Conference Proceedings of the Society for Experimental Mechanics Series

Gaëtan Kerschen *Editor*

Nonlinear Dynamics, Volume 1

Proceedings of the 33rd IMAC, A Conference and Exposition on Structural Dynamics, 2015

Springer

Conference Proceedings of the Society for Experimental Mechanics Series

Series Editor
Tom Proulx
Society for Experimental Mechanics, Inc.
Bethel, CT, USA

More information about this series at http://www.springer.com/series/8922

Gaëtan Kerschen
Editor

Nonlinear Dynamics, Volume 1

Proceedings of the 33rd IMAC, A Conference and Exposition on Structural Dynamics, 2015

Springer

Editor
Gaëtan Kerschen
Space Structures and Systems Laboratory
University of Liège
Liège, Belgium

ISSN 2191-5644 ISSN 2191-5652 (electronic)
Conference Proceedings of the Society for Experimental Mechanics Series
ISBN 978-3-319-15220-2 ISBN 978-3-319-15221-9 (eBook)
DOI 10.1007/978-3-319-15221-9

Library of Congress Control Number: 2015936670

Springer Cham Heidelberg New York Dordrecht London

Printed on acid-free paper

Springer International Publishing AG Switzerland is part of Springer Science+Business Media (www.springer.com)

Preface

Nonlinear Dynamics represents one of ten volumes of technical papers presented at the 33rd IMAC, A Conference and Exposition on Structural Dynamics, 2015, organized by the Society for Experimental Mechanics, and held in Orlando, Florida, February 2–5, 2015. The full proceedings also include volumes on Dynamics of Civil Structures; Model Validation and Uncertainty Quantification; Sensors and Instrumentation; Special Topics in Structural Dynamics; Structural Health Monitoring & Damage Detection; Experimental Techniques, Rotating Machinery & Acoustics; Shock & Vibration Aircraft/Aerospace, Energy Harvesting; and Topics in Modal Analysis.

Each collection presents early findings from experimental and computational investigations on an important area within Structural Dynamics. Nonlinearity is one of these areas.

The vast majority of real engineering structures behave nonlinearly. Therefore, it is necessary to include nonlinear effects in all the steps of the engineering design: in the experimental analysis tools (so that the nonlinear parameters can be correctly identified) and in the mathematical and numerical models of the structure (in order to run accurate simulations). In so doing, it will be possible to create a model representative of the reality which, once validated, can be used for better predictions.

Several nonlinear papers address theoretical and numerical aspects of nonlinear dynamics (covering rigorous theoretical formulations and robust computational algorithms) as well as experimental techniques and analysis methods. There are also papers dedicated to nonlinearity in practice where real-life examples of nonlinear structures will be discussed. Additionally, there are papers which discuss the results obtained by different research groups on a Round Robin exercise on nonlinear system identification.

The organizers would like to thank the authors, presenters, session organizers, and session chairs for their participation in this track.

Liège, Belgium — Gaëtan Kerschen
Nashville, TN, USA — D. Adams

Contents

Chapter 1
Interplay Between Local Frictional Contact Dynamics and Global Dynamics of a Mechanical System

M. Di Bartolomeo, F. Massi, L. Baillet, A. Culla, and A. Fregolent

Abstract Friction affects almost the entirety of the mechanical systems in relative motion. In spite of intense and long-time research activities many aspects of this phenomenon still lack of a meaningful interpretation. Some of them could be explained by not focusing only on the interface properties. In fact recent literature confirms the picture of a macroscopic frictional behaviour of a mechanical system as the outcome of a complex interaction between the local dynamics at the frictional interface (wave and rupture nucleation and propagation) and the global dynamics of the system. This paper presents the results of a 2D non-linear finite element analysis under large transformations of the onset and evolution of sliding between two isotropic elastic bodies separated by a frictional interface. The aim is to investigate the trigger of the dynamic rupture at the interface, which preludes and goes with the sliding and its interaction with the global dynamics to determine the observed macroscopic frictional behaviour (stick-slip, continuous sliding). The analysis is focused on the observed phenomena during the onset of the sliding (micro-slips, precursors, macro-slips), accounting for the frictional properties and the inertial and elastic properties of the system.

Keywords Dry friction • Stick-slip • Contact instabilities • Dynamic rupture • Body waves

1.1 Introduction

When two bodies in dry frictional contact start to move relative to each other different types of behaviour could be observed: (1) the whole interface undergoes sliding gradually, without relevant fluctuations in the frictional force, this is the case of the continuous or "smooth" sliding; (2) the system presents an unstable behaviour, characterized by strong variations of the frictional force that result in powerful vibrations transmitted to the whole system (friction-induced vibrations). This behaviour, termed as stick-slip, is related to the temporal succession of zones of the interface that start to slide and return in stick alternately; (3) the system also exhibits severe vibrations, whose origin is to be found in different types of instabilities (sprag-slip, negative friction slope, mode coupling instability, parametric resonance [1, 2]).

Friction instabilities are at the origin of very common acoustic phenomena as the creaking of door hinges, the rubbing of a shoe on the floor, the squeaking of a chalk on a board, squeal in the automotive braking system, the excitation of the violin strings by the bow (see [3] for an extensive review). Since the paper of Brace and Byerlee [4], stick-slip is also proposed as the mechanism at the origin of earthquakes, stimulating a considerable number of papers on this topic [5].

The presence of these instabilities is generally undesired. In fact the strong vibrations that they induce could bring to severe stresses acting on the system, fatigue phenomena, lack of functionality, surface damages, annoying noise etc. Issues that could affect every system/mechanism with parts in frictional contact in particular in the machine tools industry. However there are situations where, on the contrary, the stick-slip is necessary as in stringed instruments.

M. Di Bartolomeo (✉) • F. Massi
DIMA, Department of Mechanical and Aerospace Engineering,"La Sapienza" University of Rome, via Eudossiana 18, Rome 00184, Italy

LaMCoS, Contacts and Structural Mechanics Laboratory, Université de Lyon, CNRS, INSA Lyon, UMR 5259 20 rue des Sciences, F-69621 Villeurbanne, France
e-mail: mariano.dibartolomeo@uniroma1.it

L. Baillet
ISTerre, Institut des Sciences de la Terre, CNRS, Joseph Fourier University, Grenoble 1381 rue de la Piscine Domaine universitaire, St. Martin D'Heres 38400, France

A. Culla • A. Fregolent
DIMA, Department of Mechanical and Aerospace Engineering, "La Sapienz" University of Rome, via Eudossiana 18, Rome 00184, Italy

G. Kerschen (ed.), *Nonlinear Dynamics, Volume 1*, Conference Proceedings of the Society for Experimental Mechanics Series, DOI 10.1007/978-3-319-15221-9_1

Focusing our attention on the stick-slip it is often assumed that it is related to a variation of frictional resistance during sliding [6–10], resulting in a temporal succession of phases of elastic energy storage (stick phase) followed by phases of energy release (slip phase) with an associated drop of the macroscopic frictional force. In the literature, the onset of this instability was usually related to the difference between the static and the dynamic coefficient of friction, to a rate-weakening feature of the friction coefficient or to a variation of friction coefficient along the interface [11, 12]. In [13–16] it has been observed that stick-slip motion also arises in systems without such assumption, i.e. with a constant friction coefficient and no distinction between static and kinetic friction. Stick-slip in this case arises as a consequence of a dynamic instability involving the coupling between normal and tangential motion [14] or to a destabilization of the interface waves [17]. Recent works showed that the variation of frictional resistance is rather the result of both the frictional properties at the interface and the elastic and inertial properties of the system [18, 19], assuming that stick-slip configures as an interchange between the elastic energy stored into the system and its kinetic energy by means of the friction force.

This last statement places itself from the viewpoint of the recent literature which tends to consider the frictional behaviour as the result of a complex mutual interaction between the local dynamics at the frictional interface and the global dynamics of the systems rather than to be only related to the frictional characteristics of the interface [20–26].

In this new perspective the study of the local contact dynamics (wave and rupture generation and propagation) assumes a primary role. In this context in this paper the evolution of the contact forces during stick-slip instability is investigated in function of the variations of the local contact dynamics and of its relative energy flows occurring during the different phases characterizing the ruptures propagation [27].

1.2 Finite Element Model

The model (2-D, plain strain) l (Fig. 1.1) consists of two bodies kept in contact along a frictional interface by a normal force N and subjected to a relative velocity V applied at the lower boundary of the lower body. The frictional interface is governed by a classic Coulomb friction law.

Table 1.1 shows the material parameters used for the simulations. The degree of material contrast $1+\gamma = c_{S1}/c_{S2}$ [28] (c_S = shear wave speed) falls in the range of existence of the generalized Rayleigh wave (GRW) in order to account for the so called "bimaterial" effect [17, 29–33] (Table 1.2).

The simulations have been performed by the explicit dynamic finite element code PLASTD whose contact algorithm allows to calculate the mechanical quantities at the contact interface such as local contact forces, slip, velocity, contact

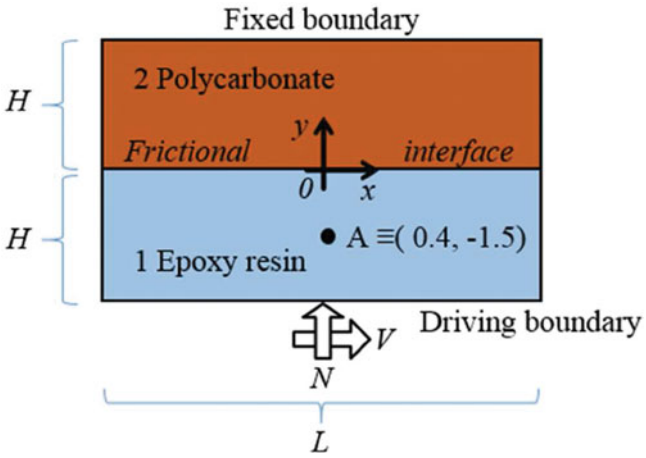

Fig. 1.1 Geometry of the 2-D bimaterial model ($H = 3$ mm $L = 10$ mm)

Table 1.1 Input data

Body	Young modulus E [GPa]	Density ρ [Kg/m^3]	Poisson ratio ν	Longitudinal wave speed c_P [m/s]	Shear wave speed c_S [m/s]	Generalized Rayleigh w. c_{GRW} [m/s]	Material contrast γ	Mass Matrix damping coeff. $\underline{\alpha}$ [s^{-1}]	Stiffness Matrix damping coeff. $\underline{\beta}$ [ms]
1.	3.9	1,300	0.33	2,100	1,062	866	0.22	40	0.5 e-6
2.	2.5	1,200	0.38	1,973	868				

Table 1.2 Simulation data

Compressive Force[a] N [N/mm]	Initial normal stress $\sigma_0 = N/L$ [MPa]	Horizontal velocity V [mm/s]	Coulomb friction coefficient μ
10	1	10	1

[a]per depth unit (2-D model)

status. This software [34] is designed for large transformations and non-linear contact behaviour; it applies an incremental Lagrange multiplier method for the contact between deformable bodies. For the dynamic study, the formulation is discretized spatially by using the finite element method and temporally by using an explicit Newmark scheme.

1.3 Results

1.3.1 Onset of the Sliding

Figure 1.2a shows the time evolution of the macroscopic (sum of the contact node components) normal and tangential contact forces at the frictional interface. At the first the normal contact force increases due to the application of the compressive force N; then the velocity V is imposed on the driving boundary (Fig. 1.1) and the tangential force increases linearly until the onset of the first sliding (time interval t_1-t_2). Afterwards the tangential force T shows irregular fluctuations in the form of a series of ramps followed by respective sudden drops, giving the typical macroscopic stick-slip pattern of Fig. 1.2 [35–38]. During the ramps the system stores elastic energy due to its deformation. When the shear contact stress locally reaches the critical value dictated by the friction law, zones of the interface switch in sliding and trigger the ruptures (in the sense of switch from local stick to slip) propagations. These ruptures can cross the whole interface, causing a global sliding and realising part of the elastic energy; the amount of released energy is proportional to the force drop at the end of every ramp.

Figure 1.3a shows the seismic profile (local slip velocity at the interface along the time) and the respective contact status along the contact surface during the time period of the force ramp delimited by the two vertical dashed lines at $t_1 = 0.725$ ms and $t_2 = 0.755$ ms in Fig. 1.2b. The colour on every seismic line represents the local status (sticking or sliding) of the contact at the interface. The area covered by every line shows the tangential local velocity of the upper side of the contact interface (that is the lower boundary of the body n° 2); the black (yellow) colour of the area indicates that the point is moving in x-negative (x-positive) direction. This graph can be considered as representative of what happens at the interface during each ramp shown in Fig. 1.2.

In macroscopic stick-slip behaviour the interface phenomena occurring during the slipping (drop of the tangential force), can be divided into three characteristic distinct phases:

1. At approximately 0.7255 ms, micro-slips (slip confined to a reduced contact zone [25]) start to appear at the interface. Each micro-slip behaves as a single nucleated rupture and radiates different types of waves along the interface and inside the bodies [26]. For a longer time ($0.7255 \div 0.732$ ms) the micro-slips coalesce with each other to form a sliding zone of about L/4 in length. Due to the energy continuously provided by the displacement of the lower body, this zone grows in width ($0.732 \div 0.735$ ms) with a sliding propagation speed of about 100 mm/s toward the left and 400 mm/s toward the right. The behaviour of the rupture propagation recovered in this first phase is consistent with the phase of propagation of the "slow front" experimentally observed in [39] and with the "stable rupture front" of [40].
2. When a sufficient number of micro-slips switches to sliding at nearly the same time they can release enough energy to sustain short range slip pulse rupture propagation (the so-called precursors); for example the supershear ruptures PR1 and PR2 in Fig. 1.3a (propagating rightwards at 1,800 m/s) [25]. As time increases, an increasing number of precursors are triggered and their distance of propagation increases, in agreement with what has been experimentally observed in [40].
3. The propagation distance of the precursors increases until the main slip event the macro-slip is triggered in the form of an extensive crack-like supershear rupture propagating rightwards (SSR 3 in Fig. 1.3a) with speed c_{rup} 1,800 m/s. As macro-slip is intended a slip that involves a large part of the interface and a relative displacement between the two bodies. At the same time a leftwards rupture front (GRR 4), again crack-like, propagates at about the GRW speed (866 m/s).

The passage of these two crack-like fronts releases most of the elastic energy and the whole interface switches to sliding state. The remaining elastic energy is discharged by subsequent pulse-like supershear ruptures (SSR 5, SSR 6). In this phase the ruptures cause local slipping with velocity an order of magnitude greater (103 mm/s) than the previous one, as can be inferred by the greater amplitude of the seismic profile oscillations. The waves generated at the interface propagate inside the two bodies as well, reaching the boundaries of the system, and are reflected exciting the dynamics of the whole system

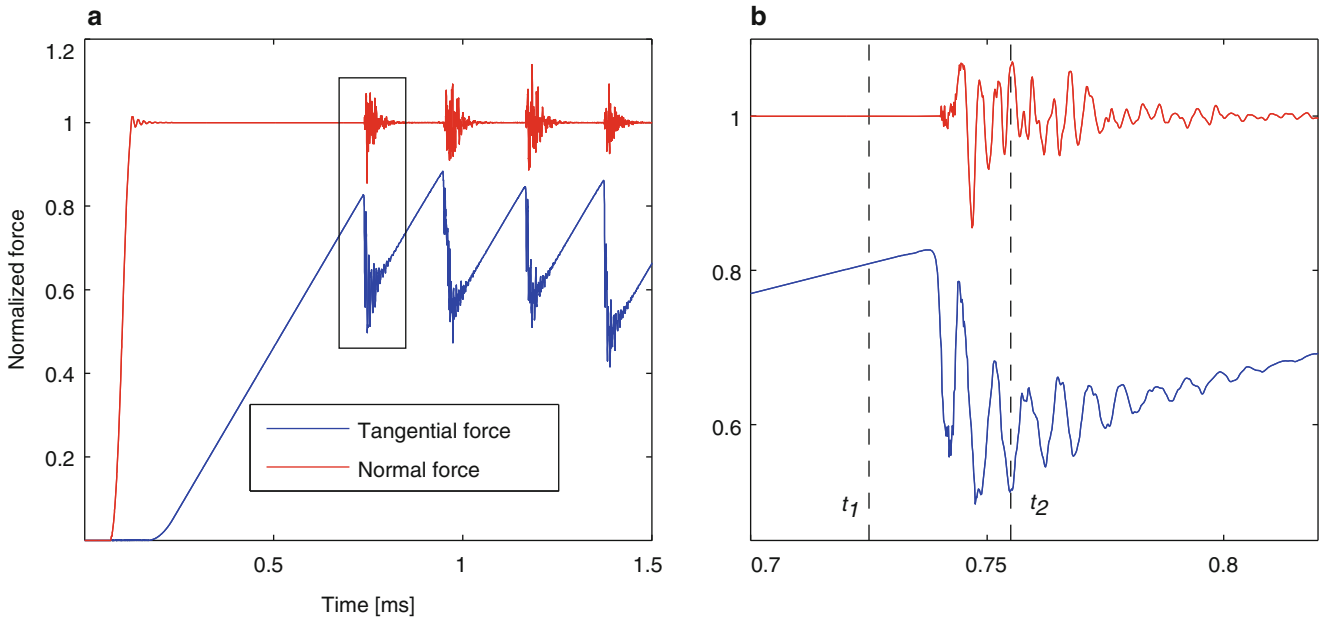

Fig. 1.2 (**a**) Time evolution of the sum of the contact forces (normalized to the compressive force N); (**b**) detail around t_1-t_2

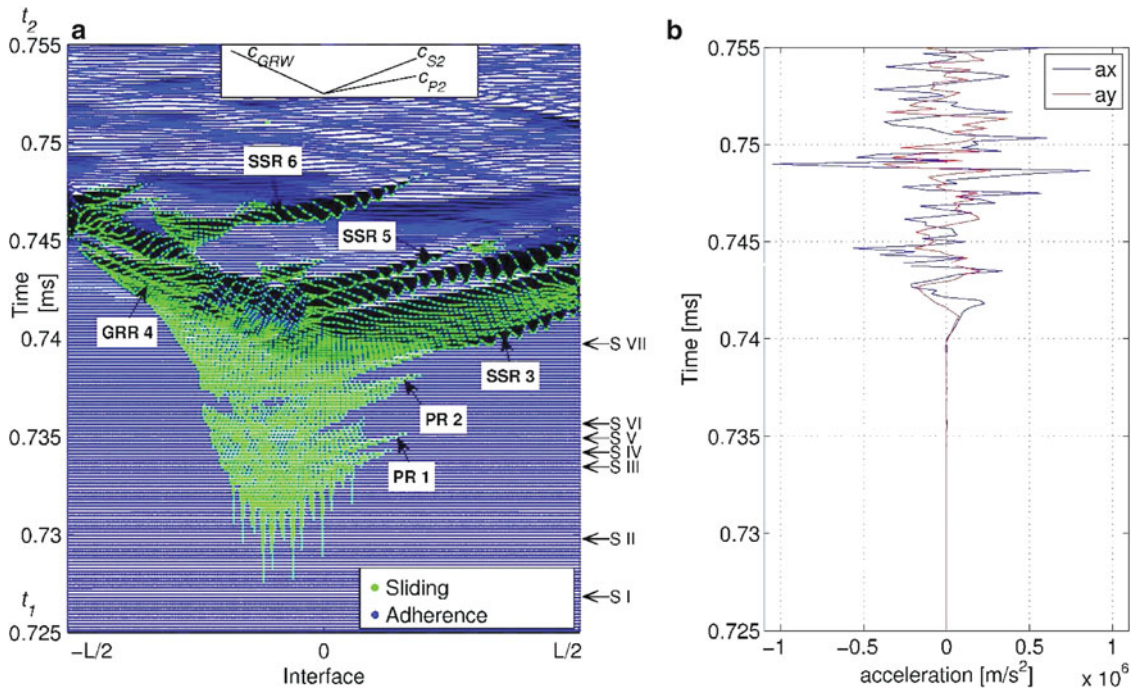

Fig. 1.3 (**a**) Seismic profile and contact status between 0.725 ÷ 0.755 ms (*dashed lines* of Fig. 1.2) *blue spots* = adherence, *green spots* = sliding, (*at the top*) directions of the wave speeds of the *upper body*, (*on the right*) stop times; (**b**) Acceleration of the point A (Fig. 1.1) during the same time interval

(friction induced vibrations). In Fig. 1.3b is reported the time evolution of the acceleration of the point A during the same interval (Fig. 1.1), it can be noted the time delay in the signal due to the distance of the point A from the interface.

After the main crack ruptures ($>t = 0.7455$ ms in Fig. 1.3a), the whole interface returns to the sticking state. Waves still cross the interface due to the reflections of the rupture fronts at the interface boundaries (and to the reflections of the body waves at the system boundaries) as can be noted by the oscillations in the seismic profile. Nevertheless their magnitude cannot trigger sliding (there are no light-grey zones on the seismic lines) and the system returns to a quasi-static evolution during which it stores the elastic energy provided by the velocity imposed to the lower body.

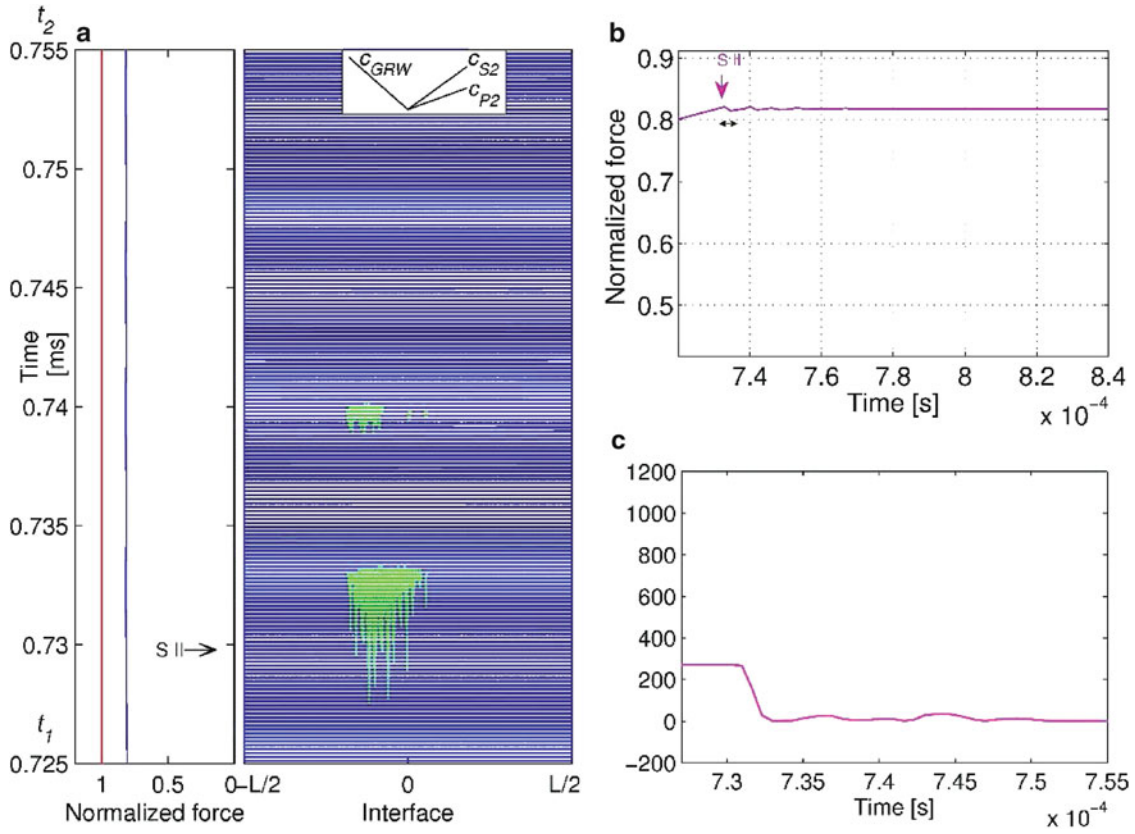

Fig. 1.4 (**a**) Seismic profile for S II (**b**) Tangential force (**c**) Seismic energy

The presented analysis shows how each phase of the stick-slip macroscopic friction behaviour can be associated with the local dynamics (wave and rupture generation) at the contact.

1.3.2 Phases Stability Analysis

In order to investigate deeply the role of each phase (microslips, precursors) in triggering the macroslip, it should be possible to isolate and individually analyse each phase. To approach this condition, the relative motion of the two bodies has been "stopped" after each phase. This allows to investigate the energy flows during each phase, and to determine if that phase could be consider "stable" or "instable" with regard to the following macroslip activation.

In particular as "stable" is intended a phase after which, if the system is stopped, the interface remains in quiet; conversely an "instable" phase means that after it the system undergoes macroslip, even if the system is stopped. A sequence of simulations have been performed and differ each other for the time, t_{stop}, at which the motion has been stopped. Figure 1.3a reports, on the right, the different stop times (SI = 0.7269e-3s, SII = 0.7299e-3, SIII = 0.7329e-3s, SIV = 0.7339e-3s, SV = 0.7350e-3s, SVI =0.7359e-3s, SVII = 0.7389e-3) used for the different simulations (S1, S2, S3, etc.). In the following by S.A. is indicated the whole simulation, without stop.

A particular attention has been placed on the modality to stop the motion between the two bodies. The interruption of the motion should take place in a time interval shorter than the time scale that characterize the different phases. Obviously the only action of reduce or stop the relative motion could affect the contact dynamics, due to the inertia forces that arise and that are inversely proportional to the applied deceleration. Reducing the braking interval Δt_b, the inertial forces increase, increasing Δt_b the inertial forces decrease but at the same time the breaking interval could cover different phases, making impossible to isolate the different effects. This fact make difficult, even impossible, to realize this type of experience in an experimental set-up, because the dynamics at the interface, during a single macroslip, is too fast compared to the possible rates of change of the macroscopic boundary conditions. The "braking" time used $\Delta t_b = 1.67$e-6s (represented in Figs. 1.4c, 1.5c, 1.6c, and 1.7c by the double arrow).

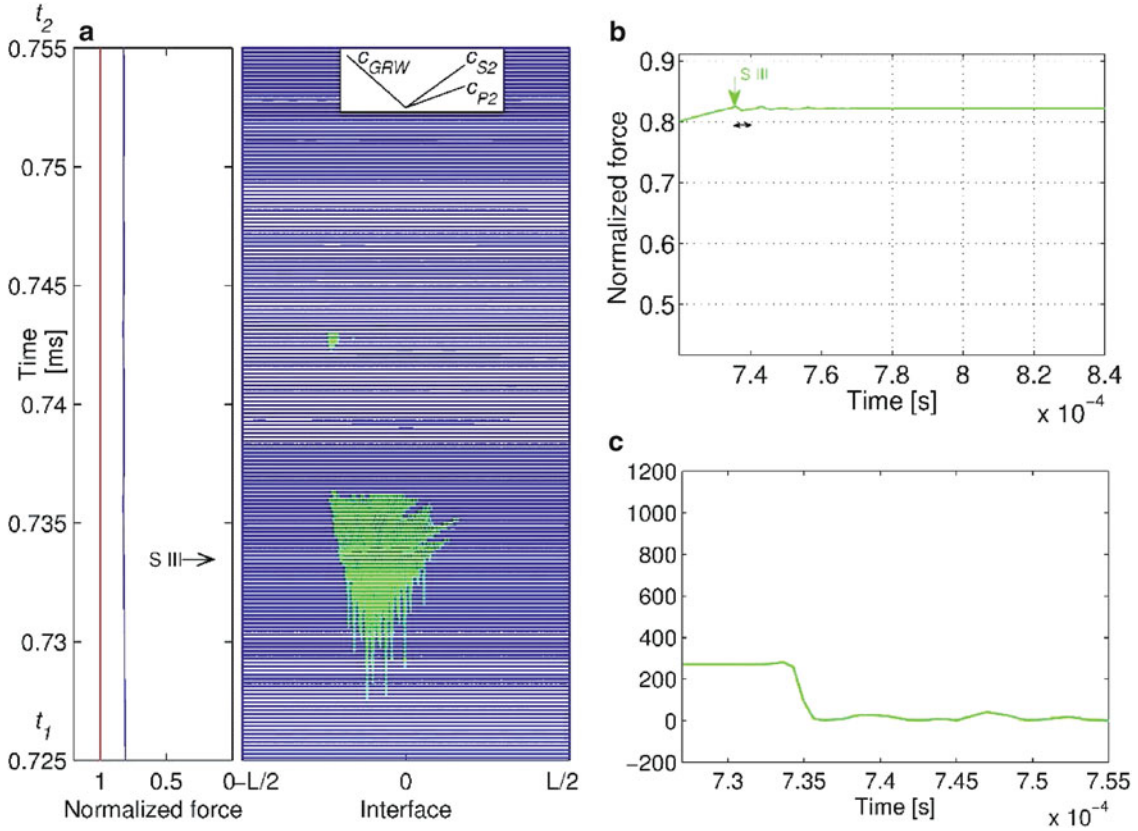

Fig. 1.5 (**a**) Seismic profile for S III (**b**) Tangential force (**c**) Seismic energy

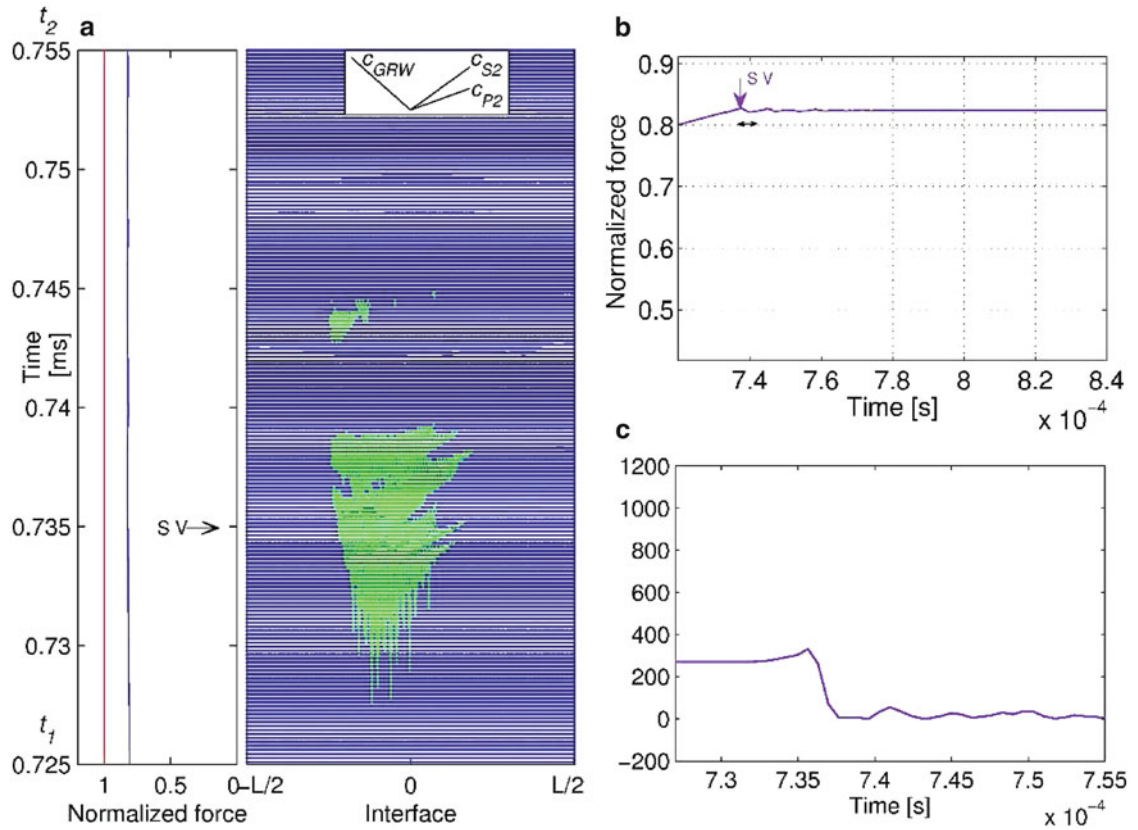

Fig. 1.6 (**a**) Seismic profile for S V (**b**) Tangential force (**c**) Seismic energy

The results have shown that are simulations that do not undergo macroslip (SI, SII, SIII, SIV and SV) and other where the macroslip occurs (SVI, SVII).

For example Fig. 1.4 shows the seismic profile (Fig. 1.4a), and the tangential force (Fig. 1.4b) for the simulation SII. It can be noted as the tangential force remains at about the same level reached at the instant of arrest. Figure 1.4c represents the seismic energy.

From the seismic profile it can be observed as during the braking interval Δt_b (black bracket) isolated microslips arise and extend their activity even after the body stops, until the interface return all in sticking state. This delay is related to the time necessary to the deceleration, applied to the lower boundary. Moreover, during the braking time the two bodies still undergo the effect of inertial forces, which active smooth oscillations following predominantly the first mode of vibration along the x direction. As can be seen in Fig. 1.4, they cause a further nucleation of microslips around 0.74 ms, i.e. after 0.06e-3s, which is consistent with the semi-period of the first mode of vibration of the system.

The seismic energy is strongly related to energy released during every events (microslips, ruptures). A definition, used mainly in the geophysics field [41], is:

$$E_{s,A} = \int_{t_1}^{t_2} v(t)^2 \, dt \tag{1.1}$$

The integral is referred to a generic point A of the solids in contact and measure the energy that arrives at the point A during the evolution of the sliding at the interface; similar to experimental geophysics where detectors measure the waves generated by earthquakes, this quantity could be measured experimentally on dedicated set-up to validate the numerical results. Even if this parameter is not an energy, missing a mass term, however it is directly related and proportional to the energy released and allows to easily examine the contribute of the different zones of the interface to the whole energy release.

It can be observed as the microslips do not give detectable signals on point A (Fig. 1.4a).

In the next SIII simulation (Fig. 1.5), the first precursors appear (PR1 in Fig. 1.3). Nevertheless, as can be observed in the figure, this rupture have not still enough magnitude to activate the macroslip. It can be also noted that also the precursor do not give detectable signals on point A (Fig. 1.5c); in fact their wave field propagating in the bulk material are quickly suppressed by the internal damping.

In the simulation SV (Fig. 1.6), other precursors appear (e.g. PR 2 in Fig. 1.3), but also in this case, these rupture do not trigger the macroslip.

To obtain the macroslip it is needed to keep the imposed relative motion until the nucleation of the main ruptures, i.e. the ruptures that cross the whole interface (Fig. 1.7), as indicated by the drop in the tangential force (Fig. 1.7b).

The seismic energy (Fig. 1.7c) shows clearly the arrival of the wave fields generated by the different ruptures at the interface (ref. Fig. 1.3). The first wave field is that relative to the propagation of the rupture SSR 3, which is also the most energetic, followed by the one corresponding to the rupture SSR 5. After that, the wave field corresponding to the rupture (GRR 4) can be noted, which is lower in magnitude due to the strong localization of the rupture 4 on the left of the interface, farther from the point A.

In Fig. 1.8 is reported the simulation unstopped (SA), it can be observed the greated magnitude of the seismic energy (Fig. 1.8c). It is interesting to note that once these ruptures nucleate, they evolve independently by the fact that the system is stopped as it can be inferred from the Fig. 1.8. That means that the energy necessary to feed them is already stored in the system and released independently from the system boundary conditions.

This preliminary analysis suggests that the system, even after the appearance of the precursors, behaves as stable (in the meaning specified above), and the macroslip is not activated by the precursor propagation. Thus, they release only the amount of energy necessary for their own propagation, up to being extinguished, and seem to be not correlated with the subsequently macroslip.

Comparing all the seismic profiles in Figs. 1.4–1.7, and 1.8, it can be observed that all the zones in sliding appear superimposable (where they exist), except for the replies of microslips due to system oscillation.

The onset and evolution of the sliding seems to follow the same pattern, and seems to be not essentially affected by the stop operation. Of course, in reality the evolution of the rupture propagation will be necessarily affected by the macroscopic dynamic response due to the inertia forces, which could trigger further ruptures after the stop. As seen before these are strongly related to the magnitude of the deceleration.

It can be inferred that the action of the imposed motion just around the onset of the sliding is limited to activate ruptures whose dynamics is led by previously stored energy. This is due to the fact that the dynamics of the ruptures evolves at time scales that are much shorter than the energy loading rate due to the imposed motion at the boundaries; consequently, the whole energy stored into the system during the time interval of Fig. 1.3 ($0.725 \div 0.755$ ms) is at least one order of magnitude much lower that the energy released during the ruptures, which is stored during the whole loading ramp (Fig. 1.2).

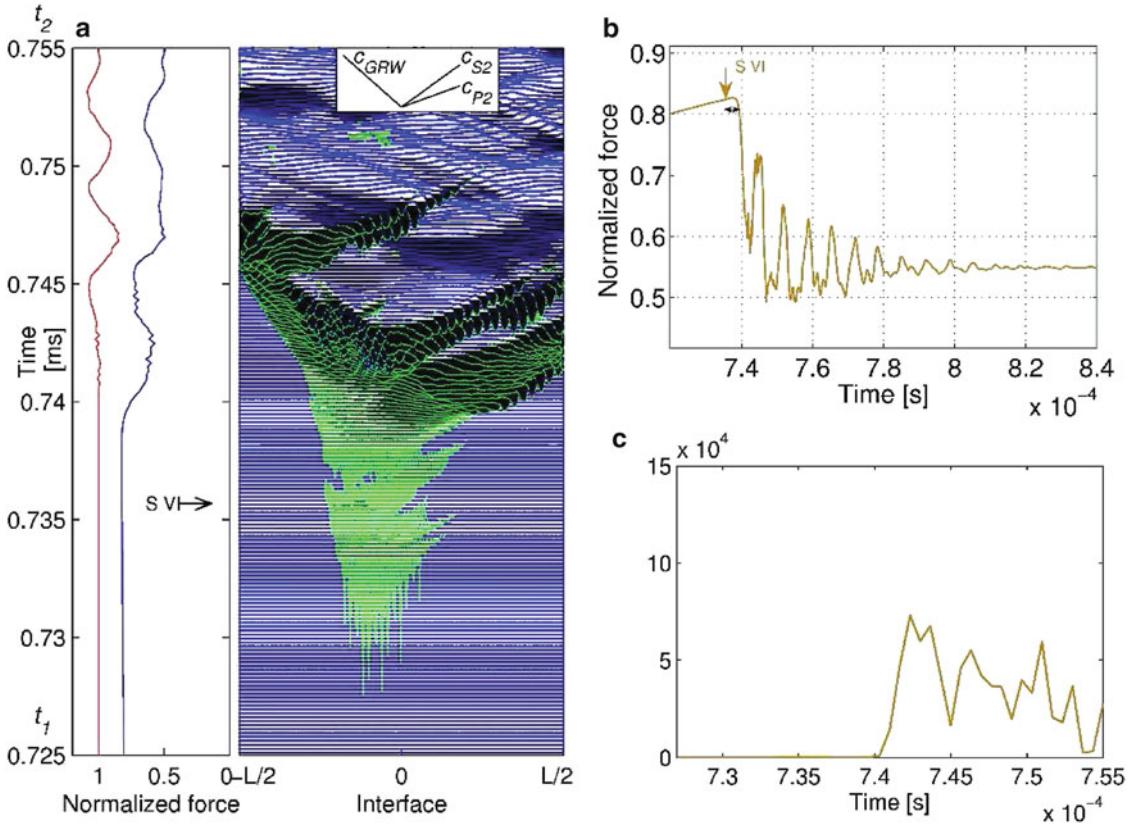

Fig. 1.7 (**a**) Seismic profile for S VI (**b**) Tangential force (**c**) Seismic energy

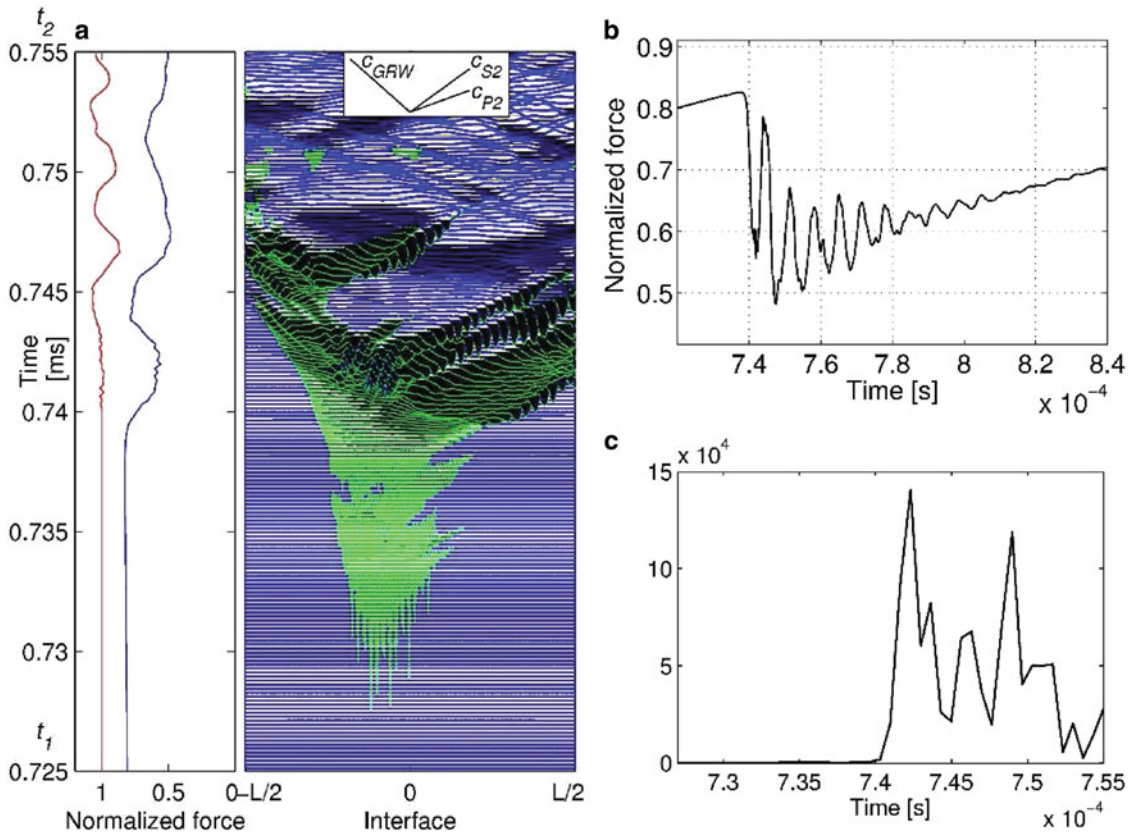

Fig. 1.8 (**a**) Seismic profile for S A (**b**) Tangential force (**c**) Seismic energy

1.4 Conclusions

In this paper the interaction between the local contact rupture dynamics and macroscopic frictional is investigated.

The macroscopic stick-slip evolution is described as a sequence of local contact phenomena: the occurrence of micro-slips is followed by the precursors, up to the macro-slip phase that brakes the whole surface and releases most of the elastic energy of the system. These results are in agreement with recent experimental observations [41, 42].

The microslips and the precursors seem to behave as stable phases with respect to the macroslip; in fact they provide only the amount of energy needed for their propagation but are not able to trigger the macroslip.

The imposed motion just around the onset of the sliding is limited to activate ruptures whose dynamics is led by previously stored energy. This is due to the fact that the dynamics of the ruptures (micro-slips, rupture and wave propagation) evolves at time scales that are much shorter than the energy loading rate due to the imposed motion;

References

1. Tonazzi D (2014) Macroscopic frictional contact scenarios and local contact dynamics: at the origins of “macroscopic stick-slip”, mode coupling instabilities and stable continuous sliding. Ph.D. thesis, University of Rome La Sapienza
2. Tonazzi D, Massi F, Culla A, Baillet L, Fregolent A, Berthier Y (2013) Instability scenarios between elastic media under frictional contact. Mech Syst Signal Process 40(2):754–766
3. Akay A (2002) Acoustics of friction. J Acoust Soc Am 111:1525
4. Brace WF, Byerlee JD (1966) Stick-slip as a mechanism for earthquakes. Science 153:990
5. Scholz CH (2002) The mechanics of earthquakes and faulting. Cambridge University Press, New York
6. Braun OM, Barel I, Urbakh M (2009) Dynamics of transition from static to kinetic friction. Phys Rev Lett 103:194301
7. Capozza R, Urbakh M (2012) Static friction and the dynamics of interfacial rupture. Phys Rev B 86:085430
8. Heslot F, Baumberger T, Perrin B (1994) Creep, stick-slip and dry-friction dynamics: experiments and a heuristic model. Phys Rev E 49:4973
9. Robbins MO, Thompson PA (1991) Critical velocity of stick-slip motion. Science 253:916
10. Trømborg J, Scheibert J, Amundsen DS, Thøgersen K, Malthe-Sørenssen A (2011) Transition from static to kinetic friction: insights from a 2D model. Phys Rev Lett 107:074301
11. Kammer DS, Yastrebov VA, Spijker P, Molinari JF (2012) On the propagation of slip fronts at frictional interfaces. Tribol Lett 48:27–32
12. Popp K, Shelter P (1990) Stick-slip vibrations and chaos. Philos Trans R Soc Lond A 332:89
13. Oden JT, Martins JAC (1985) Models and computational methods for dynamic friction phenomena. Comput Methods Appl Mech Eng 52:527
14. Martins JAC, Oden JT, Simoes FM (1990) A study of static and kinetic friction. Int J Eng Sci 28:29–92
15. Wikie B, Hill JM (2000) Stick-slip motion for two coupled masses with side friction. Int J Non-Linear Mech 35:953
16. Wensrich C (2006) Slip–stick motion in harmonic oscillator chains subject to Coulomb friction. Tribol Int 39:490
17. Adams GG (1995) Self-excited oscillations of two elastic half-spaces sliding with constant coefficient of friction. J Appl Mech 62:867
18. Persson BNJ, Popov VL (2000) On the origin of transition from slip to stick. Solid State Commun 114:261
19. Luan B, Robbins MO (2004) Effect of inertia and elasticity on stick-slip motion. Phys Rev Lett 93:036105
20. Baillet L, Link V, D’Errico S, Laulagnet B, Berthier Y (2005) Finite element simulation of dynamic instabilities in frictional sliding contact. J Tribol 127:652
21. Meziane A, D’Errico S, Baillet L, Laulangnet B (2007) Instabilities generated by friction in a pad-disc system during the braking process. Tribol Int 40:1127
22. Massi F, Berthier Y, Baillet L (2008) Contact surface topography and system dynamics of brake squeal. Wear 265:1784
23. Massi F, Rocchi J, Culla A, Berthier Y (2010) Coupling system dynamics and contact behaviour: modelling bearings subjected to environmental induced vibrations and ‘false Brinelling’ degradation. Mech Syst Signal Process 24:1068
24. Renouf M, Massi F, Saulot A, Fillot N (2011) Numerical tribology of dry contact. Tribol Int 44(7–8):834–844
25. Di Bartolomeo M, Massi F, Baillet L, Culla A, Fregolent A, Berthier Y (2012) Wave and rupture propagation at frictional bimaterial sliding interfaces: from local to global dynamics, from stick-slip to continuous sliding. Tribol Int 52:117
26. Di Bartolomeo M, Meziane A, Massi F, Baillet L, Fregolent A (2010) Dynamic rupture at a frictional interface between dissimilar materials with asperities. Tribol Int 43:1620
27. Bar-Sinai Y, Spatschek R, Brener EA, Bouchbinder E (2013) Instabilities at frictional interfaces: creep patches, nucleation, and rupture fronts. Phys Rev E 88:060403
28. Shi Z, Ben-Zion Y (2006) Dynamic rupture on a bimaterial interface governed by slip-weakening friction. Geophys J Int 165:469
29. Weertman J (1980) Unstable slippage across a fault separates elastic media of different elastic constant. J Geophys Res 85:1455
30. Ranjith K, Rice JR (2001) Slip dynamics at an interface between dissimilar materials. J Mech Phys Solids 49:341
31. Ben-Zion Y (2001) Dynamic ruptures in recent models of earthquake faults. J Mech Phys Solids 49:2209
32. Langer S, Weatherley D, Olsen-Kettle L, Finzi Y (2012) Stress heterogeneities in earthquake rupture experiments with material contrasts. J Mech Phys Solids. doi:10.1016/j.jmps.2012.11.002
33. Baillet L, Sassi T (2002) Finite element method with Lagrange multipliers for contact problems with friction. CR Mec 334:917
34. Ozaki S, Inanobe C, Nakano K (2014) Finite element analysis of precursors to macroscopic stick-slip motion in elastic materials: analysis of friction test as a boundary value problem. Tribol Lett 55:151–163

35. Prevost A, Scheibert J, Debrégeas G (2013) Probing the micromechanics of a multi-contact interface at the onset of frictional sliding. Eur Phys J E 36, 17
36. Radiguet M, Kammer DS, Gillet P, Molinari JF (2013) Survival of heterogeneous stress distributions created by precursory slip at frictional interfaces. Phys Rev Lett 111:164302
37. Svetlizky I, Fineberg J (2014) Classical shear cracks drive the onset of dry frictional motion. Nature 509:205–208
38. Trømborg J, Sveinsson HA, Scheibert J, Thøgersen K, Amundsen DS, Malthe-Sørenssen A (2014) Slow slip and the transition from fast to slow fronts in the rupture of frictional interfaces. PNAS. doi: 10.1073/pnas.1321752111
39. Ben-David O, Fineberg J (2011) Static friction coefficient is not a material constant. Phys Rev Lett 106:254301
40. Nielsen S, Taddeucci J, Vinciguerra S (2010) Experimental observation of stick-slip instability fronts. Geophys J Int 180:697
41. Occhiena C, Coviello V, Arattano M, Chiarle M, Morra Di Cella U, Pirulli M, Pogliotti P, Scavia C (2012) Analysis of microseismic signals and temperature recordings for rock slope stability investigations in high mountain areas. Nat Hazards Earth Syst Sci 12:2283–2298
42. Rubinstein SM, Cohen G, Fineberg J (2007) Dynamics of precursors to frictional sliding. Phys Rev Lett 98:226103

Chapter 2
Non-linear Dynamics of Jointed Systems Under Dry Friction Forces

Silvio Giuseppe Neglia, Antonio Culla, and Annalisa Fregolent

Abstract Dry friction devices are usually adopted to reduce structure vibrations. Generally, an optimisation procedure is required to tune the system coefficients by performing the best effect. In this paper a continuous structure coupled with a lumped dissipative system is studied. This second system is alternatively loaded by a dry friction force, so that two states can be recognized: contact and not-contact. Aim of this work is the study of the system parameters influence on the structure response when the system passes through the different states before presented. In particular, during the contact state a stick-slip motion of the lumped system is considered. The analysis is focused on the transition between chaotic and non-chaotic behaviour and on the correspondent power flows between continuous and lumped system during the motion.

Keywords Non linear dynamics • Jointed systems • Stick-slip • Bifurcation diagrams • Maximum Lyapunov exponent

2.1 Introduction

Aim of this paper is to present some results concerning the nonlinear coupling of a continuous mechanical system and a lumped one. The nonlinearity is due to a friction force between the mass of the lumped system and a moving belt.

The motion of the system is composed of a sequence of stick and slip phases: during the stick phase the relative velocity of the mass in contact with the belt is null, on the contrary during the slip phase the relative velocity controls the friction force.

In the past many works investigated this phenomenon, because in the field of applied sciences the phenomenon of friction and in particular stick-slip systems are very interesting [1–3].

In this paper a parametric analysis varying the belt velocity is performed by considering some indicators (bifurcation diagrams and Lyapunov exponents, see [3–5]). The nature of the system response is investigated in order to understand if the system exhibits a chaotic motion.

The study is also focused on the power flows between the jointed systems.

2.2 Mechanical Model

The system shown in Fig. 2.1 is made up of a continuous beam and an harmonic oscillator with two degrees of freedom driven by a belt, the belt has a constant speed v_{dr}. The two systems are linked to each other via a spring k_1.

During its motion, the mass m can have two different behaviours: it can be attached to the belt (stick motion) and moves with it, or slide on the belt (slip motion). A non constant contact force is considered through a stiffness k_3 between mass and belt along $x(t)$.

In the following, the motion equations of the global system are derived.

S.G. Neglia (✉) • A. Culla • A. Fregolent
Dipartimento di Ingegneria Meccanica e Aerospaziale, Università di Roma La Sapienza, Via Eudossiana 18, 00184 Rome, Italy
e-mail: silvio.neglia@uniroma1.it

G. Kerschen (ed.), *Nonlinear Dynamics, Volume 1*, Conference Proceedings of the Society for Experimental Mechanics Series, DOI 10.1007/978-3-319-15221-9_2

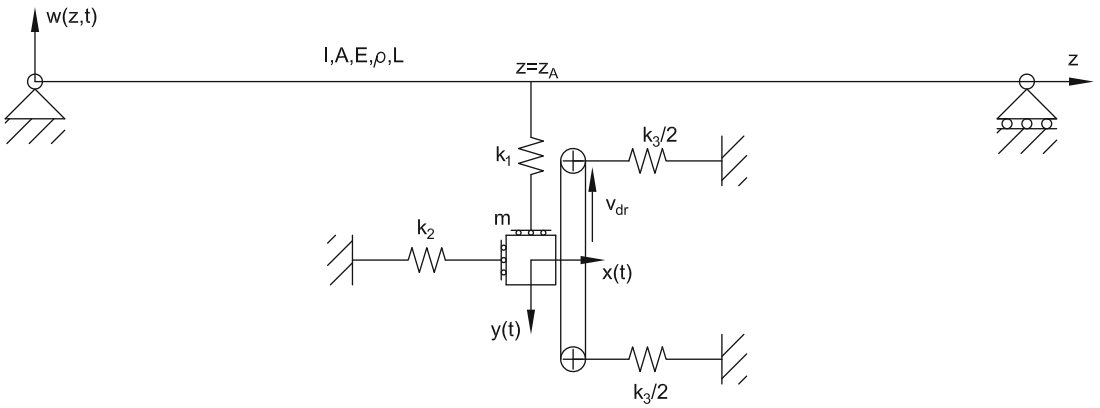

Fig. 2.1 Mechanical system

2.2.1 Dimensional Motion Equations

The continuous system is modelled using the Euler-Bernoulli theory of beam, its motion equation is expressed by the following equation:

$$EI\frac{\partial^4 w(z,t)}{\partial z^4}+\rho A\frac{\partial^2 w(z,t)}{\partial t^2}=k_1\left[y(t)-w(z,t)\right]\delta(z-z_A) \tag{2.1}$$

The beam has length L, Young modulus E, moment of inertia of area I, mass density ρ and a cross section area A.

The Dirac delta $\delta(z-z_A)$ allows to consider the influence of the harmonic oscillator in the link point $z=z_A$.

The harmonic oscillator is modelled with two degrees of freedom: $x(t)$ and $y(t)$.

Along the $x(t)$ direction the motion can be influenced of the non continuous contact between mass and belt.

There is mass-belt contact if $x(t)>0$. In this case a contact force, $N(t)$, rises and it is equal to:

$$N(t)=k_3x(t) \tag{2.2}$$

On the other hand, if there is no mass-belt contact, the normal force is $N(t)=0$.

The equation of motion along $x(t)$ is:

$$m\ddot{x}(t)+k_2x(t)+N(t)=0 \tag{2.3}$$

Along the $y(t)$ direction the stick-slip condition must be taken into account.

There is stick motion on the mass m if all the external forces acting on it are bounded in absolute value by the static friction force $T_s(t)=\mu_sN(t)$, moreover the mass velocity $\dot{y}(t)$ must be equal to the belt speed v_{dr}.

In mathematical terms the stick condition is expressed by:

$$|k_1\left[y(t)-w(z_A,t)\right]|<\mu_sN(t) \text{ and } \dot{y}(t)=v_{dr} \tag{2.4}$$

The stick motion equation is the following:

$$m\ddot{y}(t)=0 \tag{2.5}$$

The initial condition for Eq. (2.5) are:

$$\begin{cases} y(t)|_{t=0}=0 \\ \dot{y}(t)|_{t=0}=v_{dr} \end{cases} \tag{2.6}$$

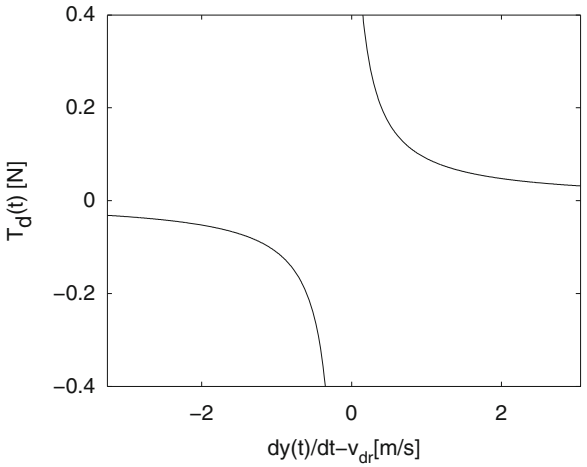

Fig. 2.2 Dynamical friction force

If the stick condition [Eq. (2.4)] is not verified, there is sliding between the mass and the belt and a dynamic friction force $T_d(t)$ rises. The slip equation of motion is:

$$m\ddot{y}(t) + k_1 \left[y(t) - w(z_A, t)\right] = T_d(t) \tag{2.7}$$

where the non linear dynamical friction force $T_d(t)$ is expressed by:

$$T_d(t) = -\frac{\mu_s N(t)}{1 + \gamma \left[\dot{y}(t) - v_{dr}\right]} \mathrm{sgn}\left[\dot{y}(t) - v_{\mathrm{dr}}\right] \tag{2.8}$$

In Fig. 2.2 the dynamic friction force plot is shown, the γ parameter represents the slope of the curve and its dimension is the inverse of the velocity.

2.2.2 Dimensionless Motion Equations

In order to generalize the problem, the general motion equation are written in a dimensionless form.

According to the Buckingham π theorem, the dimensional variables are the following:

$$\begin{cases} \alpha_1 = EI \\ \alpha_2 = L \\ \alpha_3 = \rho A \end{cases} \tag{2.9}$$

The dimensionless constants $(\cdot)^*$ are the following:

$$\begin{aligned} t^* &= t\alpha_1^{1/2}\alpha_2^{-2}\alpha_3^{-1/2} & y^*(t^*) &= y(t)\alpha_2^{-1} \\ k_1^* &= k_1\alpha_1^{-1}\alpha_2^3 & w^*(z^*, t^*) &= w(z, t)\alpha_2^{-1} \\ k_2^* &= k_2\alpha_1^{-1}\alpha_2^3 & \delta^*(z^* - z_A^*) &= \delta(z - z_A)\alpha_2 \\ k_3^* &= k_3\alpha_1^{-1}\alpha_2^3 & T_d^*(t^*) &= T_d(t)\alpha_1^{-1}\alpha_2^2 \\ m^* &= m\alpha_2^{-1}\alpha_3^{-1} & v_{dr}^* &= v_{dr}\alpha_1^{-1/2}\alpha_2\alpha_3^{1/2} \\ x^*(t^*) &= x(t)\alpha_2^{-1} & \gamma^* &= \gamma\alpha_1^{1/2}\alpha_2^{-1}\alpha_3^{-1/2} \end{aligned}$$

Substituting the dimensionless constants in Eq. (2.1), the beam dimensionless equations is obtained:

$$\frac{\partial^4 w^*(z^*,t^*)}{\partial z^{*4}} + \frac{\partial^2 w^*(z^*,t^*)}{\partial t^{*2}} = k_2^* \left[y^*(t^*) - w^*(z^*,t^*)\right] \delta^*(z^* - z_A^*) \tag{2.10}$$

The same procedure of the beam is applied to the harmonic oscillator.

Along $x^*(t^*)$ the motion equation is:

$$m^* \ddot{x}^*(t^*) + k_2^* x^*(t^*) + N^*(t^*) = 0 \tag{2.11}$$

where the mass-belt contact force is:

$$\begin{cases} N^*(t^*) = k_3^* x^*(t^*) & \text{if } x^*(t^*) > 0 \\ N^*(t^*) = 0 & \text{else} \end{cases} \tag{2.12}$$

Along $y^*(t^*)$, the motion equation of the harmonic oscillator is:

$$m^* \ddot{y}^*(t^*) = K(t^*) \tag{2.13}$$

where $K(t^*)$ is the force due to the following stick-slip condition:

$$\left|k_1^* \left[y^*(t^*) - w^*(z_A^*, t^*)\right]\right| < \mu_s N^*(t^*) \text{ and } \dot{y}^*(t^*) = v_{dr}^* \tag{2.14}$$

the force $K(t^*)$ is expressed by:

$$\begin{cases} K(t^*) = 0 & \text{(stick)} \\ K(t^*) = -k_1^* \left[y^*(t^*) - w^*(z_A^*, t^*)\right] + T_d^*(t^*) & \text{(slip)} \end{cases} \tag{2.15}$$

where the dimensionless dynamic friction force $T_d^*(t^*)$ is:

$$T_d^*(t^*) = -\frac{\mu_s N^*(t^*)}{1 + \gamma^* \left[\dot{y}^*(t^*) - v_{dr}^*\right]} \mathrm{sgn}\left[\dot{\mathrm{y}}^*(\mathrm{t}^*) - v_{\mathrm{dr}}^*\right] \tag{2.16}$$

2.2.3 Solution Method

Applying the Bubnov-Galerkin method and using the eigenfunction of the simply supported beam, it is possible to write:

$$w^*(z^*,t^*) = \sum_{i=1}^{N} \phi_i^*(z^*) q_i^*(t^*) \tag{2.17}$$

where the eigenfunctions $\phi_i^*(z^*)$ are expressed by:

$$\phi_i^*(z^*) = \sin(i\pi z^*) \tag{2.18}$$

and the beam eigenvalues are:

$$\omega_i^* = i^2 \pi^2 \tag{2.19}$$

Projecting the motion equation on a different eigenfunction basis $\phi_j^*(z^*)$, integrating on the domain and adopting the following orthonormalization conditions:

$$\begin{cases} \sum_{i=1}^{N} \int_0^1 \phi_j^*(z^*)\phi_i^{*IV}(z^*)dz^* = \omega_i^{*2}\delta_{ij} \\ \sum_{i=1}^{N} \int_0^1 \phi_j^*(z^*)\phi_i^*(z^*)dz^* = \delta_{ij} \end{cases} \tag{2.20}$$

the following N ordinary differential equations are obtained:

$$\ddot{q}_j^*(t^*) + \left[\omega_j^{*2} + k_2^*\phi_j^{*2}(z_A^*)\right] q_j^*(t^*) = k_2^* y^*(t^*)\phi_j^*(z_A^*) \quad j = 1, 2, \ldots, N \tag{2.21}$$

With the modal basis expansion expressed in Eq. (2.17) the stick condition becomes:

$$\left| k_1^* \left[y^*(t^*) - \sum_{i=1}^{N} \phi_i^*(z_A^*) q_i^*(t^*) \right] \right| < \mu_s N^*(t^*) \text{ and } \dot{y}^*(t^*) = v_{dr}^* \tag{2.22}$$

and the force $K(t^*)$:

$$\begin{cases} K(t^*) = 0 & \text{(stick)} \\ K(t^*) = -k_1^* \left[y^*(t^*) - \sum_{i=1}^{N} \phi_i^*(z_A^*) q_i^*(t^*) \right] + T_d^*(t^*) & \text{(slip)} \end{cases} \tag{2.23}$$

2.3 Results

In this section the most relevant results for the system studied are shown.

Different simulations were done in order to evaluate the sensitivity of the system solution to the variation of the belt velocity.

In Table 2.1 the dimensionless parameters used for the simulation are shown.

It is important to advance a consideration about the magnitude of the belt velocity. For small values of the velocity the system usually shows a continuous switching motion from stick to slip, while for big values of the velocity there will be an initial stick before a complete slip behavior for the whole simulation.

Therefore, the velocity range is selected in order to have the system in stick-slip motion (see Table 2.1).

2.3.1 Bifurcation Diagrams

In order to calculate the bifurcation diagram for every Lagrangian coordinates, the procedure based on the Poincaré map is used. The Lagrangian coordinates are:

$$\begin{cases} \mathcal{L}_1 = x^*(t^*) \\ \mathcal{L}_2 = y^*(t^*) \\ \mathcal{L}_3 = w^*(z_A^*, t^*) \end{cases} \tag{2.24}$$

Table 2.1 Model parameters

Variable	Value
k_1^*	1,000
k_2^*	50
k_3^*	800
m^*	10
v_{dr}^*	$10^{-4} \div 3 \cdot 10^{-2}$
z_A^*	0.3
N	10
γ^*	3

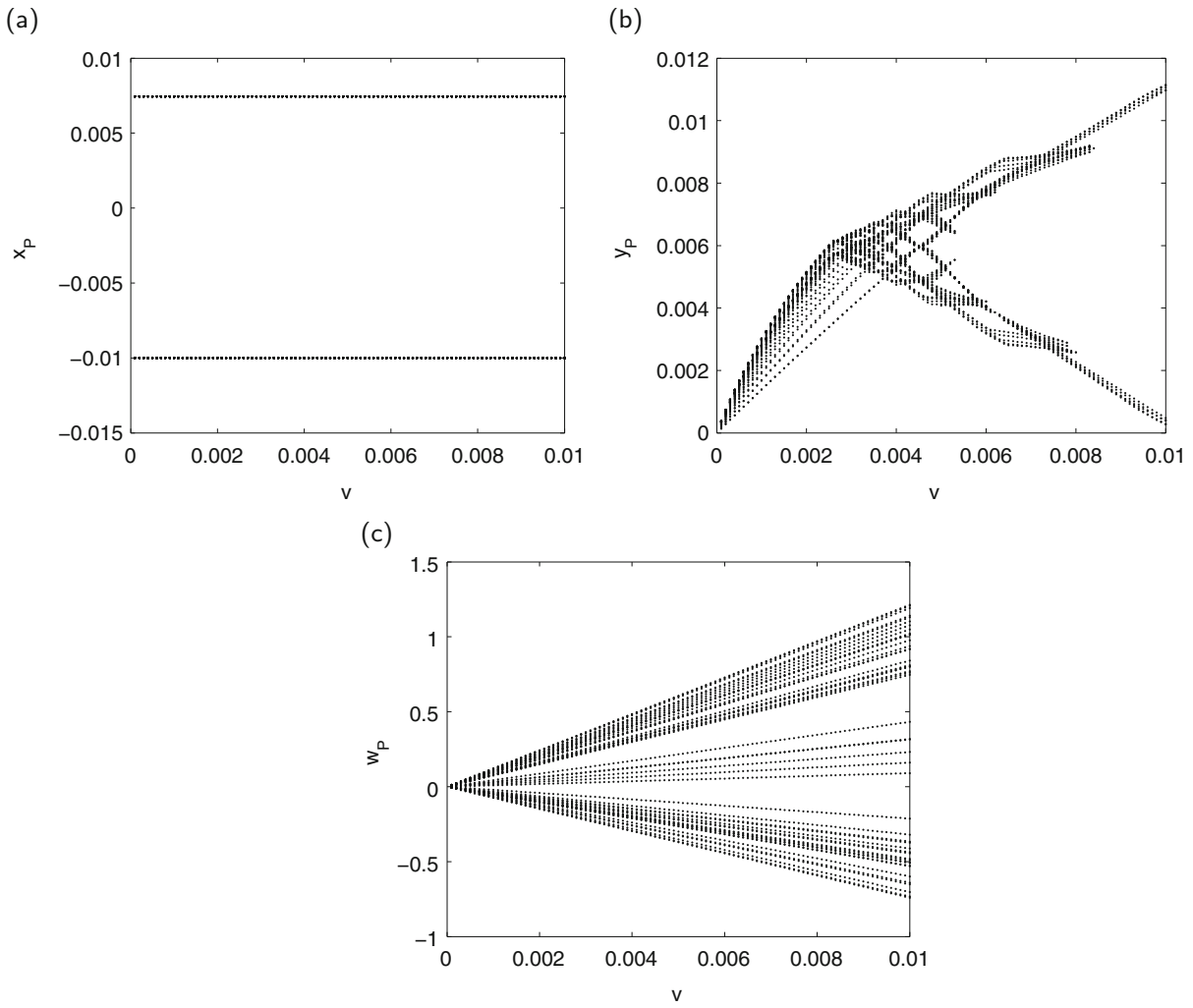

Fig. 2.3 Bifurcation diagrams of $x^*(t^*)$ (**a**), $y^*(t^*)$ (**b**) and $w^*(z_A^*, t^*)$ (**c**)

By considering the bifurcation diagram for the $\mathcal{L}_i$ coordinate, the n-dimensional phase space of the studied system can be intersected with a $(n-1)$-dimensional surface passing through $\dot{\mathcal{L}}_i = 0$. All the points $\mathcal{L}_i$ on the Poincaré section are plotted for each value of the belt speed [1, 3].

In Fig. 2.3a–c, the bifurcation diagrams of all the Lagrangian coordinates are shown for the belt velocity range $v = v_{dr}^* = 10^{-4} \div 3 \cdot 10^{-2}$.

The bifurcation diagram for $\mathcal{L}_1$ (Fig. 2.3a) shows a limit cycle for all the belt velocities, as expected. The mass motion along $x^*(t^*)$ is not affected by the beam dynamics and the stick-slip motion, does not appear.

While for $\mathcal{L}_3$ (Fig. 2.3c) the system shows a regular behaviour (for each value of the velocity v_{dr}^* there is a limit cycle that increases with the belt speed), for $\mathcal{L}_2$ (Fig. 2.3b) the system have an unpredictable motion, showing the period doubling phenomenon for a belt velocity range ($v_{dr}^* \in \left[2.5 \cdot 10^{-3}; 9 \cdot 10^{-3}\right]$), for big values of v_{dr}^* the coordinate $\mathcal{L}_2$ moves on a limit cycle. This kind of behaviour of the bifurcation diagram shows that the system response is sensitive to the variation of the belt velocity.

From the diagrams analysis, three different kind of motions can be detected for $\mathcal{L}_2$: a pure stick-slip motion ($v_{dr}^* < 2.5 \cdot 10^{-3}$), a bifurcating motion corresponding to the period doubling velocity range ($v_{dr}^* \in \left[2.5 \cdot 10^{-3}; 9 \cdot 10^{-3}\right]$) and a pure slip motion ($v_{dr}^* > 9 \cdot 10^{-3}$).

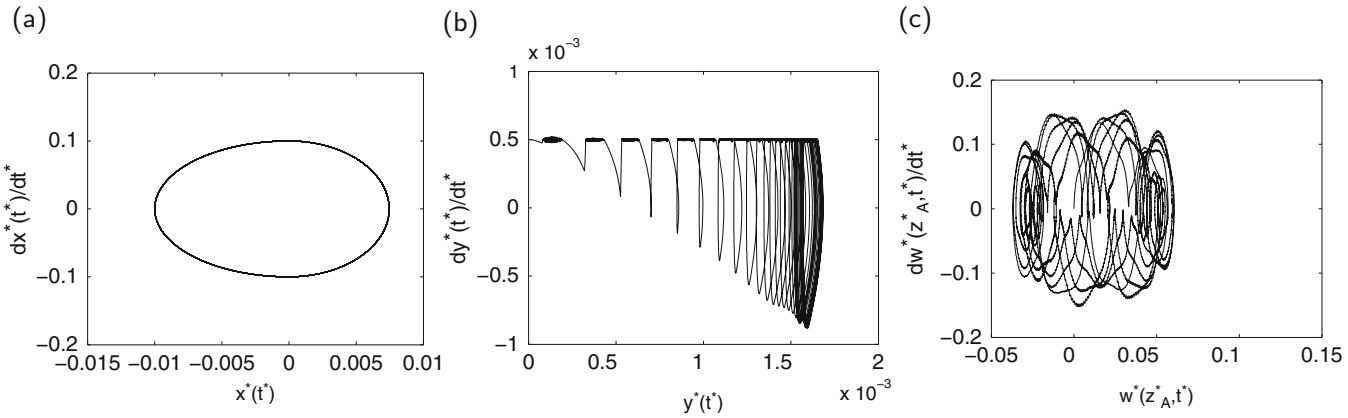

Fig. 2.4 Phase spaces of $x^*(t^*)$ (**a**), $y^*(t^*)$ (**b**) and $w^*(z_A^*, t^*)$ (**c**) at $v_{dr}^* = 0.0005$

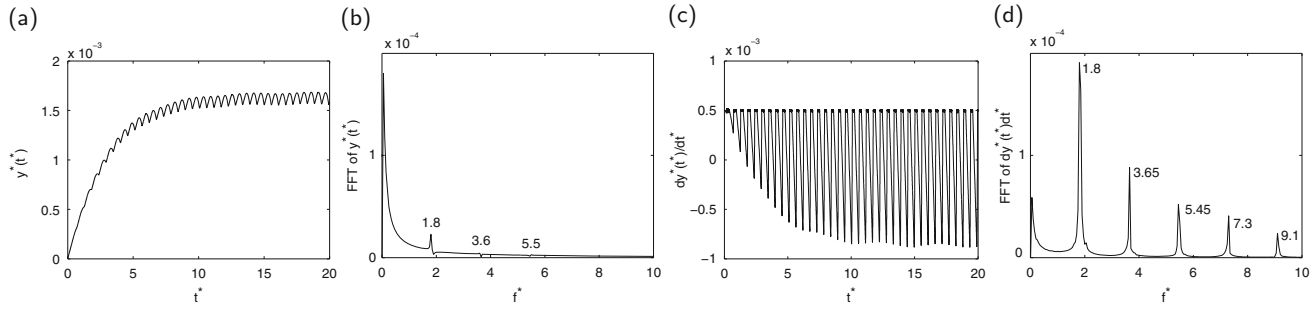

Fig. 2.5 Time evolution and FFT of $y^*(t^*)$ and $dy^*(t^*)/dt^*$ at $v_{dr}^* = 0.0005$

2.3.2 Time and Frequency Domain

For the belt speed $v_{dr}^* < 2.5 \cdot 10^{-3}$, the stick-slip behaviour is clearly shown in Figs. 2.4b and 2.5c. During the stick phase the mass velocity is constant and equal to the belt speed, while during the slip one there is a relative velocity between mass and belt.

In the time domain (see Fig. 2.5a, c) a stick-slip period $T_s = 0.54$ can be detected. The system response in the frequency domain is characterized by the stick slip frequency f_s and by its super-harmonics as shown in Figs. 2.5c and 2.6c, moreover some of them are very close the beam natural frequencies causing the excitation of some modes in the beam (see Fig. 2.6a, c).

The power exchanged between mass and belt is regular for the whole simulation, and different than zero only when the mass slides on the belt (see Fig. 2.7a, as expected; on the other hand the beam exchange more power with the mass (see Fig. 2.7c), cause of the modes excitation, and the power evolution in very irregular due to all the sub and super harmonics of the stick-slip frequency (see Fig. 2.6d).

In the bifurcating belt speed ($v_{dr}^* \in \left[2.5 \cdot 10^{-3}; 0.9 \cdot 10^{-3}\right]$) the stick-slip behaviour is visible just in the first few time steps (see Figs. 2.8 and 2.9c), but it is possible also in this case to detect a frequency $f_s = 0.25$ that is responsible the complex response of the system due to the presence of some super-harmonics of f_s (see Figs. 2.9c and 2.10c).

As shown in the bifurcation diagram in Fig. 2.3c, the beam response is predictable and its phase space increases with the belt speed, that is the reason why the power exchanged with the belt has always the same shape (see Fig. 2.11c) but different scaling factor.

The power received by the mass from the belt (see Fig. 2.11a) is less regular in this velocity range and it is influenced by the beam response (see Fig. 2.11b, d).

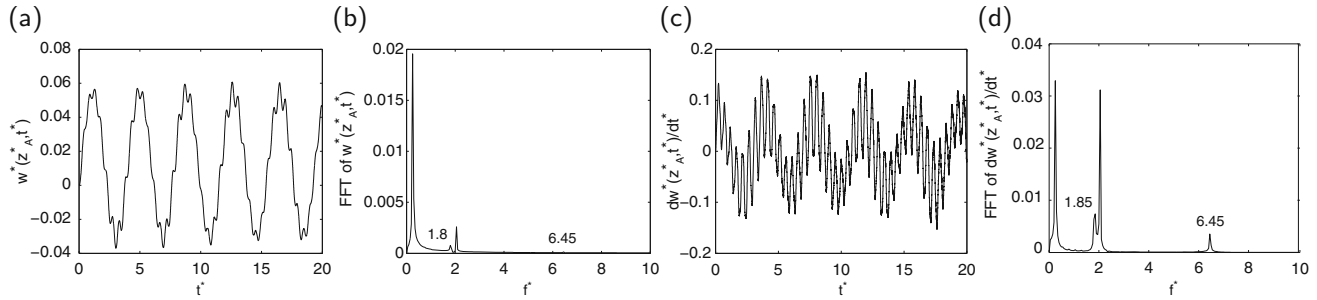

Fig. 2.6 Time evolution and FFT of $w^*(z_A^*, t^*)$ and $dw^*(z_A^*, t^*)/dt^*$ at $v_{dr}^* = 0.0005$

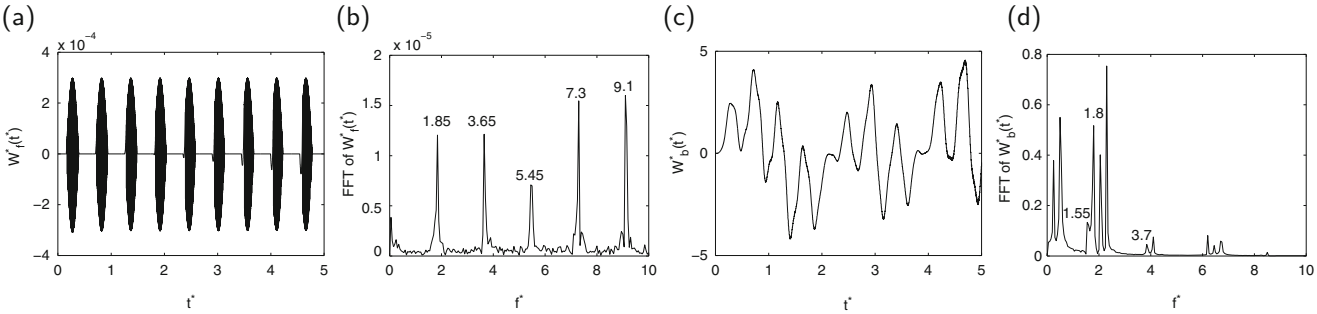

Fig. 2.7 Time evolution and FFT of the exchanged power between belt and mass $W_f^*(t^*)$ and between mass and beam $W_b^*(t^*)$ at $v_{dr}^* = 0.0005$

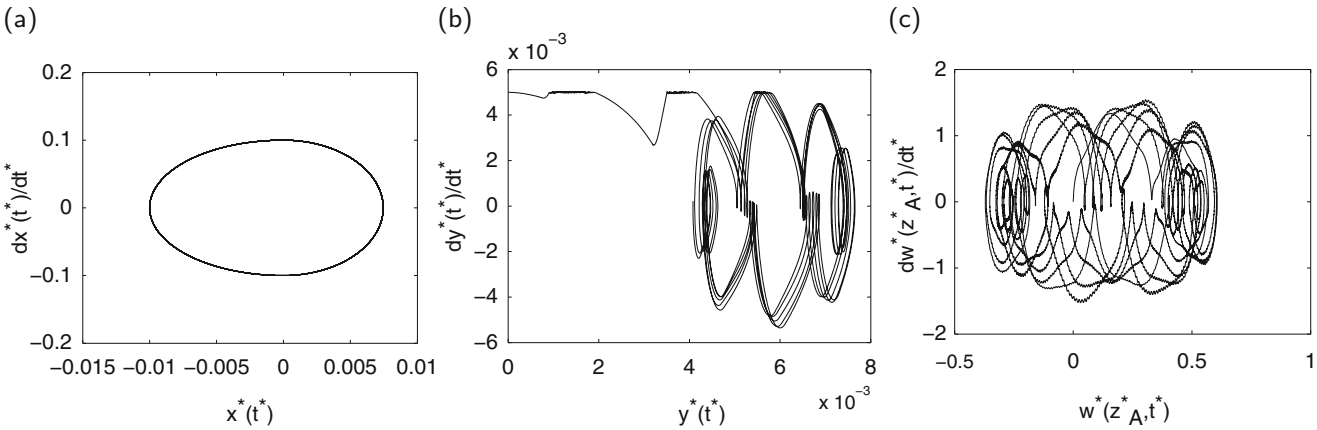

Fig. 2.8 Phase spaces of $x^*(t^*)$ (**a**), $y^*(t^*)$ (**b**) and $w^*(z_A^*, t^*)$ (**c**) at $v_{dr}^* = 0.005$

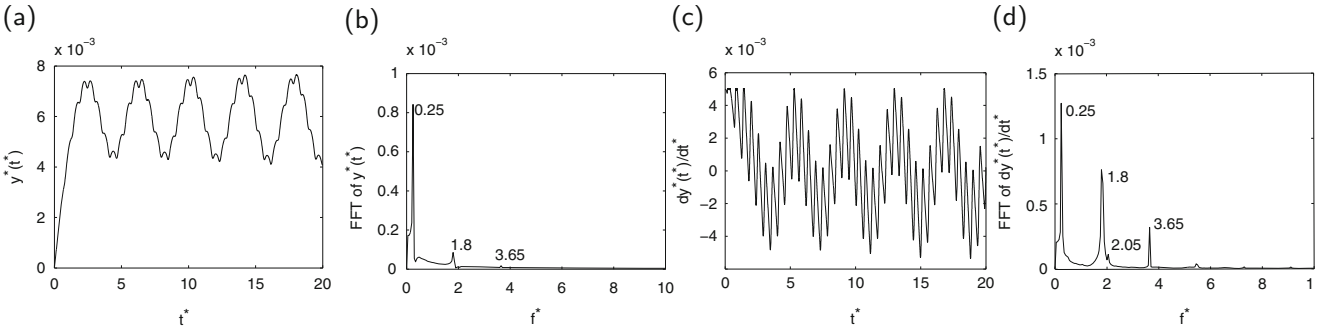

Fig. 2.9 Time evolution and FFT of $y^*(t^*)$ and $dy^*(t^*)/dt^*$ at $v_{dr}^* = 0.005$

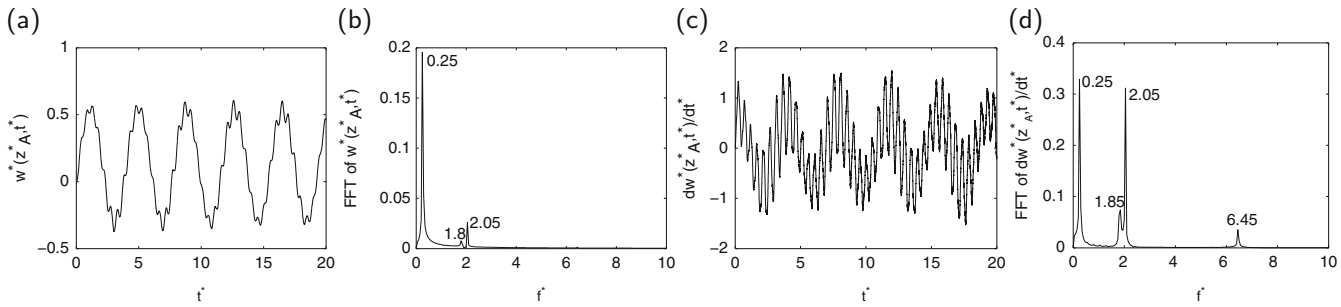

Fig. 2.10 Time evolution and FFT of $w^*(z_A^*, t^*)$ and $dw^*(z_A^*, t^*)/dt^*$ at $v_{dr}^* = 0.005$

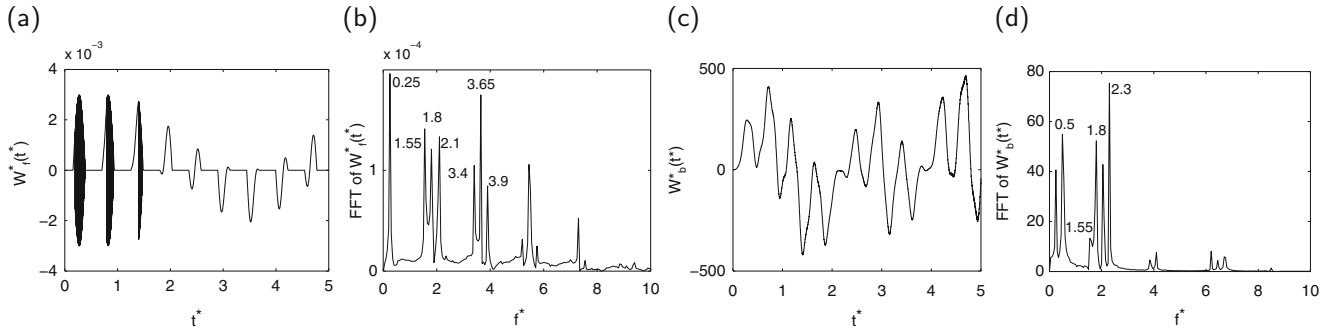

Fig. 2.11 Time evolution and FFT of the exchanged power between belt and mass $W_f^*(t^*)$ and between mass and beam $W_b^*(t^*)$ at $v_{dr}^* = 0.005$

2.3.3 Maximum Lyapunov Exponent

In order to check if the system response is sensitive to a variation of the initial conditions, the characteristic Lyapunov exponent is considered.

The stability of a generic trajectory $\bar{\mathbf{x}}(t)$, obtained by a perturbation of the initial conditions, is checked by considering its distance from the reference trajectory $\mathbf{x}(t)$. The maximum Lyapunov exponent is defined by:

$$\Lambda_{max} = \lim_{t\to\infty} \lim_{\Delta(0)\to 0} \frac{1}{t} \ln\left[\frac{\Delta(t)}{\Delta(0)}\right] \tag{2.25}$$

where $\Delta(0)$ is the perturbation of the initial condition and $\Delta(t)$ is the trajectories distance for each time [4, 5].

A positive value of the maximum Lyapunov exponent represents a divergence in time of the two considered trajectories, underlining the system dependence of the initial conditions.

For a selected belt velocity ($v_{dr}^* = 0.0005$) the maximum Lyapunov exponent has the time evolution shown in Fig. 2.12.

For few time steps the exponent reaches negative values but the dynamics of the global system exhibits its chaotic characteristic with a positive value of the exponent for the last time step and also for the most of its evolution.

Figure 2.13 shows the variation of the last value of the exponent with the belt speed, it is positive for all the belt speed range. The plot shows the three different behaviours identified in the bifurcation diagram of $\mathcal{L}_2$ (Fig. 2.3b): a stick-slip ($v_{dr}^* < 2.5 \cdot 10^{-3}$), a bifurcating ($v_{dr}^* \in \left[2.5 \cdot 10^{-3}; 9 \cdot 10^{-3}\right]$) and a pure slip range ($v_{dr}^* > 9 \cdot 10^{-3}$).

During the stick-slip range the exponents is positive but its trend is decreasing, in the bifurcating range the exponent slope is positive while in the pure slip range a new decreasing trend is shown, underlining that the system is going to reach a stable limit cycle.

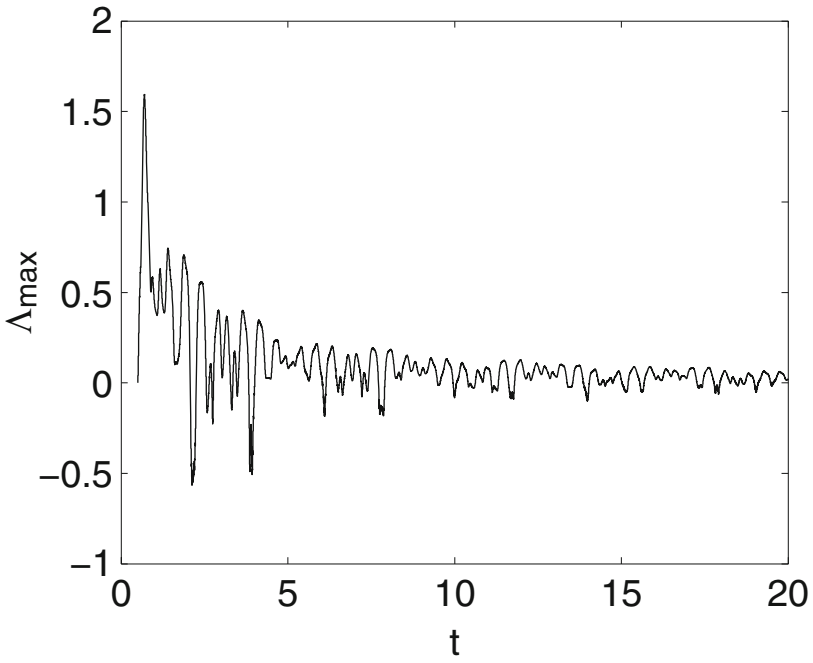

Fig. 2.12 Time evolution of the maximum Lyapunov exponent at $v_{dr}^{*} = 0.0005$

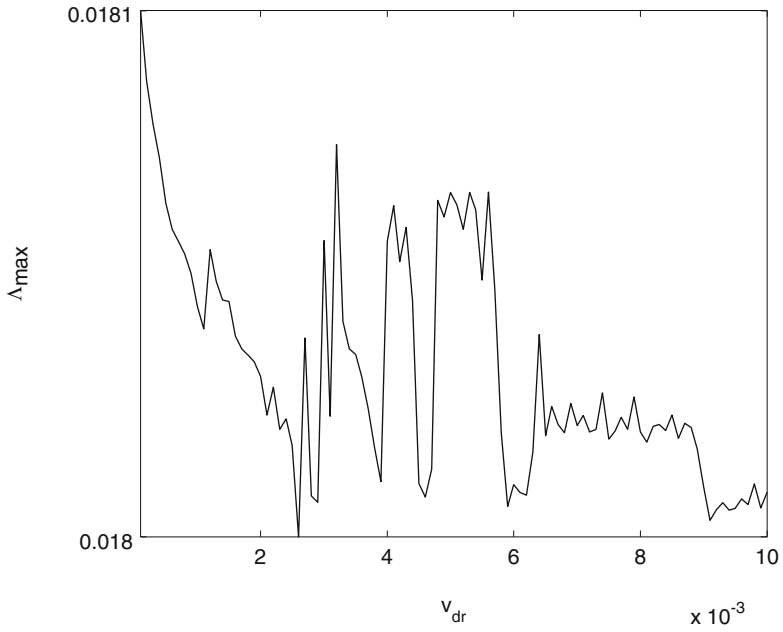

Fig. 2.13 Maximum Lyapunov exponent versus belt velocity

2.4 Concluding Remarks

In this paper the behavior of a continuous dynamical system, joint by a lumped system excited by a belt is studied.

The continuous system is modeled as an Euler-Bernoulli beam, and the coupling one is described by a two degrees of freedom harmonic oscillator excited by a belt at a constant speed along one direction.

The analysis is focused on the influence of the belt speed on the global system behavior. This induces either stick-slip phenomena (low speed of the belt) or only slip (high speed of the belt).

The system sensitivity to the variation of the belt speed and to the system initial conditions are investigated, these phenomena are studied by the bifurcation diagrams and the maximum Lyapunov exponent. Further investigations are focused to understand the chaotic nature of the phenomenon.

A particular attention is posed on the study of system response and on the power balance of the excited system. The stick-slip phenomenon induces super harmonics which effect is the excitation of the natural frequencies of the continuous system.

References

1. Galvanetto U, Bishop SR, Briseghella L (1995) Mechanical stick-slip vibrations. Int J Bifurcation Chaos 5(3):637–651
2. Cheng G, Zu JW (2004) Dynamics of a three DOF mechanical system with dry friction. J Sound Vib 275:591–603
3. Neglia SG, Culla A, Fregolent A (2014) Non-linear dynamics of stick-slip phenomena for a three DOFs mechanical system. In: Sas P (ed) Proceedings of ISMA 2014 - international conference on noise and vibration engineering, Leuven, pp 1917–1930
4. Cencini M, Cecconi F, Vulpiani A (2009) Chaos: from simple models to complex systems. World Scientific, Singapore
5. Sprott JC (2003) Chaos and time-series analysis. Oxford University Press, Oxford

Chapter 3
Prediction of Nonlinear Forced Response on Ancillary Subsystem Components Attached to Reduced Linear Systems

Sergio E. Obando, Peter Avitabile, and Jason Foley

Abstract Industrial size FE models often times involve multiple interconnected linear components with very high fidelity resolution and very refined mesh. The prediction of the dynamic characteristics of this type of system can be costly and inefficient, in particular, when localized nonlinearities are present due to coupling elements such as hard contacts, isolation mounts, gap springs, bilinear springs, etc. Reduction methodologies are currently employed in this setting to decrease the set of active degrees of freedom in the FEM and efficiently compute the nonlinear system response. For complete multi-component systems with complicated nonlinear subcomponent configurations, the dynamic response of the system will have the embedded characteristics of the appended/ancillary subcomponents but the fidelity of the model will be highly dependent on the quality and resolution of the model. Therefore, sufficient substructure information is needed for an accurate prediction of the response of the appendage and/or its coupling structure.

In this work, analytical models of a multi-component beam system with nonlinear contact interactions were created to investigate the prediction of the dynamic response of ancillary subsystem components. The ancillary structure will be assumed to be dynamically active but will not contain any degrees of freedom in the reduced model. The models will be created first at full space as a reference and then reduction techniques will be used to determine the necessary information in order to accurately predict the displacement at the appendage. The dynamic characteristics of the ancillary component will be extracted using the subcomponent information available from the system. The solution is obtained from piecewise linear approximations of the reduced order model and expansion is used to obtained system level response at all DOF.

Keywords Forced nonlinear response • Reduced order modeling • Cascaded components

Nomenclature

Symbols

$\{X_n\}$	Full Set Displacement Vector
$\{X_a\}$	Reduced Set Displacement Vector
$\{X_d\}$	Deleted Set Displacement Vector
$[M_a]$	Reduced Mass Matrix
$[M_n]$	Expanded Mass Matrix
$[K_a]$	Reduced Stiffness Matrix
$[K_n]$	Expanded Stiffness Matrix
$[U_a]$	Reduced Set Shape Matrix
$[U_n]$	Full Set Shape Matrix
$[U_a]^g$	Generalized Inverse
$[T]$	Transformation Matrix
$[T_U]$	SEREP Transformation Matrix

S.E. Obando (✉) • P. Avitabile
Structural Dynamics and Acoustic Systems Laboratory, University of Massachusetts Lowell, One University Avenue, Lowell, MA 01854, USA
e-mail: sergio.e.obando@gmail.com

J. Foley
Air Force Research Laboratory, Munitions Directorate, Fuzes Branch, Eglin Air Force Base, 306 W. Eglin Blvd, Bldg 432, Eglin AFB, Valparaiso, FL 32542-5430, USA

G. Kerschen (ed.), *Nonlinear Dynamics, Volume 1*, Conference Proceedings of the Society for Experimental Mechanics Series, DOI 10.1007/978-3-319-15221-9_3

$\{p\}$	Modal Displacement Vector
$[M]$	Physical Mass Matrix
$[C]$	Physical Damping Matrix
$[K]$	Physical Stiffness Matrix
$\overline{M}$	Diagonal Modal Mass Matrix
$\overline{K}$	Diagonal Modal Stiffness Matrix
$\overline{C}$	Diagonal Modal Damping Matrix
$[\bar{I}]$	Identity Matrix
$\{F\}$	Physical Force Vector
$\{\ddot{x}\}$	Physical Acceleration Vector
$\{\dot{x}\}$	Physical Velocity Vector
$\{x\}$	Physical Displacement Vector
$\overrightarrow{\ddot{x}}_0$	Initial Acceleration Vector
$\overrightarrow{\dot{x}}_0$	Initial Velocity Vector
$\overrightarrow{x}_0$	Initial Displacement Vector
$\overrightarrow{F}_0$	Initial Force Vector
α	Parameter for Newmark Integration
β	Parameter for Newmark Integration
Δt	Time Step

Subscript

1	State 1
2	State 2
12	State 1–2
i	Row i
j	Column j
n	Full Set of Finite Element DOF
a	Reduced Set of DOF
d	Deleted (Omitted) Set of DOF
U	SEREP
TIE	Stiffness Tie Matrix
SYS	System AB of Assembled Components

Superscript

T	Transpose
g	Generalized Inverse
k	kth Degree of Freedom
-1	Standard Inverse
A	Component A
B	Component B

Acronyms

ADOF	Reduced Degrees of Freedom
NDOF	Full Space Degrees of Freedom
DOF	Degrees of Freedom

ERMT Equivalent Reduced Model Technique
FEM Finite Element Model
MAC Modal Assurance Criterion
SEREP System Equivalent Reduction Expansion Process
TRAC Time Response Assurance Criterion

3.1 Introduction

Multi-component structural systems are commonly used in the modeling of dynamic systems. In order to simplify such complex mathematical models, peripheral/ancillary components are often times grouped as larger substructures of the total assembly. While the contribution to the dynamic characteristics of the system from the subsystem ancillary components can seem small, the accuracy of the prediction of the system level response may be compromised if a sufficiently detailed model is not used.

Industrial size FE models of this high resolution carry a large cost and lead to a significant amount of time and computational resources. For instance, the design stage of manufactured goods often times requires analysis of a multitude of configurations and scenarios that cannot be quickly evaluated. Moreover, additional challenges occur when already large intricate models involve complicated nonlinear subcomponent configuration and complex connections/coupling elements. A nonlinear solution scheme for these types of models is inefficient considering the localized nature of the nonlinearities or their overall effect at limited times on the full response of the system. In this setting, reduction methodologies are currently employed to efficiently decrease the set of active degrees of freedom (ADOF) down to a more manageable size. In particular, a family of nonlinear problems consisting of linear components interconnected with nonlinear elements allows for efficient reduced modeling and a solution composed of piecewise linear approximations.

The dynamics of this class of nonlinear problems can be accurately captured by observing the changes of state of the linear components with time while implementing efficient reduced order modeling that can be used for expansion to full field displacement as well as stress–strain prediction. This efficient approximation and modeling of structures is a result of recent developments in the computation of reduced order model response which allows for the accurate calculation of system's time response while retaining all the highly refined and complex characteristics of full finite element models. Work by Thibault [1–3] and Marinone [4–6] showed that system level response can be accurately and efficiently calculated for highly reduced system models. Moreover, Pingle [7–12] and Carr [13–16] demonstrated that the expansion of such systems can be used for the prediction of full field results as well as stress and strain from limited sets of data. Harvie and Avitabile [17–20] extended this work to include the application of expansion to nonlinear systems made out of linear components but subjected to nonlinear interactions. In that work, the expansion was greatly simplified by using the unconnected component modes to expand the response of the reduced system model as developed by Nonis [21, 22].

In this paper, multi-component structural systems are addressed in the context of retaining embedded structural information of ancillary subcomponents for the calculation of nonlinear reduced order model time response. For linear forced response, expansion was shown to return a precise approximation of the ancillary subcomponent even in cases where the reduction does not include active DOF at that subcomponent level [23]. A full space finite element model consisting of two systems, one of which contains a dynamically active ancillary subcomponent, will be reduced to a smaller set of degrees freedom and used for the prediction of the forced time response of the system as seen in Fig. 3.1. Gap-spring contact elements are introduced to generate nonlinear response between the two systems. The reduced order model (with embedded ancillary subcomponent information) will then be used to calculate the response at ADOF and then to expand back to the full space finite element model and to extract the predicted forced response of the ancillary subcomponent. This study will use SEREP [24] and ERMT (Equivalent Reduced Modeling Technique [1]) for reduction/expansion and characterization of the subsystem components from the available reduced system information.

The advantages of using reduced order models can be seen from a substantial reduction in computation time even when such systems involve nonlinear effects. The selection of degrees of freedom during the reduction process will explore whether it is necessary to include the connecting degrees of freedom of the ancillary component and the larger coupling structure or if these can be omitted as long as the preserved modes of the reduced system span the space of all modes of interest of the system. This is of particular importance in real life experimentation, as often times, measurements cannot be made exactly at the connecting degrees of freedom of multi-component structures or highly detailed finite element models are necessary to approximate the behavior of the system at those locations.

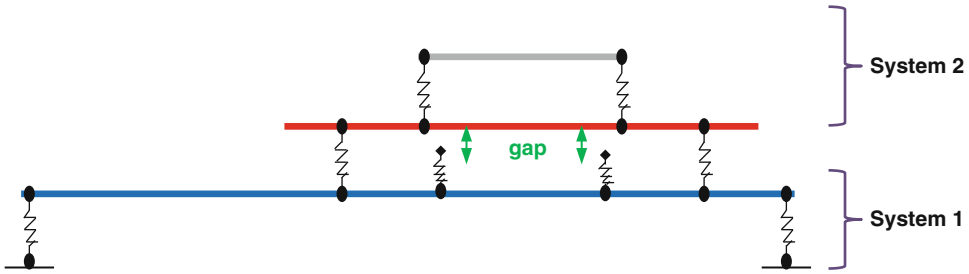

Fig. 3.1 Three beam structure consisting of two systems with active ancillary subcomponent in *grey*

3.2 Theory

The fundamentals of the study of forced response estimation and expansion/reduction of linear and nonlinear systems require a variety of theoretical topics briefly presented here. The summary starts with a description of linear multiple degree of freedom systems and continues with an overview of system modeling and mode contribution, structural dynamic modification, analytical model reduction and expansion, expansion of system modes from uncoupled component modes, forced time response computations and time correlation tools. Further information can be found in the respective references.

3.2.1 Equations of Motion for Multiple Degree of Freedom System

The general equation of motion for a multiple degree of freedom system written in matrix form is

$$[M_1]\{\ddot{x}\} + [C_1]\{\dot{x}\} + [K_1]\{x\} = \{F(t)\} \tag{3.1}$$

Assuming proportional damping, the eigensolution is obtained from

$$[\,[K_1] - \lambda\,[M_1]\,]\{x\} = \{0\} \tag{3.2}$$

The eigensolution yields the eigenvalues (natural frequencies) and eigenvectors (mode shapes) of the system. The eigenvectors are arranged in column fashion to form the modal matrix $[U_1]$. Often times, only a subset of modes is included in the modal matrix to save on computation time and due to the fact that only certain modes actually contribute to the response. Exclusion of modes results in truncation error which can be serious if key modes are excluded. Truncation error will be discussed in further detail in the structural dynamic modification section.

The physical system can be transformed to modal space using the modal matrix as

$$[U_1]^T[M_1][U_1]\{\ddot{p}_1\} + [U_1]^T[C_1][U_1]\{\dot{p}_1\} + [U_1]^T[K_1][U_1]\{p_1\} = [U_1]^T\{F(t)\} \tag{3.3}$$

Scaling to unit modal mass yields

$$\begin{bmatrix} \ddots & & \\ & I_1 & \\ & & \ddots \end{bmatrix}\{\ddot{p}_1\} + \begin{bmatrix} \ddots & & \\ & 2\xi\omega_n & \\ & & \ddots \end{bmatrix}\{\dot{p}_1\} + \begin{bmatrix} \ddots & & \\ & \Omega_1^2 & \\ & & \ddots \end{bmatrix}\{p_1\} = \left[U_1^n\right]^T\{F(t)\} \tag{3.4}$$

where $[I_1]$ is the diagonal identity matrix, $[{\Omega_1}^2]$ is the diagonal natural frequency matrix and $[2\xi\omega_n]$ is the diagonal damping matrix (assuming proportional damping). More detailed information on the equation development is contained in Ref. [25].

3.2.2 System Modeling and Mode Contribution

The approach used for the prediction of the nonlinear system response uses concepts from system modeling. In order to create multi-component models, various techniques are available for the coupling of several component models into a single

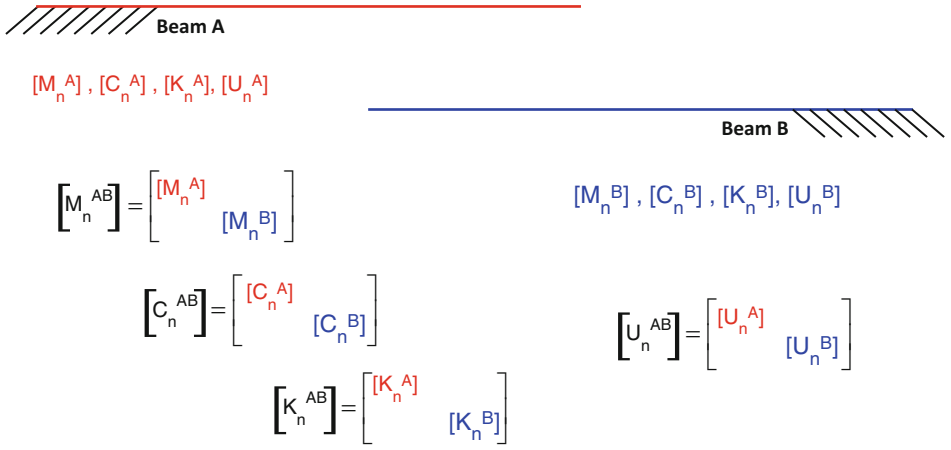

Fig. 3.2 Sample components arranged into common matrix space

system model. These system modeling techniques are used to define the various states that the system will undergo when the different nonlinear contact connections occur. The system modeling can be performed in physical space, modal space, or a combination of both physical and modal space. Consider two beams that are completely independent of one another, as illustrated in Fig. 3.2.

The two beams shown in Fig. 3.2 are completely uncoupled and will respond independent of one another when excited. A system model of the uncoupled components is generated by simply writing the variables in common matrix space, as shown in the diagram. To generate a coupled system model, specific coupling terms must be introduced at the desired locations. To include the spring(s) in the system modeling, either a modal or physical approach can be employed. The modal approach involves using Structural Dynamic Modification (SDM) and Component Mode Synthesis (CMS). The physical approach involves using a physical tie matrix to couple the beams. Both approaches involve the use of a mode contribution matrix to determine the appropriate number of component modes that contribute to the system modes. For the results presented here, physical system modeling techniques were used to generate databases for the various configurations.

3.2.2.1 Physical Space System Modeling

To form a physical system model, the mass and stiffness matrices of each component (A and B) are assembled in stacked form into the system mass and stiffness matrices. In physical space, these are coupled with a stiffness tie matrix; a mass tie can also be included if desired but not included in this work.

$$\begin{bmatrix} [M^A] & \\ & [M^B] \end{bmatrix} \{\ddot{x}\} + \left[\begin{bmatrix} [K^A] & \\ & [K^B] \end{bmatrix} + K_{TIE} \right] \{x\} = \{F\} \tag{3.5}$$

This can be cast in a modal space representation as

$$\left[\begin{bmatrix} [\overline{M}^A] & \\ & [\overline{M}^B] \end{bmatrix} \right] \begin{Bmatrix} \{\ddot{p}^A\} \\ \{\ddot{p}^B\} \end{Bmatrix} + \begin{bmatrix} [\overline{K}^A] & \\ & [\overline{K}^B] \end{bmatrix} \begin{Bmatrix} \{p^A\} \\ \{p^B\} \end{Bmatrix} + \left[[U]^T [\Delta K] [U] \right] \begin{Bmatrix} \{p^A\} \\ \{p^B\} \end{Bmatrix} = \{0\} \tag{3.6}$$

where $[\overline{M}]$ and $[\overline{K}]$ are diagonal matrices and with the mode shapes of each component stacked as

$$[U] = \begin{bmatrix} [U^A] & \\ & [U^B] \end{bmatrix} \tag{3.7}$$

Equation 3.5 is a general equation of motion in physical space; Eq. 3.6 is the modal space equation used for the eigensolution.

3.2.2.2 Structural Dynamic Modification

Structural Dynamic Modification (SDM) is a technique that uses the original mode shapes and natural frequencies of a system to estimate the dynamic characteristics due to changes in the mass and/or stiffness of the system. First, the change of mass and stiffness are transformed to modal space as shown

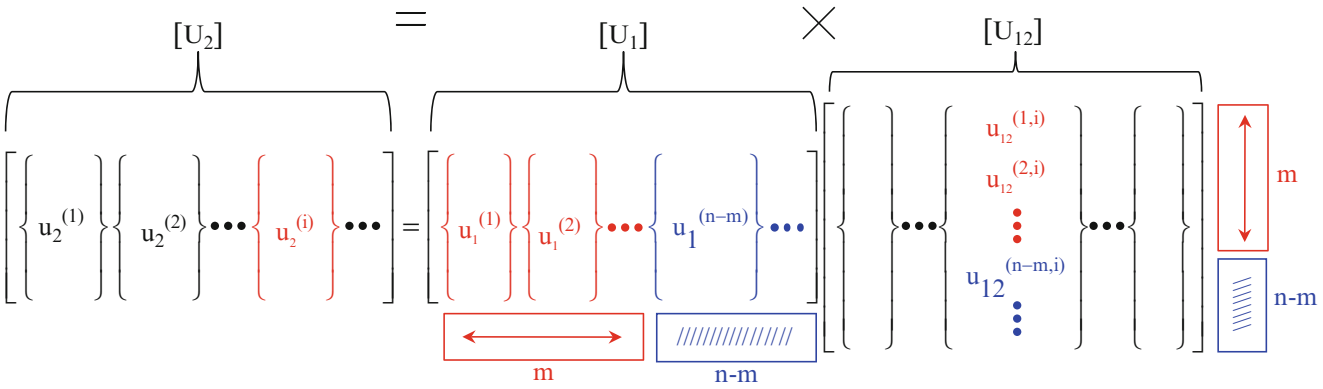

Fig. 3.3 Structural dynamic modification, mode contribution identified using U_{12} [2]

$$\left[\Delta\overline{M}_{12}\right] = [U_1]^T \left[\Delta M_{12}\right] [U_1] \tag{3.8}$$

$$\left[\Delta\overline{K}_{12}\right] = [U_1]^T \left[\Delta K_{12}\right] [U_1] \tag{3.9}$$

The modal space mass and stiffness changes are added to the original modal space equations as seem in Eq. 3.6 to obtain

$$\left[\begin{bmatrix} \ddots & & \\ & \overline{M}_1 & \\ & & \ddots \end{bmatrix} + \left[\Delta\overline{M}_{12}\right]\right] \{\ddot{p}_1\} + \left[\begin{bmatrix} \ddots & & \\ & \overline{K}_1 & \\ & & \ddots \end{bmatrix} + \left[\Delta\overline{K}_{12}\right]\right] \{p_1\} = [0] \tag{3.10}$$

The eigensolution of the modified modal space model is computed and the resulting eigenvalues are the new frequencies of the system. The resulting eigenvector matrix is the $[U_{12}]$ matrix, which is used to transform the original modes to the new modes as indicated by

$$[U_2] = [U_1]\ [U_{12}] \tag{3.11}$$

The new mode shapes are $[U_2]$. The new mode shapes are formed from linear combinations of the original mode shapes. The $[U_{12}]$ matrix shows how much each of the $[U_1]$ modes contributes to forming the new modes. Figure 3.3 shows the formation of the new mode shapes as seen on Eq. 3.11. Reference [25] has additional information on SDM.

The mode contribution matrix is used to determine which original mode shapes are necessary for the accurate reconstruction of each of the desired final mode shapes. If a dynamic response involves multiple system states, then the $[U_{12}]$ matrix must be computed for each configuration to determine the number of original system modes to appropriately span the space of the solution and avoid truncation.

3.2.3 General Reduction/Expansion Methodology and Model Updating

Model reduction is a tool used to reduce the number of degrees of freedom (DOF) in order to minimize the required computation time of an analytical model, while attempting to preserve the full DOF dynamic characteristics. The relationship between the full space and reduced space model can be written as

$$\{X_n\} = \begin{Bmatrix} X_a \\ X_d \end{Bmatrix} = [T]\{X_a\} \tag{3.12}$$

where subscript 'n' signifies the full set of DOF (NDOF), 'a' signifies the reduced set of DOF (ADOF) and 'd' is the deleted DOF (those DOF not used during the reduced computation process). The transformation matrix [T] relates the full set of NDOF to the reduced set of ADOF. The transformation matrix is used to reduce the mass and stiffness matrices as

$$[M_a] = [T]^T [M_n] [T] \text{ and } [K_a] = [T]^T [K_n] [T] \tag{3.13}$$

The eigensolution of these 'a' set mass and stiffness matrices are the modes of the reduced model. These modes can be expanded back to full space using the transformation matrix

$$[U_n] = [T\,] [U_a] \tag{3.14}$$

If an optimal 'a' set is not selected when using methods such as Guyan Condensation [26] or Improved Reduced System Technique [27], the reduced model may not perfectly preserve the dynamics of the full space model. If System Equivalent Reduction Expansion Process (SEREP) [24] is used, the dynamics of selected modes will be perfectly preserved regardless of the 'a' set selected as long as the matrix is formed from a linearly independent set of vectors. Some additional information regarding the DOF selection in regards to expansion is studied in a companion paper [28].

3.2.3.1 Expansion of System Modes from Uncoupled Component Modes

Expansion is generally used for providing full N-space mode shape information extracted from limited a-space information. The expansion to full space in this paper is based on recent work by Nonis [19, 20] showing that full N-space mode shape information for an assembled system model can be obtained using the expansion matrices from the uncoupled, unconnected, original component modes of each component. Figure 3.4 shows the entire expansion process schematically to further describe the overall procedure. Ref. [19] further details the expansion process and considerations for modes included.

While the systems studied here undergo several configurations, the expansion can be performed with a single transformation matrix obtained from the original unconnected unmodified systems. As long as the modes retained during the reduction process span the space of the full space solution of the system, the transformation matrix will produce accurate expanded predictions of the multi-configuration response. Using a single transformation matrix of the unconnected individual components/systems is much more efficient since the full space modes of the connected system are not computed.

3.2.3.2 System Equivalent Reduction Expansion Process (SEREP)

The SEREP modal transformation relies on the partitioning of the modal equations representing the system using selected DOFs and modes to obtain a reduced model that perfectly preserves the eigenvalues and eigenvectors of interest [24]. The SEREP technique utilizes the mode shapes from a full finite element solution to map to the limited set of active DOF. SEREP is not performed to achieve efficiency in the solution but rather is intended to perform an accurate mapping matrix for the transformation. The SEREP transformation matrix is formed using a subset of modes at full space and reduced space as

$$[T_U] = [U_n] [U_a]^g \tag{3.15}$$

where $[U_a]^g$ is the generalized inverse and $[T_U]$ is the SEREP transformation matrix. When the SEREP transformation matrix is used for model reduction/expansion as outlined in the previous section, the reduced model perfectly preserves the full space dynamics of the modes in $[U_n]$ [24].

3.2.4 System Forced Response Analysis

The computation of the time response developed in this paper is based on the Equivalent Reduced Model Technique (ERMT), a technique developed by Avitabile and Thibault [1–4]. This technique uses an exact reduced model representation for the calculation of the system response. Newmark integration technique [29] is used to perform the direct integration of the equations of motion for the ERMT solution process. From the known initial conditions for displacement and velocity, the initial acceleration vector is computed using the equation of motion and the applied forces as

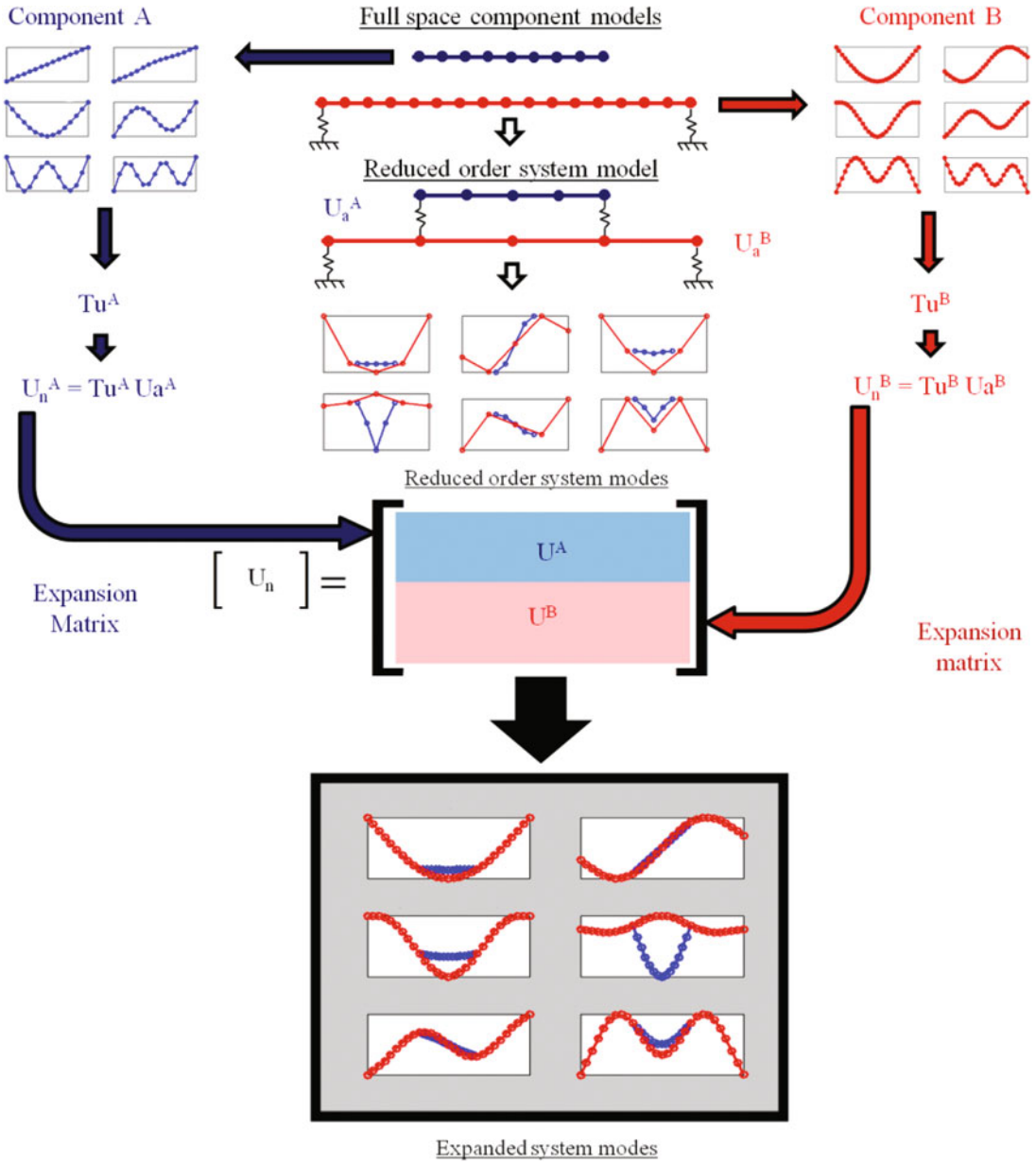

Fig. 3.4 Overall expansion process schematic using the transformation matrices from unconnected system components

$$\ddot{\vec{x}}_0 = [M]^{-1}\left(\vec{F}_0 - [C]\ \dot{\vec{x}}_0 - [K]\ \vec{x}_0\right) \tag{3.16}$$

Choosing an appropriate Δt, α, and β, the displacement vector is

$$\begin{aligned}\vec{x}_{i+1} = &\left[\tfrac{1}{\alpha(\Delta t)^2}[M] + \tfrac{\beta}{\alpha(\Delta t)}[C] + [K]\right]^{-1}\\ &\left\{\vec{F}_{i+1} + [M]\ \left(\left(\tfrac{1}{\alpha(\Delta t)^2}\right)\vec{x}_i + \left(\tfrac{1}{\alpha(\Delta t)}\right)\dot{\vec{x}}_i + \left(\tfrac{1}{2\alpha} - 1\right)\ddot{\vec{x}}_i\right)\right.\\ &\left. + [C]\ \left(\left(\tfrac{\beta}{\alpha(\Delta t)}\right)\vec{x}_i + \left(\tfrac{\beta}{\alpha} - 1\right)\dot{\vec{x}}_i + \left(\tfrac{\beta}{\alpha} - 2\right)\tfrac{\Delta t}{2}\ddot{\vec{x}}_i\right)\right\}\end{aligned} \tag{3.17}$$

The values chosen for α and β were ¼ and ½, respectively. This assumes constant acceleration and the integration process is unconditionally stable, where a reasonable solution will always be reached regardless of the time step used. However, the

time step should be chosen such that the highest frequency involved in the system response can be characterized properly to avoid numerical damping in the solution.

Following the displacement vector calculation, the acceleration and velocity vectors are computed for the next time step using

$$\dot{\vec{x}}_{i+1} = \dot{\vec{x}}_i + (1-\beta)\,\Delta t\,\ddot{\vec{x}}_i + \beta \Delta t\,\ddot{\vec{x}}_{i+1} \tag{3.18}$$

$$\ddot{\vec{x}}_{i+1} = \frac{1}{\alpha(\Delta t)^2}\left(\vec{x}_{i+1} - \vec{x}_i\right) - \frac{1}{\alpha \Delta t}\,\dot{\vec{x}}_i - \left(\frac{1}{2\alpha} - 1\right)\ddot{\vec{x}}_i \tag{3.19}$$

This process is repeated at each time step for the duration of the time response solution desired.

3.2.5 *Expansion of Reduced Order Real Time Response*

Chipman [30–33] and others [1–18] showed that a transformation matrix can be used to expand not only mode shapes, but dynamic time response data. Therefore the same principles presented above can be extended to the expansion of coupled response using uncoupled component information. The response of the coupled system at reduced space can be expanded to full space using the transformation matrices of the individual, unconnected beams systems because the dynamic characteristics of the system are directly related to the dynamic characteristics of the uncoupled components. If the $[U_{12}]$ matrix is evaluated to include enough modal information in the reduced model to accurately represent the system with the coupling elements present, then the time response of the coupled system is accurately expanded to full space using information from the uncoupled components.

For this work, nonlinear systems are analyzed where several possible configurations can exist during response. If all possible configurations are made up of linear combinations of the component mode shapes, then the expansion of nonlinear response of a reduced model can be expanded using the original transformation matrix regardless of the configurations encountered. Figure 3.5 shows the process for determining full space dynamic response of a nonlinear system using the original transformation matrices. The nonlinear contacts in green (Fig. 3.5) indicate when the spring comes in contact with the structure and thus changes from one configuration to another. Although several configurations exist within the time block shown, all modified states can be generated based on the mode shapes of the original system. Therefore only the transformation matrices of the original, uncoupled components are necessary to expand the nonlinear dynamic response of the system regardless of the configurations encountered.

3.2.6 *Time Response Correlation Tools*

In order to quantitatively compare two different time solutions, two correlation tools were employed: The Modal Assurance Criterion (MAC) and the Time Response Assurance Criterion (TRAC).

3.2.6.1 Modal Assurance Criterion (MAC)

The Modal Assurance Criterion (MAC) [34] is widely used as a vector correlation tool. In this work, the MAC was used to correlate all DOF at a single instance in time. The MAC is written as

$$MAC_{ij} = \frac{\left[\{X1_i\}^T \{X2_j\}\right]^2}{\left[\{X1_i\}^T \{X1_i\}\right]\left[\{X2_j\}^T \{X2_j\}\right]} \tag{3.20}$$

where X1 and X2 are displacement vectors. MAC values close to 1.0 indicate strong similarity between vectors, where values close to 0.0 indicate minimal or no similarity.

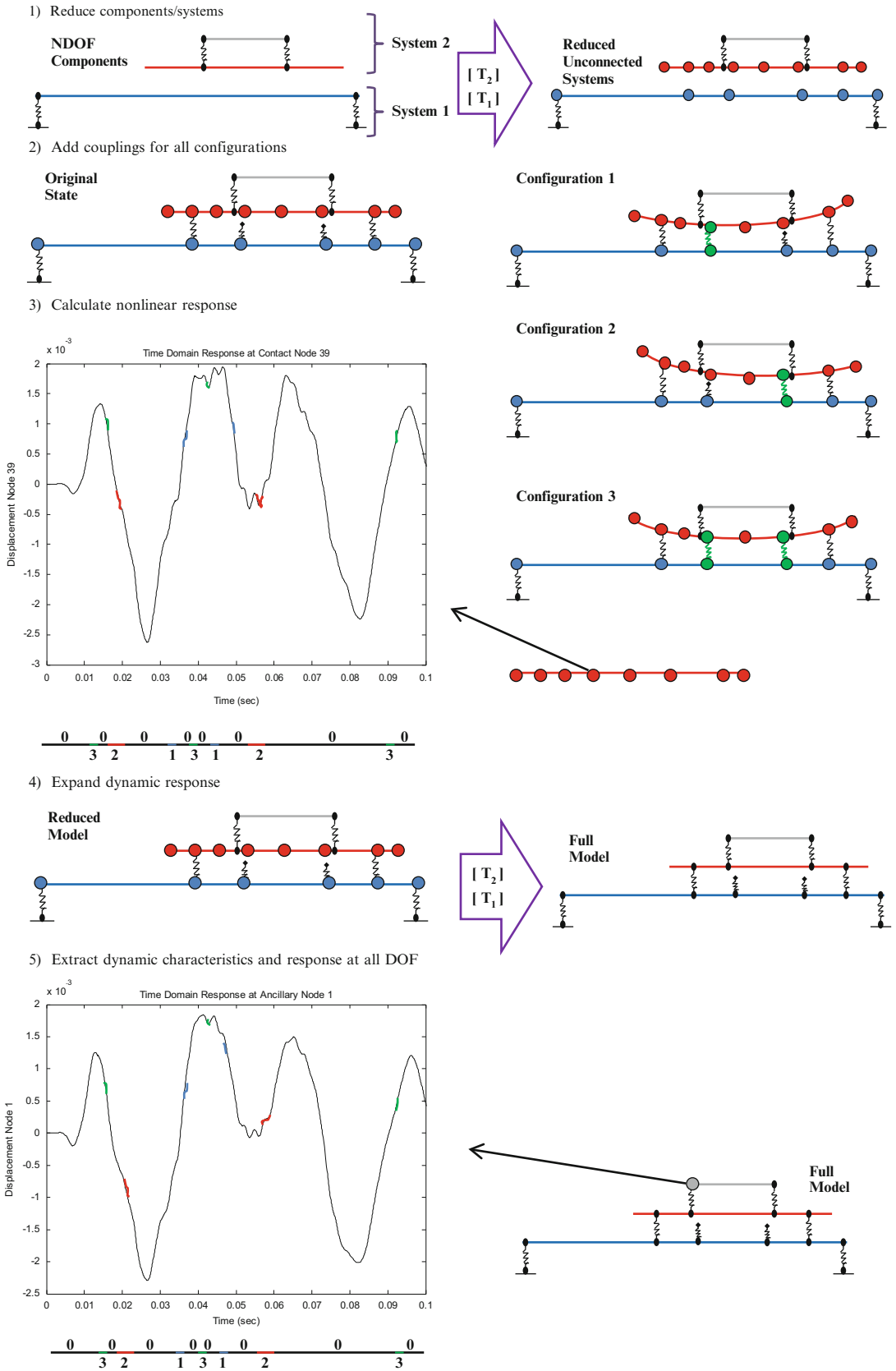

Fig. 3.5 Expansion of nonlinear response using system component mode shapes

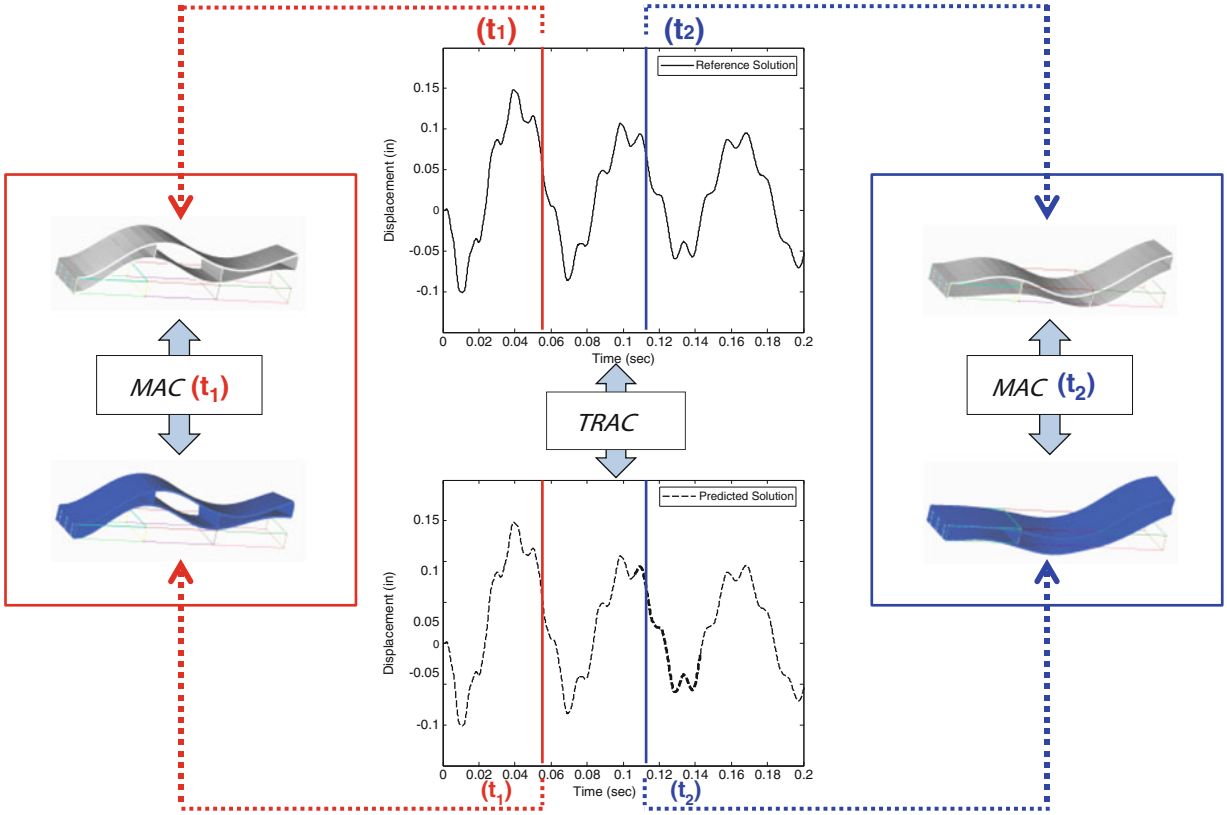

Fig. 3.6 Physical interpretation of MAC and TRAC

3.2.6.2 Time Response Assurance Criterion (TRAC)

The Time Response Assurance Criterion (TRAC) [35] quantifies the similarity between a single DOF across all instances in time. The TRAC is written as

$$\mathrm{TRAC}_{ji} = \frac{\left[\{X1_j(t)\}^T \{X2_i(t)\}\right]^2}{\left[\{X1_j(t)\}^T \{X1_j(t)\}\right]\left[\{X2_i(t)\}^T \{X2_i(t)\}\right]} \tag{3.21}$$

where X1 and X2 are time response vectors for a particular DOF. TRAC values close to 1.0 indicate strong similarity between vectors, where values close to 0.0 indicate minimal or no similarity.

In this work, the MAC is calculated between the shapes of the full space reference solution and estimated solution obtained from the reduced order model at each time step. Similarly the TRAC is used to compare the time response from the reduced order model to the time response from the full space finite element solution at each degree of freedom. A diagram detailing the two comparison techniques is shown in Fig. 3.6.

3.3 Model Description

Analytical models of a multi-component beam system were created to investigate the prediction of the dynamic response of the system including subcomponents and ancillary attachments. The models consisted of 3 beams, as illustrated in Fig. 3.1, attached asymmetrically by linear springs and such that all components are dynamically active. SEREP was used for all reduced models. Planar element beam models of the cantilevered beam were generated using MAT_SAP [36], which is a FEM program developed for MATLAB [37], and forced response calculations were performed in MATLAB using Newmark

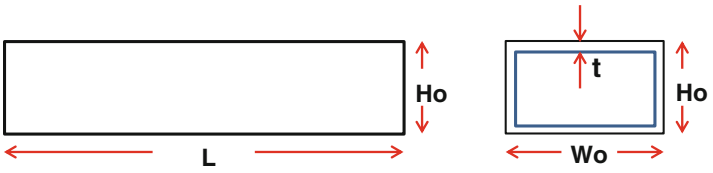

Fig. 3.7 Dimensions of top (*red*) and support/base(*blue*) beams of the analytical beam system

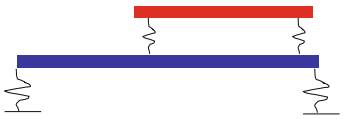

Property of Beam	Beam A	Beam B
Wo - Beam width (in)	2	3
Ho - Beam height (in)	1	4
t - Wall thickness (in)	3/8	1/8
L - Length(in)	50	140
E – Young's Modulus	10e6 psi	
ρ – Weight density	0.1 lb/in^3	
# of elements	20	70

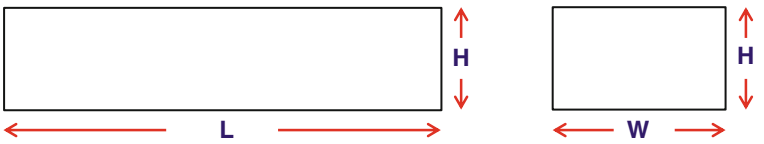

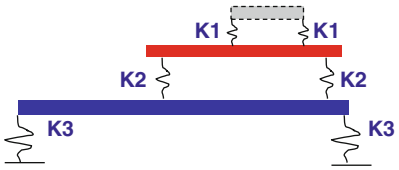

K1 & K2 = 1e6 lb/in
K3 = 1e3 lb/in

Fig. 3.8 Dimensions and characteristics of ancillary subcomponent (*grey*) of 3 beam system

Ancillary Beam Dimensions and Physical Properties	
L – Length	15 in
H – Height	0.25 in
W – Width	0.5 in
E – Young's Modulus	10e6 psi
ρ – Weight density	0.1 lb/in^3
# of Elements	10

integration scripts. The beam models were set to have dimensions and characteristics as described in Figs. 3.7 and 3.8. For all models 1 % of critical damping was used in the time response computation.

The system was subjected to a double sided force pulse at the tip of the blue beam (lowest beam) and this input force was designed as to only excite the modes in a frequency band of approximately 250 Hz as shown in Fig. 3.9. The table of frequencies for each separatecomponent and full assembled system (with and without the ancillary) can be seen in Table 3.1.

With all 100 elements of the system (i.e. 206 DOF) the full N-space reference solution to the system was calculated and served as a point of comparison for all subsequent reduced order model calculations. The nonlinear contacts were setup in two configurations, one where the contacts occurs between the blue and red beam (Case A) and one where the contact takes place at the subcomponent level (Case B) as seen in Fig. 3.10. The soft contacts are springs with a stiffness of 100 lb/in, while the hard contacts have a stiffness of 10,000 lb/in.

As studied in [23], for the linear forced response of this multi-component system the connecting DOF as well as DOF at the ancillary subcomponent are not needed in order to accurately predict the system level response. Similar conclusion will be drawn in this work, extending the prediction of the subcomponent response for nonlinear cases. However, in the nonlinear cases studied here, the location of the nonlinearity can have a significant effect on the accuracy of the prediction and on the number of modes (and DOF) required in the reduction/expansion process.

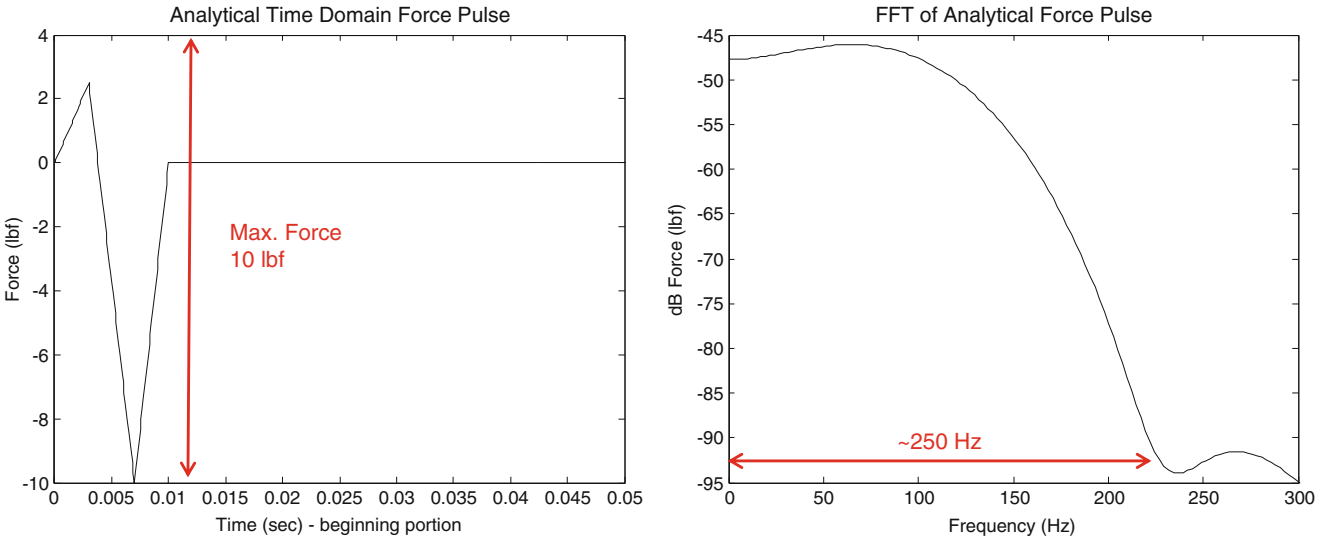

Fig. 3.9 Time (*left*) and frequency (*right*) domain plots of input analytical force pulse

Table 3.1 Frequencies of the first 15 modes of the 3 beam system (with and without ancillary) and its components

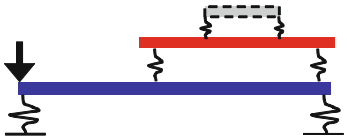

Mode	Frequency (Hz)				
	Beam A	**Beam B**	**Ancillary**	**System w/o A.C.**	**System**
1	0.0015	18.9	0.010	16.8	16.8
2	0.0024	45.9	0.014	37.6	37.5
3	87.6	80.9	224.5	68.2	68.1
4	241.4	161.4	619.0	86.9	84.6
5	473.2	299.7	1,214.3	129.1	102.1
6	782.3	489.4	2,010.4	210.5	129.1
7	1,168.8	728.2	3,011.1	282.8	210.0
8	1,633.1	1,015.5	4,223.0	343.1	282.0
9	2,175.4	1,351.0	5,653.7	477.1	343.0
10	2,796.3	1,734.7	7,302.3	645.5	396.2
11	3,496.7	2,166.4	9,071.4	716.4	477.3
12	4,277.7	2,646.2	12,046.9	959.5	645.3
13	5,140.7	3,174.1	14,493.9	1,118.7	716.3
14	6,087.4	3,750.0	17,502.7	1,311.7	88–9.0
15	7,120.0	4,373.9	21,038.3	1,617.3	960.6

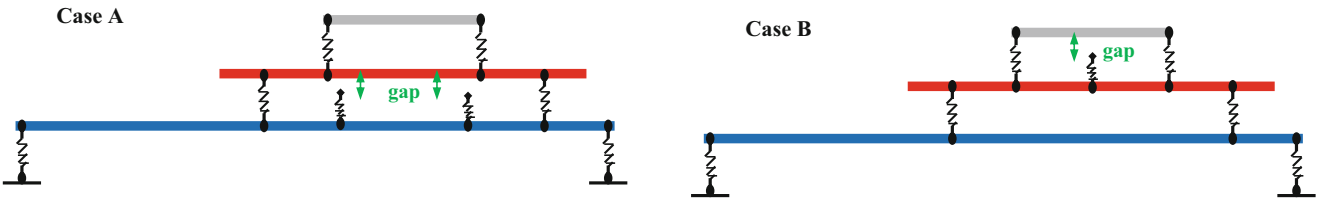

Fig. 3.10 Nonlinear gap-spring contact cases analyzed

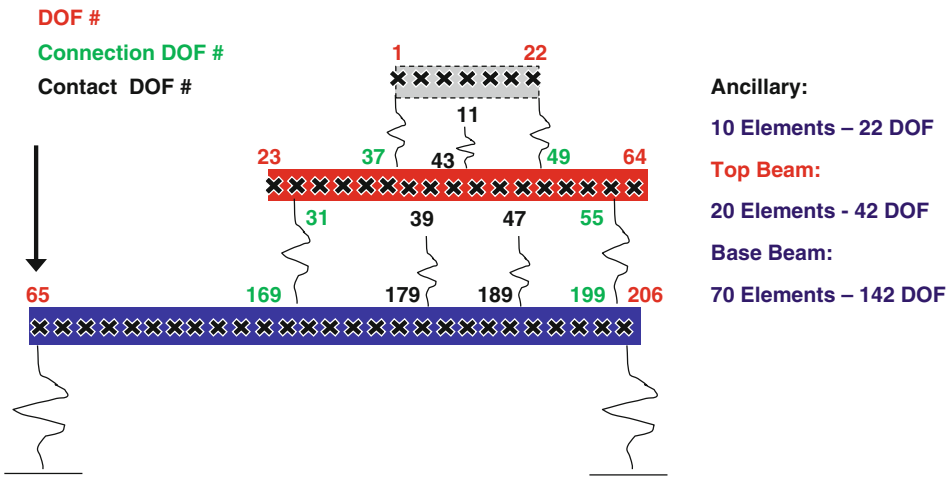

Fig. 3.11 Numbering scheme of three beam system at NDOF (206) with connection and contact locations

3.4 Cases Studied

Two nonlinear configurations of the three beam system were analyzed as shown in Fig. 3.10. The forced response of the full space reference models with 206 DOF were calculated first. Structural Dynamic Modification was used to calculate the $[U_{12}]$ matrix for each configuration of Case A and Case B. For Case A, four different configurations are possible as shown in Fig. 3.5. Similarly, Case B has two possible different configurations.

Using the calculated $[U_{12}]$ for all configurations, the necessary number of component modes were determined in order to properly characterize the system; using the force described above, the system modes must be able to characterize the response over a 250 Hz frequency span. While this is the initial frequency range of interest for any structural dynamic study, there also needs to be consideration for the nonlinear contacts which occur that may require a frequency range beyond that initially determined from the applied forcing function.

SEREP reduction was used to reduce the active DOF of the system to an 'a' set not including DOFs on the ancillary beam (except when noted). The forced responses of the reduced ADOF systems were computed. The dynamic characteristics of the ancillary subcomponent were then extracted using the system information available from the reduction process. The test cases presented here are intended to show the results when a proper set of modes are selected such that no information is lost in the reduction process as well as inaccurate reduced models where the modes do not span the full space response of the system. The arrangement of DOF and connecting DOF is illustrated in Fig. 3.11.

The cases presented here are summarized as:

Case A: Two Nonlinear Contacts Between System 1 and System 2

Case A-1: Soft Contact Reference Solution

206 DOF Total; System 1/Beam B 142 DOF; System 2 – Beam A 42 DOF and Ancillary 22 DOF.
Nonlinear Contacts of 100 lb/in at Beam A DOF 39 and 47 of System 2.

Case A-1.1: Soft Contact Reduced Model Solution with 12 Modes

12 DOF Total; Beam B – ADOF 65, 169, 179, 189, and 199;
Beam A – ADOF 23, 31, 39, 43, 47, 55 and 63.
Nonlinear Contacts of 100 lb/in at Beam A ADOF 39 and 47 of System 2.

Case A-1.2: Soft Contact Reduced Model Solution with 16 Modes

16 DOF Total; Beam B – ADOF 65, 99, 135, 169, 179, 189, 199 and 205;
Beam A – ADOF 23, 31, 35, 39, 43, 47, 55 and 63.
Nonlinear Contacts of 100 lb/in at Beam A ADOF 39 and 47 of System 2.

Case A-2: Hard Contact Reference Solution

206 DOF Total; System 1/Beam B 142 DOF; System 2 – Beam A 42 DOF and Ancillary 22 DOF.
Nonlinear Contacts of 10,000 lb/in at Beam A DOF 39 and 47 of System 2.

Case A-2.1: Hard Contact Reduced Model Solution with 21 Modes

21 DOF Total; Beam B – ADOF 65, 79, 89, 99, 109, 119, 149, 159, 169, 179, 189, 199 and 205;
Beam A – ADOF 31, 33, 39, 43, 47, 55, 57 and 61.
Nonlinear Contacts of 10,000 lb/in at Beam A ADOF 39 and 47 of System 2.

Case B: One Nonlinear Contact at System 2
Case B-1: Soft Contact Reference Solution

206 DOF Total; System 1/Beam B 142 DOF; System 2 – Beam A 42 DOF and Ancillary 22 DOF.
Nonlinear Contact of 100 lb/in at Ancillary DOF 11 of System 2.

Case B-1.1: Soft Contact Reduced Model Solution with 22 Modes with ADOF at Ancillary

22 DOF Total; Beam B – Modes 1–9 + 12, ADOF 65, 97, 117, 137, 157, 169, 177, 185, 199 and 205; Beam A – Modes 1–10 + 13 + 16, ADOF 11, 23, 29, 31, 33, 39, 43, 47, 51, 53, 55 and 63.
Nonlinear Contact 100 lb/in at Ancillary DOF 11 of System 2.

Case B-1.2: Soft Contact Reduced Model Solution with 18 Modes with No ADOF at Ancillary

18 DOF Total; Beam B – Modes 1–9 ADOF 65, 75, 97, 105, 127, 155, 169, 185, and 199;
Beam A – Modes 1–9 ADOF 25, 31, 35, 39, 43, 47, 53, 55 and 61.
Nonlinear Contact of 100 lb/in at Ancillary DOF 11 of System 2.

3.4.1 Case A: Two Nonlinear Contacts Between System 1 and System 2

3.4.1.1 Case A-1: Soft Contact Reference Solution

The NDOF unreduced subcomponents were tied together to form two systems, the support (System 1) and the top assembly (System 2). The frequencies and mode shapes of both untied and tied subcomponents were calculated for reference. The assembled 3 beam system consisting of the tied System 1 and System 2 was then tied together at full N-space and the nonlinear forced response calculated using the analytical input force of Fig. 3.9. The forced response of this NDOF (206 DOF) served as the reference solution for the reduced cases with two soft spring contacts (100 lb/in).

3.4.1.2 Component Mode Contribution – U_{12}

Calculation of the $[U_{12}]$ matrix for the system response is highly important to understand and mitigate the effects of truncation error in the reduction process. The modes from Systems 1 and System 2 required to preserve the first 5 modes of the assembled full 3 beam system were chosen using the resulting $[U_{12}]$ from all configurations (4 for Case A and 2 for Case B). Further considerations were made by taking the FFT of the response at the location of the input force and nonlinear contacts to verify if any additional modes were needed to characterize the system. As seen on the $[U_{12}]$ contribution matrix of Fig. 3.12, a total of 12 modes of the system components are required to preserve 5 modes of the assembled 3 beam system. Furthermore, mode 6 of System 2 has almost no contribution to the first 5 modes of the assembled system and could be excluded. System 1 (the blue support beam) contributes 5 modes to the reduced model while System 2 (the top red beam and its attached ancillary subcomponent) provides 7 modes. The larger contribution from system 2 is already an indication of the influence of the dynamics of the ancillary subcomponent. While some configurations required less modes than others, the maximum amount of modes in all configurations must be preserved. Moreover, Fig. 3.13 shows the FFT of the displacement

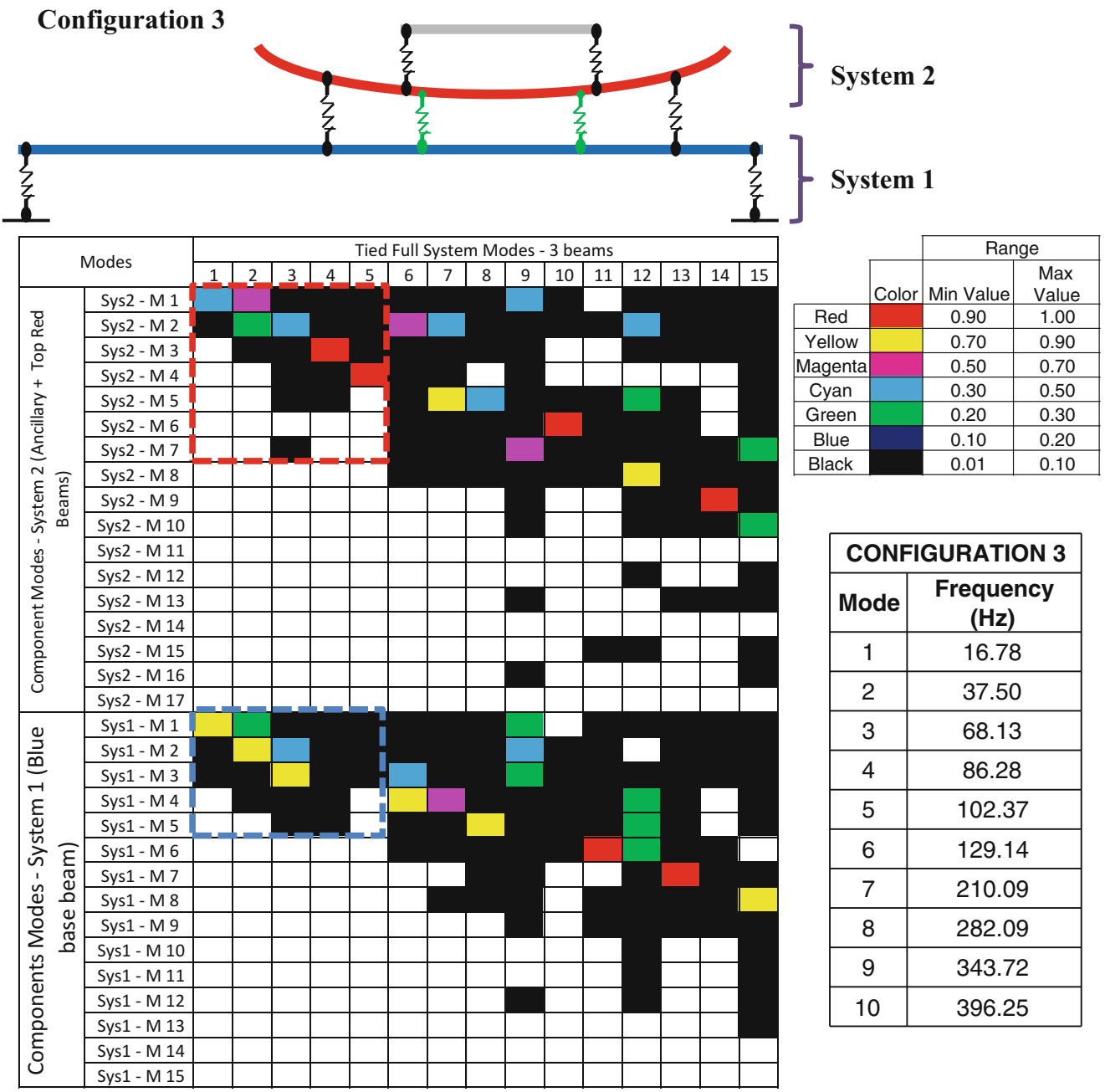

	Color	Range	
		Min Value	Max Value
Red		0.90	1.00
Yellow		0.70	0.90
Magenta		0.50	0.70
Cyan		0.30	0.50
Green		0.20	0.30
Blue		0.10	0.20
Black		0.01	0.10

CONFIGURATION 3	
Mode	**Frequency (Hz)**
1	16.78
2	37.50
3	68.13
4	86.28
5	102.37
6	129.14
7	210.09
8	282.09
9	343.72
10	396.25

Fig. 3.12 [U_{12}] matrices for configurations 3 showing the maximum number of modes needed from the components of the assembled 3 beam system

at point 39 and 47 (contact location 1 and 2) for Case A-1 indicating the need of additional modes in the reduced models due to the activation of higher order modes.

The first 5 modes of the system are in a 100 Hz band as observed in Fig. 3.12. However, the input force pulse has an excitation range of approximately 250 Hz, while the contact locations show additional modes being active in the region of 100–300 Hz as seen in Fig. 3.13. As discussed above, the [U_{12}] matrix indicates the need for 12 modes but as will be shown in the next case, additional modes are required for more accurate results.

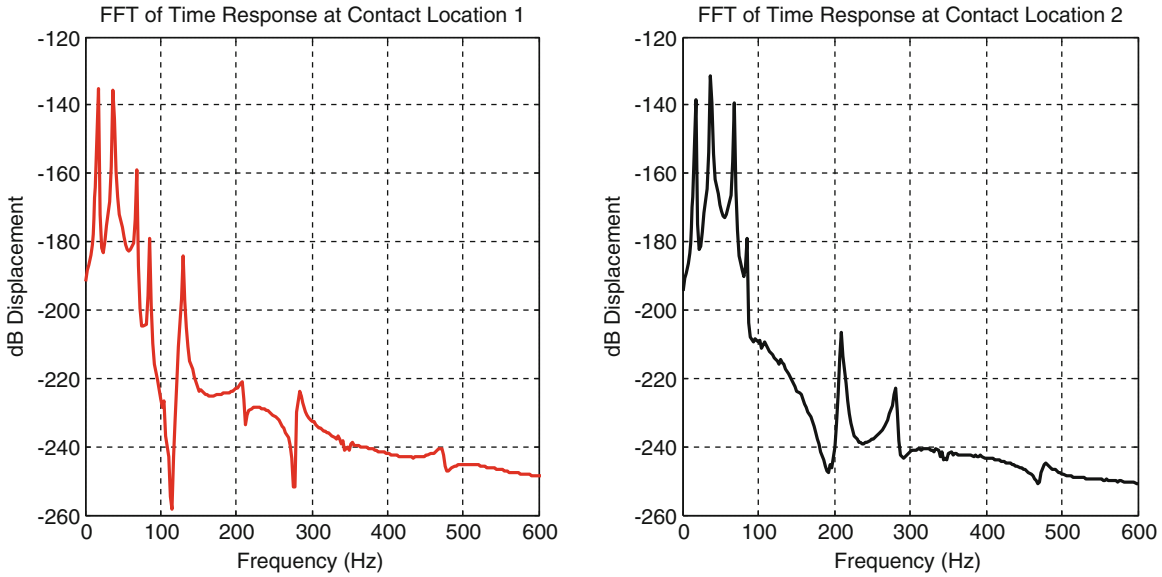

Fig. 3.13 FFT of reference time response at nonlinear soft contact locations

3.4.1.3 Overview of Reduction Process

The unconnected full space subcomponents (the 3 beams at NDOF) were first assembled into two components/assemblies, System 1 and System 2. The two systems are then connected and reduced to ADOF using SEREP reduction. The forced response is efficiently computed at ADOF and the transformation matrix of the unconnected components (obtained in the reduction process) is used to expand back to full space. The reduced models were created with emphasis in avoiding placement of active DOF at the ancillary subcomponent. The dynamics of this appendage must be predicted from the embedded information available in the reduction process. Moreover, note that only a single transformation matrix is needed for expansion even though the system goes through different configurations. This is possible because the mode shape projection vectors in the transformation matrix form a linearly independent set of vectors that span the space of the full space solution of the system. The process for the reduced model response calculation is shown in Fig. 3.14.

3.4.1.4 Case A-1.1: Soft Contact Reduced Model Solution with 12 Modes

A SEREP reduced model using 12 modes was created to illustrate the necessity for additional modes due to the interaction of the two contact springs in the response of the system. Using 12 modes for the system (5 from System 1 and 7 from System 2), the frequency range that is expected to have accurate time response prediction will likely only span about 100 Hz and is not really sufficient to obtain an accurate response. This case is included to clearly show that an appropriate set of modes must be selected otherwise poor results may be obtained; but this case does provide some results which are somewhat acceptable but can be greatly improved with the selection of more component modes which in turn provide better overall system modes. The ADOF selected were 23, 31, 39, 43, 47, 55 and 63 from Beam A and 65, 169, 179, 189, and 199 from Beam B. The nonlinear contacts occurred at ADOF 39 and 47 of System 2. Figure 3.15 shows the result of the expansion of this reduced model when compared to the full reference model of Case A-1.

While there is a good level correlation of the predicted response, the effect of the truncation of higher order modes is evident when taking a closer look at the response and FFT of the response at various points in the system. For instance, Fig. 3.16 shows the response at the contact 1 location. Using the information from the FFT and the $[U_{12}]$ matrix, a more accurate model can be obtained as will be shown in the next model.

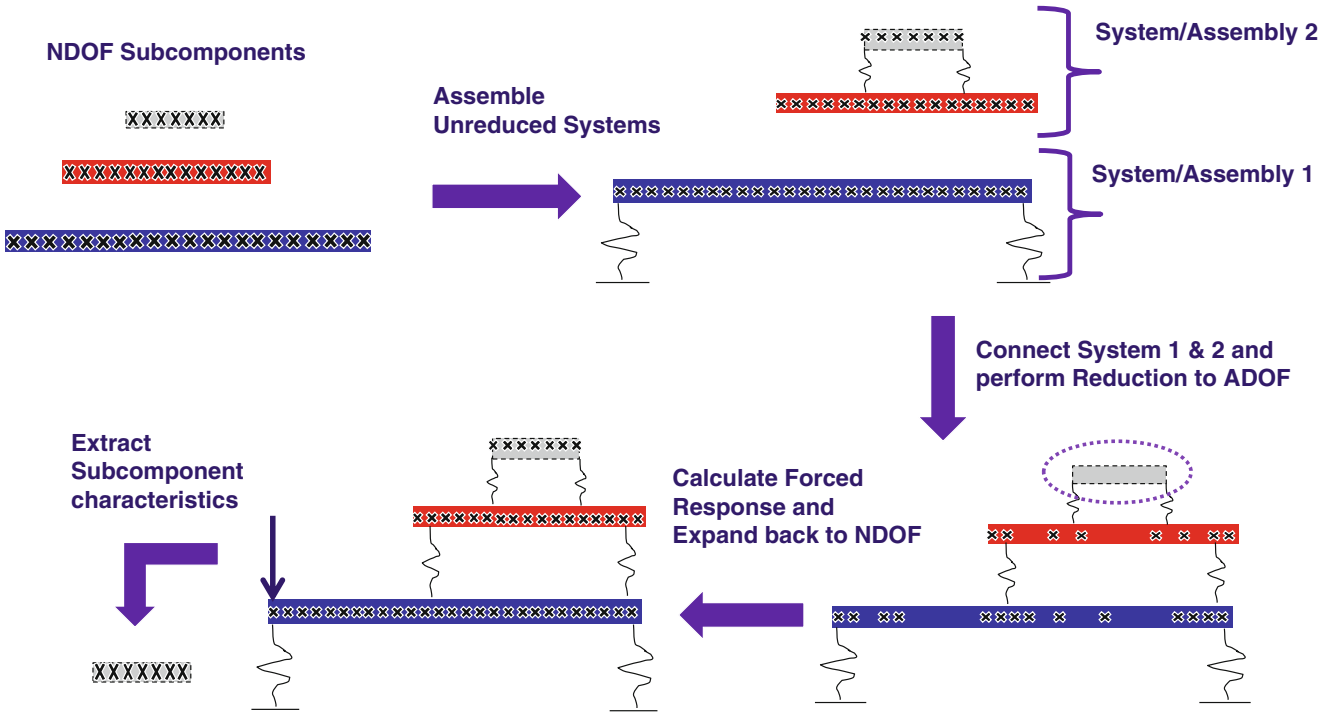

Fig. 3.14 Sequence for the development of reduced system response models

3.4.1.5 Case A-1.2: Soft Contact Reduced Model Solution with 16 Modes

A SEREP reduced model using 16 modes (8 from System 1 and 8 from System 2) was created in similar manner to that of the previous model (Case A-1.1). The ADOF selected were 23, 31, 35, 39, 43, 47, 55 and 63 from Beam A and 65, 99, 135, 169, 179, 189, 199 and 205 from Beam B. The nonlinear contacts occurred at ADOF 39 and 47 of System 2. Figure 3.17 shows the relevant portion of the $[U_{12}]$ matrix and Fig. 3.18 the comparison of the predicted response of the new model and the reference model.

Using 16 modes allows for the accurate prediction of up to 8 modes (which spans approximately 300 Hz) of the 3 beam assembled system. Comparing Figs. 3.15 and 3.18 show significant gain in accuracy across all DOF due to the addition of 4 modes to the reduced model. Figure 3.19 shows the comparison of the FFT of the displacement at the spring contact location 1 (in the same manner of that of Fig. 3.16).

The FFT of the displacement at contact location 1 in Fig. 3.19 shows that the effect of the mode truncation of the higher order modes has been highly reduced and the response is a more accurate approximation of the full NDOF solution. Note that no ADOF has been placed at the ancillary subcomponent or at the DOFs that connect the ancillary to Beam A but nevertheless the embedded information in the reduction process has successfully allowed the prediction of the time response at all NDOF.

The effect of higher order modes can be exacerbated if the type of contact is hard impact, thus producing a narrow time pulse that translates into a high order pulse in the frequency domain. The next case will explore a hard contact spring acting at two locations of the structure. A comparison of the two types of contacts, soft and hard, can be seen in Fig. 3.20.

3.4.1.6 Case A-2: Hard Contact Reference Solution

Nonlinear contacts of 10,000 lb/in were implemented instead of the soft contacts of 100 lb/in previously used. The response at NDOF was calculated for use as a reference in the next reduced model cases. New $[U_{12}]$ matrices were calculated for the 4 configurations of Case A using the hard contact. Taking the FFT of the displacement at the contact locations showed that the response is affected by a much larger range of modes as seen in Fig. 3.21.

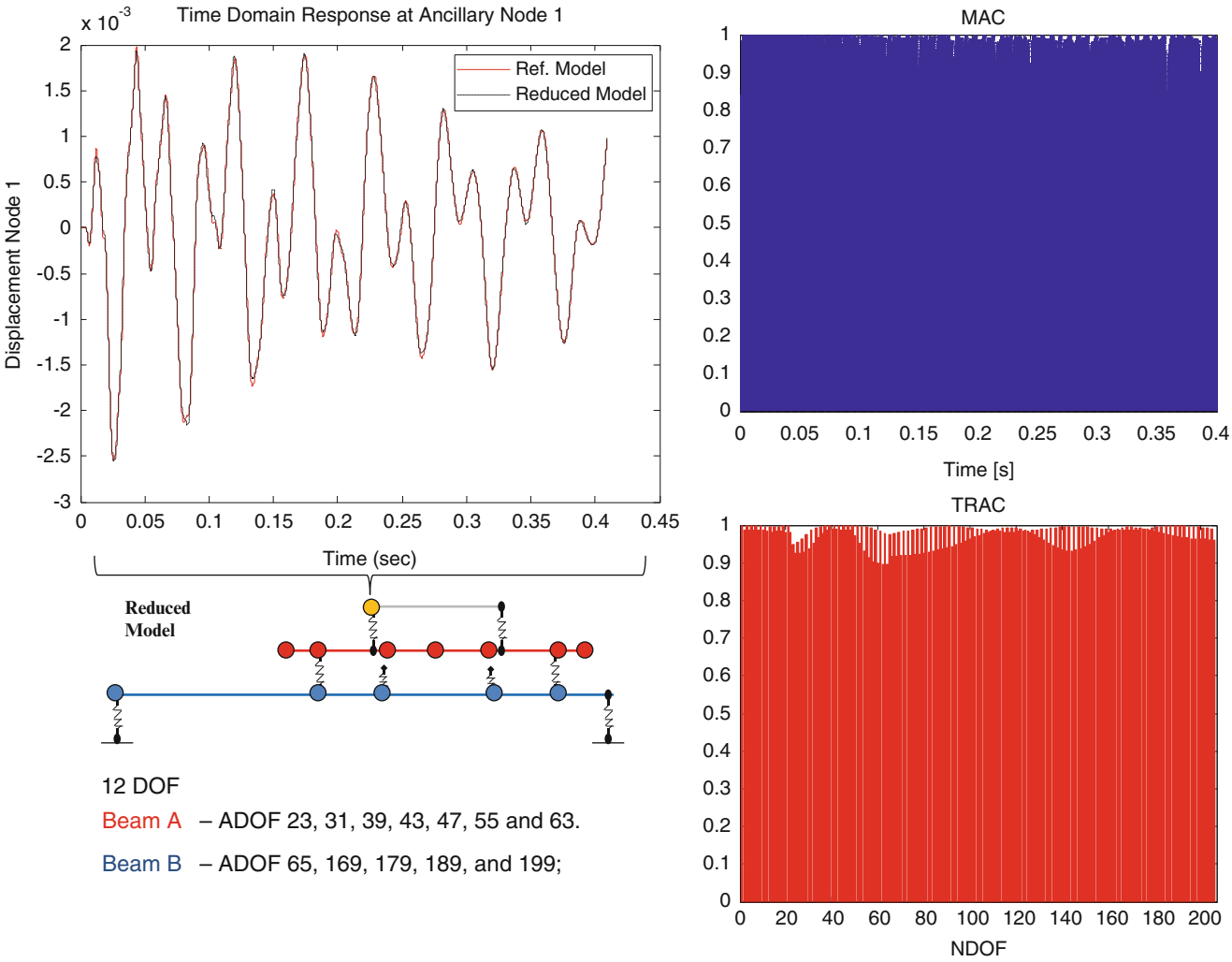

Fig. 3.15 Predicted response at ancillary from 12 DOF reduced model. MAC (*top right*) and TRAC (*bottom right*)

Figure 3.21 shows that the response of the 3 beam system with hard contacts involves high frequency modes well above 500 Hz which means up to 12 modes (or more) may be needed to accurately predict the response of the system. Figure 3.21 also list the frequencies of the hard contact case for the 4 possible configurations.

3.4.1.7 Case A-2.1: Hard Contact Reduced Model Solution with 21 Modes

Because the hard contact excites frequencies in the range of 700 Hz, the 14 or 16 mode models previously used cannot give the best approximation of the response of the system. The selection of modes preserved in the reduction must form a linearly independent set of vectors spanning the space of the full response of the system. In other words, the selected projection vectors in the transformation matrix must be able to approximate any other vector in the space as linear combinations of the mode shape vectors preserved in the reduced space. Figure 3.22 shows the $[U_{12}]$ matrix for the hard contact case using the modes of the configuration with the largest set of active modes needed to preserve the first 5 modes of the system. The red and blue squares show the modes needed to preserve the first 5 modes of the system when no additional modes are active. The green squares show the additional modes used in this case to better approximate the influence of the higher order modes due to the hard contact interactions.

The ADOF selected were 31, 33, 39, 43, 47, 55, 57 and 61 from Beam A, and ADOF 65, 79, 89, 99, 109, 119, 149, 159, 169, 179, 189, 199 and 205 from Beam B. The nonlinear contacts occurred at ADOF 39 and 47 of System 2 like in previous

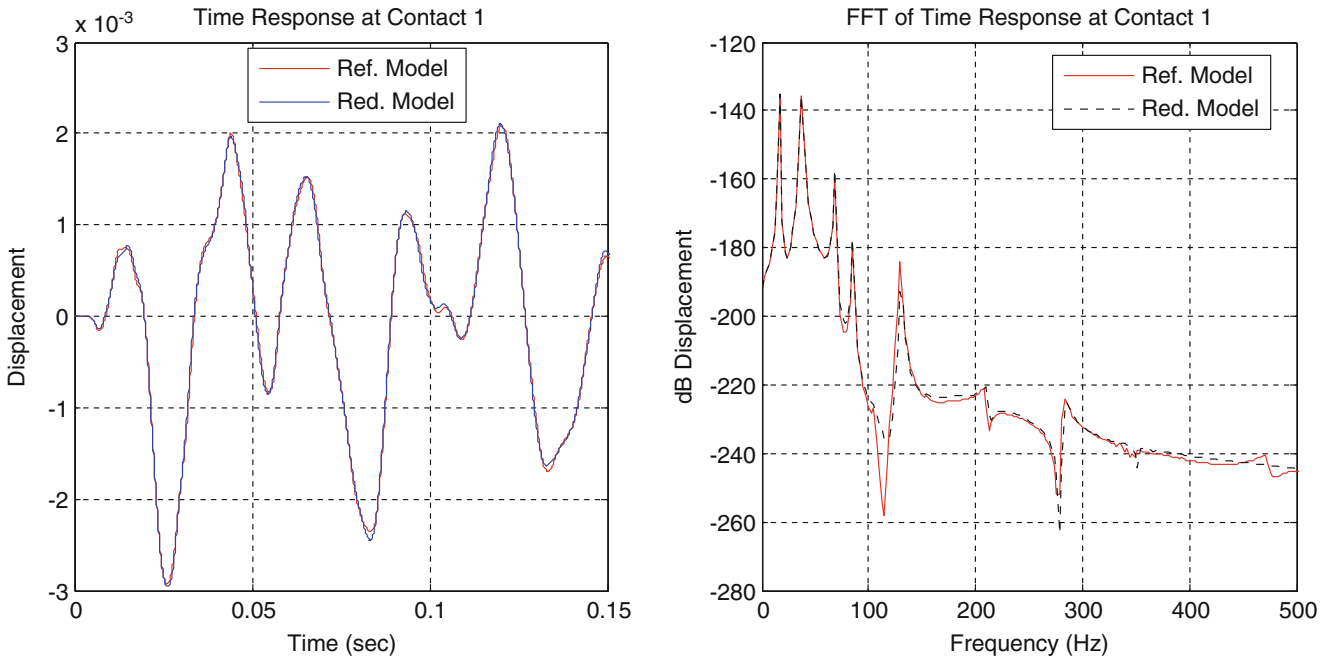

Fig. 3.16 Comparison of response (*left*) and FFT (*right*) of reference and reduced order model at spring contact location 1

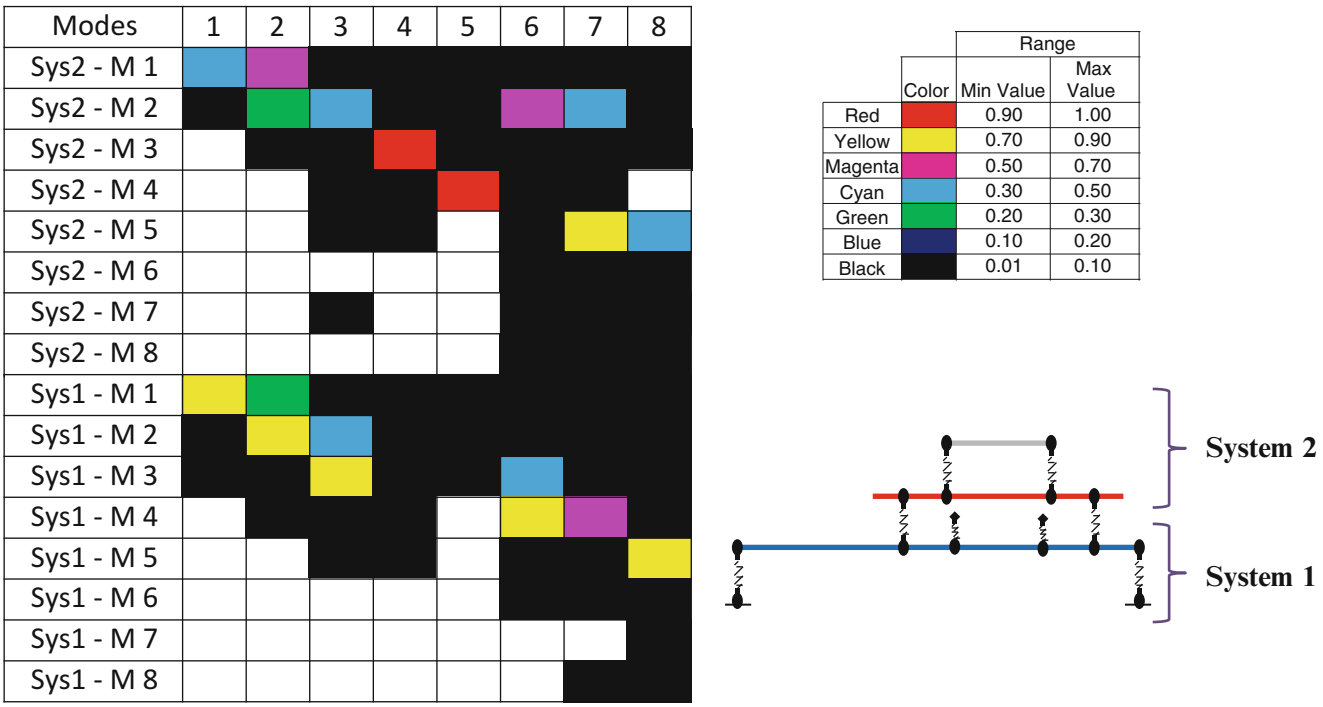

Fig. 3.17 [U_{12}] contribution matrix for model using 8 modes of each System 1 and System 2 for a total of 16 modes

cases. Note that no ADOF are placed at the ancillary subcomponent and/or connecting DOF between the ancillary and Beam A. Figure 3.23 shows the correlation and response for the 21 DOF model and the reference model.

The modes used in the reduced model resulted in an accurate approximation of the response of the NDOF system. However, the effects of mode truncation could not be completely mitigated. Additional modes could have been added, in particular for System 2. However, the 8 modes used and the ADOF selected from System 2 resulted in a more well-conditioned transformation matrix than by randomly adding DOF to the reduced model. The reduced space matrices can

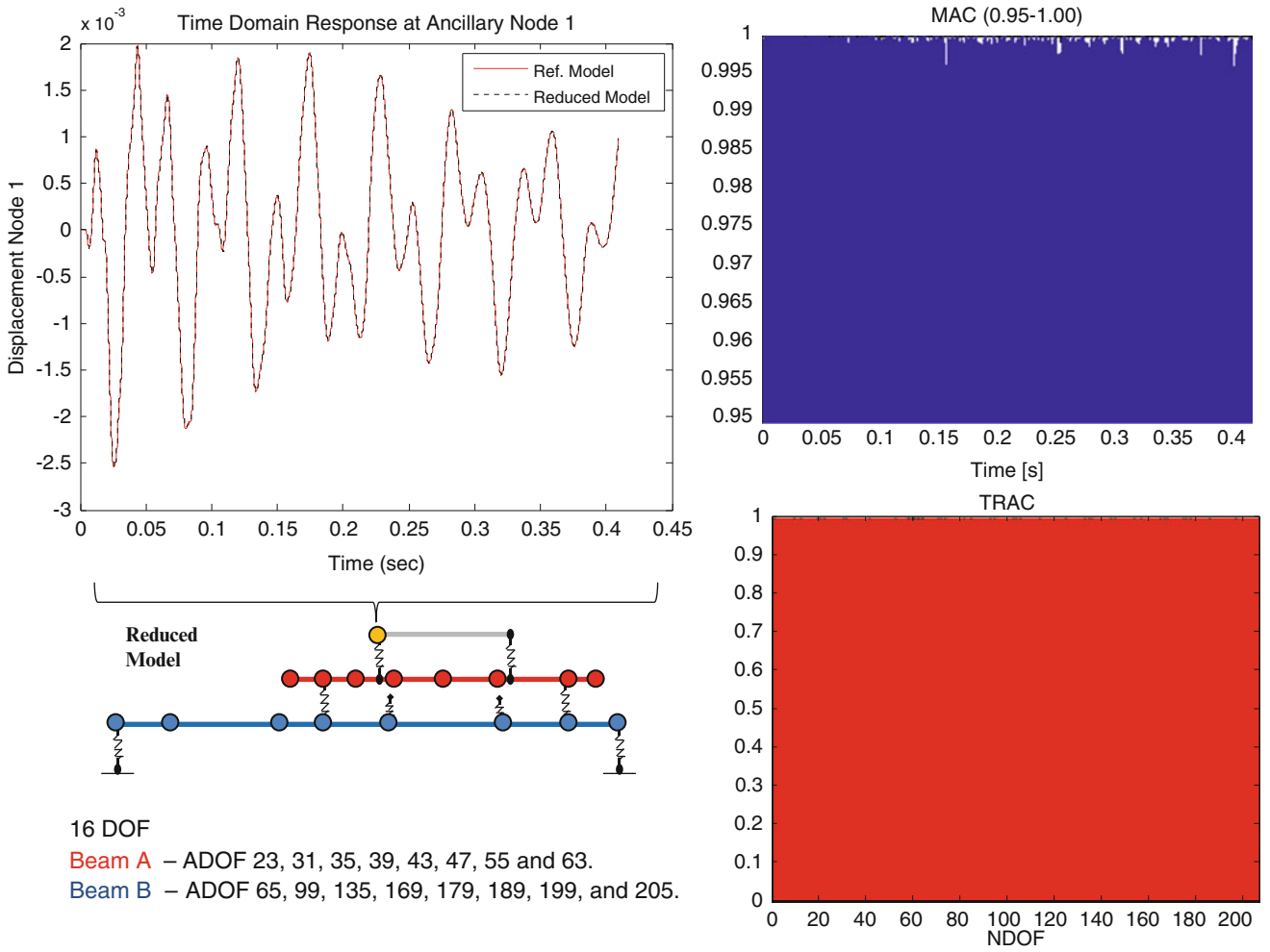

Fig. 3.18 Predicted response at ancillary node 1 from 16 DOF reduced model. MAC from 0.95 to 1.0 (*top right*) and TRAC (*bottom right*) correlation of models

become ill-conditioned for certain choice and number of DOF and the predicted response is then subjected to high levels of numerical error. Nevertheless, Fig. 3.24 shows that the FFT and response at the contact location 1 is reasonably approximated by the reduced model of 21 modes.

The cases considered thus far have shown that full field results can be obtained from reduced order models with subcomponent interactions from the embedded information preserved in the reduction process. Using the necessary number of modes in the reduced model to span the space of all modes of interest allows the response at the ancillary and any other DOF to be predicted accurately. The $[U_{12}]$ contribution matrix and the effect of the higher order modes from nonlinear interactions must be taken into account as well as the linear independence and well-determined behavior of the reduced matrices in order to obtain a good approximation of the dynamic characteristics of the system. Moreover, when proper precautions are taken to reduce the N space system to 'a' space, no ADOF are needed in the dynamically active ancillary subcomponent.

The next set of cases explores the natural extension of this work to include nonlinear contacts occurring at the ancillary subcomponent. For all the reduced models of Case A the nonlinear contact occurred at points that were preserved in the reduction process. This was done in order to check for a change of state in the system due to the springs coming in contact at those locations. However, if the contact were to occur at the ancillary subcomponent the response must be tracked at that location in order to know how the system is changing from one configuration to the other as will be discussed next.

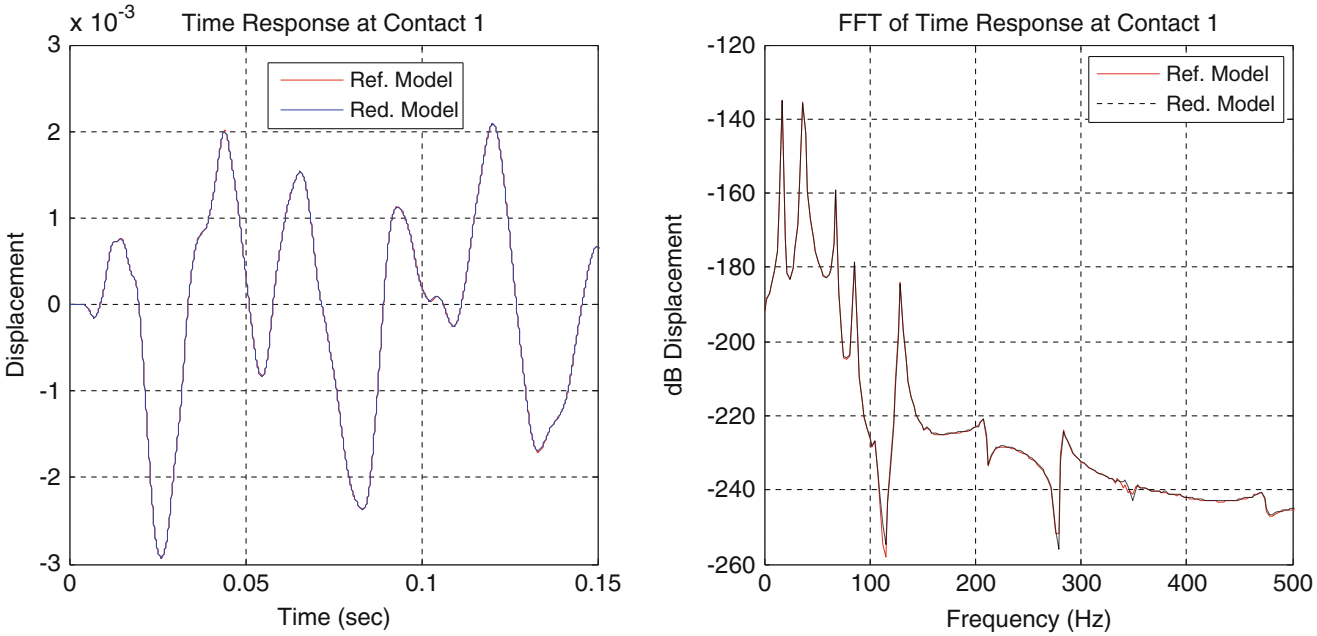

Fig. 3.19 Comparison of response (*left*) and FFT (*right*) of reference and 16 mode reduced order model at spring contact location 1

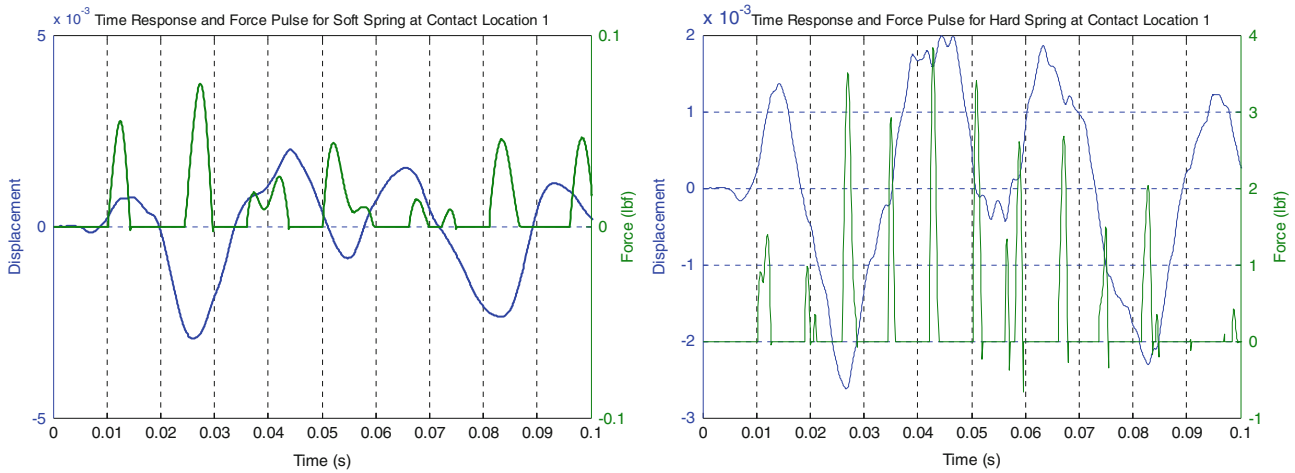

Fig. 3.20 Comparison of soft (*left*) and hard (*right*) type of nonlinear contacts at DOF 37 of the 3 beam system

3.4.2 Case B: One Nonlinear Contact at System 2

3.4.2.1 Case B-1: Soft Contact Reference Solution

The assembled 3 beam structure consisting of System 1 and System 2 (as shown in Fig. 3.1) was constructed with a single nonlinear contact of a 100 lb/in spring. The contact occurs between the ancillary subcomponent (at DOF 11) and Beam A of System 2. The full NDOF (206) response with the new contact configuration (as shown in Fig. 3.10) was calculated for used as a reference with the reduced order models. New $[U_{12}]$ contribution matrices were computed for the two possible configurations of Case B, one when the spring is not in contact and configuration 1 when the spring comes in contact with the ancillary subcomponent. As previously done in Case A, the necessary modes for an accurate prediction of the response were selected from the contribution matrix and with consideration to the higher modes that will be excited due to the hard contact nonlinear connections. Two cases are studied – one with an active DOF at the contact point and one without an active DOF at the contact point; this was studied to determine the effect of location of the active DOF.

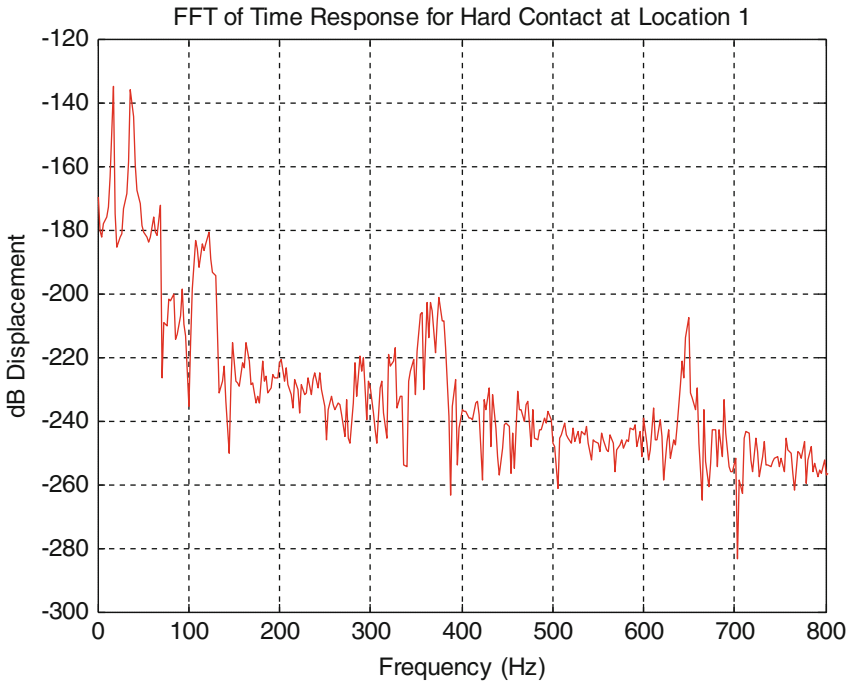

Mode	Frequency (Hz)			
	Conf. 0	Conf. 1	Conf. 2	Conf. 3
1	16.78	16.78	16.78	16.78
2	37.50	37.53	37.52	37.53
3	68.11	68.35	68.25	68.36
4	84.61	98.75	98.86	99.19
5	102.08	125.29	128.83	128.84
6	129.11	144.23	138.43	170.42
7	209.96	215.02	215.85	219.30
8	282.02	282.14	286.27	287.29
9	342.95	380.51	376.62	396.23
10	396.25	396.26	396.47	415.99
11	477.32	478.28	486.09	492.62
12	645.25	679.21	659.51	689.08
13	716.29	717.68	726.23	726.42
14	889.02	889.06	889.04	889.08
15	960.58	960.58	967.53	967.53

Fig. 3.21 FFT of reference NDOF model response at contact location 1 for hard spring (10,000 lb/in) contact

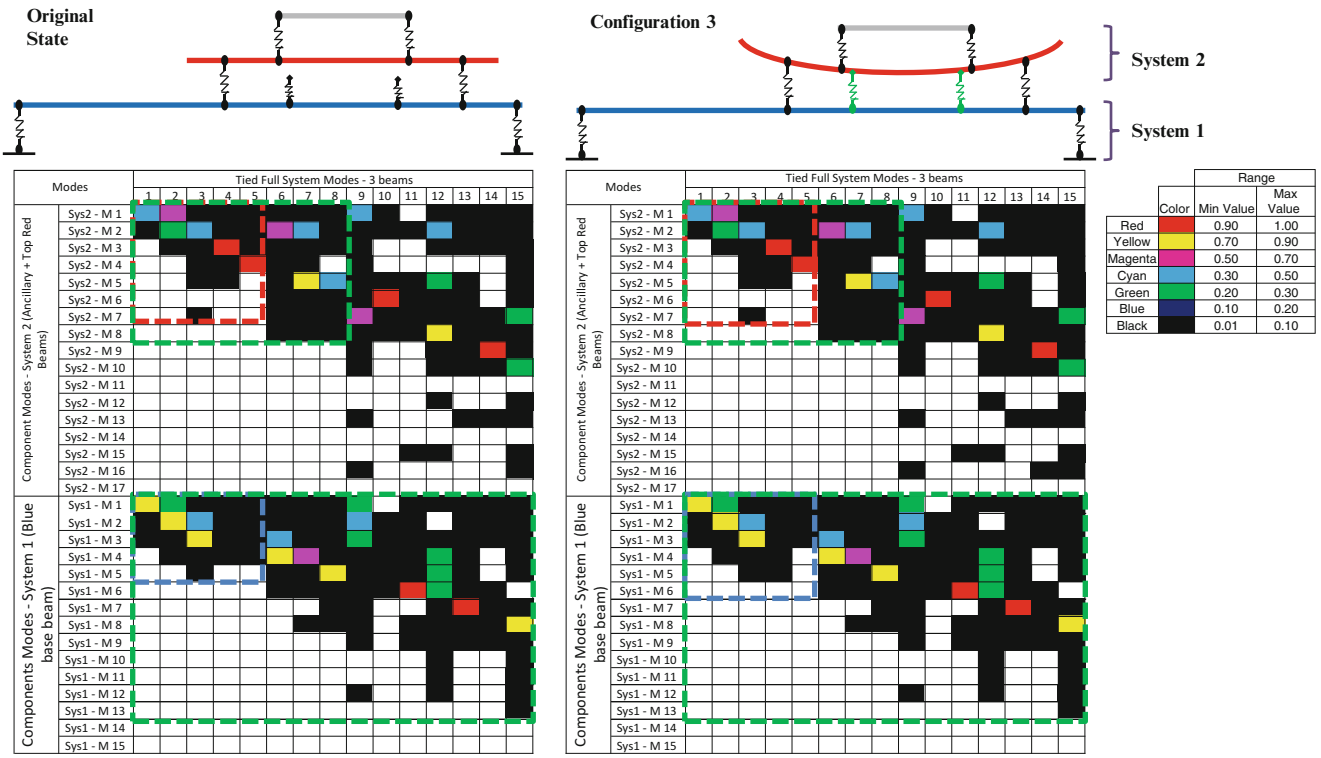

Fig. 3.22 $[U_{12}]$ matrices for configurations 0 and 3 in the hard contact case. *Blue squares* indicate modes needed from System 1, while the *red squares* indicate modes needed from System 2. *Green squares* show additional modes included due to active higher order modes in the response of the system

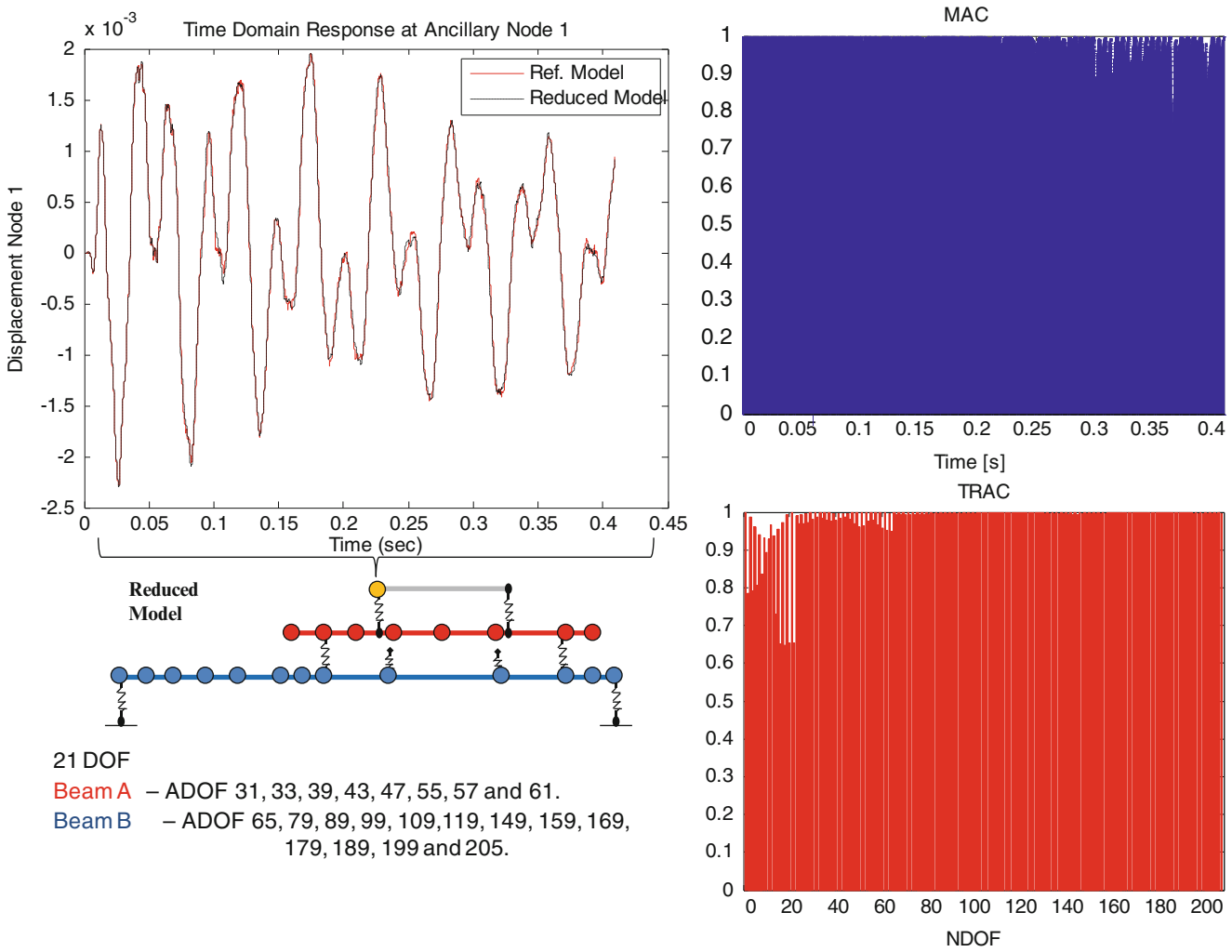

Fig. 3.23 Predicted response at ancillary node 1 from 21 DOF reduced model with hard contacts. MAC (*top right*) and TRAC (*bottom right*) correlation of models

3.4.2.2 Case B-1.1: Soft Contact Reduced Model Solution with 22 Modes with ADOF at Ancillary

A SEREP reduced model of 22 ADOF was computed using modes 1–9 and mode 12, ADOF 65, 97, 117, 137, 157, 169, 177, 185, 199 and 205 from Beam B and modes 1–10, 13 and 16, ADOF 11, 23, 29, 31, 33, 39, 43, 47, 51, 53, 55 and 63 from Beam A. Note that the nonlinear contact of 100 lb/in occurs at Ancillary DOF 11 of System 2 and this point is included in the reduced model. The modes were selected from the $[U_{12}]$ contribution matrix showing the proper number of component modes needed to form the modes of the assembled 3 beam system. Figure 3.25 shows a comparison of the displacement and FFT of the response at the contact location on the ancillary (DOF 11).

Figure 3.26 shows the displacement at node 1 of the ancillary along with the correlation of the reduced model and the reference model. The models showed high levels of correlation at all DOF. However, there are some minor differences that can be observed in the FFT of Fig. 3.25.

The differences can be attributed as in previous cases to the effect of higher order modes. The FFT of the reference model shows active high order modes above 800 Hz which occurs in the vicinity of the 18th mode of the system. Therefore, prediction of the response at all DOF with high accuracy requires modes beyond the 14 modes involved in forming the first 7 modes of the system (those modes active from the input force alone). One of the main objectives of this work is the prediction at the subcomponent level from the embedded component information in the reduction process. The next case will explore whether is possible to compute the dynamic response of the ancillary subcomponent when the nonlinear contact occurs at a DOF not in the reduced model.

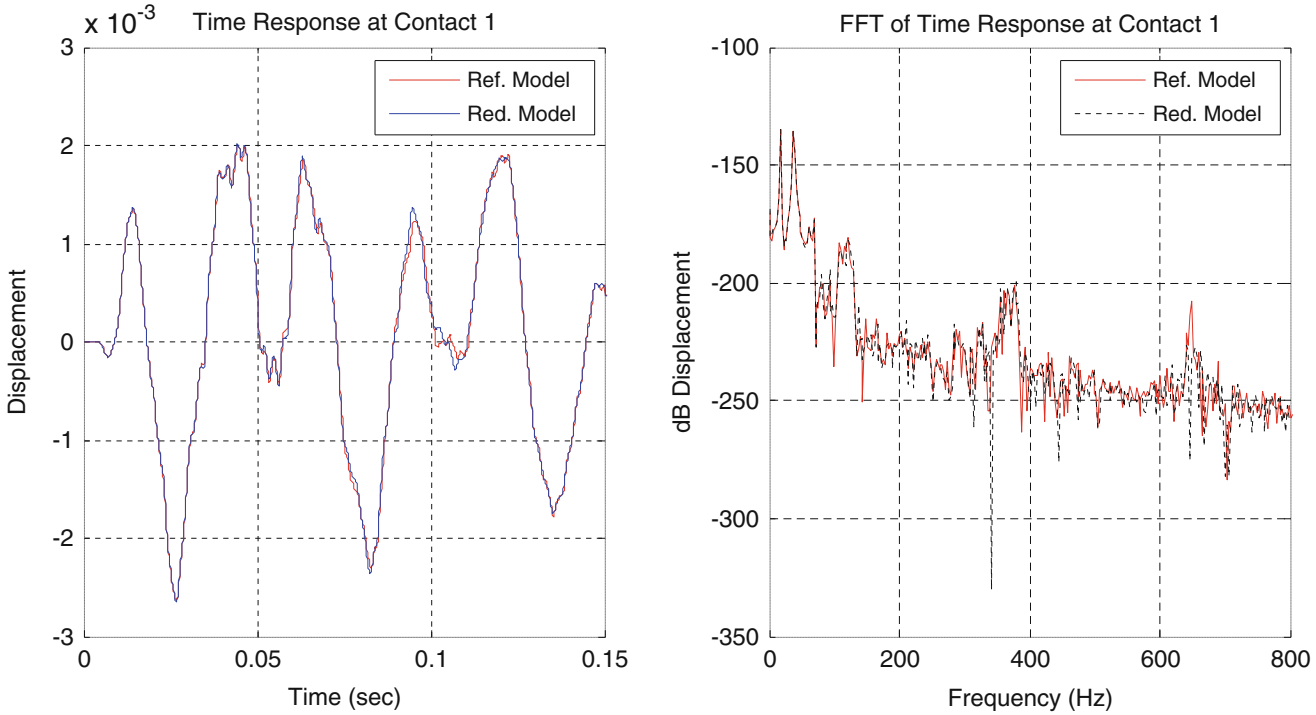

Fig. 3.24 Comparison of response (*left*) and FFT (*right*) of reference and 21 DOF reduced order model at contact location 1

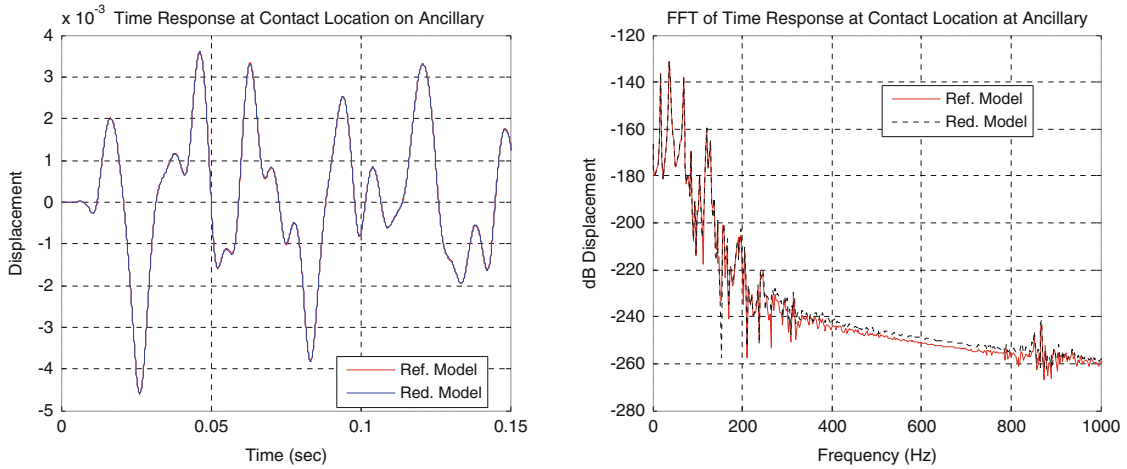

Fig. 3.25 Comparison of response (*left*) and FFT (*right*) of reference and 22 DOF reduced order model at contact location

3.4.2.3 Case B-1.2: Soft Contact Reduced Model Solution with 18 Modes with No ADOF at Ancillary

In a similar manner to that of the previous case, a reduced model of 18 modes was created without the use of an active DOF at point 11 where the nonlinear contact occurs. The reduced model consisted of modes 1–9, ADOF 65, 75, 97, 105, 127, 155, 169, 185, and 199 from Beam B and modes 1–9, ADOF 25, 31, 35, 39, 43, 47, 53, 55 and 61 from Beam A. The nonlinear contact of 100 lb/in was placed at Ancillary DOF 11 of System 2 but no ADOF were selected on the ancillary subcomponent or the connecting DOF between Beam A and the ancillary. In order to check for a change of configuration during the time response of the reduced model, the algorithm used the expansion of the displacement at time t_i for DOF 11 and then continued to the next time step t_{i+1} making the necessary adjustments if the spring came in contact with the ancillary subcomponent. Only the response at DOF 11 was expanded throughout the response since no other DOF are needed during the computation of the reduced model response. The response at 'a' space was expanded to NDOF using the transformation

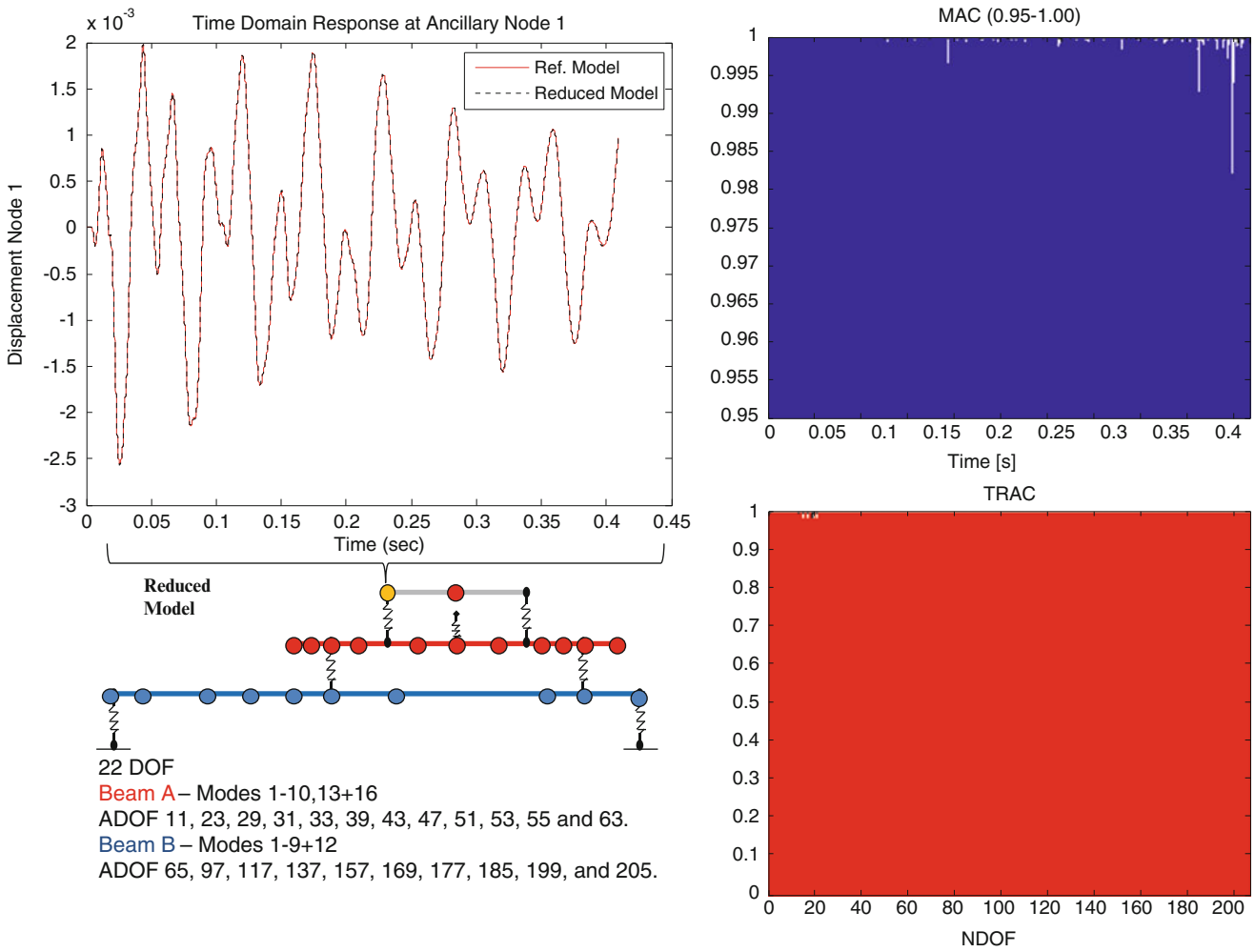

Fig. 3.26 Predicted response at ancillary node 1 from 22 DOF reduced model with soft contact. MAC from 0.95 to 1.0 (*top right*) and TRAC (*bottom right*) correlation of models

matrices (mode shape projection vectors) from the reduction process. Figure 3.27 shows a comparison of the response at point 1 of the ancillary as well as the correlation with the reference model.

The results of this reduced model show that there is an accumulation of error in the predicted system response which may be due to both mode truncation and numerical issues; but additional cases need to be explored before this is more clearly understood. Figure 3.28 shows a comparison of the response and its FFT at the contact location. In the previous case, the contact point was included in the active set of DOF. In this case, the contact point was not included. The results obtained were not as accurate and well behaved as in the previous case. This may be due to many different factors such as numerical issues, rank problems, need for more modes, and many other factors which need to be addressed in future work.

3.5 Conclusions

Nonlinear models of a multiple component structure were created to illustrate the prediction of subcomponent dynamic characteristics from embedded information in the reduction process. Models with multiple and single nonlinear contacts were considering as well as the effect of soft and hard contacts in the response. When enough modes of the unconnected components are preserved such that they form a linearly independent set of vectors spanning the space of the full response, the response was accurately predicted at all DOF of the system. The prediction at the ancillary subcomponent was successfully performed even when no active DOF were preserved in the reduced model. Additional work is needed in order to further

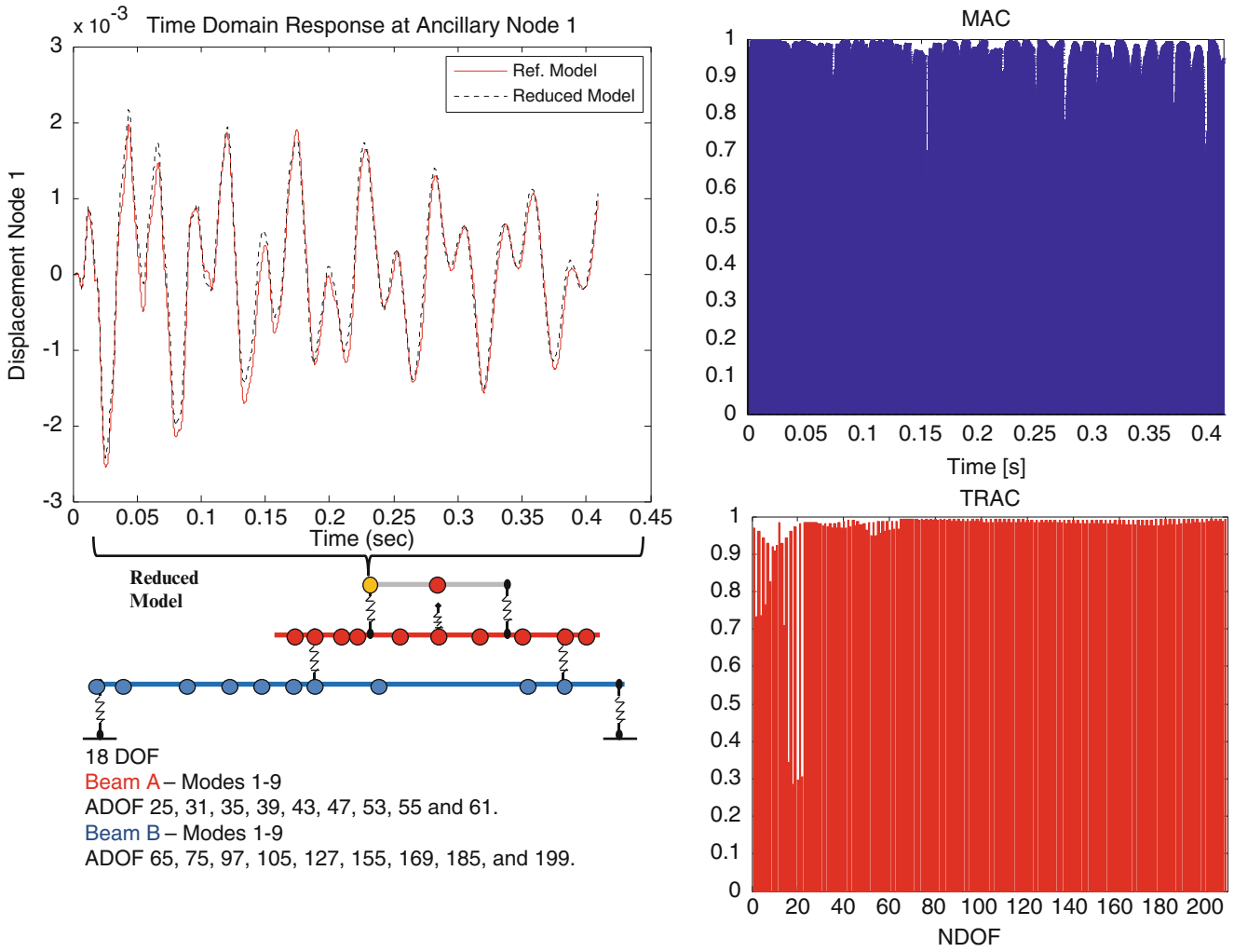

Fig. 3.27 Predicted response at ancillary node 1 from 18 DOF reduced model with soft contact. MAC (*top right*) and TRAC (*bottom right*) correlation of models

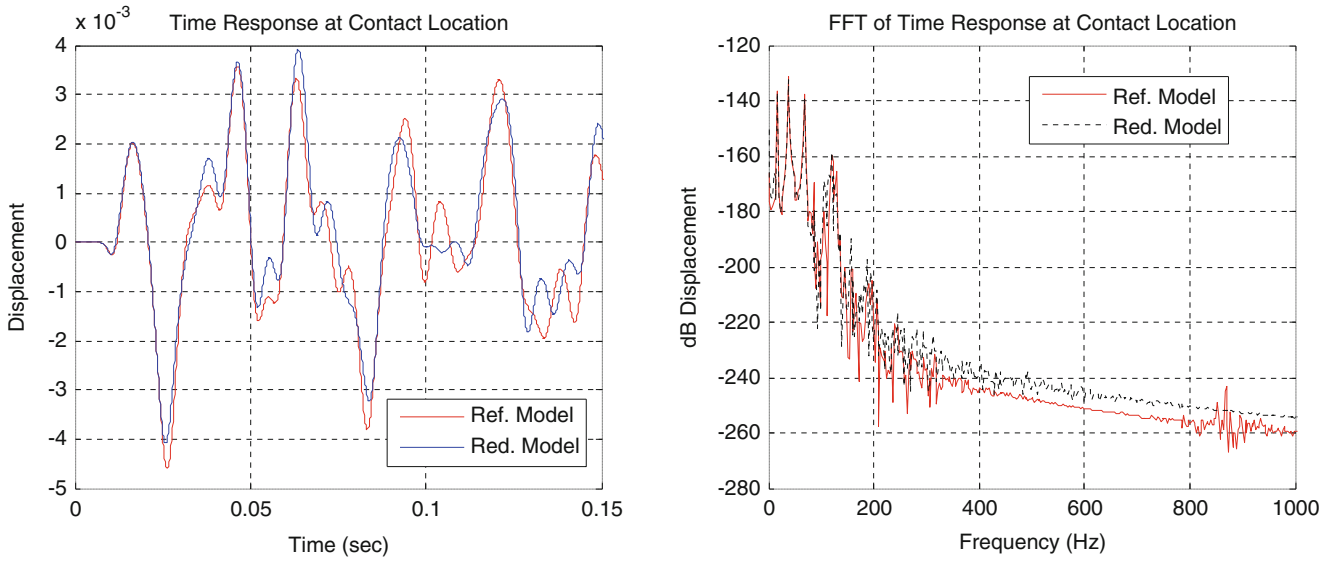

Fig. 3.28 Comparison of response (*left*) and FFT (*right*) of reference and 18 DOF reduced order model at contact location

study the effects of including the contact point as one of the active DOF for the reduced order model. Nevertheless, this work shows significant promise in the prediction of linear and nonlinear subcomponent response in cases where is not possible to place ADOF at the subcomponent level.

Acknowledgements Some of the work presented herein was partially funded by Air Force Research Laboratory Award No. FA8651-10-1-0009 "Development of Dynamic Response Modeling Techniques for Linear Modal Components". Any opinions, findings, and conclusions or recommendations expressed in this material are those of the authors and do not necessarily reflect the views of the particular funding agency. The authors are grateful for the support obtained.

References

1. Thibault L (2012) Development of equivalent reduced model technique for linear modal components interconnected with nonlinear connection elements. Master's thesis, University of Massachusetts Lowell
2. Thibault L, Avitabile P, Foley J, Wolfson J (2013) Equivalent reduced model technique for nonlinear dynamic response. Mech Syst Signal Process 36:422–455. doi:10.1016/j.ymssp.2012.07.013
3. Thibault L, Avitabile P, Foley J, Wolfson J (2012) Equivalent reduced model technique for nonlinear dynamic response. Proceedings of the thirtieth international modal analysis conference, Jacksonville
4. Marinone T, Avitabile P, Foley J, Wolfson J (2012) Efficient computational nonlinear dynamic analysis using modal modification response technique. Mech Syst Signal Process 31:67–93. doi:10.1016/j.ymssp.2012.02.011
5. Marinone T (2012) Efficient computational nonlinear dynamic analysis using modal modification response technique. Master's thesis, University of Massachusetts Lowell
6. Marinone T, Thibault L, Avitabile P (2013) Expansion of nonlinear system response using linear transformation matrices from reduced component model representations. In: Proceedings of the thirty-first international modal analysis conference, Garden Grove
7. Pingle P, Niezrecki C, Avitabile P (2011) Full field numerical stress-strain from dynamic experimental measured data. In: EURODYN 2011, Leuven
8. Avitabile P, Pingle P (2012) Prediction of full field dynamic strain from limited sets of measured data. Shock Vib 19:765–785. doi:10.3233/SAV-2012-0686
9. Pingle P, Avitabile P (2010) Prediction of full field dynamic stress/strain from limited sets of measured data. In: Proceedings of the twenty-eighth international modal analysis conference, Jacksonville
10. Pingle P, Avitabile P (2011) Limited experimental displacement data used for obtaining full-field dynamic stress/strain. In: Proceedings of the twenty-ninth international modal analysis conference, Jacksonville
11. Pingle P, Avitabile P (2011) Full field dynamic stress/strain estimation from limited sets of measured data. In: Proceedings of the twenty-ninth international modal analysis conference, Jacksonville
12. Pingle P (2010) Prediction of full-field dynamic stress/strain from limited sets of measured data. Ph.D. dissertation, University of Massachusetts Lowell
13. Carr J, Baqersad J, Niezrecki C, Avitabile P (2013) Predicting dynamic strain on wind turbine blade using digital image correlation techniques in conjunction with analytical expansion methodologies. In: Proceedings of the thirty-first international modal analysis conference, Garden Grove
14. Carr J, Baqersad J, Niezrecki C, Avitabile P (2012) Dynamic stress–strain on turbine blade using digital image correlation techniques, part 1 – static calibration. In: Proceedings of the thirtieth international modal analysis conference, Jacksonville
15. Carr J, Baqersad J, Niezrecki C, Avitabile P (2012) Dynamic stress–strain on turbine blade using digital image correlation techniques, part 2 – dynamic measurements. In: Proceedings of the thirtieth international modal analysis conference, Jacksonville
16. Carr J (2013) Application of dynamic expansion from limited measurements for full-field stress/strain on wind turbine blades. Master's thesis, University of Massachusetts Lowell
17. Harvie J (2013) Computationally efficient reduced order models for full field nonlinear dynamic strain predictions. Master's thesis, University of Massachusetts Lowell
18. Harvie J, Obando S, Avitabile P (2013) Reduced order system model nonlinear response and expansion for full field results. In: Eleventh international conference on recent advances in structural dynamics, Pisa
19. Avitabile P, Obando SE, Truong K (2014) Full field dynamic deflection and strain for linear components connected with nonlinear connectors. In: Proceedings of ISMA 2014 international conference on noise and vibration engineering, Leuven
20. Avitabile P, Harvie J, Obando SE (2014) Efficient reduced order nonlinear response with expansion for full field results. In: Proceedings of the 9th international conference on structural dynamics, EURODYN 2014, Porto
21. Avitabile P, Nonis C, Obando S (2014) System model modes developed from expansion of uncoupled component dynamic data. Stroj vestn-J Mech Eng 60(5):287–297
22. Nonis C, Thibault L, Marinone T, Avitabile P (2013) Development of full space system model modes from expansion of reduced order component modal information. In: Proceedings of the thirty-first international modal analysis conference, Los Angeles
23. Obando S, Avitabile P (2014) Prediction of forced response on ancillary subsystem components attached to reduced linear systems, vol 1, Dynamics of coupled structures. Springer, Berlin, pp 51–72
24. O'Callahan JC, Avitabile P, Riemer R (1989) System equivalent reduction expansion process. In: Proceedings of the seventh international modal analysis conference, Las Vegas
25. Avitabile P (2003) Twenty years of structural dynamic modification – a review. Sound and Vibration Magazine, pp 14–27
26. Guyan RJ (1965) Reduction of stiffness and mass matrices. AIAA J 3(2):380

27. O'Callahan JC (1989) A procedure for an Improved Reduced System (IRS) model. In: Proceedings of the seventh international modal analysis conference, Las Vegas
28. Obando SE, Avitabile P (2015) Prediction of forced response using expansion of perturbed reduced order models with inexact representation of system modes. In: Proceedings of the thirty-third international modal analysis conference, Orlando (to be published)
29. Newmark NM (1959) A method of computation for structural dynamics. J Eng Mech Div Am Soc Civ Eng 85(3):67–94
30. Chipman C, Avitabile P (2012) Expansion of transient operating data. Mech Syst Signal Process. 10.1016/j.ymssp.2012.04.013. Accepted Apr 2012
31. Chipman C, Avitabile P (2009) Expansion of transient operating data. In: Proceedings of the twenty-seventh international modal analysis conference, Orlando
32. Chipman C, Avitabile P (2008) Expansion of real time operating data for improved visualization. In: Proceedings of the twenty-sixth international modal analysis conference, Orlando
33. Chipman C (2009) Expansion of real time operating data. Master's thesis, University of Massachusetts Lowell
34. Allemang RJ, Brown DL (2007) A correlation coefficient for modal vector analysis. In: Proceedings of the first international modal analysis conference, Orlando
35. Van Zandt T (2006) Development of efficient reduced models for multi-body dynamics simulations of helicopter wing missile configurations. Master's thesis, University of Massachusetts Lowell
36. MAT_SAP/MATRIX (1986) A general linear algebra operation program for matrix analysis, Dr. John O'Callahan, University of Massachusetts Lowell
37. MATLAB R2010a, The MathWorks Inc., Natick

Chapter 4
Numerical Round Robin for Prediction of Dissipation in Lap Joints

L. Salles, C. Swacek, R.M. Lacayo, P. Reuss, M.R.W. Brake, and C.W. Schwingshackl

Abstract Joints, interfaces, and frictional contact between two substructures can be modelled as discrete nonlinearities that connect the substructures. Over the past decade, a number of phenomenologically different approaches to modelling and simulating the dynamics of a jointed structure have been proposed. This research focuses on assessing multiple modelling techniques to predict the nonlinear dynamic behaviour of a bolted lab joint, including frequency based sub-structuring methods, harmonic balance methods, discontinuous basis function methods, and high fidelity FEA approaches. The regimes in which each method is best suited are identified, and recommendations are made for how to select a modelling method and for advancing numerical modelling of discrete nonlinearities.

Keywords Nonlinear damping • Nonlinear vibration • Numerical modelling • Bolted joints • Lap joints

4.1 Introduction

The assembly of single components into a more complex structure always leads to the presence of a joint. Different assembly methods are available today, ranging from permanent connections such as welds and adhesives, to separable ones such as bolts, rivets or hooked connections. Depending on the selected joint type it represents a change in the design, and has an impact on the static and dynamic performance of the assembly. For an accurate prediction of the dynamic behaviour of the assembly the special dynamics of the joint of interest must be captured accurately.

One of the most common joint types in today's engineering applications is the bolted joint connection. The combination of a contact surface with a series of bolts to apply the required loading potentially can result in a nonlinear system. The bolts and contact stiffness can lead to a reduction in the global stiffness and relative motion in the contact can add amplitude dependent damping due to friction effects. An analytical model of an assembled structure should take these effects into account to ensure accurate predictions of the dynamic behaviour.

Several different approaches are available to deal with the bolted joint in an analysis. Rigid connections at the joints are the simplest approach, ignoring any possible influence of the joint on the response. Using a set of springs to model the reduced stiffness in the joint [1] can lead to a good agreement of predicted and measured resonance frequencies, but the damping effects due to the nonlinear friction behaviour of the joint are neglected. More advanced approaches not only include the stiffness of the bolt but also the energy dissipation due to the friction between the two contact surfaces [2], using experimental data to update and tune the model. A slightly different approach is the full three dimensional modelling of the contact interface [3] with nonlinear contact elements. It requires input parameters for the contacts, such as friction coefficient and contact stiffness [4], a linear modal model of the different components, and the normal load distribution on the contact surface.

Sandia National Laboratories is a multi-program laboratory managed and operated by Sandia Corporation, a wholly owned subsidiary of Lockheed Martin Corporations, for the U.S. Department of Energy's National Nuclear Security Administration under Contract DE-AC04-94AL85000.

L. Salles • C.W. Schwingshackl (✉)
Mechanical Engineering, Imperial College London, London, UK
e-mail: c.schwingshackl@imperial.ac.uk

C. Swacek • P. Reuss
Institute of Applied and Experimental Mechanics, University of Stuttgart, Stuttgart, Germany

R.M. Lacayo • M.R.W. Brake
Component Science and Mechanics, Sandia National Laboratories, Albuquerque, NM, USA

G. Kerschen (ed.), *Nonlinear Dynamics, Volume 1*, Conference Proceedings of the Society for Experimental Mechanics Series, DOI 10.1007/978-3-319-15221-9_4

To gain a better understanding of the capabilities of the different approaches to model the nonlinear dynamic behaviour of bolted joints, and in response to a challenge defined during the Third International Workshop on Jointed Structures in Chicago in 2012 [5], the 2014 Sandia Nonlinear Mechanics and Dynamics Summer Research Institute included a round robin numerical modelling challenge. The round robin challenge includes four different methods for the nonlinear response prediction developed at: Imperial College London, Sandia National Laboratories, and the University of Stuttgart. A straight beam (Brake-Reuß beam, detailed in Sect. 4.3) with a simple lap joint with three bolts is investigated with a transient simulation based on an Iwan model [6] (both in a reduced order and a high fidelity framework), and two different harmonic balance approaches [7, 8]. The resulting findings of the round robin are presented in this paper.

4.2 Approaches to Modeling Friction Joints

The Benchmark used for this numerical round-robin is tested with four different approaches. A transient approach based on finite elements and reduced order modelling with discontinuous basis modes is used by the Engineering Sciences Center at Sandia National Laboratories (hereafter referred to as Sandia), while the Vibration University Technology Centre at Imperial College London (hereafter referred to as Imperial) and the Institute of Applied and Experimental Mechanics at the University of Stuttgart (hereafter referred to as Stuttgart) use frequency domain approaches.

There are several notable differences between the different approaches. Qualitatively, the responses for the methods developed at Sandia are obtained in the time domain; whereas, Stuttgart and Imperial College use harmonic balance methods (HBMs) to obtain responses in the frequency domain. The Sandia transient methods are versatile in that they are developed for arbitrary excitations and nonlinear constitutive models, but at the cost of intensive computation and inaccurate frequency-space representation by Fourier transform (since a nonlinear decaying response changes the frequency behaviour). The Stuttgart and Imperial HBMs are computationally efficient, but are limited somewhat to harmonic input excitations. The two used HBM approaches differ mainly in the use of the reduction technique (Craig Bampton by Stuttgart versus Hybrid Method by Imperial), the implementation of the nonlinear forces (linearization, Stuttgart, versus alternating frequency time procedure, Imperial), and the HBM (single, Stuttgart, versus multi harmonic, Imperial). These differences will need to be kept in mind when evaluating the resulting responses of the beam.

4.2.1 Iwan Model

The four parameter Iwan model [9], is used to represent the physical mechanisms observed in measurements of the dynamic behavior of joints. The Iwan model (see Fig. 4.1a) is based on a distribution of friction sliders (Jenkins elements) that approximate the response of a jointed surface in both the micro-slip and macro-slip regimes. The four parameters that characterize the Iwan model are the tangential stiffness in the micro-slip regime, the insipient force for macro-slip, and the power law slope and exponent for the dissipation characteristics of the system as a function of excitation amplitude.

The approach taken at Sandia National Laboratories for modeling systems with frictional interfaces [6] divides the jointed surfaces into a series of contact patches (these can be as few as one patch per surface, or as many as are computationally feasible). Each of the nodes within a contact patch is rigidly connected to a new node that represents the degrees of freedom for that contact patch. This new node, in turn, is connected to the corresponding node for the contact patch on the opposite surface using an Iwan element. This modeling approach replaces the kinematics of the adjacent interfacial surfaces with a nonlinear constitutive model. The four parameters for this model generally must be determined from representative experimental data; however, a number of uncertainty approaches [10] exist for when there is an insufficient amount of data [11].

Two of the methods used by the research groups at Sandia National Laboratories include high fidelity modelling using SIERRA [12] (a massively parallel finite element program), and reduced order modelling using the method of discontinuous basis functions [13, 14]. The framework for the discontinuous basis function method is established by augmenting the linear mode shapes of a system composed of linear substructures defined by the Craig-Bampton method [15] with a series of discontinuous basis functions that are smooth everywhere except at the location of the discrete nonlinearity (i.e. joint). The mathematical definition of the discontinuous basis functions is based on the research of Reference [16], and inclusion of the discontinuous basis functions with the linear basis functions enhances the convergence properties of the system. The resulting set of nonlinear, coupled equations of motion are integrated directly in time to calculate the transient dynamic response of the system.

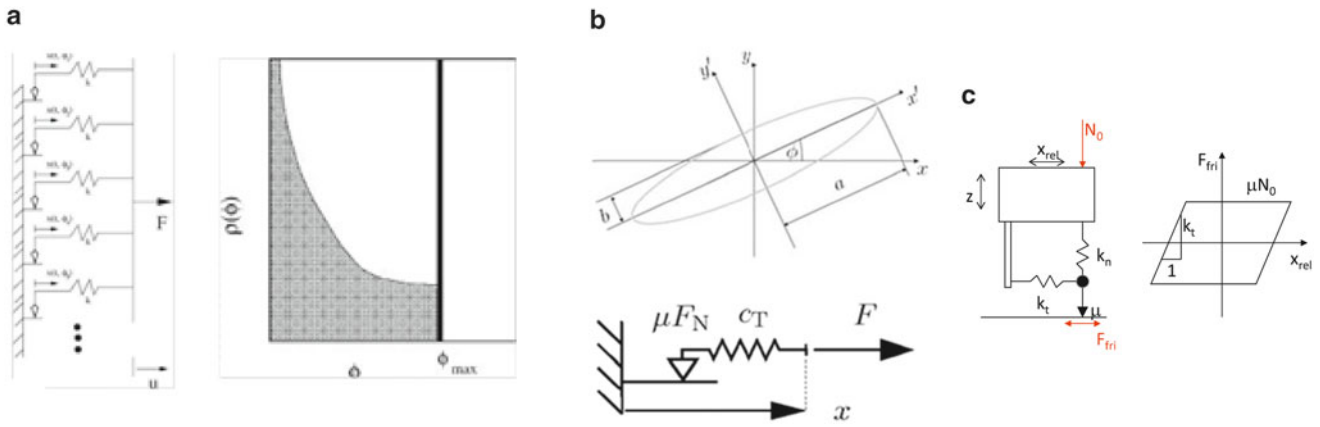

Fig. 4.1 Friction elements (**a**) Iwan model (Sandia), (**b**) Jenkins Model (Stuttgart) and 3D element (Imperial)

4.2.2 Stuttgart Approach (Harmonic Balance Method)

The Stuttgart approach [7] relies on a node-to-node contact model with friction in the tangential direction and a nonlinear contact law in the normal direction. The nonlinear contact law in a first step is used to compute the normal force at each node-to-node contact based on the applied external forces of the screws. This is established by a nonlinear static calculation and within this investigation the results presented in Sect. 3.2 are used and converted to nodal force to allow comparable conditions in the interface to be able to compare results for different methods. Further relative dynamics in the normal direction is suppressed in the present case, which means that the normal force at each node in contact is assumed as constant for the HBM calculation. In tangential direction the interface nodes can have relative displacements in two dimensions. Since in this approach only the fundamental response is considered, the resulting motion is an ellipse in the plane, Fig. 4.1b.

The friction forces are then computed for the major and minor axis a and b separately using the analytical equations for the Fourier coefficients [7] in terms of equivalent stiffness and damping of the one dimensional case. This is a further approximation that does not take into account the coupling of the friction force in two dimensions but shows reasonable results when the motion in one dimension is dominant. In the local coordinate system x' and y', the equivalent stiffness and damping matrix as well as the transformation matrix, including the angle ϕ between the local and the global coordinate system can be written as

$$\boldsymbol{K}^{l}_{hbm} = \begin{bmatrix} k^{x'}_{hbm} & 0 \\ 0 & k^{y'}_{hbm} \end{bmatrix}, \; \boldsymbol{D}^{l}_{hbm} = \begin{bmatrix} d^{x'}_{hbm} & 0 \\ 0 & d^{y'}_{hbm} \end{bmatrix}, \; \boldsymbol{T} = \begin{bmatrix} \cos\phi & \sin\phi \\ -\sin\phi & \cos\phi \end{bmatrix} \tag{4.1}$$

Transforming the matrices into the global coordinate system by

$$\boldsymbol{K}^{g}_{hbm} = \boldsymbol{T}\,\boldsymbol{K}^{l}_{hbm}\boldsymbol{T}^{T}, \; \boldsymbol{D}^{g}_{hbm} = \boldsymbol{T}\,\boldsymbol{D}^{l}_{hbm}\boldsymbol{T}^{T}, \tag{4.2}$$

a pseudo-receptance matrix in the frequency domain can be established containing the sum of all node-to-node friction contacts via

$$\boldsymbol{H}_{hbm}(\widehat{\boldsymbol{x}}) = \left((\boldsymbol{K} + \boldsymbol{K}_{hbm}(\widehat{\boldsymbol{x}})) + i\,\omega\,(\boldsymbol{D} + \boldsymbol{D}_{hbm}(\widehat{\boldsymbol{x}})) - \omega^2\boldsymbol{M}\right). \tag{4.3}$$

The linear mass and stiffness matrix contain in addition to the interface DOFs, where the friction forces act, modal dynamic information of the coupled subsystems established by the Craig-Bampton method [15]. The resulting equations of motion in the frequency domain can be arranged in an implicit form by

$$\boldsymbol{r} = \boldsymbol{H}_{hbm}(\widehat{\boldsymbol{x}})\;\widehat{\boldsymbol{x}} - \boldsymbol{f}_{ext}. \tag{4.4}$$

The residuum $\boldsymbol{r}$ is then minimised using a Nonlinear Successive Over-Relaxation Method [17] to obtain the nonlinear dynamic response. The advantage of this method is that it avoids calculating the Jacobian matrix of the equations, which is

expensive for the large number of considered degrees-of-freedom when using a standard finite-difference method to compute the derivative numerically. On the other hand, this method requires two evaluations of the nonlinear friction forces to compute the Fourier coefficients per iteration step, such that the efficiency of this method in the present case is only guaranteed by fact that the coefficients are computed analytically.

4.2.3 Imperial Approach

The Imperial-developed code, FORSE, used for the analysis of the nonlinear response of flange joints is based on the multiharmonic representation of the steady-state response and allows large scale realistic friction interface modelling. Major features of the methodology were described in [8] and only an overview of the analysis is presented in this paper. The equation of motion consists of a linear part, which is independent of the vibration amplitudes, and the nonlinear part due to the friction interfaces at the interface joint. The nonlinear equation of motion can be written as

$$\boldsymbol{K}\boldsymbol{q}(t) + \boldsymbol{C}\dot{\boldsymbol{q}}(t) + \boldsymbol{M}\ddot{\boldsymbol{q}}(t) + \boldsymbol{f}\left(\boldsymbol{q}(t)\right) - \boldsymbol{p}(t) = \boldsymbol{0}, \tag{4.5}$$

where $\boldsymbol{q}$ is a vector of displacements; $\boldsymbol{K}$, $\boldsymbol{C}$, and $\boldsymbol{M}$ are stiffness, damping and mass matrices, respectively, of the linear model; $\boldsymbol{f}$ is a vector of nonlinear friction interface forces, which is dependent on displacements and velocities of the interacting nodes, and $\boldsymbol{p}$ is a vector of periodic exciting forces. The variation of the displacements in time is represented by a restricted Fourier series, which can contain as many harmonic components as it is necessary to approximate the solution, i.e.

$$\boldsymbol{q}(t) = \boldsymbol{Q}_0 + \sum_{j=1}^{n} \boldsymbol{Q}_j^c \cos m_j \omega t + \boldsymbol{Q}_j^s \sin m_j \omega t. \tag{4.6}$$

In Eq. 4.6, $\boldsymbol{Q}$ are vectors of harmonic coefficients for the system degrees of freedom (DOFs), n is the number of harmonics that is used in the multiharmonic displacement representation, and ω is the principal vibration frequency. The flowchart of the calculations performed with the code is presented in Fig. 4.2. The contact interface elements developed in [18] (see Fig. 4.1c) are used for modelling of nonlinear interactions at contact interfaces and analytical expressions for the multiharmonic representation of the nonlinear contact forces and stiffnesses. The nonlinear algebraic system of the reduced

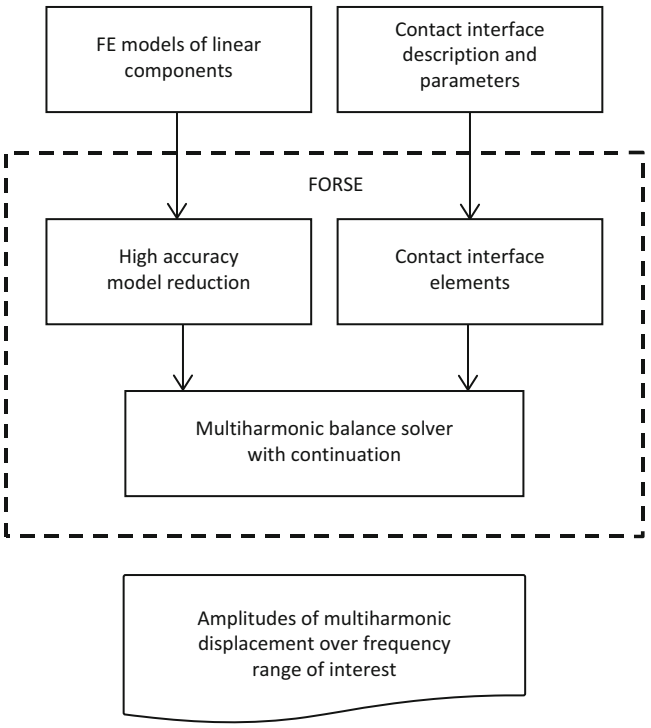

Fig. 4.2 Scheme of the forced response analysis

model is obtained using a hybrid method of reduction developed by Petrov [18], [19]. The nonlinear system in the frequency domain is

$$\tilde{\boldsymbol{Q}} = A(\omega)\left(\tilde{\boldsymbol{F}} - \tilde{\boldsymbol{F}}_{nl}\left(\tilde{\boldsymbol{Q}}\right)\right), \tag{4.7}$$

with $\tilde{Q}$ defined as the vector of the Fourier coefficients of the displacements at the interface, $A(\omega)$ the frequency response, $\tilde{F}$ is the vector of the Fourier coefficients of the excitation force and $\tilde{F}_{nl}$ is the vector of the Fourier coefficients of the nonlinear contact forces.

4.3 The Lap Joint Test Case

The test case chosen for the Round Robin investigation is the Brake-Reuss beam [20], a simple straight beam consisting of two pieces connected with a lap joint (see Fig. 4.3). The beam is made of 304 stainless steel, and has an assembled dimension of $720 \times 25 \times 25$ mm. The lap joint is located in the centre of the beam and has a length of 120 mm. Three bolt holes, spaced 30.2 mm apart, with a diameter of 8.4 mm allow the application of the required contact pressure in the joint.

4.3.1 The Finite Element Mesh

Representative linear finite element models for each side of the beam were created in Hyper Mesh and used for all four approaches (Fig. 4.4). Each side of the beam consists of 10,184 8-node hexahedral elements, with particular care taken to ensure that the mesh is congruent on either side of the contact interface. This allows for an accurate application of the nonlinear meshes for each of the methods in the round robin exercise. The contact interface has 931 nodes, as shown in Fig. 4.5. Both ends of the beam are clamped, to reduce complications in the nonlinear analysis of the joint. The nodes around the through-hole on one side of the beam are all given the same dynamic forcing load, and a single node on the hole on the other side of the interface becomes the output node of interest.

4.3.2 Nonlinear Static Analysis

A static stress analysis is used to determine the contact stress distribution in the contact interface using Code Aster and the continuous contact augmented Lagrangian formulation ($\mu = 0.6$) to obtain the most accurate stress distribution. The bolt

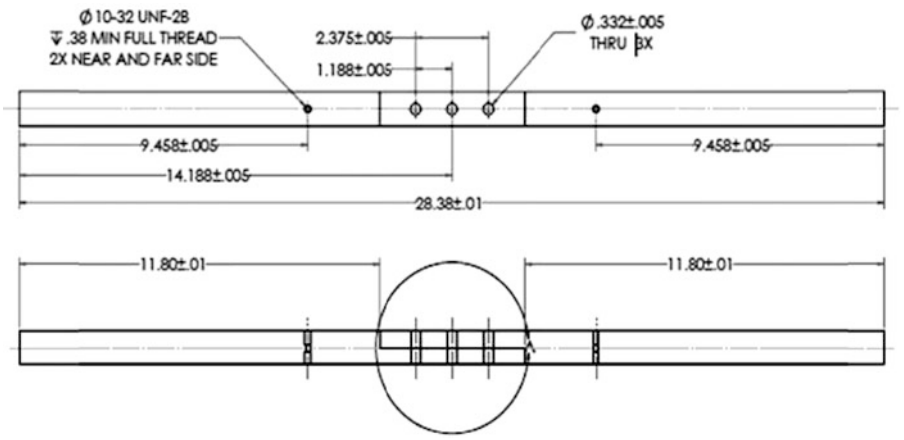

Fig. 4.3 Dimensions of the round robin beam (dimensions given in inches)

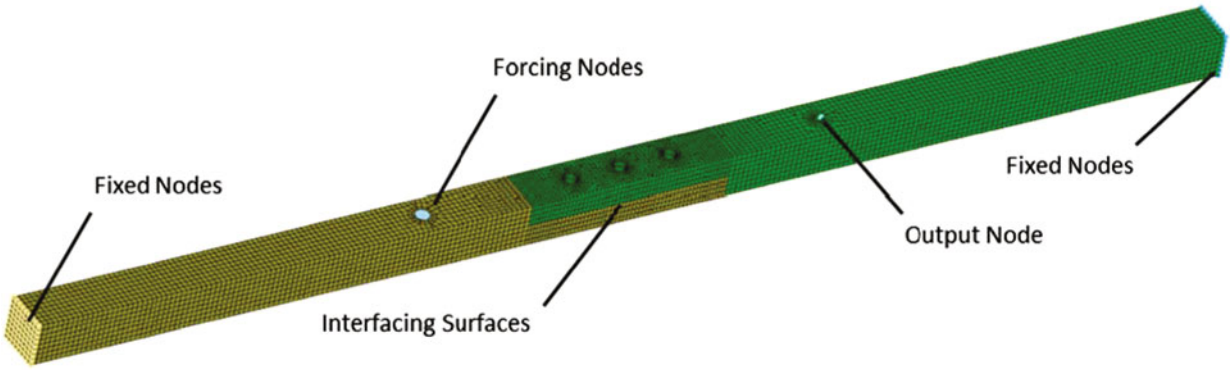

Fig. 4.4 Round Robin beam finite element model setup

Fig. 4.5 Finite element mesh at the contact interface

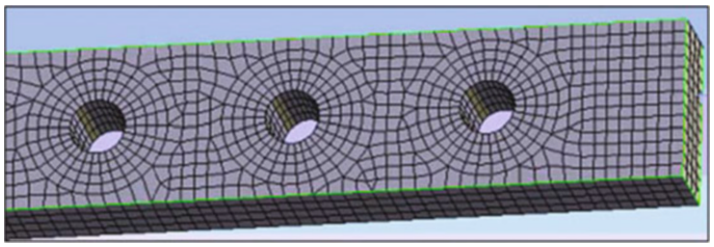

Fig. 4.6 The (**a**) calculated contact pressure and (**b**) deformation in the contact zone

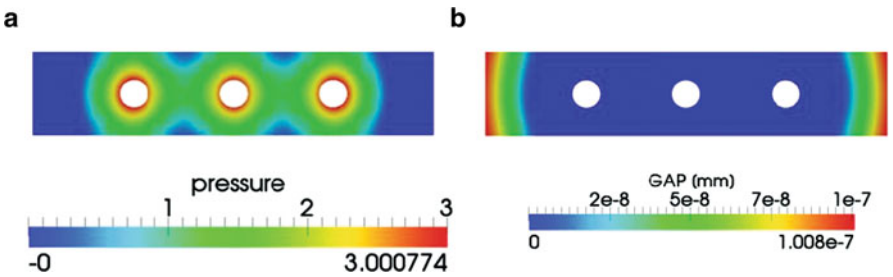

torque is subsequently applied as a constant pressure load on the outer surfaces of the beam, and several loads (between 1,000 and 12,500 N) are chosen for each bolt. The resulting pressure distribution for a load of 1,000 N can be seen in Fig. 4.6a. The high stress levels close to the bolt holes (pressure cone) reduce concentrically leading to an area of lower compression between the holes, and no stress towards the two ends of the lap joint. Figure 4.6b shows the out-of-plane displacement in the contact surface, indicating a very small opening of a gap at the two ends of the lap joint, which explains the absence of pressure in the area and leads to some interesting initial conditions for the analysis.

The linear finite element model and the calculated nonlinear static stress distribution in the lap joint are used as a starting point for the generation of the nonlinear dynamic models.

4.3.3 Nonlinear Dynamic Model

Two different modelling approaches are investigated by Sandia based on the high fidelity finite element model and a reduced order model. For both models, the joint is modelled with a four parameter Iwan model, the parameters of which (F_S, K_T, χ, and β) must be tuned to match the damping and frequency behaviour of the other methods for a meaningful comparison. The slip force F_S and tangent stiffness K_T have equivalent parameters in each of the other methods; however, the energy dissipation power law slope χ and exponent β have no equivalent representation in either of the HBMs studied in this round robin. The slip force can be interpreted as the amount of shear force necessary to instigate slip between the two interfacing surfaces and is derived from Coulomb's law. With a friction coefficient of $\mu = 0.3$ and a total normal load from the bolts of $F_N = 30{,}000$ N the friction force $F_s = \mu \bullet F_N$ becomes 9,000 N.

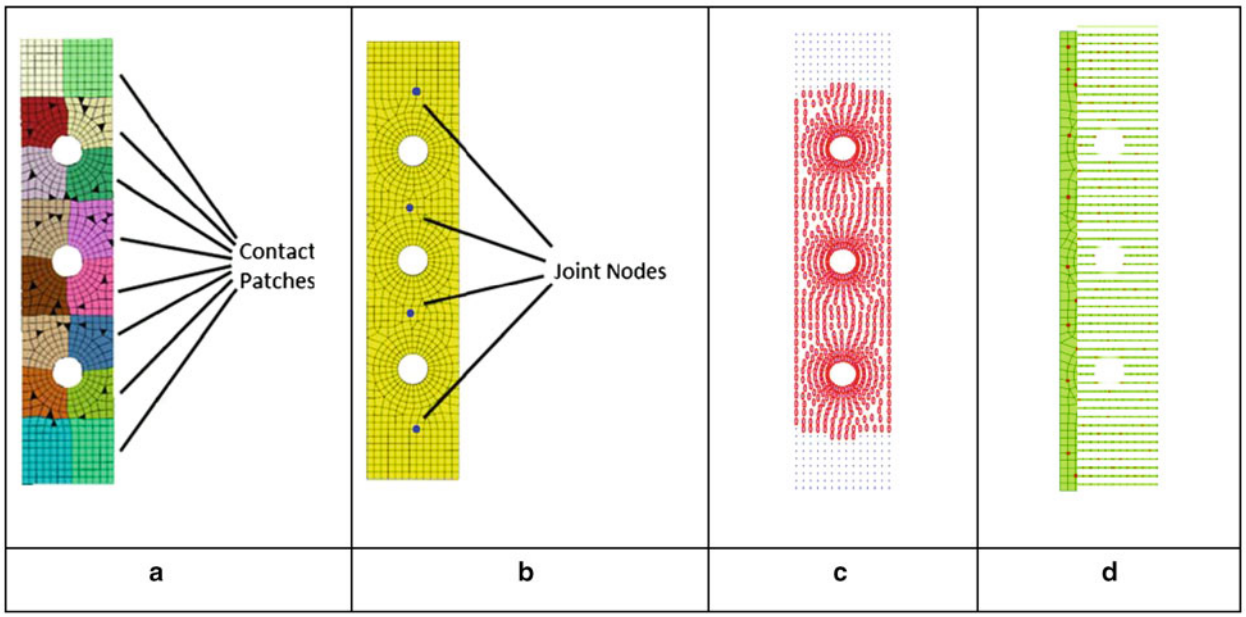

Fig. 4.7 The nonlinear models (**a**) Iwan-full, (**b**) Iwan-reduced, (**c**) HBM-Stuttgart, and (**d**) HBM-Imperial College model

The tangent stiffness value, K_T, is linked to the tangential stiffness parameters, $k_t = 50$ kN/mm^3, from the Stuttgart and Imperial approaches, but it must be adopted to represent the contact conditions in Iwan models correctly. The last two Iwan parameters, χ and β, have no known direct correspondence with the parameters of the other methods, so previous experimental data from a similar system [6] is used to derive their values.

For the simulation in Sierra [12], the two interfacing surfaces are divided into 16 contact patches each as shown in Fig. 4.7a (Iwan-full model). The two surface-tangent translational DOF are assigned 16 discrete Iwan models tuned to the parameters discussed before. The two surface-tangent rotational DOF are automatically constrained due to a zero-gap constraint in the surface-normal direction, and the surface-normal rotational DOF is given a spring with stiffness 10^9 N/rad to approximate a fixed rotation constraint due to bolt pinning. The joint model in the reduced model simulation uses four nonlinear nodes on each contact surface as indicated in Fig. 4.7b (Iwan-reduced model) with the same input parameters as above. In addition, a penalty spring model with a stiffness of 10^6 N/mm is assigned to the surface-normal DOF for each node interface. The rotational joint models do not apply for the reduced model because the rotational DOF from every node are discarded during the Craig-Bampton reduction.

The Friction Coefficient and the contact stiffness for the Stuttgart and Imperial simulations are the same as used for the Iwan models with a friction coefficient, $\mu = 0.3$, and a tangential contact stiffness, $k_t = 50$ kN/mm. The model created by Stuttgart (HBM-Stuttgart, Fig. 4.7c) has 702 nonlinear nodes at the contact interface and uses a single harmonic for the solution. The models created by Imperial College (HBM-Imperial, Fig. 4.7d) consisted of 86, 118, and 903 nonlinear elements respectively, allowing for a faster nonlinear computation with the first model, and a much more detailed analysis with the latter one. Each element has its own normal preload attributed, based on the static stress distribution form Fig. 4.6a and both a single- and a multi-harmonic analysis are used to predict the nonlinear dynamic response.

4.4 Nonlinear Dynamic Results

For both the Iwan-full and Iwan-reduced models, the displacement frequency response functions (FRF) at the output node of interest are obtained by numerically integrating the system equations of motion in the time domain, and then using the Fourier transform on the response solution. To observe the nonlinear characteristics of the Iwan joint in the frequency domain, the transient response to several impulse load excitation cases are simulated. For the Iwan-full model, the response to a Heaviside force impulse with a period of 0.01 s is simulated for peak loads of 1 kN, 10 kN, 30 kN, 100 kN, 300 kN, and 1 MN. The Iwan-reduced model uses a forcing period of 0.001 s for peak loads of 10 N, 100 N, and 1,000 N. The responses for both models are integrated over a simulation time of 0.35 s to ensure adequate frequency step size resolution after using the Fourier transform.

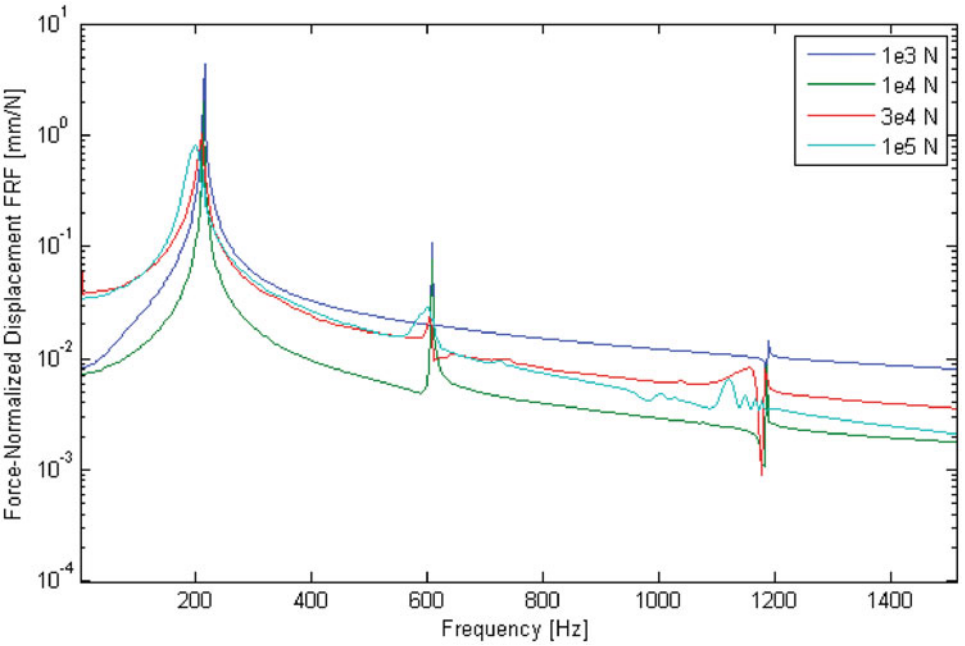

Fig. 4.8 Iwan-full model displacement frequency response functions for different forcing amplitudes

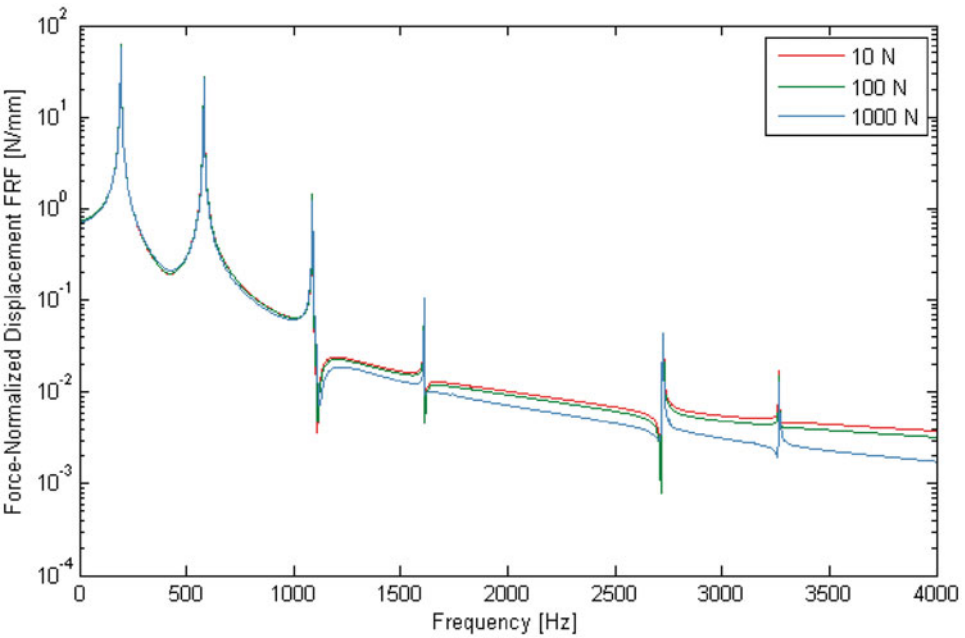

Fig. 4.9 Reduced model displacement frequency response functions for different forcing amplitudes

Figure 4.8 shows a plot of the displacement FRF for each excitation amplitude up to 100 kN, normalized to their forcing magnitude, from the Iwan-full model. As the forcing magnitude increases, the natural frequencies of the first three modes decrease and the damping increases for the first and second modes. This suggests that the joint becomes less stiff and energy dissipation increases as more energy is added to the system, which is expected. The exception to this trend appears to occur around a 10 kN excitation since both the first and third modes show a marked decrease in damping from the 1 kN case; however, this anomaly could be the result of a simulation error or further evidence of the nonlinearity of this system, and warrants further attention.

Similar to Figs. 4.8 and 4.9 shows the displacement FRF for the Iwan-reduced simulations. The nearly identical responses suggest that none of the load cases (with a maximum of 1 kN) add enough energy to the system to excite the nonlinearity in the joint. Further simulations at higher excitation amplitudes are necessary to study the effect of the joint dynamics on the response of the system.

Figure 4.10 shows the FRF near the first natural frequency obtained by the HBM-Stuttgart model with 712 contact nodes. Results for four different bolt preloads (1, 5, 10, and 15 kN) and a harmonic excitation of 100 N are shown in Fig. 4.10a.

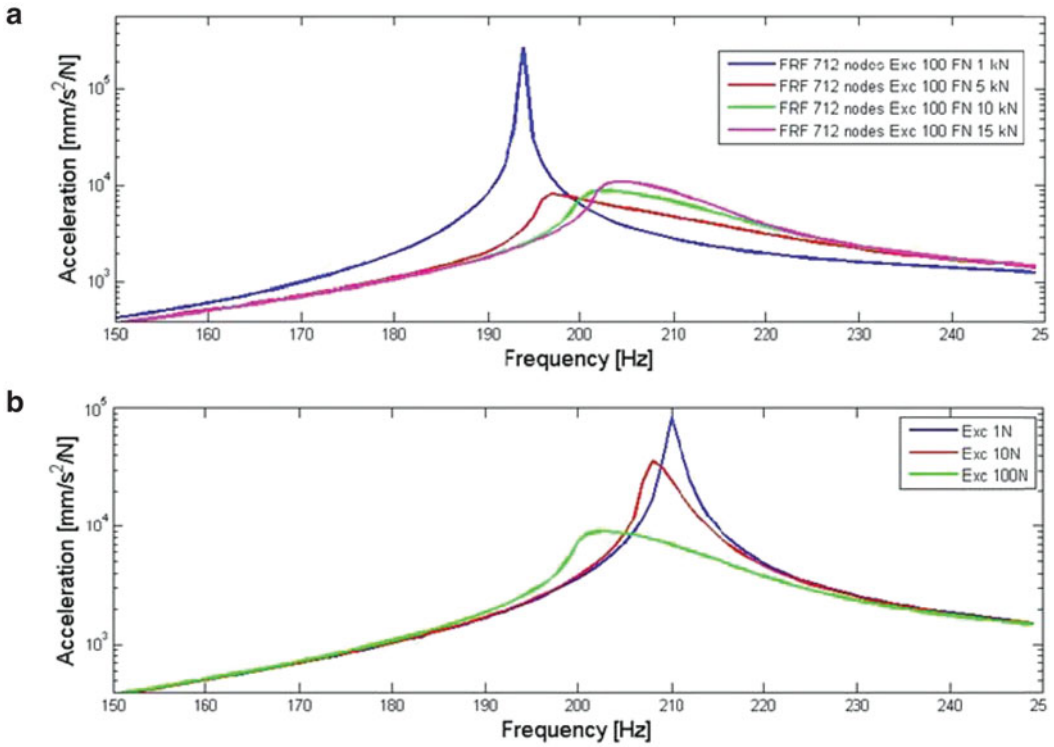

Fig. 4.10 The results from the HBM-Stuttgart model: (**a**) for varying normal load and (**b**) for varying excitation forces with 10 kN bolt loading

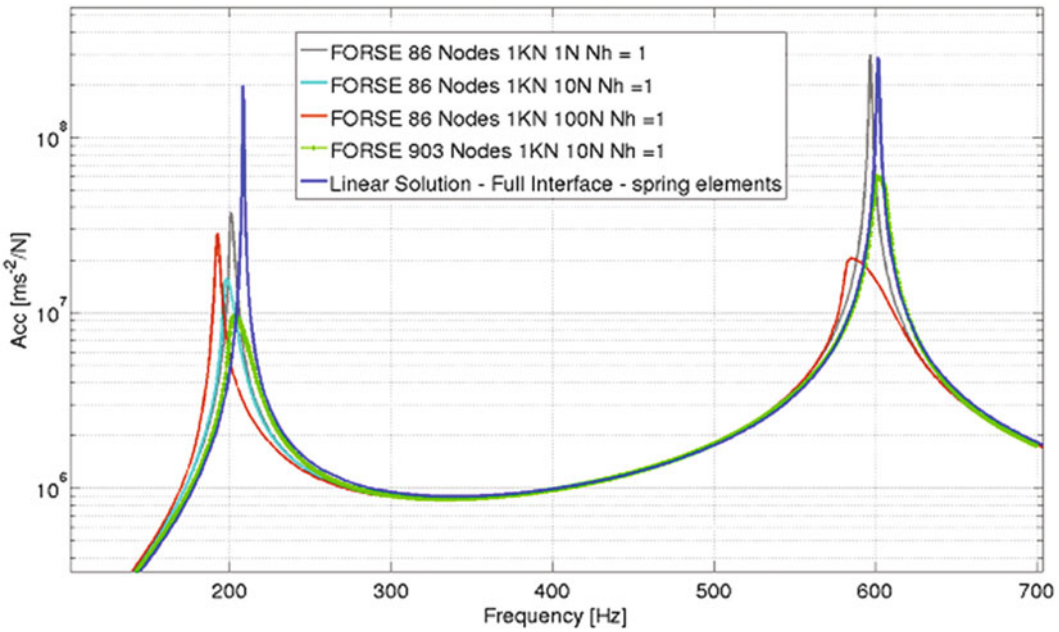

Fig. 4.11 Nonlinear frequency response prediction from the HBM-Imperial model

These results show that the behavior is nonlinear for the considered loading, in contrast to the Iwan-reduced predictions. It is interesting to observe, that the damping seems to increase with an increase in bolt load, which could potentially indicate more micro-slip in the contact zone due to a stronger static contact deformation. Figure 4.10b shows the FRF near the first natural frequency for a bolt loading of 1 kN and three excitation levels (1, 10, and 100 N). In this case the damping increases with an increasing excitation, following a more traditional understanding of the joint behavior.

Figure 4.11 shows the FRF obtained by the HBM-Imperial approach for different nonlinear models with 86 and 903 contact nodes and a linear FRF when the interface is modelled using spring elements. For varying excitation levels an

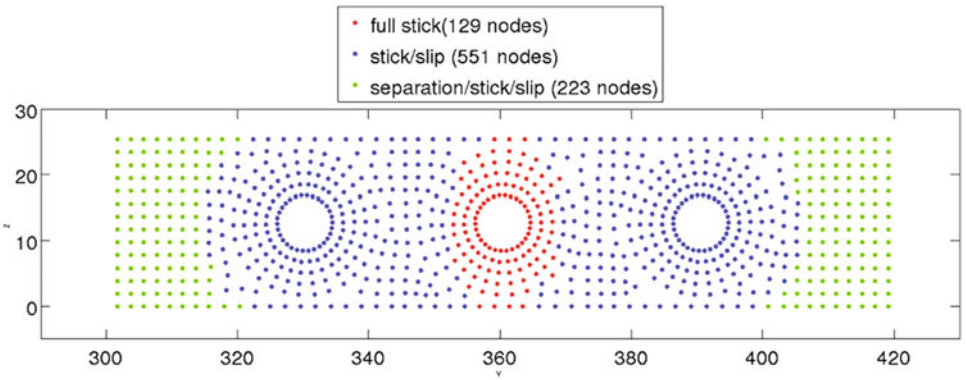

Fig. 4.12 The contact conditions in the lap joint during vibration for the HBM-Imperial model

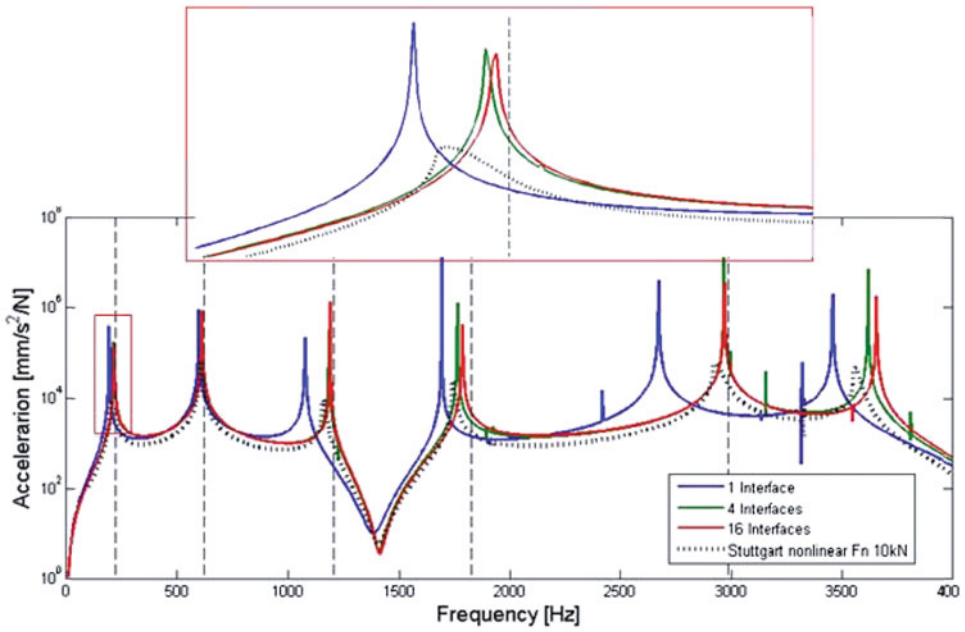

Fig. 4.13 Predicted response for different Iwan-full models and the HBM-Stuttgart model

increase in damping can be observed, which is particularly strong for the second mode. An increase in the number of contact nodes leads to a slight stiffening of the response, and predicts more damping due to a more accurate representation of the contact surface. The contact condition during one period of vibration at the resonance for the first mode in Fig. 4.12 shows that most of the contact nodes have a nonlinear behavior during the vibration period by either slipping or separating.

Figure 4.13 shows FRFs obtained from the Iwan-full model for different number of joints (1, 4, and 16) in the interface and compares the results to the HBM-Stuttgart models with a bolt preload of 10 kN. The resonance frequencies agree reasonably well, also the Iwan-full model with a single element predicts the lowest interfacial stiffness. Further, the applied transient forces for the Iwan-full model do not seem to activate the nonlinear behaviour in a similar manner as in the HBM simulations.

Figure 4.14 shows the comparison between the FRFs obtained by the HBM-Stuttgart and HBM-Imperial models. A good agreement between both approaches is observed for the single harmonic case with a large number of nonlinear elements, which is not that surprising since both approaches use a similar method for the calculation of the nonlinear response. The FRF calculated with Imperial's multi-harmonic approach shows the effect of the higher harmonics since an additional peak in the response can be detected. As the interface has been reduced to 118 nodes for the multi-harmonic analysis a small frequency shift can be observed.

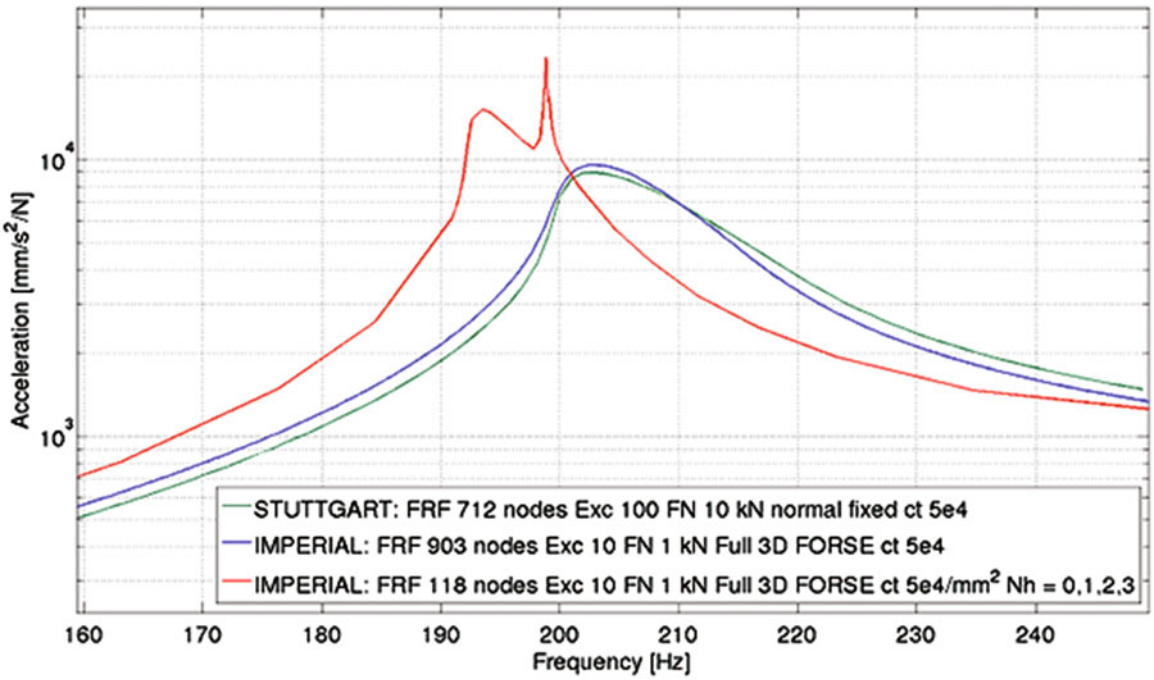

Fig. 4.14 Comparison for the HBM-Stuttgart and HBM-Imperial predictions

4.5 Conclusion

In this paper four approaches have been tested on a numerical benchmark to evaluate the current state of the art to model bolted lap joints. Two of them are frequency domain methods with contact elements based on Jenkins elements, while the other two are based on microslip Iwan elements, solved with a transient time domain analysis.

The selected lap joint beam had a strong nonlinear behaviour and it is consequently a good but quite challenging test case for the round robin exercise. Stick–slip and separation areas are present in the beam, providing a challenging task for the different approaches to capture the nonlinear response correctly. All investigated methods are able to predict a nonlinear response due to the contact surface, also some variations were observed especial between the time and the frequency domain approaches. The time domain approach seems to be unable to predict significant nonlinearity until dynamic force excitations up to three orders of magnitude higher than those of the frequency domain approach is used. The two methods based on frequency domain approaches give similar results for a single harmonic simulation but it could be observed that higher harmonics may be needed to capture the nonlinear dynamic behaviour of the joint correctly. The round robin exercise shows that the model reduction method of the contact interface can have a strong effect on the resulting nonlinear response and must be considered with care.

Since different methods (frequency domain and time domain) with different excitation approaches are used for this preliminary round robin, a direct comparison of the results is rather difficult, and a new strategy is required to efficiently compare the different approaches. This study should be seen as a first step for a numerical round robin initiated by the ASME Joints Research Group to develop a proper benchmark for the validation of future nonlinear dynamic codes.

Acknowledgements The authors would like to thank Sandia National Laboratories to support this research work during the 2014 Sandia Nonlinear Mechanics Summer Research Institute.

References

1. Luan Y, Guan Z, Cheng G, Liu S (2011) A simplified nonlinear dynamic model for the analysis of pipe structures with bolted flange joints. J Sound Vib 331:325–344
2. Boeswald M, Link M (2003) Experimental and analytical investigations of non-linear cylindrical casing joints using base excitation testing. In: IMAC XXI A conference and exposition on structural dynamics, Kissimmee, 3–6 Feb

3. Schwingshackl CW, Di Maio D, Sever I, Green JS (2013) Modeling and validation of the nonlinear dynamic behavior of bolted flange joints. Trans ASME J Eng Gas Turbines Power 135:122504-1-8
4. Schwingshackl CW, Petrov EP, Ewins DJ (2012) Measured and estimated friction interface parameters in a nonlinear dynamic analysis. Mech Syst Signal Process 28:574–584
5. Starr MJ, Brake MR, Segalman DJ, Bergman LA, Ewins DJ (2013) Proceedings of the third international workshop on jointed structures. SAND2013-6655, Sandia National Laboratories, Albuquerque
6. Segalman DJ, Gregory DL, Starr MJ, Resor BR, Jew MD, Lauffer JP, Ames NM (2009) Handbook on dynamics of jointed structures, SAND2009-4164. Sandia National Laboratories, Albuquerque
7. Bograd S, Reuss P, Schmidt A, Gaul L, Mayer M (2011) Modeling the dynamics of mechanical joints. Mech Syst Signal Process 25:2801–2826
8. Petrov EP, Ewins DJ (2002) Analytical formulation of friction interface elements for analysis of nonlinear multiharmonic vibrations of bladed discs. ASME J Turbomach 125:364–371
9. Segalman DJ (2005) A four-parameter Iwan model for lap-type joints. ASME J Appl Mech 72:752–760
10. Soize C (2010) Generalized probabilistic approach of uncertainties in computational dynamics using random matrices and polynomial chaos decompositions. Int J Numer Methods Eng 81:939–970
11. Wang XQ, Mignolet MP (2014) Stochastic Iwan-type model of a bolted joint: formulation and identification. In: IMAC XXXII A conference and exposition on structural dynamics, Orlando
12. Edwards HC (2002) Sierra framework version 3: core services theory and design. SAND2002-3616, Sandia National Laboratories, Albuquerque
13. Segalman DJ (2007) Model reduction of systems with localized nonlinearities. ASME J Comput Nonlinear Dyn 2:249–266
14. Brake MR, Segalman DJ (2013) Modeling localized nonlinear constraints in continuous systems via the method of augmentation by non-smooth basis functions. Proc Roy Soc A-Math Phys Eng Sci 469:1–20
15. Craig RR, Bampton MCC (1968) Coupling of substructures for dynamic analyses. AIAA J 6:1313–1319
16. Milman MH, Chu C-C (1994) Optimization methods for passive damper placement and tuning. J Guid Control Dyn 17:848–856
17. Cigeroglu E, Özgüven HN (2006) Nonlinear vibration analysis of bladed disks with dry friction dampers. J Sound Vib 295:1028–1043
18. Petrov EP, Ewins DJ (2004) Generic friction models for time-domain vibration analysis of bladed disks. Trans ASME J Turbomach 126: 184–192
19. Petrov EP (2011) A high-accuracy model reduction for analysis of nonlinear vibrations in structures with contact interfaces. Trans ASME J Eng Gas Turbines Power 133:102503–1–102503–10
20. Brake MR, Reuss P, Segalman DJ, Gaul L (2014) Variability and repeatability of jointed structures with frictional interfaces. In: IMAC XXXII A conference and exposition on structural dynamics, Orlando

Chapter 5
The Harmonic Balance Method for Bifurcation Analysis of Nonlinear Mechanical Systems

T. Detroux, L. Renson, L. Masset, and G. Kerschen

Abstract Because nowadays structural engineers are willing to use or at least understand nonlinearities instead of simply avoiding them, there is a need for numerical tools performing analysis of nonlinear large-scale structures. Among these techniques, the harmonic balance (HB) method is certainly one of the most commonly used to study finite element models with reasonably complex nonlinearities. However, in its classical formulation the HB method is limited to the approximation of periodic solutions. For this reason, the present paper proposes to extend the method to the detection and tracking of codimension-1 bifurcations in the system parameters space. As an application, the frequency response of a spacecraft is studied, together with two nonlinear phenomena, namely quasiperiodic oscillations and detached resonance curves. This example illustrates how bifurcation tracking using the HB method can be employed as a promising design tool for detecting and eliminating such undesired behaviors.

Keywords Continuation of periodic solutions • Bifurcation tracking • Harmonic balance method • Quasiperiodic oscillations • Detached resonance curves

5.1 Introduction

As engineering structures are designed to be lighter and operate in more severe conditions, nonlinear phenomena such as amplitude jumps, modal interactions, limit cycle oscillations and quasiperiodic (QP) oscillations are expected to occur [1]. These are phenomena that can be frequently encountered in normal operation regime, in space [2, 3] and aeroelastic [4] applications, or during GVT campaigns [5, 6]. Classical excitation signals as swept-sine and harmonic tests can already reveal nonlinear behaviors. For most of these nonlinear structures, bifurcations play a key role in the response dynamics; for example, fold bifurcations indicate a stability change for the periodic solutions, while QP oscillations are encountered in the vicinity of Neimark-Sacker (NS) bifurcations. In that regard, it seems relevant to include analysis of bifurcations while performing a parametric study of the structure.

Different algorithms and numerical methods can be found in the literature for the computation of periodic solutions and their bifurcations. Most of them build on a continuation procedure [7], as a way to study the evolution of the solutions with respect to a certain parameter, e.g., the frequency of an external excitation or a system parameter. Time domain methods, which deal with the resolution of a boundary value problem (BVP), usually prove accurate for low-dimensional structures. When applied to larger systems however, their computational burden become substantial. For example, the shooting technique [8] requires numerous time integrations that can drastically slow down the speed of the algorithm. Methods based on the orthogonal collocation, which uses a discretization of the BVP, are widely utilized in software for bifurcation detection and tracking like AUTO [9], COLSYS [10], CONTENT [11], MATCONT [12] or, more recently, COCO [13]. In spite of its high accuracy and ability to address problems with singularities, orthogonal collocation is rarely employed to study large systems, which can be explained by the considerable memory space this method requires for the discretization of the problem.

T. Detroux (✉) • L. Renson • L. Masset • G. Kerschen
Space Structures and Systems Laboratory (S3L), Structural Dynamics Research Group, Department of Aerospace and Mechanical Engineering, University of Liège, Liège, Belgium
e-mail: tdetroux@ulg.ac.be

G. Kerschen (ed.), *Nonlinear Dynamics, Volume 1*, Conference Proceedings of the Society for Experimental Mechanics Series, DOI 10.1007/978-3-319-15221-9_5

Among all methods in the frequency domain, the harmonic balance (HB) method, also known as the Fourier–Galerkin method, is certainly the most widely used. It approximates the periodic signals with their Fourier coefficients, which become the new unknowns of the problem. First implemented for analyzing linear systems, the HB method was then successfully adapted to nonlinear problems, in electrical [14] and mechanical engineering [15, 16] for example. The main advantage of the HB method is that it involves algebraic equations with less unknowns than the methods in the time domain, for problems for which low orders of approximation are sufficient to obtain an accurate solution; this is usually the case if the regime of the system is not strongly nonlinear. For this reason, the HB method has received increased attention for the last couple of years, which has led to numerous applications and adaptations of the method [17–19] and to the development of a continuation package MANLAB [20, 21]. The readers can also refer to [22] for a comparison between the HB method and orthogonal collocation in terms of convergence. Nevertheless, in spite of its performance and accuracy, to the authors' knowledge the HB method has never been extended to track bifurcations. In a previous work [23], the authors laid down the foundations for this extension, through the application to a system with two degrees of freedom (DOFs). The purpose of this work is to provide implementation details to track bifurcations of larger structures, and to illustrate how the tracking procedure can reveal and explain unexpected nonlinear phenomena.

The first part of this paper is devoted to the HB theory and its formulation in the framework of a continuation algorithm. Then Hill's method is introduced to assess the stability of periodic solutions, and to detect their bifurcations. The bifurcation tracking procedure is finally presented with its adaptations for branch point, fold and NS bifurcations. As an application, the analysis of the nonlinear dynamics of an industrial spacecraft is proposed. Starting from swept-sine and harmonic responses, nonlinear phenomena are highlighted and then studied through bifurcation detection and tracking.

5.2 Harmonic Balance Method

This section first performs a brief review of the theory of the HB method. The method will be applied to general non-autonomous nonlinear dynamical systems with n DOFs whose equations of motion are

$$\mathbf{M}\ddot{\mathbf{x}} + \mathbf{C}\dot{\mathbf{x}} + \mathbf{K}\mathbf{x} = \mathbf{f}_{ext}(\omega, t) - \mathbf{f}_{nl}(\mathbf{x}, \dot{\mathbf{x}}) = \mathbf{f}(\mathbf{x}, \dot{\mathbf{x}}, \omega, t) \tag{5.1}$$

where $\mathbf{M}$,$\mathbf{C}$ and $\mathbf{K}$ are the mass, damping and stiffness matrices respectively, $\mathbf{x}$ represents the displacements, the dots refer to the derivatives with respect to time t, $\mathbf{f}_{nl}$ represents the nonlinear forces and $\mathbf{f}_{ext}$ stands for the periodic external forces (harmonic excitation, for example) with frequency ω. The term $\mathbf{f}$ gathers both the external and nonlinear forces.

As recalled in the introduction, the periodic solutions $\mathbf{x}(t)$ and $\mathbf{f}(t)$ of Eq. (5.1) are approximated by Fourier series truncated to the N_H-th harmonic:

$$\begin{aligned} \mathbf{x}(t) &= \mathbf{c}_0^x + \sum_{k=1}^{N_H} \left(\mathbf{s}_k^x \sin\left(\frac{k\omega t}{\nu}\right) + \mathbf{c}_k^x \cos\left(\frac{k\omega t}{\nu}\right) \right) \\ \mathbf{f}(t) &= \mathbf{c}_0^f + \sum_{k=1}^{N_H} \left(\mathbf{s}_k^f \sin\left(\frac{k\omega t}{\nu}\right) + \mathbf{c}_k^f \cos\left(\frac{k\omega t}{\nu}\right) \right) \end{aligned} \tag{5.2}$$

where $\mathbf{s}_k$ and $\mathbf{c}_k$ represent the vectors of the Fourier coefficients related to the sine and cosine terms, respectively. Here it is interesting to note that the Fourier coefficients of $\mathbf{f}(t)$, $\mathbf{c}_k^f$ and $\mathbf{s}_k^f$, depend on the Fourier coefficients of the displacements $\mathbf{x}(t)$, $\mathbf{c}_k^x$ and $\mathbf{s}_k^x$. The integer parameter ν is introduced to account for some possible subharmonics of the external excitation frequency ω.

Substituting expressions (5.2) in Eq. (5.1) and balancing the harmonic terms with a Galerkin projection yields the following nonlinear equations in the frequency domain

$$\mathbf{h}(\mathbf{z}, \omega) \equiv \mathbf{A}(\omega)\mathbf{z} - \mathbf{b}(\mathbf{z}, \omega) = \mathbf{0} \tag{5.3}$$

where $\mathbf{A}$ is the $(2N_H + 1)\,n \times (2N_H + 1)\,n$ matrix describing the linear dynamics of the system, $\mathbf{z}$ is the vector containing all the Fourier coefficients of the displacements $\mathbf{x}(t)$, and $\mathbf{b}$ represents the vector of the Fourier coefficients of the external and nonlinear forces $\mathbf{f}(t)$. They have the following expressions:

$$\mathbf{A} = \begin{bmatrix} \mathbf{K} & & & & \\ & \mathbf{K} - \left(\frac{\omega}{\nu}\right)^2 \mathbf{M} & -\frac{\omega}{\nu}\mathbf{C} & & \\ & \frac{\omega}{\nu}\mathbf{C} & \mathbf{K} - \left(\frac{\omega}{\nu}\right)^2 \mathbf{M} & & \\ & & & \ddots & \\ & & & \mathbf{K} - \left(N_H \frac{\omega}{\nu}\right)^2 \mathbf{M} & -N_H \frac{\omega}{\nu}\mathbf{C} \\ & & & N_H \frac{\omega}{\nu}\mathbf{C} & \mathbf{K} - \left(N_H \frac{\omega}{\nu}\right)^2 \mathbf{M} \end{bmatrix}, \quad \mathbf{z} = \begin{bmatrix} \mathbf{c}_0^x \\ \mathbf{s}_1^x \\ \mathbf{c}_1^x \\ \vdots \\ \mathbf{s}_{N_H}^x \\ \mathbf{c}_{N_H}^x \end{bmatrix}, \quad \mathbf{b} = \begin{bmatrix} \mathbf{c}_0^f \\ \mathbf{s}_1^f \\ \mathbf{c}_1^f \\ \vdots \\ \mathbf{s}_{N_H}^f \\ \mathbf{c}_{N_H}^f \end{bmatrix} \tag{5.4}$$

In the time domain, expression (5.1) contains n equations while, in the frequency domain, expression (5.3) have $(2N_H + 1)\,n$ unknowns gathered in $\mathbf{z}$. Expression (5.3) can be seen as the equations of amplitude of (5.1): if $\mathbf{z}^*$ is a root of (5.3), then the time signals $\mathbf{x}^*$ constructed from $\mathbf{z}^*$ with (5.2) are solutions of the equations of motion (5.1) and are periodic.

5.2.1 Analytical Expression of the Nonlinear Terms and of the Jacobian Matrix of the System

Since $\mathbf{b}$ depends on $\mathbf{z}$, Eq. (5.3) is nonlinear and has to be solved iteratively (e.g., with a Newton-Raphson procedure). At each iteration, an evaluation of $\mathbf{b}$ and of $\partial\mathbf{h}/\partial\mathbf{z}$ has to be provided. If the nonlinearity is weak, in some cases $\mathbf{f}$ can be accurately approximated with a few number of harmonics N_H, and analytical relations between the Fourier coefficients of the forces $\mathbf{b}$ and of the displacements $\mathbf{z}$ can be developed together with the expression of the jacobian of the system [24–26]. When such developments are too intricate, most of the studies in the literature propose to evaluate $\mathbf{b}$ through successive transformations from frequency to time domains. For example, the alternating frequency/time-domain (AFT) technique [27] takes advantage of the fast Fourier transform to compute $\mathbf{b}$:

$$\mathbf{z} \xrightarrow{\text{FFT}^{-1}} \mathbf{x}(t) \rightarrow \mathbf{f}\left(\mathbf{x}, \dot{\mathbf{x}}, \omega, t\right) \xrightarrow{\text{FFT}} \mathbf{b}(\mathbf{z}, \omega) \tag{5.5}$$

The jacobian matrix of the system can then be computed through finite differences, which is cumbersome in terms of CPU time, or through linearization of the equations [15].

An efficient alternative consists in rewriting the inverse Fourier transform as a linear operator $\boldsymbol{\Gamma}\,(\omega)$ [28–31]. First, denoting N as the number of time samples of a discretized period of oscillation, one defines vectors $\tilde{\mathbf{x}}$ and $\tilde{\mathbf{f}}$ containing the concatenated nN time samples of the displacements and the forces, respectively, for all the DOFs:

$$\tilde{\mathbf{x}} = \begin{bmatrix} x_1\,(t_1) \\ \vdots \\ x_1\,(t_N) \\ \vdots \\ x_n\,(t_1) \\ \vdots \\ x_n\,(t_N) \end{bmatrix}, \quad \tilde{\mathbf{f}} = \begin{bmatrix} f_1\,(t_1) \\ \vdots \\ f_1\,(t_N) \\ \vdots \\ f_n\,(t_1) \\ \vdots \\ f_n\,(t_N) \end{bmatrix} \tag{5.6}$$

The inverse Fourier transform can then be written as a linear operation:

$$\tilde{\mathbf{x}} = \boldsymbol{\Gamma}\,(\omega)\,\mathbf{z} \tag{5.7}$$

with the $(nN \times (2N_H + 1)\, n)$ sparse operator

$$\boldsymbol{\Gamma}(\omega) = \left[\mathbb{I}_n \otimes \begin{bmatrix} 1 \\ 1 \\ \vdots \\ 1 \end{bmatrix} \mathbb{I}_n \otimes \begin{bmatrix} \sin(\omega t_1) \\ \sin(\omega t_2) \\ \vdots \\ \sin(\omega t_N) \end{bmatrix} \mathbb{I}_n \otimes \begin{bmatrix} \cos(\omega t_1) \\ \cos(\omega t_2) \\ \vdots \\ \cos(\omega t_N) \end{bmatrix} \dots \mathbb{I}_n \otimes \begin{bmatrix} \sin(N_H \omega t_1) \\ \sin(N_H \omega t_2) \\ \vdots \\ \sin(N_H \omega t_N) \end{bmatrix} \mathbb{I}_n \otimes \begin{bmatrix} \cos(N_H \omega t_1) \\ \cos(N_H \omega t_2) \\ \vdots \\ \cos(N_H \omega t_N) \end{bmatrix} \right] \tag{5.8}$$

where $\otimes$ and $\mathbb{I}$ stand for the Kronecker tensor product and the identity matrix, respectively. The direct Fourier transformation is written

$$\mathbf{z} = (\boldsymbol{\Gamma}(\omega))^{+} \tilde{\mathbf{x}} \tag{5.9}$$

where $^{+}$ stands for the Moore-Penrose pseudoinverse:

$$\boldsymbol{\Gamma}^{+} = \boldsymbol{\Gamma}^{T} \left(\boldsymbol{\Gamma} \boldsymbol{\Gamma}^{T} \right)^{-1} \tag{5.10}$$

According to these notations, the Fourier coefficients of the external and nonlinear forces are simply obtained by transforming the signals in the time domain back to the frequency domain:

$$\mathbf{b}(\mathbf{z}, \omega) = (\boldsymbol{\Gamma}(\omega))^{+} \tilde{\mathbf{f}} \tag{5.11}$$

The jacobian matrix of expression (5.3) with respect to the Fourier coefficients $\mathbf{z}$ can be computed as

$$\mathbf{J}_z = \frac{\partial \mathbf{h}}{\partial \mathbf{z}} = \mathbf{A} - \frac{\partial \mathbf{b}}{\partial \mathbf{z}} \tag{5.12}$$

In order to compute the derivative of $\mathbf{b}$ with respect to the Fourier coefficients of the displacements, $\mathbf{z}$, one can use the following chain rule:

$$\frac{\partial \mathbf{b}}{\partial \mathbf{z}} = \frac{\partial \mathbf{b}}{\partial \tilde{\mathbf{f}}} \frac{\partial \tilde{\mathbf{f}}}{\partial \tilde{\mathbf{x}}} \frac{\partial \tilde{\mathbf{x}}}{\partial \mathbf{z}} \tag{5.13}$$

which is rewritten with the transformation matrices

$$\frac{\partial \mathbf{b}}{\partial \mathbf{z}} = \boldsymbol{\Gamma}^{+} \frac{\partial \tilde{\mathbf{f}}}{\partial \tilde{\mathbf{x}}} \boldsymbol{\Gamma} \tag{5.14}$$

In general, the derivatives of the forces with respect to the displacements in the time domain can be expressed analytically, which makes the computation of the jacobian matrix of (5.3) faster than with the finite differences.

5.2.2 Continuation Procedure

It is usually of interest to solve (5.3) for a range of parameter values ω, rather than for a single value of the parameter. One could for example be interested in the behavior of a structure in the neighborhood of a resonance peak. A continuation scheme, coupled to the highlighted HB method, has therefore to be implemented.

Solving (5.3) for different fixed values of ω, as done with a sequential continuation procedure, fails at turning point. To overcome this issue, for this work a procedure based on tangent predictions and Moore-Penrose corrections has been selected, as proposed in the software MATCONT [12].

Denoting $\mathbf{J}_\omega$ as the jacobian of $\mathbf{h}$ with respect to the parameter ω, the search for a tangent vector $\mathbf{t}^{(i)}$ at an iteration point $\left(\mathbf{z}^{(i)}, \omega^{(i)}\right)$ along the branch reads

$$\begin{bmatrix} \mathbf{J}_z \ \mathbf{J}_\omega \\ \mathbf{t}_{(i-1)}^T \end{bmatrix} \mathbf{t}_{(i)} = \begin{bmatrix} \mathbf{0} \\ 1 \end{bmatrix} \tag{5.15}$$

The last equation in the system (5.15), imposing a scalar product of 1 between the new tangent and the previous one prevents the continuation procedure from turning back. For the first iteration of the procedure, this last row can be replaced by a condition imposing the sum of the components of the tangent to be equal to 1.

The correction stage is based on Newton's method. Introducing new optimization variables $\mathbf{v}_{(i,j)}$ initialized as $\mathbf{v}_{(i,1)} = \mathbf{t}_{(i)}$, and $\mathbf{y}_{(i,j)} = \left[\mathbf{z}_{(i,j)} \ \omega_{(i,j)}\right]^T$, the different Newton's iterations i are constructed as following:

$$\begin{aligned} \mathbf{y}_{(i,j+1)} &= \mathbf{y}_{(i,j)} - \mathbf{G}_y^{-1}\left(\mathbf{y}_{(i,j)}, \mathbf{v}_{(i,j)}\right) \mathbf{G}\left(\mathbf{y}_{(i,j)}, \mathbf{v}_{(i,j)}\right) \\ \mathbf{v}_{(i,j+1)} &= \mathbf{v}_{(i,j)} - \mathbf{G}_y^{-1}\left(\mathbf{y}_{(i,j)}, \mathbf{v}_{(i,j)}\right) \mathbf{R}\left(\mathbf{y}_{(i,j)}, \mathbf{v}_{(i,j)}\right) \end{aligned} \tag{5.16}$$

with

$$\mathbf{G}(\mathbf{y}, \mathbf{v}) = \begin{bmatrix} \mathbf{h}(\mathbf{y}) \\ \mathbf{0} \end{bmatrix}, \ \mathbf{G}_y(\mathbf{y}, \mathbf{v}) = \begin{bmatrix} \mathbf{J}_z(\mathbf{y}) \ \mathbf{J}_\omega(\mathbf{y}) \\ \mathbf{v}^T \end{bmatrix}, \ \mathbf{R}(\mathbf{y}, \mathbf{v}) = \begin{bmatrix} \left[\mathbf{J}_z(\mathbf{y}) \ \mathbf{J}_\omega(\mathbf{y})\right] \mathbf{v} \\ \mathbf{0} \end{bmatrix} \tag{5.17}$$

For a more detailed presentation of the continuation procedure, the reader can refer to [12].

5.2.3 *Stability Analysis*

The continuation procedure developed above does not indicate if a periodic solution is stable or not; therefore, a stability analysis has to be performed along the branch. In the case of time domain methods, such as the shooting technique, one usually obtains the monodromy matrix as a by-product of the procedure [8], which then provides the Floquet multipliers to study the stability of the solutions. On the other hand, in the case of frequency domain techniques such as the HB method, one preferably uses Hill's method by solving a quadratic eigenvalue problem whose components are obtained as by-products of the method. The quadratic eigenvalue problem proposed by von Groll et al. [16] for finding the Hill's coefficients as solutions of

$$\boldsymbol{\Delta}_2 \boldsymbol{\lambda}^2 + \boldsymbol{\Delta}_1 \boldsymbol{\lambda} + \mathbf{J}_z = \mathbf{0} \tag{5.18}$$

with

$$\boldsymbol{\Delta}_1 = \begin{bmatrix} \mathbf{C} & & & & \\ & \mathbf{C} & -2\frac{\omega}{\nu}\mathbf{M} & & \\ & 2\frac{\omega}{\nu}\mathbf{M} & \mathbf{C} & & \\ & & & \ddots & \\ & & & \mathbf{C} & -2N_H\frac{\omega}{\nu}\mathbf{M} \\ & & & 2N_H\frac{\omega}{\nu}\mathbf{M} & \mathbf{C} \end{bmatrix}, \ \boldsymbol{\Delta}_2 = \mathbb{I}_{(2N_H+1)} \otimes \mathbf{M} \tag{5.19}$$

can be rewritten as a linear eigenvalue problem of double size

$$\mathbf{B}_1 - \begin{bmatrix} \boldsymbol{\lambda} & \\ & \boldsymbol{\gamma} \end{bmatrix} \mathbf{B}_2 = \mathbf{0} \tag{5.20}$$

with

$$\mathbf{B}_1 = \begin{bmatrix} \boldsymbol{\Delta}_1 & \mathbf{J}_z \\ -\mathbb{I} & \mathbf{0} \end{bmatrix}, \quad \mathbf{B}_2 = -\begin{bmatrix} \boldsymbol{\Delta}_2 & \mathbf{0} \\ \mathbf{0} & \mathbb{I} \end{bmatrix} \tag{5.21}$$

The eigenvalues $\boldsymbol{\lambda}$ can thus be found among the eigenvalues of the $(2N_H + 1)\,2n \times (2N_H + 1)\,2n$ matrix

$$\mathbf{B} = \mathbf{B}_2^{-1}\mathbf{B}_1 \tag{5.22}$$

However, only $2n$ eigenvalues $\tilde{\boldsymbol{\lambda}}$ among the set $\boldsymbol{\lambda}$ approximate the Floquet exponents of the solution [32]. The other eigenvalues are only spurious and do not have any physical meaning; their number also increases with the number of harmonics N_H. As way to extract the approximations of the Floquet exponents $\tilde{\boldsymbol{\lambda}}$ from the set $\boldsymbol{\lambda}$, Moore [33] showed that one should always choose the $2n$ eigenvalues with the smallest imaginary part in modulus. The term *Floquet exponents* will be used throughout this paper for the eigenvalues $\tilde{\boldsymbol{\lambda}}$; it should however be kept in mind that these exponents are computed with Hill's method. A diagonal matrix $\tilde{\mathbf{B}}$ containing the components of $\tilde{\boldsymbol{\lambda}}$ is then constructed:

$$\tilde{\mathbf{B}} = \begin{bmatrix} \tilde{\lambda}_1 & & & \\ & \tilde{\lambda}_2 & & \\ & & \ddots & \\ & & & \tilde{\lambda}_{2n} \end{bmatrix} \tag{5.23}$$

As will be explained in Sects. 5.2.4 and 5.2.5, this matrix $\tilde{\mathbf{B}}$ plays a key role in the detection and tracking of bifurcations.

5.2.4 Detection of Bifurcations

In this work the detection and tracking of fold (F), Neimark-Sacker (NS) and branch point (BP) bifurcations is sought. The procedure proposed in this paper builds on the evaluation of *test functions* ϕ at each iteration along a continuation branch [12]; the roots of these test functions then indicate the presence of bifurcations.

According to their algebraic definitions, as explained by Seydel [34], a fold bifurcation is characterized by a rank deficiency of 1 for the jacobian matrix $\mathbf{J}_z$, and a BP bifurcation by a rank deficiency of 2. A necessary condition for fold and BP bifurcations is thus

$$|\mathbf{J}_z| = 0 \tag{5.24}$$

In order to distinguish between fold and BP bifurcations, Govaerts et al. [35] proposes the following test functions:

$$\begin{aligned} \phi_{BP} &= \begin{vmatrix} \mathbf{J}_z & \mathbf{J}_\omega \\ \mathbf{t}^T & \end{vmatrix} \\ \phi_{F,1} &= |\mathbf{J}_z| \end{aligned} \tag{5.25}$$

Fold bifurcations are found at roots of $\phi_{F,1}$, provided that ϕ_{BP} is different from 0.

One could also follow another approach, based on Floquet theory. A fold bifurcation is detected when a Floquet exponent crosses the imaginary axis along the real axis. As a consequence, the matrix of Floquet exponents $\tilde{\mathbf{B}}$ is singular at a fold bifurcation. One thus has an alternative test function $\phi_{F,2}$ written as

$$\phi_{F,2} = \left|\tilde{\mathbf{B}}\right| \tag{5.26}$$

The third type of bifurcation studied in this paper, the NS bifurcation, is detected when a pair of Floquet exponents crosses the imaginary axis as a pair of complex conjugates. Using the theory of the bialternate product [36] $\mathbf{P}_\odot$ of a $m \times m$ matrix $\mathbf{P}$

$$\mathbf{P}_\odot = \mathbf{P} \odot \mathbb{I}_m \tag{5.27}$$

which has the property to be singular when $\mathbf{P}$ has a pair of complex conjugates crossing the imaginary axis, one writes the test function for NS bifurcations as

$$\phi_{NS} = \left|\tilde{\mathbf{B}}_\odot\right| \tag{5.28}$$

Nevertheless, for large systems the values of determinants usually explode and their use leads to scaling problems. To overcome this issue, previous studies [37–39] proposed the so-called *bordering technique*. The idea behind this technique is to replace the evaluation of the determinant of a matrix $\mathbf{G}$ by the evaluation of a scalar function, herein denoted g, which vanishes as regular zero for the same system state and parameters as the determinant. Instead of

$$|\mathbf{G}| = 0 \tag{5.29}$$

it is more robust to write

$$g = 0 \tag{5.30}$$

where g is obtained by solving

$$\begin{bmatrix} \mathbf{G} & \mathbf{p} \\ \mathbf{q}^* & 0 \end{bmatrix} \begin{bmatrix} \mathbf{w} \\ g \end{bmatrix} = \begin{bmatrix} \mathbf{0} \\ 1 \end{bmatrix} \tag{5.31}$$

In this system, * denotes a conjugate transpose, and vectors $\mathbf{p}$ and $\mathbf{q}$ are chosen to ensure the nonsingularity of the matrix. When $\mathbf{G}$ is close to be singular, one preferably takes $\mathbf{q}$ and $\mathbf{p}$ close to the nullvectors of $\mathbf{G}$ and $\mathbf{G}^*$, respectively.

The test functions for BP, fold and NS bifurcations based on the bordering technique can finally be written as

$$\begin{aligned}
&\text{BPbifurcations :} \quad \phi_{BP} = g_{BP} \quad \text{with} \quad \mathbf{G}_{BP} = \begin{bmatrix} \mathbf{J}_z & \mathbf{J}_\omega \\ \mathbf{t}^T & \end{bmatrix} \\
&\text{Foldbifurcations :} \quad \begin{cases} \phi_{F,1} = g_{F,1} \quad \text{with} \quad \mathbf{G}_{F,1} = \mathbf{J}_z \\ \qquad \text{or} \\ \phi_{F,2} = g_{F,2} \quad \text{with} \quad \mathbf{G}_{F,2} = \tilde{\mathbf{B}} \end{cases} \\
&\text{NSbifurcations :} \quad \phi_{NS} = g_{NS} \quad \text{with} \quad \mathbf{G}_{NS} = \tilde{\mathbf{B}}_\odot
\end{aligned} \tag{5.32}$$

It should be noted that it is also convenient to use another test function for fold detection, namely

$$\phi_{F,3} = \mathbf{t}_{i_\omega} \tag{5.33}$$

which describes the fact that a fold bifurcation is detected when the component i_ω of the tangent prediction related to the active parameter ω changes sign [35]. This function does not require the resolution of a bordered system and therefore reduces the computational burden.

5.2.5 Tracking of Bifurcations

In order to continue codimension-1 bifurcations with respect to two parameters of the system, such as the frequency and amplitude of the forcing applied on the system, one has to append one equation to (5.3). Using the bordering technique, one obtains the following extended system:

$$\begin{cases} \mathbf{h} \equiv \mathbf{A}\mathbf{z} - \mathbf{b} = 0 \\ \\ g = 0 \end{cases} \tag{5.34}$$

where $g = g_{BP}$, g_F and g_{NS} are the solutions of bordered systems for BP, fold and NS bifurcations, respectively, with

$$\begin{aligned} &\text{BP bifurcations :} && \mathbf{G}_{BP} = \mathbf{J}_z \\ &\text{Fold bifurcations :} && \begin{cases} \mathbf{G}_{F,1} = \mathbf{J}_z \\ \quad \text{or} \\ \mathbf{G}_{F,2} = \tilde{\mathbf{B}} \end{cases} \\ &\text{NS bifurcations :} && \mathbf{G}_{NS} = \tilde{\mathbf{B}}_{\odot} \end{aligned} \tag{5.35}$$

One notices that the same additional equation, that is the fact that the determinant of $\mathbf{J}_z$ is 0, can be used either for tracking fold or BP bifurcations. Again, for fold bifurcations, one can follow either the algebraic approach using $\mathbf{J}_z$ in the bordered system, or the Floquet approach using $\tilde{\mathbf{B}}$.

During the continuation procedure, the computation of the derivatives of the additional equation is required. As shown by Govaerts [37], in the case of the bordering technique, analytical expressions for the derivatives of g with respect to one of the two active parameters α are found as

$$g_\alpha = -\mathbf{v}^* \mathbf{G}_\alpha \mathbf{w} \tag{5.36}$$

where $\mathbf{G}_\alpha$ is the derivative of $\mathbf{G}$ with respect to α, and where $\mathbf{w}$ and $\mathbf{v}$ comes from the resolution of the bordered system and its transposed version:

$$\begin{bmatrix} \mathbf{G} & \mathbf{p} \\ \mathbf{q}^* & 0 \end{bmatrix} \begin{bmatrix} \mathbf{w} \\ g \end{bmatrix} = \begin{bmatrix} \mathbf{0} \\ 1 \end{bmatrix} \tag{5.37}$$

$$\begin{bmatrix} \mathbf{G} & \mathbf{p} \\ \mathbf{q}^* & 0 \end{bmatrix}^* \begin{bmatrix} \mathbf{v} \\ e \end{bmatrix} = \begin{bmatrix} \mathbf{0} \\ 1 \end{bmatrix} \tag{5.38}$$

As a result, the only term that has to be evaluated is $\mathbf{G}_\alpha$. For g_{BP} and $g_{F,1}$, this gives

$$\frac{\partial}{\partial \alpha} \left(\mathbf{G}_{BP} \right) = \frac{\partial}{\partial \alpha} \left(\mathbf{G}_{F,1} \right) = \mathbf{J}_{z\alpha} \tag{5.39}$$

where $\mathbf{J}_{z\alpha}$ is the derivative of the jacobian $\mathbf{J}_z$ with respect to α, that can be computed through finite differences.

In the case of the Floquet approach, the derivatives read

$$\begin{aligned} &\tfrac{\partial}{\partial \alpha} \left(\mathbf{G}_{F,2} \right) = \tfrac{\partial}{\partial \alpha} \left(\tilde{\mathbf{B}} \right) \\ &\tfrac{\partial}{\partial \alpha} \left(\mathbf{G}_{NS} \right) = \tfrac{\partial}{\partial \alpha} \left(\tilde{\mathbf{B}}_{\odot} \right) = \left(\tfrac{\partial}{\partial \alpha} \left(\tilde{\mathbf{B}} \right) \right)_{\odot} \end{aligned} \tag{5.40}$$

One could directly rely on finite differences to compute the derivatives of the Floquet exponents in $\tilde{\mathbf{B}}$, that are

$$\frac{\partial}{\partial\alpha}\left(\tilde{\mathbf{B}}\right) = \begin{bmatrix} \frac{\partial\tilde{\lambda}_1}{\partial\alpha} & & & \\ & \frac{\partial\tilde{\lambda}_2}{\partial\alpha} & & \\ & & \ddots & \\ & & & \frac{\partial\tilde{\lambda}_{2n}}{\partial\alpha} \end{bmatrix} \tag{5.41}$$

However, this means that the eigenvalue problem (5.20) has to be solved $N_H + 2$ times per iteration, which is cumbersome for large systems. Instead, in this paper one computes these expressions using the properties of the derivatives of eigenvalues demonstrated by Van der Aa et al. [40]. Denoting $\mathbf{\Lambda}$ the eigenvector matrix of $\mathbf{B}$, and $\boldsymbol{\xi}$ the localization vector containing the index of the $2n$ Floquet exponents $\tilde{\boldsymbol{\lambda}}$ among the eigenvalues $\boldsymbol{\lambda}$, i.e.,

$$\tilde{\lambda}_i = \lambda_{\xi_i} \tag{5.42}$$

the eigenvalues derivatives can be computed as

$$\frac{\partial\tilde{\lambda}_i}{\partial\alpha} = \left(\mathbf{\Lambda}^{-1}\frac{\partial\mathbf{B}}{\partial\alpha}\mathbf{\Lambda}\right)_{(\xi_i,\xi_i)} \tag{5.43}$$

The only terms to be computed are thus the derivatives of $\mathbf{B}$, whose expression can be obtained from Eqs. (5.21) and (5.22). This requires the computation of the derivative of the jacobian $\mathbf{J}_z$ with respect to α, which can be performed using finite differences.

5.3 Validation of the Method on the Study of an Industrial, Complex Model with Strong Nonlinearities: The SmallSat

In this section, the HB method is used to address the continuation of periodic solutions of a large-scale structure, and the detection and tracking of their bifurcations. Analysis of nonlinear phenomena such as frequency/amplitude jumps and quasiperiodic oscillations is carried out using the outlined method.

5.3.1 Case Study: SmallSat Spacecraft

The example studied is referred to as the *SmallSat*, a structure represented in Fig. 5.1a and which was conceived by EADS-Astrium as a platform for small satellites. The interface between the spacecraft and launch vehicle is achieved via four aluminum brackets located around cut-outs at the base of the structure. The total mass of the spacecraft including the interface brackets is around 64 kg, it is 1.2 m in height and 1 m in width. It supports a dummy telescope mounted on a baseplate through a tripod, and the telescope plate is connected to the SmallSat top floor by three shock attenuators, termed *shock attenuation systems for spacecraft and adaptor* (SASSAs), whose dynamic behavior may exhibit nonlinearity.

Besides, as depicted in Fig. 5.1b, a support bracket connects to one of the eight walls the so-called *wheel elastomer mounting system* (WEMS) device which is loaded with an 8-kg dummy inertia wheel. The WEMS device is a mechanical filter which mitigates disturbances coming from the inertia wheel through the presence of a soft elastomeric interface between its mobile part, i.e. the inertia wheel and a supporting metallic cross, and its fixed part, i.e. the bracket and by extension the spacecraft. Moreover, eight mechanical stops limit the axial and lateral motions of the WEMS mobile part during launch, which gives rise to strongly nonlinear dynamical phenomena. A thin layer of elastomer placed onto the stops is used to prevent metal-metal impacts. Figure 5.2a presents a simplified though relevant modelling of the WEMS device where the inertia wheel, owing to its important rigidity, is seen as a point mass. The four nonlinear connections (NCs) between the WEMS mobile and fixed parts are labelled NC1–4. Each NC possesses a trilinear spring in the axial direction (elastomer in traction/compression plus two stops), a bilinear spring in the radial direction (elastomer in shear plus one stop) and a linear spring in the third direction (elastomer in shear). In Fig. 5.2a, linear and nonlinear springs are denoted by squares and circles, respectively.

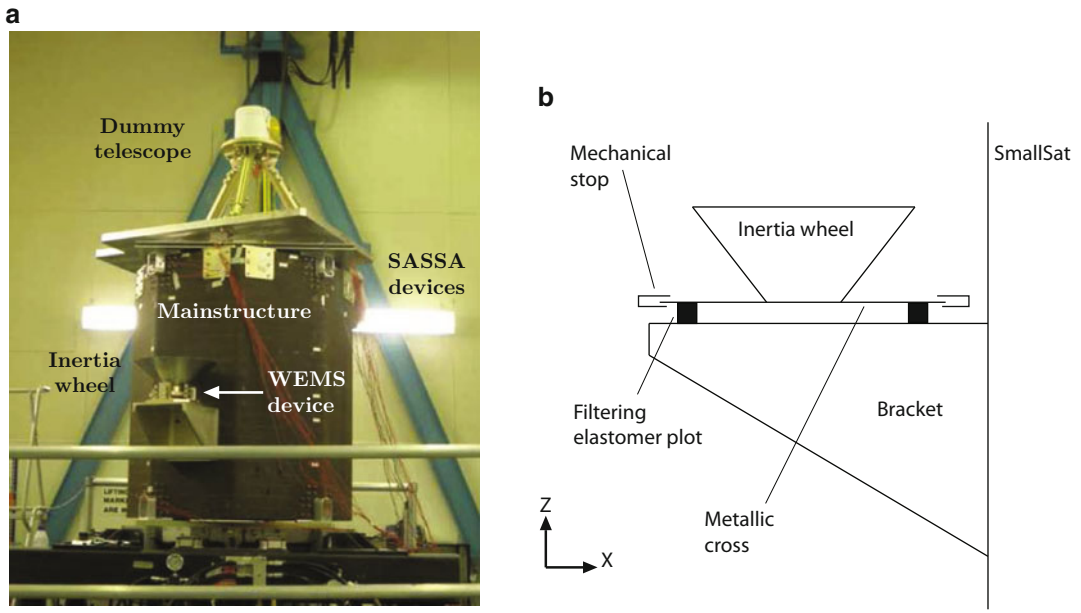

Fig. 5.1 SmallSat spacecraft equipped with an inertia wheel supported by the WEMS and a dummy telescope connected to the main structure by the SASSA isolators. (**a**) Photograph. (**b**) Schematic of the nonlinear vibration isolation device

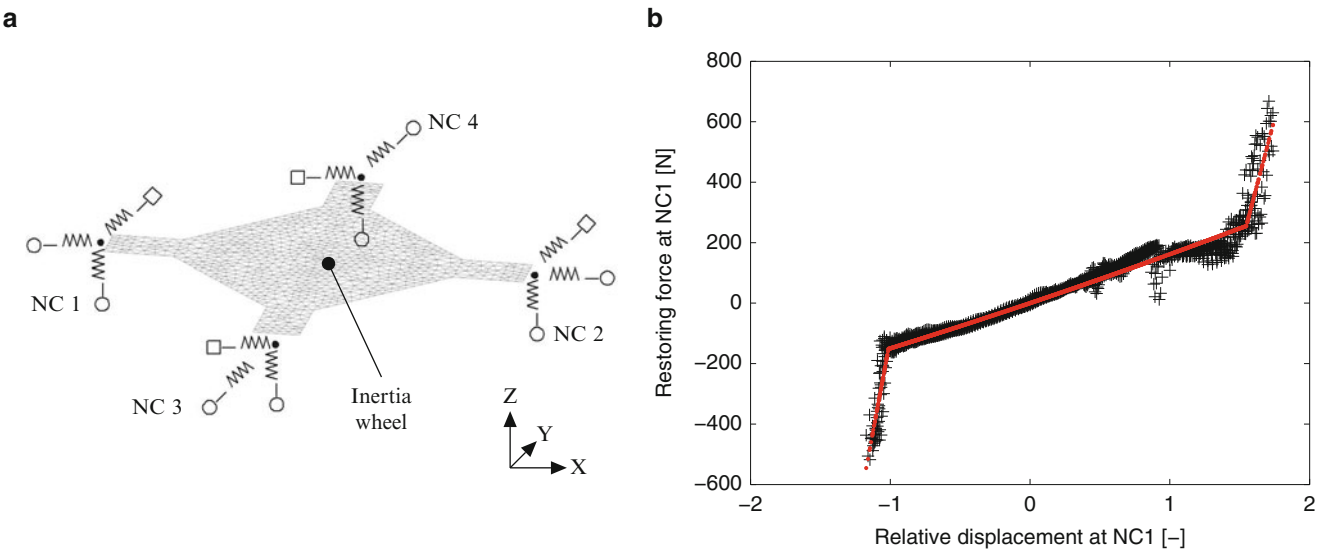

Fig. 5.2 WEMS. (**a**) Simplified modeling of the WEMS mobile part considering the inertia wheel as a point mass. The linear and nonlinear connections between the WEMS mobile and fixed parts are signaled by *squares* and *circles*, respectively. (**b**) Experimental stiffness curve of NC1 constructed using the restoring force surface method (in *black*) and fitted with a trilinear model (in *red*) (Color figure online)

A finite element model (FEM) of the SmallSat was developed and used in the present work to conduct numerical experiments. It comprises about 150,000 DOFs and the comparison with experimental data revealed its good predictive capabilities. The model consists of shell elements (octagon structure and top floor, instrument baseplate, bracket and WEMS metallic cross) and point masses (dummy inertia wheel and telescope) and meets boundary conditions with four clamped nodes. Proportional damping is considered and the high dissipation in the elastomer components of the WEMS is described using lumped dashpots with coefficients $c_{ax} = 63\,\mathrm{Ns/m}$ and $c_{lat} = 37\,\mathrm{Ns/m}$ for axial (vertical) and lateral directions, respectively; this results in a highly non-proportional damping matrix. Then, to achieve tractable nonlinear calculations,

the linear elements of the FEM were condensed using the Craig-Bampton reduction technique. This approach consists in expressing the system dynamics in terms of some retained DOFs and internal modes of vibration. Specifically, the full-scale model of the spacecraft was reduced to nine nodes (excluding DOFs in rotation), namely both sides of each NC and the vertical DOF of the inertia wheel, with ten internal modes. In total, the reduced-order model thus contains 37 DOFs. Bilinear and trilinear springs were finally introduced within the WEMS module between the NC nodes to model the nonlinearities of the connections between the WEMS and the rest of the SmallSat. To avoid numerical issues, regularization with third-order polynomials was utilized in the close vicinity of the clearances to implement C^1 continuity. The WEMS nonlinearities are the only nonlinear components introduced in the model. They were accurately identified in [2] using measured data from swept-sine base excitations at different amplitude levels. For instance, the stiffness curve characterizing NC1, identified using the restoring force surface method [41], is depicted in Fig. 5.2b. For confidentiality, clearances and displacements of the SmallSat are given through adimensionalized quantities throughout the paper.

5.3.2 Nonlinear Dynamics and Bifurcations of the SmallSat

The first part of the study of the SmallSat is carried out on the forced response of the structure for vertical excitations on the DOF of the inertia wheel. The frequency range of interest is located around the sixth mode of the structure, which corresponds to a linear frequency of 28.75 Hz. However, it was shown by Renson et al. [3] that this nonlinear mode undergoes a substantial increase in frequency due to the frequency-energy dependence of the structure.

Figure 5.3a gives the response of the NC1-Z node to a swept-sine excitation of forcing amplitude $F = 155$ N applied vertically on the inertia wheel. For this result and other swept-sine excitations throughout this paper, the applied sweep rate is 10 Hz/min. One first notices a sudden amplitude jump close to 35 Hz, which is expected for a hardening structure. Another zone of high amplitude also appears between 30 and 32 Hz, which is more surprising. A time response of the system to a single harmonic excitation of forcing amplitude $F = 155$ N and frequency $\omega = 30.5$ Hz is provided in Fig. 5.3b, i.e. in the frequency interval of the unexpected resonance. One observes that quasiperiodic oscillations occur for this operation regime, which is another phenomenon peculiar to nonlinear systems. In this case however, their importance has to be carefully assessed since they have amplitude as large as the one of the resonance.

Increasing the forcing amplitude of the swept-sine excitation further, one obtains the four responses given in Fig. 5.3c corresponding to small variations of F between 168 and 174 N. Although the responses do not significantly evolve from 168 to 170 N and from 172 to 174 N, a substantial increase in frequency and amplitude can be observed when the forcing amplitude varies from 170 to 172 N. This phenomenon, which is not often described in the technical literature, is of high interest since it leads to a resonance frequency shift of almost 4 Hz for a forcing amplitude barely increased by 2 N. For space applications with drastic structural requirements, such a behavior certainly has to be analyzed. Moreover, one notices that the quasiperiodic region is also present for these high excitation levels.

In order to explain and study the nonlinear phenomena highlighted, the HB method presented in this paper is now applied to the model. Figure 5.4a depicts the system's frequency response curve computed with $N_H = 9$ harmonics retained in the Fourier approximation and $N = 1,024$ points per period. For this result and others in the paper, no subharmonic solution is sought ($\nu = 1$). The amplitude of the periodic solutions computed is represented, that is the maximum displacement of the DOF of interest along the period. The evolution of the harmonic coefficients $\boldsymbol{\sigma}_i$ $(i = 1, \ldots, N_H)$ along the branch is given in Fig. 5.4b, where the following normalization is applied:

$$\begin{aligned} \boldsymbol{\sigma}_0 &= c_0^x \\ \boldsymbol{\sigma}_i &= \frac{\sqrt{\left(\mathbf{s}_i^x\right)^2 + \left(\mathbf{c}_i^x\right)^2}}{\sum_{k=1}^{N_H} \sqrt{\left(\mathbf{s}_k^x\right)^2 + \left(\mathbf{c}_k^x\right)^2}} \quad (i = 1, \ldots, N_H) \end{aligned} \tag{5.44}$$

From 20 to 23 Hz, only the fundamental frequency is present in the response. When the excitation enters the resonance region, the nonlinearities of the SmallSat activate other harmonics in the response such as the second and third ones. From the figure, it is also clear that the sixth and higher harmonics have a negligible participation to the response; for this reason, a number of harmonics $N_H = 5$ retained in the Fourier series is considered throughout the rest of the paper. It is also possible to show that the number of $N = 1,024$ points per period is sufficient to capture the dynamics in play.

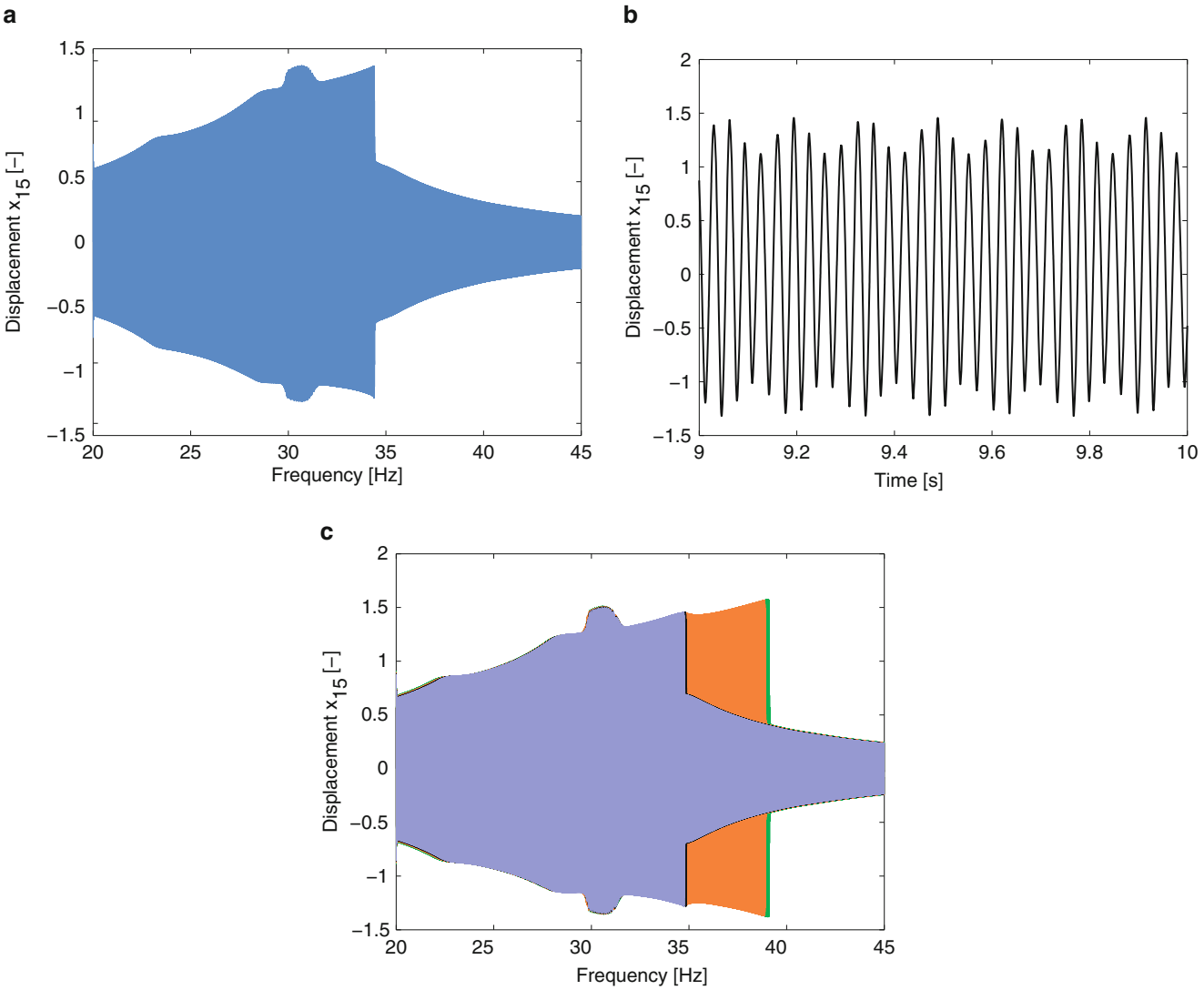

Fig. 5.3 Nonlinear dynamics of the SmallSat. Time responses of the NC1-Z node of the SmallSat for different excitations applied to the inertia wheel. (**a**) Swept-sine excitation of amplitude $F = 155$ N. (**b**) Harmonic excitation of amplitude $F = 155$ N and frequency $\omega = 30.5$ Hz. (**c**) Swept-sine excitations of amplitudes $F = 168$ (*purple curve*), 170 (*black curve*), 172 (*orange curve*) and 174 N (*green curve*) (Color figure online)

Circle and triangle markers denote the fold and NS bifurcations, respectively, that are detected along the branch in Fig. 5.4a. One observes that a pair of fold bifurcations is present in the bending segments of the resonance peak, which is due to the hardening behavior of the system. Indeed, fold bifurcations give rise to a change in stability of the periodic solutions, which explains the jump phenomenon from high to low amplitude in Fig. 5.3a, c. One also notices a pair of NS bifurcations, which means that quasiperiodic solutions can be found in their vicinity. As a verification, frequency responses computed with HB method are superimposed to swept-sine responses in Fig. 5.5a, b, for forcing amplitude $F = 155$ and 174 N, respectively. Along with the fact that the frequency responses provide accurate estimations of the displacement envelopes, as expected, one also notes that the bifurcations are directly related to the nonlinear phenomena observed. On the one hand, fold bifurcations accurately point out the location of the amplitude jump; tracking the evolution of fold bifurcations with respect to other parameters such as the forcing amplitude F or the axial damping c_{ax} could then reveal the mechanism of the phenomenon shown in Fig. 5.3c. On the other hand, the large quasiperiodic oscillations observed in Fig. 5.3a, b are created

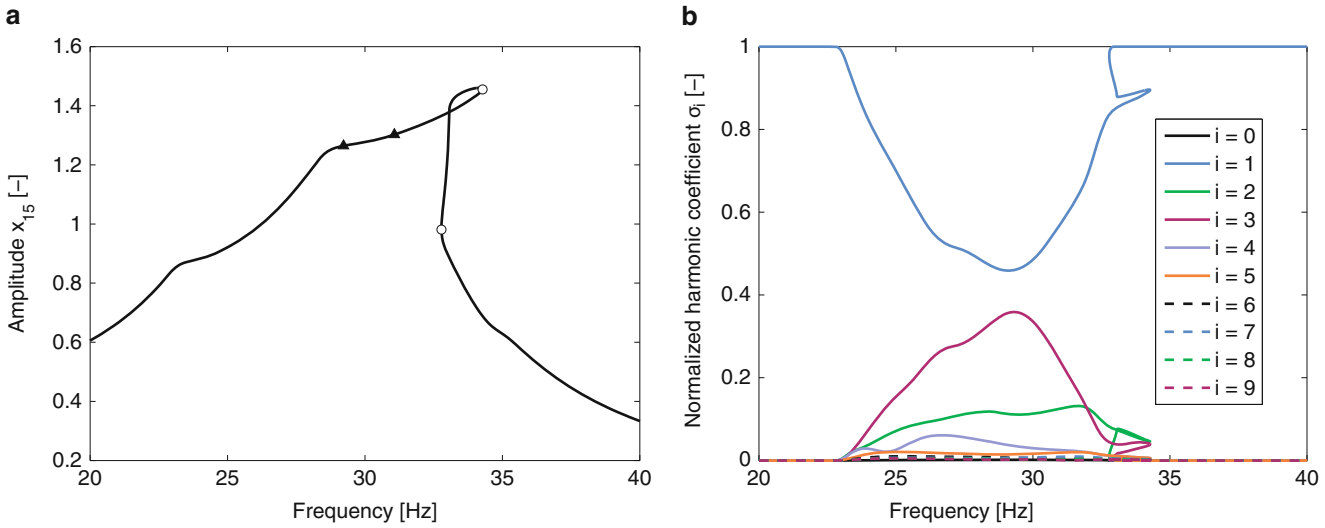

Fig. 5.4 SmallSat frequency response at NC1-Z node for harmonic excitations of amplitude $F = 155\,\mathrm{N}$ applied to the inertia wheel, obtained with the HB method. (**a**) Displacement responses with *circle markers* and *triangle markers* depicting fold and NS bifurcations, respectively. (**b**) Harmonic coefficients responses

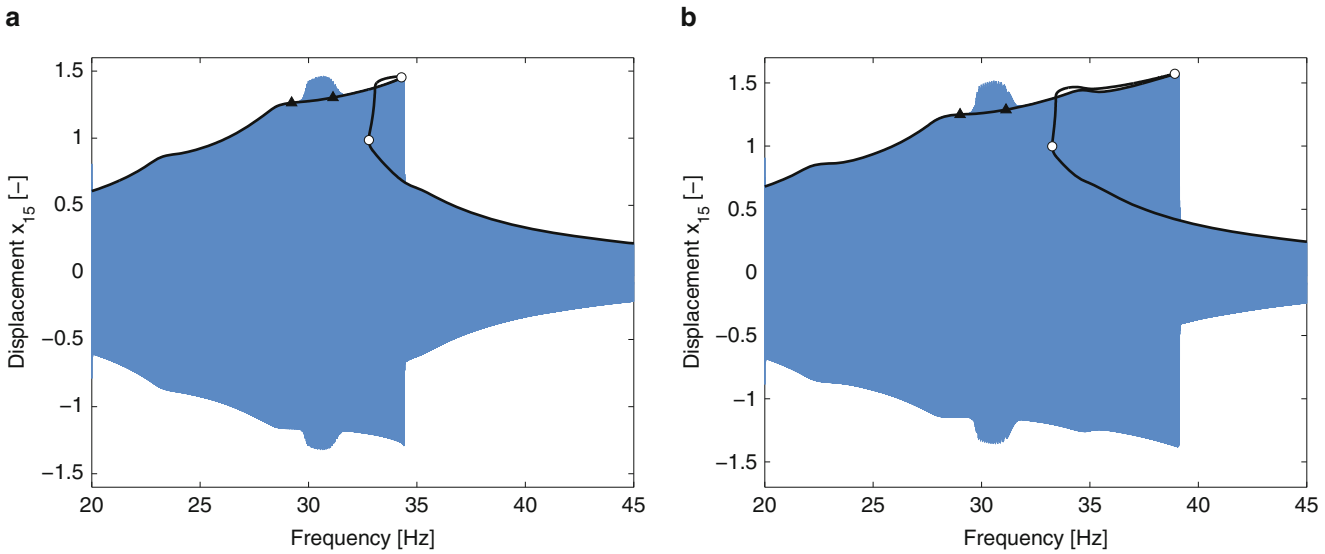

Fig. 5.5 SmallSat displacement response at NC1-Z node for excitations of amplitude (**a**) $F = 155\,\mathrm{N}$ and (**b**) $F = 174\,\mathrm{N}$ applied to the inertia wheel. The *blue lines* represent the swept-sine response obtained from time simulation, and the *black lines* are the frequency responses obtained with the HB method. *Circle markers* and *triangle markers* depict fold and NS bifurcations, respectively (Color figure online)

and eliminated at the first and second NS bifurcations, respectively; tracking the evolution of NS bifurcations with respect to a design parameter such as the axial damping c_{ax} could then indicate how one can modify the design of the SmallSat to avoid such disturbances.

5.3.3 *Influence of the Forcing Amplitude F and the Axial Damping c_{ax} on the Fold Bifurcations*

The purpose of this section is to get a deeper understanding of the frequency/jump phenomenon occurring close to the fold bifurcations. To this end, a tracking of the fold bifurcations in the codimension-2 forcing frequency-ω and amplitude-F space is performed using the technique developed in Sect. 5.2.5. Figure 5.6a represents the fold curve obtained, together

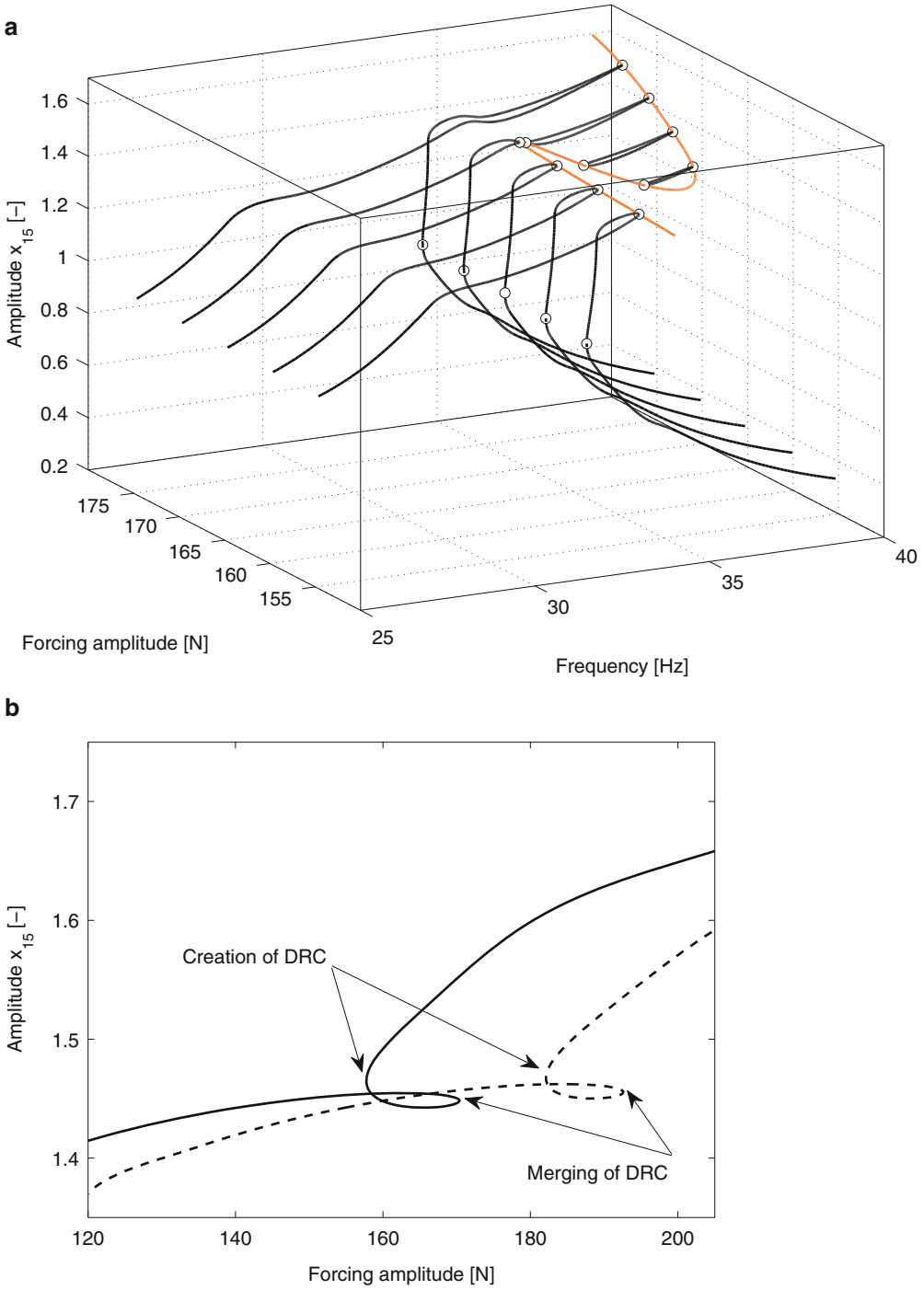

Fig. 5.6 Merging of the detached resonance curve with the main frequency response. (**a**) The *orange line* represents the branch of fold bifurcations tracked with respect to the excitation amplitude F and frequency ω. Frequency responses of the NC1-Z node for harmonic excitations of amplitude $F = 155$, 160, 170, and 175 N are also given with the *black lines*. *Circle markers* depict fold bifurcations. (**b**) Projection of the branch of fold bifurcations on the F-amplitude plane. The *solid* and *dashed lines* represent the branches for $c_{ax} = 63$ (reference) and 85 Ns/m, respectively (Color figure online)

with the frequency responses of the system for different forcing levels. Figure 5.6b also shows the projection of this curve in the F-amplitude plane. Very interestingly, the fold branch first tracks the bifurcations of the main frequency response, and then turns back to reveal *detached resonance curves* (DRC), or *isolas*, that are rarely observed for such large systems. These DRCs are created around the resonance peak at a forcing amplitude $F = 158\,\text{N}$, then expands both in frequency and amplitude, until one reaches a forcing amplitude $F = 170\,\text{N}$ at which they merge with this resonance peak. It can be shown that the upper part of the DRCs is stable; as a direct consequence, the merging of the DRC with the resonance peak leads to the sudden increase of the latter in frequency and amplitude, as highlighted in Fig. 5.3c.

Another fold curve is computed for a configuration of the SmallSat with $c_{ax} = 85\,\text{Ns/m}$, and represented in dashed line in Fig. 5.6b. While we could expect from an increase in the damping to annihilate nonlinear phenomena such as DRC, one sees that it only postpones the merging to higher forcing amplitudes and does not alter the size of the DRCs. For this system, DRCs are thus robust and deserve a careful investigation from the structural engineers.

Together with the explanations about the SmallSat dynamics they provide, these first results show that crucial information can be missed when one only performs continuation of periodic solutions. Obviously, a tracking in codimension-2 space is necessary in order to reveal DRCs.

5.3.4 *Influence of the Axial Damping c_{ax} on the NS Bifurcations*

Focusing now on NS bifurcations, one can also apply the continuation procedure presented in Sect. 5.2.5 to study the effect of a design parameter of the system such as c_{ax} on the quasiperiodic oscillations. Figure 5.7a depicts the evolution of the NS curve in the codimension-2 forcing frequency-ω and axial damping c_{ax} space, to which one superimposes frequency responses computed for $c_{ax} = 63$, 80 and 85 Ns/m. Its projection in the c_{ax}-amplitude plane is also given in Fig. 5.7b. It is interesting to note that increasing the axial damping up to a value of 84 Ns/m eliminates the NS bifurcations, while it does not significantly affect the resonance peaks.

As a verification, Fig. 5.8 shows the influence of c_{ax} on a displacement response for swept-sine excitations. At a forcing amplitude $F = 155\,\text{N}$ and for an axial damping $c_{ax} = 63\,\text{Ns/m}$, the quasiperiodic oscillations represent the part of the response with the largest amplitude. Increasing c_{ax} up to 85 Ns/m eliminates the NS bifurcations which generate these disturbances, with a small impact on the frequency of the resonance.

5.4 Conclusions

The purpose of this paper was twofold. First, it intended to extend the harmonic balance method from the computation of periodic solutions to the tracking of their bifurcations in codimension-2 parameter space. To this end, continuation techniques were adapted in order to obtain a robust and efficient algorithm able to deal with large engineering structures.

In the second part of this paper the HB method and its extension were applied to the SmallSat spacecraft, an industrial and complex model with several localized nonlinearities. Performing swept-sine excitation study on this structure revealed two types of nonlinear phenomena, namely quasiperiodic oscillations and frequency/amplitude jump due to detached resonance curves, which also involved responses of high amplitude. One then illustrated how the detection and tracking of fold and NS bifurcations can explain these phenomena, and how the design parameters of the system can be tuned to reduce their effects.

Acknowledgements The authors Thibaut Detroux, Luc Masset and Gaetan Kerschen would like to acknowledge the financial support of the European Union (ERC Starting Grant NoVib 307265).

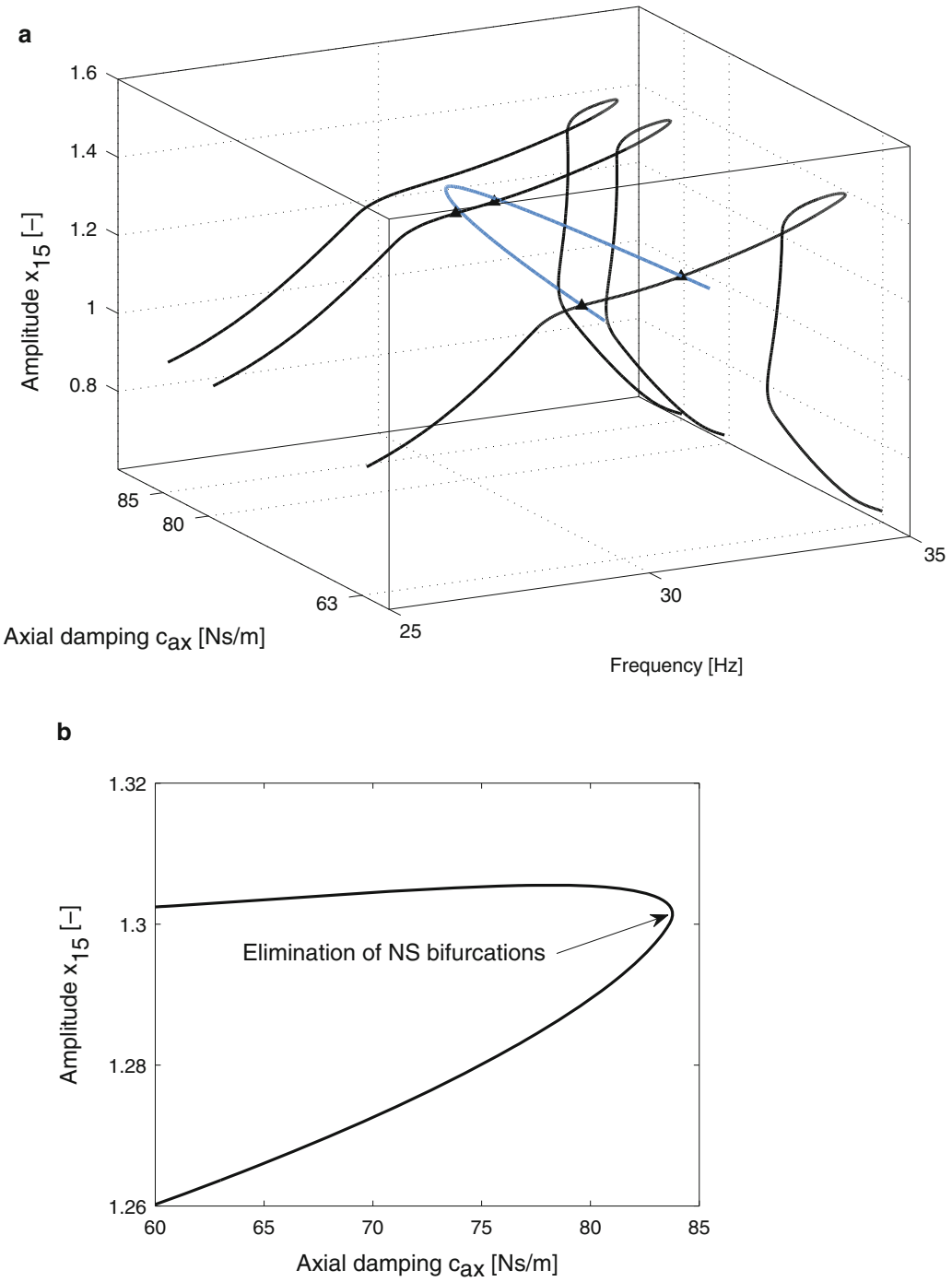

Fig. 5.7 Elimination of the NS bifurcations. (**a**) The *blue line* represents the branch of NS bifurcations tracked with respect to the axial damping coefficient c_{ax} and frequency ω. Frequency responses of the NC1-Z node for harmonic excitations of amplitude $F = 155$ N, and for configurations with $c_{ax} = 63$ (reference), 80 and 85 Ns/m are also given with the *black lines*. *Triangle markers* depict NS bifurcations. (**b**) Projection of the branch of NS bifurcations on the c_{ax}-amplitude plane (Color figure online)

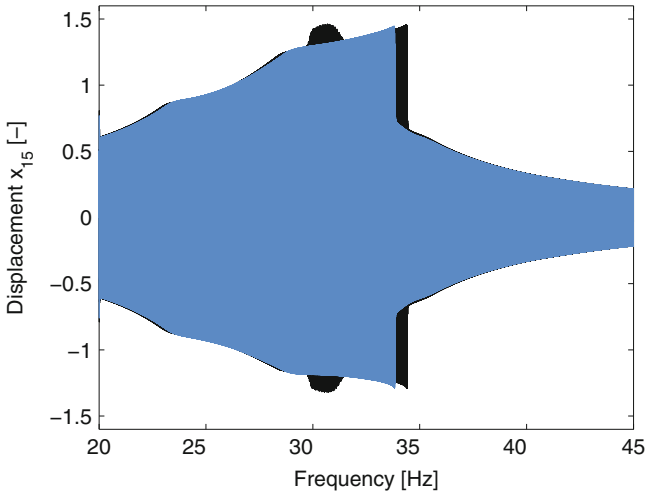

Fig. 5.8 SmallSat displacement response at NC1-Z node for swept-sine excitations of amplitude $F = 155$ N applied to the inertia wheel. The *blue line* and *green line* represent configuration with $c_{ax} = 63$ (reference) and 85 Ns/m, respectively (Color figure online)

References

1. Nayfeh AH, Mook DT (2008) Nonlinear oscillations. Wiley, New York
2. Noël J, Renson L, Kerschen G (2014) Complex dynamics of a nonlinear aerospace structure: experimental identification and modal interactions. J Sound Vib 333(12):2588–2607
3. Renson L, Noël J, Kerschen G (2015) Complex dynamics of a nonlinear aerospace structure: numerical continuation and normal modes. Nonlinear Dyn 79(2):1293–1309
4. Denegri CM (2000) Limit cycle oscillation flight test results of a fighter with external stores. J Aircraft 37(5):761–769
5. Ahlquist JR, Carreño JM, Climent H, de Diego R, de Alba J (2011) Assessment of nonlinear structural response in A400M GVT. In: Proulx T (ed) Structural dynamics, vol 3. Springer, New York, pp 1147–1155
6. Noël J-P, Renson L, Kerschen G, Peeters B, Manzato S, Debille J (2013) Nonlinear dynamic analysis of an F-16 aircraft using GVT data. In: Proceedings of the international forum on aeroelasticity and structural dynamics
7. Padmanabhan C, Singh R (1995) Analysis of periodically excited non-linear systems by a parametric continuation technique. J Sound Vib 184(1):5–58
8. Peeters M, Viguié R, Sérandour G, Kerschen G, Golinval J-C (2009) Nonlinear normal modes, part II: toward a practical computation using numerical continuation techniques. Mech Syst Signal Process 23(1):195–216
9. Doedel EJ, Champneys AR, Fairgrieve TF, Kuznetsov YA, Sandstede B, Wang X (1997) AUTO97: continuation and bifurcation software for ordinary differential equations (with HomCont), User's guide. Concordia University, Montreal. http://www.indy.cs.concordia.ca
10. Ascher U, Christiansen J, Russell RD (1979) A collocation solver for mixed order systems of boundary value problems. Math Comput 33: 659–679
11. Kuznetsov YA, Levitin VV (1995/1997) CONTENT: a multiplatform environment for analyzing dynamical systems, User's guide. Dynamical Systems Laboratory, CWI, Amsterdam. http://www.ftp.cwi.nl/pub/CONTENT
12. Dhooge A, Govaerts W, Kuznetsov YA (2003) MATCONT: a MATLAB package for numerical bifurcation analysis of ODEs. ACM Trans Math Softw (TOMS) 29(2):141–164
13. Dankowicz H, Schilder F (2011) An extended continuation problem for bifurcation analysis in the presence of constraints. J Comput Nonlinear Dyn 6(3):031003
14. Kundert KS, Sangiovanni-Vincentelli A (1986) Simulation of nonlinear circuits in the frequency domain. IEEE Trans Comput Aided Des Integr Circ Syst 5(4):521–535
15. Cardona A, Coune T, Lerusse A, Geradin M (1994) A multiharmonic method for non-linear vibration analysis. Int J Numer Methods Eng 37(9):1593–1608
16. von Groll G, Ewins DJ (2001) The harmonic balance method with arc-length continuation in rotor/stator contact problems. J Sound Vib 241(2):223–233
17. Laxalde D, Thouverez F (2009) Complex non-linear modal analysis for mechanical systems: application to turbomachinery bladings with friction interfaces. J Sound Vib 322(4):1009–1025
18. Grolet A, Thouverez F (2012) On a new harmonic selection technique for harmonic balance method. Mech Syst Signal Process 30:43–60
19. Grolet A, Thouverez F (2013) Vibration of mechanical systems with geometric nonlinearities: solving harmonic balance equations with Groebner basis and continuations methods. In: Proceedings of the colloquium calcul des structures et Modélisation CSMA, Giens
20. Arquier R (2007) Une méthode de calcul des modes de vibrations non-linéaires de structures. Ph.D. thesis, Université de la méditerranée (Aix-Marseille II), Marseille
21. Cochelin B, Vergez C (2009) A high order purely frequency-based harmonic balance formulation for continuation of periodic solutions. J Sound Vib 324(1):243–262
22. Karkar S, Cochelin B, Vergez C (2014) A comparative study of the harmonic balance method and the orthogonal collocation method on stiff nonlinear systems. J Sound Vib 333(12):2554–2567
23. Detroux T, Renson L, Kerschen G (2014) The harmonic balance method for advanced analysis and design of nonlinear mechanical systems. In: Nonlinear dynamics, vol 2. Springer, Cham, pp 19–34

24. Petrov E, Ewins D (2003) Analytical formulation of friction interface elements for analysis of nonlinear multi-harmonic vibrations of bladed disks. J Turbomach 125(2):364–371
25. Lau S, Zhang W-S (1992) Nonlinear vibrations of piecewise-linear systems by incremental harmonic balance method. J Appl Mech 59:153
26. Pierre C, Ferri A, Dowell E (1985) Multi-harmonic analysis of dry friction damped systems using an incremental harmonic balance method. J Appl Mech 52(4):958–964
27. Cameron T, Griffin J (1989) An alternating frequency/time domain method for calculating the steady-state response of nonlinear dynamic systems. J Appl Mech 56(1):149–154
28. Narayanan S, Sekar P (1998) A frequency domain based numeric–analytical method for non-linear dynamical systems. J Sound Vib 211(3):409–424
29. Bonani F, Gilli M (1999) Analysis of stability and bifurcations of limit cycles in Chua's circuit through the harmonic-balance approach. IEEE Trans Circ Syst I Fundam Theory Appl 46(8):881–890
30. Duan C, Singh R (2005) Super-harmonics in a torsional system with dry friction path subject to harmonic excitation under a mean torque. J Sound Vib 285(4):803–834
31. Kim T, Rook T, Singh R (2005) Super-and sub-harmonic response calculations for a torsional system with clearance nonlinearity using the harmonic balance method. J Sound Vib 281(3):965–993
32. Lazarus A, Thomas O (2010) A harmonic-based method for computing the stability of periodic solutions of dynamical systems. C R Mec 338(9):510–517
33. Moore G (2005) Floquet theory as a computational tool. SIAM J Numer Anal 42(6):2522–2568
34. Seydel R (2010) Practical bifurcation and stability analysis. Springer, New York
35. Govaerts W, Kuznetsov YA, De Witte V, Dhooge A, Meijer H, Mestrom W, Riet A, Sautois B (2011) MATCONT and CL MATCONT: continuation toolboxes in matlab. Technical report, Gent University and Utrech University
36. Guckenheimer J, Myers M, Sturmfels B (1997) Computing hopf bifurcations I. SIAM J Numer Anal 34(1):1–21
37. Govaerts WJ (2000) Numerical methods for bifurcations of dynamical equilibria, vol 66. SIAM, Philadelphia
38. Beyn W-J, Champneys A, Doedel E, Govaerts W, Kuznetsov YA, Sandstede B (2002) Numerical continuation, and computation of normal forms. In: Fiedler B (ed) Handbook of dynamical systems, vol. 2. Elsevier Science, North-Holland, pp 149–219
39. Doedel EJ, Govaerts W, Kuznetsov YA (2003) Computation of periodic solution bifurcations in ODEs using bordered systems. SIAM J Numer Anal 41(2):401–435
40. Van der Aa N, Ter Morsche H, MattheiJ R (2007) Computation of eigenvalue and eigenvector derivatives for a general complex-valued eigensystem. Electron J Linear Algebra 16(1):300–314
41. Masri S, Caughey T (1979) A nonparametric identification technique for nonlinear dynamic problems. J Appl Mech 46(2):433–447

Chapter 6
Nonlinear Vibrations of a Beam with a Breathing Edge Crack

Ali C. Batihan and Ender Cigeroglu

Abstract In this paper, nonlinear transverse vibration analysis of a beam with a single edge crack is studied. In literature, edge cracks are generally modeled as open cracks, in which the beam is separated into two pieces at the crack location and these pieces are connected to each other with a rotational spring to represent the effect of crack. The open edge crack model is a widely used assumption; however, it does not consider the nonlinear behavior due to opening and closing of the crack region. In this paper, a beam like structure with a breathing type crack is studied. Due to the breathing nature of the crack, crack surfaces contact with each other for some period of the motion and separate in the rest of the cycle. This nonlinear behavior of the crack region is modeled by representing the system as a single degree of freedom system (SDOF) with a bilinear stiffness by Galerkin's Method. Nonlinear differential equations of motion obtained by using Euler-Bernoulli beam theory are converted into nonlinear algebraic equations by using harmonic balance method (HBM). Under the action of a harmonic forcing, the effect of crack parameters on the vibrational behavior of the cracked beam is presented.

Keywords Breathing crack • Euler-Bernoulli beam • Galerkin's method • Harmonic balance method

6.1 Introduction

Cracks in structures may propagate and cause catastrophic failures which do not give any visible sign before failure. Therefore, identification of cracks and determination of their location and properties is very important for life prediction of mechanical systems. Because of this importance, beams with edge cracks have been an increasingly growing area of research in the last 30 years. Review paper of Dimarogonas [1] provides a collection of researches that are carried out thus far, in which analysis methods for open and breathing crack, continuous crack beam theories, dynamic characteristics of cracked beams and studies of vibration of cracked plates are considered. In majority of the literature, cracked beam is separated into two segments at the crack location and then these two segments are connected to each other by rotational springs. The most common model used in the literature is beam with an open edge crack, where the Euler-Bernoulli beam theory is utilized. Khiem et al. [2] calculated the natural frequencies of a beam with arbitrary number of cracks by using a transfer matrix method. Another research considering arbitrary number of cracks as well as taking the effects of axial loads into account was carried out by Aydın [3]. Mermertaş [4] considered a mass attachment to see the change in the natural frequencies more effectively. Method of mass attachment was also considered by Zhong et al. [5] by the application of Rayleigh's and finite element methods. Also, Mazanoğlu et al. [6] studied a non-uniform cracked beam by applying Rayleigh-Ritz and finite element methods. Besides these approaches, alternative methods were also developed. Chondros et al. [7] developed a continuous theory of cracked beams where the flexibility due to crack region was distributed along the whole beam. Chati [8] carried out the modal analysis of a beam with breathing edge crack by using finite element method. The nonlinearity due to breathing effect was modeled by a piecewise linear stiffness. Chondros et al. [9] also studied a beam with breathing edge crack. In this study, vibration characteristics due to open period and closed period were combined as a bi-linear model. Authors indicated that fatigue cracks behave as breathing cracks if the preload is sufficient. In the study of Cheng et al. [10], the breathing crack was modeled with a time dependent stiffness. Baeza et al. [11] studied breathing crack by using an analytical approach, where utilizing beam modes a modal scale factor matrix is introduced which indicates the existence of cracks. In a more recent study, sub and super harmonics of a beam with a breathing crack is studied by Giannini et al. [12] and the approach is used for crack identification where the cracked beam is modeled by finite element method. The results obtained are also compared with the results of an experiment conducted.

A.C. Batihan • E. Cigeroglu (✉)
Department of Mechanical Engineering, Middle East Technical University, Ankara 06800, Turkey
e-mail: ender@metu.edu.tr

G. Kerschen (ed.), *Nonlinear Dynamics, Volume 1*, Conference Proceedings of the Society for Experimental Mechanics Series, DOI 10.1007/978-3-319-15221-9_6

In this paper, transverse vibrations of a beam with a breathing edge crack is studied. The beam is modeled by Euler-Bernoulli beam theory and a SDOF representation of the cracked beam is obtained via Galerkin's method. For the application of Galerkin's method, trial functions that satisfy both natural and geometric boundary conditions are needed. Two different trial functions are used for this purpose. In case the crack is open, the first eigenfunction of a beam with an open crack is used whereas; the first eigenfunction of the undamaged beam is utilized in case the crack is closed. Using these two trial functions, a SDOF representation of the crack beam is obtained which contains a piecewise linear stiffness. Harmonic balance method (HBM) with multi harmonics is utilized for the solution of resulting nonlinear system and the effects of breathing crack and the parameters associated with it on higher harmonics are investigated.

6.2 Mathematical Modeling

Equation of motion of a continuous beam with an external forcing of $F(t)$ applied at location L_f can be written as follows using Euler-Bernoulli beam theory

$$EI\frac{\partial^4 w(x,t)}{\partial x^4} + c\frac{\partial w(x,t)}{\partial t} + m\frac{\partial^2 w(x,t)}{\partial t^2} = F(t)\delta\left(x - L_f\right), \tag{6.1}$$

where $w(x,t)$ is displacement of the beam in transverse direction, EI is flexural rigidity, m is mass per unit length of the beam and c is viscous damping coefficient. Using expansion theorem, the displacement of the beam can be written as follows

$$w(x,t) = \sum_{j=1}^{\infty} a_j(t)\phi_j(x), \tag{6.2}$$

where $\phi_j(x)$ is the j^{th} trial function. Utilizing a single trial function and substituting this into Eq. 6.1 results in the following ordinary differential equation

$$EIa(t)\frac{d^4\phi(x)}{dx^4} + c\dot{a}(t)\phi(x) + m\ddot{a}(t)\phi(x) = F(t)\delta\left(x - L_f\right). \tag{6.3}$$

Multiplying Eq. 6.3 by $\phi(x)$ and integrating over the spatial domain the following equation is obtained

$$m_{eq}\ddot{a}(t) + c_{eq}\dot{a}(t) + k_{eq}a(t) = F(t)\phi\left(L_f\right), \tag{6.4}$$

where

$$m_{eq} = \int_0^L m\phi(x)^2 dx, \tag{6.5}$$

$$c_{eq} = \int_0^L c\phi(x)^2 dx, \tag{6.6}$$

$$k_{eq} = \int_0^L EI\phi(x)\frac{d^4\phi(x)}{dx^4}dx. \tag{6.7}$$

Figure 6.1 shows the deformed shape of the crack beam at two different time instants. Due to breathing effect of the edge crack, the beam behaves as if it is an undamaged beam for some period of a cycle; whereas, in the rest of the cycle it behaves as a beam with an open edge crack. Consequently, beam with a breathing edge crack can be represented as a SDOF system with a piecewise linear stiffness element (or gap element) as shown in Fig. 6.2.

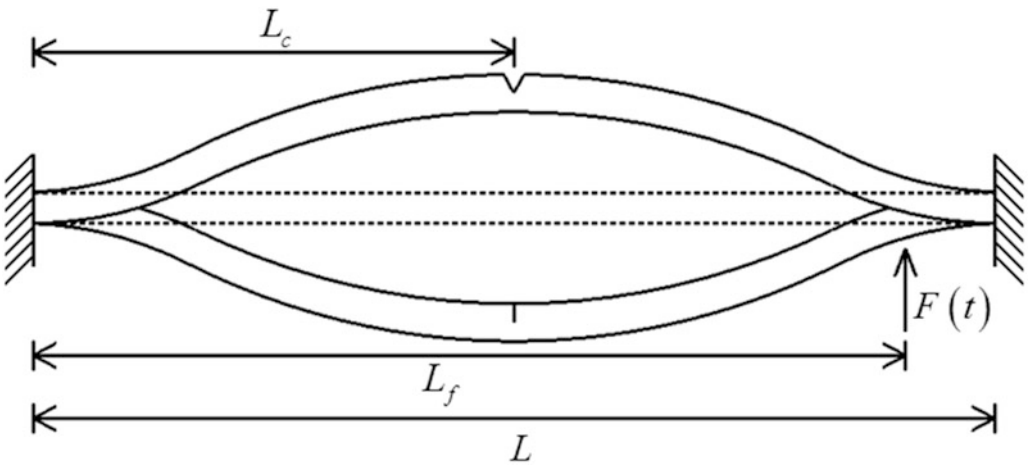

Fig. 6.1 Beam with a breathing edge crack

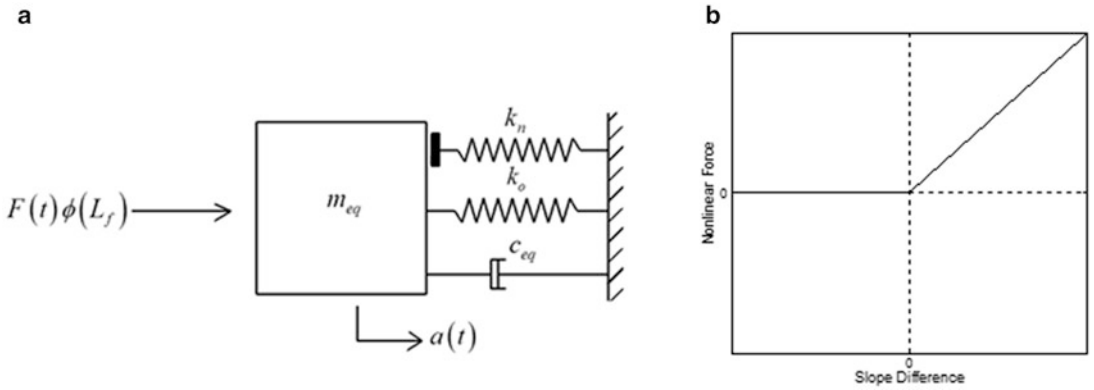

Fig. 6.2 (**a**) SDOF representation of a beam with a breathing edge crack, (**b**) Nonlinear force due to piecewise linear stiffness

Since the crack beam can be represented by two linear systems, two different trial functions corresponding to these two states are required. For the period of vibration where the crack is closed, the first eigenfunction of the undamaged beam is used as a trial function; whereas, the first eigenfunction of a beam with an open crack is used in the case of open crack. The details and derivation of these eigenfunctions can be found in [13], where the response of the left and right sides of the beam with respect to the crack are treated separately. Therefore, the first eigenfunction of a beam with an open crack is composed of two functions named as $\psi_L(x)$ for the beam segment on the left side of the crack and $\psi_R(x)$ for the beam segment on the right side of the crack. Utilizing the first eigenfunction of a beam with an open edge crack and applying Galerkin's Method, k_o and k_n can be obtained as follows,

$$k_o = EI\left(\int_0^{L_c} \psi_L(x)\frac{d^4\psi_L(x)}{dx^4}dx + \int_{L_c}^{L} \psi_R(x)\frac{d^4\psi_R(x)}{dx^4}dx\right), \tag{6.8}$$

$$k_n = k_{eq} - k_o. \tag{6.9}$$

Equation of motion of the nonlinear system given in Fig. 6.2 can be given as follows

$$m_{eq}\ddot{a}(t) + c_{eq}\dot{a}(t) + k_o a(t) + f_n(t) = F(t)\phi\left(L_f\right), \tag{6.10}$$

where $f_n(t)$ is the nonlinear force which depends on the slope difference. In this study, slope difference at the crack location of a beam with an open edge crack is used in order to identify the contact and separation of the piecewise linear stiffness.

Positive slope difference implies a closed crack; thus, a nonzero nonlinear force; whereas, a negative slope difference implies an open crack; hence, zero nonlinear force. Therefore, $f_n(t)$ can be written as

$$f_n(t) = \begin{cases} k_n a(t) & if \quad a(t)\left(\frac{d\psi_R}{dx} - \frac{d\psi_L}{dx}\right)\Big|_{x=L_c} > 0 \\ 0 & if \quad a(t)\left(\frac{d\psi_R}{dx} - \frac{d\psi_L}{dx}\right)\Big|_{x=L_c} < 0 \end{cases}. \tag{6.11}$$

6.3 Application of Harmonic Balance Method

Letting $\theta = \omega t$, $a(t)$ can be written as follows utilizing multi harmonics

$$a(\theta) = a_0 + \sum_p a_{cp} cos(p\theta) + \sum_p a_{sp} sin(p\theta), \tag{6.12}$$

where a_0, a_{cp} and a_{sp} are the bias term, coefficient of sine and cosine components, respectively. Similarly, nonlinear forcing f_n can be written as

$$f_n(\theta) = f_{n0} + \sum_p f_{ncp} cos(p\theta) + \sum_p f_{nsp} sin(p\theta), \tag{6.13}$$

where

$$f_{n0} = \frac{1}{2\pi}\int_0^{2\pi} f_n(\theta)\, d\theta, \tag{6.14}$$

$$f_{ncp} = \sum_p \left(\frac{1}{\pi}\int_0^{2\pi} f_n(\theta)\, cos(p\theta)\, d\theta\right), \tag{6.15}$$

$$f_{nsp} = \sum_p \left(\frac{1}{\pi}\int_0^{2\pi} f_n(\theta)\, sin(p\theta)\, d\theta\right). \tag{6.16}$$

Substituting Eqs. 6.12 and 6.13 into Eq. 6.10 and collecting sine and cosine terms lead to the following relation for the p^{th} harmonic

$$\begin{aligned} &\left[\left(k_{eq} - m_{eq}\omega^2 p^2\right) a_{sp} - c_{eq}\omega p a_{cp} + f_{nsp} - F_{sp}\right] sin(p\theta) \\ &+ \left[\left(k_{eq} - m_{eq}\omega^2 p^2\right) a_{cp} + c_{eq}\omega p a_{sp} + f_{ncp} - F_{cp}\right] cos(p\theta) + k_{eq} a_0 + f_{n0} = 0, \end{aligned} \tag{6.17}$$

where F_{cp} and F_{sp} are the cosine and sine components of the p^{th} harmonic of the external forcing. From Eq. 6.17, the following set of nonlinear equations are obtained

$$
\begin{aligned}
& ka_0 + f_{n0} = 0 \\
& -c\omega \begin{bmatrix} 1 & & 0 \\ & \ddots & \\ 0 & & p \end{bmatrix} \begin{Bmatrix} a_{c1} \\ \vdots \\ a_{cp} \end{Bmatrix} + \begin{bmatrix} k - m\omega^2 & & 0 \\ & \ddots & \\ 0 & & k - m\omega^2 p^2 \end{bmatrix} \begin{Bmatrix} a_{s1} \\ \vdots \\ a_{sp} \end{Bmatrix} + \begin{Bmatrix} f_{ns1} \\ \vdots \\ f_{nsp} \end{Bmatrix} - \begin{Bmatrix} F_{s1} \\ \vdots \\ F_{sp} \end{Bmatrix} = 0 \\
& \begin{bmatrix} k - m\omega^2 & & 0 \\ & \ddots & \\ 0 & & k - m\omega^2 p^2 \end{bmatrix} \begin{Bmatrix} a_{c1} \\ \vdots \\ a_{cp} \end{Bmatrix} + c\omega \begin{bmatrix} 1 & & 0 \\ & \ddots & \\ 0 & & p \end{bmatrix} \begin{Bmatrix} a_{s1} \\ \vdots \\ a_{sp} \end{Bmatrix} + \begin{Bmatrix} f_{nc1} \\ \vdots \\ f_{ncp} \end{Bmatrix} - \begin{Bmatrix} F_{c1} \\ \vdots \\ F_{cp} \end{Bmatrix} = 0.
\end{aligned} \tag{6.18}
$$

6.4 Results and Discussion

In order to study the effect of parameters of breathing edge crack, case studies are carried out on a clamped-clamped beam by using five harmonics. For the case studies, the following beam properties are used: $L = 1\,\text{m}$, $I = 2.667 \cdot 10^{-8}\,\text{m}^4$, $E = 206\,\text{GPa}$, $\rho = 7,850\,\text{kg/m}^3$, $A = 8 \cdot 10^{-4}\,\text{m}^2$, $\nu = 0.3$, $c_{eq} = 159.24\,\text{Ns/m}$, $L_f = 0.9\,\text{m}$, $F(t) = 100sin\,(\omega t)\,\text{N}$.

In Fig. 6.3, fundamental resonance frequencies for different crack ratios and crack locations are plotted. It is observed that as crack ratio increases, the change in fundamental resonance frequency is more significant. Studying Fig. 6.3b, it is observed that for the case of $L_c = 0.2$, which is very close to the location of the sign change in the slope of the beam, the effect of crack ratio on the fundamental resonance frequency is insignificant. Therefore, in crack detection problems, depending on the crack location, fundamental resonance frequency change may not give accurate results; hence, alternative features should be considered for crack detection.

Due to breathing effect of the crack, in some part of a cycle the crack remains open and in the rest of the cycle the crack remains closed. For this reason nonlinear force is almost zero for some period and nonzero in the rest of the cycle as shown in Fig. 6.4, where, the variation of the nonlinear force at the fundamental resonance frequency is plotted for one cycle at crack location of $L_c = 0.2\,\text{m}$. Even though very little change in fundamental resonance frequency is observed for $L_c = 0.2\,\text{m}$ depicted from Fig. 6.3, the nonlinear force is affected significantly as the crack ratio changes.

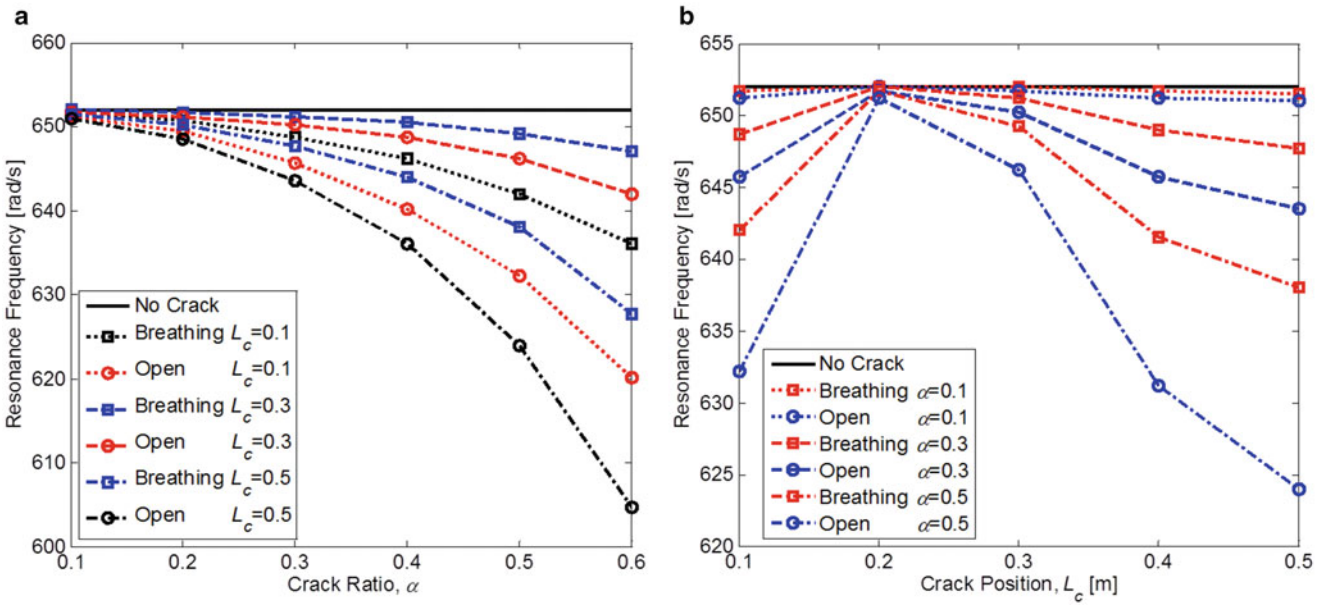

Fig. 6.3 Variation of fundamental resonance frequency with respect to (**a**) crack ratio, (**b**) crack location

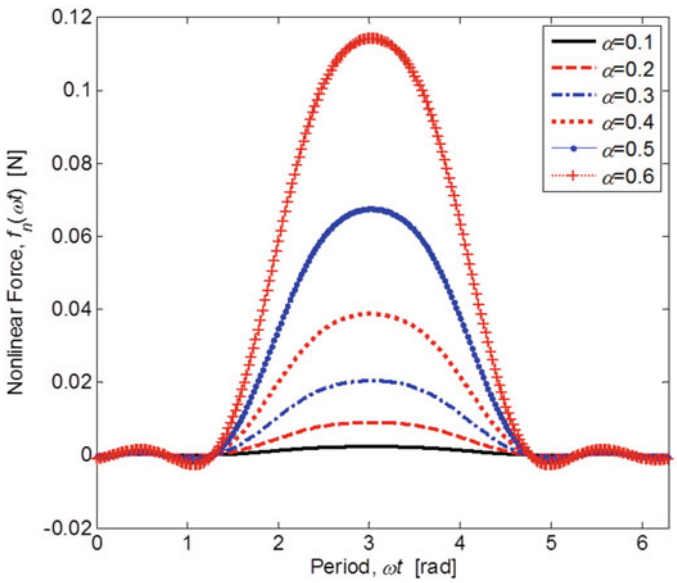

Fig. 6.4 Nonlinear force at fundamental resonance frequency in one cycle, $L_c = 0.2$ m

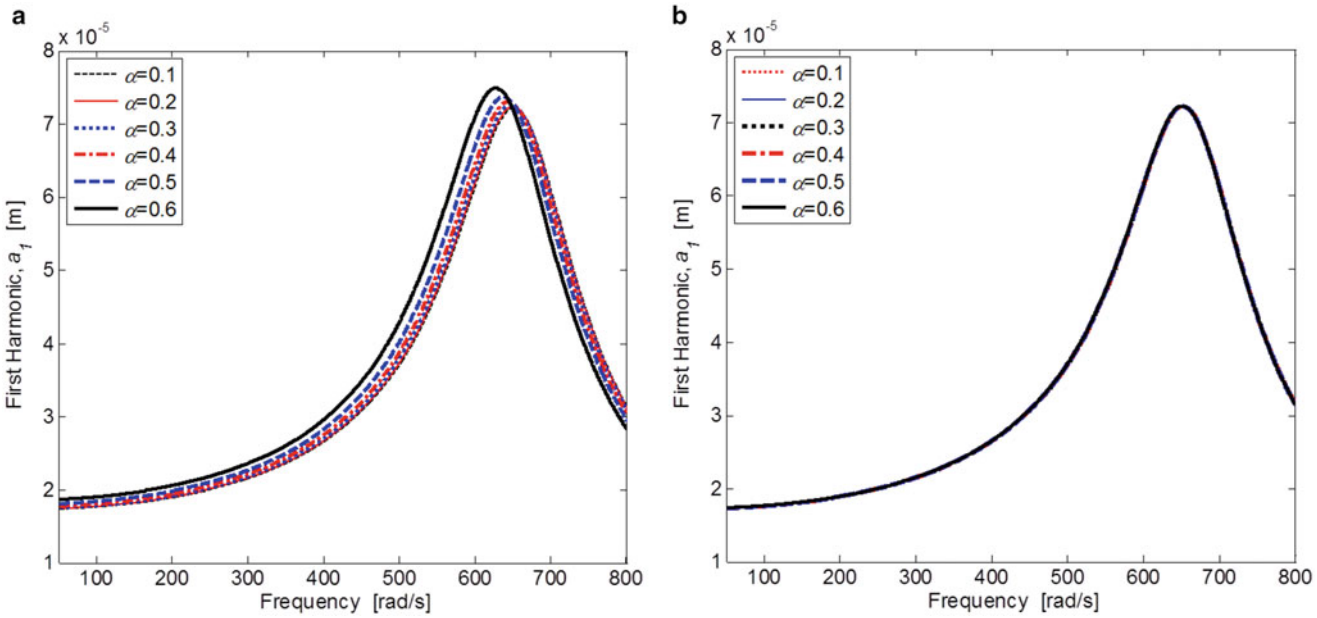

Fig. 6.5 Amplitudes of the 1st harmonic of the modal coefficient versus frequency (**a**) for $L_c = 0.5$ m and (**b**) for $L_c = 0.2$ m

In Fig. 6.5a, b, amplitudes of the first harmonic of the modal coefficient are plotted for different crack ratios for $L_c = 0.5$ m and $L_c = 0.2$ m, respectively. For the case of $L_c = 0.5$ m, the decrease in fundamental resonance frequency can be observed for increasing crack ratios. However, for the case of $L_c = 0.2$ m, no change in the amplitude of the first harmonic of the modal coefficient is observed. However, as shown in Figs. 6.6 and 6.7, bias and higher harmonics of the modal coefficient are affected significantly by the change in crack ratio for the same crack location, i.e. $L_c = 0.2$ m.

Comparison of Figs. 6.5, 6.6 and 6.7 shows that, the most dominant term on the total result is the first harmonic. However, the change in the first harmonic with respect to crack ratio is not as significant as the change in bias term and higher harmonics. To study the effect of crack ratio on the bias term and harmonics of the modal coefficient, the frequency response amplitudes at the fundamental resonance frequency (Figs. 6.5, 6.6 and 6.7 for $L_c = 0.2$ m) are normalized with respect to

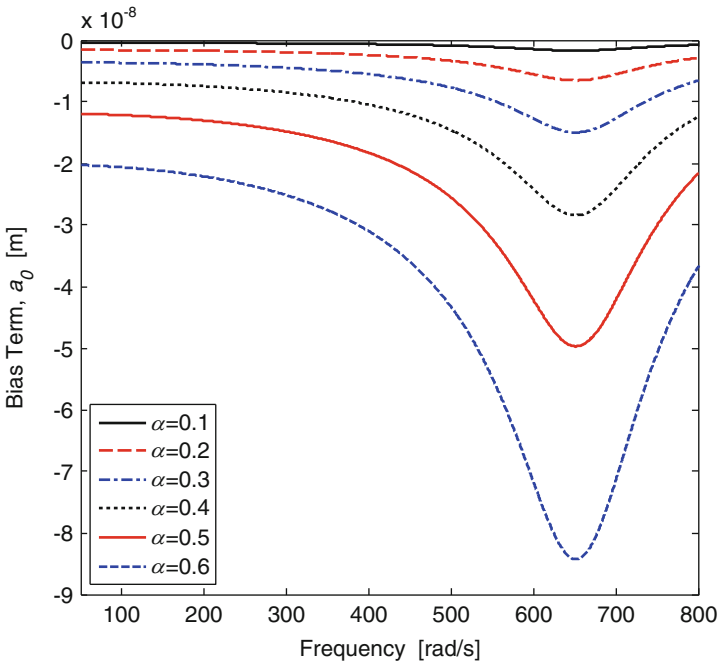

Fig. 6.6 Bias term of the modal coefficient versus frequency, $L_c = 0.2\,\text{m}$

the resonance amplitude obtained for $\alpha = 0.1$. These results are presented in Table 6.1 and Fig. 6.8 for the cases where crack is located at $L_c = 0.1\,\text{m}$, $L_c = 0.2\,\text{m}$ and $L_c = 0.4\,\text{m}$. It is observed from the results that, the effect of crack ratio on bias term, the second and the fourth harmonics is identical to each other; whereas, similar results are obtained for the third and the fifth harmonics. It can be concluded from the results obtained that odd numbered higher harmonics of the modal coefficient are more sensitive to the change in crack ratio; hence, they can be considered as a good feature for crack detection and identification, for this case study. However, it should be noted that, studying Figs. 6.6 and 6.7, the order of magnitude of the bias and second harmonic is approximately three orders greater than the third harmonic, which can be measured with less error compared to the third harmonic. Moreover, as crack location moves towards the center of the beam the multiplication factor increases slightly and for odd harmonics this change is more visible compared to the even harmonics.

Table 6.1 and Fig. 6.8 are prepared according to the amplitudes at fundamental resonance frequency. However, it is observed from Fig. 6.7 that the maximum resonance amplitudes for the higher harmonics occur at frequencies, which are inverse integer multiples of the fundamental resonance frequency. The multiplication factors are also provided at the frequency of maximum amplitude in Table 6.2. Even though the maximum amplitudes occur at different frequencies, the multiplications factors are almost the same. However, as the crack location moves towards the center of the beam the change in amplification ratio is more visible compared to the results obtained at the fundamental resonance frequency (Table 6.1).

6.5 Conclusion

In this study, vibrations of a beam with a breathing edge crack is investigated. Using a single term Galerkin's method, a SDOF piecewise linear system is developed where the nonlinear forcing term depends on the slope difference at the crack location. Case studies show that existence of a crack results in decrease in the fundamental resonance frequency of the beam, which is affected from both the crack ratio and the crack location. It is observed that the fundamental resonance frequency of the beam with a breathing edge crack is higher than the fundamental resonance frequency of the beam with an open edge crack, as expected. However, depending on the crack location the change in the fundamental resonance frequency may become insignificant. Therefore, considering only the change in fundamental resonance frequency does not always give sufficient

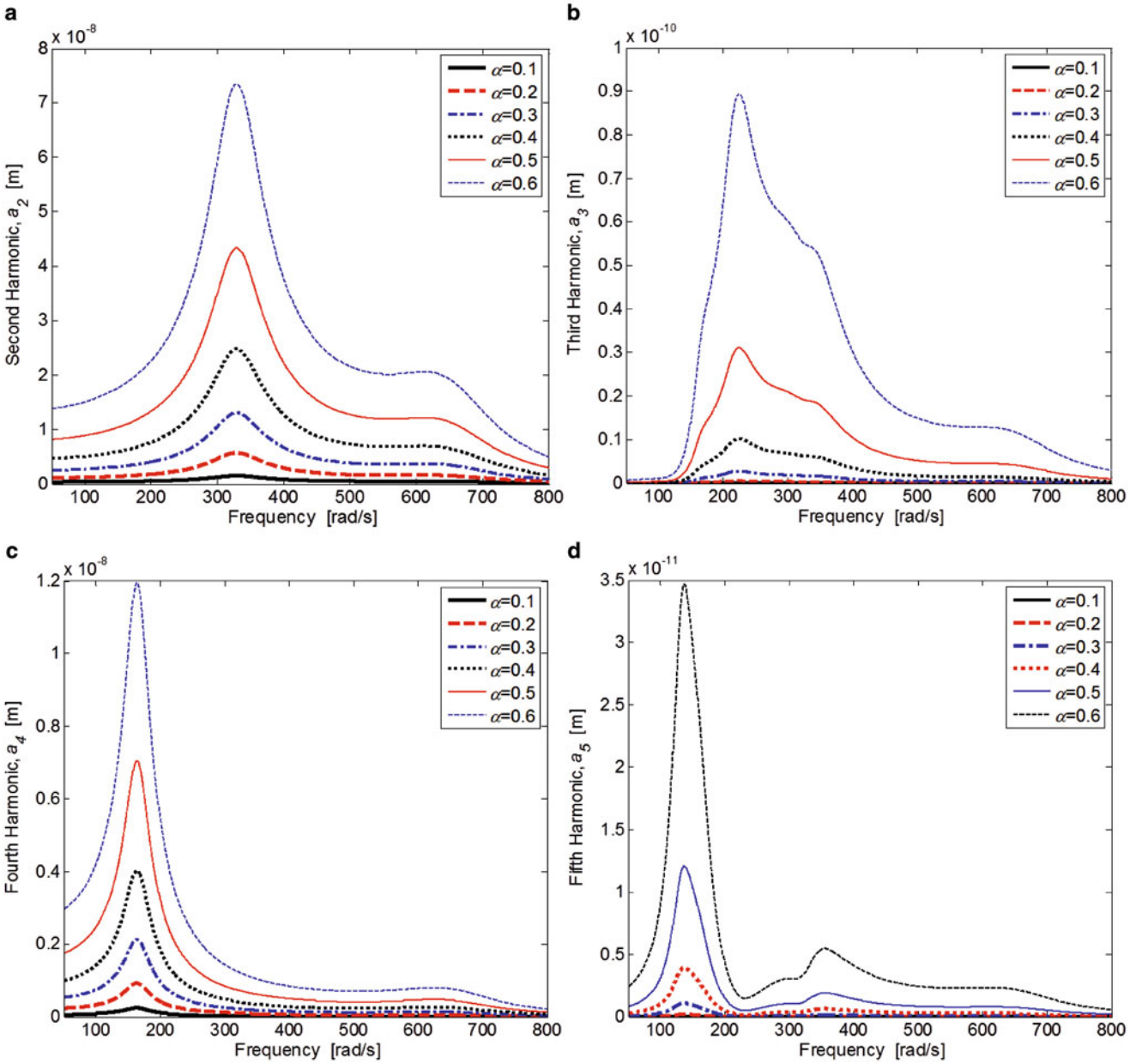

Fig. 6.7 Amplitudes of harmonics of the modal coefficient versus frequency, $L_c = 0.2\,\text{m}$

information for crack detection purposes. Consequently, alternative features are considered for crack detection problems. Effect of crack parameters on nonlinear force f_n is studied and it is observed that change in crack ratio has significant effect on the nonlinear force; however, nonlinear force cannot be measured directly. The harmonics of the modal coefficient are studied and it is observe that the most dominant harmonic on the total response is the first harmonic. However, the effect of crack parameters on the first harmonic is almost insignificant. On the other hand, if bias term and higher harmonics are investigated, it is seen that the effect of crack parameters becomes more significant which can be used as means for crack detection.

Table 6.1 Multiplication factors of bias term and harmonics of the modal coefficient

	$L_c = 0.1$ m						$L_c = 0.2$ m						$L_c = 0.4$ m					
α	0^{th}	1^{st}	2^{nd}	3^{rd}	4^{th}	5^{th}	0^{th}	1^{st}	2^{nd}	3^{rd}	4^{th}	5^{th}	0^{th}	1^{st}	2^{nd}	3^{rd}	4^{th}	5^{th}
0.1	1	1	1	1	1	1	1	1	1	1	1	1	1	1	1	1	1	1
0.2	3.86	1.00	3.84	14.68	3.83	14.69	3.86	1.00	3.86	14.91	3.86	14.89	3.88	1.00	3.87	15.00	3.88	15.00
0.3	8.77	1.00	8.71	75.58	8.71	75.56	8.87	1.00	8.87	78.67	8.87	78.60	8.97	1.00	8.97	80.11	8.97	80.09
0.4	16.35	1.01	16.24	261.45	16.21	261.14	16.86	1.00	16.83	283.50	16.85	283.38	17.22	1.01	17.21	294.07	17.20	293.83
0.5	27.79	1.01	27.62	750.70	27.52	749.43	29.45	1.00	29.42	866.20	29.45	866.47	30.65	1.02	30.66	925.43	30.55	923.78
0.6	45.07	1.02	44.78	1,955.8	44.35	1,948.2	49.96	1.00	49.84	2,487.3	49.95	2,491.4	53.49	1.03	53.50	2,785.2	52.88	2,772.2

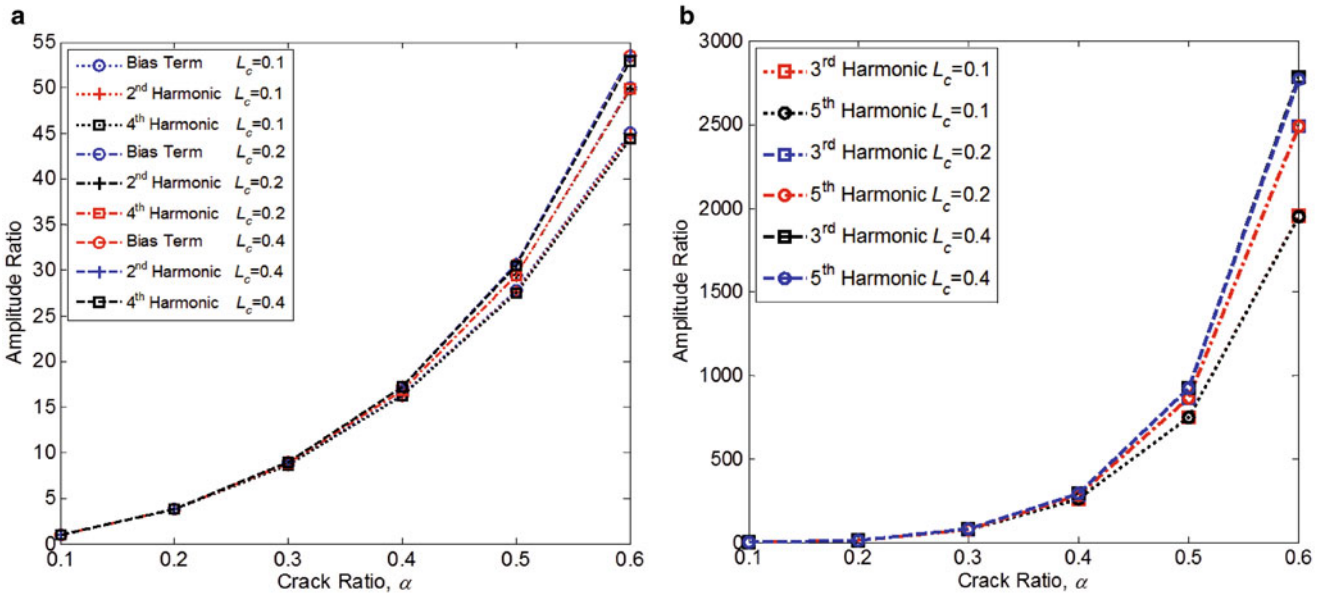

Fig. 6.8 Fundamental resonance amplitude ratios of bias and harmonics of the modal coefficient

Table 6.2 Multiplication factors for higher harmonics at the maximum amplitudes

	$L_c = 0.1$ m				$L_c = 0.2$ m				$L_c = 0.4$ m			
α	2^{nd}	3^{rd}	4^{th}	5^{th}	2^{nd}	3^{rd}	4^{th}	5^{th}	2^{nd}	3^{rd}	4^{th}	5^{th}
0.1	1	1	1	1	1	1	1	1	1	1	1	1
0.2	3.83	14.68	3.83	14.68	3.86	14.90	3.86	14.91	3.88	14.99	3.88	15.00
0.3	8.71	75.41	8.70	75.40	8.87	78.69	8.87	78.69	8.97	80	8.96	79.98
0.4	16.23	260.63	16.22	260.43	16.85	283.68	16.85	283.80	17.21	293.21	17.20	292.93
0.5	27.56	745.85	27.49	744.17	29.46	867.22	29.46	867.53	30.61	918.89	30.53	916.82
0.6	44.68	1933.0	44.33	1, 923.1	49.97	2, 494.0	49.96	2, 494.6	53.37	2, 747.7	52.88	2, 729.9

References

1. Dimarogonas AD (1996) Vibration of cracked structures: a state of the art review. Eng Fracture Mech 55(5):831–857
2. Khiem NT, Lien TV (2001) A simplified method for natural frequency analysis of multiple cracked beam. J Sound Vib 254(4):737–751
3. Aydın K (2008) Vibratory characteristics of Euler-Bernoulli beams with arbitrary number of cracks subjected to axial load. J Vib Control 14(4):485–510
4. Mermertaş V, Erol H (2001) Effect of mass attachment on the free vibration of cracked beam. In: The 8th international congress on sound and vibration, Hong Kong, China
5. Zhong S, Oyadiji SO (2008) Analytical predictions of natural frequencies of cracked simply supported beam with stationary roving mass. J Sound Vib 311:328–352
6. Mazanoğlu K, Yeşilyurt I, Sabuncu M (2009) Vibration analysis of multiple cracked non-uniform beams. J Sound Vib 320:977–989
7. Chondros TG, Dimarogonas AD, Yao J (1998) A continuous vibration cracked beam vibration theory. J Sound Vib 215(1):17–34
8. Chati M, Rand R, Mukherjee S (1997) Modal analysis of a cracked beam. J Sound Vib 207(2):249–270
9. Chondros TG, Dimarogonas AD, Yao J (2001) Vibration of a beam with a breathing crack. J Sound Vib 239(1):57–67
10. Cheng SM, Wu XJ, Wallace W (1999) Vibrational response of a beam with a breathing crack. J Sound Vib 225(1):201–208
11. Baeza L, Ouyang H (2009) Modal approach for forced vibration of beams with a breathing crack. Key Eng Mater 413–414:39–46
12. Giannini O, Casini P, Vestroni F (2013) Nonlinear harmonic identification of breathing cracks in beams. Comput Struct 129:166–177
13. Batihan AC (2011) Vibration analysis of cracked beams on elastic foundation using Timoshenko beam theory. Master thesis, Middle East Technical University

Chapter 7
Stability Limitations in Simulation of Dynamical Systems with Multiple Time-Scales

Sadegh Rahrovani, Thomas Abrahamsson, and Klas Modin

Abstract This paper focuses on the stability properties of a recently proposed *exponential* integrator particularly in simulation of highly oscillatory systems with multiple time-scales. The linear and nonlinear stability properties of the presented exponential integrator have been studied. We illustrate this with the Fermi–Pasta–Ulam (FPU) problem, a highly oscillatory nonlinear system known as a test benchmark for multi-scale time integrators. This example is also illustrative when studying the numerical resonance and algorithmic instability in the multi-time-stepping (MTS) methods, such as in exponential and/or trigonometric integration schemes, since it has no external input force and therefore no real physical resonance.

Keywords Algorithmic instability • Numerical resonance • Multiple time-scale • Exponential integrator • Linear stability

7.1 Introduction

Efficient and stable time-domain simulation is an essential step for analysis and design of engineering systems. However high model fidelity leads to large model size and multiple time-scales that often pose computational challenges in the time-integration process [1]. The reason resides in the fact that the simulation time duration is usually determined by the slow dynamics, in which we are often interested. However, the integration step-size is dictated by the system's fastest normal mode, due to the stability limitations. The main idea in multi-time-stepping (MTS) integrators is to advance the slow and fast dynamics with different time step sizes, where the slow nonlinear forces are sampled as sparsely as possible and at a rate that is independent (or almost independent) of the period of system's fastest normal mode [2]. Such large systems, with highly spread time-scales, typically arise in a vast variety of problems encountered in structural dynamic applications, as in large-scale FE analyses.

7.1.1 Motivation and Previous Work

Previous work has been conducted on efficiency superiority of the presented exponential integrator in treating large-scale FE models, particularly the ones with spatially local nonlinearity and/or uncertainty due to varying parameters [3, 4]. Moreover, the method accuracy and energy consistency in simulation of complex dynamical behavior, such as nonlinear systems with chaotic-type behavior, were investigated in [5]. This work investigates the stability performance of the method, particularly in problems with multiple time-scales by means of studying energy behavior of the numerical algorithm, which is considered as a discrete-time dynamical system. This is illustrated with the Fermi–Pasta–Ulam (FPU) problem. The FPU problem has become a benchmark for multi-scale integrators due to its rich dynamic behaviour on different time-scales, i.e. almost-harmonic motion of stiff springs on the time-scale ω^{-1}, motion of the soft springs on the time scale ω^0 and oscillatory energy exchange between stiff springs on the time scale of ω (considering ω as the frequency of the fastest normal mode of the system). Using this benchmark, the linear and nonlinear stability properties of the presented integrator has been studied.

S. Rahrovani (✉) • T. Abrahamsson
Department of Applied Mechanics, Chalmers University of Technology, Gothenburg, Sweden
e-mail: sadeghr@chalmers.se

K. Modin
Department of Mathematical Sciences, Chalmers University of Technology, Gothenburg, Sweden

G. Kerschen (ed.), *Nonlinear Dynamics, Volume 1*, Conference Proceedings of the Society for Experimental Mechanics Series, DOI 10.1007/978-3-319-15221-9_7

7.2 Numerical Integration of Highly-Oscillatory Systems

Numerical integration of highly oscillatory systems with multiple time-scales is a computationally challenging task. The computational challenge is that the explicit methods require much shorter time steps to maintain stability while the implicit methods require more force evaluations per time step [6]. To overcome this, the fast/slow splitting of dynamics is of interest, where the aim is to sample the slow forces as sparse as possible and at a rate that is independent (or almost independent) of the step-size dictated by the fastest normal mode of the system. This idea becomes more effective when the stiff/fast system can be solved analytically, as in exponential/trigonometric integration schemes, with a cost that is independent of the step size [2]. In this regard, *exponential* and *trigonometric integrators* are considered as two alternatives, designed for stable and fast simulation of systems with highly spread time-scales. The distinct feature of these integrators is the exact evaluation of the part of the solution that corresponds to the contribution of an underlying linearized system, which typically contains the fast dynamics of the system. This can help to mitigate the stiffness of the governing differential equation, which enables us to discretize the smooth nonlinear forces with a larger step size, beyond the step size dictated by the fastest normal mode of the system. This desirable feature improves the stability and efficiency properties of the numerical exponential integration schemes [7, 8], particularly when treating large-scale problems, typically encountered in large-scale FE problems. Here we describe the exponential integrators and also trigonometric integrators that are used for comparison.

7.2.1 Exponential Integrators

Consider the governing nonlinear ordinary differential equations of a multi-input-multi-output (MIMO) dynamical system, represented in first-order form,

$$\dot{\boldsymbol{x}}(t) = \boldsymbol{F}\left(\boldsymbol{x}, \boldsymbol{\theta}, \boldsymbol{f}, t\right), \; \boldsymbol{y} = \boldsymbol{C}\boldsymbol{x} \tag{7.1a,b}$$

with a given initial condition as $\boldsymbol{x}(t_0) = \boldsymbol{x}_0$ where $\boldsymbol{x} \in \Re^{N\times 1}$, $\boldsymbol{F} \in \Re^{N\times 1}$, $\boldsymbol{y} \in \Re^{n_y\times 1}$ and $\boldsymbol{C} \in \Re^{n_y\times N}$. The state vector, the right hand side vector function, and the system model parameters are denoted by $\boldsymbol{x}$, $\boldsymbol{F}$, and $\boldsymbol{\theta}$, respectively. The output vector, denoted by $\boldsymbol{y}$, is related to the state coordinates through the output matrix $\boldsymbol{C}$. The number of outputs and the number of states are denoted by n_y and N, respectively. In order to cast the governing equations into a quasi-linear form, the state-dependent terms of $\boldsymbol{F}$ can be split into a (fast/stiff) deterministic linear system and a remainder residue, created due to (slow) nonlinear/stochastic terms. Thus, in place of Eq. 7.1 with $= \boldsymbol{A}_0\boldsymbol{x} + \boldsymbol{B}^{\text{lin}}\boldsymbol{f}(t) + \boldsymbol{B}^{\text{res}}\boldsymbol{g}(\boldsymbol{x}, \boldsymbol{\theta})$, the governing equations can be rearranged into a quasi-linear form as follows,

$$\dot{\boldsymbol{x}}(t) - \boldsymbol{A}_0\boldsymbol{x} = \boldsymbol{B}^{\text{lin}}\boldsymbol{f}(t) + \boldsymbol{B}^{\text{res}}\boldsymbol{g}(\boldsymbol{x}, \boldsymbol{\theta}) \tag{7.2}$$

Here the applied time-dependent external force, represented by $\boldsymbol{f}(t)$, is projected into the state-space through the input matrix denoted by $\boldsymbol{B}^{\text{lin}} \in \Re^{N\times n_f}$ where n_f indicates the number of external inputs. The residual term, $\boldsymbol{B}^{\text{res}}\boldsymbol{g}(\boldsymbol{x}, \boldsymbol{\theta})$, can be seen as a pseudo-force that is created due to nonlinearity and/or model parameter variation. Note that this pseudo-forces $\boldsymbol{g}$ is related to the state vector through input matrix, $\boldsymbol{B}^{\text{res}}$, which is obtained based on the spatial pattern of the pseudo-forces. Thus, by integrating Eq. 7.2, the governing equations are casted into an integral form solution as follows.

$$\boldsymbol{x}(t+h) = \mathrm{e}^{h\boldsymbol{A}}\boldsymbol{x}_t + \int_t^{t+h} \mathrm{e}^{(h-s)\boldsymbol{A}}\boldsymbol{B}^{\text{lin}}\boldsymbol{f}(s)ds + \int_h^{t+h} \mathrm{e}^{(h-s)\boldsymbol{A}}\boldsymbol{B}^{\text{res}}\boldsymbol{g}\left(\boldsymbol{x}(s), \boldsymbol{\theta}\right)ds \tag{7.3}$$

This nonlinear integral form of the governing equation is called the *variation of constant formulas* or *Nonlinear Volterra Integral Equations* (NVIE's) [9]. This enables us to simulate the fast dynamics exactly while approximating the slow nonlinear pseudo-forces $\boldsymbol{g}$, with a smooth interpolation function. Since this approach makes use of matrix exponential functions, it is called *exponential integrator* [7]. Different discretization techniques, which are being used to numerically approximate the pseudo-forces, lead to different exponential integrators such as exponential-Euler, exponential-Runge–Kutta and etc. It will be explained later that the recently presented method, uses a triangular-hold discretization technique to approximate the external and pseudo forces while the integrals with approximate kernels are computed analytically. Therefore, we can call the integrator as "exponential/triangular-hold" integrator. The method will be presented in implicit and explicit implementations.

7.2.2 Trigonometric Integrators

Trigonometric integrators are a sub class of exponential integrators, which have been designed to treat conservative mechanical systems, with widely spread time-scales. Trigonometric integrators were first originated in N-body problems and molecular dynamics [10], in order to solve highly oscillatory Hamiltonian problems. Focusing on conservative systems, such as the FPU problem, is illustrative when we are studying the numerically-induced resonances and algorithmic instability, since the physical system does not have external loading and therefore real resonance. Such systems have been studied by the use of the impulse methods, which will be explained, in brief. Consider a Hamiltonian system without an external loading (this can be extended to systems with external loading). By inserting $\boldsymbol{A}$ and $\boldsymbol{B}$ matrices related to a Hamiltonian system,

$$\boldsymbol{A} = \begin{bmatrix} 0 & \mathbf{I} \\ -\boldsymbol{\Omega}^2 & 0 \end{bmatrix}, \ \boldsymbol{B} = \begin{bmatrix} 0 \\ \mathbf{I} \end{bmatrix} \tag{7.4a,b}$$

into the integral form, as in Eq. 7.3, the governing equation is simplified as

$$\begin{pmatrix} \boldsymbol{q}_{k+1} \\ \dot{\boldsymbol{q}}_{k+1} \end{pmatrix} = \begin{bmatrix} \cos(h\boldsymbol{\Omega}) & \boldsymbol{\Omega}^{-1}\sin(h\boldsymbol{\Omega}) \\ -\boldsymbol{\Omega}\sin(h\boldsymbol{\Omega}) & \cos(h\boldsymbol{\Omega}) \end{bmatrix} \begin{pmatrix} \boldsymbol{q}_k \\ \dot{\boldsymbol{q}}_k \end{pmatrix} + \int_0^h \begin{pmatrix} \boldsymbol{\Omega}^{-1}\sin((h-s)\boldsymbol{\Omega}) \\ \cos((h-s)\boldsymbol{\Omega}) \end{pmatrix} \boldsymbol{g}(\boldsymbol{q}(s))\,\mathrm{d}s \tag{7.5}$$

Here the state of the system is denoted by the displacement and velocity at each time step, i.e. $\boldsymbol{x}_{k+1} = \left[\boldsymbol{q}_{k+1}, \dot{\boldsymbol{q}}_{k+1}\right]$. Impulse/Deuflhard multi-time-stepping method,[1] also known as Verlet-I and e-RESPA, uses a trapezoidal rule to approximate the integral term on the right-hand-side of the equations, [10]. Note that this approximation is different from the one used in the presented integrator since we calculate the nonlinear integrals exactly, but based on the approximated kernels. The Impulse/Deuflhard method is time-symmetric, symplectic[2] and explicit, however, it suffers from numerical algorithmic instabilities, known as numerical/discretization resonances. This numerical resonance happens when the slow forces are sampled at a rate such that the multiplication of time step h and the fastest frequency of the system ω, i.e. $h\omega$, becomes close to an integer multiple of π. Under this condition, the period of the pseudo-force loading, created due to discretization of the nonlinear pseudo-forces, coincides with the frequency of a normal mode of corresponding linear system [11].

7.2.2.1 Mollified Impulse Methods

The mollified impulse methods are improvements of the impulse method with a better stability and accuracy properties. The idea is to modify the slow part of the potential energy and to evaluate it at "time averaged" values of the positions and then considering its gradient as the new nonlinear smooth force. Consequently, the impulse force $\boldsymbol{g}$ is replaced by a mollified conservative force, i.e. $\overline{\boldsymbol{g}} = \nabla\overline{U} = \acute{a}(\boldsymbol{q}, h)\,\boldsymbol{g}(a(\boldsymbol{q}, h))$, derived based on the modified potential that is evaluated at the average displacement, $a(\boldsymbol{q}, h)$. When the fast forces originate from a quadratic potential, it is possible to evaluate the displacement average analytically, i.e., $a(\boldsymbol{q}, h) = (h\boldsymbol{\Omega})\,\boldsymbol{q}$, where $\phi(h\boldsymbol{\Omega}) = \mathrm{sinc}(h\boldsymbol{\Omega})$ is called filter function, [10]. The mollified impulse formulation is given by,

$$\begin{pmatrix} \boldsymbol{q}_{k+1} \\ \dot{\boldsymbol{q}}_{k+1} \end{pmatrix} = \begin{bmatrix} \cos(h\boldsymbol{\Omega}) & \boldsymbol{\Omega}^{-1}\sin(h\boldsymbol{\Omega}) \\ -\boldsymbol{\Omega}\sin(h\boldsymbol{\Omega}) & \cos(h\boldsymbol{\Omega}) \end{bmatrix} \begin{pmatrix} \boldsymbol{q}_k \\ \dot{\boldsymbol{q}}_k \end{pmatrix} + \frac{h}{2} \begin{pmatrix} h\mathrm{sinc}(h\boldsymbol{\Omega})\,\phi(h\boldsymbol{\Omega})\,\boldsymbol{g}_k \\ \phi(h\boldsymbol{\Omega})\cos(h\boldsymbol{\Omega})\,\boldsymbol{g}_k + \phi(h\boldsymbol{\Omega})\,\boldsymbol{g}_{k+1} \end{pmatrix} \tag{7.6}$$

where $\boldsymbol{g}_k = \boldsymbol{g}(\phi(h\boldsymbol{\Omega})\,\boldsymbol{q}_k)$. Note that this method is an impulse method with a modified potential and therefore it remains symmetric and symplectic while providing a better stability and accuracy properties. In a more general sense, for a pair of filter functions $\Psi = \psi(h\boldsymbol{\Omega})$ and $\Phi = \phi(h\boldsymbol{\Omega})$, a symmetric explicit formulation is given in the following. Five known trigonometric methods with different filtered functions are shown in Table 7.1, as presented in [12].

$$\begin{pmatrix} \boldsymbol{q}_{k+1} \\ \dot{\boldsymbol{q}}_{k+1} \end{pmatrix} = \begin{bmatrix} \cos(h\boldsymbol{\Omega}) & \boldsymbol{\Omega}^{-1}\sin(h\boldsymbol{\Omega}) \\ -\boldsymbol{\Omega}\sin(h\boldsymbol{\Omega}) & \cos(h\boldsymbol{\Omega}) \end{bmatrix} \begin{pmatrix} \boldsymbol{q}_k \\ \dot{\boldsymbol{q}}_k \end{pmatrix} + \frac{h}{2} \begin{pmatrix} h\Psi(h\boldsymbol{\Omega})\,\boldsymbol{g}_k \\ \phi(h\boldsymbol{\Omega})\cos(h\boldsymbol{\Omega})\,\boldsymbol{g}_k + \phi(h\boldsymbol{\Omega})\,\boldsymbol{g}_{k+1} \end{pmatrix} \tag{7.7}$$

[1] Note that in problems with a quadratic fast potential both the Deuflhard method and the impulse method are identical as suggested in [10].

[2] A symplectic integrator is a scheme that intends to simulate a Hamiltonian system numerically, while it preserves its underlying symplectic structure [12].

Table 7.1 Various trigonometric methods with different filter functions

Method	$\psi(x)$	$\phi(x)$	Reference
(A)	$\text{sinc}^2(x/2)$	1	Gautschi
(B)	$\text{sinc}(x)$	1	Deuflhard
(C)	$\text{sinc}^2(x)$	$\text{sinc}(x)$	Garcia et al.
(D)	$\text{sinc}^2(x/2)$	$\text{sinc}(x)\left(1+1/3\text{sinc}^2(x/2)\right)$	Hochbruck & Lubich
(E)	$\text{sinc}^2(x)$	1	Hochbruck & Lubich

7.3 A Proposed Exponential Integration Scheme

7.3.1 On the Choice of Nominal Deterministic Model

In order to cast the differential equation $\dot{\boldsymbol{x}}(t) = \boldsymbol{F}(\boldsymbol{x}, \boldsymbol{\theta}, \boldsymbol{f}, t)$ into an integral NVIE Eq. 7.3 form, we first need to split the state-dependent part of the right-hand-side of the governing equation into a (fast/stiff) linear deterministic system and a remainder residue, consists of the (slow) nonlinear and/or stochastic part.

$$\begin{aligned} \dot{\boldsymbol{x}}(t) &= \boldsymbol{A}(\boldsymbol{x}, \boldsymbol{\theta})\boldsymbol{x} + \boldsymbol{B}^{lin}\boldsymbol{f}(t) \\ \boldsymbol{A}(\boldsymbol{x}, \boldsymbol{\theta}) &= \boldsymbol{A}_0 + [\boldsymbol{A}(\boldsymbol{\theta}, \boldsymbol{x}) - \boldsymbol{A}_0] \end{aligned} \tag{7.8a,b}$$

Note that the nominal system is state independent $\boldsymbol{A}_0 = \boldsymbol{A}_0(\boldsymbol{\theta}_0)$ and the nonlinear and/or parameter varying terms can be seen as pseudo-forces, i.e. $\boldsymbol{B}^{\text{res}}\boldsymbol{g}(\boldsymbol{x}, \boldsymbol{\theta})$, given by Eq. 7.2. One natural choice for the underlying nominal linear system is the Jacobian matrix, which corresponds to the state-dependent part of $\boldsymbol{F}$, i.e. $\boldsymbol{A}_0 = \boldsymbol{A}_\mathbf{J}$. Although the Jacobian matrix is the best linear approximation near the state $\boldsymbol{x}$, its condition number might be unbounded. To make the problem more well-condition, in such cases, the choice of the nominal linear model can be made based on a perturbation of the Jacobian matrix, i.e. $\boldsymbol{A}_0 = \boldsymbol{A}_\mathbf{J} + \Delta\boldsymbol{A}$, where $\text{cond}(\boldsymbol{A}_0) << \text{cond}(\boldsymbol{A}_\mathbf{J})$. Then, the splitting of the state-dependent parts can be done as follows.

$$\boldsymbol{A}(\boldsymbol{x}, \boldsymbol{\theta}) = \boldsymbol{A}_\boldsymbol{J} + \Delta\boldsymbol{A} + [\boldsymbol{A}(\boldsymbol{\theta}, \boldsymbol{x}) - \boldsymbol{A}_\boldsymbol{J} - \Delta\boldsymbol{A}] \tag{7.9}$$

where $\|\Delta\boldsymbol{A}\| << \|\boldsymbol{A}_\mathbf{J}\|$. Here, a perturbation of the Jacobian matrix is considered as the underlying linear model, where the condition number of the nominal linear model $\boldsymbol{A}_0$ can be controlled by adjusting the $\boldsymbol{\lambda}$ parameter,

$$\boldsymbol{A}_0 = \boldsymbol{A}_\boldsymbol{J} + \Delta\boldsymbol{A},\ \Delta\boldsymbol{A} = \boldsymbol{\lambda}\mathbf{I} \tag{7.10a, b}$$

Here, $\mathbf{I}$ is the identity matrix. Using this, the eigenvalues of the Jacobian matrix are equally shifted away from the zero axis while the eigenvectors are preserved. This is a desirable feature that can result in a better approximation of the slowly varying solution dynamics. This can be seen later in the obtained results in the FPU problem.

7.3.2 System Descritization

In a recently proposed exponential integration scheme [3–5], the triangular-order hold discretization technique is used to approximate the pseudo-forces, in the NVIE equation system Eq. 7.3, where the nonlinear convolution integrals are calculated analytically afterwards. The transfer function of this triangular-hold non-causal filter $H_\text{f}(\text{s})$ is defined by (see [13]),

$$H_\text{f}(s) = \left(\text{e}^{hs} - 2 + \text{e}^{-hs}\right)/hs^2 \tag{7.11}$$

where the fixed time-step size is introduced by h. The discrete-time equivalent of the system, with transfer function $\boldsymbol{H}(s)$, is

$$\boldsymbol{H}_\text{tri}(z) = \left((z-1)^2/hz\right)\mathcal{Z}\left\{\boldsymbol{H}(s)/s^2\right\} \tag{7.12}$$

According to the Eq. 7.3, this exponential/triangular-hold integrator leads to the following discrete system[3]

$$\begin{aligned} \boldsymbol{x}_{k+1} &= \boldsymbol{A}_d \boldsymbol{x}_k + \boldsymbol{B}_d^{lin} \boldsymbol{f}_k + \boldsymbol{B}_d^{res} \boldsymbol{g}\left(\boldsymbol{y}_k, \boldsymbol{\theta}\right) \\ \boldsymbol{y}_k &= \boldsymbol{C}_{\mathrm{d}} \boldsymbol{x}_k + \boldsymbol{D}_{\mathrm{d}}^{\mathrm{lin}} \boldsymbol{f}_k + \boldsymbol{D}_{\mathrm{d}}^{\mathrm{res}} \boldsymbol{g}\left(\boldsymbol{y}_k, \boldsymbol{\theta}\right) \end{aligned} \tag{7.13a,b}$$

where, the discrete-time system matrices are obtained, based on the continuous-time system, (for details see [13])

$$\begin{aligned} &\boldsymbol{A}_{\mathrm{d}} = e^{h\boldsymbol{A}}, \quad \boldsymbol{C}_{\mathrm{d}} = \boldsymbol{C} \\ &\boldsymbol{B}_{\mathrm{d}}^{\mathrm{lin}} = \boldsymbol{A}^{-2}\left(e^{h\boldsymbol{A}} - \boldsymbol{I}\right)^2 \boldsymbol{B}^{\mathrm{lin}} / h, \quad \boldsymbol{B}_{\mathrm{d}}^{\mathrm{res}} = \boldsymbol{A}^{-2}\left(e^{h\boldsymbol{A}} - \boldsymbol{I}\right)^2 \boldsymbol{B}^{\mathrm{res}} / h \\ &\boldsymbol{D}_{\mathrm{d}}^{\mathrm{lin}} = \boldsymbol{D}^{\mathrm{lin}} + \boldsymbol{C}\left[\boldsymbol{A}^{-2}\left(e^{h\boldsymbol{A}} - \boldsymbol{I}\right)/h - \boldsymbol{A}^{-1}\right]\boldsymbol{B}^{\mathrm{lin}}, \quad \boldsymbol{D}_{\mathrm{d}}^{\mathrm{lin}} = \boldsymbol{D}^{\mathrm{lin}} + \boldsymbol{C}\left[\boldsymbol{A}^{-2}\left(e^{h\boldsymbol{A}} - \boldsymbol{I}\right)/h - \boldsymbol{A}^{-1}\right]\boldsymbol{B}^{\mathrm{lin}} \end{aligned} \tag{7.14a–f}$$

Note that generally the input matrices, $\boldsymbol{B}_{\mathrm{d}}^{\mathrm{lin}}$ and $\boldsymbol{B}_{\mathrm{d}}^{\mathrm{res}}$ are not essentially identical since $\boldsymbol{B}^{\mathrm{lin}}$ and $\boldsymbol{B}^{\mathrm{res}}$ might be different depending on the spatial pattern of $\boldsymbol{f}$ and $\boldsymbol{g}$, respectively (This holds for $\boldsymbol{D}_{\mathrm{d}}^{\mathrm{lin}}$ and $\boldsymbol{D}_{\mathrm{d}}^{\mathrm{res}}$, as well). In the following, an implicit and explicit version of the presented exponential scheme will be presented. The implicit version is suitable for problems where the nonlinear force is spatially sparse and therefore cheap to evaluate, however, the explicit implementation is more efficient when the cost of nonlinear force evaluation is too high.

7.3.3 Implicit Implementation

Implicit numerical integrators have normally less severe stability limitations than the explicit methods, but the cost of simulating large-scale nonlinear systems with dense Jacobian matrices is usually too high. These methods are more suitable for applications such as structural dynamics and wave propagation [14], which are not severely nonlinear and particularly effective when the nonlinearity is spatially localized. In order to bring down the computational costs in such problems, a linearly implicit integrator[4] was introduced by the authors in [3–5]. Here, the presented implicit scheme, implemented in a two-stage procedure, is described briefly.

Stage 1 Automatic time-step size selection

The first stage, called *the adaptive time-step size selection step*, contains splitting the whole time sequence into equal duration time blocks, i.e. equal to $\mathcal{K}h$ which is $\mathcal{K}$ times larger than h, time step size that is used for iteratively simulating the nominal linear system. The aim in this pre-processing step is to find a suitable time block length $\mathcal{K}h$ as large as possible, while the convergence of the nonlinear pseudo-forces, obtained through an iterative linear solver, can be achieved in a reasonable number of iterations. Briefly stated, this is implemented by starting with an initial step size, equal to h, and increasing the step length to $\mathcal{K}h$ by increasing $\mathcal{K}$, as long as the convergence conditions are fulfilled. Different strategies for adaptive time step selection can be derived but it is not the main focus of this paper.

Stage 2 Time integration

The second stage contains the time stepping of the discretised system, given by the implicit formulation in Eqs. 7.13–7.14, for each time block $[t_k, t_k + \mathcal{K}h]$ (see Fig. 7.1). A prediction/correction iterative algorithm is employed to obtain the solution,

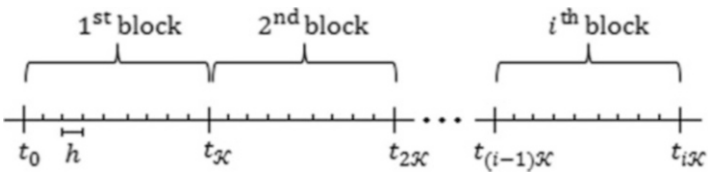

Fig. 7.1 Splitting the time sequence into separate blocks $[t_k, t_k + \mathcal{K}h]$ with $\mathcal{K}$ time increments in each block. The linearized system response is evaluated for $\mathcal{K}$ points in a time block and the pseudo-forces are obtained in a predication/updating iterative process, at the same $\mathcal{K}$ points

[3]One can use the MATLAB command sysd = c2d(sys,'foh') in order to discretize a linear-time-invariant system.

[4]Linearly implicit methods need only to solve a linear equation set, no matter the system we simulate is linear or nonlinear (see [14] for more details).

by updating the prediction for nonlinear pseudo-loading, using fixed-point iteration. This includes computing the solution of the underlying linearized system, subjected to both the external and pseudo-loadings, for each time increment, h, within the time block $\left[\mathrm{t}_{(\mathrm{i}-1)\mathcal{K}}, \mathrm{t}_{\mathrm{i}\mathcal{K}}\right]$,

$$\begin{aligned} \boldsymbol{Y}^{j} &= \left[\boldsymbol{y}_{k}^{j},\ \boldsymbol{y}_{k+1}^{j}, \ldots,\ \boldsymbol{y}_{k+\mathcal{K}}^{j}\right] \\ \boldsymbol{x}_{k+1}^{j} &= \boldsymbol{A}_{\mathrm{d}}\boldsymbol{x}_{k}^{j} + \boldsymbol{B}_{\mathrm{d}}^{\mathrm{lin}} f_{\mathrm{k}} + \boldsymbol{B}_{\mathrm{d}}^{\mathrm{res}} \boldsymbol{g}\left(\boldsymbol{y}_{k}^{j-1}, \boldsymbol{\theta}\right) \\ \boldsymbol{y}_{k}^{j} &= \boldsymbol{C}_{\mathrm{d}}\boldsymbol{x}_{k}^{j} + \boldsymbol{D}_{\mathrm{d}}^{\mathrm{lin}} f_{\mathrm{k}} + \boldsymbol{D}_{\mathrm{d}}^{\mathrm{res}} \boldsymbol{g}\left(\boldsymbol{y}_{k}^{j-1}, \boldsymbol{\theta}\right) \end{aligned} \tag{7.15a–c}$$

As mentioned, the superscript j indicates the iteration number. Note that for solving Eq. 7.15a–c, the pseudo-forces $\boldsymbol{g}$ are not computed, based on $\boldsymbol{Y}^{j}$, but based on the solution $\boldsymbol{Y}^{j-1}$ that is known from the obtained response in previous iteration.

$$\boldsymbol{G}^{j-1} = \boldsymbol{g}\left(\boldsymbol{Y}^{j-1}, \boldsymbol{\theta}\right) = \left[\boldsymbol{g}\left(\boldsymbol{y}_{k}^{j-1}, \boldsymbol{\theta}\right),\ \boldsymbol{g}\left(\boldsymbol{y}_{k+1}^{j-1}, \boldsymbol{\theta}\right), \ldots,\ \boldsymbol{g}\left(\boldsymbol{x}_{k+\mathcal{K}}^{j-1}, \boldsymbol{\theta}\right)\right] \tag{7.16}$$

Thus both the external loadings $\left[\boldsymbol{f}_{k},\ \boldsymbol{f}_{k+1}, \ldots,\ \boldsymbol{f}_{k+\mathcal{K}}\right]$ and the pseudo-forces, $\left[\boldsymbol{g}_{k}^{j-1},\ \boldsymbol{g}_{k+1}^{j-1}, \ldots,\ \boldsymbol{g}_{k+\mathcal{K}}^{j-1}\right]$, correspond to all $\mathcal{K}$ time increments within the whole time block, are considered as known deterministic inputs, used in simulation of the linearized system. Note that the method is linearly implicit meaning that the time-integration contains simulation of a linear ODE system, subjected to known inputs (at $\mathcal{K}$ time increments, in each iteration). Using the obtained response, the nonlinear pseudo-forces are updated to give

$$\boldsymbol{G}^{j} = \boldsymbol{g}\left(\boldsymbol{Y}^{j}, \boldsymbol{\theta}\right) = \left[\boldsymbol{g}\left(\boldsymbol{y}_{k}^{j}, \boldsymbol{\theta}\right),\ \boldsymbol{g}\left(\boldsymbol{y}_{k+1}^{j}, \boldsymbol{\theta}\right), \ldots,\ \boldsymbol{g}\left(\boldsymbol{y}_{k+\mathcal{K}}^{j}, \boldsymbol{\theta}\right)\right] \tag{7.17}$$

The updated pseudo-forces should be used for a new response calculation using Eq. 7.15, and this should be repeated iteratively until a specified convergence condition is fulfilled. Note that for the first iteration at each time block, the initial pseudo-forces are computed based on the response obtained from simulation of the underlying linear system subjected only to a given external loading.

$$\begin{aligned} \boldsymbol{G}^{0} &= \boldsymbol{g}\left(\boldsymbol{Y}^{\mathrm{lin}}\right) \\ \boldsymbol{Y}^{\mathrm{lin}} &= \left[\boldsymbol{y}_{k}^{\mathrm{lin}},\ \boldsymbol{y}_{k+1}^{\mathrm{lin}}, \ldots,\ \boldsymbol{y}_{k+\mathcal{K}}^{\mathrm{lin}}\right] \\ \boldsymbol{x}_{k+1}^{\mathrm{lin}} &= \boldsymbol{A}_{\mathrm{d}}\boldsymbol{x}_{k}^{\mathrm{lin}} + \boldsymbol{B}_{\mathrm{d}}^{\mathrm{lin}} \boldsymbol{f}_{k} \\ \boldsymbol{y}_{k+1}^{\mathrm{lin}} &= \boldsymbol{C}_{\mathrm{d}}\boldsymbol{x}_{k}^{\mathrm{lin}} + \boldsymbol{D}_{\mathrm{d}}^{\mathrm{lin}} \boldsymbol{f}_{k} \end{aligned} \tag{7.18a–d}$$

For each time block, the iterations are repeated until the convergence requirements are fulfilled. The criterion is based on the pseudo-forces at succeeding iterations as

$$\left\|\boldsymbol{G}^{j} - \boldsymbol{G}^{j-1}\right\| < \delta \tag{7.19}$$

It is worth mentioning that although fixed-point iteration is not suitable for large-scale problems due to the high condition number of the Jacobian matrix [15], it becomes a reasonable choice in implicit exponential integration schemes. It is because of the fact that the linear terms that usually contain the stiff and oscillatory nature of the system, are integrated exactly, in advance. Therefore the stiff terms, which can make the problem badly-conditioned, do not cause problems for convergence of the fixed-point iteration algorithm in computation of the nonlinear pseudo-forces.

7.3.4 Explicit Implementation

Explicit methods are efficient particularly when the cost of nonlinear force evaluations is high. This occurs typically when the nonlinear forces are spatially distributed and therefore the nonlinear pseudo-force is not spatially sparse anymore. In this regard, an explicit version of the exponential/triangular-hold method is being introduced. By using the same discrete-time system matrices as in Eqs. 7.13–7.14, except the $\boldsymbol{D}_{\mathrm{d}}$ matrix, the numerical integration can be implemented in an explicit form. Using this approximation, the nonlinear function is evaluated based on an approximation of the output, i.e. $\widehat{\boldsymbol{y}_{k}} = \boldsymbol{C}_{\mathrm{d}}\boldsymbol{x}_{k}$, which is dependent only on the known state values. The corresponding discrete-time system is then given by,

$$\begin{aligned} \boldsymbol{x}_{k+1} &= \boldsymbol{A}_{\mathrm{d}}\boldsymbol{x}_k + \boldsymbol{B}_{\mathrm{d}}^{\mathrm{lin}}\boldsymbol{f}_k + \boldsymbol{B}_{\mathrm{d}}^{\mathrm{res}}\boldsymbol{g}\left(\widehat{\boldsymbol{y}}_k, \boldsymbol{\theta}\right) \\ \widehat{\boldsymbol{y}_k} &= \boldsymbol{C}_{\mathrm{d}}\boldsymbol{x}_k \end{aligned} \tag{7.20a,b}$$

where the $\boldsymbol{A}_{\mathrm{d}}, \boldsymbol{B}_{\mathrm{d}}^{\mathrm{lin}}, \boldsymbol{B}_{\mathrm{d}}^{\mathrm{res}}, \boldsymbol{C}_{\mathrm{d}}$ are identical to the ones given by Eq. 7.14a–d. Note that $\boldsymbol{g}$ depends on $\widehat{\boldsymbol{y}_k}\left(\boldsymbol{x}_k\right)$ that is known, and therefore, the solution can be calculated using an explicit implementation.

7.4 The Fermi-Pasta-Ulam Benchmark Problem

We look at the Fermi-Pasta-Ulam (FPU) problem, a highly oscillatory nonlinear system known as a test benchmark for multi-scale time integrators. As given in [12], we consider the FPU problem with three stiff linear and three soft nonlinear springs, connected together in series by alternating weak cubic and stiff linear springs, shown in Fig. 7.2. Due to its rich multi-scale dynamic behaviour, the FPU problem has become a benchmark for validating the performance of numerical time integrators. This model shows different dynamical behaviour on different time scales, i.e. almost-harmonic motion of stiff springs on the time-scale ω^{-1}, the motion governed by the soft springs is on the time scale ω^0 and the energy exchange between the stiff springs is on the time scale of ω [12]. Moreover, this example is illustrative for studying the numerical resonance and/or algorithmic instability in exponential/trigonometric methods, since the system has no external input force and therefore no real resonance.

The potential energy in the FPU problem, V, is equal to the sum of the components acting on different time-scales, i.e. $V = W + U$ where W is the elastic energy in the linear stiff/fast springs and U is the potential energy in the nonlinear slow springs. Consider the second-order differential equation, $\ddot{\boldsymbol{q}} = -\nabla V\left(\boldsymbol{q}\right)$, given by

$$\ddot{\boldsymbol{q}} + \boldsymbol{\Omega}^2\boldsymbol{q} = \boldsymbol{g}\left(\boldsymbol{q}\right) \text{ with } \boldsymbol{\Omega} = \begin{bmatrix} \mathbf{0} & \mathbf{0} \\ \mathbf{0} & \omega\mathbf{I} \end{bmatrix} \tag{7.21a,b}$$

with a smooth gradient nonlinearity, denoted by $\boldsymbol{g}\left(\boldsymbol{q}\right) = -\nabla \mathrm{U}\left(\boldsymbol{q}\right)$ and $\mathbf{I}$ as the identity matrix. Note that the condition number of $\boldsymbol{\Omega}$ approaches infinity due to the multiple time-scales presents in the linear nominal system. The total energy of the system, which is a conserved quantity, is given by

$$H\left(\boldsymbol{q}, \boldsymbol{p}\right) = \frac{1}{2}\sum_{1}^{l}\left(p_{2i-1}^2 + p_{2i}^2\right) + \frac{\omega^2}{4}\sum_{1}^{l}\left(q_{2i-1} - q_{2i}\right)^2 + \sum_{1}^{l}\left(q_{2i-1} - q_{2i}\right)^4 \tag{7.22}$$

where $\boldsymbol{p}$ is the momentum vector. For the investigated case study, let $\boldsymbol{p} = \dot{\boldsymbol{q}}$ (all masses are considered to be identical, i.e. $m = 1$) and the number of point masses to be six, $2l = 6$. Considering the standard form of a highly oscillatory problem, presented in [12], a transformation is used as follows,

$$\begin{aligned} \tilde{q}_{0,i} &= \left(q_{2i-1} + q_{2i}\right)/\sqrt{2}, \;\; \tilde{q}_{1,i} = \left(q_{2i-1} + q_{2i}\right)/\sqrt{2} \\ \tilde{p}_{0,i} &= \left(p_{2i-1} + p_{2i}\right)/\sqrt{2}, \; \tilde{p}_{1,i} = \left(p_{2i-1} - p_{2i}\right)/\sqrt{2} \end{aligned} \tag{7.23a–d}$$

Following the FPU problem with $l = 3$, presented in [12], the initial condition is assumed to be

$$\tilde{q}_{0,1}(0) = 1, \quad \tilde{q}_{1,1}(0) = \omega^{-1}, \quad \tilde{p}_{0,1}(0) = 1, \quad \tilde{p}_{1,1}(0) = 1 \tag{7.24}$$

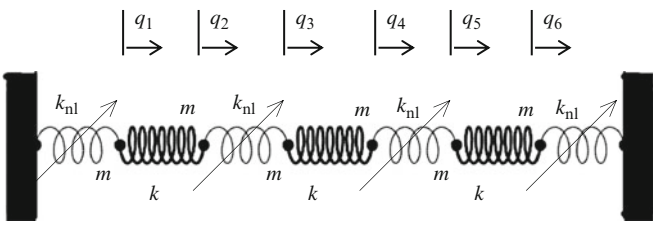

Fig. 7.2 The Fermi-Pasta-Ulam problem with six identical point masses ($2\boldsymbol{l} = 6$) connected through three identical stiff (fast) springs and three identical soft (slow) nonlinear springs. Here the parameters are considered as $\boldsymbol{m} = 1$, $\boldsymbol{k}_{\mathbf{nl}} = 4$ and $\boldsymbol{\omega}^2 = 2\boldsymbol{k}/\boldsymbol{m}$ and $\boldsymbol{m} = 1$ such that we can compare our results with the ones given in [12]

with all other initial values set to zero. Total energy is an invariant of this system. Also note that the energy in stiff springs is an adiabatic invariant (or almost conserved quantity), given by

$$I = I_1 + I_2 + I_3 \text{ with } I_j = \left(\dot{q}_{2,j}^2 + \left(\omega q_{2,j}\right)^2\right)/2 \tag{7.25a,b}$$

where I_j is the potential energy in the j^{th} stiff spring (we call it oscillatory energy as well). The elongation of the j^{th} stiff spring, $q_{1,j}$, is the j^{th} component of the lower half of $\boldsymbol{q}_2 \in \Re^3$ of $\boldsymbol{q} = (\boldsymbol{q}_1, \boldsymbol{q}_2)^{\text{T}} \in \Re^6$, decomposed according to the blocks of $\boldsymbol{\Omega}$. It is notable that the approximate preservation of these quantities can be considered as two criteria for validating the accuracy performance of a numerical integrator while the stability should be maintained, as well. In the following, in order to study the stability features of the presented integrator, we compare it to trigonometric integrators, applied to the FPU problem. In this regard, we use the specific structure of $\boldsymbol{A}$ and $\boldsymbol{B}$ system matrices for a Hamiltonian system, given by Eq. 7.4a,b, and insert it into the general form Eq. 7.3 of the presented integrator. The resulting equation is as follows

$$\begin{pmatrix} \boldsymbol{q}_{n+1} \\ \dot{\boldsymbol{q}}_{n+1} \end{pmatrix} = \begin{bmatrix} \cos(h\boldsymbol{\Omega}) & \boldsymbol{\Omega}^{-1}\sin(h\boldsymbol{\Omega}) \\ -\boldsymbol{\Omega}\sin(h\boldsymbol{\Omega}) & \cos(h\boldsymbol{\Omega}) \end{bmatrix} \begin{pmatrix} \boldsymbol{q}_n \\ \dot{\boldsymbol{q}}_n \end{pmatrix} + h \begin{pmatrix} h\text{sinc}(h\boldsymbol{\Omega})\,\text{sinc}^2(h\boldsymbol{\Omega}/2)\,\boldsymbol{g}_n \\ \text{sinc}^2(h\boldsymbol{\Omega}/2)\cos(h\boldsymbol{\Omega})\,\boldsymbol{g}_n \end{pmatrix} \tag{7.26}$$

which can be compared to the well-known trigonometric methods, presented by Eq. 7.7 and Table 7.1. It can be seen that the second term on the right-hand-side of the equation is different from trigonometric integrators, given in Table 7.1. It should be noted that the underlying nominal linear system, considered in the presented integrator, is chosen as a perturbation of the Jacobian matrix, such that the condition number of the nominal system $\boldsymbol{A}_0$ is decreased to 2510. Note that for the standard FPU problem, $\boldsymbol{A}_\mathbf{J}$, the condition number of the Jacobian matrix approaches infinity. In this regard, we have considered the nominal linear model consisting of stiff springs with stiffness k and slow springs which behaves linearly with stiffness coefficient identical to k_{nl}. Using such a proper nominal linear system, which was explained in Sect. 7.3.1, results in accuracy and stability superiority of the presented integrator, compared to LF method, see Figs. 7.3 and 7.4.

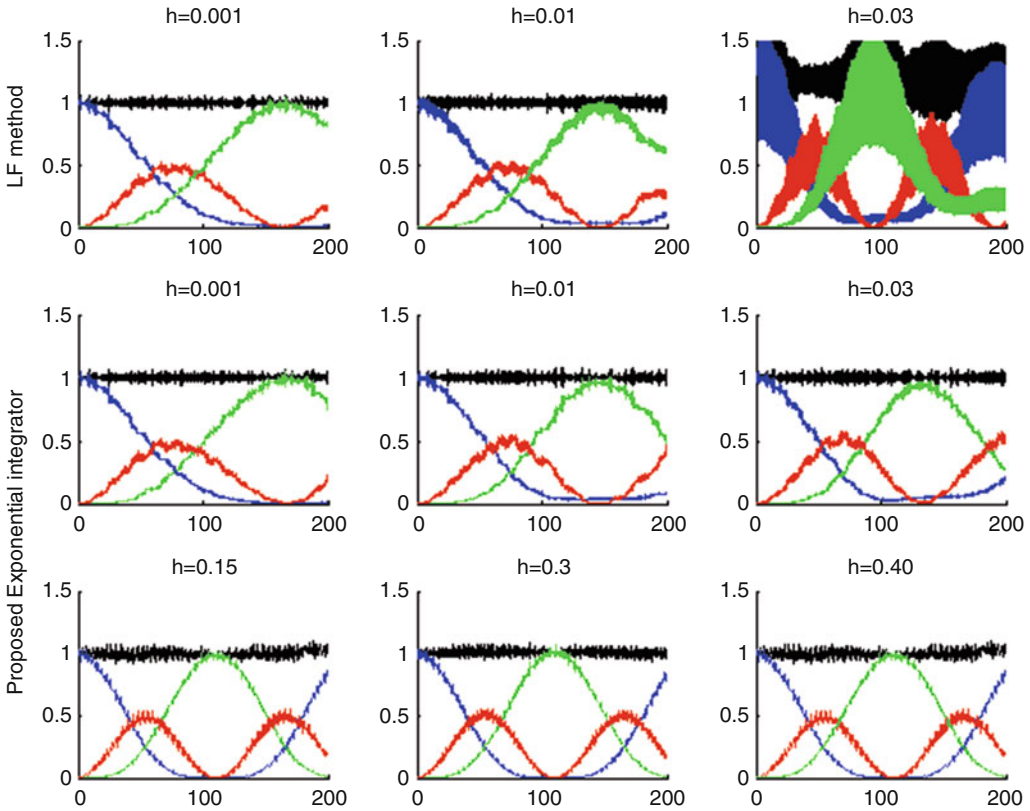

Fig. 7.3 Slow exchange of oscillatory energy between stiff springs versus time, in the Fermi-Pasta-Ulam problem with $\omega = 50$, for the presented explicit method. Oscillatory energy in the first (*blue*), second (*red*) and third stiff (*green*) springs are denoted by I_1, I_2 and I_3. The total oscillatory energy (*black*), i.e. $I = I_1 + I_2 + I_3$ is approximately preserved, i.e. I is system's adiabatic invariant

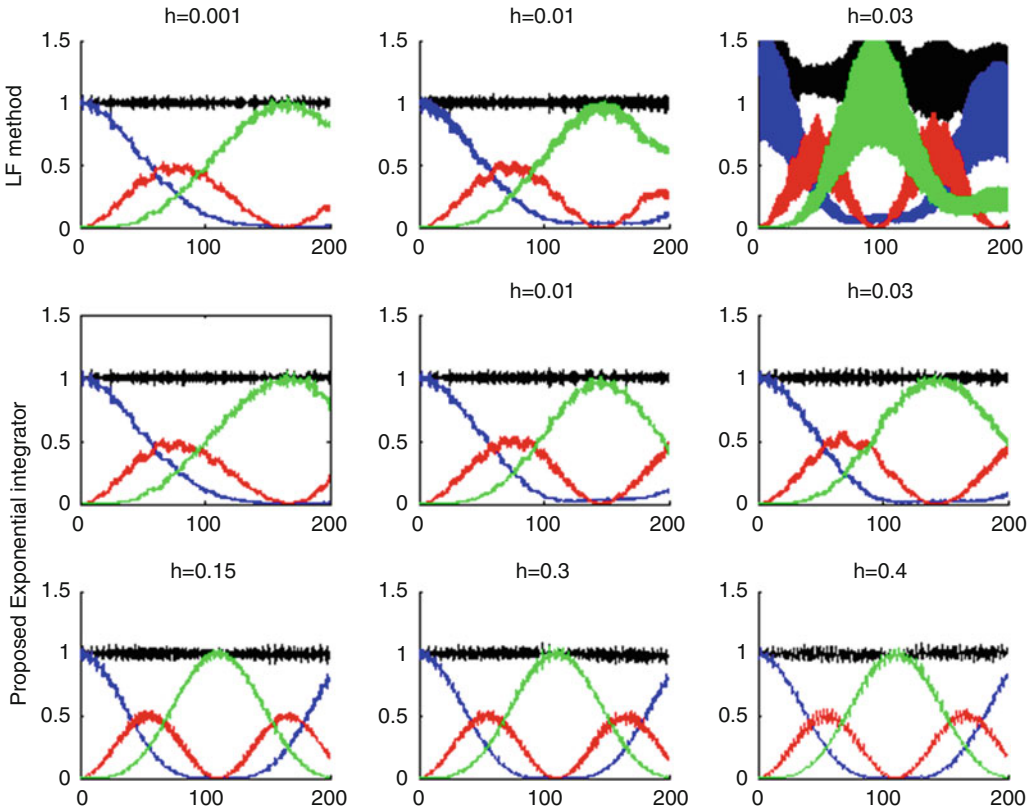

Fig. 7.4 Slow exchange of oscillatory energy between stiff springs vs time, in the Fermi-Pasta-Ulam problem with $\omega = 50$, for the presented implicit method. Oscillatory energy in the first (*blue*), second (*red*) and third stiff (*green*) springs are denoted by I_1, I_2 and I_3. The total oscillatory energy (*black*), i.e. $I = I_1 + I_2 + I_3$ is approximately preserved, i.e. I is system's adiabatic invariant

7.4.1 Linear Stability Limitations

Linear stability limitation is an important concern in numerical integration of highly oscillatory systems with multiple time-scales, particularly when we use explicit methods. To overcome this, the fast/slow splitting of dynamics is of interest, where the aim is to sample the slow forces as sparse as possible and at a rate that is independent (or almost independent) of the step-size dictated by the fastest normal mode of the system. This is the main idea behind the exponential/trigonometric integrators, such the integrator presented in this paper. To study the linear stability of the presented exponential scheme, given by Eqs. 7.22a,b, we simulate the FPU problem for different time-step sizes of h, which are even larger than h_{crit} that corresponds to the system's fastest oscillatory force. Several numerical simulations of the FPU oscillatory energy exchange are computed for the second order leap-frog (LF), [12], and the presented explicit and implicit integrator, see Figs. 7.3 and 7.4. The simulation computed by the LF with $h = 0.001$, is considered as reference. We see that the LF solution's quality degrade rapidly as the step-size approaches to the upper end of stability region, i.e. $h\omega < 2$ or equivalently at $h = 0.03$. By contrast, the presented exponential integrators, either explicit or implicit version, performs stable, also for time step up to the order of 0.03–0.4. This seems to give a better linear stability property compared to the IMEX method [16], which ensures numerical stability for step-sizes up to 0.3. As mentioned in [16], the implicit midpoint-type methods such as IMEX might suffer from numerical instability, despite their lack of linear resonances. However, at $h > 0.4$, numerical stability of the presented explicit method breaks down and the amplitude growth is without bounds. In Fig. 7.5 the oscillatory energy behaviour of the presented method (explicit version) for a longer time scale, i.e. on the ω^2 time-scale, has been considered. It is seen that the numerical energy is still reasonable and does not begin to blow up as time passes. Moreover, the excessive noise visible in simulation results, obtained by Impulse/Deuflhard method, for $h = 0.1$ (as discussed in [16]), does not exist in the results given by the presented integrator, see Fig. 7.6. This Figure shows how the triangular-hold discretization technique results in filtration of this excessive numerical noise.

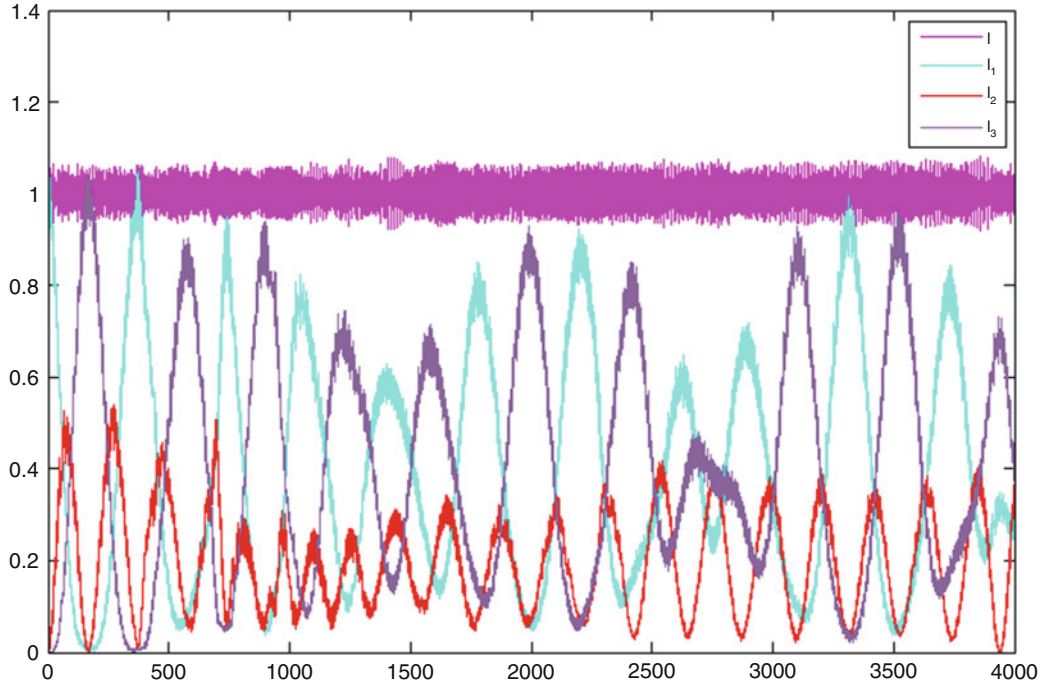

Fig. 7.5 Numerical simulation of the presented exponential scheme, for the integration time interval [0–4000] seconds. The exchange of oscillatory energy between the stiff springs and conservation of the adiabatic invariant are qualitatively correct, on the order of $\boldsymbol{\omega}^2$ time scale

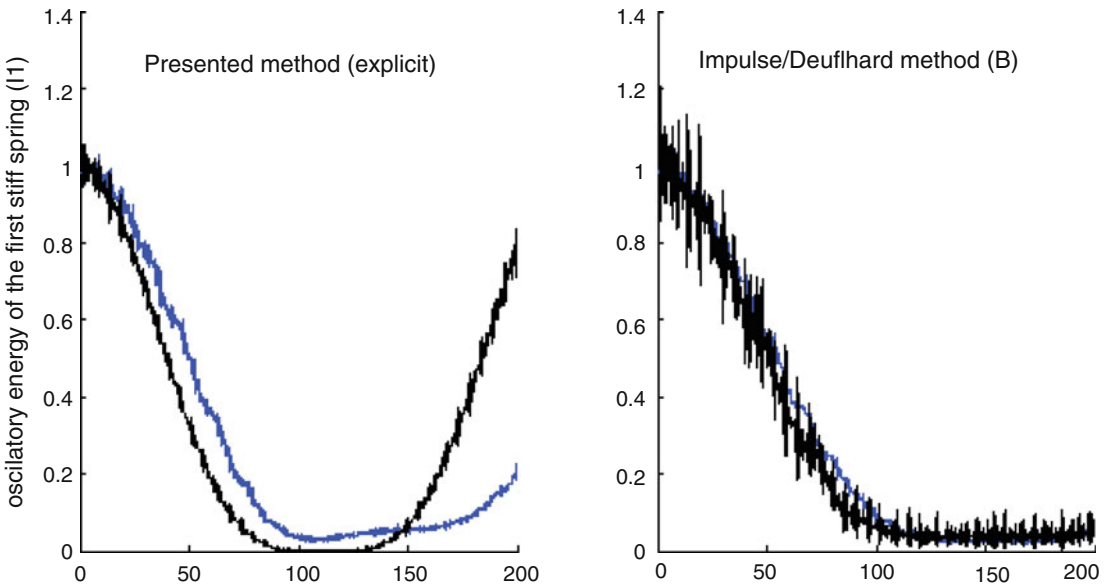

Fig. 7.6 Oscillatory energy in the first stiff spring in the FPU system versus time, on the time interval [0,200] and with $\omega = 50$ step sizes $h = 0.01$ (*green*), $h = 0.03$ (*blue*) and $h = 0.1$ (*black*)

7.4.2 Nonlinear Stability and Numerical Resonances

As discussed in previous sections, multiple-time-stepping numerical methods such as the presented exponential integrator enables us to treat highly oscillatory problems more efficiently while ensuring better linear stability properties. However, MTS methods can suffer from algorithmic nonlinear instabilities (or numerical resonances) when the step-size is some specific integer fraction of the period of the normal mode of the discrete system, i.e. integer values of $h\omega/\pi$ [10]. These instabilities, which are found to occur at certain isolated values of the step-size, are also termed "step-size resonance" [6].

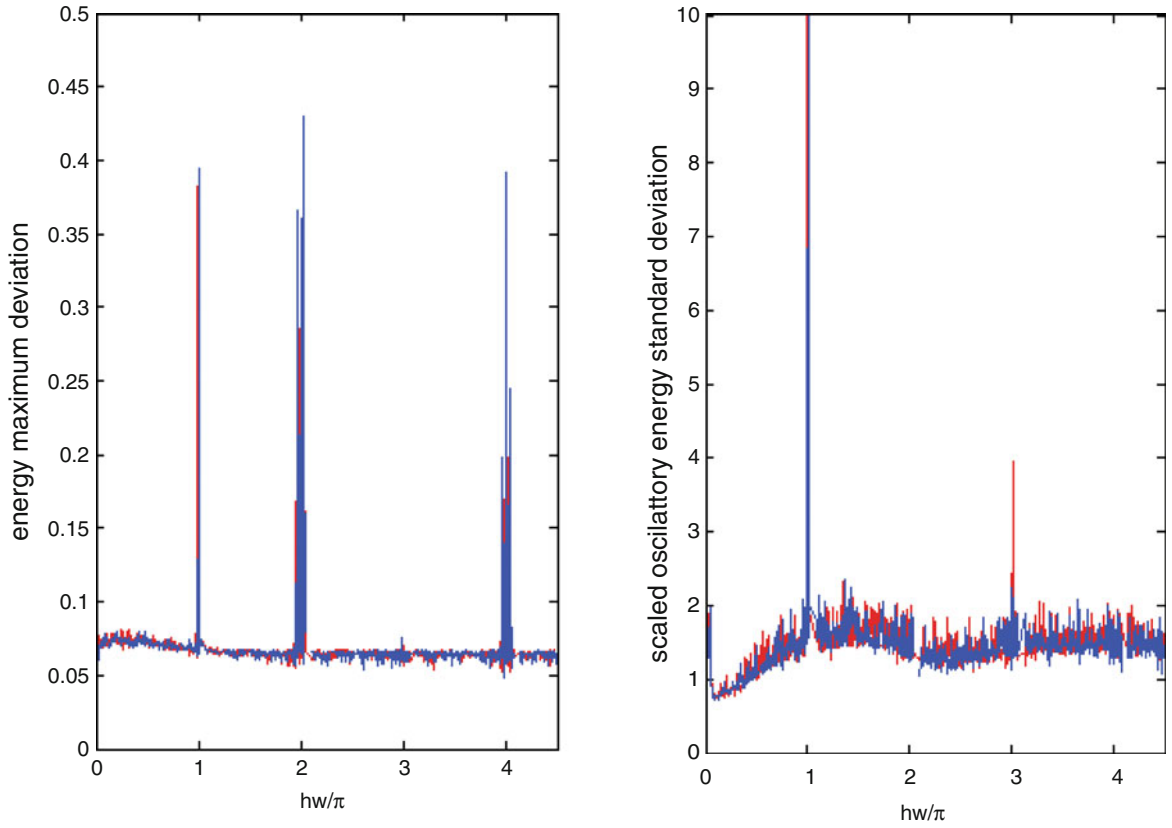

Fig. 7.7 Maximum error of total energy and standard deviation of the scaled oscillatory energy versus $h\omega/\pi$, for the FPU problem. Simulations are performed by the proposed explicit (blue) and implicit (red) on time interval [0,1000] with time step size $h = 0.02$. Zoom in pictures, for the explicit implementation, are presented in Figs. 7.8 and 7.9

Therefore, even the discrete-time linear/fast system is linearly stable alone; the introduction of the discretized slow terms (linear/nonlinear) makes things unstable. In order to study such numerically induced resonance effects, we look at the errors in the energy of numerical solution, for a fixed time step, $h = 0.02$, in the time interval [0,1000] for varying system stiffness given by ω (these values are considered the same as in [17]). It is shown in Fig. 7.7 that the total energy error increases dramatically for the resonance points and this amplitudes blow up when the system is integrated for long time intervals.

However, the presented method conserves the energy very accurately away from the numerical integrator resonance points. As mentioned in [12], among the trigonometric methods (A-E) of Table 7.1, this desirable property is valid only for integrator (A) and (D), i.e. when $(x) = \text{sinc}^2(x/2)$. For the rest of the integrators, the energy error is not small even far from the integrator resonance points and it varies for different values of ω. Note that, in general, numerical methods do not have uniform error in $h\omega$, even if they are geometric [10]. As it is shown in Fig. 7.8, the total energy error for the FPU problem approaches very large values when the integration time interval increases. Figure 7.9 shows that the oscillatory energy error of the proposed numerical algorithm is also not bounded for the odd integer values of $h\omega/\pi$, but gives a uniform error away from resonances, as shown in [10].

7.5 Concluding Results

This paper studied the stability properties of a recently proposed *exponential* integrator, focusing on stable simulation of highly oscillatory systems with multiple time-scales. The linear and nonlinear stability properties of the presented exponential integrator were studied. This was illustrated with the Fermi–Pasta–Ulam (FPU) problem, a highly oscillatory nonlinear system known as a test benchmark for multi-scale time integrators. It was shown how the exponential integrators, such as the method under study, enable us to advance the slow and fast dynamics with different time step sizes and to sample the slow nonlinear forces at a rate beyond the critical step-size, dictated by the period of system's fastest normal mode.

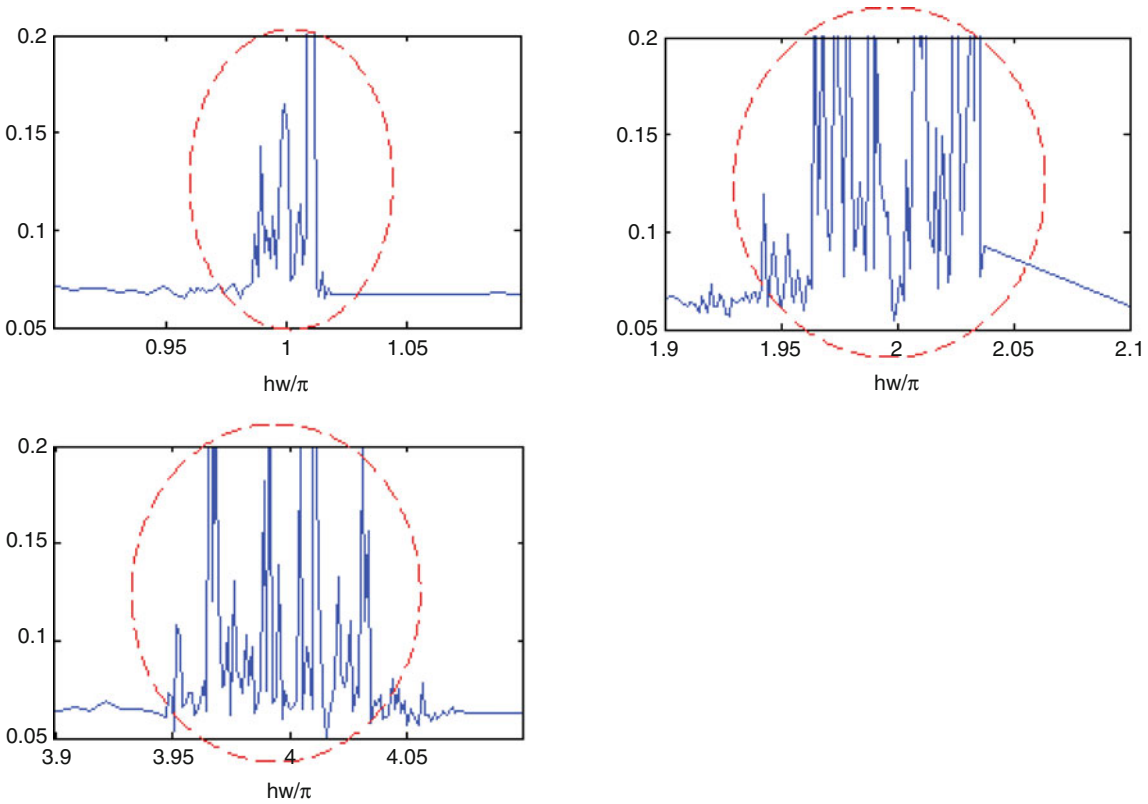

Fig. 7.8 Maximum error of total energy of the FPU problem versus $h\omega/\pi$. Simulations are performed by the proposed explicit exponential integrator on time interval [0,1000] with step size $h = 0.02$. The other three pictures are the zoom of the first picture, close to the numerical resonances points, with a finer frequency resolution

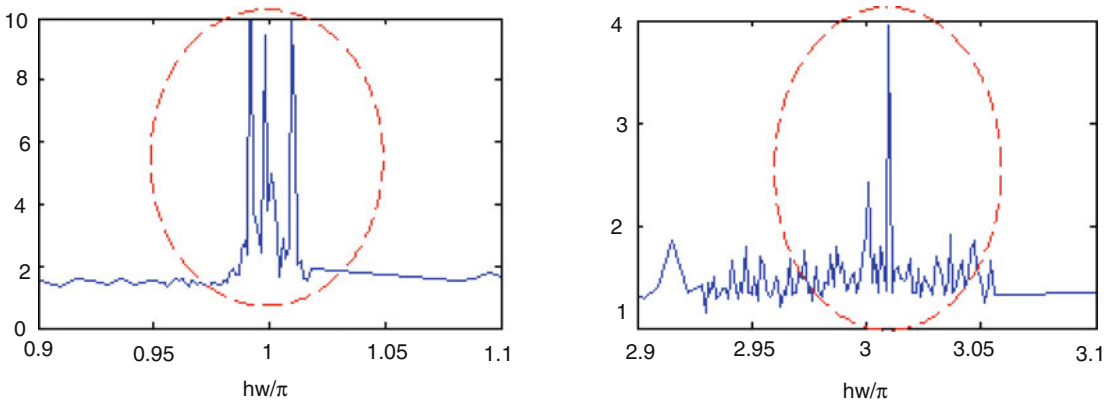

Fig. 7.9 Standard deviation of scaled oscillatory energy of the FPU problem versus $h\omega/\pi \in [0-4.5]$. Simulations are performed on time interval [0,1000] with $h = 0.02$. Oscillatory energy is scaled by ω and shifted by a reference solution, (i.e. $\omega\left[\sigma I\left(\omega\right) - I(0)\right]\Big)$ such that the reference solution is unitary. The other two pictures are the zoom of the first picture, close to the numerical resonances points, with a finer frequency resolution

References

1. Sou KC, de Weck OL (2005) Fast time-domain simulation for large-order linear time-invariant state space systems. Int J Numer Methods Eng 63(5):681–708
2. Sanz-Serna JM (2008) Mollified impulse methods for highly oscillatory differential equations. SIAM J Numer Anal 46(2):1040–1059
3. Rahrovani S, Abrahamsson T, Modin K (2014) An efficient exponential integrator for large nonlinear stiff systems part 1: theoretical investigation. Conference proceedings of the society for experimental mechanics series, vol 2, Orlando, pp 269–280

4. Rahrovani S, Abrahamsson T, Modin K (2014) An efficient exponential integrator for large nonlinear stiff systems part 2: symplecticity and global error analysis. Conference proceedings of the society for experimental mechanics series, vol 2, Orlando, pp 269–280
5. Rahrovani S, Abrahamsson T, Modin K (2014) Integration of hamiltonian systems with a structure preserving algorithm. Proceedings of ISMA2014 and USD2014, Leuven, pp 2915–2929
6. Reich S, Leimkuhlera B (2001) A reversible averaging integrator for multiple time-scale dynamics. J Comput Phys 171(1):95–114
7. Ostermann A, Hochbruck M (2010) Exponential integrators. Acta Numer 19:209–286
8. Cox SM, Matthews PC (2002) Exponential time differencing for stiff systems. J Comput Phys 176(2):430–455
9. Gaurav WSF, Johnsson E (2011) Efficient uncertainty quantification of dynamical systems with local nonlinearities and uncertainties. Probab Eng Mech 26(4):561–569
10. Dion O'Neale (2009) Preservation of phase space structure in symplectic integration, Ph.D. thesis
11. García-Archilla B, Sanz-Serna JM, Skeel RD, Sanz-Serna JM (1998) Long-time-step methods for oscillatory differential equations. SIAM J Sci Comput 20(3):930–963
12. Hairer E, Lubich C, Wanner G (2001) Geometric numerical integration – structure preserving algorithms for ordinary differential equations. Springer, Berlin
13. Franklin GF, Powell JD, Workman ML (1998) Digital control of dynamic systems. Ellis-Kagle Press, Half Moon Bay
14. Zhang M, Skeel R (1997) Cheap implicit symplectic integrators. Appl Numer Math 25(2–3):297–302
15. Beylkin G, Keiser JM (1997) On the adaptive numerical solution of nonlinear partial differential equations in Wavelet bases. J Comput Phys 132(2):231–259
16. Grinspun E, Stern A (2009) Implicit-explicit variational integration of highly oscillatory problems. SIAM Multiscale Model Simul 7(4):1779–1794
17. Stern A, Mclachlan RI (2014) Modified trigonometric integrators. SIAM J Numer Anal 52:1378–1397

Chapter 8
Coupled Parametrically Driven Modes in Synchrotron Dynamics

Alexander Bernstein and Richard Rand

Abstract This work concerns the dynamics of a type of particle accelerator called a synchrotron, in which particles are made to move in nearly circular orbits of large radius. The stability of the transverse motion of such a rotating particle may be modeled as being governed by Mathieu's equation. For a train of two such particles the equations of motion are coupled due to plasma interactions and resistive wall coupling effects.

In this paper we study a system consisting of a train of two such particles which is modeled as two coupled nonlinear Mathieu equations with delay coupling. In particular we investigate the stability of two coupled parametrically forced linear normal modes.

Keywords Parametric excitation • Coupled oscillators • Mathieu equation • Stability analysis • Synchrotron

8.1 Introduction

The synchrotron is a particle accelerator in which a "particle" actually consists of a group of electrons in a "bunch." We ignore the interactions of electrons inside each bunch and treat the entire bunch as a single particle.

Each bunch leaves an electrical disturbance behind it as it traverses around the synchrotron, and these wake fields are the main source of coupling in the model. The coupling is mediated by several sources, including resistive wall coupling, ion coupling, and the electron cloud effect. The wake fields can persist through entire orbits.

The ensemble of all bunches is called a "train." When modeled as several interacting bunches, each bunch is coupled to the wake of the bunch in front of it. When modeled as a train, the train interacts with itself after a full orbit. We will combine both of these into one cohesive model.

The particle is made to move in a circle-like orbit through the use of about 100 magnets. The magnets are an external force dictating the path of the electron, and the circular nature of this path means that the forcing is periodic in rotation angle θ; using $\theta = \omega t$, the forcing is periodic in time as well. We can express this forcing function as a Fourier series, and we shall approximate this series by the first couple of terms in it, namely the constant term and the first cosine term.

We model each bunch as a scalar variable $x_i(t), i = 1, \ldots, n$. Here x_i is the vertical displacement above equilibrium of the center of mass of the ith bunch. Each x_i is modeled as an oscillator, and we write:

$$\begin{aligned} \ddot{x_1} + (\delta + \epsilon \cos t)\, x_1 + \epsilon\gamma x_1^3 &= \beta \sum_{j=1}^{n} x_j(t-T) \\ \ddot{x_i} + (\delta + \epsilon \cos t)\, x_i + \epsilon\gamma x_i^3 &= \beta \sum_{j=1}^{n} x_j(t-T) + \alpha x_{i-1}, \quad i = 2, \ldots, n \end{aligned} \tag{8.1}$$

A. Bernstein (✉)
Center for Applied Mathematics, Cornell University, Ithaca, NY, USA
e-mail: ab2334@cornell.edu

R. Rand
Department of Mathematics, Cornell University, Ithaca, NY, USA

Department of Mechanical and Aerospace Engineering, Cornell University, Ithaca, NY, USA

G. Kerschen (ed.), *Nonlinear Dynamics, Volume 1*, Conference Proceedings of the Society for Experimental Mechanics Series, DOI 10.1007/978-3-319-15221-9_8

When modeling the train as a single unit, we are concerned with the forces on it due to the disturbance left at a given point by itself, one cycle ago. This effect will be modeled as a delay term, where the delay is the time to rotate through one cycle. β represents the strength of this coupling (Meller, personal communication to author RR on 12-27-13).

When modeling the interaction between bunches, each bunch influences the bunch behind it in the train. Since the time for a bunch to move to the position occupied by the previous bunch is small relative to the time needed to traverse the entire circumference of the synchrotron, the bunch-to-bunch interactions are not modeled with delay terms. α represents the strength of this coupling (Meller, personal communication to author RR on 12-27-13).

The simplest case is a single bunch, $n = 1$. Here we only consider the effect of delayed self feedback:

$$\ddot{x_1} + (\delta + \epsilon\nu\cos t)x_1 = \beta x_1(t - T) \tag{8.2}$$

A system of this type has been investigated by Morrison and Rand [1]. It was shown that the region of instability associated with 2:1 subharmonic resonance can be eliminated by choosing the delay T long enough.

8.2 Model 1

In this paper we study a system of two bunches (Eq. (8.1) with $n = 2$), in which we ignore nonlinear terms as well as delay. The equations are:

$$\begin{aligned} \ddot{x} + (\delta + \epsilon\cos t)\, x &= \beta(x + y) \\ \ddot{y} + (\delta + \epsilon\cos t)\, y &= \beta(x + y) + \alpha x \end{aligned} \tag{8.3}$$

We uncouple these equations with the following linear transformation:

$$x = u + v, \qquad y = \sqrt{\frac{\beta + \alpha}{\beta}}(u - v) \tag{8.4}$$

giving

$$\begin{aligned} \ddot{u} + (\Omega_u^2 + \epsilon\cos t)\, u &= 0 \\ \ddot{v} + (\Omega_v^2 + \epsilon\cos t)\, v &= 0 \end{aligned} \tag{8.5}$$

where

$$\begin{aligned} \Omega_u^2 &= \delta - \beta - \sqrt{\beta(\beta + \alpha)} \\ \Omega_v^2 &= \delta - \beta + \sqrt{\beta(\beta + \alpha)} \end{aligned} \tag{8.6}$$

The system has thus been reduced to a pair of uncoupled Mathieu equations, each of the form:

$$\ddot{z} + (\Delta + \epsilon\cos t)\, z = 0 \tag{8.7}$$

As is well known, this equation exhibits a 2:1 subharmonic resonance in the neighborhood of $\Delta = 1/4$. The boundaries of the associated tongue of instability are given by:

$$\Delta = \frac{1}{4} \pm \frac{\epsilon}{2} + O(\epsilon^2) \tag{8.8}$$

Comparison of Eqs. (8.6) and (8.8) gives the instability tongues as $\Omega_i^2 = \frac{1}{4} \pm \frac{\epsilon}{2}$, or in terms of the parameter δ, the two tongues become:

$$\delta = \frac{1}{4} + \beta \pm \sqrt{\beta(\beta + \alpha)} \pm \frac{\epsilon}{2} + O(\epsilon^2) \tag{8.9}$$

$$\delta_0 = \frac{1}{4} + \beta \pm \sqrt{\beta(\beta + \alpha)} \tag{8.10}$$

$$\delta_1 = \pm\frac{1}{2} \tag{8.11}$$

It is clear from this result that the introduction of α and β only affects δ_0. Graphically, this means that as the parameters α, β change, the tongue of instability is translated left or right in the δ-ϵ plane, and the slopes of the transition curves remain the same.

Four graphs of the transition curves are shown on the next page. The shaded regions are unstable and the unshaded regions are stable.

8.3 Model 2

Another model we investigated was one where the coupling terms were O(ϵ). In this model, the equations are:

$$\begin{aligned} \ddot{x} + (\delta + \epsilon\cos t)\, x &= \epsilon\beta(x + y) \\ \ddot{y} + (\delta + \epsilon\cos t)\, y &= \epsilon\beta(x + y) + \epsilon\alpha x \end{aligned} \tag{8.12}$$

We will employ the technique of harmonic balance to find expressions for the transition curves to order ϵ [2]. We assume a solution can be found of the form:

$$\begin{aligned} x &= A\cos\tfrac{t}{2} + B\sin\tfrac{t}{2} \\ y &= C\cos\tfrac{t}{2} + D\sin\tfrac{t}{2} \end{aligned} \tag{8.13}$$

And substitute these equations into (8.12).

After using some trig identities we obtain:

$$\begin{aligned} 0 = {} & \frac{\epsilon B}{2}\sin\frac{3t}{2} + \frac{\epsilon A}{2}\cos\frac{3t}{2} \\ & + \left(B\delta - \epsilon\beta D - \epsilon\beta B - \frac{\epsilon B}{2} - \frac{B}{4}\right)\sin\frac{t}{2} \\ & + \left(A\delta - \epsilon\beta C - \epsilon\beta A + \frac{\epsilon A}{2} - \frac{A}{4}\right)\cos\frac{t}{2} \end{aligned}$$

$$\begin{aligned} 0 = {} & \frac{\epsilon D}{2}\sin\frac{3t}{2} + \frac{\epsilon C}{2}\cos\frac{3t}{2} \\ & + \left(D\delta - \epsilon\beta D - \epsilon\beta B - \epsilon\alpha B - \frac{\epsilon D}{2} - \frac{D}{4}\right)\sin\frac{t}{2} \\ & + \left(C\delta - \epsilon\beta C - \epsilon\beta A - \epsilon\alpha A + \frac{\epsilon C}{2} - \frac{C}{4}\right)\cos\frac{t}{2} \end{aligned}$$

Since we only care about O(ϵ) we disregard the $\cos\frac{3t}{2}$ and $\sin\frac{3t}{2}$ terms. Taking the coefficients of the remaining trigonometric functions to be zero, we obtain four equations in A, B, C, and D. Writing this as a matrix, we get

$$\begin{bmatrix} -\frac{(4\beta-2)\epsilon-4\delta+1}{4} & 0 & -\epsilon\beta & 0 \\ -(\alpha+\beta)\epsilon & 0 & -\frac{(4\beta-2)\epsilon-4\delta+1}{4} & 0 \\ 0 & -\frac{(4\beta+2)\epsilon-4\delta+1}{4} & 0 & -\epsilon\beta \\ 0 & -(\alpha+\beta)\epsilon & 0 & -\frac{(4\beta+2)\epsilon-4\delta+1}{4} \end{bmatrix} \tag{8.14}$$

For this system to have a nontrivial solution, the determinant must be zero. This produces the equation:

$$-\frac{((4\beta-2)\epsilon-4\delta+1)^2\left(\frac{((4\beta+2)\epsilon-4\delta+1)^2}{16}-\beta(\alpha+\beta)\epsilon^2\right)}{16}$$
$$+\beta(\alpha+\beta)\epsilon^2\left(\frac{((4\beta+2)\epsilon-4\delta+1)^2}{16}-\beta(\alpha+\beta)\epsilon^2\right)=0 \tag{8.15}$$

With the solution:

$$\delta=\frac{1}{4}+\epsilon\left(\beta\pm\sqrt{\beta(\beta+\alpha)}\pm\frac{1}{2}\right)+O(\epsilon^2) \tag{8.16}$$

As in Model 1, we write δ in the form $\delta=\delta_0+\epsilon\delta_1+O(\epsilon^2)$ to obtain

$$\delta_0=\frac{1}{4} \tag{8.17}$$

$$\delta_1=\beta\pm\sqrt{\beta(\beta+\alpha)}\pm\frac{1}{2} \tag{8.18}$$

Unlike in Model 1, here the introduction of α and β only affects δ_1. Graphically, this means that as the parameters α,β change, the tongue of instability narrows or widens while intersecting the same point on the δ-axis.

Four graphs of the transition curves are shown on the next page. The shaded regions are unstable and the unshaded regions are stable.

8.4 Results

There are a few important observations to make about the tongues of instability.

8.4.1 Model 1

The first is that a small stable region appears between the tongues of instability, and it grows in size as both parameters α and β increase. Thus, while most of the graph becomes more unstable as the coupling increases, there is a region where the system actually becomes more stable.

The second observation to note is how these transition curves change with respect to both parameters. When β is increased, one of the tongues stays relatively still while the other tongue moves to the right. This causes the intersection of the tongues to move both up and to the right. When α is increased, the tongue on the left moves further to the left and the tongue on the right moves further to the right. This movement is balanced so that the intersection of the tongues moves straight up.

8.4.2 Model 2

Unlike in Model 1, there is no small stable region in Model 2 that grows in size with the parameters α,β. More explicitly, there is no region that becomes more stable as α and β are increased; all unstable regions stay unstable as the parameters increase.

8.5 Conclusion

In this paper we showed the distinct effects that the two types of coupling, α and β, have on the system. Furthermore, we showed that both effects are relevant to the problem and are worth considering when mathematically modeling the synchrotron, and that the nature of the instability depends on the way in which the coupling is modeled.

Note that both models give the same result when ϵ is fixed and α, β vary. As an example, suppose $\epsilon = 0.1$ and we take $\alpha = \beta = 0.01$ in Model 1. Then the values of δ where the stability changes are given by $\delta_{crit} = (0.1957, 0.2958)$. For Model 2 we'd have to use the parameter values $\alpha = 0.1$, $\beta = 0.1$, since the coupling is $\epsilon\alpha$, $\epsilon\beta$ and $\epsilon = 0.1$. Using these values in Model 2 gives the same δ_{crit} values as the ones in Model 1.

The difference between these models comes when the parameters α, β are fixed and ϵ is allowed to vary. In this case we get the transition curves shown in Figs. 8.1 and 8.2.

For future papers we will explore the effects of delay and nonlinearity on this model.

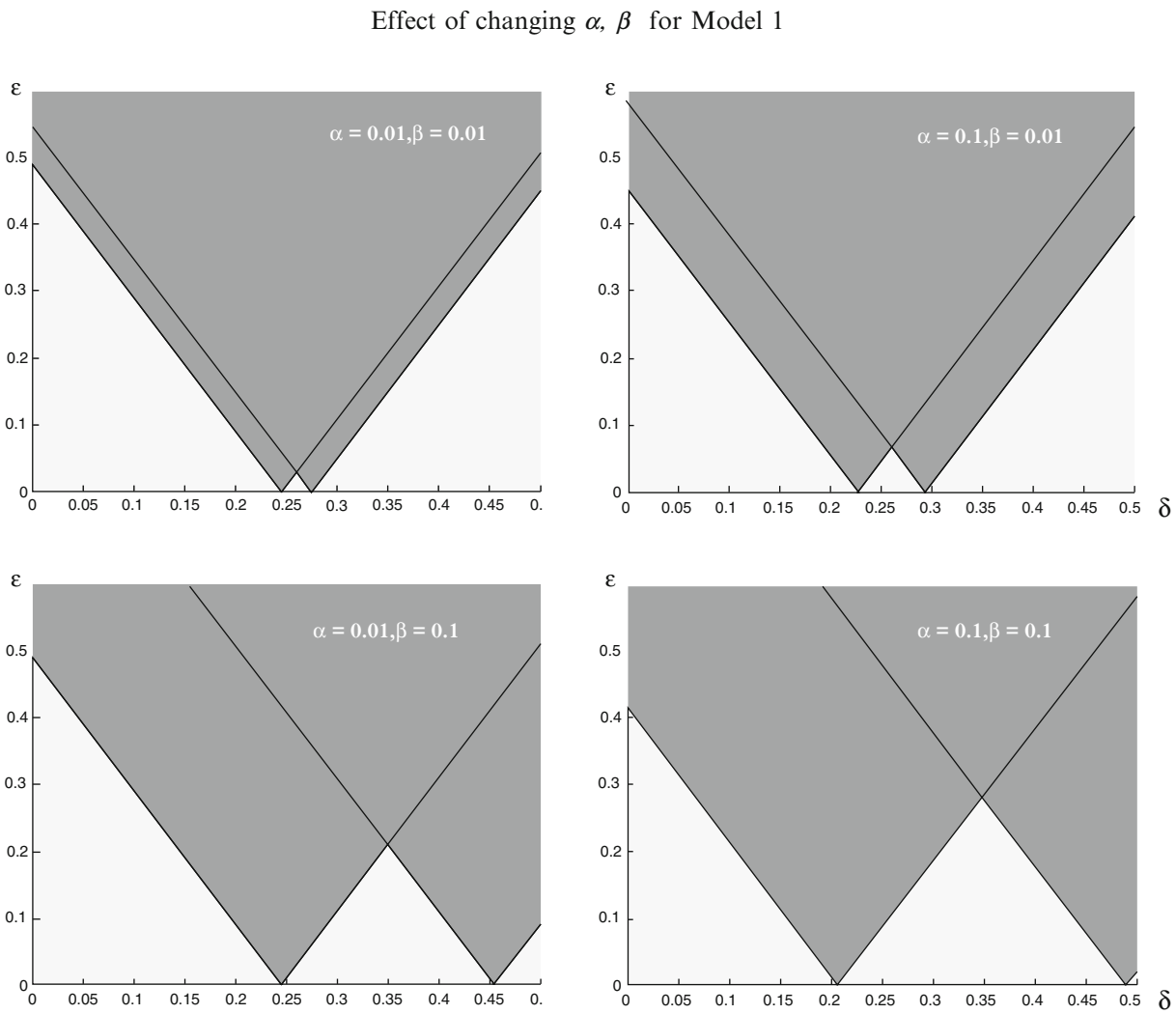

Fig. 8.1 *Shaded regions* are unstable, *unshaded regions* are stable

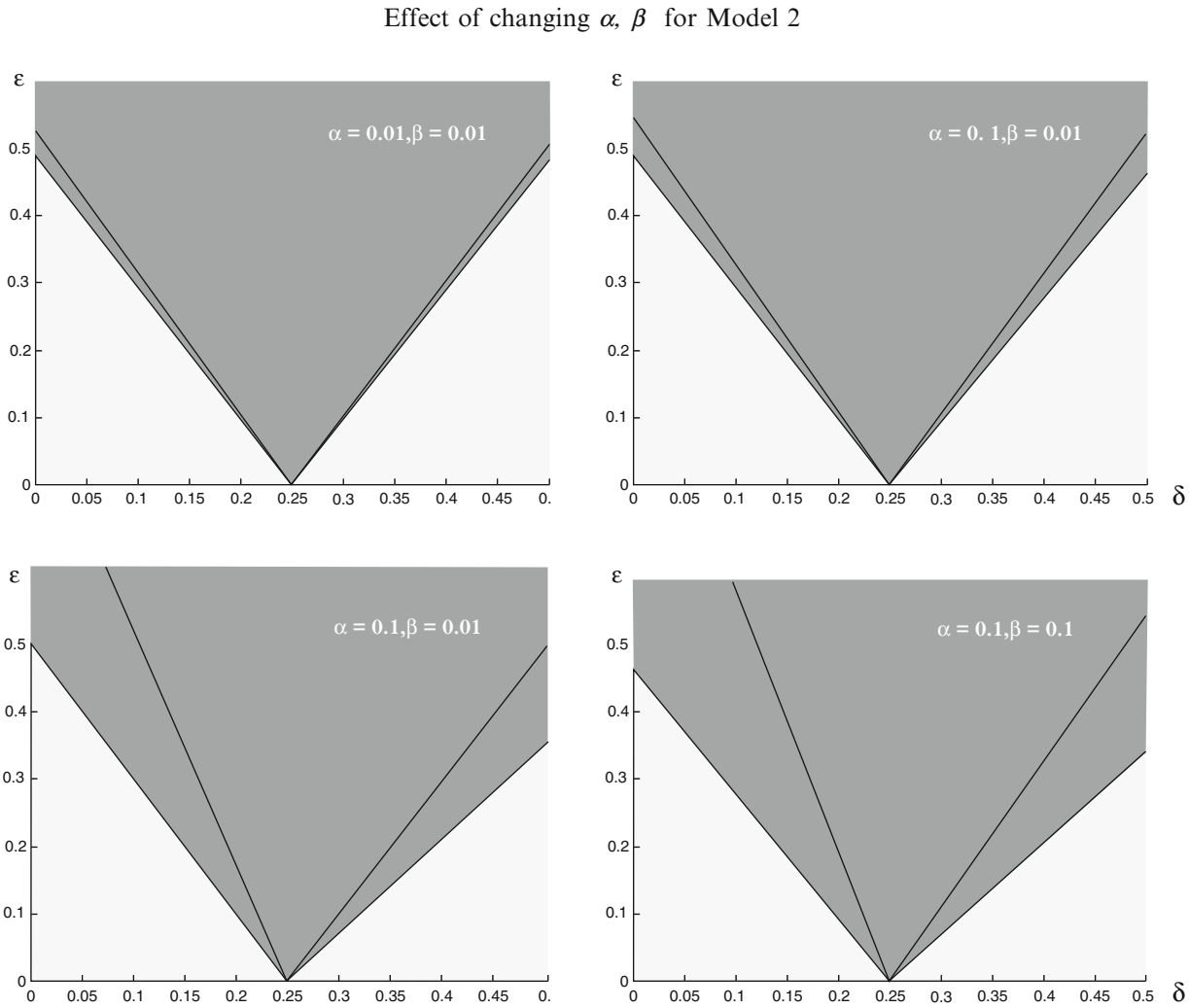

Fig. 8.2 *Shaded regions* are unstable, *unshaded regions* are stable

Acknowledgements The authors wish to thank their colleagues J. Sethna, D. Rubin, D. Sagan and R. Meller for introducing us to the dynamics of the Synchrotron.

References

1. Morrison TM, Rand RH (2007) Resonance in the delayed nonlinear Mathieu equation. Nonlinear Dyn 341–352. doi:10.1007/s11071-006-9162-5
2. Rand RH (2012) Lecture notes in nonlinear vibrations. The Internet-First University Press, New York. http://www.ecommons.library.cornell.edu/handle/1813/28989

Chapter 9
Relating Backbone Curves to the Forced Responses of Nonlinear Systems

T.L. Hill, A. Cammarano, S.A. Neild, and D.J. Wagg

Abstract Backbone curves describe the steady-state responses of unforced, undamped systems, therefore they do not directly relate to any specific forcing and damping configuration. Nevertheless, they can be used to understand the underlying dynamics of nonlinear systems subjected to forcing and damping. Building on this concept, in this paper we describe an analytical technique used to predict the onset of internally-resonant modal interactions in an example system. In conjunction with backbone curve analysis, which can be used to predict the possibility of internally-resonant behaviour, this approach provides an analytical tool for understanding and quantifying internally-resonant regions in the forced responses.

Keywords Backbone curves • Second-order normal forms • Modal analysis • Modal interaction • Modal reduction

9.1 Introduction

As many engineering systems becoming increasingly lightweight and flexible, the ability to model the behaviour resulting from nonlinear characteristics is becoming increasingly important. Although there exist many powerful numerical techniques for the modelling of nonlinear dynamical systems, analytical approaches are often more desirable. This is because analytical descriptions can offer greater insight into the mechanisms behind the dynamical behaviour [1], as well as providing efficient tools for procedures such as optimisation [2]. One dynamic phenomenon that is of particular importance in many nonlinear structures is internal resonance. Internal resonance occurs when the response of one underlying linear mode of a system is triggered by the actions of another, and is commonly seen in structures such as cables, beams, membranes and plates [3, 4].

Some of the analytical techniques that are typically employed for the analysis of nonlinear systems include harmonic balancing [5], multiple scales [6], nonlinear normal modes [7, 8] and normal forms [9, 10]. These techniques may be used to describe the responses of unforced, undamped nonlinear systems, referred to here as *backbone curves*. Although these backbone curves can be used to determine the underlying behaviour of the system, they cannot be related to a specific forced response. Furthermore, many analytical approaches cannot be extended to include forcing and damping, whilst with others their inclusion often proves difficult.

In this paper we first show how the backbone curves may be used to determine whether internal resonance may be observed in the system. We then present a method that may be used to predict the onset of internal resonance in forced and damped responses, and describe regions in which internal resonance will be seen.

9.2 Second-Order Normal form Technique

9.2.1 The Example System

In this paper we consider the forced and damped two-mass nonlinear oscillator shown in Fig. 9.1—a system similar to that described in [11]. This system consists of two masses, both of mass m. These masses are connected to ground by two identical cubic nonlinear springs, both with the force-displacement relationship $F = k(\delta x) + \alpha(\delta x)^3$. The masses are also grounded

T.L. Hill (✉) • A. Cammarano • S.A. Neild
Department of Mechanical Engineering, University of Bristol, Queen's Building, University Walk, Bristol BS8 1TR, UK
e-mail: tom.hill@bristol.ac.uk

D.J. Wagg
Department of Mechanical Engineering, University of Sheffield, Sir Frederick Mappin Building, Mappin Street, Sheffield S1 3JD, UK

G. Kerschen (ed.), *Nonlinear Dynamics, Volume 1*, Conference Proceedings of the Society for Experimental Mechanics Series, DOI 10.1007/978-3-319-15221-9_9

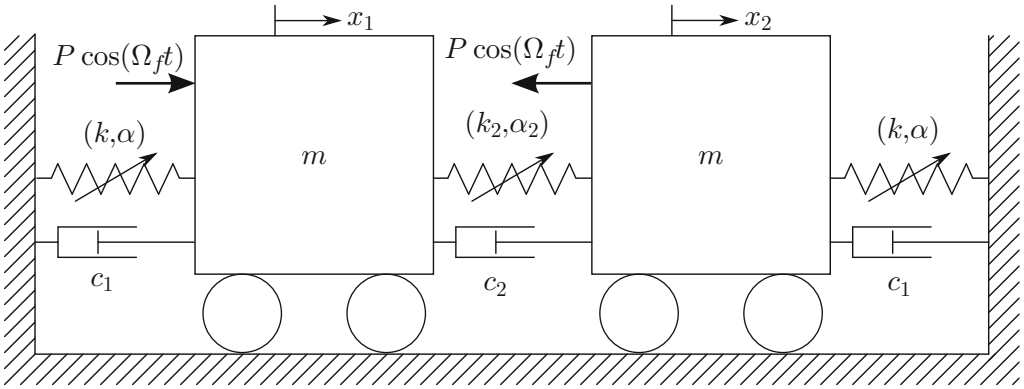

Fig. 9.1 Schematic of a forced and damped, two-degree-of-freedom, symmetric oscillator with cubic nonlinear springs

by two identical linear dampers, both with damping constant c. Another cubic nonlinear spring connects the masses, with the force-displacement relationship $F = k_2(\delta x) + \alpha_2(\delta x)^3$, and a linear damper, with damping constant c_2, connects the masses. The displacement of the masses are denoted x_1 and x_2 and are both forced sinusoidally at amplitude P and frequency Ω_f, as shown in Fig. 9.1. This forcing is in anti-phase, such that the system has a symmetric in structure and applied load.

The equations of motion for this system may be written

$$\mathbf{M}\ddot{\mathbf{x}} + \mathbf{C}\dot{\mathbf{x}} + \mathbf{K}\mathbf{x} + \mathbf{\Gamma}_x(\mathbf{x}) = \mathbf{P}_x \cos(\Omega_f t), \tag{9.1}$$

where $\mathbf{M}$, $\mathbf{C}$ and $\mathbf{K}$ are the mass, damping and linear stiffness matrices respectively, and $\mathbf{\Gamma}_x(\mathbf{x})$ and $\mathbf{P}_x$ are vectors of the nonlinear terms and forcing amplitudes, written

$$\mathbf{\Gamma}_x(\mathbf{x}) = \begin{pmatrix} \alpha x_1^3 + \alpha_2 (x_1 - x_2)^3 \\ \alpha x_2^3 - \alpha_2 (x_1 - x_2)^3 \end{pmatrix}, \qquad \mathbf{P}_x(\mathbf{x}) = \begin{pmatrix} P_{x1} \\ P_{x2} \end{pmatrix} = \begin{pmatrix} P \\ -P \end{pmatrix}. \tag{9.2}$$

9.2.2 Applying the Second-Order Normal form Technique

We now use the second-order normal form technique to transform the equations of motion, Eq. (9.1), into a set of time-invariant equations describing the dynamical behaviour. Before applying this technique, we first combine the damping and nonlinear terms into the vector $\mathbf{N}_x$, allowing us to write Eq. (9.1) as

$$\mathbf{M}\ddot{\mathbf{x}} + \mathbf{K}\mathbf{x} + \mathbf{N}_x(\mathbf{x}, \dot{\mathbf{x}}) = \mathbf{P}_x \cos(\Omega_f t). \tag{9.3}$$

The first step of this technique is the linear modal transform, written $\mathbf{x} = \mathbf{\Phi}\mathbf{q}$, where $\mathbf{\Phi}$ is the modeshape matrix, whose nth column describes the modeshape of the nth linear mode. For the system considered here, the modeshape matrix may be written

$$\mathbf{\Phi} = \begin{bmatrix} 1 & 1 \\ 1 & -1 \end{bmatrix}. \tag{9.4}$$

Thus, applying this transform to Eq. (9.3) leads to the modal equation of motion, written

$$\ddot{\mathbf{q}} + \mathbf{\Lambda}\mathbf{q} + \mathbf{N}_q(\mathbf{q}, \dot{\mathbf{q}}) = \mathbf{P}_q \cos(\Omega_f t), \tag{9.5}$$

where $\mathbf{q}$ is a vector of modal displacements, $\mathbf{N}_q(\mathbf{q}, \dot{\mathbf{q}})$ is a vector of nonlinear and modal damping terms, $\mathbf{P}_q$ is a vector of modal forcing terms and $\mathbf{\Lambda}$ is a diagonal matrix whose nth leading diagonal term is the square of the nth linear natural

Table 9.1 The parameters describing the example system

Parameter	m	ω_{n1}	ω_{n2}	α	α_2	ζ	P
Value	1	1	1.005	0.4	0.05	0.004	0.006

frequency, ω_{nn}^2. For this system, these may be written

$$\mathbf{\Lambda} = \begin{bmatrix} \omega_{n1}^2 & 0 \\ 0 & \omega_{n2}^2 \end{bmatrix} = \frac{1}{m}\begin{bmatrix} k & 0 \\ 0 & k+2k_2 \end{bmatrix}, \qquad \mathbf{P}_q = \begin{pmatrix} P_{q1} \\ P_{q2} \end{pmatrix} = \frac{1}{2m}\begin{pmatrix} P_{x1}+P_{x2} \\ P_{x1}-P_{x2} \end{pmatrix} = \frac{1}{m}\begin{pmatrix} 0 \\ P \end{pmatrix},$$
$$\mathbf{N}_q = \begin{pmatrix} 2\zeta_1\omega_{n1}\dot{q}_1 \\ 2\zeta_2\omega_{n2}\dot{q}_2 \end{pmatrix} + \frac{\alpha}{m}\begin{pmatrix} q_1^3+3q_1q_2^2 \\ \gamma q_2^3+3q_1^2q_2 \end{pmatrix}, \quad \text{where:} \quad \begin{pmatrix} 2\zeta_1\omega_{n1} \\ 2\zeta_2\omega_{n2} \end{pmatrix} = \frac{1}{m}\begin{pmatrix} c \\ c+2c_2 \end{pmatrix}, \tag{9.6}$$

where P_{qn} and ζ_n are the linear modal forcing amplitude and modal damping constant of the nth linear mode respectively, and $\gamma = 1 + (8\alpha_2/\alpha)$. Here we assume that the damping constants are equal for both modes, i.e. $\zeta_1 = \zeta_2 = \zeta$, which, from Eq. (9.6), is true when $\frac{c_2}{c} = \frac{1}{2}\left(\frac{\omega_{n2}}{\omega_{n1}} - 1\right)$.

The system that is considered here may be described by the parameters in Table 9.1 and we consider the cases where the forcing frequency is in the close vicinity of the linear natural frequencies.

The next step of the second-order normal form technique is the forcing transform, applied to Eq. (9.5) to give

$$\ddot{\mathbf{v}} + \mathbf{\Lambda}\mathbf{v} + \mathbf{N}_v(\mathbf{v}, \dot{\mathbf{v}}) = \mathbf{P}_v \cos(\Omega_f t). \tag{9.7}$$

The purpose of this transform is to remove any modal forcing whose frequency is not in the vicinity of the linear natural frequency of the mode on which it is acting. As we are considering forcing frequencies in the vicinity of the linear natural frequencies (which are close—see Table 9.1), this transform is unity, and we may write

$$\mathbf{q} = \mathbf{v}\,, \qquad \mathbf{N}_q(\mathbf{q}, \dot{\mathbf{q}}) = \mathbf{N}_v(\mathbf{v}, \dot{\mathbf{v}})\,, \qquad \mathbf{P}_q = \mathbf{P}_v\,. \tag{9.8}$$

The final step of the technique is the nonlinear near-identity transform, written $\mathbf{v} = \mathbf{u} + \varepsilon\mathbf{h}$, where $\mathbf{u}$ and $\mathbf{h}$ are the fundamental and harmonic components of $\mathbf{v}$ respectively. The bookkeeping parameter ε is used to denote that $\mathbf{h}$ is small in comparison with $\mathbf{u}$. Assuming that the fundamental component of the nth linear mode is sinusoidal, we may write

$$u_n = u_{np} + u_{nm} = \frac{U_n}{2}\left(\mathrm{e}^{+\mathrm{j}(\omega_{rn}t - \phi_n)} + \mathrm{e}^{-\mathrm{j}(\omega_{rn}t - \phi_n)}\right), \tag{9.9}$$

where U_n, ω_{rn} and ϕ_n are the amplitude, response frequency and phase (with respect to the forcing) of the fundamental component of v_n respectively. The subscripts p and m denote the positive and negative (plus and minus) signs of the exponents respectively. As, in the example considered here, the linear natural frequencies are close, we may assume that the response frequencies are equal, i.e. $\omega_{r1} = \omega_{r2} = \Omega$ where Ω is the *common response frequency*.

Along with the harmonics, $\mathbf{h}$. it is also assumed that the nonlinear terms are small, i.e. $\mathbf{N}_v(\mathbf{v}, \dot{\mathbf{v}}) = \varepsilon\mathbf{N}_v(\mathbf{v}, \dot{\mathbf{v}})$. Thus, making the substitution $\mathbf{v} = \mathbf{u} + \varepsilon\mathbf{h}$ into $\varepsilon\mathbf{N}_v(\mathbf{v}, \dot{\mathbf{v}})$ allows us to make the order ε^1 approximation $\varepsilon\mathbf{N}_v(\mathbf{u} + \varepsilon\mathbf{h}, \dot{\mathbf{u}} + \varepsilon\dot{\mathbf{h}}) \approx \varepsilon\mathbf{N}_v(\mathbf{u}, \dot{\mathbf{u}})$. From Eqs. (9.6)–(9.9) this approximation allows us to write

$$\mathbf{N}_v(\mathbf{u}, \dot{\mathbf{u}}) = 2\mathrm{j}\zeta\Omega\begin{pmatrix} \omega_{n1}\left(u_{1p} - u_{1m}\right) \\ \omega_{n2}\left(u_{2p} - u_{2m}\right) \end{pmatrix} + \frac{\alpha}{m}\begin{pmatrix} \left(u_{1p}+u_{1m}\right)^3 + 3\left(u_{1p}+u_{1m}\right)\left(u_{2p}+u_{2m}\right)^2 \\ 3\left(u_{1p}+u_{1m}\right)^2\left(u_{2p}+u_{2m}\right) + \gamma\left(u_{2p}+u_{2m}\right)^3 \end{pmatrix}. \tag{9.10}$$

The nonlinear near-identity transform results in the resonant equation of motion, written

$$\ddot{\mathbf{u}} + \mathbf{\Lambda}\mathbf{u} + \mathbf{N}_u(\mathbf{u}, \dot{\mathbf{u}}) = \mathbf{P}_u \cos(\Omega_f t), \tag{9.11}$$

where $\mathbf{N}_u(\mathbf{u}, \dot{\mathbf{u}})$ is a vector of resonant nonlinear and damping terms and $\mathbf{P}_u = \mathbf{P}_v$. The nth element of the vector $\mathbf{N}_u(\mathbf{u}, \dot{\mathbf{u}})$ is populated with the terms from the nth element of $\mathbf{N}_v(\mathbf{u}, \dot{\mathbf{u}})$ that are resonant with the nth mode. As, in the example considered here, both modes resonate at the common response frequency, Ω, $\mathbf{N}_u$ is populated with terms that resonate at Ω. The response

frequency of the terms in $\mathbf{N}_v$ is determined by defining the vector $\mathbf{u}^*$ which contains all unique combinations of u_{np} and u_{nm} that appear in $\mathbf{N}_v(\mathbf{u}, \dot{\mathbf{u}})$. As, from Eq. (9.10), $\mathbf{N}_v(\mathbf{u}, \dot{\mathbf{u}})$ contains 24 unique terms, $\mathbf{u}^*$ is a $\{24 \times 1\}$ vector. We also define the $\{2 \times 24\}$ coefficient matrices $[n_v]$ and $[n_u]$, that allow us to write

$$\mathbf{N}_v = [n_v]\mathbf{u}^* \qquad \text{and} \qquad \mathbf{N}_u = [n_u]\mathbf{u}^* \,. \tag{9.12}$$

The ℓth element of $\mathbf{u}^*$ may be written

$$u^*_\ell = \prod_{k=1}^{2} u_{kp}^{s_{\ell kp}} u_{kp}^{s_{\ell km}} \,, \tag{9.13}$$

where $s_{\ell kp}$ and $s_{\ell km}$ are the exponents of the u_{kp} and u_{km} in u^*_ℓ respectively. Using these, we may calculate the $\{2 \times 24\}$ matrix $\boldsymbol{\beta}$, whose $\{n,\ \ell\}$th element may be calculated using

$$\beta_{n\ell} = \left(\left[\sum_{k=1}^{2} \left\{ s_{\ell kp} - s_{\ell km} \right\} \omega_{rk} \right]^2 - \omega_{rn}^2 \right) = \left(\left[\sum_{k=1}^{2} \left\{ s_{\ell kp} - s_{\ell km} \right\} \right]^2 - 1 \right) \Omega^2 \,. \tag{9.14}$$

The elements in $\boldsymbol{\beta}$ with a value of zero correspond to elements in $[n_v]$ that describe the coefficients of resonant terms. Thus, in order to populate $\mathbf{N}_u$ with resonant terms, we use

$$n_{u,n\ell} = \begin{cases} n_{v,n\ell} & \text{if} \quad \beta_{n\ell} = 0 \,, \\ 0 & \text{if} \quad \beta_{n\ell} \neq 0 \,. \end{cases} \tag{9.15}$$

The non-zero elements in $\boldsymbol{\beta}$ correspond to coefficients that are used to describe the harmonics. As we are assuming the harmonics to be negligible here, this step is neglected, however for details of this see [12].

Using Eqs. (9.10), (9.13), (9.14) and (9.15), we may calculate $[n_v]$, $\mathbf{u}^*$ and $\boldsymbol{\beta}$ as

$$[n_v]^T = \frac{\alpha}{m} \begin{bmatrix} \kappa_1 & 0 \\ -\kappa_1 & 0 \\ 1 & 0 \\ 3 & 0 \\ 3 & 0 \\ 1 & 0 \\ 3 & 0 \\ 6 & 0 \\ 3 & 0 \\ 3 & 0 \\ 6 & 0 \\ 3 & 0 \\ 0 & \kappa_2 \\ 0 & -\kappa_2 \\ 0 & 3 \\ 0 & 3 \\ 0 & 6 \\ 0 & 6 \\ 0 & 3 \\ 0 & 3 \\ 0 & \gamma \\ 0 & 3\gamma \\ 0 & 3\gamma \\ 0 & \gamma \end{bmatrix}, \quad \mathbf{u}^* = \begin{bmatrix} u_{1p} \\ u_{1m} \\ u_{1p}^3 \\ u_{1p}^2 u_{1m} \\ u_{1p} u_{1m}^2 \\ u_{1m}^3 \\ u_{1p} u_{2p}^2 \\ u_{1p} u_{2p} u_{2m} \\ u_{1p} u_{2m}^2 \\ u_{1m} u_{2p}^2 \\ u_{1m} u_{2p} u_{2m} \\ u_{1m} u_{2m}^2 \\ u_{2p} \\ u_{2m} \\ u_{1p}^2 u_{2p} \\ u_{1p}^2 u_{2m} \\ u_{1p} u_{1m} u_{2p} \\ u_{1p} u_{1m} u_{2m} \\ u_{1m}^2 u_{2p} \\ u_{1m}^2 u_{2m} \\ u_{2p}^3 \\ u_{2p}^2 u_{2m} \\ u_{2p} u_{2m}^2 \\ u_{2m}^3 \end{bmatrix}, \quad \boldsymbol{\beta}^T = \Omega^2 \begin{bmatrix} 0 - \\ 0 - \\ 8 - \\ 0 - \\ 0 - \\ 8 - \\ 8 - \\ 0 - \\ 0 - \\ 0 - \\ 0 - \\ 8 - \\ -0 \\ -0 \\ -8 \\ -0 \\ -0 \\ -0 \\ -0 \\ -8 \\ -8 \\ -0 \\ -0 \\ -8 \end{bmatrix}, \tag{9.16}$$

where $\kappa_1 = \mathrm{j}2\zeta\Omega\omega_{n1}(m/\alpha)$ and $\kappa_2 = \mathrm{j}2\zeta\Omega\omega_{n2}(m/\alpha)$. The elements in $\boldsymbol{\beta}$ that contain a dash $(-)$ correspond to elements in $[n_v]$ that contain a zero, thus are of no importance.

We may now identify the coefficients of resonant terms in $[n_v]$ as those elements that correspond to a zero in $\boldsymbol{\beta}$. Once we have used Eq. (9.16) to populate $[n_u]$ we can use Eq. (9.12) to find N_u as

$$\mathbf{N}_u = 2\zeta \begin{pmatrix} \omega_{n1}\dot{u}_1 \\ \omega_{n2}\dot{u}_2 \end{pmatrix} + \frac{3\alpha}{m} \begin{pmatrix} u_{1p}u_{1m}u_1 + 2u_{2p}u_{2m}u_1 + u_{1p}u_{2m}^2 + u_{1m}u_{2p}^2 \\ \gamma u_{2p}u_{2m}u_2 + 2u_{1p}u_{1m}u_2 + u_{1p}^2u_{2m} + u_{1m}^2u_{2p} \end{pmatrix}. \tag{9.17}$$

We may the substitute Eq. (9.17) into Eq. (9.11) to find the resonant equation of motion, in which all terms resonate at the common response frequency, Ω.

9.2.3 Finding the Backbone Curves of the Example System

Backbone curves describe the unforced, undamped responses of a system. Therefore, the backbone curves of the example system may be found using the resonant equation of motion, Eq. (9.11), when the forcing and damping is set to zero, i.e. $\zeta = 0$ and $\mathbf{P}_u^T = [0,\ 0]$. From Eqs. (9.11) and (9.17) this leads to

$$\boldsymbol{\Lambda}\mathbf{u} - \Omega^2\mathbf{u} + \frac{3\alpha}{m} \begin{pmatrix} u_{1p}u_{1m}u_1 + 2u_{2p}u_{2m}u_1 + u_{1p}u_{2m}^2 + u_{1m}u_{2p}^2 \\ \gamma u_{2p}u_{2m}u_2 + 2u_{1p}u_{1m}u_2 + u_{1p}^2u_{2m} + u_{1m}^2u_{2p} \end{pmatrix} = 0\,. \tag{9.18}$$

It can be seen, from Eq. (9.9), that Eq. (9.18) may be written

$$\boldsymbol{\Upsilon}^+\mathrm{e}^{+\mathrm{j}\Omega t} + \boldsymbol{\Upsilon}^-\mathrm{e}^{-\mathrm{j}\Omega t} = 0\,, \tag{9.19}$$

where $\boldsymbol{\Upsilon}^+$ and $\boldsymbol{\Upsilon}^-$ are complex conjugates. Therefore, it is determined that $\boldsymbol{\Upsilon}^+ = 0$, which may be written

$$\boldsymbol{\Upsilon}^+ = \frac{1}{2} \begin{pmatrix} \left[\omega_{n1}^2 - \Omega^2 + \frac{3\alpha}{4m}\left\{ U_1^2 + U_2^2\left(2 + \mathrm{e}^{+\mathrm{j}2(\phi_1-\phi_2)}\right)\right\}\right] U_1\mathrm{e}^{-\mathrm{j}\phi_1} \\ \left[\omega_{n2}^2 - \Omega^2 + \frac{3\alpha}{4m}\left\{\gamma U_2^2 + U_1^2\left(2 + \mathrm{e}^{-\mathrm{j}2(\phi_1-\phi_2)}\right)\right\}\right] U_2\mathrm{e}^{-\mathrm{j}\phi_2} \end{pmatrix} = 0\,, \tag{9.20}$$

which may be simplified to

$$\left[\omega_{n1}^2 - \Omega^2 + \frac{3\alpha}{4m}\left\{ U_1^2 + U_2^2\left(2 + \mathrm{e}^{+\mathrm{j}2(\phi_1-\phi_2)}\right)\right\}\right] U_1 = 0\,, \tag{9.21a}$$

$$\left[\omega_{n2}^2 - \Omega^2 + \frac{3\alpha}{4m}\left\{\gamma U_2^2 + U_1^2\left(2 + \mathrm{e}^{-\mathrm{j}2(\phi_1-\phi_2)}\right)\right\}\right] U_2 = 0\,. \tag{9.21b}$$

The imaginary parts of Eqs. (9.21) both lead to $\sin(2|\phi_1 - \phi_2|) = 0$. Therefore we may determine that

$$\mathrm{e}^{\mathrm{j}2|\phi_1-\phi_2|} = \cos(2|\phi_1 - \phi_2|) = \pm 1 = p. \tag{9.22}$$

Therefore, if $p = +1$, the fundamental components of the two linear modes are in-phase or in anti-phase, and if $p = -1$ the fundamental components are $\pm 90°$ out-of-phase. In [1] it is shown that $p = -1$ is not a valid solution for the parameters used here, hence substituting $p = +1$ into Eqs. (9.21) leads to

$$\left[\omega_{n1}^2 - \Omega^2 + \frac{3\alpha}{4m}\left\{U_1^2 + 3U_2^2\right\}\right] U_1 = 0\,, \tag{9.23a}$$

$$\left[\omega_{n2}^2 - \Omega^2 + \frac{3\alpha}{4m}\left\{\gamma U_2^2 + 3U_1^2\right\}\right] U_2 = 0\,. \tag{9.23b}$$

Aside from the trivial solution in which $U_1 = U_2 = 0$, corresponding to no motion, there exists two solutions in which $U_2 = 0$ and $U_1 = 0$ independently. These single-mode solutions are denoted *S1* and *S2* and are described by

$$S1: \quad U_2 = 0\,, \quad \Omega^2 = \omega_{n1}^2 + \frac{3\alpha}{4m} U_1^2\,, \tag{9.24}$$

$$S2: \quad U_1 = 0\,, \quad \Omega^2 = \omega_{n2}^2 + \frac{3\alpha\gamma}{4m} U_2^2\,. \tag{9.25}$$

There also exists two solutions in which U_1 and U_2 are non-zero simultaneously. These solutions, denoted $S3^+$ and $S3^-$ (or $S3^\pm$ when referring to both), have identical frequency-amplitude relationships given by

$$S3^\pm: \qquad U_1^2 = \left(1 - 4\frac{\alpha_2}{\alpha}\right) U_2^2 - \frac{2m}{3\alpha}\left(\omega_{n2}^2 - \omega_{n1}^2\right), \tag{9.26a}$$

$$\Omega^2 = \frac{3\omega_{n1}^2 - \omega_{n2}^2}{2} + \frac{3(\alpha - \alpha_2)}{m} U_2^2\,. \tag{9.26b}$$

However, from Eq. (9.22), the backbone curves $S3^+$ and $S3^-$ correspond to solutions in which u_1 and u_2 are in-phase and in anti-phase respectively. This may be written as

$$S3^+: \quad |\phi_1 - \phi_2| = 0\,, \qquad S3^-: \quad |\phi_1 - \phi_2| = \pi\,. \tag{9.27}$$

Figure 9.2 shows the backbone curves along with the forced response of this system. The backbone curves are represented by light-blue and dashed-red lines for the stable and unstable sections respectively (where the stability has been calculated

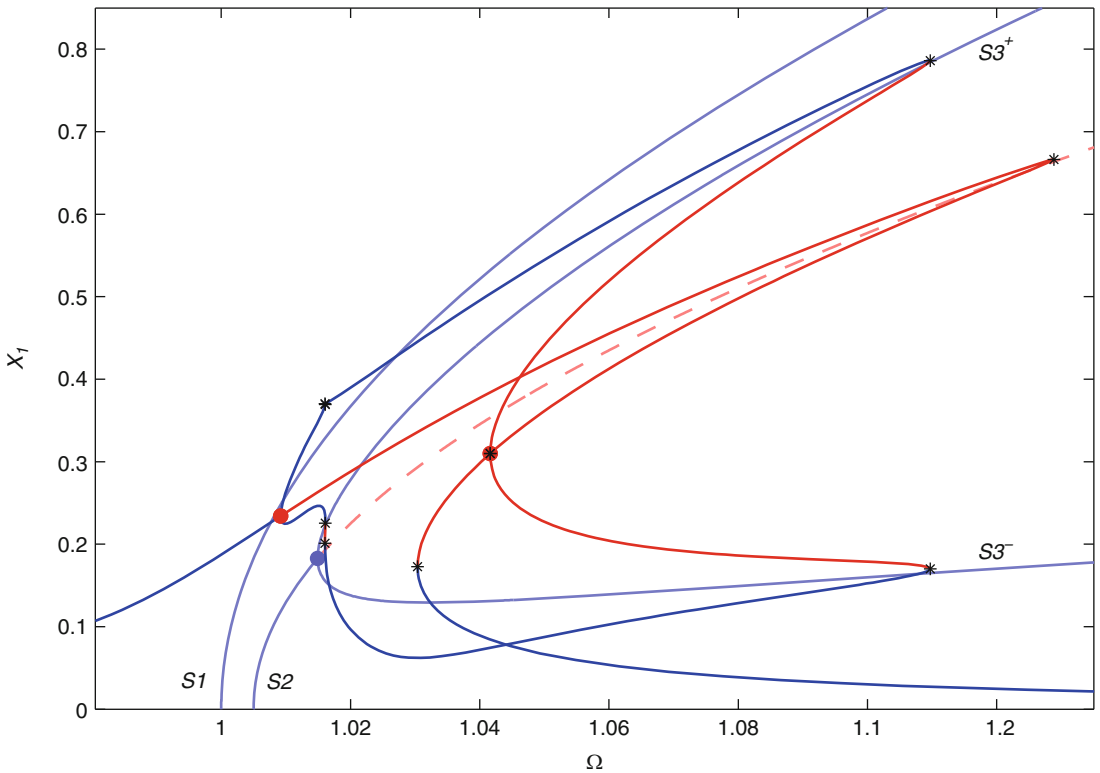

Fig. 9.2 The backbone curves and forced responses for the example system. This is shown in the projection of the forcing frequency, Ω, against the amplitude of displacement of the first mass, X_1. *Solid-blue* and *solid-red lines* show stable and unstable forced responses respectively. *Light-blue* and *dashed-red lines* show the stable and unstable backbone curves respectively. *Large-red dots* show the bifurcations from the second-mode-only forced response onto the mixed-mode forced response and *black asterisks* represent fold bifurcations. A *light-blue dot* shows the pitchfork bifurcation from the backbone curve *S2*, onto $S3^\pm$ (Color figure online)

using the method described in [13]). A light-blue dot shows a bifurcation on *S2*, leading to the branches $S3^{\pm}$ and an unstable section of *S2*. As *S2* is composed only of u_2, see Eq. (9.25), and $S3^{\pm}$ are composed of both u_1 and u_2, this bifurcation is representative of the onset of an internal resonance between the first and second linear modes. Further discussion of this bifurcation is given in [11]. The stable and unstable forced responses are shown by solid-blue and solid-red lines respectively. Additionally, black asterisks represent fold bifurcations and large-red dots show the bifurcations from the second-mode-only forced response branch onto the mixed-mode branch. These forced responses have been calculated using the numerical continuation software AUTO-07p [14], which also provides the stability of the branches and the bifurcations.

Figure 9.2 clearly demonstrates the relationship between the backbone curves and the forced responses of this system. It can be seen that the second-mode-only Duffing-like forced branch envelops *S2* (a second-mode-only backbone curve). Additionally, the bifurcation on *S2* that leads to the mixed-mode backbone curves $S3^{\pm}$ is similar to the bifurcations on the second-mode-only forced branch that leads to mixed-mode forced branches, and these mixed-mode branches also tend-towards $S3^{\pm}$. This relationship shows that the backbone curves may be used to determine whether internal resonance may be seen in a particular structure. However, backbone curves alone cannot be used to determine whether internal resonance will be triggered for a given forcing and damping, or where the onset of internal resonance will be seen. The following section describes an analytical approach that may be used to describe the onset of internal resonance.

9.3 Internal Resonance

Internal resonance occurs when a non-directly forced (NDF) linear mode exhibits a response. In Eq. (9.6) it can be seen that the forcing is only applied to the second linear mode (i.e. the first mode is NDF). Through backbone curve analysis we can determine whether multiple-mode solutions exist, such as $S3^{\pm}$ in the example system. Understanding the onset of internal resonance helps to provide insight into the mechanisms behind the forced responses of a system and may be used, for example, to aid the process of modal reduction as we are able to define if and when particular interactions become significant.

9.3.1 Internal Resonance in the Example System

Internal resonance may be defined as an instability of the zero-amplitude solution of an NDF mode. To determine the stability of a zero-solution, a similar approach to that taken in [13] may be used. First, we allow the amplitude and phase of the NDF mode to vary slowly with time. For the system considered here this is denoted $U_1 = U_1(\varepsilon t)$ and $\phi_1 = \phi_1(\varepsilon t)$, such that we may write

$$u_1 = u_{1p} + u_{1m} = U_{1p}(\varepsilon t)\mathrm{e}^{+\mathrm{j}\Omega t} + U_{1m}(\varepsilon t)\mathrm{e}^{-\mathrm{j}\Omega t}\,, \tag{9.28}$$

where the complex conjugates $U_{1p}(\varepsilon t)$ and $U_{1m}(\varepsilon t)$ may be written

$$U_{1p}(\varepsilon t) = \frac{1}{2}U_1(\varepsilon t)\mathrm{e}^{-\mathrm{j}\phi_1(\varepsilon t)}\,, \qquad U_{1m}(\varepsilon t) = \frac{1}{2}U_1(\varepsilon t)\mathrm{e}^{+\mathrm{j}\phi_1(\varepsilon t)}\,. \tag{9.29}$$

Using Eq. (9.28) we write the first and second time derivatives of u_1 as

$$\dot{u}_1 = \mathrm{j}\Omega\left(U_{1p}\mathrm{e}^{+\mathrm{j}\Omega t} - U_{1m}\mathrm{e}^{-\mathrm{j}\Omega t}\right) + \mathcal{O}(\varepsilon^1)\,, \tag{9.30a}$$

$$\ddot{u}_1 = \mathrm{j}\varepsilon 2\Omega\left(U'_{1p}\mathrm{e}^{+\mathrm{j}\Omega t} - U'_{1m}\mathrm{e}^{-\mathrm{j}\Omega t}\right) - \Omega^2 u_1 + \mathcal{O}(\varepsilon^2)\,, \tag{9.30b}$$

where $\bullet' = \frac{\mathrm{d}\bullet}{\mathrm{d}(\varepsilon t)}$ and Eqs. (9.30a) and (9.30b) are truncated at order ε^0 and ε^1 respectively. As $\dot{u}_1$ components only appear in terms of order ε^1 (as damping is assumed to be small), substituting Eqs. (9.30) into the equation of motion will result in an overall order of accuracy of ε^1.

Next, we substitute Eq. (9.30) into the resonant equation of motion for the first mode, Eq. (9.11), which may be written

$$\ddot{u}_1 + \omega_{n1}^2 u_1 + N_{u,1} = 0\,, \tag{9.31}$$

where $N_{u,1}$ is the first element of $\mathbf{N}_u$. Since we are interested in the onset of instability of the zero-amplitude solution we can consider u_1 to be small. Hence we may eliminate terms that are composed of the product of more than one component of u_{1p} and u_{1m}. From this, and using Eq. (9.17), we may write Eq. (9.31) as

$$\ddot{u}_1 + \omega_{n1}^2 u_1 + 2\zeta\omega_{n1}\dot{u}_1 + \frac{3\alpha}{m}\left(2u_{2p}u_{2m}u_1 + u_{1p}u_{2m}^2 + u_{1m}u_{2p}^2\right) = 0\,, \tag{9.32}$$

which, using Eqs. (9.28) and (9.30), may be written

$$\begin{aligned}&\left[\mathrm{j}2\Omega\left(U_{1p}' + \zeta\omega_{n1}U_{1p}\right) + \left(\omega_{n1}^2 - \Omega^2\right)U_{1p} + \frac{3\alpha}{m}\left(2U_{2p}U_{2m}U_{1p} + U_{2p}^2U_{1m}\right)\right]\mathrm{e}^{+\mathrm{j}\Omega t}\\ &-\left[\mathrm{j}2\Omega\left(U_{1m}' + \zeta\omega_{n1}U_{1m}\right) - \left(\omega_{n1}^2 - \Omega^2\right)U_{1m} - \frac{3\alpha}{m}\left(2U_{2p}U_{2m}U_{1m} + U_{2m}^2U_{1p}\right)\right]\mathrm{e}^{-\mathrm{j}\Omega t} = 0\,.\end{aligned} \tag{9.33}$$

It can be seen that Eq. (9.33) may be written in the form of Eq. (9.19). Therefore, the contents for the square brackets in Eq. (9.33) may each be equated to zero, and written as

$$U_{1p}' = \frac{\mathrm{j}}{2\Omega}\left[\left(\omega_{n1}^2 - \Omega^2\right)U_{1p} + \frac{3\alpha}{m}\left(2U_{2p}U_{2m}U_{1p} + U_{2p}^2U_{1m}\right)\right] - \zeta\omega_{n1}U_{1p}\,, \tag{9.34a}$$

$$U_{1m}' = \frac{-\mathrm{j}}{2\Omega}\left[\left(\omega_{n1}^2 - \Omega^2\right)U_{1m} + \frac{3\alpha}{m}\left(2U_{2p}U_{2m}U_{1m} + U_{2m}^2U_{1p}\right)\right] - \zeta\omega_{n1}U_{1m}\,. \tag{9.34b}$$

We now let $\mathbf{U}_1' = \mathbf{f}(\mathbf{U}_1)$, where $\mathbf{U}_1 = [U_{1p}\,,\, U_{1m}]^T$ such that

$$\mathbf{f}(\mathbf{U}_1) = \frac{\mathrm{j}}{2\Omega}\begin{pmatrix}\mathrm{j}2\Omega\zeta\omega_{n1}U_{1p} + \left(\omega_{n1}^2 - \Omega^2\right)U_{1p} + \dfrac{3\alpha}{m}\left(2U_{2p}U_{2m}U_{1p} + U_{2p}^2U_{1m}\right)\\ \mathrm{j}2\Omega\zeta\omega_{n1}U_{1m} - \left(\omega_{n1}^2 - \Omega^2\right)U_{1m} - \dfrac{3\alpha}{m}\left(2U_{2p}U_{2m}U_{1m} + U_{2m}^2U_{1p}\right)\end{pmatrix}. \tag{9.35}$$

We then use $\bar{\mathbf{U}}_1$ to denote $\mathbf{U}_1$ at equilibrium, and $\varepsilon\hat{\mathbf{U}}_1$ to denote a small perturbation. Hence, applying a small perturbation from the equilibrium to $\mathbf{U}_1$, we may write

$$\mathbf{U}_1' = \bar{\mathbf{U}}_1' + \varepsilon\hat{\mathbf{U}}_1' = \mathbf{f}\left(\bar{\mathbf{U}}_1 + \varepsilon\hat{\mathbf{U}}_1\right) = \mathbf{f}\left(\bar{\mathbf{U}}_1\right) + \varepsilon\mathbf{f}_{\mathbf{U}_1}\left(\bar{\mathbf{U}}_1\right)\hat{\mathbf{U}}_1 + \mathcal{O}\left\{\varepsilon^2\right\}\,, \tag{9.36}$$

where we have used a Taylor expansion and $\mathbf{f}_{\mathbf{U}_1}$ is the derivative of $\mathbf{f}$ with respect to $\mathbf{U}_1$. Using $\bar{\mathbf{U}}_1' = \mathbf{f}\left(\bar{\mathbf{U}}_1\right)$, we may use Eq. (9.36) to make the order ε^1 approximation

$$\hat{\mathbf{U}}_1' \approx \mathbf{f}_{\mathbf{U}_1}\left(\bar{\mathbf{U}}_1\right)\hat{\mathbf{U}}_1\,. \tag{9.37}$$

From Eq. (9.37) it can be seen that if the real parts of the eigenvalues of $\mathbf{f}_{\mathbf{U}_1}$ are positive, the solution is unstable. The eigenvalues may be calculated by finding $\mathbf{f}_{\mathbf{U}_1}$ from Eq. (9.35) as

$$\mathbf{f}_{\mathbf{U}_1} = \frac{\mathrm{j}}{2m\Omega}\begin{bmatrix}\mathrm{j}2m\Omega\zeta\omega_{n1} + \left(\omega_{n1}^2 - \Omega^2\right)m + 6\alpha U_{2p}U_{2m} & 3\alpha U_{2p}^2\\ -3\alpha U_{2m}^2 & \mathrm{j}2m\Omega\zeta\omega_{n1} - \left(\omega_{n1}^2 - \Omega^2\right)m - 6\alpha U_{2p}U_{2m}\end{bmatrix}. \tag{9.38}$$

We may now use Eq. (9.38) to calculate the eigenvalues $\lambda_{1,2}$ as

$$\lambda_{1,2} = -\zeta\omega_{n1} \pm \frac{\sqrt{\left[3\alpha U_2^2\right]^2 - \left[4m\left(\omega_{n1}^2 - \Omega^2\right) + 6\alpha U_2^2\right]^2}}{8m\Omega}\,. \tag{9.39}$$

As instability, i.e. internal resonance, will occur when $\Re\{\lambda\} > 0$, we are interested in the region defined by

$$\Re\left\{\sqrt{\left[3\alpha U_2^2\right]^2 - \left[4m\left(\omega_{n1}^2 - \Omega^2\right) + 6\alpha U_2^2\right]^2}\right\} > 8m\Omega\zeta\omega_{n1}\,. \tag{9.40}$$

When $\Omega^2 > \omega_{n1}^2 + \frac{3\alpha}{4m}U_2^2$ then the left-hand-side of Eq. (9.40) is non-zero and we may write

$$\left(\frac{3\alpha}{4m}U_2^2\right)^2 > (2\Omega\zeta\omega_{n1})^2 + \left(\omega_{n1}^2 - \Omega^2 + \frac{6\alpha}{4m}U_2^2\right)^2\,. \tag{9.41}$$

This defines the region where a zero-amplitude response in the first mode is unstable. Hence a mixed-mode response, containing both u_1 and u_2 must emerge from the boundary of this region.

Figure 9.3 shows the internally-resonant regions for the example system. The light-red shaded area represents the internally-resonant region, as predicted using Eq. (9.41). It can be seen that all second-mode-only forced responses within this region are unstable (represented by a solid-red line) and the points at which these responses intersect the boundary of the region coincide with bifurcations onto mixed-mode responses. This is representative of the triggering of an internally resonant response, i.e. the first mode is an NDF mode exhibiting a response due to internal interactions with the second, directly forced, mode.

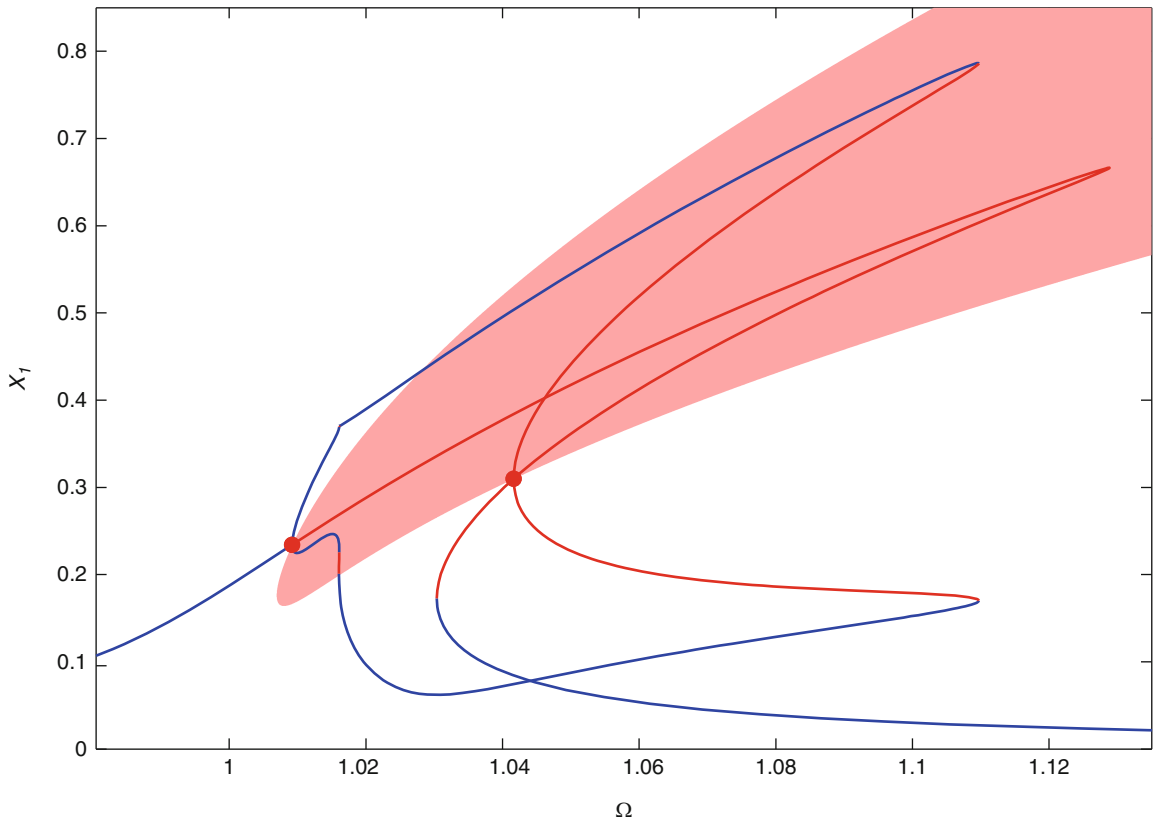

Fig. 9.3 The forced responses and internally-resonant region for the example system. This is shown in the projection of the forcing frequency, Ω, against the amplitude of displacement of the first mass, X_1. *Solid-blue* and *solid-red lines* show stable and unstable forced responses respectively. *Large-red dots* show the bifurcations from the second-mode-only forced response onto the mixed-mode forced response. The *light-red shaded area* represents the region in which a second-mode-only response is unstable, and an internal resonance is triggered (Color figure online)

9.4 Conclusions

In this paper we have shown how the backbone curves of a system can be used to determine whether internal resonance may be observed. We have also introduced a method for finding the regions in which internally resonant behaviour may be triggered. This method is derived using the second-order normal from technique, which may also be used to find the backbone curves of the system. As the internally-resonant regions are calculated independently of forcing, they may be used to understand the mechanisms behind the internal resonance for any forcing conditions (assuming the forcing meets the requirements for internal resonance).

This technique may be used to better understand the internally-resonant behaviour of structures such as cables, beams, plates and shells. As the backbone curves and internally-resonant regions may be described analytically, this approach provides and efficient tool for design and optimisation. The main limitation of the use of the internally-resonant region is that it cannot be used to determine the behaviour of the system in regions where internal resonance has been triggered. For example, a small region at low amplitude may lead to a very large amplitude internally-resonant response. However, the backbone curves may be used to provide some insight into the structure of the internally-resonant response.

References

1. Hill TL, Cammarano A, Neild SA, Wagg DJ (2015) Out-of-unison resonance in weakly nonlinear coupled oscillators. Proc R Soc A, p 471
2. Cammarano A, Neild SA, Burrow SG, Wagg DJ, Inman DJ (2014) Optimum resistive loads for vibration-based electromagnetic energy harvesters with a stiffening nonlinearity. J Intell Mater Syst Struct 25:1757–1770
3. Lewandowski R (1996) On beams membranes and plates vibration backbone curves in cases of internal resonance. Meccanica 31:323–346
4. Marsico MR, Tzanov V, Wagg DJ, Neild SA, Krauskopf B (2011) Bifurcation analysis of a parametrically excited inclined cable close to two-to-one internal resonance. J Sound Vib 330:6023–6035
5. Tondl A, Ruijgrok T, Verhulst F, Nabergoj R (2000) Autoparametric resonance in mechanical systems. Cambridge University Press, Cambridge
6. Glendinning P (1994) Stability, instability and chaos: an introduction to the theory of nonlinear differential equations. Cambridge texts in applied mathematics. Cambridge University Press, Cambridge
7. Kerschen G, Peeters M, Golinval JC, Vakakis AF (2009) Nonlinear normal modes, Part I: a useful framework for the structural dynamicist. Mech Syst Signal Process 23:170–194
8. Peeters M, Viguié R, Sérandour G, Kerschen G, Golinval JC (2009) Nonlinear normal modes, Part II: toward a practical computation using numerical continuation techniques. Mech Syst Signal Process 23:195–216
9. Murdock J (2002) Normal forms and unfoldings for local dynamical systems. Springer, New York
10. Neild SA (2012) Approximate methods for analysing nonlinear structures. In: Wagg DJ, Virgin L (eds) Exploiting nonlinear behavior in structural dynamics. CISM courses and lectures, vol 536. Springer, Vienna, pp 53–109
11. Cammarano A, Hill TL, Neild SA, Wagg DJ (2014) Bifurcations of backbone curves for systems of coupled nonlinear two mass oscillator. Nonlinear Dyn 77:311–320
12. Neild SA, Wagg DJ (2011) Applying the method of normal forms to second-order nonlinear vibration problems. Proc R Soc A 467:1141–1163
13. Xin ZF, Neild SA, Wagg DJ, Zuo ZX (2013) Resonant response functions for nonlinear oscillators with polynomial type nonlinearities. J Sound Vib 332:1777–1788
14. Doedel EJ, with major contributions from Champneys AR, Fairgrieve TF, Kuznetsov YuA, Dercole F, Oldeman BE, Paffenroth RC, Sandstede B, Wang XJ, Zhang C (2008) AUTO-07P: continuation and bifurcation software for ordinary differential equations. Concordia University, Montreal. http://cmvl.cs.concordia.ca

Chapter 10
Nonlinear Modal Interaction Analysis for a Three Degree-of-Freedom System with Cubic Nonlinearities

X. Liu, A. Cammarano, D.J. Wagg, S.A. Neild, and R.J. Barthorpe

Abstract The majority of work in the literature on modal interaction is based on two degree-of-freedom nonlinear systems with cubic nonlinearities. In this paper we consider a three degree-of-freedom system with nonlinear springs containing cubic nonlinear terms. First the undamped, unforced case is considered. Specifically the modal interaction case that occurs when all the underlying linear modal frequencies are close is considered (i.e. $\omega_{n1} : \omega_{n2} : \omega_{n3} \simeq 1 : 1 : 1$). In the case considered, due to the symmetry of the system, the first mode is linear and not coupled with the other two modes. The analysis is carried out by using a normal form transformation to obtain the nonlinear backbone curves of the undamped, unforced response. In addition, the frequency response function (FRF) of the corresponding lightly damped and harmonically forced system obtained from the continuation software AUTO-07p is compared with the backbone curves to show its validity for predicting the nonlinear resonant frequency and amplitude. A comparison of the results gives an insight into how modal interactions in the forced-damped response can be predicted using just the backbone curves, and how this might be applied to predict resonant responses of multi-modal nonlinear systems more generally.

Keywords Backbone curve • 3-DoF nonlinear oscillator • Nonlinear modal interaction • Cubic nonlinearity • Second-order normal form method

10.1 Introduction

In this paper, we consider the nonlinear modal behaviour of a three-degree-of-freedom (3-DOF) lumped mass system. In particular we consider the potential modal interactions that can occur by analysing the backbone curves, i.e the response of the equivalent undamped, unforced system. This is because, in common with the majority of vibration examples that lend themselves to modal analysis, the lightly damped dynamic behaviour is largely determined by the properties of the underlying Hamiltonian dynamic system.

The motivation for this study is that when multi-degree-of-freedom systems have weak nonlinearities, then internal resonance effects become significant. In fact these types of resonance effects have extensively been studied because they are often related to unwanted vibration effects in structures. Most of the literature is for undamped, unforced systems, and includes beams, cables, membranes, plates and shells—see for example [1, 9, 13, 15]. Several different analytical approaches have been used to approach this type of problem, such as perturbation methods, [10] nonlinear normal modes (NNMs) [8, 12, 14] or normal form analysis [2, 6, 11, 16]. Similar 3-DOF systems have been analysed using NNMs in the context of nonlinear vibration suppression [7].

In this paper we demonstrate the resonance effects by considering two configurations of an in-line three-degree-freedom(3-DOF) nonlinear oscillators with small forcing and light damping. In Sect. 10.2 we describe the two different configurations of in-line oscillator. Then, in Sect. 10.3, we apply a normal form transformation method [11] to the 3-DOF systems. Having found the normal form, in Sect. 10.4 the backbone curves are computed. These curves are then used to infer the dynamic behaviour of the system, which in turn can be used or interpret the forced, damped behaviour. Conclusions are drawn in Sect.10.5.

X. Liu (✉) • D.J. Wagg • R.J. Barthorpe
Department of Mechanical Engineering, University of Sheffield, Sheffield S1 3JD, UK
e-mail: xuanang.liu@sheffield.ac.uk

A. Cammarano • S.A. Neild
Department of Mechanical Engineering, University of Bristol, Bristol BS8 1TR, UK

G. Kerschen (ed.), *Nonlinear Dynamics, Volume 1*, Conference Proceedings of the Society for Experimental Mechanics Series, DOI 10.1007/978-3-319-15221-9_10

10.2 In-Line Nonlinear 3-DOF Oscillators

The first 3-DOF system considered here is shown schematically in Fig. 10.1. Three lumped massed, all of mass m, have displacements x_1, x_2 and x_3 and are forced sinusoidally at amplitudes P_1, P_2 and P_3 respectively at frequency Ω. The two outside masses are connected to the ground via linear viscous dampers with damping constant c_n, and via nonlinear springs, with linear spring stiffness k_n and cubic stiffness κ_n. The middle mass is also connected to the two side masses via a linear viscous damper and nonlinear springs.

The second 3-DOF system configuration is shown schematically in Fig. 10.2. All three masses are connected to the ground via a linear viscous damper, c_n, and a linear springs, k_n, and the middle mass is connected to the two end masses via linear viscous dampers and the cubic nonlinear springs.

Generally, the governing motion equations of the multi-degree-of-freedom (MDOF) nonlinear vibration system under single-frequency-sinusoidal excitations can be expressed as,

$$\mathbf{M}\ddot{\mathbf{x}} + \mathbf{C}\dot{\mathbf{x}} + \mathbf{K}\mathbf{x} + \mathbf{N}_{\mathbf{x}}(\mathbf{x}) = \mathbf{P}\cos(\Omega t), \tag{10.1}$$

where $\mathbf{M}$, $\mathbf{C}$ and $\mathbf{K}$ are the mass, damping and stiffness matrices ($n \times n$), respectively; $\mathbf{x}$, $\dot{\mathbf{x}}$ and $\ddot{\mathbf{x}}$ are the displacement, velocity and acceleration vectors ($n \times 1$), respectively; $\mathbf{N}_{\mathbf{x}}(\mathbf{x})$ is the nonlinear force vector ($n \times 1$) and $\mathbf{P}$ is the external force amplitude vector ($n \times 1$).

For both of our nonlinear oscillator configurations, the linear damping matrix $\mathbf{C}$ and external sinusoidal force amplitude vector can be written as,

$$\mathbf{C} = \begin{bmatrix} C_1 & -C_4 & 0 \\ -C_4 & C_2 & -C_5 \\ 0 & -C_5 & C_3 \end{bmatrix}, \qquad \mathbf{P} = \begin{pmatrix} P_1 \\ P_2 \\ P_3 \end{pmatrix}. \tag{10.2}$$

But their stiffness matrices and nonlinear terms vectors are different. For the nonlinear oscillator in Fig. 10.1, its specific stiffness matrix $\mathbf{K}$ and the cubic nonlinear force vector $\mathbf{N}_{\mathbf{x}}(\mathbf{x})$ are given by,

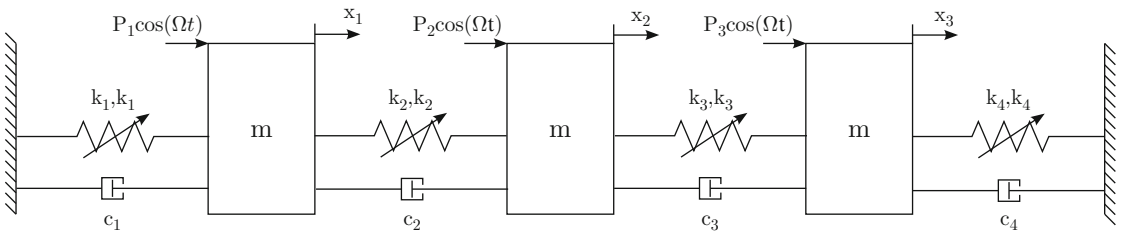

Fig. 10.1 In-line, 3-DOF nonlinear oscillator. The middle mass is respectively connected to the two masses at the end and the two end masses are connected to the ground via a linear spring, a nonlinear cubic spring and a linear viscous damper. All three masses are excited by the single-frequency-sinusoidal forces

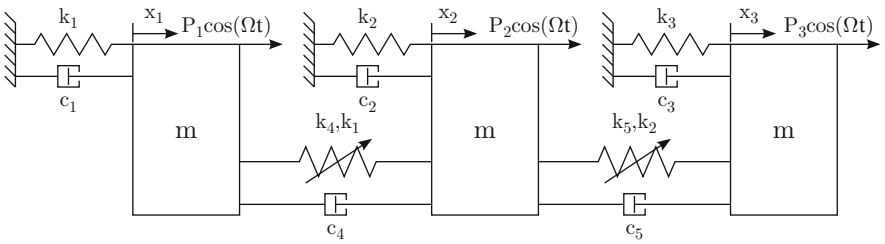

Fig. 10.2 In-line, 3-DOF nonlinear oscillator. All three masses are connected to the ground with a linear spring and a viscous damper and the middle mass links the masses at two ends via a linear spring, a nonlinear cubic spring and a linear viscous damper. All three masses are excited by the single-frequency-sinusoidal forces

$$\mathbf{K}^I = \begin{bmatrix} k_1+k_2 & -k_2 & 0 \\ -k_2 & k_2+k_3 & -k_3 \\ 0 & -k_3 & k_3+k_4 \end{bmatrix}, \qquad \mathbf{N}_\mathbf{x}^I(\mathbf{x}) = \begin{pmatrix} \kappa_1 x_1^3 + \kappa_2 (x_1 - x_2)^3 \\ \kappa_2 (x_2 - x_1)^3 + \kappa_3 (x_2 - x_3)^3 \\ \kappa_3 (x_3 - x_2)^3 + \kappa_4 x_3^3 \end{pmatrix}, \tag{10.3}$$

while for the other oscillator which is shown in Fig. 10.2, its stiffness matrix $\mathbf{K}$ and nonlinear force vector $\mathbf{N}_\mathbf{x}(\mathbf{x})$ (superscripts are used to indicate the two oscillators) are,

$$\mathbf{K}^{II} = \begin{bmatrix} k_1+k_4 & -k_4 & 0 \\ -k_4 & k_2+k_4+k_5 & -k_5 \\ 0 & -k_5 & k_3+k_5 \end{bmatrix}, \qquad \mathbf{N}_\mathbf{x}^{II}(\mathbf{x}) = \begin{pmatrix} \kappa_1 (x_1 - x_2)^3 \\ \kappa_1 (x_2 - x_1)^3 + \kappa_2 (x_2 - x_3)^3 \\ \kappa_2 (x_3 - x_2)^3 \end{pmatrix}. \tag{10.4}$$

10.3 Application of the Second-Order Normal Form Method

Now, we apply a normal form technique which is the second-order normal form method [11] to investigate the modal interaction within the nonlinear 3-DOF oscillator. Here, we firstly consider the case with no damping and no forcing. In this case the equation of motion for both systems is given by

$$\mathbf{M}\ddot{\mathbf{x}} + \mathbf{K}\mathbf{x} + \mathbf{N}_\mathbf{x}(\mathbf{x}) = \mathbf{0}. \tag{10.5}$$

First by applying the linear modal transformation to Eq. (10.5) to decouple the linear terms, we get the linear modal decomposition equation in terms of the new modal coordinate $\mathbf{q}$ as

$$\ddot{\mathbf{q}} + \Lambda\mathbf{q} + \mathbf{N}_\mathbf{q}(\mathbf{q}) = \mathbf{0}, \tag{10.6}$$

where $\mathbf{q}$ is the modal coordinates and Λ is a diagonal matrix of the squares of the corresponding linearised natural frequencies ω_{n1}, ω_{n2} & ω_{n3}, and the $\mathbf{N}_\mathbf{q}(\mathbf{q})$ is the nonlinear modal force vector,

$$\mathbf{N}_\mathbf{q}(\mathbf{q}) = \mathbf{n}_\mathbf{q}\mathbf{q}^*, \tag{10.7}$$

where coefficient matrix $\mathbf{n}_\mathbf{q}$ and nonlinear element vector $\mathbf{q}^*$ are, in general

$$\mathbf{n}_\mathbf{q}^\mathbf{T} = \begin{bmatrix} \alpha_{11} & \alpha_{21} & \alpha_{31} \\ \alpha_{12} & \alpha_{22} & \alpha_{32} \\ \alpha_{13} & \alpha_{23} & \alpha_{33} \\ \alpha_{14} & \alpha_{24} & \alpha_{34} \\ \alpha_{15} & \alpha_{25} & \alpha_{35} \\ \alpha_{16} & \alpha_{26} & \alpha_{36} \\ \alpha_{17} & \alpha_{27} & \alpha_{37} \\ \alpha_{18} & \alpha_{28} & \alpha_{38} \\ \alpha_{19} & \alpha_{29} & \alpha_{39} \\ \alpha_{10} & \alpha_{20} & \alpha_{30} \end{bmatrix}, \qquad \mathbf{q}^* = \begin{bmatrix} q_1^3 \\ q_1^2 q_2 \\ q_1 q_2^2 \\ q_2^3 \\ q_2^2 q_3 \\ q_2 q_3^2 \\ q_3^3 \\ q_1 q_3^2 \\ q_1^2 q_3 \\ q_1 q_2 q_3 \end{bmatrix}. \tag{10.8}$$

Substituting $q_n \rightarrow u_n = u_{np} + u_{nm}$ gives the functional form of $\mathbf{u}^*$ vector and coefficient vector $\mathbf{n}_\mathbf{u}$ as below, and simultaneously, values for $\beta_{k,l}$ can be computed using

$$\beta_{k,l} = \left[\sum_{n=1}^{N} \left\{ (s_{npl} - s_{nml}) \omega_{rn} \right\} \right]^2 - \omega_{rk}^2, \tag{10.9}$$

with the assumption that $\omega_{r2} = r\omega_{r1}$ and $\omega_{r3} = r'\omega_{r1}$,

$$\mathbf{u}^* = \begin{bmatrix} u_{1p}^3 \\ u_{1p}^2 u_{1m} \\ u_{1p} u_{1m}^2 \\ u_{2p}^3 \\ u_{1p}^2 u_{2p} \\ u_{1p} u_{1m} u_{2p} \\ u_{1m}^2 u_{2p} \\ u_{1p}^2 u_{2m} \\ u_{1p} u_{1m} u_{2m} \\ u_{1m}^2 u_{2m} \\ u_{1p} u_{2p}^2 \\ u_{1p} u_{2p} u_{2m} \\ u_{1p} u_{2m}^2 \\ u_{1m} u_{2p}^2 \\ u_{1m} u_{2p} u_{2m} \\ u_{1m} u_{2m}^2 \\ u_{2p}^3 \\ u_{2p}^2 u_{2m} \\ u_{2p} u_{2m}^2 \\ u_{2m}^3 \\ u_{2p}^2 u_{3p} \\ u_{2p} u_{2m} u_{3p} \\ u_{2m}^2 u_{3p} \\ u_{2p}^2 u_{3m} \\ u_{2p} u_{2m} u_{3m} \\ u_{2m}^2 u_{3m} \\ u_{2p} u_{3p}^2 \\ u_{2p} u_{3p} u_{3m} \\ u_{2p} u_{3m}^2 \\ u_{2m} u_{3p}^2 \\ u_{2m} u_{3p} u_{3m} \\ u_{2m} u_{3m}^2 \\ u_{3p}^3 \\ u_{3p}^2 u_{3m} \\ u_{3p} u_{3m}^2 \\ u_{3m}^3 \\ u_{1p} u_{3p}^2 \\ u_{1p} u_{3p} u_{3m} \\ u_{1p} u_{3m}^2 \\ u_{1m} u_{3p}^2 \\ u_{1m} u_{3p} u_{3m} \\ u_{1m} u_{3m}^2 \\ u_{1p}^2 u_{3p} \\ u_{1p} u_{1m} u_{3p} \\ u_{1m}^2 u_{3p} \\ u_{1p}^2 u_{3m} \\ u_{1p} u_{1m} u_{3m} \\ u_{1m}^2 u_{3m} \\ u_{1p} u_{2p} u_{3p} \\ u_{1p} u_{2p} u_{3m} \\ u_{1p} u_{2m} u_{3p} \\ u_{1p} u_{2m} u_{3m} \\ u_{1m} u_{2p} u_{3p} \\ u_{1m} u_{2p} u_{3m} \\ u_{1m} u_{2m} u_{3p} \\ u_{1m} u_{2m} u_{3m} \end{bmatrix} \quad \mathbf{n}_\mathbf{u}^\mathbf{T} = \begin{bmatrix} \alpha_{11} & \alpha_{21} & \alpha_{31} \\ 3\alpha_{11} & 3\alpha_{21} & 3\alpha_{31} \\ 3\alpha_{11} & 3\alpha_{21} & 3\alpha_{31} \\ \alpha_{11} & \alpha_{21} & \alpha_{31} \\ \alpha_{12} & \alpha_{22} & \alpha_{32} \\ 2\alpha_{12} & 2\alpha_{22} & 2\alpha_{32} \\ \alpha_{12} & \alpha_{22} & \alpha_{32} \\ \alpha_{12} & \alpha_{22} & \alpha_{32} \\ 2\alpha_{12} & 2\alpha_{22} & 2\alpha_{32} \\ \alpha_{12} & \alpha_{22} & \alpha_{32} \\ \alpha_{13} & \alpha_{23} & \alpha_{33} \\ 2\alpha_{13} & 2\alpha_{23} & 2\alpha_{33} \\ \alpha_{13} & \alpha_{23} & \alpha_{33} \\ \alpha_{13} & \alpha_{23} & \alpha_{33} \\ 2\alpha_{13} & 2\alpha_{23} & 2\alpha_{33} \\ \alpha_{13} & \alpha_{23} & \alpha_{33} \\ \alpha_{14} & \alpha_{24} & \alpha_{34} \\ 3\alpha_{14} & 3\alpha_{24} & 3\alpha_{34} \\ 3\alpha_{14} & 3\alpha_{24} & 3\alpha_{34} \\ \alpha_{14} & \alpha_{24} & \alpha_{34} \\ \alpha_{15} & \alpha_{25} & \alpha_{35} \\ 2\alpha_{15} & 2\alpha_{25} & 2\alpha_{35} \\ \alpha_{15} & \alpha_{25} & \alpha_{35} \\ \alpha_{15} & \alpha_{25} & \alpha_{35} \\ 2\alpha_{15} & 2\alpha_{25} & 2\alpha_{35} \\ \alpha_{15} & \alpha_{25} & \alpha_{35} \\ \alpha_{16} & \alpha_{26} & \alpha_{36} \\ 2\alpha_{16} & 2\alpha_{26} & 2\alpha_{36} \\ \alpha_{16} & \alpha_{26} & \alpha_{36} \\ \alpha_{16} & \alpha_{26} & \alpha_{36} \\ 2\alpha_{16} & 2\alpha_{26} & 2\alpha_{36} \\ \alpha_{16} & \alpha_{26} & \alpha_{36} \\ \alpha_{17} & \alpha_{27} & \alpha_{37} \\ 3\alpha_{17} & 3\alpha_{27} & 3\alpha_{37} \\ 3\alpha_{17} & 3\alpha_{27} & 3\alpha_{37} \\ \alpha_{17} & \alpha_{27} & \alpha_{37} \\ \alpha_{18} & \alpha_{28} & \alpha_{38} \\ 2\alpha_{18} & 2\alpha_{28} & 2\alpha_{38} \\ \alpha_{18} & \alpha_{28} & \alpha_{38} \\ \alpha_{18} & \alpha_{28} & \alpha_{38} \\ 2\alpha_{18} & 2\alpha_{28} & 2\alpha_{38} \\ \alpha_{18} & \alpha_{28} & \alpha_{38} \\ \alpha_{19} & \alpha_{29} & \alpha_{39} \\ 2\alpha_{19} & 2\alpha_{29} & 2\alpha_{39} \\ \alpha_{19} & \alpha_{29} & \alpha_{39} \\ \alpha_{19} & \alpha_{29} & \alpha_{39} \\ 2\alpha_{19} & 2\alpha_{29} & 2\alpha_{39} \\ \alpha_{19} & \alpha_{29} & \alpha_{39} \\ \alpha_{10} & \alpha_{20} & \alpha_{30} \\ \alpha_{10} & \alpha_{20} & \alpha_{30} \\ \alpha_{10} & \alpha_{20} & \alpha_{30} \\ \alpha_{10} & \alpha_{20} & \alpha_{30} \\ \alpha_{10} & \alpha_{20} & \alpha_{30} \\ \alpha_{10} & \alpha_{20} & \alpha_{30} \\ \alpha_{10} & \alpha_{20} & \alpha_{30} \\ \alpha_{10} & \alpha_{20} & \alpha_{30} \end{bmatrix} \quad \boldsymbol{\beta}^T = \omega_{r1}^2 \begin{bmatrix} 8 & 9-r^2 & 9-r'^2 \\ 0 & 1-r^2 & 1-r'^2 \\ 0 & 1-r^2 & 1-r'^2 \\ 8 & 9-r^2 & 9-r'^2 \\ r^2+4r+3 & 4r+4 & r^2+4r+4-r'^2 \\ r^2-1 & 0 & r^2-r'^2 \\ r^2-4r+3 & -4r+4 & r^2-4r+4-r'^2 \\ r^2-4r+3 & -4r+4 & r^2-4r+4-r'^2 \\ r^2-1 & 0 & r^2-r'^2 \\ r^2+4r+3 & 4r+4 & r^2+4r+4-r'^2 \\ 4r^2+4r & 3r^2+4r+1 & 4r^2+4r+1-r'^2 \\ 0 & 1-r^2 & 1-r'^2 \\ 4r^2-4r & 3r^2-4r+1 & 4r^2-4r+1-r'^2 \\ 4r^2-4r & 3r^2-4r+1 & 4r^2-4r+1-r'^2 \\ 0 & 1-r2 & 1-r'2 \\ 4r^2+4r & 3r^2+4r+1 & 4r^2+4r+1-r'^2 \\ 9r^2-1 & 8r^2 & 9r^2-r'^2 \\ r^2-1 & 0 & r^2-r'^2 \\ r^2-1 & 0 & r^2-r'^2 \\ 9r^2-1 & 8r^2 & 9r^2-r'^2 \\ 4r^2+4rr'+r'^2-1 & 3r^2+4rr'+r'^2 & 4r^2+4rr' \\ r'^2-1 & r'^2-r^2 & 0 \\ 4r^2-4rr'+r'^2-1 & 3r^2-4rr'+r'^2 & 4r^2-4rr' \\ 4r^2-4rr'+r'^2-1 & 3r^2-4rr'+r'^2 & 4r^2-4rr' \\ r'^2-1 & r'^2-r^2 & 0 \\ 4r^2+4rr'+r'^2-1 & 3r^2+4rr'+r'^2 & 4r^2+4rr' \\ r^2+4rr'+4r'^2-1 & 4rr'+4r'^2 & r^2+4rr'+3r'^2 \\ r^2-1 & 0 & r^2-r'^2 \\ r^2-4rr'+4r'^2-1 & -4rr'+4r'^2 & r^2-4rr'+3r'^2 \\ r^2-4rr'+4r'^2-1 & -4rr'+4r'^2 & r^2-4rr'+3r'^2 \\ r^2-1 & 0 & r^2-r'^2 \\ r^2+4rr'+4r'^2-1 & 4rr'+4r'^2 & r^2+4rr'+3r'^2 \\ 9r'^2-1 & 9r'^2-r^2 & 8r'^2 \\ r'^2-1 & r'^2-r^2 & 0 \\ r'^2-1 & r'^2-r^2 & 0 \\ 9r'^2-1 & 9r'^2-r^2 & 8r'^2 \\ 4r'+4r'^2 & 1+4r'+4r'^2-r^2 & 1+4r'+3r'^2 \\ 0 & 1-r^2 & 1-r'^2 \\ -4r'+4r'^2 & 1-4r'+4r'^2-r^2 & 1-4r'+3r'^2 \\ -4r'+4r'^2 & 1-4r'+4r'^2-r^2 & 1-4r'+3r'^2 \\ 0 & 1-r^2 & 1-r'^2 \\ 4r'+4r'^2 & 1+4r'+4r'^2-r^2 & 1+4r'+3r'^2 \\ 3+4r'+r'^2 & 4+4r'+r'^2-r^2 & 4+4r' \\ r'^2-1 & r'^2-r^2 & 0 \\ 3-4r'+r'^2 & 4-4r'+r'^2-r^2 & 4-4r' \\ 3-4r'+r'^2 & 4-4r'+r'^2-r^2 & 4-4r' \\ r'^2-1 & r'^2-r^2 & 0 \\ 3+4r'+r'^2 & 4+4r'+r'^2-r^2 & 4+4r' \\ (1+r+r')^2-1 & (1+r+r')^2-r^2 & (1+r+r')^2-r'^2 \\ (1+r-r')^2-1 & (1+r-r')^2-r^2 & (1+r-r')^2-r'^2 \\ (1-r+r')^2-1 & (1-r+r')^2-r^2 & (1-r+r')^2-r'^2 \\ (1-r-r')^2-1 & (1-r-r')^2-r^2 & (1-r-r')^2-r'^2 \\ (1-r-r')^2-1 & (1-r-r')^2-r^2 & (1-r-r')^2-r'^2 \\ (1-r+r')^2-1 & (1-r+r')^2-r^2 & (1-r+r')^2-r'^2 \\ (1+r-r')^2-1 & (1+r-r')^2-r^2 & (1+r-r')^2-r'^2 \\ (1+r+r')^2-1 & (1+r+r')^2-r^2 & (1+r+r')^2-r'^2 \end{bmatrix} \tag{10.10}$$

By viewing the $\boldsymbol{\beta}$ matrix, the zero terms represent the unconditionally-resonant terms which should be kept in the dynamic equation for u. Furthermore, there are also additional conditionally-resonant terms depending on the value of r and r'. For example, $r, r' = 1, 3, \frac{1}{3}$ will lead further zero terms in the $\boldsymbol{\beta}$ matrix. For both unconditionally- and conditionally-resonant terms, the corresponding terms in $\mathbf{n_u}$ as equal to those in $\mathbf{n}$. Here, as an example, consider the case that r and $r' \neq 1, 3, \frac{1}{3}$, such that there is no conditionally resonance terms and the resulting dynamic equations are, (Note that this special case is inconsistent with the $\omega_{n1} : \omega_{n2} : \omega_{n3} \simeq 1 : 1 : 1$ case considered elsewhere in this paper.)

$$\begin{aligned}
&\ddot{u}_1 + \omega_{n1}^2 u_1 + 3\alpha_{11}\left[u_{1p}^2 u_{1m} + u_{1p} u_{1m}^2\right] + 2\alpha_{13}\left[u_{1p}u_{2p}u_{2m} + u_{1m}u_{2p}u_{2m}\right] + 2\alpha_{18}\left[u_{1p}u_{3p}u_{3m} + u_{1m}u_{3p}u_{3m}\right] = 0,\\
&\ddot{u}_2 + \omega_{n2}^2 u_2 + 3\alpha_{24}\left[u_{2p}^2 u_{2m} + u_{2p} u_{2m}^2\right] + 2\alpha_{22}\left[u_{1p}u_{1m}u_{2p} + u_{1p}u_{1m}u_{2m}\right] + 2\alpha_{26}\left[u_{2p}u_{3p}u_{3m} + u_{2m}u_{2p}u_{3m}\right] = 0,\\
&\ddot{u}_3 + \omega_{n3}^2 u_3 + 3\alpha_{37}\left[u_{3p}^2 u_{3m} + u_{3p} u_{3m}^2\right] + 2\alpha_{35}\left[u_{2p}u_{2m}u_{3p} + u_{2p}u_{2m}u_{3m}\right] + 2\alpha_{39}\left[u_{1p}u_{1m}u_{3p} + u_{1p}u_{1m}u_{3m}\right] = 0.
\end{aligned} \tag{10.11}$$

Substituting $u_{ip} = (U_i/2)\, e^{j(\omega_{ri}t - \phi_i)}$ and $u_{im} = (U_i/2)\, e^{-j(\omega_{ri}t - \phi_i)}$ into Eq. (10.11) and balancing the coefficients of $e^{j\omega_{ri}t}$ and $e^{-j\omega_{ri}t}$, we can get the time-independent equations

$$\begin{aligned}
&\left[-\omega_{r1}^2 + \omega_{n1}^2 + 3\alpha_{11}U_1^2 + 2\alpha_{13}U_2^2 + 2\alpha_{18}U_3^2\right] U_1 = 0,\\
&\left[-\omega_{r2}^2 + \omega_{n2}^2 + 3\alpha_{24}U_2^2 + 2\alpha_{22}U_1^2 + 2\alpha_{26}U_3^2\right] U_2 = 0,\\
&\left[-\omega_{r3}^2 + \omega_{n3}^2 + 3\alpha_{37}U_3^2 + 2\alpha_{35}U_2^2 + 2\alpha_{39}U_1^2\right] U_3 = 0.
\end{aligned} \tag{10.12}$$

Three solutions to Eq. (10.12) can be found by successively setting U_1 , U_2 and U_3 to zero and the results are,

$$S1: \quad U_1 \neq 0, U_2 = U_3 = 0, \quad \omega_{r1}^2 = \omega_{n1}^2 + \frac{3}{4}\alpha_{11}U_1^2, \tag{10.13}$$

$$S2: \quad U_2 \neq 0, U_1 = U_3 = 0, \quad \omega_{r2}^2 = \omega_{n2}^2 + \frac{3}{4}\alpha_{24}U_2^2, \tag{10.14}$$

$$S3: \quad U_3 \neq 0, U_1 = U_2 = 0, \quad \omega_{r3}^2 = \omega_{n3}^2 + \frac{3}{4}\alpha_{37}U_3^2. \tag{10.15}$$

Here $S1$, $S2$ and $S3$ are the expressions of the backbone curve branches of the modal coordinates for the non-modal-interaction case.

10.4 Backbone Curve and FRF Results

In order to show how the backbone curve obtained by the second-order normal form method can present the information of the modal interaction within a nonlinear oscillator, we choose the second nonlinear system (shown in Fig. 10.2) with specific parameters as a example for illustration. Here, to simplify the mathematical presentation, we choose the oscillator to be symmetric, which means the linear stiffness $k_1 = k_2 = k_3 = k$ and $k_4 = k_5 = k'$ and the cubic nonlinear stiffness $\kappa_1 = \kappa_2 = \kappa$.

Therefore, through linear modal transformation, the linear modal natural frequencies can be calculated to be $\omega_{n1} = \sqrt{k}$, $\omega_{n2} = \sqrt{k + k'}$ and $\omega_{n3} = \sqrt{k + 3k'}$. To make these modal frequencies be close, k' is supposed to be small and there will exist the possibility for the nonlinear modes to interact. Hence, for a $1 : 1 : 1$ resonance we set $r = r' = 1$. Submitting the frequencies ratios values into the $\boldsymbol{\beta}$ matrix derived in Sect. 10.3, picking out the resonant terms into $\mathbf{n}$ and following the same process in last section, we obtain the time-independent equations like Eq. (10.12) to be,

$$\begin{aligned}
&\left[-\omega_{r1}^2 + \omega_{n1}^2\right] U_1 = 0,\\
&\left[-\omega_{r2}^2 + \omega_{n2}^2 + \frac{3}{4}\mu\left\{U_2^2 + (18 + 9p)U_3^2\right\}\right] U_2 = 0,\\
&\left[-\omega_{r3}^2 + \omega_{n3}^2 + \frac{3}{4}\mu\left\{27U_3^2 + (6 + 3p)U_2^2\right\}\right] U_3 = 0.
\end{aligned} \tag{10.16}$$

where $\mu = \kappa/m$ and $p = e^{j2(|\phi_2 - \phi_3|)}$. The $|\phi_2 - \phi_3|$ represents the phase difference between mode 2 and 3. Using the same procedure as that in Sect. 10.3, there exist three independent backbone branches labelled $S1$, $S2$ and $S3$,

$$S1: \quad U_1 \neq 0, U_2 = U_3 = 0, \quad \omega_{r1}^2 = \omega_{n1}^2, \tag{10.17}$$

$$S2: \quad U_2 \neq 0, U_1 = U_3 = 0, \quad \omega_{r2}^2 = \omega_{n2}^2 + \frac{3}{4}\mu U_2^2, \tag{10.18}$$

$$S3: \quad U_3 \neq 0, U_1 = U_2 = 0, \quad \omega_{r3}^2 = \omega_{n3}^2 + \frac{81}{4}\mu U_3^2. \tag{10.19}$$

It can be noticed that the branch for u_1 is linear and it is actually not coupled with the other two modes, where mode 2 and 3 would potentially interact with each other which will be affected by p. If u_2 and u_3 are both active, Eq. (10.16) can be written as

$$\Omega^2 = \omega_{n2}^2 + \frac{3}{4}\mu\left\{U_2^2 + (18 + 9p)U_3^2\right\} = \omega_{n3}^2 + \frac{3}{4}\mu\left\{27U_3^2 + (6 + 3p)U_2^2\right\}. \tag{10.20}$$

For Eq. (10.20) to be real, the phase difference terms should be, $p = \pm 1$. $p = 1$ and $p = -1$ represent the in-unison and out-of-unison resonances respectively. The full discussion of the value chosen of p and its corresponding physical meaning can be found in [3, 5]. So, here by setting $p = +1$ yields two extra backbone curves, labelled $S4^+$ and $S4^-$, with the phase difference

$$S4^+ : |\phi_2 - \phi_3| = 0, \qquad S4^- : |\phi_2 - \phi_3| = \pi, \tag{10.21}$$

and their corresponding backbone branch expressions,

$$\begin{aligned} S4^{\pm}: \quad & U_2^2 = \frac{\omega_{n2}^2 - \omega_{n3}^2}{6\mu}, \\ S4^{\pm}: \quad & \Omega^2 = \frac{9\omega_{n2}^2 - \omega_{n3}^2}{8} + \frac{81}{4}\mu U_3^2. \end{aligned} \tag{10.22}$$

The case where $p = -1$ yields a further two backbone curves, denoted $S5^+$ and $S5^-$. They are characterised by the phase differences,

$$S5^+ : |\phi_2 - \phi_3| = +\pi/2, \qquad S5^- : |\phi_2 - \phi_3| = -\pi/2. \tag{10.23}$$

Substituting $p = 1$ into Eq. (10.20) gives the amplitude and response frequency relationships

$$\begin{aligned} S5^{\pm}: \quad & U_2^2 = \frac{2(\omega_{n2}^2 - \omega_{n3}^2)}{3\mu} - 9U_3^2, \\ S5^{\pm}: \quad & \Omega^2 = \frac{3\omega_{n2}^2 - \omega_{n3}^2}{2}. \end{aligned} \tag{10.24}$$

It should be noted that if μ is positive Eqs. (10.22) and (10.24) will be complex (assumed $\omega_{n3} > \omega_{n2}$) and lose its physical meaning. Hence, the $S4^{\pm}$ and $S5^{\pm}$ branches exist and the corresponding nonlinear modal interaction only happens when the cubic spring stiffness κ is negative, i.e. the system is a softening nonlinear case. Also it can be seen from Eq. (10.24) that as the frequency of $S5^{\pm}$ will not vary with the mode amplitude and as the mode amplitude cannot infinitely increase the $S5^{\pm}$ backbone branch will be a vertical line with a limited length.

Figure 10.3 shows the backbone curves for the cases where $\omega_{n1} = 1$, $\omega_{n2} = 1.005$, $\omega_{n3} = 1.015$ and $\kappa = -0.05$. All panels show the backbone curves in the projection of response frequency against a displacement. The first column shows the amplitude of displacement of the fundamental response of u_1, u_2 and u_3 and the second shows that of the lumped masses x_1, x_2 and x_3. The labelled $S1$, $S2$ and $S3$ branches are the independent resonant backbone curve. The $S4^+$, $S4^-$, $S5^+$ and $S5^-$ branches are the interacting ones in which case mode 2 and mode 3 are both activated and the mode phase differences are 0, π, $+\pi/2$ and $-\pi/2$ respectively. Note that as $S5^{\pm}$ will coincide with $S1$, $S5^{\pm}$ backbone curves are indicated by short cross lines in Fig. 10.3.

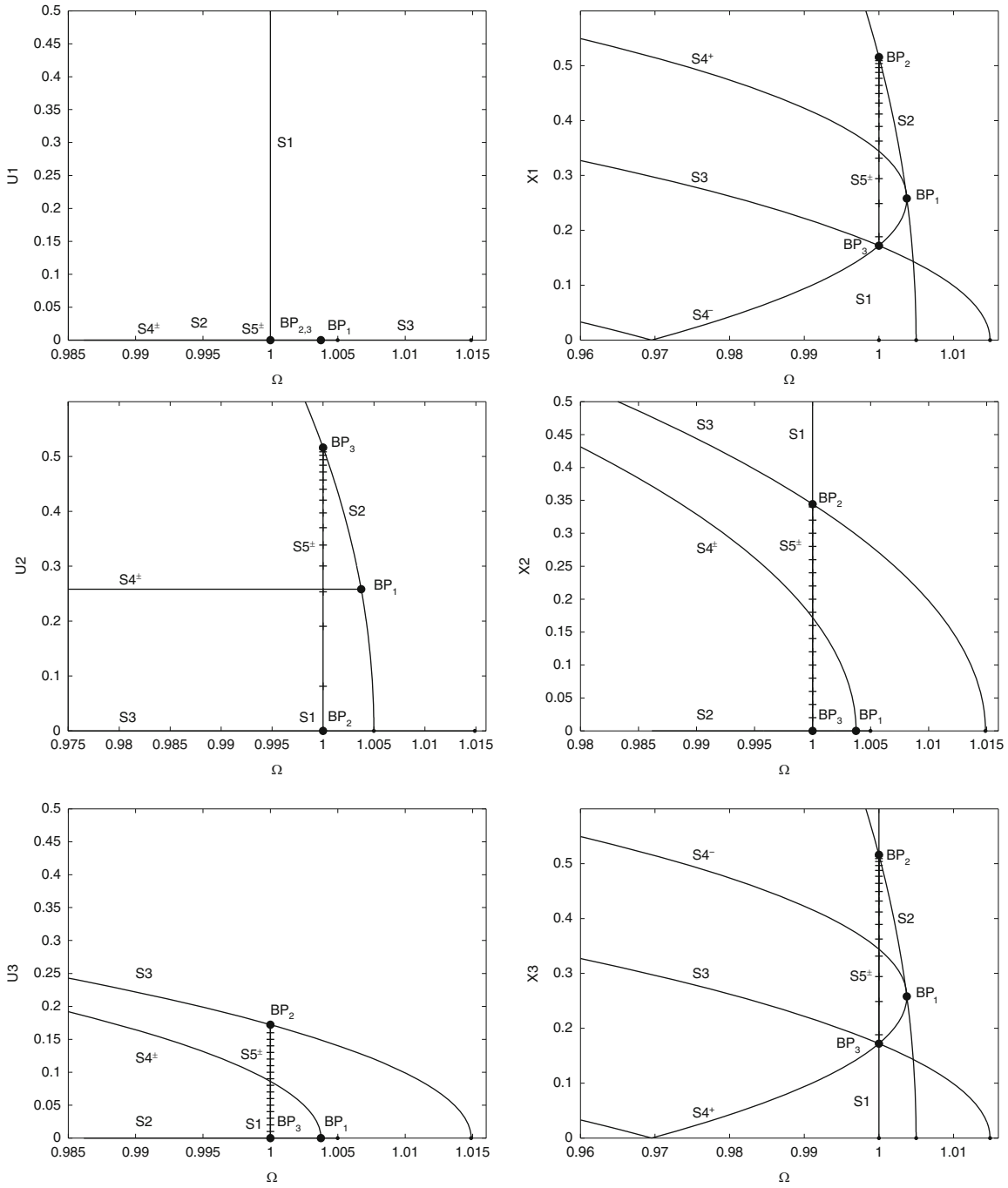

Fig. 10.3 Backbone curves for the oscillator with the physical parameters $k_1 = k_2 = k_3 = 1$, $k_3 = k_4 = 0.01$ and $\kappa_1 = \kappa_2 = -0.05$, so the modal natural frequencies are $\omega_{n1} = 1$, $\omega_{n2} = 1.005$ and $\omega_{n3} = 1.015$. The panels in the first and second column show the modal and physical results respectively. Stable solutions are shown with *solid lines*, whereas unstable solutions are represented by *dashed line*. Bifurcation points are noted by *BP*. Note that as $S5^{\pm}$ would overlap $S1$, $S5^{\pm}$ backbone curves are indicated by *short cross lines* for distinction

To further demonstrate the ability of the backbone curve in determining the response of the system to an external forcing, we show a brief example of the relationship between the forced response and the backbone curves. The same fundamental system as above is used and it is forced in the second mode, $[P_{m1}, P_{m2}, P_{m3}] = [0, 15, 0] \times 10^{-4}$ (corresponding physical mass force is $[P_1, P_2, P_3] = [15, 0, -15] \times 10^{-4}$) with a damping ratio of $\zeta = 0.001$. The forced response has been computed from an initial steady state solution, found with numerical integration in MATLAB, which is then continued in forcing frequency using the software AUTO-07p [4].

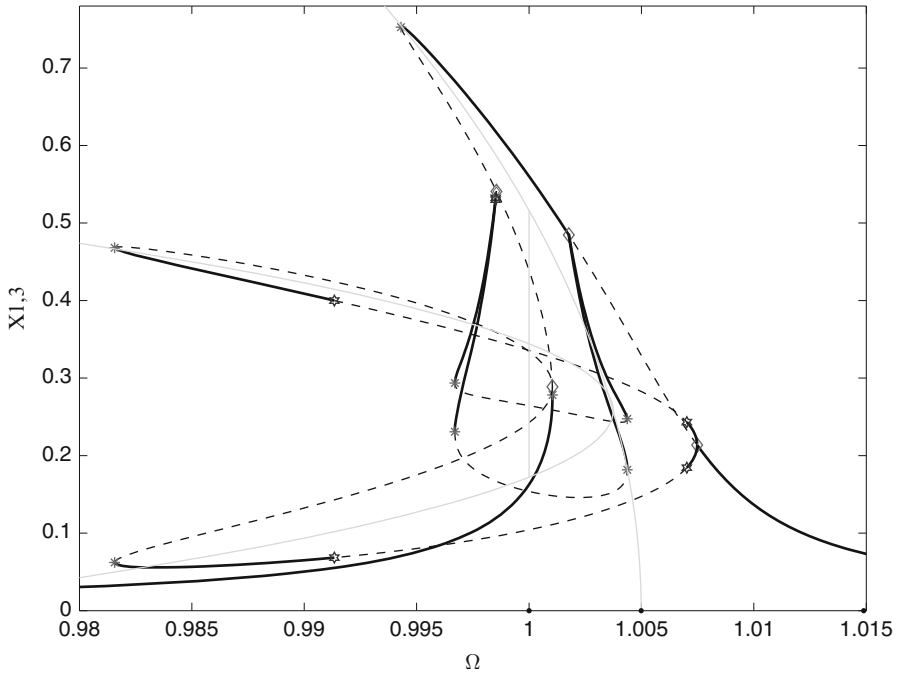

Fig. 10.4 Backbone curves and the amplitude response of the first and third masses when the system is forced in only the second mode (i.e. $[P_{m1}, P_{m2}, P_{m3}] = [0, 0.0015, 0]$) with parameters $m = 1$, $\omega_{n1} = 1$, $\omega_{n2} = 1.005$, $\omega_{n3} = 1.015$, $\kappa_1 = \kappa_2 = -0.05$, $c_1 = c_2 = c_3 = 0.002$, $c_4 = c_5 = 0$ and $[P_1, P_2, P_3] = [0.0015, 0, -0.0015]$. The *diamond*, *star* and *asterisk* indicate branch, torus bifurcation and fold points. The *black solid lines* and *thin dash lines* represent the stable and unstable amplitude response respectively. The *grey lines* represent the backbone curves. Note that as forcing is in the second mode only, the backbone branches $S1$ (containing mode 1 only) and $S3$ (containing mode 3) have not been plotted here

Figure 10.4 shows the forced response of the first and third masses, X_1 and X_3 (due to the system symmetry) for the system whose backbone curves are presented in the first panel of the second column in Fig. 10.3. In Fig. 10.4, it can be observed that the response of the typical softening Duffing oscillator is following the $S2$ backbone where the response is confined to just the second mode. On the right stable and left unstable Duffing oscillator response branches, two branch bifurcation points, marked by quadrangles, respectively leading to two branches which follow $S4^+$ and $S4^-$ backbone curves respectively. Still one pair of response branches is stable and the other is unstable. These branches are the responses composed of both second and third modes with the phase difference 0 and π respectively. In the center part of Fig. 10.4, there are four stable branches which also bifurcate from the Duffing oscillator response and they appear to be attracted to $S5^{\pm}$. There four curves seems to be the response composed of second mode and third mode but with the phase difference $+\pi/2$ and $-\pi/2$. Besides, it can be seen that all the peaks amplitude points are close to our backbone curve branches. Therefore, the result shows that the backbone curve obtained by the second-order normal form method provides a good way for understanding the modal interaction within the nonlinear 3-DOF oscillator system.

10.5 Conclusions

In this paper, we have considered the nonlinear modal behaviour of a three-degree-freedom (3-DOF) lumped mass system. In particular we considered the potential modal interactions that can occur by analysing the backbone curves of the undamped, unforced system. This is an important topic because the majority of vibration examples that relate to modal analysis are lightly damped and therefore the dynamic behaviour is largely determined by the properties of the underlying undamped dynamic system.

First the undamped, unforced case was considered. In particular the modal interaction case that occurs when all the underlying linear modal frequencies are close was considered (i.e. $\omega_{n1} : \omega_{n2} : \omega_{n3} \simeq 1 : 1 : 1$). In this case the first mode is linear because of the symmetry of the system and the other two modes will potentially interact with each other when the special parameters are chosen. We showed how this system can be analysed using a normal form transformation to obtain the

nonlinear backbone curves of the undamped, unforced response. Following this the frequency response function (FRF) of the corresponding lightly damped and harmonically forced system was obtained using the continuation software AUTO-07p. This result was compared with the backbones curve to show its validity for predicting the nonlinear resonant frequency and amplitude.

References

1. Amabili M (2008) Nonlinear vibrations and stability of shells and plates. Cambridge University Press, Cambridge
2. Arnold VI (1988) Geometrical methods in the theory of ordinary differential equations. Springer, New York
3. Cammarano A, Hill T, Neild S, Wagg D (2014) Bifurcations of backbone curves for systems of coupled nonlinear two mass oscillator. Nonlinear Dyn 77(1–2):311–320
4. Doedel EJ, Champneys AR, Fairgrieve TF, Kuznetsov YA, Dercole F, Oldeman BE, Paffenroth RC, Sandstede B, Wang XJ, Zhang C (2008) AUTO-07P: continuation and bifurcation software for ordinary differential equations. Concordia University, Montreal. http://cmvl.cs.concordia.ca
5. Hill TL, Cammarano A, Neild SA, Wagg DJ (2015) Our-of-unison resonance in weakly-nonlinear oscillator. Proc R Soc Lond A 471(2173):p.20140659
6. Jezequel L, Lamarque CH (1991) Analysis of nonlinear dynamic systems by the normal form theory. J Sound Vib 149(3):429–459
7. Kerschen G, Kowtko JJ, McFarland DM, Bergman LA, Vakakis AF (2007) Theoretical and experimental study of multimodal targeted energy transfer in a system of coupled oscillators Nonlinear Dyn 47:285–309
8. Kerschen G, Peeters M, Golinval JC, Vakakis AF (2009) Nonlinear normal modes, Part I: a useful framework for the structural dynamicist. Mech Syst Signal Process 23(1, Sp. Iss. SI):170–194
9. Lewandowski R (1996) On beams, membranes and plates backbone curves in a cases of internal resonance. Meccanica 31:323–346
10. Nayfeh AH, Mook DT (1995) Nonlinear oscillations. Wiley, New York
11. Neild SA, Wagg DJ (2011) Applying the method of normal forms to second-order nonlinear vibration problems. Proc R Soc Lond A 467(2128):1141–1163
12. Pierre C, Jiang DY, Shaw S (2006) Nonlinear normal modes and their application in structural dynamics. Math Prob Eng 2006:10847
13. Rega G, Lacarbonara W, Nayfeh A, Chin C (1999) Multiple resonances in suspended cables: direct versus reduced-order models. Int J Nonlinear Mech 34(5):901–924
14. Touzé C, Amabili M (2006) Nonlinear normal modes for damped geometrically nonlinear systems: application to reduced-order modelling of harmonically forced structures. J Sound Vib 298(4–5):958–981
15. Touzé C, Thomas O, Chaigne A (2002) Asymmetric non-linear forced vibrations of free-edge circular plates. Part 1: Theory. J Sound Vib 258(4):649–676
16. Wagg DJ, Neild SA (2009) Nonlinear vibration with control. Springer, New York

Chapter 11
Passive Flutter Suppression Using a Nonlinear Tuned Vibration Absorber

Giuseppe Habib and G. Kerschen

Abstract Limit cycle oscillations (LCOs) occur in many mechanical systems and they are often a source of danger. The addition of a relatively small mass to the host system, attached through a linear spring and a damper (linear tuned vibration absorber, LTVA), significantly improves its stability. The use of a purely nonlinear spring in the absorber (nonlinear energy sink, NES) increases the frequency bandwidth of the absorber, reduce LCO amplitude and avoid subcritical bifurcation at the loss of stability. Recently, a nonlinear tuned vibration absorber (NLTVA) has been proposed, whose restoring force is tailored according to the functional form of the nonlinearity of the primary system. The NLTVA is designed to exploit the positive features of both the LTVA and the NES. In this paper we show that the NLTVA can compensate the detrimental effect of the nonlinearities of the primary system. In other words, the coupled system exhibits a linear-like dynamics, similar to the same system without structural nonlinearities. Considering a Van der Pol—Duffing oscillator as primary system, a closed-form solution for the local compensation of nonlinearities is obtained analytically. Numerical continuation techniques show that the compensation is valid also for large amplitudes of the response.

Keywords Limit cycle oscillations • Vibration absorber • Nonlinearity synthesis • Stability analysis • Bifurcation analysis

11.1 Introduction

Limit cycle oscillations (LCOs) are encountered in a number of real engineering applications including aircraft [1, 2], machine tools [3, 4], automotive disk brakes [5, 6] and oil-drilling rigs [7]. LCOs often limit the performance and can also endanger the safety of operation [8].

Active control strategies have been proposed as a means of counteracting LCOs [9–11]. These references have shown that active control can be used to raise the threshold above which LCOs occur. However, active control is also limited by its requirements in terms of energy or space for actuators. Furthermore, delay in the feedback loop can generate unexpected instabilities [12, 13] whereas saturation of the actuators can limit the robustness of stability [14].

Passive vibration absorbers are another alternative for mitigating undesired LCOs. Specifically, the linear tuned vibration absorber (LTVA), which comprises a small mass attached to the host system through a damper and a spring, has been widely studied in the literature [15–21]. In most of these works, the system under investigation is the classical Van der Pol (VdP) oscillator. References [17, 18] provide simple rules to properly tune the LTVA parameters, while references [20, 21] study the post-bifurcation behavior of the coupled system. In [22], a nonlinear damping element was added in parallel with the LTVA to decrease the maximum LCO amplitude. Other nonlinear vibration absorbers, including the autoparametric vibration absorber [23, 24], the nonlinear energy sink [25–27] and the hysteretic tuned vibration absorber [28], have also been considered to increase the effectiveness of vibration attenuation.

The main idea of this study is to utilize the nonlinear tuned vibration absorber (NLTVA) for LCO suppression. This absorber, first introduced in [29], possesses a linear spring and a nonlinear spring whose mathematical form is determined according to the nonlinearity in the host system. Following references [15–21], the linear spring coefficient is determined to maximize the stable region of the trivial solution of the host system. Subsequently, the nonlinear spring is designed to ensure supercritical behavior and to mitigate the LCOs in the postcritical range. A fundamental result of this paper is that, if properly designed, the linear and nonlinear springs of the NLTVA can complement each other giving rise to a very effective LCO

G. Habib (✉) • G. Kerschen
Space Structures and Systems Laboratory (S3L), Structural Dynamics Research Group, Department of Aerospace and Mechanical Engineering, University of Liège, Liège, Belgium
e-mail: giuseppe.habib@ulg.ac.be; g.kerschen@ulg.ac.be

G. Kerschen (ed.), *Nonlinear Dynamics, Volume 1*, Conference Proceedings of the Society for Experimental Mechanics Series, DOI 10.1007/978-3-319-15221-9_11

suppression and management strategy. The example that will serve to validate the proposed developments is the Van der Pol–Duffing (VdPD) oscillator [30], which is a paradigmatic model for the description of self-excited oscillations. The bifurcation behavior of the VdPD oscillator was studied in [31, 32] whereas its stabilization using active control was proposed in [33–35].

The paper is organized as follows. Section 11.2 introduces the three design objectives pursued in this paper. In Sect. 11.3, optimal values for the linear parameters of the NLTVA are determined using stability analysis of the coupled system. Section 11.4 investigates the bifurcations occurring at the loss of stability and proposes an analytical tuning rule for the nonlinear coefficient of the NLTVA. In Sect. 11.5, the reduction of the LCO amplitude in the postcritical range is discussed. Local and global analyses are carried out using normal form theory and the MATCONT software, respectively. Finally, conclusions are drawn in Sect. 11.6.

11.2 Problem Formulation

The primary system considered throughout this work is the Van der Pol–Duffing (VdPD) oscillator:

$$m_1 q_1'' + c_1 \left(q_1^2 - 1\right) q_1' + k_1 q_1 + k_{nl1} q_1^3 = 0 \tag{11.1}$$

where m_1, c_1, k_1 and k_{nl1} are the oscillator's mass, damping and the coefficients of the linear and cubic springs, respectively. For instance, for an in-flow wing, the terms $c_1 \left(q_1^2 - 1\right) q_1'$ and $k_{nl1} q_1^3$ would model the fluid-structure interaction and the structural nonlinearity, respectively. The trivial equilibrium point of the system loses stability when $\mu_1 = c_1/2\sqrt{k_1 m_1} = 0$. Loss of stability occurs through either a supercritical Hopf bifurcation or a subcritical Hopf bifurcation. This latter scenario is dangerous, because stable large-amplitude LCOs can co-exist with the stable equilibrium point [36].

The objective of the present study is to mitigate, or even completely eliminate, the LCOs of the VdPD oscillator through the attachment of a fully passive nonlinear vibration absorber, termed the NLTVA [29]. One salient feature of the NLTVA compared to existing nonlinear absorbers is that the absorber's load-deflection curve is not imposed a priori, but it is rather synthesized according to the nonlinear restoring force of the primary system. The equations of motion of the coupled VdPD and NLTVA system are:

$$\begin{aligned} &m_1 q_1'' + c_1 \left(q_1^2 - 1\right) q_1' + k_1 q_1 + k_{nl1} q_1^3 + c_2 \left(q_1' - q_2'\right) + g\left(q_1 - q_2\right) = 0 \\ &m_2 q_2'' + c_2 \left(q_2' - q_1'\right) - g\left(q_1 - q_2\right) = 0 \end{aligned} \tag{11.2}$$

where m_2 and c_2 are the absorber's mass and viscous damping, respectively. The NLTVA is assumed to have a generic smooth elastic force $g(q_1 - q_2)$ with $g(0) = 0$.

The design problem is as follows. The mass ratio $\varepsilon = m_2/m_1$ (and, hence, the absorber mass) is prescribed by obvious practical constraints; $\varepsilon = 0.05$ is considered in the numerical examples of this paper. The damping coefficient c_2 and the absorber's stiffness $g(q_1 - q_2)$ should be determined so as to:

1. Maximize the stable region of the VdPD oscillator by displacing the Hopf bifurcation toward large positive values of μ_1 (Fig. 11.1a);
2. Avoid a catastrophic bifurcation scenario by transforming the potentially subcritical Hopf bifurcation of the VdPD into a supercritical Hopf bifurcation of the coupled system (Fig. 11.1b);
3. Reduce the amplitude of the remaining LCOs (Fig. 11.1c).

These three design objectives are studied in detail in the next three sections.

11.3 Elimination of Limit Cycles Through Stability Analysis

The first design objective is to stabilize the trivial solution of the VdPD oscillator for values of μ_1 greater than 0. Because the stability of an equilibrium point of a nonlinear system is governed only by the local underlying linear system, the NLTVA should comprise a linear spring for increased flexibility, i.e., $g\left(q_1 - q_2\right) = k_2 \left(q_1 - q_2\right) + g_{nl}\left(q_1 - q_2\right)$. The system of interest for the stability analysis is therefore

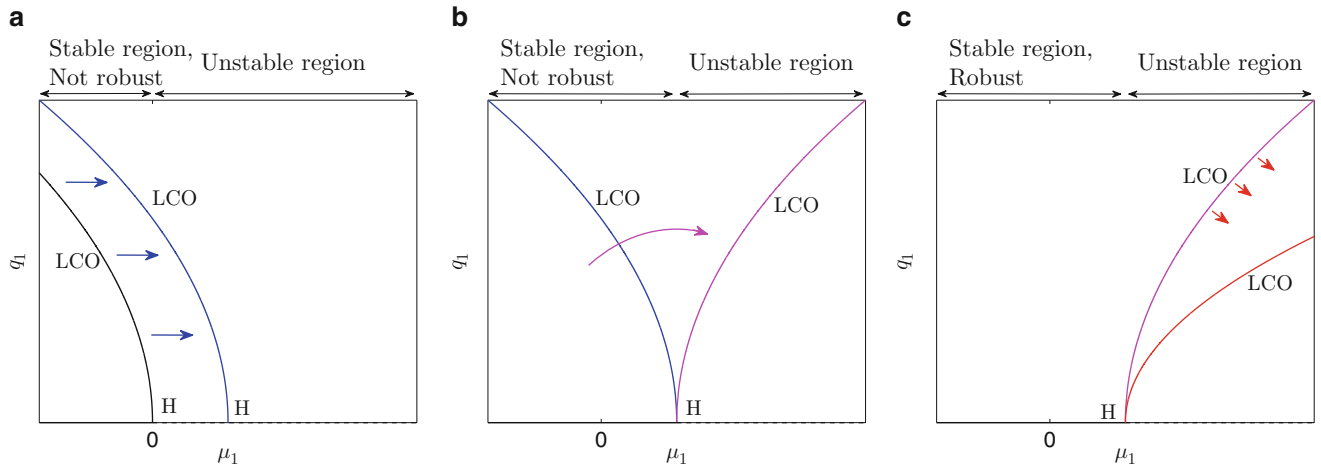

Fig. 11.1 Subcritical VdPD oscillator with an attached NLTVA. (**a**) Enlargement of the stable region of the equilibrium point of the VdPD oscillator; (**b**) transformation of the subcritical Hopf bifurcation into a supercritical Hopf bifurcation; (**c**) reduction of the amplitude of the remaining LCOs. H stands for Hopf bifurcation

$$\begin{aligned} m_1 q_1'' - c_1 q_1' + k_1 q_1 + c_2 \left(q_1' - q_2'\right) + k_2 \left(q_1 - q_2\right) = 0 \\ m_2 q_2'' + c_2 \left(q_2' - q_1'\right) + k_2 \left(q_2 - q_1\right) = 0 \end{aligned} \tag{11.3}$$

Introducing the variables $\omega_{n1}^2 = k_1/m_1$, $\omega_{n2}^2 = k_2/m_2$, $\mu_2 = c_2/(2m_2\omega_{n2})$, $\gamma = \omega_{n2}/\omega_{n1}$, the dimensionless time $\tau = t/\omega_{n1}$ and the variable $q_d = q_1 - q_2$, and recasting the equations in matrix form yield

$$\begin{bmatrix} 1 & 0 \\ 0 & 1 \end{bmatrix} \begin{bmatrix} \ddot{q}_1 \\ \ddot{q}_d \end{bmatrix} + \begin{bmatrix} -2\mu_1 & 2\mu_2\gamma\varepsilon \\ -2\mu_1 & 2\mu_2\gamma\left(1+\varepsilon\right) \end{bmatrix} \begin{bmatrix} \dot{q}_1 \\ \dot{q}_d \end{bmatrix} + \begin{bmatrix} 1 & \gamma^2\varepsilon \\ 1 & \gamma^2\left(1+\varepsilon\right) \end{bmatrix} \begin{bmatrix} q_1 \\ q_d \end{bmatrix} = \begin{bmatrix} 0 \\ 0 \end{bmatrix} \tag{11.4}$$

or in compact form $\mathbf{M}\ddot{\mathbf{q}} + \mathbf{C}\dot{\mathbf{q}} + \mathbf{K}\mathbf{q} = \mathbf{0}$. The dot indicates derivation with respect to the dimensionless time τ.

As reported for a similar system in [20], the trivial solution of Eq. (11.4) is asymptotically stable if and only if the roots of the characteristic polynomial $\det\left(z^2\mathbf{M}\ddot{\mathbf{q}} + z\mathbf{C}\dot{\mathbf{q}} + \mathbf{K}\mathbf{q}\right) = 0$ have negative real parts. Figure 11.2a depicts the stability chart in the μ_1, μ_2, γ space obtained from direct evaluation of the roots. The surface, which represents the stability boundary, peaks along the μ_1 axis at point C, meaning that the trivial solution can no longer be stable beyond this point. Performing the stability analysis through Routh-Hurwitz criterion the coordinates of point C can be found analytically. These allow us to define the optimal values of μ_2 and γ to maximize the value of μ_1 that gives stability, namely

$$\mu_{2\text{opt}} = \frac{1}{2}\sqrt{\frac{\varepsilon}{1+\varepsilon}}, \quad \gamma_{\text{opt}} \frac{1}{\sqrt{1+\varepsilon}} \tag{11.5}$$

which gives $\mu_{1\text{max}} = \sqrt{\varepsilon}/2$.

11.4 Enforcement of Supercritical Hopf Bifurcations Through Normal Form Analysis

The second design objective is to ensure the robustness of the trivial solution, i.e., no stable LCO can coexist with the stable equilibrium, as depicted in Fig. 11.1b. Since supercritical Hopf bifurcations are sought in the coupled system, a detailed investigation of the bifurcations occurring at the loss of stability is the main focus of the present section. Because bifurcation characterization depends on the nonlinear coefficient of the NLTVA, this analysis will allow us to define the optimal value of this coefficient whereas the linear coefficients of the NLTVA should remain close to their optimal values (11.5), i.e., $\gamma = 0.976$ and $\mu_2 = 0.109$ for $\varepsilon = 0.05$.

Another key element that remains to be determined is the mathematical expression of the NLTVA's elastic force $g(q_1 - q_2)$. A reasoning based upon local analysis is adopted herein. First, fractional-order terms are not considered, since they would be

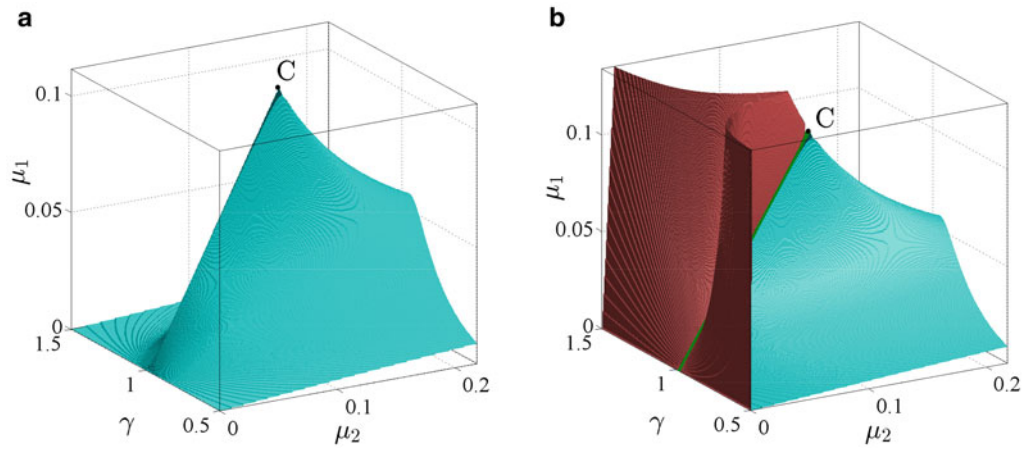

Fig. 11.2 Stability chart in the μ_1, μ_2, γ space for $\varepsilon = 0.05$. The *blue surface* (**a**, **b**) indicates the stability boundary whereas the *red surface* (**b**) indicates the boundary of the region with four eigenvalues with positive real parts. The coupled system loses stability through double Hopf bifurcations along the *green line* (**b**) (Color figure online)

transformed into terms of integer orders by the Taylor series expansion during bifurcation analysis. Terms of degree higher than 3 have negligible effects on the local dynamics; they would be neglected during the transformation into normal form. Although it is difficult to anticipate it without performing the analysis, quadratic terms give much less freedom for tuning the NLTVA compared to cubic terms. For these reasons, the nonlinear spring of the NLTVA is chosen to be cubic, and, hence, the coupled system writes

$$\begin{aligned} m_1 q_1'' + c_1\left(q_1^2 - 1\right) q_1' + k_1 q_1 + k_{nl1} q_1^3 + c_2\left(q_1' - q_2'\right) + k_2\left(q_1 - q_2\right) \\ + k_{nl2}\left(q_1 - q_2\right)^3 = 0 \\ m_2 q_2'' + c_2\left(q_2' - q_1'\right) + k_2\left(q_2 - q_1\right) + k_{nl2}\left(q_2 - q_1\right)^3 = 0 \end{aligned} \tag{11.6}$$

Considering dimensionless coordinates, we transform the system into first-order differential equations

$$\begin{bmatrix} \dot{x}_1 \\ \dot{x}_2 \\ \dot{x}_3 \\ \dot{x}_4 \end{bmatrix} = \begin{bmatrix} 0 & 1 & 0 & 0 \\ -1 & 2\mu_1 & -\gamma^2\varepsilon & -2\mu_2\gamma\varepsilon \\ 0 & 0 & 0 & 1 \\ -1 & 2\mu_1 & -\gamma^2(1+\varepsilon) & -2\mu_2\gamma(1+\varepsilon) \end{bmatrix} \begin{bmatrix} x_1 \\ x_2 \\ x_3 \\ x_4 \end{bmatrix} + \begin{bmatrix} 0 \\ -2\mu_1 x_1^2 x_2 - \alpha_3 x_1^3 - \beta_3 \varepsilon x_3^3 \\ 0 \\ -2\mu_1 x_1^2 x_2 - \alpha_3 x_1^3 - \beta_3 (1+\varepsilon) x_3^3 \end{bmatrix} \tag{11.7}$$

or in compact form $\dot{\mathbf{x}} = \mathbf{W}\mathbf{x} + \mathbf{b}$. The variables $x_1 = q_1$, $x_2 = \dot{q}_1$, $x_3 = q_d$, $x_4 = \dot{q}_d$, $\alpha_3 = k_{nl1}/k_1$ and $\beta_3 = k_{nl2}/(k_1\varepsilon)$ have been introduced in these equations.

When stability is lost, one or two pairs of complex conjugate eigenvalues of $\mathbf{W}$ leave the left half plane, which corresponds to single or double Hopf bifurcation, respectively. As reported in [20], a double Hopf bifurcation is likely to occur when $\gamma = \gamma_{\text{opt}}$ and $\mu_2 \leq \mu_{\text{opt}}$. This assertion is confirmed in Fig. 11.2b, which superposes the boundary of the region with four eigenvalues with positive real parts on the stability boundary of Fig. 11.2a. If the coupled system loses stability along the green line where two pairs of complex conjugate eigenvalues have zero real part, a double Hopf bifurcation is encountered.

11.4.1 Single Hopf Bifurcation

The analysis is first focused on the single Hopf bifurcation scenario for which $\mathbf{W}$ has a pair of complex conjugate eigenvalues with zero real part $\lambda_{1,2} = k_1 \pm j\omega_1$ and two other eigenvalues λ_3 and λ_4 with negative real parts. Defining a transformation matrix through the eigenvectors of $\mathbf{W}$, we can decouple the linear part of the system. Then, applying a center manifold

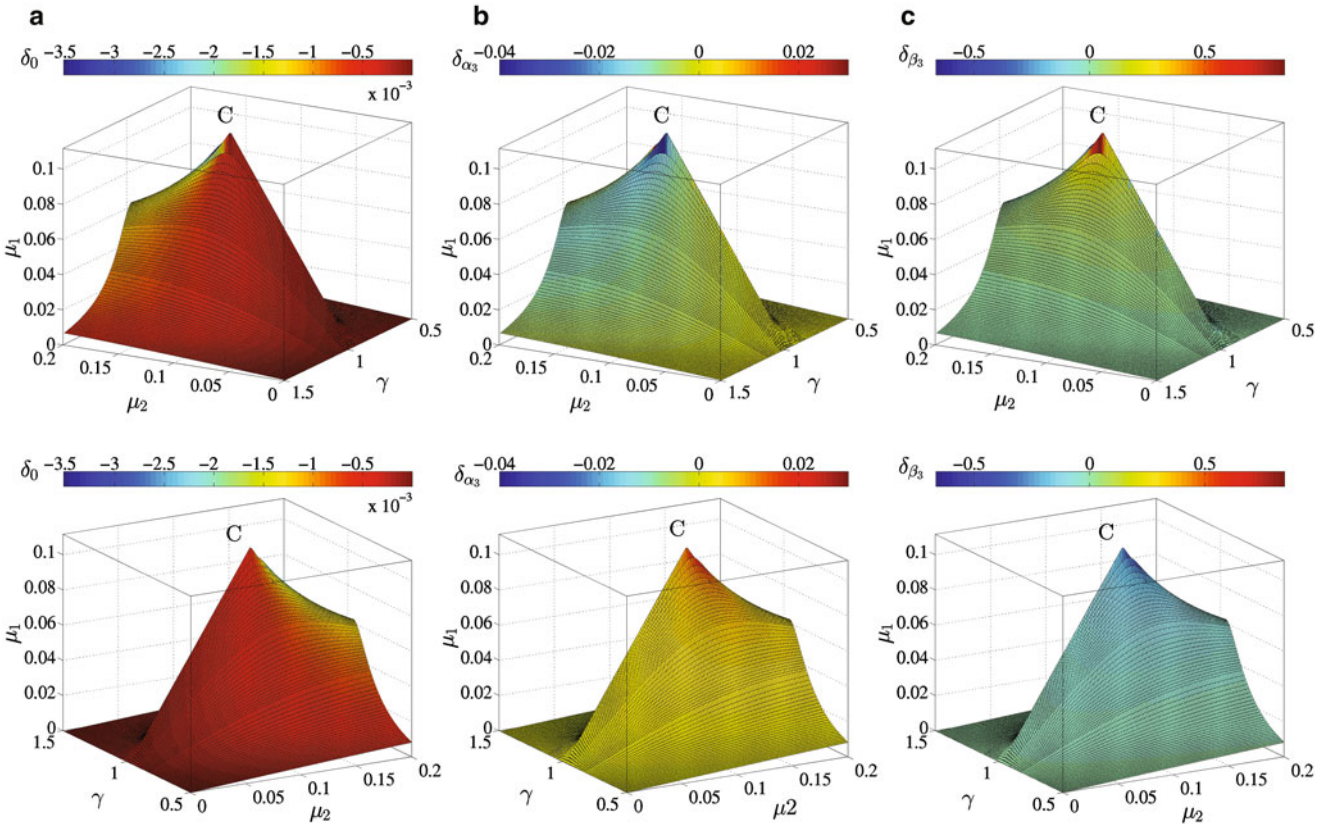

Fig. 11.3 Values of (**a**) δ_0, (**b**) δ_{α_3} and (**c**) δ_{β_3} along the stability boundary in the μ_1, μ_2, γ space for $\varepsilon = 0.05$. The *color* indicates the value of the corresponding coefficient. To facilitate the visualization, two different views of the same surface are given (*top* and *bottom plots*) (Color figure online)

reduction it is possible to eliminate the variable not related to the bifurcation, reducing the dimension of the system without affecting the local dynamics. Performing then a transformation in complex form, a near identity transformation and a transformation in polar coordinates, we obtain the normal form of a Hopf bifurcation, i.e.

$$\dot{r} = k_1 r + \delta r^3. \tag{11.8}$$

Equation (11.8) has solutions $r_0 = 0$ and $r^* = \sqrt{-k_1/\delta}$. The coefficient δ can be expressed as a linear function of the nonlinear coefficients α_3 and β_3:

$$\delta = \delta_0(\varepsilon, \gamma, \mu_1, \mu_2) + \delta_{\alpha_3}(\varepsilon, \gamma, \mu_1, \mu_2)\alpha_3 + \delta_{\beta_3}(\varepsilon, \gamma, \mu_1, \mu_2)\beta_3, \tag{11.9}$$

where δ_0, δ_{α_3}, and δ_{β_3} are defined analytically in the procedure just briefly described.

From Eq. (11.8), we see that the bifurcation is supercritical if $\delta < 0$ and subcritical if $\delta > 0$. Our objective should therefore be to design the nonlinear spring β_3 of the NLTVA to impose negative values of δ. Ideally, this nonlinear tuning should be carried out in the vicinity of γ_{opt} and $\mu_{2\text{opt}}$ so as to maintain LCO onset at large values of μ_1. Figure 11.3 displays the values of the coefficients δ_0, δ_{α_3} and δ_{β_3} along the stability boundary in the μ_1, μ_2, γ space. Figure 11.4 considers a section of these plots for $\mu_2 = 1.1\mu_{2\text{opt}} = 0.12$ for which stability is lost through a single Hopf bifurcation.

The case of a LTVA (i.e., $\beta_3 = 0$) attached to the VdPD is investigated, and positive values of α_3 are first considered. Because δ_0 is always negative (this means that the system with no structural nonlinearity is always supercritical), our attention should be focused on the value of δ_{α_3}. Figures 11.3b and 11.4b evidence a symmetric behavior for δ_{α_3}, i.e., it is positive (negative) below (above) $\gamma \approx \gamma_{\text{opt}}$. This uncertainty on the sign of δ_{α_3} in the region of optimum tuning poses an important practical difficulty, because a supercritical bifurcation cannot confidently be enforced in this region. The solution to avoid a catastrophic bifurcation scenario is to detune the NLTVA toward larger values of γ, which guarantees negative values of δ_{α_3}. However, this detuning is associated with a significant decrease in the value of $\mu_{1\text{max}}$. For instance, considering $\gamma = 1$ decreases $\mu_{1\text{max}}$ by approximately 30 %. Following a similar reasoning, we conclude that the NLTVA should be detuned toward smaller values of γ for negative values of α_3.

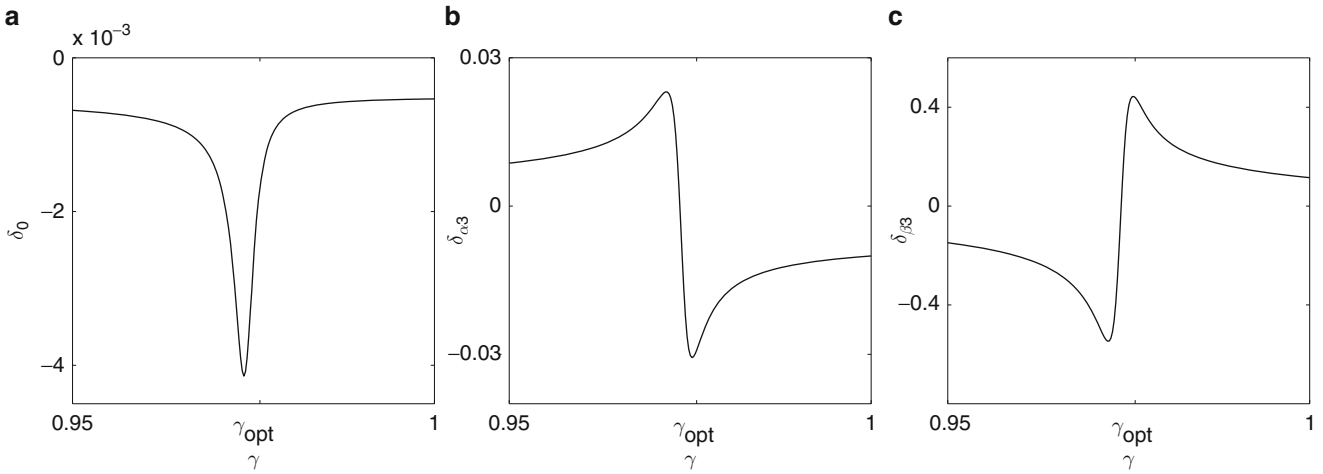

Fig. 11.4 Values of (**a**) δ_0, (**b**) δ_{α_3} and (**c**) δ_{β_3} for $\mu_2 = 0.12$ and $\varepsilon = 0.05$

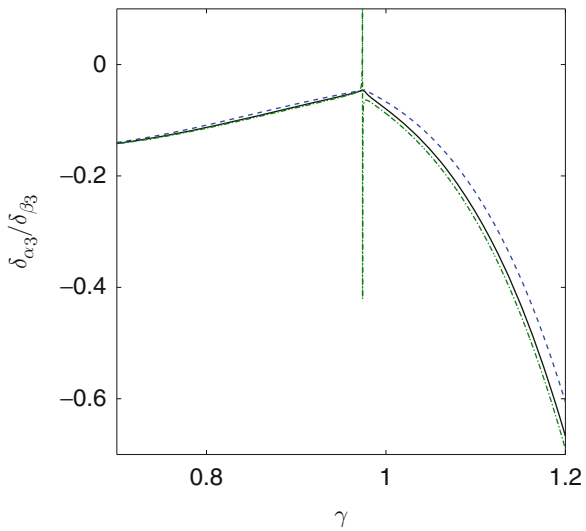

Fig. 11.5 Ratio $\delta_{\alpha_3}/\delta_{\beta_3}$ as a function of γ for fixed values of μ_2 and $\varepsilon = 0.05$. *Dashed blue lines*: $\mu_2 = 0.07$, *solid black lines*: $\mu_2 = \mu_{2\text{opt}} = 0.1091$, *dash-dotted green lines*: $\mu_2 = 0.12$. The *dash-dotted green curve* goes to infinity when $\delta_{\beta_3} = 0$; this is not a problem because δ_{α_3} goes to 0 almost at the same time (Color figure online)

The NLTVA presents increased flexibility with respect to the LTVA, because β_3 represents an additional tuning parameter. However, Figs. 11.3c and 11.4c show that the sign of δ_{β_3} in the optimal tuning region is as difficult to predict as for δ_{α_3}. Interestingly, δ_{α_3} and δ_{β_3} have consistently an opposite sign, which is confirmed by plotting their ratio in Fig. 11.5. Since $\delta_{\alpha_3}/\delta_{\beta_3} \approx -0.05$ close to γ_{opt}, $\delta_{\alpha_3}\alpha_3 + \delta_{\beta_3}\beta_3 \approx 0$ if $\beta_3 \approx 0.05\alpha_3$. In other words, the potentially detrimental effect of the structural nonlinearity of the VdPD on the bifurcation behavior can be compensated through a proper design of the NLTVA's nonlinearity. Unlike the LTVA, the NLTVA can therefore be designed to enforce supercritical bifurcations in the optimal tuning region. At this stage, we provide a further justification of the cubic nonlinearity of the NLTVA. For a quadratic spring in the NLTVA, Eq. (11.9) would comprise the term $\delta_{\beta_2}\beta_2^2$ instead of $\delta_{\beta_3}\beta_3$. The compensation effect would not be achievable, because the sign of $\delta_{\beta_2}\beta_2^2$ could not be influenced by β_2.

11.4.2 Two Intersecting Single Hopf Bifurcations

Although the investigation of the double Hopf bifurcation that occurs along the green line in Fig. 11.2b is beyond the scope of this paper, the separate analysis of the two intersecting single Hopf bifurcations gives already some insight into the dynamics. The eigenvalues of $\mathbf{W}$ at point C are $\lambda_{1,2} = \pm j$ and $\lambda_{3,4} = \pm j/\sqrt{1+\varepsilon}$. By performing the analysis outlined in the previous section, first considering $\lambda_{1,2}$ as the critical eigenvalues and then $\lambda_{3,4}$, we obtain respectively

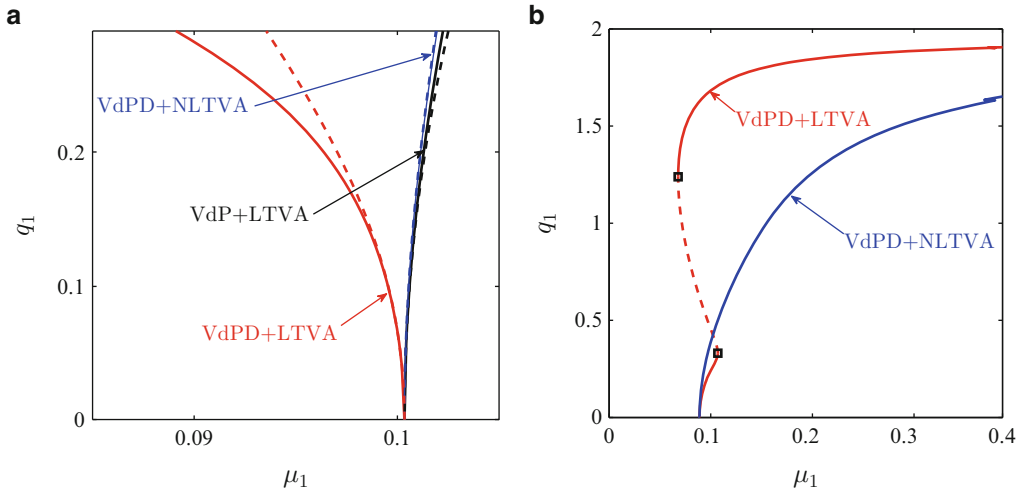

Fig. 11.6 Bifurcation diagrams for $\mu_2 = 0.12$ and $\varepsilon = 0.05$. (**a**) $\gamma = 0.970$, (**b**) $\gamma = 0.985$. *Black*: VdP+LTVA ($\alpha_3 = 0$ and $\beta_3 = 0$); *red*: VdPD+LTVA ($\alpha_3 = 0.3$ and $\beta_3 = 0$); *blue*: VdPD+NLTVA ($\alpha_3 = 0.3$ and $\beta_3 = 0.0136$). *Dashed lines*: numerical results (MATCONT); *solid lines*: analytical results (Color figure online)

$$\delta_{1,2} = \frac{1}{8}\left(-\frac{\varepsilon\sqrt{\varepsilon}}{1+\varepsilon} + \frac{3\sqrt{\varepsilon}}{1+\varepsilon}\alpha_3 - \frac{3(1+\varepsilon)}{\sqrt{\varepsilon}}\beta_3\right) \tag{11.10}$$

$$\delta_{3,4} = \frac{3}{8}\left(-\sqrt{\varepsilon}\alpha_3 + \frac{(1+\varepsilon)^2}{\sqrt{\varepsilon}}\beta_3\right). \tag{11.11}$$

The remarkable feature of Eqs. (11.10) and (11.11) is that the ratio between δ_{α_3} and δ_{β_3} is $\delta_{\alpha_3}/\delta_{\beta_3} = -\varepsilon/(1+\varepsilon)^2$ and it is constant. The important practical consequence of this result is that the effect of α_3 can be locally entirely compensated by $\beta_3 = \varepsilon/(1+\varepsilon)^2\alpha_3$. It can be shown in fact that this ratio is constant along the whole line of double Hopf bifurcations. We also note that this formula is in excellent agreement with the expression $\delta_{\alpha_3}/\delta_{\beta_3} \approx -0.05$ obtained in the single Hopf case for $\varepsilon = 0.05$.

11.4.3 Proposed Tuning Rule for the Nonlinear Coefficient of the NLTVA

According to the analysis in the previous sections, a fundamental result of this paper is that a properly-tuned NLTVA can annihilate the effect of the structural nonlinearity of the VdPD. Even though it is strictly valid along the line of double Hopf bifurcations, the tuning rule proposed herein for the nonlinear coefficient is

$$\beta_3 = \varepsilon/(1+\varepsilon)^2\alpha_3. \tag{11.12}$$

We anticipate that this rule is also valid in regions of single Hopf bifurcations, which is verified in this section.

The bifurcation diagrams predicted using the analytical developments of Sect. 11.4.1 and the numerical continuation software MATCONT [37] are depicted in Fig. 11.6. Slightly detuned linear parameters, i.e., $\mu_2 = 0.12$, $\gamma = 0.97/0.985$, are considered to show the robustness of our findings. Loss of stability occurs through a single Hopf bifurcation for the two parameter sets. Figure 11.6 presents an excellent qualitative agreement between the analytical and numerical curves; the quantitative differences observed at higher values of q_1 are due to the fact that the analytical results are only valid locally. When there is no structural nonlinearity ($\alpha_3 = 0$ and $\beta_3 = 0$), the bifurcation remains supercritical, and the LTVA works effectively on the classical VdP oscillator. The introduction of the structural nonlinearity ($\alpha_3 = 0.3$) in the VdP oscillator gives rise to a subcritical or supercritical bifurcation in Fig. 11.6a, b, respectively. This result confirms the difficulty to predict the bifurcation behavior of the coupled VdPD and LTVA system in the optimal region; it also highlights the detrimental role played by the structural nonlinearity of the VdPD oscillator. Conversely, the introduction of nonlinearity in the absorber

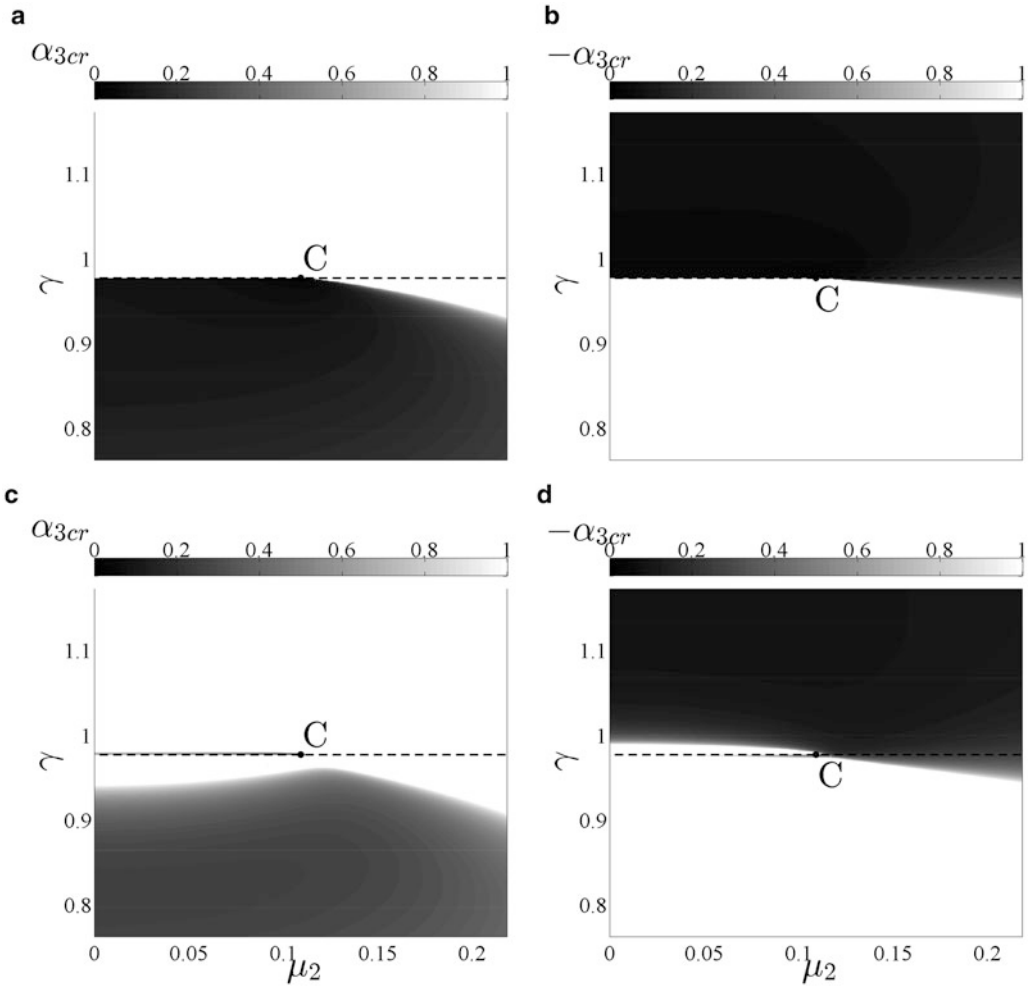

Fig. 11.7 Maximal value of α_3 below which supercritical bifurcations for the LTVA (**a**, **b**) and NLTVA (**c**, **d**) are guaranteed ($\varepsilon = 0.05$, $\beta_3 = 0$ (**a**, **b**) and $\beta_3 = \varepsilon/(1+\varepsilon)^2\alpha_3$). (**a**, **c**) Positive values of α_3; (**b**, **d**) negative values of α_3. The *dashed line* corresponds to $\gamma = \gamma_{\text{opt}}$ and the *dot* to $\mu_2 = \mu_{2\text{opt}}$

($\beta_3 = 0.0136$) allows to guarantee a supercritical bifurcation, as for the system without nonlinearity. The compensation effect brought by the NLTVA is therefore clearly demonstrated.

For a more global perspective, Fig. 11.7a, b display the maximal value of α_3 below which supercritical bifurcations for the LTVA are encountered. To avoid very large values in the vicinity of double Hopf bifurcations, the color map was trimmed at 1. It is seen that the point C of optimal tuning of γ and μ_2 lies at the boundary between 0 and 1, resulting in a design with virtually zero robustness. For positive (negative) values of α_3, the solution for a robust absorber is to increase either γ or μ_2 (decrease γ), which necessarily results in an earlier LCO onset, i.e., $\mu_{1\text{max}} < \sqrt{\varepsilon}/2$.

Figure 11.7c, d represent the same results for the NLTVA. For positive values of α_3, point C now lies well inside the region where supercriticality is guaranteed, which clearly highlights the benefit of the NLTVA. For negative values of α_3, the optimal point lies close to the boundary between 0 and 1, which means that there is much less margin for a robust design than for positive α_3. However, compared to the LTVA with negative α_3, the NLTVA still possesses a larger region of supercritical behavior. Specifically, there is a new region $\gamma \approx \gamma_{\text{opt}}$ and $\mu_2 < \mu_{2\text{opt}}$ in which supercritically can be guaranteed.

Finally, Fig. 11.8 presents the probability to have a supercritical bifurcation as a function of α_3 (in absolute value). To reflect a realistic design scenario, uncertainty of $\pm$ 1 % and $\pm$ 5 % on the values of γ and μ_2 around point C, respectively, are considered. Again, the superiority of the NLTVA over the LTVA is evident in these plots.

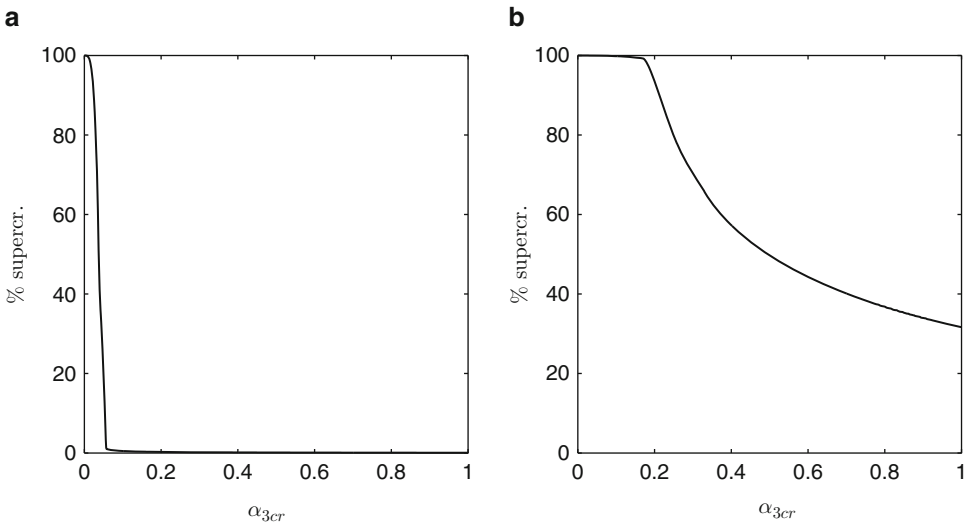

Fig. 11.8 Probability to have a supercritical bifurcation for different values of α_3 (in absolute value). (**a**) LTVA; (**b**) NLTVA. γ and μ_2 are within $\pm 1\,\%$ and $\pm 5\,\%$ of the corresponding optimum value, respectively

11.5 Reduction of the Amplitude of Limit Cycle Oscillations

At this stage, the linear and nonlinear parameters of the NLTVA have been designed through stability (Sect. 11.3) and bifurcation (Sect. 11.4) analyses, respectively. There is therefore no much freedom left to mitigate the amplitudes of the LCOs in the post-bifurcation regime.

11.5.1 Local Analysis

Considering the normal form of a Hopf bifurcation, the amplitude of the generated LCOs is proportional to $\sqrt{-k_1/\delta}$, where k_1 is the real part of the eigenvalue related to the bifurcation (see Sect. 11.4.1). Because $k_1 = 0$ at the loss of stability, we consider its linear approximation, i.e., $k_1 \approx (\mathrm{d}k_1/\mathrm{d}\mu_1)\,|_{\mu_1=\mu_{1\mathrm{cr}}}(\mu_1 - \mu_{1\mathrm{cr}})$. The LCO amplitude in the vicinity of the loss of stability is therefore

$$r \approx \sqrt{-\left.\frac{\mathrm{d}k_1}{\mathrm{d}\mu_1}\right|_{\mu_1=\mu_{1\mathrm{cr}}} \frac{\mu_1 - \mu_{1\mathrm{cr}}}{\delta}}, \tag{11.13}$$

The maximal value of the LCO in physical space (q_1^*), computed performing backward the transformation through which the normal form was obtained, is represented along the stability boundary in Fig. 11.9. It can be observed that the amplitude of the LCOs is minimized close to the optimal tuning region, which signifies that the design of the previous sections is also relevant for LCO mitigation.

11.5.2 Global Analysis

The previous analytical developments are valid only in the neighborhood of the bifurcation leading to LCO onset. The MATCONT software [37] is now utilized to investigate large-amplitude LCOs.

Figure 11.10a, b plot bifurcation diagrams for the case of a single Hopf bifurcation at the loss of stability. The same parameter values as those in Fig. 11.6 are used, but greater values of q_1 are investigated. A major difference with the local analysis is that fold bifurcations that can turn supercritical behavior into subcritical behavior are now encountered, which confirms the importance of global analysis. If the pair of folds that appears for the NLTVA in Fig. 11.10a cannot be considered as particularly detrimental, this is not the case for the LTVA in Fig. 11.10b, where bistability in a significant portion of the stable region compromises the robustness of the linear absorber.

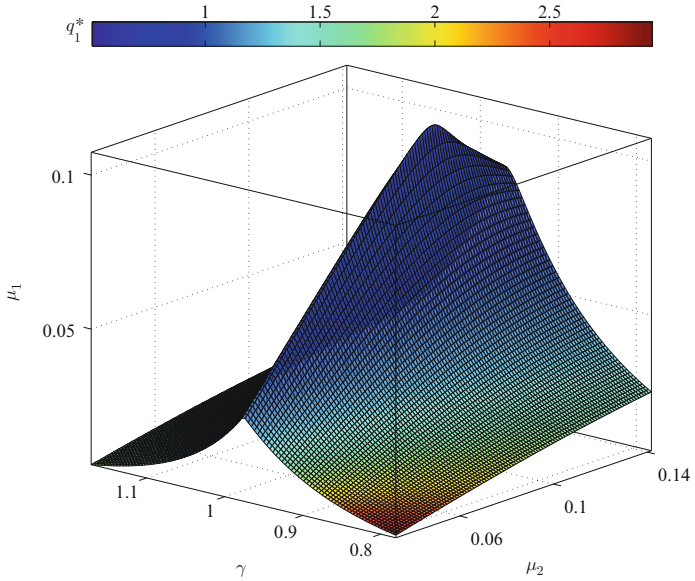

Fig. 11.9 LCO amplitude along the stability boundary for $\alpha_3 = 0.08$, $\varepsilon = 0.05$, $\beta_3 = \varepsilon/(1+\varepsilon)^2\alpha_3 = 0.0036$ and $\mu_1 - \mu_{1\text{cr}} = 0.01$

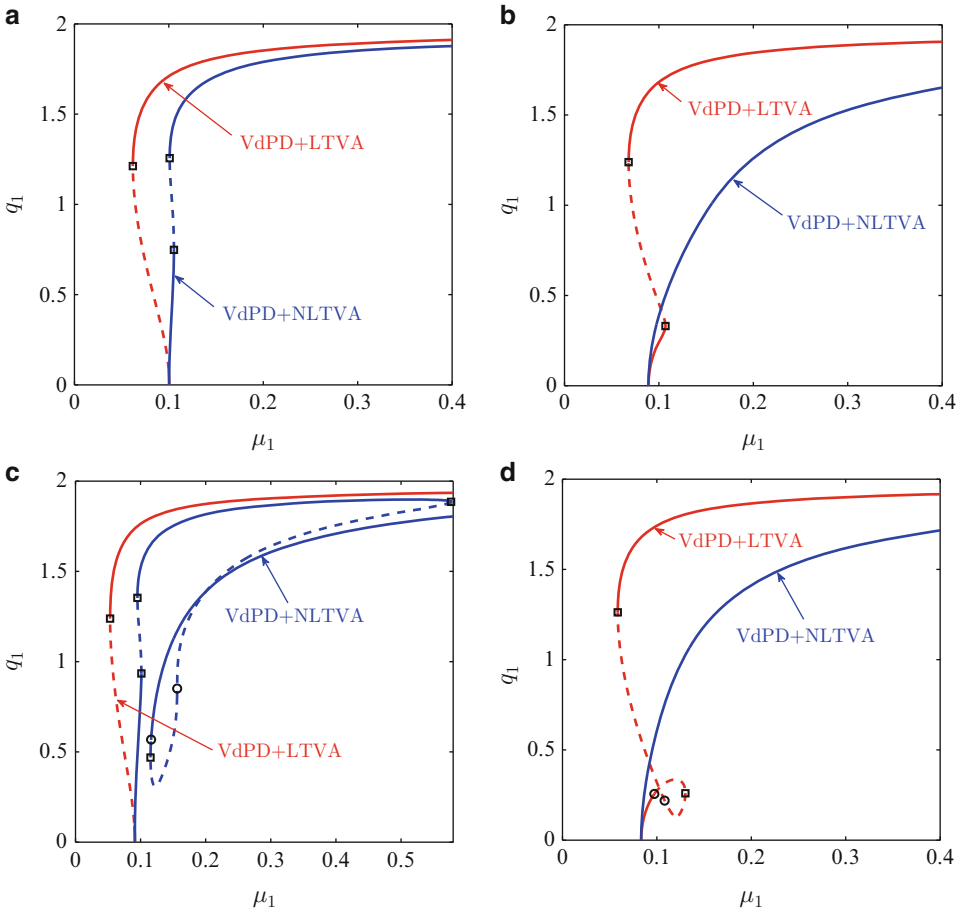

Fig. 11.10 Bifurcation diagrams for $\mu_2 = 0.12$ (**a**, **b**) and $\mu_2 = 0.097$ (**c**, **d**), $\alpha_3 = 0.3$ and $\varepsilon = 0.05$. (**a**, **c**) $\gamma = 0.970$, (**b**, **d**) $\gamma = 0.985$. *Red*: VdPD+LTVA ($\beta_3 = 0$); *blue*: VdPD+NLTVA ($\beta_3 = 0.0136$). *Squares*: fold bifurcations; *circles*: secondary Hopf bifurcations (Color figure online)

Figure 11.10c, d represent the same results for a lower value of μ_2 for which a double Hopf bifurcation is expected. The bifurcation diagrams are more complex with secondary Hopf (or Neimark-Sacker) bifurcations observed both for the LTVA and NLTVA; their analysis is beyond the scope of this paper. Apart from these new bifurcations, we note that the general trend of the curves is similar to that in Fig. 11.10, demonstrating a certain robustness of the absorbers with respect to parameter variations.

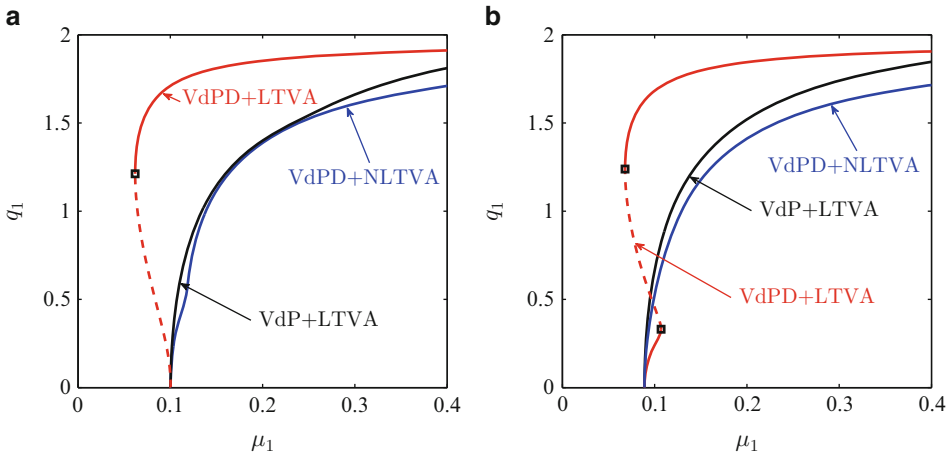

Fig. 11.11 Bifurcation diagrams for $\mu_2 = 0.12$ and $\varepsilon = 0.05$. (**a**) $\gamma = 0.970$, (**b**) $\gamma = 0.985$. *Black*: VdP+LTVA ($\alpha_3 = 0$ and $\beta_3 = 0$); *red*: VdPD+LTVA ($\alpha_3 = 0.3$ and $\beta_3 = 0$); *blue*: VdPD+NLTVA ($\alpha_3 = 0.3$ and $\beta_3 = 0.018$). *Squares*: fold bifurcations (Color figure online)

Figure 11.11 considers again the single Hopf case, but with a slightly greater value of the nonlinear coefficient of the NLTVA, i.e., $\beta_3 = 0.018$ instead of 0.0136. The NLTVA clearly outperforms the LTVA: not only LCO amplitudes are significantly smaller, but there is the complete absence of dangerous bistable regions. Another important result is the strong resemblance between the behaviors of the VdP+LTVA and VdPD+NLTVA systems. This suggests that the compensation of the nonlinearity of the VdPD by the nonlinearity of the NLTVA, which was observed in previous sections, is also valid at larger amplitudes.

11.6 Conclusions

The purpose of this paper was to investigate the performance of the NLTVA for suppression of self-excited oscillations of mechanical systems. A distinct advantage of this absorber is the complementary roles played by the linear and nonlinear springs.

Thanks to detailed stability and bifurcation analyses, a complete analytical design of the NLTVA, i.e., $\gamma = 1/\sqrt{1+\varepsilon}$, $\mu_2 = \sqrt{\varepsilon}/(2\sqrt{1+\varepsilon})$ and $\beta_3 = \varepsilon/(1+\varepsilon)^2\alpha_3$, was obtained. Although the double Hopf bifurcation scenario was not investigated herein, the preference should still be given to loss of stability through single Hopf bifurcations, which gives rise to simpler dynamics. This scenario can be enforced by, e.g., a small increase in the absorber damping μ_2. The numerical validation of the analytical predictions also highlighted the benefit of considering a slightly greater value of the nonlinear coefficient β_3 compared to that suggested by the analytical formula.

Eventually, the NLTVA was shown to be effective for LCO suppression and mitigation, as it maximizes the stability of the trivial equilibrium point, guarantees supercritical bifurcations and reduces the amplitude of the remaining LCOs. Another interesting feature of the NLTVA is that its nonlinearity can be tuned to annihilate the effects of the potentially detrimental nonlinearity of the primary system. This compensation mechanism is appealing and clearly deserves more attention in future studies.

Acknowledgements The authors G. Habib and G. Kerschen would like to acknowledge the financial support of the European Union (ERC Starting Grant NoVib 307265).

References

1. Denegri CM Jr (2000) Limit cycle oscillation flight test results of a fighter with external stores. J Aircraft 37:761–769
2. Trickey ST, Virgin LN, Dowell EH (2002) The stability of limit cycle oscillations in a nonlinear aeroelastic system. Proc R Soc A 458:2203–2226
3. Stepan G (2001) Modelling nonlinear regenerative effects in metal cutting. Philos Trans R Soc A 359:739–757
4. Mann BP, Bayly PV, Davies MA, Halley JE (2004) Limit cycles, bifurcations and accuracy of the milling process. J Sound Vib 277:31–48
5. von Wagner U, Hochlenert D, Hagedorn P (2007) Minimal models for disk brake squeal. J Sound Vib 302:527–539

6. Coudeyras N, Sinou JJ, Nacivet S (2009) A new treatment for predicting the self-excited vibrations of nonlinear systems with frictional interfaces: the constrained harmonic balance method with application to disc brake squeal. J Sound Vib 379:1175–1199
7. Depouhon A, Detournay E (2014) Instability regimes and self-excited vibrations in deep drilling systems. J Sound Vib 333:2019–2039
8. Griffin OM, Skop RA (1973) The vortex-excited resonant vibrations of circular cylinders. J Sound Vib 31:235–249
9. Ko J, Kurdila A, Strganac T (1997) Nonlinear control of a prototypical wing section with torsional nonlinearity. J Guid Control Dyn 20:1181–1189
10. Papatheou E, Tantaroudas ND, Da Ronch A, Cooper JE, Mottershead JE (2013) Active control for flutter suppression: an experimental investigation. In: Proceedings of the international forum on aeroelasticity and structural dynamics (IFASD), Bristol, 2013
11. van Dijk NJM, van de Wouw N, Doppenberg EJJ, Oosterling JAJ, Nijmeijer H (2012) Robust active chatter control in the high-speed milling process. IEEE Trans Control Syst Technol 20:901–917
12. Stepan G (1989) Retarded dynamical systems: stability and characteristic functions. Longman, New York
13. Niculescu SI, Gu K (2004) Advances in time-delay systems. Springer, Berlin
14. Habib G, Rega G, Stepan G (2012) Nonlinear bifurcation analysis of a single-DoF model of a robotic arm subject to digital position control. J Comput Nonlinear Dyn 8:011009
15. Mansour WM (1972) Quenching of limit cycles of a van der Pol oscillator. J Sound Vib 25:395–405
16. Tondl A (1975) Quenching of self-excited vibrations equilibrium aspects. J Sound Vib 42:251–260
17. Rowbottom MD (1981) The optimization of mechanical dampers to control self-excited galloping oscillations. J Sound Vib 75:559–576
18. Fujino Y, Abe M (1993) Design formulas for tuned mass dampers based on a perturbation technique. Earthq Eng Struct Dyn 22:833–854
19. Natsiavas S (1993) Vibration absorbers for a class of self-excited mechanical systems. J Appl Mech 60:382–387
20. Gattulli V, Di Fabio F, Luongo A (2001) Simple and double Hopf bifurcations in aeroelastic oscillators with tuned mass dampers. J Franklin Inst 338:187–201
21. Gattulli V, Di Fabio F, Luongo A (2003) One to one resonant double hopf bifurcation in aeroelastic oscillators with tuned mass dampers. J Sound Vib 262:201–217
22. Gattulli V, Di Fabio F, Luongo A (2004) Nonlinear tuned mass damper for self-excited oscillations. Wind Struct 7:251–264
23. Haxton RS, Barr ADS (1972) The autoparametric vibration absorber. J Manuf Sci Eng 94:119–125
24. Vyas A, BajaJ AK (2001) Dynamics of autoparametric vibration absorbers using multiple pendulums. J Sound Vib 246:115–135
25. Lee YS, Vakakis AF, Bergman LA, McFarland DM (2006) Suppression of limit cycle oscillations in the Van der Pol oscillator by means of passive nonlinear energy sinks. Struct Control Heal Monitor 13:41–47
26. Gendelman OV, Bar T (2010) Bifurcations of self-excitation regimes in a Van der Pol oscillator with a nonlinear energy sink. Physica D 239:220–229
27. Luongo A, Zulli D (2014) Aeroelastic instability analysis of NES-controlled systems via a mixed multiple scale/harmonic balance method. J Vib Control 20:1985–1998
28. Lacarbonara W, Cetraro M (2011) Flutter control of a lifting surface via visco-hysteretic vibration absorbers. Int J Aeronaut Space Sci 2:331–345
29. Habib G, Detroux T, Viguié R, Kerschen G (2015) Nonlinear generalization of Den Hartog's equal-peak method. Mech Syst Signal Process. Elsevier 52:17–28
30. Guckenheimer J, Holmes P (1983) Nonlinear oscillations, dynamical systems and bifurcations of vectors fields. Springer, New York
31. Ebelin W, Herzel H, Richert W, Schimansky-Geier L (1986) Influence of noise on Duffing-Van der Pol oscillators. J Appl Math Mech 66:141–146
32. Szemplinska-Stupnicka W, Rudowski J (1997) The coexistence of periodic, almost periodic and chaotic attractors in the Van der Pol–Duffing oscillator. J Sound Vib 199:165–175
33. Xu J, Chung KW (2003) Effects of time delayed position feedback on a van der Pol–Duffing oscillator. Physica D 180:17–39
34. Ji JC, Hansen CH (2006) Stability and dynamics of a controlled van der Pol–Duffing oscillator. Chaos Solitons Fractals 28:555–570
35. Li X, Ji JC, Hansen CH, Tan C (2006) The response of a Duffing–van der Pol oscillator under delayed feedback control. J Sound Vib 91:644–655
36. Nayfeh AH, Balachandran B (2007) Applied nonlinear dynamics, analytical, computational, and experimental methods. Wiley, New York
37. Dhooge A, Govaerts W, Kuznetsov YA (2003) MATCONT: a MATLAB package for numerical bifurcation analysis of ODEs. J ACM Trans Math Softw 29:141–164

Chapter 12
Nonlinear Vibrations of a Flexible L-shaped Beam Using Differential Quadrature Method

Hamed Samandari and Ender Cigeroglu

Abstract Flexible L-shaped beams are integrated sub-components of several navy and space structures where overall response of the system is affected by these structures. Hence, an understanding of the dynamical properties of these structural systems is required for their design and control. Recent studies show that the dynamic response of beam like structures undergoing large deformation is nonlinear in nature where phenomenon such as jump and chaotic response can be detected.

In this study, nonlinear free vibrations of L-shaped beams are studied using a continuous beam model with a focus on the internal resonance of these structures. Nonlinearity considered is due to large deflection of the beams (geometric nonlinearity). Hamilton principle and Euler Bernoulli beam theory are used to obtain the nonlinear equations of motion. The differential quadrature method (DQM) is utilized to discretize the partial differential equations of motion in spatial domain, which resulted in a nonlinear set of ordinary differential equations of motion in time domain. Harmonic balance method is used to convert the ordinary differential equations of motion into a set of nonlinear algebraic equations which is solved numerically. Numerical simulations, based on the mathematical model, are presented to analyze the nonlinear responses of the L-shape beam structure.

Keywords Nonlinear vibrations • L-shaped beam • Differential quadrature method • Geometric nonlinearity • Euler-Bernoulli beam theory

12.1 Introduction

Flexible structures composed of beams are one of the most important components of engineering structures [1]. Recent studies confirmed that response of these structures are affected significantly by their geometric nonlinearity as they go through large deflections. Understanding the nonlinear dynamics of flexible structures becomes more essential with recent advances in science and deployment of these structures in advance engineering structures such as space stations and energy harvesters [2, 3], Among flexible beam structures, L-shaped beam structures are the most common ones and the dynamics of them have been studied by several researchers in the past decades. Haddow et al. [4] were one of the first who studied the planar dynamic responses of a flexible L-shaped beam-mass structure analytically and experimentally. Later, similar structures are studied by Nayfeh and Zavodney [5], Nayfeh and Balachandran [6–8], and several other researchers [9–14]. The internal resonance of an L-shaped beam structure is studied in [15, 16] where motion of the structure is limited by using several stops. In a detailed study, Nayfeh and Pai (2004) [1] have investigated the nonlinear dynamics of a similar structure to primary-resonant excitations, experimentally and theoretically. These studies confirmed that periodic and chaotic solutions, saddle-node and Hopf bifurcations and saturation phenomena can exist for the case of L-shaped beam structures. However, in all of these studies a reduced order model, two degrees of freedom model, is used to study the dynamics of the system. The reduced order model is obtained by utilizing a single trial function, which is the exact eigenfunction of the relevant linear system, in Galerkin type methods. However for nonlinear systems, the resulting nonlinear eigenfunctions can be significantly different than the eigenfunctions of the linear system, and depending on the nonlinearity, it may not be possible to capture the nonlinear characteristics correctly by using a single trial function [17–19]. Therefore, to determine the dynamics of L-shaped beams correctly, methods that can model and approximate the nonlinear eigenfunctions of the structure is required.

In the present study, nonlinear free vibrations of a flexible L-shaped beam is investigated using Differential quadrature method (DQM). DQM is a well-developed numerical method for quick solutions of linear and nonlinear partial differential equations. Furthermore, application of DQM eliminates the need for finding suitable trial functions that satisfies all the

H. Samandari • E. Cigeroglu (✉)
Department of Mechanical Engineering, Middle East Technical University, Ankara 06800, Turkey
e-mail: ender@metu.edu.tr

G. Kerschen (ed.), *Nonlinear Dynamics, Volume 1*, Conference Proceedings of the Society for Experimental Mechanics Series, DOI 10.1007/978-3-319-15221-9_12

boundary conditions and different boundary conditions can be studied with no extra effort. The nonlinear equations of motions are obtained by using Hamilton Principle and variational approach. Results indicate that in addition to equations of motion, boundary condition equations are also affected by nonlinear terms which can be treated by DQM very easily compared to Galerkin type methods.

12.2 Modeling

In this section the governing nonlinear partial differential equations of motion for an L-shaped beam are derived. As shown in Fig. 12.1, the structure is constructed from two beams one of which is connected to the free end of the other and a concentrated mass on each one of them. The structure is assumed to vibrate in plane where its motion in axial and transverse directions are denoted by $u_i(x,t)$ and $w_i(x,t)$ in which subscript i stands for the first and second beam. Based on the Euler–Bernoulli beam theory and the nonlinear strain–displacement relationship of Von Karman type [20], the relation between displacement field and strain can be written as follows

$$\varepsilon_i\left(x_i, z_i\right) = x_1 + \frac{1}{2}\left(\frac{\partial w_i\left(x_i, t\right)}{\partial x_i}\right)^2 - z_i \frac{\partial^2 w_i\left(x_i, t\right)}{\partial {x_i}^2}, \tag{12.1}$$

where x_i is the axial coordinate along the beam, t is the temporal variable, and $\varepsilon_i(x_i, z_i)$ is the corresponding strain at (x_i, z_i).

Using Hook's stress-strain law, i.e. $\sigma_i = E_i \varepsilon_i$, the potential energy stored in the beams due to bending can be written as follows

$$V = V_1 + V_2, \tag{12.2}$$

$$\begin{aligned} V_i &= \frac{1}{2}\int_0^{L_i}\int_A \sigma_i \cdot \varepsilon_i\left(x_i, z_i\right)\, dA\, dx = \frac{1}{2}\int_0^{L_i}\int_A E_i \cdot \left(\frac{\partial u_i}{\partial x_i} + \frac{1}{2}\left(\frac{\partial w_i}{\partial x_i}\right) - z\frac{\partial^2 w_i}{\partial {x_i}^2}\right)^2 dA\, dx_i \\ &= \frac{1}{2}\int_0^{L_i} E_i A_i \left(\frac{\partial u_i}{\partial x_i} + \frac{1}{2}\left(\frac{\partial w_i}{\partial x_i}\right)\right)^2 dx_i + \frac{1}{2}\int_0^{L_i} E_i I_i \left(\frac{\partial^2 w_i}{\partial {x_i}^2}\right)^2 dx_i, \end{aligned} \tag{12.3}$$

where $i = 1, 2$ indicating the first and second beams, respectively.

The total kinetic energy is composed of four items, two of which are related to the beams and the remaining two is related to the concentrated masses, which can be written as follows

$$T = \sum_i T_i = T_1 + T_2 + T_3 + T_4, \tag{12.4}$$

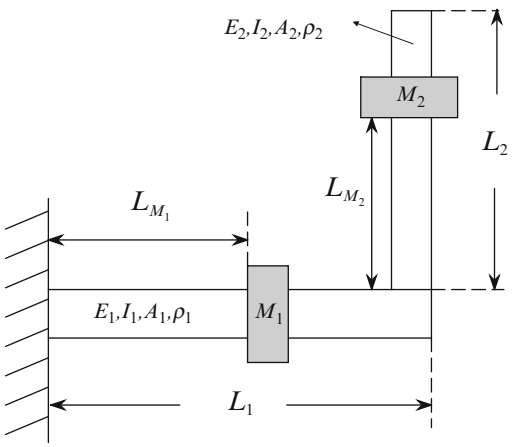

Fig. 12.1 Schematic of an L-shaped beam structure

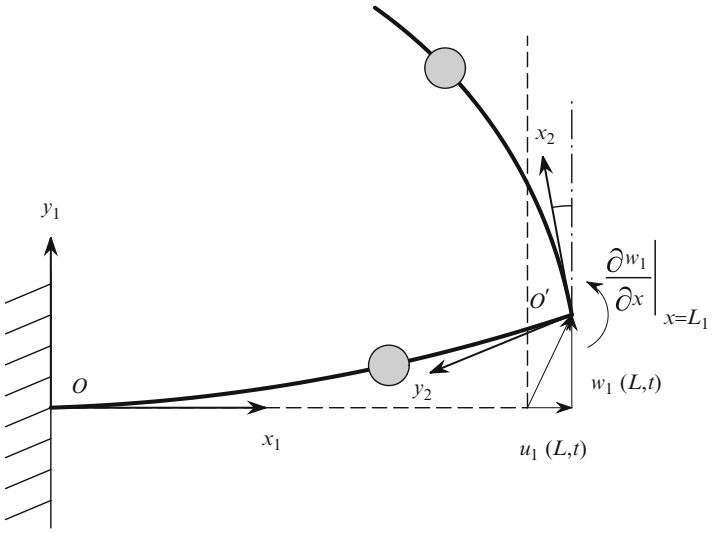

Fig. 12.2 Coordinate frames used

where

$$T_1 = \frac{1}{2}\int_0^{L_1} \rho_1 A_1 \cdot \dot{u}_1^2 \, dx_1 + \frac{1}{2}\int_0^{L_1} \rho_1 A_1 \cdot \dot{w}_1^2 \, dx_1, \tag{12.5}$$

$$T_2 = \frac{1}{2}\int_0^{L_2} \rho_2 A_2 \cdot \left(\left(\dot{u}_2 + \dot{w}_1|_{x_1=L_1}\right)^2 + \left(\dot{w}_2 + x_2 \dot{w}_1' \,|_{x_1=L_1} - \dot{u}_1|_{x_1=L_1}\right)^2 \right) dx_2, \tag{12.6}$$

$$T_3 = \frac{1}{2} M_1 \left(\int_0^{L_1} \dot{w}_1^2 \delta\left(x_1 - L_{M_1}\right) dx_1 + \int_0^{L_1} \dot{u}_1^2 \delta\left(x_1 - L_{M_1}\right) dx_1 \right), \tag{12.7}$$

$$T_4 = \frac{1}{2} M_2 \left(\int_0^{L_2} \left(\dot{w}_1\left(L_1\right) + \dot{u}_2\right)^2 \delta\left(x_2 - L_{M_2}\right) dx_2 + \int_0^{L_2} \left(\dot{w}_2 + x_2 \dot{w}_1'\left(L_1\right) - \dot{u}_1\left(L_1\right)\right)^2 \delta\left(x_2 - L_{M_2}\right) dx_2 \right), \tag{12.8}$$

T_1 and T_2 represent the kinetic energy of the first and second beams, respectively, whereas T_3 and T_4 stand for the kinetic energy of the concentrated masses. It is worth noting that as shown in Fig. 12.2, the reference frame of $x_2 O' y_2$ of the second beam is a moving coordinate frame with respect to inertial reference frame of $x_1 O y_1$. As a result, the kinetic energy of the second beam given by Eq. 12.6 contains terms related to motion of the first beam. $\delta(x)$ is the Dirac delta function, dots and primes represents partial derivatives with respect to temporal variable t and spatial coordinate x_i.

Hamilton's integral can be written as follows

$$\int_{t_1}^{t_2} \delta\left(T - V\right) \, dt = \int_{t_1}^{t_2} \delta T \, dt - \int_{t_1}^{t_2} \delta V \, dt = 0, \tag{12.9}$$

which is used to obtain the nonlinear equations of motion of the L-shaped beam. Substituting the potential energy and kinetic energy expression into Eq. 12.9, and setting the coefficients of δu_i, δw_i equal to zero lead to the following equations of motion for the first and second beams, respectively

$$-\left(\rho_1 A_1 + M_1 \delta\left(x_1 - L_{M_1}\right)\right) \ddot{u}_1 + \left[E_1 A_1 \left(u_1' + \frac{1}{2}\left(w_1'\right)^2 \right) \right]' = 0, \tag{12.10}$$

$$-\left(\rho_1 A_1 + M_1\delta\left(x_1 - L_{M_1}\right)\right)\ddot{w}_1 - E_1 I_1\, w_1^{(4)} + \left[E_1 A_1\left(u_1' + \frac{1}{2}\left(w_1'\right)^2\right)w_1'\right]' = 0, \tag{12.11}$$

$$-\left(\rho_2 A_2 + M_2\delta\left(x_2 - L_{M_2}\right)\right)\left(\ddot{u}_2 + \ddot{w}_1\left(L_1\right)\right) + \left[E_2 A_2\left(u_2' + \frac{1}{2}\left(w_2'\right)^2\right)\right]' = 0, \tag{12.12}$$

$$-\left(\rho_2 A_2 + M_2\delta\left(x_2 - L_{M_2}\right)\right)\left(\ddot{w}_2 + x_2\ddot{w}_1'\left(L_1\right) - \ddot{u}_1\left(L_1\right)\right) - E_2 I_2\, w_2^{(4)} + \left[E_2 A_2\left(u_2' + \frac{1}{2}\left(w_2'\right)^2\right)w_2'\right]' = 0, \tag{12.13}$$

Disregarding the kinetic energy due to axial motion of the beams i.e. $\ddot{u}_i = 0$ and integrating Eqs. 12.10 and 12.12 along the beam length and substituting in Eqs. 12.11 and 12.13, the equations of motion can be simplified as follows

$$-\left(\rho_1 A_1 + M_1\delta\left(x_1 - L_{M_1}\right)\right)\ddot{w}_1 - E_1 I_1\, w_1^{(4)} + \frac{E_1 A_1}{2L_1}\left(\int_0^{L_1}\left(w_1'\right)^2 dx_1\right)w_1'' = 0, \tag{12.14}$$

$$\begin{aligned}-\left(\rho_2 A_2 + M_2\delta\left(x_2 - L_{M_2}\right)\right)\left(\ddot{w}_2 + x_2\ddot{w}_1'\left(L_1\right)\right) - E_2 I_2\, w_2^{(4)} + \left(\frac{E_2 A_2}{2L_2}\int_0^{L_1}\left(w_1'\right)^2 dx_1\right)w_2'' \\ + \left(\rho_2 A_2 + M_2\delta\left(x_2 - L_{M_2}\right)\right)\ddot{w}_1\left(L_1\right)\left(w_2' - \left(0.5L_2 - x_2\right)w_2''\right) = 0,\end{aligned} \tag{12.15}$$

with the following nonlinear boundary conditions: for the first beam

$$w_1(0) = 0, \tag{12.16}$$

$$w_1'(0) = 0, \tag{12.17}$$

$$-\left(\int_0^{L_2}\left(\rho_2 A_2 + M_2\delta\left(x_2 - L_{M_2}\right)\right)dx_2\right)\ddot{w}_1\left(L_1\right) + E_1 I_1\, w_1'''\left(L_1\right) - \frac{E_1 A_1}{2L_1}\left(\int_0^{L_1}\left(w_1'\right)^2 dx_1\right)w_1'\left(L_1\right) = 0, \tag{12.18}$$

$$\int_0^{L_2}\left(\rho_2 A_2 + M_2\delta\left(x_2 - L_{M_2}\right)\right)\left(\ddot{w}_2 + x_2\ddot{w}_1'\left(L_1\right)\right)x_2 dx_2 + E_1 I_1\, w_1''\left(L_1\right) = 0, \tag{12.19}$$

and for the second beam

$$w_2(0) = 0, \tag{12.20}$$

$$w_2'(0) = 0, \tag{12.21}$$

$$E_2 I_2\, w_2'''\left(L_2\right) - \left(0.5L_2\left(\rho_2 A_2 + M_2\delta\left(x_2 - L_{M_2}\right)\right)\ddot{w}_1\left(L_1\right) + \frac{E_2 A_2}{2L_2}\int_0^{L_1}\left(w_1'\right)^2 dx_1\right)w_2'\left(L_2\right) = 0, \tag{12.22}$$

$$E_2 I_2\, w_2''\left(L_2\right) = 0. \tag{12.23}$$

12.3 Application of Differential Quadrature Method

Differential quadrature method (DQM) approximates the derivatives of a function with respect to a spatial variable at a given discrete point by a weighted linear summation of function values at all the discrete points in the computational domain. For example, the m^{th} derivative of a function $W_i(x)$ at the n^{th} point, x_n, can be estimated by [21]

$$W_i{}^{(m)}(x_n) = \sum_{j=1}^{N} c_{n,j}^{(m)}\, {}_jW_i = \left(c_{n,1}^{(m)}\ c_{n,2}^{(m)} \cdots c_{n,N}^{(m)}\right) \cdot \left({}_1W_i\ {}_2W_i \cdots {}_NW_i\right)^T = \mathbf{c_n^{(m)}}^T \cdot \mathbf{W}_i, \tag{12.24}$$

where $W_i^{(m)}(x_n)$ is the m^{th} order derivative of $W_i(x)$ at point x_n, ${}_jW_i = W_i\left(x_j\right)$, and N is the number of grid points utilized in the discretization of the partial derivatives. $c_{n,j}{}^{(m)}\ (j = 1, \ldots, N)$ are the weighting coefficients for the m^{th} derivative estimation of the n^{th} point, which are pre-determined [18, 21]. Further details on the utilizing DQM can be found in [18].

Assuming a harmonic solution in time for the beams, i.e. $w_i(x_i, t) = W_i(x_i) \cdot \cos(\omega t)$, the partial differential equation of motion given by Eqs. 12.14 and 12.15 can be converted into ordinary differential equations in the spatial domain x_i. Furthermore, substituting the DQM derivative approximations given by Eq. 12.24, the following nonlinear algebraic equations in matrix form is obtained

$$(\mathbf{K_L} + \mathbf{K_{NL}})_{2N\times 2N} \cdot \left\{\begin{matrix}\mathbf{W}_1\\ \mathbf{W}_2\end{matrix}\right\} = \omega^2 \mathbf{M}_{2N\times 2N} \cdot \left\{\begin{matrix}\mathbf{W}_1\\ \mathbf{W}_2\end{matrix}\right\} \tag{12.25}$$

$\mathbf{M}$, $\mathbf{K_L}$, and $\mathbf{K_{NL}}$ represent the mass, linear stiffness, and nonlinear stiffness matrices, respectively. Similarly, boundary condition equations can be written in matrix form as follows

$$\left(\mathbf{K_{BCs}} + \mathbf{K_{BCs}^{NL}} - \omega^2 \mathbf{M_{BCs}}\right) \cdot \left\{\begin{matrix}\mathbf{W}_1\\ \mathbf{W}_2\end{matrix}\right\} = 0 \tag{12.26}$$

where $\mathbf{K_{BCs}}$, $\mathbf{K_{BCs}^{NL}}$, and $\mathbf{M_{BCs}}$ indicate the mass, linear stiffness and nonlinear stiffness matrices associated with boundary equations. Considering the interior and boundary grid points (nodes) separately and using matrix manipulation, Eqs. 12.25 and 12.26 can be re-written as follows

$$\mathbf{K_D^{NL}} \cdot \mathbf{x_B} + \left(\mathbf{K_L^*} + \mathbf{K_{NL}^*} - \omega^2 \mathbf{M^*}\right) \cdot \mathbf{x_s} = \mathbf{0} \tag{12.27}$$

$$\left(\mathbf{K_B} + \mathbf{K_B^{NL}} - \omega^2 \mathbf{M_B}\right) \cdot \mathbf{x_B} + \left(\mathbf{K_s} + \mathbf{K_s^{NL}} - \omega^2 \mathbf{M_s}\right) \cdot \mathbf{x_s} = \mathbf{0} \tag{12.28}$$

Where

$$\mathbf{x_B} = \left({}_1W_1, {}_2W_1, {}_{N-1}W_1, {}_NW_1 \,|\, {}_1W_2, {}_2W_2, {}_{N-1}W_2, {}_NW_2\right)^T_{8\times 8} \tag{12.29}$$

$$\mathbf{x_s} = \left({}_3W_1\ {}_4W_1 \cdots {}_{N-2}W_1 \,\big|/\, {}_3W_2\ {}_4W_2 \cdots {}_{N-2}\ W_2\right)^T_{(2N-8)\times(2N-8)} \tag{12.30}$$

The definitions and dimensions of the above matrices are given in Table 12.1.

Solving $\mathbf{x_B}$ from Eq. 12.28 and substituting it into Eq. 12.27 and simplifying the resulting expression, the following nonlinear algebraic equation is obtained

$$\left[\left(\mathbf{K_L^*} + \mathbf{K_{NL}^*} - \omega^2 \mathbf{M^*}\right) - \mathbf{K_D}\left(\mathbf{K_B} + \mathbf{K_B^{NL}} - \omega^2 \mathbf{M_B}\right)^{-1}\left(\mathbf{K_s} + \mathbf{K_s^{NL}} - \omega^2 \mathbf{M_s}\right)\right] \cdot \mathbf{x_s} = 0 \tag{12.31}$$

However, even though boundary nodes are not present in the residual function, due to nonlinear matrices, $\mathbf{K_B^{NL}}$ and $\mathbf{K_s^{NL}}$, the equation indirectly depends on $\mathbf{x_B}$ as expressed by Eq. 12.28 as well. In order to overcome this difficulty, Eqs. 12.31 and 12.28 are solved simultaneously by using Newton's method with arc-length continuation details of which are given in Cigeroglu and Samandari [17]. The residual vector function used in Newton's method is defined as follows

Table 12.1 Dimension of matrices

	Description	Size
Equation of motion		
$\mathbf{K_D^{NL}}$	Displacement dependent nonlinear stiffness matrix for boundary nodes	$(2N-8)\times 8$
$\mathbf{K_L^*}$	Linear stiffness matrix for interior nodes	$(2N-8)\times(2N-8)$
$\mathbf{K_{NL}^*}$	Displacement dependent nonlinear stiffness matrix for interior nodes	$(2N-8)\times(2N-8)$
$\mathbf{M}^*$	Mass matrix for interior nodes	$(2N-8)\times(2N-8)$
Boundary condition equations		
$\mathbf{K_B}$	Stiffness matrix of boundary nodes	8×8
$\mathbf{K_B^{NL}}$	Displacement dependent nonlinear stiffness matrix of boundary nodes	8×8
$\mathbf{M_B}$	Mass matrix for boundary nodes	8×8
$\mathbf{K_s}$	Stiffness matrix for interior nodes	$8\times(2N-8)$
$\mathbf{K_s^{NL}}$	Displacement dependent nonlinear stiffness matrix for interior nodes	$8\times(2N-8)$
$\mathbf{M_s}$	Mass matrix for interior nodes	$8\times(2N-8)$

$$\mathbf{r}\left(\begin{Bmatrix}\mathbf{x_s}\\ \mathbf{x_B}\end{Bmatrix},\omega\right)=\left[\frac{\left(\mathbf{K_L^*}+\mathbf{K_{NL}^*}-\omega^2\mathbf{M}^*\right)-\mathbf{K_D}\left(\mathbf{K_B}+\mathbf{K_B^{NL}}-\omega^2\mathbf{M_B}\right)^{-1}\left(\mathbf{K_s}+\mathbf{K_s^{NL}}-\omega^2\mathbf{M_s}\right)}{\left(\mathbf{K_B}+\mathbf{K_B^{NL}}-\omega^2\mathbf{M_B}\right)}\middle|\frac{\mathbf{0}}{\mathbf{K_s}+\mathbf{K_s^{NL}}-\omega^2\mathbf{M_s}}\right]\begin{Bmatrix}\mathbf{x_s}\\ \mathbf{x_B}\end{Bmatrix} \tag{12.32}$$

12.4 Results

The material and geometric parameters of the L-shaped beams used in this study are given in Table 12.2. Two set of parameters: Structure 1 and Structure 2 are defined to study the effect of key parameters of the beams on system response. In order to present the results in a proper form, the linear and nonlinear natural frequencies are normalized with respect to the first linear natural frequency of Structure 1 and Structure 2. Furthermore, vibration amplitudes are normalized with respect to $\sqrt{I_1/A_1}$.

Firstly, linear vibrations of the structures are studied and verified with available results in literature. It is worth mentioning that available results in literature are generally limited to the cases with simple and uniform geometry due to the limits of the methods used which requires exact eigenfunction of the system which is hard to find even for linear non-uniform cases. It is worth mentioning that a comparison function can be used in cases where the exact eigenfunction is unknown. However, the selected function should satisfy the nonlinear boundary conditions determined for this problem which requires significant effort. On the other hand, it is possible to overcome these difficulties very easily by using DQM, since similar to finite element methods, DQM works based on the values of functions at discrete points and it does not require any pre-knowledge of the system mode shapes. In the following sections using the proposed approach, linear and nonlinear free vibrations of L-shaped beams are studied.

12.4.1 Linear Vibrations

For the DQM analysis presented, the effect of number of grid points on the linear natural frequency of system is studied, where it is detected that the natural frequencies obtained are identical when the number of grid points is larger or equal to 14. Hence, in all the results presented, 18 grid points are used which is observed to be sufficient for the nonlinear cases as well. Table 12.3 shows a comparison between the results of the present study and the analytical results reported by [12] for a uniform L-shaped beam without any concentrated mass. For this case, parameters of Structure 1 given in Table 12.2 are used for the analysis. Identical results to the one reported in [12] are obtained.

The first two natural frequencies of the system for two cases are given in Table 12.4 and the corresponding mode shapes of the system are given in Fig. 12.3. It is worth noting that, for Structure 1, the first and the second beams have identical parameters; whereas, for Structure 2, the key parameters of beams are modified such that second natural frequency becomes approximately equal to two times of the first natural frequency of the system.

Table 12.2 Numerical values of system parameters

	Structure 1		Structure 2	
Parameter	1st beam	2nd beam	1st beam	2nd beam
Cross section height	0.5 mm	0.5 mm	1.69 mm	0.56 mm
Cross section width	10 mm	10 mm	12.83 mm	12.80 mm
Beam length	500 mm	500 mm	154.51 mm	152.40 mm
Young's modulus	200 GPa	200 GPa	200 GPa	250 GPa
Density	7,680 Kg/m^3	7,680 Kg/m^3	7,680 Kg/m^3	7,680 Kg/m^3
Mass of concentrated mass on beam	0 Kg	0 Kg	0 Kg	0.040 Kg
Position of concentrated mass on beam	0 mm	0 mm	0 mm	55.9 mm

Table 12.3 Comparison between results of present study and available results in literature

Frequency parameter $\beta(\omega = \beta^2\sqrt{EI_1/\rho A_1 L_1^4})$	Values	
	Present study	[12]
First	1.082488	1.082488
Second	1.786316	1.786316
Third	3.969206	3.969206
forth	4.805330	4.805330
Fifth	7.098548	7.098548

Table 12.4 First two natural frequencies of system-shaped beams

	Structure 1	Structure 2
First natural frequency, ω_1	5.431372 Hz	10.764607
Second natural frequency, ω_2	14.790400 Hz	21.854607
ω_2/ω_1	2.723143	2.030228

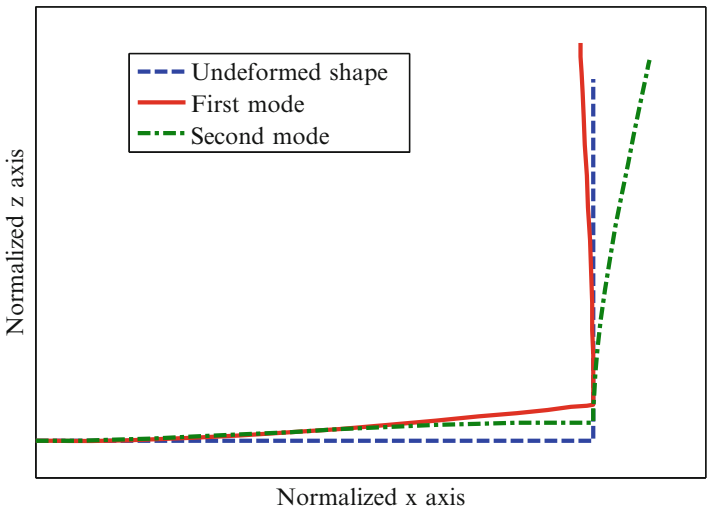

Fig. 12.3 First two linear mode shapes of the system

12.4.2 Nonlinear Free Vibrations

Figure 12.4 compares the variation of normalized nonlinear natural frequency of Structure 1 vibrating in the first mode of vibration obtained from the proposed approach including and excluding the effects of nonlinear terms in the boundary conditions and Galerkin method. The results of Galerkin's method are obtained considering a single trail function of the relevant linear system in the solution as it is been used in previous studies in literature. Results show that the nonlinear terms in boundary conditions have a significant effect on the variation of normalized nonlinear natural frequency. It is worth noting that the results of DQM disregarding the nonlinear terms and Galerkin's method are in good agreement. This is an expected result, since the mode shape anticipated by the DQM is very similar to the one used in Galerkin's method when nonlinear terms in the boundary equations are disregarded.

In Fig. 12.5, variation of normalized nonlinear natural frequency of Structure 1 vibrating in the first and the second vibration modes as a function of maximum vibration amplitude of the first and the second beam is given. Results show that

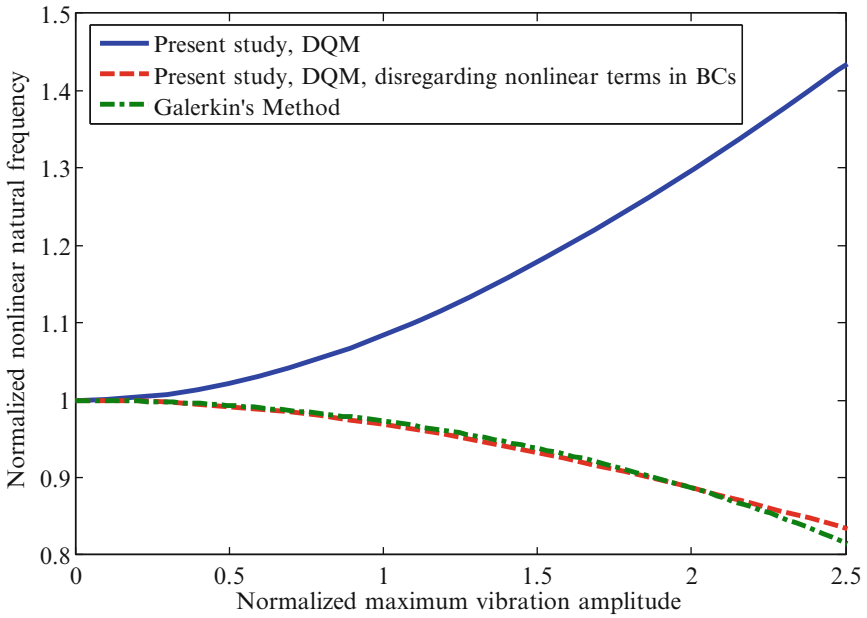

Fig. 12.4 Variation of normalized nonlinear natural frequency of Structure 1 with respect to normalized maximum vibration amplitude of the first beam

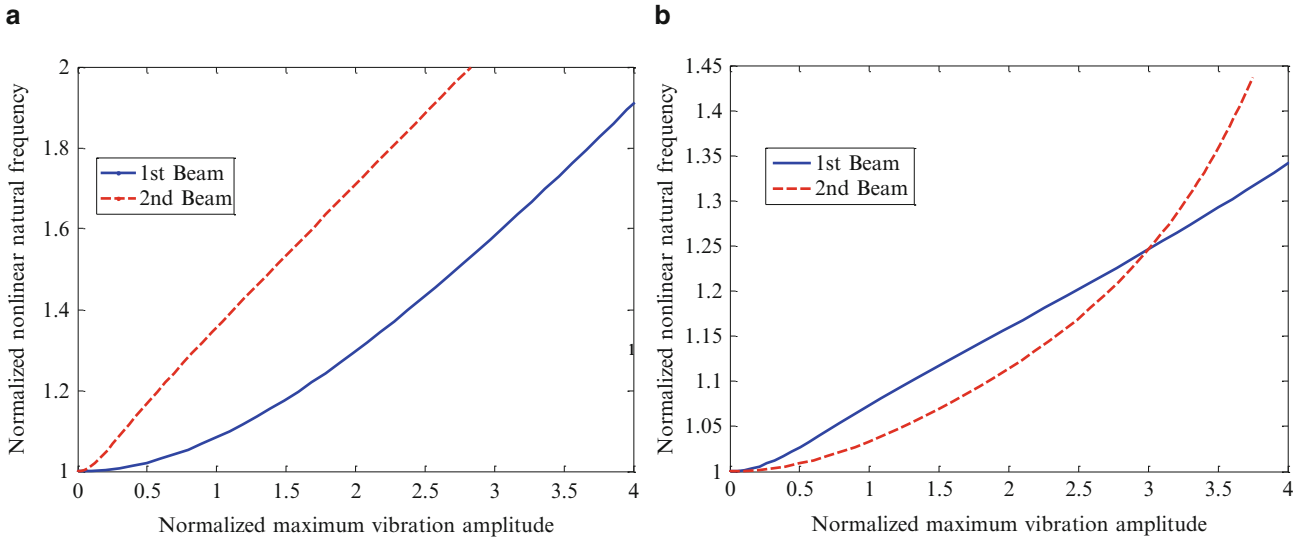

Fig. 12.5 Variation of normalized nonlinear natural frequency of Structure 1 (**a**) 1st mode (**b**) 2nd mode

the normalized nonlinear natural frequency increases as the normalized maximum vibration amplitude increases for both vibration modes. It is observed that the increase in the normalized nonlinear natural frequency is larger in the first mode compared to second mode. Figure 12.6 shows variation of normalized nonlinear natural frequency of Structure 2 vibrating in the first and the second vibration modes. It should be noted that the key parameters of Structure 2 is modified in such a way that the second natural frequency of the system is approximately two times of its first natural frequency. A hardening effect is also detected for this case as the maximum vibration amplitude increases. Studying the results given in Figs. 12.5 and 12.6, it can be observed that in the first vibration mode of Structure 1, beam 1 has larger vibration amplitude with respect to beam 2; whereas, the reverse is true for Structure 2. At the first vibration mode, the ratio of the vibration amplitudes of beam 2 to beam 1 for Structure 2 is significantly larger than the ratio of vibration amplitudes of beam 1 to beam 2 for Structure 1. At the second vibration mode, for Structure 1, both beams have comparable maximum vibration amplitudes; whereas, for Structure 2, beam 2 has a larger amplitude with respect to beam 1 and the amplitude ratio is larger than the ratio of the first vibration mode.

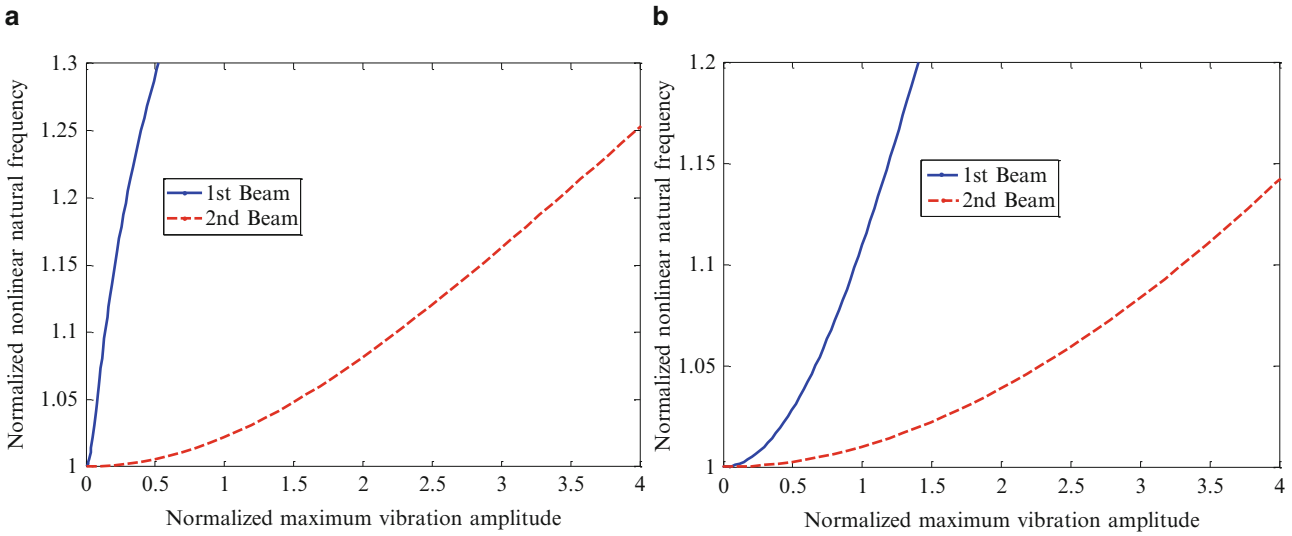

Fig. 12.6 Variation of normalized nonlinear natural frequency of Structure 2 (**a**) 1st mode (**b**) 2nd mode

12.5 Conclusion

In the present study, nonlinear free vibrations of an L-shaped beam is investigated. Hamilton's principle is used to obtain the nonlinear equations of motion and corresponding boundary conditions. It is shown that in addition to the equations of motion, boundary conditions are also affected by nonlinearities introduced by large deflections of the structure. In order to solve the resulting eigenvalue problem, differential quadrature method is used. Application of the DQM makes it possible to consider higher vibration modes of the structure in the discretization which cannot be done due to complexity in Galerkin type methods and especially due to nonlinear boundary conditions. Numerical case studies are performed and the results obtained by the present method is compared with Galerkin's method with a single trial function, which is the eigenfunction of the linear system. It is observed that Galerkin's method fails in predicting the system behavior correctly, since the trial function used cannot include the effects of nonlinearity in boundary conditions. On the other hand, it is possible to treat nonlinear boundary conditions by DQM; hence, it predicts the behavior of the structure correctly.

References

1. Nayfeh AH, Pai PF (2004) Linear and nonlinear structural mechanics. Wiley, Hoboken
2. Erturk A, Renno JM, Inman DJ (2009) Modeling of piezoelectric energy harvesting from an L-shaped beam-mass structure with an application to UAVs. J Intell Mater Syst Struct 20:529–544
3. Karami MA, Inman DJ (2010) Analytical modeling and experimental verification of the vibrations of the zigzag microstructure for energy harvesting. J Vib Acoust 133(1):011002. doi: 10.1115/1.4002783
4. Haddow A, Barr A, Mook D (1984) Theoretical and experimental study of modal interaction in a two-degree-of-freedom structure. J Sound Vib 97:451–473
5. Nayfeh A, Zavodney L (1988) Experimental observation of amplitude-and phase-modulated responses of two internally coupled oscillators to a harmonic excitation. J Appl Mech 55:706–710
6. Nayfeh A, Balachandran B (1990) Experimental investigation of resonantly forced oscillations of a two-degree-of-freedom structure. Int J Non Linear Mech 25:199–209
7. Balachandran B, Nayfeh A (1990) Nonlinear motions of beam-mass structure. Nonlinear Dyn 1:39–61
8. Balachandran B, Nayfeh A (1991) Observations of modal interactions in resonantly forced beam-mass structures. Nonlinear Dyn 2:77–117
9. Nayfeh A, Balachandran B, Colbert M, Nayfeh M (1989) An experimental investigation of complicated responses of a two-degree-of-freedom structure. J Appl Mech 56:960–967
10. Cao DX, Zhang W, Yao MH (2009) Theoretical and experimental investigation of an L-shape beam structure, Smasis 2008. In: Proceedings of the Asme conference on smart materials, adaptive structures and intelligent systems – 2008, vol 2, pp 437–442
11. Cao DX, Zhang W, Yao MH (2010) Analytical and experimental studies on nonlinear characteristics of an L-shape beam structure. Acta Mech Sinica 26:967–976
12. Gurgoze M (1998) On the dynamic analysis of a flexible L-shaped structure. J Sound Vib 211:683–688

13. Onozato N, Nagai K-i, Maruyama S, Yamaguchi T (2012) Chaotic vibrations of a post-buckled L-shaped beam with an axial constraint. Nonlinear Dyn 67:2363–2379
14. Oueini SS, Nayfeh AH, Pratt JR (1998) A nonlinear vibration absorber for flexible structures. Nonlinear Dyn 15:259–282
15. Pun D, Lau SL, Liu YB (1996) Internal resonance of an L-shaped beam with a limit stop.1. Free vibration. J Sound Vib 193:1023–1035
16. Pun D, Lau SL, Liu YB (1996) Internal resonance of an L-shaped beam with a limit stop.2. Forced vibration. J Sound Vib 193:1037–1047
17. Cigeroglu E, Samandari H (2012) Nonlinear free vibration of double walled carbon nanotubes by using describing function method with multiple trial functions. Physica E 46:160–173
18. Cigeroglu E, Samandari H (2014) Nonlinear free vibrations of curved double walled carbon nanotubes using differential quadrature method. Physica E 64:95–105
19. Shaw SW, Pierre C (1994) Normal modes of vibration for non-linear continuous systems. J Sound Vib 169:319–347
20. Rao J (1999) Dynamics of plates. Alpha Science, New Delhi
21. Tornabene F, Fantuzzi N, Ubertini F, Viola E (2015) Strong formulation finite element method based on differential quadrature: a survey. Appl Mech Rev 67(2):020801. doi: 10.1115/1.4028859

Chapter 13
Theoretical and Experimental Analysis of Bifurcation Induced Passive Bandgap Reconfiguration

Michael J. Mazzoleni, Brian P. Bernard, Nicolas Garraud, David P. Arnold, and Brian P. Mann

Abstract This paper presents a theoretical analysis and experimental validation of passively reconfigurable bandgaps in a 1D chain of oscillators. Nonlinearities in the system result in a morphing of the bandgap structure when the excitation amplitude passes a certain threshold. Specifically, an asymmetric bistability is used to achieve amplitude dependent filtering through passive bandgap reconfiguration. The experimental system consists of a 1D chain of axially aligned pendulums arranged in dimer unit cells with nearest neighbor coupling. Repulsive magnets are used to induce bistability in the pendulums. Comparisons between experiments and theory show good agreement.

Keywords Vibrations • Wave propagation • Bandgaps • Bifurcations • Bistability

13.1 Introduction

Wave propagation through periodic structures is a phenomenon of interest in mechanical, photonic, and electrical systems [1–3]. The study of wave propagation behavior in periodic structures has led to significant advances in signal processing, wave guiding, and vibration absorption technologies [4]. Periodic structures typically exhibit two fundamental modes: propagation and attenuation [5, 6]. In recent years, there has been significant interest in the design and development of metamaterials that have desirable wave propagation characteristics. One of the primary focuses of these studies is the manipulation of bandgaps in periodic structures.

Bandgaps are attenuation zones that exist between two propagation zones, and it is often desirable to tune these bandgaps for specific applications. Currently, there are two main approaches for tuning bandgap behavior. The first approach is based on design methodologies and utilizes careful selection of material properties and geometries [7–10]. However, once designed, the bandgap structures of these systems are fixed. The second approach is based on active control and tunes the bandgap behavior through component replacements, variable adjustments, and manual switching [11–14]. This approach enables the bandgap structure to reconfigure itself, but it requires human intervention and is not suitable for autonomous operation.

This paper builds upon previous studies conducted by the authors and presents a method for achieving passive bandgap reconfiguration, which enables the bandgap structure to alter its wave propagation characteristics in response to its environment [15, 16]. Therefore, this system is autonomous and adaptable. The system described in this paper achieves amplitude dependent filtering, which allows waves of a given frequency to propagate below a certain amplitude threshold. However, once the amplitude crosses that threshold, a bifurcation occurs and the waves are attenuated. A theoretical model is presented to explain this phenomenon, and an experimental setup is used to validate the model.

M.J. Mazzoleni (✉) • B.P. Mann
Dynamical Systems Laboratory, Department of Mechanical Engineering and Materials Science, Duke University, Durham, NC 27708, USA
e-mail: michael.mazzoleni@duke.edu; brian.mann@duke.edu

B.P. Bernard
Autonomous Systems Laboratory, Department of Mathematics, Schreiner University, Kerrville, TX 78028, USA
e-mail: bpbernard@schreiner.edu

N. Garraud • D.P. Arnold
Interdisciplinary Microsystems Group, Department of Electrical and Computer Engineering, University of Florida, Gainesville, FL 32611, USA
e-mail: darnold@ufl.edu

G. Kerschen (ed.), *Nonlinear Dynamics, Volume 1*, Conference Proceedings of the Society for Experimental Mechanics Series, DOI 10.1007/978-3-319-15221-9_13

13.2 Math Model

This section presents a mathematical model that describes the wave propagation characteristics of a 1D array of axially aligned pendulums. The pendulum array consists of repeating dimer unit cells consisting of two pendulums, and each pendulum is torsionally coupled to its neighbors. A schematic of this pendulum system is shown in Fig. 13.1. The system's bandgap regions are calculated by applying periodic boundary conditions to the system, assuming a traveling wave solution, and solving the resulting eigenvalue problem. Reconfigurable bandgaps are made possible by introducing bistability into the system through a nonlinear restoring torque. If the bistability is asymmetric, then the system will have two distinct bandgap profiles.

13.2.1 Equations of Motion

Consider a unit cell of the pendulum array which consists of two coupled pendulums with periodic boundary conditions and with a nonlinear restoring torque $f(\theta_2)$ applied to the second pendulum. The pendulums are assumed to be rods which each have a lumped mass added to them. The system will only exhibit a bandgap region when these masses are different. A homogeneous unit cell will result in a system with no bandgaps. The governing equations of motion for this system are

$$I\ddot{\theta}_1 + \left(\epsilon m_1 + \frac{m}{2}\right) gL \sin\theta_1 + 2k\left(\theta_1 - \theta_2\right) = 0, \tag{13.1}$$

$$I\ddot{\theta}_2 + \left(\epsilon m_2 + \frac{m}{2}\right) gL \sin\theta_2 + 2k\left(\theta_2 - \theta_1\right) + f\left(\theta_2\right) = 0, \tag{13.2}$$

where θ_j is the angular displacement of the jth pendulum, I is the mass moment of inertia of each pendulum, L is the length of each pendulum, ϵ is the ratio of the location of the added mass vs. the length of each pendulum rod, m is the mass of each pendulum rod, k is the linear torsional coupling constant between any two adjacent pendulums, g is the acceleration due to gravity, and m_j is the mass added to the jth pendulum. If $\epsilon = 1$, then the masses m_j are located at the tips of the pendulum rods. For convenience, the dimensionless time variable $\tau = t\sqrt{g/L}$ can be introduced and Eqs. (13.1) and (13.2) can be rewritten in dimensionless form as

$$\theta_1'' + \eta \sin\theta_1 + \kappa_1\left(\theta_1 - \theta_2\right) = 0, \tag{13.3}$$

$$\theta_2'' + \mu \sin\theta_2 + \kappa_2\left(\theta_2 - \theta_1\right) + F\left(\theta_2\right) = 0, \tag{13.4}$$

where $\theta_j'' = d^2\theta_j/d\tau^2 = \ddot{\theta}_j L/g$, $\eta = \left(6\epsilon\alpha + 3\right)/\left(6\epsilon^2\alpha + 2\right)$, $\mu = \left(6\epsilon\beta + 3\right)/\left(6\epsilon^2\beta + 2\right)$, $\kappa_1 = 6\kappa/\left(3\epsilon^2\alpha + 1\right)$, $\kappa_2 = 6\kappa/\left(3\epsilon^2\beta + 1\right)$, $F\left(\theta_2\right) = 3f\left(\theta_2\right)/\left(3\epsilon^2\beta + 1\right)mgL$, $\alpha = m_1/m$, $\beta = m_2/m$, and $\kappa = k/mgL$.

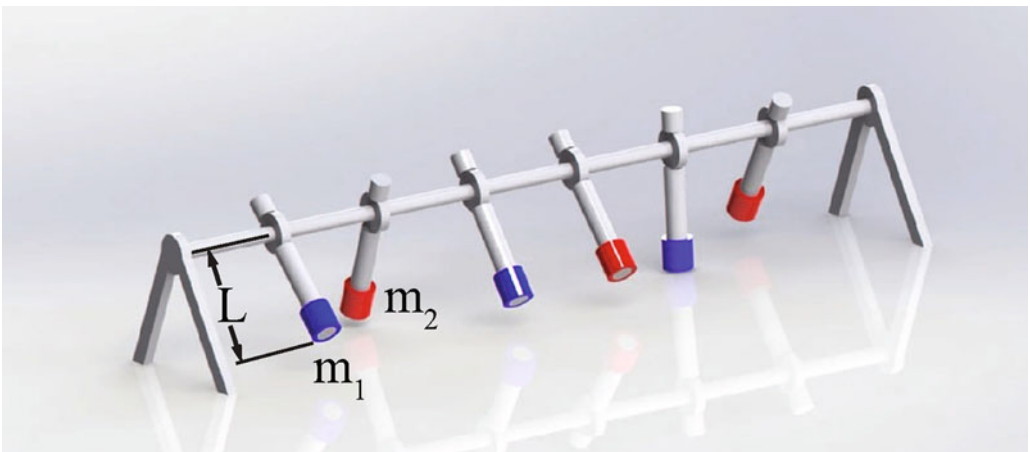

Fig. 13.1 Schematic of a 1D array of axially aligned pendulums. The pendulums are assumed to be rods of length L which each have a lumped mass added to them. Each unit cell consists of two pendulums, and the masses can differ between the two pendulums

13.2.2 Bandgap Calculations

To determine the system's bandgap structure, a traveling wave solution can be assumed in the form

$$\theta_j = A_j e^{i(j\gamma - \tilde{\omega}\tau)}, \tag{13.5}$$

where A_j is the amplitude of the jth pendulum's oscillations, γ is the wavenumber, and $\tilde{\omega}$ is the dimensionless propagation frequency. A standard eigenvalue problem can be formulated by substituting Eq. (13.5) into Eqs. (13.3) and (13.4) and then linearizing the system about an equilibrium, resulting in

$$\left[S(\gamma) - \tilde{\omega}^2 I\right] A = 0, \tag{13.6}$$

where

$$S(\gamma) = \begin{bmatrix} \kappa_1 + \eta & -\kappa_1 \cos\gamma \\ -\kappa_2 \cos\gamma & \kappa_2 + \mu + \sigma \end{bmatrix}, \tag{13.7}$$

and σ is the linearized value of $F(\theta_2)$ for a given equilibrium. Equation (13.6) can then be solved to construct the bandgap structure of the system. For bandgap calculations, it is only necessary to consider values of γ within the first Brillouin zone [17]. Therefore, the reduced wavenumber γN should be varied from 0 to π, where $N = 2$ for this system since each unit cell consists of two pendulums. Bandgaps are attenuation zones that exist between two propagation zones, and they can only exist in nonhomogeneous periodic structures. If $\alpha = \beta$, then no bandgaps will exist. An example of a system with no bandgaps can be see in Fig. 13.2a, while Fig. 13.2b provides an example of a system with a bandgap. For frequencies in the bandgap region, traveling waves will attenuate instead of propagate. For a bistable system, Eq. (13.6) must be solved for both equilibria in order to determine both bandgap profiles. For practical applications it is necessary to convert the dimensionless frequencies into dimensional frequencies using the following scaling convention: $\omega = \tilde{\omega}\sqrt{g/L}$.

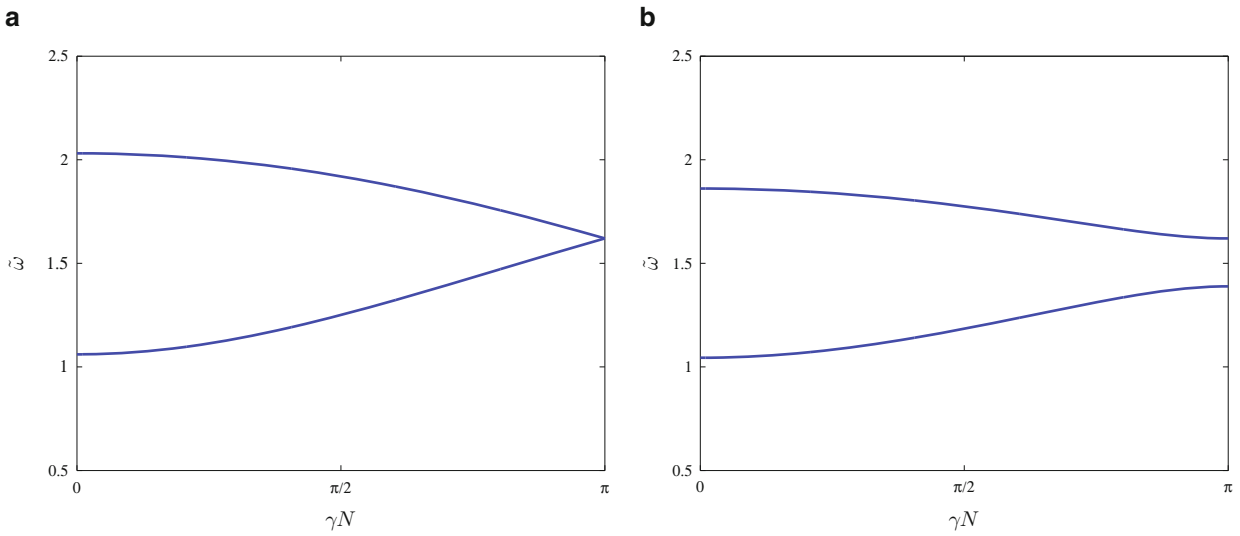

Fig. 13.2 For both of these plots, propagation zones are represented by the frequency ranges where solutions (*lines*) exist, and attenuation zones are represented by the frequency ranges where solutions do not exist (*blank space*). Plot (**a**) shows the homogeneous case where $\alpha = \beta = 1$ and no bandgaps exist. Instead, a single propagation zone exists for $1.06 < \tilde{\omega} < 2.03$. Plot (**b**) shows the existence of a bandgap region between the two propagation zones at $1.04 < \tilde{\omega} < 1.39$ and $1.62 < \tilde{\omega} < 1.86$ when $\alpha = 1$ and $\beta = 2$. For both plots, $\epsilon = 1$, $\kappa = 1$, and $\sigma = 0$. Bistability has not yet been introduced to the system, so there is only one bandgap profile for a given set of parameters

13.3 Experimental System

This section describes a set of experiments that were used to demonstrate the phenomenon of reconfigurable bandgaps. An experimental system consisting of 14 axially aligned pendulums was built, and can be seen in Fig. 13.3. The pendulums were torsionally coupled to each other using elastic bands, and magnetic interactions were used to generate the nonlinear restoring torques necessary for creating a bistable system. The system parameters were selected so that the bistability was asymmetric, resulting in two distinct bandgap profiles for the system. The first pendulum was connected to a vertical shaker that was used to excite the system, and a coupling mechanism was used to convert the translational input into a rotational input. Frequency sweeps were used to verify the two distinct bandgap profiles, and the experimental results closely matched the theoretically predicted system behavior. An amplitude sweep was then used to demonstrate amplitude dependent filtering through passive bandgap reconfiguration, and the system successfully transitioned from one bandgap configuration to the other during the experiment after an amplitude threshold was passed.

13.3.1 Bandgap Predictions

Bistability was introduced to the system through magnetic interactions. For each unit cell, a cylindrical magnet was attached to the rod of the second pendulum as the added mass (m_2). No additional mass was added to the first pendulum ($m_1 = 0$). Additional magnets were placed on a platform below the second pendulum in each unit cell, and the magnets were oriented in such a way so that they produced a repulsive magnetic force. The platforms were arranged so that they induced an asymmetric bistability in the system. The nonlinear restoring torque $f(\theta_2)$ that was created by the magnetic interactions was calculated analytically using a magnetic dipole model and numerically verified using COMSOL [16]. A plot of the potential energy for a unit cell can be seen in Fig. 13.4a. The potential energy function is the sum of the magnetic potential energy and gravitational potential energy for the system, and the placement of the magnetic platforms was manipulated to ensure that the system was asymmetrically bistable. The resulting bandgap profiles for the system can be seen in Fig. 13.4b. It can be clearly seen that the shallow well has a propagation zone in the same frequency range that the deep well has an attenuation zone. This is an important property of the system, as it enables amplitude dependent filtering.

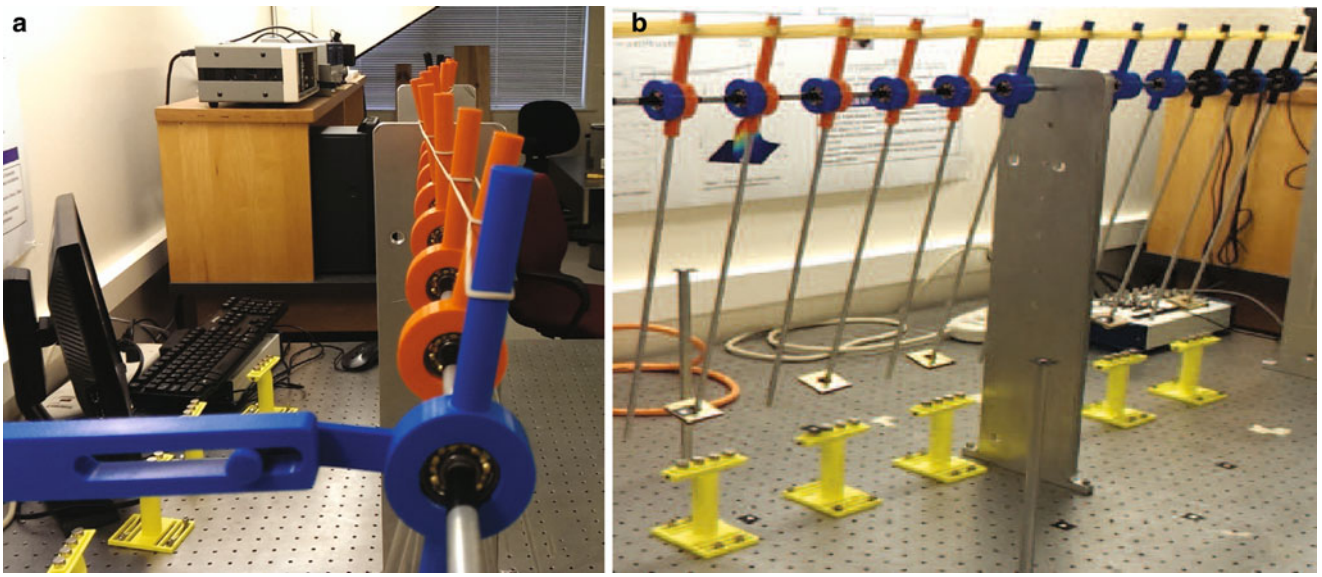

Fig. 13.3 Photographs of the experimental setup. Photo (**a**) shows the coupling mechanism that converts the translational motion of the shaker into a rotational input to the system. Photo (**b**) shows the pendulums in the shallow well configuration. The experimental system has the following parameter values: $m = 0.0347\,\text{kg}$, $m_1 = 0$, $m_2 = 0.0807\,\text{kg}$, $L = 0.4250\,\text{m}$, and $\epsilon = 0.9412$. In the shallow well, $k = 0.4203\,\text{Nm/rad}$ and $\sigma = 6.1219$. In the deep well, $k = 0.4033\,\text{Nm/rad}$ and $\sigma = 0.9083$. The stiffness values were obtained experimentally from the elastic bands used to couple the pendulums, and the values are slightly different for the two cases due to a nonlinear relationship between coupling strength and displacement. However, for inter-well behavior the coupling can be considered linear since the angular displacements are relatively small

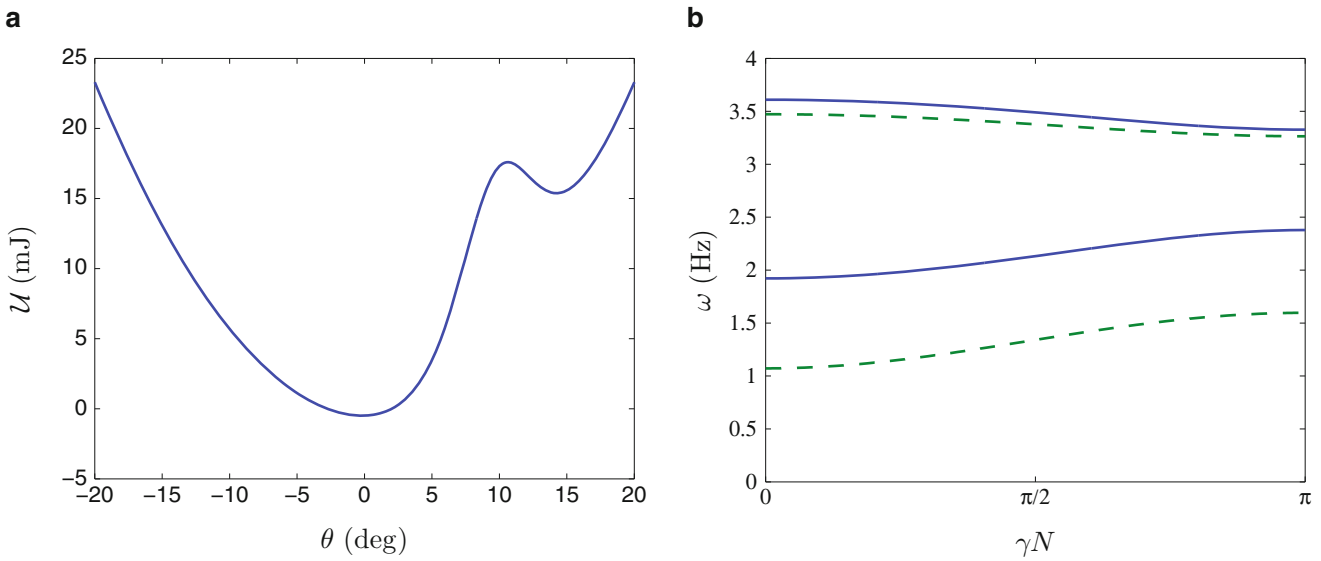

Fig. 13.4 Plot (**a**) shows the asymmetric potential energy function of a unit cell, where $\mathcal{U}$ is the potential energy of the system. Notice that there is a deep well and a shallow well. Plot (**b**) shows the bandgap profiles for the two wells. The shallow well (*solid blue lines*) has a bandgap region between the two propagation zones at 1.92 Hz $< \omega <$ 2.38 Hz and 3.33 Hz $< \omega <$ 3.61 Hz, while the deep well (*dashed green line*) has a bandgap region between the two propagation zones at 1.07 Hz $< \omega <$ 1.60 Hz and 3.26 Hz $< \omega <$ 3.47 Hz. Note that the shallow well has a propagation zone in the same frequency range that the deep well has an attenuation zone (Color figure online)

13.3.2 Frequency Sweeps

Frequency sweeps were conducted to verify the bandgap structures predicted in Fig. 13.4b. For each well, a forward and reverse frequency sweep was performed. Video capture technology was used to determine the angular displacements of the pendulums during the frequency sweeps [16]. The results of these frequency sweeps for all oscillators can be seen in Fig. 13.5, which clearly shows that two distinct propagation zones exist in each well, with a bandgap region in between. In Fig. 13.6, the response of the fifth oscillator is analyzed for each frequency sweep to verify that the system's bandgap structure matches the theoretically predicted propagation and attenuation zones. The fifth oscillator was arbitrarily selected for this analysis, and it can be seen from Fig. 13.5 that its behavior matches the behavior of the other oscillators.

13.3.3 Amplitude Sweep

An amplitude sweep was used to demonstrate amplitude dependent filtering through passive bandgap reconfiguration. The pendulums were placed in the shallow well configuration, and the excitation frequency was set to 2.1 Hz, which falls in the propagation zone for the shallow well and the bandgap region of the deep well, as seen in Fig. 13.4b. The excitation amplitude was then slowly ramped up. After approximately 160 s, a bifurcation occurred and the pendulums escaped from the shallow well into the deep well, and the system reconfigured its bandgap properties. It took approximately 1 min for transient effects to fade away, but then the amplitude of oscillations for the pendulums was almost zero, even though the excitation amplitude was still increasing. This experiment successfully demonstrates amplitude dependent filtering through passive bandgap reconfiguration, and the experimental results can be seen in Fig. 13.7. Plot (a) analyzes the response of the fifth oscillator and clearly demonstrates that the system's behavior switched from propagation to attenuation after the bifurcation occurred and transient effects settled down. Plot (b) verifies that the excitation amplitude was steadily increasing throughout the experiment. Plot (c) shows that all of the pendulums transitioned from the shallow well to the deep well nearly simultaneously. Video capture technology was used to determine the angular displacements of the pendulums during the amplitude sweep [16]. This experiment successfully demonstrated amplitude dependent filtering, as waves were allowed to propagate through the system as long their amplitude was below the bifurcation threshold. After crossing the threshold, passive bandgap reconfiguration occurred and waves were attenuated instead of propagated through the system.

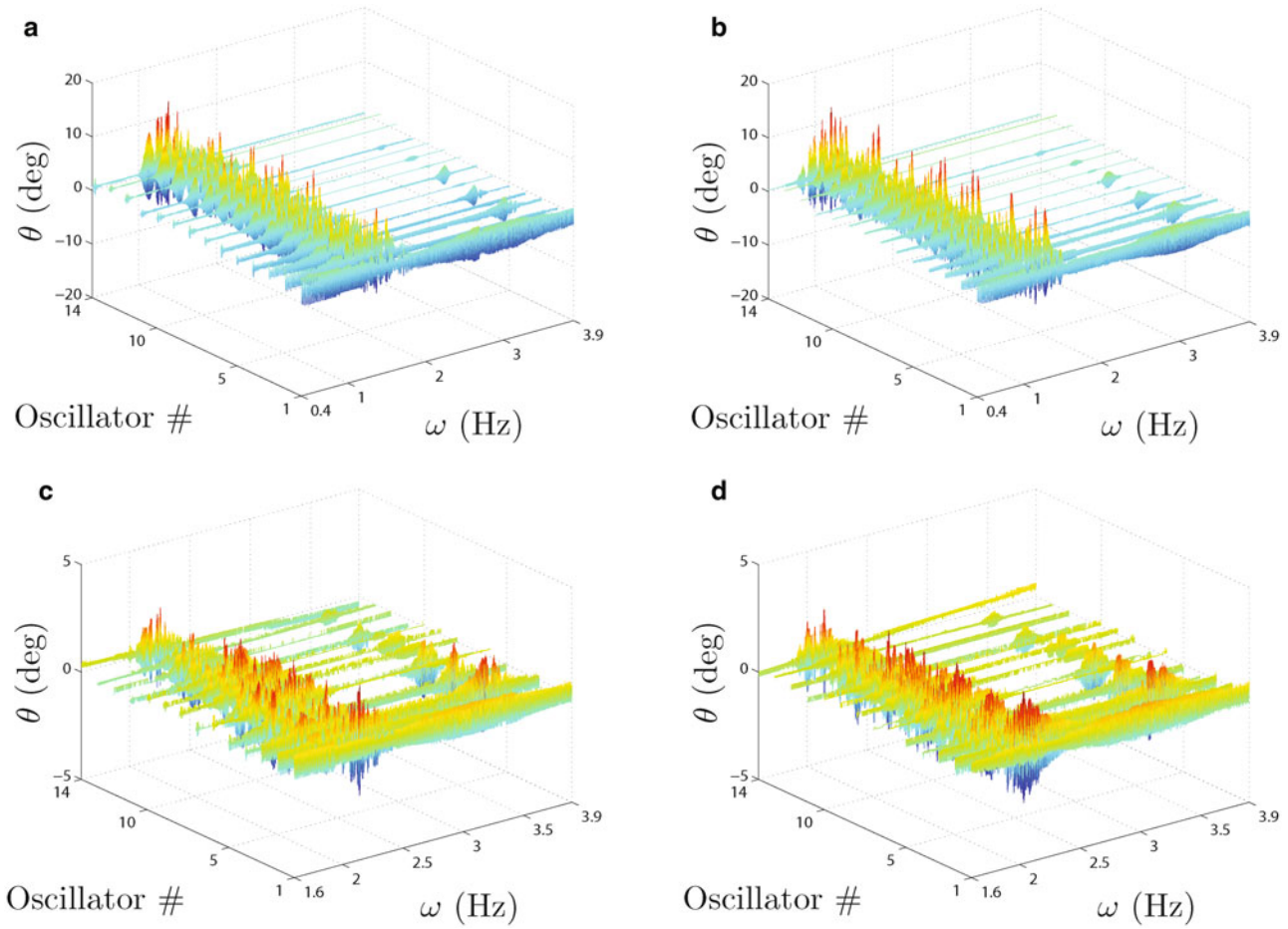

Fig. 13.5 These plots show the experimental results of various frequency sweeps in the pendulum assembly, and it can be seen that two distinct propagation zones exist in each well, with a bandgap region in between. Plot (**a**) shows the forward frequency sweep for the deep well, plot (**b**) shows the reverse frequency sweep for the deep well, plot (**c**) shows the forward frequency sweep for the shallow well, and plot (**d**) shows the reverse frequency sweep for the shallow well. The first oscillator behaves differently from the rest because it is being directly driven by the vertical shaker. The last oscillator also behaves slightly differently due to boundary effects

13.4 Conclusion

This paper presents a mathematical model that describes the bandgap structure for a 1D chain of bistable oscillators, and shows that introducing an asymmetric bistability into the system will result in two distinct bandgap structures. Bandgaps are attenuation zones that exist between two propagation zones, and it is often desirable to tune these bandgaps for specific applications. This paper shows that the system can be tuned so that it can achieve amplitude dependent filtering through passive bandgap reconfiguration. This enables waves to propagate through the system as long their amplitude is below a critical threshold. After crossing the threshold, passive bandgap reconfiguration occurs and waves are attenuated instead of propagated through the system. An experimental system was constructed to demonstrate this phenomenon, and comparisons between experiments and theory show good agreement.

Acknowledgements The authors would like to thank Xiao Wen, Jake Greenstein, Charlie Arentzen, and Jared Little for their contributions to this project. This project was primarily funded by the NSF through grants CMMI-1300307 and CMMI-1300658, and it was also supported by the ARO.

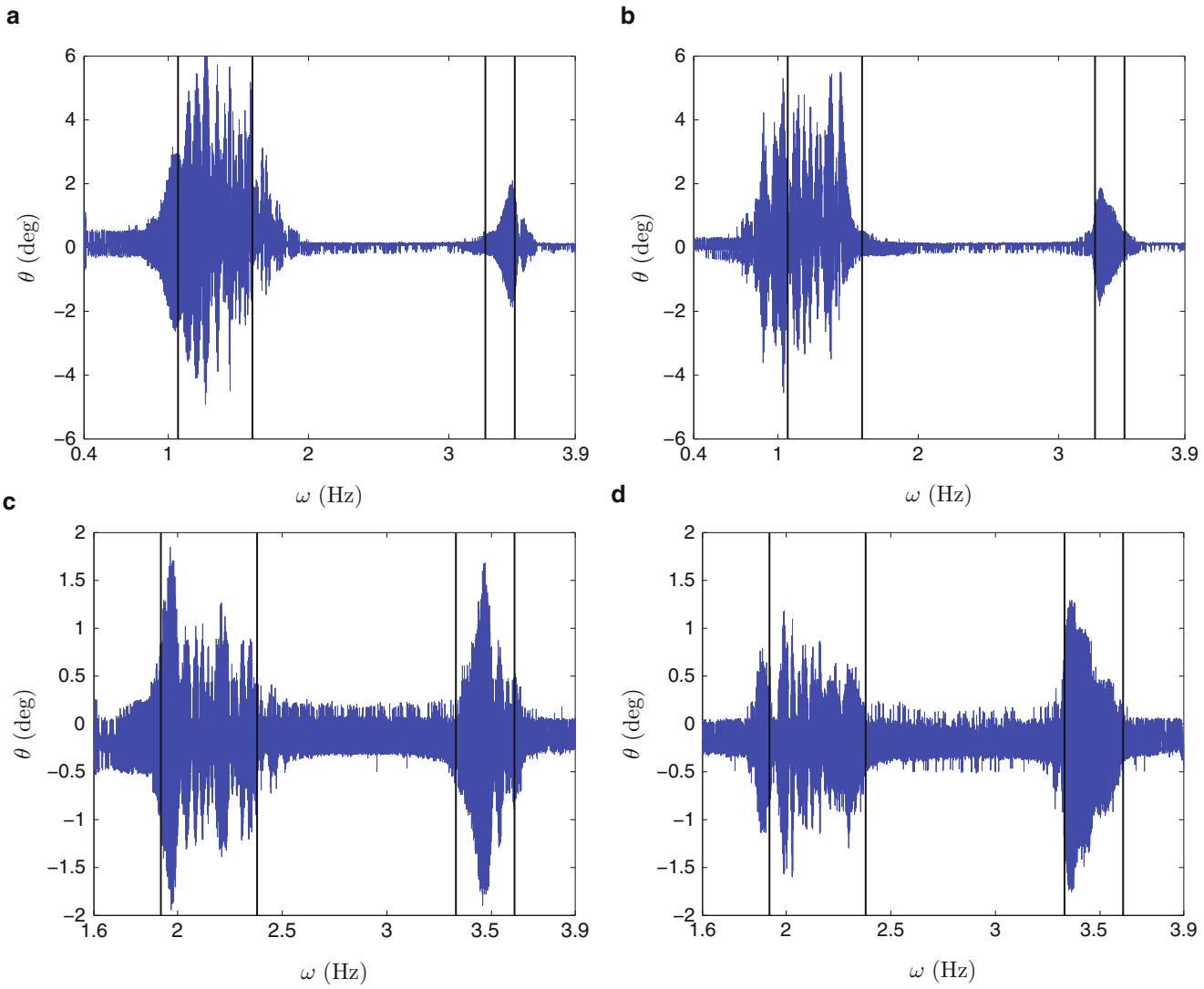

Fig. 13.6 These plots analyze the experimental response of the fifth oscillator of the pendulum assembly during various frequency sweeps, and it can be seen that the system's behavior closely matches the theoretically predicted propagation and attenuation zones. The fifth oscillator was arbitrarily selected for this analysis, and it can be seen from Fig. 13.5 that its behavior matches the behavior of the other oscillators. Plot (**a**) shows the forward frequency sweep for the deep well, plot (**b**) shows the reverse frequency sweep for the deep well, plot (**c**) shows the forward frequency sweep for the shallow well, and plot (**d**) shows the reverse frequency sweep for the shallow well. The propagation zones for the system are identified by the vertical black lines at their borders. Oscillations sometimes appear outside the propagation zones, which can be attributed to transient effects during the sweeps

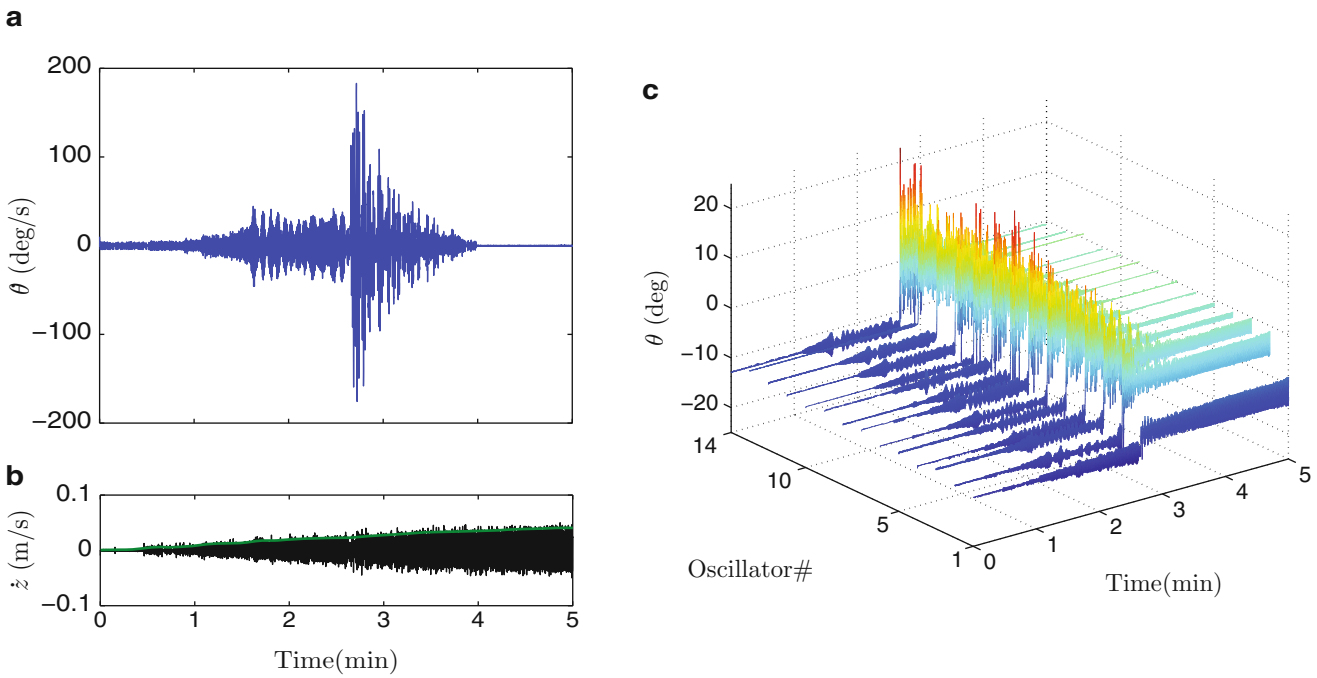

Fig. 13.7 These plots demonstrates amplitude dependent filtering through passive bandgap reconfiguration. Plot (**a**) analyzes the fifth oscillator in the pendulum assembly during an amplitude sweep, and shows how the amplitude of oscillations increases until a bifurcation occurs and the system transitions from the propagation zone in the shallow well to the attenuation zone in the deep well. After transient effects fade away, the system's oscillations are almost zero, even though the amplitude of excitation for the system is still increasing. Plot (**b**) verifies that the excitation amplitude was steadily increasing throughout the experiment ($\dot{z}$ is the velocity of the vertical shaker input). Plot (**c**) shows that all of the pendulums transitioned from the shallow well to the deep well nearly simultaneously. The first oscillator behaves differently from the rest because it is being directly driven by the vertical shaker

References

1. Friesecke G, Wattis JAD (1994) Existence theorem for solitary waves on lattices. Commun Math Phys 161:391–418
2. Lazaridi AN, Nesterenko VF (1985) Observation of a new type of solitary waves in a one-dimensional granular medium. J Appl Mech Tech Phys 26:405–408
3. Mead DJ (1996) Wave propagation in continuous periodic structures: research contributions from Southampton, 1964–1995. J Sound Vib 190:495–524
4. Brillouin L (1953) Wave propagation in periodic structures. Dover, New York
5. Kushwaha MS, Halevi P, Dobrzynski L, Djafari-Rouhani B (1993) Acoustic band structure of periodic elastic composites. Phys Rev Lett 71:2022–2025
6. Kushwaha MS, Halevi P, Martinez G, Dobrzynski L, Djafari-Rouhani B (1994) Theory of acoustic band-structure of periodic elastic composites. Phys Rev B Condens Matter Mater Phys 49:2313–2322
7. Daraio C, Nesterenko VF, Herbold EB, Jinn S (2006) Energy trapping and shock disintegration in a composite granular medium. Phys Rev Lett 96:058002
8. Zhou XZ, Wang YS, Zhang C (2009) Effects of material parameters on elastic band gaps of two-dimensional solid phononic crystals. J Appl Phys 106:014903
9. Sun HX, Zhang SY, Shui XJ (2012) A tunable acoustic diode made by a metal plate with periodical structure. J Appl Phys 100:103507
10. Doney R, Sen S (2006) Decorated, tapered, and highly nonlinear granular chain. Phys Rev Lett 97:155502
11. Zhou W, Mackie DM, Taysing-Lara M, Dang G, Newman PG, Svensson S (2006) Novel reconfigurable semiconductor photonic crystal-mems device. Solid State Electron 50:908–913
12. Edalati A, Boutayeb H, Denidni TA (2007) Band structure analysis of reconfigurable metallic crystals: effect of active elements. J Electromagn Waves Appl 21:2421–2430
13. Herbold EB, Kim J, Nesterenko VF, Wang SY, Daraio C (2009) Pulse propagation in a linear and nonlinear diatomic periodic chain: effects of acoustic frequency band-gap. Acta Mech 205:85–103
14. Yang XS, Wang BZ, Zhang Y (2004) Pattern-reconfigurable quasi-yagi microstrip antenna using a photonic band gap structure. Microw Opt Technol Lett 42:296–297
15. Bernard BP, Mann BP (2013) Passive band-gap reconfiguration born from bifurcation asymmetry. Phys Rev E Stat Nonlinear Soft Matter Phys 88:052903
16. Bernard BP, Mazzoleni MJ, Garraud N, Arnold DP, Mann BP (2014) Experimental investigation of bifurcation induced bandgap reconfiguration. J Appl Phys 116:084904
17. Jensen JS (2003) Phononic band gaps and vibrations in one- and two-dimensional mass-spring structures. J Sound Vib 266:1053–1078

Chapter 14
A Model of Evolutionary Dynamics with Quasiperiodic Forcing

Elizabeth Wesson and Richard Rand

Abstract Evolutionary dynamics combines game theory and nonlinear dynamics to model competition in biological and social situations. The replicator equation is a standard paradigm in evolutionary dynamics. The growth rate of each strategy is its excess fitness: the deviation of its fitness from the average. The game-theoretic aspect of the model lies in the choice of fitness function, which is determined by a payoff matrix.

Previous work by Ruelas and Rand investigated the Rock-Paper-Scissors replicator dynamics problem with periodic forcing of the payoff coefficients. This work extends the previous to consider the case of quasiperiodic forcing. This model may find applications in biological or social systems where competition is affected by cyclical processes on different scales, such as days/years or weeks/years.

We study the quasiperiodically forced Rock-Paper-Scissors problem using numerical simulation, and Floquet theory and harmonic balance. We investigate the linear stability of the interior equilibrium point; we find that the region of stability in frequency space has fractal boundary.

Keywords Replicator equation • Quasiperiodic forcing • Floquet theory • Harmonic balance • Numerical integration

14.1 Introduction

The field of evolutionary dynamics combines game theory and nonlinear dynamics to model population shifts due to competition in biological and social situations. One standard paradigm [3, 9] uses the replicator equation,

$$\dot{x}_i = x_i(f_i(\mathbf{x}) - \phi), \quad i = 1, \ldots, n \tag{14.1}$$

where x_i is the frequency, or relative abundance, of strategy i; the unit vector $\mathbf{x}$ is the vector of frequencies; $f_i(\mathbf{x})$ is the fitness of strategy i; and ϕ is the average fitness, defined by

$$\phi = \sum_i x_i f_i(\mathbf{x}). \tag{14.2}$$

The replicator equation can be derived [10] from an exponential model of population growth,

$$\dot{\xi}_i = \xi_i f_i, \quad i = 1, \ldots, n \tag{14.3}$$

where ξ_i is the population of strategy i, assuming that f_i depends only on the frequencies: $f_i = f_i(\mathbf{x})$. The derivation consists of a simple change of variables: $x_i \equiv \xi_i / p$ where $p = \sum_i \xi_i$ is the total population.

The game-theoretic component of the replicator model lies in the choice of fitness functions. Define the payoff matrix $A = (a_{ij})$ where a_{ij} is the expected reward for a strategy i individual vs. a strategy j individual. We assume the population

E. Wesson (✉)
Center for Applied Mathematics, Cornell University, Ithaca, NY 14853, USA
e-mail: enw27@cornell.edu

R. Rand
Cornell University, Ithaca, NY 14853, USA

G. Kerschen (ed.), *Nonlinear Dynamics, Volume 1*, Conference Proceedings of the Society for Experimental Mechanics Series, DOI 10.1007/978-3-319-15221-9_14

is well-mixed, so that any individual competes against each strategy at a rate proportional to that strategy's frequency in the population. Then the fitness f_i is the total expected payoff for strategy i vs. all strategies:

$$f_i(\mathbf{x}) = (A\mathbf{x})_i = \sum_j a_{ij} x_j. \tag{14.4}$$

In this work, we generalize the replicator model to systems in which the payoff coefficients are quasiperiodic functions of time. Previous work by Ruelas and Rand [7, 8] investigated the Rock-Paper-Scissors replicator dynamics problem with periodic forcing of the payoff coefficients. We also consider a forced Rock-Paper-Scissors system. The quasiperiodically forced replicator model may find applications in biological or social systems where competition is affected by cyclical processes on different scales, such as days/years or weeks/years.

14.2 The Model

14.2.1 Rock-Paper-Scissors Games with Quasiperiodic Forcing

Rock-Paper-Scissors (RPS) games are a class of three-strategy evolutionary games in which each strategy is neutral vs. itself, and has a positive expected payoff vs. one of the other strategies and a negative expected payoff vs. the remaining strategy. The payoff matrix is thus

$$A = \begin{pmatrix} 0 & -b_2 & a_1 \\ a_2 & 0 & -b_3 \\ -b_1 & a_3 & 0 \end{pmatrix}. \tag{14.5}$$

We perturb off of the canonical case, $a_1 = \cdots = b_3 = 1$, by taking

$$A = \begin{pmatrix} 0 & -1 - F(t) & 1 + F(t) \\ 1 & 0 & -1 \\ -1 & 1 & 0 \end{pmatrix} \tag{14.6}$$

where the forcing function F is given by

$$F(t) = \epsilon((1-\delta)\cos\omega_1 t + \delta\cos\omega_2 t). \tag{14.7}$$

For ease of notation, write $(x_1, x_2, x_3) = (x, y, z)$. The dynamics occur in the simplex

$$S \equiv \{(x, y, z) \in \mathbb{R} \,|\, x, y, z \in [0, 1]\} \tag{14.8}$$

but since x, y, z are the frequencies of the three strategies, and hence $x + y + z = 1$, we can eliminate z using $z = 1 - x - y$. Therefore, the region of interest is T, the projection of S into the $x - y$ plane:

$$T \equiv \{(x, y) \in \mathbb{R} \,|\, x, y, x + y \in [0, 1]\}. \tag{14.9}$$

See Fig. 14.1. Thus the replicator equation (14.1) becomes

$$\dot{x} = -x(x + 2y - 1)(1 + (x - 1)F(t)) \tag{14.10}$$

$$\dot{y} = y(2x + y - 1 - x(x + 2y - 1)F(t)) \tag{14.11}$$

Note that $\dot{x} = 0$ when $x = 0$, $\dot{y} = 0$ when $y = 0$, and

$$\dot{x} + \dot{y} = (x + y - 1)(xF(t)(x + 2y - 1) - x + y) \tag{14.12}$$

so that $\dot{x} + \dot{y} = 0$ when $x + y = 1$, which means that $x + y = 1$ is an invariant manifold. This shows that the boundary of T is invariant, so trajectories cannot escape the region of interest.

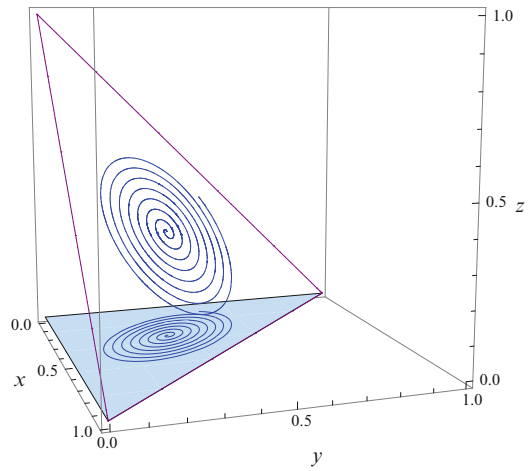

Fig. 14.1 A curve in S and its projection in T

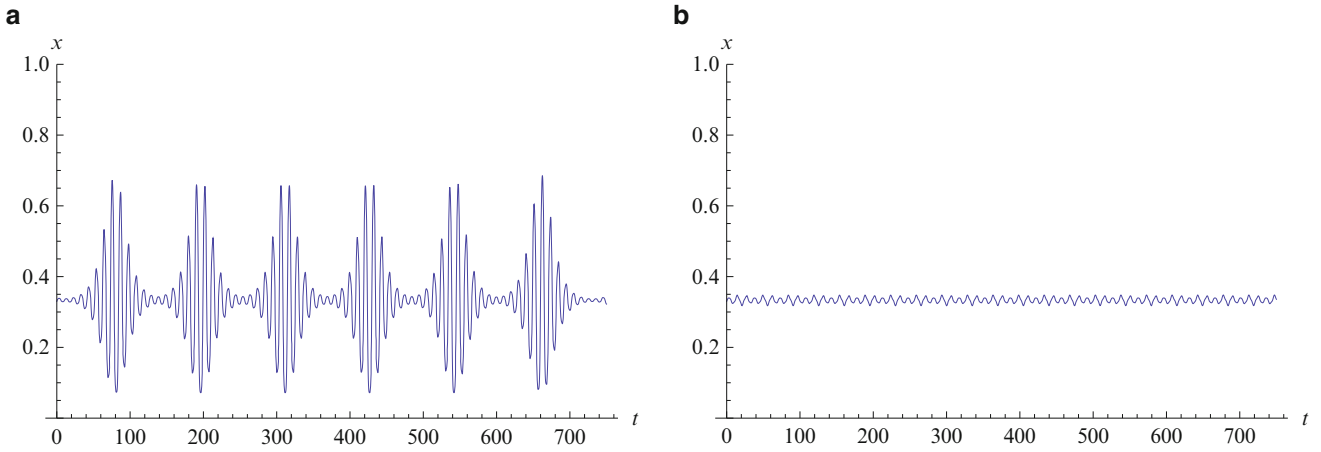

Fig. 14.2 Numerical solutions for $x(t)$ with identical initial conditions $x(0) = y(0) = 0.33$ and parameters $\epsilon = 0.9, \delta = 0.6$, but with different ω_1, ω_2. (**a**) $\omega_1 = \omega_2 = 1.2$. (**b**) $\omega_1 = \omega_2 = 0.9$

It is known [4] that in the unperturbed case ($\epsilon = 0$) there is an equilibrium point at $(x, y) = (\frac{1}{3}, \frac{1}{3})$, and the interior of T is filled with periodic orbits. We see from Eqs. (14.10)–(14.11) that this interior equilibrium point persists when $\epsilon \neq 0$. Numerical integration suggests that the Lyapunov stability of motions around the equilibrium point depends sensitively on the values of ω_1 and ω_2. See Fig. 14.2. We investigate the stability of the interior equilibrium using Floquet theory and harmonic balance, as well as by numerical methods.

14.2.2 Linearization

To study the linear stability of the equilibrium point, we set $x = u + \frac{1}{3}$, $y = v + \frac{1}{3}$, substitute these into (14.10)–(14.11) and linearize, to obtain

$$\dot{u} = -\frac{1}{9}(u + 2v)(3 + 2F(t)) \tag{14.13}$$

$$\dot{v} = \frac{1}{9}(F(t)(u + 2v) + 3(2u + v)). \tag{14.14}$$

The linearized system (14.13)–(14.14) can also be written [6] as a single second-order equation on u, by differentiating (14.13) and substituting in expressions for $\dot{v}$ from (14.14) and v from (14.13). This gives us

$$g(t)\ddot{u} - \dot{g}(t)\dot{u} - \frac{1}{9}g^2(t)u = 0 \tag{14.15}$$

where

$$g(t) = -3 - 2F(t) = -3 - 2\epsilon((1-\delta)\cos\omega_1 t + \delta\cos\omega_2 t). \tag{14.16}$$

Now that we have a linear system with coefficients that are functions of time, we use Floquet theory to determine the stability of the origin.

14.3 Floquet Theory

Floquet theory is concerned with systems of differential equations of the form

$$\frac{dx}{dt} = M(t)x, \quad M(t+T) = M(t). \tag{14.17}$$

We have the system (14.13)–(14.14), which can be written as

$$\begin{bmatrix} \dot{u} \\ \dot{v} \end{bmatrix} = \frac{1}{9}\begin{bmatrix} g(t) & 2g(t) \\ \frac{1}{2}(9-g(t)) & -g(t) \end{bmatrix}\begin{bmatrix} u \\ v \end{bmatrix} \equiv B(t)\begin{bmatrix} u \\ v \end{bmatrix} \tag{14.18}$$

where $g(t)$ is as in (14.16).

In general, $B(t)$ is not periodic, since ω_1 and ω_2 are rationally independent. However, the set of points for which ω_1 and ω_2 are rationally dependent is dense in the $\omega_1 - \omega_2$ plane, and solutions of (14.18) must vary continuously with ω_1 and ω_2, so it is reasonable to consider only the case that $F(t)$, and hence $g(t)$ and $B(t)$, are in fact periodic.

Assume that $\omega_2 = \frac{a}{b}\omega_1$ in lowest terms, where a and b are relatively prime integers. Then we can make the change of variables $\tau = \omega_1 t$, so $\omega_2 t = \frac{a}{b}\tau$. Since a and b are relatively prime, we see that F, and hence g and B, have period $T = 2\pi b$ in τ. Thus (14.18) becomes

$$\begin{bmatrix} u' \\ v' \end{bmatrix} = \frac{1}{\omega_1}B(\tau)\begin{bmatrix} u \\ v \end{bmatrix}, \quad B(\tau + 2\pi b) = B(\tau) \tag{14.19}$$

where u' indicates $du/d\tau$. This has the same form as (14.17), so we can apply the results of Floquet theory.

Suppose that there is a fundamental solution matrix of (14.19),

$$X(\tau) = \begin{bmatrix} u_1(\tau) & u_2(\tau) \\ v_1(\tau) & v_2(\tau) \end{bmatrix} \tag{14.20}$$

where

$$\begin{bmatrix} u_1(0) \\ v_1(0) \end{bmatrix} = \begin{bmatrix} 1 \\ 0 \end{bmatrix}, \quad \begin{bmatrix} u_2(0) \\ v_2(0) \end{bmatrix} = \begin{bmatrix} 0 \\ 1 \end{bmatrix}. \tag{14.21}$$

Then the Floquet matrix is $C = X(T) = X(2\pi b)$, and stability is determined by the eigenvalues of C:

$$\lambda^2 - (\mathrm{tr}C)\lambda + \det C = 0. \tag{14.22}$$

We can show [5] that $\det C = 1$, as follows. Define the Wronskian

$$W(\tau) = \det X(\tau) = u_1(\tau)v_2(\tau) - u_2(\tau)v_1(\tau). \tag{14.23}$$

Notice that $W(0) = \det X(0) = 1$. Then taking the time derivative of W and using (14.19) gives

$$\begin{aligned}\frac{dW}{d\tau} &= u_1'(\tau)v_2(\tau) + u_1(\tau)v_2'(\tau) - u_2'(\tau)v_1(\tau) - u_2(\tau)v_1'(\tau) \\ &= \frac{1}{9\omega_1}\left(g(\tau)(u_1 + 2v_1)v_2 + \frac{1}{2}u_1(9u_2 - (u_2 + 2v_2)g(\tau))\right. \\ &\quad \left. -g(\tau)(u_2 + 2v_2)v_1 - \frac{1}{2}u_2(9u_1 - (u_1 + 2v_1)g(\tau))\right) = 0. \end{aligned} \tag{14.24}$$

This shows that $W(\tau) = 1$ for all τ, and in particular $W(T) = \det C = 1$. Therefore,

$$\lambda = \frac{\mathrm{tr}C \pm \sqrt{\mathrm{tr}C^2 - 4}}{2} \tag{14.25}$$

which means [5] that the transition between stable and unstable solutions occurs when $|\mathrm{tr}C| = 2$, and this corresponds to periodic solutions of period $T = 2\pi b$ or $2T = 4\pi b$.

Given the period of the solutions on the transition curves in the $\omega_1 - \omega_2$ plane, we use harmonic balance to approximate those transition curves.

14.4 Harmonic Balance

We seek solutions to (14.15) of period $4\pi b$ in τ:

$$u = \sum_{k=0}^{\infty} \alpha_k \cos\left(\frac{k\tau}{2b}\right) + \beta_k \sin\left(\frac{k\tau}{2b}\right). \tag{14.26}$$

Since $\omega_2 = \frac{a}{b}\omega_1$ where a and b are relatively prime, any integer k can be written as $na + mb$ for some integers n and m [2, 11]. That is, there is a one-to-one correspondence between integers k and ordered pairs (m, n). We can therefore write the solution as

$$u = \sum_{m=0}^{\infty}\sum_{n=-\infty}^{\infty} \alpha_{mn} \cos\left(\frac{ma + nb}{2b}\tau\right) + \beta_{mn} \sin\left(\frac{ma + nb}{2b}\tau\right) \tag{14.27}$$

$$= \sum_{m=0}^{\infty}\sum_{n=-\infty}^{\infty} \alpha_{mn} \cos\left(\frac{m\omega_2 + n\omega_1}{2}t\right) + \beta_{mn} \sin\left(\frac{m\omega_2 + n\omega_1}{2}t\right). \tag{14.28}$$

We substitute a truncated version of (14.28) into (14.15), expand the trigonometric functions and collect like terms. This results in cosine terms whose coefficients are functions of the α_{mn}, and sine terms whose coefficients are functions of the β_{mn}. Let the coefficient matrices of these two sets of terms be Q and R, respectively. In order for a nontrivial solution to exist, the determinants of both coefficient matrices must vanish [5]. We solve the equations $\det Q = 0$ and $\det R = 0$ for relations between ω_1 and ω_2. This gives the approximate transition curves seen in Fig. 14.3.

It has been shown [6, 7] that in a periodically forced RPS system (i.e. $\delta = 0$ in our model) there are tongues of instability emerging from $\omega_1 = 2/n\sqrt{3}$ in the $\omega_1 - \epsilon$ plane. Our harmonic balance analysis is consistent with this: we observe bands of instability around $\omega_1 = 2/\sqrt{3}$ and $\omega_2 = 2/\sqrt{3}$, which get broader as ϵ increases. We also see narrower regions of instability along the lines $n\omega_1 + m\omega_2 = 2/\sqrt{3}$, for each n, m used in the truncated solution (14.28).

Thus the boundary of the region of instability exhibits self-similarity when we consider $\omega_1, \omega_2 \in [0, 2^{1-k}]$ for $k = 0, 1, \ldots$.

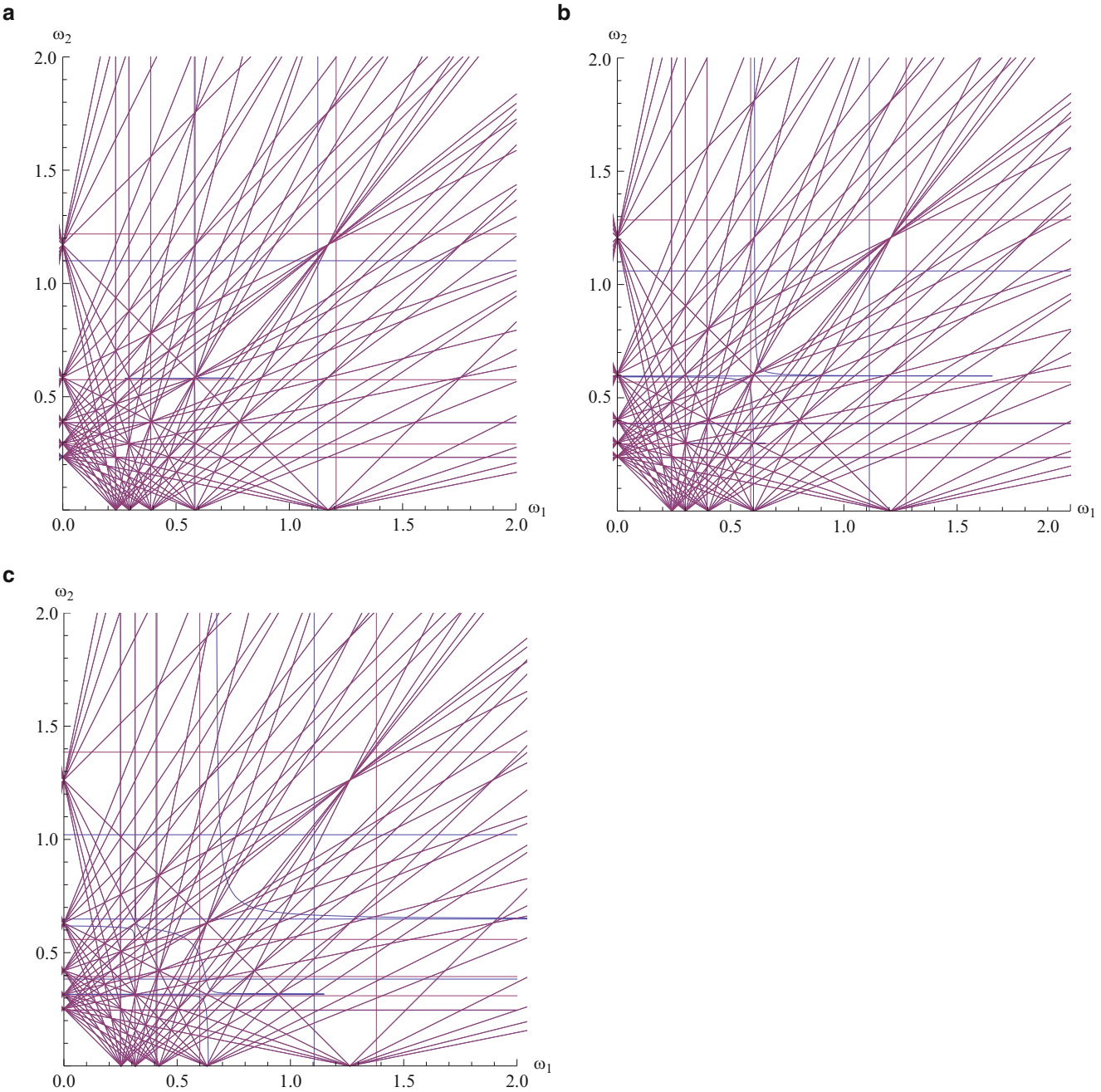

Fig. 14.3 Transition curves predicted by harmonic balance with $-5 \leq m \leq 5, 0 \leq n \leq 5$ for various values of ϵ. (**a**) $\epsilon = 0.5, \delta = 0.6$. (**b**) $\epsilon = 0.9, \delta = 0.6$. (**c**) $\epsilon = 1.3, \delta = 0.6$

14.5 Numerical Integration

In order to check the results of the harmonic balance method, we generate an approximate stability diagram by numerical integration of the linearized system (14.15).

For randomly chosen parameters $(\omega_1, \omega_2) \in [0, 2]$, we choose random initial conditions $(u(0), \dot{u}(0))$ on the unit circle—since the system is linear, the amplitude of the initial condition needs only to be consistent between trials. We then integrate the system for 1,000 time steps using `ode45` in Matlab. This is an explicit Runge-Kutta (4,5) method that is recommended in the Matlab documentation for most non-stiff problems. We considered a motion to be unstable if $\max |u(t)| > 10$. The set

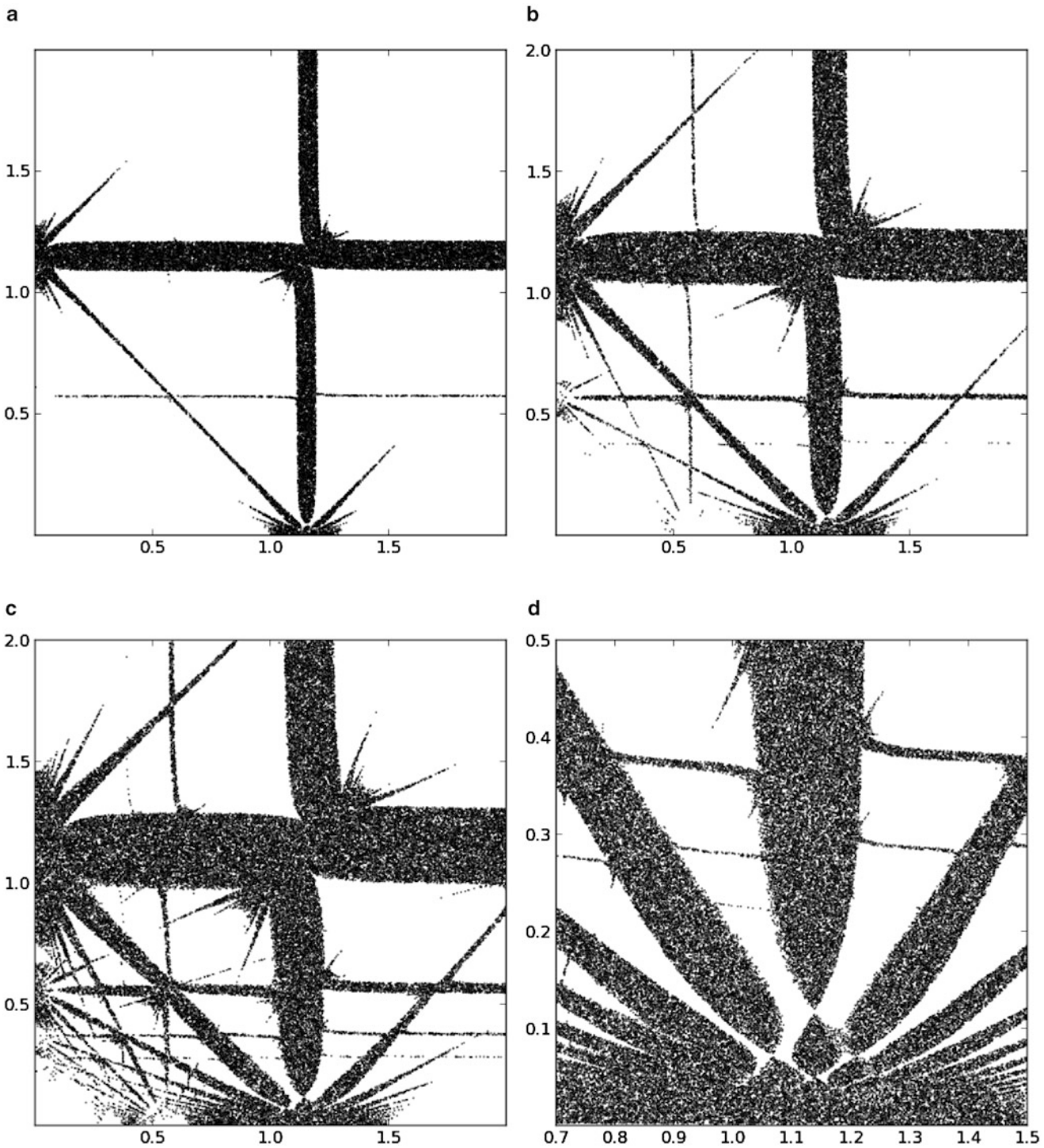

Fig. 14.4 Plots of unstable points in the (ω_1, ω_2) plane for various values of ϵ. (**a**) $\epsilon = 0.5, \delta = 0.6$. (**b**) $\epsilon = 0.9, \delta = 0.6$. (**c**) $\epsilon = 1.3, \delta = 0.6$. (**d**) Detail view: $\epsilon = 1.3, \delta = 0.6$

of points (ω_1, ω_2) corresponding to unstable motions were plotted using `matplotlib.pyplot` in Python. See Fig. 14.4. Each plot in Fig. 14.4 contains approximately 5×10^4 points.

We note that the unstable regions given by numerical integration appear to be consistent with the transition curves predicted by harmonic balance (Fig. 14.3). The regions of instability around $\omega_1 = 2/\sqrt{3}$ and $\omega_2 = 2/\sqrt{3}$ are visible for all tested values of ϵ and δ, and as ϵ increases, more tongues of the form $n\omega_1 + m\omega_2 = 2/\sqrt{3}$ become visible.

14.6 Lyapunov Exponents

A second, and more informative, numerical approach for determining stability is the computation of approximate Lyapunov exponents. This is a measure of a solution's rate of divergence from the equilibrium point [1], and is defined as

$$\lambda = \limsup_{t\to\infty} \frac{1}{t} \ln |u(t)|. \tag{14.29}$$

If the limit is finite, then $u(t) \sim e^{\lambda t}$ or smaller as $t \to \infty$. A positive Lyapunov exponent indicates that the solution is unstable.

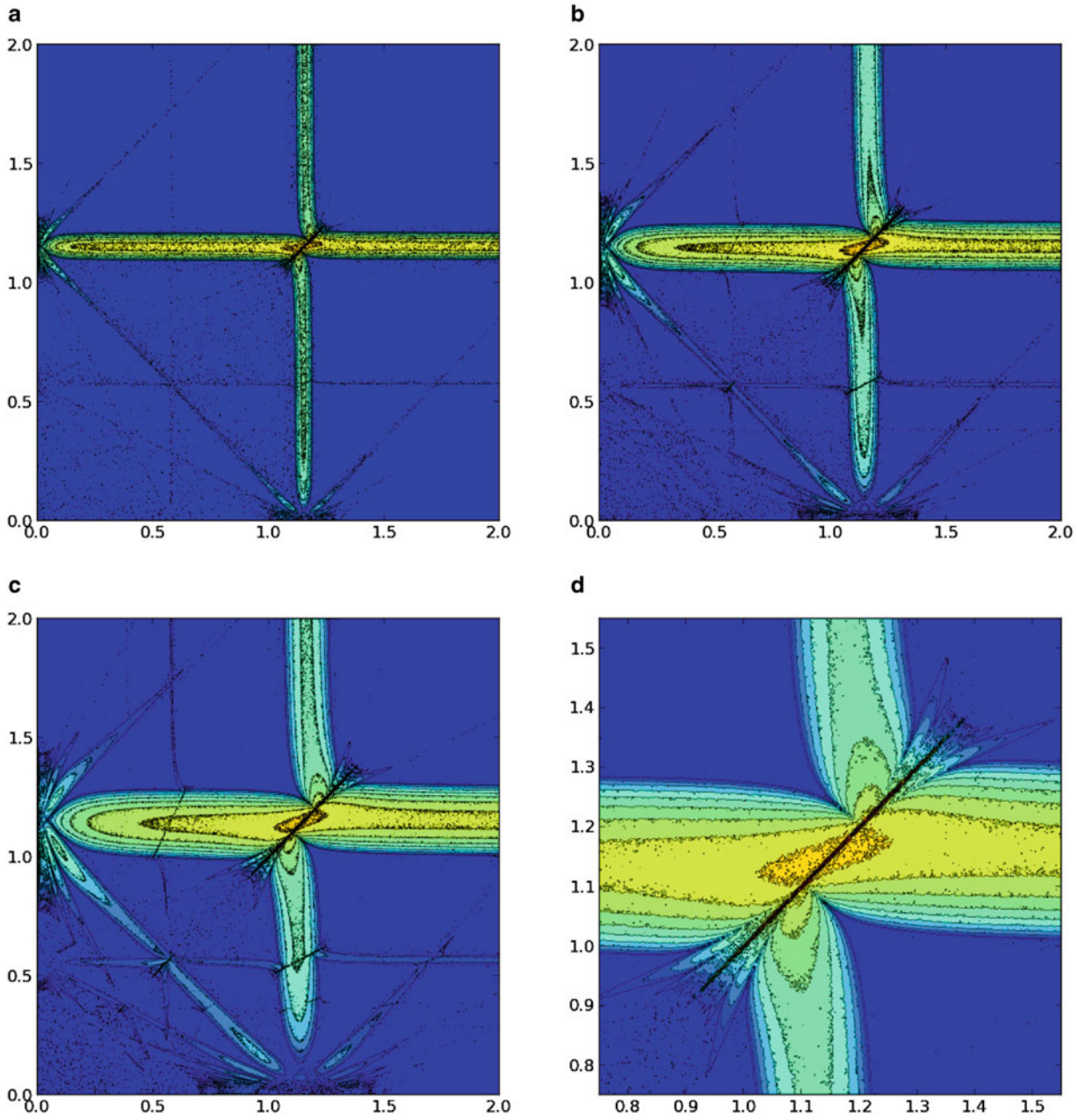

Fig. 14.5 Contour plot of Lyapunov exponents in the (ω_1, ω_2) plane for various values of ϵ. (**a**) $\epsilon = 0.5, \delta = 0.6$. Contours between $\lambda = 0$ and $\lambda = 0.04$. (**b**) $\epsilon = 0.9, \delta = 0.6$. Contours between $\lambda = 0$ and $\lambda = 0.08$. (**c**) $\epsilon = 1.3, \delta = 0.6$. Contours between $\lambda = 0$ and $\lambda = 0.12$. (**d**) Detail view: $\epsilon = 1.3, \delta = 0.6$. Contours as in (**c**)

We do not find any negative Lyapunov exponents, but note [5] that the system (14.15) can be converted to a Hill's equation

$$\ddot{z} - z\left(\frac{4g(t)^3 + 27\dot{g}(t)^2 - 18g(t)\ddot{g}(t)}{36g(t)^2}\right) = 0 \tag{14.30}$$

by making the change of variables $u = \sqrt{g(t)}z$. Since $\sqrt{g(t)}$ is bounded, u is bounded if and only if z is bounded. And since there is no dissipation in (14.30), stable solutions correspond to $\lambda = 0$.

We approximate the Lyapunov exponents numerically by integrating as above, and taking

$$\lambda \approx \sup_{900<t<1000} \frac{1}{t} \ln |u(t)|. \tag{14.31}$$

See Fig. 14.5. The shape of the unstable region is the same as in Fig. 14.4, but this method allows us to see a sharp increase in unstable solutions' rate of growth along the line $\omega_1 = \omega_2$.

14.7 Conclusion

The replicator equation with quasiperiodic perturbation may be used to model biological or social systems where competition is affected by cyclical processes on different scales. We have investigated the linear stability of the interior equilibrium point for RPS systems with quasiperiodic perturbation, using Floquet theory and harmonic balance, as well as numerical integration and numerical computation of Lyapunov exponents. We find that stability depends sensitively on the frequencies ω_1 and ω_2, and that the region of instability in the $\omega_1 - \omega_2$ plane exhibits self-similarity.

References

1. Guckenheimer J, Holmes P (1983) Nonlinear oscillations, dynamical systems, and bifurcations of vector fields. Springer, New York
2. Herstein I (1975) Topics in algebra, 2nd edn. Wiley, New York
3. Hofbauer J, Sigmund K (1998) Evolutionary games and population dynamics. Cambridge University Press, Cambridge
4. Nowak M (2006) Evolutionary dynamics. Belknap Press of Harvard University Press, Cambridge, MA
5. Rand R (2012) Lecture notes on nonlinear vibrations. Published online by The Internet-First University Press. http://ecommons.library.cornell.edu/handle/1813/28989
6. Rand R, Yazhbin M, Rand D (2011) Evolutionary dynamics of a system with periodic coefficients. Commun Nonlinear Sci Numer Simul 16:3887–3895
7. Ruelas R, Rand D, Rand R (2012) Nonlinear parametric excitation of an evolutionary dynamical system. J. Mech Eng Sci Proc Inst Mech Eng C 226:1912–1920
8. Ruelas R, Rand D, Rand R (2013) Parametric excitation and evolutionary dynamics. J Appl Mech 80:051013
9. Sigmund K (2011) Introduction to evolutionary game theory, Chap. 1. In: Sigmund K (ed) Evolutionary game dynamics. Proceedings of symposia in applied mathematics, vol 69, pp 1–26. American Mathematical Society, Providence
10. Taylor P, Jonker L (1978) Evolutionarily stable strategies and game dynamics. Math Biosci 40(1–2):145–156
11. Zounes R, Rand R (1998) Transition curves for the quasi-periodic mathieu equation. Siam J Appl Math 40(4): 1094–1115

Chapter 15
Experimental Demonstration of a 3D-Printed Nonlinear Tuned Vibration Absorber

C. Grappasonni, G. Habib, T. Detroux, and G. Kerschen

Abstract Engineering structures are designed to be lighter and more flexible, hence reducing the extent of application of linear dynamic models. Concurrently, vibration mitigation is required for enhancing the performance, comfort or safety in real-life applications. Passive linear vibration absorbers are purpose-built, often designed using Den Hartog's equal-peak strategy. However, nonlinear systems are known to exhibit frequency-energy-dependent oscillations which linear absorbers cannot effectively damp out. In this context, the paper introduces a new nonlinear tuned vibration absorber (NLTVA) whose nonlinear functional form is tailored according to the frequency-energy dependence of the nonlinear primary structure. The NLTVA design aims at ensuring equal peaks in the nonlinear receptance function for an as large as possible range of forcing amplitudes, hence generalizing Den Hartog's method to nonlinear systems. Our focus in this study is on experimental demonstration of the NLTVA performance using a primary structure consisting of a cantilever beam with a geometrically nonlinear component at its free end. The absorber is implemented using a doubly-clamped beam fabricated thanks to 3D printing. The NLTVA performance is also compared with that of the classical linear tuned vibration absorber.

Keywords Nonlinear resonances • Tuned vibration absorber • Equal-peak method • 3D printing • Experimental demonstration

15.1 Introduction

Engineering structures must often operate in a harsh dynamic environment. Passive vibration absorbers have therefore been exploited to mitigate the resonant vibrations with a limited increase in weight. Linear tuned vibration absorbers (LTVA) are commonly designed using the well-established Den Hartog's equal-peak strategy [1]. However, in view of its narrow bandwidth, the LTVA can be ineffective when the primary structure exhibits frequency-energy-dependent nonlinear oscillations. In this context, a nonlinear counterpart to the classical LTVA would be extremely beneficial, and several nonlinear absorbers have been proposed in the literature, see, e.g., [2–5].

The concept of a nonlinear tuned vibration absorber (NLTVA) was introduced by the authors in [6]. One unconventional aspect of the NLTVA is that the mathematical form of its restoring force is tailored according to the nonlinear restoring force of the primary system. The NLTVA parameters are then determined using a nonlinear generalization of Den Hartog's equal-peak method. In the present study, the NLTVA effectiveness is verified experimentally on a primary structure consisting of a cantilever beam with a geometrically nonlinear component at its free end.

The procedure that we propose herein to design and validate the NLTVA is sketched in Fig. 15.1. Starting from an experimentally-characterized structure, an equivalent nonlinear single-degree-of-freedom (SDOF) modal model of the targeted resonance is first derived (Sect. 15.2). From the nonlinear modal model, the analytic tuning procedure developed in [6] provides the absorber's parameters, and, in particular, its load-deflection characteristic (Sect. 15.3). The NLTVA is then implemented using doubly-clamped geometrically nonlinear beams which are fabricated using 3D printers. The mechanical and geometrical properties of the nonlinear beams are also obtained analytically (Sect. 15.4). Finally, the NLTVA performance is verified experimentally through sine sweep testing at different excitation levels (Sect. 15.5).

C. Grappasonni (✉) • G. Habib • T. Detroux • G. Kerschen
Space Structures and Systems Laboratory (S3L), Department of Aerospace and Mechanical Engineering, University of Liège, Liège, Belgium
e-mail: chiara.grappasonni@ulg.ac.be; giuseppe.habib@ulg.ac.be; tdetroux@ulg.ac.be; g.kerschen@ulg.ac.be

G. Kerschen (ed.), *Nonlinear Dynamics, Volume 1*, Conference Proceedings of the Society for Experimental Mechanics Series, DOI 10.1007/978-3-319-15221-9_15

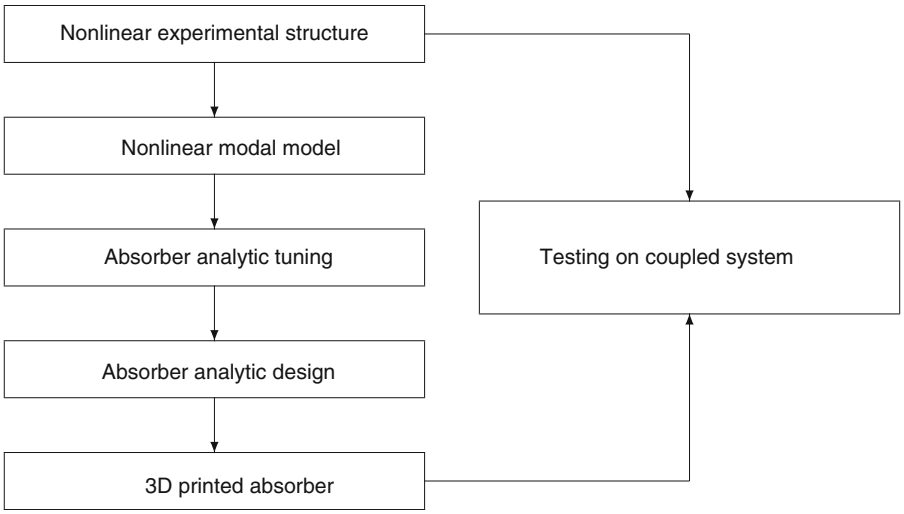

Fig. 15.1 Proposed procedure for NLTVA design and performance validation

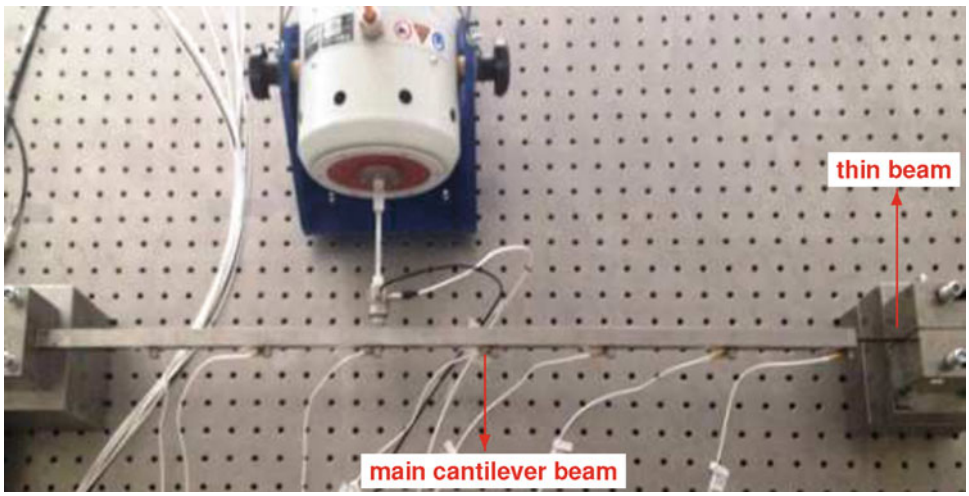

Fig. 15.2 Experimental setup of the nonlinear beam

Table 15.1 Modal parameters of the first two modes of the underlying linear structure

Mode	Natural frequency (Hz)	Damping ratio (%)
1	31.05	0.12
2	145.68	0.05

15.2 Primary System Description

The primary system considered throughout this work is a benchmark that was originally proposed in [7] and that was studied by a number of research groups across the world. The set-up, shown in Fig. 15.2, is a monolithic structure made of 42CrMo4 steel that comprises a cantilever beam with a very thin beam at its tip. The thin beam can exhibit large-displacement-related effects (i.e., mid-plane stretching effects) and behaves as a hardening nonlinearity. Around the first resonance, the system can be modeled as a Duffing oscillator.

The structure was instrumented with seven accelerometers which span the beam regularly. A shaker located 0.3 m far from the clamped root was used to apply the excitation measured through a load cell. The signal acquisition was performed using the LMS SCADAS mobile and the LMS Test.LAB Structures Acquisition programs. The frequency-domain nonlinear subspace identification (FNSI) method [8] was used to determine the coefficient of the cubic spring modelling the nonlinear effect of the thin beam. The value that was identified from high-level random data with a 16 Nrms forcing amplitude was 2.37×10^9 N/m^3. In addition, the FNSI method provided the modal parameters of the underling linear system listed in Table 15.1.

Table 15.2 SDOF models of the nonlinear beam for the configurations with LTVA/NLTVA

Configuration	m_1	c_1	k_1	k_{nl1}
W/o support (LTVA)	0.2893 kg	0.1357 Ns/m	1.1009×10^4 N/m	2.3703×10^9 N/m^3
W/ support (NLTVA)	0.4090 kg	0.2509 Ns/m	1.0660×10^4 N/m	2.3703×10^9 N/m^3

The procedure for the tuning of the absorbers in [6] relies on the assumption of a SDOF primary system, which holds here, because the nonlinear beam has well-separated modes (Table 15.1). The mitigation of the resonance of the first beam mode is targeted. The frequency bandwidth of interest is therefore limited to [10–50] Hz. The physical mass of the beam m_{beam} is 1.105 kg. The effective mass m_1, damping c_1 and stiffness k_1 of the first mode can be calculated with respect to the degree of freedom to which the nonlinearity is attached. As depicted in Fig. 15.4, unlike the LTVA which is realized using a cantilever beam, the NLTVA is implemented using a doubly-clamped beam that needs a support to be mounted on the primary structure. This support of mass $m_{supp} = 0.14$ kg is therefore part of the primary system for the coupled beam and NLTVA system. The effective mass of the first mode increases by a factor of 40 %, and the first natural frequency decreases by about 21 %. Table 15.2 summarizes the parameters of the nonlinear SDOF model of the beam around its first resonance, which can be seen as a Duffing oscillator.

15.3 Linear and Nonlinear Den Hartog's Equal-Peak Methods

15.3.1 The Linear Tuned Vibration Absorber (LTVA)

The steady-state response of an undamped SDOF system subjected to a harmonic excitation at a constant frequency can be suppressed using an undamped linear tuned vibration absorber, as proposed by Frahm in 1909 [9]. However, the LTVA performance deteriorates significantly when the excitation frequency varies. To improve the performance robustness, damping was introduced in the absorber by Ormondroyd and Den Hartog [10]. The equations of motion of the coupled system are

$$\begin{aligned} m_1\ddot{x}_1 + k_1 x_1 + c_2(\dot{x}_1 - \dot{x}_2) + k_2(x_1 - x_2) &= F\cos\omega t \\ m_2\ddot{x}_2 + c_2(\dot{x}_2 - \dot{x}_1) + k_2(x_2 - x_1) &= 0 \end{aligned} \tag{15.1}$$

where $x_1(t)$ and $x_2(t)$ are the displacements of the harmonically-forced primary system and of the damped LTVA, respectively. Den Hartog proposed two approximate formulas for choosing the stiffness and damping ratio of the absorber in order to minimize the maximal value of the receptance function. In practice, the minimization corresponds to force the two resonant peaks to have the same height. Interestingly, it is only recently that the exact solution to this problem was found [11]. The introduction of linear damping into the primary system complicates further the problem. A series solution for minimizing the maximal frequency response was proposed in [12] and writes

$$\begin{aligned} m_2 &= \epsilon m_1 \\ k_2 &= \epsilon k_1 \left[\frac{1}{1+\epsilon} - \mu_1 \frac{1}{1+\epsilon}\sqrt{\frac{1}{2(1+\epsilon)}\left(3+4\epsilon-\frac{AB}{2+\epsilon}\right)} + \mu_1^2 \frac{C_0 - 4(5+2\epsilon)AB}{4(1+\epsilon)^2(2+\epsilon)(9+4\epsilon)} \right]^2 \\ c_2 &= 2\sqrt{k_2 m_2}\left[\sqrt{\frac{3\epsilon}{8(1+\epsilon)}} + \mu_1 \frac{60+63\epsilon+16\epsilon^2-2(3+2\epsilon)AB}{8(1+\epsilon)(2+\epsilon)(9+4\epsilon)} + \right. \\ &\quad \left. \mu_1^2 \frac{C_1(A+B)\sqrt{2+\epsilon} + C_2(A-B)\sqrt{\epsilon}}{32(1+\epsilon)(2+\epsilon)^2(9+4\epsilon)^3\sqrt{2\epsilon(1+\epsilon)}} \right] \end{aligned} \tag{15.2}$$

Table 15.3 SDOF model of the LTVA and NLTVA

	m_2	c_2	k_2	k_{nl2}
LTVA	3.315×10^{-2} kg	2.279 Ns/m	1.014×10^3 N/m	–
NLTVA	3.735×10^{-2} kg	1.959 Ns/m	8.161×10^2 N/m	2.896×10^7 N/m^3

where

$$\begin{aligned}
\mu_1 &= \frac{c_1}{2\sqrt{m_1 k_1}} \\
A &= \sqrt{3(2+\epsilon) - \sqrt{\epsilon(2+\epsilon)}} \\
B &= \sqrt{3(2+\epsilon) + \sqrt{\epsilon(2+\epsilon)}} \\
C_0 &= 52 + 41\epsilon + 8\epsilon^2 \\
C_1 &= -1296 + 2124\epsilon + 6509\epsilon^2 + 5024\epsilon^3 + 1616\epsilon^4 + 192\epsilon^5 \\
C_2 &= 48168 + 112887\epsilon + 105907\epsilon^2 + 49664\epsilon^3 + 11632\epsilon^4 + 1088\epsilon^5
\end{aligned} \tag{15.3}$$

and $\epsilon = m_2/m_1$ is the mass ratio. We note that Eq. (15.2) reduce to Den Hartog's approximate formulas[13] for undamped main system ($\mu_1 = 0$):

$$\begin{aligned}
k_2 &= \epsilon k_1 \left[\frac{1}{1+\epsilon}\right]^2 \\
c_2 &= 2\sqrt{k_2 m_2}\sqrt{\frac{3\epsilon}{8(1+\epsilon)}}
\end{aligned} \tag{15.4}$$

Considering the harmonically-forced, lightly-damped Duffing oscillator derived in Sect. 15.2, the performance of the LTVA attached to this nonlinear system is investigated. The equations of motion of the coupled system are

$$\begin{aligned}
m_1\ddot{x}_1 + c_1\dot{x}_1 + k_1 x_1 + k_{nl1}x_1^3 + c_2(\dot{x}_1 - \dot{x}_2) + k_2(x_1 - x_2) &= F\cos\omega t \\
m_2\ddot{x}_2 + c_2(\dot{x}_2 - \dot{x}_1) + k_2(x_2 - x_1) &= 0.
\end{aligned} \tag{15.5}$$

The tuning of the LTVA is performed considering a physical mass ratio, $\epsilon_{phys} = m_2/(m_{beam})$, of 3 %. This constraint directly sets the LTVA mass to 3.315×10^{-2} kg, and, as a consequence, the effective mass ratio is $\epsilon = m_2/m_1 = 11.46\,\%$. The parameters of the optimal LTVA, calculated from Eq. (15.2) with the values given in Table 15.2, are listed in Table 15.3.

Figure 15.3a shows the ratio between the displacement response at beam tip and the applied force for various forcing amplitudes, namely $F = 1.0$ N, $F = 3.5$ N, $F = 6.5$ N and $F = 9.5$ N. The frequency response curves are computed using a path-following algorithm combining shooting and pseudo-arclength continuation [14]. For low values of forcing amplitude, the two resonant peaks have similar amplitude, which validates the effectiveness of the equal-peak rule for linear regimes of motions. However, increasing the forcing amplitude activates the nonlinearity of the thin beam. As a result, the amplitude of the second resonant peak increases significantly, which confirms that the LTVA is ineffective in nonlinear regimes of motion.

15.3.2 The Nonlinear Tuned Vibration Absorber (NLTVA)

In [6], following previous studies [15, 16], a nonlinear vibration absorber, termed the nonlinear tuned vibration absorber (NLTVA), was proposed. One unconventional feature of this absorber is that the mathematical form of the restoring force is not determined a priori, but it is chosen as a "mirror" of the primary system's restoring force. In other words, if the primary system presents linear and cubic springs, the NLTVA should also possess linear and cubic springs. The absorber parameters are then determined so as to ensure equal peaks in nonlinear regimes of motion, giving rise to an effective reduction of the resonance response in a large range of forcing amplitudes.

The equations of motion of the Duffing oscillator of Sect. 15.2 with an attached NLTVA are

$$m_1\ddot{x}_1 + c_1\dot{x}_1 + k_1 x_1 + k_{nl1}x_1^3 + c_2(\dot{x}_1 - \dot{x}_2) + k_2(x_1 - x_2) + k_{nl2}(x_1 - x_2)^3 = F\cos\omega t$$

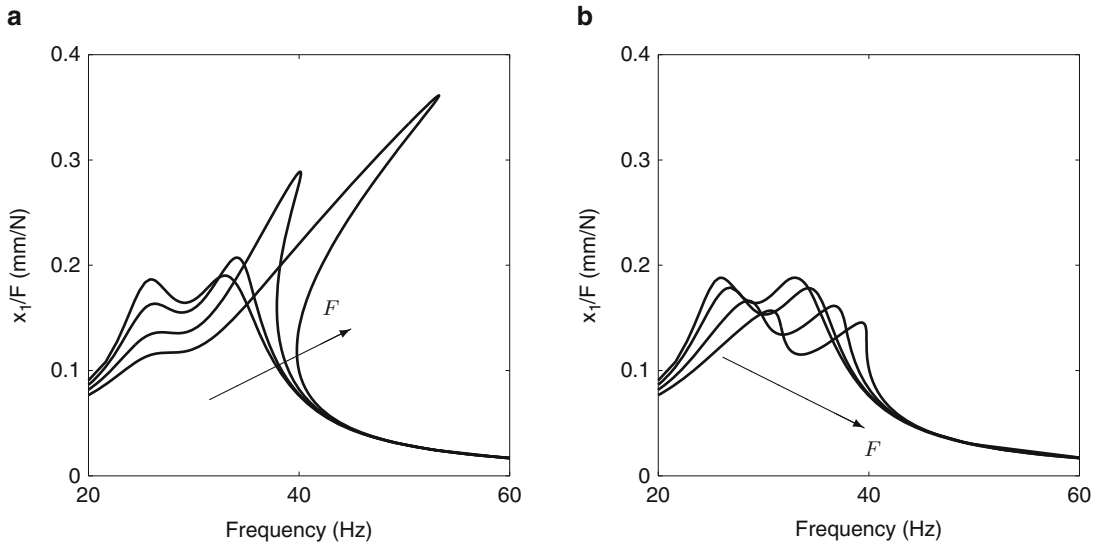

Fig. 15.3 Ratio between the frequency response and the force in a Duffing oscillator with the LTVA or the NLTVA attached. For the different curves the forcing amplitude is $F = 1.0\,\text{N}$, $F = 3.5\,\text{N}$, $F = 6.5\,\text{N}$ and $F = 9.5\,\text{N}$. (**a**) LTVA. (**b**) NLTVA

Table 15.4 Polyjet digital ABS material properties

Young modulus	Density	Elongation at break	Minimum thickness
1,950 MPa	1,175 kg/m^3	32 %	0.5 mm

$$m_2\ddot{x}_2 + c_2(\dot{x}_2 - \dot{x}_1) + k_2(x_2 - x_1) + k_{nl2}(x_2 - x_1)^3 = 0 \tag{15.6}$$

The tuning rules for the linear parameters of the NLTVA, k_2 and c_2, are those presented in Eq. (15.2). For the nonlinear coefficient k_{nl2}, it is provided in reference [6]:

$$k_{nl2} = \frac{2\epsilon^2}{(1+4\epsilon)} k_{nl1} \tag{15.7}$$

An interesting observation is that the ratio between the two nonlinear stiffnesses is linear and depends only on the mass ratio ϵ, a quite surprising finding for a nonlinear system. As for the LTVA, a physical mass ratio, $\epsilon_{phys} = m_2/(m_{beam} + m_{supp})$, of 3 % is considered. Hence, the NLTVA mass is 3.735×10^{-2} kg, and the effective mass ratio is $\epsilon = m_2/m_1 = 9.13\,\%$. The NLTVA parameters can be calculated from Eqs. (15.2, 15.7) and Table 15.2; they are listed in Table 15.3.

The effectiveness of the NLTVA is proved in Fig. 15.3b for the same primary system already considered for the LTVA. It can be noted that the strong detuning characterizing the LTVA does no longer occur. When the forcing amplitude F increases, the peaks of the frequency response function x_1/F remain equal or almost equal for the largest forcing amplitude.

15.4 Practical Realization of LTVA and NLTVA Using Cantilever and Doubly-Clamped Beams

Different beam models are used for the LTVA and NLTVA, since the stiffness requirements for the tuning are not the same. Specifically, linear cantilever beams are considered for the practical implementation of the LTVA, whereas nonlinear doubly-clamped beams are considered for the NLTVA. Both absorbers were manufactured using a Stratasys 3D printer with the Polyjet Digital ABS material. This material is specifically designed to simulate engineering plastics with high strength, and it also offers the possibility to create thin-walled parts. The mechanical properties are given in Table 15.4.

Table 15.5 Geometrical dimensions of the cantilever and doubly-clamped beams

Beam	Length	Width	Thickness	Mass
Cantilever (LTVA)	263.0 mm	10.4 mm	10.4 mm	3.3×10^{-2} kg
Doubly-clamped (NLTVA)	236.5 mm	4.5 mm	4.4 mm	0.6×10^{-2} kg

15.4.1 LTVA Cantilever Beam

The design of a linear cantilever beam of mass m_2 and of first natural frequency $\omega_2 = \sqrt{k_2/m_2}$ is a classical problem that, solved with respect to the beam length L, yields

$$L = \left(\frac{1.875^4 E m_2}{12\omega_2^2 \rho^2}\right)^{1/5} \tag{15.8}$$

where E is the material's Young modulus and ρ is the material's density. To guarantee that the beam behaves linearly, large deflections have to be avoided for the operating loading conditions. Therefore, a squared cross section of thickness t and width w

$$t = w = \left(\frac{m_2}{\rho L}\right)^{1/2} \tag{15.9}$$

is utilized. The geometrical dimensions of the cantilever beam are obtained from the parameters in Table 15.3 and are listed in Table 15.5.

15.4.2 NLTVA Doubly-Clamped Beam

According to the mirror rule, the NLTVA should behave as a Duffing oscillator around the resonance of interest. Doubly-clamped beams are suitable candidates for NLTVA realization, because the mid-plane stretching effect, not present in cantilever beams, can quickly activate nonlinear behaviors. Another advantage is that the geometrical dimensions of uniform doubly-clamped beams can be derived analytically as functions of only the linear k_2 and nonlinear k_{nl2} stiffness coefficients in Eqs. (15.2) and (15.7), respectively:

$$k_2 = 2\pi^4 \frac{EI}{L^3}, \qquad k_{nl2} = \pi^4 \frac{EA}{8L^3} \tag{15.10}$$

in which A and I are the cross-section area and momentum of inertia, respectively. The analytic derivation is explained in [17].

It is interesting to observe that the coefficient of the nonlinear term depends on the axial stiffness of the beam EA, as in [18]. Therefore, the cross-section dimensions are the geometrical parameters driving the design. In fact, the ratio between the nonlinear and linear coefficients depends only on the area and the momentum of inertia. For rectangular cross sections, the thickness t can be directly deduced from this relationship

$$t = \sqrt{\frac{3k_2}{4k_{nl2}}} \tag{15.11}$$

whereas the beam length L and the cross-section width w can be chosen to satisfy the following constraint

$$\frac{L^3}{w} = \frac{\pi^4 E t}{8k_{nl2}} \tag{15.12}$$

Once the material is chosen, the design of a rectangular doubly-clamped beam capable to follow a prescribed cubic load-deflection curve reduces to a problem that admits multiple solutions. An additional constraint can therefore still be imposed (e.g., manufacturing limitations). The linear and nonlinear stiffness coefficients in Table 15.3 are used to evaluate the

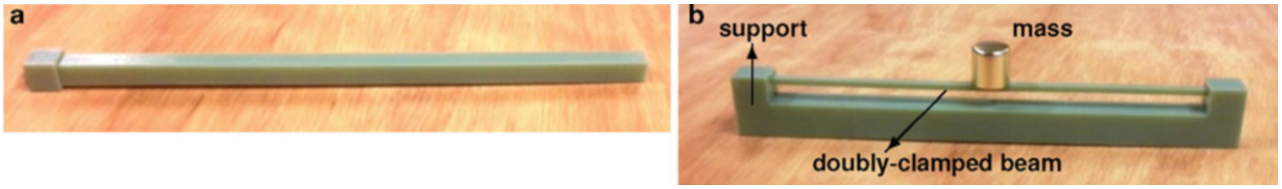

Fig. 15.4 (**a**) LTVA and (**b**) NLTVA manufactured using 3D-printing

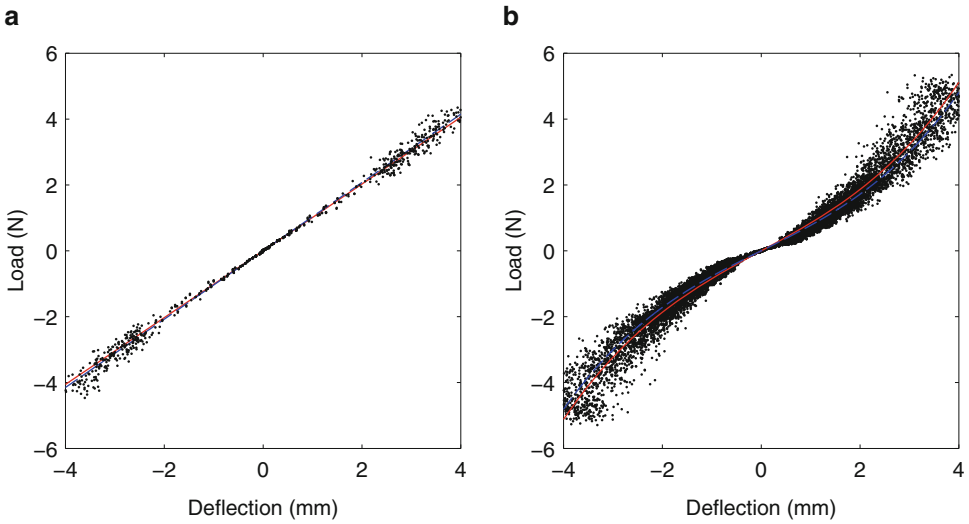

Fig. 15.5 Stiffness curves of the 3D-printed absorbers: prescribed (*red lines*), measured (*black dots*) and fitted (*blue dashed lines*) curves. (**a**) LTVA. (**b**) NLTVA (Color figure online)

geometrical dimensions of the doubly-clamped beam from Eqs. (15.11)–(15.12), and the results are given in Table 15.5. We remark that the mass of the designed doubly-clamped beam is much lower than the value assigned to m_2 in Table 15.3; a lumped mass is then added at midspan so that the nonlinear beam behaves as a SDOF NLTVA. We also note that there was no attempt at tuning the NLTVA damping through, e.g., the selection of a proper material.

15.4.3 Experimental Characterization of the Manufactured Absorbers

The LTVA and NLTVA were manufactured using 3D-printing and are shown in Fig. 15.4. Specifically, the doubly-clamped beam and its support were produced as a monolithic structure to ensure appropriate clamped-clamped boundary conditions.

In order to characterize the manufactured absorbers, the restoring force surface (RFS) method was employed since it yields a convenient visualization of the restoring force. For this purpose, the absorbers were mounted on the shaker, and a base excitation test was carried out using sine sweep around the first resonance. The accelerations at the base $\ddot{x}_{base}$ and at the point on the beam experiencing the maximum deflection (i.e., the tip of the cantilever beam and the midspan of the doubly-clamped beam) $\ddot{x}$ were measured and integrated once and twice to evaluate velocities and displacements, respectively. The RFS method relies on Newton's second law of motion, which can be written for the case under investigation as

$$m\,\ddot{x} + f(x - x_{base}, \dot{x} - \dot{x}_{base}) = 0 \tag{15.13}$$

where f is the restoring force of the system. If the relative displacement is defined as $y = x - x_{base}$, this equation recasts into

$$f(y, \dot{y}) = -m\,\ddot{x} \tag{15.14}$$

A direct access to a nonparametric estimate of the restoring force surface defined by the triplets $(y,\ \dot{y},\ -m\,\ddot{x})$ is then obtained. The intersection of this surface with the zero-velocity plane provides the stiffness curve. Figure 15.5 represents the experimentally-evaluated stiffness curves for the LTVA and the NLTVA. There is a very close agreement between the measured and prescribed stiffness curves, both for the LTVA and NLTVA. Fitting with measured LTVA curves with a line

provides an estimate of the linear stiffness equal to 1.037×10^3 N, which is only in error of 2 % with respect to the prescribed value. For the NLTVA, the fitting with a polynomial with linear and cubic terms provides the linear and cubic coefficients, i.e., 7.449×10^2 N/m and 2.861×10^7 N/m^3, respectively. They correspond to an error of 9 % and 1 %, respectively. Finally, we notice that the experimental dots in Fig. 15.5 closely follow the prescribed curves for small deflections, whereas they are more scattered at the outer limits of the interval. This is attributed to the extrapolation of the points of the stiffness curve using the RFS method. Indeed, the points of the 3D surface with relative velocity practically equal to 0 are not in sufficient number to draw the stiffness curve, and this curve has to be traced by considering points with small, but non-zero, relative velocity. A dependency of the load on the relative velocity was also responsible for the scattering of the outer points.

15.5 Experimental Demonstration of LTVA and NLTVA Performance

In this section the LTVA and NLTVA are attached to the nonlinear beam, as depicted in Fig. 15.6. The first objective is to confirm that the LTVA is effective only in linear regimes of motion, as discussed in Sect. 15.3.1. The second objective is to demonstrate that this limitation can be overcome by the NLTVA, as claimed in Sect. 15.3.2.

The coupled beam and LTVA system is first analyzed. Figure 15.7a plots the amplitude of the displacement at the main beam tip where the nonlinearity is located for sine sweep excitation at low level. Two resonance peaks of unequal amplitudes are observed. This discrepancy can be explained by analyzing the force signal measured at the interface between the structure and the shaker, represented in Fig. 15.7b. In fact, the experimental test is not performed at constant forcing level, although the voltage provided to the shaker is kept constant. Specifically, drops in the force amplitude can be noted at the resonant frequencies, a phenomenon that is typically encountered during vibration testing. However, the corresponding frequency response function (FRF) depicted in Fig. 15.7c displays two equal peaks, which validates the LTVA design and the effectiveness of this absorber for linear regimes. When the driving signal provided to the shaker is doubled, the displacement amplitude increases as in Fig. 15.7d, and the resonance peaks seem to get closer. Nevertheless, the drops in the corresponding forcing amplitude are not equal, as shown in Fig. 15.7e. The FRF in Fig. 15.7f presents two peaks of unequal amplitude, meaning that a detuning of the LTVA has happened.

Figure 15.8a–c depict the plots of the NLTVA performance for low-level sine sweep excitation. The FRF in Fig. 15.8c shows two equal peaks, which can be considered as a proof of the NLTVA effectiveness when the system behaves linearly. The presence of the NLTVA support affects the primary structure's resonances, as already point out in Sect. 15.2. Therefore, the NLTVA curves are shifted toward lower frequencies in contrast to the LTVA. Nevertheless, this effect does not affect the findings of this paper, because the absorbers were tuned accordingly. Figure 15.8d–f presents the displacement, force and FRF amplitude, respectively, when the driving signal provided to the shaker is doubled. The two resonance peaks in the FRF remains equal although the energy supplied to the system is high enough to activate the nonlinearity in the thin beam. Unlike the LTVA, the NLTVA is still effective at this forcing level.

In order to better quantify the detuning of the LTVA caused by the frequency-energy dependence of the oscillations, Fig. 15.9a shows the displacement amplitude of the two resonant peaks at their corresponding force amplitudes for various excitation levels. The peak amplitudes are equal for low forcing amplitudes, but then they rapidly diverge from each other

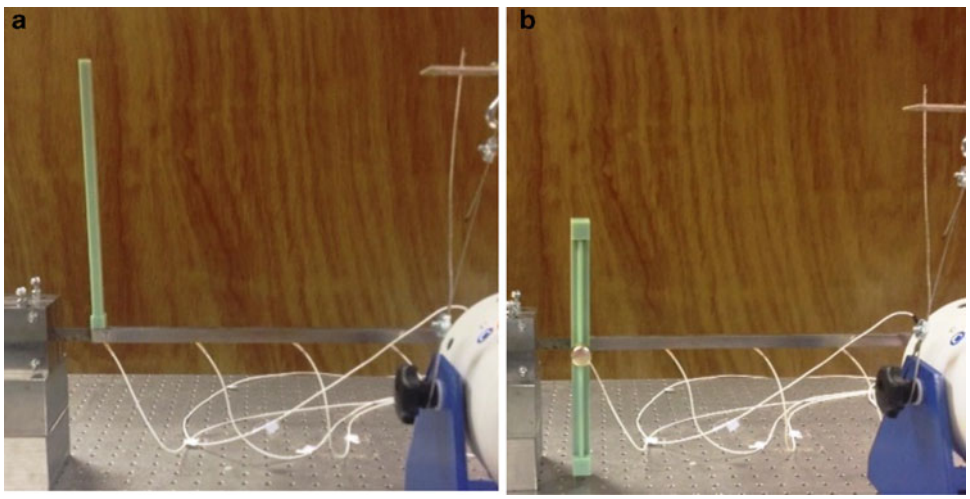

Fig. 15.6 Primary structure with attached (**a**) LTVA and (**b**) NLTVA

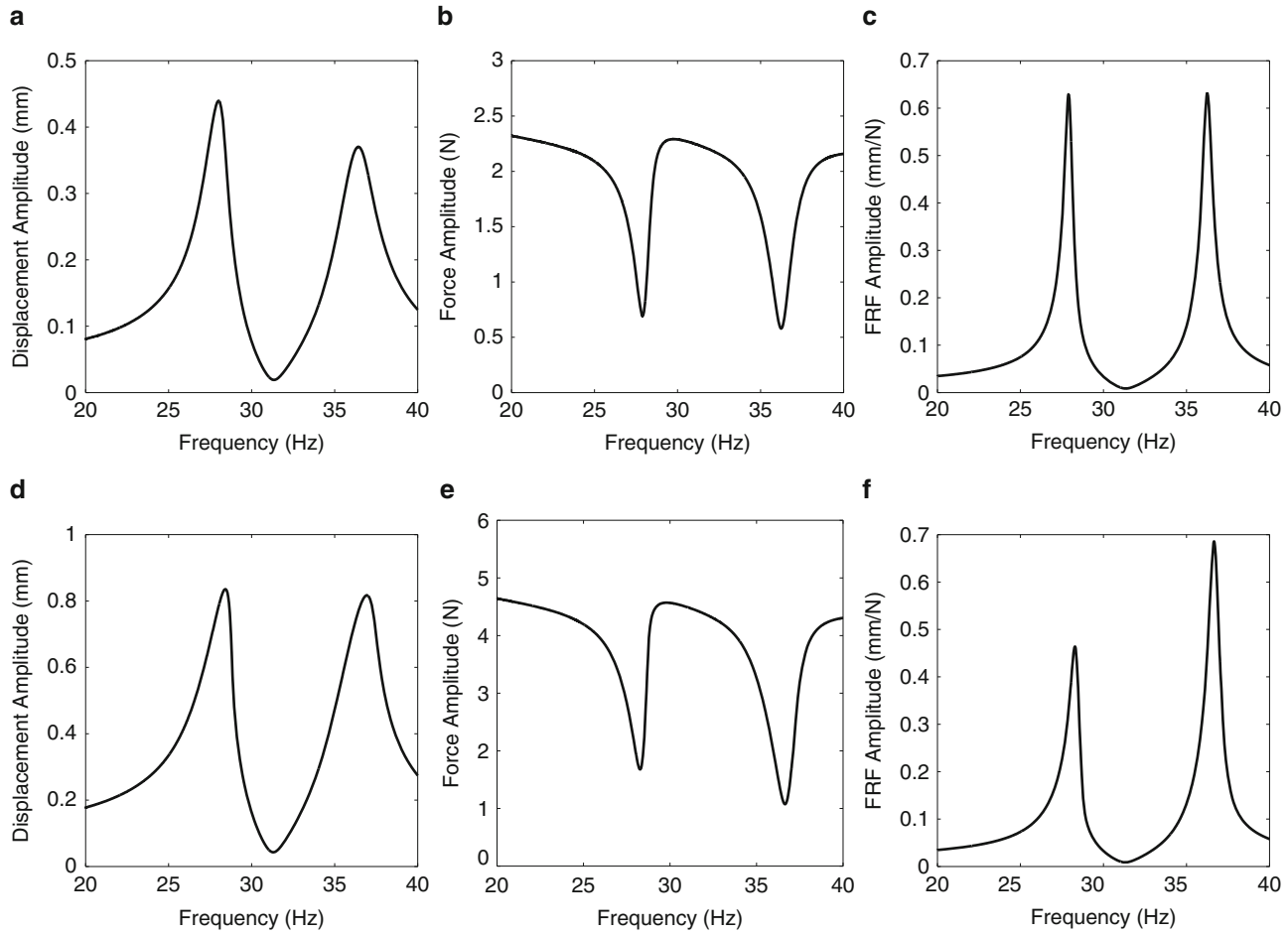

Fig. 15.7 Experimental responses of the primary system with an attached LTVA (sine sweep excitation). (**a**, **d**) Displacement amplitude at the main beam tip, (**b**, **e**) force amplitude at the driving point, (**c**, **f**) FRF amplitude, for low and high excitation levels, respectively

for forces greater than 1 N. After this point the amplitude of one resonant peak increases significantly making the absorber ineffective. For the NLTVA, two resonant peaks with virtually the same amplitude are observed for all considered excitation levels in Fig. 15.9b, which is a confirmation of the excellent performance of the nonlinear absorber.

A final remark is that the coupled primary structure and NLTVA system seems to obey the superposition principle in Fig. 15.9b. Indeed, the response increases almost linearly with the forcing amplitude, whereas the coupled system vibrates in nonlinear regimes of motion. It therefore seems that the addition of a nonlinear attachment to a nonlinear system can somehow provides more linear dynamics. This interesting phenomenon will be investigated more closely in future studies.

15.6 Concluding Remarks

The objective of this study was to verify experimentally the effectiveness of a new nonlinear tuned vibration absorber, the NLTVA. A complete procedure starting from the experimental identification of the primary structure to the testing of the coupled system was also proposed. An important feature of this methodology is that the nonlinear doubly-clamped beam implementing the NLTVA in practice and manufactured using 3D printing could be designed by resorting only to analytic formulas. The experimental test campaign demonstrated that the NLTVA clearly outperforms its linear counterpart (the LTVA), since this former absorber is able to maintain equal peaks in nonlinear regimes of motion.

Acknowledgements The authors would like to acknowledge the financial support of the European Union (ERC Starting Grant NoVib 307265). The authors also want to thank LMS A Siemens Business for providing access to the LMS Test.Lab software.

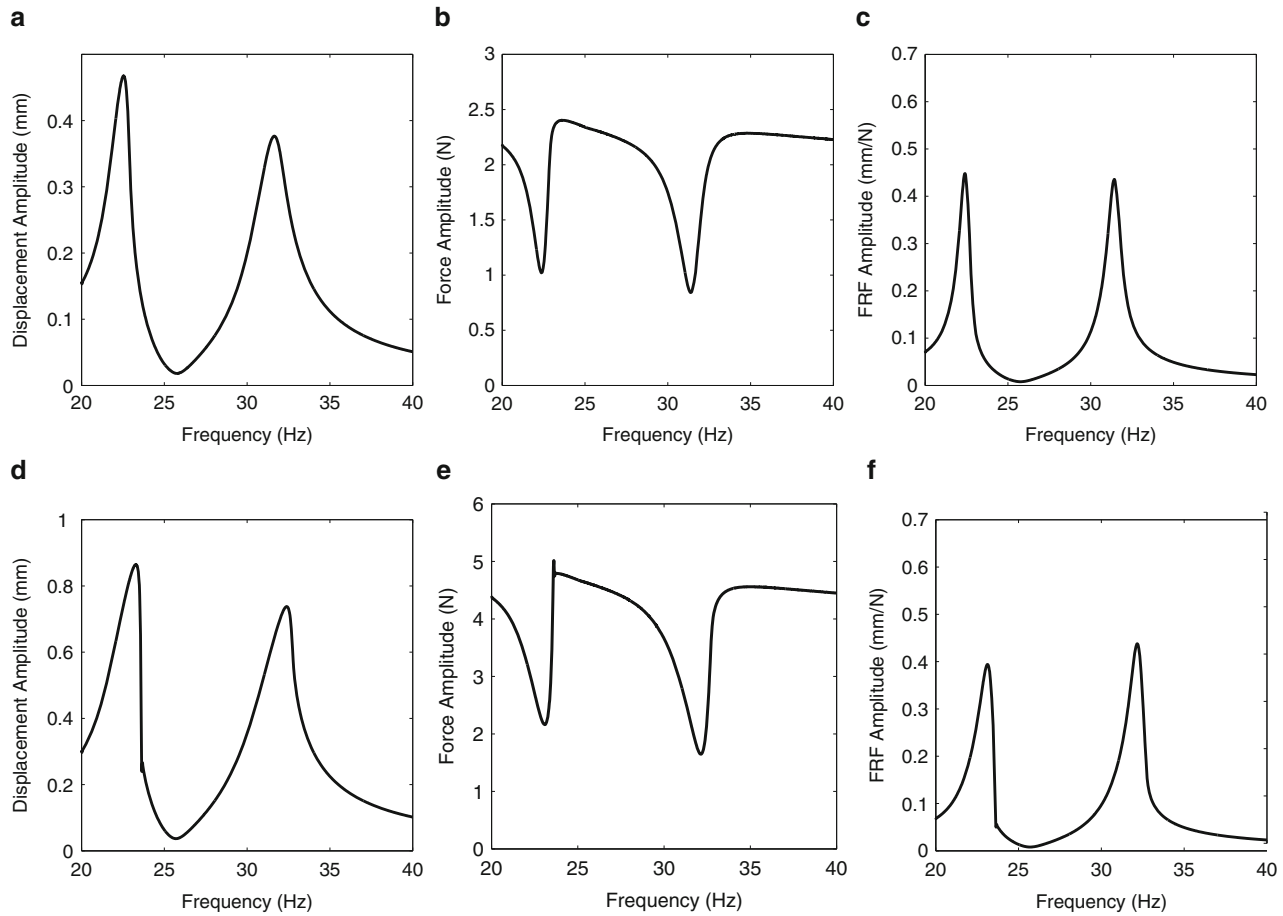

Fig. 15.8 Experimental responses of the primary system with an attached NLTVA (sine sweep excitation). (**a**–**d**) Displacement amplitude at the main beam tip, (**b**–**e**) force amplitude at the driving point, (**c**–**f**) FRF amplitude, for low and high excitation levels, respectively

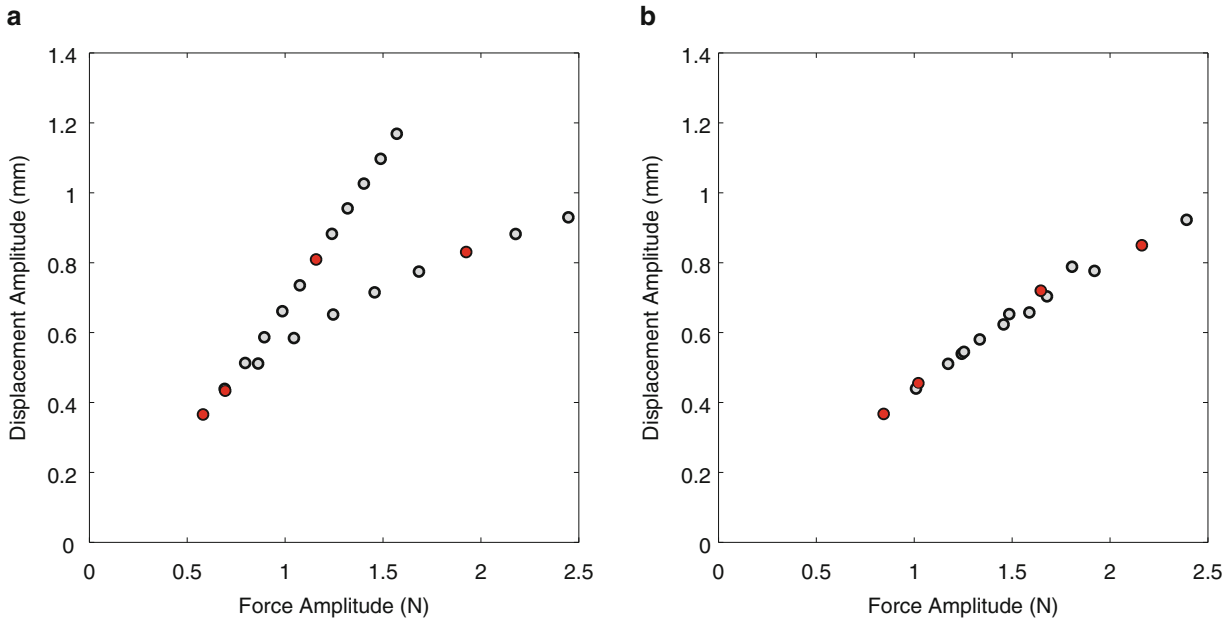

Fig. 15.9 Amplitude of the resonance peaks at the tip of the primary beam for increasing forcing amplitudes ((**a**) LTVA and (**b**) NLTVA). The *red dots* represent the values in Figs. 15.7 and 15.8 (Color figure online)

References

1. Den Hartog JP (1934) Mechanical vibrations. McGraw-Hill, New York
2. Oueini S, Nayfeh A (2000) Analysis and application of a nonlinear vibration absorber. J Vib Control 6:999–1016
3. Vyas A, Bajaj A (2001) Dynamics of autoparametric vibration absorbers using multiple pendulums. J Sound Vib 246:115–135
4. Vakakis A, Gendelman OV (2001) Energy pumping in nonlinear mechanical oscillators, Part II: resonance capture. J Appl Mech 68:42–48
5. Vakakis AF, Gendelman O, Bergman LA, McFarland DM, Kerschen G, Lee YS (2009) Nonlinear targeted energy transfer in mechanical and structural systems. Solid mechanics and its applications. Springer, Netherlands
6. Habib G, Detroux T, Viguié R, Kerschen G (2015) Nonlinear generalization of Den Hartog's equal-peak method. Mech Syst Signal Process, Elsevier, 52:17–28
7. Thouverez F (2003) Presentation of the ECL benchmark. Mech Syst Signal Process 17:195–202
8. Noël JP, Kerschen G (2013) Frequency-domain subspace identification for nonlinear mechanical systems. Mech Syst Signal Process 40:701–717
9. Frahm H (1909) Device for damping vibrations of bodies. US Patent 989958, 1909
10. Ormondroyd J, Den Hartog JP (1928) The theory of the dynamic vibration absorber. Trans ASME 50:9–22
11. Asami T, Nishihara O (2003) Closed-form exact solution to H∞ optimization of dynamic vibration absorbers (application to different transfer functions and damping systems). J Vib Acoust 125:398–405
12. Asami T, Nishihara O, Baz AM (2002) Analytical solutions to H∞ and H_2 optimization of dynamic vibration absorbers attached to damped linear systems. J Vib Acoust 124:284–295
13. Den Hartog JP (1985) Mechanical vibrations. McGraw-Hill, New York
14. Peeters M, Viguié R, Sérandour G, Kerschen G, Golinval JC (2009) Nonlinear normal modes, Part II: toward a practical computation using numerical continuation. Mech Syst Signal Process 23:195–216
15. Viguié R, Kerschen G (2010) On the functional form of a nonlinear vibration absorber. J Sound Vib 329(25):5225–5232
16. Denman HH (1992) Tautochronic bifilar pendulum torsion absorbers for reciprocating engines. J Sound Vib 159(2):251–277
17. Grappasonni C, Habib G, Detroux T, Wang F, Kerschen G, Jensen J (2014) Practical design of a nonlinear tuned vibration absorber. In: Proceedings of the ISMA 2014 conference, 2014
18. Senturia S (2001) Microsystem design, vol 3. Kluwer Academic Publishers, Boston

Chapter 16
The Effect of Gravity on a Slender Loop Structure

Lawrence N. Virgin, Raymond H. Plaut, and Elliot V. Cartee

Abstract The deformation and vibration of vertical, highly flexible loops are investigated primarily from an experimental perspective. Both upright and hanging loops are considered with a small clamped length. The effects of self-weight on the loop static deformation and lowest frequency for in-plane symmetric vibrations are determined. Good agreement is attained between some theoretical results (based on an inextensible elastica model) and the experimental data. An interesting phenomenon of adjacent, co-existing solutions is also described.

Keywords Nonlinear mechanics • Elastica • Vibration • Co-existing equilibria • Experiments

16.1 Introduction

Thin elastic structures may be sufficiently lightweight and slender that gravity competes with elastic stiffness in determining equilibrium shapes and natural frequencies [1]. This paper describes a relatively simple system configured in a closed loop-like geometry, see Fig. 16.1a [2]. A key non-dimensional parameter is $\bar{w} = WL^3/EI$ in which W is the weight per unit length (and equivalent to ρAg), L is the arc-length of the loop, and EI is flexural rigidity (the product of Young's modulus, E, and the second moment area of the cross-section, $I = bd^3/12$).For practical reasons we have a relatively short, finite clamp length, C, as shown in Fig. 16.1. In this figure the orientation is upright, with a finite length of the loop resting on the foundation, but the hanging down case is easily obtained by flipping the direction of gravity and defining negative values of $\bar{w}$ for this case (with no foundation).

Since the loop is made of an initially flat, thin, sheet of material with width b (into the page), and thickness d, we see that $\bar{w}$ scales with L^4 and d^2, for the same material, and it's interesting to note the independence of this parameter on width, b, see Fig. 16.1b. That is, for long, thin shapes ($\bar{w} \to \infty$) the weight effect dominates, whereas for short, thick shapes ($\bar{w} \to 0$) the elastic stiffness dominates. For the latter case we obtain close to a circle (of diameter L/π), the familiar elastic ring from conventional structural mechanics [3]. Given the fact that weight and stiffness both scale linearly with b it seems that a narrow ring-like structure should have the same general behavior as a wide roll-type structure (not unlike a roll of carpet). However, in this paper we shall focus most attention on systems in which these competing effects are of comparable influence. Some representative shapes for both the upright and hanging orientations are shown in Fig. 16.2. In the extreme case, with $\bar{w} \to \infty$ we would expect $Y_c \to 0$ for the upright orientation, and $|Y_c| \to L/2$ for the hanging down orientation.

In this paper we shall mostly focus on the upright orientation since this tends to exhibit more interesting behavior. The static deformation metric will be based largely on the vertical distance of the mid-point Y_c from the support point. The lowest natural frequencies about these shapes are also of interest, and they are reported too. We non-dimensionalize the mid-point deflection using $y = Y_c/L$ and the natural frequency using $\Omega = \omega L^2\sqrt{W/EIg}$, and examine both of these characteristics as a function of $\bar{w}$. A limited amount of results from numerical analysis are included for comparison purposes, but their derivation is not reported here. The analysis is based on solving the governing partial differential equations in terms of arc-length coordinates using a shooting method. Further details of this type of elastica analysis, in which the determination of the flat resting portion of the shape in the upright configuration is a key step, can be found in [4].

L.N. Virgin (✉)
Department of Mechanical Engineering and Materials Science, Duke University, Durham, NC 27708, USA
e-mail: l.virgin@duke.edu

R.H. Plaut
Department of Civil and Environmental Engineering, Virginia Tech, Blacksburg, VA 24061, USA

E.V. Cartee
Department of Mathematics, Cornell University, Ithaca, NY 14850, USA

G. Kerschen (ed.), *Nonlinear Dynamics, Volume 1*, Conference Proceedings of the Society for Experimental Mechanics Series, DOI 10.1007/978-3-319-15221-9_16

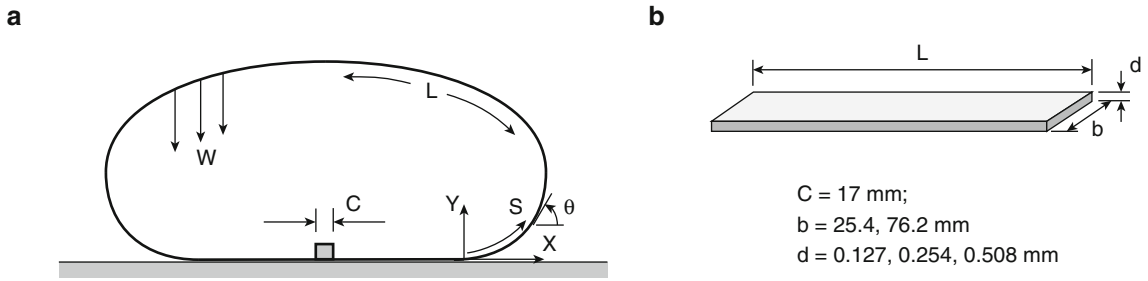

Fig. 16.1 The geometry of a loop structure, (**a**) supported by a rigid table, (**b**) initially flat, thin strips make up the loop

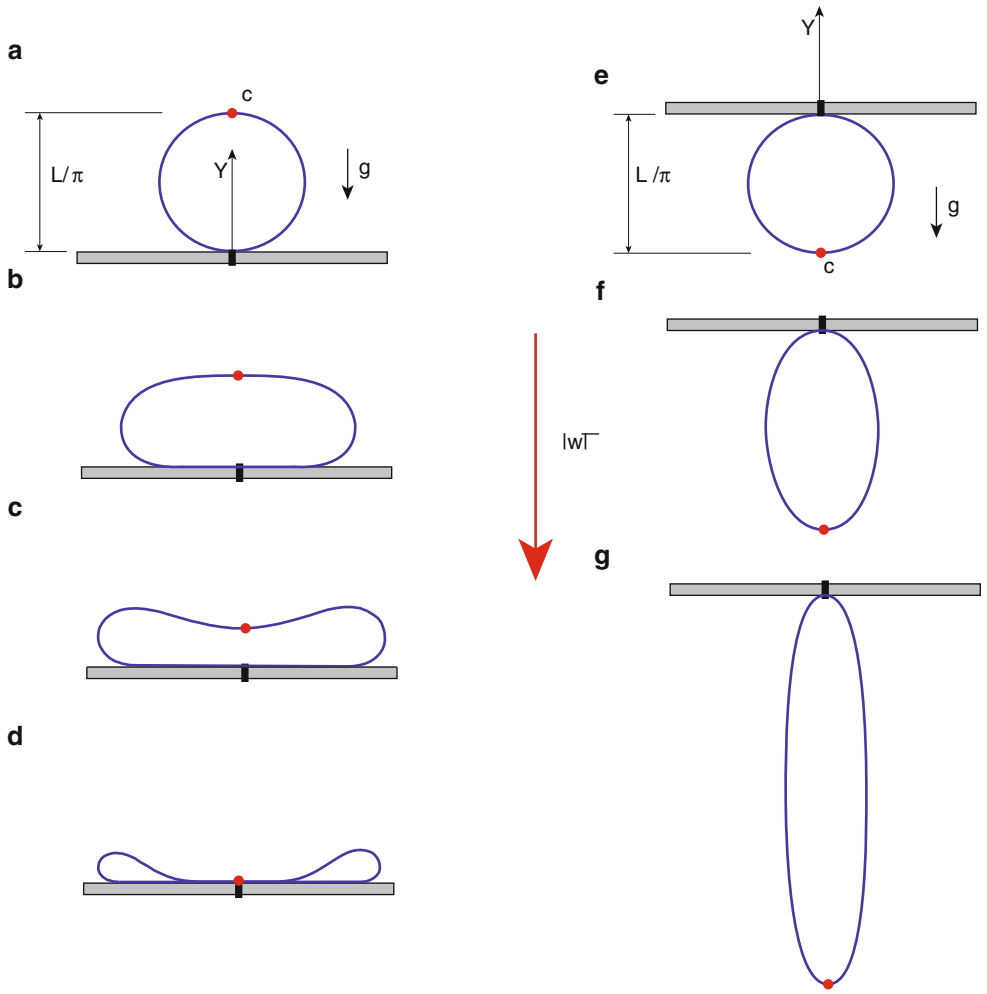

Fig. 16.2 Sample shapes for different lengths or weights, (**a**)–(**d**) upright; (**e**)–(**g**) hanging

16.2 The Experimental System

The material used in this work is polycarbonate, with Young's modulus $E = 2.25\,\text{GPa}$, and density $\rho = 1.18 \times 10^{-3}\,\text{g/mm}^3$. Two widths b are chosen: 25.4 and 76.2 mm; three thicknesses, d: 0.127, 0.254, and 0.508 mm; and the length, L is the primary control parameter. Although the scaling suggests the width b does not play a role in the mechanics, it will be seen later that there is a non-negligible (and in fact very interesting) effect associated with the width dimension, and not captured by the 2D planar analysis.

A photographic image of the experimental system is shown in Fig. 16.3. An initially flat strip of polycarbonate is bent elastically to form a loop, which is then clamped (with a finite but small clamp length of $C = 17\,\text{mm}$). Thus, even for very short lengths the equilibrium shape is not quite circular. A laser proximity sensor measures the central vertical height

Fig. 16.3 An image of the experimental loop and measurement system. Width $b = 76.2\,\text{mm}$

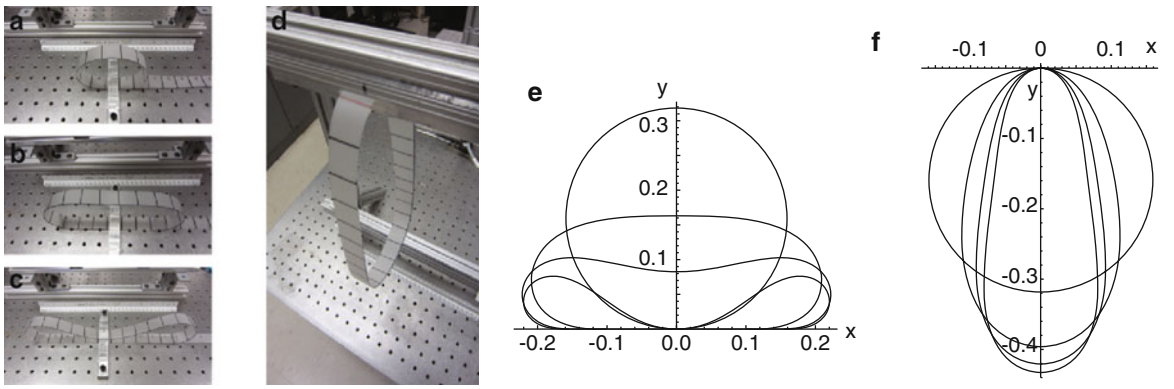

Fig. 16.4 (**a**)–(**d**) Some typical experimental deflected shapes (width $b = 25.4\,\text{mm}$), (**e**)–(**f**) sample numerical results

of the loop, Y_c, primarily as a function of loop length L, and hence $\bar{w}$. At each L the loop is subject to a small vertical perturbation. This leads to a decaying transient oscillation from which a natural frequency can be extracted using appropriate signal processing. The damping in the system is light, such that there is no appreciable difference between the damped and undamped natural frequencies.

16.3 Results

Figure 16.4 shows a sample of results in terms of equilibrium configurations for different lengths. Parts (a)–(d) show equilibrium shapes for the upright and hanging configurations. Parts (e) and (f) show some numerical results, although for a clamp length of zero, with $\bar{w} = 0, \pm 500, \pm 1000, \pm 1500$ for these cases. As mentioned previously, the key measurement is the vertical height of the loop, and specifically its deviation from a circular elastic stiffness-dominated shape. At a certain length the upright loop collapses onto itself in a pancake-type shape.

16.3.1 Results in Dimensional Terms

Figure 16.5 summarizes the static central deflection Y_c (mm) as a function of length L (mm) for three different thicknesses $d = 0.127$ (red), 0.254 (blue), 0.508 (black) mm, and a width b of 25.4 mm. These results correspond to the upright configuration, $\bar{w} > 0$. The requirement for elastic behavior limits the testing of very short arc-lengths (tightly wound loops), and the initial linearity of the three curves suggests a stiffness-dominated result as expected. As the length of the strip increases the loop height increases, initially, but then starts to reduce as the weight/stiffness ratio increases. The thickest strip is able to 'grow' to a relatively larger shape ($\bar{w}$ depends on the inverse square of the thickness). Part (b) plots the lowest

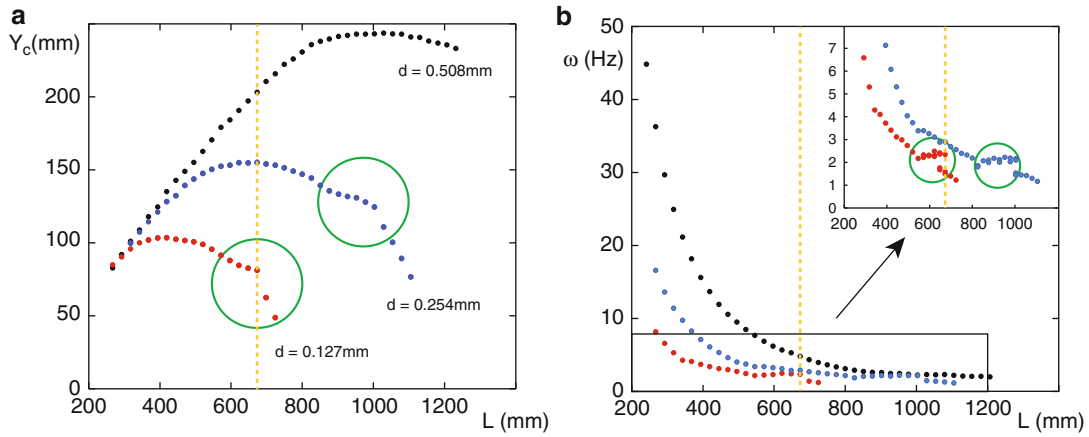

Fig. 16.5 (**a**) Central deflection versus arc-length, (**b**) lowest symmetric natural frequency versus arc-length (color figure online)

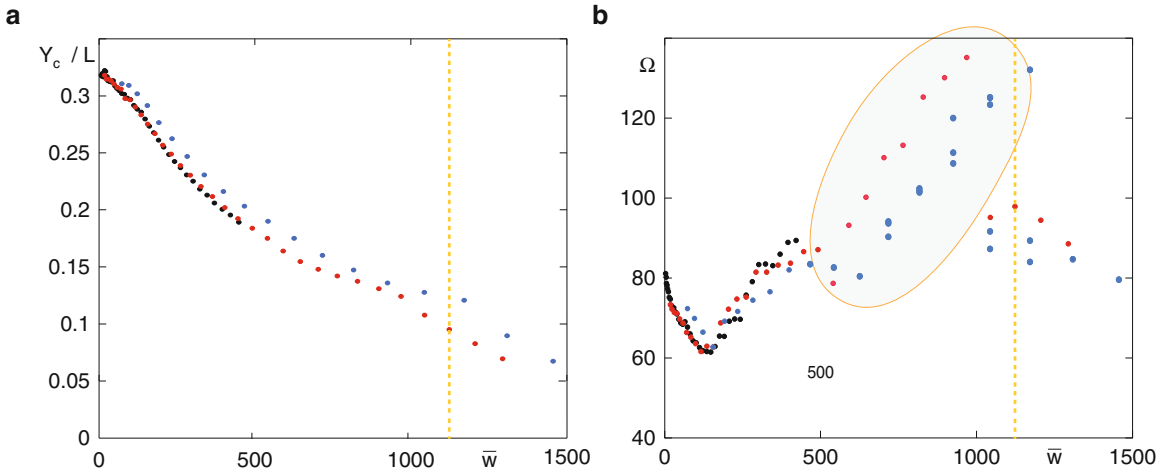

Fig. 16.6 (**a**) Non-dimensional central deflection, (**b**) non-dimensional natural frequency (color figure online)

symmetric natural frequency again as a function of length. For long lengths the frequency becomes very low, especially for the thinnest strip. This figure also contains a blow-up to feature an interesting (and unexpected) phenomenon, highlighted by the green circles, that we shall return to later.

16.3.2 Results in Non-dimensional Terms

We now recast these results in non-dimensional terms. Both central vertical deflection and the lowest symmetric natural frequency are plotted against $\bar{w}$ in Fig. 16.6. The data collapses onto a single universal curve in general. The intercept with the y-axis in part (a) corresponds to an almost circular shape with $Y_c/L \to 1/\pi$. The paucity of black data points (the thickest strip) for larger $\bar{w}$ is based on practical limitations in handling relatively large loops in the experimental apparatus. The frequencies show an interesting 'dip' in the behavior as the underlying equilibrium shape undergoes considerable change. Note that there appears to be a region of $\bar{w}$ for which the data does *not* fall onto the single curve, and also does not appear to 'belong' to the underlying curve elsewhere. This area is shown shaded in Fig. 16.6b and is related to the kinks in the dimensional results, although the nondimensionalization in part (a) does not seem to make this effect as apparent.

Figure 16.7 shows a comparison between experimental and numerical results now including the hanging down configuration as well. The small discontinuity for $\bar{w} \approx 0$ is associated with the finite clamp length. Agreement is generally good [4].

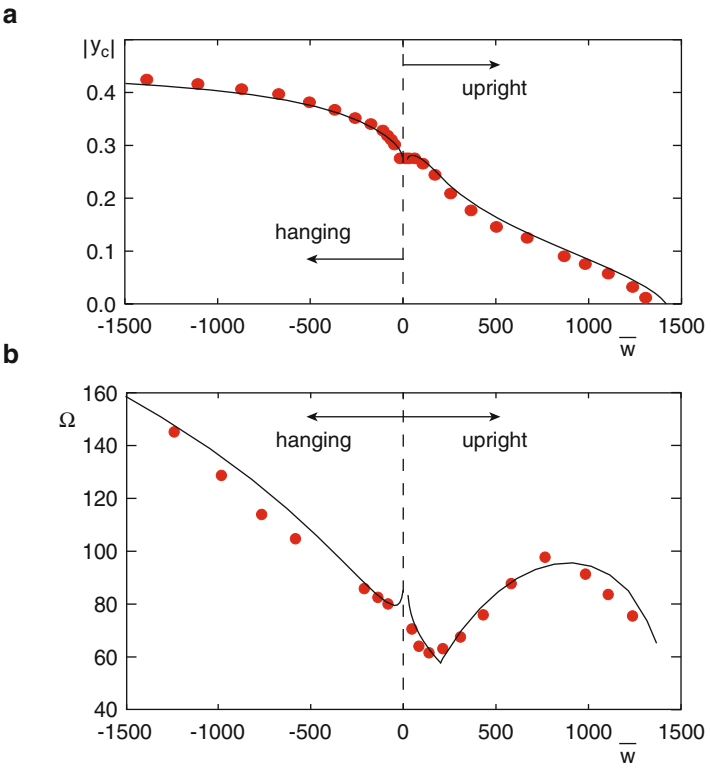

Fig. 16.7 Comparison between theory (*black lines*) and experimental data (*red dots*), (**a**) central deflection, (**b**) natural frequency. Width $b = 25.4$ mm (Color figure online)

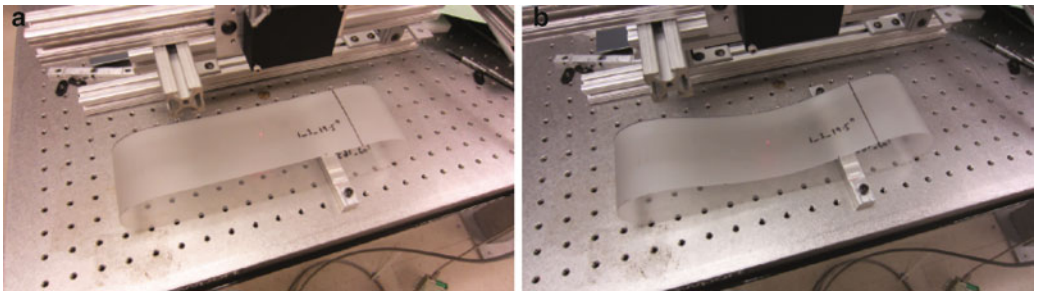

Fig. 16.8 Images of the two co-existing equilibrium shapes. $\bar{w} = 1{,}170$, $L = 673$ mm, $d = 0.127$ mm, $b = 76.2$ mm, (a) upper equilibrium shape, (b) lower equilibrium shape

16.3.3 An Interesting Feature

Mention has already been made of the small discontinuities appearing in Fig. 16.5, and indicated by the green circles. Over this range of $\bar{w}$ a region of hysteresis was observed, *but only for the wider of the strips*. In this range it was possible to observe two coexisting equilibria, and corresponding to the case in which the top part of the loop was close to horizontal. It was apparent that there was a certain 'plate-like' effect [5–7] along this top portion for the wider strip, and the behavior could be perturbed between two alternative adjacent equilibria. Figure 16.8 shows images of the two shapes, at exactly the same system parameters. It should be noted that the system was only marginally stable in an overall lateral sense at these parameter values.

Figure 16.9 shows a time series in which the system is perturbed between the two stable equilibria. The perturbations are indicated by the dark blue marks along the top axis in this figure. This case, and the images in the previous figure, correspond to $\bar{w} = 1{,}170$ ($L = 673, b = 76.2, d = 0.127$ mm) and also correspond to the dashed orange lines in Figs. 16.5 and 16.6.

The difference in the dominant natural frequency about these two equilibrium shapes is apparent. The vertical separation at the center corresponds to about 27 mm, and, with different lengths it was possible to find co-existing solutions with other vertical separations including the case in which the lower shape included a portion resting on the foundation. It should be reiterated that this behavior was not observed in the case in which $b = 25.4$ mm, which as we have stated, does not influence

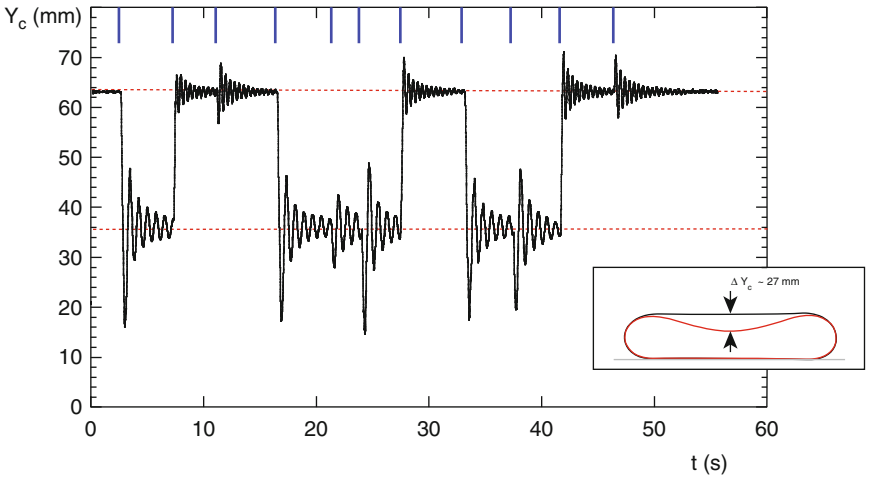

Fig. 16.9 A time series of small induced oscillations about, and between, the co-existing equilibrium shapes. $\bar{w} = 1{,}170$, $L = 673\,\text{mm}$, $d = 0.127\,\text{mm}$, $b = 76.2\,\text{mm}$

the non-dimensional ratio $\bar{w}$, again suggesting an additional, plate-like effect, possibly associated with anticlastic bending, but measurement in the width direction were not taken.

16.4 Conclusions

For very slender structures, in a gravitational field, the effect of weight can be as influential in determining equilibrium shapes as conventional elastic stiffness. For a loop structure, supported by a substrate, this results in squashed equilibrium shapes; if the loop is suspended below a support, then elongated, stretched equilibrium shapes result. A non-dimensional parameter determines the competing influences of weight and elastic stiffness. At one end of the spectrum the behavior is independent of gravitational effects and elastic stiffness dominates, as in conventional structural analysis. At the other end of the spectrum a structure will act more like a string (if hanging down) or collapse almost flat (if supported from below). The intermediate cases are most interesting and are here subject to systematic experimental study. The experimental data are closely predicted by some theoretical results. The appearance of co-existing (stable equilibrium) shapes at the same parameter values and accompanying hysteresis proved to be an unexpected but interesting feature. This behavior seems to be associated with two-dimensional bending and would not, therefore, be captured by the planar elastica analysis.

References

1. Virgin LN (2007) Vibration of axially loaded structures. Cambridge University Press, Cambridge, UK
2. Wang CY, Watson LT (1981) Equilibrium of heavy elastic cylindrical shells. J Appl Mech 48:582–586
3. Zakrzhevskii AK, Tkachenko VF, Khoroshilov VS (2010) Natural modes and frequencies of in-plane vibrations of a fixed elastic ring. Int Appl Mech 46:1420–1427
4. Plaut RH, Virgin, LN (2014) Deformation and vibration of upright loops on a foundation and of hanging loops. Int J Solids Struct 51:3067–3075
5. Bellow DG, Ford G, Kennedy JS (1965) Anticlastic behavior of flat plates. Exp Mech 5:227–232
6. Conway HD, Nickola WE (1965) Anticlastic action of flat sheets in bending. Exp Mech 5:115–119
7. Campanile LF, Jahne R, Hasse A (2011) Exact analysis of the bending of wide beams by a modified elastica approach. J Mech Eng Sci 225:2759–2764

Chapter 17
Wave Propagation in a Materially Nonlinear Rod: Numerical and Experimental Investigations

Yu Liu, Andrew J. Dick, Jacob Dodson, and Jason Foley

Abstract In order to facilitate an efficient and high fidelity analysis of nonlinear wave propagation, a modified Newton-Raphson iterative method is developed in order to improve the computational performance of the alternating wavelet-time finite element method (AWT-FEM). A non-dimensional model of a materially nonlinear rod is developed and a metric is constructed to quantify nonlinear dispersion in the response. A parametric study is conducted in order to investigate the influence of the nonlinear coefficient and other system parameters on the nonlinear behavior by using the modified AWT-FEM. An experimental investigation is performed by using a rod structure with a strong hardening-type material nonlinearity in order to verify the predicted phenomenon.

Keywords Rod • Wave propagation • Nonlinear • Wavelet • High fidelity simulation

17.1 Introduction

Many structures in industrial applications are subject to extreme impact loading conditions with high amplitude and short duration, which can result in high frequency content in the force profile and significantly magnify the nonlinear behavior in the response. With the development of novel materials and the advance of new structures and devices [1, 2], investigation of nonlinear behavior and its relation to system parameters and impact conditions has significant importance.

The source of nonlinearity can be divided into three categories: material, geometric, and boundary conditions [3]. In this study, the research is focused on the influence of material nonlinearity on the impact wave response. The material nonlinearity results from a nonlinear constitutive relationship between stress σ and strain ε. It is assumed that the impact conditions produce a wave response in an intermediate strain regime, for metals and polymers the range is typically characterized from 10^{-6} to 10^{-3}. The influence of geometric nonlinearity resulting from large deformation is not considered here. The case of plastic deformation and damage of the material is also not considered here.

In order to solve the problem of impact wave response in nonlinear structures, various numerical methods have been developed. The finite element method (FEM) [3] is a commonly adopted approach to simulate the structural response to impulsive loads. The FEM uses approximate shape functions in the time-domain to predict the response. A limitation of FEM is that spurious oscillations may be introduced into the response by numerical dispersion and dissipation and undermine the fidelity of simulation [4, 5].

The spectral finite element method (SFEM) [6, 7] was developed to obtain high fidelity result for linear structures under impact loading. The calculation is transformed into the frequency-domain by using fast Fourier transform (FFT). The exact wave solution is adopted as the spectrally-dependent shape functions. A finite element procedure is implemented to approximate the spatial domain. For linear problem, only one element is needed for a homogeneous structural component with constant cross-section. This method can predict impact wave response with perfect accuracy for linear problems. However, for structures with material nonlinearity under extreme impact loading, convolution operations may be involved and cause the implementation process to become computationally prohibitive. Also due to the limitation of FFT, a wrap-around issue may occur to transfer the response back to the beginning of time series and corrupt the result [7].

Y. Liu • A.J. Dick (✉)
Nonlinear Phenomena Laboratory, Department of Mechanical Engineering and Materials Science, Rice University, Houston, TX 77005, USA
e-mail: andrew.j.dick@rice.edu

J. Dodson • J. Foley
Fuzes Branch, Munitions Directorate, Air Force Research Laboratory, Eglin AFB, FL, USA

G. Kerschen (ed.), *Nonlinear Dynamics, Volume 1*, Conference Proceedings of the Society for Experimental Mechanics Series, DOI 10.1007/978-3-319-15221-9_17

In the authors' previous work, a new method called the alternating wavelet-time finite element method (AWT-FEM) is developed to study nonlinear wave propagation [8]. A spectrally-uncoupled wavelet transform is designed to replace the FFT as the transformation technique. A wavelet-based extrapolation technique [9, 10] is employed to implement a non-periodic time boundary in order to avoid the wrap-around issue. A direct iterative algorithm is constructed to set up an alternating procedure between the specifically designed wavelet-domain and the time-domain. This method has been applied for numerical and experimental study of wave propagation in nonlinear structures [8, 11].

In this research, a modified version of AWT-FEM is applied to study wave propagation in a rod composed of polyurethane and sugar. Sugar is added to the polyurethane to increase the stiffness properties. The polyurethane rod is modeled with a material nonlinearity. Numerical simulation and parametric study are conducted to explore the influence of system parameters and impact conditions on the nonlinear behavior in the response. An experimental investigation is performed in order to characterize the predicted phenomenon.

In the next section, the non-dimensionalized version of an elementary rod theory model with a material nonlinearity is developed. A version of AWT-FEM by using the modified Newton-Raphson algorithm is also introduced. In the third section, a parametric study is performed to explore the influence of system parameter and impact conditions on the nonlinear behavior in the response. In the fourth section, the experimental system and observed wave propagation are presented with comparisons to the numerical simulation results.

17.2 Modeling

A constitutive law with a quadratic nonlinear term in the positive intermediate strain regime [12, 13] is chosen as shown in Eq. (17.1)

$$\sigma = E(\varepsilon + \alpha\varepsilon^2), \tag{17.1}$$

where α is the nonlinear coefficient, σ represents stress, E is the Young's modulus, and ε represents strain.

By assuming a linear strain-displacement relationship and using the extended Hamilton's principle, the governing equation of motion for a rod model with material nonlinearity is obtained as follows

$$EA\frac{\partial^2 u}{\partial x^2} - \rho A\frac{\partial^2 u}{\partial t^2} + 2\alpha EA\frac{\partial u\,(x,t)}{\partial x}\frac{\partial^2 u\,(x,t)}{\partial x^2} = 0, \tag{17.2}$$

where A represents the cross sectional area, ρ represents the density, and u is the axial displacement.

The dimensionless version of Eq. (17.2) is obtained through a non-dimensionalization process with respect to time t and rod length L as

$$\bar{u}'' - \ddot{\bar{u}} + 2\bar{\alpha}\bar{u}'\bar{u}'' = 0, \tag{17.3}$$

where the over-bar represents the non-dimensionalized version of the corresponding variable. The over-dot and prime symbols are used to represent time and spatial derivatives, respectively. The relationship between dimensional and non-dimensional variables are

$$\begin{aligned} u &= \bar{u}L, \\ x &= \bar{x}L, \\ t &= \bar{t}\sqrt{\frac{\rho AL^2}{EA}}. \end{aligned} \tag{17.4}$$

The spectrally-uncoupled wavelet transform [9] combined with a wavelet extrapolation technique is conducted to transform Eq. (17.3) into the specifically designed wavelet domain as

$$\hat{\bar{u}}'' - \lambda^2\hat{\bar{u}} + \hat{\bar{Q}} = 0, \tag{17.5}$$

where $Q = 2\alpha EA\frac{\partial u(x,t)}{\partial x}\frac{\partial^2 u(x,t)}{\partial x^2}$ is the nonlinear term in the time-domain.

By following a spectral finite element procedure, a matrix form of Eq. (17.5) is obtained as

$$\mathbf{K}(\lambda_j)\mathbf{q}_j = \mathbf{F} + \mathbf{Q}, \tag{17.6}$$

where the subscript j represents the wavelet point, $\mathbf{K}$ is the spectrally-dependent dynamic stiffness matrix, $\mathbf{q}$ is the spectral nodal displacement vector, $\mathbf{F}$ is the equivalent nodal force term for the distributed external load, and $\mathbf{Q_N}$ is the equivalent nodal force term for the nonlinear term.

The residual term at a given wavelet point j is defined as

$$\mathbf{R} = \mathbf{K}(\lambda_j)\mathbf{q}_j - \mathbf{Q} - \mathbf{F}. \tag{17.7}$$

By using a Taylor's series expansion and only keeping the first order term, the residual term is approximated as

$$\mathbf{R}(\mathbf{q}_j) = \mathbf{R}(\mathbf{q}_j)^{r-1} + \left(\frac{\partial \mathbf{R}}{\partial \mathbf{q}_j}\right)^{r-1} \delta \mathbf{q}_j, \tag{17.8}$$

where r represents the iteration number.

The partial derivative term is defined as the tangent stiffness matrix. In the wavelet-domain, the explicit evaluation of components of the tangent stiffness is computationally prohibitive. In the modified Newton-Raphson algorithm, it is replaced by a pre-calculated constant matrix in order to avoid updating the value of the tangent stiffness at every iteration. A convenient choice is made here to use the linear spectral stiffness matrix $\mathbf{K}(\lambda_j)$. The step size at each iteration is calculated as

$$\mathbf{K}(\lambda_j)\delta \mathbf{q}_j = -\mathbf{R}, \tag{17.9}$$

$$\mathbf{q}_j^{r+1} = \mathbf{q}_j^r + \delta \mathbf{q}_j. \tag{17.10}$$

The AWT-FEM procedure is adopted here to solve the result. At each iteration, the linear response is used as the initial values. The linear spectrally-dependent dynamic stiffness matrix $\mathbf{K}(\lambda_j)$ is computed and stored. An alternating wavelet-time framework is followed. At each iteration, the values of nonlinear terms are calculated in the time-domain. The results are transformed into the wavelet-domain to update values of $\mathbf{Q}$ and the residual $\mathbf{R}$. The incremental step $\delta \mathbf{q}_j$ and the value of $\mathbf{q}_j^{r+1}$ are computed by using Eq. (17.9). This computational process is performed to all wavelet points. The results are then transformed back to the time-domain to update the values of the nonlinear term for the next iteration. This alternating iterative process is repeated until a predefined error measure satisfies a given threshold.

17.3 Parametric Study

A free-free rod is chosen for parametric study in this section. It is subject to an impact load and a mid-point is chosen as the observation location to analyze the wave response. A dimensionless metric R_n is defined as the relative root-mean-square difference between the nonlinear and linear velocity response at this point in order to quantitatively measure the nonlinear distortion of wave shape, as shown in Eq. (17.11)

$$R_n = \sqrt{\frac{1}{N}\sum_{i=1}^{N}\left(\frac{V_n(i) - V_l(i)}{V_l(i)}\right)^2}, \tag{17.11}$$

where V_n is the nonlinear response, V_l is the linear response, i is the index of the time series, and N is the number of sampling points.

The nonlinear coefficient $\bar{\alpha}$ has significant influence on the nonlinear behavior in the response. In order to isolate its influence in the parametric study, the force condition is fixed with the duration $T_f = 0.25$ and the amplitude $A = 3 \times 10^4$, which are chosen to make the response stay in the intermediate strain value regime.

As shown in Fig. 17.1, by increasing the magnitude of $\bar{\alpha}$, the value of R_n is increased, which indicates a stronger nonlinear behavior existing in the response. This trend is true for both positive and negative values.

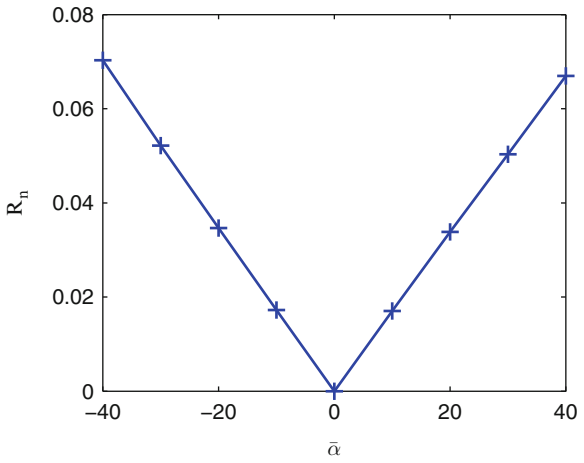

Fig. 17.1 Parametric study of the nonlinear dispersion in rod model with respect to the nonlinear coefficient $\bar{\alpha}$

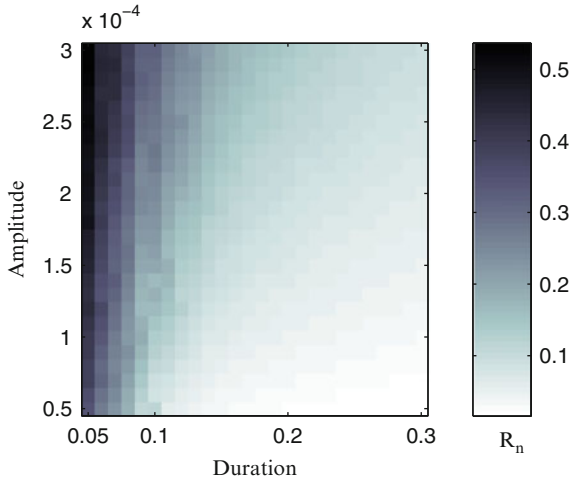

Fig. 17.2 Nonlinear dispersion in rod model with respect to the impact amplitude and duration

By fixing the nonlinear coefficient $\alpha = 30$, a study is conducted to explore the influence of force conditions on the nonlinear behavior in the response. The impact amplitude A is varied from 0.5×10^{-4} to 3×10^{-4} and impact duration T_f is varied from 0.05 to 0.3. As shown in Fig. 17.2, by increasing the impact amplitude and decreasing the duration, the value of R_n is increased. A larger impact amplitude pushes the response into a larger strain value regime which is more sensitive to nonlinearity. A shorter impact duration T_f can generate higher frequency content and further magnify the wave speed differences between frequencies in the response.

17.4 Experiments

The experiment test apparatus was set up at the AFRL Shock Dynamics Laboratory, as shown in Fig. 17.3. It consists of a 50 in. long bar of polyurethane with sugar, a 0.166 in. thin aluminum disk as the front interface, and a 6 in. steel striker. The thin aluminum disk is a modification of the long incident bar used in previous experiments [11] in order to avoid energy loss and wave reflection at the interface. There are six 120 Ohm Kyowa Semiconductor strain gages attached to the polymer bar at locations 5″, 6″, 10″, 20″, 30″, and 40″. Both bending waves and axial waves are collected. Only the axial waves are of interest in this study and signals at location 5″, 10″, 20″, and 30″ are clear for further analysis, as shown in Fig. 17.4.

The responses at the four locations are shown in Fig. 17.5. A initial pulse occurs at 0.02 s at location 5″. It travels along the bar and arrives at location 30″ at 0.0211 s. The duration of the impact is around 0.01 s. This impact duration is too long for the wave propagation in the polymer bar, where the wave speed can reach 530 m/s. The response is also still in the linear regime since the maximum strain value is smaller than 1.5×10^{-4}. A second pulse occurs around 0.05 s, which might results from slipping on the Teflon bearings.

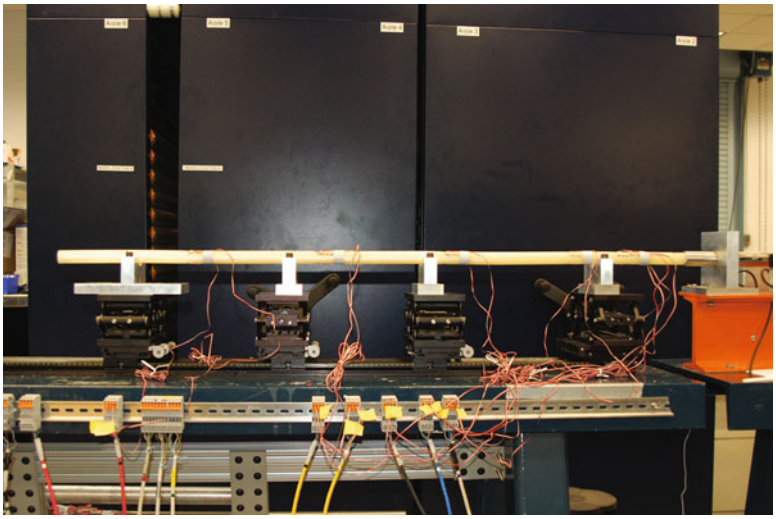

Fig. 17.3 Experimental setup

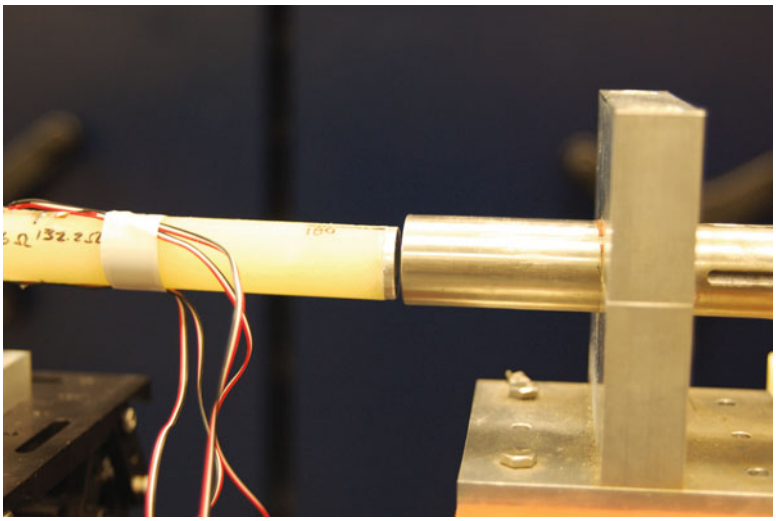

Fig. 17.4 Thin metal interface

The comparison between the experimental data and the simulated response at location 20″ are shown in Fig. 17.6. The two results are close to each other. The distortion of wave shape in the experimental results is consistent in all locations. It might be related to the reflection at the interface between the aluminum thin disk and the polymer bar.

17.5 Conclusion and Future Work

In this study, the alternating wavelet-time finite element method was applied to study the impact wave response in a materially nonlinear polymer bar. A parametric study was conducted to explore the influence of system parameters and impact conditions on the nonlinear behavior. A strong nonlinear constitutive relationship at the intermediate strain value regime characterized by a nonlinear coefficient $\bar{\alpha}$, a large impact amplitude, and a short impact duration, can magnify the nonlinear behavior in the response.

An experimental study was also conducted to verify the nonlinear wave response in a polymer bar. Due to the limitation of current setup, the impact amplitude and duration cannot push the wave response into a strong nonlinear regime. Numerical simulation results are used to verify the general trend of the pulse profile. The parametric study also indicates the potential

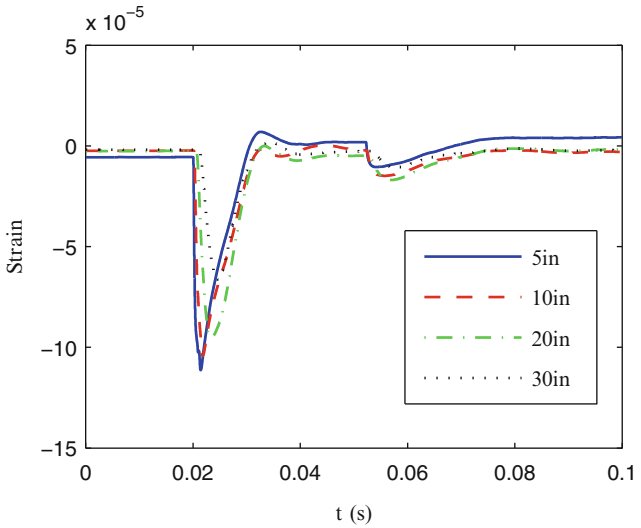

Fig. 17.5 Experimentally measured strain time series data at four locations along the polymer bar

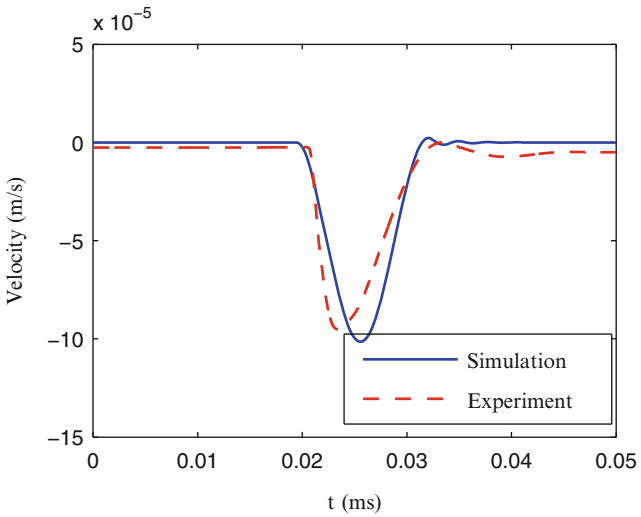

Fig. 17.6 Compairison of simulated (solid) and experimental (dashed) propagating wave data for the 20" location on polymer bar

range of impact conditions sensitive to nonlinear behavior. In the future, modifications to the experimental setup will be made in order to verify the nonlinear effect.

References

1. Mitra M, Gopalakrishnan S (2006) Wave propagation analysis in carbon nanotube embedded composite using wavelet based spectral finite elements. Smart Mater Struct 15(1):104
2. Gopalakrishnan S, Mitra M (2010) Wavelet methods for dynamical problems: with application to metallic, composite, and nano-composite structures. CRC Press, New York
3. Reddy JN (2004) Nonlinear finite element analysis. Oxford University Press, New York
4. Ham S, Bathe K-J (2012) A finite element method enriched for wave propagation problems. Comput Struct 94:1–12
5. Idesman AV (2007) A new high-order accurate continuous galerkin method for linear elastodynamics problems. Comput Mech 40(2):261–279
6. Doyle JF (1989) Wave propagation in structures. Springer, Berlin
7. Doyle J (1988) A spectrally formulated finite element for longitudinal wave propagation. Int J Anal Exp Modal Anal 3:1–5
8. Liu Y and Dick AJ (2014) On the Role of Boundary Conditions in the Nonlinear Dynamic Response of Simple Structures. In R Allemang (Ed.) Topics in Modal Analysis II, Vol. 8, pp. 135–143, Switzerland: Springer International Publishing. DOI: 10.1007/978-3-319-04774-4_13

9. Williams JR, Amaratunga K (1997) A discrete wavelet transform without edge effects using wavelet extrapolation. J Fourier Anal Appl 3(4):435–449
10. Beylkin G (1992) On the representation of operators in bases of compactly supported wavelets. SIAM J Numer Anal 29(6):1716–1740
11. Liu Y, Dick AJ, Dodson J and Foley J (2014) Nonlinear High Fidelity Modeling of Impact Load Response in a Rod. In R Allemang (Ed.) Topics in Modal Analysis II, Vol. 8 pp. 129–134, Switzerland: Springer International Publishing. DOI: 10.1007/978-3-319-04774-4_12
12. Nayfeh AH, Mook DT (2008) Nonlinear oscillations.Wiley, Weinheim
13. Zhang S, Zhuang W (1987) The strain solitary waves in a nonlinear elastic rod. Acta Mech Sin 3(1):62–72

Chapter 18
Experimental Nonlinear Dynamics and Chaos of Post-buckled Plates

R. Wiebe and D. Ehrhardt

Abstract Panels and plates are an important structural element in many engineering applications, such as aircraft skin panels, ship hulls, and civil shell structures. These structures, particularly when their boundaries are in some way constrained, exhibit highly nonlinear behavior (e.g. spring hardening) even for relatively small deformations due to induced axial loading. An extreme, but highly important, example is dynamic snap-through buckling of curved or post-buckled thin panels. This phenomena is well represented in the literature, both for plates and for the simplified case of curved beams. The majority of the experimental studies, especially for panels, have been carried out using either wind tunnels or acoustic drivers to generate transverse loading. While this is directly applicable to real-world scenarios, say aircraft panel loading, it does not permit direct control of the loads that are applied. In this work, we instead apply loads to a thermally buckled panel using an electrodynamic shaker. This, along with the use of digital image correlation to capture the full field dynamic response allows for a complete picture of the complex characteristics of dynamic snap-through.

Keywords Nonlinear dynamics • Experimental mechanics • Snap-through • Chaos

18.1 Introduction

Given their common use as structural elements, plates and curved panels have been studied extensively in the past. The work that most closely matches what will be presented in this paper is [1], in which the nonlinear dynamics and snap-through of a thermally buckled plate under acoustic excitation is investigated experimentally. It is shown that regions of snap-through occur near linear resonance, and not surprising is more likely for larger loading magnitudes. Given the bistability of buckled plates, it is perhaps not surprising that, at least qualitatively, this mirrors the response of, in decreasing spatial complexity, buckled beams [2], and the double-well Duffing equation. In [3, 4] it is shown that the double-well Duffing equation yields surprising sensitivity to forcing parameters, with certain parameters yielding multiple co-existing response types.

The response of the Duffing equation hints that a buckled plate (which may be represented by a double-well Duffing type equation for first-mode response) may also present similar sensitivity in forcing parameter space, a characteristic which would certainly be of interest to engineers designing shell and plate type structures. Figure 18.1 shows the initially (nominally) flat, thermally-buckled aluminum plate with clamped boundary conditions all around that is used in this investigation (mounting visible in photo). The plate dimensions were $0.5 \times 165 \times 216$ mm. The plate was thermally buckled using two heat lamps. All tests were performed after the plate had reached a steady-state temperature. The rise of the center of the plate at the steady-state temperature was $h \approx 1$ mm. Forcing was applied inertially by mounting the plate in its frame to an MB Dynamics electrodynamic shaker (not visible in photo). The benefit of using a shaker, rather than standard wind-tunnel or acoustic testing, is that the harmonic forcing frequency, and amplitude could be easily and independently controlled. Random, or combined random and harmonic forcing could also be applied using this arrangement, however this paper is limited to harmonic forcing results. The displacement was measured using dynamic digital image correlation DIC. The use of DIC allowed for a vast improvement over more traditional vibrometers as this made it possible to obtain displacement time series at any location of interest.

R. Wiebe (✉)
College of Engineering, University of Washington, Seattle, WA 98195, USA
e-mail: rwiebe@uw.edu

D. Ehrhardt
College of Engineering, University of Wisconsin, Madison, WI 53706, USA
e-mail: dehrhardt@wisc.edu

G. Kerschen (ed.), *Nonlinear Dynamics, Volume 1*, Conference Proceedings of the Society for Experimental Mechanics Series, DOI 10.1007/978-3-319-15221-9_18

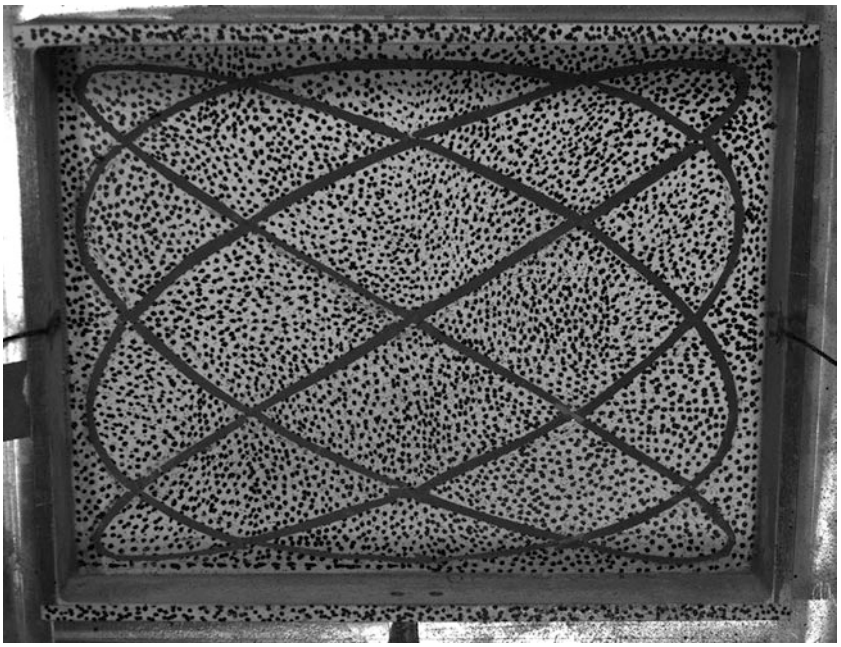

Fig. 18.1 Aluminum plate painted with speckle pattern for DIC data acquisition. The mounting frame provided clamped boundary conditions on all edges. The lissajous curves were applied to allow for scanning laser data acquisition (not discussed herein)

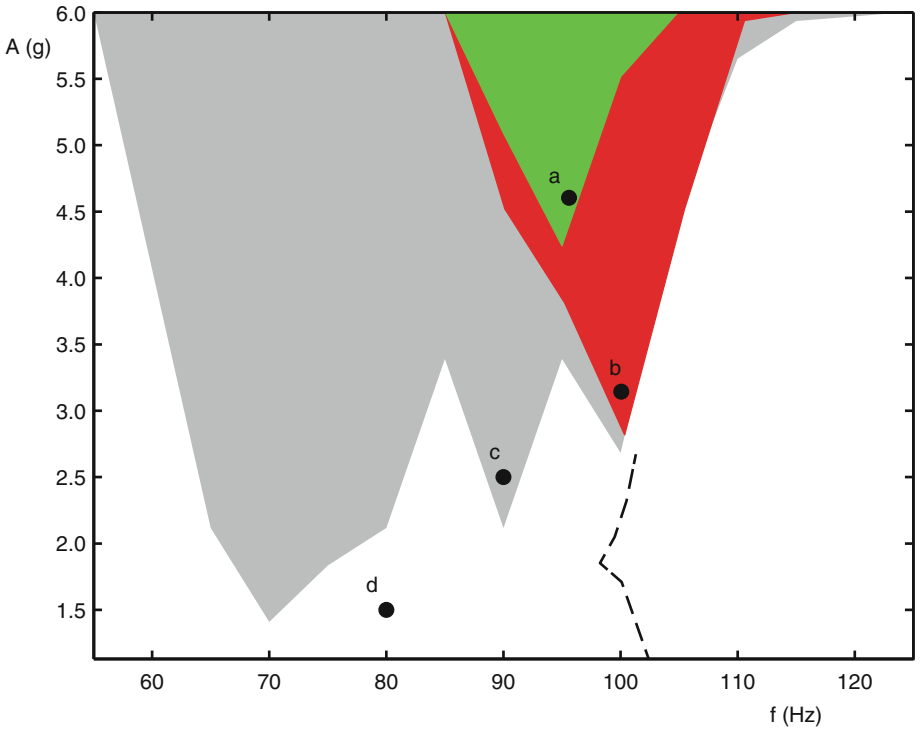

Fig. 18.2 Response-type plot of buckled plate under harmonic loading. The forcing amplitude is given in multiples of g (acceleration due to gravity), while the frequency is given in Hz. Four response types were observed, (*white*) non-snap, (*green*) P1 snap-through, (*red*) chaotic snap-through, (*gray*) co-existing chaotic snap-through and non-snap. The first nonlinear normal mode (*dashed black curve*) is also shown (Color figure online)

18.2 Experimental Results

The results of an experimental parametric study are presented as a response-type plot in Fig. 18.2. This figure divides the forcing parameter space into four response types. In the white regions of parameter space, the response was entirely non-snap-through, i.e. single-well. A typical time series of the plate measured at its center point (for parameters at point d) can be seen in Fig. 18.3d. In an engineering design context, this would be a preferable structural response. At the other extreme, the green region contains forcing parameters that resulted in period 1 snap-through. A time series of this response (for the parameters at point a) is shown in Fig. 18.3a. This is effectively the highest rate of snap-through that one could expect, and is thus likely to lead to the most rapid degradation through fatigue. The red shaded region instead resulted in chaotic

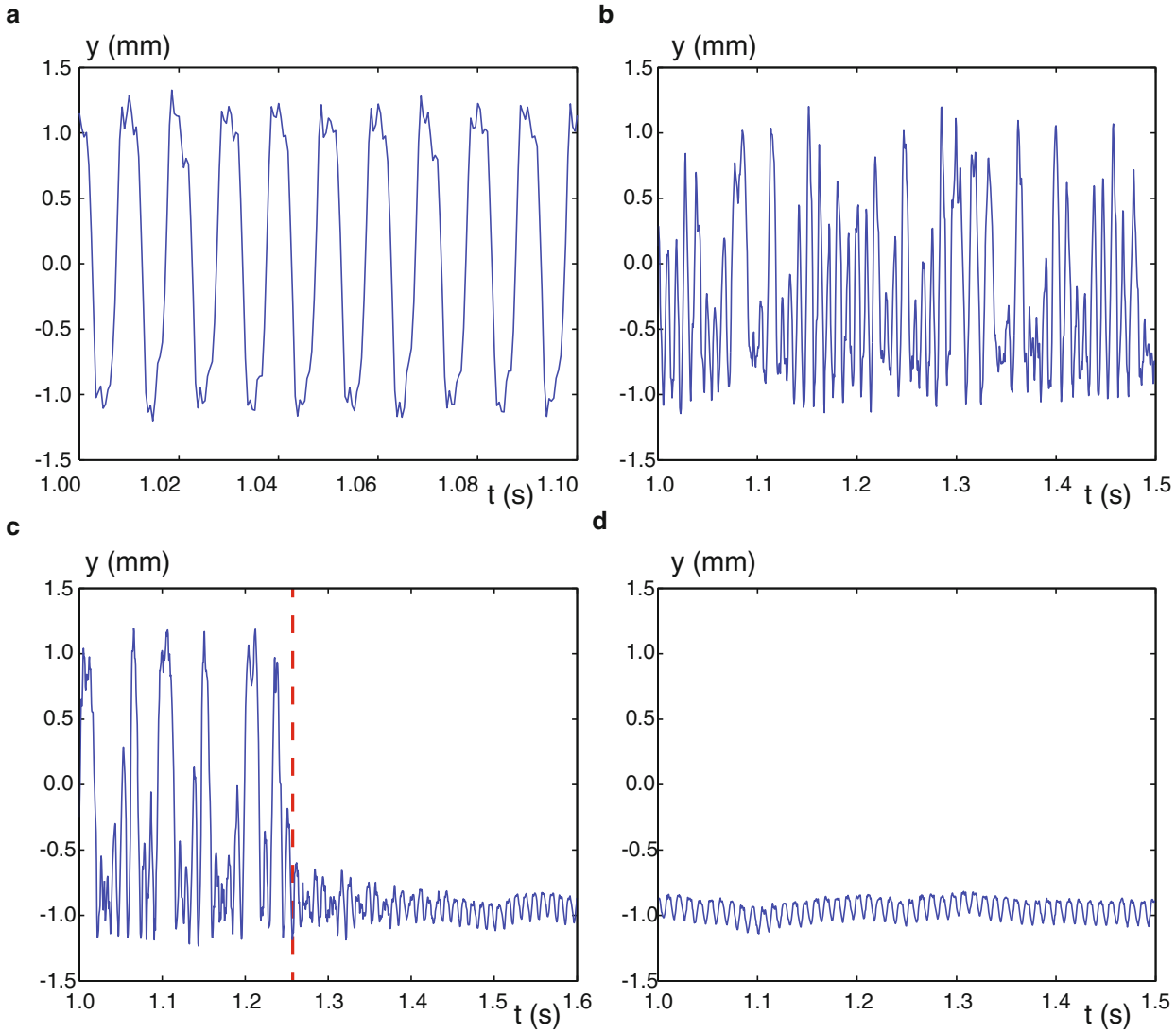

Fig. 18.3 Sample plate center-displacement time series. Parts (**a**) through (**d**) correspond to the labels (**a**) through (**d**) in Figure 18.2. The *vertical dashed line* in part (**c**) indicates an external perturbation

snap-through (also see point b and Fig. 18.3b), which yields a lower average snap-through rate than P1 snap-through. Finally, the gray shaded region denotes forcing parameters that lead to co-existing snap-through and non-snap-through response. As an example, the two response types that coexist for point c are shown in Fig. 18.3c. The gray region shows that this structure also exhibits sensitivity to initial conditions in terms of final response type, along with sensitivity to parameters. In part (c) an external perturbation (impacting the beam with a small hammer, vertical dashed line) was used to 'kick' the system between the competing response types. While the green region produces the most violent, highest-energy, response, the gray region is perhaps the most critical, as it could easily lull a designer into a false sense of security about the structural response.

Figure 18.2 was obtained using slow amplitude ramp-up and ramp-down tests at 15 different frequencies in 5 Hz increments. The boundaries between different response-type regions of parameter space were obtained by visual observation of the response, and are thus subject to some error. Tests were, however, repeated multiple times to ensure quality of the results. The boundary of the gray region was particularly difficult to observe. These boundaries were initially approximated by first ramping the amplitude up, then down at a given frequency. The amplitude at which chaotic (or periodic) snap-through occurred on the ramp-up was assumed to be in the vicinity of the gray-red (or gray-green) boundary. Then on the down-sweep, the amplitude at which snap-through ceased was assumed to be near the white-gray boundary. These approximate parameter locations were then examined further using multiple random perturbations (hitting the plate with a small hammer) to find at exactly which forcing amplitude the co-existing non-snap and snap-through behavior ceased to exist. The sliver of

red-type response the divides the green and gray response types is suspect, as the transient behavior was quite long in this region, making difficult to distinguish chaotic response from long transience leading to periodic behavior. This sliver does not appear in the response-type plot of the double-well Duffing equation [3]. The seemingly ragged gray-white boundary is, at least qualitatively, similar to what is observed in the double-well Duffing equation, which is almost certainly fractal. The 5 Hz grid used experimentally, however, is much to coarse to prove or disprove the existence of fractal boundaries in this plot.

The first linear natural frequency of the plate about the buckled configuration was $f_0 \approx 108$ Hz. When compared with the lowest point of the red response type, which occurs at $f \approx 100$ Hz, it could be stated that this system presents a softening type behavior. An interesting method of characterizing the transition form linear to increasingly nonlinear behavior is given by the nonlinear normal modes (NNMs) of the response. These modes are extensions of the linear modes, in that they exhibit 'vibration in unison' (although other definitions exist), and present a promising approach for characterizing nonlinear vibrations, or as mode shapes in reduced order modeling [5]. The details of NNMs will not be discussed herein (see [6] for further details), however, as a point of interest the first NNM of the buckled plate (dashed black curve in Fig. 18.2) can be seen to approach the critical minimum snap-through point. If this is indeed the case, it would serve as another useful application of NNMs in detecting snap-through. Note that the NNM connects to the linear natural frequency of $f_0 \approx 108$ Hz, however, the plot is cut off at a forcing amplitude of 1 g.

18.3 Conclusions

Thermally buckled plates are shown experimentally to exhibit extreme sensitivity to initial conditions (chaos and co-existing solutions) and forcing parameters (sudden changes in the response-type plot) under harmonic loading. This has consequences in the structural design of curved plates and shells, as designers must be careful to ensure that they have captured the worst case, or limit state, of the system of interest.

Acknowledgements The authors wish to thank S.M. Spottswood for granting access to the Air Force Research Laboratory equipment, and for his help in the laboratory.

References

1. Murphy KD, Virgin LN, Rizzi SA (1996) Experimental snap-through boundaries for acoustically excited thermally buckled plates. Exp Mech 36(4):312–317
2. Chandra Y, Wiebe R, Stanciulescu I, Virgin LN, Spottswood SM, Eason TG (2013) Characterizing dynamic transitions associated with snap-through of clamped shallow arches. J Sound Vib 332(22):5837–5855
3. Wiebe R, Spottswood SM (2014) Co-existing responses and stochastic resonance in post-buckled structures: a combined numerical and experimental study. J Sound Vib 333(19):4682–4694
4. Ueda Y (1991) Survey of regular and chaotic phenomena in the forced duffing oscillator. Chaos Solitons Fractals 1(3):199–231
5. Allen MS, Kuether RJ (2012) Substructuring with nonlinear subcomponents: a nonlinear normal mode perspective. In: Proceedings of the Society for Experimental Mechanics, Jacksonville, FL, pp 109–121
6. Kerschen G, Peeters M, Golinval J-C, Vakakis AF (2009) Nonlinear normal modes, part i: a useful framework for the structural dynamicist. Mech Syst Signal Process 23(1):170–194

Chapter 19
Control-Based Continuation of a Hybrid Numerical/Physical Substructured System

David A.W. Barton

Abstract Control-based continuation is a relatively new technique for tracking the orbits and bifurcations in a physical experiment under parameter variations. It leverages ideas from the dynamical systems community, particularly from numerical continuation, and combines them with feedback control. A related idea is that of hybrid testing, whereby a physical system is substructured into two parts: one physical and one numerical. The two substructures are connected in real-time via actuators and sensors to form a closed system. This methodology enables the testing of large-scale structures without needing to build everything.

In this paper, we will present initial results from combining these two methodologies and we show how the nonlinear dynamics and bifurcations of a particular coupled system can be explored systematically even though a model for the full system is not available. The principal benefit of combining these two methods is that parameter studies become much more straightforward—the numerical model contains numerous parameters that can be adjusted programmatically allowing for an extensive investigation of the full system.

Keywords Nonlinear dynamics • Feedback control • Numerical continuation • Real-time substructuring • Bifurcations

19.1 Introduction

Modal analysis is an extremely successful approach to analysing the dynamics of physical structures that are inherently linear in their response [7]. However, many modern structures are inherently nonlinear in their response; due to a focus on efficiency and high performance, materials and structures are being pushed significantly beyond the linear regime [15]. In spite of numerous attempts by different authors (for example [4]), it has proved extremely difficult to design a similarly successful methodology for investigating nonlinear systems.

Part of the challenge associated with nonlinear systems is that they can undergo qualitative changes in behaviour (so-called bifurcations) as system parameters change. One example of this is the onset of chatter at a Hopf bifurcation when machining; at some critical speed or depth of cut the cutting tool starts to oscillate causing a degradation of the surface being cut [8]. It is unlikely that a single method will ever be able to characterise such a wide range of physical phenomena.

The dynamical systems community has made significant progress towards creating a suite of versatile methods for analysing nonlinear systems that exist as numerical models. One such method in this suite is numerical continuation, which allows solutions of a nonlinear system to be tracked as a system parameter is varied continuously [12]. Any bifurcations that are encountered can also be tracked automatically. AUTO-07p [6] and COCO [5] are two open-source packages for numerical continuation.

Control-based continuation is an attempt to extend numerical continuation into the physical domain. By wrapping a physical experiment in a feedback control loop, unstable states and bifurcations can be investigated directly [13, 14]. The key challenge is to choose the appropriate control inputs to both ensure stability and simultaneously ensure that the control input is non-invasive (i.e., it does not change the dynamics of the system). The challenge of making the control input non-invasive is typically achieved using a Newton iteration on the physical experiment [3] but in certain circumstances a simple fixed-point iteration can suffice [2].

Control-based continuation bears a strong similarity to the scheme proposed by [9] which makes use of OGY control [10] to track periodic orbits of a tapping-mode atomic force microscope. However, control-based continuation can be argued to be more general since a particular control scheme may be used, for example Pygragas-time delayed feedback control [11].

D.A.W. Barton (✉)
Department of Engineering Mathematics, University of Bristol, Merchant Venturers Building, Woodland Road, Bristol BS8 1UB, UK
e-mail: david.barton@bristol.ac.uk

G. Kerschen (ed.), *Nonlinear Dynamics, Volume 1*, Conference Proceedings of the Society for Experimental Mechanics Series, DOI 10.1007/978-3-319-15221-9_19

Moreover, the control scheme itself need not be non-invasive; instead a Newton iteration can be used to render a more traditional linear feedback controller non-invasive via an iterative procedure.

Real-time dynamic substructuring otherwise known as hybrid testing is a means of dynamically testing a large scale structure by concentrating on the parts of the structure which are not well modelled. A common approach is to build a physical representation of the parts of the structure which are thought to behave nonlinearily and implement a numerical model of the remainder of the structure. The physical substructure and the numerical substructure are then connected via actuators and sensors to create a closed loop. For an overview of this method see the review of [16]. Since real-time substructuring uses a numerical model in the loop, there is easy access to a wide range of system parameters which can be changed as the simulation is running. As such, combining control-based continuation and real-time substructuring provides a wealth of opportunities.

In this paper we outline a particular test problem and show how the methods of control-based continuation and real-time dynamic substructuring can be applied to enable a thorough investigation of the system in question. Results from numerical studies are presented.

19.2 Experimental Set-Up

19.2.1 A Test Problem

As an initial test problem, we consider the example of a nonlinear tuned-mass-damper (TMD) attached to linear base structure, the response of which is well described by a single mode. The nonlinearity in the TMD is a result of the spring stiffness which follows a cubic polynomial form. This example is investigated extensively using numerical methods (in particular numerical continuation) by Alexander and Schilder [1]. The equations of motion of the system are given by

$$\ddot{x}_1 + 2\gamma_1\dot{x}_1 - 2\varepsilon\gamma_2\Omega\,(\dot{x}_2 - \dot{x}_1) + x_1 - \varepsilon\Omega^2\,(x_2 - x_1) - \varepsilon\Omega_N^2\,(x_2 - x_1)^3 = \Gamma\sin(\omega t), \tag{19.1a}$$

$$\ddot{x}_2 + 2\gamma_2\Omega\,(\dot{x}_2 - \dot{x}_1) + \Omega^2\,(x_2 - x_1) + \Omega_N^2\,(x_2 - x_1)^3 = 0, \tag{19.1b}$$

where ε is the mass ratio between the two substructures, γ_1 and γ_2 are damping coefficients, Ω and Ω_N are frequency ratios, Γ is the forcing amplitude and ω is the forcing frequency. A schematic drawing is shown in Fig. 19.1a and a photograph of the experimental realisation of the nonlinear TMD is shown in Fig. 19.1b.

The numerical investigation of [1] shows that (19.1) can exhibit a range of nonlinear phenomena when excited with multiple excitation frequencies including multiple stable states and 'detached' resonance curves (so-called isolas) which are caused by saddle-node bifurcations. Other bifurcations such as Neimark-Sacker bifurcations (torus bifurcations) can also be found for some parameter values. Since the study in [1] is motivated by engineering buildings to withstand earthquakes, the use of a complicated forcing function appropriate. However, for the purposes of this study, single frequency sinusoidal forcing is sufficient. (Note that any time-periodic forcing could, in principle, be considered with the methodologies discussed here.)

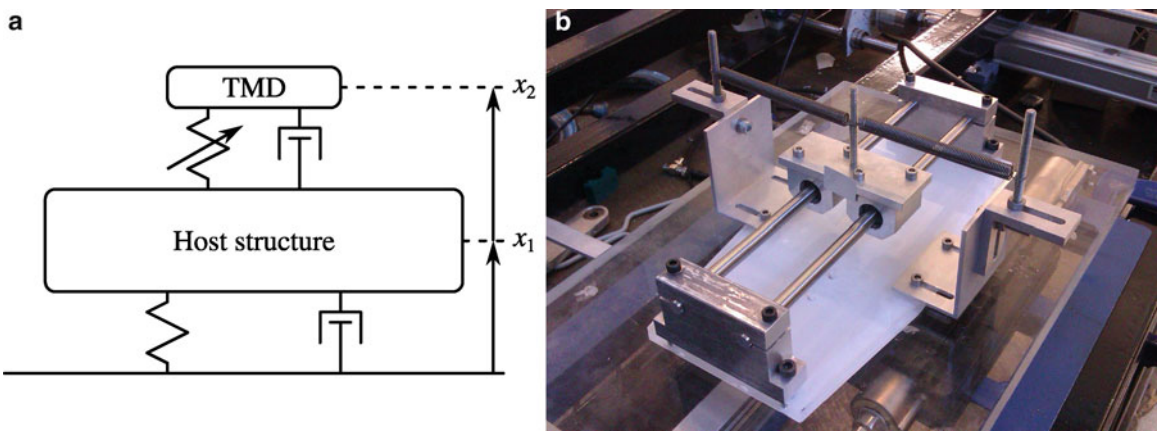

Fig. 19.1 Panel (**a**) shows a schematic of the physical system corresponding to (19.1). Panel (**b**) shows an experimental realisation of the nonlinear tuned-mass-damper using a mass mounted on linear bearings with springs mounted perpendicular to the direction of motion to provide the nonlinearity

19.2.2 Real-Time Dynamic Substructuring and Control-Based Continuation

In this paper, we consider the case where the base structure and its excitation is implemented as a numerical model (the numerical substructure). The nonlinear TMD is implemented as a physical experiment (the physical substructure) that is coupled to the numerical model using a high precision electrodynamic actuator (a Spektra APS 113 long stroke shaker) and a load cell (RDP model 31 50N load cell).

When using real-time dynamic substructuring, a numerical model is typically running in real-time, responding to inputs from the physical substructure and providing force outputs to a shaker to close the feedback loop. In the context of control-based continuation this real-time numerical model is not required. Instead, a fixed input to the physical substructure is chosen and then iteratively refined (typically after every few periods of forcing but there are no particular timing requirements) based on the output measurements. For this a numerical root-finder is used, for example a Newton-Broyden iteration as has been used in previous implementations of control-based continuation.

The benefit of not using a real-time numerical model is that delay effects due to computation and actuation times are no longer an issue. It is well known that in some real-time dynamic substructuring experiments that these delays can make the experiment unconditionally unstable. Since the input to the physical substructure is iteratively refined, there are no such issues when combining real-time dynamic substructuring with control-based continuation.

19.3 Results

As an initial proof of concept, some initial results from numerical continuation applied to (19.1) are shown in Fig. 19.2. To obtain these results, the numerical continuation software COCO [5] is used with a Fourier discretisation of (19.1). Panels (a)–(f) of Fig. 19.2 show the frequency response functions of (19.1) for different values of forcing amplitude Γ. The other parameter values are set to $\gamma_1 = 0.02$, $\gamma_2 = 0.05$, $\Omega = 0.5$, $\Omega_N = 0.05$, and $\varepsilon = 0.1$ (values taken from [1]).

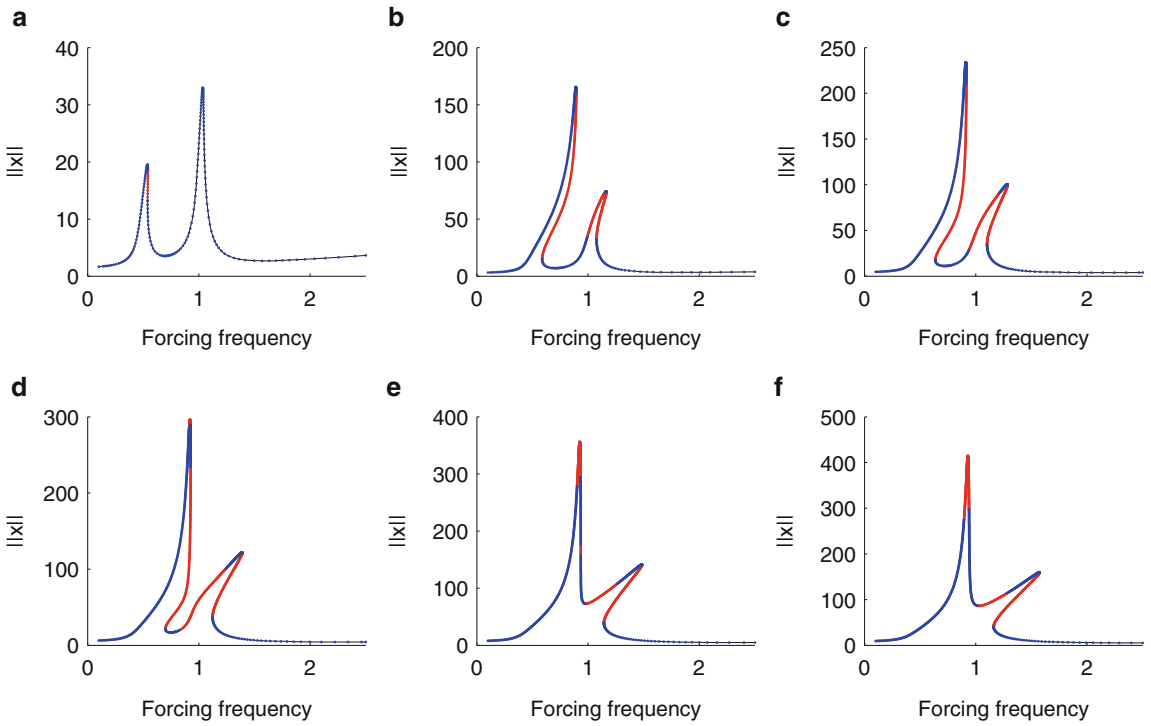

Fig. 19.2 A series of numerical continuations in the forcing frequency ω for different values of Γ. Stable periodic motion is marked in *blue* whereas unstable periodic motion is marked in *red*. The frequency responses show the two resonances associated with the nonlinear TMD and the host structure. Hardening spring characteristics are evident from the existence of folds in the frequency responses. In addition to the folds (or saddle-node bifurcations) the system also undergoes pitchfork bifurcations which account for the other stability losses. (**a**) $\Gamma = \frac{1}{3}$, (**b**) $\Gamma = \frac{2}{3}$, (**c**) $\Gamma = 1$, (**d**) $\Gamma = \frac{4}{3}$, (**e**) $\Gamma = \frac{5}{3}$, and (**f**) $\Gamma = 2$ (Color figure online)

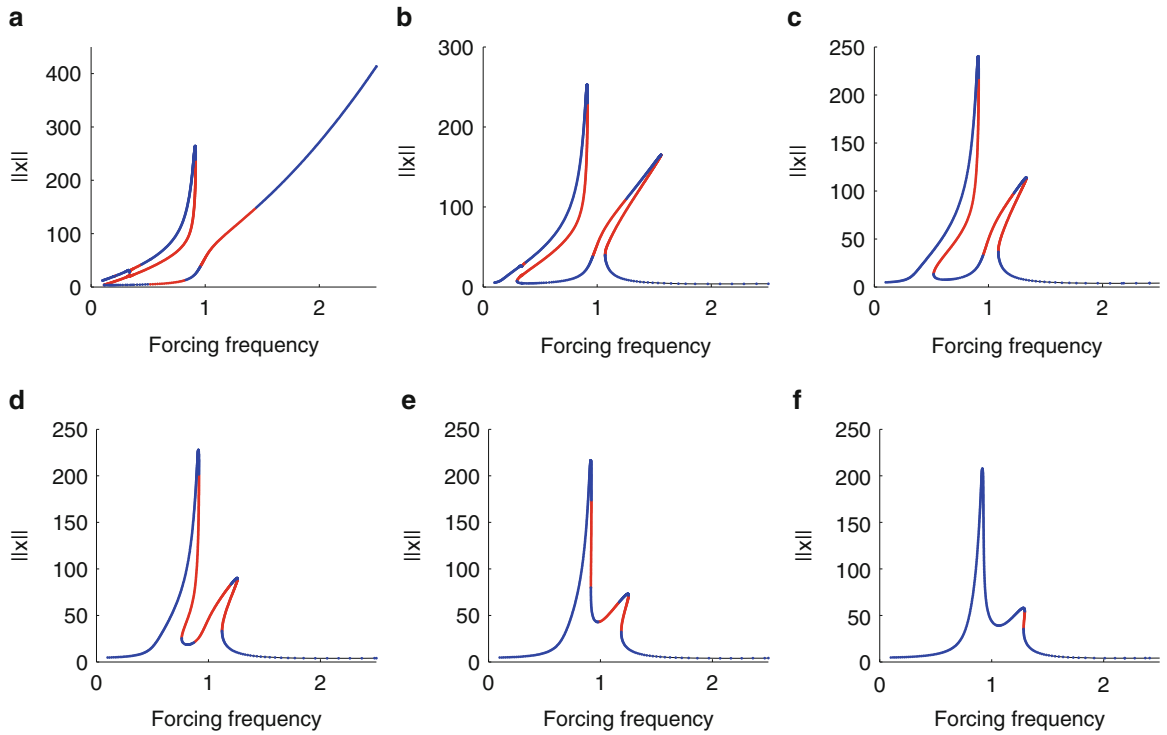

Fig. 19.3 A series of numerical continuations in the forcing frequency ω for different values of Ω. Stable periodic motion is marked in *blue* whereas unstable periodic motion is marked in *red*. While the results are rather similar to those shown in Fig. 19.2, they are achieved by altering the frequency ratio between the substructures—something that is only possible by combining control-based continuation with real-time dynamic substructuring. (**a**) $\Omega = 0$, (**b**) $\Omega = \frac{1}{5}$, (**c**) $\Omega = \frac{2}{5}$, (**d**) $\Omega = \frac{3}{5}$, (**e**) $\Omega = \frac{4}{5}$, and (**f**) $\Omega = 1$ (Color figure online)

It is clear from Fig. 19.2 that as the forcing amplitude is increased, the nonlinear behaviour significantly influences the dynamics. Hysteresis and amplitude dependency in the frequency response functions are clear and, in addition, there exist multiple pitchfork bifurcations where the system loses stability due to energy transfers between the two modes of the system.

The results shown in Fig. 19.2 while of interest are easily obtainable using standard methodologies (though tracking of the unstable orbits may require control-based continuation). However, Fig. 19.3 shows results that cannot be obtained using standard methodologies without a significant investment of time and effort—panels (a)–(f) of Fig. 19.3 also show frequency response functions but this time for different values of the frequency ratio Ω between the substructures. Achieving different frequency ratios in an experiment is likely to be difficult and time consuming, if it is possible at all. However, by combining control-based continuation and real-time dynamic substructure, it is relatively straightforward to achieve these results when the physical substructure is the nonlinear TMD.

Acknowledgements D.A.W.B. is supported by EPSRC grant EP/K032739/1 and would like to acknowledge the help of Alicia Gonzalez-Buelga and Simon Neild in the development of the experimental rig.

References

1. Alexander NA, Schilder F (2009) Exploring the performance of a nonlinear tuned mass damper. J Sound Vib 319(1):445–462
2. Barton DAW, Sieber J (2013) Systematic experimental exploration of bifurcations with noninvasive control. Phys Rev E 87(5):052916. doi:10.1103/PhysRevE.87.052916
3. Barton DAW, Mann BP, Burrow SG (2012) Control-based continuation for investigating nonlinear experiments. J Vib Control 18(4):509–520. ISSN 1077-5463, 1741-2986. doi:10.1177/1077546310384004
4. Carrella A, Ewins DJ (2011) Identifying and quantifying structural nonlinearities in engineering applications from measured frequency response functions. Mech Syst Signal Process 25(3):1011–1027
5. Dankowicz H, Schilder F (2013) Recipes for continuation, vol 11. SIAM, Philadelphia
6. Doedel EJ, Champneys AR, Dercole F, Fairgrieve TF, Kuznetsov YA, Oldeman B, Paffenroth RC, Sandstede B, Wang XJ, Zhang CH (2007) Auto-07p: continuation and bifurcation software for ordinary differential equations. Technical report. http://indy.cs.concordia.ca/auto/

7. Ewins DJ (1986) Modal testing: theory and practice, vol 2. Research Studies Press, Letchworth
8. Insperger T, Barton DAW, Stepan G (2008) Criticality of hopf bifurcation in state-dependent delay model of turning processes. Int J Non-Linear Mech 43(2):140–149. doi:/10.1016/j.ijnonlinmec.2007.11.002
9. Misra S, Dankowicz H, Paul MR (2008) Event-driven feedback tracking and control of tapping-mode atomic force microscopy. Proc R Soc A 464(2096):2113–2133. doi:10.1098/rspa.2007.0016
10. Ott E, Grebogi C, Yorke JA (1990) Controlling chaos. Phys Rev Lett 64(11):1196–1199. doi:10.1103/PhysRevLett.64.1196
11. Pyragas K (1992) Continuous control of chaos by self-controlling feedback. Phys Lett A 170(6):421–428
12. Seydel R (2010) Practical bifurcation and stability analysis. Interdisciplinary applied mathematics, vol 5, 3rd edn. Springer, New York
13. Sieber J, Krauskopf B (2008) Control based bifurcation analysis for experiments. Nonlinear Dyn 51(3):365–377. doi:10.1007/s11071-007-9217-2.
14. Sieber J, Gonzalez-Buelga A, Neild SA, Wagg DJ, Krauskopf B (2008) Experimental continuation of periodic orbits through a fold. Phys Rev Lett 100(24):244101
15. Wagg D, Neild S (2009) Nonlinear vibration with control: for flexible and adaptive structures, vol 170. Springer, Heidelberg
16. Williams MS, Blakeborough A (2001) Laboratory testing of structures under dynamic loads: an introductory review. Phil Trans R Soc Lond A Math Phys Eng Sci 359(1786):1651–1669

Chapter 20
Towards Finite Element Model Updating Based on Nonlinear Normal Modes

Simon Peter, Alexander Grundler, Pascal Reuss, Lothar Gaul, and Remco I. Leine

Abstract Local nonlinearities typically occur due to large deformation in certain parts of a structure or due to the presence of nonlinear coupling elements. Often the dynamic behavior of such elements is a priori unknown and has to be investigated experimentally before they can be included in numerical calculations. In this contribution an integrated method for estimation of linear as well as nonlinear system parameters based on the nonlinear normal modes (NNMs) of the structure is proposed. The characteristics of the nonlinear and linear parts of an assembly both contribute to its NNMs. Assuming that the functional form of the nonlinearity is known or can be estimated through non-parametric identification techniques, this feature can be exploited for the purpose of model updating. For the updating process the measured and calculated NNMs of a system are compared and their difference is minimized. In this context the numerical calculation of NNMs is performed using the Harmonic Balance Method (HBM). The properties of the proposed method are demonstrated on the numerical example of a 4DOF oscillator with a cubic nonlinearity. Furthermore, the effectiveness of the method is shown by updating the FE-model of a beam with cubic nonlinearity based on experimental data.

Keywords Nonlinear normal modes • FE-model updating • Nonlinear identification • Harmonic balance method

20.1 Introduction

In linear structures updating of FE-parameters is one of the standard tools for the adjustment of analytical models based on experimental data [1, 2]. There exist various methods and different criteria e.g. based on Frequency Response Functions or modal data. However, in reality most systems behave in a nonlinear way as for example local nonlinearities are caused by joints or geometric nonlinearities due to large displacements. Additionally, nonlinear material properties may be relevant. All of these nonlinearities can remarkably affect the systems overall behavior and therefore cause linear model updating techniques to fail. In these cases the nonlinearities must be identified and included in the analytical model.

For identification the of nonlinear systems there exist numerous techniques [3, 4], yet many of them are limited to SDOF systems or weak nonlinearity and some are difficult to relate to a clear physical meaning [5]. Others treat the linear parts of the structure separated from the nonlinear parts [6] which is on the one hand more complicated as it requires a combination of several measurements and analytical methods for the same structure and on the other hand it is sometimes difficult to isolate the effects of nonlinearities in coupled structures [7].

This contribution addresses some of these issues by using the concept of Nonlinear Normal Modes for a structural model updating. This concept was pioneered by Rosenberg [8] and provides a clear mathematical and physical framework as well as a conceptual relation to linear modes [9]. Therefore, it recently received increasing attention in the structural dynamics community [10, 11]. Rosenberg defines NNMs as synchronous periodic motion of a conservative system. This definition is restrictive in a certain sense, as it refers to conservative systems only. Still, for lightly damped systems as considered in this paper, the NNMs of the underlying conservative system are closely related to the characteristics of the damped system. It should be mentioned at this point that the numerical methods can be extended to non-conservative systems [12–14] and there are also approaches for the extension of experimental methods [15].

The idea of using the NNMs of a system to identify parameters and to update experimental models is based on the fact that NNMs contain both: information about the underlying linear system as well as information about the nonlinear behavior.

S. Peter (✉) • A. Grundler • P. Reuss • L. Gaul • R.I. Leine
Institute of Applied and Experimental Mechanics, University of Stuttgart, Pfaffenwaldring 9, 70550 Stuttgart, Germany
e-mail: peter@iam.uni-stuttgart.de

G. Kerschen (ed.), *Nonlinear Dynamics, Volume 1*, Conference Proceedings of the Society for Experimental Mechanics Series, DOI 10.1007/978-3-319-15221-9_20

In this context, the article focuses on linear systems with local nonlinearities that may strongly affect the overall behavior of the system. Particularly, the influence of a local cubic nonlinearity is considered in the following, but the extension to any other conservative nonlinearity is straightforward.

The general strategy of the method is outlined in Sect. 20.2. In Sect. 20.3 the calculation method for the simulated NNMs which is based on the Harmonic Balance Method including higher harmonics is described in some detail. Subsequently, in Sect. 20.4, some properties of the proposed method are examined on a 4DOF lumped mass system. Afterwards, the functionality of the method is demonstrated on a real experimental setup consisting of a beam with attached cubic spring element in Sect. 20.5. The paper closes with a conclusion and some aspects of future work in Sect. 20.6.

20.2 Model Updating Methodology

In this section an integrated methodology for updating of linear and nonlinear parameters of a system is described. The method is based on the comparison of experimental and analytical backbone curves (BBCs) associated to the NNMs. Hence, the fundamental property of NNMs which will be exploited for the update, is the frequency-energy dependence or frequency-amplitude dependence respectively. Figure 20.1 schematically shows the method used for the update which consists of two main steps: one is the numerical calculation of the NNM, which is described in the next section, and the other one is the experimental extraction of the NNM's frequency-energy dependence, which will be briefly addressed in Sect. 20.5.

Based on this, the idea is to minimize the difference between experimental BBCs (BBC_{ei}) and analytical BBCs (BBC_{ai}) leading to the objective function of the updating process

$$\Delta = \sum_{i}^{l} \|(BBC_{ai} - BBC_{ei})\| \rightarrow min. \tag{20.1}$$

In this objective function l denotes the total number of NNMs considered for the update. The difference between the measured and simulated NNMs can be expressed in terms of the difference of the associated backbone curves which can be minimized in a least squares sense

$$\|BBC_{ai} - BBC_{ei}\| = \sum_{j}^{n} (BBC_{ai}(\chi_j, \boldsymbol{\alpha}) - BBC_{ei}(\chi_j))^2, \tag{20.2}$$

where χ_j are the points where the BBCs are analytically evaluated and measured respectively. For minimization of the objective function a Nelder-Mead simplex algorithm is used and generally all unknown system parameters which are included in the parameter vector $\boldsymbol{\alpha}$ can be updated simultaneously to obtain a best fit of the analytical model to the experimental results. The vector $\boldsymbol{\alpha}$ can contain linear system parameters, nonlinear system parameters or both.

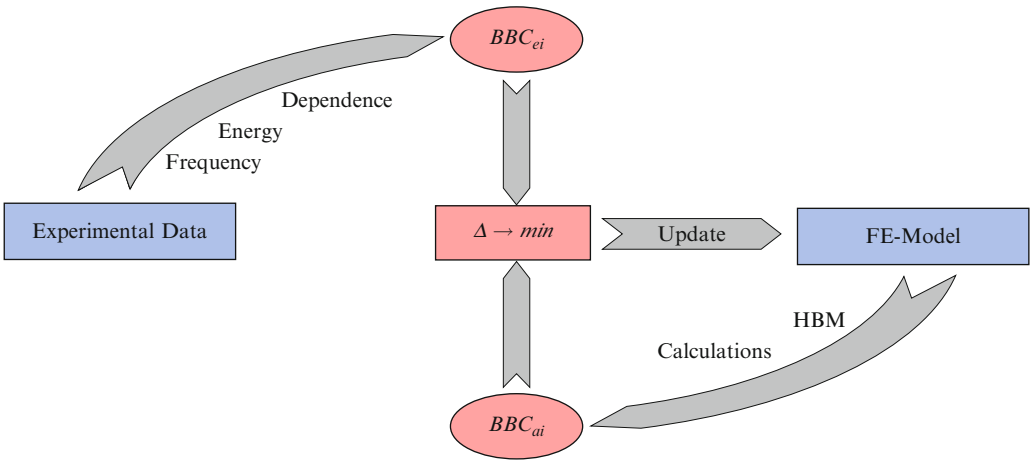

Fig. 20.1 Scheme for FE-model update based on nonlinear normal modes

20.3 Harmonic Balance Method for NNM Calculation

There are several methods for the numerical calculation of NNMs like for example shooting methods [11, 16] and also different versions of HBM [14, 17] based methods. In this paper the method of choice is based on the HBM in combination with analytical formulations for nonlinear forces due to three main reasons:

1. The high computational performance also for large scale structures.
2. The filtering property of the HBM in connection with NNM calculations.
3. The direct comparability of calculated results with experimental data.

The significance of the first point is obvious as an updating process may require numerous function evaluations to reach the best parameters. The second point will be described in more detail at the end of this section and the last point in the context of the experimental example in Sect. 20.5.

In general an autonomous, undamped mechanical system can be represented by the equation of motion

$$\boldsymbol{M}\ddot{\boldsymbol{x}} + \boldsymbol{K}\boldsymbol{x} + \boldsymbol{F}_{\mathrm{nl}}(\boldsymbol{x}, t) = \boldsymbol{0}, \tag{20.3}$$

where $\boldsymbol{M}$ denotes the mass matrix, $\boldsymbol{K}$ the linear stiffness matrix and $\boldsymbol{F}_{\mathrm{nl}}(\boldsymbol{x}, t)$ represents a vector of nonlinear, conservative forces. In this particular case of a conservative system a simplified HBM ansatz of the form

$$\boldsymbol{x}(t) = \hat{\boldsymbol{x}}_0 + \sum_{\nu=1}^{\nu_{\mathrm{h}}} \hat{\boldsymbol{x}}_\nu \cos(\nu\omega t) \tag{20.4}$$

can be made, taking into account a number of ν_{h} higher harmonics. This ansatz contrasts to the general HBM ansatz in the way that only the cosine part (or sine part) of the Fourier series has to be taken into account. This is due to the autonomous and conservative nature of the system which makes the phase arbitrary and constant. With this ansatz for the calculation of the solution for the displacement amplitudes $\hat{\boldsymbol{x}}_\nu$ in Eq. (20.4) the nonlinear forces $\boldsymbol{F}_{\mathrm{nl}}(\boldsymbol{x}, t)$ can be developed in a Fourier series dependent on the displacement $\boldsymbol{x}$ leading to

$$\boldsymbol{F}_{\mathrm{nl}}(\boldsymbol{x}, t) = \hat{\boldsymbol{F}}_{\mathrm{nl},0} + \sum_{\nu=1}^{\nu_{\mathrm{h}}} \hat{\boldsymbol{F}}_{\mathrm{nl},\nu} \cos(\nu\omega t). \tag{20.5}$$

Using these Fourier series the equation of motion can be transformed into a matrix form in the frequency domain yielding

$$\underbrace{\begin{bmatrix} \boldsymbol{K} & \boldsymbol{0} & \boldsymbol{0} & \cdots & \boldsymbol{0} \\ \boldsymbol{0} & \boldsymbol{H}_{\mathrm{lin},1} & \boldsymbol{0} & \cdots & \boldsymbol{0} \\ \vdots & \vdots & \vdots & \ddots & \vdots \\ \boldsymbol{0} & \boldsymbol{0} & \boldsymbol{0} & \cdots & \boldsymbol{H}_{\mathrm{lin},\nu_{\mathrm{h}}} \end{bmatrix}}_{\boldsymbol{H}_{\mathrm{lin}}} \underbrace{\begin{bmatrix} \hat{\boldsymbol{x}}_0 \\ \hat{\boldsymbol{x}}_1 \\ \vdots \\ \hat{\boldsymbol{x}}_{\nu_{\mathrm{h}}} \end{bmatrix}}_{\hat{\boldsymbol{x}}} + \underbrace{\begin{bmatrix} \hat{\boldsymbol{F}}_{\mathrm{nl},0}(\hat{\boldsymbol{x}}_0, \hat{\boldsymbol{x}}_1, \ldots, \hat{\boldsymbol{x}}_{\nu_{\mathrm{h}}}) \\ \hat{\boldsymbol{F}}_{\mathrm{nl},1}(\hat{\boldsymbol{x}}_0, \hat{\boldsymbol{x}}_1, \ldots, \hat{\boldsymbol{x}}_{\nu_{\mathrm{h}}}) \\ \vdots \\ \hat{\boldsymbol{F}}_{\mathrm{nl},\nu_{\mathrm{h}}}(\hat{\boldsymbol{x}}_0, \hat{\boldsymbol{x}}_1, \ldots, \hat{\boldsymbol{x}}_{\nu_{\mathrm{h}}}) \end{bmatrix}}_{\hat{\boldsymbol{f}}_{\mathrm{nl}}\left(\hat{\boldsymbol{x}}, \omega\right)} = \begin{bmatrix} \boldsymbol{0} \\ \boldsymbol{0} \\ \vdots \\ \boldsymbol{0} \end{bmatrix}, \tag{20.6}$$

$$\text{with} \quad \boldsymbol{H}_{\mathrm{lin},\nu} = \boldsymbol{K} - (\nu\omega)^2 \boldsymbol{M}. \tag{20.7}$$

As the nonlinear forces depend on the amplitudes and this relation is not known explicitly in the frequency domain the equation has to be solved iteratively. For this purpose a Newton-like method is used along with a continuation method. The system of equations in Eq. (20.6) consists of $N + 1$ equations and $N + 2$ unknowns as the frequency is unknown as well as all entries of the displacement vector $\hat{\boldsymbol{x}}$. To circumvent the problem of an underdetermined system a normalization is performed. This normalization can be made with respect to the total energy in the system or to the amplitude of a specific DOF. In an experimental setup it is difficult to measure the total energy of the system, hence in this case the normalization will be made with respect to a chosen DOF. For the solution with the Newton method a Jacobian matrix of the system has to be calculated. This calculation is the key factor for the computational performance of the solution algorithm, but the details are beyond the scope of this paper. For a detailed description of the analytical approach for the nonlinear force and Jacobian matrix calculation applied to the cubic nonlinearity and the description of the solution method the reader is referred to [18].

As already mentioned an interesting property of the HBM in context with NNM calculation is the filtering characteristic, which means that depending on the ansatz function in Eq. (20.4) certain internal resonances can be neglected and still the global trend of the NNM is represented correctly [17]. This is shown in Fig. 20.2 through the example of the first mode of a beam with cubic nonlinearity similar to the one depicted in Fig. 20.7. It can be observed that the calculation with five harmonics shows two internal resonances: one of type 1:3 and one of type 1:5 which are both caused by modal interactions of the first mode with the second mode. In contrast, the calculation with three harmonics filters out the 1:5 internal resonance and the calculation with one harmonic also the 1:3 internal resonance. This is apparent as the solution can only contain motions governed by frequencies included in the ansatz in Eq. (20.4). However, in regions apart from the internal resonances the frequency-energy dependency as well as the mode shapes which are depicted in Fig. 20.2 on the right are captured quite well even with the rough single harmonic approximation.

This is particularly interesting, when it is a priori known which harmonics have a major effect or even lead to internal resonances and hence should be included in the calculations. This is the case in the application of model updating, when experimental data exists prior to the numerical calculation of the NNMs.

20.4 Parametric Study of an Example System

Before some practical aspects of the proposed method are demonstrated, it has to be stated that this is by no means a complete study of all relevant factors that can influence the performance of the updating process. The following investigations of a four degree of freedom (4DOF) lumped mass system with cubic nonlinearity is rather an exemplary selection of some factors which might be of interest for the subsequent experimental demonstration. The 4DOF system considered as numerical example is displayed in Fig. 20.3.

For this system a reference calculation of the NNMs is made, which will be put in place of the experimental data in Fig. 20.1. This provides the advantage that the system parameters are actually known and can be varied for testing purpose.

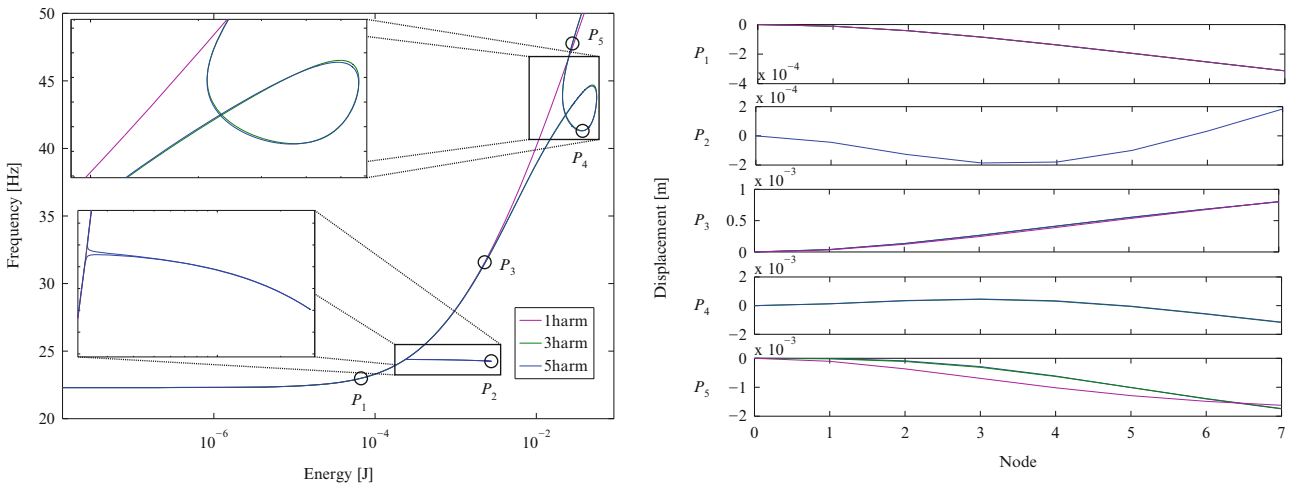

Fig. 20.2 *Left*: Filtering of HBM with different number of harmonics for the first mode of a beam with cubic nonlinearity. *Right*: Comparison of the mode shapes for the points $P1$ to $P5$ with different numbers of harmonics

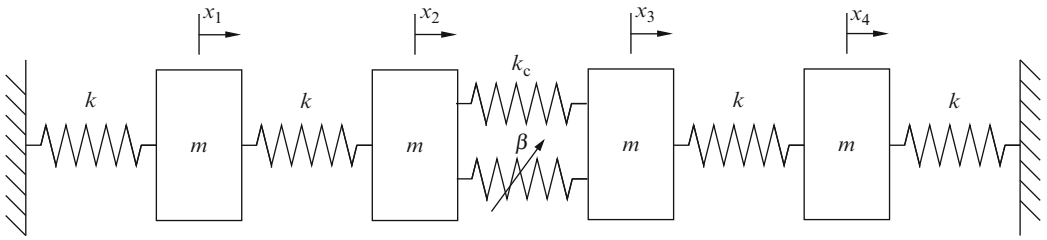

Fig. 20.3 4DOF system with cubic coupling element

Table 20.1 Parameters of reference system and parameter range for start values

Parameter	Value	Unit	Start parameter range (%)
m	1	kg	±20
k	1	N/m	±20
k_c	1	N/m	±30
β	0.5	N/m^3	±30

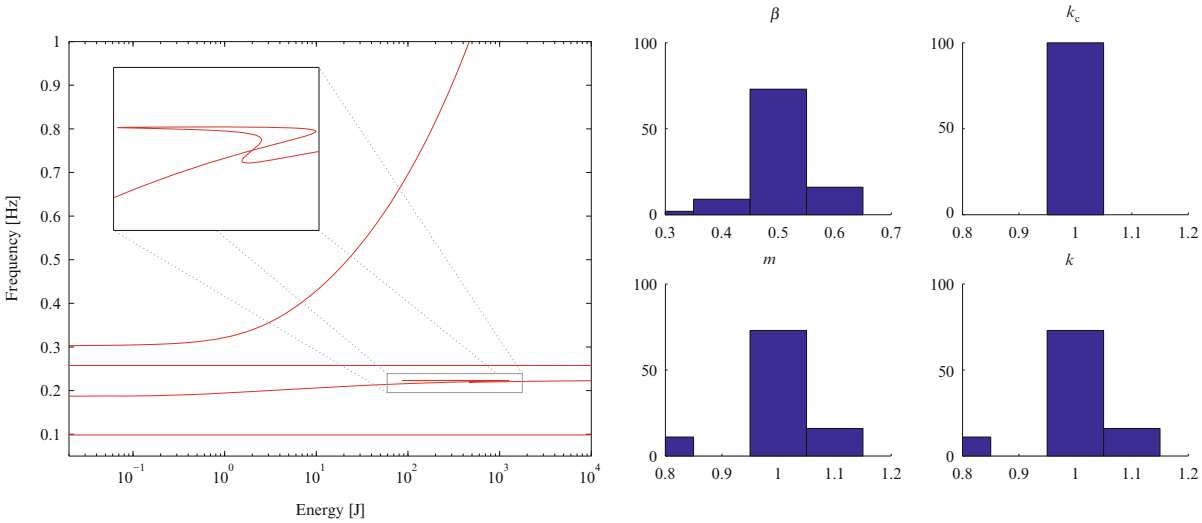

Fig. 20.4 *Left*: Frequency energy plot for reference system (three harmonics). *Right*: Results of parameter update for maximum energy $E_{max} = 10^1$ J

The parameters of the reference system are listed in Table 20.1 and the Frequency Energy Plot (FEP) is shown in Fig. 20.4. For each of the following parametric studies a number of 100 different start parameter sets is used. Based on the reference solution the start setup with randomly distributed parameters in a certain range around the actual parameters of the system is chosen and the performance of the updating process is investigated. The range for the start parameters is listed in Table 20.1.

The first factor having an influence on the performance of the algorithm is the selected energy range for the update. For the investigation of this factor only a single harmonic approximation is used to avoid internal resonances distorting the significance of the results. For very low energy the system behaves approximately linear. Therefore, it is hard to find a good parameter estimation of the nonlinear parameter β if the regarded energy range is too low. This can be seen in Fig. 20.4 (right), where the low energy range leads to problems in estimating especially the nonlinear parameter. On the other hand the probability that the updating algorithm reaches local minima and thus fails, increases with very high energy ranges, as can be observed in Fig. 20.5 (right). Furthermore, in a real experimental setup it is difficult to measure at high energy levels as the system is then subject to high loads which can cause damage. This will indeed be the limiting factor in the experimental investigation in the next section. Also the computational time for the analytic model naturally increases with increasing energy range. Hence, it is desired to select a trade-off energy range for the update, such as in Fig. 20.5 (left), which means that the amplitudes are high enough that the effect of the nonlinearity is significant but as low as possible to prevent damage of the experimental setup, avoid local minima and to increase the computational performance. In any case, for the most start parameters the updated parameters are significantly closer to the real parameters and provide a good model for further investigations.

A second point which obviously influences the updating process is the number of harmonics taken into account. One consequence of the consideration of higher harmonics is that the system in Eq. (20.6) apparently increases in size, which makes the calculations more expensive. Another effect is the occurrence of internal resonances. This feature of NNMs leads to multi-valued curves in the FEP, like in Fig. 20.4 (left), and causes problems in the updating with the basic least squares objective function. A conceivable workaround is the change of the normalization to a specific DOF or even a higher harmonic of a DOF instead of the total energy. However, a detailed study of the effect of internal resonances on the model updating is still an open question for future research. For the following experimental demonstration internal resonances do not play a role and if one stays away from the internal resonances the consideration of the higher harmonics does not have a significant effect on the performance of the updating algorithm, as can be observed in Fig. 20.6 (left).

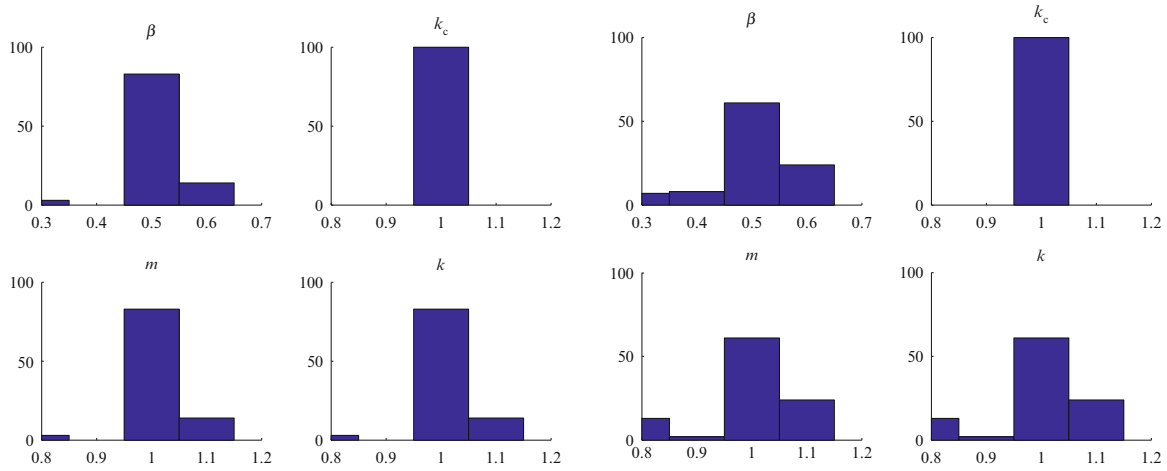

Fig. 20.5 *Left*: Results of parameter update for maximum energy $E_{max} = 10^2$ J. *Right*: Results of parameter update for maximum energy $E_{max} = 10^4$ J

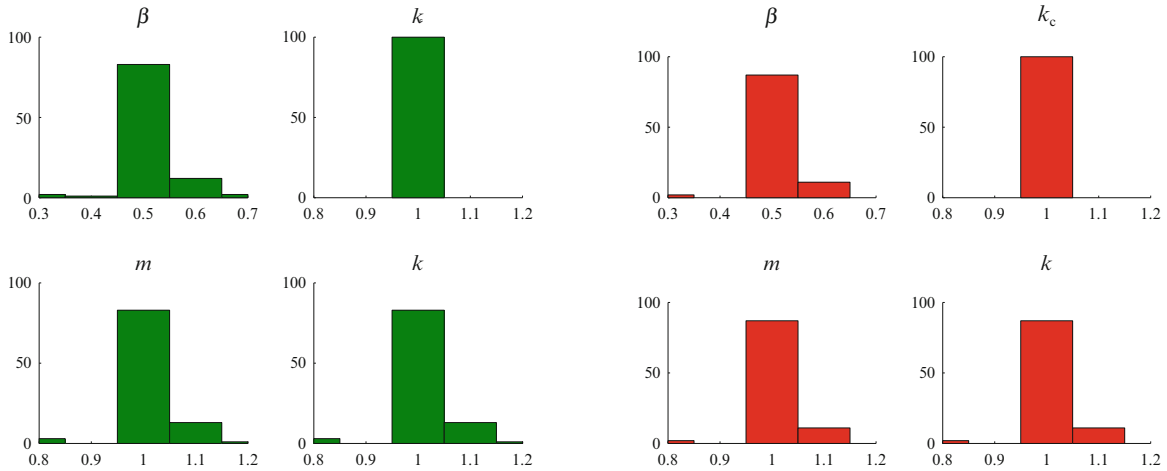

Fig. 20.6 *Left*: Results of parameter update for maximum energy $E_{max} = 1e2$ J and three harmonics. *Right*: Results of parameter update for maximum energy $E_{max} = 1e2$ J and modes 1, 2 and 4

The third aspect which will be regarded is that in an experiment it is sometimes difficult to obtain complete and accurate measurements of all NNMs. In Fig. 20.6 (right) the results for the update with only three of the NNMs of the system is run. All other settings are the same like in Fig. 20.5 (left). Comparison of both results shows that it is possible to get a similar quality of the results with an incomplete set of modes. However, one has to be careful as for example in the regarded system not all modes are affected by the nonlinearity and the choice of the wrong modes might cause the update, especially of the nonlinear parameter, to fail. So for an experimental setup one should generally have some idea about how the modes look like before choosing the NNMs considered for the updating.

In summary, the parametric study shows that even for poorly estimated start parameters the updating mostly converges to reasonable solutions and one has some freedom in choosing the amplitude range for the update, the number of harmonics and the number of modes taken into account.

20.5 Model Updating Results for Beam with Cubic Nonlinearities

In this section the proposed method is applied to a real experimental setup. The system consists of a clamped beam with a small beam at the tip and is similar to the ECL benchmark beam [19]. The small beam will encounter large displacements and therefore show cubic behavior as already reported in several publications before [20, 21]. The main beam is modeled by

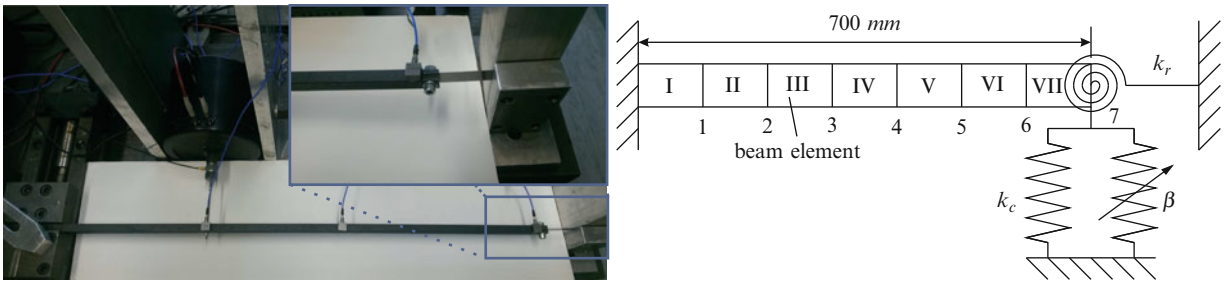

Fig. 20.7 *Left*: Photo of the experimental setup. *Right*: Schematic sketch of the numerical model

Table 20.2 Start parameters of model update for the beam structure and updated parameters

Parameter	Value before update	Value after update	Unit
E	165	186	GPa
k_c	8,000	5,525	N/m
k_r	300	217	Nm/rad
β	300×10^6	203×10^6	N/m^3

a total number of seven beam elements and 14DOFs. In the analytical model the small beam at the tip is replaced by linear translational and rotational springs with spring constants k_c and k_r respectively as well as a cubic spring with constant β. A photo of the experimental setup and a sketch of the numerical model is shown in Fig. 20.7.

The experimental extraction of the NNMs follows the approach of Peeters [20], who proposed a method which consists of three steps:

1. Tuning of the excitation to a single mode based on a phase quadrature criterion.
2. Turning off the excitation and measuring the free decay response.
3. Extracting the ridge of the Wavelet Transform (WT) of the free decay response.

With this method it is possible to extract the time-frequency dependence of a single NNM. In combination with calculation of the ridge of the WT the frequency-amplitude dependence can be reconstructed as well as the evolution of the NNM shape over amplitude with respect to the measured points. An advantage of the WT in combination with the HBM is that the WT decomposes the signal into its frequency components. Hence, the result of the WT of the time signal can be directly related to the respective harmonic coefficients of the HBM based calculations of the NNM.

For the measurements the beam is excited on node 2 with an electrodynamic shaker and tuned to a single mode. Then the excitation is switched off and the free decay is recorded. In this experimental setup the acceleration is measured with three accelerometers located at nodes $2, 4$ and 7. For the updating only the first two NNMs are taken into account as it is difficult and time consuming to accurately measure all NNMs. Still, the first two modes together with the three measured points provide a sufficient data base to start a parameter update for the parameters of the small coupling beam which will be expressed in terms of k_c, k_r, β and the Young's modulus E of the main beam.

The first five harmonics were included in the calculations as these were found to be significant in the experimental results. Yet, in the objective function only the first harmonic component was compared to the respective component of the measured results. Due to the nature of the wavelet transform yielding frequency-decomposed amplitudes for all times of the free decay it is generally possible to extract frequency-amplitude dependencies of all harmonics of the measurement. Based on this an arbitrary harmonic or even multiple harmonics can be included in the objective function for the updating. Typically the first harmonic governs the time signal and therefore is the natural choice as it provides a reasonable signal-to-noise ratio. In some cases, especially in the presence of internal resonances, it might be interesting to chose another harmonic component or multiple harmonics for the objective function. The use of the frequency-amplitude dependence of three measured points simultaneously implies an update based on frequency-amplitude dependence of each point and the relation of their amplitudes dependent on the instantaneous frequency. Thus, some additional information about the amplitude dependent NNM shape evaluated at these three points is included as well.

The parameters of an exemplary start setup before the update are listed in Table 20.2 and compared to the updated parameters. Even for such a poor start parameter estimation the updating procedure converges to a reasonable solution. For comparison the Young's modulus of the main beam was also estimated by a linear modal analysis as 185 GPa which is a deviation less than 1 % compared to the Young's modulus estimated by the nonlinear model update. Generally, the method

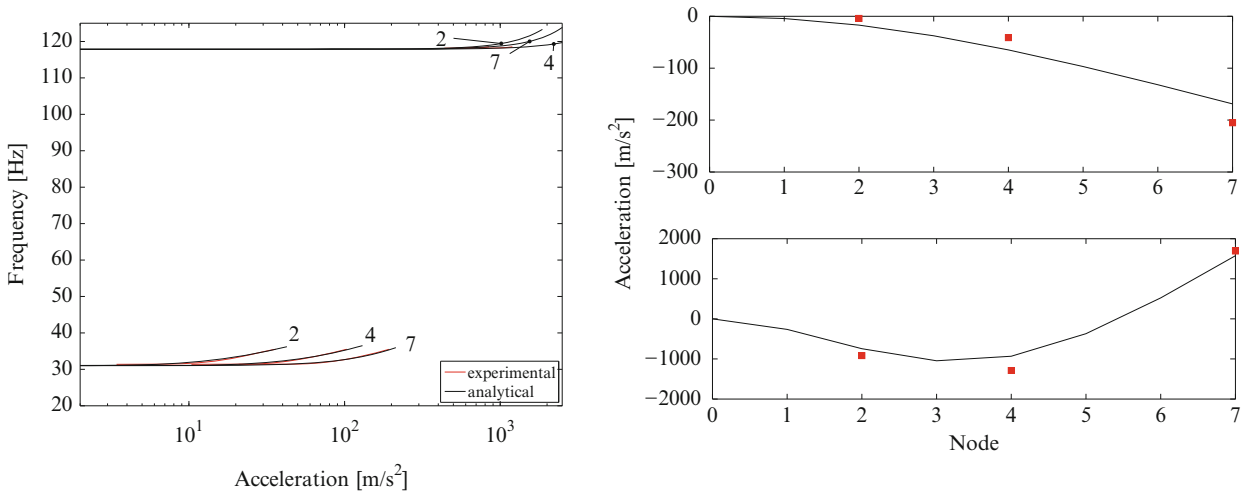

Fig. 20.8 *Left*: Comparison of first harmonic of frequency-amplitude dependence of analytical and experimental. *Right*: Comparison of the mode shapes for the measured nodes 2, 4, 7 with the analytical mode shape (*top*: mode 1 at 34.5 Hz, *bottom*: mode 2 at 118.5 Hz)

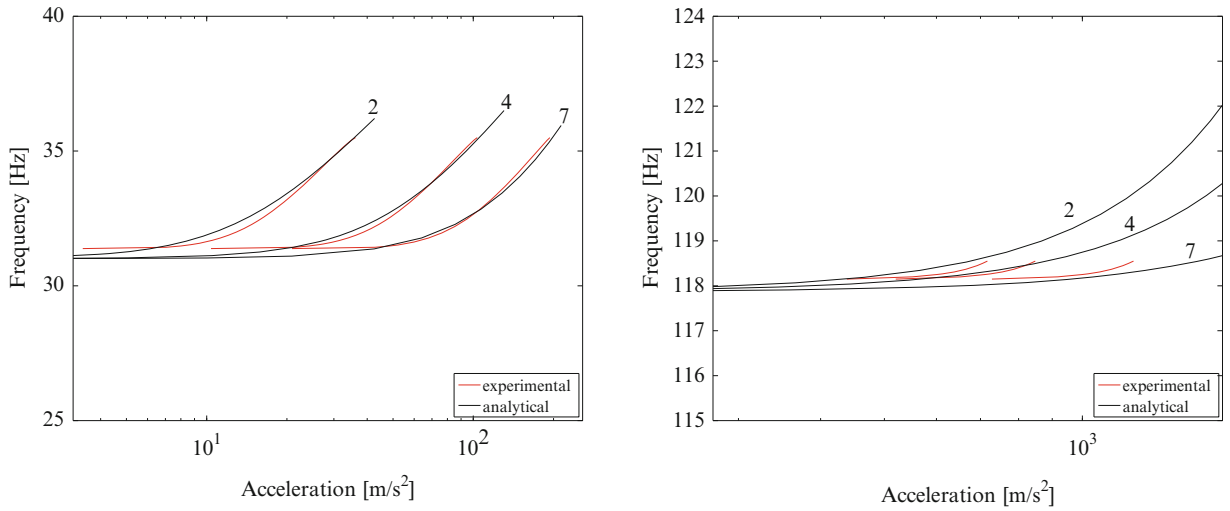

Fig. 20.9 *Left*: Zoom on the frequency-amplitude dependence curve of first NNM for points 2, 4 and 7. *Right*: Zoom on the frequency-amplitude dependence curve of second NNM for points 2, 4 and 7

seems not very sensitive on the start parameters and provides very similar updating results for different start parameters within a wide range. Also the computational time which is for the update with five harmonics around 90 s on a 3.2 GHz Intel i5 desktop computer seems acceptable.

Figure 20.8 shows a comparison of the results of the updated analytical model and the measured NNMs for the first two modes and all three measured points (nodes 2, 4, 7) on the beam. On the right the frequency-amplitude dependence is depicted for both, analytical and experimental results. Especially the first NNM shows very good agreement over a large amplitude range. For the second NNM it was difficult to obtain an accurate measurement for a wide amplitude range. However, in the range which could be measured the agreement is also satisfying. The mode shapes for the first two NNMs of the beam at a medium amplitude level, with corresponding frequencies of 34.5 Hz for the first and 118.5 Hz for the second NNM, are compared on the right of Fig. 20.8 and show good agreement as well.

Figure 20.9 shows a zoom on the frequency-amplitude dependence curves of the first (left) and the second (right) NNM for the experimental and the numerical results for the considered nodes.

20.6 Conclusion and Future Work

This paper presents a method for the integration of local nonlinearities in a structural model updating procedure based on the NNMs of the structure. With this method linear and nonlinear system parameters have been identified simultaneously. For the updating a least squares minimization of the difference between the measured BBCs and the analytical BBCs is used. The analytical calculations are made with a HBM ansatz taking into account higher harmonics. Experimentally the NNMs were extracted as the ridges of the WTs of free decay measurements in resonance. The updating algorithm was tested on a numerical test case of a lumped mass system and some features of the method were illustrated. Subsequently, the updating was successfully applied to a real experimental setup consisting of a beam structure with cubic nonlinearity. It has been shown that the application of the HBM is reasonable in this context as the computational algorithm provides fast calculations which is required for an updating with numerous function evaluations. Also the filtering of internal resonances and the direct comparability of HBM results with measured WTs of the free decay responses are interesting features of the method. For the experimental setup it turns out that a critical point is the accurate measurement of the NNMs over a broad amplitude range and for all NNMs. The free decay measurement method which was applied is also time consuming as it requires to measure each mode separately. Nevertheless, even experimental results for smaller amplitude ranges, for few measured points and an incomplete set of considered NNMs were sufficient to successfully identify parameters of the beam structure.

In future research the method will be applied to more complex structures. In this context the consideration of other nonlinearities including non-smooth and non-conservative ones will be a challenge as well as the improvement of the methods for the measurements and the updating algorithm. Another interesting point which has to be analyzed in more detail is the effect of internal resonances in the context of the model updating.

References

1. Mottershead JE, Friswell MI (1993) Model updating in structural dynamics: a survey. J Sound Vib 167:347–375
2. Friswell MI, Mottershead JE (1995) Finite element model updating in structural dynamics. Kluwer Academic Publishers, Dordrecht
3. Worden K, Tomlinson GR (2001) Nonlinearity in structural dynamics. Institute of Physics Publishing, Bristol
4. Kerschen G,Worden K, Vakakis AF, Golinval J-C (2006) Past, present and future of nonlinear system identification in structural dynamics. Mech Syst Signal Process 20:505–592
5. Feeny BF, Kappagantu R (1998) On the physical interpretation of proper orthogonal modes in vibrations. J Sound Vib 211:607–616
6. Masri SF, Miller RK, Saud AF, Caughey TK (1987) Identification of nonlinear vibrating structures: part II - applications. J Appl Mech 109:607–616
7. Böswald M, Füllekrug U (2014) Non-linear identification of multi-degree of freedom systems using the restoring force surface method. In: Proceedings of ISMA 2014
8. Rosenberg RM (1960) Normal modes of nonlinear dual-mode systems. J Appl Mech 27:263–268
9. Vakakis AF, Manevitch LI, Mikhlin YV, Pilipchuk VN, Zevin AA (1996) Normal modes and localization in nonlinear systems. Wiley, New York
10. Kerschen G, Peeters M, Golinval J-C, Vakakis AF (2009) Nonlinear normal modes, part I: a useful framework for the structural dynamicist. Mech Syst Signal Process 23:170–194
11. Peeters M, Vigui R, Srandour G, Kerschen G, Golinval J-C (2009) Nonlinear normal modes, part II: toward a practical computation using numerical continuation techniques. Mech Syst Signal Process 23:195–216
12. Shaw SW, Pierre C (1993) Normal modes for non-linear vibratory systems. J Sound Vib 164:85–124
13. Laxalde D, Thouverez F (2009) Complex non-linear modal analysis for mechanical systems: application to turbomachinery bladings with friction interfaces. J Sound Vib 322:1009–1025
14. Krack M, Panning-von Scheidt L, Wallaschek J (2013) A method for nonlinear modal analysis and synthesis: application to harmonically forced and self-excited mechanical systems. J Sound Vib 332:6798–6814
15. Staszewski WJ (1998) Identification of non-linear systems using multi-scale ridges and skeletons of the wavelet transform. J Sound Vib 214:639–658
16. Kuether RJ, Allen MS (2014) A numerical approach to directly compute nonlinear normal modes of geometrically nonlinear finite element models. Mech Syst Signal Process 46:1–15
17. Detroux T, Renson L, Kerschen G (2014) The harmonic balance method for advanced analysis and design of nonlinear mechanical systems. In: Proceedings of the IMAC-XXXII, Orlando
18. Peter S, Schreyer F, Reuss P, Gaul L (2014) Consideration of local stiffening and clearance nonlinearities in coupled systems using a generalized harmonic balance method. In: Proceedings of ISMA 2014
19. Thouverez F (2003) Presentation of the ECL benchmark. Mech Syst Signal Process 17:195–202
20. Peeters M, Kerschen G, Golinval JC (2010) Dynamic testing of nonlinear vibrating structures using nonlinear normal modes. J Sound Vib 330:486–509
21. Meyer S (2003) Modellbildung und Identifikation von lokalen nichtlinearen Steifigkeits- und Dämpfungseigenschaften in komplexen strukturdynamischen finite elemente modellen. Ph.D. thesis, Universität Kassel

Chapter 21
Experimental Modal Analysis of Nonlinear Structures Using Broadband Data

J.P. Noël, L. Renson, C. Grappasonni, and G. Kerschen

Abstract The objective of the present paper is to develop a rigorous identification methodology of nonlinear normal modes (NNMs) of engineering structures. This is achieved by processing experimental measurements collected under broadband forcing. The use of such a type of forcing signal allows to excite multiple NNMs simultaneously and, in turn, to save testing time. A two-step methodology integrating nonlinear system identification and numerical continuation of periodic solutions is proposed for the extraction of the individual NNMs from broadband input and output data. It is demonstrated using a numerical cantilever beam possessing a cubic nonlinearity at its free end. The proposed methodology can be viewed as a nonlinear generalization of the phase separation techniques routinely utilized for experimental modal analysis of linear structures. The paper ends with a comparison between this new nonlinear phase separation technique and a previously-developed nonlinear phase resonance method.

Keywords Nonlinear normal modes • Experimental data • Broadband excitation • Nonlinear system identification • Numerical continuation

21.1 Introduction

Experimental modal analysis of linear engineering structures is now well-established and mature [1]. It is routinely practiced in industry, in particular during on-ground certification of aircraft and spacecraft structures [2–4], using two specific approaches, namely phase resonance and phase separation methods. Phase resonance testing, also known as force appropriation, consists in exciting the normal modes of interest one at a time using a multipoint sine forcing at the corresponding natural frequency [5]. Conversely, in phase separation testing, several normal modes are excited simultaneously using either broadband or swept-sine forcing, and are subsequently identified using appropriate linear system identification techniques [6, 7].

The existence of nonlinear behavior in dynamic testing, at least in certain regimes of motion, is today a challenge the structural engineer is more and more frequently confronted with. In this context, the development of a nonlinear counterpart to experimental modal analysis would be extremely beneficial. An interesting approach is the so-called nonlinear resonant decay method introduced by Wright and co-workers [8, 9]. In this approach, a burst of a sine wave is applied to the structure at the undamped natural frequency of a normal mode, and enables small groups of modes coupled by nonlinear forces to be excited. A nonlinear curve fitting in modal space is then carried out using the restoring force surface method. The identification of modes from multimodal nonlinear responses has also been attempted in the past few years. For that purpose, advanced signal processing techniques have been utilized, including the empirical mode decomposition [10–12], time-frequency analysis tools [13] and machine learning algorithms [14]. Multimodal identification relying on the synthesis of frequency response functions using individual mode contributions has been proposed in [15, 16]. The difficulty with these approaches is the absence of superposition principle in nonlinear dynamics, preventing the response of a nonlinear system from being decomposed into the sum of different modal responses.

In the present study, we adopt the framework offered by the theory of nonlinear normal modes (NNMs) to perform experimental nonlinear modal analysis. The concept of normal modes was generalized to nonlinear systems by Rosenberg in the 1960s [17, 18] and by Shaw and Pierre in the 1990s [19]. NNMs possess a clear conceptual relation with the classical linear normal modes (LNMs) of vibration, while they provide a solid mathematical tool for interpreting a wide

J.P. Noël (✉) • L. Renson • C. Grappasonni • G. Kerschen
Space Structures and Systems Laboratory (S3L), Aerospace and Mechanical Engineering Department, University of Liège, Liège, Belgium
e-mail: jp.noel@ulg.ac.be; l.renson@ulg.ac.be; chiara.grappasonni@ulg.ac.be; g.kerschen@ulg.ac.be

G. Kerschen (ed.), *Nonlinear Dynamics, Volume 1*, Conference Proceedings of the Society for Experimental Mechanics Series, DOI 10.1007/978-3-319-15221-9_21

class of nonlinear dynamic phenomena, see, e.g., [20–23]. There now exist effective algorithms for their computation from mathematical models [24–27]. For instance, the NNMs of full-scale aircraft and spacecraft structures and of a turbine bladed disk were computed in [28–30], respectively.

A nonlinear phase resonance method exploiting the NNM concept was first proposed in [31], and was validated experimentally in [32]. Following the philosophy of force appropriation and relying on a nonlinear generalization of the phase lag quadrature criterion, this nonlinear phase resonance method excites the targeted NNMs one at a time using a multipoint, multiharmonic sine forcing. The energy-dependent frequency and modal curve of each NNM are then extracted directly from the experimental time series by virtue of the invariance principle of nonlinear oscillations. Applications of nonlinear phase resonance testing to moderately complex experimental structures were recently reported in the technical literature, in the case of a steel frame in [33] and of a circular perforated plate in [34].

The objective of the present paper is to develop a rigorous identification methodology of NNMs by processing experimental measurements collected under broadband forcing. The use of such a type of forcing signal allows, in contrast with a phase resonance approach, to excite multiple NNMs simultaneously and, in turn, to save testing time. A two-step methodology integrating nonlinear system identification and numerical continuation of periodic solutions is proposed for the extraction of the individual NNMs from broadband input and output data. More specifically, the frequency-domain nonlinear subspace identification (FNSI) method, introduced in [35], is first applied to measured data to derive an undamped experimental model of the nonlinear structure of interest, assuming an accurate characterization of the nonlinearities. Secondly, a numerical algorithm implementing pseudo-arclength continuation [25] is exploited to compute the NNMs of the structure based on the experimentally-derived model.

The paper is organized as follows. The fundamental properties of NNMs defined as periodic solutions of the underlying undamped system are briefly reviewed in Sect. 21.2. The existing nonlinear phase resonance method introduced in [31] is also described. In Sect. 21.3, the two building blocks of the proposed NNM identification methodology, namely the FNSI method and the pseudo-arclength continuation algorithm, are presented in detail. The methodology is demonstrated in Sect. 21.4 using numerical experiments on a cantilever beam possessing a cubic nonlinearity at its free end. Since it can be viewed as a nonlinear generalization of linear phase separation techniques, the proposed methodology is also compared in Sect. 21.5 with the previously-developed nonlinear phase resonance method. The conclusions of the study are finally summarized in Sect. 21.6.

21.2 Brief Review of Nonlinear Normal Modes (NNMs) and Identification Using Phase Resonance

In this work, an extension of Rosenberg's definition of a NNM is considered [23]. Specifically, a NNM is defined as a nonnecessarily synchronous, periodic motion of the undamped, unforced system

$$\mathbf{M}\,\ddot{\mathbf{q}}(t) + \mathbf{K}\,\mathbf{q}(t) + \mathbf{f}(\mathbf{q}(t)) = 0 \tag{21.1}$$

where $\mathbf{M}$ and $\mathbf{K} \in \mathbb{R}^{n_p \times n_p}$ are the mass and linear stiffness matrices, respectively; $\mathbf{q} \in \mathbb{R}^{n_p}$ is the generalized displacement vector; $\mathbf{f}(\mathbf{q}(t)) \in \mathbb{R}^{n_p}$ is the nonlinear restoring force vector encompassing elastic terms only; n_p is the number of degrees of freedom (DOFs) of the system. This definition of a NNM may appear to be restrictive in the case of nonconservative systems. However, as shown in [23], the topology of the underlying conservative NNMs of a system yields considerable insight into its damped dynamics.

Because a salient feature of nonlinear systems is the frequency-energy dependence of their oscillations, the depiction of NNMs is conveniently realized in a frequency-energy plot (FEP). A NNM motion in a FEP is represented by a point associated with the fundamental frequency of the periodic motion, and with the total conserved energy accompanying the motion. A branch in a FEP details the complete frequency-energy dependence of the considered mode. By way of illustration, the FEP of the two-DOF system described by the equations

$$\begin{aligned} \ddot{q}_1 + (2\,q_1 - q_2) + 0.5\,q_1^3 &= 0 \\ \ddot{q}_2 + (2\,q_2 - q_1) &= 0 \end{aligned} \tag{21.2}$$

is plotted in Fig. 21.1. The plot consists of two branches corresponding to the in-phase and out-of-phase synchronous NNMs of the system. These fundamental NNMs are the direct nonlinear extension of the corresponding LNMs. The nonlinear modal

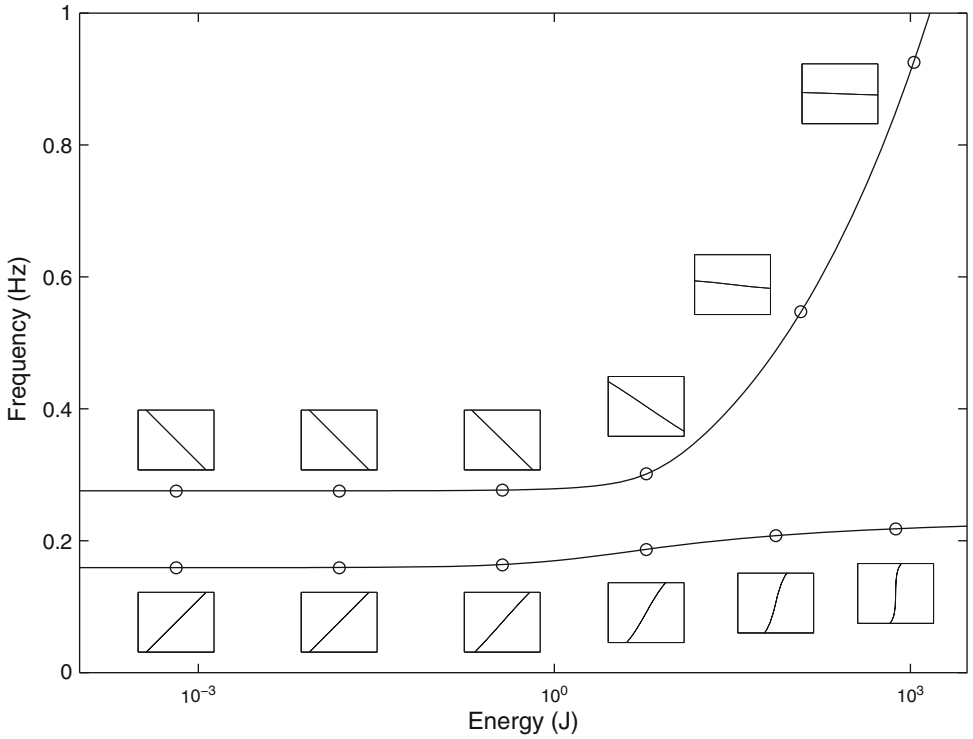

Fig. 21.1 FEP of the two-DOF system described by Eq. (21.2). NNM motions depicted in displacement space are *inset*. The horizontal and vertical axes in these plots are the displacements of the first and second DOF of the system, respectively

parameters, i.e. the frequencies of oscillation and the modal curves, are found to depend markedly on the energy. In particular, the frequency of the two fundamental NNMs increases with the energy level, revealing the hardening characteristic of the cubic stiffness nonlinearity in the system.

The absence of superposition principle in nonlinear dynamics renders by no means straightforward the identification of NNMs from broadband measurements (see Sect. 21.3). However, two essential properties of linear systems are preserved in the presence of nonlinearity. First, forced resonances of nonlinear systems occur in the neighborhood of NNMs [20]. Second, NNMs obey the invariance principle, which states that if the motion is initiated on one specific NNM, the remaining NNMs are quiescent for all time [19].

These two properties were exploited in [31] to develop a rigorous nonlinear phase resonance method based on sine data. The procedure comprises two steps, as illustrated in Fig. 21.2. During the first step, termed NNM force appropriation, the system is excited to induce a single-NNM motion at a prescribed energy level. This step is facilitated by a generalized phase lag quadrature criterion applicable to nonlinear systems [31]. This criterion asserts that a structure vibrates according to an underlying conservative NNM if the measured responses possess, for all harmonics, a phase difference of 90° with respect to the excitation. The second step of the procedure, termed NNM free-decay identification, turns off the excitation to track the energy dependence of the appropriated NNM. The associated modal parameters are extracted directly from the free damped system response through time-frequency analysis. This nonlinear phase resonance method was found to be highly accurate but, as linear phase resonance testing, very time-consuming. In addition, to reach the neighborhood of the resonance where a specific NNM lives may require a cumbersome trial-and-error approach to deal with the shrinking basins of attraction along forced resonance peaks. The methodology described in the next section precisely addresses these two issues.

21.3 Identification Methodology of Nonlinear Normal Modes (NNMs) Under Broadband Forcing

The methodology proposed in this paper for the identification of NNMs using broadband measurements is presented in Fig. 21.3. It comprises two major steps. The first step consists in processing acquired input and output data to construct an experimental undamped model of the nonlinear structure of interest. In the present study, this model takes the form of a set of first-order equations in the state space. In a second step, the energy-dependent frequencies and modal curves of the excited NNMs are computed individually by applying a numerical continuation algorithm to the undamped model equations.

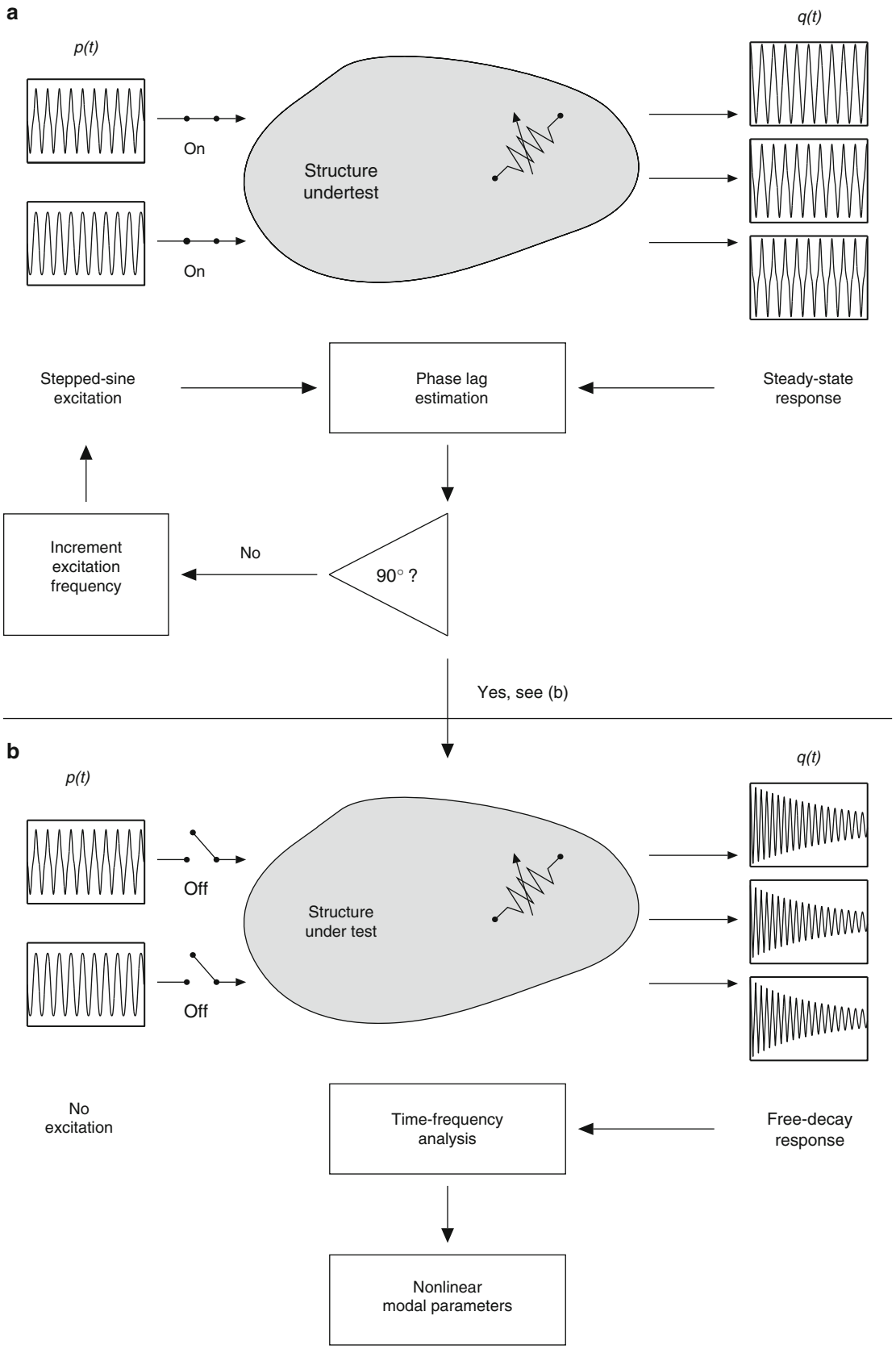

Fig. 21.2 Experimental modal analysis of nonlinear systems using a nonlinear phase resonance method [31]. (**a**) NNM force appropriation; (**b**) NNM free-decay identification

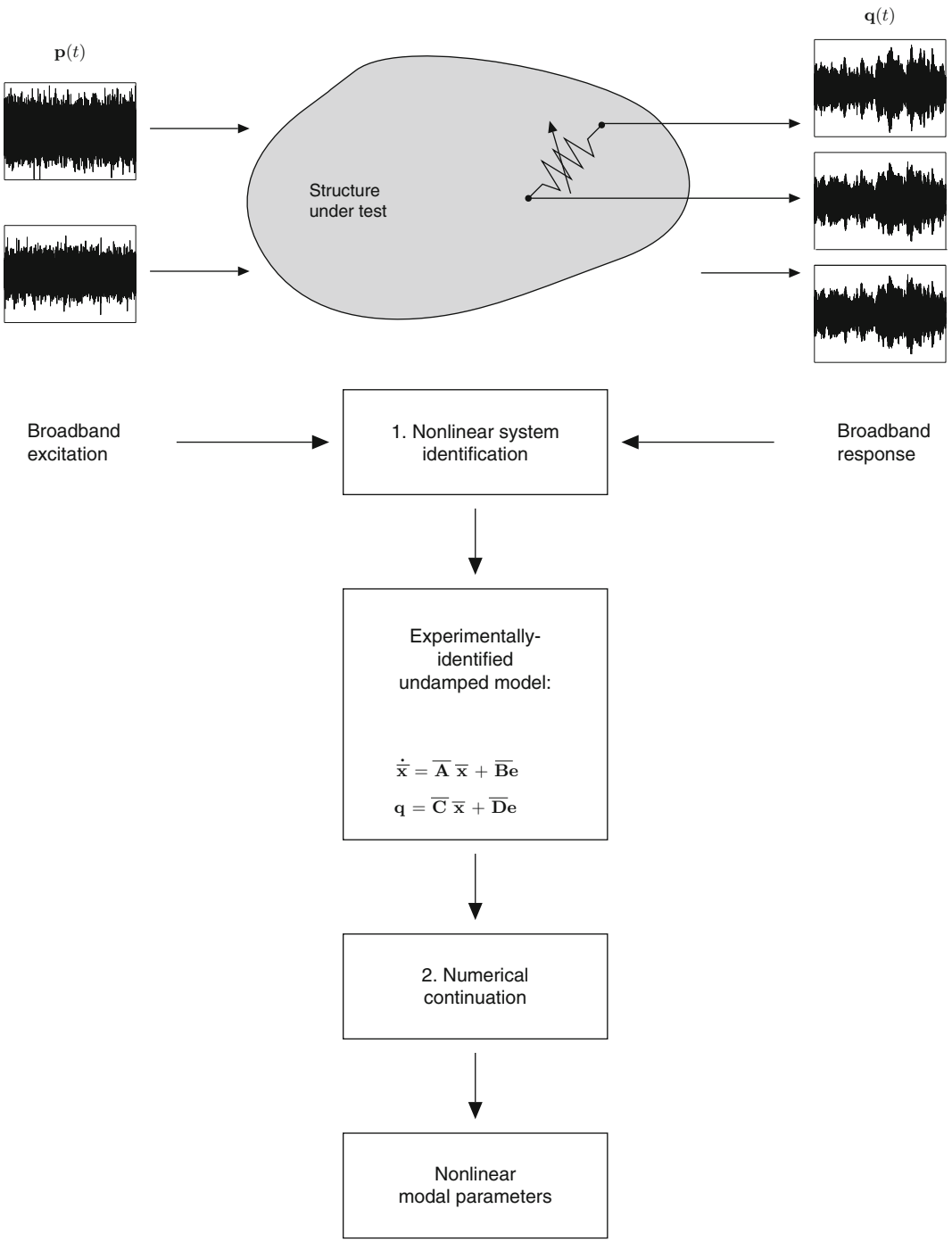

Fig. 21.3 Proposed methodology for the identification of NNMs based on broadband measurements. It comprises two major steps, namely nonlinear system identification and numerical continuation

Section 21.3.1 describes how the experimental state-space model can be derived in the frequency domain by employing the FNSI method. Section 21.3.2 next outlines one existing algorithm, based on pseudo-arclength continuation, for the computation of NNMs defined as periodic solutions.

21.3.1 Experimental Identification of an Undamped Nonlinear State-Space Model

In the present section, the experimental extraction of a nonlinear undamped model of the structure under test is achieved by means of a subspace identification technique, termed FNSI method [35]. The FNSI method is capable of deriving models of nonlinear vibrating systems directly from measured data, and without resorting to a preexisting numerical model, e.g. a finite element model. It is applicable to multi-input, multi-output structures with high damping and high modal density, and makes no assumption as to the importance of nonlinearity in the measured dynamics [36, 37]. It will also be shown in this section that the application of the FNSI method requires the measurement of the applied forces together with the dynamic responses throughout the structure, including at the driving points and across the nonlinear components.

21.3.1.1 Nonlinear Model Equations in the Physical Space

The vibrations of damped nonlinear systems obey Newton's second law of dynamics

$$\mathbf{M}\,\ddot{\mathbf{q}}(t) + \mathbf{C}_v\,\dot{\mathbf{q}}(t) + \mathbf{K}\,\mathbf{q}(t) + \mathbf{f}(\mathbf{q}(t), \dot{\mathbf{q}}(t)) = \mathbf{p}(t) \tag{21.3}$$

where $\mathbf{C}_v \in \mathbb{R}^{n_p \times n_p}$ is the linear viscous damping matrix; $\mathbf{p}(t) \in \mathbb{R}^{n_p}$ is the generalized external force vector; $\mathbf{f}(\mathbf{q}(t), \dot{\mathbf{q}}(t)) \in \mathbb{R}^{n_p}$ is the nonlinear restoring force vector encompassing elastic and dissipative terms. Note that Eq. (21.3) represents the damped and forced generalization of Eq. (21.1). The nonlinear restoring force term in Eq. (21.3) is expressed by means of a linear combination of known basis functions $\mathbf{h}_a(\mathbf{q}(t), \dot{\mathbf{q}}(t))$ as

$$\mathbf{f}(\mathbf{q}(t), \dot{\mathbf{q}}(t)) = \sum_{a=1}^{s} c_a\,\mathbf{h}_a(\mathbf{q}(t), \dot{\mathbf{q}}(t)). \tag{21.4}$$

In this sum, the coefficients c_a associated with the nonlinear basis functions $\mathbf{h}_a(\mathbf{q}(t), \dot{\mathbf{q}}(t))$ play a role similar to the linear stiffness and viscous damping coefficients contained in the matrices $\mathbf{K}$ and $\mathbf{C}_v$ in Eq. (21.3), respectively. Note that the total number of basis functions s introduced in the model may be larger than the number of physical nonlinearity sources in the system, as multiple model terms are generally required to capture the behavior of a single nonlinear component.

Given measurements of $\mathbf{p}(t)$ and $\mathbf{q}(t)$ or its derivatives, and an appropriate selection of the functionals $\mathbf{h}_a(t)$, the application of the FNSI method in the present study aims at constructing a state-space model describing the undamped dynamics associated with Eq. (21.3). Models in the state space are appealing because of their intrinsic capability to represent systems with multiple inputs and outputs. They can also be effectively utilized to predict the response of the system under a given forcing function by direct time integration (see Sect. 21.3.2).

21.3.1.2 Feedback Interpretation and State-Space Model Equations

The FNSI approach builds on a block-oriented interpretation of nonlinear structural dynamics, which sees nonlinearities as a feedback into the linear system in the forward loop [38], as illustrated in Fig. 21.4. This interpretation boils down to moving the nonlinear internal forces in Eq. (21.3) to the right-hand side, and viewing them as additional external forces applied to the underlying linear structure, that is,

$$\mathbf{M}\,\ddot{\mathbf{q}}(t) + \mathbf{C}_v\,\dot{\mathbf{q}}(t) + \mathbf{K}\,\mathbf{q}(t) = \mathbf{p}(t) - \sum_{a=1}^{s} c_a\,\mathbf{h}_a(\mathbf{q}(t), \dot{\mathbf{q}}(t)). \tag{21.5}$$

Without loss of generality, it is assumed in this section that the structural response is measured in terms of generalized displacements. Defining the state vector $\mathbf{x} = \left(\mathbf{q}^T \;\; \dot{\mathbf{q}}^T\right)^T \in \mathbb{R}^{n_s}$, where $n_s = 2\,n_p$ is the dimension of the state space and T the matrix transpose, Eq. (21.5) is recast into the set of first-order equations

$$\begin{cases} \dot{\mathbf{x}}(t) = \mathbf{A}\,\mathbf{x}(t) + \mathbf{B}\,\mathbf{e}(t) \\ \mathbf{q}(t) = \mathbf{C}\,\mathbf{x}(t) + \mathbf{D}\,\mathbf{e}(t) \end{cases} \tag{21.6}$$

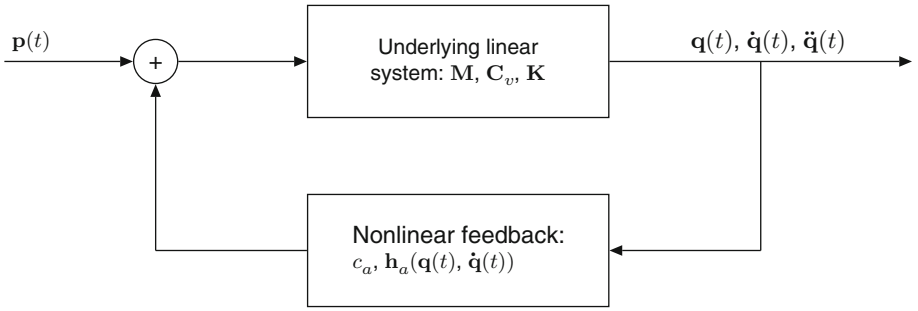

Fig. 21.4 Feedback interpretation of nonlinear structural dynamics [38]

where the vector $\mathbf{e} \in \mathbb{R}^{(s+1)\,n_p}$, termed *extended input vector*, concatenates the external forces $\mathbf{p}(t)$ and the nonlinear basis functions $\mathbf{h}_a(t)$. The matrices $\mathbf{A} \in \mathbb{R}^{n_s \times n_s}$, $\mathbf{B} \in \mathbb{R}^{n_s \times (s+1)\,n_p}$, $\mathbf{C} \in \mathbb{R}^{n_p \times n_s}$ and $\mathbf{D} \in \mathbb{R}^{n_p \times (s+1)\,n_p}$ are the state, extended input, output and direct feedthrough matrices, respectively. State-space and physical-space matrices correspond through the relations

$$\mathbf{A} = \begin{pmatrix} \mathbf{0}^{n_p \times n_p} & \mathbf{I}^{n_p \times n_p} \\ -\mathbf{M}^{-1}\,\mathbf{K} & -\mathbf{M}^{-1}\,\mathbf{C}_v \end{pmatrix} ; \mathbf{B} = \begin{pmatrix} \mathbf{0}^{n_p \times n_p} & \mathbf{0}^{n_p \times n_p} & \mathbf{0}^{n_p \times n_p} & \dots & \mathbf{0}^{n_p \times n_p} \\ \mathbf{M}^{-1} & -c_1\,\mathbf{M}^{-1} & -c_2\,\mathbf{M}^{-1} & \dots & -c_s\,\mathbf{M}^{-1} \end{pmatrix}$$

$$\mathbf{C} = \begin{pmatrix} \mathbf{I}^{n_p \times n_p} & \mathbf{0}^{n_p \times n_p} \end{pmatrix} ; \mathbf{D} = \mathbf{0}^{n_p \times (s+1)\,n_p} \tag{21.7}$$

where $\mathbf{0}$ and $\mathbf{I}$ are the zero and identity matrices, respectively. It should be remarked that no identifiability condition constrains the number of measured displacements, provided that the nonlinear basis functions $\mathbf{h}_a(\mathbf{q}(t), \dot{\mathbf{q}}(t))$ can be formed from the recorded channels [35]. This implies that the nonlinear components in the structure must be instrumented on both sides in order to measure the relative displacement and velocity required in the formulation of the nonlinear basis functions $\mathbf{h}_a(\mathbf{q}(t), \dot{\mathbf{q}}(t))$, as illustrated in Fig. 21.3.

The FNSI estimation of the four system matrices $\mathbf{A}$, $\mathbf{B}$, $\mathbf{C}$ and $\mathbf{D}$ is achieved in the frequency domain using a classical subspace resolution scheme. This resolution essentially involves the reformulation of Eq. (21.6) in matrix form, and the computation of estimates of $(\mathbf{A}, \mathbf{B}, \mathbf{C}, \mathbf{D})$ through geometrical manipulations of input and output data. The interested reader is referred to [35] for a complete introduction to the theoretical and practical aspects of the FNSI method.

21.3.1.3 Conversion from State Space to Physical and Modal Space

The identified state-space model $(\mathbf{A}, \mathbf{B}, \mathbf{C}, \mathbf{D})$ can be converted into estimates of (1) the nonlinear coefficients c_a and (2) the underlying linear modal properties of the system. Linear and nonlinear system properties will prove useful in the construction of undamped state-space model equations in Sect. 21.3.1.4. They will also prove convenient to assess the quality of the identification in Sects. 21.4.1.3 and 21.4.1.4. The complexity of the conversion addressed in this subsection stems from an unknown similarity transformation of the state-space basis within which the FNSI model is derived [35]. Because the nonlinear coefficients c_a are elements of the matrix $\mathbf{B}$, they vary according to the choice of the basis in which $\mathbf{B}$ is calculated. Therefore, the estimates of c_a cannot be obtained from a direct inspection of $\mathbf{B}$.

To achieve the conversion to physical and modal space, the transfer function matrix $\mathbf{G}_s(\omega)$ associated with the state-space model is formed as

$$\mathbf{G}_s(\omega) = \mathbf{C}\left(j\omega\,\mathbf{I}^{n_s \times n_s} - \mathbf{A}\right)^{-1}\mathbf{B} + \mathbf{D} \tag{21.8}$$

where ω is the pulsation and j the imaginary unit. Matrix $\mathbf{G}_s(\omega)$ is an invariant system property with respect to any similarity transformation of the state-space basis [39]. It can be expressed in terms of the physical and modal properties of the system by substituting Eq. (21.4) into Eq. (21.3) in the frequency domain, which leads to

$$\mathbf{G}^{-1}(\omega)\mathbf{Q}(\omega) + \sum_{a=1}^{s} c_a\,\mathbf{H}_a(\omega) = \mathbf{P}(\omega) \tag{21.9}$$

where $\mathbf{G}(\omega) = \left(-\omega^2\,\mathbf{M} + j\,\omega\,\mathbf{C}_v + \mathbf{K}\right)^{-1}$ is the frequency response function (FRF) matrix of the underlying linear system, and where $\mathbf{Q}(\omega)$, $\mathbf{H}_a(\omega)$ and $\mathbf{P}(\omega)$ are the continuous Fourier transforms of $\mathbf{q}(t)$, $\mathbf{h}_a(t)$ and $\mathbf{p}(t)$, respectively. The concatenation of $\mathbf{P}(\omega)$ and $\mathbf{H}_a(\omega)$ into the extended input spectrum $\mathbf{E}(\omega)$ finally gives

$$\mathbf{Q}(\omega) = \mathbf{G}(\omega)\left[\,\mathbf{I}^{n_p\times n_p}\; -c_1\,\mathbf{I}^{n_p\times n_p}\;\ldots\;-c_s\,\mathbf{I}^{n_p\times n_p}\,\right]\mathbf{E}(\omega) = \mathbf{G}_s(\omega)\,\mathbf{E}(\omega). \tag{21.10}$$

Matrix $\mathbf{G}(\omega)$ is simply extracted using Eqs. (21.8) and (21.10) as the first n_p columns of matrix $\mathbf{G}_s(\omega)$. Subsequently, the nonlinear coefficients c_a are computed from the other columns of $\mathbf{G}_s(\omega)$ given the knowledge of $\mathbf{G}(\omega)$.

Moreover, the system damped and undamped natural frequencies, denoted ω_i and $\omega_{i,0}$, respectively, can be estimated together with the unscaled mode shape vectors $\boldsymbol{\psi}^{(i)} \in \mathbb{R}^{n_s}$ by solving the eigenvalue problem associated with the state matrix $\mathbf{A}$, that is,

$$\mathbf{A}\,\boldsymbol{\psi}^{(i)} = \lambda_i\,\boldsymbol{\psi}^{(i)},\quad i = 1,..,n_s. \tag{21.11}$$

The imaginary part $\mathcal{I}(\lambda_i)$ and the absolute value $|\lambda_i|$ of the complex eigenvalues λ_i provide the damped and undamped natural frequencies, respectively. Moreover, the state-space mode shape vectors $\boldsymbol{\psi}^{(i)}$ are converted into the corresponding physical-space modes $\tilde{\boldsymbol{\phi}}^{(i)}$ utilizing the output matrix $\mathbf{C}$ as

$$\tilde{\boldsymbol{\phi}}^{(i)} = \mathbf{C}\,\boldsymbol{\psi}^{(i)}. \tag{21.12}$$

Each mode shape vector $\tilde{\boldsymbol{\phi}}^{(i)}$ can be scaled using the residue $R_{kk}^{(i)}$ of the driving point FRF $G_{kk}(\omega)$ of the underlying linear system formulated as

$$G_{kk}(\omega) = \sum_{i=1}^{n_p} \frac{R_{kk}^{(i)}}{j\,\omega - \lambda_i} + \frac{R_{kk}^{(i)^*}}{j\,\omega - \lambda_i^*} \tag{21.13}$$

where k is the location of the excited DOF within the n_p DOFs of the structure, and where a star denotes the complex conjugate operation. Equation (21.13) is an overdetermined algebraic system of equations with n_p unknowns and as many equations as the number of processed frequency lines. The ith scaled mode shape vector at the driving point $\phi_k^{(i)}$ is finally obtained by enforcing a unit modal mass, i.e.

$$R_{kk}^{(i)} = \frac{\phi_k^{(i)}\,\phi_k^{(i)}}{2\,j\,\omega_{i,0}}, \tag{21.14}$$

while the other components of the mode shape vector $\tilde{\boldsymbol{\phi}}^{(i)}$ are scaled accordingly.

It should be noted that the mode scaling adopted in this section is rigorously valid if the linear damping mechanisms in the tested structure are proportional to the mass and stiffness distributions [40]. This assumption is compatible with the presence of weak damping. This implies that the mode shape vector at the driving point $\phi_k^{(i)}$ is real-valued in Eq. (21.14). In general, experimental mode shapes are however complex-valued. They can be enforced to be real by rotating each mode in the complex plane by an angle equal to the mean of the phase angles of the mode components, and subsequently neglecting the imaginary parts of the rotated components.

21.3.1.4 Removal of Damping Terms in the Identified State-Space Model

The removal of damping terms in the identified state-space model is necessary to allow the calculation of undamped NNMs as defined in Sect. 21.2. This is achieved in this subsection by recasting Eq. (21.6) into modal space. For that purpose, the vector of modal coordinates $\overline{\mathbf{q}}(t) \in \mathbb{R}^{n_p}$ is introduced as

$$\mathbf{q}(t) = \boldsymbol{\Phi}\,\overline{\mathbf{q}}(t) \tag{21.15}$$

where $\boldsymbol{\Phi} \in \mathbb{R}^{n_p\times n_p}$ is the matrix of the scaled mode shape vectors $\boldsymbol{\phi}^{(i)}$, and where a bar signals a vector or a matrix expressed in modal space. It is known that the projection of Eq. (21.5) into modal space yields

$$\mathbf{I}^{n_p \times n_p}\,\ddot{\overline{\mathbf{q}}}(t) + \overline{\mathbf{C}}_v\,\dot{\overline{\mathbf{q}}}(t) + \overline{\mathbf{K}}\,\overline{\mathbf{q}}(t) = \mathbf{\Phi}^T\,\mathbf{p}(t) - \sum_{a=1}^{s} c_a\,\mathbf{\Phi}^T\,\mathbf{h}_a(\mathbf{q}(t), \dot{\mathbf{q}}(t)) \tag{21.16}$$

where $\mathbf{\Phi}^T\,\mathbf{M}\,\mathbf{\Phi} = \overline{\mathbf{M}} = \mathbf{I}^{n_p \times n_p}$ since the linear mode shapes were unit-mass-scaled in the previous subsection, $\mathbf{\Phi}^T\,\mathbf{C}_v\,\mathbf{\Phi} = \overline{\mathbf{C}}_v$ and $\mathbf{\Phi}^T\,\mathbf{K}\,\mathbf{\Phi} = \overline{\mathbf{K}}$. The projected stiffness matrix $\overline{\mathbf{K}}$ is a diagonal matrix populated with the squared values of the undamped frequencies $\omega_{i,0}$, i.e. $\text{diag}\left(\overline{\mathbf{K}}\right) = \left(\omega_{1,0}^2\ \omega_{2,0}^2\ \ldots\ \omega_{n_p,0}^2\right)$.

Therefore, defining the modal state vector $\overline{\mathbf{x}} = \left(\overline{\mathbf{q}}^T\ \dot{\overline{\mathbf{q}}}^T\right)^T \in \mathbb{R}^{n_s}$, Eq. (21.16) can be reformulated in the form of the two first-order relations

$$\begin{cases} \dot{\overline{\mathbf{x}}}(t) = \overline{\mathbf{A}}\,\overline{\mathbf{x}}(t) + \overline{\mathbf{B}}\,\mathbf{e}(t) \\ \mathbf{q}(t) = \overline{\mathbf{C}}\,\overline{\mathbf{x}}(t) + \overline{\mathbf{D}}\,\mathbf{e}(t) \end{cases} \tag{21.17}$$

where the state, extended input, output and direct feedthrough matrices in modal space are given by

$$\overline{\mathbf{A}} = \begin{pmatrix} \mathbf{0}^{n_p \times n_p} & \mathbf{I}^{n_p \times n_p} \\ -\overline{\mathbf{K}} & -\overline{\mathbf{C}}_v \end{pmatrix};\ \overline{\mathbf{B}} = \begin{pmatrix} \mathbf{0}^{n_p \times n_p} & \mathbf{0}^{n_p \times n_p} & \mathbf{0}^{n_p \times n_p} & \ldots & \mathbf{0}^{n_p \times n_p} \\ \mathbf{\Phi}^T & -c_1\,\mathbf{\Phi}^T & -c_2\,\mathbf{\Phi}^T & \ldots & -c_s\,\mathbf{\Phi}^T \end{pmatrix}$$

$$\overline{\mathbf{C}} = \begin{pmatrix} \mathbf{\Phi} & \mathbf{0}^{n_p \times n_p} \end{pmatrix};\ \overline{\mathbf{D}} = \mathbf{0}^{n_p \times (s+1)\,n_p}. \tag{21.18}$$

Undamped state-space model equations in modal space can finally be constructed by imposing zero damping in Eq. (21.18), that is $\overline{\mathbf{C}}_v = \mathbf{0}^{n_p \times n_p}$. The nonlinear coefficients c_a, the undamped frequencies $\omega_{i,0}$ and the scaled mode shape matrix $\mathbf{\Phi}$ in Eq. (21.18) are obtained via Eqs. (21.10), (21.11) and (21.14), respectively.

Note that, in a real measurement setup, the structure of interest is tested over a limited frequency interval, typically encompassing a few tens of modes depending on the input bandwidth and the sampling frequency. Assuming that $m < n_p$ linear modes are excited and identified given input and output data, this results into the truncation of the diagonal of $\overline{\mathbf{K}}$ such that $\text{diag}\left(\overline{\mathbf{K}}\right) = \left(\omega_{1,0}^2\ \omega_{2,0}^2\ \ldots\ \omega_{m,0}^2\right)$. The dimension of the scaled mode shape matrix $\mathbf{\Phi}$ is similarly truncated to m columns.

21.3.2 Computation of the Individual NNMS in the State Space Using Numerical Continuation

According to their definition given in Sect. 21.2 in the conservative case, NNMs can be sought numerically as periodic solutions of the governing nonlinear equations of motion, i.e. Eq. (21.17) in the proposed identification methodology. To this end, a two-step algorithm is exploited in the present study combining shooting and pseudo-arclength continuation. This section provides a succinct description of the two techniques. The interested reader is referred to [25] for more in-depth comments.

Shooting is a popular numerical technique for solving the two-point boundary-value problem associated with the periodicity condition

$$\mathbf{S}(\mathrm{T}, \overline{\mathbf{x}}_{p0}) \equiv \overline{\mathbf{x}}_p(\mathrm{T}, \overline{\mathbf{x}}_{p0}) - \overline{\mathbf{x}}_{p0} = \mathbf{0} \tag{21.19}$$

where $\mathbf{S}(\mathrm{T}, \overline{\mathbf{x}}_{p0})$ is called the shooting function. It expresses the difference between the final state at time T of the system $\overline{\mathbf{x}}_p(\mathrm{T}, \overline{\mathbf{x}}_{p0})$ and the initial state of the system $\overline{\mathbf{x}}_{p0}$. A solution $\overline{\mathbf{x}}_p(t, \overline{\mathbf{x}}_{p0})$ is periodic if

$$\overline{\mathbf{x}}_p(t, \overline{\mathbf{x}}_{p0}) = \overline{\mathbf{x}}_p(t + \mathrm{T}, \overline{\mathbf{x}}_{p0}) \tag{21.20}$$

where T is the minimal period. In a shooting algorithm, the period T and the initial conditions $\overline{\mathbf{x}}_{p0}$ realizing a periodic motion are found iteratively. More specifically, direct numerical integration is carried out to obtain an initial guess of the periodic solution, which is corrected by means of a Newton-Raphson procedure to converge to the actual solution. In this work, time integration is performed using a fifth-order Runge-Kutta scheme with an automatic selection of the time step.

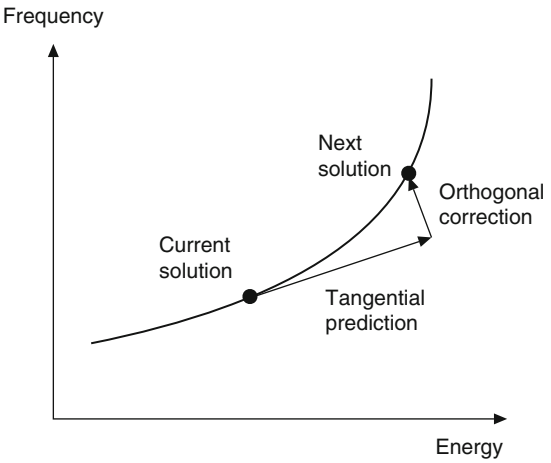

Fig. 21.5 Computation of a family of periodic solutions using a pseudo-arclength continuation scheme including prediction and correction steps

One notes that the truncation of $\overline{\mathbf{K}}$ and $\mathbf{\Phi}$ in Eq. (21.18) according to the m identified linear modes discards high-frequency modes in the experimental model. This allows a reasonably large time step to be considered during time integration, which may substantially reduce the computational burden.

Another important remark in the resolution of the boundary-value problem formulated in Eq. (21.19) is that the phase of the periodic solutions is not unique. If $\bar{\mathbf{x}}_p(t)$ is a solution of Eq. (21.17), then $\bar{\mathbf{x}}_p(t + \Delta t)$ is geometrically the same solution in state space for any Δt. Hence, an additional condition $s(\bar{\mathbf{x}}_{p0}) = 0$, termed phase condition, is specified to remove the arbitrariness of the initial conditions. Following the approach in [25], the modal velocities $\dot{\bar{\mathbf{q}}}_0$ are set equal to zero. In summary, an isolated NNM motion is computed by solving the augmented two-point boundary-value problem defined by the two relations

$$\begin{aligned} \mathbf{S}(\mathrm{T}, \bar{\mathbf{x}}_{p0}) &= 0 \\ s(\bar{\mathbf{x}}_{p0}) &= 0. \end{aligned} \tag{21.21}$$

To obtain the family of periodic solutions that describe the considered NNM, shooting is combined with a pseudo-arclength continuation technique. Starting from a known periodic solution, continuation proceeds in two steps, namely a prediction and a correction, as illustrated in Fig. 21.5. In the prediction step, a guess of the next periodic solution along the NNM branch is generated in the direction of the tangent vector to the branch at the current solution. Next, the prediction is corrected using a shooting procedure, forcing the variations of the period and the initial conditions to be orthogonal to the prediction direction. Note that this shooting-continuation algorithm was used to construct Fig. 21.1.

21.4 Numerical Demonstration Using a Cantilever Beam Possessing a Cubic Nonlinearity

In this section, the developed methodology for the identification of NNMs is demonstrated based on numerical experiments carried out on the nonlinear beam structure proposed as a benchmark during the European COST Action F3 [41]. This structure consists of a main cantilever beam whose free end is connected to a thin beam clamped on the other side. The thin beam can exhibit geometrically nonlinear behavior for sufficiently large displacements. It should be noted that the same case study was investigated to demonstrate the nonlinear phase resonance method developed in [31, 32].

The finite element model of the structure considered in this work is represented in Fig. 21.6 and is identical to the experimentally-updated model in [32]. It comprises 14 two-dimensional beam elements for the main beam and three elements for the thin beam. As shown in [35, 42], the nonlinear dynamics induced by the thin beam can be modeled through a grounded cubic spring associated with a coefficient c_1, and positioned at the connection between the two beams. The geometrical and mechanical properties of the structure are listed in Tables 21.1 and 21.2, respectively.

Numerical experiments were conducted by direct time integration using a nonlinear Newmark scheme. To this end, a linear damping matrix $\mathbf{C}_v$ was introduced in the model via a proportionality relation with the mass and stiffness matrices, i.e.

$$\mathbf{C}_v = \alpha\mathbf{K} + \beta\mathbf{M}, \tag{21.22}$$

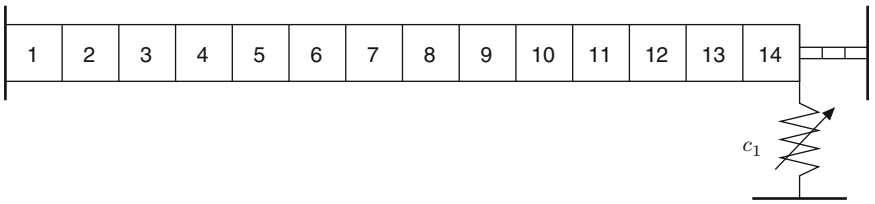

Fig. 21.6 Finite element model of the nonlinear beam

Table 21.1 Geometrical properties of the nonlinear beam

	Length (m)	Width (mm)	Thickness (mm)
Main beam	0.7	14	14
Thin beam	0.04	14	0.5

Table 21.2 Mechanical properties of the nonlinear beam

Young's modulus (N/m^2)	Density (kg/m^3)	Nonlinear coefficient c_1 (N/m^3)
$2.05\ 10^{11}$	7,800	$8\ 10^9$

Table 21.3 Linear natural frequencies ω_0 and damping ratios ϵ of the first three bending modes of the nonlinear beam

Mode	Natural frequency ω_0 (Hz)	Damping ratio ε (%)
1	31.28	1.28
2	143.64	0.29
3	397.87	0.14

with $\alpha = 3\ 10^{-7}$ and $\beta = 5$. The resulting linear natural frequencies and damping ratios of the first three bending modes of the beam structure are given in Table 21.3. The sampling frequency during time simulation was set to 60,000 Hz to ensure the accuracy of the integration. Synthetic time series were then decimated down to 3,000 Hz for practical use, considering low-pass filtering to avoid aliasing.

21.4.1 Identification Using the FNSI Method Under a Multisine Excitation

According to the scheme in Fig. 21.3, the proposed testing procedure starts with the application of a broadband excitation signal to the nonlinear beam structure. Note that the FNSI method can address classical random excitations, including Gaussian noise, periodic random, burst random and pseudo random signals. Stepped-sine and swept-sine excitations are not applicable because of the inability of the FNSI method to handle nonstationary signals, i.e. signals with time-varying frequency content [35]. One opts herein for pseudo random signals, also known as random phase multisine signals. A random phase multisine is a periodic random signal with a user-controlled amplitude spectrum, and a random phase spectrum drawn from a uniform distribution. If an integer number of periods is measured, the amplitude spectrum is perfectly realized, unlike Gaussian noise. One of the other main advantages of a multisine is that its periodic nature can be utilized to separate the transient and the steady-state responses of the system. This, in turn, eliminates the systematic errors due to leakage in the identification.

A multisine excitation with a flat amplitude spectrum and a root-mean-squared (RMS) amplitude of 15 N was applied vertically to node 4 of the structure. The excited band spans the 5–500 Hz interval to encompass the three linear modes of interest. The response of the nonlinear beam was simulated over ten periods of 32,768 samples each, nine periods of which were discarded to achieve steady-state conditions. Figure 21.7a, b shows the amplitude spectrum and the phase spectrum of one period of the considered multisine input, respectively. The complete signal containing ten periods is depicted in Fig. 21.7c, where one specific period is highlighted in gray. Finally, the decay of the transient response measured at the main beam tip is illustrated in logarithmic scaling in Fig. 21.7d. The latter plot was obtained by subtracting from the entire signal the last period of measurement, assumed to be in steady state.

21.4.1.1 Selection of the Nonlinear Basis Functions

The application of the FNSI method to measured data requires the selection of appropriate basis functions $\mathbf{h}_a(\mathbf{q}(t), \dot{\mathbf{q}}(t))$ to describe the nonlinearity in the system. This task, referred to as the characterization of nonlinearity, is in general challenging because of the various sources of nonlinear behavior that may exist in engineering structures, and the plethora of

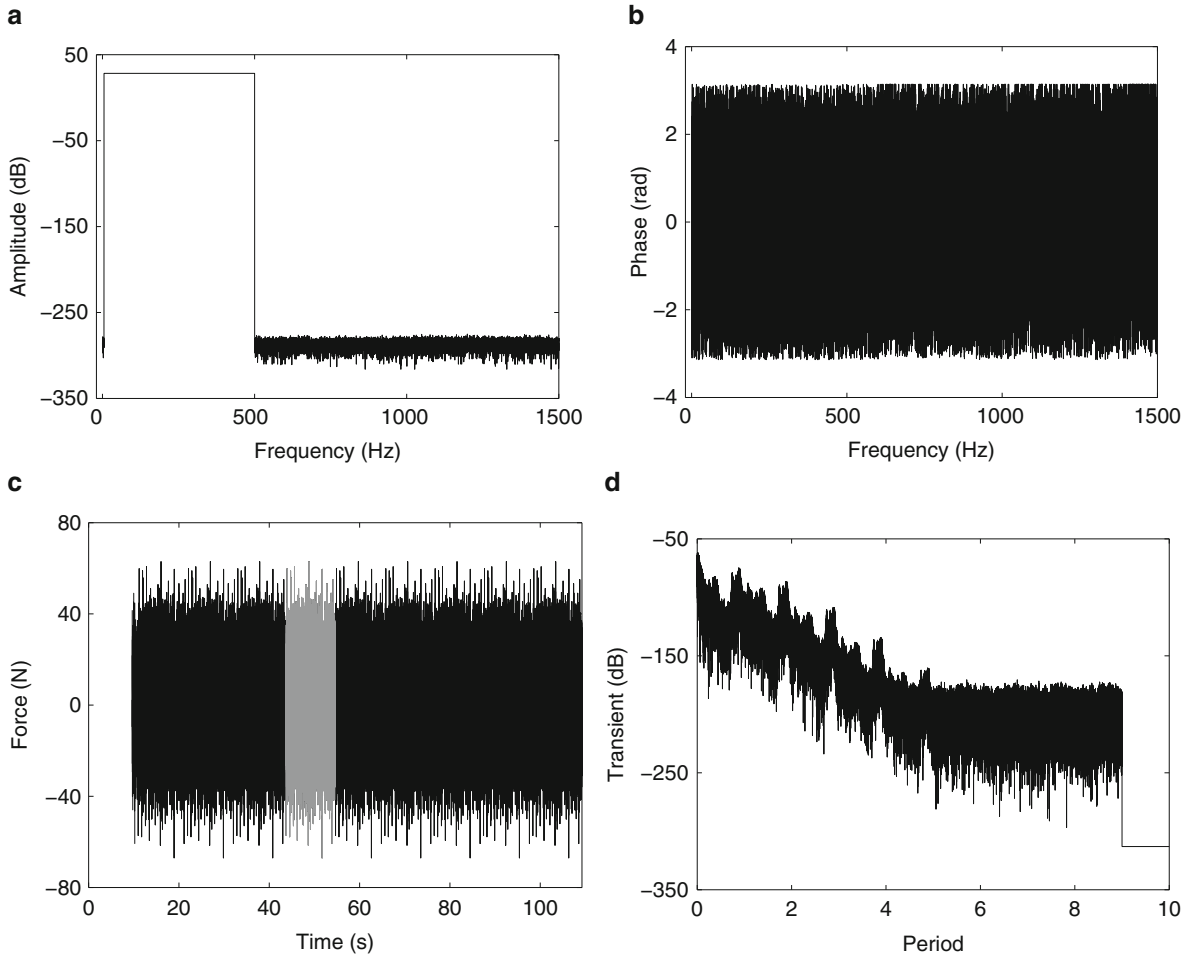

Fig. 21.7 Random phase multisine excitation signal. (**a**, **b**) Amplitude and phase spectrum of a single period; (**c**) complete signal containing ten periods with one specific period highlighted in *gray*; (**d**) decay of the transient response at the main beam tip in logarithmic scaling

dynamic phenomena they may cause [43]. One possible approach to discriminate between different candidate nonlinearity models is the use of a subspace identification error criterion, as detailed in [36]. Characterization may also be partly bypassed by resorting to mathematical functionals capable of representing a vast class of nonlinearities, such as high-order polynomials [44], neural networks [45] or splines [37]. In this study, we assume the knowledge of nonlinear functional form associated with the thin beam, namely a cubic restoring force in displacement.

21.4.1.2 Selection of the Model Order

The order of the state-space model derived using the FNSI method is equal to twice the number of linear modes activated in the measured data [35]. This order is conveniently estimated using a stabilization diagram, similarly to the current practice in linear system identification. Figure 21.8 charts the stabilization of the natural frequencies, damping ratios and mode shapes of the structure computed at 15 N RMS for model orders up to 20. In this diagram, the modal assurance criterion (MAC) is utilized to quantify the correspondence between mode shapes at different orders. Figure 21.8 shows full stabilization of the first three modes of the structure at order 6. Note that full stabilization symbols only appear at order 8. However, since this is tested between successive model orders taking as reference the lowest order, equal stabilization is also achieved at order 6, which is therefore selected to avoid spurious poles.

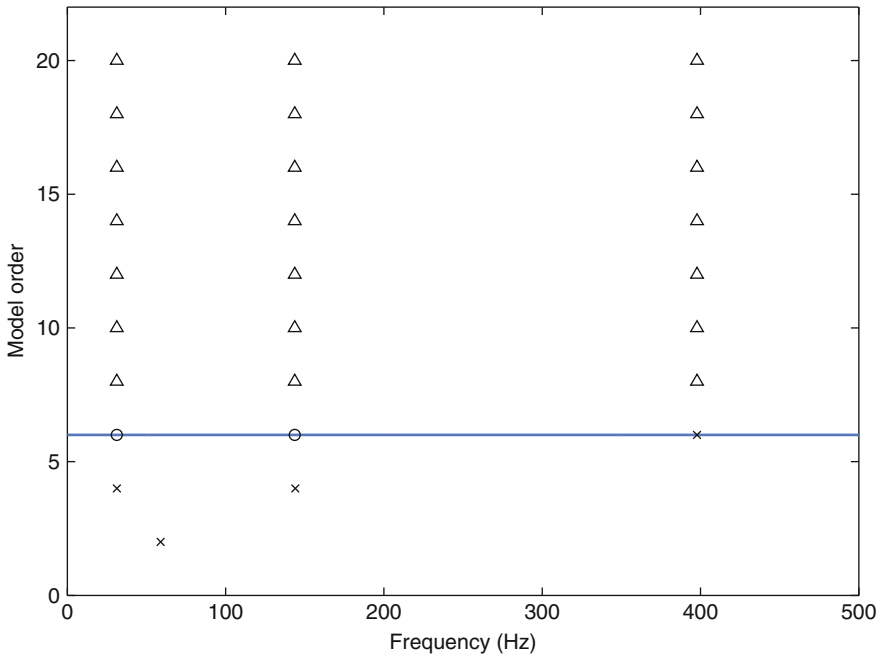

Fig. 21.8 Stabilization diagram. *Cross*: stabilization in natural frequency; *circle*: extra stabilization in MAC; *triangle*: full stabilization. Stabilization thresholds in natural frequency, damping ratio and MAC are 1 %, 5 % and 0.98, respectively. The *blue line* indicates the selected order (Color figure online)

Table 21.4 Relative errors on the estimated natural frequencies and damping ratios (in %) and diagonal MAC values of the first three modes of the beam computed at order 6

Mode	Error on ω_0 (%)	Error on ε (%)	MAC
1	0.0004	−0.0175	1.00
2	−0.0020	0.0180	1.00
3	−0.0144	−0.0461	1.00

21.4.1.3 Estimation of the Underlying Linear Properties

Table 21.4 lists the relative errors on the estimated natural frequencies and damping ratios together with the diagonal MAC values. The results in this table demonstrate the ability of the FNSI method to recover accurately the modal properties of the underlying linear structure from nonlinear data. The overall quality of the linear parameter estimates is confirmed in Fig. 21.9a, b, where the exact FRF at the main beam tip is compared with the corresponding FRF synthesized using the FNSI method at 15 N RMS for the first and second modes of the structure, respectively. The FRFs calculated at high level using a linear estimator are also visible in the two plots, and highlight the importance of the nonlinear distortions affecting the beam dynamics. Note that, since the considered nonlinearity is a function of the displacement at the main beam tip, the distortions appearing around the first mode are more substantial. For the same reason, the third bending mode is only marginally impacted at 15 N RMS, and is hence not depicted.

21.4.1.4 Estimation of the Nonlinear Coefficient

The nonlinear coefficient c_1 is estimated using Eq. (21.10) and is consequently a spectral quantity, i.e. it is complex-valued and frequency-dependent. This is an attractive property because the significance of its frequency variations and imaginary part turns out to be particularly convenient to assess the quality of the identification. Figure 21.10a, b depicts the real and imaginary parts of the coefficient, respectively. The real part shows almost no dependence upon frequency, and the imaginary part is more than three orders of magnitude smaller (see Table 21.5). Table 21.5 gives the averaged value of the nonlinear coefficient, the relative error and the ratio between its real and imaginary parts in logarithmic scaling. This table reveals the excellent agreement between the identified and exact coefficients.

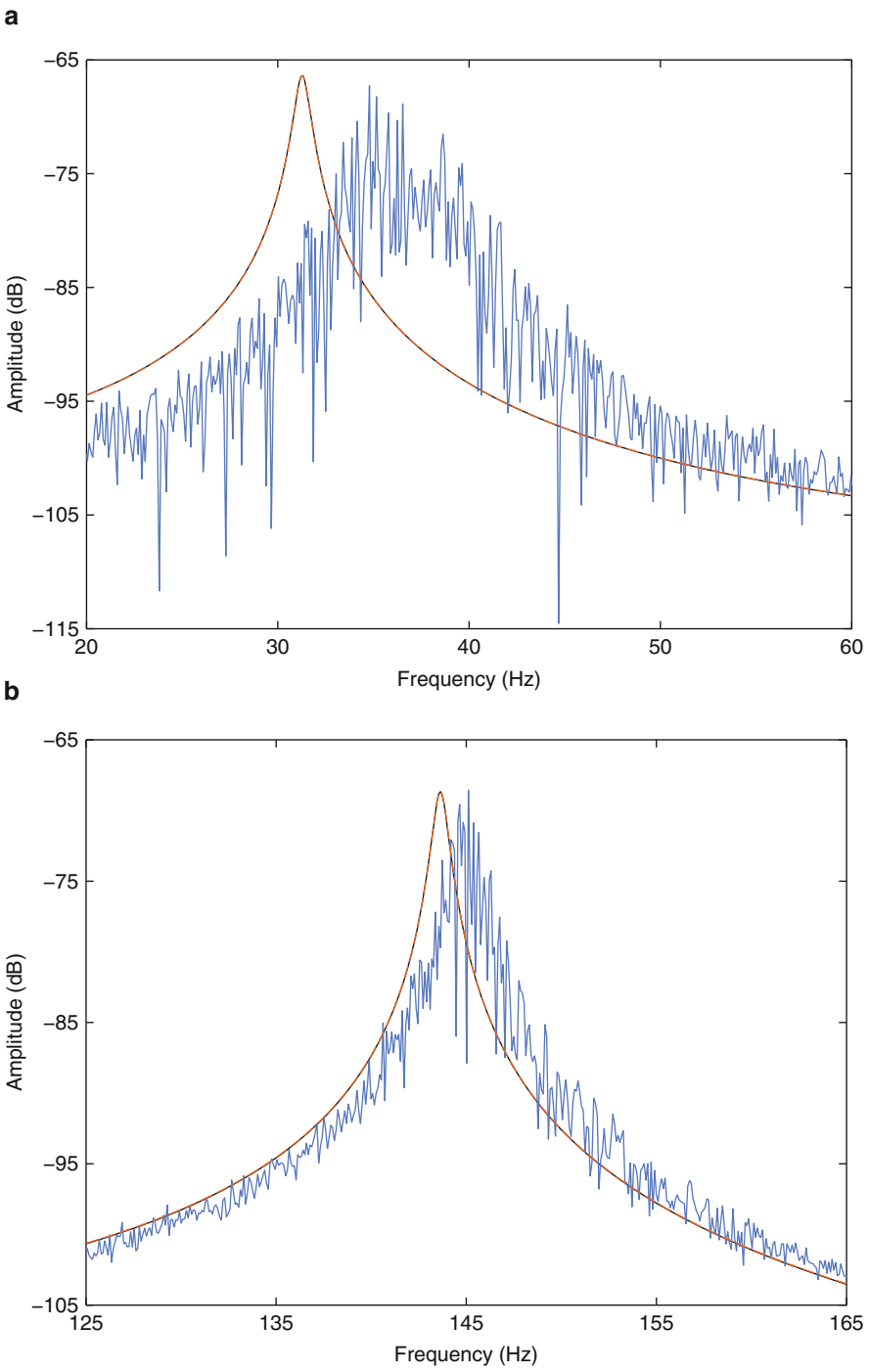

Fig. 21.9 Comparison between the exact linear FRF at the main beam tip (in *black*) and the corresponding curve synthesized using the FNSI method at high level (in *orange*), i.e. at 15 N RMS. The FRF calculated using a linear estimator at high level is also superposed (in *blue*). (**a**) First mode; (**b**) second mode (Color figure online)

21.4.1.5 Removal of Damping Terms

Damping terms are finally removed from the identified nonlinear state-space model $(\mathbf{A}, \mathbf{B}, \mathbf{C}, \mathbf{D})$ following the constructive procedure of Sect. 21.3.1.4. The resulting undamped model equations form the basis of the subsequent computation of NNMs using numerical techniques.

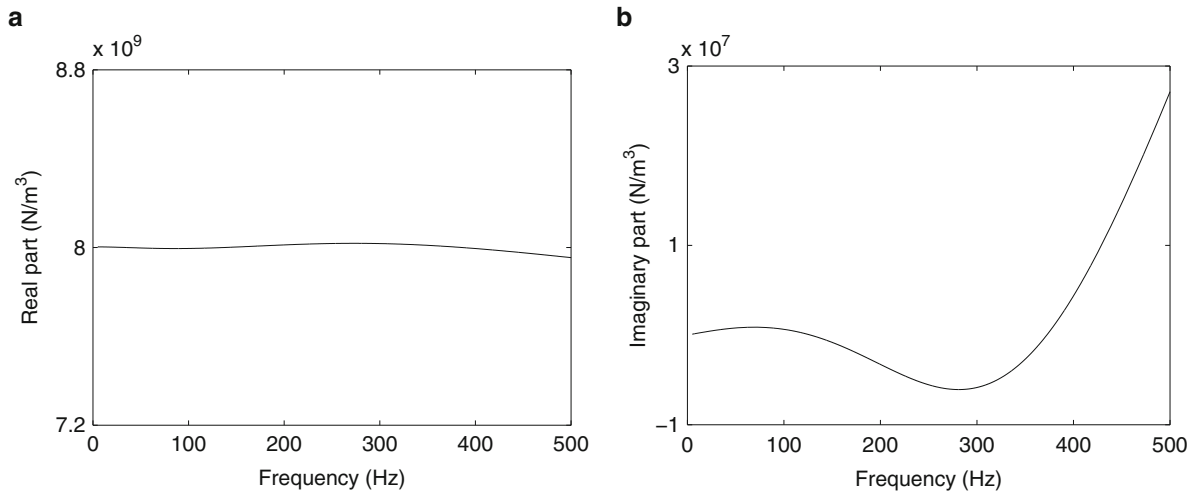

Fig. 21.10 Complex and frequency-dependent estimate of the nonlinear coefficient c_1. (**a**) Real part; (**b**) imaginary part

Table 21.5 Estimate of the nonlinear coefficient c_1

Exact value (GN/m^3)	Real part (GN/m^3)	Error (%)	Log_{10} (real/imag.)
8	8.0005	0.0062	3.72

Real part averaged over 5–500 Hz, relative error (in %) and ratio between the real and imaginary parts (in logarithmic scaling)

21.4.2 Computation of the First Two NNMS Using Continuation

In this section, the algorithm of Sect. 21.3.2 is applied to the undamped model equations identified in Sect. 21.4.1 to compute the first two NNMs of the beam structure. Note that the third mode is not analyzed herein as it involves virtually no nonlinear distortions. Figure 21.11 shows the evolution of the frequency of the first bending mode of the structure as a function of the amplitude of the motion evaluated at the main beam tip. The use of a displacement amplitude as horizontal axis in this plot is justified by the absence of direct access to the total conserved energy associated with the considered mode in experimental conditions [32]. The identified frequency-amplitude curve depicted in orange in Fig. 21.11 is seen to closely match with the exact NNM presented in black, proving the accuracy of the proposed identification methodology. This is confirmed through the comparison between the exact and identified modal shapes inserted in Fig. 21.11 at four specific amplitude levels, namely 0.2, 0.4, 0.6 and 0.8 mm. Similar conclusions are drawn from the quality of the identification of the second mode of the nonlinear beam plotted in Fig. 21.13.

It should be underlined that the results in Fig. 21.11 demonstrate the validity of the NNM identification methodology for strongly nonlinear regimes of motion. Specifically, a hardening of almost 8 Hz of the natural frequency is found to be accurately captured in this plot. This substantial frequency shift corresponds to an amplitude of motion of 1 mm at the main beam tip, which is twice the thickness of the thin beam. The importance of nonlinearity in the beam dynamics is well evidenced in Fig. 21.12a, b, where the first NNM of the structure is represented in the configuration space for amplitudes of 0.2 and 0.8 mm, respectively. The configuration space is spanned in this figure by the displacements measured at nodes 4 and 14, i.e. at the driving point and the main beam tip, respectively. One observes that, at low amplitude level in Fig. 21.12a, the NNM is a straight line, whereas it corresponds to a curved line for high amplitudes in Fig. 21.12b, revealing the appearance of harmonics in the time series. A similar analysis is achieved in Fig. 21.14a, b for the second NNM of the beam. These two graphs show that, owing to the displacement nature of the involved nonlinearity, higher-frequency modes are less impacted by harmonic distortions, and translate into straight lines in configuration space even for large amplitudes of motion.

One finally points out that the amplitude axes in Figs. 21.11 and 21.13 were arbitrarily limited to 1 mm. This choice relates to the validity range of the amplitude-dependent periodic solutions calculated based on an experimental model derived using broadband data. In this study, the amplitude interval over which the continuation was performed was merely selected by observing that the maximum amplitude of displacement recorded in Sect. 21.4.1 at the main beam tip under multisine forcing was of the order of 1 mm. Moreover, the frequency shifts noticed in Fig. 21.9a, b through the blue curves are seen to be consistent with the extent of the frequency axes in Figs. 21.11 and 21.13. However, a rigorous evaluation of the validity ranges of identified frequency-amplitude plots remains an open question and should deserve more investigation.

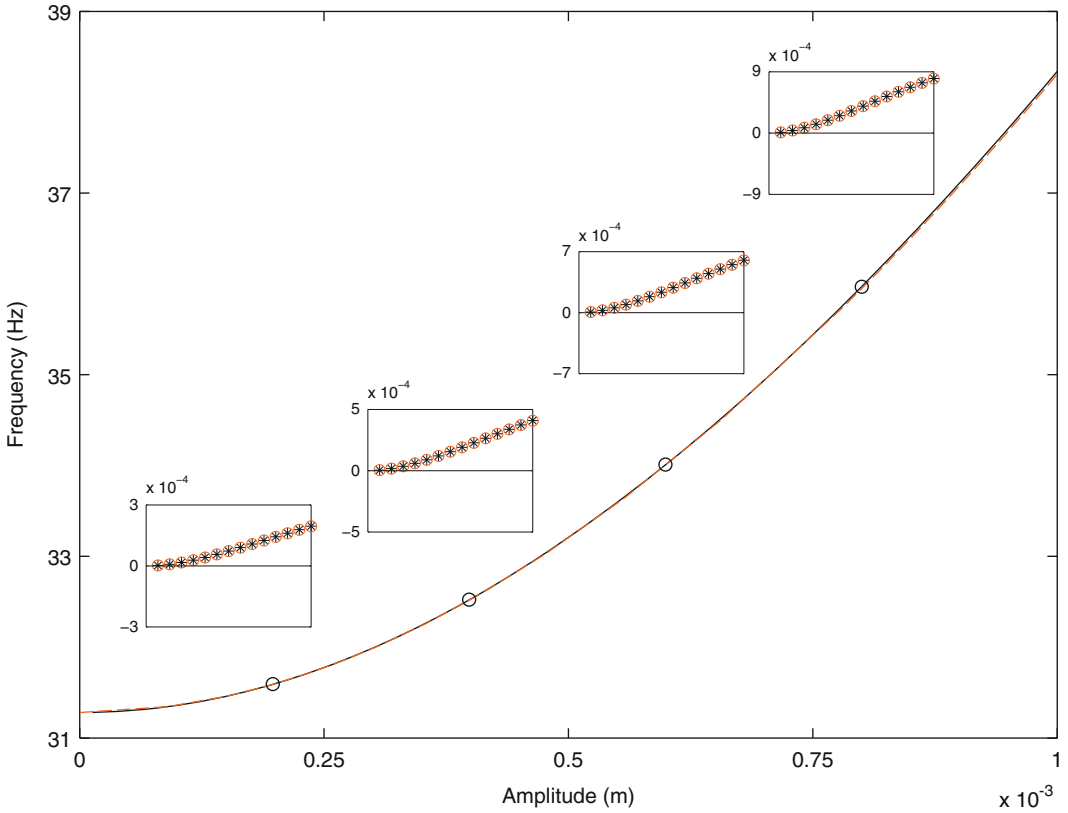

Fig. 21.11 Comparison between the theoretical (in *black*) and identified (in *orange*) frequency-amplitude evolution of the first NNM of the nonlinear beam. The NNM shapes (displacement amplitudes of the main beam) at four amplitude levels, namely 0.2, 0.4, 0.6 and 0.8 mm, are *inset* (Color figure online)

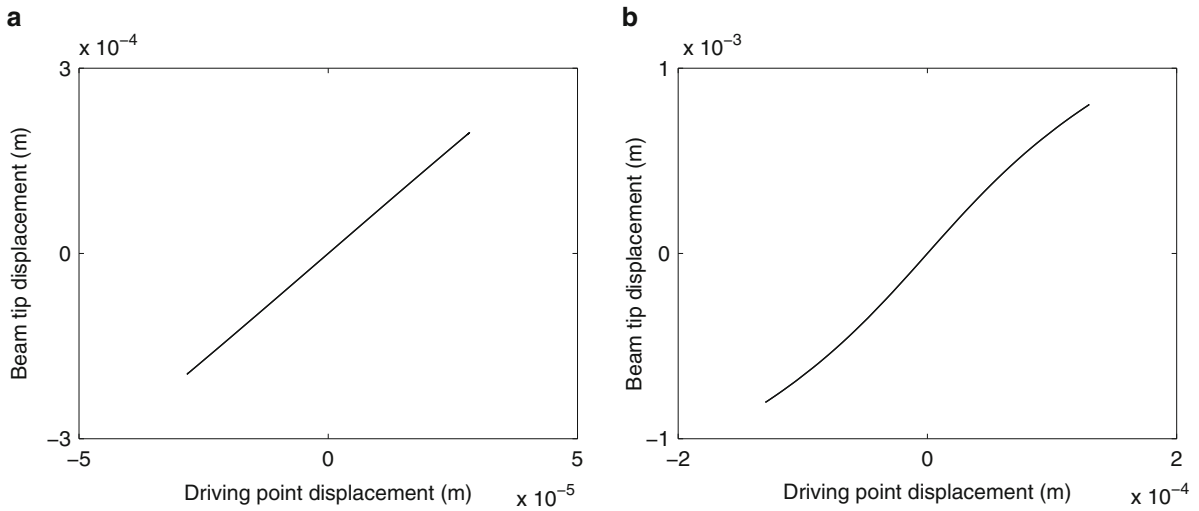

Fig. 21.12 First NNM of the nonlinear beam represented in configuration space at two amplitude levels. The configuration space is constructed using the displacements measured at the driving point and the main beam tip. (**a**) 0.2 mm ; (**b**) 0.8 mm

21.5 Comparison with NNMs Identified Using Nonlinear Phase Resonance

This final section is dedicated to a comparison between the identification methodology proposed in this work, which can be seen as a generalization of the classical linear phase separation testing techniques, and the nonlinear phase resonance approach of [31]. As explained in Sect. 21.2 and depicted in Fig. 21.2, the first step of the nonlinear phase resonance testing

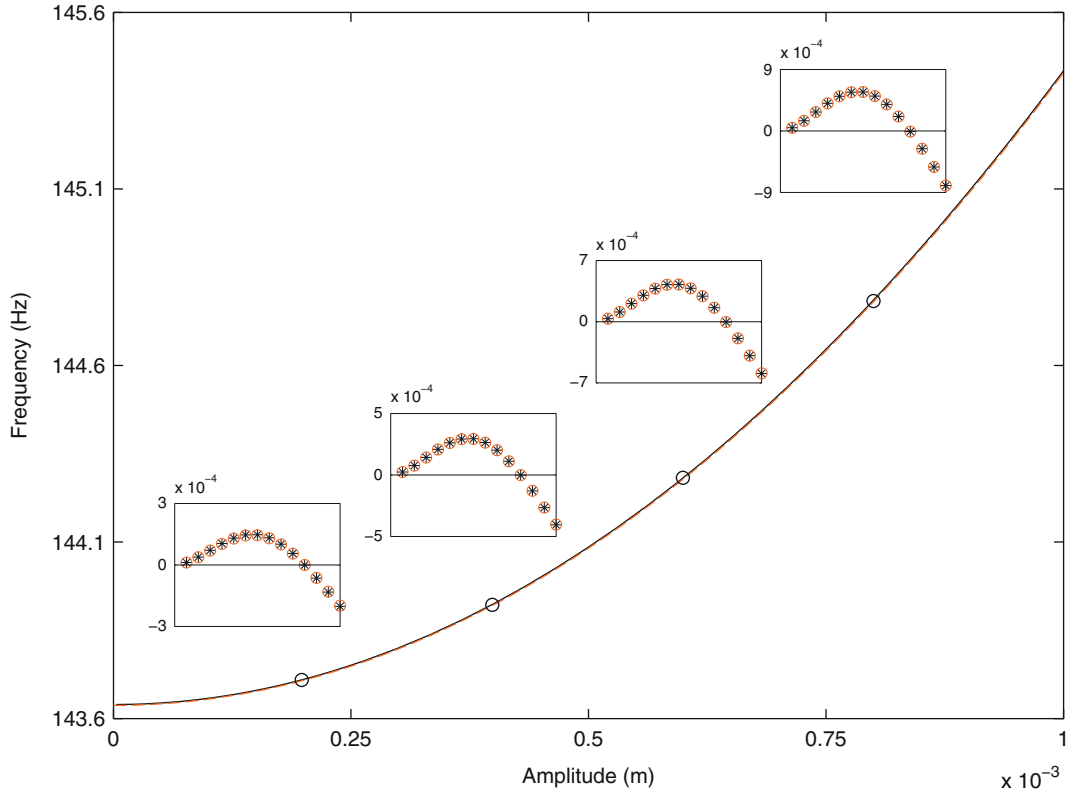

Fig. 21.13 Comparison between the theoretical (in *black*) and identified (in *orange*) frequency-amplitude evolution of the second NNM of the nonlinear beam. The NNM shapes (displacement amplitudes of the main beam) at four amplitude levels, namely 0.2, 0.4, 0.6 and 0.8 mm, are *inset* (Color figure online)

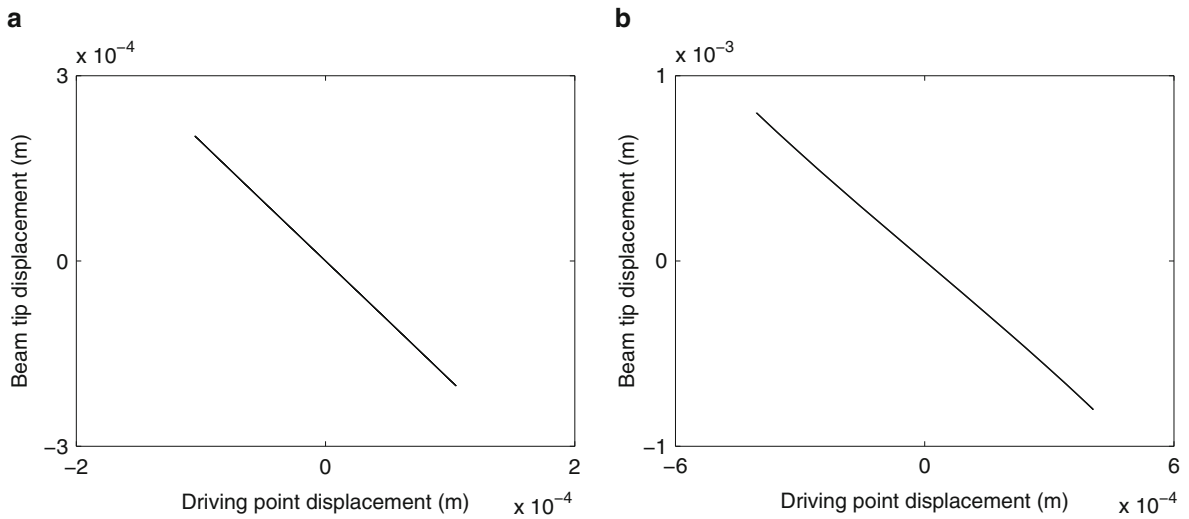

Fig. 21.14 Second NNM of the nonlinear beam represented in configuration space at two amplitude levels. The configuration space is constructed using the displacements measured at the driving point and the main beam tip. (**a**) 0.2 mm; (**b**) 0.8 mm

procedure is the appropriation of the NNM of interest. This is realized by tuning the frequency of a stepped-sine excitation so as to induce of a single-NNM motion of the system. This step is facilitated by a generalized phase lag quadrature criterion, which can be translated into a force appropriation indicator equal to 1 at resonance [32]. NNM appropriation is illustrated in Fig. 21.15a, b in the case of the first mode of the nonlinear beam. The excitation is a 4 N sine signal applied to node 4 of the structure. Figure 21.15a plots the evolution of the appropriation indicator with respect to the forcing frequency. It reaches a

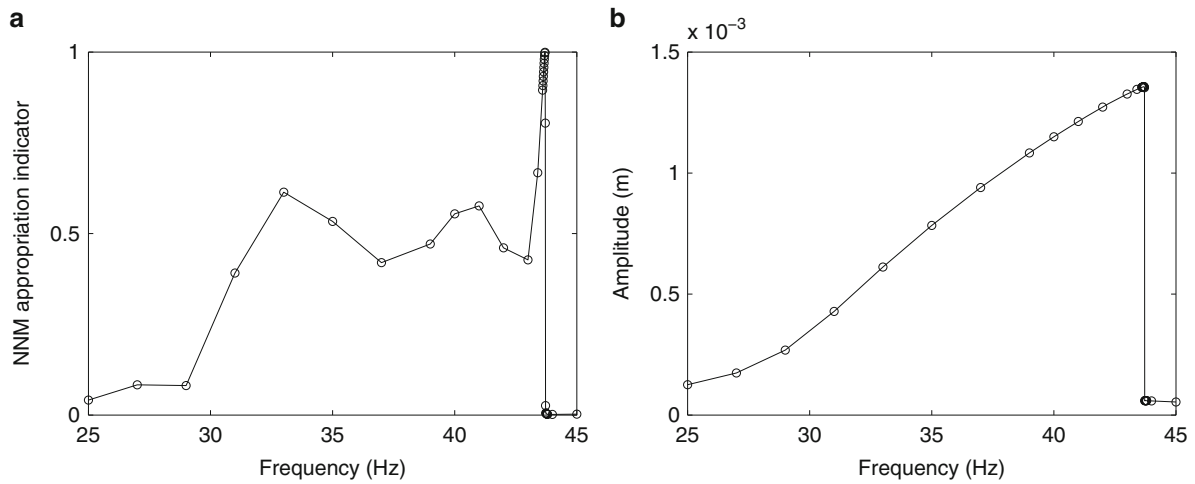

Fig. 21.15 Appropriation of the first NNM of the beam structure in the nonlinear phase resonance method. (**a**) NNM appropriation indicator; (**b**) amplitude of the response at the main beam tip

value equal to 1 for a frequency close to 43.7 Hz. The corresponding amplitude of the forced response measured at the main beam tip is depicted in Fig. 21.15b. This graph shows the distorted frequency response of the first mode and the sudden jump occurring as soon as resonance is passed.

When the considered NNM is appropriated, the second step of the nonlinear phase resonance procedure is to turn off the excitation in order to observe the free decay of the system along the NNM branch. A time-frequency analysis of the decaying time response is then carried out to extract the frequency-energy dependence of the mode. This is achieved in Fig. 21.16 where the wavelet transform of the displacement measured at beam tip during the free decay is represented. The ridge of the wavelet, i.e. the locus of maximum amplitude with respect to frequency, is presented as a black line, and is seen to closely coincide with the NNM identified in the previous section and plotted in orange. The comparable accuracy of the phase separation and phase resonance approaches is confirmed by the modal shapes superposed at four amplitude levels in Fig. 21.16. The results in this figure, together with the analysis of the second NNM appropriation reported in Figs. 21.17 and 21.18, clearly confirm the claimed accuracy of the NNM identification methodology developed in the present paper. In summary, Table 21.6 lists the strengths and limitations of the two methodologies.

21.6 Conclusion

The present paper introduced a methodology capable of extracting experimentally the nonlinear normal modes (NNMs) of vibrating systems from measurements collected under broadband forcing. This is the first methodology suffering from no restriction regarding the strength of the nonlinearities and the modal coupling. It relies on the joint utilization of nonlinear system identification and numerical continuation of periodic solutions. The methodology can be viewed as the ideal complement to a previously-developed approach for the identification of NNMs from sine data. Together, they provide rigorous generalizations of the testing procedures routinely exploited for experimental modal analysis of linear engineering structures.

Further work will focus on the experimental demonstration of the methodology proposed herein. In this context, the use of splines will be investigated in order to bypass the a priori assumption of a mathematical model for the nonlinearities. Another research direction is the extension of the methodology to systems with damping nonlinearities through the direct computation of damped NNMs based on the experimentally-derived state-space model.

Acknowledgements The author J.P. Noël is a Postdoctoral Researcher of the *Fonds de la Recherche Scientifique – FNRS* which is gratefully acknowledged. The author L. Renson is a Marie-Curie COFUND Postdoctoral Fellow of the University of Liège, co-funded by the European Union. The authors C. Grappasonni and G. Kerschen would like to acknowledge the financial support of the European Union (ERC Starting Grant NoVib 307265).

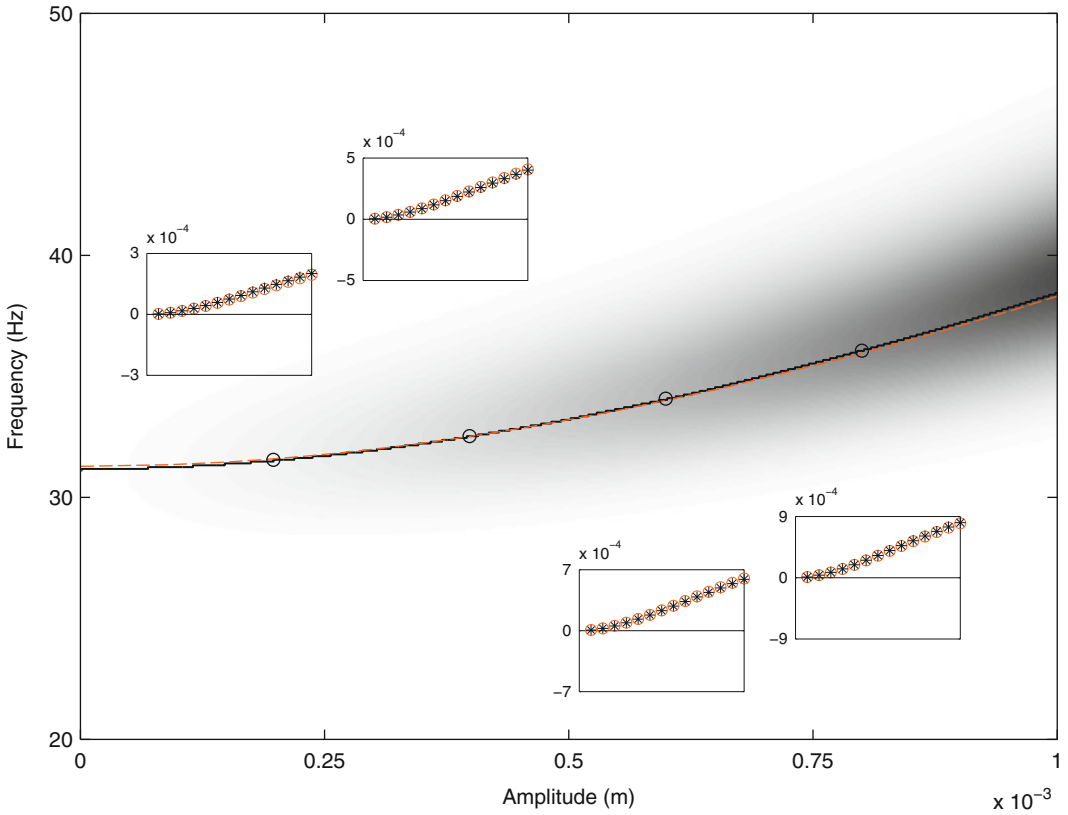

Fig. 21.16 Decay along the first NNM branch calculated using time-frequency analysis (in *black*) and corresponding NNM obtained in Sect. 21.4.2 using the proposed identification methodology (in *orange*). The NNM shapes (displacement amplitudes of the main beam) at four amplitude levels, namely 0.2, 0.4, 0.6 and 0.8 mm, are *inset* (Color figure online)

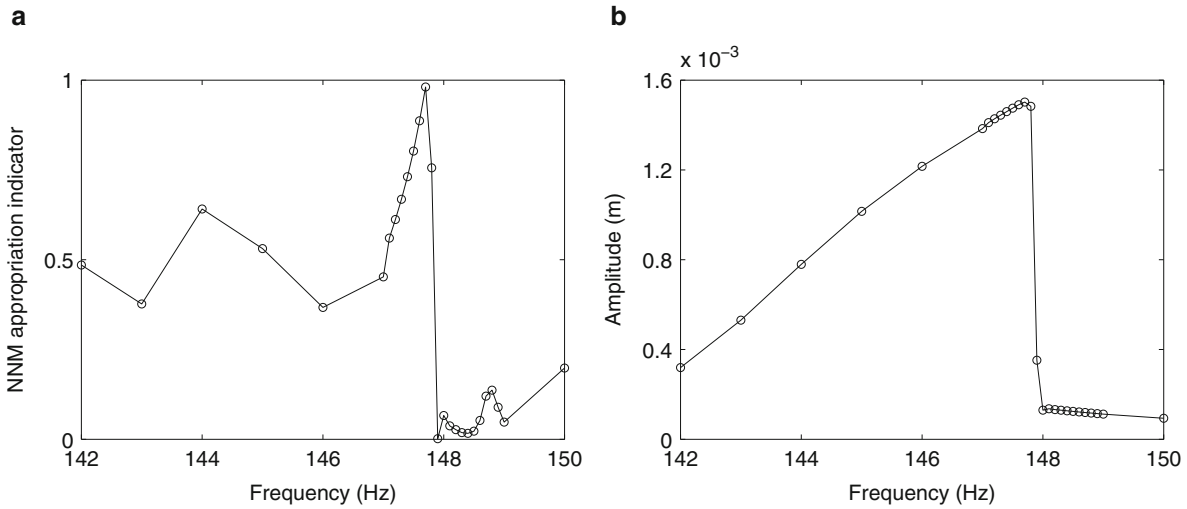

Fig. 21.17 Appropriation of the second NNM of the beam structure in the nonlinear phase resonance method. (**a**) NNM appropriation indicator; (**b**) amplitude of the response at the main beam tip

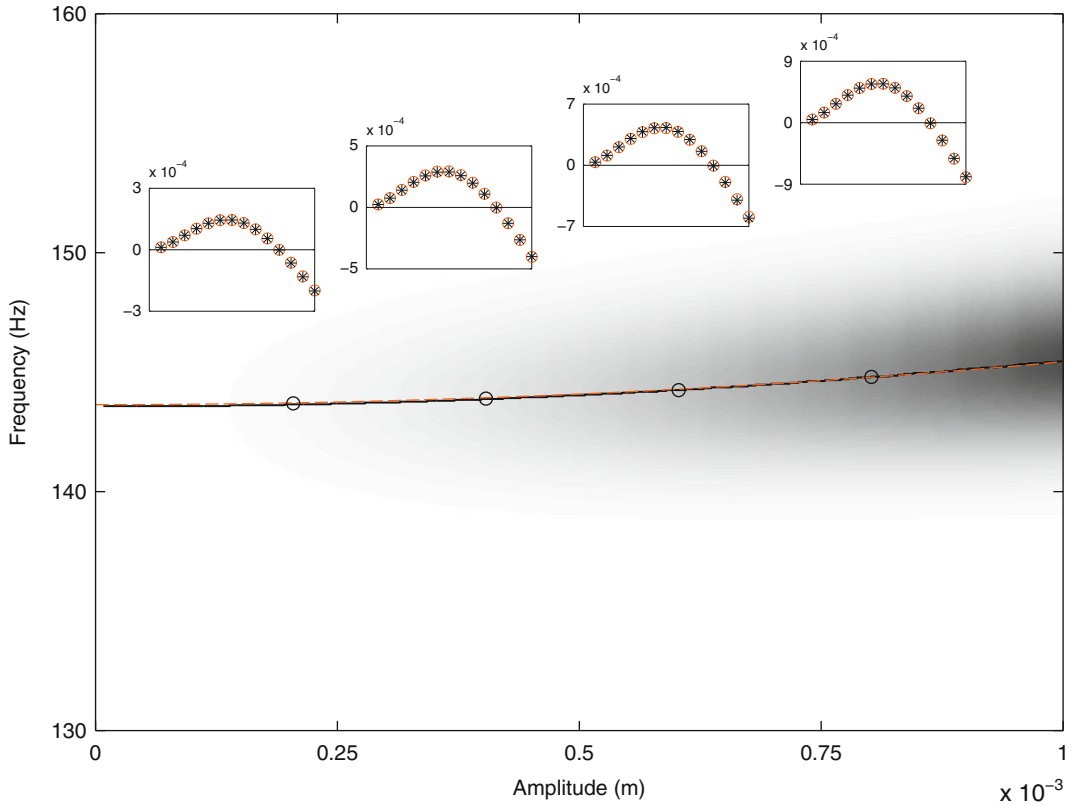

Fig. 21.18 Decay along the second NNM branch calculated using time-frequency analysis (in *black*) and corresponding NNM obtained in Sect. 21.4.2 using the proposed identification methodology (in *orange*). The NNM shapes (displacement amplitudes of the main beam) at four amplitude levels, namely 0.2, 0.4, 0.6 and 0.8 mm, are *inset* (Color figure online)

Table 21.6 Comparison of the strengths and limitations of the two methodologies

Nonlinear phase separation method	Nonlinear phase resonance method
Fast (multiple NNMs simultaneously)	Time-consuming (one NNM at a time, and difficulty to reach resonance)
Need of an experimental model	Model-free
Classical random excitation can be utilized	Multi-harmonic forcing is needed
Nonlinear components must be instrumented on both sides	Multiple shakers are needed and must be turned off
Nonlinearity characterization is required	Limited information needed about the nonlinearities
Damping in the experimental model must be removed	Undamped NNMs are directly obtained

References

1. Ewins D (2006) A future for experimental structural dynamics. In: Proceedings of the international conference on noise and vibration engineering (ISMA), Leuven, Belgium
2. Peeters B, Climent H, de Diego R, de Alba J, Ahlquist J, Carreño J, Hendricx W, Rega A, Garcia G, Deweer J, Debille J (2008) Modern solutions for ground vibration testing of large aircraft. In: Proceedings of the 26th international modal analysis conference (IMAC), Orlando, FL
3. Göge D, Böswald M, Füllekrug U, Lubrina P (2007) Ground vibration testing of large aircraft: state of the art and future perspectives. In: Proceedings of the 25th international modal analysis conference (IMAC), Orlando, FL
4. Grillenbeck A, Dillinger S (2011) Reliability of experimental modal data determined on large spaceflight structures. In: Proceedings of the 29th international modal analysis conference (IMAC), Jacksonville, FL
5. Wright J, Cooper J, Desforges M (1999) Normal-mode force appropriation - theory and application. Mech Syst Signal Process 13:217–240
6. Peeters B, Van der Auweraer H, Guillaume P, Leuridan, J (2004) The PolyMAX frequency-domain method: a new standard for modal parameter estimation? Shock Vib 11(3–4):395–409
7. Van Overschee P, De Moor B (1996) Subspace identification for linear systems: theory, implementation and applications. Kluwer Academic Publishers, Dordrecht
8. Atkins P, Wright J, Worden K (2000) An extension of force appropriation to the identification of non-linear multi-degree of freedom systems. J Sound Vib 237:23–43
9. Platten M, Wright JR, Dimitriadis G, Cooper J (2009) Identification of multi-degree of freedom non-linear systems using an extended modal space model. Mech Syst Signal Process 23:8–29
10. Poon C, Chang C (2007) Identification of nonlinear elastic structures using empirical mode decomposition and nonlinear normal modes. Smart Struct Syst 3:423–437
11. Vakakis A, Bergman L, McFarland D, Lee Y, Kurt M (2011) Current efforts towards a non-linear system identification methodology of broad applicability. Proc Inst Mech Eng C J Mech Eng Sci 225:2497–2515
12. Eriten M, Kurt M, Luo G, Vakakis A, McFarland D, Bergman L (2013) Nonlinear system identification of frictional effects in a beam with bolted connection. Mech Syst Signal Process 39:245–264
13. Pai P (2011) Time-frequency characterization of nonlinear normal modes and challenges in nonlinearity identification of dynamical systems. Mech Syst Signal Process 25:2358–2374
14. Worden K, Green P (2014) A machine learning approach to nonlinear modal analysis. In: Proceedings of the 32nd international modal analysis conference (IMAC), Orlando, FL
15. Gibert C (2003) Fitting measured frequency response functions using non-linear modes. Mech Syst Signal Process 17:211–218
16. Chong Y, Imregun M (2001) Development and application of a nonlinear modal analysis technique for MDOF systems. J Vib Control 7: 167–179
17. Rosenberg R (1962) The normal modes of nonlinear n-degree-of-freedom systems. J Appl Mech 29:7–14
18. Rosenberg R (1966) On nonlinear vibrations of systems with many degrees of freedom. Adv Appl Mech 9:217–240
19. Shaw S, Pierre C (1993) Normal modes for non-linear vibratory systems. J Sound Vib 164(1):85–124
20. Vakakis A, Manevitch L, Mlkhlin Y, Pilipchuk V, Zevin A (1996) Normal modes and localization in nonlinear systems. Wiley, New York
21. Lacarbonara W, Camillacci R (2004) Nonlinear normal modes of structural systems via asymptotic approach. Int J Solids Struct 41:5565–5594
22. Touzé C, Amabili M (2006) Nonlinear normal modes for damped geometrically nonlinear systems: application to reduced-order modelling of harmonically forced structures. J Sound Vib 298:958–981
23. Kerschen G, Peeters M, Golinval J, Vakakis A (2009) Nonlinear normal modes. Part I: a useful framework for the structural dynamicist. Mech Syst Signal Process 23(1):170–194
24. Arquier R, Bellizzi S, Bouc R, Cochelin B (2006) Two methods for the computation of nonlinear modes of vibrating systems at large amplitudes. Comput Struct 84:1565–1576
25. Peeters M, Viguié R, Sérandour G, Kerschen G, Golinval J (2009) Nonlinear normal modes. Part II: toward a practical computation using numerical continuation techniques. Mech Syst Signal Process 23(1):195–216
26. Laxalde D, Thouverez F (2009) Complex non-linear modal analysis of mechanical systems: application to turbomachinery bladings with friction interfaces. J Sound Vib 322:1009–1025
27. Renson L, Deliége G, Kerschen G (2014) An effective finite-element-based method for the computation of nonlinear normal modes of nonconservative systems. Meccanica 49(8):1901–1916
28. Kerschen G, Peeters M, Golinval J, Stephan C (2013) Nonlinear modal analysis of a full-scale aircraft. J Aircr 50:1409–1419
29. Renson L, Noël J, Kerschen G (2014) Complex dynamics of a nonlinear aerospace structure: numerical continuation and normal modes. Nonlinear Dyn 79(2):1293–1309
30. Krack M, Panning-von Scheidt L, Wallaschek J (2014) A method for nonlinear modal analysis and synthesis: application to harmonically forced and self-excited mechanical systems. J Sound Vib 332(25):6798–6814
31. Peeters M, Kerschen G, Golinval J (2011) Dynamic testing of nonlinear vibrating structures using nonlinear normal modes. J Sound Vib 330:486–509
32. Peeters M, Kerschen G, Golinval J (2011) Modal testing of nonlinear vibrating structures based on nonlinear normal modes: experimental demonstration. Mech Syst Signal Process 25:1227–1247
33. Zapico-Valle J, Garcia-Dieguez M, Alonso-Camblor R (2013) Nonlinear modal identification of a steel frame. Eng Struct 56:246–259
34. Ehrhardt D, Harris R, Allen M (2014) Numerical and experimental determination of nonlinear normal modes of a circular perforated plate. In: Proceedings of the 32nd international modal analysis conference (IMAC), Orlando, FL
35. Noël J, Kerschen G (2013) Frequency-domain subspace identification for nonlinear mechanical systems. Mech Syst Signal Process 40:701–717
36. Noël J, Marchesiello S, Kerschen G (2014) Subspace-based identification of a nonlinear spacecraft in the time and frequency domains. Mech Syst Signal Process 43:217–236

37. Noël J, Kerschen G, Foltête E, Cogan S (2014) Grey-box identification of a nonlinear solar array structure using cubic splines. Int J Non-linear Mech 67:106–118
38. Adams D, Allemang R (2000) A frequency domain method for estimating the parameters of a non-linear structural dynamic model through feedback. Mech Syst Signal Process 14:637–656
39. Marchesiello S, Garibaldi L (2008) A time domain approach for identifying nonlinear vibrating structures by subspace methods. Mech Syst Signal Process 22:81–101
40. Géradin M, Rixen D (1997) Mechanical vibrations: theory and applications to structural dynamics. Wiley, Chichester
41. Thouverez F (2003) Presentation of the ECL benchmark. Mech Syst Signal Process 17(1):195–202
42. Kerschen G, Lenaerts V, Golinval J (2003) Identification of a continuous structure with a geometrical non-linearity. Part I: conditioned reverse path method. J Sound Vib 262:889–906
43. Kerschen G, Worden K, Vakakis A, Golinval J (2006) Past, present and future of nonlinear system identification in structural dynamics. Mech Syst Signal Process 20:505–592
44. Platten M, Wright J, Cooper J, Dimitriadis G (2009) Identification of a nonlinear wing structure using an extended modal model. J Aircr 46(5):1614–1626
45. Fan Y, Li C (2002) Non-linear system identification using lumped parameter models with embedded feedforward neural networks. Mech Syst Signal Process 16(2–3):357–372

Chapter 22
Measurement of Nonlinear Normal Modes Using Mono-harmonic Force Appropriation: Experimental Investigation

David A. Ehrhardt, Matthew S. Allen, and Timothy J. Beberniss

Abstract A structure undergoing large amplitude deformations can exhibit nonlinear behavior which is not predicted by traditional linear theories. Structures with some initial curvature offer an additional complication due to buckling and snap through phenomena, and can exhibit softening, hardening and, internal resonance. As a structure transitions into a region of nonlinear response, a structure's nonlinear normal modes (NNMs) can provide insight into the forced responses of the nonlinear system. Mono-harmonic excitations can often be used to experimentally isolate a dynamic response in the neighborhood of a single NNM. This is accomplished with an extension of the modal indicator function and force appropriation to ensure the dynamic response of the structure is on the desired NNM. This work explores these methods using two structures: a nominally-flat beam and a curved axi-symmetric plate. Single-point force appropriation is used by manually tuning the excitation frequency and amplitude until the mode indicator function is satisfied for the fundamental harmonic. The results show a reasonable estimate of the NNM backbone, the occurrence of internal resonance, and couplings between the underlying linear modes along the backbone.

Keywords Nonlinear normal mode • Experimental force appropriation • Continuous scan laser doppler vibrometry (CSLDV) • Digital image correlation (DIC)

22.1 Introduction

Over the past several decades a suite of testing and modeling approaches, under the title of modal analysis, has been developed for linear structures under dynamic loading. The term linear is important here since characterization of a structure using modal analysis is based on quantifying the structure in terms of invariant properties inherent to the structure. With the quantification of these structural properties, (e.g., resonant frequencies, damping ratios, mode shapes, etc.) a complex structure can be described with a small number of known variables in linear response regimes. However, these properties lose their invariance when a structure is in a nonlinear response regime caused by large amplitude loading conditions (thermal, acoustic, mechanical, etc.). Therefore, techniques created for linear structures can not be directly applied to nonlinear behavior since the structural properties become functions of input energy. An understanding of this energy dependent behavior informs the design of critical components and can be exploited to dissipate energy throughout the structure or aid in failure prediction. So new experimental methods are sought to address nonlinear behavior while preserving the simplicity and connection to the linear design and test paradigms.

Linear experimental modal analysis techniques can be classified into two groups: phase separation and phase resonance methods. There are certainly other classifications of modal analysis techniques, but this is done for convenience of the following discussion. The most popular and easiest implemented methods available today for linear structures are phase separation methods, which excite several or all linear normal modes of interest at a single time with the use of broadband or swept-sine excitation. The modes of vibration can be separated in these measurements using the phase information between the input force and measured response allowing the assessment of natural frequencies, mode shapes, and damping ratios. A good reference for this type of testing and analysis can be found [1, 2]. In contrast, phase resonance testing methods [3–5] for linear structures focus on a single mode of vibration using a multi-point mono-harmonic forcing vector, and are less popular in linear experimental modal analysis because they can be time-consuming. With phase resonance, a mode of

D.A. Ehrhardt (✉) • M.S. Allen
Department of Engineering Physics, University of Wisconsin-Madison, Madison, WI 53706, USA
e-mail: dehrhardt@wisc.edu; msallen@engr.wisc.edu

T.J. Beberniss
Structural Sciences Centers, Air Force Research Laboratory, Wright-Patterson AFB, Dayton, OH 45433, USA

G. Kerschen (ed.), *Nonlinear Dynamics, Volume 1*, Conference Proceedings of the Society for Experimental Mechanics Series, DOI 10.1007/978-3-319-15221-9_22

vibration is isolated in a test when the phase relationship between the applied harmonic force and measured displacement response fulfills phase lag quadrature. In other words, all degrees of freedom displace synchronously with a phase lag of 90° from the harmonic input force.

The use of these methods with nonlinear vibrations require an extended definition of a mode of vibration since a nonlinear mode is energy dependent and can involve complex interactions between modes. Rosenberg [6] initially defined a nonlinear normal mode (NNM) as a *synchronous solution* of the nonlinear system, but this definition has been extended to include *not necessarily synchronous solutions* of the conservative nonlinear equations of motion [7, 8]. Oscillations of this nature provide significant insight into the structure's free and forced responses, including complex dynamics such as bifurcations, internal resonances, and a strong dependence on input energy. Additionally, the damped dynamics of the system can often be interpreted based on the topological structure and bifurcations of the NNMs of the underlying un-damped system.

The extension of phase separation techniques to characterize a structure's nonlinear response has seen much attention in the form of system identification as shown in [9, 10] which is by no means a complete list of references. Developed phase separation methods have not been readily applied to industrial practice except for low order systems. Phase resonance methods have been extended to the measurement of NNMs through the implementation of different methods of force appropriation. Atkins et al [11] presented a force appropriation of nonlinear systems (FANS) method using a multi-point multi-harmonic force vector to isolate a linear normal mode (LNM) of interest. This permits the direct nonlinear characteristics of the isolated mode to be calculated without modal coupling terms. Peeters et al [12, 13] showed that a multi-point multi-harmonic sine wave could isolate a single NNM. For application to real world structures, it was then demonstrated that a single-point single harmonic force could be used to isolate a response in the neighborhood of a single NNM with good accuracy [12, 14]. In these investigations, once phase lag quadrature was met, the input force was turned off and the response allowed to decay tracing the backbone of the NNM. Building off of this work, Ehrhardt et al [15] used step sine testing to measure the response around a specific NNM and at several input forcing levels leading to nonlinear frequency response functions (FRFs). From these FRFs, responses in the neighborhood of the NNM can be isolated from measured responses.

This investigation focuses on measuring the first linear normal mode of a flat beam and curved axi-symmetric plate and its nonlinear continuation on the NNM at higher energies. Modal interactions from internal resonances are also detected but not rigorously isolated since the main NNM backbone is the primary focus of this investigation. The next section provides some background information regarding NNMs including important characteristics and expected NNMs from finite element models (FEMs). An examination of force appropriation and its application to experimentally isolate an NNM is also presented. Section 22.3 offers a description of the geometric properties of both structures and Sect. 22.4 then discusses results from the application of force appropriation to the measurement of NNMs for both structures.

22.2 Nonlinear Normal Modes

22.2.1 Numerically Calculated NNMs

For an in-depth description of NNMs, their fundamental properties, and methods of calculation, the reader is referred to [7, 8]. Of interest, NNMs have been shown to capture complicated dynamics such as bifurcations, modal interactions, and large energy dependence of the fundamental frequency of vibration. These characteristics can be presented compactly in a frequency-energy plot (FEP) where the change in fundamental frequency of vibration is presented as a function of input energy. Due to these appealing characteristics, much has been done to expand and apply the NNM concept to finite element models (FEMs) [16, 17].

In previous works, finite element models were created for the structures studied here: the flat clamped-clamped beam in [16] and the curved axi-symmetric plate from the exhaust system of a large diesel engine in [15]. Results from the calculation of the first NNM for both of these models is shown in Figs. 22.1 and 22.2. For reference, a demarcation is added to these plots showing where a maximum displacement of the structure would be equal to one thickness of the structure (e.g. 0.76 mm for the beam and 1.52 mm for the plate).

As seen in the FEP presented in Fig. 22.1a, the flat beam shows a characteristic spring hardening, or an increase in fundamental frequency of vibration with increased input energy as discussed in [18, 19]. The large change in fundamental frequency of vibration is captured on the backbone of the NNM and is observed for relatively small input energies. Two regions of internal resonance appear as branches off of the backbone curve, also observed in Fig. 22.1a. These branches indicate 5:1 (near 88 Hz) and 12:1 (near 120 Hz) internal resonances in the response of the beam. For comparison with experimental measurements, it is helpful to examine the deformation of the beam at points along the FEP which are indicated

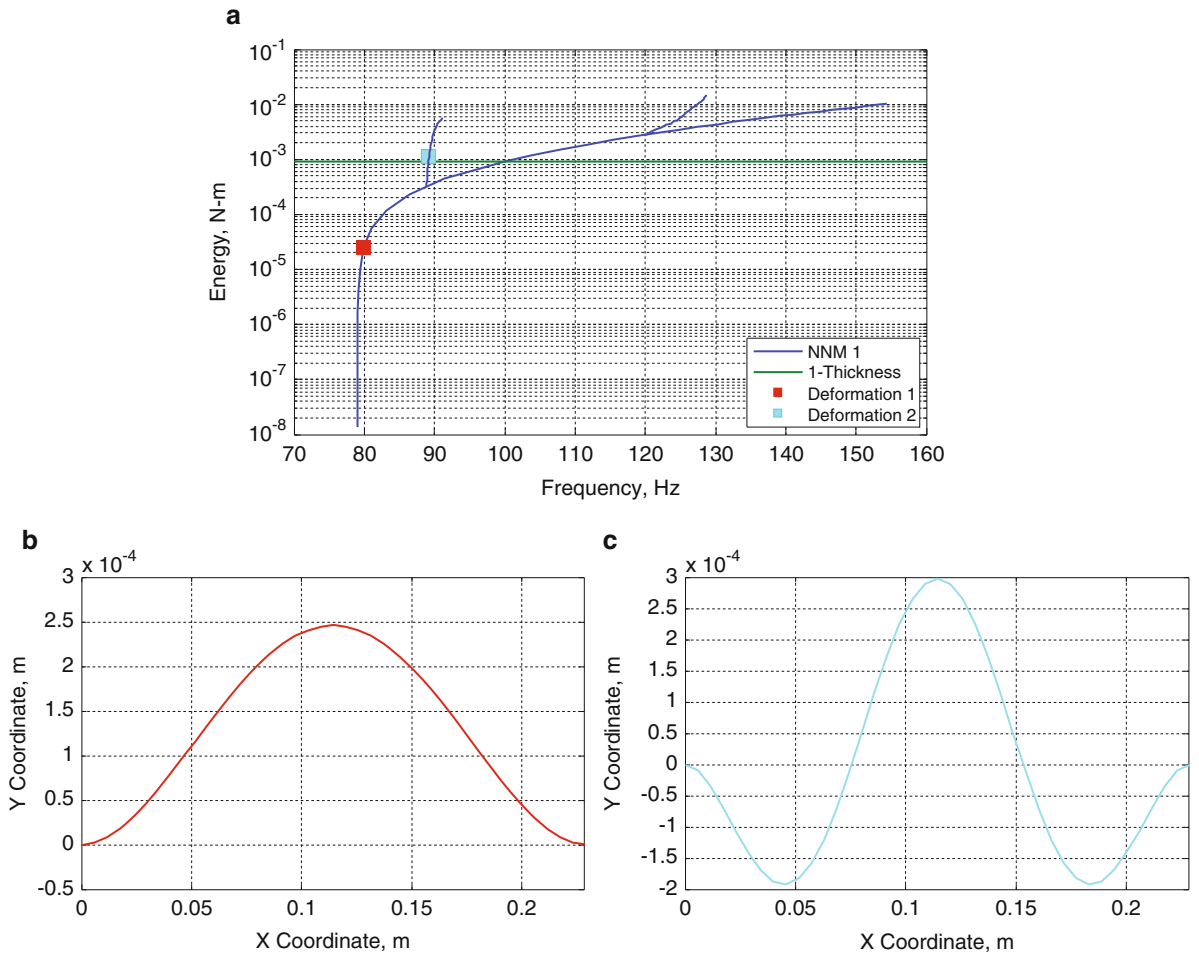

Fig. 22.1 Numerical NNM 1 for flat clamped-clamped beam – (**a**) frequency-energy plot, (**b**) deformation 1 shape, (**c**) deformation 2 shape

in Fig. 22.1a. Deformation 1, shown in Fig. 22.1b, resembles a mode shape for the first natural frequency of a clamped-clamped beam showing little change in linear shape at this low energy. Deformation 2, shown in Fig. 22.1c, resembles a mode shape for the third natural frequency of a clamped-clamped beam showing the effect an internal resonance has on the overall deformation of the beam. The mode 3 shape becomes more pronounced at higher energies on the internal resonance branch, and less pronounced at lower energies on the internal resonance branch. So, while the mode 3 shape is not dominant at lower energies, the interaction between these modes is still visible as will be shown in the experimental results for this NNM.

Figure 22.2a shows the first NNM FEP for the curved axi-symmetric plate. The numerically calculated backbone was determined with a reduce-order model (ROM) where the continuation of the first linear normal mode to higher energies was isolated. While this removes the ability to calculate internal resonances in the plate, this one mode ROM still provides insight into the frequency-energy dependence of NNM 1. As observed here, the NNM undergoes a change in the characteristic nonlinearity as the fundamental frequency of vibration undergoes a decrease prior to increasing. This softening to hardening characteristic can commonly be found in curved structures [20, 21]. Similar to the flat beam, deformations of the plate can also be examined at points along the FEP. Since only mode 1 was used to calculate the NNM, Deformation 1 and 2, shown in Fig. 22.2b, c, are purely mode 1 shapes with different scale factors. The effect of higher modes on an initially flat axi-symmetry plate was examined numerically in. Modes 1 and 6 were both found to be important to describe the response along the NNM backbone providing insight to possible modal interactions.

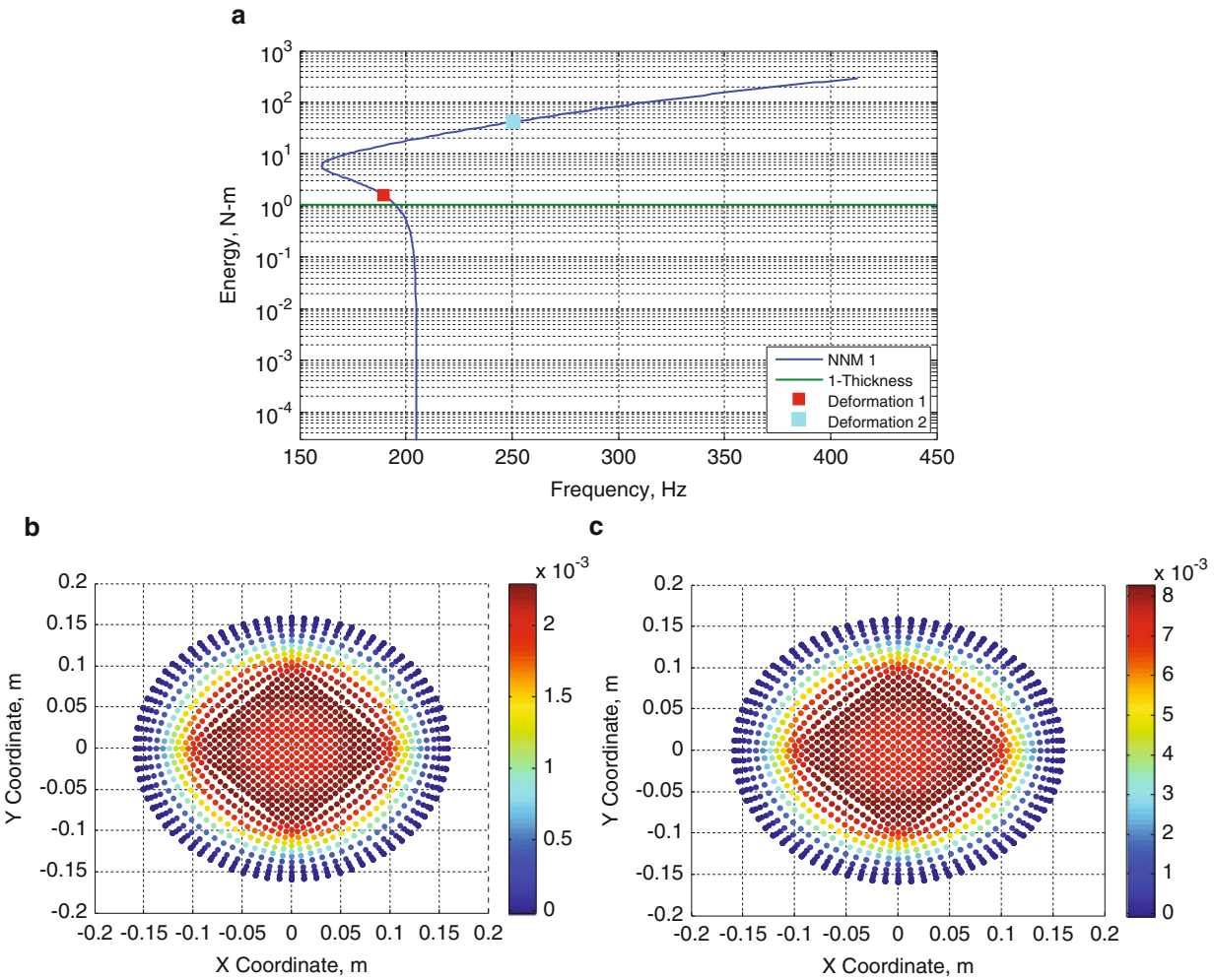

Fig. 22.2 NNM 1 for axi-symmetric plate – (**a**) frequency-energy plot, (**b**) deformation 1 shape, (**c**) deformation 2 shape

22.2.2 Measuring NNMs with Force Appropriation

The implementation of force appropriation to isolate a NNM requires an extension of the phase lag quadrature as discussed in [13] and is repeated here for clarification. The nonlinear forced response of a structure with viscous damping can be represented in matrix form by Eq. 22.1, where [M] is the mass matrix, [C] is the damping matrix, [K] is the stiffness matrix, f_{nl} is the nonlinear restoring force that is a function of $x(t)$, and $p(t)$ is the external excitation. An un-damped NNM is defined as a periodic solution to Eq. 22.2, and is the response of the system in Eq. 22.1 when Eq. 22.3 is satisfied for all response harmonics. Simply stated, the response of a structure is on the NNM when the forcing function exactly cancels the damping forces in the structure. This approach was used on the clamped-clamped beam studied in this work.

For the circular plate, an inertial load (base excitation) was used where the displacement of the structure is proportional to a rigid body mode, $\psi_{RB} a_b(t)$, so the negative of the base acceleration is shown to be equal to [C] , and hence there is a certain phase relationship between the velocity of the structural response and the base acceleration. The phase relationship between input force and velocity response can be determined by writing the displacement and velocity as Fourier cosine and sine series as shown in Eq. 22.4. From the defined relationships, an appropriated force is obtained when the applied base acceleration is 180° out of phase with the response velocity. Methods of force appropriation to experimentally isolate a NNM have been used with success on a beam with localized nonlinearity [12], an aircraft with nonlinear joints [14], and an axi-symmetric plate [15]. A structure is defined to respond on an isolated NNM when all harmonics of the response fulfill the phase lag criterion. Building on this work, and the methodology of NNM calculation presented in [17], force appropriation is experimentally applied using a mono-harmonic excitation to isolate the response of the structures in the neighborhood of the desired NNM. For one NNM, the response of the structure is first isolated in the linear range at low energy. After

measurement, an increase of input energy is made and the input frequency is adjusted until the phase lag criterion is fulfilled again. Subsequent increase of input energy and changes of frequency are then made until the range of response for the desired NNM is measured.

$$\mathbf{M}\ddot{\mathbf{x}}(t) + \mathbf{C}\dot{\mathbf{x}}(t) + \mathbf{K}\mathbf{x}(t) + \mathbf{f}_{nl}\left(\mathbf{x}(t)\right) = \mathbf{p}(t) \tag{22.1}$$

$$\mathbf{M}\ddot{\mathbf{x}}(t) + \mathbf{K}\mathbf{x}(t) + \mathbf{f}_{nl}\left(\mathbf{x}(t)\right) = 0 \tag{22.2}$$

$$\mathbf{C}\dot{\mathbf{x}}(t) = \mathbf{p}(t) = -\mathbf{M}\boldsymbol{\psi}_{RB} a_b(t) \tag{22.3}$$

$$\begin{aligned} a_b(t) &= \sum_{k=1}^{\infty} \{a_k\} \sin(k\omega t) \\ \mathbf{x}(t) &= \sum_{k=1}^{\infty} \{\mathbf{X}_k\} \cos(k\omega t) \\ \dot{\mathbf{x}}(t) &= -\sum_{k=1}^{\infty} \{\mathbf{X}_k\} k\omega \sin(k\omega t) \end{aligned} \tag{22.4}$$

22.3 Structure Description

22.3.1 Beam Description

The first device undertest for this investigation is a precision-machined feeler gauge made from high-carbon, spring-steel in a clamped-clamped configuration previously studied in [22]. The beam had an effective length of 228 mm, a nominal width of 12 mm, and a thickness of 0.76 mm. All presented dimensions are nominal and subject to variation from clamping and stress variations from machining process to obtain the desired thickness. Prior to clamping, the beam was prepared for three dimensional digital image correlation (3D-DIC) and continuous-scan laser Doppler vibrometry (CSLDV) as discussed in [23] and shown in Fig. 22.3. Locations of the initial laser Doppler vibrometry (LDV) measurements are also shown at the center of the beam and 12 mm to the left of the first measurement. The clamping force was provided by the two 6.35-28 UNF-2B bolts located on the inside of the clamping fixture, which is the same fixture used in [22]. After clamping the beam to the fixture, a single-input single-output modal hammer test was performed on the beam so natural frequencies and damping ratios could be identified. Results for the first seven modes are shown in Table 22.1.

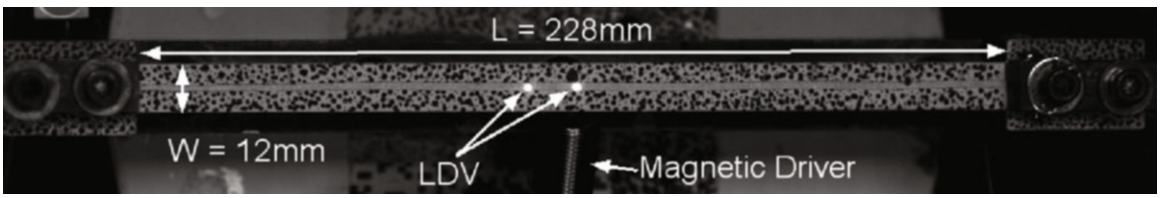

Fig. 22.3 Beam specimen

Table 22.1 Linear (low amplitude) natural frequencies of flat clamped-clamped beam

	Mode 1	Mode 2	Mode 3	Mode 4	Mode 5	Mode 6	Mode 7
f, Hz	63.8	193.4	392.7	659.8	855.9	994.1	1396.5
$\zeta 1$, %	0.91	0.25	0.21	0.17	0.12	0.14	0.13

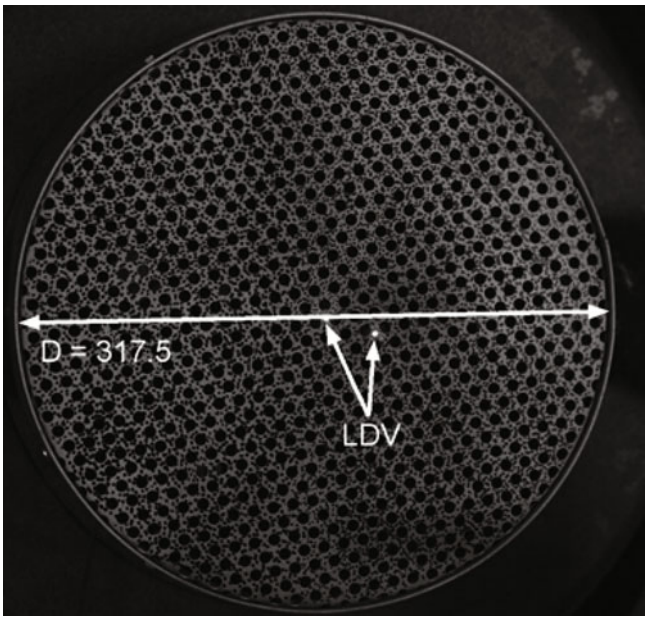

Fig. 22.4 Final mounted perforated plate

Table 22.2 Linear (low amplitude) natural frequencies of curved axi-symmetric plate

	Mode 1	Mode 2	Mode 3	Mode 4	Mode 5	Mode 6	Mode 7	Mode 8	Mode 9
f, Hz	202.2	324	342.8	489.7	509.9	554.1	697.2	777.9	794.2
$\zeta 1$, %	0.2	0.13	0.31	0.092	0.15	0.087	0.11	0.49	0.43

22.3.2 Plate Description

The second article under investigation is a circular perforated plate with rolled ends which is shown in Fig. 22.4 and previously studied in [15]. A mechanical punch was used to create the circular perforations in a flat 16 gauge (1.52 mm thick) 409 stainless steel plate in an array of equilateral triangles with 10.16 mm long edges. Once this process was completed, the plate was formed around a 317.5 mm diameter mold with the excess trimmed so a lip of 12 mm remained. The plate was then welded to a 89 mm high cylinder made from a 14 gauge (1.9 mm thick) 409 stainless steel plate that was cold rolled to the 317.5 mm diameter as shown in Fig. 22.1b. The welded plate assembly was then bolted to a 317.5 mm diameter by 19 mm thick aluminum fixture with twelve 6.4 mm evenly spaced holes. Figure 22.4 also shows the location of the single point laser Doppler vibrometers (LDV). After mounting, a single-input single-output modal hammer test was performed on the plate so natural frequencies and damping ratios could be identified. Results for the first nine modes are shown in Table 22.2. CSLDV was not used in this measurement due to the discontinuities from the perforations. It is important to note that all stated dimensions are nominal and subject to variation. Additionally, the processes the plate is subjected to can induce residual stresses in the structure which also might modify the dynamics of the plate in its final configuration. While this system is relatively simple compared to the engine to which it is designed to be attached, work will show how important it is to have a test to validate any computational models that are created; there are a variety of subtle details that might easily be neglected initially, and yet they could change the response considerably.

22.3.3 Experimental Setup

The final mounted beam and plate are shown in Fig. 22.5. For this experimental setup, there are three systems: (1) exciter/controller, (2) full-field measurement systems, and (3) system for force appropriation:

1. Excitation was provided by two separate mechanisms, both controlled in an open-loop using a Wavetek Variable Phase Synthesizer. The beam was excited by a magnetic driver with a Piezo Amplifier. The input force exerted by the magnetic driver was measured using a force transducer mounted to a solid base between the magnetic driver and input location. Due to the weight and size of the curved axi-symmetric plate, the magnetic driver did not produce sufficient force, so

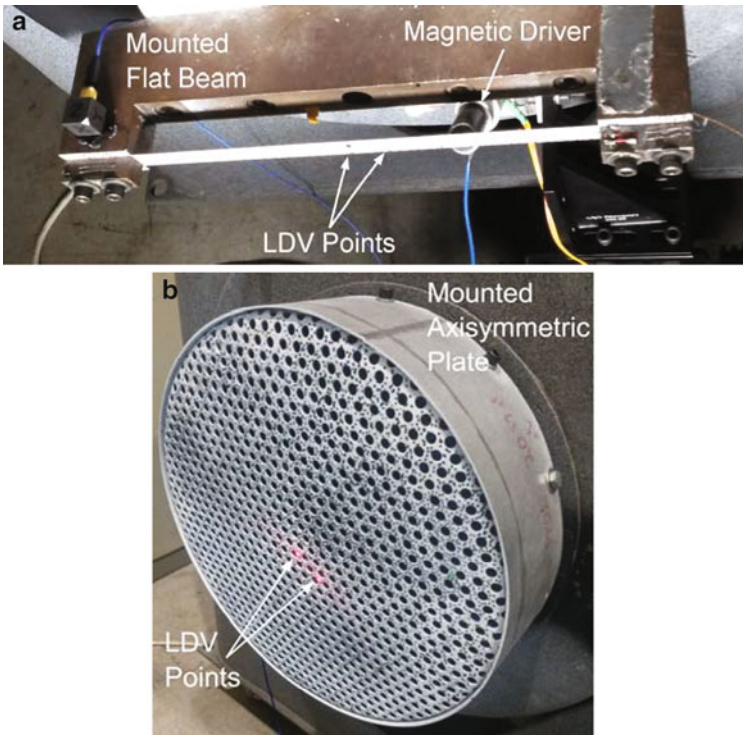

Fig. 22.5 Experimental setup. (**a**) Close up of clamped beam, (**b**) close up of axi-symmetric plate

excitation was provided by shaking a base on which the plate was mounted with a 5,000 N MB dynamics shaker and power amplifier. Excitation for this setup is provided through the mounting base at a set excitation acceleration. This type of excitation limits the ability to examine asymmetric modes and keep the plate response in a linear regime.

2. Full-field measurements were taken of the structures using a combination of Continuous-scan laser Doppler vibrometry (CSLDV) and high speed three dimensional digital image correlation (3D-DIC). Details for both of these measurement techniques can be found [23]. Due to the discontinuities of the perforations, CSLDV was only used on the flat clamped-clamped beam.
3. A second laser Doppler vibrometer (LDV) is used to measure the response of the plate as it is subjected to a single frequency sinusoid at a specified excitation amplitude. The voltage input to the exciter was measured as well as the input force for the magnetic driver and the base acceleration for the shaker. The velocity response and input voltage signals were analyzed in real time using a Onosoki FFT Analyzer to track the phase between the signals. Here, the input voltage was used instead of the measured force/acceleration to limit noise contamination from the measurement sensors. The measured force/acceleration signals were compared after measurement to ensure the correct phase relationship between input and response was maintained. Natural frequencies could then be determined by adjusting the frequency until the input voltage and response velocity are 180° out of phase since the appropriation is between a force and velocity. In a post processing step, the phase relationship for the fundamental harmonic was examined more precisely and the phase relationships for the higher harmonics were computed as well. In the future it would be ideal to be able to monitor all of the phase relationships in real time.

22.4 Results

22.4.1 Clamped-Clamped Beam

Using the described methodology and equipment, mono-harmonic force appropriation was used to measure the first NNM of the flat clamped-clamped beam and a curved axi-symmetric plate. The structural response was measured at each appropriated force amplitude once steady-state was achieved. Figure 22.6 shows the resulting FEP for the flat clamped-clamped beam with the energy of the system represented by the maximum velocity of the beam measured 12 mm left of center and plotted against the fundamental frequency of vibration. Similar to the numerically calculated FEP, a large spring hardening characteristic

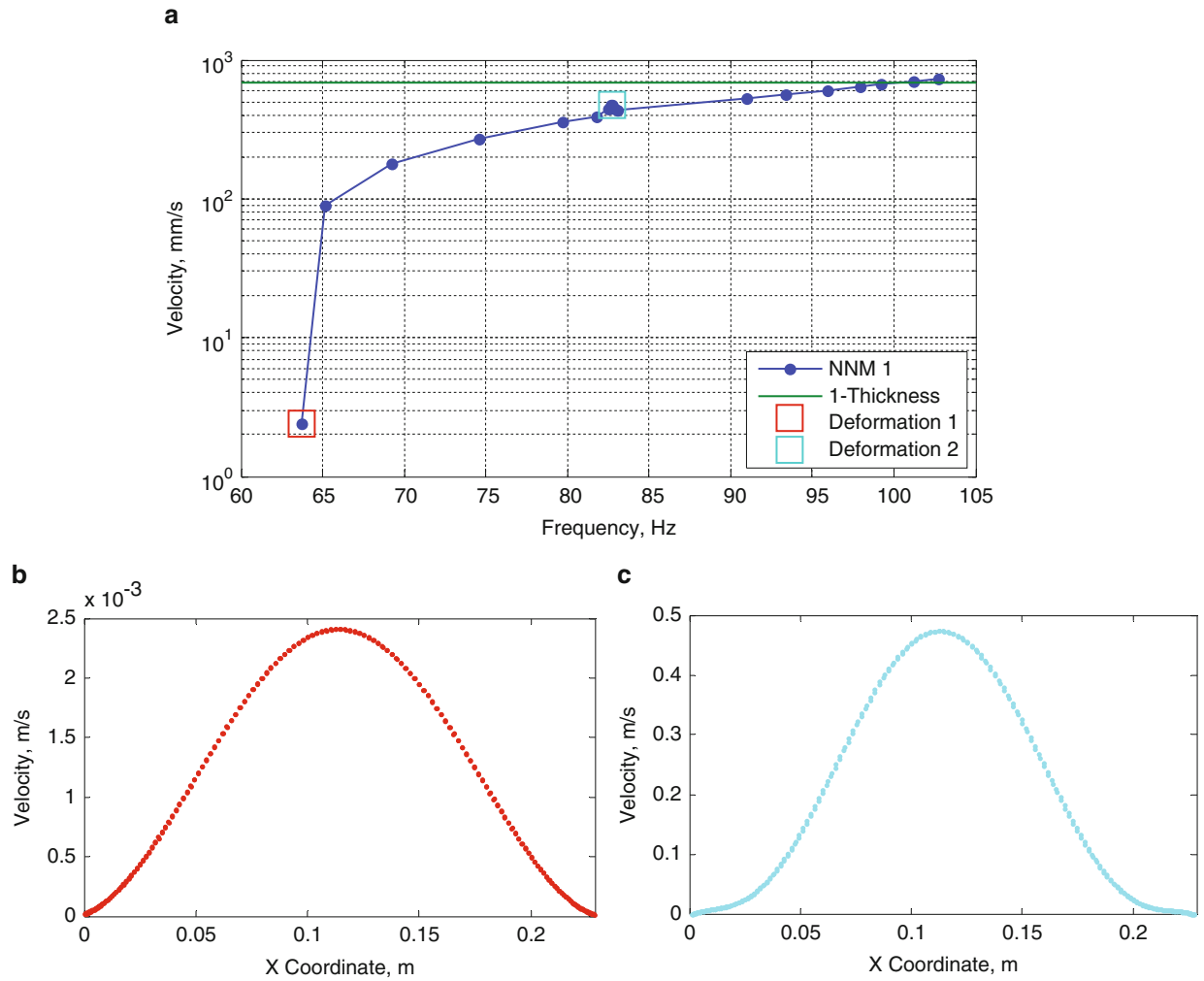

Fig. 22.6 Experimental NNM 1 for flat clamped-clamped beam – (**a**) frequency-velocity plot, (**b**) deformation 1 shape, (**c**) deformation 2 shape

is observed as the beam response approaches a beam thickness. The experimental results show a 36 Hz change (or a 50 % shift in frequency) when the response amplitude approaches the beam thickness. For comparison, the numerical results show a 22 Hz change. However, no effort was made to tune the boundary conditions in the numerical model to match those in the experiment, so some disagreement is to be expected. Though measured and predicted backbones vary significantly, it is interesting that both show a 5:1 modal interaction, which is visible in the measured FEP as a collection of points near 82 Hz. Figures 22.6b and c show the deformation shapes at the selected points on the experimental FEP in Fig. 22.6a, found using CSLDV. The deformation at the point marked Deformation 1 in Fig. 22.4b shows that, at low energy, the response resembles the first linear mode. At the point marked Deformation 2, which is near the bottom of the internal resonance branch, there is a visible change in shape near the root. If measurements were taken further up this modal interaction one would presumably see mode 3 begin to dominate the overall deformation shape of the beam as was predicted by the analytical model, but this was not pursued further here.

The conclusion that the jump in the data near 82 Hz is a modal interaction can be verified by an examination of the spectral content. The amplitude of the fast-Fourier transform (FFT) coefficients of the first seven harmonics is shown in Fig. 22.7a. The evolution of the amplitudes of the higher harmonics show where the 5:1 modal interaction occurs at a 30 % change of frequency in the measured NNM. The presence of the modal interaction is predominant in the 3rd, 5th, and 7th harmonics of the response. In these harmonics, larger amplitudes are observed when the response is in the region of the modal interaction, and the amplitude decreases once the response has passed the modal interaction where the 5th and 3rd harmonic show more dominance. Since single-point mono-harmonic force appropriation is used, an examination of the phase of the harmonics of the response with the input force is important to determine the quality of appropriation. Figure 22.5b shows how the phase of the first seven harmonics evolve throughout the test, where a phase of $-180°$ would be perfect appropriation since force

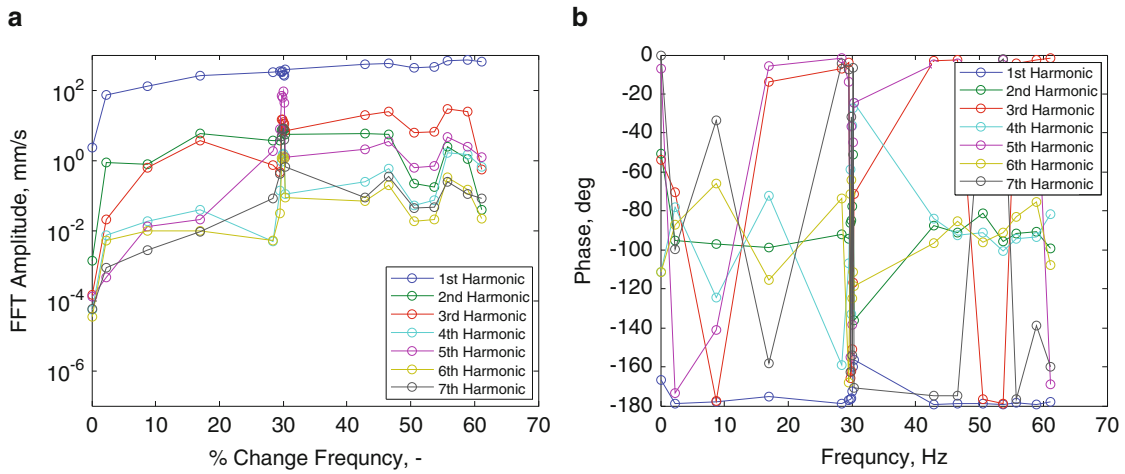

Fig. 22.7 NNM results for the flat clamped-clamped beam – (**a**) FFT amplitude of harmonics in the response and (**b**) phase results of harmonics in the response

and velocity are examined. As expected, the 1st harmonic shows good appropriation throughout measurements except when the response is near the modal interaction and near the initial linear region of the test. Since the modal interaction includes a greater contribution of higher harmonics in the global response of the beam, difficulty of appropriation might be expected in this region. Difficulty of appropriation at lower amplitudes could be due to noise contamination of the velocity measurements at low response amplitudes. The remaining harmonics show a large variability of appropriation due to the use of mono-harmonic force appropriation, but could presumably be improved if higher-harmonic inputs were added to the forcing signal. Indeed, in the simulation study in [17] Kuether found that it was necessary to include higher harmonics to isolate an NNM if the energy was sufficiently high. At even higher energies it also became important to apply a multi-point force.

A useful examination of how the deformation of the beam evolves at each harmonic along the backbone curve can be made with the use of full field measurements. Figure 22.8a–h shows a selection of normalized deformation patterns along the beam for selected harmonics. These shapes could be decomposed into the modes of the structure in order to determine how modal interactions change along the backbone. Figures 22.8a–g describe how the first seven harmonics of the response change with increasing frequency. The second plotted line (green) shows the harmonic response at the modal interactions previously discussed. Figure 22.8a shows how the 1st harmonic evolves from the lowest energy on the backbone curve to the highest with minimal variation from mode 1 of the beam. The line corresponding to the modal interaction is not shown here since the harmonic deformation changes little. Figure 22.8b shows how the 2nd harmonic transitions from a predominantly mode 1 deformation to a mode 2 deformation where a large skew of mode 1 is observed at the modal interaction. Figure 22.8c shows a similar result for the 3rd harmonic, where the deformation transitions from a mode 1 deformation to a higher mode of deformation. For the higher harmonics, shown in Fig. 22.8e–g, the dominant response has the shape of mode 3, which continues to higher odd harmonics (9th and 11th), shown in Fig. 22.8h. Figure 22.8h also shows shapes for the 8th and 10th harmonics at their maximum values which correlate to higher order mode shapes of a beam.

The results presented above provide a wealth of information regarding the frequency-energy behavior of the structure and the way in which the deformation evolves with increasing energy. This information can be critical when seeking to develop a model to correctly simulate the response of the structure.

22.4.2 Circular Plate

Figure 22.9 shows the experimentally measured NNM of the curved axi-symmetric plate with the velocity response measured at the LDV point located at the [x,y] coordinates of [0.01,−0.03]. Similar to the numerically calculated NNM in Fig. 22.9b, the experimentally measured NNM shows the characteristic spring softening to hardening effect or a decrease of the fundamental frequency of vibration which begins to increase at a specific input force level. Unfortunately, limited data was gathered on the structure in the linear region of response due to inadequate capabilities of the shaker to obtain lower forcing amplitudes. Also, the plate cracked when a higher input force amplitude was attempted, so further testing at low amplitudes was impossible. Failure initially occurred at the [x,y] coordinates of [−0.01,−0.01] which can be identified in Fig. 22.9c, d.

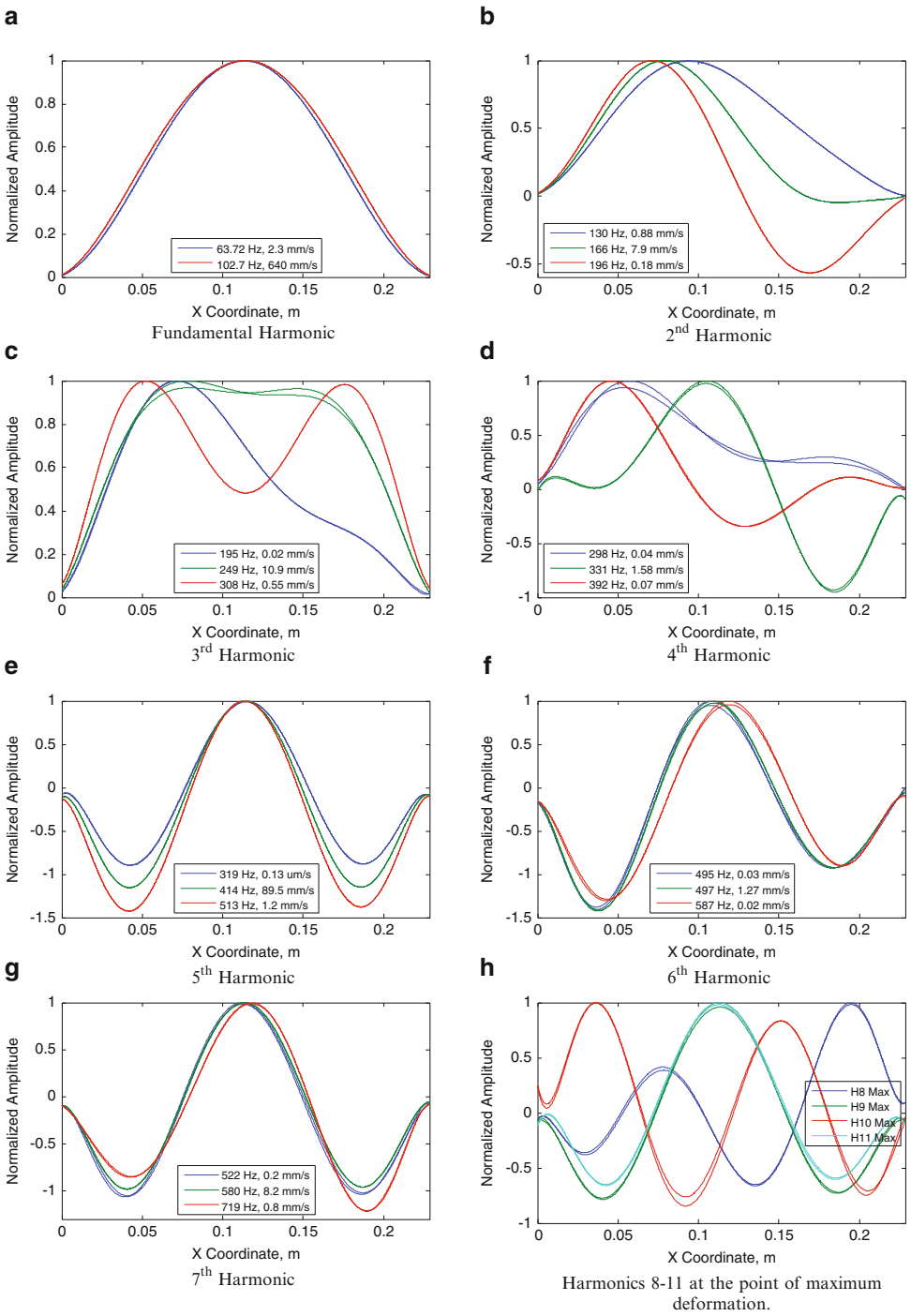

Fig. 22.8 Deformation pattern for each harmonic in the response of the beam at three points along backbone curve. The legend shows the frequency from which these harmonics were extracted and the peak velocity amplitude in each shape. The peak velocities can be compared with those of the 1st harmonic to assess the relative importance of each shape to the overall deformation

With the use of high speed 3D-digital image correlation, maximum deformation shapes of the plate at low and higher energy are shown in Fig. 22.9b–e. Figure 22.9b, c show the deformation shape at the low energy point marked "deformation 1" in Fig. 22.9a. The deformation at this frequency-energy point resemble mode 1 of a flat plate as expected in linear results. Figure 22.9d, e show the deformation shape at the high energy point, or deformation 2 also shown in Fig. 22.9a.

To obtain further insights, the measured response is decomposed into its harmonics in Fig. 22.10a. Interestingly, this shows that while the fundamental harmonic is dominant at low amplitude, as the response begins to turn from softening to hardening the harmonics become large, the 3rd harmonic in particular being equal to the first. Hence, while no internal resonances are present the response of this NNM is multi-modal along the backbone. Unfortunately, the phase of the harmonics, shown in Fig. 22.10b reveal that the higher harmonics for the plate are not in quadrature and so one cannot be sure that the NNM

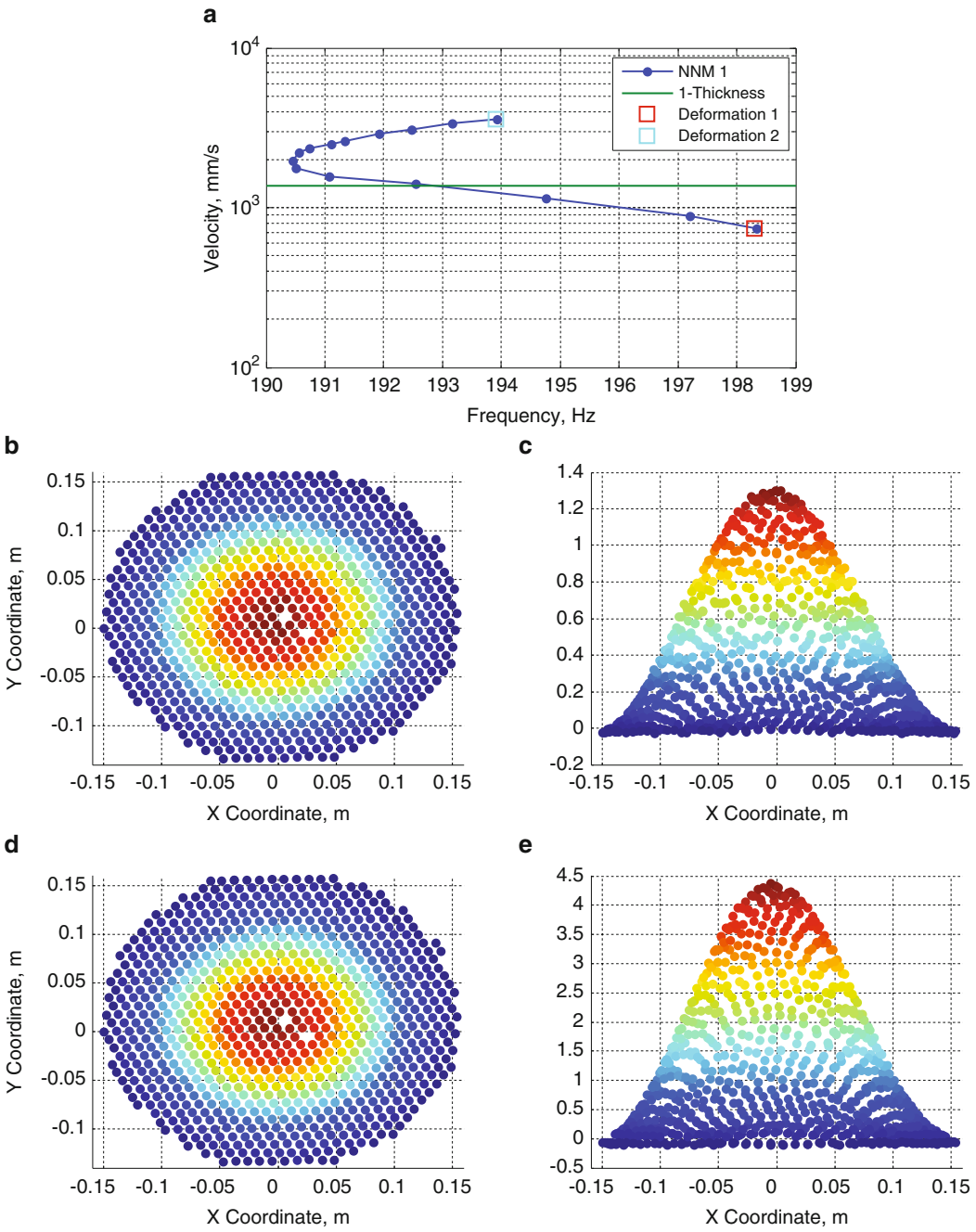

Fig. 22.9 Experimental NNM 1 for axi-symmetric plate – (**a**) frequency-velocity plot, (**b**) deformation 1 shape, top view, (**c**) deformation 1 shape, side view, (**d**) deformation 2 shape, top view, (**e**) deformation 2 shape, side view

has been isolated. The 1st harmonic stays near 180° phase, but it is less accurate in the spring hardening regime. This is most likely due to the increase of modal interaction at this point. The phase is worse than expected for all harmonics, but the reason is not fully understood at this time.

The full field deformation shapes were again computed for each harmonic to better understand the evolution of the response along the backbone, and are shown in Fig. 22.11. It is particularly interesting to note that the response near the 3rd harmonic takes on a shape similar to the 6th linear mode of the plate. In [24] a finite element model of a similar plate (but with no initial curvature) was studied and linear Modes 1 and 6 were both found to be important to describe the response along the NNM backbone. At the highest level on the FEP, the measurements show that the magnitude of this shape is on the same order of the fundamental harmonic. It is also interesting to note the broadening of the deformation shape around the 1st

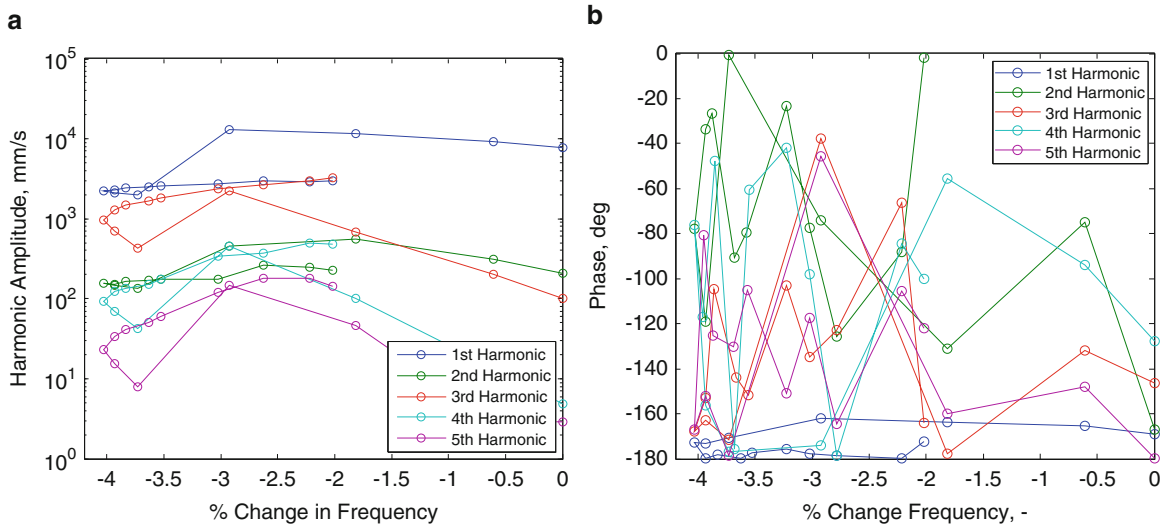

Fig. 22.10 NNM results for the axi-symmetric plate – (**a**) FFT amplitude of harmonics in the response and (**b**) phase results of harmonics in the response

harmonic of deformation 1 and deformation 2, shown in Fig. 22.11a, b. The 5th harmonic, which becomes important only at the last point computed on the NNM. The shapes of the 4th and 5th harmonics suggests that a complicated response occurs in this regime with the inclusion of multiple higher order mode shapes, and this may have been a factor contributing to the failure of the plate.

22.5 Conclusion

The results shown here demonstrate the capability of mono-harmonic force appropriation in two structures exhibiting rich dynamics. The measured response of the flat beam shows the ability to achieve a quality dynamic response in the neighborhood of the beam's first NNM with only mono-harmonic force. In addition to capturing the expected frequency-energy relationship, a modal interaction between the first and third mode of the beam was identified, though not isolated. The measured response of the curved axi-symmetric plate also showed the ability to achieve a dynamic response in the neighborhood of the first NNM of a more complex structure. The quality of the appropriated response for the plate was not on the same level of the beam when looking at the phase of the input and response possibly demonstrating a limitation of a mono-harmonic force to appropriate the response in the neighborhood of the expected NNM.

More work is needed to extend this method of force appropriation for complex structures possibly incorporating multi-harmonic and/or multi-point inputs. As the method of appropriation becomes more complex, higher harmonic amplitude and phase relationships would need to be distinguished in-situ to tune the appropriation. However, even with the relatively simplistic appropriation methodology demonstrated here, results show an adequate identification of the frequency-energy relationship of a structure and insight to modal interactions. So, small improvements in the force appropriation could greatly increase the ability to measure higher energy responses and isolation of modal interactions.

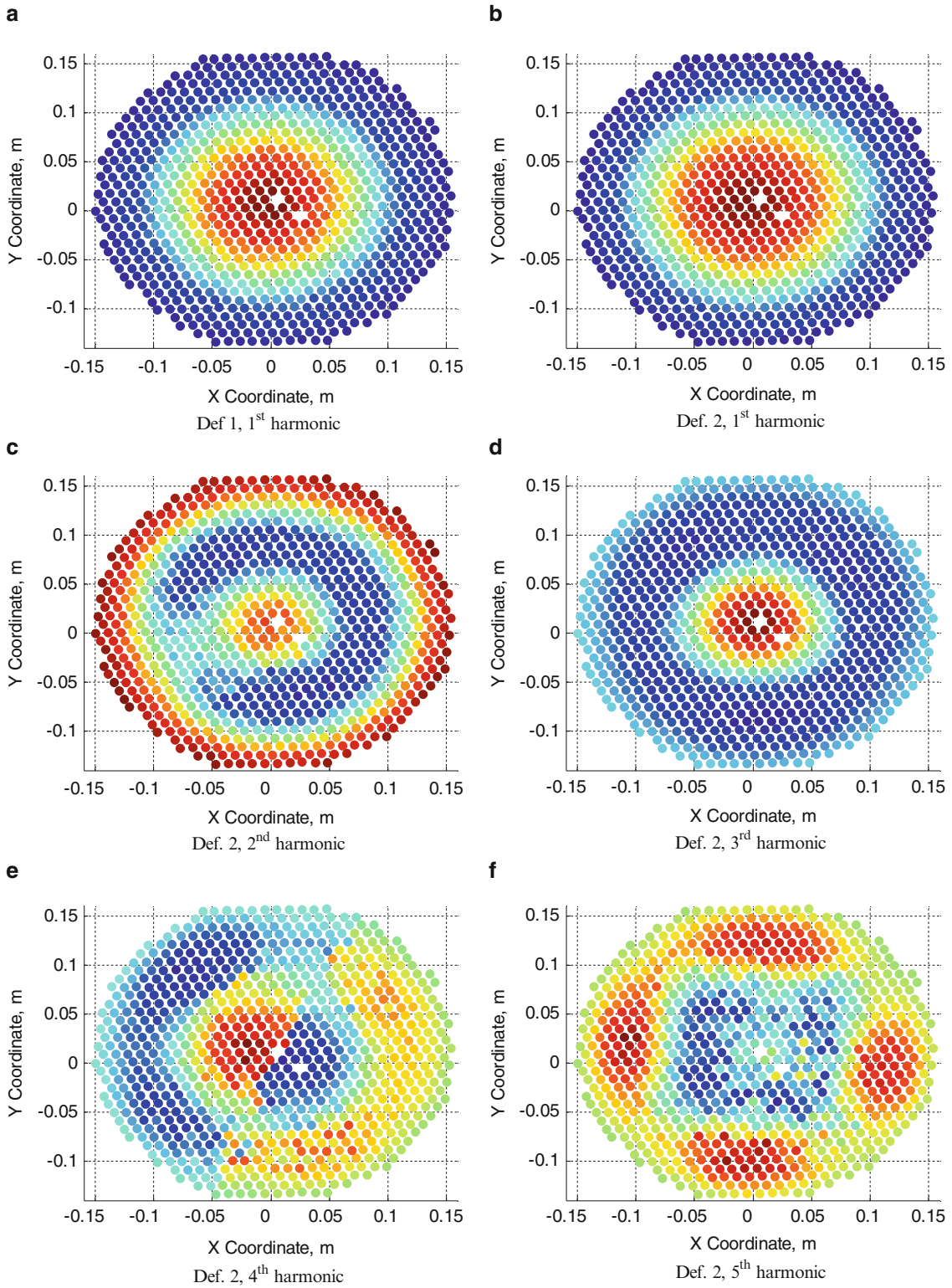

Fig. 22.11 Deformation patterns of plate at various harmonics for two points along the backbone curve: (**a**) 1st harmonic of deformation 1, (**b–f**) 1st harmonic, 2nd harmonic, 3rd harmonic, 4th harmonic, and 5th harmonics respectively of deformation 2

References

1. Ewins DJ (2000) Modal analysis theory, practice, and application, 2nd edn. Research Studies Press LTD., Baldock, Hertfordshire, England
2. Allemang RJ, Brown DL (1998) A unified matrix polynomial approach to modal identification. J Sound Vib 211:301–322
3. Lewis RC, Wrisley DL (1950) A system for the excitation of pure natural modes of complex structure. J Aeronaut Sci (Institute of the Aeronautical Sciences) 17:705–722, 1950/11/01
4. Fraeijs de Veubeke B (1956) A variational approach to pure mode excitation based on characteristic phase lag theory. North Atlantic Treaty Organization, Advisory Group for Aerospace Research and Development, Paris
5. Wright JR, Cooper JE, Desforges MJ (1999) Normal mode force appropriation – theory and application. Mech Syst Signal Process 13:217–240
6. Rosenberg RM (1960) Normal modes of nonlinear dual-mode systems. J Appl Mech 27:263–268
7. Vakakis AF, Manevitch LI, Mikhlin YV, Pilipchuk VM, Zeven AA (1996) Normal modes and localization in nonlinear systems. Wiley, New York
8. Kerschen G, Peeters M, Golinval JC, Vakakis AF (2009) Nonlinear normal modes, part I: a useful framework for the structural dynamicist. Mech Syst Signal Process 23:170–194
9. Kerschen G, Worden K, Vakakis AF, Golinval J-C (2006) Past, present and future of nonlinear system identification in structural dynamics. Mech Syst Signal Process 20:505–592
10. Worden K, Tomlinson GR (2001) Nonlinearity in structural dynamics: detection, identification, and modeling. Institute of Physics, Bristol/Philadelphia
11. Atkins PA, Wright JR, Worden K (2000) An extension of force appropriation to the identification of non-linear multi-degree of freedom systems. J Sound Vib 237:23–43
12. Peeters M, Kerschen G, Golinval JC (2011) Modal testing of nonlinear vibrating structures based on nonlinear normal modes: experimental demonstration. Mech Syst Signal Process 25:1227–1247
13. Peeters M, Kerschen G, Golinval JC (2011) Dynamic testing of nonlinear vibrating structures using nonlinear normal modes. J Sound Vib 330:486–509
14. Peeters M, Kerschen G, Golinval JC, Stéphan C, Lubrina P (2011) Nonlinear normal modes of a full-scale aircraft. In: Proulx T (ed) Modal analysis topics, vol 3. Springer, New York, pp 223–242
15. Ehrhardt D, Harris R, Allen M (2014) Numerical and experimental determination of nonlinear normal modes of a circular perforated plate. International modal analysis conference XXXII, Orlando, pp 239–251
16. Kuether RJ, Allen MS (2014) A numerical approach to directly compute nonlinear normal modes of geometrically nonlinear finite element models. Mech Syst Signal Process 46:1–15
17. Kuether RJ, Allen MS (2012) Computing nonlinear normal modes using numerical continuation and force appropriation, presented at the 24th conference on mechanical vibration and noise
18. Gordon RW, Hollkamp JJ (2011) Reduced-order models for acoustic response prediction. Air Force Research Laboratory, AFRL-RB-WP-TR-2011-3040, Dayton
19. Hollkamp JJ, Gordon RW (2008) Reduced-order models for nonlinear response prediction: implicit condensation and expansion. J Sound Vib 318:1139–1153
20. Virgin LN (2007) Vibration of axially loaded structures. Cambridge University Press, Cambridge, UK
21. Virgin LN (2000) Introduction to experimental nonlinear dynamics: a case study in mechanical vibration. Cambridge University Press, Cambridge, UK
22. Gordon RW, Hollkamp JJ, Spottswood SM (2003) Non-linear response of a clamped-clamped beam to random base excitation, presented at the VIII international conference on recent advances in structural dynamics, Southampton
23. Ehrhardt D, Yang S, Beberniss T, Allen M (2014) Mode shape comparison using continuous-scan laser Doppler vibrometry and high speed 3D digital image correlation. In: International modal analysis conference XXXII, Orlando, pp 321–331
24. Kuether RJ, Deaner B, Allen MS, Hollkamp JJ (2014) Evaluation of geometrically nonlinear reduced order models with nonlinear normal modes. AIAA J, (Submitted)

Chapter 23
Nonlinear System Identification Through Backbone Curves and Bayesian Inference

A. Cammarano, P.L. Green, T.L. Hill, and S.A. Neild

Abstract Nonlinear structures exhibit complex behaviors that can be predicted and analyzed once a mathematical model of the structure is available. Obtaining such a model is a challenge. Several works in the literature suggest different methods for the identification of nonlinear structures. Some of the methods only address the question of whether the system is linear or not, others are more suitable for localizing the source of nonlinearity in the structure, only a few suggest some quantification of the nonlinear terms. Despite the effort made in this field, there are several limits in the identification methods suggested so far, especially when the identification of a multi-degree of freedom (MDOF) nonlinear structure is required.

This work presents a novel method for the identification of nonlinear structures. The method is based on estimating backbone curves and the relation between backbone curves and the response of the system in the frequency domain. Using a Bayesian framework alongside Markov chain Monte Carlo (MCMC) methods, nonlinear model parameters were inferred from the backbone curves of the response and the Second Order Nonlinear Normal Forms which gives a relationship between the model and the backbone curve. The potential advantage of this method is that it is both efficient from a computation and from an experimental point of view.

Keywords Identification • Nonlinear vibrations • Markov Chain Monte Carlo • Bayesian inference • Nonlinear normal forms

23.1 Introduction

In the last decades the scientific community has shown a growing interest in the dynamics of nonlinear structures. This is mainly due to the increasing demand for lighter structures where the same level of safety is guaranteed and, eventually, the region of operation is extended. When the structures are particularly light, in order to assess the safety of the structure, large deflections have to be taken into account, but the theory commonly used to study the dynamics of structures relies on the assumption of linear behavior. This assumption is not true for larger deformations.

Many authors have developed numerical tools able to capture the nonlinear behavior in structures. Although the resulting numerical models give great insight into the physics and the mechanisms that govern the nonlinear behavior, a correct characterization of the nonlinear laws that characterize such behavior in a real structure is still challenging.

The problem of defining such a law is commonly referred to as "nonlinear identification". Unlike linear identification, where the basic assumption is that the structure can be described by a set of linear equations and that only the coefficients of such linear equations are unknown, in nonlinear identification both the coefficients and the form of the equations are to be found.

Several nonlinear identification techniques attempted to linearize the behavior of the system in the neighborhood of a parameter set (see for example [1, 2]). This is equivalent to describing the system in terms of a set of linear oscillators, each able to reproduce the response of the system for a particular range of amplitude. Although this approach has the advantage of re-introducing some of the tools of linear analysis, it comes with many disadvantages. One of the main disadvantages is that these techniques are able to describe the system only when the nonlinear contribution to the response is extremely small. Also it is essential that the response does not go through any bifurcation. When these requirements are not met, other techniques are to be preferred.

A. Cammarano (✉) • T.L. Hill • S.A. Neild
Department of Mechanical Engineering, University of Bristol, Queen's Building, University Walk, Bristol BS8 1TR, UK
e-mail: andrea.cammarano@bristol.ac.uk

P.L. Green
Department of Mechanical Engineering, University of Sheffield, Sir Frederick Mappin Building, Mappin Street, Sheffield S1 3JD, UK

G. Kerschen (ed.), *Nonlinear Dynamics, Volume 1*, Conference Proceedings of the Society for Experimental Mechanics Series, DOI 10.1007/978-3-319-15221-9_23

A set of techniques that overcome this limitation is based on the restoring force surface [3]. This technique, using some features of the surface that relate the restoring force to its state variables, provides a way to estimate the nonlinear parameters. This approach is incredibly powerful for single degrees of freedom systems where the equivalent parameters can be extracted by studying the intersection of the surface with planes characterized by either zero velocities or zero displacement—zero planes. When the number of degrees of freedom increases, the construction of these surfaces becomes more complicated and the interpretation of the intersection with the zero-planes is not trivial. Besides, building these surfaces requires the acquisition of a great number of time histories which can be incredibly time consuming.

It has long been established that probabilistic parameter estimates of nonlinear systems can be realized through the use of a Bayesian framework. This often involves inferring a set of parameters from a measured time history (see [4] for example). One drawback of the techniques is that the input data are compared with simulated data generated through the integration of differential equations. This process can be extremely time demanding.

In this work we present a different approach that uses the Bayesian framework in conjunction with the nonlinear normal forms [5, 6]. The advantage of this approach is that the normal forms provide a useful framework to reduce a complex nonlinear model to a set of algebraic equations. The method does not require forced responses but instead uses the resonant decay which provides an estimation of the backbone curves of the system. The equations provided by the second order nonlinear normal forms are then used to investigate the set of nonlinear parameters that minimizes the error between simulated and input data.

After a brief introduction to nonlinear normal forms and how they can be used for identification purposes, a brief overview of the application of the Bayesian inference for identification with the nonlinear normal forms is provided. Then, a simulated two-degree of freedom nonlinear system with known nonlinear parameters is used to show the procedure to assess the accuracy of the identification technique. Finally, after a brief discussion of the results, the conclusions are drawn.

23.2 Nonlinear Normal Forms and Backbone Curves

A description of the second order nonlinear normal forms can be found in [6, 7]. Here, for sake of simplicity, a brief description in general terms is provided.

The concept behind the nonlinear normal forms [5] is that a set of nonlinear differential equations can be simplified by applying a set of transformations that separates the effect of the nonlinear terms, retaining only those that are more influential for the description of the response. The second order nonlinear normal forms [6], a variation of the original formulation, is particularly convenient for describing the dynamics of structures. In fact, the equations of motion are always expressed in terms of second order differential equations. The second order normal forms avoid the need to rewrite the set of equation in terms of a Cauchy problem (i.e. to reduce the system to the first order).

In this work the second order nonlinear normal forms are used to find algebraic equations that describe the backbone curves of the system. To find the backbone curves, the system has to be considered unforced and undamped. Therefore, the damping and forcing terms must be removed from the equations, which can then be transformed using the following transformations:

- A linear modal transform—the system is projected onto the linear modes (i.e. the modes of the underlying linear system).
- A nonlinear near-identity transform—this removes any non-resonant terms from each equation of motion.

Once these transforms are applied, each mode is described by an equation of motion consisting only of the terms resonating at one frequency—the response frequency (ω_{ri} for the ith mode—close to the linear natural frequency ω_{ni}). This way, the harmonic components of the equation are balanced, and any time-dependence removed. We invite the reader to note that the frequency at which the ith mode responds is named here as ω_{ri}, whereas ω_{ni} is the ith underlying linear natural frequency.

Broadly adopting the notation used by [8], we write the resulting unforced modal dynamics as

$$\ddot{\mathbf{v}} + \mathbf{\Lambda}\mathbf{v} + \mathbf{N}_v(\mathbf{v}, \dot{\mathbf{v}}) = 0, \tag{23.1}$$

where $\mathbf{v}$ is a vector of modal displacements, $\mathbf{\Lambda}$ is a diagonal matrix having the ith diagonal term equal to ω_{ni}^2 and $\mathbf{N}_v$ contains the nonlinear terms, which are assumed to be small. The final step in the technique is the near-identity nonlinear transform $\mathbf{v} \rightarrow \mathbf{u}$

$$\begin{gathered} \mathbf{v} = \mathbf{u} + \mathbf{H}(\mathbf{u}, \dot{\mathbf{u}}) \\ \ddot{\mathbf{v}} + \mathbf{\Lambda}\mathbf{v} + \mathbf{N}_v(\mathbf{v}, \dot{\mathbf{v}}) = 0 \qquad \longrightarrow \qquad \ddot{\mathbf{u}} + \mathbf{\Lambda}\mathbf{u} + \mathbf{N}_u(\mathbf{u}, \dot{\mathbf{u}}) = 0, \end{gathered} \tag{23.2}$$

where $\mathbf{H}$ stores all the terms that do not contribute to the fundamental response. All nonlinear terms resonating at ω_{ri}, for the ith mode, are collected in $\mathbf{N}_u$. A general solution for the ith component of the fundamental response $\mathbf{u}$ can be written as $u_i = u_{ip} + u_{im} = U_i e^{j\omega_{ri}tc} + U_i e^{-j\omega_{ri}t+\phi_i}$, where U_i represents the amplitude of the sinusoidal response and ϕ_i its phase. Substituting this solution for $\mathbf{u}$ in Eq. (23.2), and writing $\mathbf{N_u}(\mathbf{u}, \dot{\mathbf{u}}) = [\mathbf{N_u}]\mathbf{u}^*$ and $\mathbf{H}(\mathbf{u}, \dot{\mathbf{u}}) = [\mathbf{H}]\mathbf{u}^*$ as a linear combination of all nonlinear terms, where in general the lth element in the vector $\mathbf{u}^*$ is

$$u_\ell^* = \prod_{i=1}^{I} \left\{ u_{ip}^{s_{\ell ip}} u_{im}^{s_{\ell im}} \right\}, \tag{23.3}$$

it is possible to eliminate the time dependency from Eq. (23.2) and write the response of the system in terms of algebraic equations. The coefficients of these linear combinations can be found following the procedure described in [7]. Since the response is now expressed in terms of algebraic equations, relating the response to the change in parameters becomes extremely simple and computationally efficient. This is one of the great advantage of performing the identification of the parameters of the system using these equations, rather than the original differential equations.

23.3 Identification with Bayesian Inference

In the previous section, the second order nonlinear normal forms were used to find algebraic expression for a generic backbone curve of the system. To use these expressions for identification purposes, the backbone curve of the system must be estimated with an experimental procedure. For this purpose the techniques introduced by Feldman in [9] is used.

This techniques requires that the system is excited with a step sine so that the maximum amplitude response on one resonant peak is reached (red star in Fig. 23.1). Once this response is achieved, the forcing is stopped and the free response of the system is measured.

Because the system was vibrating around a resonant peak, the initial condition for the free vibration is also compatible with that resonance, hence the system response decays along its backbone curve (for more details see [10]). A schematic representation of this method is shown in Fig. 23.1. Here the response to the swept sine is represented with a dotted line, the resonant peak, where the forcing is stopped, is indicated with a red star and the backbone curve followed by the decaying signal is represented by a thick solid black line. The complete response of the system is shown with a thin line. The response is shown in solid black if stable, dashed red if unstable.

Note that the maximum amplitude response is in the proximity of a fold bifurcation (after which the response becomes unstable). This means that it is impossible to reach the peak (the basin of attraction of that solution is almost null and any small perturbation makes the solution jump to the lower solution). For this reason, when conducting the experiment, the forcing has to be stopped before the resonant peak. From numerical simulation it seems this does not cause any problem in the estimation of the backbone curve, since the free response rapidly converges to it.

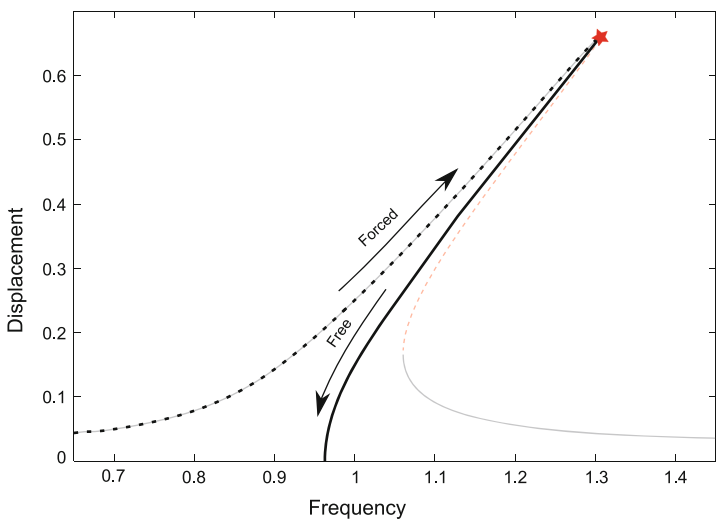

Fig. 23.1 Schematic of the backbone curve estimation with the free decay curve method. The *thin lines* represent the frequency response around resonance (*grey solid curves* show the stable responses whereas *red dashed lines* represent the unstable responses). The system is forced with a step sine until the forced response (*black dots*) reaches the resonant peak (*red star*). At this point the forcing is brought to zero and the damping in the system causes the response of the system to freely decay to zero (Color figure online)

Once the free vibration has been measured, the estimation of the backbone curve can be done by considering the period between too consecutive zeros and the amplitude of the signal at that instant of time (since the signal is decaying an average value on the interval is considered). For the backbone curves to be used with the nonlinear normal forms, they need to be expressed in terms of the underlying linear modal coordinates. This can be achieved applying the modal transform to the measured physical displacements. The modal transform can be obtained by running an initial test at low amplitude so that the nonlinear contribution is very small. This test is also needed to find the linear natural frequencies.

Once the backbone curves are evaluated, the Bayesian inference can be used. Here a brief description of the method is provided. For more details see [4].

Using Bayes' rule

$$P(\boldsymbol{\theta}|\mathcal{D},\mathcal{M}) = \frac{P(\mathcal{D}|\boldsymbol{\theta},\mathcal{M})P(\boldsymbol{\theta}|\mathcal{M})}{P(\mathcal{D}|\mathcal{M})} \tag{23.4}$$

it is possible to evaluate the probability that parameter vector assumes a value *boldsymbol*θ given data $\mathcal{D}$ and a model structure $\mathcal{M}$. In this case, the data consist of the measured values of $U_{1,n}$ and $U_{2,n}$ along the backbone curves together with the corresponding frequencies ω_{rn}. Here with the subscript n we indicate the resonance. So $U_{1,1}$ is the component U_1 of the first backbone curve. From now on the data are separated in two sets: the set of the $U_{1,n}$ values and their corresponding response frequency ω_{rn} is named $\mathcal{D}_1$ and the set of the $U_{2,n}$ values together with their response frequency $\mathcal{D}_2$.

The vector of parameters $\boldsymbol{\theta}$ contains all the parameters that must be identified. The model $\mathcal{M}$, in this case is the algebraic equation derived from the second order normal forms that maps values of ω_{rn} in values of $U_{1,n}$ and $U_{2,n}$.

To define the likelihood $P(\mathcal{D}|\boldsymbol{\theta},\mathcal{M})$, we assume that, for a given model $\mathcal{M}$ and a parameter set $\boldsymbol{\theta}$, the probability of witnessing $U_{1,n}$ and $U_{2,n}$ are mutually independent, so that

$$P(\mathcal{D}|\boldsymbol{\theta},\mathcal{M}) = P(\mathcal{D}_1|\boldsymbol{\theta},\mathcal{M})P(\mathcal{D}_2|\boldsymbol{\theta},\mathcal{M}). \tag{23.5}$$

Also it is assumed that the PDF describing the probability of witnessing a data point is given by a Gaussian distribution with mean equal to the model output,

$$P(U_1^{(i)}|\boldsymbol{\theta},\mathcal{M}) = \mathcal{N}(\hat{U}_1^{(i)}(\boldsymbol{\theta}),\sigma_1^2), \tag{23.6}$$

$$P(U_2^{(i)}|\boldsymbol{\theta},\mathcal{M}) = \mathcal{N}(\hat{U}_2^{(i)}(\boldsymbol{\theta}),\sigma_2^2). \tag{23.7}$$

Here the $\hat{U}_1$ and $\hat{U}_2$ are the output values of the model $\mathcal{M}$ for U_1 and U_2 (the hat indicates that this values are simulated) and therefore they are a function of the parameters $\boldsymbol{\theta}$. The parameters σ_1 and σ_2 can be included in the parameter vector and considered as unknown for the problem.

It is also assumed that there is mutual independence between the data points, that is

$$P(U_1^{(i)},U_1^{(j)}|\mathcal{D},\mathcal{M}) = P(U_1^{(i)}|\boldsymbol{\theta},\mathcal{M})P(U_1^{(j)}|\mathcal{D},\mathcal{M}), \tag{23.8}$$

$$P(U_2^{(i)},U_2^{(j)}|\mathcal{D},\mathcal{M}) = P(U_2^{(i)}|\boldsymbol{\theta},\mathcal{M})P(U_2^{(j)}|\mathcal{D},\mathcal{M}). \tag{23.9}$$

Under these assumptions the likelihood of the data set $\mathcal{D}$ given a parameter set $\boldsymbol{\theta}$ and a model $\mathcal{M}$ is

$$P(\mathcal{D}|\boldsymbol{\theta},\mathcal{M}) = \prod_{i=1}^{N} \mathcal{N}(\hat{U}_1^{(i)}(\boldsymbol{\theta}),\sigma_1^2)\mathcal{N}(\hat{U}_2^{(i)}(\boldsymbol{\theta}),\sigma_2^2). \tag{23.10}$$

In Eq. (23.4) the distribution $P(\boldsymbol{\theta}|\mathcal{M})$ is the prior distribution, that is a probability distribution representing the knowledge of $\boldsymbol{\theta}$ before the data are known. In this work the prior is assumed to have a uniform distribution. The denominator of Eq. (23.4) can be seen as a normalizing constant which ensure that the integral of the posterior distribution over the support of the prior is equal to 1.

To generate the samples from the posterior we use a Markov chain Monte Carlo (MCMC). In particular for this work we used the Simulated Annealing algorithm which involves targeting the sequence of distributions:

$$\pi_{\beta_j} \propto P(\mathcal{D}|\boldsymbol{\theta},\mathcal{M})^{\beta_j} P(\boldsymbol{\theta}|\mathcal{M}) \qquad j = 1,2,\ldots \tag{23.11}$$

where β_1, β_2, β_3, is a sequence which increases monotonically from 0 to 1—the annealing schedule. Using Eq. (23.4) an adaptive annealing schedule was chosen. This ensures that the information content of the data (measured using the Shannon entropy) is introduced into the target distribution at a constant rate [11]. Moreover, to avoid local traps, multiple Markov chain can be grown in parallel.

23.4 Nonlinear Identification of a 2-DOF Nonlinear Oscillator

In this section a two mass system featuring a nonlinear spring is presented. This system is used to produce a set of numerical data which can be used for the nonlinear identification. As the system is simulated the characteristics are known and so allows us to verify the accuracy of the identified parameters using the proposed technique.

A schematic of the system is provided in Fig. 23.2. Both masses are connected to ground and between each other with linear springs and viscous dampers. All the springs have the same stiffness value K of 1 N/m, the external dampers (labeled C)have a damping constant of 1×10^{-3} Ns/m and the central dampers (labeled C_2) have a damping constant of 5×10^{-4} Ns/m. The spring between ground and the first mass has an additional cubic term with a nonlinear coefficient κ of 0.5 N/m^3.

In this example, the system has not been excited as previously described. Since the system presented is simulated, it was possible to reverse the time flow and start the time decay from a solution in the close proximity of zero. The advantage of this method is that when the amplitude of vibration approaches zero, the system behaves linearly and the initial displacement can be chosen so that it is compatible with the modeshape corresponding to the nth mode of the underlying linear system. In this case, the eigenvectors of the underlying linear system are $[1, 1]$ and $[1, -1]$. A simulation starting from $[\delta, \delta]$ is used to generate a time history from which the first backbone curve can be estimated. The same approach, starting from an initial displacement of $[\delta, -\delta]$ gives the time history to estimate the second backbone curve. Here with δ we mean a generic small displacement.

The backbone curve, estimated evaluating the instantaneous frequency at the zero crossing, are then used as input data for the Bayesian technique illustrated in the previous section. For this test we hypothesized that the number of nonlinear springs and their position were known and that only the value of the nonlinearity was unknown. Using the nonlinear normal forms, analytical expressions for the backbone curves of a system featuring two masses and three linear springs are derived:

$$S1 : \left(\omega_{n1}^2 - \omega_{r1}^2\right) U_1 + \frac{3}{8m}\left[\kappa \left(U_1 + U_2\right)^3\right] = 0, \tag{23.12}$$

$$S2 : \left(\omega_{n2}^2 - \omega_{r2}^2\right) U_2 + \frac{3}{8m}\left[\kappa \left(U_1 + U_2\right)^3\right] = 0. \tag{23.13}$$

In the model, the number of nonlinear springs is one and its position is known: this simplified the derivation of the backbone curves. Also, only one nonlinear parameter has to be identified. For the estimation of the nonlinear parameter a uniform distribution for the prior has been used. The limit of the distribution for each parameter are listed in Table 23.1.

The parameter vector $\boldsymbol{\theta}$ in this case is made of the nonlinear parameter κ and the variance of the data around the value estimated by the model. To find the parameter vector 8,000 posterior samples were generated using MCMC.

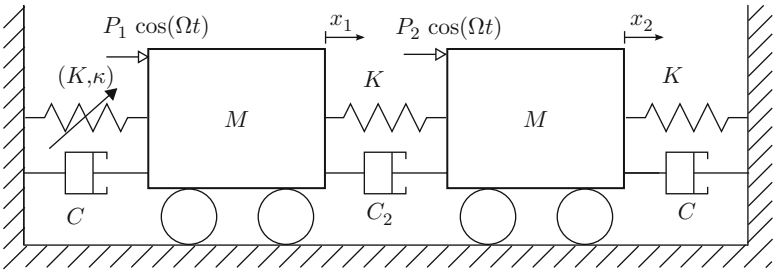

Fig. 23.2 A schematic diagram of the nonlinear two-mass oscillator

Table 23.1 Parameter limits for the prior distribution

Parameter	Lower limit	Upper limit
κ	0	1
σ_1	0	0.5
σ_2	0	0.5

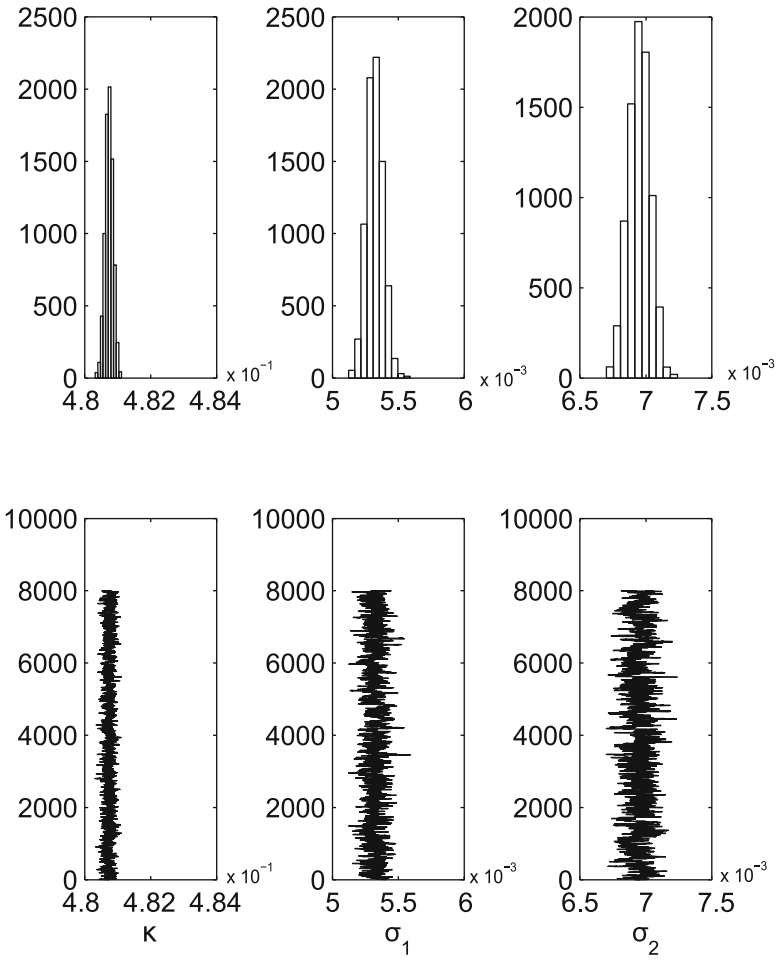

Fig. 23.3 Parameter distribution in the data generated by the MCMC. Each of the three columns of figures shows the evolution of one the parameters (*bottom*) and its histogram (*top*). The mean nonlinear coefficient κ is estimated to be 4.81 N/m^3. The *second* and the *third columns* show the values of σ_1 and σ_2 for the distribution of the input data around the values predicted by the model

The identification methods predicted a mean value for κ of 0.481 N/m^3 as shown in Fig. 23.3 whereas the real value was 0.5 N/m^3. Figures 23.4 and 23.5 show the measured backbone curves (black dots), the most probable backbone curves identified by the techniques using the estimated value of κ (red lines). Also the $\pm 3\ \sigma$ intervals (delimited by the blue curves) are shown. The estimated backbone curve, the predicted ones and the interval limits are very close to each other: from the figures they are barely distinguishable. The backbone curves in Figs. 23.4 and 23.5 are represented in terms of the amplitude of the fundamentals U_1 and U_2 respectively. This representation has been chosen to be consistent with the variable used in the identification methods. Other representations are possible (for example in terms of the physical coordinates).

23.5 Conclusions

A procedure for identifying nonlinear system has been described. The method, based on the second order nonlinear normal forms, uses a Bayesian framework to find probabilistic estimates of the parameters of a nonlinear system. The advantage of this technique over other techniques using a Bayesian framework is that the simulated data are obtained using algebraic equations rather than differential equations. This results in reduced computation time and in the possibility of comparing the input data with a higher number of nonlinear functions. After the introduction of the techniques, a numerical model of a 2DOF nonlinear oscillator has been used to provide input data for the identification procedure. In the previous section, the identification procedure was implemented on the simulated data and more insight into the technique provided. The parameter used for the simulation was correctly identified by the identification method shown in this work with an error of 5%. For this initial test, the position and the number of nonlinear springs were assumed as known. Future work will assess whether this technique is able to localize the nonlinearity and if the estimation error can be reduced.

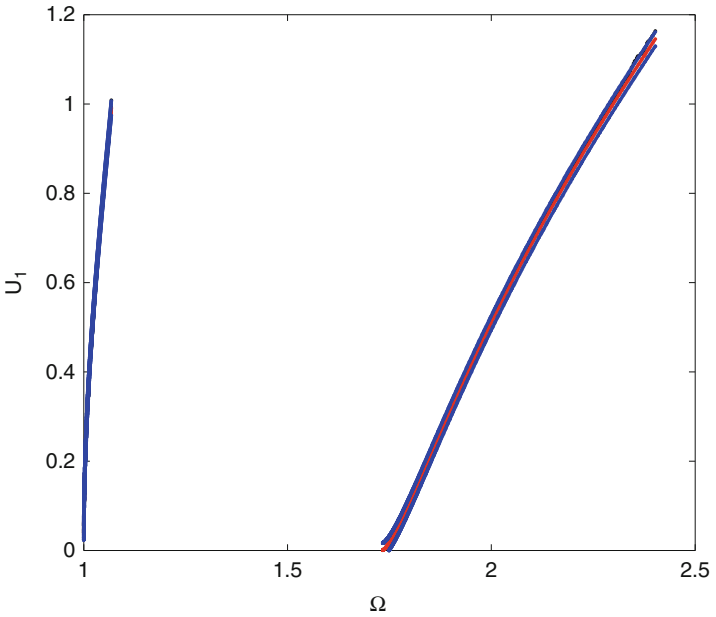

Fig. 23.4 Backbone curves (U_1 component): estimated backbone curve (*black dots*), identified backbone curve (*red dots*) and limit of the $\pm 3\ \sigma_1$ region (*blue dots*). Both the $S1$ and the $S2$ backbone curves are shown (Color figure online)

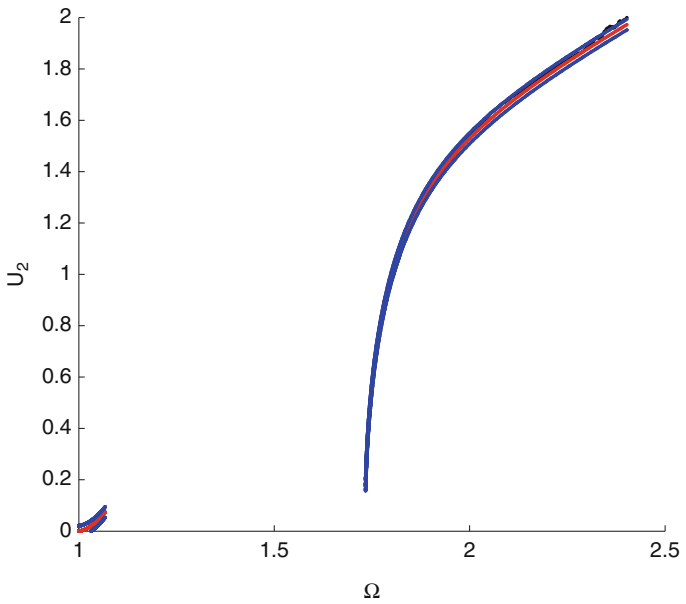

Fig. 23.5 Backbone curves (U_2 component): estimated backbone curves (*black dots*), identified backbone curves (*red dots*) and limit of the $\pm 3\ \sigma_2$ region (*blue dots*). Both the $S1$ and the $S2$ backbone curves are shown (Color figure online)

Acknowledgements The authors would like to acknowledge the support of the Engineering and Physical Sciences Research Council. A. Cammarano and P.L.Green are supported by EPSRC Programme Grant "Engineering Nonlinearity" EP/K003836/1. T.L. Hill is supported by an EPSRC studentship and S.A. Neild is supported by EPSRC Fellowship EP/K005375/1.

References

1. Carrella A, Ewins DJ (2011) Identifying and quantifying structural nonlinearities in engineering applications from measured frequency response functions. Mech Syst Signal Process 25(3):1011–1027
2. Josefsson A, Magnevall M, Ahlin K (2007) On nonlinear parameter estimation with random noise signals. In: Proceedings of IMAC XXV
3. Worden K, Tomlinson GR (2010) Nonlinearity in structural dynamics: detection, identification and modelling. CRC Press, Boca Raton, pp 286–376
4. Green PL (2014) Bayesian system identification of a nonlinear dynamical system using a novel variant of Simulated Annealing. Mech Syst Signal Process. doi:10.1016/j.ymssp.2014.07.010

5. Nayfeh AH (1993) Method of normal forms. Wiley, New York
6. Neild SA, Wagg DJ (2011) Applying the method of normal forms to second order nonlinear vibration problems. Proc R Soc Lond A 467: 1141–1163
7. Neild SA (2012) Approximate methods for analysing nonlinear structures. Exploiting nonlinear behavior in structural dynamics. Springer, New York, pp 53–109
8. Cammarano A, Hill TL, Neild SA, Wagg DJ (2013) Bifurcations of backbone curves for systems of coupled nonlinear two mass oscillator. Nonlinear Dyn 1–10. doi:10.1007/s11071-014-1295-3
9. Feldman M (1994) Non-linear system vibration analysis using Hilbert transform—I. Free vibration analysis method'Freevib'. Mech Syst Signal Process 8(2):119–127
10. Kerschen G, Peeters M, Golinval JC, Vakakis AF (2009) Nonlinear normal modes, Part I: a useful framework for the structural dynamicist. Mech Syst Signal Process 23:170–194
11. Green PL (2014) Bayesian system identification of nonlinear dynamical systems using a fast MCMC algorithm. In: Proceedings of ENOC 2014, European nonlinear dynamics conference

Chapter 24
Experimental Nonlinear Identification of an Aircraft with Bolted Connections

G. De Filippis, J.P. Noël, G. Kerschen, L. Soria, and C. Stephan

Abstract Aircraft structures are known to be prone to nonlinear phenomena, especially as they constantly become lighter and hence more flexible. One specific challenge that is regularly encountered is the modeling of the mounting interfaces between aircraft subcomponents. Indeed, for large amplitudes of vibration, such interfaces may loosen and, in turn, trigger complex mechanisms such as friction and clearances. In this context, the present work intends to investigate the nonlinear dynamics of the Morane–Saulnier Paris aircraft, accessible at ONERA. This aircraft possesses multiple bolted connections between two external fuel tanks and wing tips. The objective of the paper is specifically to carry out an adequate identification of the numerous nonlinearities affecting the dynamics of this full-scale structure. Nonlinearity detection and the subsequent subspace-based parameter estimation have been performed on experimental data, collected during an on-ground test campaign. Nonlinearity detection is first achieved by the comparison of frequency response functions estimated at low excitation level, with those obtained at high amplitude level, yielding insight towards accurately characterizing the behavior of the bolted connections. Then, a nonlinear subspace identification method is applied to measured data to estimate the linear and nonlinear parameters of the structure and novel strategies and tools that overcome specific arisen problems are developed.

Keywords Nonlinear system identification • Frequency-domain subspace method • Full-scale aircraft • Cubic splines • Spurious poles

24.1 Introduction

The increasing levels of performance demanded to aircraft structures can require the implementation of design procedures and options that may, in turn, lead to the activation of some nonlinear phenomena. Numerous works reporting on the evidence of existing nonlinearities in aerospace applications can be found in the technical literature, as, to give only some examples, [1–3]. Classical linear subspace-based methods [4] have recently been generalized to handle these occurrences [5, 6]. Specifically, the frequency-domain nonlinear subspace identification (FNSI) method has been proved to successfully deal with grey-box models, affected by many nonlinearities [7].

In this paper, the FNSI methodology is applied for the first time to a full-scale structure, the Morane–Saulnier Paris aircraft. This aircraft presents multiple bolted connections between the wings and two external fuel tanks, located at the wing tips. The experimental identification requires that a considerable number of output locations are utilized on the aircraft main body and at the two the ends of the mounting interfaces, where nonlinear behaviors are expected to arise. Due to the presence of many nonlinearities, a relevant number of basis functions are included in the FNSI routine. The development of novel tools and strategies is carried out to overcome the problems related to the high dimensionality of the consequent inverse problem. Moreover, classical subspace methods do not provide the user with the possibility of selecting among the

G. De Filippis (✉) • L. Soria
Dipartimento di Meccanica, Matematica e Management, Politecnico di Bari, Bari, Italy
e-mail: giovanni.defilippis@poliba.it; leonardo.soria@poliba.it

J.P. Noël • G. Kerschen
Space Structures and Systems Laboratory (S3L), Aerospace and Mechanical Engineering Department, University of Liège, Liège, Belgium
e-mail: jp.noel@ulg.ac.be; g.kerschen@ulg.ac.be

C. Stephan
ONERA – The French Aerospace Lab, Châtillon, France
e-mail: cyrille.stephan@onera.fr

G. Kerschen (ed.), *Nonlinear Dynamics, Volume 1*, Conference Proceedings of the Society for Experimental Mechanics Series, DOI 10.1007/978-3-319-15221-9_24

poles computed at a given model order. This means that, in the usual procedure, all the calculated poles have to be included, the physical as the spurious ones. To avoid this drawback, an appropriate strategy is employed, that allows for removing the undesired spurious poles.

Linear identification is first performed at low amplitude level, with the aim of collecting the modal parameters. Then, the comparison between frequency response functions (FRFs) estimated at low and at high amplitude level is employed for detecting the overall nonlinear behavior of the structure. Afterward, the FNSI method is applied to estimate the underlying linear properties and the nonlinear restoring forces. Finally, a novel strategy for spurious poles' removal is applied to the identified model.

24.2 Description of the Aircraft and of the Experimental Setup

The structure is the airframe of the Morane–Saulnier Paris aircraft, represented in Fig. 24.1. This French jet aircraft was built during the 1950s and was used as a trainer and liaison aircraft. The structural configuration under consideration corresponds to the aircraft without its jet engines and standing on the ground through its three landing gears with deflated tires. A specimen of this airplane is present in ONERA's laboratory. It is used for training engineers and technicians for ground vibration tests (GVT) and for research purposes. GVT exhibit nonlinear behavior in the connection between the wings and external fuel tanks located at the wing tip.

A total of 38 accelerometers is employed to instrument the structure, of which eight tri-axial sensors are positioned at the two ends of each of the four wing-tank bolted attachments (Fig. 24.2), where, thus, nonlinearities are mainly expected to be located. Two small-size shakers, one visible in Fig. 24.1, are used to apply pure broad-band random excitation inputs to the two wings, along the vertical direction. The adopted sampling frequency is equal to 400 Hz. Acceleration and force signals are both recorded at the driving points, located below the fuel tanks (Fig. 24.3), by means of impedance heads.

In this paper, all the output channels related to bolted attachments are denoted by a label of the form abc:D, where a is Ri or Le, for indicating the right or the left side of the aircraft, respectively, b is Fr or Re, when referring to the front or the rear bolted connection, and c is Wi or Ta, if the considered node belongs to the wing or to the tank, respectively. More over, D represents the channel direction (X, Y, or Z), evaluated with respect to a fixed reference frame, having the X-axis coinciding with the longitudinal axis of the aircraft, but directed from the nose to the tail, the vertical, Z-axis, pointing upward, and the Y-axis chosen to form a right-handed cartesian coordinate system. Both the ends of the bolted connections are included when the character c is imposed equal to BC. To give an example of this nomenclature, the label LeReWi:Y denotes the output channel referred to the left rear bolted connection, node on the wing, along the Y direction. In the case of input channels, instead, we need only to distinguish between the left (LeIn:Z) and the right (RiIn:Z) excitation.

Fig. 24.1 Morane–Saulnier Paris aircraft

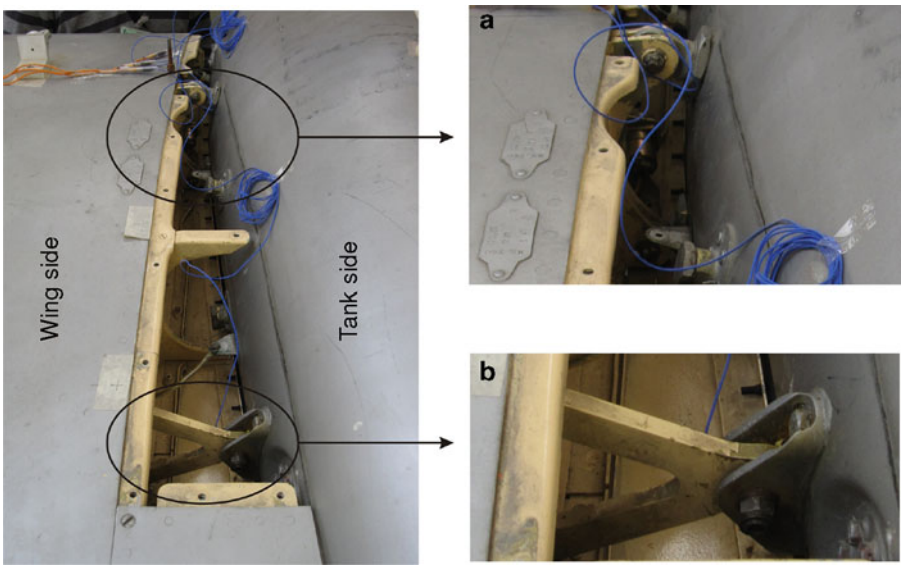

Fig. 24.2 Connection between external fuel tank and wing tip (*top view*). Close-up of (**a**) front and (**b**) rear bolted attachments

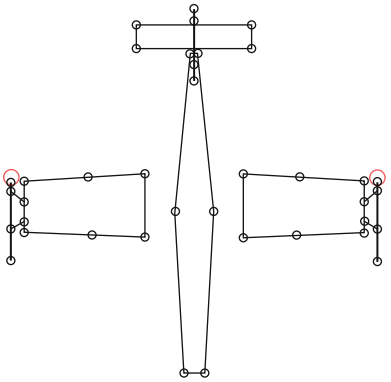

Fig. 24.3 Layout of the experimental setup (*top view*). *Black circles*: output locations; *red circles*: driving points (Color figure online)

24.3 Nonlinear Subspace Identification in the Frequency Domain

The FNSI method derives models of mechanical systems possessing localised nonlinearities directly from measured data, and without resorting to a preexisting numerical model, e.g. a finite element model [6]. It is applicable to multi-input, multi-output structures with high nonproportional damping and high modal density, and makes no assumption as to the importance of nonlinearity in the measured dynamics [8]. The vibrations of such nonlinear systems are governed by Newton's second law

$$\mathbf{M}\,\ddot{\mathbf{q}}(t) + \mathbf{C}\,\dot{\mathbf{q}}(t) + \mathbf{K}\,\mathbf{q}(t) + \mathbf{g}(\mathbf{q}(t), \dot{\mathbf{q}}(t)) = \mathbf{p}(t) \tag{24.1}$$

where $\mathbf{M}, \mathbf{C}, \mathbf{K} \in \mathbb{R}^{n \times n}$ are the mass, linear viscous damping and linear stiffness matrices, respectively; $\mathbf{q}(t)$ and $\mathbf{p}(t) \in \mathbb{R}^n$ are the generalized displacement and external force vectors, respectively; $\mathbf{g}(t) \in \mathbb{R}^n$ is the essentially nonlinear, i.e. non-linearizable, restoring force vector encompassing elastic and dissipative contributions, and n is the number of degrees of freedom (DOFs) of the structure obtained after spatial discretization. The amplitude, direction, location and frequency content of the excitation $\mathbf{p}(t)$ determine in which regime, linear or nonlinear, the structure behaves. The effects of the r lumped nonlinear components in the system are represented using a linear-in-the-parameters model of the form

$$\mathbf{g}(\mathbf{q}(t), \dot{\mathbf{q}}(t)) = \sum_{a=1}^{r} \sum_{b=1}^{s_a} c_{a,b}\, \mathbf{h}_{a,b}(\mathbf{q}(t), \dot{\mathbf{q}}(t)). \tag{24.2}$$

In this double sum, s_a is the number of nonlinear basis functions $\mathbf{h}_{a,b}(\mathbf{q}(t), \dot{\mathbf{q}}(t))$ selected to describe the a-th nonlinearity, and $c_{a,b}$ are the associated coefficients. The total number of nonlinear basis functions introduced in the model is equal to $s = \sum_{a=1}^{r} s_a$. Linearity in the parameters avoids an iterative optimization process, and issues related to initialization and convergence thereof.

Given measurements of $\mathbf{p}(t)$ and $\mathbf{q}(t)$ or its derivatives, and an appropriate selection of the functionals $\mathbf{h}_{a,b}(t)$, the FNSI algorithm aims at computing estimates of (1) the FRF matrix

$$\mathbf{H}(\omega) = \left(-\omega^2\,\mathbf{M} + \mathrm{j}\,\omega\,\mathbf{C} + \mathbf{K}\right)^{-1} \tag{24.3}$$

describing the underlying linear properties of the system in Eq. (24.1), where ω is the frequency and j the imaginary unit, and (2) the nonlinear coefficients $c_{a,b}$ in Eq. (24.2).

The identification methodology essentially builds on a block-oriented interpretation of nonlinear structural dynamics, which sees nonlinearities as a feedback into the linear system in the forward loop [9], as illustrated in Fig. 24.4. This interpretation boils down to moving the nonlinear internal forces in Eq. (24.1) to the right-hand side, and viewing them as additional external forces applied to the underlying linear structure, that is

$$\mathbf{M}\,\ddot{\mathbf{q}}(t) + \mathbf{C}\,\dot{\mathbf{q}}(t) + \mathbf{K}\,\mathbf{q}(t) = \mathbf{p}(t) - \sum_{a=1}^{r}\sum_{b=1}^{s_a} c_{a,b}\,\mathbf{h}_{a,b}(\mathbf{q}(t), \dot{\mathbf{q}}(t)). \tag{24.4}$$

Based on Eq. (24.4), the parameter estimation problem is solved in the frequency domain by processing a user-selected number of frequency lines in the measured band. A state-space representation of Eq. (24.4) is first extracted directly from frequency-domain data using robust tools from numerical analysis, including QR and singular value decompositions. The calculated state-space parameters are secondly converted into the modal space to estimate the underlying linear FRF matrix $\mathbf{H}(\omega)$, and to the physical space to estimate the nonlinear coefficients $c_{a,b}$. Figure 24.5 presents an overview of the identification methodology. The interested reader is referred to [6] for a detailed introduction to the theoretical and practical aspects of the FNSI method.

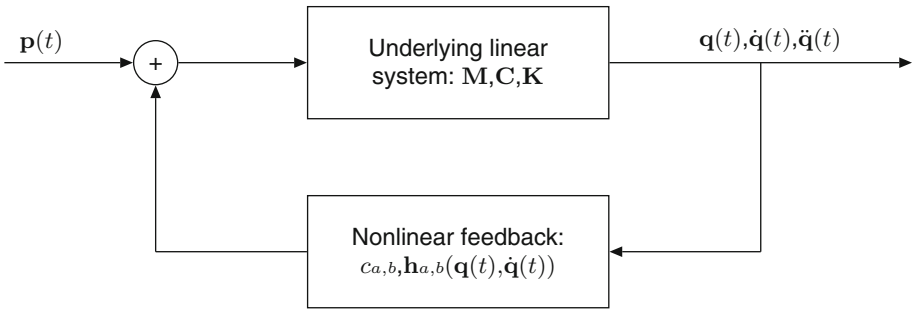

Fig. 24.4 Feedback interpretation of nonlinear structural dynamics [9]

1. Select appropriate basis functions $\mathbf{h}_{a,b}(\mathbf{q}(t),\dot{\mathbf{q}}(t))$ to represent the nonlinearities.
2. Choose the number of processed frequency lines in the measured band.
3. Determine the order of the state-space representation of Eq. 4 and calculate its parameters from frequency-domain data.
4. Convert the state-space model to modal space to estimate the underlying linear FRF matrix $\mathbf{H}(\omega)$.
5. Convert the state-space model to physical space to estimate the nonlinear coefficients $c_{a,b}$.

Fig. 24.5 Overview of the FNSI methodology

24.4 Linear Analysis at Low Level and Nonlinearity Detection

When the system is excited with low amplitude level inputs, the nonlinearities affecting the bolted connections are not activated. This means that data acquired at low level can be utilized to perform a linear identification of the structure. To this aim, a band-limited (7–45 Hz) white-noise signal is applied to the aircraft, having a root-mean-square (RMS) amplitude of 4.4 N. In this conditions, the FNSI method can be employed for obtaining the linear modal parameters of the structure. Since we, here, focus only on the identification of the first five modes, the frequency band of analysis ranging from 7 to 21.5 Hz is considered. A detailed motivation of this choice is reported in Sect. 24.5.2.

Figure 24.6 shows the linear properties extracted by the FNSI method for model orders up to 50. This stabilization diagram leads to the identification of five mode shapes, whose natural frequencies and damping ratios are listed in Table 24.1. The obtained results are therein compared with those estimated by using another state-of-the-art algorithm, i.e. the poly-reference Least-Squares Complex Frequency Domain (p-LSCFD [10]). Furthermore, in Fig. 24.7 the comparison of results is performed by means of the modal assurance criterion (MAC [11]). By considering what is shown we may conclude that the two methods give basically the same results, both in terms of natural frequencies and mode shapes, while a bias error inevitably affects the estimate of the damping ratios. However, a good agreement is found when comparing FRFs synthesized by the FNSI method and those obtained with the H1 estimator (Fig. 24.8).

A second random data set measured at high level (44 N RMS) is then analyzed to detect and locate in the frequency domain the modes triggering nonlinear mechanisms. Since all the considered mode shapes involve to a certain extent the wings' deformation, all the frequencies seem to be affected by nonlinear distortions. To give an example, the deformed shapes of modes 2 and 4 are depicted in Fig. 24.9a, b, respectively.

In Fig. 24.10, the comparison between the low- and high-level FRFs is presented. A softening behavior is clearly visible for all the first three modes, included in the range from 9 to 13 Hz. Modes 4 and 5 represent the most critical configurations in terms of deformed shapes. During the resonance, in fact, the bolted attachments are activated through a combination of wing

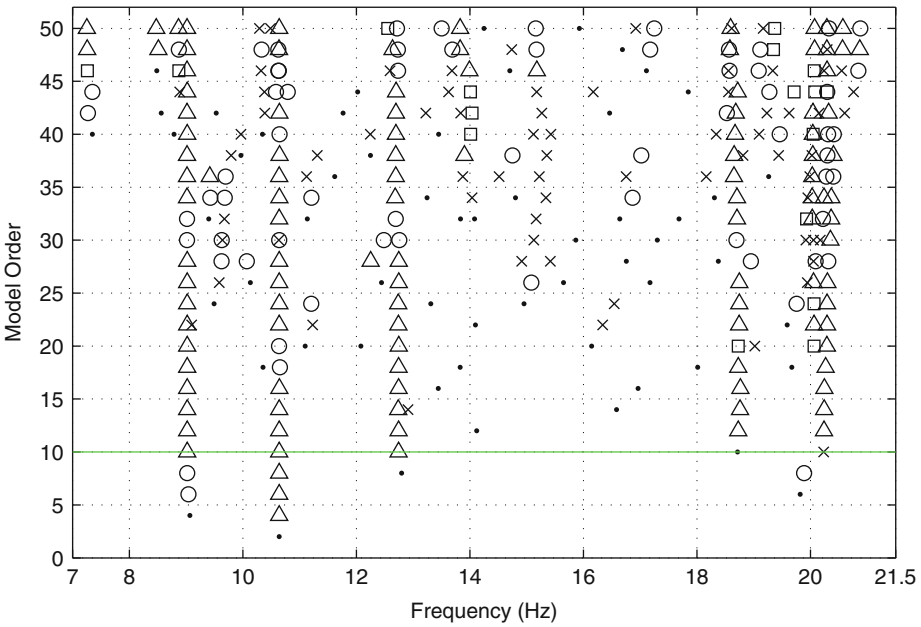

Fig. 24.6 Stabilization diagram computed by the FNSI method at low level (4.4 N RMS). *Dot*: no stabilization in natural frequency; *cross*: stabilization in natural frequency; *square*: extra stabilization in damping ratio; *circle*: extra stabilization in MAC value; *triangle*: full stabilization. Stabilization thresholds for natural frequency, damping ratio and MAC value are 2 %, 10 % and 0.95, respectively. The *green line* indicates the selected model order (Color figure online)

Table 24.1 Comparison between FNSI and p-LSCFD results

	FNSI		p-LSCFD		Discrepancy	
Mode	f_n (Hz)	ζ (%)	f_n (Hz)	ζ (%)	δ_f (%)	δ_ζ(%)
1	9.02	0.29	9.02	0.32	0.00	9.38
2	10.64	0.78	10.64	0.78	0.00	0.00
3	12.75	0.67	12.70	0.56	0.39	19.64
4	18.71	1.34	18.64	2.10	0.38	36.19
5	20.23	0.86	20.11	0.84	0.60	2.38

Estimated natural frequencies (f_n) and damping ratios (ζ) in the 7–21.5 Hz band

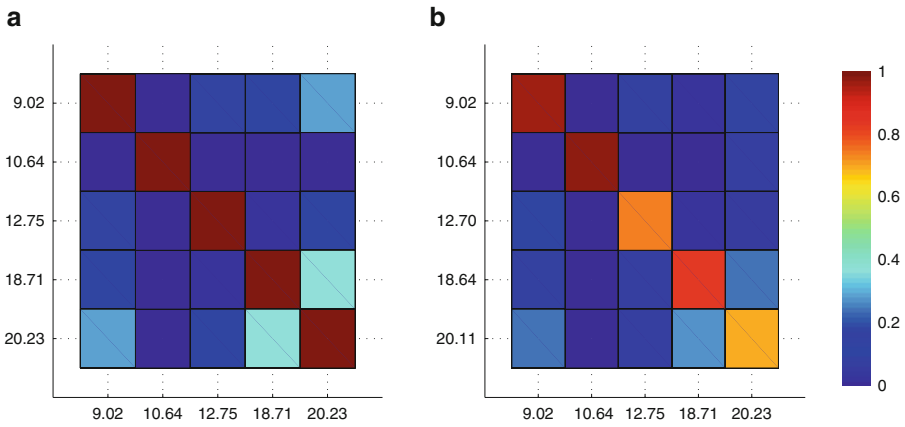

Fig. 24.7 Comparison between FNSI and p-LSCFD results. (**a**) AutoMAC for FNSI method; (**b**) MAC between FNSI and p-LSCFD mode sets (Color figure online)

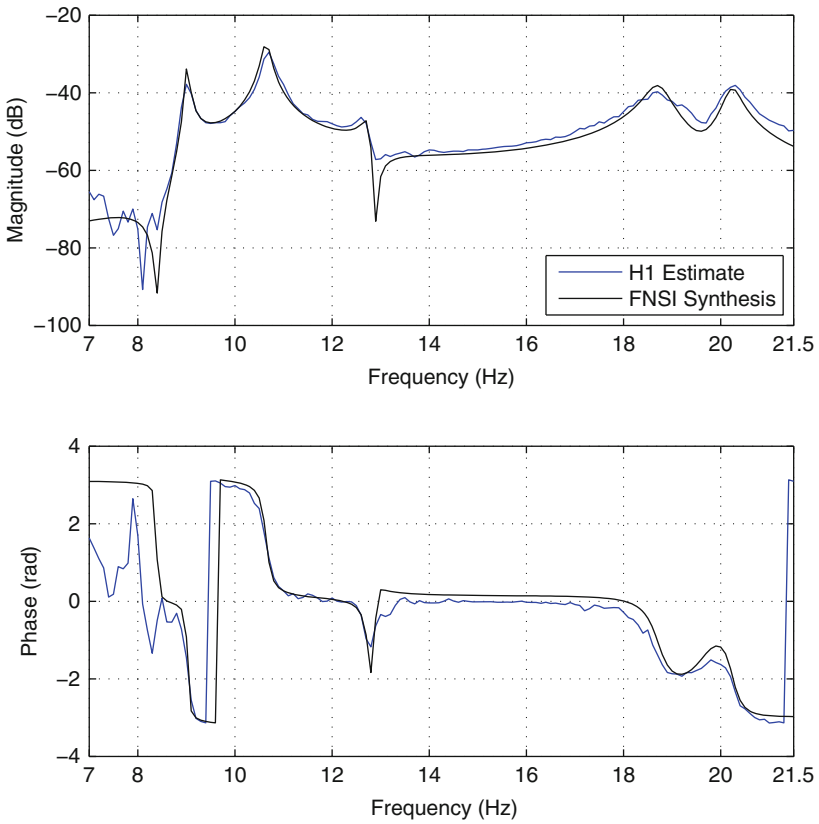

Fig. 24.8 FRF LeReWi:Y/RiIn:Z. Comparison between H1 estimate and FNSI synthesis at low level (4.4 N RMS) (Color figure online)

bending and torsion. As a consequence, the related modal parameters are strongly affected by nonlinear distortions. Since the peak located at 18.7 Hz is more depressed at high level, the interpretation of the nonlinear behavior becomes arduous. However, by looking at the phase plot, one may conclude that the noticeable curve translation is still induced by softening effect. We instead demonstrate in what follows, that this phenomenon can likely to be attributed to loosening in the bolted connections. In fact, even if at high level an overall softening effect has been detected, we later show that some connections can exhibit a combined softening-hardening behavior.

24.5 Nonlinearity Identification at High Level

To obtain a nonlinear subspace model of the aircraft at the high 44 N RMS level, a five-step procedure is followed (see Fig. 24.5). The first step is an appropriate selection of the nonlinear basis functions $\mathbf{h}_{a,b}\left(\mathbf{q}\left(t\right),\dot{\mathbf{q}}\left(t\right)\right)$ defined in Eq. (24.2). The analysis reported in Sect. 24.4 has revealed that the physical phenomena activating the nonlinear behavior of the structure

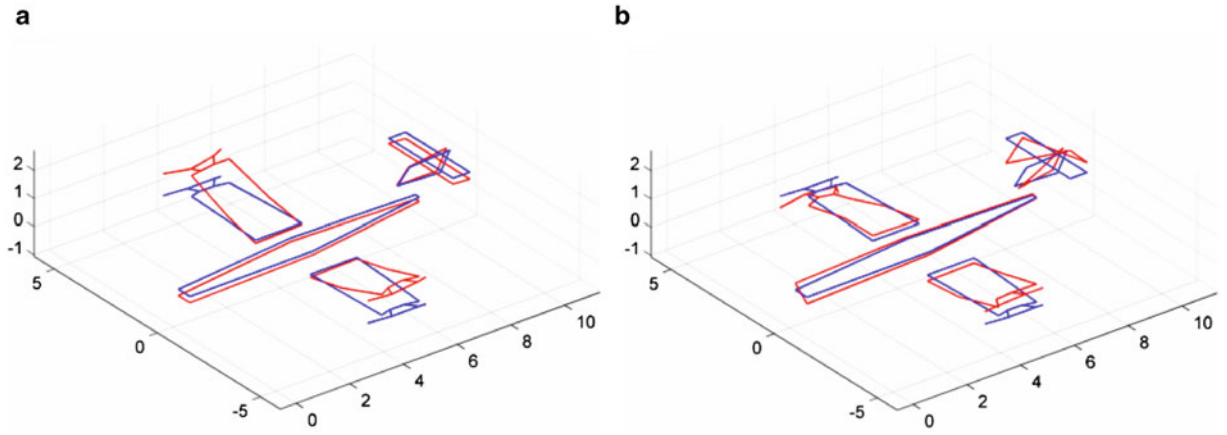

Fig. 24.9 Deformed shapes corresponding to modes 2 and 4 identified at low level (4.4 N RMS). Geometrical dimensions are given in meters. (**a**) Mode 2 (10.64 Hz) and (**b**) mode 4 (18.71 Hz). *Blue* and *red lines* indicate the undeformed and deformed shapes, respectively (Color figure online)

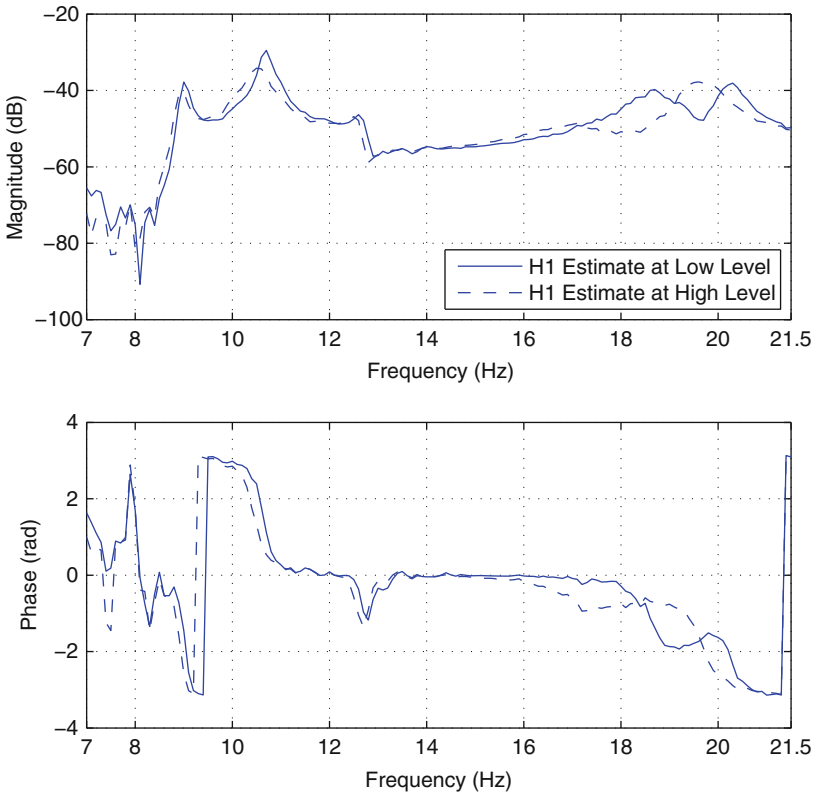

Fig. 24.10 FRF LeReWi:Y/RiIn:Z. Comparison between H1 estimate at low (4.4 N RMS) and high (44 N RMS) levels (Color figure online)

are complex and numerous. Since the aircraft is equipped with four bolted attachments and the acceleration is measured at the two ends along each direction, 24 output channels are candidate to form the right basis functions. In the following section, two useful tools are introduced: (1) cubic splines, that avoid the selection of physics-based functional forms; (2) the comparison approach, that allows for evaluating the influence of the selected basis functions on the retrieved underlying linear properties.

24.5.1 Selection of Appropriate Basis Functions

For the sake of simplicity and without loss of generality, the scope of this section is restricted to an elastic nonlinear restoring force $g(q(t))$ in the single-DOF case. Let q be divided into L segments of arbitrary length and defined by their abscissas, denoted by q_k for $k = 1, \ldots, L+1$. Each abscissa is associated with an ordinate g_k, together defining a knot (q_k, g_k) of the spline. Thus, if q is a displacement value in between knots k and $k+1$, the corresponding point of a cubic-spline-based approximation of $g(q(t))$ is given by [12]

$$\begin{aligned} g(q(t)) = {} & (2t^3 - 3t^2 + 1)\, g_k + (-2t^3 + 3t^2)\, g_{k+1} + (t^3 - 2t^2 + t)(q_{k+1} - q_k)\, g'_k \\ & + (t^3 - t^2)(q_{k+1} - q_k)\, g'_{k+1} \end{aligned} \tag{24.5}$$

where t is the normalised displacement $\frac{q - q_k}{q_{k+1} - q_k}$. The computation of the first derivatives $g'_k = \partial g_k / \partial q_k$ can be achieved by forcing the cubic spline and its first two derivatives to be continuous across each of the interior knots. This results in $L-1$ linear constraint equations

$$\begin{aligned} & \frac{g'_{k-1}}{q_k - q_{k-1}} + 2\left(\frac{1}{q_k - q_{k-1}} + \frac{1}{q_{k+1} - q_k}\right) g'_k + \frac{g'_{k+1}}{q_{k+1} - q_k} \\ & = 3\left(\frac{g_k - g_{k-1}}{(q_k - q_{k-1})^2} + \frac{g_{k+1} - g_k}{(q_{k+1} - q_k)^2}\right). \end{aligned} \tag{24.6}$$

Since the essentially nonlinear restoring force $g(q(t))$ is zero and has zero slope at equilibrium, one should also enforce, in the segment containing the abscissa of the equilibrium point, that

$$\begin{aligned} & (t_0^3 - 2t_0^2 + t_0)(q_{k+1} - q_k)\, g'_k + (t_0^3 - t_0^2)(q_{k+1} - q_k)\, g'_{k+1} \\ & = -(2t_0^3 - 3t_0^2 + 1)\, g_k - (-2t_0^3 + 3t_0^2)\, g_{k+1} \end{aligned} \tag{24.7}$$

and

$$(3t_0^2 - 4t_0 + 1)(q_{k+1} - q_k)\, g'_k + (3t_0^2 - 2t_0)(q_{k+1} - q_k)\, g'_{k+1} = 6(t_0 - t_0^2)(g_k - g_{k+1}) \tag{24.8}$$

where $t_0 = \frac{-q_k}{q_{k+1} - q_k}$. Equations (24.6)–(24.8) constitute $L+1$ relations that uniquely define the $L+1$ parameters $g'_1, \ldots, g'_{L+1}$ as functions of the ordinates of the knots $g_1, \ldots, g_{L+1}$. The first derivatives can thus be substituted in Eq. (24.5) to compute the basis functions associated with the ordinates. These basis functions correspond to the terms $\mathbf{h}_{a,b}(t)$ introduced as additional external forces in the FNSI algorithm, as described in Sect. 24.3.

The optimal number of knots in the definition of the splines should rigorously be sought by minimizing the difference, in some metric, between the predictions of the nonlinear model and measured data. In practice, an acceptable number of knots can be found by a trial and error approach, by maximizing the accuracy of the underlying linear properties of the system, estimated from nonlinear data. However, when a large number of outputs is employed to form the basis functions, the inverse problem becomes difficult to be solved. This is mainly due to the high dimensionality of data matrices involved in the computation. This means that the maximum allowed number of basis functions is inevitably influenced by the size of the data set utilized in the identification.

In this framework, the comparison approach represents a novel strategy, developed to solve the above described problems. The main idea is to single out the minimum number of outputs and the simplest functional forms, which are able to retrieve at high level enough accurate underlying linear properties. The first step is to collect natural frequencies, damping ratios and real mode shapes estimated by the FNSI method at low level. Tolerance thresholds are imposed by the analyst to these three parameters. In particular, the tolerance on natural frequencies is utilized to form the acceptance regions. Of course, the number of these regions has to be equal to the number of the collected natural frequencies. Then, at high level, the outputs that are candidates to form the basis functions have to be combined in a series of scheduled experiments. The underlying linear properties are extracted for all the combinations and for each model order. The obtained solutions are stacked in the acceptance regions and the discarded linear properties are immediately classified as non comparable in natural frequency. At each model order, at least one admitted solution must be found in all the acceptance regions. An ultimate step is needed to reveal the so called comparable model orders, in which the underlying linear properties are retrieved within certain tolerance limits. A graphical tool, that we name comparison diagram, is developed to make simple and effective the visualization of the

comparable model orders and of equivalent solutions. On the x-axis, the natural frequencies are represented, while the model orders are given on the y-axis; horizontal green lines indicate the comparable model orders. As in the case of stabilization diagram, several situations are labeled with different symbols: The dot denotes no equivalence in natural frequency, the cross represents equivalence in natural frequency, the square and the circle stand for extra equivalence in damping ratio and in MAC value, the triangle refers to fully equivalent solutions.

For the investigated aircraft, the modal parameters estimated at low level are collected in Table 24.1. Comparison thresholds for natural frequency, damping ratio and MAC value are set to 1.25 %, 10 % and 0.95, respectively. The motivation of these choices is later discussed in Sect. 24.5.4. We choose to include in each experiment, only one direction for each bolted connection. Thus, employing a full factorial Design of Experiments with four factors (the four attachments) and three levels (the three directions), a table of 81 possible combinations is obtained. With this strategy, only eight of the 24 output channels related to the bolted connections have to be included in the FNSI routine. By the comparison approach, it is found that splines with five knots on relative displacements are the simplest functional forms able to suitably capture the physical mechanisms activating the nonlinear phenomena. It is worth to here stress the reduced dimensionality of the consequent inverse problem, that encompasses 20 basis functions, two external forces, 32 outputs for the aircraft main body and eight outputs for the bolted connections.

24.5.2 Choice of the Processed Bandwidth

As anticipated in Sect. 24.4, the bandwidth processed for the identification ranges from 7 to 21.5 Hz. This choice is principally made for reducing the computational burden. In fact, the dimensionality reduction operated through the comparison approach may become not sufficient when the FNSI method has to deal with a considerable number of basis functions. The restriction of the bandwidth is helpful for avoiding memory issues, even if does not allow for preserving the nonlinear distortions usually appearing outside the whole band of excitation (from 7 to 45 Hz). Owing to this dimensionality, time-domain identification techniques, as, in particular, the subspace method proposed in [5], are likely to suffer from computational memory issues, because of their inability to reject less informative measured samples. Moreover, few methods in the technical literature are capable of reliably handling a large amount of nonlinear coefficients. For instance,the conditioned reverse path method [13] estimates the coefficients sequentially, i.e. errors are accumulated throughout the identification process, and would probably lead to very large errors in the present case study. Another example is the nonlinear identification through feedback of the outputs method [9], whose estimation accuracy is known to decrease rapidly as the number of parameters increases.

24.5.3 Determination of the Model Order

The third step in Fig. 24.5 is the determination of the model order. One can notice that, here, the information about the poles' stabilization may become ambiguous and difficult to be interpreted (Fig. 24.11). In modal analysis, the stabilization diagram is often used to assist the analyst in separating the physical system poles from the mathematical ones. Since the linear identification has been accomplished at low level, the correct physical poles have been already collected. This means that in the comparison diagram the spurious poles are a priori discarded, since they are classified as non comparable in natural frequency at the beginning of the analysis. On the contrary, the stabilization diagram may lead to the selection of stable, but not comparable underlying linear properties. These considerations remark the importance of the proposed strategy, in which the comparison approach represents a useful methodology that allows for: (1) refining the localization of nonlinearities, and (2) revealing the presence of comparable model orders.

24.5.4 Estimation of the Underlying Linear Properties

In Fig. 24.12 we show the comparison diagram corresponding to the experiment that involves the outputs denoted as RiReBC:Z, RiFrBC:Z, LeReBC:Y and LeFrBC:X. Three consecutive model orders, i.e. the 42, 44 and 46, are found to be comparable. An extra equivalence in the MAC value is evident only for the first mode. Depending on the chosen model order, the damping ratio may result comparable on the third or on the second mode. Of course, these outcomes are absolutely dependent on the imposed tolerance limits. We stress that the comparison approach is really sensitive to tolerance fixed on

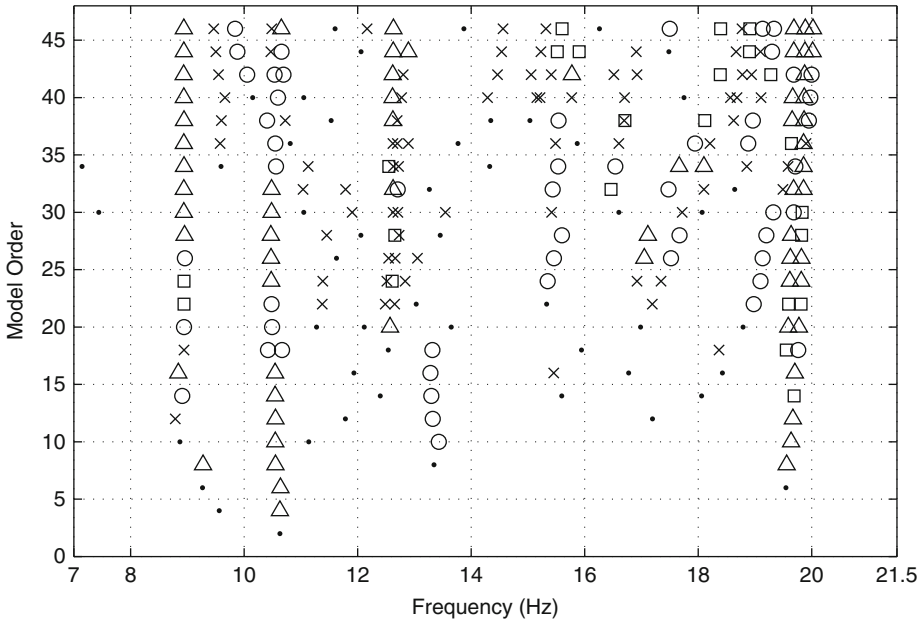

Fig. 24.11 Stabilization diagram computed by the FNSI method at high level (44 N RMS). *Dot*, *crosses*, *squares*, *circles* and *triangles* are defined similarly to Fig. 24.6

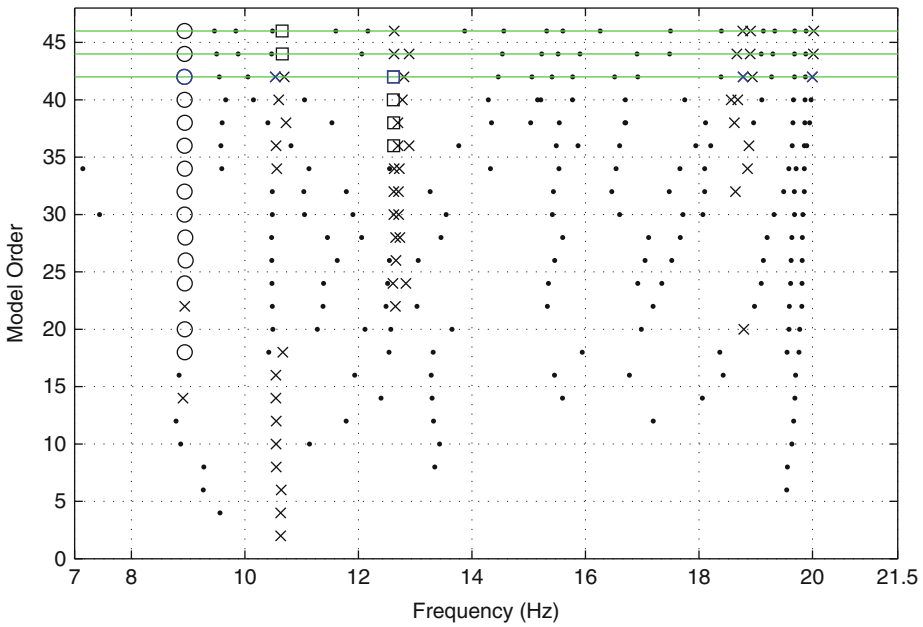

Fig. 24.12 Comparison diagram computed at high level (44 N RMS). Splines with five knots on relative displacements of the outputs denoted as RiReBC:Z, RiFrBC:Z, LeReBC:Y and LeFrBC:X are included in the FNSI routine. *Dot*: no equivalence in natural frequency; *cross*: equivalence in natural frequency; *square*: extra equivalence in damping ratio; *circle*: extra equivalence in MAC value; *triangle*: full equivalence. Comparison thresholds for natural frequency, damping ratio and MAC value are 1.25 %, 10 % and 0.95, respectively. The *green lines* are the comparable model orders and the *blue marks* indicate the selected system poles (Color figure online)

the natural frequencies, mainly owing to the construction of the acceptance regions. Obviously, the larger are these regions, the higher is the chance of finding comparable model orders. On the opposite, using strict tolerance values leads to the estimate of more accurate underlying linear properties. Moving from these considerations, the analyst is suggested to set the comparison thresholds according to the application. In Fig. 24.10 a small shift can be noticed for the first 3 peaks of the FRF estimated at high level. This means that, for the present investigation, the adoption of severe tolerance limits is strongly recommended.

The FRF LeReWi:Y/RiIn:Z synthesized by the FNSI at model order 42 is depicted in Fig. 24.13. When compared to the synthesis obtained at low level, many additional peaks are now visible, which corresponds to the numerous spurious poles present at this model order. Due to the extra equivalence on the damping ratio, a good agreement is observable only at the third resonant frequency (12.75 Hz). A useful way to improve this result is presented in Sect. 24.6.

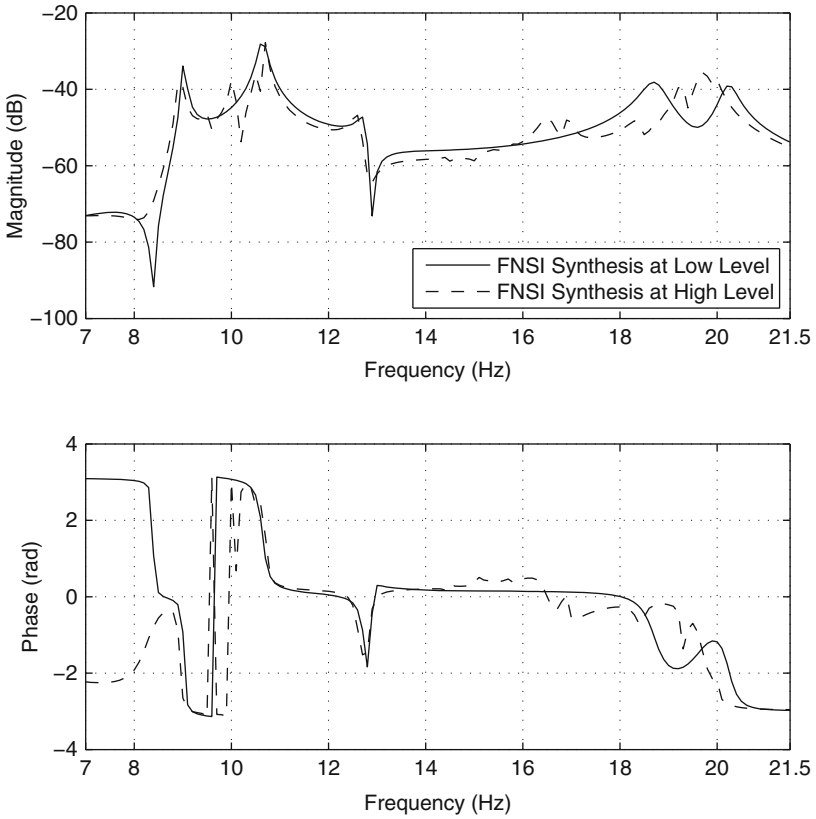

Fig. 24.13 FRF LeReWi:Y/RiIn:Z. Comparison between FNSI synthesis at low (4.4 N RMS) and high (44 N RMS) levels

Table 24.2 Ratio between averaged real and imaginary parts in logarithmic scaling

Location	Coefficient 1	Coefficient 2	Coefficient 3	Coefficient 4	Coefficient 5
RiReBC:Z	0.16	−0.10	0.92	0.33	0.08
RiFrBC:Z	1.84	0.80	1.38	1.33	1.02
LeReBC:Y	0.16	−0.90	1.70	−0.42	0.98
LeFrBC:X	0.87	−0.38	0.02	−0.71	−1.10

The estimate is performed in the 13–14 Hz band

24.5.5 Estimation of the Nonlinear Coefficients

With the last step in Fig. 24.5, the state-space model is converted to the physical space, in order to visualize the restoring forces, fitted by using cubic splines. To this end, the conversion scheme detailed in [6] is utilized. As a result, the nonlinear coefficients identified from the extended FRF matrix $\mathbf{H}_e(\omega)$ are spectral quantities, i.e. are complex-valued and frequency-dependent. A reliable identification, together with an appropriate selection of the basis functions, should make the imaginary parts much smaller than the corresponding real parts. The coefficients' frequency dependence should also remain small. These indications are usually utilized as criteria for the quality assessment of the estimated nonlinear parameters. In Fig. 24.14, we illustrate the real and the imaginary parts of the complex-valued coefficients related to the output LeFrBC:X, whose estimation results to be that more affected by errors. The variations along the frequency axis are located at the same positions of the selected modal parameters. As one can clearly observe, on both the curves the spurious poles give rise to sharpest peaks, in turn, heavily affecting the average values of the estimated coefficients. To mitigate this effect, the frequency range for the conversion is restricted to the flat zone ranging from 13 to 14 Hz (Fig. 24.14). In this range, the ratios between the averaged real and imaginary parts are computed, actually revealing the output LeFrBC:X as the worst estimated among the four of the experiment (see the fourth row of Table 24.2). This result is even improved in the next section (Sect. 24.6), by using an appropriate strategy specifically designed for removing the spurious poles.

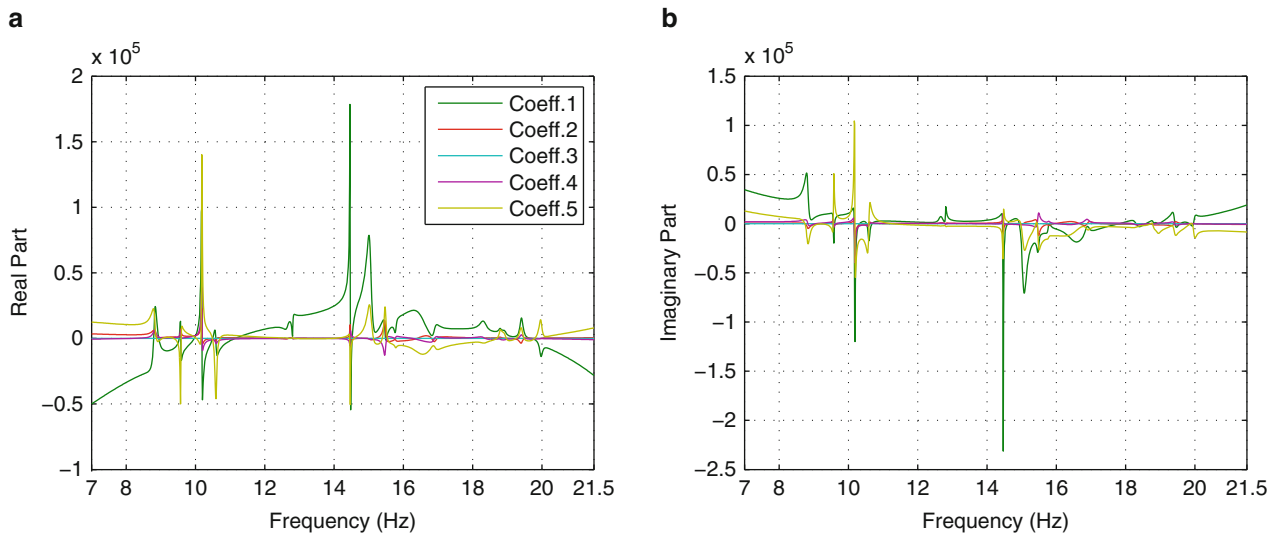

Fig. 24.14 Complex-valued estimates of the five nonlinear coefficients related to the output LeFrBC:X in the full bandwidth (7–21.5 Hz) (Color figure online)

24.6 Proposed Strategy for Removing Spurious Poles and Improved Results

The presence of the spurious poles can be attributed to many different causes, e.g. noise on the data, modeling errors, computational issues, etc. Classical subspace methods do not provide the user with the possibility of selecting poles computed at a given model order, not allowing for discarding the spurious ones. In the usual procedure, in fact, all the poles have to be included. To avoid this drawback, an appropriate novel strategy is employed for removing the spurious poles. In the first part of the FNSI method, the underlying linear properties are directly computed from the continuous state and output matrices $\mathbf{A}_c \in \mathbb{R}^{2n\times 2n}$ and $\mathbf{C} \in \mathbb{R}^{l\times 2n}$. Then, the discrete extended input and direct feedthrough matrices $\mathbf{B}_d^e \in \mathbb{R}^{2n\times(m+s)}$ and $\mathbf{D}^e \in \mathbb{R}^{l\times(m+s)}$ are calculated by defining the transfer function matrix $\mathbf{G}_s(k)$ associated with the state-space model

$$\mathbf{G}_s(k) = \mathbf{C}\left(z_k\mathbf{I}^{n\times n} - \mathbf{A}_d\right)^{-1}\mathbf{B}_d^e + \mathbf{D}^e \tag{24.9}$$

and minimizing the weighted difference between the measured and modeled output spectra in a linear least-squares sense

$$\mathbf{B}_d^e, \mathbf{D}^e = \arg\min \sum_{k=1}^{F} \mathbf{W}^2(k)\left|\mathbf{Y}(k) - \mathbf{H}_e(k)\,\mathbf{E}(k)\right|^2 \tag{24.10}$$

where $z_k = \mathrm{e}^{\mathrm{j}2\pi k/\mathrm{N}}$ is the Z-transform variable for discrete-time models, $\mathbf{W}(k)$ is a real-valued weighting function, $\mathbf{Y}(k)$ and $\mathbf{E}(k)$ represent the output spectra and the extended input vector, F denotes the number of frequency samples, the subscripts c and d refer to continuous and discrete time models, while l and m indicate the number of outputs and the number of inputs involved in the identification, respectively. The continuous-time state-space matrices can be converted in discrete-time form by means of the following relations, considering a sampling frequency f_s

$$\mathbf{A}_d = \mathrm{expm}\left(\mathbf{A}_c/f_s\right) \qquad \mathbf{B}_d^e = \left(\mathrm{expm}\left(\mathbf{A}_c/f_s\right) - \mathbf{I}^{2n\times 2n}\right)\mathbf{A}_c^{-1}\mathbf{B}_c^e \tag{24.11}$$

where expm indicates the matrix exponential. The employed procedure for the removal of spurious poles consists in the reduction of the dimensionality of the state-space matrices. From the eigenvalue decomposition of $\mathbf{A}_c$ the poles of the system and the eigenvectors are collected in $\mathbf{\Lambda}_c \in \mathbb{C}^{2n\times 2n}$ and $\mathbf{V} \in \mathbb{C}^{2n\times 2n}$, respectively. Once n_p poles are selected by the analyst, the corresponding diagonal terms in $\mathbf{\Lambda}_c$ are extracted and a reduced matrix of system poles is obtained $\bar{\mathbf{\Lambda}}_c \in \mathbb{C}^{2n_r\times 2n_r}$ ($n_r = 2\cdot n_p$). The same procedure of extraction is repeated on the columns of $\mathbf{V}$, leading to $\bar{\mathbf{V}} \in \mathbb{C}^{2n\times 2n_r}$. The reduced output matrix $\bar{\mathbf{C}} \in \mathbb{C}^{l\times 2n_r}$ is, thus, calculated in modal coordinates

$$\bar{\mathbf{C}} = \mathbf{C}\bar{\mathbf{V}} \tag{24.12}$$

and the following Eq. (24.13) is utilized to replace Eq. (24.9) in the minimization problem, in order to derive the $\bar{\mathbf{B}}_d^e$ and $\mathbf{D}^e$ matrices

$$\mathbf{G}_s(k) = \bar{\mathbf{C}}\left(z_k\mathbf{I}^{n\times n} - \bar{\mathbf{\Lambda}}_d\right)^{-1}\bar{\mathbf{B}}_d^e + \mathbf{D}^e. \tag{24.13}$$

The array $\bar{\mathbf{B}}_d^e \in \mathbb{C}^{2n_r\times(m+s)}$ is the discrete extended input matrix represented in modal coordinates. We comment that for converting $\bar{\mathbf{\Lambda}}_c$ and $\bar{\mathbf{B}}_d^e$ to discrete and continuous time forms the same relations holding for $\mathbf{A}_c$ and $\mathbf{B}_d^e$ (Eq. (24.11)) can be employed, respectively. Finally, the extended FRF matrix $\mathbf{H}_e(\omega)$ is estimated and the typical scheme for conversion to the physical space can be applied to retrieve the nonlinear coefficients.

In the comparison diagram of Fig. 24.12 the blue marks indicate the selected system poles at model order 42. In Table 24.3, the linear properties identified at low level (see Sect. 24.4), together with the associated frequencies estimated at high level are reported. As one can see, the error values are respectful of the imposed comparison thresholds and this means that, since strict tolerances can be fixed on natural frequencies, a consequent matching is found between estimates at low and high levels. Differently, the overall estimate of damping ratios is less satisfactory. The damping ratios that present higher discrepancies are those corresponding to modes 4 and 5. Probably, this fact may be related to the activation of nonlinear phenomena involving damping forces. This behavior, already singled out during the detection step, is further stressed and put in evidence by the comparison diagram. In fact, the last region ranging from 17 to 21 Hz is very confused and really affected by the presence of not comparable solutions. We even comment that the splines utilized in the present identification are not able to capture this kind of behavior, being solely defined on the relative displacement. Future investigations will be made in this direction.

The results presented in Table 24.3 have a direct influence on the synthesis of FRFs. The same FRF described in the previous section (Sect. 24.5), i.e. the one of output LeReWi:Y/RiIn:Z, is depicted in Fig. 24.15, where five distinct peaks are now clearly visible also at high level. Due to a more reliable estimate of the damping ratio, a good agreement is confirmed for the third mode, and a relevant improvement is also achieved in the cases of the first two frequencies, as evidenced by the phase plot. Again by inspecting the comparison between FRF syntheses, we may conclude that mode 4 and 5 are the most distorted and, as expected, a huge discrepancy is observed in the magnitude plot.

Again, the last step is the conversion of the reduced state-space model to the physical space. In Fig. 24.16 the complex-valued coefficients estimated by the FNSI method in the whole frequency bandwidth are represented. With respect to Fig. 24.14 the diagram appears highly improved. The sharpness of the peaks is now mitigated both for the real and the imaginary parts. Extremely interesting results are obtained by performing the estimate in the frequency range from 15 to 16.5 Hz (see Table 24.4), where the ratio between the averaged real and imaginary parts, in log scale, are now positive for all the coefficients, meaning that, finally, a good estimate has been accomplished. We comment that the trend of the estimated nonlinear restoring forces is consistent with the nature of the bolted connections (see Fig. 24.17). In fact, a combined softening-hardening behavior can be observed for RiReBC:Z, RiFrBC:Z and LeReBC:Y, while in the case of output LeFrBC:X, a simple softening effect is found out. It is worth to stress that due the high stiffness, the nonlinear behavior of bolted connections is activated in the very small scale of relative displacements (10^{-2} mm). Moreover, a high density of points is present inside the softening region ($\pm 3\cdot 10^{-2}$ mm), that may probably explain the overall softening behavior observed in the detection step (Sect. 24.4), and that can now certainly considered imputable to loosening in the attachments.

Table 24.3 Comparison between FNSI estimates at low and high levels

	FNSI at low level		FNSI at high level		Error	
Mode	f_n (Hz)	ζ (%)	f_n (Hz)	ζ (%)	ϵ_f (%)	ϵ_ζ(%)
1	9.02	0.29	8.94	0.42	0.89	44.83
2	10.64	0.78	10.54	0.50	0.94	35.90
3	12.75	0.67	12.62	0.72	1.02	7.46
4	18.71	1.34	18.78	0.16	0.37	88.06
5	20.23	0.86	20.00	0.20	1.14	76.74

Estimated natural frequencies (f_n) and damping ratios (ζ) in the 7–21.5 Hz band. The fourth and the fifth columns refers to underlying linear properties selected in Fig. 24.12

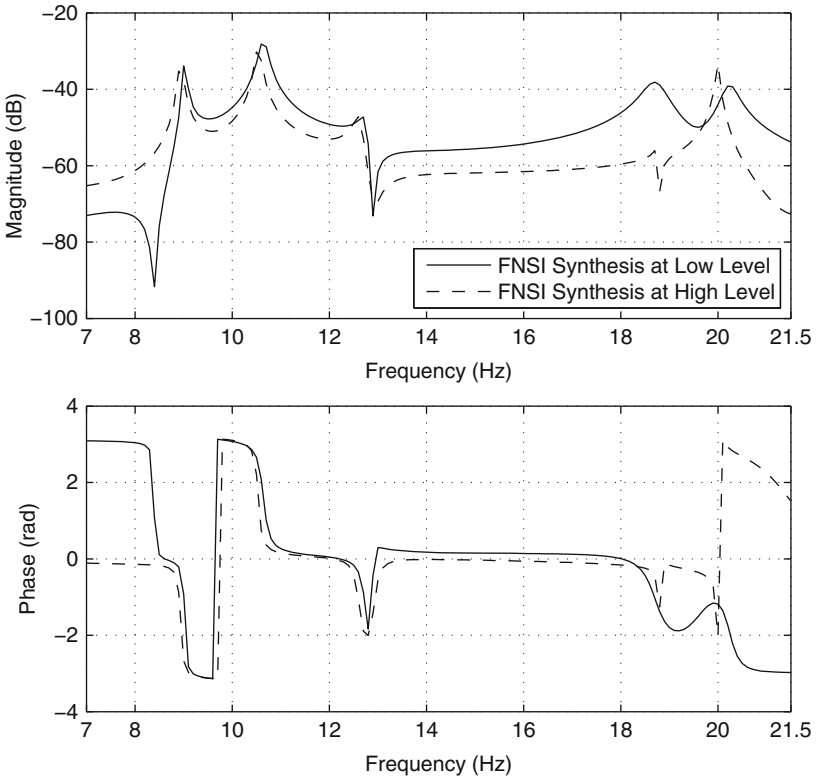

Fig. 24.15 Improved FRF LeReWi:Y/RiIn:Z. Comparison between FNSI synthesis at low (4.4 N RMS) and high (44 N RMS) levels. The selected poles are depicted in Fig. 24.12

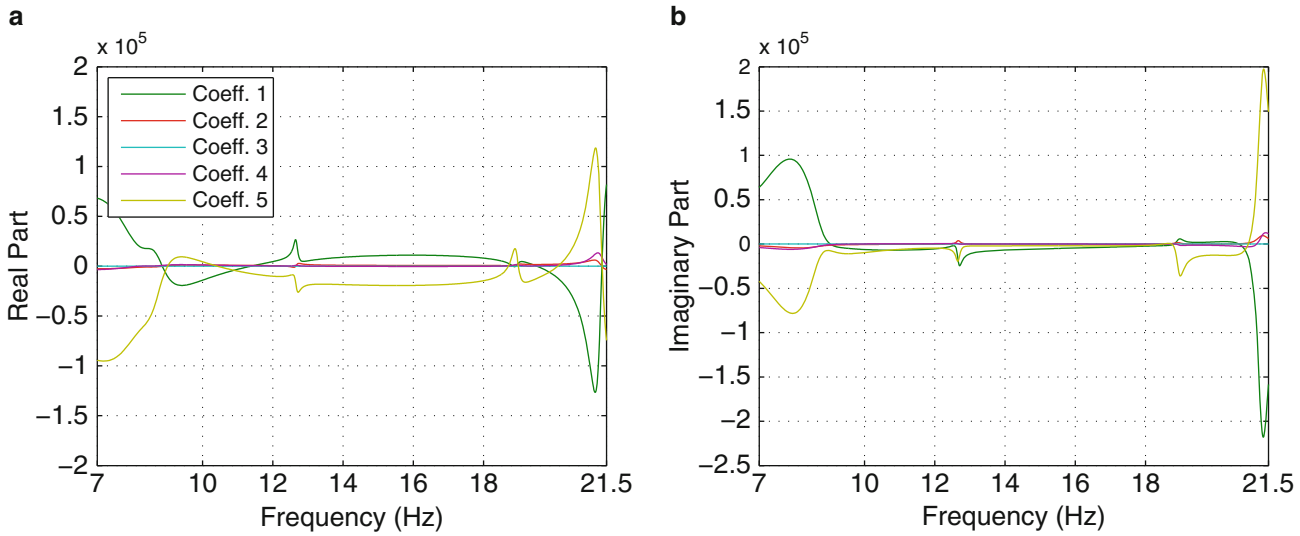

Fig. 24.16 Improved complex-valued estimates of the five nonlinear coefficients related to the output LeFrBC:X in the full bandwidth (7–21.5 Hz). The selected poles are depicted in Fig. 24.12 (Color figure online)

Table 24.4 Improved ratio between averaged real and imaginary parts in logarithmic scaling

Location	Coefficient 1	Coefficient 2	Coefficient 3	Coefficient 4	Coefficient 5
RiReBC:Z	0.96	1.72	1.94	1.68	0.95
RiFrBC:Z	0.98	1.68	1.25	1.78	1.05
LeReBC:Y	0.52	0.85	0.57	1.06	0.08
LeFrBC:X	0.36	1.00	0.40	1.64	0.97

The estimate is performed in the 15–16.5 Hz band. The selected poles are depicted in Fig. 24.12

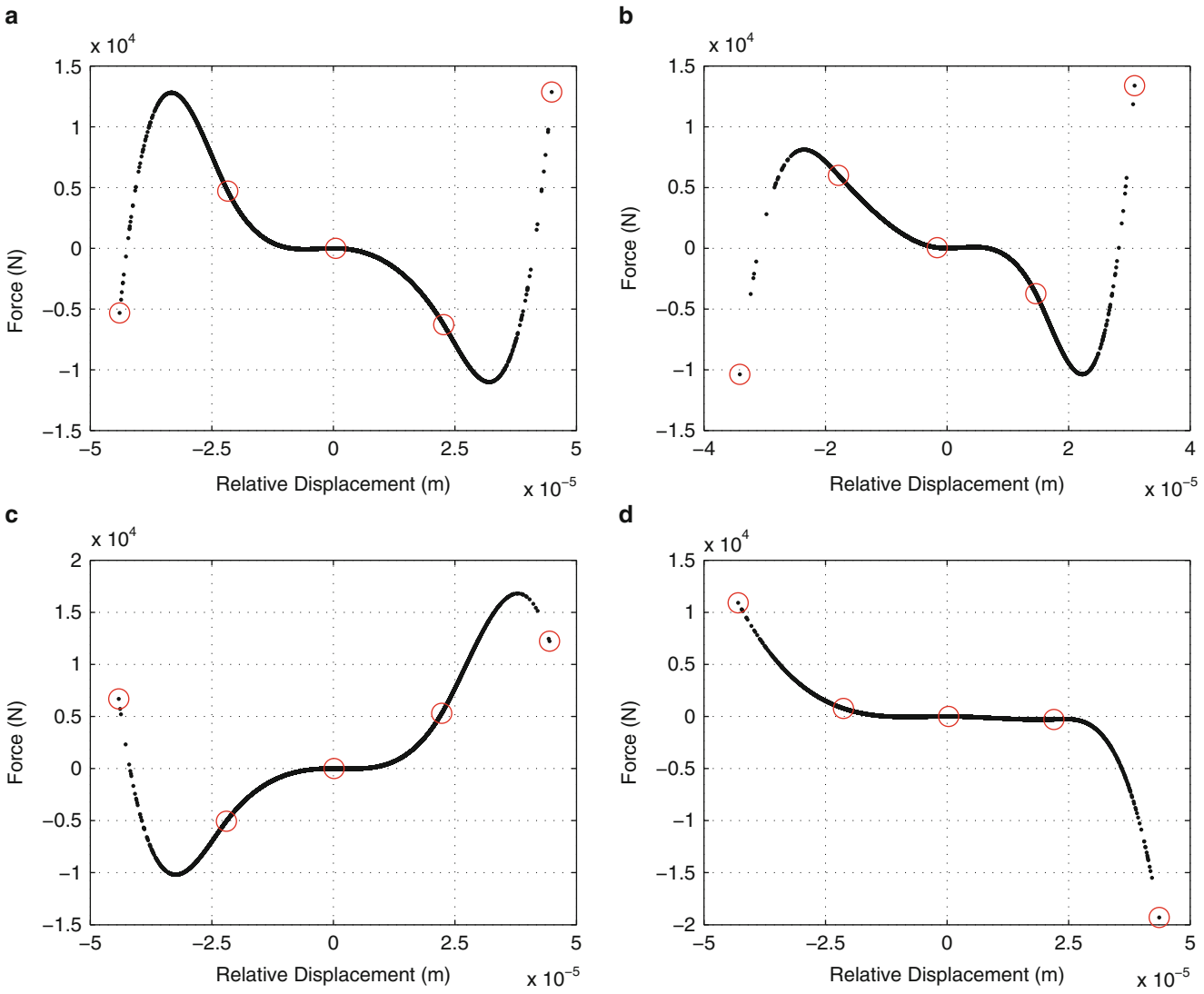

Fig. 24.17 Improved nonlinear stiffness curves reconstructed at high level (44 N RMS) at different output locations. *Red circles* localise the five chosen knots of the splines. The selected poles are depicted in Fig. 24.12. (**a**) RiReBC:Z. (**b**) RiFrBC:Z. (**c**) LeReBC:Y. (**d**) LeFrBC:X (Color figure online)

24.7 Conclusions

In the presented research, new tools and strategies have been implemented in the FNSI methodology to tackle the experimental identification of a full-scale aircraft, affected by the presence of many nonlinearities. The strength of the proposed comparison approach consists in the possibility of reducing the dimensionality of the inverse problem, avoiding the memory issues that may arise when large data sets are employed. On the other hand, the nonlinear identification can be carried out without loosing relevant information that might be related to the not included outputs. In addition, this strategy can be utilized to evaluate the capability of the chosen basis functions of encompassing the activated nonlinear phenomena. In this context, the limits of the stabilization analysis have been exploited at high level. A new visualization tool, named comparison diagram, is used to reveal the existence of comparable model orders in which the underlying linear properties are recovered within certain tolerance limits. At high level, cubic splines with five knots on the relative displacement, related to the selected outputs, are included in the FNSI routine. An improved agreement is found when comparing FRFs synthesized at low and high levels, after a novel procedure for spurious poles' removal is applied. In the end, the estimated nonlinear restoring forces have proved to be consistent with the nature of the bolted connections. Despite the fact that an overall softening behavior has been observed in the detection step, the estimates have revealed an additional combined softening-hardening behavior,

that is certainly imputable to loosening in the attachments. A less satisfying agreement is found out on estimates of damping ratios at high level, that may be probably related to the activation of nonlinear phenomena involving the damping forces. In the present study splines on velocity were not considered, but this will be the focus of our future investigations. More over, to refine the achieved results effort will be spent for improving the proposed novel tools and procedures.

Acknowledgements The author J.P. Noël is a Postdoctoral Researcher of the *Fonds de la Recherche Scientifique – FNRS* which is gratefully acknowledged. The author G. De Filippis attends his Ph.D. course at Politecnico di Bari, with scholarship funded, through the PON `01_02380`, by the Ministry of Education, University, and Research, which is even gratefully acknowledged.

References

1. Ahlquist JR, Carreño JM, Climent H, de Diego R, de Alba J (2011) Assessment of nonlinear structural response in A400M GVT. In: Proulx (ed) Structural dynamics, vol 3. Springer, New York, pp 1147–1155
2. Carrella A, Ewins D (2011) Identifying and quantifying structural nonlinearities in engineering applications from measured frequency response functions. Mech Syst Signal Process 25(3):1011–1027
3. Noël J-P, Renson L, Kerschen G, Peeters B, Manzato S, Debille J (2013) Nonlinear dynamic analysis of an F-16 aircraft using GVT data. In: Proceedings of the international forum on aeroelasticity and structural dynamics
4. Van Overschee P, De Moor B (1996) Subspace identification for linear systems: theory, implementation and applications. Kluwer Academic Publishers, Dordrecht
5. Marchesiello S, Garibaldi L (2008) A time domain approach for identifying nonlinear vibrating structures by subspace methods. Mech Syst Signal Process 22:81–101
6. Noël J, Kerschen G (2013) Frequency-domain subspace identification for nonlinear mechanical systems. Mech Syst Signal Process 40:701–717
7. Noël J, Kerschen G, Foltête E, Cogan S (2014) Grey-box identification of a non-linear solar array structure using cubic splines. Int J Non-linear Mech 67(0):106–119
8. Noël J, Marchesiello S, Kerschen G (2014) Subspace-based identification of a nonlinear spacecraft in the time and frequency domains. Mech Syst Signal Process 43:217–236
9. Adams D, Allemang R (2000) A frequency domain method for estimating the parameters of a non-linear structural dynamic model through feedback. Mech Syst Signal Process 14:637–656
10. Peeters B, Van der Auweraer H, Guillaume P, Leuridan J (2004) The PolyMAX frequency-domain method: a new standard for modal parameter estimation? Shock Vib 11(3–4):395–409
11. Heylen W, Lammens S, Sas P (2007) Modal Analysis theory and testing. Katholieke Universteit Leuven, Departement Werktuigkunde, Leuven
12. De Boor C (1978) A practical guide to splines. Springer, New York
13. Richards C, Singh R (1998) Identification of multi-degree-of-freedom non-linear systems under random excitations by the “reverse path” spectral method. J Sound Vib 213(4):673–708

Chapter 25
Non linear Finite Element Model Validation of a Lap-Joint

A. delli Carri and D. Di Maio

Abstract It is commonly accepted that bolted structures can present nonlinearities caused by contact conditions, and that these are severely exercised for large vibration amplitudes. Several researches have targeted these joints' nonlinear behaviour and experimental model validations have demonstrated to be successful.

An earlier publication of the authors demonstrates that nonlinearities identified in modal space can be correlated with the same ones identified in the physical space using the reverse path method. A dumbbell test rig was designed and manufactured so as to have two lap joints connecting the two weights placed at either ends of the bolted beam. The test structure was modelled by both two degrees of freedom lump parameter model and Finite Element. The nonlinearities were identified in the first stage of this research work and validated by using a simple spring mass model.

The objective of this paper is to show how to model the nonlinear dynamics of the dumbbell test structure using a standard FE package. The validated nonlinear characteristics of the lap-joint will be modelled in the FE environment and prediction of nonlinear responses will be correlated with the experimental ones.

Keywords Nonlinearities • Modal testing • Experimental data • Model updating • Lap-joint

25.1 Introduction

The coupling between components is commonly achieved by joining two components together. A tight connection is built by two components (or more) and both structures will share a common area of contact. Bolted joints are the most common ones in engineering and, for example, looking at engine aircraft casings several bolted joints are used for achieving seal tight conditions between the two casing components. From an Finite Element Analysis (FEA) perspective, joints can be modelled, and often are, as springs connecting two components; this way preserving the flexibility of the joint itself. Instead, the modelling of the contact conditions is seldom performed because challenging and very time consuming. Many FEA solvers are still based on time step integration analysis. An attempt of modelling the contact interface between two simple bolted flanges was performed in [1] with very interesting results. The predictive FE capability available for that project allowed a rapid prediction of forced responses. However, an important requirement had to be satisfied in order to model and predict correctly forced responses and that was the actual area in contact between the two components' surfaces. So, joint modelling is difficult despite the simplicity of this mechanical component such as a bolt and a nut. Recent literature presented advanced modelling of joints but also alternative ways (to time integration) of predicting responses. Some of the most recent ones are available in [2–10]. It is clear from those readings that the equations describing joints' models are not that simple (nor trivial) and that FEA seems to be still far in the background because of the expensive computational cost.

Writing this article the authors decided to question themselves on this: "Would it be possible to identify an adequate number of nonlinear terms and use those for FE modelling so as to predict, in its simplest form, a nonlinear forced response of a lap-joint?". In fact, the experimental model validation reported in [1] showed that FE modelling can be done but at a cost of defining the correct contact surface between the two assemblies. Keeping in mind that these conditions are not easily to satisfy then this research work initiated by looking at the dynamics of a lap-joint in dumbbell test configuration [11]. The experimental approach was based on the identification of the nonlinearity by using Reverse Path method. This is not a new technique and, in fact, it is possible to read about recent works carried out by other authors in [12–14]. However, the novelty in [11] was to bridge two domains, such as the modal and the physical space. This paper aims to start from this latter finding and explore how to use identified nonlinear terms within an FEA environment. Therefore, experimentalist must never lose

A. delli Carri • D. Di Maio (✉)
University of Bristol, Bristol, UK
e-mail: dario.dimaio@bristol.ac.uk

G. Kerschen (ed.), *Nonlinear Dynamics, Volume 1*, Conference Proceedings of the Society for Experimental Mechanics Series, DOI 10.1007/978-3-319-15221-9_25

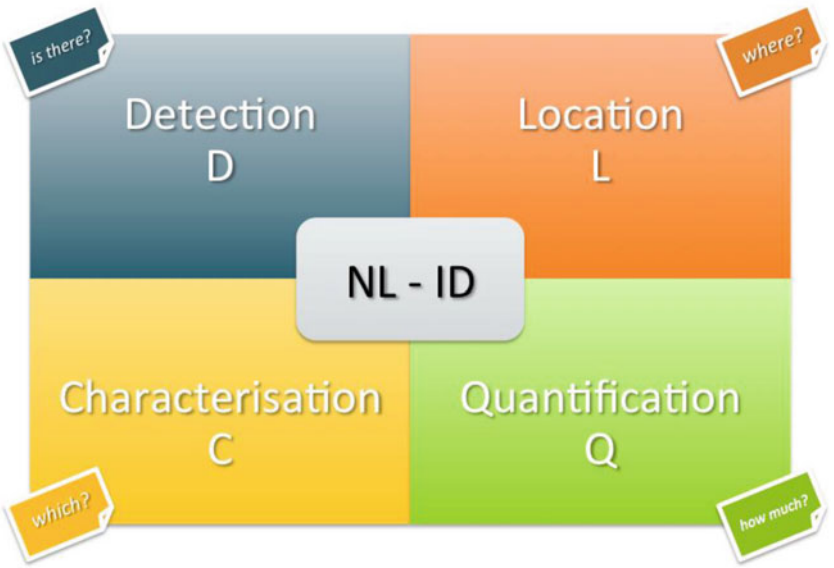

Fig. 25.1 The modular approach in physical space

sight of the ultimate purpose of their analysis: to build a mathematical model able to describe the complex dynamics behind the nonlinear structure. For this purpose, the nonlinear elements identified in the physical space are far easier to implement in an FE model, which is the industry standard for a mathematical representation of structures.

During the last years, many methods have been developed in order to get more insights into the rich dynamics of a nonlinear system, but they can be categorised into two main branches:

- Modal space approaches
- Physical space approaches.

The modal space methods usually exploit the concept that a system can still be decomposed into its modal components, although giving up all those properties that made this approach appealing in the first place – like superposition and homogeneity – and the arise of issues like modal interactions. On the other side, the methods that exploit the physical space of a system have the clear advantage to retain all the information about the physical locations of the nonlinear elements, while describing such elements with mathematical laws that could be eventually implemented in lumped parameters models or FEM. The downside of these methods is that they often lead to intensive computations and the need for a thorough way to validate their estimations.

For clarity, both modal and physical space go by acquisition of physical quantities, such as vibrations, at specific location on a test structure.

The physical space approach has also the capability to deal with nonlinearities in a modular fashion, not seeking for a jack-of-all-trades, monolithic algorithm but relying on a toolbox of different methods, each of which capable of answering to one or more of the four main questions about the nonlinear elements (Fig. 25.1):

- Is there nonlinear behaviour? (**D**etection)
- What kind of nonlinearity? (**C**haracterisation)
- Where are the nonlinear elements located? (**L**ocation)
- How strong are these nonlinearities? (**Q**uantification)

In the last 2 years, the authors have conducted a thorough review of the available methods and algorithms for nonlinear modal testing [15, 16] and while all of them are founded on a solid mathematical basis, only few of them could actually cope with the hurdles of an experimental environment.

While it is usually straightforward to assess that a structure under test experiences some degree of nonlinear behaviour (e.g. by looking at distortions in FRFs) it is much harder to locate the source of the nonlinearity and its functional form. The Reverse Path method has been proven to be a valuable tool for location and characterisation, requiring just a standard broadband test. Once the locations and functional forms of the nonlinearities have been assessed, the only unknowns left are the coefficients (i.e. the "strengths") of those nonlinearities. Towards this end, one can use the recently developed Frequency Nonlinear Subspace Identification method [17] or – once developed a nonlinear model – rely on standard updating techniques.

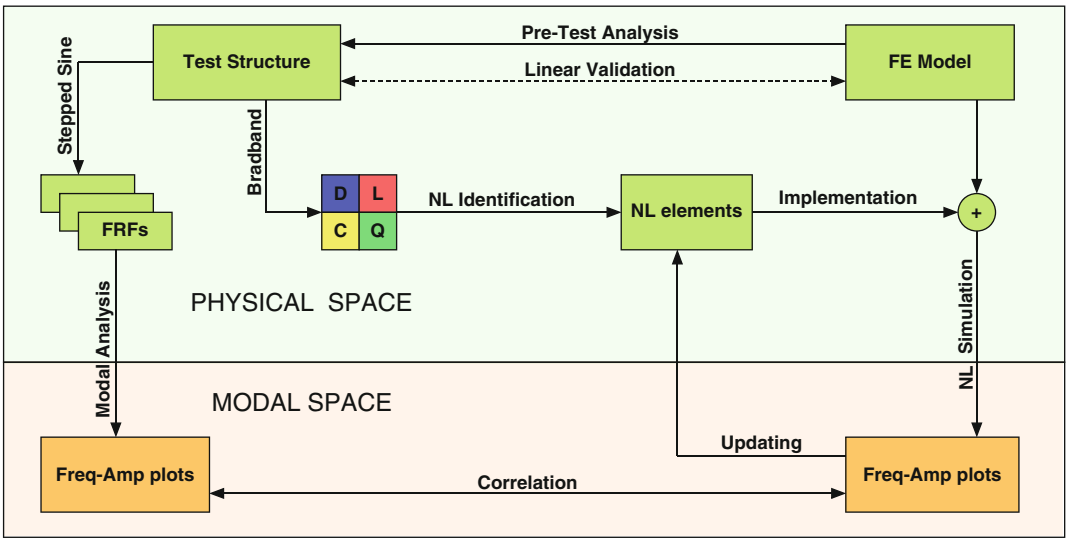

Fig. 25.2 Flowchart of the procedure followed in this paper

Fig. 25.3 Test structure

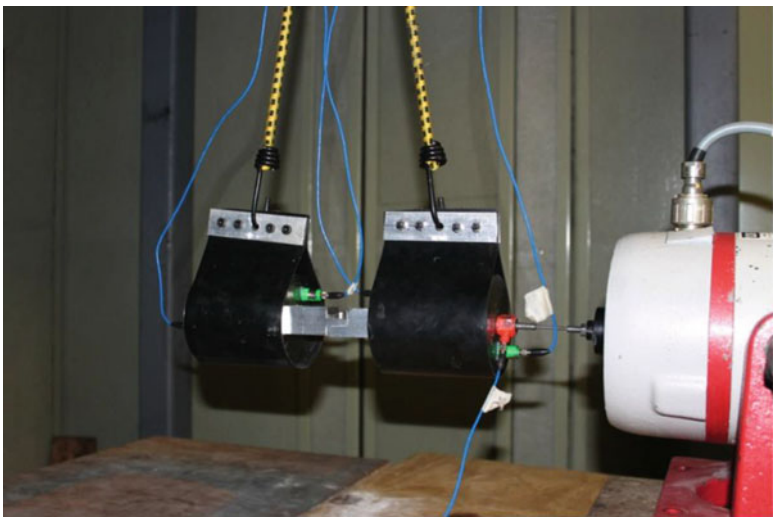

Since there is the need for a thorough validation of the results, the authors developed a procedure that will assess the goodness of the estimation (Fig. 25.2). This relies on the presence of a linearly validated model that will at some point incorporate the estimated nonlinear elements:

The test structure must be tested two times in order to validate the results.

The first test will be performed using stepped sine excitation (left branch). Once the FRFs have been collected, they can be analysed in modal space using classical modal analysis and any method capable of extracting – even approximately – the frequency-amplitude relationship of each mode. This relationship will be the main correlation variable and updating target.

The second test will use a broadband excitation (right branch). Analysing this broadband data with the previously discussed physical space toolbox, one will retrieve a set of estimated nonlinear elements. Those elements could be then implemented into the linear model. The validation step can be finally carried out in the modal space: from the left branch, the frequency-amplitude relationships are correlated with the same relationships retrieved by the model using a nonlinear simulation. Since there are now nonlinear parameters in the model, the procedure can provide an updating loop over these parameters in order to minimise any estimation error. In this work the authors seek to validate the non-linear forced response of a lap-joint using the previously discussed toolbox of physical-space based algorithms. The test structure is represented in Fig. 25.3. It consists of an axial lap-joint specimen with two stainless steel 4 kg masses at each end.

The purpose of the masses is to bring down the natural frequencies and exacerbate the main axial mode of vibration. The specimen itself is made of aluminium and consists in two squared-section blocks; each connected to the mass with a single

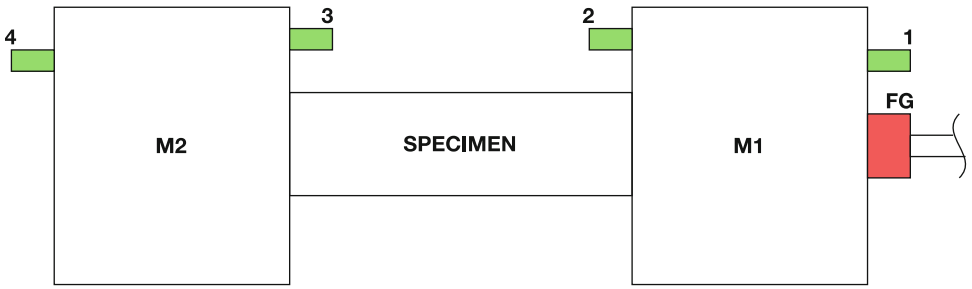

Fig. 25.4 Test setup scheme

10/32 UNF bolt and coupled to each other with two M5 bolts. The "dumbbell" structure was then instrumented with four mono-axial accelerometers placed at the ends of the masses and a force gauge along the axial direction (Fig. 25.4).

The authors acknowledge the redundancy of having two accelerometers on the same mass, but this configuration will make the location phase of the nonlinearities much less trivial. Finally, the dumbbell was supported with two belts around the masses and suspended in free-free conditions by means of elastic bungees. This configuration was aimed to avoid any undesired strains at the joint but the ones acting along the axial direction.

25.2 Testing and Modelling

25.2.1 Broadband and Stepped Sine Tests

Referring to the flowchart in Fig. 25.2, two tests have been performed on the structure in order to (i) extract the nonlinear elements and (ii) validate the resulting nonlinear model.

Broadband tests were performed at two different levels (0.5 V and 5 V), in order to get a preliminary assessment of the FRFs of the structure and the high-level time histories required by the Reverse Path method.

Due to the energy of the signal being spread over a wide frequency range, the broadband excitation often deals a linearized FRF. In Figs. 25.5 and 25.6 the two FRFs at low and high excitation level are shown. DOF #3 was chosen because it is the degree of freedom just across the joint, with respect to the excitation (refer to Fig. 25.4).

At high level of excitation (Fig. 25.6) one can notice a severe drop in coherence in correspondence of frequencies that are two times the natural frequencies of the structure. This is a clear indication of nonlinear behaviour, and will be useful later for the detection step. This behaviour is noticeable even at low level for the highest peak (Fig. 25.5) mainly because the disconnection created by the joint is exerted even at low amplitudes of vibration.

After a preliminary modal analysis, the main resonance peak was identified as being the axial mode of interest, as expected.

Following the other branch of Fig. 25.2, stepped sine excitation was carried out as a pure tone excitation in a frequency range between 1,200 Hz and 1,360 Hz with a frequency resolution of 0.2 Hz. The test was then repeated for five force levels (1, 3, 5, 7, 10 and 15 N). During a stepped sine test, the entire energy of the shaker is transferred into the structure tone by tone, leading to an exacerbation of any nonlinear behaviour (Fig. 25.7).

The measured FRFs show a clear distortion of the response curves as the excitation force is increased, therefore demonstrating the amplitude dependency of the nonlinear phenomenon. It is clear that one shall seek for a nonlinear element that could grant the model a softening behaviour. One expert eye will notice from the response curves that the softening behaviour of the stiffness is not associated with an attenuation of the peak response of the same curves.

25.2.2 Models

Since there is only one real mode of interest, it is straightforward and easy to create a single degree of freedom model of the structure. After a quick modal analysis at low vibration level, one can retrieve the following system:

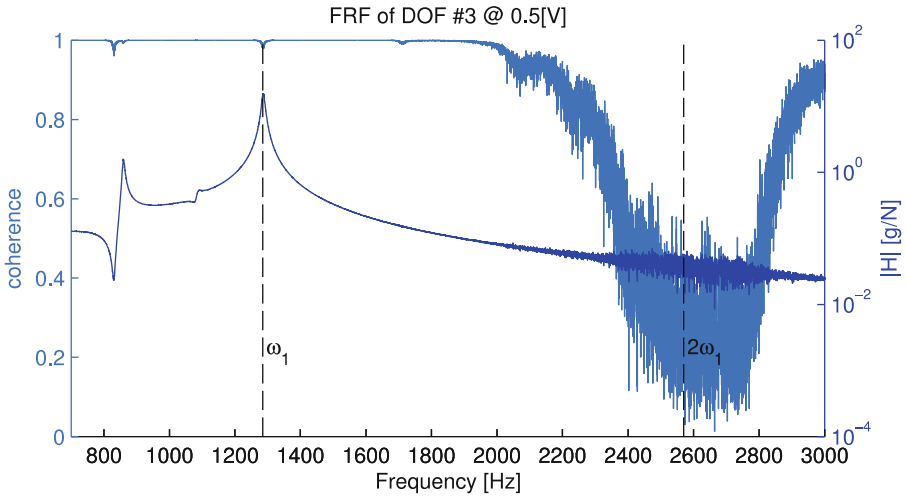

Fig. 25.5 FRF and coherence (broadband) at low level of excitation

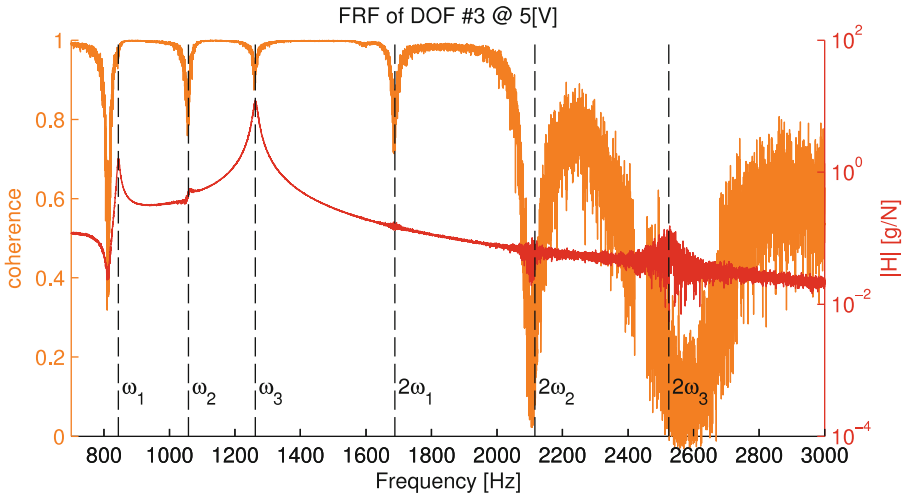

Fig. 25.6 FRF and coherence (broadband) at high level of excitation

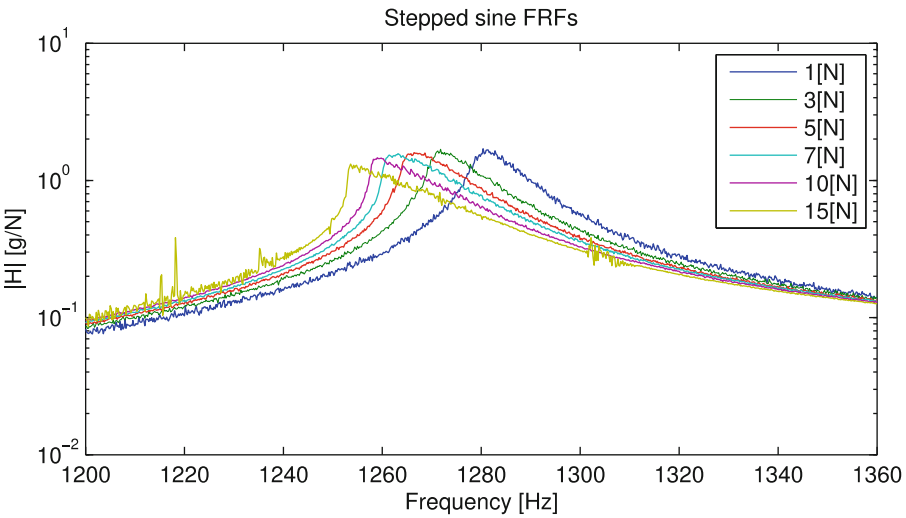

Fig. 25.7 FRFs (stepped sine) at different excitation levels

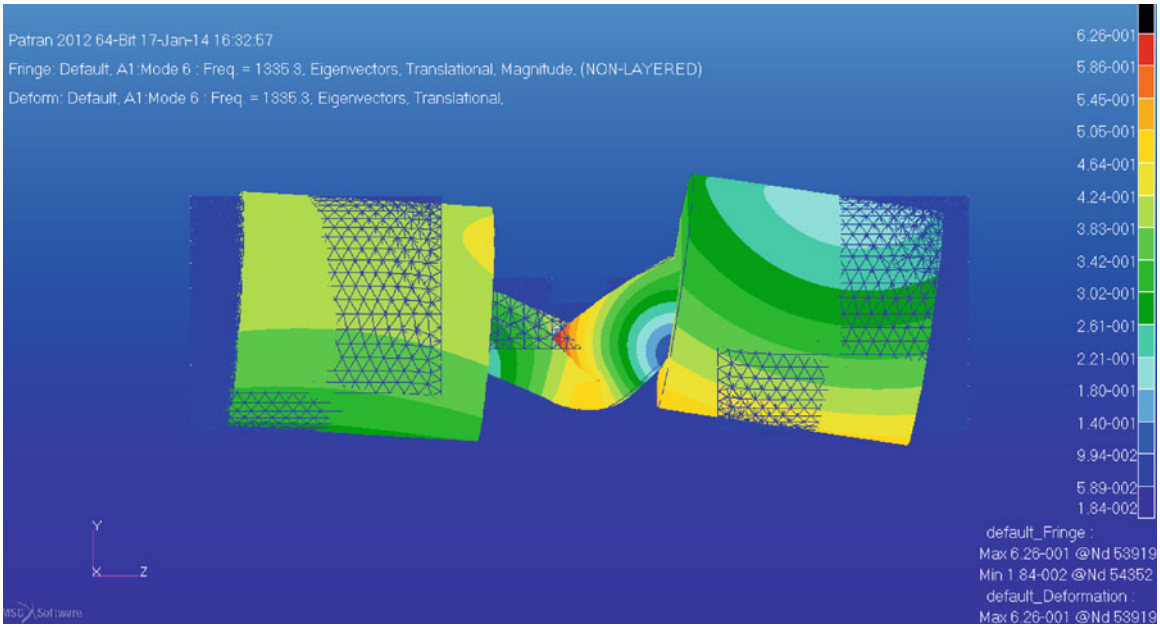

Fig. 25.8 Main axial mode of FE model at 1,335 Hz

$$m\ddot{x} + c\dot{x} + kx + \sum_{i}^{M} \gamma_i g_i\,(w_i) = F \sin(\Omega t) \tag{25.1}$$

Where $m = 4$ Kg, $c = 645$ Ns/m, $k = 2.67452$ E + 8 N/m. The nonlinear part (highlighted in red) contains information about the quantification coefficient γ, the characterisation function $g\,(\bullet)$ and the location $w = x_p - x_q$ of each nonlinear element.

An FE model of the structure was created and analysed using standard software packages (MSC PATRAN/NASTRAN, DSS ABAQUS). The joint had to be modelled with a tie constraint rigidly coupling the surfaces together in order to run an analytical modal analysis, since any contact condition would have not been translated into the stiffness matrix of the system. This is the main issue of the currently available commercial FE packages. The main axial mode is shown in Fig. 25.8. This is the only mode shape of interest due to the peculiarity of the experimental setup (refer to Fig. 25.4) but it is the mode that provides the most useful loading of the joint specimen.

Although being a rough model, it can be argued that the mode calculated with the FE analysis, agrees well enough with the experimental data. In fact, the natural frequency of the main axial mode is around 1,280[Hz], while the one retrieved by FE analysis is 1,335[Hz]. This is mainly is due to the tie constraints of the surfaces that is likely to stiffen the modelled structure. However, this will be the base on top of which one will implement the nonlinear elements identified with the aid of nonlinear analysis.

25.3 Nonlinear Analysis

25.3.1 Detection

The detection step is generally straightforward. In this case we have collected two main evidences of nonlinear behaviour:

(i) From the stepped-sine tests, it is clear the amplitude-dependency of the FRFs, which in a linear case are invariants for the system (Fig. 25.7).
(ii) From the broadband tests, it is noticeable the severe drop in coherence. While a drop in coherence is generally caused by noise or unmeasured spurious inputs, a drop at an integer multiple of the natural frequencies of the system is usually caused by extra harmonic content in the response signal that causes the FRFs to appear noisy (Fig. 25.6). This extra content is caused by nonlinear behaviour occurring in the structure.

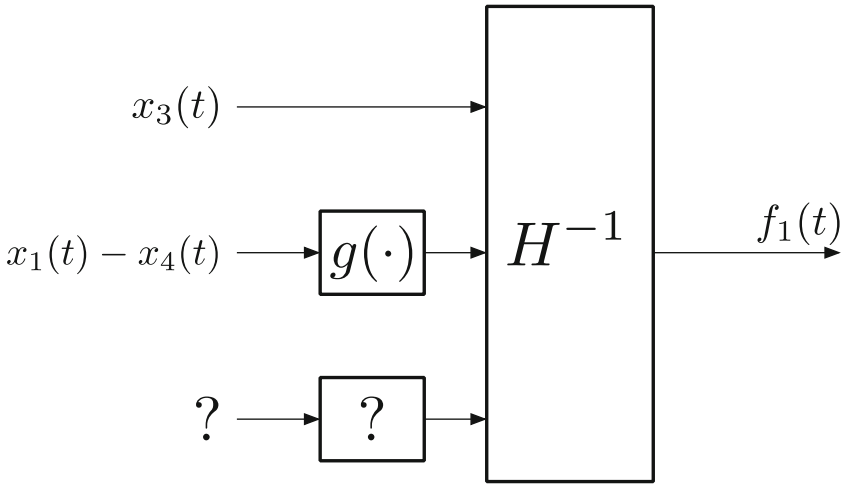

Fig. 25.9 Reverse path method

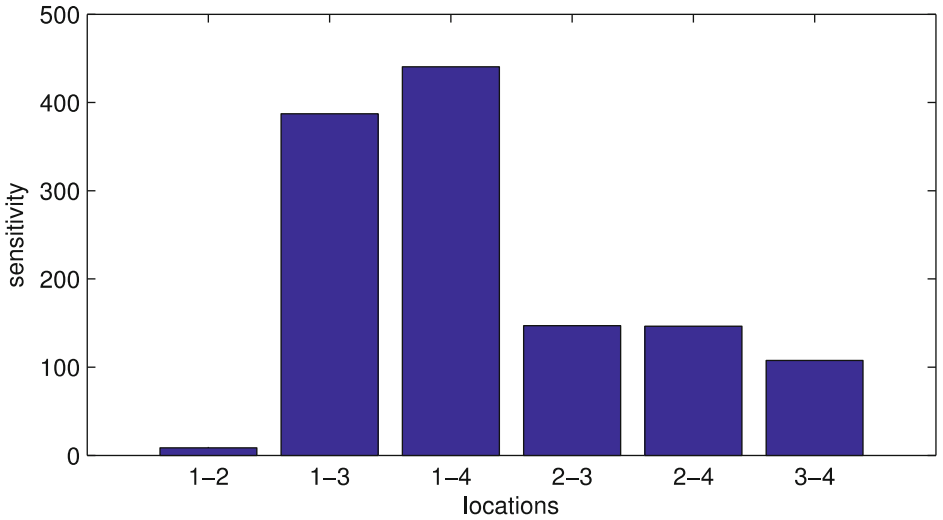

Fig. 25.10 Location plot: the most sensitive location is found among the DOFs across the joint

25.3.2 Location

The location step is performed via Reverse Path method. The main idea is to improve the poor coherence by re-casting the equation of motion of a nonlinear system with force at the outputs and responses – linear and nonlinear – at the input. hence the term "reverse path".

Collecting the broadband time histories responses at high level and treating the nonlinearities as feedback terms, the location method is to run a sensitivity analysis about the locations that have the most influence on the coherence of the underlying linear system (Fig. 25.9).

Figure 25.10 shows the coherence sensitivity associated with all the potential nonlinear locations. It is straightforward to notice that the sensitivity is higher when accounting for two DOFs that lie across the joint, while the sensitivity is low or very low when accounting the DOFs that lie on the same side of the joint.

Thus, it is possible to locate the nonlinearity between DOFs #1 and #4. However, in this particular case, any combination of DOFs lying across the joint would have been acceptable.

25.3.3 Characterisation

Once the nonlinear element has been localised, using the same Reverse Path method it is possible to seek for a nonlinear relationship that will improve the coherence of the underlying linear model. To do so, a monomial model (25.2) with variable exponent has been fed into the system and the resulting coherences calculated.

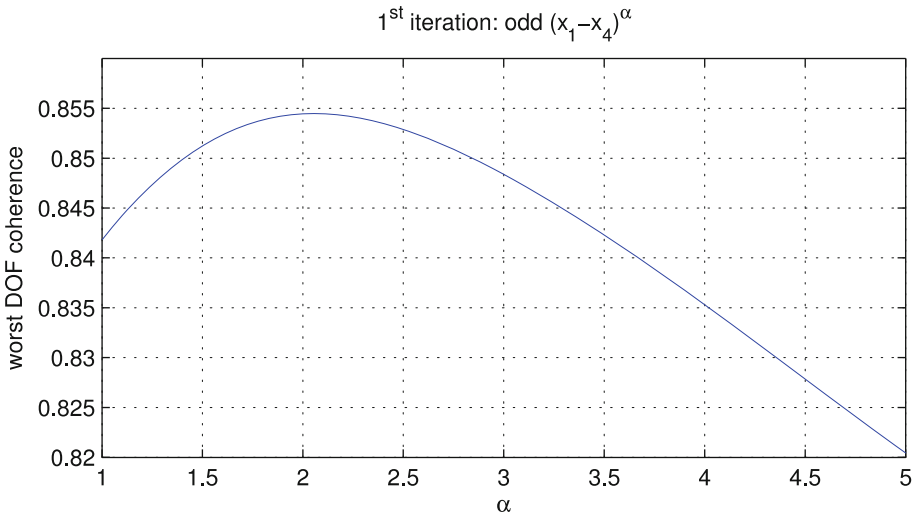

Fig. 25.11 Characterisation plot: the exponent that best improves the coherence is 2.1

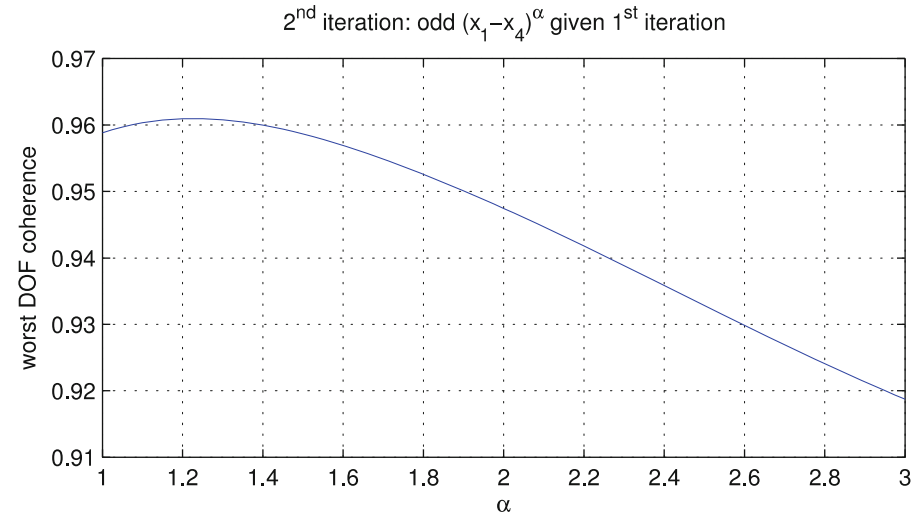

Fig. 25.12 Characterisation plot, second iteration: the exponent that best improves the coherence is now 1.2

$$F_{NL} = \text{sign}\,(x_1 - x_4) \cdot \text{abs}(x_1 - x_4)^{\alpha} \tag{25.2}$$

Figure 25.11 shows the results of this process: one can notice that the best result is achieved with an exponent of 2.1, with a coherence of 85.5 % in the bandwidth of interest 700:3,000 [Hz]

One can now take another iteration in order to try and improve the coherence further. The same monomial model has been fed into the system, given the first iteration:

$$F_{NL} = \text{sign}\,(x_1 - x_4)\,\text{abs}(x_1 - x_4)^{2.1} + \text{sign}\,(x_1 - x_4)\,\text{abs}(x_1 - x_4)^{\alpha} \tag{25.3}$$

The result of this second iteration is shown in Fig. 25.12. In this case the exponent is 1.2 and the coherence is 96 %

25.3.4 Quantification

After the location and characterisation steps, it is possible to plot the final coherence achieved by the now nonlinear system. Figures 25.13 and 25.14 show respectively the coherence indices for each degree of freedom prior and after identification as well as the full coherence functions in the bandwidth of interest 700:3000[Hz] for the driving point and the worst coherent point prior and after the identification.

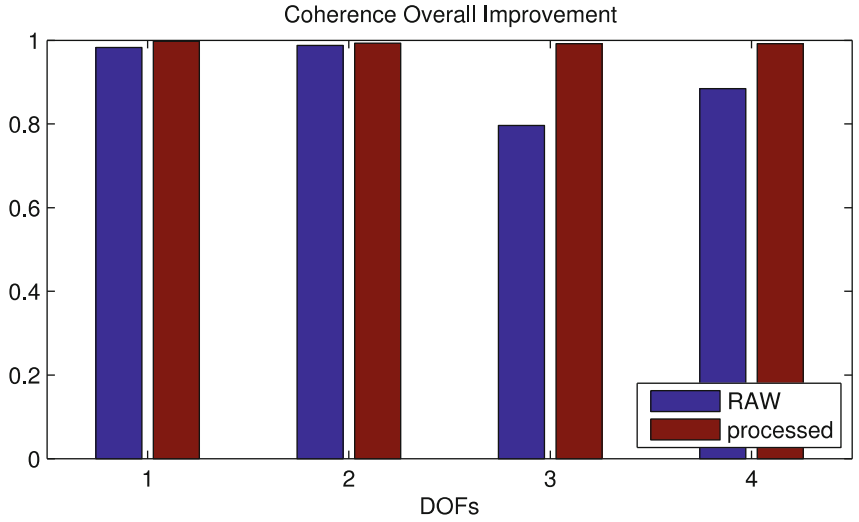

Fig. 25.13 Coherence improvement after identification

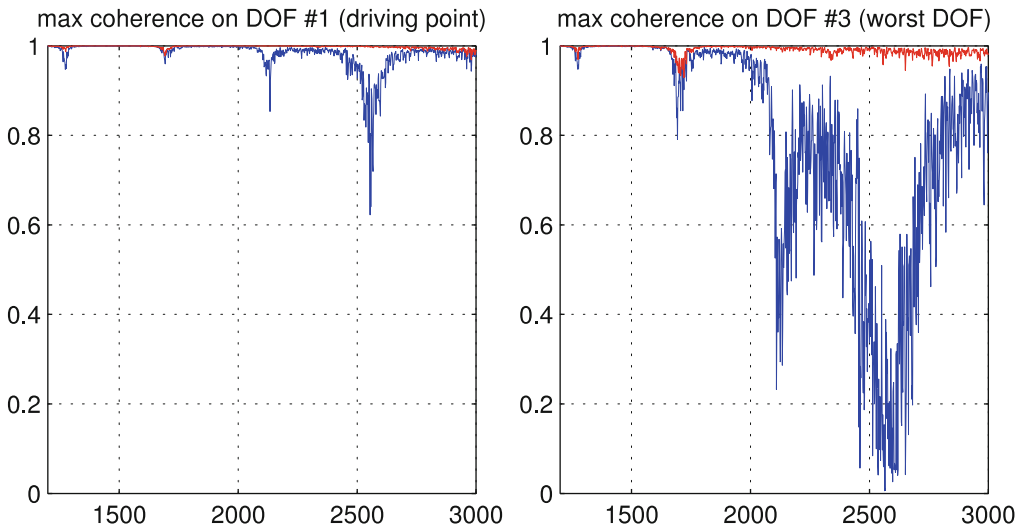

Fig. 25.14 Coherence improvement of driving point (*left*) and worst coherent point (*right*)

The Reverse Path method is also able to quantify the coefficients of the retrieved nonlinearities, but with much less reliability. However, this estimation will be a good starting point for the upcoming updating loop.

One expects the nonlinear coefficients to be constant and real valued, but the Reverse Path method deals frequency-dependent complex ones; the retrieved coefficients will then be the average value of their real part. Figure 25.15 shows the real part of the coefficients retrieved using the information of the underlying linear system and their average, which will be used as a starting value for the upcoming updating loop.

25.4 Correlation and Models Updating

25.4.1 SDOF Correlation and Updating

In order to correlate the SDOF model with the experimental data, simulations of FRFs were produced using the equation of motion (25.1), now with the totally known nonlinear part.

With $\gamma_1 = -4.85\ \mathrm{E}+13\ \mathrm{N/m^{2.1}}$ and $\gamma_2 = -2.74\ \mathrm{E}+9\ \mathrm{N/m^{1.2}}$. All simulations were performed using the same levels of excitation force used for the experimental measurements (Fig. 25.7). The simulations for single tone excitation were

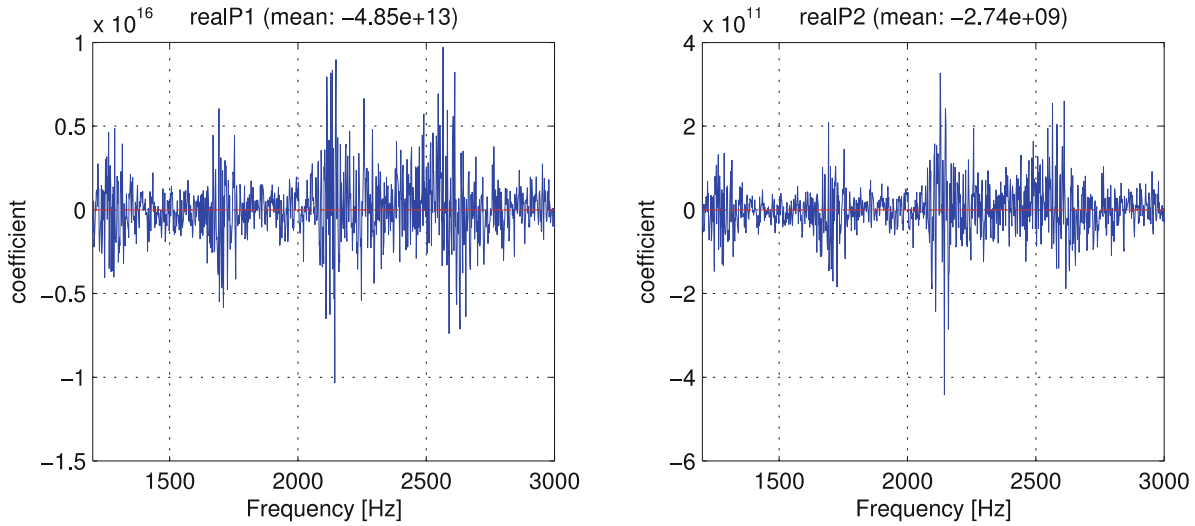

Fig. 25.15 Estimated nonlinear coefficients $\gamma 1$ (*left*) and $\gamma 2$ (*right*)

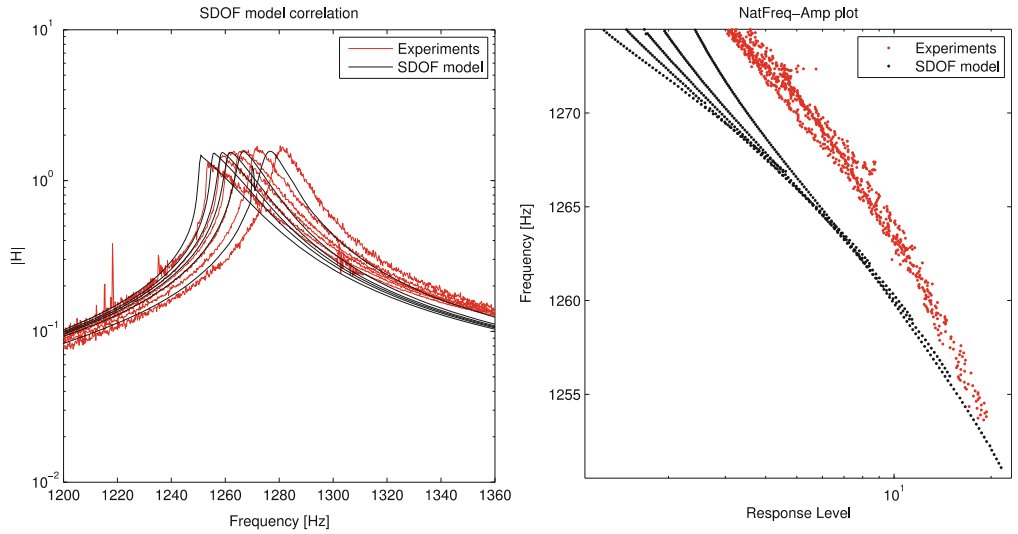

Fig. 25.16 SDOF model correlation

performed by means of a classical Runge–Kutta fixed time integration. Both the theoretical and experimental frequency response functions are plotted in Fig. 25.16.

The results look promising but are far from being good. Since the weak link in the analysis chain is to be found in the quantification step of the Reverse Path method, the estimated coefficients γ_1 and γ_2 have been chosen as the only parameters to update. As one can notice from Fig. 25.17, the updating step successfully turns the model into a more reliable representation of the physical phenomenon, setting the γ coefficients to a value of $-1.8\,\mathrm{E}+13$ and $-3\mathrm{E}+8$.

25.4.2 Nonlinear FE Model Validation

One of the main issues of nonlinear FE packages is their lack of frequency-domain nonlinear solvers. In order to retrieve a nonlinear FRF, one must perform an explicit pure tone time-domain simulation for each frequency point of interest, and construct the FRF taking the ratio of the FFT of the response (at the fundamental, since it will contain extra harmonic content) versus the FFT of the excitation. While this is an affordable method for SDOF models, FE models usually contains thousands of nodes. In this case the modeller must take good care of reducing the number of nodes, exploiting symmetry and artifices in order to ease the computational burden.

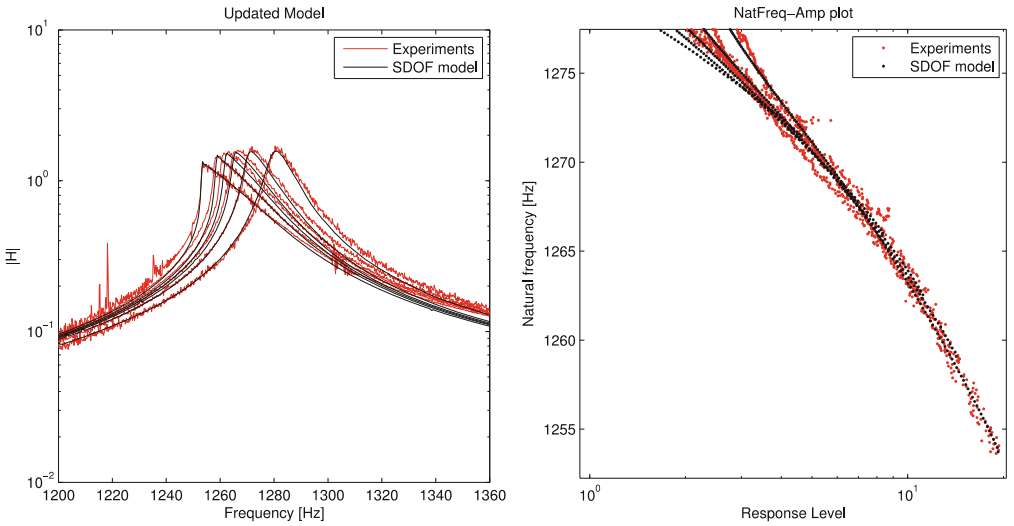

Fig. 25.17 SDOF model after updating on nonlinear coefficients

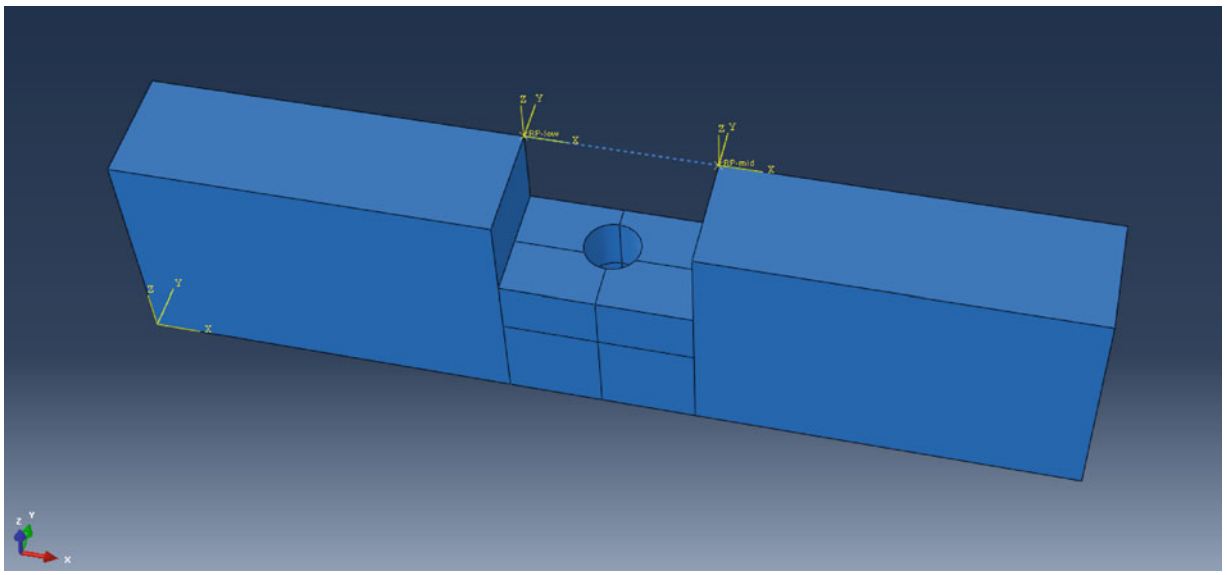

Fig. 25.18 FE model with nonlinear element across the joint

In this case, in order to reduce the number of nodes, the test structure was sliced along its only symmetry axis and the big cylindrical masses were replaced by point masses of equal value (Fig. 25.18).

The nonlinear element included in the simulation was a nonlinear spring of equation (25.4), as retrieved from the nonlinearity characterisation and updating step.

$$F_{NL} = k\,(x_1 - x_2) + \gamma_1 \cdot \text{sign}\,(x_1 - x_2) \cdot \text{abs}(x_1 - x_2)^{2.1} + \gamma_2 \cdot \text{sign}\,(x_1 - x_2) \cdot \text{abs}(x_1 - x_2)^{1.2} \tag{25.4}$$

It was placed in the centreline of the interface and across the joint, as indicated by the nonlinearity location step. This particular spring restrained the motion in the axial direction only; in order to avoid that unmeasured relative degrees of freedom could pollute the solution or make it unstable.

Pure-tone time-domain simulations were performed ranging from 1,200 Hz to 1,360 Hz, with a frequency resolution of 2[Hz]. The simulations were repeated for 1 N and 15 N force levels. The results are shown in Fig. 25.19.

As one can notice from figures Figs. 25.19 and 25.20, the FRFs of the FE model are not as good as the ones of the previously updated SDOF model. This may be caused by the not perfect point mass values or the approximate material properties, but these results represent nonetheless a good starting point for a further updating.

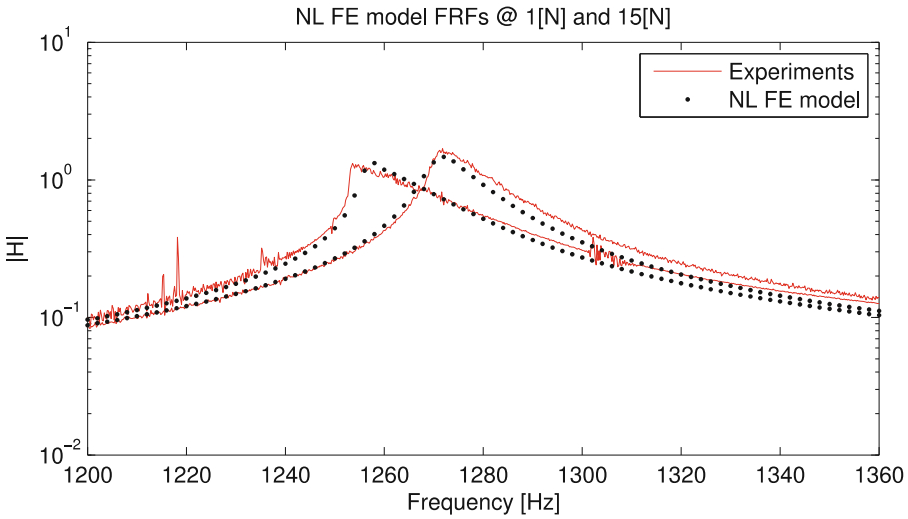

Fig. 25.19 Updated FE model FRFs

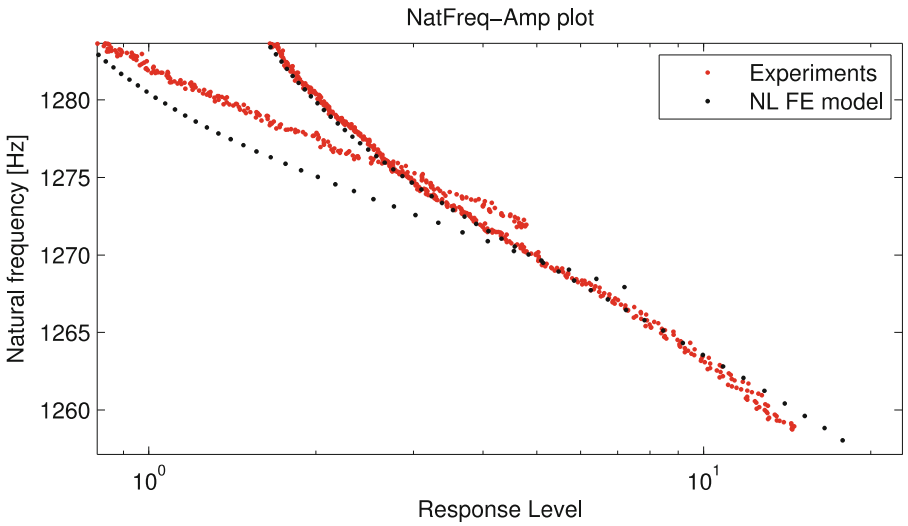

Fig. 25.20 Natural frequency amplitude relationships for the updated FE model

However, it is now theoretically possible to use standard updating techniques and calculate sensitivities for the newly introduced parameters (nonlinear coefficients, nonlinear exponents) in order to achieve a perfect match. Unfortunately, the available commercial updating software packages do not allow the introduction of these new nonlinear parameters, so one must rely on some custom made tools.

25.5 Conclusions

This paper presented a strategy for dealing with nonlinearities observed from a coupled structure such as a lap-joint in a dumbbell test rig configuration. This simple test rig can be modelled as a Single Degree Of Freedom (SDOF) because the main nonlinear dynamics is identified in one mode of vibration which is caused by the two weights to be in out of phase motion to each other. The type of nonlinearity is identified as softening behaviour, such as the peak response leans to lower frequencies for high vibration amplitudes. The strategy of **D**, **L**, **C** and **Q** identified the nonlinear elements from the dynamic response of the system. These elements were used to build a simple SDOF and simulate the frequency responses functions for different level of excitation force. These were processed by Complex-FRF analysis and compared with the results obtained from the measured ones. The results matched very well after some model updating. The final aim of this paper was to be able to connect the two components by a single spring element, the dynamics of which had to comply with the nonlinear terms identified from the tests. Simulations carried out by using the proposed FE model of the dumbbell test rig produced good data. It was not possible to refine the simulations by model updating because of the time integration analysis method, which turned to be lighter than using contact conditions but, inevitably, still prohibitive.

Future studied will be focussed on the use of Multi-Harmonic Balance Method. This type of solver combined with the ability of defining the right equation describing the coupling between the two assemblies will boost the capability of predicting forced responses of coupled structures. Clearly, this study was focussed on a single element connecting the two components but the authors are aware of this restrictive (and unrealistic) assumption. Future works will also need to address this point by increasing the study on a more comprehensive model updating process.

References

1. Schwingshackl CW, Di Maio D, Sever I, Green JS (2013) Modeling and validation of the nonlinear dynamic behavior of bolted flange joints. J Eng Gas Turbines Power 135(12):122504
2. Zucca S, Firrone CM (2014) Nonlinear dynamics of mechanical systems with friction contacts: coupled static and dynamic multi-harmonic balance method and multiple solutions. J Sound Vib 333(3):916–926
3. Mohammadali M, Ahmadian H (2014) Efficient model order reduction for dynamic systems with local nonlinearities. J Sound Vib 333(6):1754–1766
4. Festjens H, Chevallier G, Dion JL (2014) Nonlinear model order reduction of jointed structures for dynamic analysis. J Sound Vib 333(7):2100–2113
5. Noël JP, Renson L, Kerschen G (2014) Complex dynamics of a nonlinear aerospace structure: experimental identification and modal interactions. J Sound Vib 333(12):2588–2607
6. Ahmadian H, Rajaei M (2014) Identification of Iwan distribution density function in frictional contacts. J Sound Vib 333(15):3382–3393
7. Rahmani AM, Ervin EK (2014) Frequency response of an impacting lap joint. J Nonlinear Dyn 2014:1–10
8. Mehrpouya M, Graham E, Park SS (2014) Identification of multiple joint dynamics using the inverse receptance coupling method. J Vib Control. doi:10.1177/1077546314523306
9. Reuss P, Kruse S, Peter S, Morlock F, Gaul L (2014) Identification of nonlinear joint characteristic in dynamic substructuring. In: Mayes R, Rixen D, Allen M (eds) Topics in experimental dynamic substructuring, vol 2 SE – 3. Springer, New York, pp 27–36
10. Shiki S, Lopes V Jr, da Silva S (2014) Identification of nonlinear structures using discrete-time Volterra series. J Braz Soc Mech Sci Eng 36(3):523–532
11. delli Carri A, Di Maio D, Lucchetti A, Sever IA (2014) Experimental model validation of a non-linear structure with lap-joint using the physical space approach. In: International conference on noise and vibration engineering, pp 1185–1198
12. Garibaldi L (2003) Application of the conditioned reverse path method. Mech Syst Signal Process 17(1):227–235
13. Magnevall M, Josefsson A, Ahlin K, Broman G (2012) Nonlinear structural identification by the 'reverse path' spectral method. J Sound Vib 331(4):938–946
14. Muhamad P, Sims ND, Worden K (2012) On the orthogonalised reverse path method for nonlinear system identification. J Sound Vib 331(20):4488–4503
15. dell Carri A, Ewins DJ (2014) A systematic approach to modal testing of nonlinear structures. In: Allemang R, De Clerck J, Niezrecki C, Wicks A (eds) Topics in modal analysis, vol 7 SE – 25. Springer, New York, pp 273–286
16. delli Carri, A., and D. J. Ewins (2014) Assessment and Validation of Nonlinear Identification Techniques Using Simulated Numerical and Real Measured Data. Topics in Modal Analysis II, Vol 8. Springer International Publishing, pp 285–298
17. Noël JP, Kerschen G (2013) Frequency-domain subspace identification for nonlinear mechanical systems. Mech Syst Signal Process 40(2):701–717

Chapter 26
Experimental Validation of Pseudo Receptance Difference (PRD) Method for Nonlinear Model Updating

Güvenç Canbaloğlu and H. Nevzat Özgüven

Abstract In real life applications most of the structures have nonlinearities, which restrict us applying model updating techniques available for linear structures. Well-established FRF based model updating methods would easily be extended to a nonlinear system if the FRFs of the underlying linear system (linear FRFs) could be experimentally measured. When frictional type of nonlinearity co-exists with other types of nonlinearities, it is not possible to obtain linear FRFs experimentally by using low level forcing. Pseudo Receptance Difference (PRD) method, recently developed by the authors, calculates linear FRFs of a nonlinear structure by using FRFs measured at various forcing levels, and simultaneously identifies multiple nonlinearities in the system. Then any model updating method can be used to update the linear part of the mathematical model. In this present work, the PRD method is used to predict the linear FRFs from nonlinear FRFs, and the inverse eigensensitivity method is employed to update the linear finite element (FE) model of a nonlinear structure. A real nonlinear T-beam test structure is used to validate the accuracy of the proposed method. First, the linear FRFs are calculated from nonlinear FRFs measured at different forcing levels, and simultaneously, the nonlinearities in the structure are identified. Then the FE model of the linear part of the structure is updated. Finally, the accuracy of the updated nonlinear model of the test structure is demonstrated by comparing the calculated and measured FRFs of the test structure at several different forcing levels.

Keywords Nonlinear model updating • Nonlinearity • Nonlinear identification • Friction nonlinearity • Nonlinear structures

26.1 Introduction

Accurate prediction of the dynamic response of a structure is a vital step in the design stage of engineering structures. FE method is the most common numerical method used for obtaining dynamic response of engineering structures. However, usage of FE methods may yield certain inaccuracies arising from modeling errors, Due to these errors experimental and FE method results do not always match perfectly. Therefore FE models need to be updated by using the experimental results and changing some of the parameters used in the FE model.

Various model updating methods were developed in order to correct the mathematical models. However most of the model updating methods available in literature are for linear systems. Nalitolela et al. [1] proposed a method which is based on exact model reduction and perturbation of both the actual structure and its analytical model by adding mass or stiffness in order to produce accurate dynamic models. Roy et al. [2] proposed direct energy approach to relate the kinetic and strain energies of each part of a FE model to the experimental data. Brughmans et al. [3] applied a FE model updating technique, based on a forward sensitivity formulation, to a twin propeller commuter aircraft. Link and Zhang [4] applied different updating techniques to a test structure in order to investigate the sensitivity of updating results in these methods. Jung and Ewins [5] studied the application of the inverse eigensensitivity method for model updating using arbitrarily chosen macro elements to a simple frame. In order to investigate the potential errors causing the discrepancies between analytical and experimental normal modes, Miccoli and Agostoni [6] used the sensitivity analysis. Hemez [7] studied an updating method which is based

G. Canbaloğlu (✉)
Department of Mechanical Engineering, Middle East Technical University, Ankara 06800, Turkey

MGEO Division, ASELSAN Inc., Ankara 06750, Turkey
e-mail: gcanbal@aselsan.com.tr

H.N. Özgüven
Department of Mechanical Engineering, Middle East Technical University, Ankara 06800, Turkey
e-mail: ozguven@metu.edu.tr

G. Kerschen (ed.), *Nonlinear Dynamics, Volume 1*, Conference Proceedings of the Society for Experimental Mechanics Series, DOI 10.1007/978-3-319-15221-9_26

on sensitivity approach for damped FE models. A new model updating method is proposed by Lenoir et al. [8] which is based on the modal synthesis of experimental forced responses. Mottershead et al. [9] studied the effect of the selection of different updating parameters in the model updating of an aluminum space frame. In order to update a bridge structure Jung et al. [10] presented a hybrid optimization technique based on the genetic algorithm and Nelder-Mead simplex. Kozak et al. [11] proposed a new error localization method and an updating routine and applied the routine in different case studies. In a more recent work Boulkaibet et al. [12] studied the use of the Shadow Hybrid Monte Carlo technique to determine the selection of updating parameters. Fei and Jiang [13] studied the criteria of evaluating initial models that will be used in the updating procedure. In a very recent work, Boulkaibet et al. [14] proposed the use of Separable Shadow Hybrid Monte Carlo method for the updating of FE models. Hemez [15] briefly overviewed the first 30 years of FE model updating development, from the mid-1960s to the mid-1990s and categorized FE model updating methods into broad categories that each offers their own benefits and limitations.

Since most of the structures have nonlinear behavior, it is vital to have model updating techniques for nonlinear structures as well. Hasselman et al. [16] studied Principal Components Analysis which is based on singular value decomposition of a collection of response time history, for nonlinear model correlation and updating. In a later work Anderson and Hasselman [17] addressed the issue of the minimizing the correlation of parameter estimates in the updating of nonlinear systems. Burton et al. [18] studied the combined model reduction and singular value decomposition approach for model updating of nonlinear structures. Silva et al. [19] studied harmonic balance, constitutive relation error, restoring force surface and Karhunen-Loève decomposition methods for nonlinear model updating, and compared with each other. Canbaloglu and Özgüven, very recently, developed a method to obtain linear FRFs of nonlinear structures having multiple nonlinearities including friction type of nonlinearity, from nonlinear FRF measurements [20] and used this method in the nonlinear model updating approach proposed [21]. The method is validated by applying the method developed to a nonlinear test system.

For nonlinear structures, it is possible to use model updating techniques developed for the linear systems, if the linear dynamic behaviors of the structure are obtained which may require identification of nonlinearity first. Kerschen et al. [22] presented a literature survey which is one of the most detailed nonlinear system identification literature surveys in which more than 400 papers were cited. The method developed by Canbaloglu and Özgüven [20] aims to obtain linear FRFs of a nonlinear structure from FRF measurements, without fully identifying nonlinearities, the ultimate goal being to update linear model parameters of a nonlinear structure having multiple nonlinearities including friction type of nonlinearity. Very recently, Doranga and Wu studied [23] the Nonlinear Resonant Decay method for parameter identification of nonlinear dynamic systems. Grappasonni et al. [24] presented a method for identification of an experimental cantilever beam with a geometrically nonlinear thin beam clamped with prestress. Aykan and Altuntop [25] implemented the method developed for parametrically identifying nonlinearities from measured frequency response functions [26] to a gearbox. Londono and Cooper [27] developed a technique for the experimental identification of structures exhibiting geometric nonlinearities, in particular aircraft with highly flexible wings. In this study, the method [20, 21] developed by the authors for nonlinear model updating, is experimentally validated by applying the approach to a real nonlinear T-beam test structure. First, the linear FRFs are calculated from nonlinear FRFs measured at different forcing levels, and simultaneously the nonlinearities in the structure are identified. Then the FE model of the linear part of the structure is updated. Finally, in order to demonstrate the accuracy of the updated nonlinear model of the test structure, predicted and measured FRFs of the test structure are compared at several different forcing levels.

26.2 Theory

The model updating method recently developed by Canbaloglu and Özgüven [20, 21] is used in this study for updating the FE model of a nonlinear structure. Since the theory of the method is given in detail in Refs. [20] and [21], just a very brief summary is presented here.

For a nonlinear system, it is possible to write the following equation.

$$[\Delta] = \left[\Delta_f\right] + [\Delta_{HF}] = \left[H^{NL}\right]^{-1} - \left[H^{L}\right]^{-1} \tag{26.1}$$

where $[\Delta]$, $[\Delta_f]$, $[\Delta_{HF}]$, $[H^{NL}]$, $[H^L]$ are the nonlinearity matrix, nonlinearity matrix due to friction, nonlinearity matrix due to remaining nonlinearities that are dominant at high forcing levels of excitation, response level dependent nonlinear and linear FRF matrices, respectively. Measuring FRFs experimentally several times at the same frequency but at different forcing levels the following set of equations can be written:

$$[\Delta_{HF}]_{i+1} - [\Delta_f]_1 = [H^{NL}]_{i+1}^{-1} - [H^{NL}]_1^{-1} \qquad i = 1, 2, \ldots, (n-1) \tag{26.2}$$

In Eq. 26.2, subscript 1 indicates low forcing case and subscripts 2, 3, … n indicate high forcing cases. The detailed derivation of the formulation can be found in [20]. The nonzero elements in the nonlinearity matrices at the left hand sides which can be written as polynomial functions of response amplitudes with unknown coefficients are the describing functions of the corresponding nonlinearities. Polynomial fit for *(n-1)* data points is applied in a least square sense and the equation of the corresponding regression curve is obtained in order to find the unknown coefficients. By comparing the terms of the regression equation with the corresponding describing functions, nonlinearities are identified and then linear FRFs can easily be calculated as [20]

$$[H^L]_1 = \left[[H^{NL}]_1^{-1} - [\Delta_f]_1\right]^{-1} \tag{26.3}$$

One of the drawbacks of the above equation is that it requires the full matrix inversions. Therefore the formulation is improved for nonlinear structures where the nonlinearity is local [21]. For local nonlinearities it possible to partition the nonlinearity matrix as

$$[\Delta] = \begin{bmatrix} [\Delta_{aa}] & [0] \\ [0] & [0] \end{bmatrix} \tag{26.4}$$

where subscript *a* represents coordinates where nonlinear elements are connected ("nonlinear coordinates" in short). Pre-multiplying all the terms in Eq. 26.1 by $[H^L]$, post-multiplying by $[H^{NL}]$ and using Eq. 26.4 for the nonlinearity matrix, the following equation is obtained:

$$\begin{bmatrix} [H^L{}_{aa}] & [H^L{}_{ab}] \\ [H^L{}_{ba}] & [H^L{}_{bb}] \end{bmatrix} \begin{bmatrix} [\Delta_{aa}] & [0] \\ [0] & [0] \end{bmatrix} \begin{bmatrix} [H^{NL}{}_{aa}] & [H^{NL}{}_{ab}] \\ [H^{NL}{}_{ba}] & [H^{NL}{}_{bb}] \end{bmatrix} = \begin{bmatrix} [H^L{}_{aa}] & [H^L{}_{ab}] \\ [H^L{}_{ba}] & [H^L{}_{bb}] \end{bmatrix} - \begin{bmatrix} [H^{NL}{}_{aa}] & [H^{NL}{}_{ab}] \\ [H^{NL}{}_{ba}] & [H^{NL}{}_{bb}] \end{bmatrix} \tag{26.5}$$

Here subscript *b* corresponds to linear coordinates.

Considering the first submatrix of the resultant matrix and performing some matrix manipulations, the linear FRF matrix for the nonlinear coordinates can be obtained as [21]

$$[H^L{}_{aa}]_1 = \left[[H^{NL}{}_{aa}]_1^{-1} - [\Delta_f]_1\right]^{-1} \tag{26.6}$$

It is obvious that for locally nonlinear structures computational effort will be considerably reduced by using the above equation compared with Eq. 26.3. Once the linear FRFs are calculated by using Eq. 26.6, then they can be used in the model updating process of a FE model. Note that in several model updating methods having FRFs of limited number of coordinates is sufficient. Therefore, having FRF of even a single coordinate may be enough for model updating.

One of the common methods used for model updating is the inverse eigensensitivity method [28], which is based on the following equation:

$$\{\Delta r\} = [S]\{\Delta p\} \tag{26.7}$$

Here, $\{r\}$ is the response vector composed of mode shapes and natural frequencies, $\{p\}$ is the parameter vector composed of geometrical parameters or material properties used in the FE model, and $[S]$ is the modal sensitivity matrix. Modal sensitivity matrix $[S]$ can be written as

$$[S] = \begin{bmatrix} S_{r_1}{}^{p_1} & \cdots & S_{r_1}{}^{p_m} \\ \vdots & \ddots & \vdots \\ S_{r_n}{}^{p_1} & \cdots & S_{r_n}{}^{p_m} \end{bmatrix} \tag{26.8}$$

In Eq. 26.8, $S_{r_n}{}^{p_m}$ stands for the sensitivity of the n^{th} response to the m^{th} updating parameter. For complex structures it is easier to calculate the sensitivities by numerical differentiation. In this study, centered difference approximation with $O(h^4)$ is used to obtain the sensitivities as given in the following equation:

$$r'(p_i) = \frac{-r(p_{i+2}) + 8r(p_{i+1}) - 8r(p_{i-1}) + r(p_{i-2})}{12\Delta p} \tag{26.9}$$

After obtaining the sensitivity matrix $[S]$ and $\{\Delta r\}$ vector, $\{\Delta p\}$ which gives the changes required to be made in parameter vector, can be obtained from the following equation:

$$\{\Delta p\} = [S]^{-1}\{\Delta r\} \tag{26.10}$$

26.3 Experimental Study

In this section, PRD method developed recently [20] is applied to a nonlinear experimental test system. The test system is a T-beam which is similar to the test rig used by Ferreira [29] and also by Siller [30]. Using the PRD method, both linear FRFs and the nonlinearities in the system are obtained from experimentally measured nonlinear FRFs.

26.3.1 Experimental Setup

The test set-up is a T-beam which consists of a cantilever beam with its free end is maintained between two thin identical beams having fixed-fixed boundary conditions. The thin beams which are attached to the free end of the cantilever beam are the main source of nonlinearity in the test structure. The dimensions of the T-beam are given in Fig. 26.1.

In order to maintain the fixed boundary conditions, beams are manufactured longer than their original dimensions, so that adequate parts of the beams are fixed between fixture blocks. The material used for the beams is St37. The test rig used in the experiments is shown in Fig. 26.2.

In the experiments performed in this study, the structure is excited with B&K Type 4808 modal shaker via a push-rod. In order to increase the excitation level of the shaker, B&K Type 2712 power amplifier is used. Acceleration responses and the forces applied are measured with B&K Type 4507B accelerometer and B&K Type 8230-002 force transducer, respectively. In all the measurements, as a data acquisition system, B&K Type 3560C frontend is used. The equipment used in the experiments is shown in Fig. 26.3.

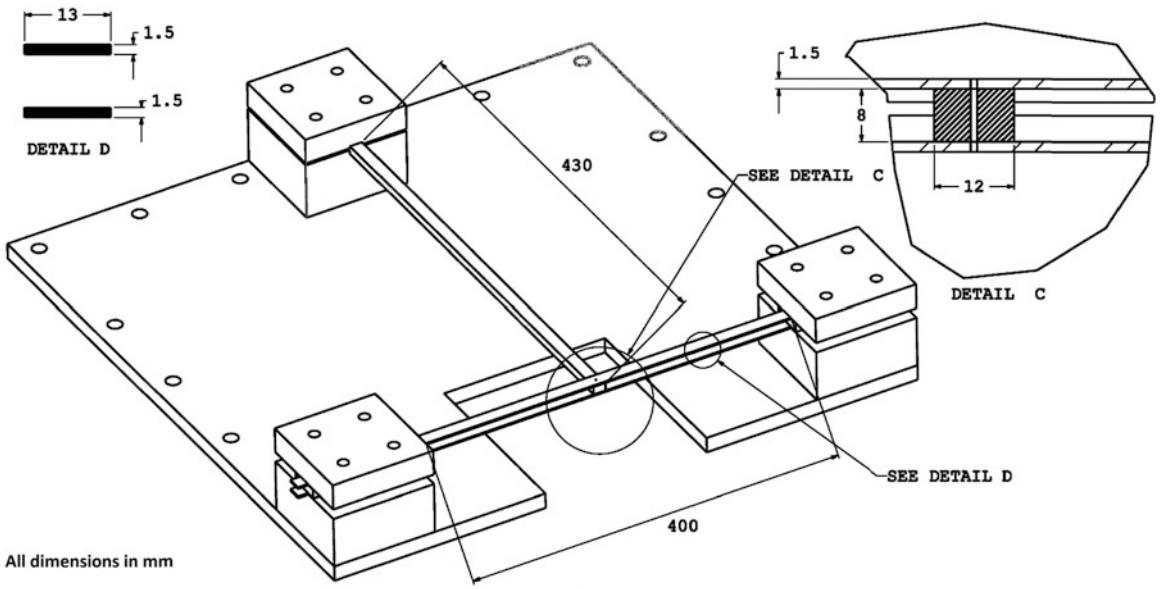

Fig. 26.1 Nonlinear T-beam test system

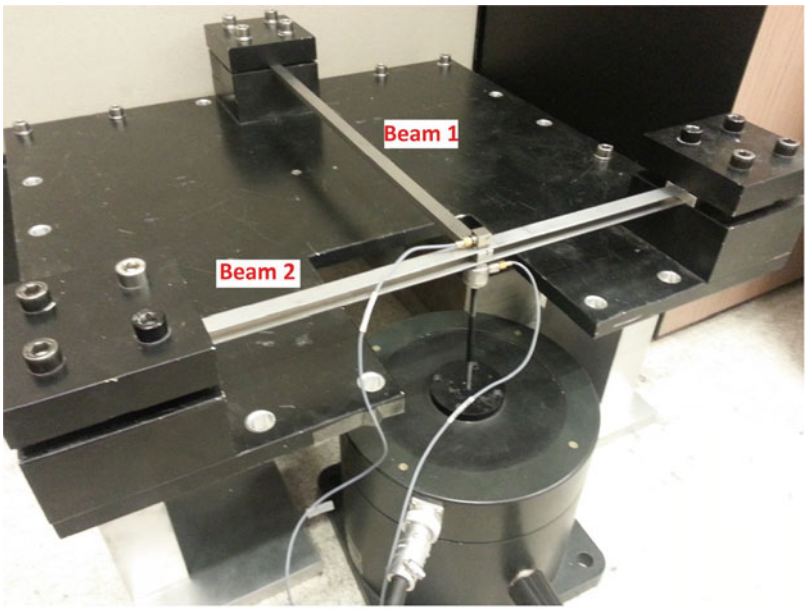

Fig. 26.2 Test rig used in the experiment

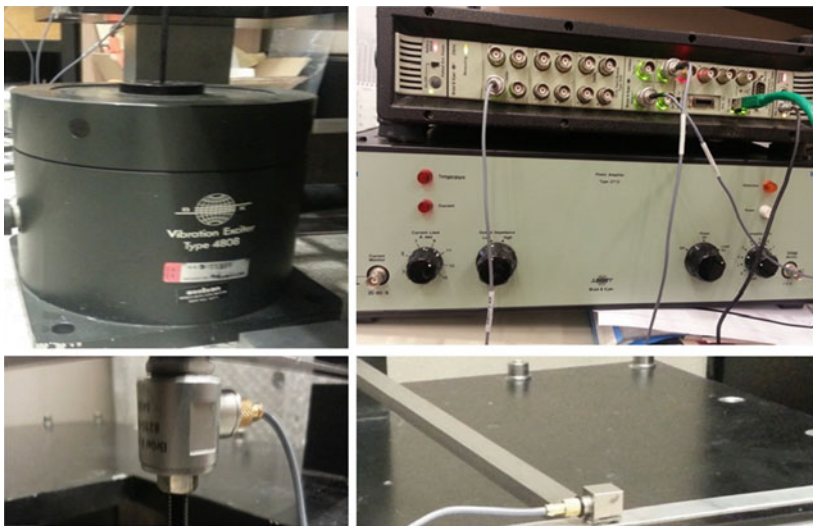

Fig. 26.3 View of the equipment used in the experiments

26.3.2 First Set of Experiments

In order to apply the PRD method, a set of experiments is conducted on the test setup. Firstly, the structure is excited with a random excitation. Since the method proposed by Canbaloglu and Özgüven [20, 21] depends on frequency of excitation, and it is shown that method works better around a linear resonance frequency of the structure, a quick test which does not excite nonlinearities considerably is made. In random excitation, low excitation signal level is selected and using this excitation type, driving point FRF at the tip of beam 1 in transverse direction is measured. The frequency range is selected between 0 and 100 Hz and a frequency resolution of 0.25 Hz is used in the measurements. In order to eliminate the noise in measurements, 130 averages are taken. After the analysis of the measurements, driving point FRF at the tip of beam 1 in transverse direction is obtained as shown in Fig. 26.4.

From Fig. 26.4, it is observed that the first resonance of the structure in transverse direction is around 41 Hz. Therefore in order to apply the proposed method, the structure is excited at around that frequency with a pure sine excitation at different forcing levels. The structure is excited at a low forcing level and then at a number of high forcing levels. The advantage of this method is that, there is no need for any vibration controller as in the cases of constant forcing or constant amplitude testing over a certain frequency range.

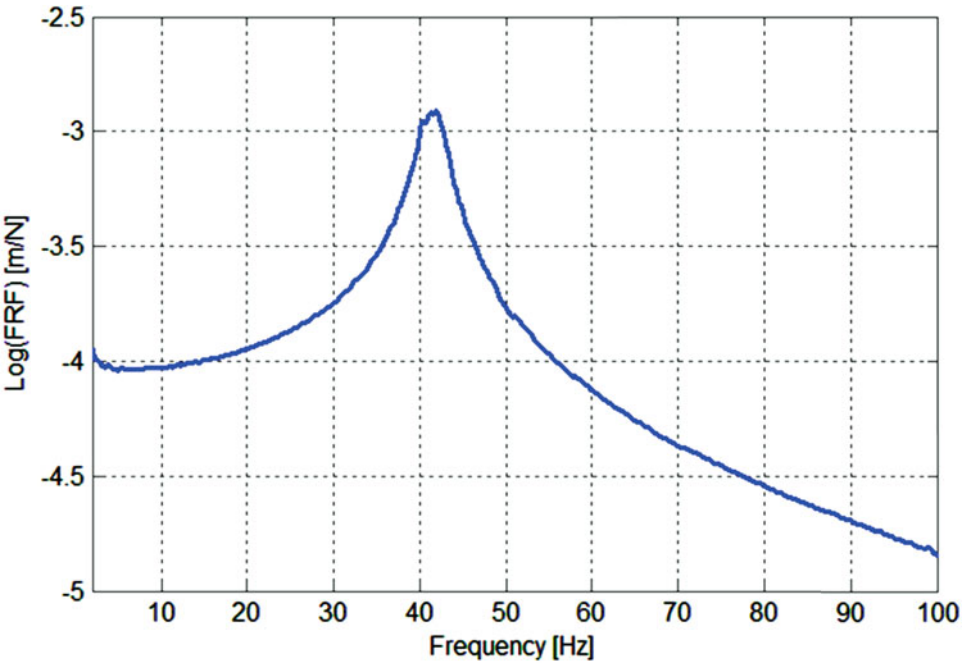

Fig. 26.4 The driving point FRF at the tip of beam 1 in transverse direction

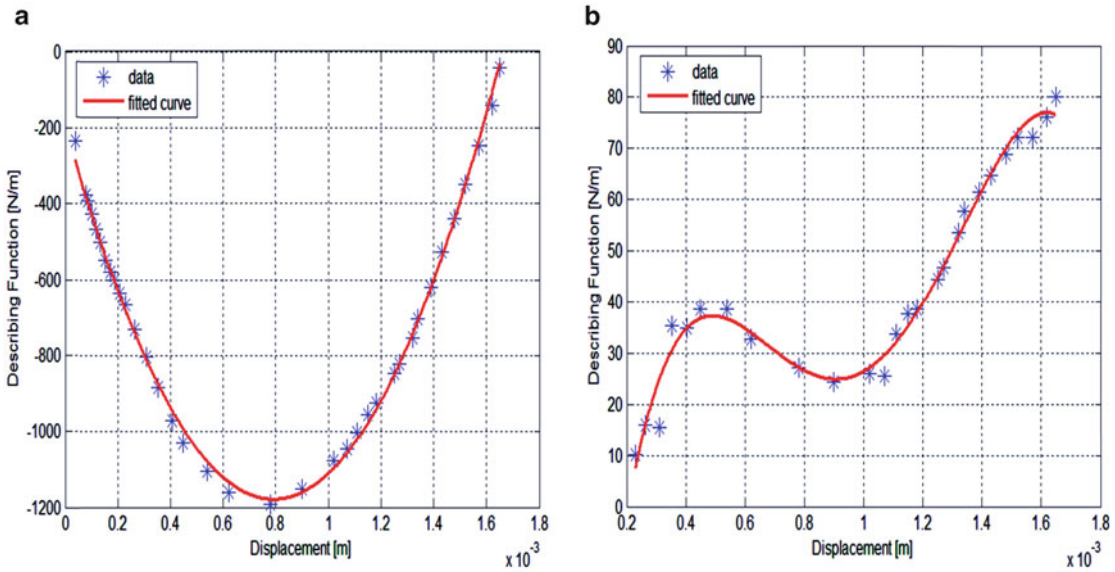

Fig. 26.5 Calculated describing function (**a**) Real part (**b**) Imaginary part

In order to study the effect of choosing different frequencies of excitation on the performance of the method, two different excitation frequencies (39 Hz, 40 Hz) are used and for each of these excitation frequencies, describing functions of the nonlinearities are obtained by using the method proposed.

26.3.2.1 Application of the PRD Method at Excitation Frequency 39 Hz

In Fig. 26.5, the calculated real and imaginary parts of the describing function obtained from experimental measurements by using PRD method and the corresponding fitted curves are shown.

For the real part of describing function, 2nd order, for the imaginary part of the describing function 4th order polynomials are fit. The coefficients estimated are given in Table 26.1.

Table 26.1 Coefficients of the polynomials fit to the data for real and imaginary parts of the describing function

	p_4	p_3	p_2	p_1	p_0
Real part of describing function $p_2x^2 + p_1x + p_0$	–	–	1.56×10^9	-2.48×10^6	-190
Imaginary part of describing function $p_4x^4 + p_3x^3 + p_2x^2 + p_1x + p_0$	-2.74×10^{14}	1.10×10^{12}	-1.49×10^9	8.0×10^5	-109

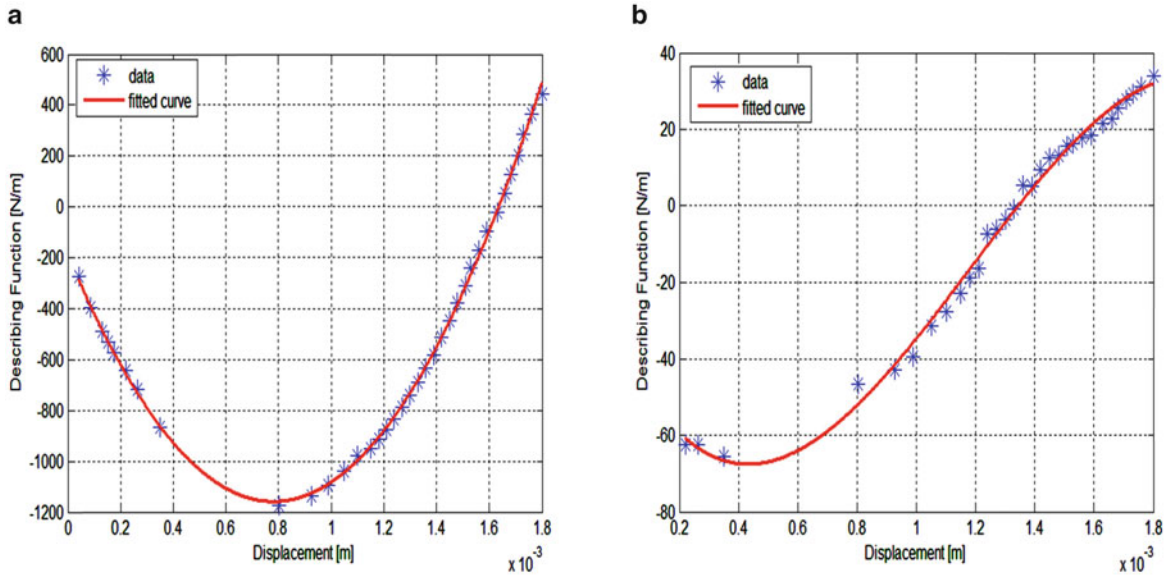

Fig. 26.6 Calculated describing function (**a**) Real part (**b**) Imaginary part

Table 26.2 Coefficients of the polynomials fit to the data for real and imaginary part of the describing function

	p_3	p_2	p_1	p_0
Real part of describing function $p_2x^2 + p_1x + p_0$	–	1.59×10^9	-2.49×10^6	-181
Imaginary part of describing function $p_3x^3 + p_2x^2 + p_1x + p_0$	-6.0×10^{10}	2.15×10^8	-1.52×10^5	-36

26.3.2.2 Application of the PRD Method at Excitation Frequency 40 Hz

In Fig. 26.6, calculated real and imaginary parts of the describing function obtained from experimental measurements by using PRD method and the corresponding fitted curves are shown.

For the real part of describing function, 2nd order, for the imaginary part of the describing function 3rd order polynomials are fit. The coefficients estimated are given in Table 26.2.

If we compare the coefficients for the real part of describing functions obtained using the measurements at 39 Hz and 40 Hz, it can be observed that coefficients are very close to each other. However when coefficients for the imaginary part of describing functions obtained by using the measurements at 39 Hz and 40 Hz are observed, it is seen that there are differences between the coefficients.

As a final test in this set of experiments, a constant low forcing level excitation experiment is performed between 37 Hz and 47 Hz. Stepped sine constant force test is performed for the given test set-up. Frequency resolution of 0.25 Hz is used in the experiment. Pure sine signal is used as the excitation signal. However, in order to make constant force vibration testing over the frequency range, a control strategy is needed in the experiments. This control is maintained manually by checking the forcing level and changing the excitation voltage supplied to the shaker iteratively for each frequency point. In Fig. 26.7, measured FRFs at F = 0.05 N are shown.

It is observed from the Fig. 26.7 that, the FRFs measured at F = 0.05 N seem like a linear FRF, which is an expected result.

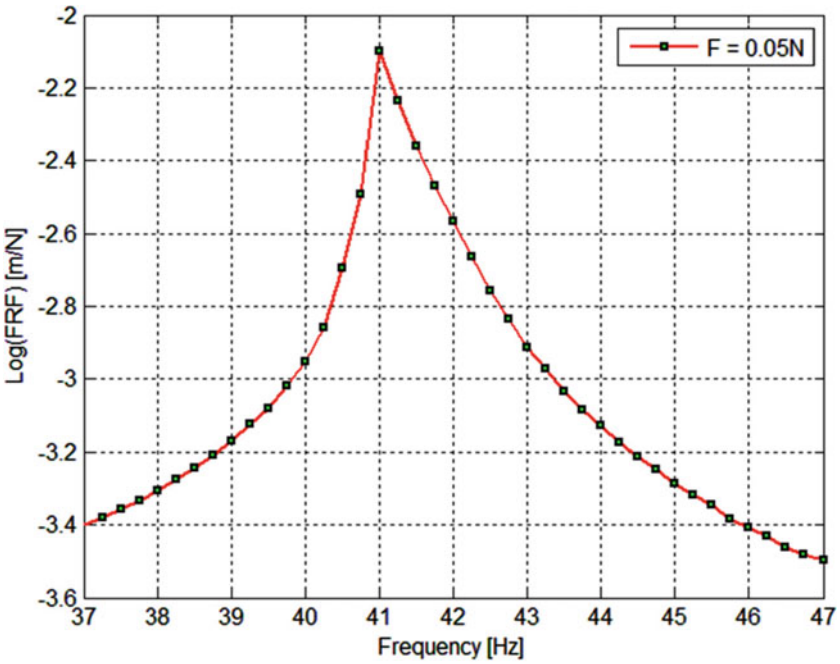

Fig. 26.7 Measured FRF at F = 0.05 N

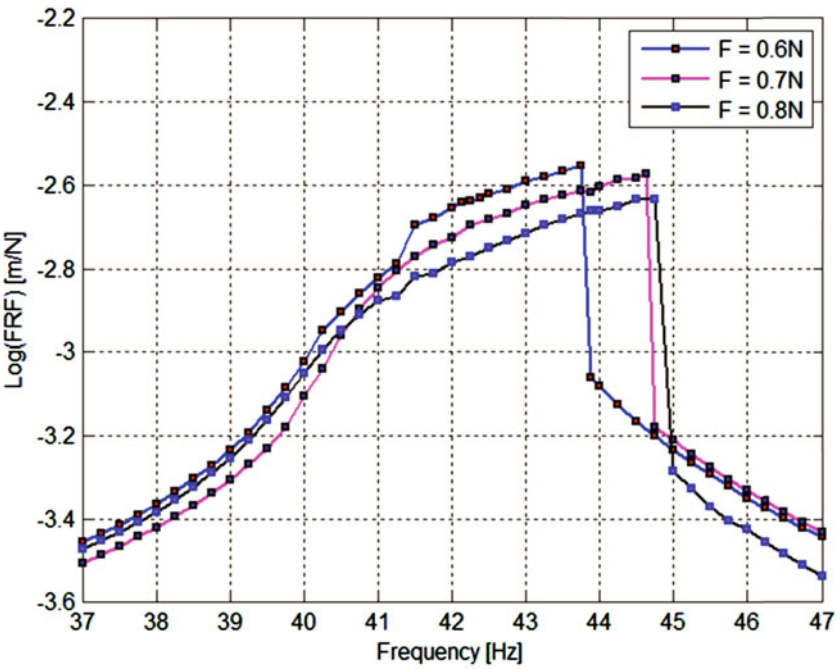

Fig. 26.8 Measured FRF at F = 0.6 N, F = 0.7 N, F = 0.8 N

26.3.3 Second Set of Experiments

In the second set of experiments, the aim is to perform the measurements which will be used to verify the PRD method and the model updating approach proposed. A set of stepped sine constant force tests is performed on the given set-up. Frequency resolution of 0.25 Hz is used in the experiment. Similarly, the constant force excitation is maintained by manually checking the forcing level and changing the excitation voltage supplied to the shaker at each frequency point. The structure is excited with 3 different forcing levels (F = 0.6 N, F = 0.7 N, F = 0.8 N). The measured FRFs are shown in Fig. 26.8.

26.4 Application of the PRD Method

Using the describing function values obtained and the FRF values measured at F = 0.05 N in the first set of experiments, linear FRF of the structure is predicted by applying PRD method. Since, describing function values are obtained at two different excitation frequencies, in order to study the effects of test frequency on the performance of the method, two separate linear FRF curves are predicted. The two linear FRF curves predicted by using the describing functions obtained from experiments made at 39 Hz and 40 Hz are compared with the FRFs measured at F = 0.05 N in Fig. 26.9, and with each other in Fig. 26.10.

As can be observed from Fig. 26.9, FRFs measured at low forcing level (F = 0.05 N) deviate from the linear FRFs obtained by using the proposed PRD method. It was recently shown [21] that PRD method yields the FRFs of the underlying linear system in a nonlinear system accurately; therefore it can be concluded here that FRFs measured even at a very low forcing level may not represent the linear FRF accurately, which is consistent with the observations made in a recent study [26].

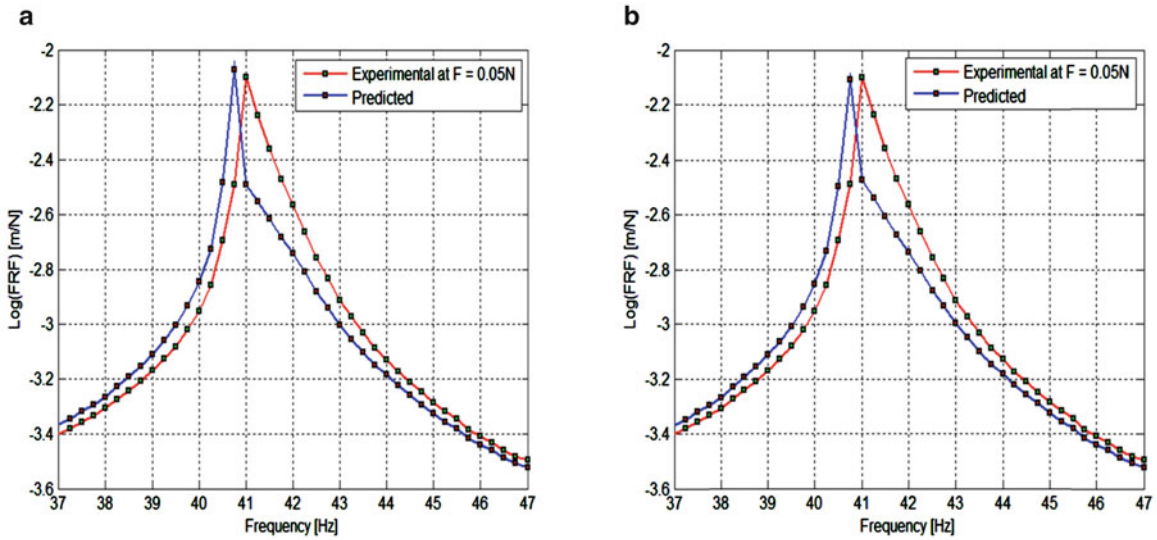

Fig. 26.9 Comparison of linear FRF at F = 0.05 N and predicted linear FRF by using PRD method using experiments conducted at (**a**) 39 Hz (**b**) 40 Hz

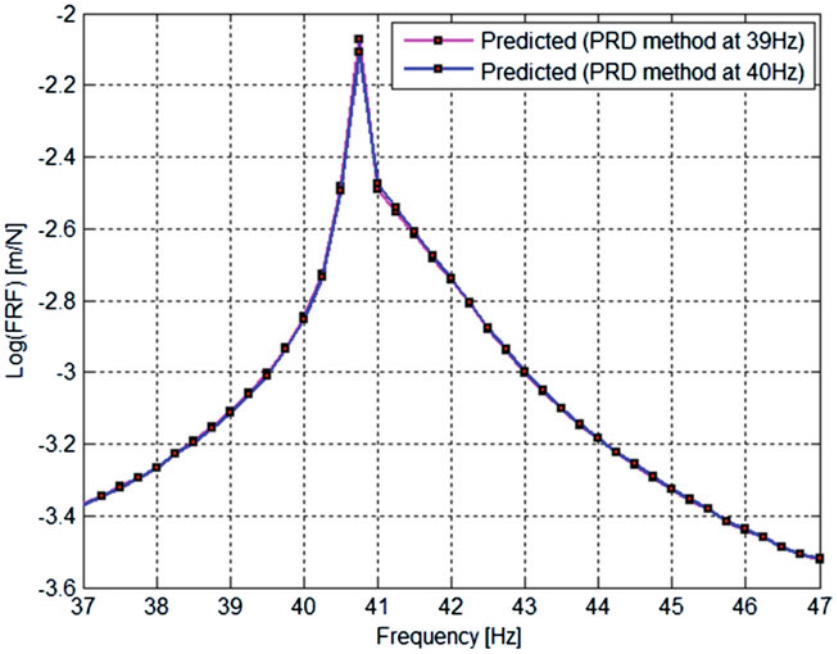

Fig. 26.10 Comparison of predicted linear FRF by using PRD method using experiments conducted at 39 Hz and 40 Hz

Furthermore, it is observed from Fig. 26.10 that linear FRFs obtained using the describing functions identified from the tests made at 39 Hz and 40 Hz are very close to each other, although the imaginary parts of the describing functions identified from these tests are slightly different from each other.

26.5 Model Updating of the Test System and Verification of the Updated Model

In this section, linear FE model of the test system is built in ANSYS and then the linear FE model is updated by employing the approach proposed. The accuracy of the updated nonlinear model of the test structure is also demonstrated. First, the PRD method is applied; thus the describing functions representing the nonlinearity in the system are identified and the linear FRFs are predicted from the measured nonlinear FRFs. Secondly, the linear FE model of the test structure is updated by using the linear FRFs and applying inverse eigensensitivity method. Using the identified nonlinearity and updated linear FE model updated nonlinear model of the test structure is constructed. Finally, predicted and measured FRFs of the test structure are compared at different forcing levels in order to demonstrate the accuracy of the updated nonlinear model of the system.

The FE model of the test structure is shown in Fig. 26.11 and the material properties used in the initial FE model is given Table 26.3.

The first natural frequency and the driving point FRF at the tip of beam 1 in Z (transverse) direction are calculated in ANSYS by using the FE model. Comparisons of the natural frequency and linear FRFs obtained from FE analysis with those obtained from experiments by using PRD method are given in Table 26.4 and Fig. 26.12, respectively.

As can be seen in Table 26.4 and Fig. 26.12, there are discrepancies between the results; therefore the FE model of the test structure needs to be updated. Since most of the uncertainty is generally in modulus of elasticity of the materials, as an updating parameter in FE model, the modulus of elasticity is selected. For the selected parameter, element of the sensitivity matrix is calculated using the centered difference approximation with $O(h^4)$ which is given in Eq. 26.9, at each iteration step. After five iterations, updating parameter is converged to 188 GPa. The convergence graph of this parameter is given in Fig. 26.13.

Using the converged value of E, the FE model is updated. Then the first natural frequency of the updated linear model is calculated and compared with that of initial FE model, as well as with the natural frequency obtained from experiments by using PRD method in Table 26.5.

As can be seen in Table 26.5, the first natural frequency is very accurately estimated by using the updated FE model. In Fig. 26.14, the linear FRFs obtained by using PRD method from experimentally measured nonlinear FRFs are compared with those calculated from, initial and updated FE models. As can be seen in Fig. 26.14, considerable improvement is obtained when updated FE model is used.

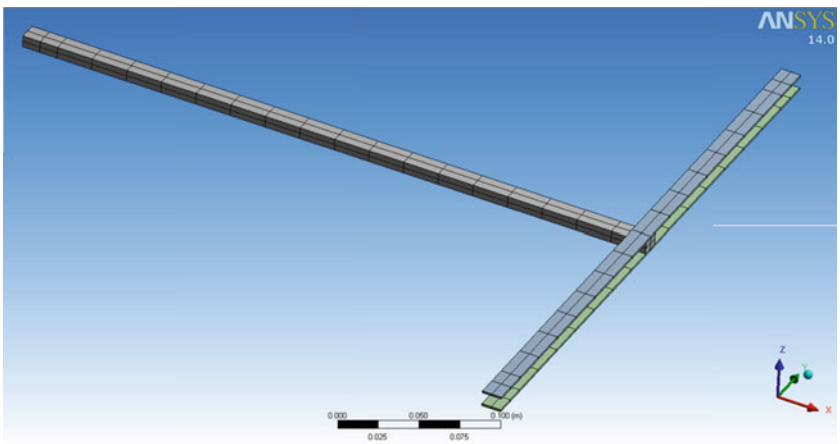

Fig. 26.11 FE model of the test structure

Table 26.3 Material properties used in the initial FE model

	Modulus of elasticity (E) (GPa)	Poisson's ratio (ν)	Density (ρ) (kg/m^3)
Beam1	210	0.3	7,850
Beam2	210	0.3	7,850

Table 26.4 Comparison of the first natural frequency obtained from initial FE model with the experimental value obtained by using PRD method

Mode number	Natural frequency (PRD method) (Hz)	Natural frequency (initial FE model) (Hz)	Error (%)
1	40.75	43.1	5.77

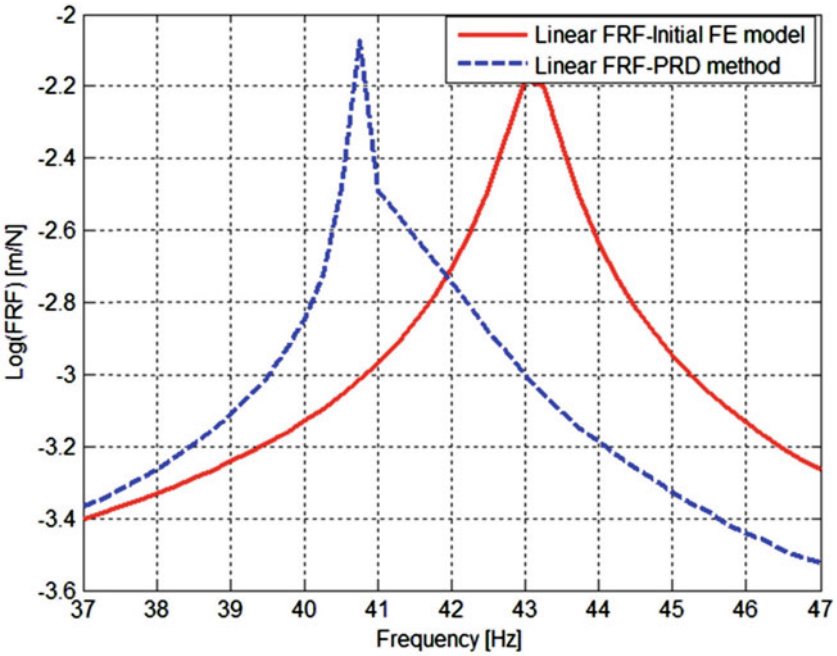

Fig. 26.12 Comparison of the linear FRFs obtained from initial FE model with those obtained by using PRD method

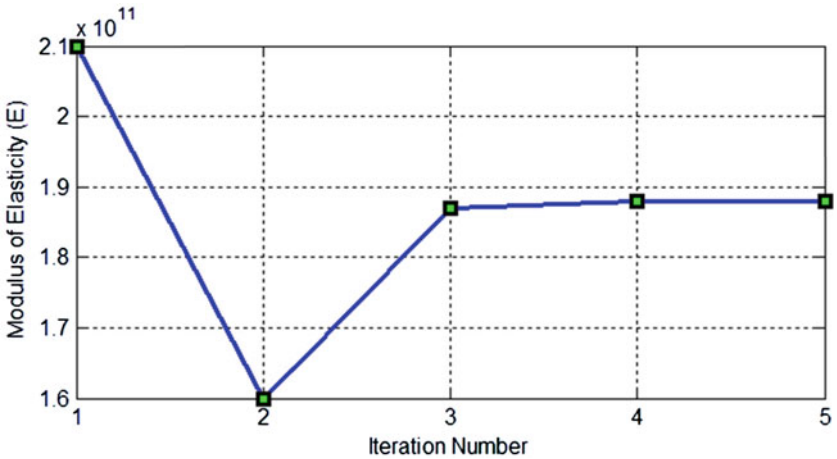

Fig. 26.13 Convergence of the modulus of elasticity of the beams

Table 26.5 Comparison of the first natural frequency obtained from initial and updated FE models with experimental value obtained by using PRD method

Mode number	Natural frequency (PRD method) (Hz)	Natural frequency (initial FE model) (Hz)	Error (%)	Natural frequency (updated FE model) (Hz)	Error (%)
1	40.75	43.1	5.77	40.75	0.00

Since the ultimate goal is to have accurate nonlinear response predictions from the updated model, nonlinear FRFs measured experimentally for F = 0.6 N, F = 0.7 N and F = 0.8 N are compared with those obtained from the initial and updated models (composed of original and updated FE combined with identified nonlinearity). The results are given in Fig. 26.15. As observed in Fig. 26.15 there is a considerable improvement in the FRFs calculated with the updated model for all forcing levels.

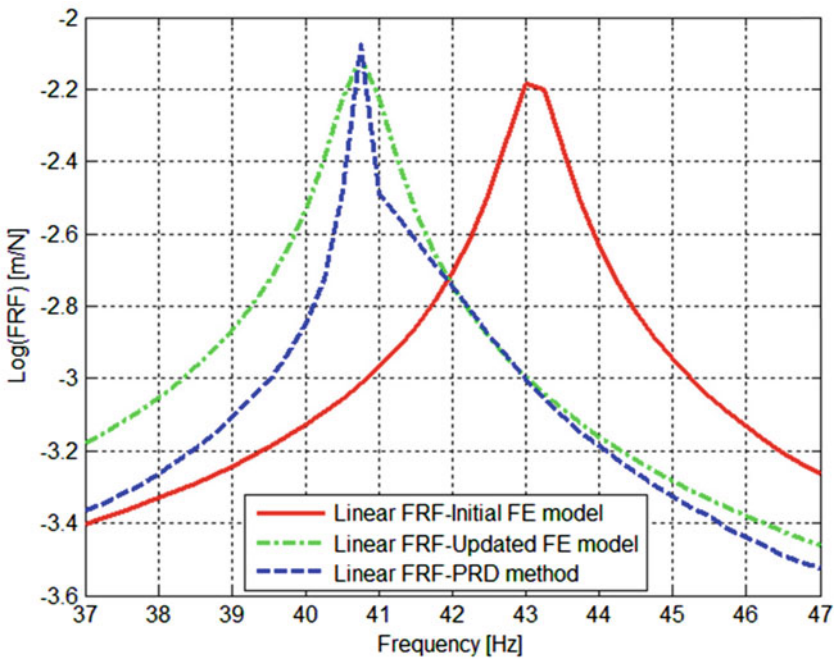

Fig. 26.14 Comparison of the linear FRF obtained by using PRD method from experimentally measured values, with those calculated from, initial and updated FE models

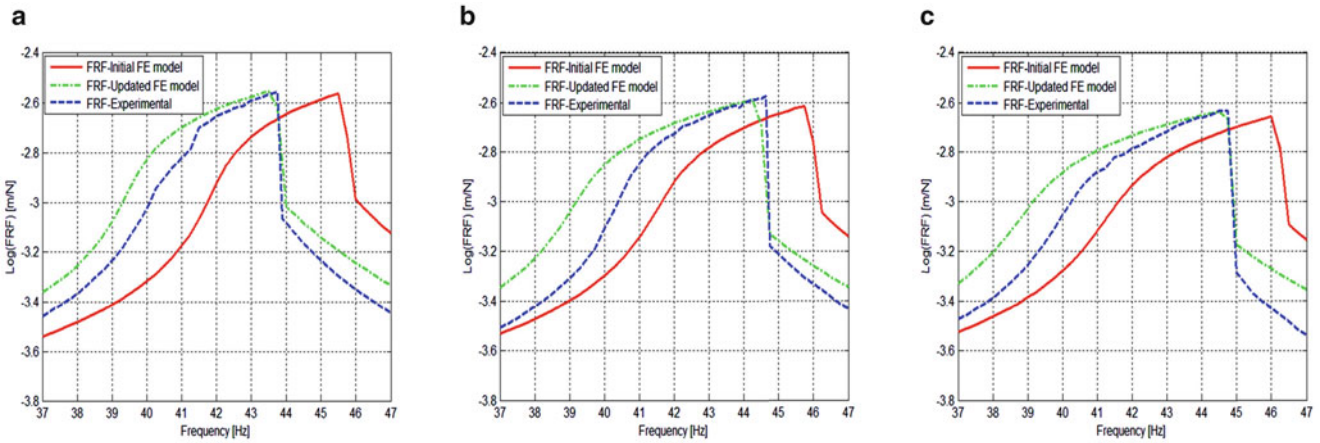

Fig. 26.15 Comparison of FRFs obtained from initial and updated models with the experimental ones for (**a**) F = 0.6 N (**b**) F = 0.7 N (**c**) F = 0.8 N

26.6 Summary and Conclusions

In this study, a nonlinear T-beam test structure is used to validate the accuracy of the nonlinear model updating approach suggested. Pseudo Receptance Difference (PRD) method, recently developed by the authors [20] calculates the linear FRFs of a nonlinear structure by using nonlinear FRFs experimentally measured at various forcing levels. The method, at the same time, identifies nonlinearities in the system. In the approach suggested, first, the linear FRFs are calculated from experimentally measured nonlinear FRFs, and the nonlinearities in the structure are identified. Then by using the linear FRFs obtained employing PRD method, FE model of the linear part of the structure is updated. In this work the inverse eigensensitivity method is used to update the linear FE model. Finally, the accuracy of the updated nonlinear model of the test structure is demonstrated by comparing calculated and measured FRFs of the nonlinear test structure at several different forcing levels.

In the experiments, firstly the structure is excited with a random excitation in order to find the range of frequencies where the first resonance occurs. Then, in order to apply the PRD method, the structure is excited at a constant frequency (which is close to the resonance frequency of the underlying linear system) with a pure sine excitation at different forcing levels. Finally, a set of stepped sine constant force experiments is performed on the test structure in order to measure nonlinear FRFs at various forcing levels.

Computationally; by applying the PRD method, first the describing functions of the nonlinearities are identified from test results, and then using these describing functions and the FRF values measured at low forcing level, linear FRFs of the structure are predicted. In the model updating of the FE model of the linear part of the structure, the predicted linear FRFs of the test system are used.

In this study it is shown that in a nonlinear structure, FRFs measured at a low forcing level ($F = 0.05$ N, in this experimental work) may deviate from the actual FRFs of the linear part of the system. So it can be concluded that if sufficiently low forcing level cannot be applied in the experiments, or if there is friction type of nonlinearity in the system along with other types of nonlinearity, then the linear FRFs cannot be directly measured accurately. It is furthermore experimentally demonstrated that PRD method is very successful in predicting linear FRFs of a nonlinear structure from measured nonlinear FRFs. It is also observed that the frequency at which the experiments are made for the application of PRD method does not have a considerable effect on the accuracy of the predicted linear FRFs, as long as it is close to the resonance frequency.

Finally, the nonlinear model updating approach proposed is validated in this experimental study by comparing the nonlinear FRFs measured at various forcing levels, with those obtained from the original and updated models (which are defined by the original and updated FE models combined with identified nonlinearity). It is shown that with the updated nonlinear model considerable improvements can be obtained in predicting FRFs of a nonlinear structure at different forcing levels.

References

1. Nalitolela NG, Penny JET, Friswell MI (1990) Updating structural parameters of a finite element model by adding mass or stiffness to the system. In: Proceedings of the 8th international modal analysis conference, Kissimmee, pp 836–842
2. Roy NA, Girard A, Dupuis PE (1991) A direct energy approach for updating dynamic finite element models. In: Proceedings of the 9th international modal analysis conference, Florence, pp 51–57
3. Brughmans M, Hrycko G, Wyzykowski J (1991) Application of FEM model correlation and updating techniques on an aircraft using test data of a ground vibration survey. In: Proceedings of the 9th international modal analysis conference, Florence, pp 517–525
4. Link M, Zhang L (1992) Experience with different procedures for updating structural parameters of analytical models using test data. In: Proceedings of the 10th international modal analysis conference, San Diego, pp 730–738
5. Jung H, Ewins DJ (1992) Error sensitivity of the inverse eigensensitivity method for model updating. In: Proceedings of the 10th international modal analysis conference, San Diego, pp 1051–1056
6. Miccoli G, Agostoni F (1993) Modal updating using sensitivity analysis. In: Proceedings of the 11th international modal analysis conference, Kissimmee, pp 683–689
7. Hemez FM (1996) Advanced tools for updating damped finite element models using static modal and flexibility data. In: Proceedings of the 14th international modal analysis conference, Dearborn, pp 511–517
8. Lenoir D, Cogan S, Lallement G, Bricout JN (1998) Model updating by modal synthesis of experimental forced responses. In: Proceedings of the 16th international modal analysis conference, Santa Barbara, pp 399–405
9. Mottershead JE, Mares C, Friswell MI, James S (2000) Model updating of an aluminium space-frame using different parameter sets. In: Proceedings of the 18th international modal analysis conference, San Antonio, pp 576–583
10. Jung DS, Kim CY, Kang JH (2007) Hybrid optimization technique based on GA-NMS for FE model updating. In: Proceedings of the 25th international modal analysis conference, Orlando
11. Kozak MT, Cömert MD, Özgüven HN (2007) Model updating routine based on the minimization of a new frequency response based index for error localization. In: Proceedings of the 25th international modal analysis conference, Orlando, pp 84–95
12. Boulkaibet I, Mthembu L, Marwala T, Friswell MI, Adhikari S (2013) Finite element model updating using the shadow hybrid Monte Carlo technique. In: Proceedings of the 31st international modal analysis conference, Orange County
13. Fei Q, Jiang D (2014) Evaluating initial model for dynamic model updating: criteria and application. In: Proceedings of the 32nd international modal analysis conference, Orlando
14. Boulkaibet I, Mthembu L, Marwala T, Friswell MI, Adhikari S (2014) Finite element model updating using the separable shadow hybrid Monte Carlo technique. In: Proceedings of the 32nd international modal analysis conference, Orlando
15. Hemez FM (2014) A brief history of 30 years of model updating in structural dynamics. In: Proceedings of the 32nd international modal analysis conference, Orlando
16. Hasselman TK, Anderson MC, Gan W (1998) Principal components analysis for nonlinear model correlation, updating and uncertainty evaluation. In: Proceedings of the 16th international modal analysis conference, Santa Barbara, pp 644–651
17. Anderson MC, Hasselman TK (2000) Minimizing parameter correlation in nonlinear model updating. In: Proceedings of the 18th international modal analysis conference, San Antonio, pp 109–115
18. Burton TD, Hemez FM, Rhee W (2000) Combined model reduction/SVD approach to nonlinear model updating. In: Proceedings of the 18th international modal analysis conference, San Antonio, pp 116–123
19. Silva SD, Cogan S, Foltete E, Buffe F (2008) Metrics for non-linear model updating in mechanical systems. In: Proceedings of the 26th international modal analysis conference, Orlando

20. Canbaloglu G, Özgüven HN (2013) Obtaining linear FRFs for model updating in structures with multiple nonlinearities including friction. Topics in nonlinear dynamics, volume 1: proceedings of the 31st IMAC, a conference on structural dynamics, Garden Grove, California, pp 145–157
21. Canbaloglu G, Özgüven HN (2014) Model updating of nonlinear structures. In: Proceedings of the 32nd international modal analysis conference, Orlando
22. Kerschen G, Worden K, Vakakis AF, Golinval JC (2006) Past, present and future of nonlinear system identification in structural dynamics. Mech Syst Signal Process 20:505–592
23. Doranga S, Wu CQ (2014) Parameter identification for nonlinear dynamic systems via multilinear least square estimation. In: Proceedings of the 32nd international modal analysis conference, Orlando
24. Grappasonni C, Noel JP, Kerschen G (2014) Subspace and nonlinear-normal-modes-based identification of a beam with softening-hardening behaviour. In: Proceedings of the 32nd international modal analysis conference, Orlando
25. Aykan M, Altuntop E (2014) Parametric nonlinearity identification of a gearbox from measured frequency response data. In: Proceedings of the 32nd international modal analysis conference, Orlando
26. Aykan M, Özgüven HN (2013) Identification of restoring force surfaces in nonlinear MDOF systems from FRF data using nonlinearity matrix. In: Proceedings of the 31st international modal analysis conference, Garden Grove
27. Londono JM, Cooper JE (2014) Experimental identification of a system containing geometric nonlinearities. In: Proceedings of the 32nd international modal analysis conference, Orlando
28. Collins JD, Hart GC, Hasselman TK, Kennedy B (1974) Statistical identification of structure. AIAA J 12(2):185–190
29. Ferreira JV (1998) Dynamic response analysis of structures with nonlinear components. Ph.D. thesis, Department of Mechanical Engineering, Imperial College London
30. Siller HRE (2004) Non-linear modal analysis methods for engineering structures. Ph.D. thesis, Department of Mechanical Engineering, Imperial College London/University of London

Chapter 27
Systems with Bilinear Stiffness: Extraction of Backbone Curves and Identification

Julian M. Londono, Simon A. Neild, and Jonathan E. Cooper

Abstract With the need to improve system performance, aerospace and automotive structures are being designed with much lighter construction and also much less inherent damping. A consequence of this is that structural nonlinearities have a much greater effect on the static and dynamic performance. Although there has been significant effort recently towards the extension of modal analysis to identify structural nonlinearities, these techniques are still not at a stage where they can be used on industrial size structures. This paper describes an experimental investigation on a structure model containing two bilinear stiffness elements. A method for the estimation of the characteristic backbone curves of the nonlinear system is first discussed and then used to characterise the active nonlinear elements from experimental data. Conclusions are drawn as to the most effective way to extend the proposed method for future industrial applications.

Keywords Bilinear stiffness • Experimental identification • Resonance decay method • Identification of nonlinearities

27.1 Introduction

The development of novel materials together with the increasing computational capabilities have brought to light a variety of novel and more efficient design solutions to diverse engineering problems. These solutions usually result in extremely flexible structures that are particularly susceptible to exhibiting nonlinear effects that occur at large structural deflections. Others structural systems can also combine nonlinear phenomena due to discontinuities (like mobile joints or connections) and nonlinear material properties. Therefore, the understanding of nonlinear dynamic systems and their performance in operational and under extreme loading conditions is an increasingly important research topic with potentially strong impact in many industrial sectors.

One useful tool capable of offering a better understanding of the behaviour of nonlinear systems is the backbone curve [11, 12]. This defines the natural frequency as a function of the amplitude of the system response when neither damping nor forcing are present.

This paper studies a scaled structural model that features two bilinear stiffness elements. The model is, at a first approximation, linear at low vibration levels but the contribution of the nonlinear elements becomes significant at larger excitation levels. Our interest is to investigate the free vibration response originated from initial conditions belonging to particular steady-state responses of the nonlinear system. The Resonance Decay Method (RDM) [6] is used here, as this enables the excitation of individual modes of the system independently. Once the structure is vibrating at the desired resonance condition, the forcing is removed and the resulting free vibration response can be analysed. This strategy has proven to be able to isolate distinct characteristics of the examined nonlinear system [1, 10].

One promising technique for nonlinear identification consists in curve-fitting the resulting decay response directly to identify active nonlinear elements [4, 6]. This requires prior knowledge of the nature of the nonlinearity to be curve-fitted. The problem of deciding which terms are required for an accurate identification has previously been addressed using some forms of the Forward Selection, Backward Elimination or other techniques based on soft computing [5, 9]. Notwithstanding, a suitable strategy to select proper candidates of the nonlinearities is still unclear.

In this paper, the RDM method is used to excite the structure at a number of resonance frequencies that enables measurements to be made in regimes where the nonlinearities are more active. This facilitates both the estimation of backbone curves from the experimental decay records and more information to be contained in the backbone curves, thus enabling a appropriate identification of the nonlinearities.

J.M. Londono (✉) • S.A. Neild • J.E. Cooper
Faculty of Engineering, University of Bristol, Queens Building, University Walk, Bristol BS8 1TR, UK
e-mail: Julian.Londono@bristol.ac.uk

G. Kerschen (ed.), *Nonlinear Dynamics, Volume 1*, Conference Proceedings of the Society for Experimental Mechanics Series, DOI 10.1007/978-3-319-15221-9_27

27.2 Backbone Curves from Experimental Data

Our interest is to examine free vibration responses originated from initial conditions that lay on one steady-state condition of the system. This strategy has proven to be able to isolate distinct characteristics of the examined dynamical system. Consequently, in this approach the signal used to estimate the backbone curves of the nonlinear structure is generated in accordance with the Resonance Decay Method (RDM) [6]. In this technique, individual modes of the system can be excited independently by applying an appropriated force pattern. Such a force pattern is determined by using the normal-force mode appropriation method, that enables for extracting the undamped natural frequency and normal-modes shapes of a linearised structural system [13]. After the appropriated force pattern is computed, this is applied to the system at the relevant frequency using harmonic excitation. The input is then removed and the model undergoes free vibration from the steady-state reached. As long as the level of vibration in the steady-state is large enough to activate the structural nonlinearities, the generated decaying response can be use to estimate the system's backbone curves that offer significant information about the system and its dynamic variables.

Two main features namely instantaneous frequency and amplitude envelope are estimated in the interest of revealing the active nonlinear elements.

While there are many procedures for calculating instantaneous frequency such as the Wigner–Ville distribution [7] and the Hilbert transform [3], the process used here is based on the detection of the zero-crossing points of the response signal. Once the sequence of the crossing times (t^o) is properly determined, the first estimation of the instantaneous frequency is computed as the inverse of the instantaneous period along one complete cycle. This frequency is assigned to the crossing time at the centre of this respective interval. Imperfects in the prediction arising from noise and other sampling issues are smoothed out by means of a moving average (MA) filter. In spite of its simplicity, the moving average filter exhibits excellent properties in reducing random noise while is able to retain a sharper step response. Hence, the final estimation of the instantness frequency derives from a processed data that retains only the dominant frequency variation along time. We note that this procedure assumes that the instantaneous frequency estimated is not significantly altered by the dissipative forces acting on the system.

To estimate the instantaneous amplitude envelope over time, the maximum absolute value of the decaying response and its corresponding occurring time are measured within each interval $\{t_i^o, t_{i+1}^o\}$. These sequence of numbers is used in conjunction with a standard polynomial interpolating function to determine the value of the envelope amplitude at the same times at which the instantaneous frequency has been evaluated.

As a final step, the backbone curve can be obtained as a function of above estimated instantaneous frequency and amplitude enveloped parametrised by time.

27.3 Experimental Example

Results of a model structure containing two element with bilinear stiffness are used here to illustrate the applicability of backbone curves as a tool for characterising and modelling nonlinear systems. The test structure approximately represents the configuration of an aircraft wing having two underwing stores (e.g., engines) with nonlinear pylon connections. The model consists of a rectangular aluminium plate hung by bungee chords and two lumped masses suspended underneath via pylon plates, as shown in Fig. 27.1.

The nonlinear connection is built by fixing the pylon plates onto the wing using two bespoke clamps. This connecting element features internal curve surfaces that produce a characteristic nonlinear behaviour (see details in Fig. 27.1b). This wing structure was previously tested in [10] using the RDM approach. The model is excited by an electrodynamic shaker (LDS V201) and instrumented with nine piezoelectric accelerometers (PCB 33M07) and one force sensors (PCB 208C03) to measure the shaker driving force. Additionally, a laser Doppler vibrometer (PDV-100) is used to measure the velocity in the horizontal direction of one of the stores. Laser readings are used only to verify the processed data after numerically integrating the acquired acceleration signals. The vibration tests were controlled and recorded by using the data acquisition systems LMS SCADAS Lab.

A number of tests were performed to gain insights into the overall structural behaviour of the wing model. To begin with, the pylon connection was tested statically to determine the actual nonlinearity acting on the system. Figure 27.2 (left) shows the resulting bilinear hardening stiffness exhibited by the clamped connection of one of the pylons when it is loaded in a pseudo-static test cyclically. Several dynamic tests were also conducted at different applied vibration levels. The driving force employed to vibrate the model was a burst random signal with a bandwidth of 256 Hz. Figure 27.2 presents five FRFs

Fig. 27.1 Test structure representing the configuration of an aircraft wing having two underwing stores supported by pylons. (**a**) General view of the experiment setup. (**b**) Detailed view of the nonlinear connection

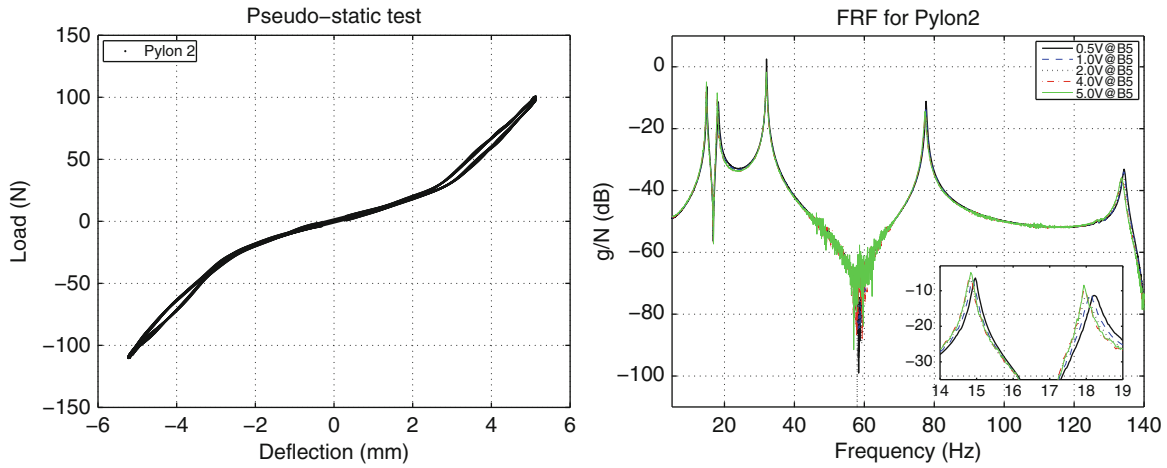

Fig. 27.2 Pseudo-static test on one isolated clamp connection showing a bilinear hardening stiffness (*left*). Set of FRFs for different levels of vibration via random excitation. Note the softening effect exhibited by the resonance peaks in the zoomed box (*right*)

for different increasing levels of excitation. In their estimation, 25 averages are considered. It can be seen that the FRFs do not overlay each other for several modes indicating the presence of nonlinearities. Interestingly, the zoomed plot within the figure revels a clear softening effect that is opposite to what might be expected from the preliminary pseudo-static tests. This fact will be further discuss later. We note that the frequency shift is mainly exhibited by the first and second resonance frequencies located around 16 and 18 Hz respectively.

Classical modal testing [2] is used to obtain the shapes corresponding to the first four vibration modes, see Fig. 27.3. The first and second modes describe the stores moving in anti-phase and in phase respectively. Whereas the third and fourth correspond to modes that are dominated by the first and second bending modes of the wing respectively, with minimal interaction of the stores. Therefore, the nonlinear behaviour is expected to mainly affect the structure when vibrating in one of the first two modes. In the present paper, we only discuss the results associated with to the first resonance frequency.

Following the procedure described above for the experimental estimation of backbone curves, the first tasks consists in applying the RDM method for the first resonance frequency in order to obtain suitable decay records. After applying the normal-force mode appropriation method [13], results showed that not more than one shaker is required to properly excite the first mode and thus obtain the desired system's resonance condition. Sinusoidal excitation in force-control mode is applied to the test specimen at the first resonance frequency of the underlying linear system. The forcing frequency is gradually tuned until the amplitude of the response rises in magnitude and is large enough to activate the nonlinearity. When the system response reaches the state-steady condition, the shaker is turned off and the decay response recorded.

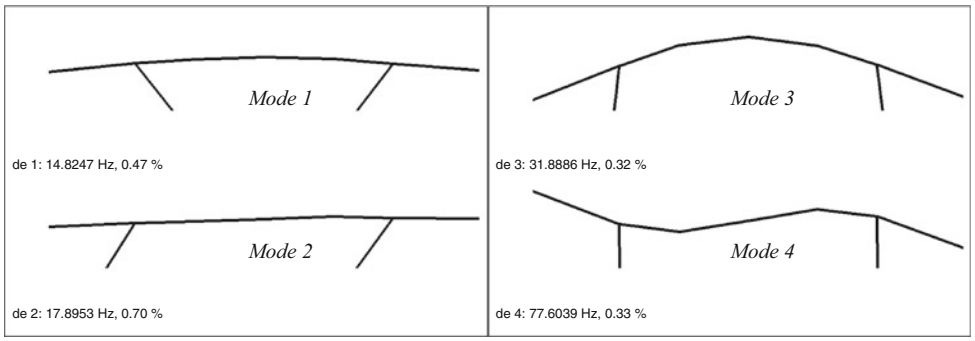

Fig. 27.3 First four mode shapes of the underlying linear system of the test model

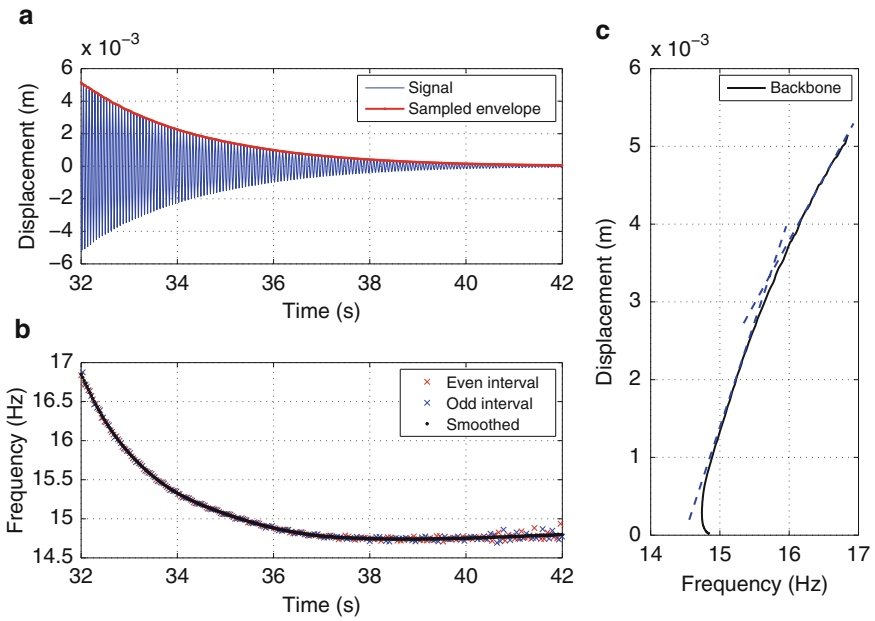

Fig. 27.4 Estimation of backbone curve from experimental decay data after achieving resonance condition for the first frequency (Displacements of store 2). (**a**) Decaying signal and the estimated envelope; (**b**) instantaneous frequency; (**c**) backbone curve

The amplitude envelope and instantaneous frequency are then estimated for individual displacement records in physical space. The displacements have been calculated via double integration of the accelerometer signals. Figure 27.4a presents the decaying record of the store 2 originated from the steady-state condition at the first resonance frequency. The red line corresponds to the estimation of the amplitude envelope. Figure 27.4b shows the initial approximation of the instantaneous frequency with coloured crosses and the final estimation with black dots. The backbone curve produced is presented in Fig. 27.4c.

Some interesting aspects can be seen in these results. First of all, the bilinear characteristic of the nonlinear connection can be seen in the backbone curve presented in Fig. 27.4c. Thus, the nonlinearity could be characterised by this means. With help of two auxiliary dashed lines, the inflexion point seems to be consistent with the one in Fig. 27.2a. In addition, it can be seen that the dispersion of the estimation of the instantaneous frequency become larger when the amplitude of oscillation is small. This is due to the fact that the accuracy of the measurements is reduced at that range of vibration as the signal-to-noise ratio is critically low.

The matrix of the first four mode shapes of the underlining linear system is presented in (27.1). The first seven rows correspond to the accelerometers located on the wing plate, and the last two rows, to the accelerometers located in the stores as shown in Fig. 27.1. This matrix can be used to operate a linear transformation on the decay records and thus obtain the structural response in terms of linear modal coordinates.

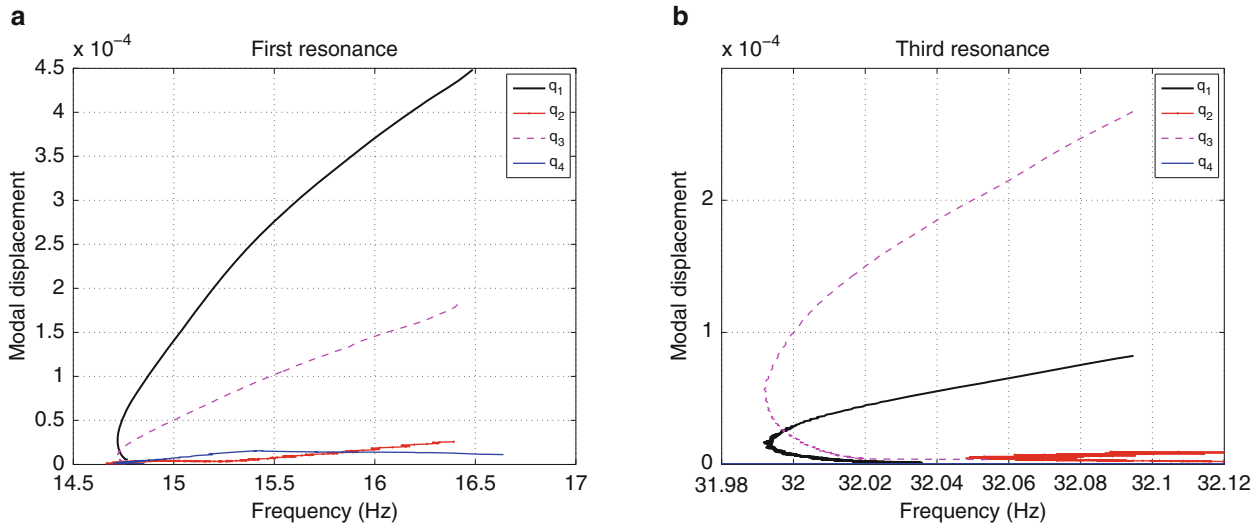

Fig. 27.5 Backbone curves estimated from experimental data in terms of the modal coordinates q_1 to q_4. (**a**) From decay after achieving steady-state response at the first resonance. (**b**) From decay after achieving steady-state response at the third resonance

$$\Phi = \begin{bmatrix} -0.249 & 0.074 & -1.418 & -1.068 \\ -0.031 & 0.085 & -0.120 & 0.140 \\ 0.097 & 0.046 & 0.668 & 0.413 \\ 0.153 & 0.004 & 1.000 & 0.005 \\ 0.106 & -0.046 & 0.661 & -0.415 \\ -0.009 & -0.092 & -0.073 & -0.153 \\ -0.205 & -0.084 & -1.293 & 1.000 \\ 1.000 & 1.000 & -0.165 & -0.008 \\ -1.171 & 0.942 & 0.165 & -0.017 \end{bmatrix} \tag{27.1}$$

The procedure for estimating the backbone curves can then be applied independently to each decaying response of the system expressed in terms of the linear modal space. Figure 27.5a presents the resulting backbone curves estimated when projected onto the linear modal coordinates q_1, q_2, q_3 and q_4, from decaying signals corresponding to the first resonance frequency. Notice that the dominant backbone curve corresponds to the first linear modal coordinated q_1 (black solid line). An expected result as the structure was harmonically excited around the frequency corresponding to the first resonance. Note that this curve also shows the bilinear characteristic of the nonlinear stiffness. Furthermore, it can be seen that when the structural response is large and the influence of the nonlinearity is much more significant, the backbone curve in terms of the third modal coordinate q_3 starts to rise too. This is a nonlinear effect that can be recognised as an interaction between linear modes since the structural response can not be fully represented by a single linear mode anymore; in fact, the backbone curve relates directly to the nonlinear normal modes of the system [8]. Note that this aspect could be exploit to include additional coupled terms into the modal equations for nonlinear system identification purposes.

With the aim of verifying the aforementioned modal interaction, the RDM method is applied again, this time for the third resonance. As before a sinusoidal excitation in force-control mode is applied to the test specimen at an appropriate resonance frequency until the system reaches the state-steady response, then the shaker is turned off and the decaying signals recorded. Figure 27.5b presents the resulting backbone curves estimated with respect to the modal coordinates q_1, q_2, q_3 and q_4, from decaying signals that belong to the third resonance frequency. These results not only show that the structural responses can not be fully represented by the third modal coordinate only (magenta dashed line), but also confirm the interaction between modes 1 and 3, as the response in terms of the first linear modal coordinate is significant.

These results indicates that most of the structural response for the first and third resonance frequency (and so the information of the nonlinearity) is contained in both backbone curves q_1 and q_3. We recall that the backbone curve defines the natural frequency as a function of the amplitude of the system response when neither damping nor forcing are present. Thus, we can write for each resonance a modal equation of the form

$$\ddot{q}_i + \omega_i^2 q_i + f_{NL}(q_{1_i}, q_{3_i}) = 0\,; \quad \forall i = 1, 3 \tag{27.2}$$

Table 27.1 Best set of coefficients that fits Eq. (27.4) to the backbone curves presented in Fig. 27.5

i-th resonance	ω_i	Fitted coefficients ($\times 10^6$)				
		a_{1i}	a_{2i}	a_{3i}	a_{4i}	a_{5i}
1	14.924	−8.356	−0.989	1.928	−0.251	0.541
3	32.015	−1.954	−0.303	0.228	0.192	−0.090

where ω_i is the i-th natural frequency of the underlying linear system and f_{NL} is a nonlinear function of the first and third modal coordinates at the i-th resonance q_{1_i} and q_{3_i} that represents the nonlinear characteristics shown in Fig. 27.5a. This can be transformed into

$$-\omega^2 + \omega_i^2 + \frac{1}{q_i} f_{NL}(q_{1_i}, q_{3_i}) = 0\,; \quad \forall i = 1, 3 \tag{27.3}$$

where ω is the instantaneous frequency in the backbone curve. By using the experimental data summarised in the backbone curves in Fig. 27.5, Eq. (27.4) can be curve-fitted for both resonance cases.

The contribution of quadratic and cubic stiffness in the nonlinear function f_{NL} are assumed here for illustrative purposes only. Thus, it can be written that

$$f_{NL} = a_{1i} q_i + (a_{2i} q_{1_i} + a_{3i} q_{3_i})^2 + (a_{4i} q_{1_i} + a_{5i} q_{3_i})^3\,; \quad \forall i = 1, 3 \tag{27.4}$$

We note that a specific form for the nonlinear coupling has been selected for the quadratic term, since the more general form would have been $b_{1i} q_{1_i}^2 + b_{2i} q_{1_i} q_{3_i} + b_{3i} q_{3_i}^2$. A similar consideration can be made with respect to the cubic term. Table 27.1 presents the results after carrying out a numerical optimisation procedure that finds the best set of coefficients that fits Eq. (27.4) to the experimentally obtained backbone curves presented in Fig. 27.5.

A similar discussion can be made with reference to the responses around the second and fourth resonance frequencies. The RDM can be applied to vibrate the structure appropriately, generate the decaying records and estimate the backbone curves. After considering the modal interactions, they can be curve-fitted to complete the model for the test structure on the linear modal space.

27.4 Conclusions

The prediction of the performance of nonlinear structural systems is an increasingly important research topic. Among other analysing tools, backbone curves stand out as they offer a better understanding of the dynamical behaviour of the nonlinear structure. They are also able to reveal the nature of nonlinearities exhibited by the structural response. This approach is well suited to investigate structures primarily linear but that contain active nonlinear elements which become significant at larger levels of excitation.

In this paper a model structure containing bilinear stiffness elements was studied. Results demonstrated that the proposed procedure is capable of achieving a sharp estimation of the backbone curves from experimental data. The backbone curves were able to reveal the bilinear characteristic of the nonlinearity from appropriately obtained experimental data. It is worth mentioning that the backbone curves can offer important information to identify the modal coupling caused by the active nonlinearities. This can be exploit to pinpoint the non-zero off diagonal terms of the matrix of modal stiffness when identifying a suitable mathematical model for the structure under test. More studies are required to establish a strategy to extract the non-linear structural parameters from a set of backbone curves. This will allow for a complete identification of the nonlinear system.

Acknowledgements The present work was funded by the Engineering and Physical Sciences Research Council (EPSRC) in the UK as part of the Programme Grant EP/K003836/1. Prof. Neild is supported by the EPSRC Fellowship EP/K005375/1 and Prof. Cooper is supported by the Royal Academy of Engineering in the UK through the RAEng Airbus Sir George White Chair in Aerospace Engineering. These financial supports are gratefully acknowledged.

References

1. Charmbalis G, Londono J, Cooper JE (2013) Vibration testing of aeroelastic structures containing geometric stiffness nonlinearities. American Institute of Aeronautics and Astronautics, Boston, pp 8–11
2. Ewins D (2000) Modal testing: theory, practice and application. Engineering dynamics series, 2nd edn. RSP Ltd., Baldock, Hertfordshire
3. Feldman M (1994) Non-linear system vibration analysis using Hilbert transform–I. Free vibration analysis method 'FREEVIB'. Mech Syst Signal Process 8:119–127
4. Londono JM, Cooper JE (2014) Experimental identification of a system containing geometric nonlinearities. In: De Clerck J (ed) Topics in modal analysis I. Conference proceedings of the society for experimental mechanics series, vol 7. Springer International Publishing, New York, pp 253–260
5. Mao K, Billings S (1999) Variable selection in non-linear systems modelling. Mech Syst Signal Process 13:351–366
6. Naylor S, Platten M, Wright J, Cooper J (2004) Identification of multi-degree of freedom systems with nonproportional damping using the resonant decay method. J Vib Acoust 126:298–306
7. Neild S, McFadden P, Williams M (2003) A review of time-frequency methods for structural vibration analysis. Eng Struct 25:713–728
8. Peeters M, Kerschen G, Golinval J (2011) Modal testing of nonlinear vibrating structures based on nonlinear normal modes: experimental demonstration. Mech Syst Signal Process 25:1227–1247
9. Platten MF, Wright JR, Worden K, Dimitrladis G, Cooper JE (2007) Non-linear identification in modal space using a genetic algorithm approach for model selection. Int J Appl Math Mech 3:72–89
10. Platten MF, Wright JR, Cooper JE, Dimitriadis G (2009) Identification of a nonlinear wing structure using an extended modal model. J Aircraft 46:1614–1626
11. Wagg DJ, Neild SA (2010) Nonlinear vibration with control. Solid mechanics and its applications, vol 170. Springer, Dordrecht
12. Worden K, Tomlinson G (2001) Nonlinearity in structural dynamics: detection, identification and modelling. IOP Publishing Ltd., Bristol/Philadelphia
13. Wright J, Cooper J, Desforges M (1999) Normal-mode force appropriation – theory and application. Mech Syst Signal Process 13:217–240

Chapter 28
Simplifying Transformations for Nonlinear Systems: Part I, An Optimisation-Based Variant of Normal Form Analysis

N. Dervilis, K. Worden, D.J. Wagg, and S.A. Neild

Abstract This paper introduces the idea of a 'simplifying transformation' for nonlinear structural dynamic systems. The idea simply stated; is to bring under one heading, those transformations which 'simplify' structural dynamic systems or responses in some sense. The equations of motion may be cast in a simpler form or decoupled (and in this sense, nonlinear modal analysis is encompassed) or the responses may be modified in order to isolate and remove certain components. It is the latter sense of simplification which is considered in this paper. One can regard normal form analysis in a way as the removal of superharmonic content from nonlinear system response. In the current paper, this problem is cast in an optimisation form and the differential evolution algorithm is used.

Keywords Nonlinearity • Differential evolution • Optimisation • Simplifying transformation • Superharmonics

28.1 Introduction

The machine learning methods that are introduced in this paper via an optimisation algorithm that aims to address the problem of validity relating to the modal analysis of nonlinear structures. Modal analysis is an important tool in structural dynamics as it is used to understand the dynamical characteristics of the structure. Many methods have been proposed in recent years regarding nonlinear analysis, such as nonlinear normal modes or the method of normal forms [1–10].

The motivation for this paper comes from the problem of how to transform second-order equations of motion into a simpler form, as vibration problems are naturally expressed via such differential equations. The method of normal forms can be used as an analytical tool when vibration problems are surrounded by nonlinearities in order to recast the equations of motion in a simpler form.

One can regard normal form analysis in a way as the removal of some superharmonic content from nonlinear system response. In the current work, this problem is cast in an optimisation form and the differential evolution algorithm is used. The advantage of this data-based approach introduced here is that complicated algebraic analysis is not needed and the details of the equations of motion are not required.

The layout of the paper is as follows. Section 28.2 covers the main features of the optimisation algorithm and the proposed transformation, while Sect. 28.3 gives an example of nonlinear analysis based on the technique that is mentioned in Sect. 28.2. The paper finishes with some overall conclusion and future work.

28.2 Simplifying Transformation Strategy and Differential Evolution

In vibration analysis, the relationship between system resonances and external forcing is particularly important especially when nonlinearities are present. Using the approach that is proposed here, leads to a simpler form when simulating resonant behaviour by removing the dominant superharmonic.

N. Dervilis (✉) • K. Worden • D.J. Wagg
Dynamics Research Group, Department of Mechanical Engineering, University of Sheffield, Mappin Street, Sheffield S1 3JD, UK
e-mail: n.dervilis@sheffield.ac.uk

S.A. Neild
Department of Mechanical Engineering, Queens Building, University of Bristol, Bristol BS8 1TR, UK

G. Kerschen (ed.), *Nonlinear Dynamics, Volume 1*, Conference Proceedings of the Society for Experimental Mechanics Series, DOI 10.1007/978-3-319-15221-9_28

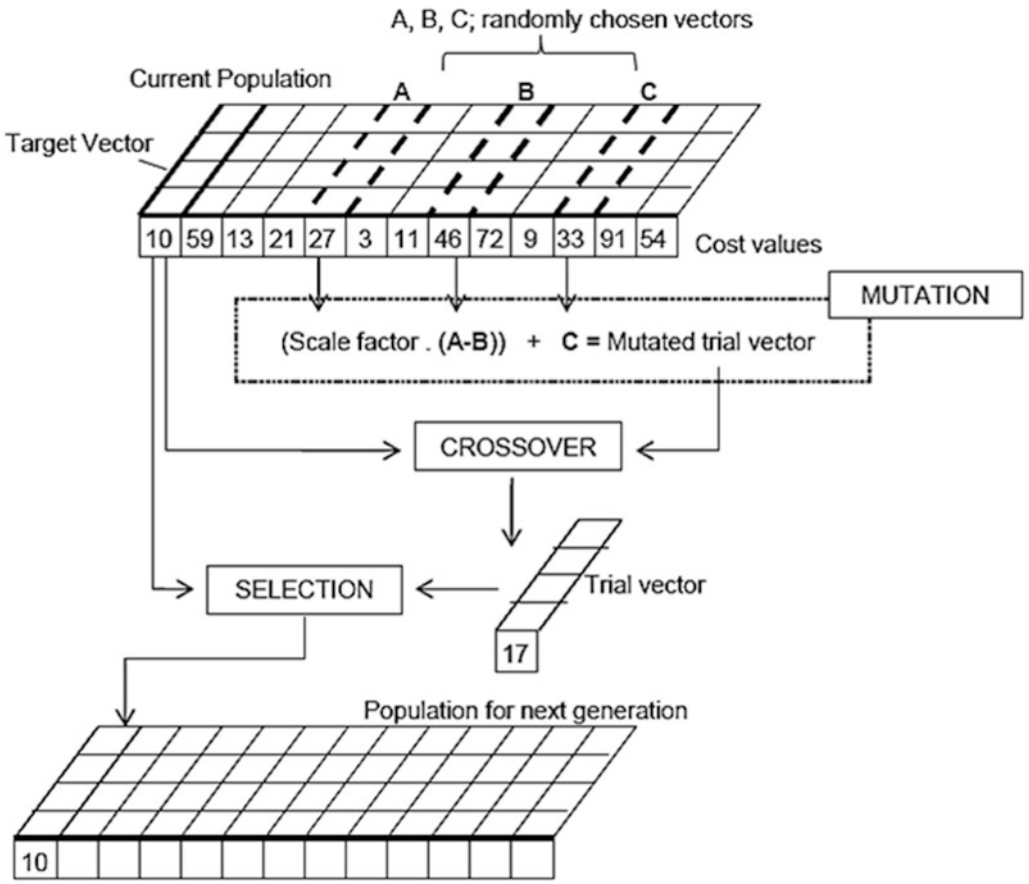

Fig. 28.1 Schematic of a typical differential evolution algorithm [14]

The transformation is as simple as a polynomial expansion. Adopting a machine learning approach, one can learn the undetermined coefficients from measured data, freeing the system from the dominant superharmonic.

A different approach to both analytic solutions and pattern recognition methods is to treat the removal of superharmonic content from nonlinear system response in terms of an optimisation problem, where the aim is to choose parameters such that the new signal is free from the first superharmonic that appears at three times the natural frequency (for a symmetric nonlinearity). For this purpose, a nonlinear optimisation algorithm based on differential evolution will be used here. For the purposes of this paper a brief description of differential evolution is given and readers are referred to [11–13] for more details. A section will follow with results using the technique on data simulated to represent the theoretical situation that was discussed.

Differential evolution, introduced by Storn and Price [12], is an evolutionary algorithm in the same sense as a genetic algorithm that begins with an initial population of trial solutions to a problem and via successive cycles of mutation, crossover and selection computes an optimal set of solutions. These trial solution are subject to a suitable objective function, in respect to the given problem. In turn, for the current analysis the trial solutions are a vector of parameter guesses that satisfy the condition that the new signal is a simplified transformation as described before.

The optimisation algorithm is summarised in Fig. 28.1. The routine, although seeming complicated, follows a smooth but powerful procedure. An initial population of parameter vectors are randomly generated. Then to each parameter vector of this initial population, the objective function specifies a cost value and a new generation of solutions is born from this initial population. A target vector is chosen from the initial population and then a trial vector is created by ‘mutation’. Mutation takes two random parameter vectors A and B according to Fig. 28.1 from the population and subtracts one from the other by multiplying it by some constant or scaling factor and finally adds it to a third randomly chosen parameter vector (C) from the initial population. The trial vector can be considered as the ‘child’ of the target vector and the mutated vector.

After this chain of actions a new parameter vector is born between mutated trial vector and the target vector and the procedure is called ‘crossover’. A predefined hyperparameter determines if the trial vector takes a parameter value from the

target vector or the mutated vector. This new vector will then be selected for the next generation if its cost value is lower than that of the target vector. If not, the target vector is forwarded to the next generation population. This procedure is repeated several times and as the process evolves through a chain of generations, parameter vectors with low cost values will be constructed.

In this analysis a slight variation of DE was used called self-adaptive differential evolution (SADE) [11, 13]. This algorithm evolves in a similar fashion to the DE procedure except that it also learns which values of scaling factor and hyperparameter are most likely to result in a trial vector that will be forwarded to the next generation, giving faster convergence compared to DE algorithm. The main advantage of using this evolutionary population based tool in respect to the parameter estimation problem is that the algorithm will potentially converge on the global minimum cost value rather than a local minimum.

For the purposes of the nonlinear simplifying transformation, a suitable objective function must be chosen on the basis of isolating and remove certain components (superharmonics).

28.3 An Example

The system of interest will be a nonlinear one-DOF lumped parameter system (see Fig. 28.2). Data were simulated using a fixed-step fourth-order Runge-Kutta algorithm with harmonic excitation and the associated displacement was extracted. The model parameters adopted were: $m = 1$, $c_1 = 0.001$, $k_1 = 50$, $k_{nl} = 10^3$. The nonlinearity that is assumed is cubic.

Figure 28.3 shows the resulting power spectral density (PSD) for the simulated physical variable. The method that is used in order to calculate the power spectral densities (PSDs) which follow is the Welch method based on time averaging over short, modified periodograms which could decolour the effect of different random excitation inputs [15]. The signals are split into sections and the periodograms of each section are averaged. Through the Welch method these data sections are overlapped and a window, such as the Hanning window is applied in order to filter each section. The overlapping of the signal sections is usually either 50 % (as in this paper) or 75 %.

For all the graphs the vertical axis is the **PSD of displacement** and the **frequency is in Hz**.

As can be seen, the third order superharmonic (which as expected appeared at three times the natural frequency) is the dominant trend in the signal. Following this evidence a simplifying transformation of a polynomial expansion is adopted in the form of:

$$z(i) = a + by(i) + cy(i)^3 + dy(i)^5 \tag{28.1}$$

where $\{z\}$ is the transformed signal, $\{y\}$ is the initial signal and $[a, b, c, d]$ the undetermined parameters of the polynomial expansion.

The task of the optimisation algorithm is to determine the polynomial coefficients and at the same time transform the new signal by zeroing the first dominant superharmonic that appears at three times from the natural frequency.

As can be seen in Fig. 28.4 the method that is introduced successfully removes the superharmonic. However, as can be noted in Fig. 28.5 if the frequency spectrum is widened then the second superharmonic (fifth order) is rising in magnitude to counter balance the reduction of the third order superharmonic. This problem will be investigated in the second part of this paper.

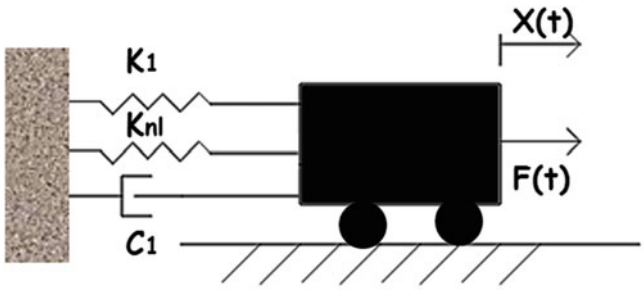

Fig. 28.2 Nonlinear one-DOF lumped parameter system

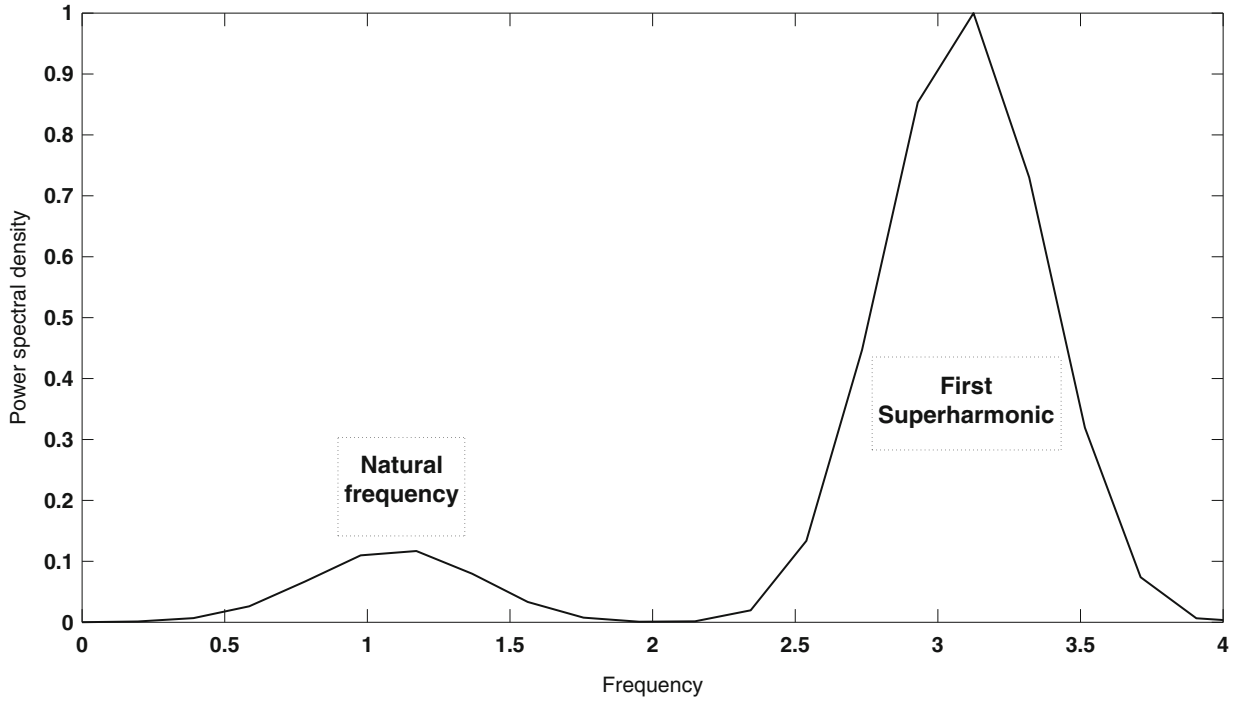

Fig. 28.3 PSD for physical variable

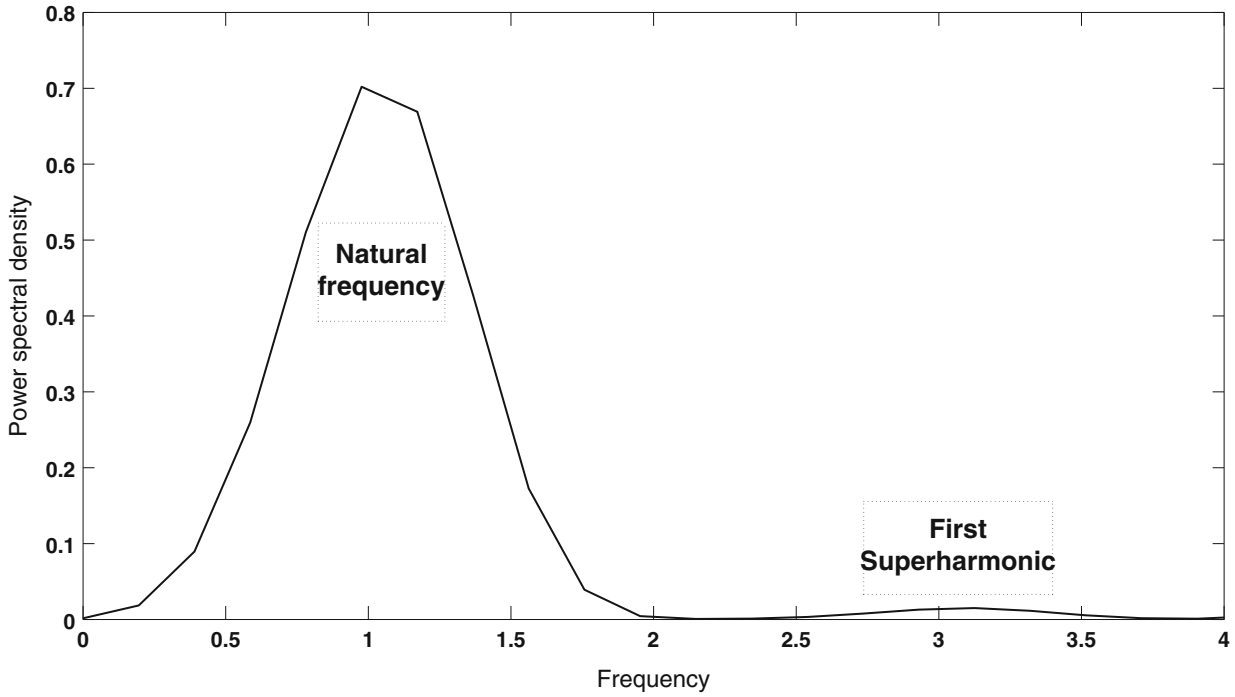

Fig. 28.4 PSD for transformed variable

28.4 Conclusion

The purpose of this paper is to highlight the key utility of some machine learning methods, not only for dynamic analysis of structure but as well as a method of simplification for nonlinear mechanical systems. The main benefit of the approach taken here is that complicated algebraic analysis is not necessary. Furthermore, the physical equations of the system are

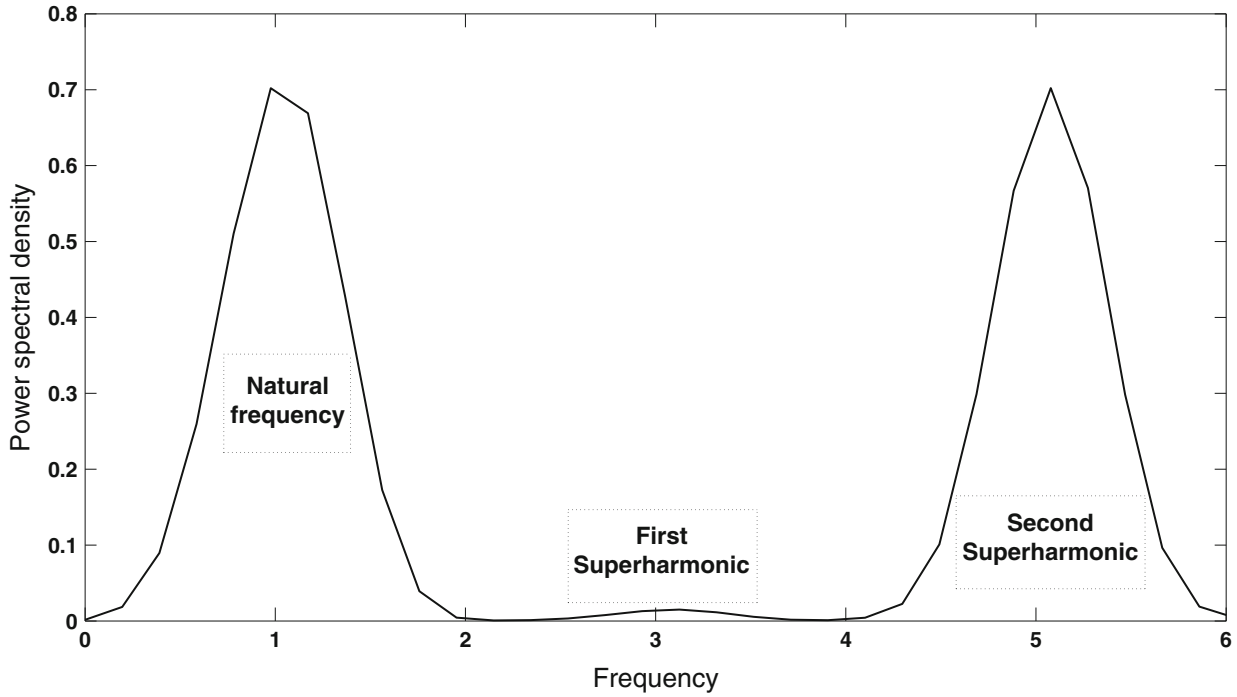

Fig. 28.5 PSD for transformed variable including second superharmonic (fifth order)

not needed. As a result, this machine learning approach is suited to experimental investigation of nonlinear systems using only the measured output responses. A further work in the second part of this paper investigates the appearance of higher order superharmonics.

Acknowledgements The support of the UK Engineering and Physical Sciences Research Council (EPSRC) through grant reference number EP/J016942/1 and EP/K003836/2 is gratefully acknowledged.

References

1. Kerschen G, Golinval J-C, Vakakis AF, Bergman LA (2005) The method of proper orthogonal decomposition for dynamical characterization and order reduction of mechanical systems: an overview. Nonlinear Dyn 41(1–3):147–169
2. Vakakis AF (1997) Non-linear normal modes (nnms) and their applications in vibration theory: an overview. Mech Syst Signal Process 11(1):3–22
3. Worden K, Tomlinson GR (2000) Nonlinearity in structural dynamics: detection, identification and modelling. CRC Press, Boca Raton
4. Worden K, Tomlinson GR (2001) Nonlinearity in experimental modal analysis. Philos Trans R Soc Lond Ser A Math Phys Eng Sci 359(1778):113–130
5. Worden K, Green PL (2014) A machine learning approach to nonlinear modal analysis. In: Catbas FN (ed) Dynamics of civil structures, vol 4. Springer, New York, pp 521–528
6. Rosenberg RM (1962) The normal modes of nonlinear n-degree-of-freedom systems. J Appl Mech 29(1):7–14
7. Shaw SW, Pierre C (1993) Normal modes for non-linear vibratory systems. J Sound Vib 164(1):85–124
8. Neild SA, Wagg DJ (2011) Applying the method of normal forms to second-order nonlinear vibration problems. Proc R Soc A Math Phys Eng Sci 467(2128):1141–1163
9. Poncelet F, Kerschen G, Golinval J-C, Verhelst D (2007) Output-only modal analysis using blind source separation techniques. Mech Syst Signal Process 21(6):2335–2358
10. Dervilis N, Wagg DJ, Green PL, Worden K (2014) Nonlinear modal analysis using pattern recognition. In: Proceedings of ISMA2014, pp 3017–3027
11. Worden K, Manson G, Sohn H, Farrar CR (2005) Extreme value statistics from differential evolution for damage detection. In: Proceedings of the 23rd international modal analysis conference (IMAC XXIII), Orlando, pp 2009–3
12. Storn R, Price K (1997) Differential evolution—a simple and efficient heuristic for global optimization over continuous spaces. J Global Optim 11(4):341–359

13. Qin AK, Suganthan PN (2005) Self-adaptive differential evolution algorithm for numerical optimization. In: The 2005 IEEE congress on evolutionary computation, vol 2. IEEE, pp 1785–1791
14. Cross E (2012) On structural health monitoring in changing environmental and operational conditions. Ph.D. thesis
15. Welch P (1967) The use of fast fourier transform for the estimation of power spectra: a method based on time averaging over short, modified periodograms. IEEE Trans Audio Electroacoust 15(2):70–73

Chapter 29
Simplifying Transformations for Nonlinear Systems: Part II, Statistical Analysis of Harmonic Cancellation

N. Dervilis, K. Worden, D.J. Wagg, and S.A. Neild

Abstract The first paper in this short sequence described the idea of a simplifying transformation and applied the concept to a numerical optimisation-based variant of normal form analysis. The idea of the numerical normal form transformation was simply to eliminate or reduce the contribution of a pre-defined set of harmonics in the system response. It was shown that reducing the defined harmonics could lead to amplification of other components of the response. The idea of the current paper is to conduct a Monte Carlo worst-case analysis to investigate how badly unconstrained harmonics might be amplified by the optimisation.

Keywords Nonlinearity • Differential evolution • Optimisation • Simplifying transformation • Superharmonics

29.1 Introduction

In the first part of short series of these papers, a data-based approach in order to produce simplifying transformations for nonlinear systems was introduced. The machine learning methods that were utilised in the previous paper via optimisation algorithm aimed to determine the polynomial coefficients of a simplifying transformation and at the same time transform the new signal by zeroing the third order dominant superharmonic. However, the fifth order superharmonic was observed to rise in magnitude to counter balance the reduction of the third order superharmonic.

The motivation for this paper is to conduct a Monte Carlo worst-case analysis to investigate how badly unconstrained harmonics might be amplified by the optimisation and specifically the fifth order one.

The layout of the paper is as follows. Section 29.2 covers the main features of the optimisation algorithm and the Monte Carlo simulation, while Sect. 29.3 gives an example of nonlinear modal analysis based on the technique that is mentioned in Sect. 29.2. The paper finishes with some overall conclusion and future work.

29.2 Differential Evolution

As, explained in part one of this study the transformation is as simple as a polynomial expansion. Adopting a machine learning approach, one can learn the undetermined coefficients from measured data, freeing the system from the dominant superharmonic.

For this purpose, a nonlinear optimisation algorithm based on differential evolution will be used here. For the purposes of this paper a brief description of differential evolution is given and readers are referred to [1–3] for more details. A section will follow with results using the technique on data simulated to represent the theoretical situation that was discussed.

Differential evolution, was introduced by Storn and Price [2] and is an evolutionary algorithm in the same sense as a genetic algorithm that begins with an initial population of trial solutions to a problem and via successive cycles of mutation, crossover and selection computes an optimal set of solutions. These trial solution are subject to a suitable objective function,

N. Dervilis (✉) • K. Worden • D.J. Wagg
Dynamics Research Group, Department of Mechanical Engineering,
University of Sheffield, Mappin Street, Sheffield S1 3JD, UK
e-mail: n.dervilis@sheffield.ac.uk

S.A. Neild
Department of Mechanical Engineering, Queens Building, University of Bristol, Bristol BS8 1TR, UK

G. Kerschen (ed.), *Nonlinear Dynamics, Volume 1*, Conference Proceedings of the Society
for Experimental Mechanics Series, DOI 10.1007/978-3-319-15221-9_29

in respect to the given problem. In turn, for the current analysis the trial solutions are a vector of parameter guesses that satisfy that the new signal is a simplified transformation as described before.

Although, the routine seems complicated it follows a smooth but powerful procedure. An initial population of parameter vectors are randomly generated. Then to each parameter vector of this initial population, the objective function specifies a cost value and a new generation of solutions is born from this initial population. A target vector is chosen from the initial population and then a trial vector is created by "mutation". Mutation takes two random parameter vectors from the population and subtracts one from the other by multiplying it by some constant or scaling factor and finally adds it to a third randomly chosen parameter vector from the initial population.

After this chain of actions a new parameter vector is born between the mutated trial vector and the target vector and the procedure is called "crossover". A predefined hyperparameter determines if the trial vector takes a parameter value from the target vector or the mutated vector. This new vector will then be selected for the next generation if its cost value is lower than that of the target vector. If not, the target vector is forwarded to the next generation population. This procedure is repeated several times and as the process evolves through a chain of generations, a parameter vector with low cost values will be constructed.

In this analysis a slight variation of DE was used called self-adaptive differential evolution (SADE). For more detailed analysis the reader is referred to part one paper and references [1, 3].

For the purposes of nonlinear simplifying transformation, a suitable objective function must be chosen on the basis of isolating and remove certain components (superharmonics).

A simplifying transformation of a polynomial expansion is adopted in the form of:

$$z(i) = a + by(i) + cy(i)^3 + dy(i)^5 \tag{29.1}$$

where $\{z\}$ is the transformed signal, $\{y\}$ is the initial signal and $[a, b, c, d]$ the undetermined parameters of the polynomial expansion.

The task of the optimisation algorithm is to determine the polynomial coefficients and the same time transform the new signal by zeroing the first dominant superharmonic that appears three times from the natural frequency.

29.3 An Example

The system of interest will be a nonlinear Duffing oscillator of the form described by the following equation:

$$\ddot{y} + 2\zeta\omega_n\dot{y} + \omega_n^2 y + ay^3 = f \tag{29.2}$$

where ω is the natural frequency, ζ is the damping ratio, f is the harmonic excitation and a the nonlinearity parameter.

Data were simulated using a fixed-step fourth-order Runge-Kutta algorithm with harmonic excitation and the associated displacement was extracted. The model parameters adopted were: $m = 1$, $\zeta = [0.001, 1]$, $a = [10^3, 10^5]$ and $\omega_n = 1$. The nonlinearity that is assumed is cubic.

The method that is used in order to calculate the power spectral densities (PSDs) is the Welch method based on time averaging over short, modified periodograms which could decolour the effect of different random excitation inputs [4]. The signals are split into sections and the periodograms of each section are averaged. Through the Welch method these data sections are overlapped and a window, such as the Hanning window is applied in order to filter each section. The overlapping of the signal sections is usually either 50 % (as in this paper) or 75 %.

29.3.1 Monte Carlo Simulation

In order to investigate how badly unconstrained harmonics might be amplified by the optimisation and especially the fifth order one, a Monte Carlo simulation was conducted. The procedure can be described as follows:

- Data were simulated using a fixed-step fourth-order Runge-Kutta algorithm with harmonic excitation and the associated displacement was extracted. The difference is that the ζ and a were sampled from a uniform distribution between the values described before.

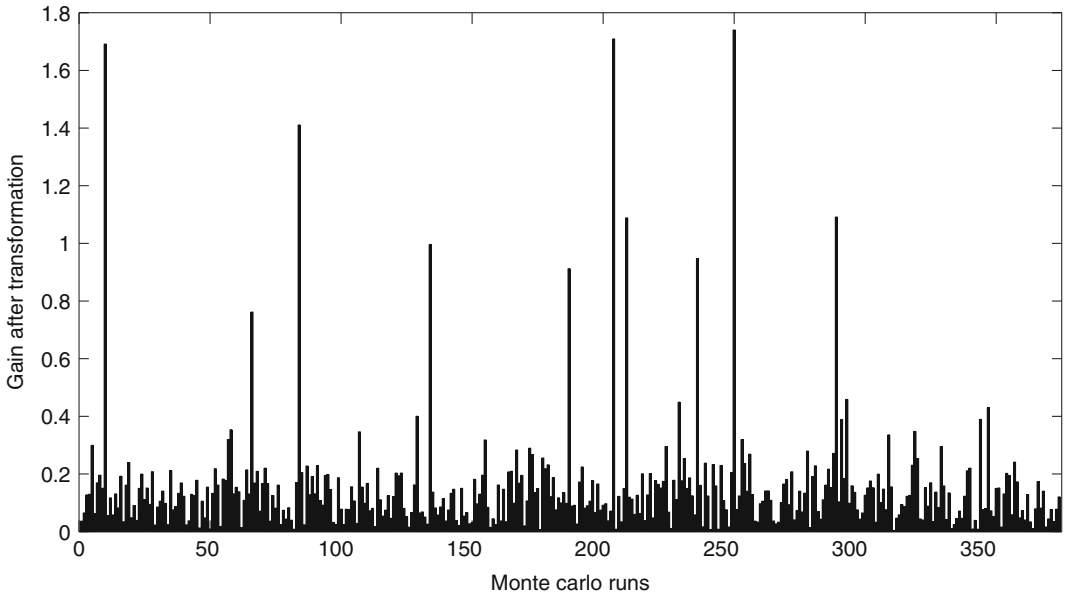

Fig. 29.1 Gain of nonlinear system after transformation for the maximum amplitude of the third order harmonic

- The optimisation algorithm determines the polynomial coefficients and the same time transforms the new signal by zeroing the third order superharmonic.
- The largest (i.e. extreme), value of the third and fifth order superharmonic is recorded for each trial and each value is stored.
- The process is repeated for a large number of trials in order to generate an array of extreme numbers.

29.3.2 Discussion

In order to produce a meaningful measure of how successful was the transformation through these several Monte Carlo trials and create a clear image of how bad the fifth harmonic behaves, the gain index was computed. Gain is simply given by the following equation:

$$Gain = \frac{\text{value after transformation}}{\text{value before transformation}}. \tag{29.3}$$

As can be seen in Fig. 29.1 the method that is introduced successfully removes the superharmonic as the gain index is very low (below one). However, as can be noted in Fig. 29.1, there are some few trials that SADE did not reach the global minimum. In contrast in Fig. 29.2 there is a confirmation of what was observed in the previous work. The fifth order superharmonic is arising in magnitude to counter balance the reduction of the third order superharmonic.

In Fig. 29.3 a normal test plot is used in order to investigate whether processed (transformed) data of the fifth harmonic exhibits the standard normal or Gaussian distribution. The green straight line gives the normal density function and one has to check the plotted points, and see how well they fit the normal line. In Fig. 29.3 the data points bend down and to the right of the green line which is an indication of a long tail to the left or left skew. This conclusion can also be seen in Fig. 29.4 where the histogram of the gain amplitude of the fifth order harmonic is presented.

The red line in Fig. 29.4 represents the threshold (gain value one) after which the gain of the fifth harmonic increases as result of minimising the third harmonic. It is very clear that the majority of the runs give gain magnitudes much higher that one. This confirms statistically what was expected via the simplifying transformation.

If one computes the logarithm of the actual values and then draws a normal test plot as can be seen in Fig. 29.5 then the data starts above the normal green line, bends to follow it and ends above. This indicates long tails which means more variance than one would expect in a normal distribution. However, compared to previous Fig. 29.3 the data appears to be

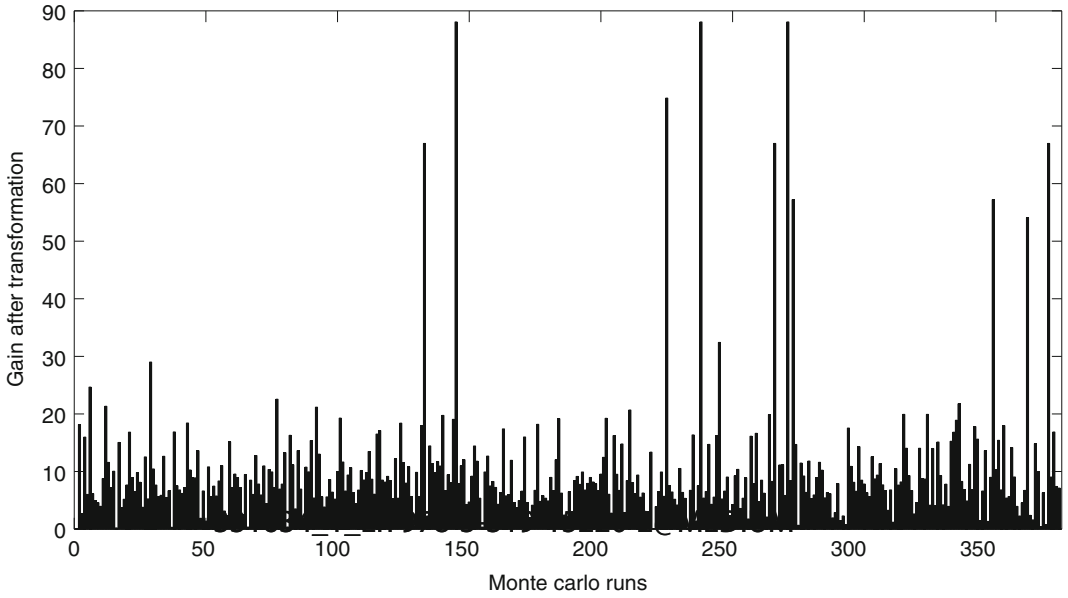

Fig. 29.2 Gain of nonlinear system after transformation for the maximum amplitude of the fifth order harmonic

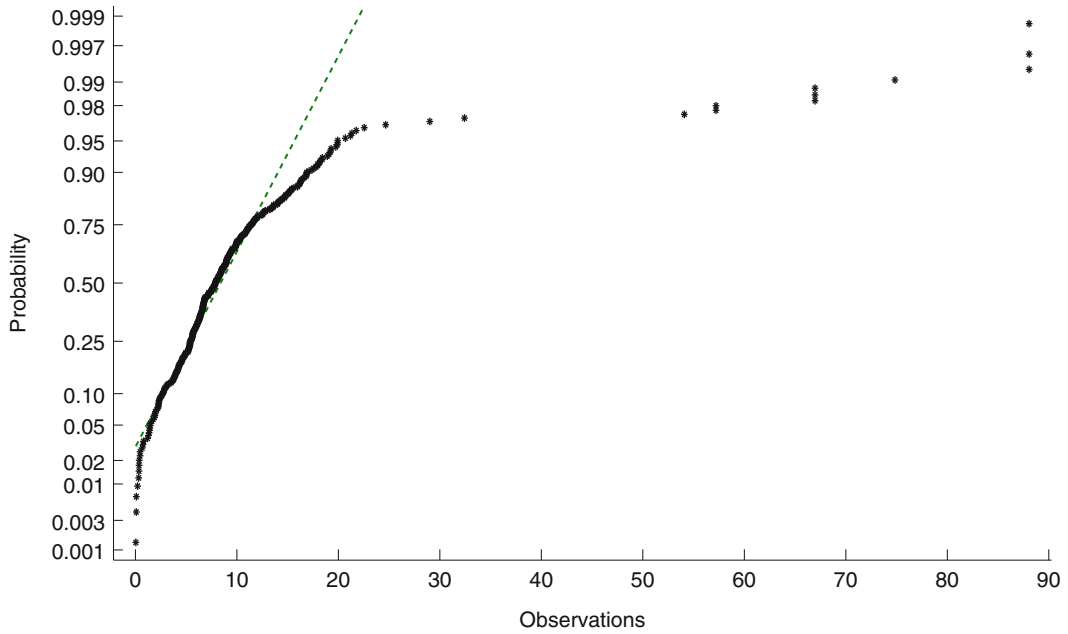

Fig. 29.3 Normal probability plot or normal quartile plots

more Gaussian and this can also be seen in Fig. 29.6 where the histogram of the gain amplitude of the fifth order harmonic is presented and the normal density function is fitted (purple dotted line).

Again, the red line in Fig. 29.4 represents the threshold after (right) which the gain of the fifth harmonic increases as result of minimising the third harmonic. It is very clear that the majority of the runs give gain magnitudes much higher that one. Also, the data appears to be more Gaussian which could be proved useful in order to derive meaningful statistics.

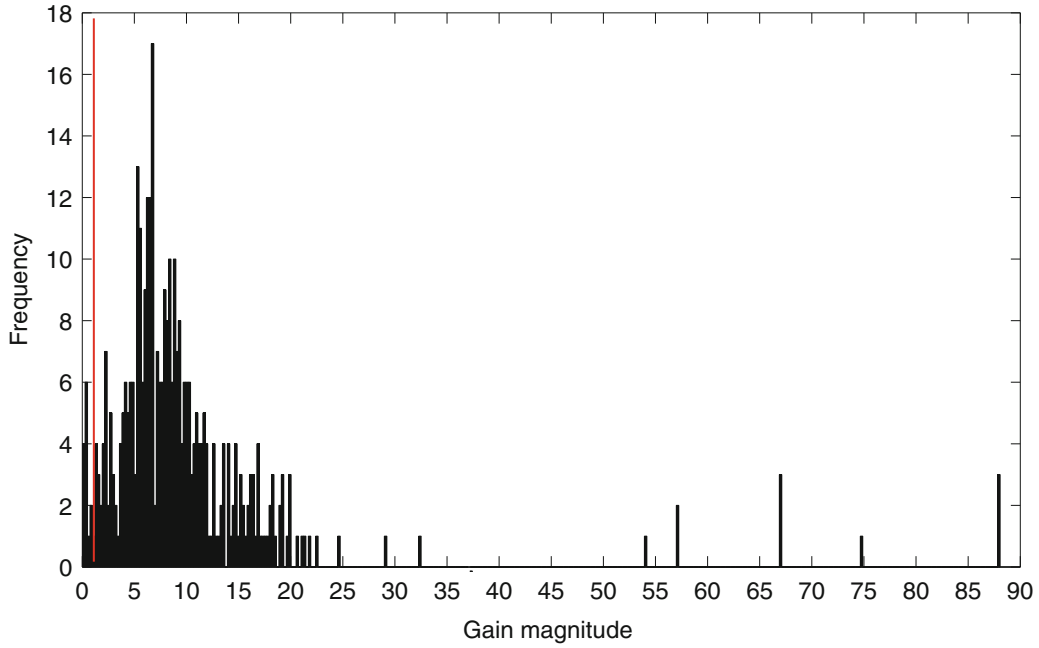

Fig. 29.4 Histogram of the maximum amplitude of the fifth order harmonic

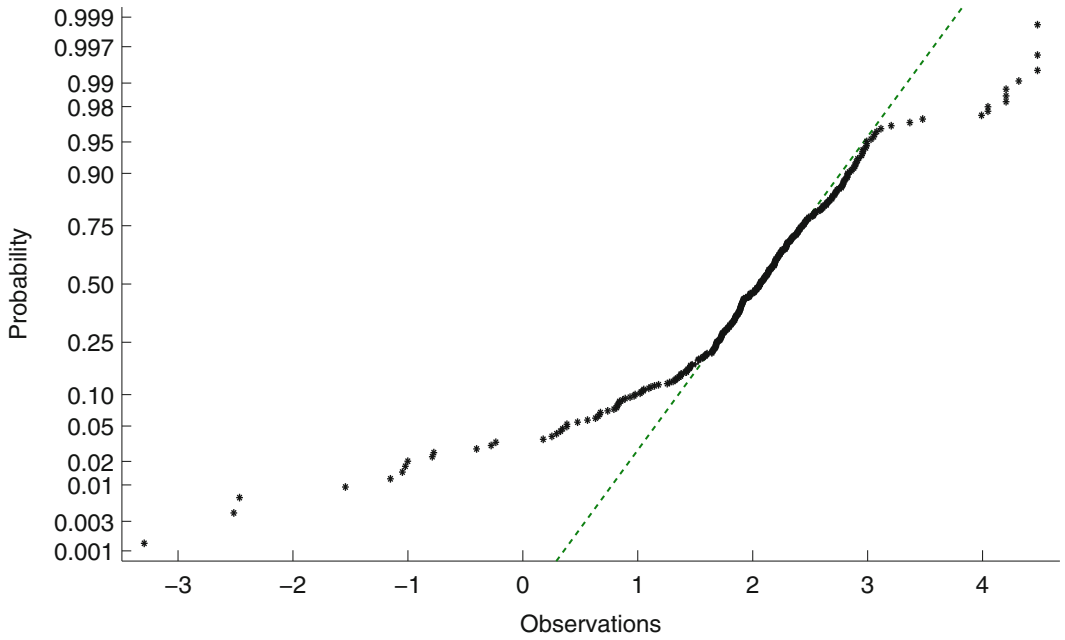

Fig. 29.5 Normal probability plot or normal quartile plots in the logarithmic scale

29.4 Conclusion

The purpose of this paper is to highlight the key utility of some machine learning methods, not only for dynamic analysis of structure but as well as a method of simplification for nonlinear mechanical systems. The main benefit of the approach taken here is that complicated algebraic analysis is not necessary. Furthermore, the physical equations of the system are not needed. As a result, this machine learning approach is suited to experimental investigation of nonlinear systems using only

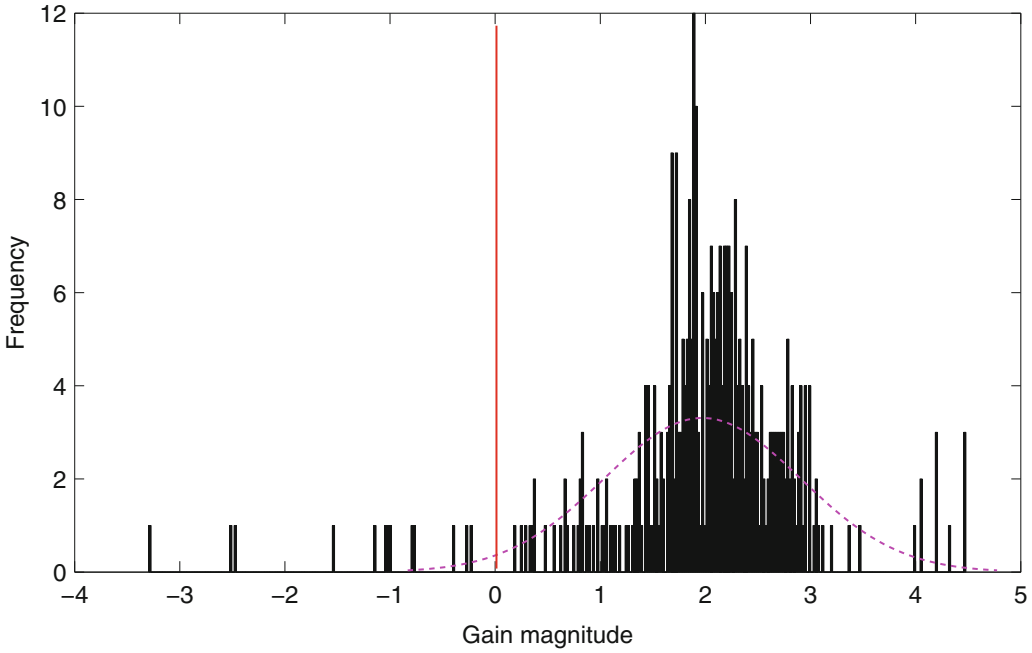

Fig. 29.6 Histogram of the maximum amplitude of the fifth order harmonic in the logarithmic scale

the measured output responses. A further work is under preparation that deals with MDOF systems, where one attempts to remove interaction/combination frequencies from MDOF system responses. One might regard this as a means of decoupling the degrees of freedom.

Acknowledgements The support of the UK Engineering and Physical Sciences Research Council (EPSRC) through grant reference number EP/J016942/1 and EP/K003836/2 is gratefully acknowledged.

References

1. Worden K, Manson G, Sohn H, Farrar CR (2005) Extreme value statistics from differential evolution for damage detection. In: Proceedings of the 23rd international modal analysis conference (IMAC XXIII), pp 2009–3
2. Storn R, Price K (1997) Differential evolution–a simple and efficient heuristic for global optimization over continuous spaces. J Glob Optim 11(4):341–359
3. Qin AK, Suganthan PN (2005) Self-adaptive differential evolution algorithm for numerical optimization. In: The 2005 IEEE congress on evolutionary computation, vol 2. IEEE, Edinburgh, pp. 1785–1791
4. Welch P (1967) The use of fast fourier transform for the estimation of power spectra: a method based on time averaging over short, modified periodograms. IEEE Trans Audio Electroacoust 15(2):70–73

Chapter 30
Considerations for Indirect Parameter Estimation in Nonlinear Reduced Order Models

Lorraine C.M. Guerin, Robert J. Kuether, and Matthew S. Allen

Abstract Over the past few decades, there have been many developments in techniques that extract a reduced order model (ROM) from a geometrically nonlinear finite element model. The enforced displacement ROM strategy that is of interest in this work is known as an indirect approach because it does not require altering the finite element code. Instead, one uses a series of static displacement fields applied to the nonlinear finite element model to estimate the nonlinear stiffness coefficients in the reduced equations. Geometric nonlinearity causes the bending and membrane displacements to become coupled, and the enforced displacements method requires that the kinematics of the membrane motion be explicitly included in the basis using either axial vibration modes or dual modes. This work explores the accuracy of the enforced displacements ROM strategy by comparing the efficiency of these basis vectors, as well as the use of three different parameter estimation procedures and the effect of scaling factors on the static load cases used to generate the ROM. The different modeling decisions are shown to have a very significant effect on the accuracy of the ROMs, and the comparisons are used to suggest best practices that result in the most accurate ROMs. These issues are explored using finite element models of a flat geometrically nonlinear beam with fixed-fixed boundary conditions and a flat geometrically nonlinear exhaust cover plate. The effect of each of the modeling decisions on the resulting enforced displacement ROM is evaluated by computing the Nonlinear Normal Modes (NNMs) of the full finite element model and comparing them with the NNMs calculated from the ROMs. The NNMs offer a powerful metric that indicates whether or not the ROM captures a variety of important physics in the original model.

Keywords Reduced order modeling • Geometric nonlinearity • Nonlinear dynamics • Nonlinear normal modes • Finite element analysis

30.1 Introduction

One popular modeling approach in structural dynamics uses finite element analysis (FEA) to generate the discretized equations of motion. Detailed meshes may be needed to capture precise geometric features of a realistic structure, for example, the stiffeners in an aircraft panel, so a large number of degrees-of-freedom (DOF) may be needed to accurately describe the motion. Furthermore, when the model exhibits large deformations, the equations of motion become nonlinear and the computational cost increases dramatically. As a result, many efforts have been put forth over the last few decades to develop reduced order modeling strategies for geometrically nonlinear FEA models [1, 2]. One class of reduction methods, referred to as *indirect* methods, uses a Galerkin approach to reduce the equations using a smaller set of modal DOF. An additional nonlinear term persists in the modal equations due to the geometric nonlinearity, whose coefficients are determined through a series of static load cases. This paper explores some of the challenges with producing accurate nonlinear reduced order models (ROMs) using the enforced displacement procedure [3], particularly issues related to mode selection, parameter estimation and displacement scaling factors.

The enforced displacement procedure was first developed by Muravyov and Rizzi in [3]. A set of component modes describe the kinematics of a geometrically nonlinear FEA model, and are used to reduce the full model down to a low order set of modal equations. These equations have a linear modal mass and modal stiffness term that can be determined analytically since one typically has access to the linear mass and stiffness matrices in a commercial FEA package. However, the nonlinear terms are usually not available unless one has access to the internals of the software. Assuming that the material is linear elastic, and a quadratic strain–displacement relation is used, the nonlinear restoring force in modal form is a quadratic

L.C.M. Guerin (✉) • R.J. Kuether • M.S. Allen
Department of Engineering Physics, University of Wisconsin, Madison, WI 53706, USA
e-mail: lguerin@wisc.edu; rkuether@wisc.edu; msallen@engr.wisc.edu

G. Kerschen (ed.), *Nonlinear Dynamics, Volume 1*, Conference Proceedings of the Society for Experimental Mechanics Series, DOI 10.1007/978-3-319-15221-9_30

and cubic polynomial function of the modal displacements with unknown stiffness coefficients. To determine these values, the nonlinear FEA model is enforced to take the shape of the scaled component mode shapes, or a combination of these shapes, and a static analysis is performed to solve for the reactions forces to hold each shape. The nonlinear stiffness terms in the modal equations are determined using a series of these displacements and reaction forces.

The bending-membrane coupling must be accounted for explicitly when creating ROMs using the enforced displacement procedure. As the model experiences large bending deflections, membrane stretching can occur, so both bending and membrane type component modes are explicitly needed in the basis set. This paper explores two approaches to capture these kinematics, namely the use of axial vibration modes, and the dual modes method in [4]. Another modeling consideration is the procedure used to fit the nonlinear stiffness coefficients based on a series of static solutions. The method referred to as RANSTEP throughout this paper, which was first introduced in [3], uses special combinations of modal displacements to solve for a small number of coefficients at a time. The coefficients could also be found by setting up a least squares problem involving all of the static load solutions [5]. Finally, the effect of scaling on the static displacement fields is explored in this paper using the constant modal scaling (CS) method proposed originally in [3] along with the constant modal displacement (CD) approach used in [6–8]. The results presented here will show that the resulting accuracy of the ROM equations greatly depends on the procedures used to fit the nonlinear stiffness coefficients and capture the membrane motions.

Rizzi and Przekop explored the effect of basis selection on the resulting ROM equations in [9], and assessed the accuracy of the ROM by comparing its response to random inputs with the response of the full-order model (which is quite expensive to compute). The authors recently suggested that a more rigorous comparison between two ROMs could be made by comparing their nonlinear normal modes and used this to compare two ROM procedures [6]. The nonlinear normal mode [10, 11], which is defined as a *not necessarily synchronous periodic response of the undamped nonlinear equations of motion,* provides an excellent metric for comparison between ROMs and the full FEA model since these solutions are independent of any external forces, and capture a wide range of response amplitudes seen by the nonlinear system. Previous works have shown that if the NNMs predicted by the ROM converge, then the response predictions also tend to be accurate [12, 13]. The work presented in this paper is an extension of the work in [6], but here we only focus on variations on the enforced displacement procedure. The effect of mode selection, methods to identify the nonlinear stiffness terms, and the scaling on the static load cases are all explored simultaneously to attempt to determine the best practices when using the enforced displacements ROM approach.

The paper is organized as follows. Section 30.2 reviews the theory of the enforced displacement reduction strategy, along with considerations for mode selection, scaling of the static load cases, and identification of nonlinear stiffness terms. The results in Sects. 30.3 and 30.4 demonstrate the reduction strategy applied to a geometrically nonlinear flat beam with clamped-clamped boundary conditions. The nonlinear normal modes are used to compare a set of ROM equations generated with different variations on the enforced displacements procedure, showing that the ROM predictions can diverge from those predicted by the full FEA model in certain cases. Section 30.5 presents the results from a more complicated model of an exhaust cover plate with geometric nonlinearity, using the best practices learned from the beam model. Section 30.6 presents the conclusions.

30.2 Theoretical Development

The equations of motion for a geometrically nonlinear, N degree-of-freedom (DOF) system, discretized by the finite element method can be written as

$$\mathbf{M}\ddot{\mathbf{x}}(t) + \mathbf{K}\mathbf{x}(t) + \mathbf{f}_{NL}(\mathbf{x}) = \mathbf{f}(t) \tag{30.1}$$

where $\mathbf{M}$ and $\mathbf{K}$ are the $N \times N$ mass and stiffness matrices, respectively and the $N \times 1$ displacement and acceleration vectors are respectively represented as $\mathbf{x}(t)$ and $\ddot{\mathbf{x}}(t)$. The $N \times 1$ external force vector is denoted as $\mathbf{f}(t)$, while $\mathbf{f}_{NL}(\mathbf{x})$ is the $N \times 1$ nonlinear restoring force vector due to the geometric nonlinearity.

The size of the equations of motion are reduced using a coordinate transformation based on a set of component modes. The relationship between physical and generalized coordinates is described as

$$\mathbf{x}(t) = \mathbf{T}\mathbf{q}(t) \tag{30.2}$$

where $\mathbf{q}(t)$ is the $m \times 1$ time-dependent modal displacement vector and $\mathbf{T}$ is the $N \times m$ matrix of component modes. A subset of m basis vectors are included in each column of $\mathbf{T}$, such that the degrees-of-freedom are significantly reduced ($m << N$). By substituting Eq. (30.2) into Eq. (30.1), and pre-multiplying by $\mathbf{T}^{\mathbf{T}}$, the reduced equations of motion become

$$\widehat{\mathbf{M}}\ddot{\mathbf{q}} + \widehat{\mathbf{K}}\mathbf{q} + \mathbf{T}^{\mathrm{T}}\mathbf{f}_{NL}\left(\mathbf{Tq}\right) = \mathbf{T}^{\mathrm{T}}\mathbf{f}(t) \tag{30.3}$$

$$\widehat{\mathbf{M}} = \mathbf{T}^{\mathrm{T}}\mathbf{MT} \tag{30.4}$$

$$\widehat{\mathbf{K}} = \mathbf{T}^{\mathrm{T}}\mathbf{KT} \tag{30.5}$$

The $()^{\mathrm{T}}$ operator represents the transpose operator. The nonlinear restoring force in the modal form of the equation can be generalized as

$$\mathbf{T}^{\mathrm{T}}\mathbf{f}_{NL}\left(\mathbf{Tq}\right) = \boldsymbol{\theta}(\mathbf{q}) \tag{30.6}$$

which is a nonlinear function of each of the displacements in $\mathbf{q}$. For linear elastic materials with quadratic strain–displacement relationships, it has been shown in previous works [1, 2] that the r^{th} nonlinear restoring force in modal form may be written as

$$\theta_r\left(q_1, q_2, \ldots, q_m\right) = \sum_{i=1}^{m}\sum_{j=i}^{m} B_r\left(i, j\right) q_i q_j + \sum_{i=1}^{m}\sum_{j=i}^{m}\sum_{k=j}^{m} A_r\left(i, j, k\right) q_i q_j q_k$$
$$r = 1, 2, \ldots, m \tag{30.7}$$

where B_r are the quadratic nonlinear stiffness coefficients and A_r are the cubic nonlinear stiffness coefficients for the r^{th} nonlinear modal equation. Within most commercial finite element packages, the nonlinear stiffness matrices are inaccessible, and therefore they must be determined indirectly by applying a set of forces or displacements to the FEA model.

There are several methods to evaluate the nonlinear stiffness coefficients. In this paper, the enforced displacement (ED) procedure is used exclusively. The ED process uses specific static displacements fields (i.e. linear combinations of the component modes in $\mathbf{T}$) that are enforced on the model using any suitable commercial FEA solver. For example, the c^{th} static displacement can be a combination of up to three component modes given as

$$\mathbf{x}_c = \mathbf{T}_i\widehat{q}_i + \mathbf{T}_j\widehat{q}_j + \mathbf{T}_k\widehat{q}_k \tag{30.8}$$

where the $N \times 1$ vector $\mathbf{x}_c$ is an enforced displacement for the c^{th} static load case, and each component mode denoted with subscript i, j, or k is scaled with the scalar amplitude $\widehat{q}$. The FEA software computes the reaction force, $\mathbf{f}_{T,c}$, necessary to hold the displacement field $\mathbf{x}_{\mathrm{c}}$, which can be broken into linear and nonlinear internal force components by the relation

$$\mathbf{f}_{T,c} = \mathbf{f}_L + \mathbf{f}_{NL} = \mathbf{K}\mathbf{x}_c + \mathbf{f}_{NL}\left(\mathbf{x}_c\right) \tag{30.9}$$

After computing the nonlinear reaction force $\mathbf{f}_{T,c}$, a series of these displacement and forces can be used to determine the nonlinear stiffness coefficients in Eq. (30.7), as will be reviewed in Sect. 30.2.3.

30.2.1 Selection of Modes

Mode selection becomes particularly important for finite element models with geometric nonlinearity. It is common to use the linearized, mass normalized vibration modes φ_r as basis vectors, which are computed from the eigenvalue problem $\left(\mathbf{K} - \omega_r^2\mathbf{M}\right)\boldsymbol{\varphi}_r = \mathbf{0}$. It is important to explicitly include the appropriate bending and membrane modes for the reduction basis of the ED procedure in order to capture the kinematics of this bending-membrane coupling. The higher frequency membrane motions can be incorporated into the basis by either including axial vibration modes, or using an alternative set of component modes referred to as dual modes. Guidance for the computation and selection of each type of membrane mode is provided below.

30.2.1.1 Axial Vibration Modes

Many works have used axial modes to capture the membrane effects [1, 6, 9, 14] for enforced displacement ROMs. Since these membrane motions are typically driven by large deformations of the bending modes, a set of these axial modes can be selected and augmented to each bending mode in the basis set as done in [6]. The augmented axial vibration modes for the r^{th} bending mode are determined by applying a force proportional to that bending mode shape to the finite element model as

$$\mathbf{Kx} + \mathbf{f}_{NL}(\mathbf{x}) = \mathbf{M}\boldsymbol{\varphi}_r \widehat{f}_r \tag{30.10}$$

The force amplitude $\widehat{f}_r$ should be large enough to excite the nonlinearity in the response such that the displacements contain components of the r^{th} bending mode as well as components of other modes that are statically coupled to that mode. The static displacement is then projected onto all the linear, mass normalized modes as $\mathbf{q} = \boldsymbol{\Phi}^{\mathrm{T}}\mathbf{Mx}$, and axial modes with the largest contribution to the response should be selected as the axial basis augmented to the r^{th} bending mode. For flat structures, the distinction for axial and bending type motion is clear. However, curved structures tend to produce vibrations modes that are coupled between transverse and in-plane deformations making it more difficult to distinguish between the two. This approach is discussed in more detail in [6].

30.2.1.2 Dual Modes

A systematic approach to generating the membrane basis was developed by Kim et al. using the concept of the dual mode [4]. The dual modes are computed from a pre-selected set of bending mode shapes using static forces applied to the nonlinear structure. There are three types of dual modes, which are referred to as first, second, and third generation dual modes. For the first generation dual mode, a static force proportional to only one bending mode is applied to the FEA model, given as

$$\mathbf{f}_T = \mathbf{M}\boldsymbol{\varphi}_r \widehat{f}_r \tag{30.11}$$

Again, $\widehat{f}_r$ is the scaling value on the applied force that sufficiently excites a nonlinear response. Using a commercial finite element package, the resulting static displacement field is computed as $\mathbf{u}_r$. The residual component of the response, that which remains after removing the component of the r^{th} bending mode φ_r, is isolated by the following relationship

$$\mathbf{v}_r^{(1)} = \mathbf{u}_r - \boldsymbol{\varphi}_r^T \mathbf{M}\mathbf{u}_r \boldsymbol{\varphi}_r \tag{30.12}$$

where $\mathbf{v}_r$ represents the remaining displacement field. This field contains the membrane motion due to bending displacement in the r^{th} mode. The notation $^{(1)}$ denotes that this type of response is used to compute a first generation the dual mode. A set of first generation dual modes are computed for all bending modes in the basis set.

Similarly, second generation dual modes result from an applied static force that is a linear combination of two bending mode shapes, such as

$$\mathbf{f}_T = \mathbf{M}\boldsymbol{\varphi}_i \widehat{f}_i + \mathbf{M}\boldsymbol{\varphi}_j \widehat{f}_j \tag{30.13}$$

The linear bending modes components are subtracted from the resultant displacement field as given below

$$\mathbf{v}_{ij}^{(2)} = \mathbf{u}_{ij} - \boldsymbol{\varphi}_i^T \mathbf{M}\mathbf{u}_{ij} \boldsymbol{\varphi}_i - \boldsymbol{\varphi}_j^T \mathbf{M}\mathbf{u}_{ij} \boldsymbol{\varphi}_j \tag{30.14}$$

Third generation dual modes are found by applying forces made up of linear combinations of three bending modes.

The final computational step for the dual modes basis is to make the dual modes mutually orthonormal with respect to the linear modes and the mass matrix. Each dual mode is orthonormalized with respect to the mass matrix using a Gram-Schmidt procedure, so the final orthonormal basis vectors $\boldsymbol{\Xi}_{ijk}^{(g)}$ are found using the following.

$$\boldsymbol{\Xi}_{ijk}^{(g)} = \mathbf{v}_{ijk}^{(g)} - \sum_{l=1}^{p} \boldsymbol{\varphi}_l \boldsymbol{\varphi}_l^T \mathbf{M}\mathbf{v}_{ijk}^{(g)} \tag{30.15}$$

The subscripts *i, j,* and *k* represent the linear mode(s) used to generate the dual mode, superscript *g* represents the type of dual mode (first, second, or third generation), and *p* represents the number of linear bending modes in the basis. For further details, see [4].

30.2.2 Scaling of Modes

Two scaling methods are used in this paper when determining the displacement magnitude $\widehat{q}$ of each component mode in Eq. (30.8). The displacement level dictates the level of nonlinearity excited during the static load cases used to fit the nonlinear stiffness coefficients. The two scaling approaches are the constant modal scaling (CS) method and the constant modal displacement (CD) method. Using the CD approach from [6], a scaling value $\widehat{q}_r$ for the r^{th} modal displacement is defined as

$$\widehat{q}_r = CD_r = \frac{w_{\max,r}}{\max\limits_{d}(\mathbf{T}_r)} \tag{30.16}$$

where $w_{\max,r}$ is the desired maximum displacement in physical coordinates for the r^{th} mode, and $\max\limits_{d}(\mathbf{T}_r)$ is the maximum displacement (i.e. ignoring any rotations) in the r^{th} component mode shape. The CD method sets a specific scaling factor for each mode in the displacement fields generated by Eq. (30.8). The authors have found that it is important to determine adequate scaling levels for the bending and membrane modes in order to obtain accurate ROM equations. One approach to guide the range of appropriate scaling values is to create a set of single-mode ROMs, which ultimately have one quadratic and one cubic nonlinear stiffness term. By tracking the nonlinear stiffness coefficients as a function of the maximum displacement, $w_{\max,r}$, the coefficients should converge around a range of scaling levels, indicating that the geometric nonlinearity is sufficiently exercised.

Previous works on the enforced displacement procedure have used what is referred to here as the CS approach, as recommended in [3]. The CS factor takes the CD scaling factor for the lowest frequency mode in the basis set in Eq. (30.16), and uses the same scaling factor for all modes in the basis set as $\widehat{q}_r = \mathrm{CD}_1$. The scaling factor is chosen based on the maximum displacement of the first bending mode included in the ROM, allowing for no control over the displacement level of the other modes in the basis. Displacements on the order of the thickness of the structure are recommended in [3], however the results in Sect. 30.3 show that this approach may not always produce the most accurate model.

Mignolet, Perez, Wang and others have also employed the enforced displacements procedure successfully to many structures [2, 7, 8, 15]. They typically set CD_r for each mode such that each bending mode displaces 1.0 times the thickness and a displacement < 1.0 times the thickness for the axial or dual modes. The optimal CD values are problem dependent and so they typically employ a few values near 1.0 thickness and check whether the ROM coefficients vary significantly. They also typically use the cleaning procedure described in [15] to set to zero any cubic $\mathrm{A}_r(r, r, r)$ and quadratic $\mathrm{B}_r(r, r)$ terms involving only one axial (or dual) mode. Finally, it should be noted that their approach to determine the ROM coefficients differs slightly from that outlined in Sect. 30.2.3.3 in that they estimate both the linear and nonlinear terms in the ROM from the results of the static load cases. The linear terms can then be compared against the known linear natural frequencies to check the consistency of the results; they may vary from the linear natural frequencies if too large of loads have been applied. This approach was not implemented in this work, but it should be kept in mind as it may explain some of the differences between the scaling values that worked best in this work and those reported in their works.

30.2.3 Identification of Nonlinear Stiffness Coefficients

30.2.3.1 Least Squares Method

The nonlinear stiffness coefficients may be evaluated using the least squares method, which employs a pseudo-inverse of a data matrix to determine the nonlinear stiffness coefficients for the r^{th} modal equation in a single computation. From Eq. (30.6) and a given static solution to the c^{th} load case in Eq. (30.8), the quasi-static modal equations can be rearranged as

$$\sum_{i=1}^{m}\sum_{j=i}^{m} B_r(i,j)\,\widehat{q}_i\widehat{q}_j + \sum_{i=1}^{m}\sum_{j=i}^{m}\sum_{k=j}^{m} A_r(i,j,k)\widehat{q}_i\widehat{q}_j\widehat{q}_k = \mathbf{T}_r^T\mathbf{f}_{T,c} - \mathbf{T}_r^T\mathbf{K}\mathbf{x}_c \tag{30.17}$$

For P static load cases of different permutations of the mode displacement fields, the relation for the nonlinear stiffness terms for the r^{th} equation can be written generally as

$$\begin{bmatrix} \widehat{q}_1{}^2[1] & \widehat{q}_1\widehat{q}_2[1] & \dots & \widehat{q}_m{}^2[1] & \widehat{q}_1{}^3[1] & \widehat{q}_1{}^2\widehat{q}_2[1] & \dots & \widehat{q}_m{}^3[1] \\ \widehat{q}_1{}^2[2] & \widehat{q}_1\widehat{q}_2[2] & \dots & \widehat{q}_m{}^2[2] & \widehat{q}_1{}^3[2] & \widehat{q}_1{}^2\widehat{q}_2[2] & \dots & \widehat{q}_m{}^3[2] \\ \vdots & \vdots & \vdots & \vdots & \vdots & \vdots & & \\ \widehat{q}_1{}^2[P] & \widehat{q}_1\widehat{q}_2[P] & \dots & \widehat{q}_m{}^2[P] & \widehat{q}_1{}^3[P] & \widehat{q}_1{}^2\widehat{q}_2[P] & \dots & \widehat{q}_m{}^3[P] \end{bmatrix} \begin{Bmatrix} B_r(1,1) \\ B_r(1,2) \\ \vdots \\ B_r(m,m) \\ A_r(1,1,1) \\ A_r(1,1,2) \\ \vdots \\ A_r(m,m,m) \end{Bmatrix} = \begin{Bmatrix} \mathbf{T}_r^{\mathrm{T}}\mathbf{f}_{T,1} - \mathbf{T}_r^T\mathbf{K}\mathbf{x}_1 \\ \mathbf{T}_r^{\mathrm{T}}\mathbf{f}_{T,2} - \mathbf{T}_r^T\mathbf{K}\mathbf{x}_2 \\ \vdots \\ \mathbf{T}_r^{\mathrm{T}}\mathbf{f}_{T,P} - \mathbf{T}_r^T\mathbf{K}\mathbf{x}_P \end{Bmatrix} \tag{30.18}$$

Note that each row will contain at most contributions from up to three modes. The algebraic equation in Eq. (30.18) is simplified as

$$\mathbf{G}\boldsymbol{\kappa}_r = \widehat{\mathbf{F}}_r \tag{30.19}$$

where $\mathbf{G}$ represents the data matrix of modal displacements, $\boldsymbol{\kappa}_r$ represents the vector of unknown coefficients for the r^{th} modal equation, and $\widehat{\mathbf{F}}_r$ represents the difference between the modal reaction force and linear contribution of the internal force. The unknown coefficients for the r^{th} modal equations are determined by computing the pseudo-inverse of the data matrix $\mathbf{G}$ in Eq. (30.19). The data matrix is independent of the modal equation being evaluated, so the pseudo-inverse needs to be computed only once. Only the right hand side of Eq. (30.19) need be updated to compute the coefficients for each of the modes described by the subscript r.

30.2.3.2 Least Squares, Constrained Method

The least squares, constrained method evaluates the nonlinear stiffness coefficients with a similar procedure as the least squares method. For multi-mode ROMs, dependency relations between the nonlinear stiffness coefficients are enforced during the fitting procedure. The relations are given as

$$B_k(i,j) = B_i(j,k) = B_j(i,k) \tag{30.20}$$

$$B_i(i,j) = 2B_j(i,i) \tag{30.21}$$

$$A_i(i,i,j) = 3A_j(i,i,i) \tag{30.22}$$

$$A_i(i,j,j) = A_j(i,i,j) \tag{30.23}$$

$$A_l(i,j,k) = A_k(i,j,l) \tag{30.24}$$

$$A_j(i,j,k) = 2A_i(j,j,k) = 2A_k(i,j,j) \tag{30.25}$$

These relations are enforced to ensure that the nonlinear stiffness matrices remain symmetric. The least squares, constrained method must solve for the nonlinear stiffness terms for all of the modal equations with a single pseudo-inverse of a modified data matrix, rather than just the r^{th} equation as done before. This matrix is larger than that in Eq. (30.19). The size of the matrix is not important from the view of computational cost, since the computations in Eqs. (30.18), (30.19), (30.20), (30.21), (30.22), (30.23), (30.24), and (30.25) are negligible compared to the cost required to solve the static load cases in the FEA code. However, larger matrices may exacerbate ill-conditioning in the fitting process leading to less accurate ROMs. Further details on both of the least squares methods can be found in [5].

30.2.3.3 RANSTEP Method

The RANSTEP method determines the nonlinear stiffness coefficients for each modal equation in a series of steps that involve inverting much smaller data matrices. The method solves for the unknown coefficients in sequential steps, beginning with the single-mode displacement fields

$$\begin{aligned} \mathbf{x}_1 &= +\mathbf{T}_i \widehat{q}_i \\ \mathbf{x}_2 &= -\mathbf{T}_i \widehat{q}_i \end{aligned} \tag{30.26}$$

The resulting quasi-static nonlinear modal equations for each mode $r = 1, 2, \ldots, m$ can be written in modal coordinates as

$$\begin{aligned} \mathbf{T}_r^T \mathbf{f}_{T,1} - \mathbf{T}_r^T \mathbf{K} \mathbf{x}_1 &= B_r\,(i,i)\,\widehat{q}_i \widehat{q}_i + A_r\,(i,i,i)\,\widehat{q}_i \widehat{q}_i \widehat{q}_i \\ \mathbf{T}_r^T \mathbf{f}_{T,2} - \mathbf{T}_r^T \mathbf{K} \mathbf{x}_2 &= B_r\,(i,i)\,\widehat{q}_i \widehat{q}_i - A_r\,(i,i,i)\,\widehat{q}_i \widehat{q}_i \widehat{q}_i \end{aligned} \tag{30.27}$$

This relation provides an algebraic equation, similar to the form in Eq. (30.17), as

$$\begin{bmatrix} \widehat{q}_i{}^2\,[1] & \widehat{q}_i{}^3\,[1] \\ \widehat{q}_i{}^2\,[2] & \widehat{q}_i{}^3\,[2] \end{bmatrix} \begin{Bmatrix} B_r\,(i,i) \\ A_r\,(i,i,i) \end{Bmatrix} = \begin{Bmatrix} \mathbf{T}_r^T \mathbf{f}_{T,1} - \mathbf{T}_r^T \mathbf{K} \mathbf{x}_1 \\ \mathbf{T}_r^T \mathbf{f}_{T,2} - \mathbf{T}_r^T \mathbf{K} \mathbf{x}_2 \end{Bmatrix} \tag{30.28}$$

By inverting the 2×2 matrix of modal displacements, the nonlinear stiffness coefficients $B_r(i,i)$ and $A_r(i,i,i)$ can be identified for modes $r = 1, 2, \ldots\ m$ and using all load cases involving modes $i = 1,2, \ \ldots\ m$.

Similarly, the displacement fields that are combinations of two modes

$$\begin{aligned} \mathbf{x}_1 &= +\mathbf{T}_i \widehat{q}_i + \mathbf{T}_j \widehat{q}_j \\ \mathbf{x}_2 &= -\mathbf{T}_i \widehat{q}_i - \mathbf{T}_j \widehat{q}_j \\ \mathbf{x}_3 &= +\mathbf{T}_i \widehat{q}_i - \mathbf{T}_j \widehat{q}_j \end{aligned} \tag{30.29}$$

and the coefficients from Eq. (30.28) are used to determine the $B_r(i,j)$, $A_r(i,i,j)$, and $A_r(i,j,j)$ coefficients. The displacement fields combining three modes

$$\mathbf{x}_1 = +\mathbf{T}_i \widehat{q}_i + \mathbf{T}_j \widehat{q}_j + \mathbf{T}_k \widehat{q}_k \tag{30.30}$$

are used along with all the other computed nonlinear stiffness terms to compute the $A_r(i,j,k)$ coefficients. Further details can be found in [3].

30.3 Numerical Results: Comparison of Parameter Estimation Method and Scaling Method

The least squares method, both constrained and unconstrained, and the RANSTEP method were first evaluated on a clamped-clamped beam with geometric nonlinearity. The nonlinear beam model, constructed of structural steel, was 228.6 mm (9 in.) long, with a cross section of 12.7 mm (0.5 in.) wide by 0.787 mm (0.031 in.) thick. The material properties are listed below in Table 30.1. The beam was modeled with forty B31 beam elements in Abaqus®, resulting in 117 DOF. In this section, only the axial vibration modes were used to capture the membrane kinematics, as ED ROMs were successfully obtained using these modes on this particular model in [6]. Dual modes are used to model the membrane motions in Sect. 30.4. The ROMs using axial vibration modes were computed with each of the different fitting procedures described in Sect. 30.2.3, along with the two scaling methods in Sect. 30.2.2. The nonlinear normal modes were computed from the reduced equations of motion using the algorithm in [16] and compared to the exact NNMs computed directly from the full FEA model using the AMF algorithm in [17]. The comparison to the full order model allows one to determine at which energy, or response levels, the solutions to the ROM equations deviate from the full model.

Table 30.1 Material properties of clamped-clamped beam

Young's modulus	Shear modulus	Density
$E = 204.8$ GPa (29,700 ksi)	$G = 80.0$ GPa (11,600 ksi)	$\rho = 7{,}870$ kg/m^3 (7.36×10^{-4} lb-s^2/in^4)

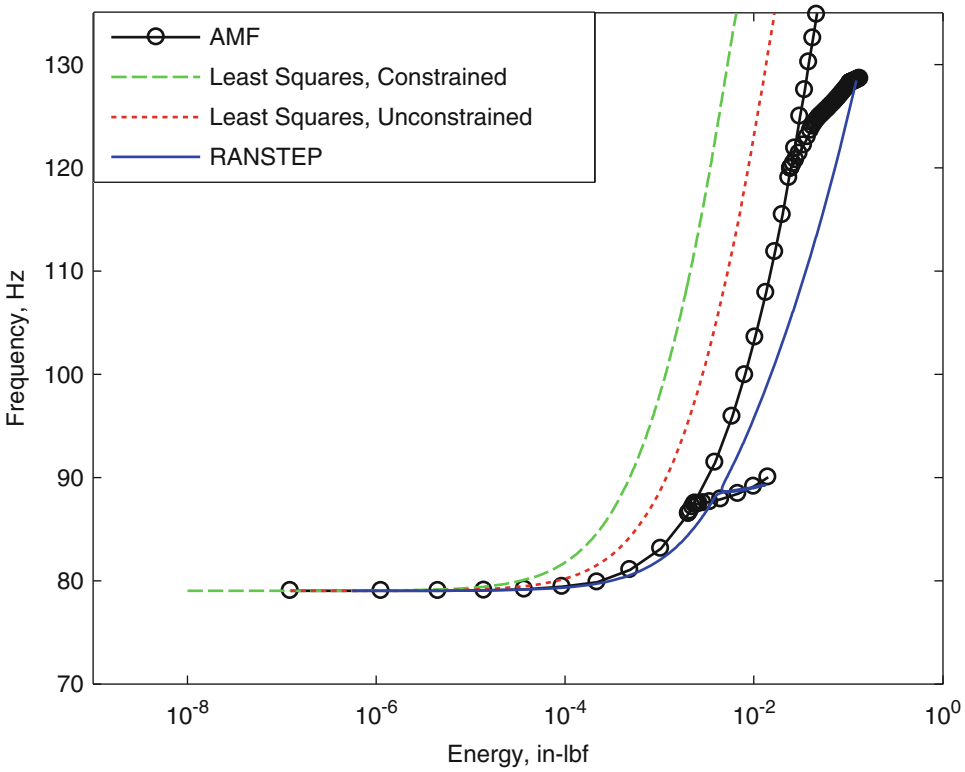

Fig. 30.1 Plot of NNM 1 using modes (1, 3, 5, 7, 26, 39, 45, 47, 49, 51, 53, 55) and a CS scaling set to a maximum displacement of 1.0 times the thickness for mode 1. The (*black circles*) show NNM 1 computed with the AMF algorithm, and ROMs built with the (*green dashed*) least squares constrained method (*red dotted*), least squares method, and (*blue solid*) RANSTEP method

Based on the results from [6], a ROM was successfully computed for the clamped-clamped beam using bending modes 1, 3, 5 and 7, augmented with axial modes 26, 39, 45, 47, 49, 51, 53, 55. The axial modes were chosen based on the static responses discussed in Sect. 30.2.1.1, such that two associated axial modes were added for every bending mode. This basis is used throughout Sect. 30.3 in order to understand how the parameter estimation schemes and scaling factors affect the resulting ROM. The original development of the enforced displacement method by Muravyov and Rizzi suggested using the constant scaling (CS) method to scale each mode during the static displacement fields. The sensitivity of the ED method was observed by using two different CS factors, namely when the first mode was displaced to 3.0 times the beam thickness (referred as CS (3.0)), and 1.0 times the thickness (CS (1.0)). After computing the ROM with these scaling factors, and each of the parameter estimation schemes, the first NNM was computed from the reduced equations and compared to the full order model results (denoted as AMF in the figure legend). These results are presented on the frequency energy plot (FEP) in Figs. 30.1 and 30.2, where the frequency represents the fundamental frequency of the periodic response, and the energy represents the conserved energy (potential plus kinetic) as the structure vibrates in that NNM.

Many interesting observations can be made from these results, and since each ROM used the same basis vectors, the discrepancy can be attributed to the CS scaling level and parameter estimation method. For the smaller CS factor in Fig. 30.1, none of the parameter estimation schemes predicted to correct results. The ROM estimated with RANSTEP was softer than the AMF results, while the two least square methods predicted a stiffer NNM. (Softer or stiffer refers to the fact that at a given energy level the frequency is either lower or higher than the actual frequency, respectively.) These results show that the CS factor of 1.0 is not an adequate scaling factor, even though it was on the order of the beam thickness, as originally recommended.

The results in Fig. 30.2 show the same ROMs but instead with a CS factor set to 3.0 times the beam thickness. At this scaling level, the ROM with RANSTEP produced very accurate results as the first NNM nearly coincides with the AMF results. The ROM with RANSTEP captured solutions along the backbone of the NNM, and also captured the two modal interactions (i.e. the tongues emanating from the backbone around 88 and 120 Hz). Each of the least squares methods were again inaccurate, even though they estimate the nonlinear stiffness coefficients from the same static responses at the same scaling level. Apparently ill-conditioning in the equations leads to higher sensitivity to errors, ultimately producing inaccurate predictions of the NNM. The RANSTEP approach is clearly the favorable method to estimate the nonlinear coefficients, however, one must carefully select the scaling amplitudes to obtain accurate results.

The results in Figs. 30.1 and 30.2 defy the conventional wisdom, which suggests that scaling on the order of the beam thickness will give a valid ROM. The root cause was investigated by computing a single-mode ROM with a particular mode

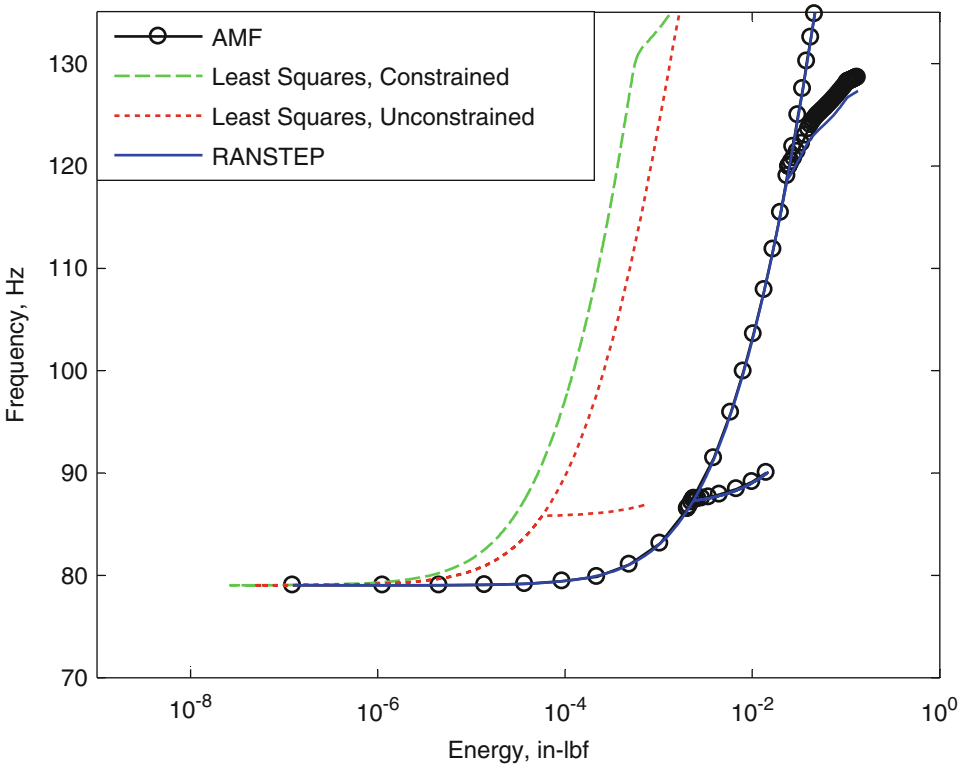

Fig. 30.2 Plot of NNM 1 using modes (1, 3, 5, 7, 26, 39, 45, 47, 49, 51, 53, 55) and a CS scaling set to a maximum displacement of 3.0 times the thickness for mode 1. The (*black circles*) show NNM 1 computed with the AMF algorithm, and ROMs built with the (*green dashed*) least squares constrained method (*red dotted*), least squares method, and (*blue solid*) RANSTEP method

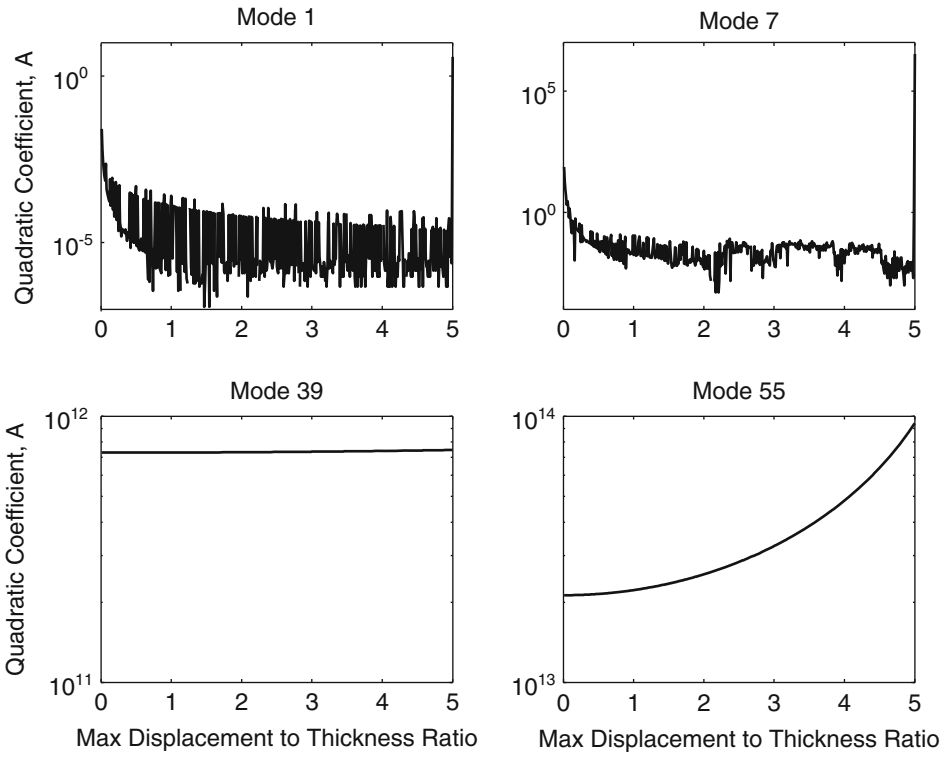

Fig. 30.3 For modes 1, 7, 39 and 55, the effect of scaling is shown for the computed absolute value of the quadratic stiffness term, B1(1,1), of a single-mode ROM

in the basis set, and tracking how the nonlinear quadratic and cubic stiffness coefficients changed with scaling level. Since the difference in the NNM essentially traces back to the stiffness coefficients at the different scaling levels, this provided insight into the scaling range over which each mode could be accurately estimated. Examining a higher and lower mode for both the bending and membrane modes, the absolute values of the stiffness coefficients versus scaling level for bending modes 1 and 7 and membrane modes 39 and 55 are shown in Figs. 30.3 and 30.4.

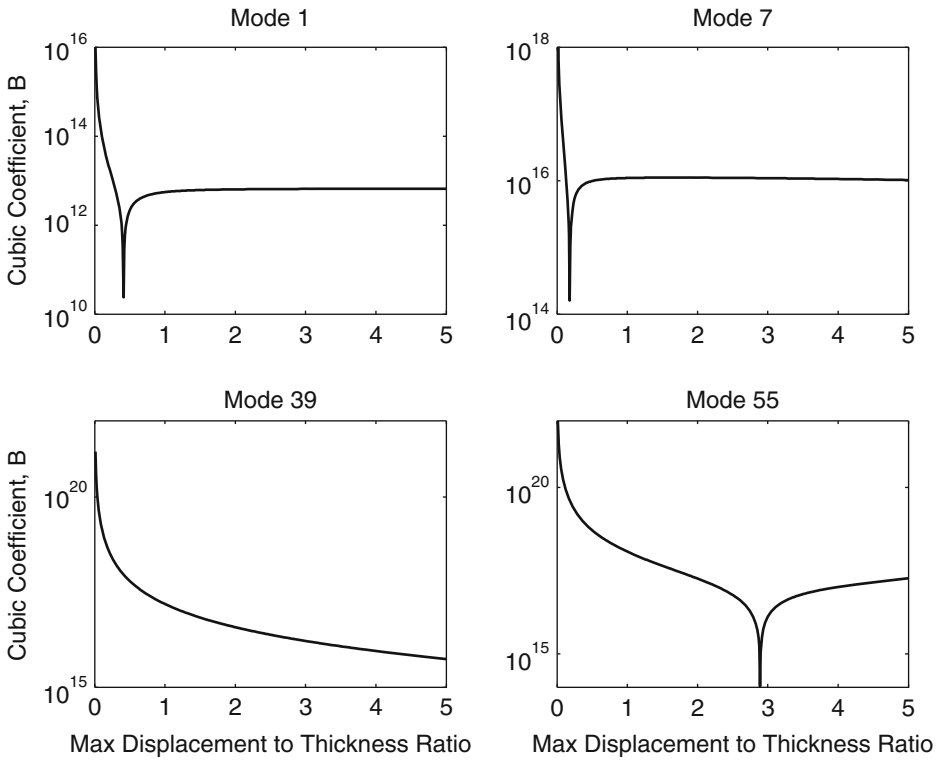

Fig. 30.4 For modes 1, 7, 39 and 55, the effect of scaling is shown for the computed absolute value of the cubic stiffness term, $A_1(1,1,1)$, of a single-mode ROM

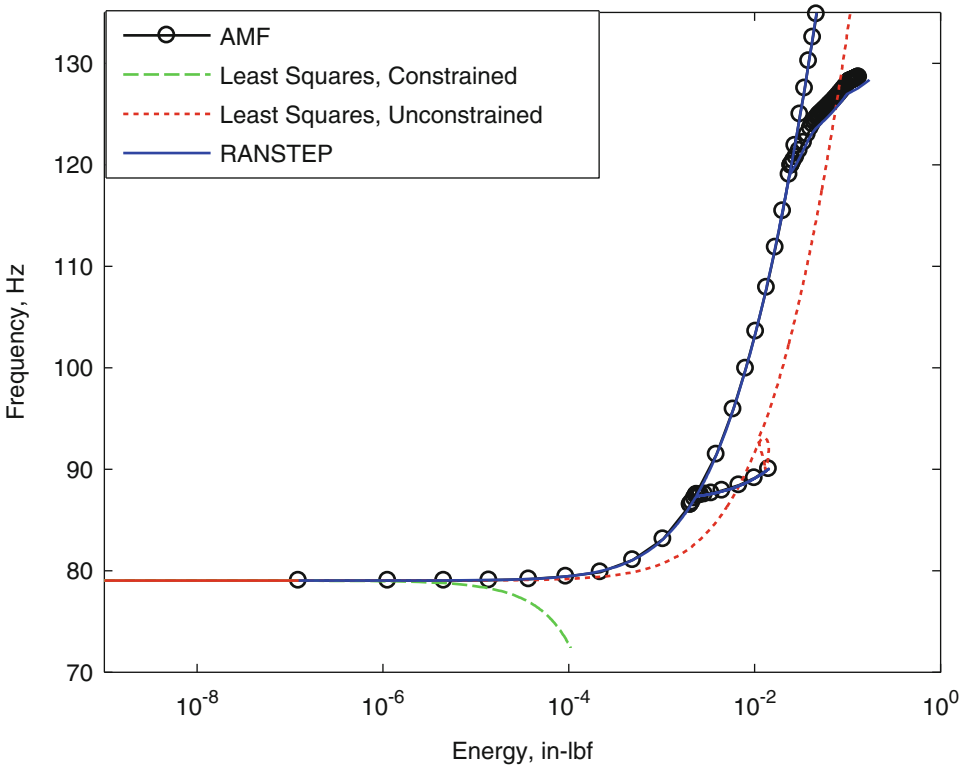

Fig. 30.5 Plot of NNM 1 using modes (1, 3, 5, 7, 26, 39, 45, 47, 49, 51, 53, 55) and a CD scaling set to a maximum displacement of 3.0 times the thickness for all bending modes, and 1.0 times the thickness for all axial modes. The (*black circles*) show NNM 1 computed with the AMF algorithm, and ROMs built with the (*green dashed*) least squares constrained method (*red dotted*), least squares method, and (*blue solid*) RANSTEP method

Table 30.2 Equivalent displacement levels of each mode when using CS set to 3.0 times the thickness

Mode	1	3	5	7	26	39	45	47	49	51	53	55
Equivalent CD levels	3.00	2.85	2.84	2.85	2.67	2.67	2.67	2.54	2.67	2.67	2.67	2.54

For the two bending modes, the quadratic coefficients in Fig. 30.3 were essentially zero, which was expected for the bending modes of a flat structure, but is still informative to see the level of scatter and the regimes where they are estimated to be small. The two axial vibration modes produced quadratic terms that were nonzero. The quadratic term for mode 39 was nearly constant over the entire displacement range, however $B_1(1,1)$ for mode 55 appeared to increase as the scaling increased. The cubic terms were less consistent throughout the scaling range for all of the modes. For both bending modes, the cubic terms were increasing by several orders of magnitude as the displacement tended towards zero. Between displacements of 0 and 1.0 times the beam thickness, the predicted $A_1(1,1,1)$ term dropped down about two orders of magnitude, but began to stabilize as the scaling went above 1.0.

The "bend" of the first NNM predicted in Figs. 30.1 and 30.2 strongly depends on the cubic stiffness coefficient associated with bending mode 1. For mode 1 in Fig. 30.4, scaling of 1.0 times the beam thickness produced a value of $A_1(1,1,1) = 5.52 \cdot 10^{12}$ lbf/in^3, while a scaling of 3.0 produced a value of $6.51 \cdot 10^{12}$ lbf/in^3. The coefficient on mode 1 did not converge until around the range of 2.0 or 3.0 times the beam thickness, which may explain why the scaling of CS (3.0) produced more accurate results than CS (1.0). Unlike the bending modes, the quadratic and cubic terms for the axial modes do not converge within the range of the scaling shown in Figs. 30.3 and 30.4.

The optimal scaling can vary for each mode in the basis, and hence this was the motivation for using the CD scaling method which allows the scaling level to be chosen individually for each mode (recall that the CS method only allows control of the displacement level on the lowest frequency bending mode). New ROMs were again produced using the same basis and parameter estimation schemes, however this time using the CD scaling method. Each of the bending modes was scaled to 3.0 times the beam thickness, while the axial modes were scaled to 1.0 times the beam thickness. Since there was no clear consistency in the coefficients produced by the axial modes in Figs. 30.3 and 30.4, the 1.0 factor was chosen in order to avoid the large spikes in the quadratic or cubic term. The results for NNM 1 are shown in Fig. 30.5.

With the CD scaling method, the ROM with RANSTEP again produced very accurate results, however the least squares methods produced erroneous NNMs. Even though no difference was observed when using the CS or CD scaling with RANSTEP, the CD method provides more flexibility in the selection of scaling each mode during the fitting process. The connection between the CD scaling method, and CS is shown below in Table 30.2, where the equivalent CD factor is given for each mode when using CS (3.0). It can be seen that the displacements on each mode with CS are not drastically different from those used in Fig. 30.5, except that the axial modes are displaced slightly higher (2.5 times the thickness compared to 1.0). The level of the reaction force required to enforce an axial displacement by one thickness tends to be much larger than that required in bending, so the reduced scaling on the axial modes reduced the axial force levels and any associated numerical ill-conditioning, explaining why least squares improved in Fig. 30.5 compared to the results in Fig. 30.2.

30.4 Numerical Results: Axial Modes Versus Dual Modes

The results in Sect. 30.3 showed that the RANSTEP estimation procedure was clearly the preferred method for parameter estimation and that CD scaling was adequate. In this section, the bending modes Eqs. (30.1, 30.3, 30.5, and 30.7) will be used exclusively with RANSTEP and CD in order to evaluate the effect of using dual modes instead of axial modes. The ROMs used in the previous section used 12 modes to capture the response of only four bending modes, so one would hope that a more compact model could be found. Recall from Sect. 30.2.1.2 that three types of dual modes exist, namely generation one, two and three. In the following, a generation one dual mode estimated from bending mode 1 will be referred to as "dual 1" or "D1", and a generation two dual mode with bending modes 1 and 3 will be referred as "dual 1-3" or "D1-3".

Before generating ROMs with the dual mode basis, the appropriate scaling levels for these modes were investigated by computing the single-mode ROMs, and observing how the absolute values of the stiffness coefficients evolved with displacement level. The results for duals 1 and 1–3 are shown in Fig. 30.6.

It was determined that these dual modes should be scaled to 1.0 times the beam thickness when using them to estimate the ROMs, exactly as done with the axial modes in the previous section. There were no large spikes around this value observed in Fig. 30.6 for the dual modes of interest, implying that this would be a safe displacement level to use. The work by Kim et al. [4] discussed the use of dual modes with the enforced displacement procedure, and suggested the use of different

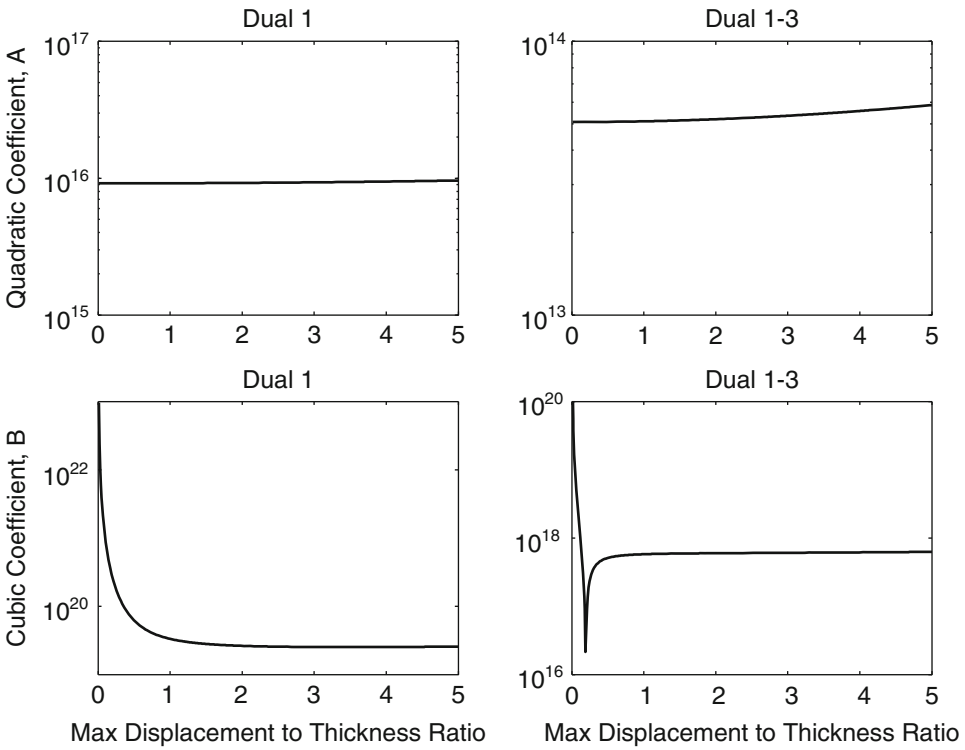

Fig. 30.6 Variation in the absolute values of the cubic and quadratic stiffness terms, $B_1(1,1,1)$ and $A_1(1,1,1)$ for dual modes D1 and D1-3, respectively

Table 30.3 Description of dual mode basis used to generate the ED ROMs

Description	Dual modes included
Generation 1 duals	$\Xi_1^{(1)}, \Xi_3^{(1)}, \Xi_5^{(1)}, \Xi_7^{(1)}$
Generation 1 and 2 duals	$\Xi_1^{(1)}, \Xi_3^{(1)}, \Xi_5^{(1)}, \Xi_7^{(1)}, \Xi_{13}^{(2)}, \Xi_{15}^{(2)}, \Xi_{17}^{(2)}, \Xi_{35}^{(2)}, \Xi_{37}^{(2)}, \Xi_{57}^{(2)}$
Mode 1 dominant duals	$\Xi_1^{(1)}, \Xi_{13}^{(2)}, \Xi_{15}^{(2)}, \Xi_{17}^{(2)}, \Xi_{135}^{(3)}, \Xi_{137}^{(3)}, \Xi_{157}^{(3)}$

combinations of specific dual modes. For example, they discuss using only dual modes computed from one of the dominant bending modes. In the case where bending modes 1, 3, 5, and 7 were used in the basis and mode 1 was expected to be dominant in the responses of interest, then only the dual modes (1, 1-3, 1-5, 1-7, 1-3-5, 1-3-7, 1-5-7) would be included in the ROM. To evaluate the use of dual modes to capture the in-plane kinematics, ROMs were created with only generation one dual modes, generation one and two dual modes, and mode 1 dominant dual modes (see Table 30.3 for a list of dual modes included in each ROM). The resulting ROMs were computed with the RANSTEP method and CD with each bending mode scaled to 3.0 times the thickness and the appropriate duals to 1.0. The ROMs were then compared based on their computed nonlinear normal modes. The results are shown in Fig. 30.7.

The ROM with the mode 1 dominant dual modes (green dashed) performed best when compared to the full order model, as it captured solutions along the backbone as well as the two modal interactions. When using only generation one dual modes (blue solid), the resulting ROM was able to accurately predict solutions along the backbone, but not along the modal interactions. For example, the modal interaction at 88 Hz was an interaction with NNM 3. Since using only generation one dual modes did not include $\Xi_{13}^{(2)}$ or any other higher order dual modes, the necessary kinematics were not available in the ROM to fully capture this interaction. When using generation one and two dual modes (red dotted), the ROM was able to capture this interaction, further implying that the higher order kinematics were important.

There was one additional challenge with the ROM that was built with generation one and two dual modes; the authors were not able to compute NNM solutions beyond 100 Hz with this ROM. (Notice that the red dotted line in Fig. 30.7 does not continue past this point.) A similar observation was made when a ROM was constructed including all of generation one, two, and three dual modes (not shown here). With this ROM the continuation algorithm could not compute past the linear range of the NNM so its NNM was not included in Fig. 30.7. Apparently some of these higher generation modes introduce some instability in the ROM equations at certain amplitude levels. One would hope that adding additional basis vectors to the ROM would improve the results, or at the very least have no ill effect on the results so this behavior is certainly undesirable. The cleaning procedure [15] briefly mentioned in Sect. 30.2.2 would perhaps help with this issue, although it was not explored in this paper.

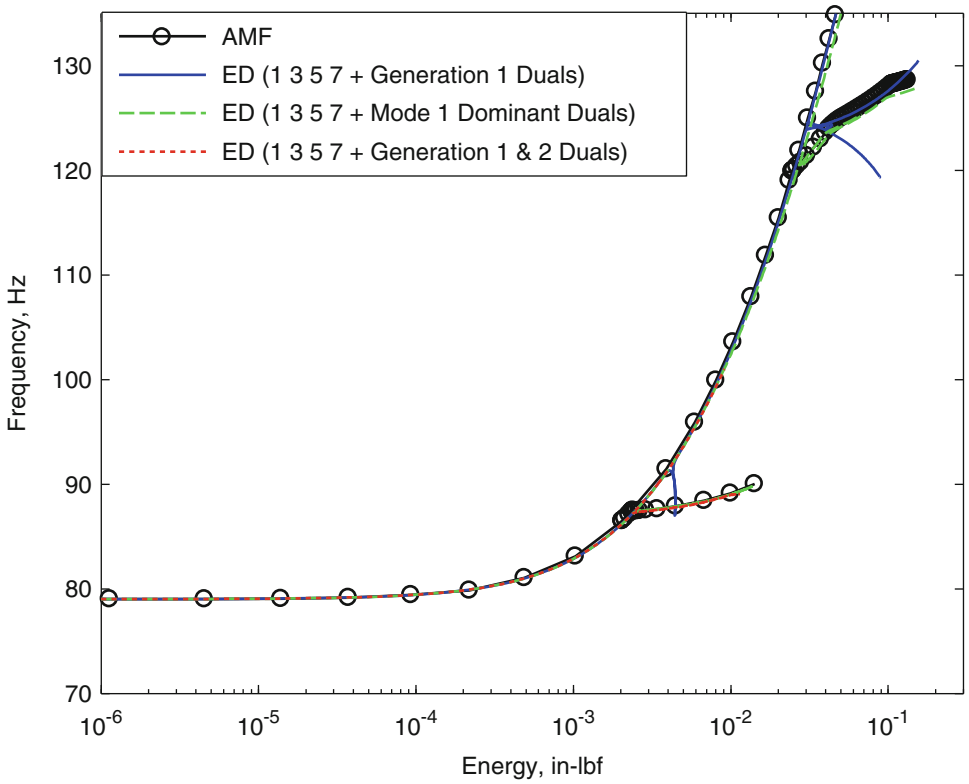

Fig. 30.7 Plot of NNM 1 using bending modes (1, 3, 5, 7) and various combinations of dual modes. A CD scaling factor was set to a maximum displacement of 3.0 times the thickness for all bending modes, and 1.0 times the thickness for all dual modes. The (*black circles*) show NNM 1 computed with the AMF algorithm, and ROMs built with the (*blue solid*) generation 1 dual modes (*green dashed*), mode 1 dominant dual modes, and (*red dotted*) generation 1 and 2 dual modes

30.5 Numerical Results: FEA Model of Exhaust Cover Plate

A more complicated model is used now to evaluate the ability of the enforced displacement ROMs to accurately predict NNMs of a structure for which an analytical solution is intractable. The FEA model of interest is a perforated exhaust cover plate and is shown in Fig. 30.8. A similar model was studied in [6, 17], but the model here has an improved mesh. When the authors originally investigated this model, they found that it was difficult to identify axial modes to augment the bending modes and hence an accurate ROM was not obtained in [6]. Here, the problem is revisited in an attempt to model the in-plane kinematics with dual modes.

The exhaust cover plate is 317.5 mm (12.5 in.) in diameter with a uniform thickness of 1.5 mm (0.059 in.). It is constructed of structural steel with a mass density of 7,800 kg/m^3 (7.29 · 10-4 lb-s^2/in^4) and a Young's modulus of 208 GPa (30,160 ksi). The Abaqus® model has a total of 1,440 S4 shell elements, and a total of 8,886 DOF. The boundary conditions were approximated as fixed along the bottom ring of the plate in order to account for the relatively rigid boundary to which the plate is welded.

The first NNM of the nonlinear plate model was computed using the AMF algorithm, and used to compare five different ROMs. Four of the ROMs used bending modes (1 and 6), and "axial" modes (126, 135, 142, 157, 169, 375). These "axial" modes were selected based on the static displacement results in Sect. 30.2.1.1, however each selected mode shape still had noticeable transverse deformation and no true in-plane modes were identified. Another ROM was created with the same bending modes, but instead with all the first and second generation dual modes ($\Xi_1^{(1)}$, $\Xi_6^{(1)}$, $\Xi_{16}^{(2)}$). For all cases, the RANSTEP parameter estimation procedure was used, and the CD scaling factors were selected such that the bending modes and membrane (axial or dual) modes were displaced between 0.5 and 3.0 times the plate thickness. The frequency-energy behavior of the NNMs estimated from these ROMs are shown in Fig. 30.9.

The enforced displacement ROMs that were built with axial modes and scaled the bending modes to a maximum displacement of 3.0 times the thickness predicted stiffer NNMs than the full order model, as expected from previous works [6]. The ROM that was built with axial modes and scaled the bending and membrane modes to a maximum displacement of 1.0 times the thickness predicted slightly stiffer behavior at lower energies and then slightly softer behavior at higher energies. For any of these first three ROMs with axial modes in the legend of Fig. 30.9, the accuracy may be acceptable for some purposes. However, the last ROM created with axial modes predicted unphysical behavior, likely due to the low scaling factors used during the static loads to fit the nonlinear coefficients. Additional kinematics are needed to

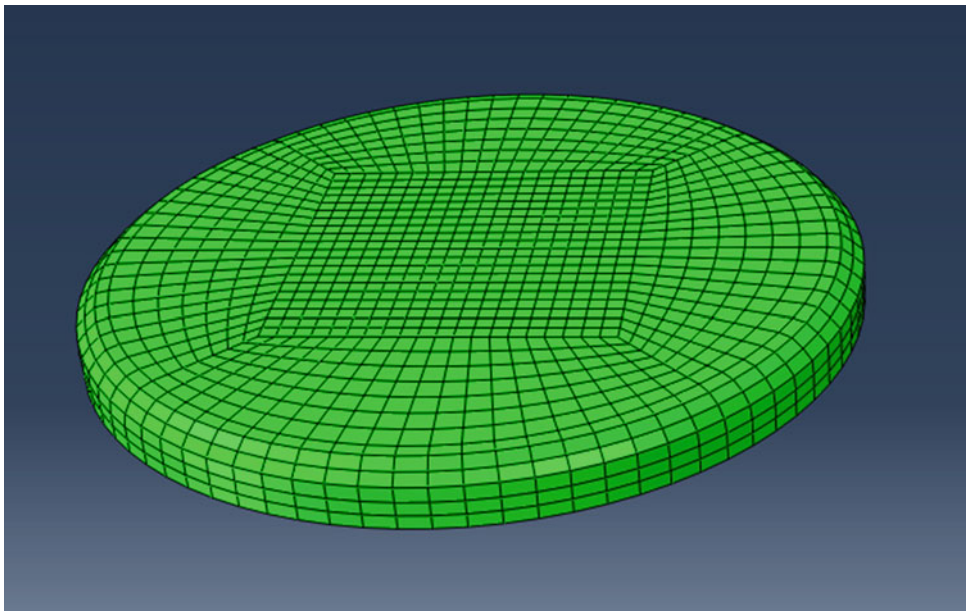

Fig. 30.8 A geometrically nonlinear finite element model of an exhaust cover panel

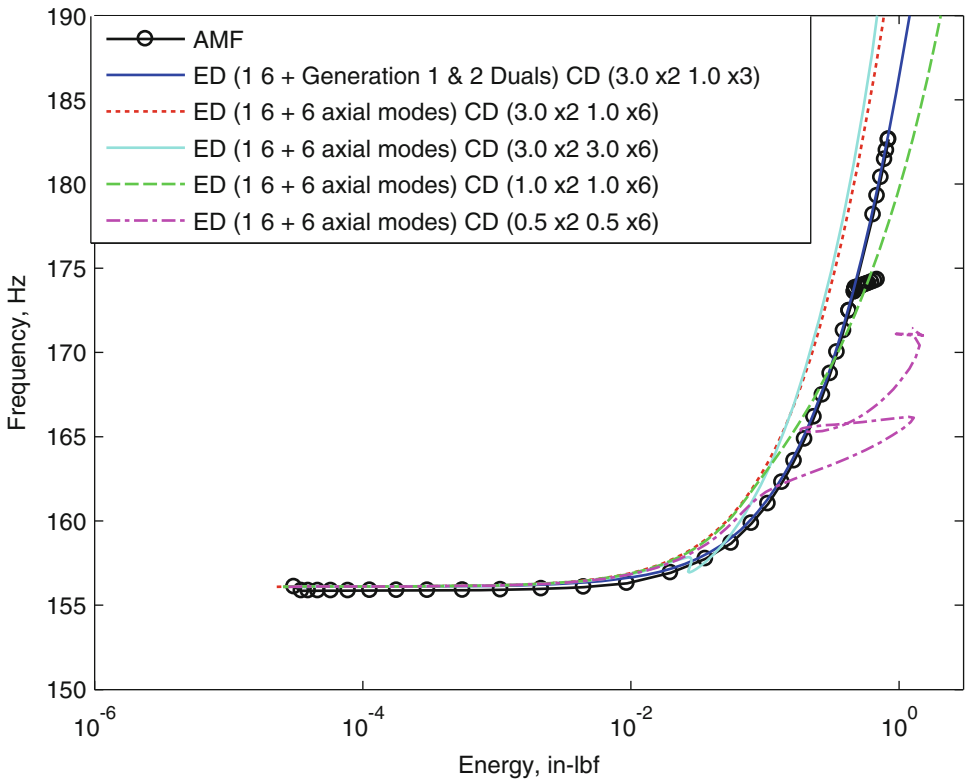

Fig. 30.9 Plot of NNM 1 using bending modes (1 and 6) with either all generation one and two dual modes ($\Xi_1^{(1)}$, $\Xi_6^{(1)}$, $\Xi_{16}^{(2)}$), or six axial modes (126, 135, 142, 157, 169, 375). Various values for the CD scaling factors were used for the bending and membrane modes and the parameters were fit with RANSTEP. The (*black circles*) show NNM 1 computed with the AMF algorithm

improve the accuracy of this model when using axial modes, but it is difficult to determine which modes are needed. Plus, the model already has three times as many axial modes as it does bending modes, so additional modes increase the cost required to build the ROM. The ROM with dual modes worked very well as the predicted backbone coincided with the AMF results almost perfectly. This ROM was not able to capture the modal interaction near 175 Hz, however this is to be expected because this internal resonance was an interaction with NNM 15, a bending motion that was not included in the basis set. The use of dual modes provided a systematic approach to model the in-plane deformations, with only 3 in-plane component mode shapes, and provided very accurate results for the exhaust cover plate model.

30.6 Conclusion

This work has explored the effect of the various decisions to generate a ROM using the enforced displacement procedure by comparing the accuracy of its computed nonlinear normal modes. The results in Sect. 30.3 clearly showed that the RANSTEP procedure was much more robust at estimating the coefficients in the reduced order models than the least squares procedure. This may also suggest that one can expect RANSTEP to be less sensitive to the amplitude of the load cases than the least squares approach. The effect of the scaling of the modal displacements on these ROMs was also investigated. So long as RANSTEP was used, either scaling method was found to be accurate as long as the bending modes were displaced a few times the beam thickness. Previous works have made general recommendations of using a displacement on the order of the thickness [3]. However, this discrepancy could be attributed to the fact that we assumed the linear term on the ROM equation was determined from an eigenvalues solution, whereas in the works by Perez, they fit this when fitting the nonlinear terms. The CD scaling method is recommended based on the flexibility it allows to displace each mode in the basis set.

This work has also explored the number of axial or dual modes that are needed to obtain an accurate ROM. For the systems studied here it was sometimes possible to obtain an accurate ROM by simply selecting those axial modes that were statically coupled to each of the bending modes in the basis. This worked for the beam but the ROM for the exhaust plate seemed to converge slowly to the true NNM and there was noticeable inaccuracy even after several axial modes had been included. In contrast, when dual modes were used, an accurate ROM for the exhaust plate was obtained with only two bending modes and three dual modes. For the beam, the dual modes consistently produced ROMs that accurately captured the backbone of the NNM. However, only the ROM with mode 1 dominant duals captured the internal resonances correctly. Additionally, several of the ROMs with dual modes could not be integrated at large response amplitudes, presumably due to small errors in some of the nonlinear coefficients. It was noted that Mignolet, Perez and Wang [2, 7, 8, 15] typically use the cleaning procedure in the papers just cited to set certain terms in the ROM to zero. Perhaps this is a critical step when using these methods. However, it is important to note that cleaning can only be done when the structure is flat since one needs to be able to classify each mode as either axial or bending. For a curved structure, all modes contain bending and membrane components, making it difficult to apply this approach.

In summary, the results so far confirm the effectiveness of the enforced displacements procedure so long as the best practices outlined above are used. It seems to exhibit some sensitivity to the displacement levels but these can be addressed by computing single-mode ROMs at different scaling levels and seeing how the coefficients change. These ROMs tend to produce larger reduced order models since the membrane modes need to be explicitly included in the basis, and these can be hard to identify. Dual modes seem to be promising as a means of obtaining an efficient ROM with relatively few membrane degrees of freedom, but some expertise is still required to choose a set of dual modes that will be accurate while keeping the ROM small.

Acknowledgements The authors gratefully acknowledge the support of the Air Force Office of Scientific Research under grant number FA9550-11-1-0035, administered by Dr. David Stargel of the Multi-Scale Structural Mechanics and Prognosis Program. The authors also wish to thank Dr. Joseph Hollkamp and the Structural Sciences Center at the Air Force Research Laboratory for providing the Abaqus® interface that was used in this work as well as for many helpful suggestions and discussions regarding the ROM modeling and Dr. Stephen Rizzi for providing an implementation of the RANSTEP code and suggestions regarding how to use it effectively. The authors are also grateful to Ricardo Perez (Universal Technologies Inc. and AFRL) for his insights and comments regarding how to create accurate ROMs.

References

1. Hollkamp JJ, Gordon RW, Spottswood SM (2005) Nonlinear modal models for sonic fatigue response prediction: a comparison of methods. J Sound Vib 284:1145–1163
2. Mignolet MP, Przekop A, Rizzi SA, Spottswood SM (2013) A review of indirect/non-intrusive reduced order modeling of nonlinear geometric structures. J Sound Vib 332:2437–2460
3. Muravyov AA, Rizzi SA (2003) Determination of nonlinear stiffness with application to random vibration of geometrically nonlinear structures. Comput Struct 81:1513–1523
4. Kim K, Radu AG, Wang XQ, Mignolet MP (2013) Nonlinear reduced order modeling of isotropic and functionally graded plates. Int J Non-Lin Mech 49:100–110
5. Gordon RW, Hollkamp JJ (2011) Reduced-order models for acoustic response prediction. AFRL-RB-WP-TR-2011-3040, July 2011
6. Kuether RJ, Deaner BJ, Hollkamp JJ, Allen MS (2014) Evaluation of geometrically nonlinear reduced order models with nonlinear normal modes. AIAA J (submitted)
7. Perez R, Wang XQ, Mignolet MP (2014) Nonintrusive structural dynamic reduced order modeling for large deformations: enhancements for complex structures. J Comput Nonlin Dyn 9:031008–031008

8. Perez RA (2012) Multiscale reduced order models for the geometrically nonlinear response of complex structures. PhD, Arizona State University
9. Rizzi SA, Przekop A (2005) The effect of basis selection on static and random acoustic response prediction using a nonlinear modal simulation. NASA TP-2005-213943
10. Kerschen G, Peeters M, Golinval JC, Vakakis AF (2009) Nonlinear normal modes. Part I. A useful framework for the structural dynamicist. Mech Syst Signal Process 23:170–194
11. Vakakis AF (1997) Non-linear normal modes (NNMs) and their applications in vibration theory: an overview. Mech Syst Signal Process 11:3–22
12. Kuether RJ, Brake MR, Allen MS (2014) Evaluating convergence of reduced order models using nonlinear normal modes. Presented at the 32nd international modal analysis conference (IMAC XXXII), Orlando
13. Schoneman JD, Allen MS, Kuether RJ (2014) Relationships between nonlinear normal modes and response to random inputs. Presented at the 5th AIAA/ASME/ASCE/AHS/SC structures, structural dynamics, and materials conference, National Harbor
14. Rizzi SA, Przekop A (2008) System identification-guided basis selection for reduced-order nonlinear response analysis. J Sound Vib 315:467–485
15. Wang XQ, Perez RA, Mignolet MP, Capillon R, Soize C (2013) Nonlinear reduced order modeling of complex wing models. In: 54th AIAA/ASME/ASCE/AHS/ASC structures, structural dynamics, and materials conference, Boston
16. Peeters M, Viguié R, Sérandour G, Kerschen G, Golinval JC (2009) Nonlinear normal modes, Part II: toward a practical computation using numerical continuation techniques. Mech Syst Signal Process 23:195–216
17. Kuether RJ, Allen MS (2014) A numerical approach to directly compute nonlinear normal modes of geometrically nonlinear finite element models. Mech Syst Signal Process 46:1–15

Chapter 31
Nonlinear Model Updating Methodology with Application to the IMAC XXXIII Round Robin Benchmark Problem

Mehmet Kurt, Keegan J. Moore, Melih Eriten, D. Michael McFarland, Lawrence A Bergman, and Alexander F Vakakis

Abstract We develop a new nonlinear model updating strategy based on global/local nonlinear system identification of general mechanical systems. The approach relies on analyzing system time series in the frequency-energy domain by constructing Hamiltonian, and forced/damped frequency-energy plots (FEPs). The system parameters are then characterized and updated by matching the backbone branches of the FEPs with the frequency-energy wavelet transforms of experimental and/or computational time series. The main advantage of this method is that no nonlinearity model is assumed a priori, and the system model is updated solely based on simulation and/or experimental results. By matching the frequency-energy plots of the benchmark system and its reduced order model, we show that we are able to retrieve the global dynamics in the frequency and energy ranges of interest, identify bifurcations, characterize local nonlinearities, and accurately reconstruct time series.

Keywords Nonlinear model updating • Nonlinear system identification • Frequency-energy plots • Reduced-order modeling

31.1 Introduction

Predictions from analytical and computational models are often called into question when they conflict with test results. *Model updating* concerns the correction of these models by processing and integrating dynamic response data from test structures [1]. More specifically, finite element – FE model updating emerged in the 1990s as a topic thought to be very crucial for the design, construction and maintenance of mechanical systems and other engineering structures [2]. Reviews of existing FE model updating techniques are given in [1–4]. These give a clear overview of sensitivity-based updating methods. Sensitivity-based FE model updating methods have been embraced for damage assessment and structural health monitoring applications, e.g., [5–7], but have been limited in application to linear systems.

We note, however, that the existing model updating methodologies don't account for strongly nonlinear effects on the global dynamics, i.e., of the system dynamics over broad frequency and energy ranges, so they are only applicable to specific classes of dynamical systems; in addition, some functional form should be assumed for modeling the system nonlinearities. On the contrary, the nonlinear model updating methodology proposed in this work relies solely on measured time series, with no a priori assumption regarding the nonlinearity of the system. Hence, the proposed methodology is data driven and applicable to a broad range of dynamical systems.

M. Kurt (✉)
Department of Bioengineering, Stanford University, Stanford, CA 94305, USA
e-mail: mehmetkurtt@gmail.com

K.J. Moore • A.F. Vakakis
Department of Mechanical Science and Engineering, University of Illinois, Urbana, IL 61801, USA

M. Eriten
Department of Mechanical Engineering, University of Wisconsin at Madison, Madison, WI 53706, USA

D.M. McFarland • L.A. Bergman
Department of Aerospace Engineering, University of Illinois, Urbana, IL 61801, USA

G. Kerschen (ed.), *Nonlinear Dynamics, Volume 1*, Conference Proceedings of the Society for Experimental Mechanics Series, DOI 10.1007/978-3-319-15221-9_31

31.2 Proposed Model Updating Methodology

In Fig. 31.1, the general outline of the proposed nonlinear model updating approach for a given dynamical system is presented. The first step is the measurement of the time series of the system responses. In order to estimate the global frequency-energy of the dynamics we measure time series from a number of sensors throughout the system under transient excitation. Afterwards, we estimate the instantaneous frequency, amplitude and the energy of the measured time series by applying numerical wavelet transforms (WTs), and superposing the resulting WT spectra onto a 'reference' frequency-energy plot – FEP representing the different branches of nonlinear periodic solutions of the underlying Hamiltonian system (i.e., the dynamical system with damping and forcing terms removed). A very useful feature of the 'reference' FEP for system identification purposes is its relation to the transient dynamics of the corresponding weakly damped system. This is due to the fact that *the effect on the dynamics of weak damping is expected to be parasitic*; that is, instead of introducing 'new' dynamics, weak damping just causes transitions of the transient damped dynamics between branches of normal modes of the underlying Hamiltonian system leading to multi-frequency nonlinear dynamical transitions. It has been shown that the superposition of a frequency-energy plot (FEP) depicting the periodic orbits of the underlying Hamiltonian system to the wavelet transform (WT) spectra of the corresponding weakly damped responses represents a suitable tool for analyzing energy exchanges and transfers taking place in the damped system [8–10]. Therefore, by utilizing this (empirical) frequency-energy dependence obtained from the superposition of the WT spectra onto the 'reference' FEP, we arrive at a nonlinearity model, since we can infer the properties of the nonlinearities in the frequency-energy domain, provided that the transient data covers the energy and frequency range of interest to the study. The parameters of the nonlinearity model are then optimized by comparing the numerical frequency-energy dependence derived from the simulations to the 'reference' Hamiltonian FEP computed numerically, e.g., using the software NNMcont as described by [11].

31.3 Application to the Benchmark Problem

In this section, the proposed nonlinear model updating strategy will be applied to the benchmark problem posed to the system identification community in the IMAC XXXIII held in Orlando, Florida between February 2–5, 2015, as a Round Robin Exercise on Nonlinear System Identification. The benchmark files used in this exercise, which is a protected code that can be simulated at 8 sensing locations depicted in Fig. 31.2. The considered structure consists of two facing clamped steel beams connected by a non-identified flexible element, in Fig. 31.2. The purpose of the exercise is to identify and model the nonlinear characteristics of this unknown element by using only the outputs of the system, which is exactly the solid foundation of our NSI, reduced order modeling and nonlinear model updating methodologies. The two beams lay on two parallel planes, so that the connecting element is inclined. The length of each beam is 300 mm, the width 20 mm, and the

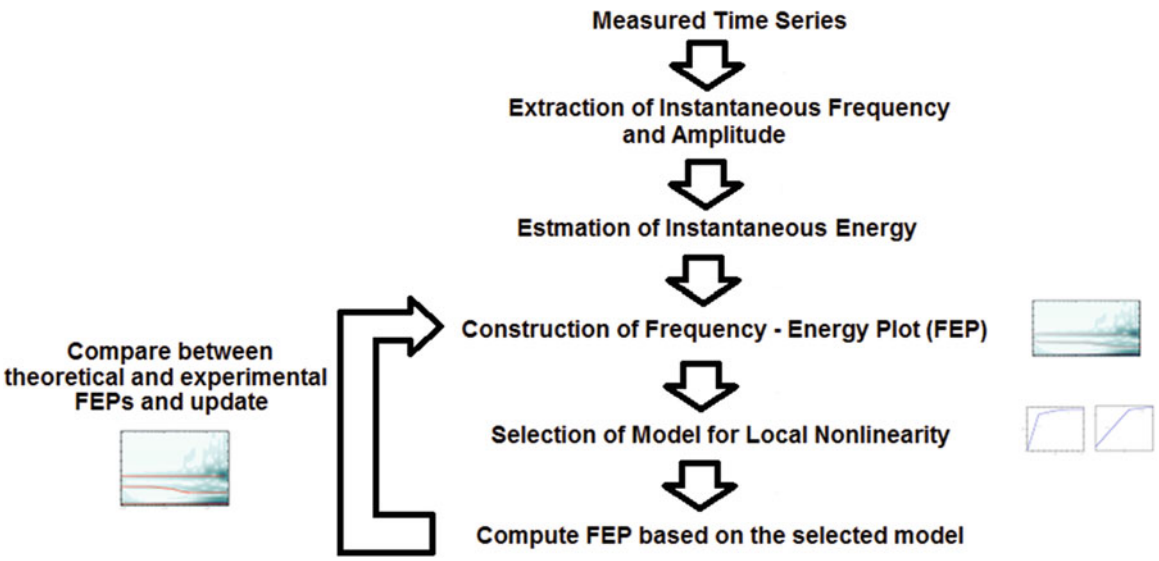

Fig. 31.1 Schematic diagram of the proposed nonlinear model updating approach

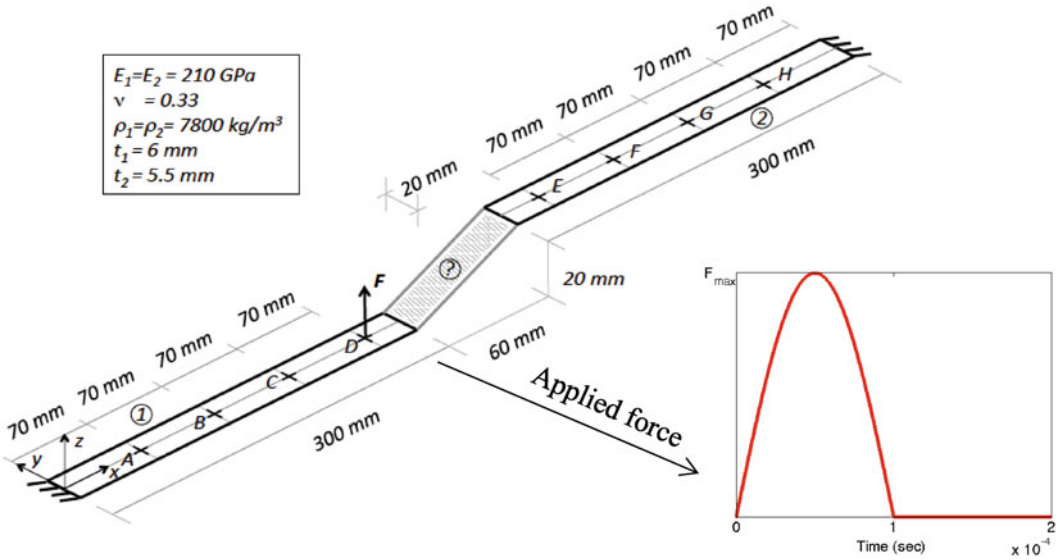

Fig. 31.2 Benchmark structure. The two clamped beams are connected by a non-identified element. The applied force in the positive direction on sensor D is indicated

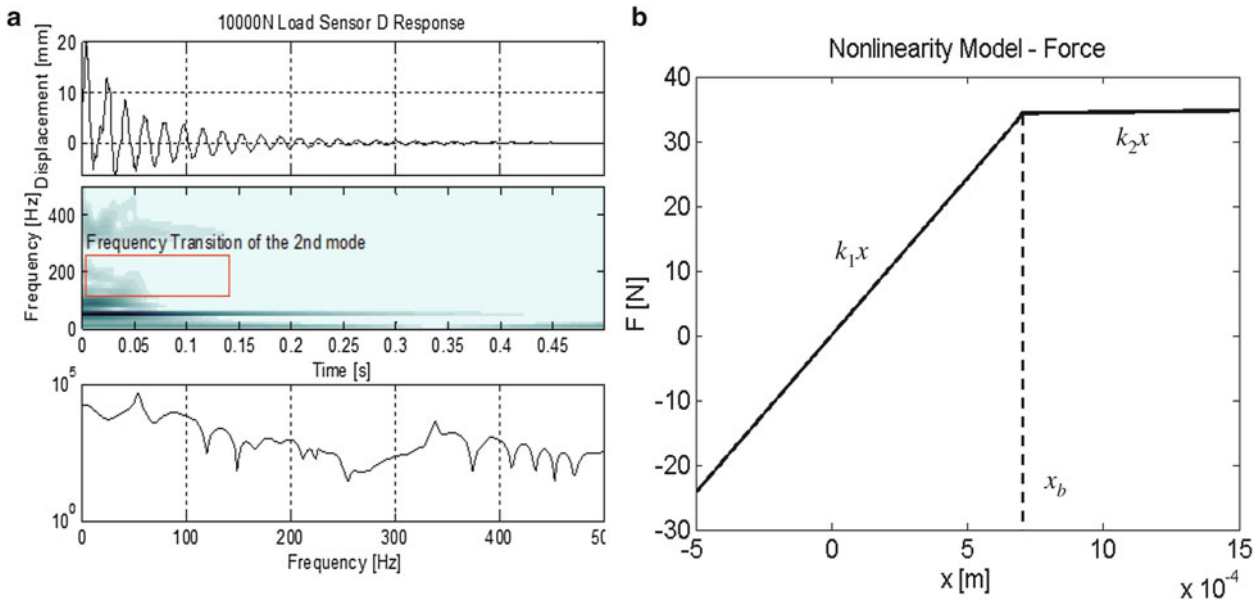

Fig. 31.3 (**a**) Benchmark output at Point D for a 10,000 N load (*cf.* Fig. 31.2) (**b**) Modeling of the nonlinear properties for the "non-identified" connection in Fig. 31.2

thicknesses of the two members are 6 mm and 5.5 mm, respectively. The linear, elastic material adopted for the beams is characterized by a Young modulus E = 210 GPa, a Poisson ratio $\nu = 0.33$, and a density $\rho = 7{,}800$ Kg/m^3. Eight sensors are placed along the beams, in the locations specified in Fig. 31.2 (point A, B, C, D, E, F, G and H) from which displacements, velocities and accelerations in direction z can be measured. A time dependent force in z direction can be applied at one sensor point per time. The system has an operational limit that cannot be exceeded. The limit is set at 40 mm: if the displacement any point of the structure exceeds this value, the time integration stops.

We perform impulse tests on the given system in order to obtain transient responses that will be useful in obtaining the frequency-energy dependence of the system, The applied force, shown in Fig. 31.2, is a half-sine signal with a duration of 0.1 ms, applied close to the tip of the first beam, point D in Fig. 31.2. The benchmark output with a 10,000 N impulse load at Point D is shown in Fig. 31.3a. We should especially point out the interesting frequency transition of the second mode, highlighted in Fig. 31.3a. By studying the wavelet transform of the transient data both in time and energy domain,

we conclude that we should have a member which gets softer in one bending direction after some energy level, thus after some critical displacement value, x_b, which is similar to a buckling-type behavior. The displacement curve for the proposed membrane model is shown in Fig. 31.3b.

In order to simulate the benchmark system with the proposed nonlinearity model shown in Fig. 31.3b, we model the system each beam is modeled by a 30 degree of freedom (DOF) finite element (FE) model using beam elements each with 2 DOF. A Guyan static reduction technique is used to remove the rotational DOFs resulting in 15 translational DOFs for each beam. The unknown membrane is modeled as a two piece linear spring (*cf.* Fig. 31.3b) and is assumed to be massless. The first stiffness constant of the two piece spring, k_1, is found by matching the eigenvalues calculated from the FE model with the eigenvalues determined from FFT plots of the Benchmark outputs. The second stiffness constant, k_2, and the transition displacement point x_b are determined by matching the Hamiltonian frequency energy plots (FEP) with the wavelet transform (WT) of the Benchmark output time series plotted in the energy-frequency domain. This is done by calculating the instantaneous kinetic energy of each beam using the velocities output by the Benchmark code and a four DOF FE model for each beam. The Hamiltonian FEPs are calculated using a two DOF FE model for each beam and using the numerical continuation code created by Peeters et al. [11]. Our optimized values are found to be $k_1 = 48575\frac{N}{m}$, $k_2 = 500\frac{N}{m}$, $x_b = 0.0007$ m. The FE model is analyzed using MATLAB's ode45 for an impulse *(cf.* Fig. 31.2) of 1 N at sensor D for the linear case and an impulse (*cf.* Fig. 31.2) of 10,000 N. The comparisons for linear and strongly nonlinear cases with the direct benchmark outputs are depicted in Fig. 31.4. We observe that our simulations with the optimized nonlinearity model yield a very good match both in time and frequency domain.

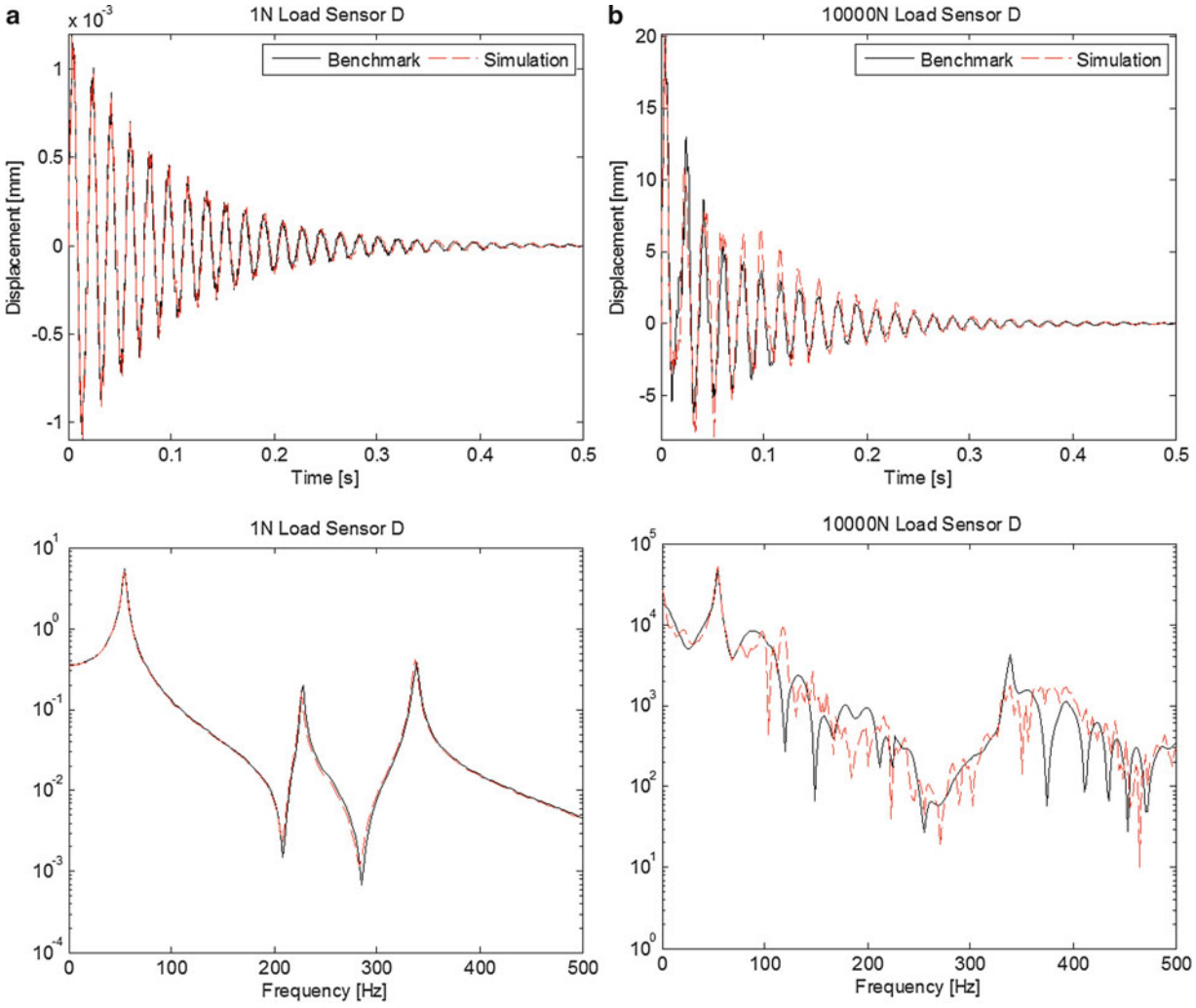

Fig. 31.4 Displacement time series and the resulting FFT plot for the Benchmark output and the simulation output for (**a**) the linear case and (**b**) the highly nonlinear case; benchmark time series, simulation time series

31.4 Concluding Remarks

In this section, a nonlinear model updating strategy based on global/local nonlinear system identification of a broad class of nonlinear systems was proposed. The approach relied on analyzing the system in the frequency-energy domain by constructing Hamiltonian or forced and damped frequency – energy plots (FEPs) and comparing against the frequency-energy dependencies of the data obtained from transient dynamics. The proposed methodology was applied to the benchmark problem with a system consisting of two facing steel cantilever beams coupled with an "unknown" nonlinear element, whose parameters were optimized and the underlying dynamics was successfully reproduced for linear and strongly nonlinear regions.

References

1. Mottershead JE, Friswell MI (1993) Model updating in structural dynamics: a survey. J Sound Vib 167(2):347–375
2. Friswell M, Mottershead JE (1995) Finite element model updating in structural dynamics. Springer, Dordrecht
3. Hemez FM, Doebling SW (2001) Review and assessment of model updating for non-linear, transient dynamics. Mech Syst Signal Process 15(1):45–74
4. Datta BN (2002) Finite-element model updating, eigenstructure assignment and eigenvalue embedding techniques for vibrating systems. Mech Syst Signal Process 16(1):83–96
5. Teughels A, Maeck J, De Roeck G (2002) Damage assessment by FE model updating using damage functions. Comput Struct 80(25):1869–1879
6. Brownjohn JMW, Xia P-Q, Hao H, Xia Y (2001) Civil structure condition assessment by FE model updating: methodology and case studies. Finite Elem Anal Des 37(10):761–775
7. Link M, Rohrmann RG, Pietrzko S (1996) Experience with automated procedures for adjusting the finite element model of a complex highway bridge to experimental modal data. In: Proceedings-Spie of the international society for optical engineering, Spie International Society For Optical, pp 218–225
8. Kerschen G, McFarland DM, Kowtko JJ, Lee YS, Bergman LA, Vakakis AF (2007) Experimental demonstration of transient resonance capture in a system of two coupled oscillators with essential stiffness nonlinearity. J Sound Vib 299(4–5):822–838
9. Andersen D, Starosvetsky Y, Vakakis A, Bergman L (2012) Dynamic instabilities in coupled oscillators induced by geometrically nonlinear damping. Nonlin Dyn 67(1):807–827
10. Remick K, Vakakis A, Bergman L, McFarland DM, Quinn DD, Sapsis TP (2013) Sustained high-frequency dynamic instability of a nonlinear system of coupled oscillators forced by single or repeated impulses: theoretical and experimental results. J Vib Acoust 136(1):011013–011013
11. Peeters M, Viguié R, Sérandour G, Kerschen G, Golinval J-C (2009) Nonlinear normal modes, Part II: toward a practical computation using numerical continuation techniques. Mech Syst Signal Process 23(1):195–216

Chapter 32
Bridging the Gap Between Nonlinear Normal Modes and Modal Derivatives

Cees Sombroek, Ludovic Renson, Paolo Tiso, and Gaetan Kerschen

Abstract Nonlinear Normal Modes (NNMs) have a clear conceptual relation to the classical linear normal modes (LNMs), yet they offer a solid theoretical framework for interpreting a wide class of non-linear dynamical phenomena with no linear counterpart. The main difficulty associated with NNMs is that their calculation for large-scale models is expensive, particularly for distributed nonlinearities. Repeated direct time integrations need to be carried out together with extensive sensitivity analysis to reproduce the frequency-energy dependence of the modes of interest.

In the present paper, NNMs are computed from a reduced model obtained using a quadratic transformation comprising LNMs and Modal Derivatives (MDs). Previous studies have shown that MDs can capture the essential dynamics of geometrically nonlinear structures and can greatly reduce the computational cost of time integration.

A direct comparison with the NNMs computed from another standard reduction technique highlights the capability of the proposed reduction method to capture the essential nonlinear phenomena. The methodology is demonstrated using simple examples with 2 and 4 degrees of freedom.

Keywords Model reduction • Nonlinear normal modes • Modal derivatives • Quadratic manifold transformation

32.1 Introduction

The manifestation of nonlinear phenomena during the vibration testing of aerospace structures is frequently reported in the technical literature (e.g., for the Airbus A400M [1] and for the F-16 aircraft [2]). A common source of nonlinearity is the junction between structural components where freeplay and complex damping mechanisms can be present. The stringent constraints on weight also lead to more flexible structures where geometrical nonlinear effects are present due to large displacements and rotations.

Though frequently ignored in practice, the presence of nonlinearity poses important challenges as novel dynamical phenomena with no linear counterpart may be observed. Modal interactions, for instance, couple the vibration modes of a structure and can lead to energy transfers that can in turn jeopardize the structural integrity (cf. [3]). Addressing nonlinearity as early as in the design becomes therefore important.

In this context, the concept of nonlinear normal modes (NNMs) proved useful. First introduced in the 1960s by Rosenberg, NNMs were defined as families of synchronous periodic oscillations [4, 5]. An extended definition considering NNMs as *(non-necessarily synchronous) periodic motions* was then proposed in [6] to account for modal interactions during which the periodic motion contains the frequencies of at least two interacting modes. Considered as the direct extension of linear vibration modes (VMs) to nonlinear systems, NNMs allow to rigorously interpret nonlinear dynamical phenomena such as mode localization, internal resonances and mode bifurcations [7].

With the advances in computing power and in computer methods, recent years witnessed the development of computational methods for NNMs. In [8], shooting and pseudo-arclength continuation methods are combined to calculate NNMs. Alternatively, the harmonic balance and asymptotic numerical methods are used in [9]. The main difficulty associated with NNMs is that their calculation for large-scale models is expensive. If the aforementioned techniques were applied to real-life structures [3, 10], the systems mainly consisted in large linear structures with localized nonlinearities. In this case, classical

C. Sombroek (✉) • P. Tiso
Delft University of Technology, Delft, Netherlands
e-mail: c.s.m.sombroek@student.tudelft.nl

L. Renson • G. Kerschen
University of Liege, Liege, Belgium

G. Kerschen (ed.), *Nonlinear Dynamics, Volume 1*, Conference Proceedings of the Society for Experimental Mechanics Series, DOI 10.1007/978-3-319-15221-9_32

linear reduction methods, such as the Craig–Bampton or the Rubin techniques, can be used to accurately and effectively reduce the dimensionality of the linear system. However, for systems with nonlinear geometrical effects, nonlinearities are distributed between all DOFs and such linear approach proved ineffective.

In previous contributions [11–13], an effective model reduction of geometrically nonlinear problems was achieved by combining VMs and modal derivatives (MDs) in a single basis. Time simulations showed that the essential dynamics of the structures was captured while computational efforts were effectively reduced. Simple, this approach has however the drawback of largely increasing the size of the reduced-order model as the number of MDs grows quadratically with the number of degrees of freedom (DOF).

In this paper, we present and investigate an alternative approach where VMs and MDs are combined in a quadratic coordinate transformation. The proposed method fully exploits the second-order Taylor-series expansion of the displacement vector with respect to a reduced set of vibration modes. This differs from previous works where a linear basis with additional coordinates for each MDs was built.

The paper is organized as follows. Section 32.2 introduces the governing equations of motion and Sect. 32.3 presents the underlying theory behind classical Galerkin model reduction techniques and introduces the concept of modal derivatives. In Sect. 32.4, the new quadratic transformation is derived. The method used for computing NNMs is briefly introduced in Sect. 32.5. The quadratic manifold approach is exploited in Sect. 32.6 using examples with 2 and 4 DOFs. A direct comparison with the NNMs computed from the full system and from systems reduced with the Galerkin method are used to discuss the performance of the proposed method.

32.2 Governing Equations

We seek the solution of the space discretized equation of motion of a generic system:

$$\begin{cases} \mathbf{M}\ddot{\mathbf{y}}(t) + \mathbf{K}\mathbf{y}(t) + \mathbf{f}^{nl}(\mathbf{y}(t)) = \mathbf{p}(t) \\ \mathbf{y}(0) = \mathbf{y}_0 \\ \dot{\mathbf{y}}(0) = \dot{\mathbf{y}}_0, \end{cases} \tag{32.1}$$

where $\mathbf{y}(t) \in \mathbb{R}^n$ is the generalized displacement vector, $\mathbf{M} \in \mathbb{R}^{n\times n}$ and $\mathbf{K} \in \mathbb{R}^{n\times n}$ are the mass and linear stiffness matrices, respectively, $\mathbf{f}^{nl}(\mathbf{y}(t)) : \mathbb{R}^n \mapsto \mathbb{R}^n$ is the nonlinear force vector and $\mathbf{p}(t) \in \mathbb{R}^n$ is the time dependent applied load vector. Note that we explicitly separate the linear and the nonlinear internal forces. The initial conditions for the displacement and the velocity vector are indicated with $\mathbf{y}_0$ and $\dot{\mathbf{y}}_0$, respectively. From this point on, the time dependency is omitted for clarity.

32.3 Galerkin Projection

In practical applications, the size n of Eq. (32.1) is usually large. The number of unknowns can be reduced to k, with $k \ll n$, by projecting the displacement field $\mathbf{y}$ on a suitable reduced order basis (ROB) $\boldsymbol{\Psi} \in \mathbb{R}^{n\times k}$ of time-independent vectors, as:

$$\mathbf{y} \approx \boldsymbol{\Psi}\mathbf{q}, \tag{32.2}$$

where $\mathbf{q}(t) \in \mathbb{R}^k$ is the vector of modal amplitudes. The governing equations can then be projected on the chosen basis $\boldsymbol{\Psi}$ in order to make the equilibrium residual orthogonal to the subspace in which the solution $\mathbf{q}$ is sought. This results in a reduced system of k nonlinear equations:

$$\boldsymbol{\Psi}^T\mathbf{M}\boldsymbol{\Psi}\ddot{\mathbf{q}} + \boldsymbol{\Psi}^T\mathbf{K}\boldsymbol{\Psi}\mathbf{q} + \boldsymbol{\Psi}^T\mathbf{f}^{nl}(\boldsymbol{\Psi}\mathbf{q}) = \boldsymbol{\Psi}^T\mathbf{p}, \tag{32.3}$$

or, equivalently,

$$\hat{\mathbf{M}}\ddot{\mathbf{q}} + \hat{\mathbf{K}}\mathbf{q} + \hat{\mathbf{f}}^{nl}(\boldsymbol{\Psi}\mathbf{q}) = \hat{\mathbf{p}}. \tag{32.4}$$

The reduced mass matrix $\hat{\mathbf{M}}$ and stiffness matrix $\hat{\mathbf{K}}$ do not depend on $\mathbf{q}$ and can be calculated offline. We refer to the numerical solution $\mathbf{y}$ of Eq. (32.1) as the *full* solution, while $\mathbf{u} = \boldsymbol{\Psi}\tilde{\mathbf{q}}$ is called *reduced* solution, $\tilde{\mathbf{q}}$ being the solution of Eq. (32.4). The key of a good reduction method is to find a suitable ROB $\boldsymbol{\Psi}$ that is able to reproduce the full solution with a good, hopefully controlled, accuracy. Note here that Galerkin projection is not strictly the only possible choice, since also the Petrov–Galerkin method can be applied. In this method, the ROB for the left projection is different than the ROB for the primary variable. Usually, the Galerkin method is preferred in structural dynamics applications because of the symmetry and positive definiteness of the tangential operators.

32.3.1 Vibration Modes

Let us consider a static equilibrium position $\mathbf{y}_{eq}$ when the applied load is constant and given by $\mathbf{p}_{eq}$. We can then linearize the system of equations (32.1) around such configuration assuming that the motion $\mathbf{u}$ around $\mathbf{y}_{eq}$ is small, i.e. $\mathbf{y} = \mathbf{y}_{eq} + \mathbf{u}$, $\ddot{\mathbf{y}} = \ddot{\mathbf{u}}$. The linearized dynamic equilibrium equations become:

$$\mathbf{M}\ddot{\mathbf{u}} + \mathbf{K}\mathbf{u} = \mathbf{s} \tag{32.5}$$

where $\mathbf{s}$ is a small load variation from $\mathbf{p}_{eq}$. The eigenvalue problem associated to Eq. (32.5) writes:

$$\left(\mathbf{K} - \omega_i^2\mathbf{M}\right)\phi_i = \mathbf{0}, \quad i = 1, 2, \ldots, n \tag{32.6}$$

and its solution provides n vibration modes (VMs) ϕ_i and associated natural frequencies ω_i^2. In linear modal analysis, the displacement vector $\mathbf{u}$ can be expressed as a linear combination of $m < n$ VMs as:

$$\mathbf{u} = \sum_{i=1}^{m} \phi_i(\mathbf{y}_{eq}) q_i = \boldsymbol{\Phi}\mathbf{q} \tag{32.7}$$

where $\boldsymbol{\Phi} = [\phi_1 \ldots, \phi_m] \in \mathbb{R}^{n \times m}$. In linear analysis, the VMs ϕ_i are constant, i.e. they form a ROB that spans the small motion $\mathbf{u}$ around $\mathbf{y}_{eq}$. We discuss the implication of large displacements on the ROB in the next section.

32.3.2 Modal Derivatives

The projection of the governing equations on a reduction basis formed by a reduced set of VMs is a well-known technique for linear structural dynamics. The main advantage of this technique is that the resulting reduced model consists of a system of uncoupled equations that can therefore be solved separately. As discussed in the introduction, several attempts have been made to extend the vibration modes projection for nonlinear analysis. The main limitation of such an approach lies in the fact that the vibration basis changes as the configuration of the system changes. It is therefore required to upgrade the basis during the numerical time integration to account for the effect of the nonlinearity.

When the displacements cannot be considered as small, the VMs change with respect to the configuration. We can therefore express the displacement vector $\mathbf{u}$ as

$$\mathbf{u} = \sum_{i=1}^{M} \boldsymbol{\phi}_i(\mathbf{y}_{eq} + \mathbf{u}) q_i \tag{32.8}$$

where the dependence of the VMs on the displacement is highlighted. If Eq. (32.8) is expanded in Taylor series around the equilibrium configuration $\mathbf{y}_{eq}$:

$$\mathbf{u} = \sum_{i=1}^{M} \boldsymbol{\phi}_i(\mathbf{u}) q_i = \frac{\partial \mathbf{u}}{\partial q_i}\Big|_{\mathbf{u}=\mathbf{0}} q_i + \frac{1}{2}\frac{\partial^2 \mathbf{u}}{\partial q_i \partial q_j}\Big|_{\mathbf{u}=\mathbf{0}} q_{iq_j} + \ldots \tag{32.9}$$

The derivatives of the displacement vector with respect to the modal amplitudes q_i can be computed from Eq. (32.8), and are:

$$\frac{\partial \mathbf{u}}{\partial q_i} = \boldsymbol{\phi}_i + \frac{\partial \boldsymbol{\phi}_j}{\partial q_i} q_j \tag{32.10}$$

and

$$\frac{\partial^2 \mathbf{u}}{\partial q_i \partial q_j} = \frac{\partial \boldsymbol{\phi}_i}{\partial q_j} + \frac{\partial \boldsymbol{\phi}_j}{\partial q_i} + \frac{\partial^2 \boldsymbol{\phi}_k}{\partial q_i \partial q_j} q_k. \tag{32.11}$$

When evaluated at $\mathbf{y} = \mathbf{y}_{eq}$, they become:

$$\frac{\partial \mathbf{u}}{\partial q_i}\Big|_{\mathbf{u}=\mathbf{0}} = \boldsymbol{\phi}_i \tag{32.12}$$

and

$$\frac{\partial^2 \mathbf{u}}{\partial q_i \partial q_j}\Big|_{\mathbf{u}=\mathbf{0}} = \frac{\partial \boldsymbol{\phi}_i}{\partial q_j} + \frac{\partial \boldsymbol{\phi}_j}{\partial q_i}. \tag{32.13}$$

The term (32.12) is the VM, while $\frac{\partial \boldsymbol{\phi}_i}{\partial q_j}$ is the MD: it represents how the VM $\boldsymbol{\phi}_i$ changes when the system is perturbed in the shape of VM $\boldsymbol{\phi}_j$.

A way to compute $\frac{\partial \boldsymbol{\phi}_i}{\partial q_j}$ is to differentiate the eigenvalue problem (32.6) with respect to the modal amplitudes:

$$\left[\mathbf{K}_{eq} - \omega_i^2 \mathbf{M}\right] \frac{\partial \boldsymbol{\Phi}_i}{\partial q_j} + \left[\frac{\partial \mathbf{K}_{eq}}{\partial q_j} - \frac{\partial \omega_i^2}{\partial q_j} \mathbf{M}\right] \boldsymbol{\Phi}_i = \mathbf{0}, \tag{32.14}$$

together with orthogonality condition

$$\boldsymbol{\Phi}_i^T \mathbf{M} \frac{\partial \boldsymbol{\Phi}_i}{\partial q_j} = \mathbf{0}, \quad \forall, i, j = 1, \ldots, m, \tag{32.15}$$

that must be added to in order to (32.14) to make the expansion (32.9) unique. Essentially, Eq. (32.14) yields the sensitivity of the VMs with respect to the modal amplitudes. In previous contributions [11–13], it has been shown that an effective ROB for geometrically nonlinear problems of the type governed by Eq. (32.1) can be formed by combining dominant VMs with some MDs, as:

$$\boldsymbol{\Psi} = [\boldsymbol{\Phi}_1, \ldots, \boldsymbol{\Phi}_m, \ldots, \frac{\partial \boldsymbol{\Phi}_i}{\partial q_j}, \ldots], \tag{32.16}$$

While simple and effective, this approach bears the drawback of largely increasing the size of the ROB, as the number of MDs grows quadratically with m. We present in Sect. 32.4 an alternative approach that fully exploits the structure of Eq. (32.9).

32.4 Reduction with Quadratic Manifold

The expansion (32.9) essentially provides a quadratic mapping $\mathbf{U}(\mathbf{q}) : \mathbb{R}^m \mapsto \mathbb{R}^n$ between the modal coordinates $\mathbf{q}$ and the physical displacements $\mathbf{u}$. Compactly, we can write:

$$\mathbf{u} = \mathbf{U}(\mathbf{q}) = \boldsymbol{\Phi}\mathbf{q} + \frac{1}{2}\boldsymbol{\Theta}(\mathbf{q}, \mathbf{q}) \tag{32.17}$$

where the third order tensor $\boldsymbol{\Theta} \in \mathbb{R}^{n\times n\times n}$ writes componentwise:

$$\Theta_{Iij} = \frac{\partial \phi_i}{\partial q_j} + \frac{\partial \phi_j}{\partial q_i} \tag{32.18}$$

and $\Theta_{Iij} = \Theta_{Iji}$.

The velocity and acceleration are then expressed as functions of the modal coordinates q_I as

$$\dot{\mathbf{u}} = \Phi\dot{\mathbf{q}} + \Theta(\dot{\mathbf{q}}, \mathbf{q}) \tag{32.19}$$

and

$$\ddot{\mathbf{u}} = \Phi\ddot{\mathbf{q}} + \Theta(\ddot{\mathbf{q}}, \mathbf{q}) + \Theta(\dot{\mathbf{q}}, \dot{\mathbf{q}}), \tag{32.20}$$

respectively. The tangent space $\mathbf{V}(\mathbf{q}) \in \mathbb{R}^{n\times m}$ is computed as:

$$\mathbf{V} = \frac{\partial \mathbf{U}}{\partial \mathbf{q}} = \boldsymbol{\Phi} + \boldsymbol{\Theta}(\mathbf{q}, \cdot) \tag{32.21}$$

The notation $\boldsymbol{\Theta}(\mathbf{q}, \cdot)$ is to be intended, componentwise, as $\Theta_{Iij}q_i = \Theta_{Iij}q_j$. When inserting the quadratic manifold approximation (32.17) in the governing equation (32.1) and projecting on the tangent subspace (32.21) we obtain the reduced governing equations:

$$\ddot{\mathbf{q}} + \mathbf{M}_3(\mathbf{q}, \ddot{\mathbf{q}}, \mathbf{q}) + \mathbf{M}_3(\mathbf{q}, \dot{\mathbf{q}}, \dot{\mathbf{q}}) + \mathbf{V}^T\mathbf{f}^{int}(\mathbf{U}(\mathbf{q})) = \mathbf{V}^T\mathbf{p} \tag{32.22}$$

where $\mathbf{M}_{3Iijk} = \Theta_{iIJ}\mathbf{M}_{ij}\Theta_{jKL}$ and orthogonality and mass-normalization has been employed. As compared to the Galerkin projected equations (32.4) when VMs and MDs are used to form the ROB, the reduced system (32.22) is much more compact (size m as compared to size $m + m^2$). This approach is analogous to [14], where the nonlinear manifold is constructed via a static condensation procedure.

32.5 Nonlinear Normal Modes

In the conservative case, NNMs can be sought numerically as periodic solutions of the governing nonlinear equations of motion, i.e., Eqs. (32.1), (32.4), (32.22) for the full system, the system reduced using a Galerkin-type projection, and the QM approach, respectively. To this end, the two-step algorithm presented in [8] is exploited in the present study. This section provides a succinct description of the shooting and pseudo-arclength techniques used in the algorithm.

Shooting is a popular numerical technique for solving the two-point boundary-value problem associated with the periodicity condition

$$\mathbf{H}(T, \mathbf{z}_{p_0}) = \mathbf{z}_p(T, \mathbf{z}_{p_0}) - \mathbf{z}_{p_0} = \mathbf{0} \tag{32.23}$$

where $\mathbf{H}(T, \mathbf{z}_{p_0})$ is called the shooting function, and $\mathbf{z}$ is the state vector of the system. $\mathbf{H}$ expresses the difference between the final state at time T of the system $\mathbf{z}_p(T, \mathbf{z}_{p_0})$ and the initial state of the system $\mathbf{z}_{p_0}$. A solution $\mathbf{z}_p(t, \mathbf{z}_{p_0})$ is periodic if $\mathbf{z}_p(t, \mathbf{z}_{p_0}) = \mathbf{z}_p(t + T, \mathbf{z}_{p_0})$ where T is the minimal period. In a shooting algorithm, the period T and the initial conditions $\mathbf{z}_{p_0}$ realizing a periodic motion are found iteratively. More specifically, direct numerical integration is carried out to obtain an initial guess of the periodic solution, which is corrected by means of a Newton–Raphson procedure to converge to the actual solution. In this work, time integration is performed using a fifth-order Runge–Kutta scheme with an automatic selection of the time step.

Another important remark in the resolution of the boundary-value problem formulated in Eq. (32.23) is that the phase of the periodic solutions is not unique. If $\mathbf{z}_p(t)$ is solution of the equations of motion, then $\mathbf{z}_p(t + \Delta t)$ is geometrically the same solution in state space for any Δt. Hence, an additional condition $h(\mathbf{z}_{p_0}) = 0$, termed phase condition, is specified to

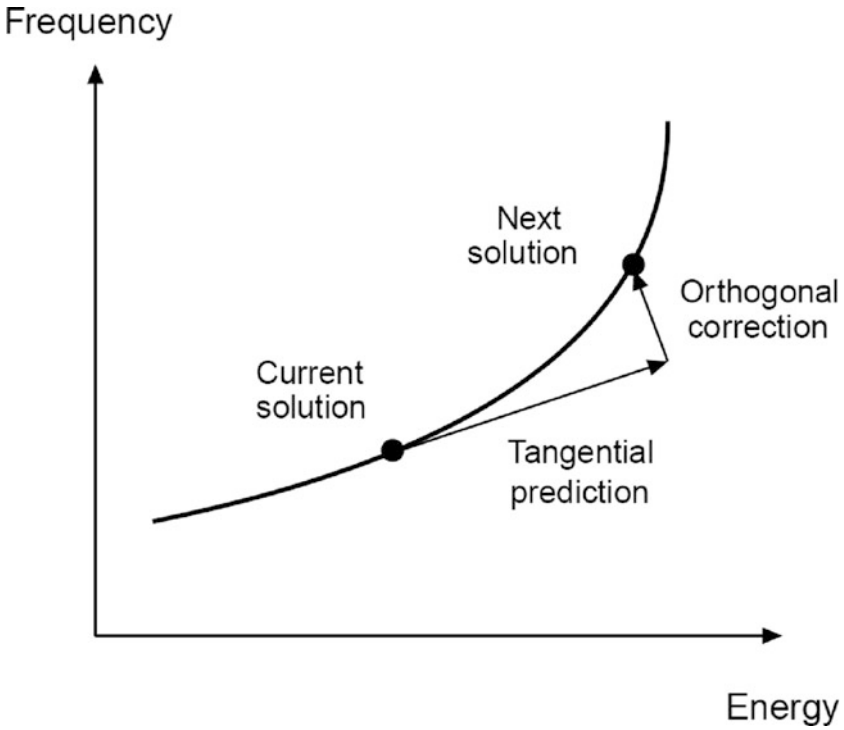

Fig. 32.1 Schematic representation of the prediction and correction steps of the pseudo-arclength continuation scheme

remove the arbitrariness of the initial conditions. Following the approach in [8], the modal velocities are set equal to zero. In summary, an isolated NNM motion is computed by solving the augmented two-point boundary-value problem defined by the two relations

$$\mathbf{H}(T, \mathbf{z}_{p_0}) = \mathbf{0}, \tag{32.24}$$

$$h(\mathbf{z}_{p_0}) = 0. \tag{32.25}$$

To obtain the family of periodic solutions that describe the considered NNM, shooting is combined with a pseudo-arclength continuation technique. Starting from a known periodic solution, continuation proceeds in two steps, namely a prediction and a correction, as illustrated in Fig. 32.1. In the prediction step, a guess of the next periodic solution along the NNM branch is generated in the direction of the tangent vector to the branch at the current solution. Next, the prediction is corrected using a shooting procedure, forcing the variations of the period and the initial conditions to be orthogonal to the prediction direction.

32.6 Numerical Examples

We intend here to present simple tests to compare the exact NNMs obtained via continuation method to the NNMs calculated with the MDs based reduced order models (32.4) and (32.22). This is done using two examples containing 2 DOFs and 4 DOFs respectively.

32.6.1 2DOF Example

First a two DOFs system is examined with geometrical nonlinearities (quadratic and cubic) arising from second order terms in the strain tensor. The configuration of the system is shown in Fig. 32.2. The equations of motion for the system write:

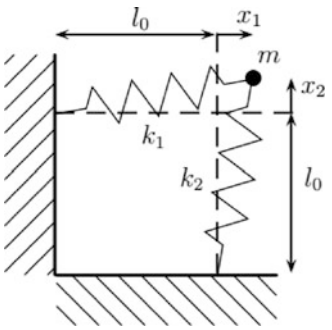

Fig. 32.2 Schematic representation of the 2 DOF system

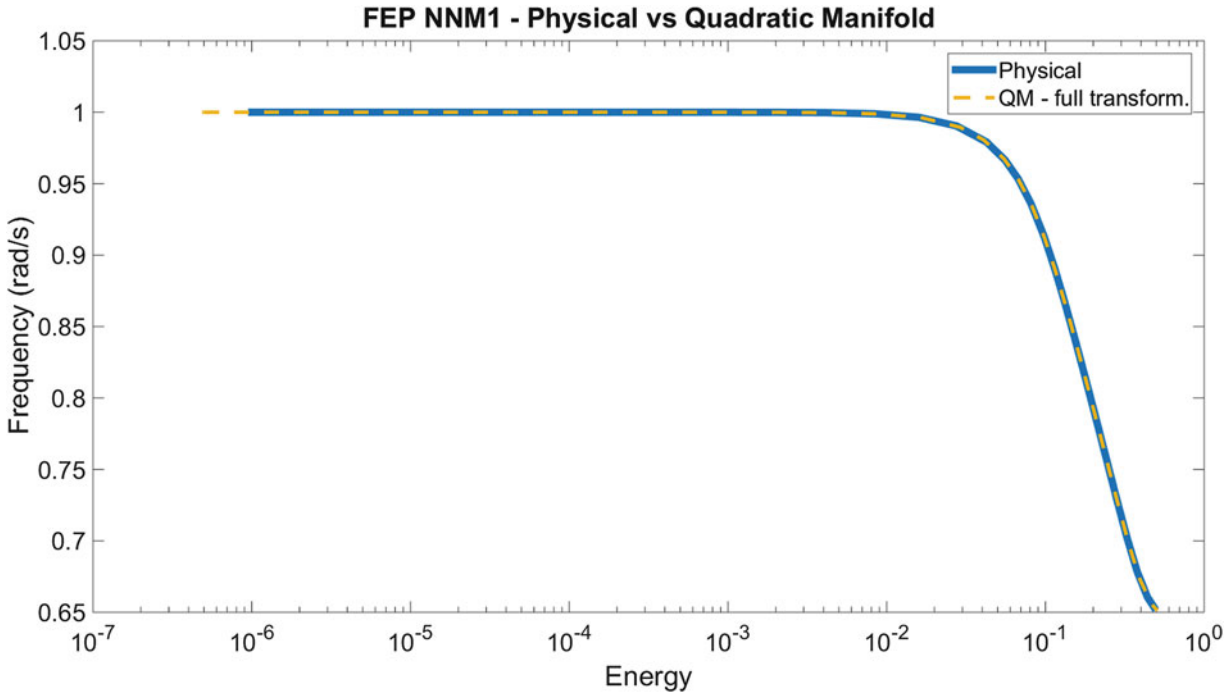

Fig. 32.3 FEP of first nonlinear normal mode

$$\begin{cases} m\ddot{x}_1 + k_1 x_1 + k_2 x_1 x_2 + \frac{3k_1 x_1^2}{2} + \frac{k_1 x_2^2}{2} + \frac{(k_1+k_2)x_1}{2}\left(x_1^2 + x_2^2\right) = 0 \\ m\ddot{x}_2 + k_2 x_2 + k_1 x_1 x_2 + \frac{3k_2 x_2^2}{2} + \frac{k_2 x_1^2}{2} + \frac{(k_1+k_2)x_2}{2}\left(x_1^2 + x_2^2\right) = 0 \end{cases} \tag{32.26}$$

where the parameters are set to be $k_1 = k_2 = 1$ N/m and $m = 1$ kg such that the eigenfrequencies of the system become $\omega_1 = 1$ rad/s and $\omega_2 = \sqrt{3}$ rad/s.

To validate the proposed quadratic manifold formulation, the NNMs are computed in physical space, and with the proposed quadratic manifold Eq. (32.17) with two modal coordinates, so no reduction. NNM1 and NMM2 are presented in Figs. 32.3 and 32.4 using a frequency energy plot (FEP) (as suggested by [8]). From these figures, it is confirmed that considering two modes provides a full system transformation that results in the same exact FEP.

Next the reduction methods are used to compute NNM motion in a reduced sense. For the Galerkin projection two ROB are formed containing $[\phi_i]$ and $\left[\phi_i, \frac{\partial \phi_i}{\partial q_j}\right]$ respectively. Note that in the latter situation the system is actually not reduced, and therefore must produce the exact NNM. The quadratic manifold computation was carried out with a single modal coordinate q.

From the FEPs, shown in Figs. 32.5 and 32.6, it is clear that the Galerkin projection with the modal derivative enhanced ROB produces the exact NNM. Regarding the results with actual reduction, the QM captures correctly the global trend of the FEP whereas the GP is qualitatively correct for the second NNM and wrong for the first one. One can also note that, for the first NNM, the branch computed with the QM deviates earlier from the true solution than the branch obtained with GP.

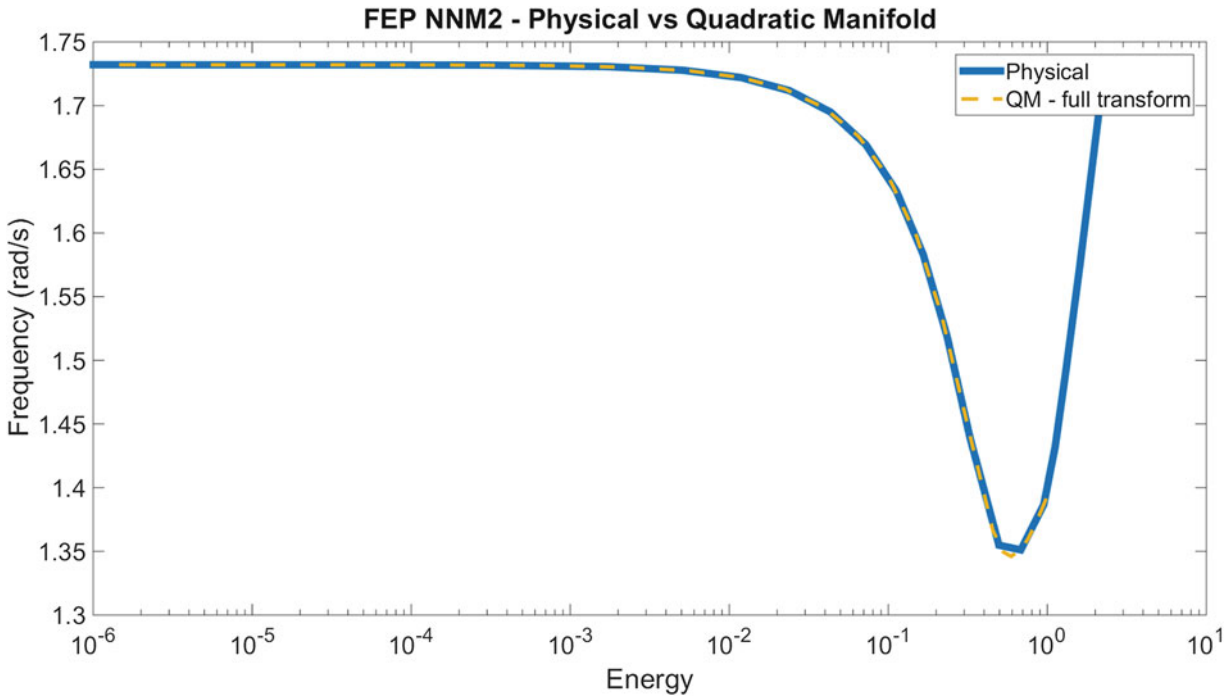

Fig. 32.4 FEP of second nonlinear normal mode

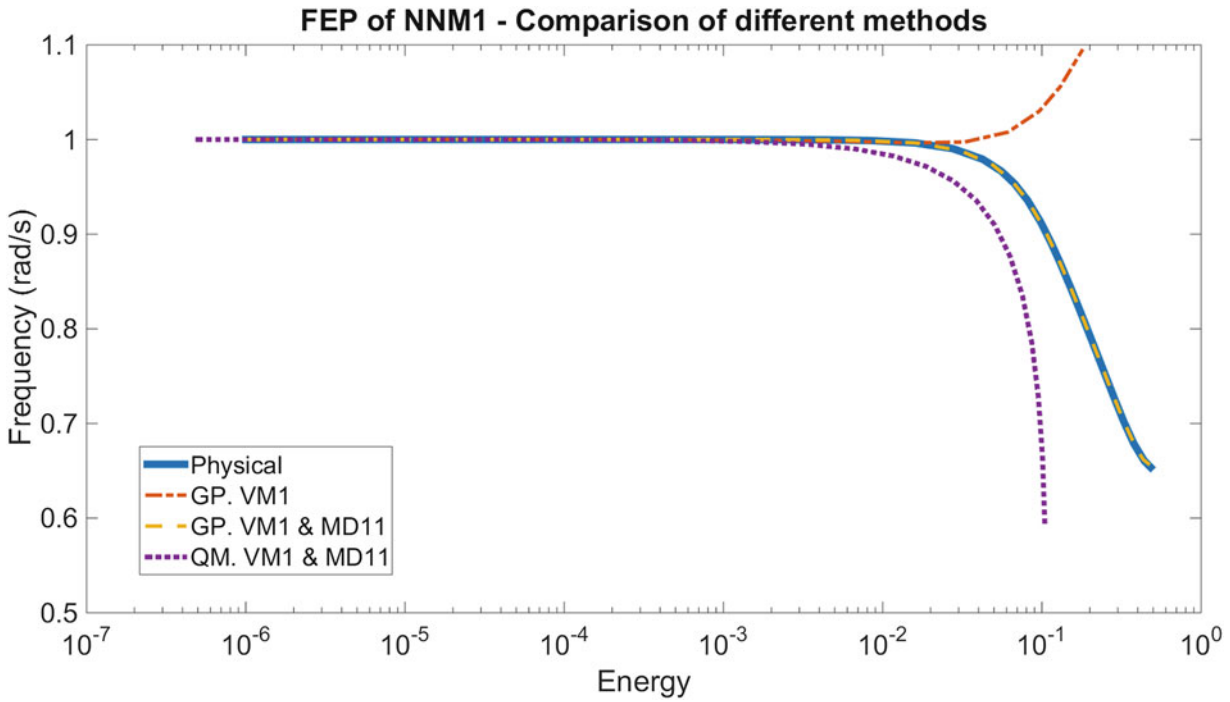

Fig. 32.5 Comparison of the reduction methods in the FEP of NNM1

32.6.2 4DOF Example

The second example contains 4 DOF, and the nonlinearities are again of geometrical nature. The configuration is presented in Fig. 32.7. The equations of motions are given by:

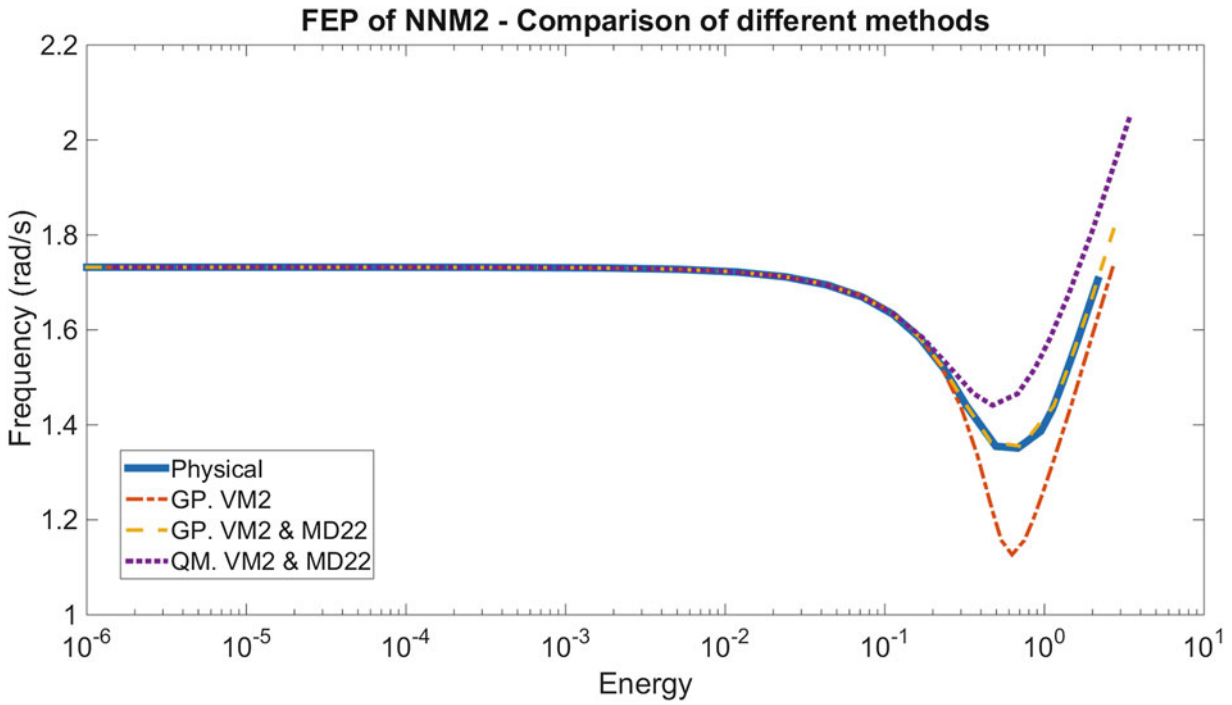

Fig. 32.6 Comparison of the reduction methods in the FEP of NNM2

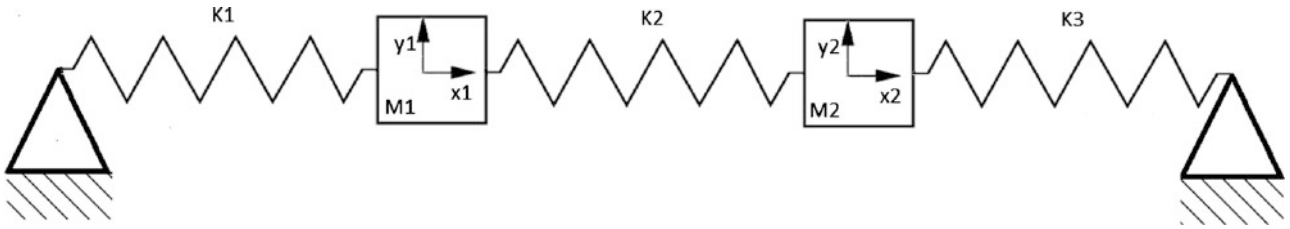

Fig. 32.7 Schematic representation of the 4 DOF system

$$\begin{cases} m_1\ddot{x}_1 - \frac{k_2(l_0-x_1+x_2)\left((y_1-y_2)^2+(l_0-x_1+x_2)^2-L_0^2\right)}{2L_0^2} + \frac{k_1(l_0+x_1)\left((l_0+x_1)^2-L_0^2+y_1^2\right)}{2L_0^2} = 0 \\ m_1\ddot{y}_1 + \frac{k_1 y_1\left((l_0+x_1)^2-L_0^2+y_1^2\right)}{2L_0^2} + \frac{k_2(y_1-y_2)\left((y_1-y_2)^2+(l_0-x_1+x_2)^2-L_0^2\right)}{2L_0^2} = 0 \\ m_2\ddot{y}_1 - \frac{k_3(l_0-x_2)\left((l_0-x_2)^2-L_0^2+y_2^2\right)}{2L_0^2} + \frac{k_2(l_0-x_1+x_2)\left((y_1-y_2)^2+(l_0-x_1+x_2)^2-L_0^2\right)}{2L_0^2} = 0 \\ m_2\ddot{y}_2 - \frac{k_2(y_1-y_2)\left((y_1-y_2)^2+(l_0-x_1+x_2)^2-L_0^2\right)}{2L_0^2} + \frac{k_3 y_2\left((l_0-x_2)^2-L_0^2+y_2^2\right)}{2L_0^2} = 0 \end{cases} \tag{32.27}$$

where the parameters are set to be $k_1 = k_2 = k_3 = 1$ N/m, $m_1 = m_2 = 1$ kg and the original lengths of the springs are $L_0 = 0.4$ m. A pretension is applied by suspending the masses at a distance $l_0 = 0.5$ m from the hinges and each other. The pretension is applied to separate the eigenfrequencies of the in plane and out of plane motion, these frequencies are $\omega_1 = 0.53$ rad/s, $\omega_2 = 0.92$ rad/s, $\omega_3 = 1.36$ rad/s and $\omega_4 = 2.35$ rad/s.

The first nonlinear normal modes obtained with the full system and both reduction methods is presented in Fig. 32.8 accompanied by a close up for very small energy (Fig. 32.9). The results in both figures indicate that the QM is less accurate compared to a classical GP. However, if we look at the results in a frequency-amplitude plot (see Figs. 32.10 and 32.11), the QM is able to approximate the motion in both in and out of plane motion up to approximately 30 % of the suspended spring lengths, whilst the GP can only approximate the result in one direction (not along x_1). From this point of view, the QM improved the results with respect to a simple GP.

The results for the second NNM are presented in Figs. 32.12, 32.13 and confirm our initial observations. More precisely, the QM is here more accurate than the GP throughout the energy range considered.

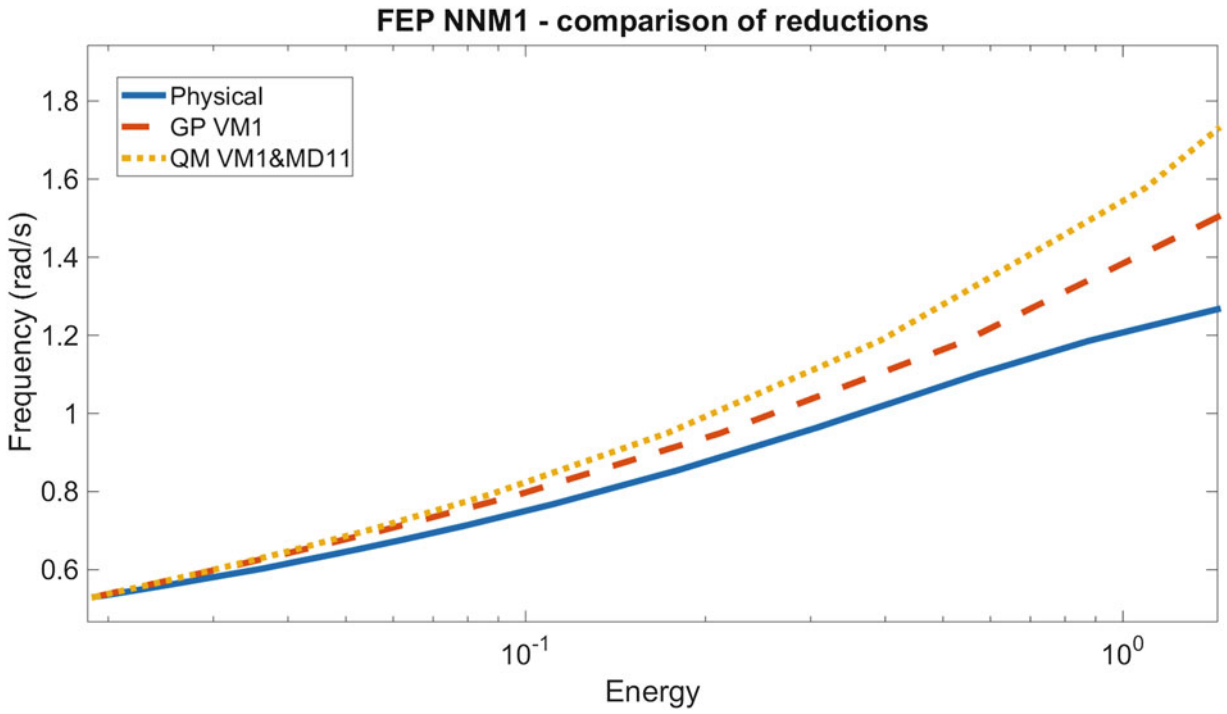

Fig. 32.8 NNM1 FEP, reduction methods compared with exact physical NNM

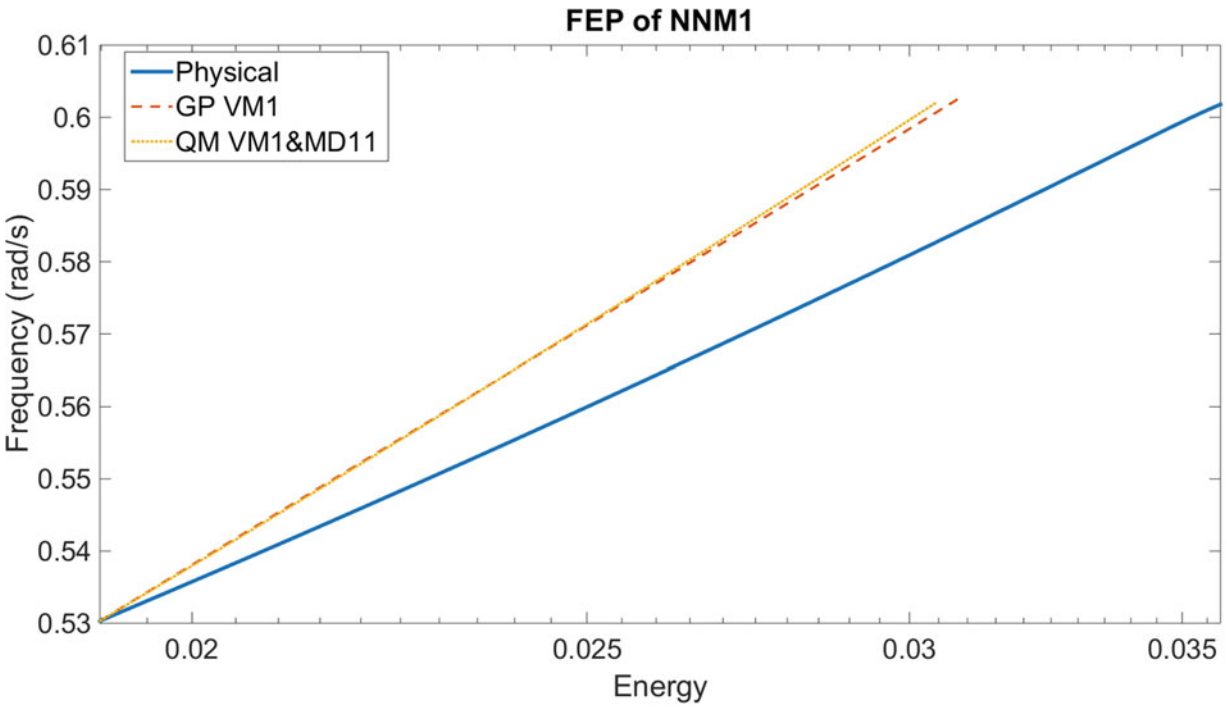

Fig. 32.9 Close up of NNM1 FEP, reduction methods compared with exact physical NNM

32.7 Conclusions

In this paper, a quadratic coordinate transformation combining linear VMs and their corresponding MDs was presented. In comparison with classical Galerkin reduction methods where each MD is associated with an independent DOF in the reduced system, the proposed method allows to further reduce the size of the dynamical system while accounting for the

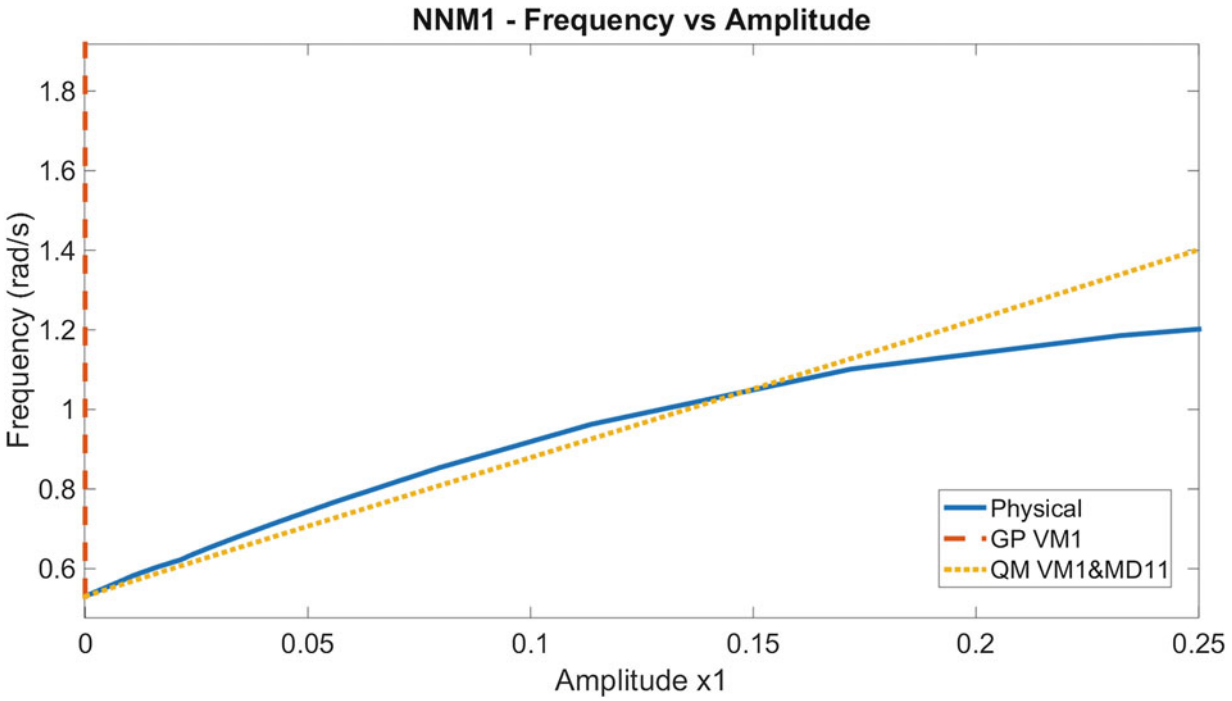

Fig. 32.10 NNM1 frequency amplitude plot for x_1

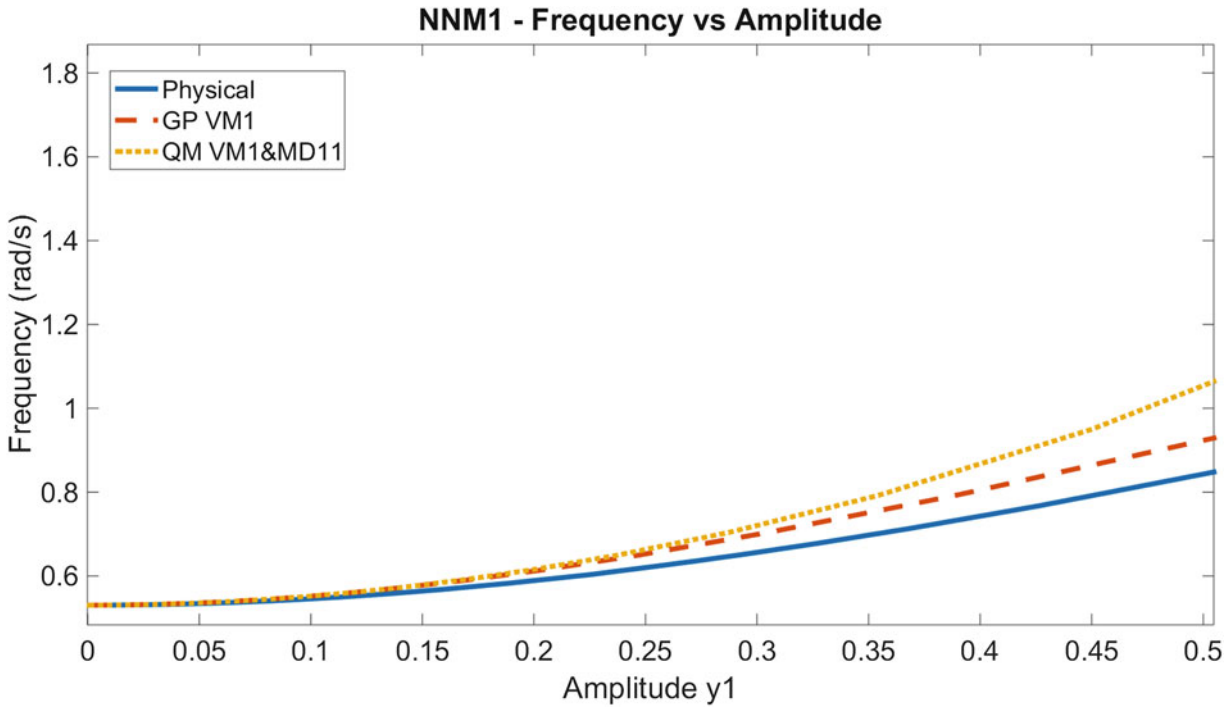

Fig. 32.11 NNM1 frequency amplitude plot for y_1

change of the VMs due to nonlinearities. The QM reduction was applied to two examples with 2 and 4 DOFs, respectively. For reduced-order models of same dimensions, the QM reduction showed to improve the results obtained with the simple Galerkin projection.

We however stress that the presented results are only preliminary and further investigations should be conducted. In particular, the improvements brought by the QM were only present for very low energies (or amplitudes).

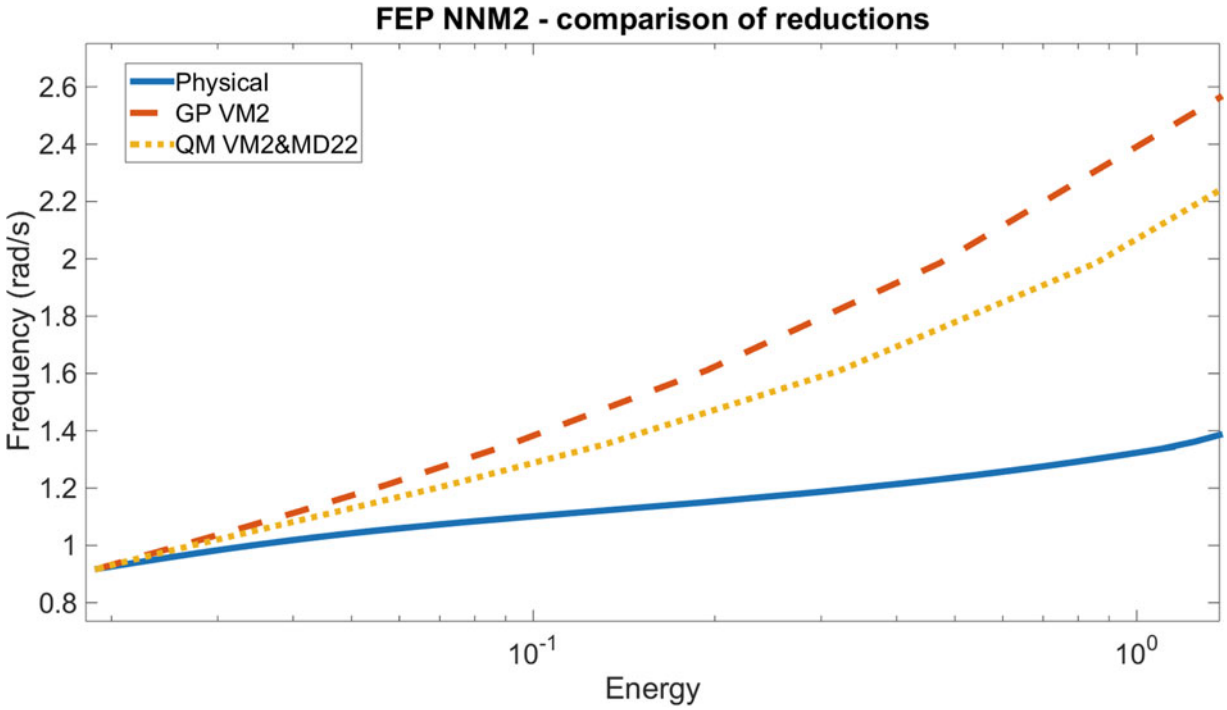

Fig. 32.12 NNM2 FEP, reduction methods compared with exact physical NNM

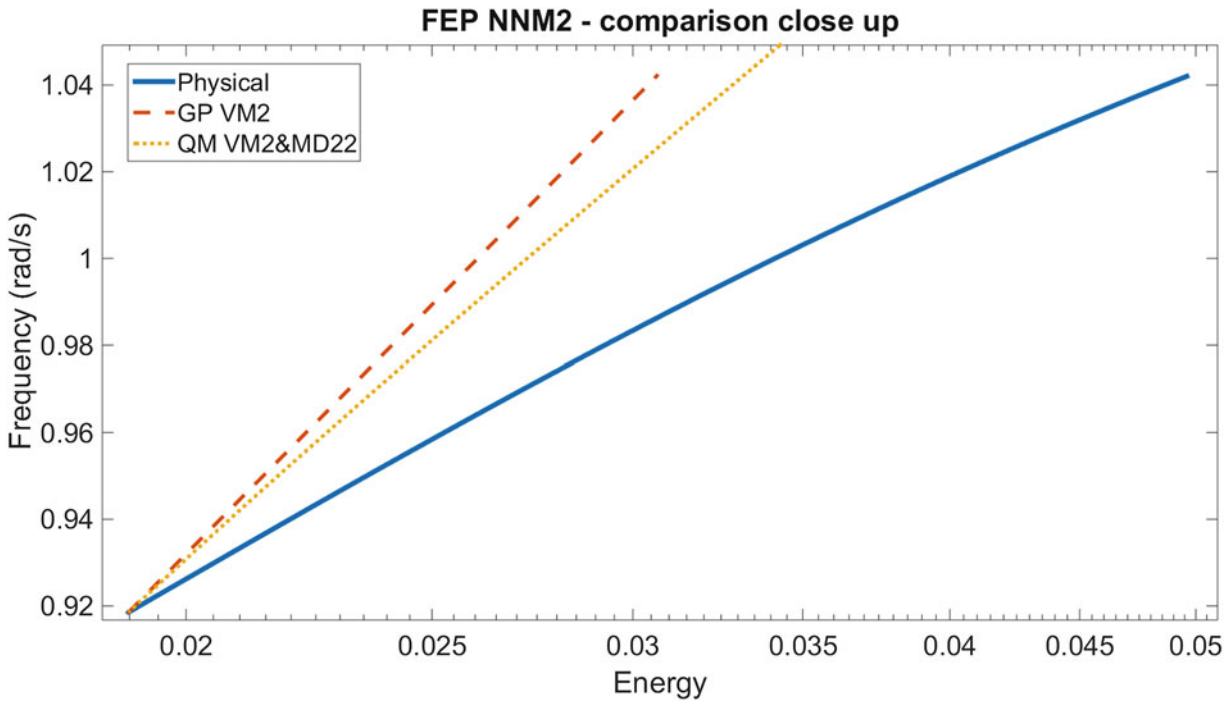

Fig. 32.13 Close up of NNM2 FEP, reduction methods compared with exact physical NNM

Acknowledgement The author L. Renson is a Marie-Curie COFUND Postdoctoral Fellow of the University of Liège, co-funded by the European Union

References

1. Ahlquist JR, Carreño JM, Climent H, de Diego R, de Alba J (2010) Assessment of nonlinear structural response in A400M GVT. In: Proceedings of the international modal analysis conference, Jacksonville, 2010
2. Noël JP, Renson L, Kerschen G, Peeters B, Manzato S, Debille J (2013) Nonlinear dynamic analysis of an F-16 aircraft using GVT data. In: Proceedings of the international forum on aeroelasticity and structural dynamics, Bristol, 2013
3. Renson L, Noël JP, Kerschen G (2015) Complex dynamics of a nonlinear aerospace structure: numerical continuation and normal modes. Nonlinear Dyn. doi:10.1007/s11071-014-1743-0
4. Rosenberg RM (1960) Normal modes of nonlinear dual-mode systems. J Appl Mech 27(2):263–268
5. Rosenberg RM (1966) On nonlinear vibrations of systems with many degrees of freedom. Adv Appl Mech 9:155–242
6. Lee YS, Kerschen G, Vakakis AF, Panagopoulos P, Bergman L, McFarland DM (2005) Complicated dynamics of a linear oscillator with a light, essentially nonlinear attachment. Physica D 204(1–2):41–69
7. Vakakis AF, Manevitch LI, Mlkhlin YV, Pilipchuk VN, Zevin AA (2008) Normal modes and localization in nonlinear systems. Wiley-VCH Verlag GmbH, Weinheim
8. Peeters M, Viguié R, Sérandour G, Kerschen G, Golinval JC (2009) Nonlinear normal modes, part II: toward a practical computation using numerical continuation techniques. Mech Syst Signal Process 23(1):195–216
9. Arquier R, Bellizzi S, Bouc R, Cochelin B (2006) Two methods for the computation of nonlinear modes of vibrating systems at large amplitudes. Comput Struct 84(24–25):1565–1576
10. Kerschen G, Peeters M, Golinval JC, Stéphan C (2013) Nonlinear modal analysis of a full-scale aircraft. J Aircr 50(5):1409–1419
11. Idelsohn SR, Cardona A (1985) A reduction method for nonlinear structural dynamic analysis. Comput Methods Appl Mech Eng 49(3):253–279
12. Tiso P (2011) Optimal second order reduction basis selection for nonlinear transient analysis. In: Modal analysis topics, vol 3. Springer, New York, pp 27–39
13. Wenneker F, Tiso P (2014) A substructuring method for geometrically nonlinear structures. In: Dynamics of coupled structures, vol 1. Springer, Heidelberg
14. Rutzmoser JB, Rixen DJ, Tiso P (2014) Model order reduction using an adaptive basis for geometrically nonlinear structural dynamics. In: Conference on noise and vibration engineering, Leuven, 20–25 Sept 2014

Chapter 33
Validation of Nonlinear Reduced Order Models with Time Integration Targeted at Nonlinear Normal Modes

Robert J. Kuether and Mathew S. Allen

Abstract Recently, nonlinear reduced order models (ROMs) of large scale finite element models have been used to approximate the nonlinear normal modes (NNMs) of detailed structures with geometric nonlinearity distributed throughout all of its elements. The ROMs provide a low order representation of the full model, and are readily used with numerical continuation algorithms to compute the NNMs of the system. In this work, the NNMs computed from the reduced equations serve as candidate periodic solutions for the full order model. A subset of these are used to define a set of initial conditions and integration periods for the full order model and then the full model is integrated to check the quality of the NNM estimated from the ROM. If the resulting solution is not periodic, then the initial conditions can be iteratively adjusted using a shooting algorithm and a Newton–Raphson approach. These converged solutions give the true NNM of the finite element model, as they satisfy the full order equations, and they can be compared to the ROM predictions to validate the ROM at selected points along the NNM branch. This gives a load-independent metric that may provide confidence in the accuracy of the ROM while avoiding the excessive cost of computing the complete NNM of the full order model. This approach is demonstrated on two models with geometric nonlinearity: a beam with clamped-clamped boundary conditions, and a cantilevered plate used to study fatigue and crack propagation.

Keywords Reduced order modeling • Geometric nonlinearity • Nonlinear normal modes • Periodic orbits • Finite element analysis

33.1 Introduction

Geometric nonlinearity can be encountered in almost any structure where the thickness of a member is small enough that it can deform significantly while the material remains in the linear elastic regime. The development of reduced order models of such systems has been motivated by the efforts of the United States Air Force (USAF) and the National Aeronautics and Space Administration (NASA) to model and design reusable hypersonic aircraft. At hypersonic speeds (Mach > 5) the aerodynamic pressure is sufficient to cause skin panels to vibrate nonlinearly. Additionally, thermal loads can lead to buckling and highly nonlinear vibration of the panel between two buckled states. Similar issues are encountered in stealth aircraft as exhaust from engines, which are buried within the structure to minimize their thermal signature, impinges on structural panels. While these are certainly two extreme environments, it is important to note that geometric nonlinearity can also be encountered in a variety of more common situations. For example, when accelerated endurance tests are performed on structures with thin sheet metal panels, the increased loads may cause the panels, and hence the structure, to behave nonlinearly. This could invalidate the endurance test if the nonlinearity is not considered. As a rule of thumb, a thin panel will tend to behave nonlinearly if the displacement is on the order of the panel thickness, as bending deformations induce axial stretching. This is illustrated schematically in Fig. 33.1 for a clamped-clamped beam.

Finite element codes have been capable of geometrically nonlinear quasi-static analysis for several decades. On today's computers, this type of analysis is feasible for models containing tens or perhaps even hundreds of thousands of degrees of freedom, with solution times on the order of tens of minutes to several hours, respectively. This capability can also be used to compute the transient, dynamic response of the structure, essentially by solving a quasi-static problem at each time step. However, considering the short time steps that are typically required and the time span over which analysis must be performed to obtain meaningful results, a dynamic analysis tends to take thousands if not millions of times longer. Hence,

R.J. Kuether • M.S. Allen (✉)
Department of Engineering Physics, University of Wisconsin, Madison, WI 53706, USA
e-mail: rkuether@wisc.edu; msallen@engr.wisc.edu

G. Kerschen (ed.), *Nonlinear Dynamics, Volume 1*, Conference Proceedings of the Society for Experimental Mechanics Series, DOI 10.1007/978-3-319-15221-9_33

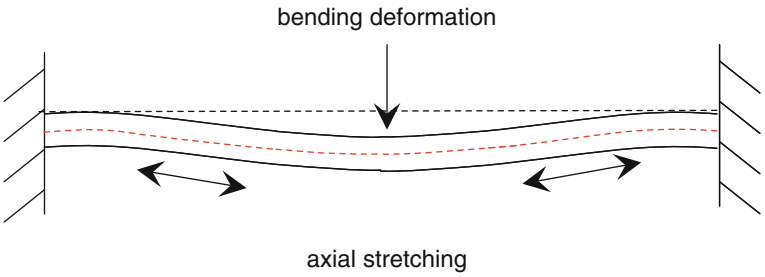

Fig. 33.1 Schematic of clamped-clamped beam subject to bending loads. When the deformations are small axial stretching can be neglected, but for large deformations the total stiffness increases as the beam must both bend and stretch axially to accommodate the deformation

these analyses are far too expensive to be practical as a design tool except perhaps on relatively simple structures or when considering short dynamic events.

Fortunately, in the past few decades Reduced Order Modeling (ROM) approaches have been developed which can extract a lower order dynamic model from a detailed finite element model of a geometrically nonlinear structure and then its response can be computed very inexpensively. The first approach of this kind seems to have been presented by Nash [1], and other early contributors included Segalman and Dohrmann [2, 3], McEwan [4] and Muravyov and Rizzi [5]. All of these methods use a small number of nonlinear quasi-static analyses to extract a low order model for the structure, typically using the structure's linear modal deformation shapes as a basis to describe the nonlinear response. As long as the method used accounts for the way that axial stretching is induced as the structure vibrates in these low order bending modes, an accurate and efficient reduced order model can be obtained. The works by Hollkamp and Gordon [6, 7] provide an excellent review and thorough explanation of the methods. A recent review [8] provides additional perspective on the myriad of methods that have been developed.

While these methods show tremendous promise, it can still be very challenging to create an accurate reduced order model for a real structure. To succeed, not only must one include all of the linear modes that participate in the response, but the static load cases used to determine the ROM must be chosen such that an appropriate level of nonlinearity is excited in each mode's response. If the loads are too small the numerical procedure becomes ill-conditioned and if they are too large they may induce coupling between many modes so that fitting a low order model becomes unacceptable. Furthermore, the number of static load cases required scales with more than the third power of the number of modes (or about the second power for a recent method [9]), so there is strong motivation to use the minimum number of modes that will be adequate.

In order to validate the ROM, most works (see, e.g. [6, 9–12]) have generated responses from either a static or dynamic load applied to the full order finite element model and compared this expensive set of truth data to the response predicted by the ROM. From this truth data, the modes and load levels used to generate the ROM are fine tuned until it agrees acceptably with these results. However, with this approach one cannot assure that the model will suitably agree with the results predicted by the full order model at a different load level, or load type. The authors recently proposed to instead compare the Nonlinear Normal Modes (NNMs) [13–15] of the candidate ROMs and to use them as a metric to gauge the convergence of the ROM [16–18]. Nonlinear modes are typically depicted on a frequency versus amplitude or frequency versus energy plot, which shows how each natural frequency evolves as the response amplitude changes, capturing a more complete amplitude range involving the geometric nonlinearity, independent of any external forces. The NNMs are easy to relate, qualitatively at least, to the response of the structure to sinusoidal [19], transient [17] or even random [20] excitation, so they still provide a powerful connection back to the response to external loads. As a result, the NNMs provide an informative means for comparing two or more candidate ROMs.

This paper builds upon the foundation established in [18], but instead here we discuss in more detail the general procedure that is used to arrive at a valid ROM so that its NNMs agree with the true NNMs of the structure as the number of modes included increases. This paper now proposes to use the deformations found by a ROM to integrate the full model subject to those initial conditions at certain locations along the NNM curve in order to evaluate whether the ROM predicts an NNM solution or not. If the solution is not periodic, than these deformations serve as an initial guess in a shooting algorithm [21] that iterates on the dynamic simulation of the full finite element model over one period until it exhibits a periodic response (to some tolerance) and hence a true NNM. This avoids the lengthy computational effort required to fully resolve the NNM of interest using the continuation algorithm in [21], particularly because one can circumvent the internal resonances where much of the computational effort is expended. These concepts are illustrated on a clamped-clamped beam, one of the simplest structures that exhibits geometric nonlinearity, and on a much more complicated 32,000 DOF model of a specimen used to study the fatigue behavior of Titanium [22].

The paper is outlined as follows. Sect. 33.2 briefly reviews the ROM modeling strategy and the definition of nonlinear normal modes used in this work. The general procedure for generating candidate ROMs and checking the computed NNM solutions on the full order model is also discussed. In Sect. 33.3 the methods are applied to a clamped-clamped beam,

capitalizing on the work presented in [18, 21]. The methods are then applied to a fatigue specimen, where the true NNMs are too expensive to compute in detail, providing insight into how these approaches may fare in industrial practice. The conclusions are then presented in Sect. 33.4.

33.2 Theoretical Development

While damping can be included in a ROM [6], the nonlinearity due to large deformations only depends on displacements so this work focuses on the conservative model for the system. After discretization by the finite element method, the system can be represented as,

$$\mathbf{M}\ddot{\mathbf{x}} + \mathbf{K}\mathbf{x} + \mathbf{f}_{NL}(\mathbf{x}) = \mathbf{f}(t) \tag{33.1}$$

where $\mathbf{M}$ and $\mathbf{K}$ are the $N \times N$ linear mass and stiffness matrices and the geometric nonlinearity exerts a nonlinear restoring force through the $N \times 1$ vector, $\mathbf{f}_{NL}(\mathbf{x})$. Note that this nonlinear internal force is purely a static effect. The external loads are accounted for by including the $N \times 1$ vector $\mathbf{f}(t)$, and the $N \times 1$ vectors $\mathbf{x}(t)$ and $\ddot{\mathbf{x}}(t)$ are the displacement and acceleration, respectively.

33.2.1 Review of Reduced Order Modeling

A reduced order model is obtained by presuming that the response can be well represented using a small set of mode shapes $\left(\mathbf{K} - {\omega_r}^2\mathbf{M}\right)\boldsymbol{\varphi}_r = 0$ so that,

$$\mathbf{x}(t) = \boldsymbol{\Phi}_m \mathbf{q}(t) \tag{33.2}$$

Each column in the $N \times m$ mode shape matrix, $\boldsymbol{\Phi}_m$, is a mass normalized mode shape vector, φ, and $\mathbf{q}(t)$ is a vector of time-dependent modal displacements. The vectors in $\boldsymbol{\Phi}_m$ are truncated to a small set mode shapes, typically reducing the number of degrees of freedom down to a few tens, or even fewer, of modal coordinates, so $m << N$.

After applying the modal transformation to the full order equations in Eq. 33.1, the equation of motion for each modal degree of freedom becomes

$$\ddot{q}_r + \omega_r^2 q_r + \theta_r(q_1, q_2, \ldots, q_m) = \boldsymbol{\varphi}_r^{\mathrm{T}}\mathbf{f}(t) \tag{33.3}$$

where ω_r is the linear natural frequency, $()^{\mathrm{T}}$ is the transpose operator and q_r is the r^{th} modal displacement. The nonlinearity couples the modal degrees of freedom so the nonlinear modal restoring force is generally a function of all of the modal displacements $\theta_r(\mathbf{q}) = \boldsymbol{\varphi}_r^{\mathrm{T}}\mathbf{f}_{NL}(\boldsymbol{\Phi}_m\mathbf{q})$. The response of the modes that are excluded from the modal basis is hoped to be negligible. The theory for geometric nonlinearity reveals that the nonlinear modal restoring force can be modeled with second and third order polynomials, which are shown to be

$$\theta_r(q_1, q_2, \ldots, q_m) = \sum_{i=1}^{m}\sum_{j=i}^{m} B_r(i,j) q_i q_j + \sum_{i=1}^{m}\sum_{j=i}^{m}\sum_{k=j}^{m} A_r(i,j,k) q_i q_j q_k \tag{33.4}$$

The scalars B_r and A_r are the coefficients of the quadratic and cubic nonlinear stiffness terms, respectively, for the r^{th} equation of motion. One approach to determine these coefficients is the Implicit Condensation and Expansion (ICE) method [10], where a series of static loads are applied to the full order model having the shape

$$\mathbf{f} = c_r \mathbf{M}\boldsymbol{\varphi}_r \tag{33.5}$$

with a scaling term c_{r} defined for the r^{th} mode in the basis set. Note that this force would only cause deformation in a single mode if the system were linear. The *nonlinear* static response of the structure is found in response to the force in Eq. 33.5, and the process is repeated for each mode in the basis and for combinations of up to three modes. With a series of these forces and resulting nonlinear responses, a least squares problem is set up to solve for nonlinear stiffness coefficients B_r and A_r.

Another popular ROM approach, termed the Enforced Displacement (ED) method, involves the converse static solutions where a series of modal displacements are applied to the structure and a quasi-static analysis extracts the reaction forces required to hold that displacement [5, 9]. Those forces and displacements are used to solve a series of smaller algebraic equations for the coefficients B_r and A_r. Because a least squares problem is avoided, this method tends to be more numerically stable but it does not implicitly capture the axial effects so axial modes must be included to obtain accurate results.

33.2.2 Review of Nonlinear Normal Modes

The nonlinear normal mode definition used throughout this work is based on the extended definition by Vakakis, Kerschen and others [13, 14], where an NNM is a *not necessarily synchronous periodic solution to the conservative, nonlinear equations of motion*. Each NNM must satisfy the condition of periodicity, and can account for motions that are not synchronous which occur when two or modes interact at a specific integer frequency ratio. Nonlinear modes are typically depicted on a frequency versus energy plot, or FEP, which shows how the natural frequency evolves as the response amplitude changes, revealing many qualitative insights into the amplitude dependent dynamics. Even though the property of superposition and orthogonality no longer hold for the NNM, they are still conceptually useful in the identification of nonlinear dynamics as they form the backbone to the nonlinear forced response curves [13, 14], offer metrics for comparison between nonlinear modeling domains [17, 18, 23–25], and closely follow the freely decaying response of a lightly damped structure as energy dissipates [13, 26].

A pseudo-arclength continuation algorithm, developed originally by Peeters et al. [27], is used throughout this work to compute the NNMs of each of the undamped reduced order models. For the low order m-DOF systems represented by Eqs. 33.3 and 33.4 with $\mathbf{f}(t) = \mathbf{0}$, there exist m nonlinear normal mode branches that each initiate at a linear mode at low energy, or low response amplitude. (Continuation algorithms need an initial solution in order to start tracing an NNM branch, and the linear mode solutions at low energy provide an excellent starting point.) The continuation algorithm uses the shooting technique to find a set of initial conditions and an integration period that satisfy periodicity as the amplitude in the response changes. A shooting function is defined as,

$$\mathbf{H}\left(T, \mathbf{q}_0, \dot{\mathbf{q}}_0\right) = \begin{Bmatrix} \mathbf{q}\left(T, \mathbf{q}_0, \dot{\mathbf{q}}_0\right) \\ \dot{\mathbf{q}}\left(T, \mathbf{q}_0, \dot{\mathbf{q}}_0\right) \end{Bmatrix} - \begin{Bmatrix} \mathbf{q}_0 \\ \dot{\mathbf{q}}_0 \end{Bmatrix} = \{\mathbf{0}\}, \tag{33.6}$$

where T is the period of integration, and $\mathbf{q}_0$ and $\dot{\mathbf{q}}_0$ are the initial modal displacements and velocities, respectively, for a candidate ROM. The ROM equations must be integrated over a period T subject to the initial conditions $\mathbf{q}_0$ and $\dot{\mathbf{q}}_0$ to evaluate whether or not these variables produce an NNM motion. The periodicity condition is based on a numerical tolerance $\varepsilon_{\text{shoot}}$, such that an NNM motion is obtained when

$$\frac{\left\|\mathbf{H}\left(T, \mathbf{q}_0, \dot{\mathbf{q}}_0\right)\right\|}{\left\| \begin{Bmatrix} \mathbf{q}_0 \\ \dot{\mathbf{q}}_0 \end{Bmatrix} \right\|} < \varepsilon_{\text{shoot}} \tag{33.7}$$

Typically a numerical tolerance $\varepsilon_{\text{shoot}}$ on the order of 10^{-4} to 10^{-6} is used, depending on the accuracy of the numerical time integration scheme. Once periodicity is satisfied, an NNM solution is uniquely defined by $\mathbf{q}_0$, $\dot{\mathbf{q}}_0$, and T, which is used with the continuation algorithm to predict a new periodic solution at a slightly different energy level. A step size controller determines the magnitude of the prediction step based on the number of iterations taken during the preceding correction steps.

33.2.3 Proposed Procedure for Generating a Valid ROM

The authors have developed the following procedure to obtain a valid ROM for a finite element model of interest using its computed NNMs as a convergence metric, as originally proposed in [18]. The analyst must first select the frequency and energy range of interest, and ultimately choose which nonlinear normal modes it should accurately compute. In this section, the procedure is outlined for a ROM that will only capture the NNM that initiates from the r^{th} mode of interest. Note that the procedure is similar for a ROM that needs to accurately compute many different NNMs.

1. For a given force amplitude c_r in Eq. 33.5, compute both the linear and nonlinear static response for the r^{th} mode of interest. As an initial guess, determine the load scaling c_r that would give one thickness of deformation for the linear response.
   (a) If the ratio of the nonlinear displacement to the linear displacement is not between about 0.85 and 0.90, or 1.15 and 1.10, repeat with a larger or smaller load. This general rule of thumb has been found [6, 18] to activate the nonlinearity sufficiently so that B_r and A_r can be accurately determined from the static load cases.
2. Use $\mathbf{q} = \mathbf{\Phi}^T\mathbf{M}\mathbf{x}$ to compute the modal displacement of each mode in response to the load case in step (1). Identify any modes that are strongly coupled (statically) to the mode of interest.
3. Compute a 1-Mode ROM using only the r^{th} mode and compute the NNM from those equations.
4. Add a few of the modes that were most strongly coupled to the r^{th} mode in step (2). For the added modes, determine the appropriate scale levels, and compute a multi-mode ROM with the new mode set.
5. Recompute the NNM using the improved multi-mode ROM of interest. Compare the NNM with that found in step (3).
6. If the NNM has not converged, one can either:
   (a) Repeat the analysis in steps (4) through (5) by adding any additional modes to the ROM identified from step (2) and using the appropriate load levels.
   (b) Consider whether smaller or larger load levels should be used when generating the multi-mode ROM and repeat steps (4) through (5).

In the authors' previous work, the convergence of the ROM was evaluated based on the NNMs, just as outlined above, but these results were ultimately deemed accurate by comparing those to the NNM computed directly from the full finite element model using the Applied Modal Force (AMF) continuation algorithm in [21]. The AMF results are costly for large scale models since the continuation algorithm uses many time integrations of the full model to iterate on the initial conditions to satisfy the shooting function at many point along the NNM branch. The authors also found that much computational effort was wasted seeking to map out the NNM branch through internal resonances where several modes respond and the frequency-energy behavior is complicated, hence requiring many prediction/correction steps. This work approaches the final validation step a little differently. Instead of running AMF on the full model to get the truth data, the NNM computed from the ROMs using the procedure above is checked at a few points on the curve by integrating the full model subject to the initial conditions found using the ROMs, thus requiring fewer numerical simulations on the full model.

Specifically, suppose that one ROM denoted ROM_A, involving a certain set of modal coordinates $\mathbf{q}_\text{ROM}$ (for example, the result for the ICE (1,3,5,7) ROM in Sect. 33.3.1 includes q_1, q_3, q_5 and q_7) produces a periodic response at a certain point along the frequency energy curve with initial conditions $\mathbf{q}_{\text{ROM},0}$, $\dot{\mathbf{q}}_{\text{ROM},0}$ and integration period T. These initial conditions are then used to compute the initial bending displacement at each point in the FE model using

$$\mathbf{x}_{\text{b},0} = \mathbf{\Phi}_\text{ROM}\mathbf{q}_{\text{ROM},0} \tag{33.8}$$

and similarly for the velocities. Then the expansion procedure in ICE [10] is used to compute the corresponding membrane deformations $\mathbf{x}_{\text{m},0}$ and the two are added $\mathbf{x}_{\text{tot},0} = \mathbf{x}_{\text{b},0} + \mathbf{x}_{\text{m},0}$ to estimate the total deformation of the structure corresponding to the point of interest. The result is then used as the initial condition for the full FE model. Note that when the enforced displacements procedure is used the membrane modes are explicitly included in the ROM so Eq. 33.8 produces the total deformation $\mathbf{x}_{\text{tot},0}$ directly.

The finite element model is integrated subject to these initial conditions and the response after one cycle is extracted. This is then used to check the quality of the solution for the NNM at this point by computing the shooting function (in terms of the displacements only) as,

$$\mathbf{H}\left(T, \mathbf{x}_{\text{tot},0}, \dot{\mathbf{x}}_{\text{tot},0}\right) = \mathbf{x}\left(T, \mathbf{x}_{\text{tot},0}, \dot{\mathbf{x}}_{\text{tot},0}\right) - \mathbf{x}_{\text{tot},0} \tag{33.9}$$

The convergence metric is similar to the one in Eq. 33.7, such that

$$\frac{\left\|\mathbf{H}\left(T, \mathbf{x}_{\text{tot},0}, \dot{\mathbf{x}}_{\text{tot},0}\right)\right\|}{\left\|\mathbf{x}_{\text{tot},0}\right\|} = \varepsilon \tag{33.10}$$

In previous works [21] the authors used a tolerance threshold of 10^{-4} to realize a periodic solution within a finite element code. This procedure is repeated at a few key points of interest on the NNM and used to assess how well the ROM represents the full finite element model.

If the candidate initial conditions do not provide an adequate periodic solution, then the Newton–Raphson approach can be used to iterate on the initial conditions supplied by the ROM until the shooting function is satisfied to a preferred numerical tolerance. This is the same approach used in the shooting portion of the AMF algorithm in [18] with the initial conditions determined as follows. First, a nonlinear static analysis is performed to compute the reaction forces, $\mathbf{f}_{\text{tot},0}$, required to hold the structure at the displacement $\mathbf{x}_{\text{tot},0}$ estimated from the ROM. Then, those reaction forces are projected onto each of the modes in the ROM basis as,

$$\widehat{\mathbf{f}}_{\text{tot},0} = \boldsymbol{\Phi}_{\text{ROM}}{}^{\text{T}}\mathbf{f}_{\text{tot},0} \tag{33.11}$$

where $\widehat{\mathbf{f}}_{\text{tot},0}$ is the $m \times 1$ vector of modal force amplitudes. The initial conditions $\mathbf{x}_{\text{FE},0}$ used to evaluate the shooting function in Eq. 33.9 are then determined by solving the nonlinear static response of the full model to the force $\mathbf{M}\boldsymbol{\Phi}_{\text{ROM}}\widehat{\mathbf{f}}_{\text{tot},0}$. The full finite element model is integrated to these initial conditions to check for periodicity, and the free variables $\widehat{\mathbf{f}}_{\text{tot},0}$ and T are updated using a Newton–Raphson approach until the shooting function is satisfied. Additional modal forces can be added if convergence is not obtained, as outlined in [21]

33.3 Numerical Results

The proposed approach was applied to two different geometrically nonlinear finite element models: a clamped-clamped beam that was modeled with forty B31 beam elements, and a flat cantilevered plate with over 30,000 degrees of freedom. Both models were created and evaluated in Abaqus®, although in other works Nastran® [9] and Ansys® [16] have also been shown to have similar capabilities.

33.3.1 Clamped-Clamped Beam from [18, 21]

The ROMs of the clamped-clamped beam and the approach used to find them were described thoroughly in [16, 18], so only the final result will be highlighted here and used to explore whether the metric in Eqs. 33.9 and 33.10 can be effectively used to discern between candidate ROMs. In [18], a 1-mode ROM denoted ICE (1) (e.g. a ROM generated with Implicit Condensation and Expansion with only mode 1 in the basis) was found to accurately capture the backbone of the beam's first NNM, and a ROM that included modes 1, 3, 5 and 7, denoted ICE (1,3,5,7), captured the backbone more accurately and also two of its modal interactions. An ED (1) ROM will also be considered here, as an example of a ROM that does not as accurately reflect the structure. Recall that axial modes must be included in the Enforced Displacement method to obtain an accurate ROM. In [18] the authors show that an ED (1,26,39) ROM can be created that has similar accuracy to the ICE (1) ROM. The frequency energy plot (FEP) of the first NNM computed from each of these models is shown in Fig. 33.2a.

One can see that the FEPs predicted by the ICE (1) and ICE (1,3,5,7) ROMs agree very well with each other, except for the fact that the former misses the 5:1 modal interaction with NNM 3 at 88 Hz. Because these successive ROMs agree along the backbone, one might expect that they correspond to the true NNM, but in practice it can sometimes be difficult to be sure that convergence has been achieved. For example, it is possible that a ROM with additional degrees of freedom, for example an ICE (1,3,5,7,9,11) ROM, will encounter numerical ill conditioning and give a different answer. As a first attempt to evaluate the quality of these ROMs, four points were selected (as shown with markers in Fig. 33.2a) and the full model was integrated over one cycle with the initial conditions corresponding to those of the ROM at each of these points. The shooting tolerance was then computed using Eq. 33.10 and the result is shown in Fig. 33.2b. The most refined ROM gave a tolerance near 0.001, indicating that the full finite element model very nearly satisfies the shooting function for the initial conditions that the ROM supplies. For reference, the authors used a tolerance of 0.0001 in the AMF algorithm described in [21] to compute the "true" NNMs of this structure. Similarly, the results show that the ICE (1) ROM is quite adequate in some cases while one can expect errors of $0.1 < \varepsilon < 0.5$ if the ED (1) ROM is used.

Certainly this evaluation of four points is not nearly as robust as the comparisons that were used in [18], where the NNMs from each ROM were compared with the NNMs computed from the full FEA model. However, it only took about 30 s per point to evaluate the shooting function in Eq. 33.9, while the AMF algorithm would take about two hours to compute the backbone of this NNM over the same range, and even more time for the internal resonances. On larger systems this difference will be even more dramatic. The time histories of the nodal transverse displacements are shown in Fig. 33.3 for the solutions near 115 Hz in Fig. 33.2a, revealing the degree to which the displacements differ from a true, periodic response (and hence

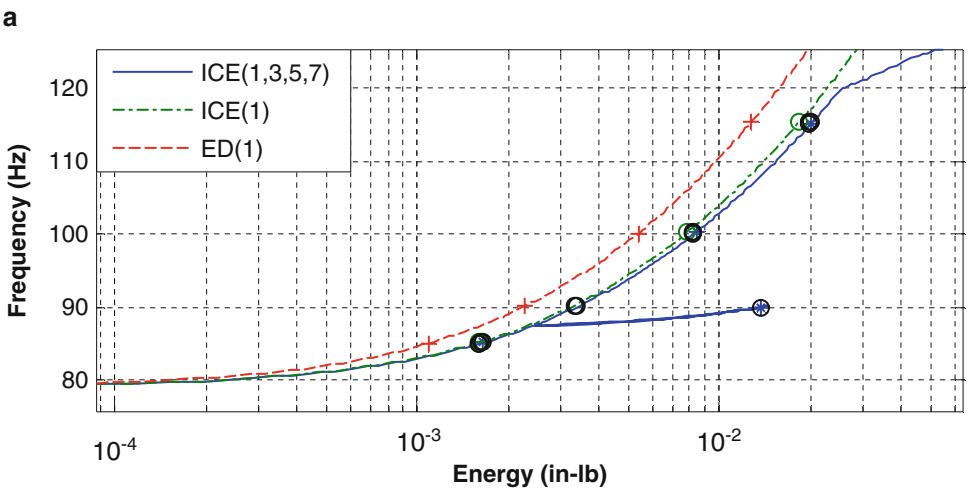

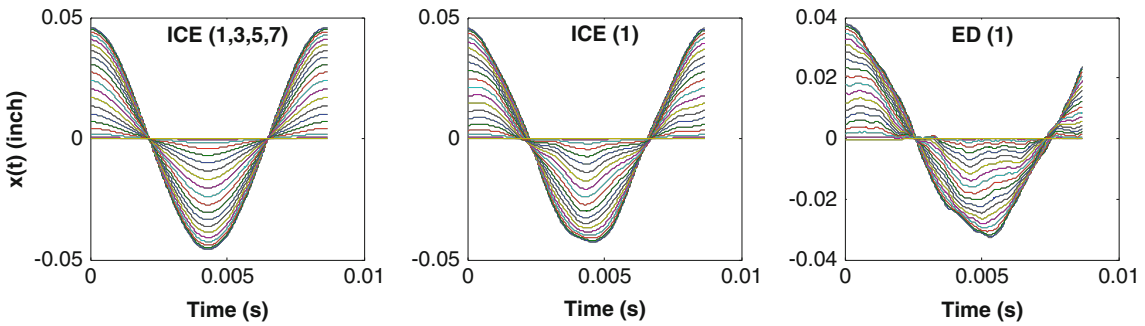

Fig. 33.2 (**a**) Frequency-energy plot showing the first NNM of various ROMs, and (*black circles*) represent converged NNMs with the full FE model. (**b**) Base 10 logarithm of the shooting tolerance, ε, in Eq. 33.10

Fig. 33.3 Time histories found after integrating the full FEA model subject to the initial conditions prescribed by each of the ROMs for the points near 115 Hz in the FEP in Fig. 33.2

an NNM). The response from the ICE (1,3,5,7) ROM initial conditions appears to be periodic, whereas the ED (1) ROM clearly does not predict the correct initial conditions to satisfy the full model. One could similarly compute the time history of a different quantity of interest, such as strain or stress, to determine whether its deviation from perfect periodic motion is large enough to invalidate life predictions or other key quantities of interest.

To further evaluate the quality of the ROMs, the black circles shown in Fig. 33.2a are converged NNM solutions using the shooting algorithm to drive the tolerance below 0.0001, as done in the AMF algorithm. The initial conditions were seeded from each of the ROMs at the four points of interest. During the Newton–Raphson iteration, the period of integration was held fixed, therefore the algorithm only converged on solutions with the same initial frequency. Therefore, the percent errors in the ROM energy and true energy, as shown in Table 33.1, can be used to gauge how close the ROM is to the truth model. For each of the points on the ICE (1,3,5,7), the shooting algorithm took at most two iterations (approximately 7 min) to converge below a tolerance of $\varepsilon < 0.0001$. The algorithm converged in anywhere between two to four iterations with the

Table 33.1 Percent error of energy after AMF shooting converged to true NNM solution

Point	Energy error ED (1)	Energy error ICE (1)	Energy error ICE (1,3,5,7)
1	56.4 %	8.4 %	1.8 %
2	51.2 %	4.8 %	1.8 %
3	47.8 %	2.4 %	0.1 %
4	46.0 %	1.3 %	0.1 %

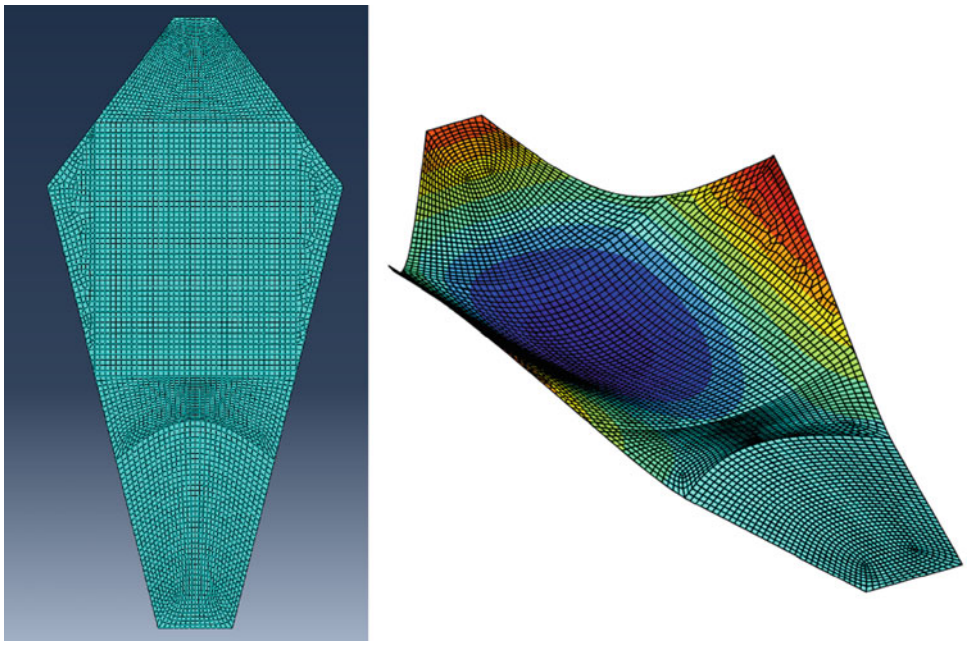

Fig. 33.4 (*left*) Finite element model used to model the cantilevered flat plate (*right*) 7th bending mode

ICE (1) NNM as starting guesses, and between three to five for the ED (1) NNM. The results suggests that if fewer than about 15 points on the NNM were desired then it would be cheaper (for this system) to compute the ROM first and then use its NNM to seed the shooting algorithm at each desired point.

The NNMs predicted by the ICE (1,3,5,7) ROM match the energy, within 2 % error, of that predicted by the NNM of the full model at 4 frequency locations along the NNM: three points along the backbone and one along the tongue of the 5:1 internal resonance with NNM 3. Also, the initial conditions predicted by the ICE (1,3,5,7) ROM reasonably satisfies the periodicity condition from the full FE model at the same four points. Both of these observations suggest that one can have confidence that the other solutions along the backbone are also accurate, and that the ROM has converged to solutions on NNM 1. The fact that the NNM has converged has important implications. For example, if the structure is lightly damped, then one can show [19], that the forced response of the ROM (in the worst case resonant condition) is also likely to agree over this same range of energy.

33.3.2 Cantilevered Plate

The next system studied is a cantilevered plate used to test the fatigue strength of materials and to validate models that simulate crack growth [28]. The shape of the plate and sinusoidal clamp at the bottom edge cause this plate to have a two-stripe mode (mode with two vertical node lines) where the region of highest stress is in the center of the top portion of the plate. The design was optimized to minimize the stresses near the clamp because it is difficult to control the stress field and to limit crack initiation in that region. The plate was modeled with a total of 5,378 nodes using a mixture of S3 and S4 shell elements, as shown in Fig. 33.4. The material properties of the model are those of a titanium alloy, having a Young's Modulus of 17.92 Mpsi, density of 0.164 lb/in^3, and a Poisson's ratio of 0.291. The thickness of the plate was 0.0511 in. Springs are connected to each node below the curve in the out of plane direction. The bottom edge of the plate is constrained in the vertical direction and the bottom-left node is constrained in the horizontal direction. The model was updated based on experimental data to determine the stiffness of the springs (k = 141 lb/in for the model used in this work), and a comparison of the linear natural frequencies of the plate are shown below in Table 33.2.

Table 33.2 Linear natural frequencies of the cantilevered plate

Mode number	Experimental Nat. Freq. (Hz)	FE Nat. Freq. (Hz)
1	27.7	28.424
2	98.6	99.501
3	167.9	169.71
4	437.6	436.95
5	566.0	567.65
6	756.9	754.03
7	861.1	848.07
8	1,041.3	1,048.6
9	1,206.5	1,188.8
10	1,378.5	1,370.6
11	1,408.4	1,396.4
12	1,608.9	1,607.5
13	2,043.3	1,983.6
14	2,062.8	2,066.3

The key mode of interest of this plate is the two stripe mode, Mode 7, which is the only mode that is significantly excited during fatigue testing. During the endurance test, the plate is excited with a base excitation at a monoharmonic frequency near Mode 7's natural frequency and typically at a large enough response amplitude to cause the plate to exhibit significant geometric nonlinearity. As a result, it is important to capture the 7th NNM when creating a ROM that will be used to model the response to such harmonic excitation. O'Hara and Hollkamp have successfully predicted both the direction and the rate of crack growth using a reduced order model in combination with the generalized finite element method (GFEM) [28]. When selecting a modal basis for the ROM, one should include any modes that are nonlinearly coupled with linear Mode 7, as these will influence the deformation field, and hence stress distribution, that will drive crack growth.

As a result, Mode 7 was used to seed the process presented in Sect. 33.2.3 and various load scales were applied using Eq. 33.5 to evaluate its nonlinearity and the modes statically coupled to it. The result is shown below in Fig. 33.5, where the vertical axis shows the modal displacement amplitude, and the horizontal axis shows the maximum linear displacement to thickness ratio if the force in the shape of Mode 7 were applied to the linear structure. A force-displacement analysis with 60 static solutions takes about 17 min for this model. This analysis revealed that the displacement must reach between 2 and 4 plate thicknesses to see appreciable nonlinearity. The results of these loadings were also used to determine which linear modes of the structure were activated and hence statically coupled to Mode 7. As shown in Fig. 33.5, Modes 1, 3 and 6 are most strongly coupled (statically) to Mode 7, so they were the next candidates to add to the model.

On the first iteration, a one mode ROM was created with a force that would have displaced Mode 7 two times the thickness, denoted ICE (7) CD (2). Based on the couplings observed above, a 4-mode ROM was then created and additional static load cases were performed for Mode 1 and 3 and linear displacements CD (10,3,1,2) were determined to be suitable (the values for Modes 1 and 3 were determined through additional force-displacement calculations, while that for Mode 6 was assumed to avoid computing an additional set of static load cases). These displacements caused nonlinear displacements that, respectively, had the following ratios relative to the computed linear displacement: 0.995, 0.84965, 0.6174, 1.1476. The first value is well outside the desired range of 0.85–0.9, but little nonlinearity was expected from this fundamental cantilever mode. It was hoped that this load level would be adequate to assure that the ROM did not prematurely predict nonlinear response in this mode, while being small enough to avoid contaminating the other modes. For reference a second ROM was created with the same modes and using CD (1,1,1,1), which could be considered an approach based on blindly applying a rule of thumb. Finally, an even higher order ICE (1,3,6,7,9,10,12) ROM was generated with the load case CD(10,3,1,2,1,1,1), referred to as Case 1. Case 2 was also generated with the same modes, but instead using half as large of force amplitudes when creating the ROM.

Figure 33.6 shows the NNM for Mode 7 computed with each of these ROMs. The NNM computation has revealed that there are quite significant differences between the five ROMs and the variations are such that it is difficult to say which of these ROMs might be most accurate. One might wonder, which load cases will give the best results? Will adding modes increase the accuracy due to the more complete modal basis, or decrease it as numerical ill conditioning becomes more severe?

Three points were identified on the NNM computed with each of the ROMs, as shown with black squares in Fig. 33.6, and were used to initiate a transient response on the full finite element model. About 42 min were required to compute each of the nonlinear transients and to write the response (at all nodes) to disk at all time instants during the response. The resulting shooting tolerances in Eq. 33.10 are summarized in Table 33.3, suggesting that both of the seven mode ROMs are similar

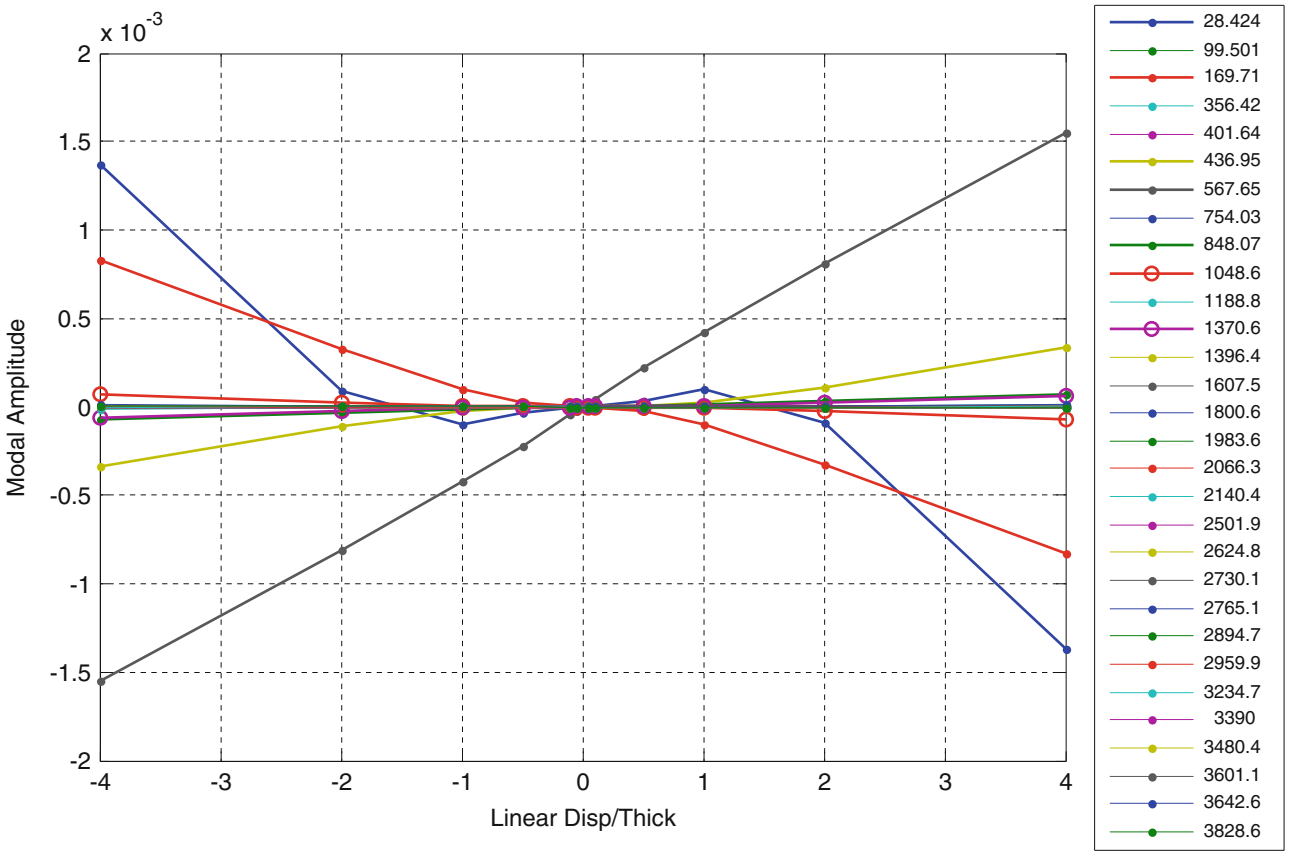

Fig. 33.5 Force-displacement analysis of the plate when a force in the shape of Mode 7 is applied to the nonlinear finite element model. The *colored lines* represent the modal amplitudes of the statically coupled modes, whose linear natural frequencies are in the legend

and quite close to the true NNM of the FEA model at the first two points. At the higher energy level, these ROMs apparently deviate quite a bit from the true NNM, so the ROM may need to be further refined if that regime is of interest. At point 1 the ICE (1,3,6,7) ROMs agree fairly closely with the higher order ROMs, so either of these might be close to the true NNM as well, explaining why the FEPs of all the multi-mode ROMs nearly agree around 580 Hz in Fig. 33.6.

In order to illustrate how these values of ε relate to the error in the solution, the time history of modal displacements over the integration period is shown for points 1, 2 and 3 using the ICE (1, 3, 6, 7, 9, 10, 12) CD (10, 3, 1, 2, 1, 1, 1) ROM. The physical displacements from the full finite element model were projected onto the unit displacement normalized modes, such that the modal degrees of freedom have units of inches. Each of these time histories are plotted below in Fig. 33.7, showing just the first 8 most dominant modes of each response from the full order model.

The integrated response from points 1 and 2 show that the solution is nearly periodic, although point 2 begins to have significant contributions from the other modes coupled to Mode 7. The significant error in ε for the response at point 3 may be attributed to the fact that modes 14, 16 and 18 become excited, indicating that these modes are dynamically coupled to Mode 7 and may need to be included in the ROM to more accurately compute NNM 7. It is interesting that there is noticeable difference in modal amplitude of Mode 7 from $t = 0$ to the final time. This suggests that this mode is not well represented in the ROM or that coupling with other modes has caused it to deviate from a periodic response. The time histories show how ε reveals the inaccuracy of the ROM at point 3, however the response at points 1 and 2 would be considered acceptable.

Based on these results, the next step would be to generate a ROM with additional modes (14, 16 and 18) and track how the NNM computed from the new ROM compares to the ones in Fig. 33.6. The initial conditions from these NNMs could then be used to seed the shooting algorithm discussed in Sect. 33.2.3, providing further insight into the location of the true NNM of the full order model and whether any of the ROMs capture these solutions. Neither of these items were explored in this work, but will certainly be considered in the future. Also, so far only NNM 7 has been studied in detail, but in reality it is significantly affected by the other NNMs that are extensions of the linear modes in the basis. Modal interactions with NNM 7 are strongly dependent on the accuracy of the other NNMs generated by the ROM, therefore it would probably be wise to assess the convergence of those NNMs.

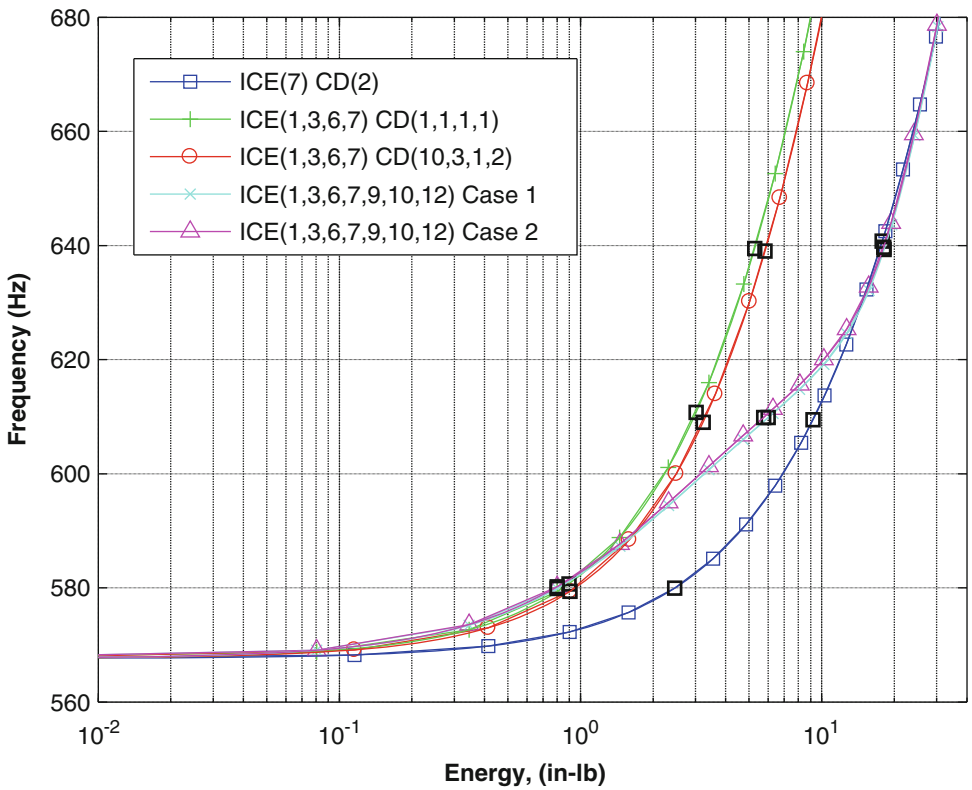

Fig. 33.6 Estimate of 7th NNM computed from various ROMs of the cantilevered plate. In the last two lines of the legend, Case 1 corresponds to CD(10,3,1,2,1,1,1) while Case 2 used forces half as large with CD(5,1.5,0.5,1, 0.5, 0.5, 0.5)

Table 33.3 Values of shooting function tolerance, ε, from Eq. 33.10 for the points shown with black squares in Fig. 33.6

Point	Frequency (Hz)	ε ICE (7) CD (2)	ε ICE (1,3,6,7) CD (1,1,1,1)	ε ICE (1,3,6,7) CD (10,3,1,2)	ε ICE (1,3,6,7,9,10,12) CD (10,3,1,2,1,1,1)	ε ICE (1,3,6,7,9,10,12) CD (5,1.5,0.5,1,0.5,0.5,0.5)
1	580	0.241	0.0853	0.0875	0.00896	0.00897
2	610	0.344	0.205	0.216	0.0663	0.0657
3	640	0.396	0.267	0.278	0.177	0.173

33.4 Conclusion

This work explores a systematic approach to obtain validated reduced order models from finite element models with geometric nonlinearity based on their computed nonlinear normal modes. Ideally, as more modes are added to the basis set, or the scaling of the loads are adjusted, these low order equations should converge and accurately predict the NNMs of the full order model. In this paper, the ROMs provide a set of initial conditions from the predicted NNM, which are integrated with the full order model to check the quality of the ROM. A small set of points along the branch can be selected to span the desired range of response amplitude, covering a more complete operating range of interest. If the initial conditions of the ROMs do not produce periodic motions, they can be iteratively adjusted using the shooting algorithm and a Newton–Raphson approach in hopes of converging on a true NNM. These converged solutions provide further insight into the deficiencies of the ROM. This approach avoids the need to run the costly AMF continuation algorithm [21] to trace the full NNM branch directly from the full finite element model, which has shown to require many more time integrations, and has a tendency to waste a lot of computational effort when tracing out the internal resonances.

The approach was demonstrated on a simple beam with geometric nonlinearity and fixed boundary conditions at both ends. The ICE ROM had nearly converged on the backbone of the 1st NNM using only a single-mode ROM, and captured one of the beams internal resonances when using four modes. The initial conditions supplied by these ROMs were integrated with the full finite element model and produced acceptable NNMs. Even the converged NNMs found with the shooting algorithm agreed very well with these ROMs, validating them at various energies and frequencies. The single-mode ED

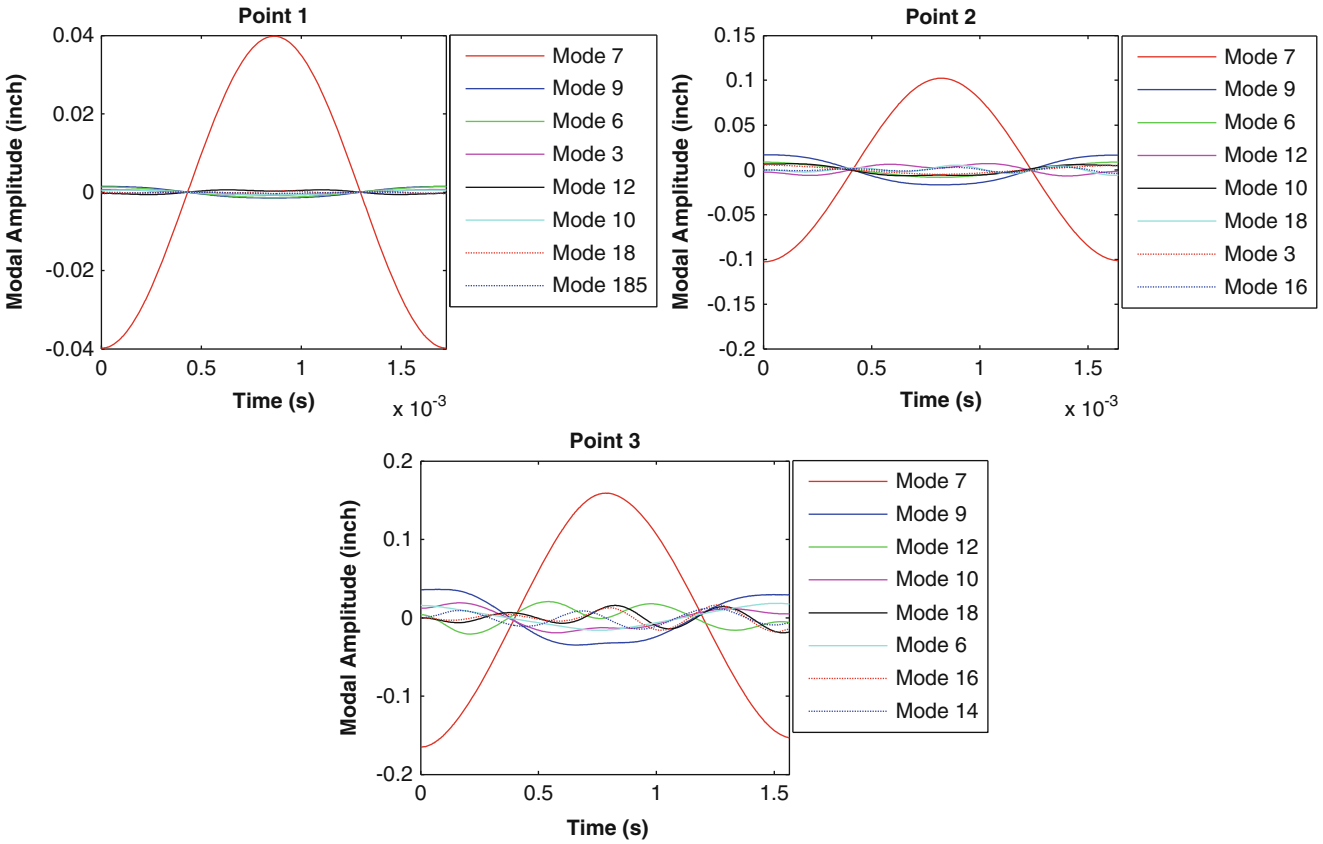

Fig. 33.7 Time histories of the integrated response of the full order model for the points shown with *black squares* in Fig. 33.6 using the ICE (1, 3, 6, 7, 9, 10, 12) CD (10, 3, 1, 2, 1, 1, 1) ROM. The first eight most dominant modal displacements are shown over one integration period

ROM did not perform as well (as predicted due to the lack of membrane modes in the basis) since the estimated backbone was much stiffer than the true NNM, resulting in integrated responses that were clearly not periodic and FEPs that were far of from the true NNM. A cantilever plate model with 32,000 degrees of freedom was used as an industrial application where this approach might be useful. The ICE ROMs with various mode shapes showed that the 7th NNM of interest was difficult to accurately capture, as no convergence was observed in the FEPs. Integrating the initial conditions at three points along the branch with each ROM revealed that the ROMs may be converging at lower energies, but more deformation shapes would be needed in the ROM basis to capture the higher energy response. The results revealed that as more modes were added to the basis, the evaluation of the shooting function improved, suggesting that the ROMs were converging to the true solution.

This procedure shows great promise as an approach to validate a ROM without having to run very many overly expensive time simulations on the full order model. One can choose the operating range of interest for the ROM, and validate it at those energy levels, or frequencies. The NNM is independent of any external forces applied to the structure, providing a more robust comparison metric between candidate ROMs and the full order model. In future works, additional modes will be added to the ICE ROM of the cantilever plate in hopes of further improving the prediction of the 7th NNM. Also, the shooting algorithm will be used to find true NNMs at select points along the backbone, in hopes of guiding further improvements to the ROM procedure, or validating the existing ones. Other NNMs will be considered as well.

Acknowledgements The authors gratefully acknowledge the support of the Air Force Office of Scientific Research under grant number FA9550-11-1-0035, administered by the Dr. David Stargel of the Multi-Scale Structural Mechanics and Prognosis Program. The authors also wish to thank Dr. Joseph Hollkamp and the Structural Sciences Center at the Air Force Research Laboratory for providing the Abaqus® interface that was used in this work as well as for many helpful suggestions and discussions regarding the ROM modeling.

References

1. Nash M (1977) Nonlinear structural dynamics by finite element modal synthesis. PhD, Department of Aeronautics, Imperial College
2. Segalman DJ, Dohrmann CR (1996) Method for calculating the dynamics of rotating flexible structures, Part 1: derivation. J Vib Acoust Trans ASME 118:313–317
3. Segalman DJ, Dohrmann CR, Slavin AM (1996) Method for calculating the dynamics of rotating flexible structures, Part 2: example calculations. J Vib Acoust Trans ASME 118:318–322
4. McEwan MI, Wright JR, Cooper JE, Leung AYT (2001) A combined modal/finite element analysis technique for the dynamic response of a non-linear beam to harmonic excitation. J Sound Vib 243:601–624
5. Muravyov AA, Rizzi SA (2003) Determination of nonlinear stiffness with application to random vibration of geometrically nonlinear structures. Comput Struct 81:1513–1523
6. Gordon RW, Hollkamp JJ (2011) Reduced-order models for acoustic response prediction. AFRL-RB-WP-TR-2011-3040, July 2011
7. Hollkamp JJ, Gordon RW, Spottswood SM (2005) Nonlinear modal models for sonic fatigue response prediction: a comparison of methods. J Sound Vib 284:1145–1163
8. Mignolet MP, Przekop A, Rizzi SA, Spottswood SM (2013) A review of indirect/non-intrusive reduced order modeling of nonlinear geometric structures. J Sound Vib 332:2437–2460
9. Perez R, Wang XQ, Mignolet MP (2014) Nonintrusive structural dynamic reduced order modeling for large deformations: enhancements for complex structures. J Comput Nonlin Dyn 9:031008
10. Hollkamp JJ, Gordon RW (2008) Reduced-order models for nonlinear response prediction: implicit condensation and expansion. J Sound Vib 318:1139–1153
11. Przekop A, Guo X, Rizzi SA (2012) Alternative modal basis selection procedures for reduced-order nonlinear random response simulation. J Sound Vib 331:4005–4024
12. Rizzi SA, Przekop A (2008) System identification-guided basis selection for reduced-order nonlinear response analysis. J Sound Vib 315:467–485
13. Kerschen G, Peeters M, Golinval JC, Vakakis AF (2009) Nonlinear normal modes. Part I. A useful framework for the structural dynamicist. Mech Syst Signal Process 23:170–194
14. Vakakis AF (1997) Non-linear normal modes (NNMs) and their applications in vibration theory: an overview. Mech Syst Signal Process 11:3–22
15. Vakakis AF, Manevitch LI, Mikhlin YN, Pilipchuk VN, Zevin AA (1996) Normal modes and localization in nonlinear systems. Wiley, New York
16. Allen MS, Kuether RJ, Deaner BJ, Sracic MW (2012) A numerical continuation method to compute nonlinear normal modes using modal coordinates. In: 53rd AIAA/ASME/ASCE/AHS/ASC structures, structural dynamics, and materials conference, Honolulu
17. Kuether RJ, Brake MR, Allen MS (2014) Evaluating convergence of reduced order models using nonlinear normal modes. Presented at the 32nd international modal analysis conference (IMAC XXXII), Orlando
18. Kuether RJ, Deaner BJ, Hollkamp JJ, Allen MS (2014) Evaluation of geometrically nonlinear reduced order models with nonlinear normal modes. AIAA J (submitted)
19. Peeters M, Kerschen G, Golinval JC (2011) Dynamic testing of nonlinear vibrating structures using nonlinear normal modes. J Sound Vib 330:486–509
20. Schoneman JD, Allen MS, Kuether RJ (2014) Relationships between nonlinear normal modes and response to random inputs. Presented at the 5th AIAA/ASME/ASCE/AHS/SC structures, structural dynamics, and materials conference, National Harbor
21. Kuether RJ, Allen MS (2014) A numerical approach to directly compute nonlinear normal modes of geometrically nonlinear finite element models. Mech Syst Signal Process 46:1–15
22. O'Hara PJ, Hollkamp JJ (2014) Modeling vibratory damage with reduced-order models and the generalized finite element method. J Sound Vib 333:6637–6650
23. Ehrhardt D, Harris R, Allen M (2014) Numerical and experimental determination of nonlinear normal modes of a circular perforated plate. In: De Clerck J (ed) Topics in modal analysis I, volume 7. Springer, Cham, pp 239–251
24. Peeters M, Kerschen G, Golinval JC (2011) Modal testing of nonlinear vibrating structures based on nonlinear normal modes: experimental demonstration. Mech Syst Signal Process 25:1227–1247
25. Zapico-Valle JL, García-Diéguez M, Alonso-Camblor R (2013) Nonlinear modal identification of a steel frame. Eng Struct 56:246–259
26. Ardeh HA, Allen MS (2013) Investigating cases of jump phenomena in a nonlinear oscillatory system. Presented at the 31st international modal analysis conference (IMAC XXXI), Garden Grove
27. Peeters M, Viguié R, Sérandour G, Kerschen G, Golinval JC (2009) Nonlinear normal modes, Part II: toward a practical computation using numerical continuation techniques. Mech Syst Signal Process 23:195–216
28. George TJ, Seidt J, Herman Shen MH, Nicholas T, Cross CJ (2004) Development of a novel vibration-based fatigue testing methodology. Int J Fatigue 26:477–486

Chapter 34
Model Order Reduction of Nonlinear Euler-Bernoulli Beam

Shahab Ilbeigi and David Chelidze

Abstract Numerical simulations of large-scale models of complex systems are essential to modern research and development. However these simulations are also problematic by requiring excessive computational resources and large data storage. High fidelity reduced order models (ROMs) can be used to overcome these difficulties, but are hard to develop and test. A new framework for identifying subspaces suitable for ROM development has been recently proposed. This framework is based on two new concepts: (1) *dynamic consistency* which indicates how well does the ROM preserve the dynamical properties of the full-scale model; and (2) *subspace robustness* which indicates the suitability of ROM for a range of initial conditions, forcing amplitudes, and system parameters. This framework has been tested on relatively low-dimensional systems; however, its feasibility for more complex systems is still unexplored.

A 58 degree-of-freedom fixed-fixed nonlinear Euler-Bernoulli beam is studied, where large-amplitude forcing introduces geometrical nonlinearities. The responses of the beam subjected to both harmonic and random loads are obtained using finite difference method. The ROM subspaces are identified using the framework with both Proper Orthogonal Decomposition (POD) and Smooth Orthogonal Decomposition (SOD). POD- and SOD-based ROMs are then compared and fidelity of the new framework is evaluated.

Keywords Model order reduction • Dynamic consistency • Subspace robustness • Geometrical nonlinearity • Proper and smooth orthogonal decomposition

34.1 Introduction

Even with today's advances in computing technologies, long-time simulations of complex systems (e.g., molecular/multi-body/computational fluid dynamics, rationale drug template design or large-scale structural finite element models) are difficult. Such large- scale models can be unburdened of unnecessary computations using reduced order models (ROMs) [1]. However, not all ROMs are faithful. A faithful ROM is valid over a range of system parameters, initial conditions and input functions [1, 2].

There are different methods for model reduction of linear and nonlinear systems. For linear systems, these methods are well established. Such methods include Galerkin reduction using linear normal modes (LNMs) [3, 4] Krylov subspaces projection [5], and proper orthogonal decomposition (POD, also known as, singular value decomposition, principal component analysis, and Karhunen-Loeve Decomposition) [6–12]. However, in most cases the complexity of the system is caused by its nonlinearity. Many techniques are proposed for reduction of nonlinear models. These techniques include, but are not limited to, inertial manifold approximation, linearization about the equilibrium point [13, 14], center manifold theory [15, 16], nonlinear normal modes (NNMs) [17–20], and POD.

Commonly used methodologies for model reduction of nonlinear systems can be categorized in two groups. In the first method, the nonlinear manifold is approximated using NNMs [17–20]. Although the nonlinear manifold has the lowest dimension needed, it is limited with the difficulty of the analytical calculations used in the approximation. Besides, the nonlinear manifold identified for a given energy may be different for other energy levels [1].

In the second method, the nonlinear system can be projected onto a linear subspace spanned by a set of appropriate basis functions [6, 11]. These bases can be identified by proper orthogonal modes (POMs) and smooth orthogonal modes (SOMs) in POD and SOD methods, respectively. By definition, POMs are limited to be orthogonal; hence, they capture the nonlinear manifold by a higher dimensional linear subspace than SOMs [1]. Furthermore, in contrast to POD, SOD considers

S. Ilbeigi • D. Chelidze (✉)
Department of Mechanical, Industrial and Systems Engineering, University of Rhode Island, Kingston, RI 02881, USA
e-mail: chelidze@egr.uri.edu

G. Kerschen (ed.), *Nonlinear Dynamics, Volume 1*, Conference Proceedings of the Society for Experimental Mechanics Series, DOI 10.1007/978-3-319-15221-9_34

both spatial and temporal characteristics of the data set. In particular, SOD identifies coordinates (smooth orthogonal coordinates- or SOCs) that have both minimal temporal roughness and maximal spatial variance. Therefore, SOD obtains the smoothest low dimensional approximation of a high dimensional system.

The fidelity of a ROM can be investigated by raising two questions: (1) "How well does it approximate the full-scale system?" and (2) "Is it valid over a wide range of system's level of energy?" A recently developed framework [1, 2] addresses these questions. This framework is based on two concepts: dynamical consistency and subspace robustness. These concepts were used to estimate the lowest dimensional subspaces suitable for ROM for both POD and SOD. It was shown that using SOD, the dynamics of a nonlinear system can be captured in a lower dimensional ROM. However, the studied system was relatively low-dimensional and thus the fidelity of the framework as well as the performance of the SOD are needed to be explored for more complex nonlinear systems.

To this aim, a nonlinear Euler-Bernoulli beam is modeled based on the explicit finite difference scheme. The geometrically nonlinear regime, which governs this system, has an interesting full-scale model solution with high-amplitude transverse and low-amplitude axial vibrations. Thus, its full state-space model is a combination of coordinates having very low and high variances. The ability of the POD in capturing the dynamics of this system is in question since it only looks at these variances. Using the new framework, the ROM subspaces are identified for both POD and SOD and their performances are contrasted. Prior to doing that, a brief review on nonlinear model reduction theory, dynamical consistency and subspace robustness is provided.

34.2 Nonlinear Model Reduction

Full-scale model of a deterministic dynamical system has the following form:

$$\dot{y} = f\,(y, t) \tag{34.1}$$

where $y \in \mathbb{R}^n$ is a dynamic state variable, $f : \mathbb{R}^n \times \mathbb{R} \to \mathbb{R}^n$ is some nonlinear flow, $t \in \mathbb{R}$ is time, and $n \in \mathbb{N}$ is usually twice the number of the system's degrees-of-freedom. The state variable trajectories data can be arranged in the matrix $Y = [y_1,\ y_2,\ \ldots,\ y_n] \in \mathbb{R}^{m \times n}$. A basis for Y can be calculated using either POD or SOD using the procedure explained in [1]. These most dominant k-dimensional bases are arranged in the matrix $P_k = [e_1,\ e_1, \ldots,\ e_k]$. Now, using a coordinate transformation of $q = P_k\ Y \in \mathbb{R}^n$ to give the reduced state variable, the corresponding ROM is:

$$\dot{q} = P_k^{\dagger} f\,(P_k\ q, t) \tag{34.2}$$

where $(.)^{\dagger}$ indicates the pseudoinverse of (.).

34.3 Model Reduction Subspace Selection

The appropriate subspace for model reduction can be selected based on a newly developed criterion [1]. This criterion quantifies two concepts: dynamical consistency – which demonstrates how well the linear subspace embeds the nonlinear manifold – and subspace robustness –which explains the sensitivity of the subspace to changes in system's level of energy. Here, these concepts are briefly reviewed. A more complete description can be found in [1].

34.3.1 Dynamical Consistency

The idea behind dynamical consistency is based on the unfolding of an attractor used in delay coordinate embedding [21] and can be determined by the premise behind a method of false nearest neighbors [22]. A linear subspace used for model reduction is said to be dynamically consistent if the resultant trajectories are deterministic and smooth. The metric for dynamical consistency is defined as the ratio of the number of false nearest neighbors (FNN) over the total number of nearest neighbor pairs in a particular k-dimensional subspace:

$$\zeta^k = 1 - \frac{N_{fnn}^k}{N_{nn}} \tag{34.3}$$

where N_{fnn}^{k} is the estimated number of FNNs in k-dimensional subspace, and N_{nn} is the total number of nearest neighbor pairs used in the estimation. If ζ^{k} is close to unity, then that k-dimensional subspace is dynamically consistent.

34.3.2 Subspace Robustness

Unlike linear normal mode subspaces that are unique and insensitive to the level of energy, the robustness of the subspaces obtained by data analysis methods should be determined. In order to quantify the subspace robustness, the basis vectors, which span the k-dimensional subspace for s systems with different level of energy, form a matrix $\mathbf{S} \in \mathbb{R}^{n \times ks}$. Then, the corresponding subspace robustness γ_{s}^{k} is given by the following expression:

$$\gamma_{s}^{k} = \left| 1 - \frac{4}{\pi} \arctan \sqrt{\frac{\sum_{i=k+1}^{n} \sigma_{i}^{2}}{\sum_{i=1}^{k} \sigma_{i}^{2}}} \right| \tag{34.4}$$

where σ_{i} ' s are proper orthogonal values of the matrix $\mathbf{S}$.

34.4 Nonlinear Euler-Bernoulli Beam

In this work, a ROM for vibrations of a high-dimensional nonlinear Euler-Bernoulli beam is investigated. A physical beam model is shown in Fig. 34.1. The mathematical model of this system is described in classical books devoted to spatial objects dynamics [23, 24]; here only the governing differential equations are given:

$$\begin{aligned} &\rho A \frac{\partial^2 u}{\partial t^2} + d_2 \frac{\partial u}{\partial t} - EA \left(\frac{\partial^2 u}{\partial x^2} + \frac{\partial w}{\partial x} \frac{\partial^2 w}{\partial x^2} \right) = 0 \\ &\rho A \frac{\partial^2 w}{\partial t^2} + EI \frac{\partial^4 w}{\partial x^4} + d_1 \frac{\partial w}{\partial t} - EA \left(\frac{\partial u}{\partial x} \frac{\partial^2 w}{\partial x^2} + \frac{\partial^2 u}{\partial x^2} \frac{\partial w}{\partial x} + \frac{3}{2} \frac{\partial^2 w}{\partial x^2} \left(\frac{\partial w}{\partial x} \right)^2 \right) = q\,(x,\ t)\,, \end{aligned} \tag{34.5}$$

where ρ is viscosity, E is Young's modulus of elasticity, A is the area of beam section, I is moment of inertia, d_1 and d_2 are damping coefficients, and $q(x, t)$ is transverse forcing. Also, $u(x, t)$ and $w(x, t)$ denote for axial and transverse vibrations, respectively. The beam under investigation is fixed-fixed at its ends with the following boundary conditions that are attached to Eq. (34.5):

$$w\,(0,\ t) = w\,(a,\ t) = u\,(0,\ t) = u\,(a,\ t) = \left. \frac{\partial w\,(x,\ t)}{\partial x} \right|_{x=0} = \left. \frac{\partial w\,(x,\ t)}{\partial x} \right|_{x=a} = 0 \tag{34.6}$$

In this case, both transverse and longitudinal displacements at beam's ends, as well as tangents to the slope at its ends are equal to zero. Besides, the following initial conditions are considered for the beam:

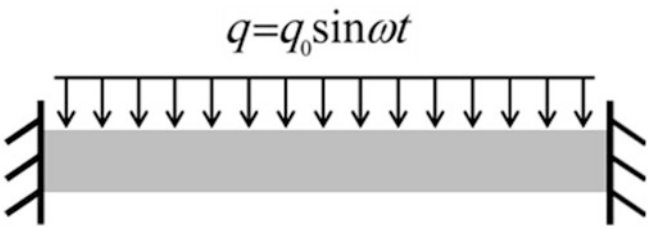

Fig. 34.1 Model of the nonlinear Euler-Bernoulli beam

$$
\begin{aligned}
w(x,\ t) &= w_0(x,\ t) \\
u(x,\ t) &= u_0(x,\ t) \\
\frac{\partial w(x,\ t)}{\partial t} &= \dot{w}_0(x,\ t) \\
\frac{\partial u(x,\ t)}{\partial t} &= \dot{u}_0(x,\ t)
\end{aligned}
\tag{34.7}
$$

For small transverse vibrations, the two equations given in Eq. (34.5) reduce to one linear equation, which only accounts for transverse vibrations. In that case, axial vibrations are very small and negligible. For large deflections, axial displacements are taken into account, which introduces geometrical nonlinearity to the system. There is no exact analytical solution for the nonlinear system; however, a finite-dimensional model of the system can be solved numerically using finite difference method. The method is described in next section.

34.4.1 Full-Dimensional System Model

The full-dimensional state-space model of the system in matrix form can be obtained using FDM. The space coordinate of the beam, as shown in Fig. 34.2, is meshed using $M + 2$ nodes. The parameters u_i and w_i indicate axial and transverse displacements of the i-th node. The space derivatives in Eq. (34.5) are substituted by their second order finite difference approximation $O(\Delta x^2)$ which are given as follows:

$$
\begin{aligned}
&\frac{\partial u}{\partial x} = \frac{u_{i+1} - u_{i-1}}{2\ \Delta x},\ \frac{\partial^2 u}{\partial x^2} = \frac{u_{i+1} - 2u_i + u_{i-1}}{\Delta x^2},\ \frac{\partial w}{\partial x} = \frac{w_{i+1} - w_{i-1}}{2\ \Delta x},\ \frac{\partial^2 w}{\partial x^2} = \frac{w_{i+1} - 2w_i + w_{i-1}}{\Delta x^2}, \\
&\frac{\partial^4 w}{\partial x^4} = \frac{w_{i+2} - 4w_{i+1} + 6w_i - 4w_{i-1} - w_{i-2}}{\Delta x^4},
\end{aligned}
\tag{34.8}
$$

where Δx is space mesh size. After simplifying, this leads to the following systems of ordinary differential equations:

$$
\begin{cases}
\ddot{w}_i + \alpha\ \dot{w}_i = H_i(x,t) \\
\ddot{u}_i + \beta\ \dot{u}_i = G_i(x,t)
\end{cases}
\quad \text{for } i = 1,\ 2,\ \ldots,\ M,
\tag{34.9}
$$

where $\alpha = \frac{d_1}{\rho A}$ and $\beta = \frac{d_2}{\rho A}$.

The boundary and initial conditions can be treated using two fictitious space layers, which are illustrated in Fig. 34.2. Therefore, using finite difference approximation one obtain:

$$
w_i(0) = w_{i0};\ \dot{w}_i(0) = \dot{w}_{i0};\ u_i(0) = u_{i0};\ \dot{u}_i(0) = \dot{u}_{i0}.
\tag{34.10}
$$

By introducing $y_i = w_i,\ y_{M+i} = u_i,\ y_{2M+i} = \dot{w}_i$ for $i = 1, \ldots, M$, the system can be written as $4M$-dimensional first-order equation in $y = \left[w_i\ u_i\ \dot{w}_i\ \dot{u}_i \right]^T \in \mathbb{R}^n,\ n = 4M$ as:

$$
\dot{\mathbf{y}} = \mathbf{A}\mathbf{y} + \mathbf{f}(y,t)
\tag{34.11}
$$

where $\mathbf{f}(y,t) = \left[\mathbf{0}_{1\times 2M}\ H_1(x,y,t)\ \ldots\ H_M(x,y,t)\ G_1(x,y,t)\ \ldots\ G_M(x,y,t) \right]^T \in \mathbb{R}^n$ and $\mathbf{A} = \begin{bmatrix} \mathbf{0}\ \mathbf{0} & \mathbf{I} & \mathbf{0} \\ \mathbf{0}\ \mathbf{0} & \mathbf{0} & \mathbf{I} \\ \mathbf{0}\ \mathbf{0} & -\alpha\mathbf{I} & \mathbf{0} \\ \mathbf{0}\ \mathbf{0} & \mathbf{0} & -\beta\mathbf{I} \end{bmatrix}$,

where $\mathbf{0} \in \mathbb{R}^{M\times M}$ is a zero matrix and $\mathbf{I} \in \mathbb{R}^{M\times M}$ is an identity matrix.

Equation (34.11) represents the full-dimensional mathematical model of the system. It is solved via Adams-Bashforth method with the accuracy of $O(\Delta t^4)$, where Δt is the time step. The matrix form of POD-based ROM or SOD-based ROM can be expressed as:

$$
\dot{\mathbf{q}} = \mathbf{P}_k{}^T \mathbf{A}\ \mathbf{P}_k\ \mathbf{q} + \mathbf{P}_k{}^T \mathbf{f}(y,t)
\tag{34.12}
$$

where $\mathbf{P}_k$ could be the most dominant k-dimensional POMs or the most dominant k-dimensional SOMs.

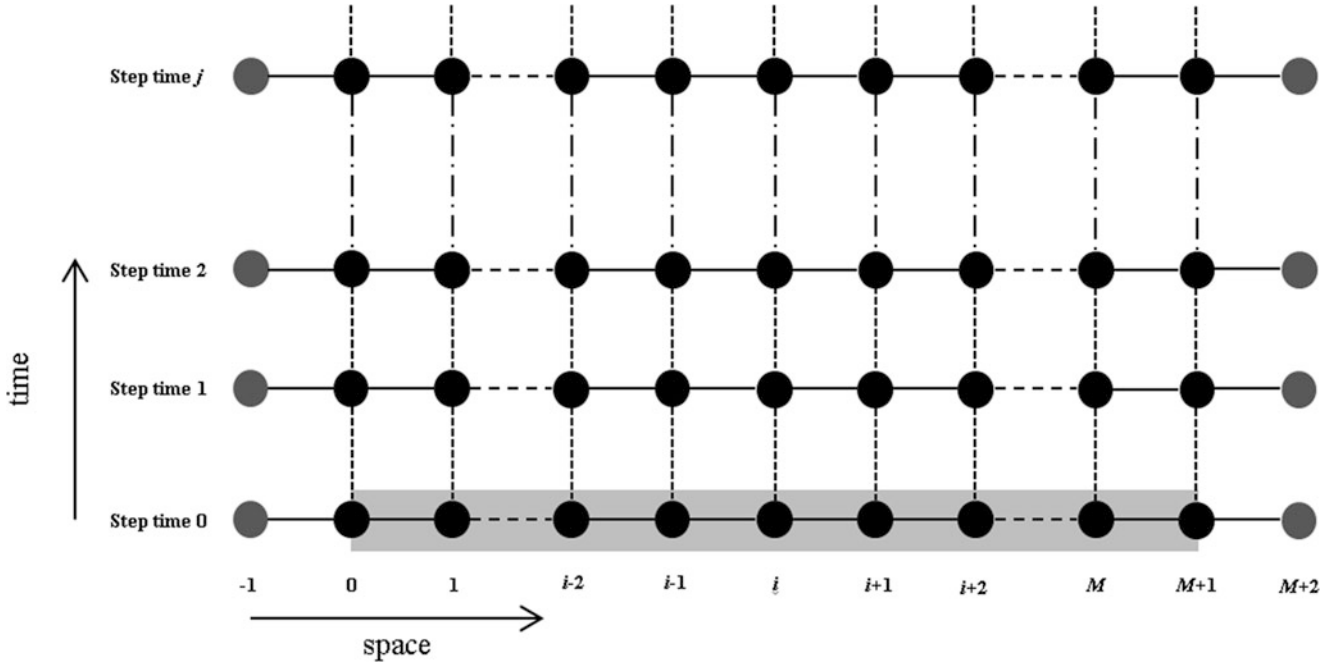

Fig. 34.2 Numerical scheme

34.5 Results and Discussion

34.5.1 Full-Dimensional Model

The space coordinate of the beam is meshed using $M = 29$ nodes. Thus, the full state space model is 116-dimensional, which means that 116 equations are needed to be solved simultaneously. The beam is assumed to be made of aluminum with density $\rho = 2710\ \text{kg/m}^3$, Young's Modulus $E = 69$ Gpa, dissipation ratios $\alpha = 1.845$ and $\beta = 0$. The beam's dimensions are $0.01\ \text{m} \times 0.01\ \text{m} \times 1\ \text{m}$. A harmonic transverse force $q = q_0 \sin \omega t$ is applied to the beam. For forcing frequency $\omega = 200$ Hz, and the parameter q_0 is used as a bifurcation parameter. The bifurcation diagram for the transverse vibrations of the beam's middle point is shown in Fig. 34.3. To obtain this diagram, the first 200 cycles of harmonic forcing are not used to eliminate transient. The next 200 cycles are then used in the calculations. The bifurcation diagram starts at $q_0 = 1$ with zero initial conditions. As the amplitude of forcing increases, new trajectories follow the previous solutions. A rich dynamical behavior, which includes chaotic response, can be observed in Fig. 34.3. For instance, the solution (transverse vibrations of the middle point) for some values of q_0 obtained using the full-dimensional model is depicted in Fig. 34.4.

The axial vibration of the most far end nodes has larger magnitude than other nodes. The phase space portrait of the most far left node, for the same values as in Fig. 34.4, are depicted in Fig. 34.5. It can be seen that their magnitudes are much smaller than those of the transverse vibrations. Therefore, the full-dimensional state space vector space has big variances in the coordinates corresponding to the transverse vibrations, but small variances for those corresponding to axial vibrations. POD-based MOR only considers the variances in configuration space while SOD-based MOR not only considers the spatial variances but also looks at the temporal characteristics of the trajectories in the full-dimensional state-space model. Thus, the authors expect SOD to capture the dynamic of the system in a lower-dimensional subspace. In next section, the results of both POD-and SOD-based MOR are discussed.

34.5.2 Reduced Order Model

To identify the modal structure using both POD and SOD, the beam is excited for a comparably long time by an appropriately filtered random forcing. This guarantees that nearly all the state space is explored and all dominant frequencies of the beam are covered. A set of 30 randomly driven trajectory data is used to estimate the subspaces robustness using the

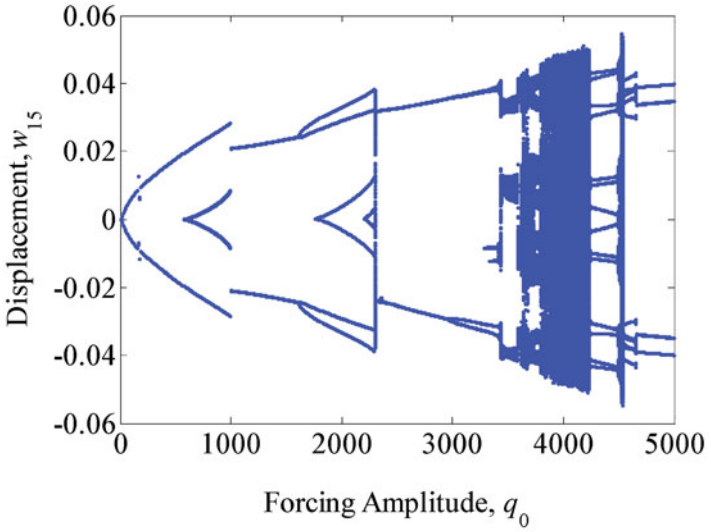

Fig. 34.3 Bifurcation diagram

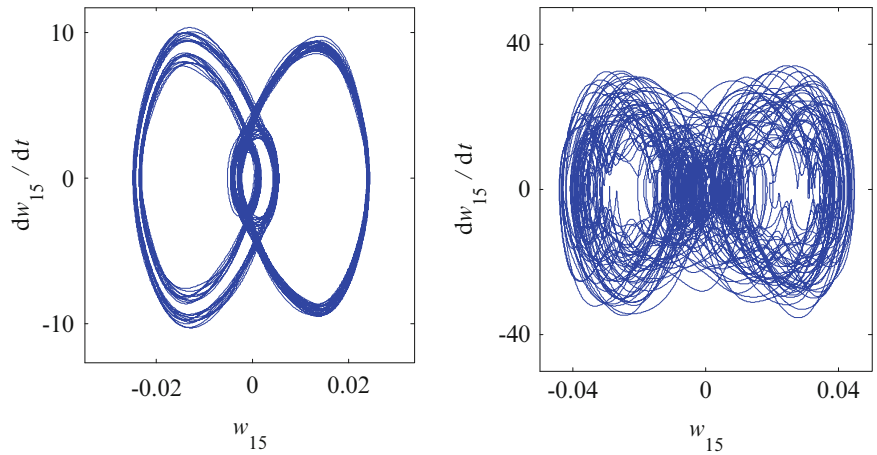

Fig. 34.4 transverse vibrations of the middle of beam: $q_0 = 760$ (*left*), $q_0 = 3900$ (*right*)

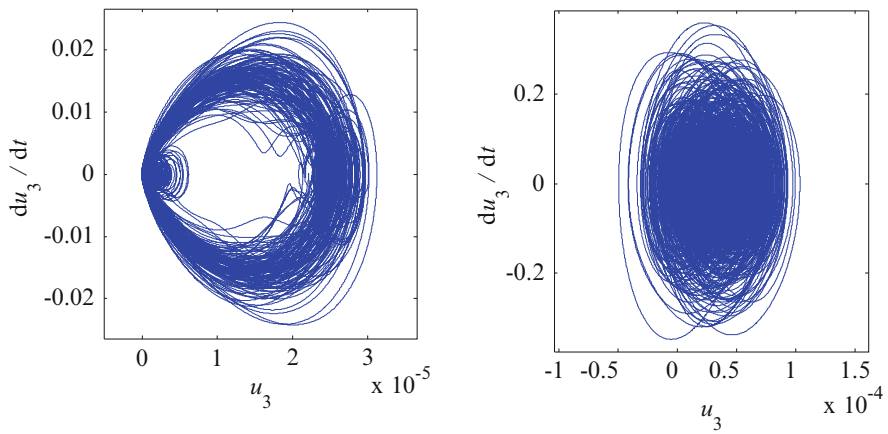

Fig. 34.5 axial vibrations of the most far left node on the beam: $q_0 = 760$ (*left*), $q_0 = 3900$ (*right*)

aforementioned procedure. Figure 34.6 illustrates the subspace robustness for all k-dimensional subspaces of the full-scale model. Each quantity in this figure gives a measure of sensitivity of its corresponding k-dimensional subspace to different forcing conditions. According to this figure, for $k \geq 13$, SOD subspace robustness is close to unity. The POD subspace robustness is not monotonic. It reaches unity at $k = 58$, however, suddenly drops by increasing the number of the modes.

The dynamical consistency is shown in Fig. 34.7 for both POD- and SOD-based ROMs. To estimate the dynamical consistency, the k-dimensional subspaces obtained from randomly driven data are used to project full dimensional space

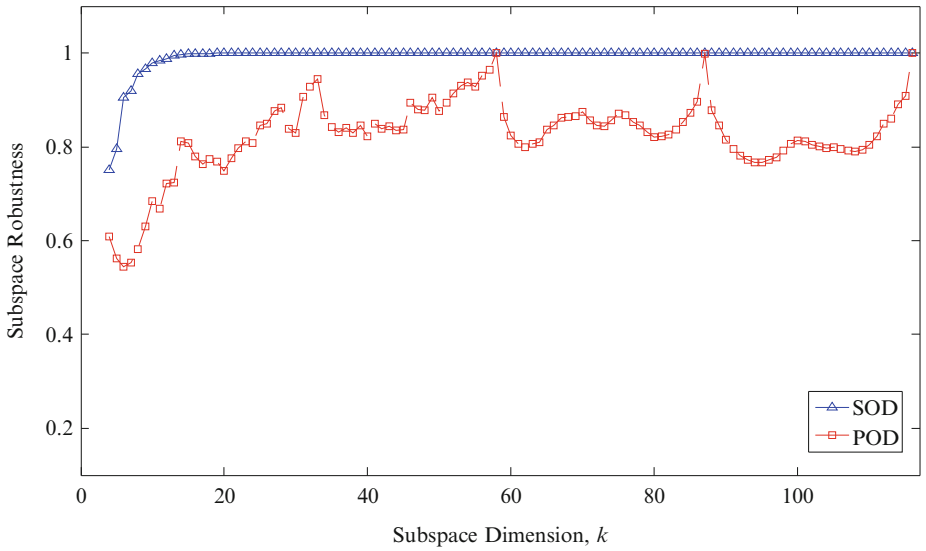

Fig. 34.6 Subspace robustness for randomly driven system

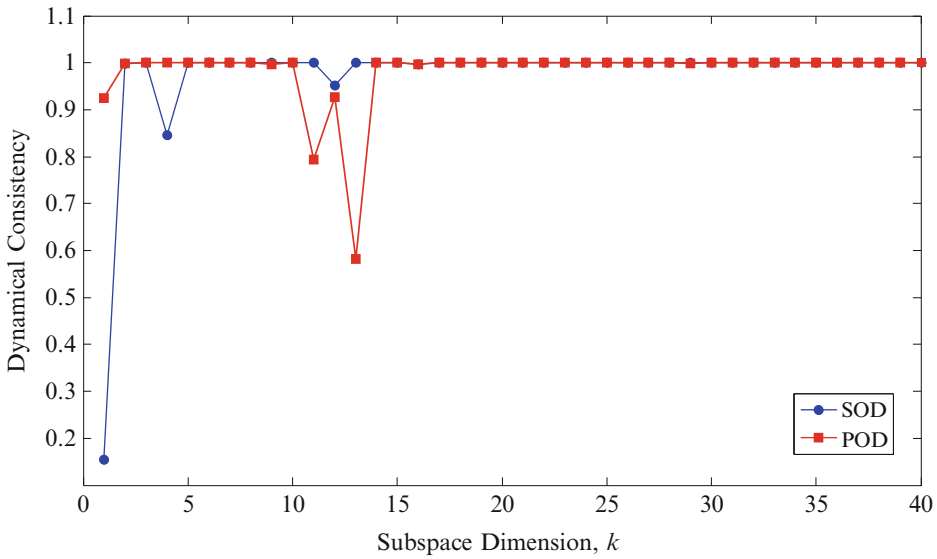

Fig. 34.7 Dynamical consistency

of harmonic data. This figure demonstrates that results for dynamical consistency of POD and SOD are similar, except for $k = 4,\ 11$ and 13, where POD subspaces are more consistent.

Now, the extracted modes can be used for building the POD- and SOD-based ROMs to simulate the solution of the full-scale model under harmonic forcing. The lowest dimensional SOD-based ROM, which is stable, has the dimension 47. Figure 34.8 depicts the results for POD- and SOD-based ROMs for harmonic forcing with $q_0 = 10$. Comparison with the full-scale model trajectories shows that POD-based ROM is not stable. To get a stable POD-based ROM, it has to be at least 65-dimensional.

In Fig. 34.9, the POD- and SOD-based ROM, obtained for a range of forcing amplitudes, are compared to full-scale model trajectories. It can be seen that SOD-based ROMs capture dynamic in a lower dimension. A 49-dimensional SOD-based ROM is able to reproduce good results while POD-based ROM needs at least 65 dimensions for that. POD-based ROM with dimension lower than 65 are not stable. Some SOD-based ROM with dimension lower than 49 had fairly good correlation with the full-scale model, however, failed after very few cycles of harmonic forcing.

The instability of lower dimensional ROMs is most likely to be due to the explicit nature of the FDM, which was used for solving both full-scale and reduced order models. However, another possibility, which could explain this problem, is the weak coupling between axial and transverse displacement of the nodes. This results in small magnitude of the data corresponding to state variables of the axial nodes in the full dimensional state space. Therefore, it might be difficult for both POD and SOD to identify the corresponding subspaces of these data properly. Nevertheless, SOD was shown to have a better performance in identifying these subspaces.

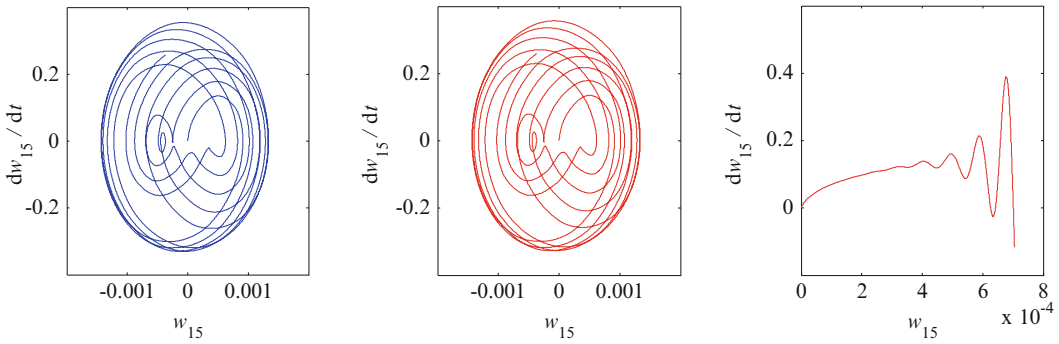

Fig. 34.8 Full-scale and ROM trajectories for periodic loading with $q_0 = 10$ and $\omega = 200$ Hz; Full-scale model (*left*), random SOD- based ROM (*middle*), random POD- based ROM (*right*)

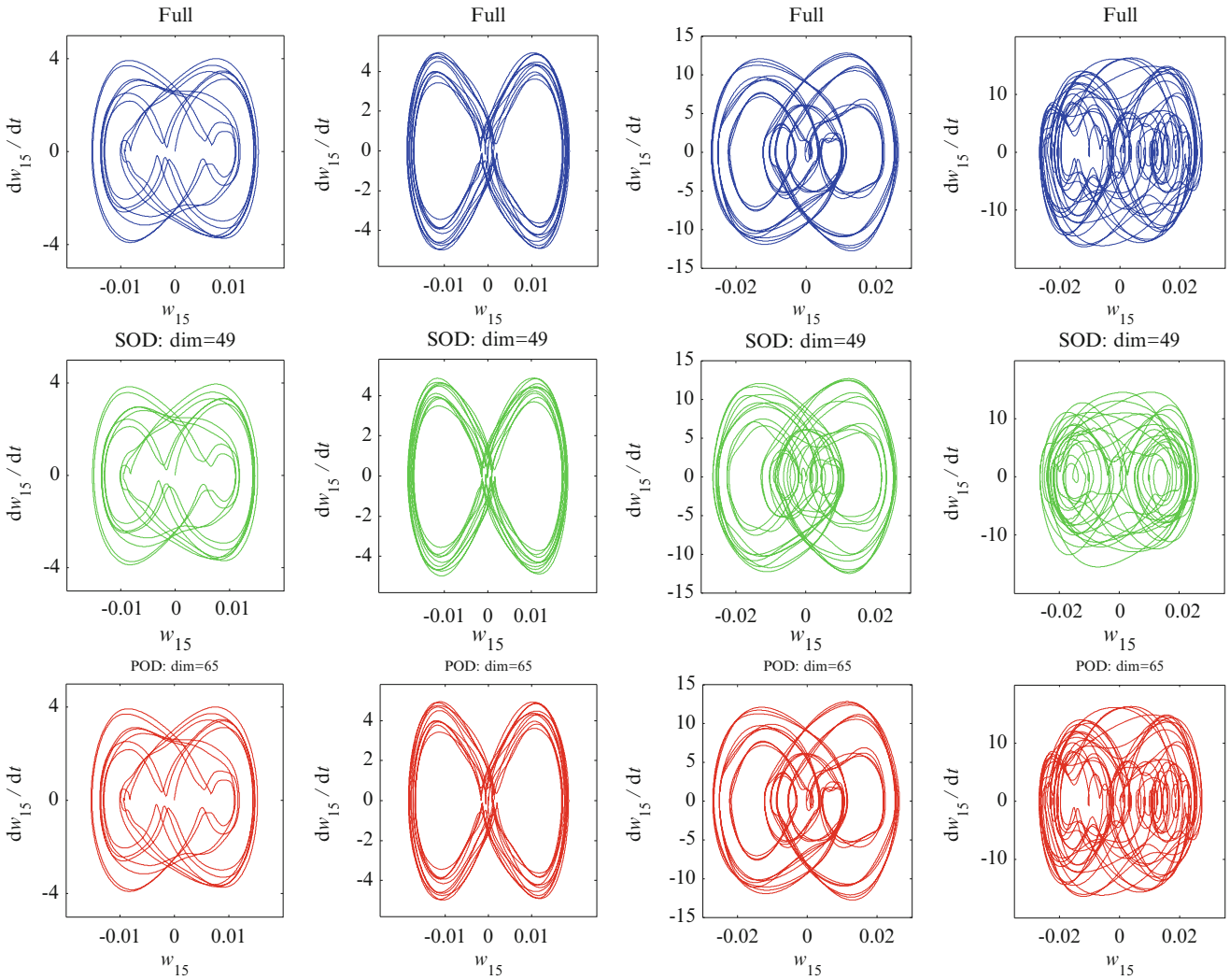

Fig. 34.9 POD- and SOD-based ROMs for $\omega = 200$ Hz and different forcing amplitudes: $f = 300$ (column 1), $f = 500$ (column 2), $f = 800$ (column 3) and $f = 1000$ (column 4)

34.6 Conclusion

The full state-space model of a nonlinear Euler-Bernoulli beam was obtained using FDM. POD and SOD subspaces for this system were obtained and their dynamical consistency and subspace robustness were evaluated. SOD subspaces were shown to be more robust than those of POD. Obtained subspaces were also used for building the ROMs of the system. ROM simulations showed that SOD-based ROM captures the dynamic of the full-scale system in a relatively lower dimensional space.

Although SOD had a better performance than POD, our effort for obtaining lower dimensional models failed. As discussed, that could be due to either instability of the advised numerical scheme or incapability of both POD and SOD. This problem should be addressed with different systems, where couplings between different coordinates are weak while either an analytical-based numerical method or implicit numerical scheme is available. This system would have geometric nonlinearity and its model can be solved using implicit methods. An example of such a system is a grid of masses, connected by springs and dampers, with two degree of freedom for each mass.

Acknowledgement The authors would like to thank National Science Foundation under Grant No. 1100031.

References

1. Chelidze D (2014) Identifying robust subspaces for dynamically consistent reduced-order models. Nonlinear Dyn 2:123–130
2. Segala DB, Chelidze D (2013) Robust and dynamically consistent reduced order models. In: ASME 2013 international mechanical engineering congress and exposition. American Society of Mechanical Engineers, pp V04BT04A010–V04BT04A010
3. Foias C, Jolly MS, Kevrekidis IG, Sell GR, Titi ES (1988) On the computation of inertial manifolds. Phys Lett A 131(7):433–436
4. Pesheck E, Pierre C, Shaw SW (2002) A new Galerkin-based approach for accurate non-linear normal modes through invariant manifolds. J Sound Vib 249(5):971–993
5. Feldmann P, Freund RW (1995) Efficient linear circuit analysis by Padé approximation via the Lanczos process. Comput Aid Des Integr Circuit Syst 14(5):639–649
6. Amabili M, Sarkar A, Paıdoussis MP (2003) Reduced-order models for nonlinear vibrations of cylindrical shells via the proper orthogonal decomposition method. J Fluids Struct 18(2):227–250
7. Georgiou I (2005) Advanced proper orthogonal decomposition tools: using reduced order models to identify normal modes of vibration and slow invariant manifolds in the dynamics of planar nonlinear rods. Nonlinear Dyn 41(1–3):69–110
8. Hall K, Thomas J, Dowell E (1999) Reduced-order modelling of unsteady small-disturbance flows using a frequency-domain proper orthogonal decomposition technique. In 37th Aerospace Science Meeting and Exhibit, no. AIAA Paper 99-0655
9. Kerschen G, Golinval JC, Vakakis AF, Bergman LA (2005) The method of proper orthogonal decomposition for dynamical characterization and order reduction of mechanical systems: an overview. Nonlinear Dyn 41(1–3):147–169
10. Rathinam M, Petzold LR (2003) A new look at proper orthogonal decomposition. SIAM J Numer Anal 41(5):1893–1925
11. Smith TR, Moehlis J, Holmes P (2005) Low-dimensional modeling of turbulence using the proper orthogonal decomposition: a tutorial. Nonlinear Dyn 41(1–3):275–307
12. Willcox K, Peraire J (2002) Balanced model reduction via the proper orthogonal decomposition. AIAA J 40(11):2323–2330
13. Phillips JR (2003) Projection-based approaches for model reduction of weakly nonlinear, time-varying systems. IEEE Trans Comput Aid Design Integr Circuits Syst 22(2):171–187
14. Bai Z (2002) Krylov subspace techniques for reduced-order modeling of large-scale dynamical systems. Appl Num Math 43(1):9–44
15. Carr J (1981) Applications of centre manifold theory. Springer-Verlag
16. Guckenheimer J, Holmes P (1983) Nonlinear oscillations, dynamical systems, and bifurcations of vector fields, vol 42. Springer, New York
17. Shaw S, Pierre C (1991) Non-linear normal modes and invariant manifolds. J Sound Vib 150(1):170–173
18. Shaw SW, Pierre C (1993) Normal modes for non-linear vibratory systems. J Sound Vib 164(1):85–124
19. Shaw SW, Pierre C (1994) Normal modes of vibration for non-linear continuous systems. J Sound Vib 169(3):319–347
20. Vakakis AF (1997) Non-linear normal modes (NNMs) and their applications in vibration theory: an overview. Mech Syst Signal Process 11(1):3–22
21. Sauer T, Yorke JA, Casdagli M (1991) Embedology. J Stat Phys 65(3–4):579–616
22. Kennel MB, Brown R, Abarbanel HD (1992) Determining embedding dimension for phase-space reconstruction using a geometrical construction. Phys Rev A 45(6):3403
23. Volmir AS (1974) The nonlinear dynamics of plates and shells. No FTD-HC-23-851-74. Foreign Technology DIV Wright-Patterson AFB OH
24. Virgin LN (2007) Vibration of axially loaded structures, 393rd edn. Cambridge University Press, New York

Chapter 35
Identification of Dynamic Nonlinearities of Bolted Structures Using Strain Analysis

D. Di Maio

Abstract This work investigates the identification of the nonlinear behaviour of bolted structures through experimental and numerical analysis. Friction joints (especially bolted joints) generate nonlinear dynamic behaviours in a bolted assembled structure subject to dynamic loadings (especially high level vibrations) due to energy dissipation. The causes of nonlinearities are multiple and the ones related to joints will be researched in this piece of work. Although numerical simulation of nonlinear dynamic behaviour is complex, Finite Element models of a bolted flange will be used for strain analysis in order to develop a strategy for test planning of nonlinear vibration testing. Experimental tests and parameters that can be used to identify the joint nonlinearities will be used for developing correlation methods.

Keywords Modal testing • Joints • Nonlinearity • Strain

35.1 Introduction

Bolted assemblies are widely used in the mechanical industry. Understanding their dynamic behaviour is critical in a design process. Most of bolted assemblies used in engines (especially aircraft gas turbines) are subject to high levels of vibrations. Then, it is necessary to understand how the structure behaves under such loading conditions. Both numerical and experimental modal analysis have been well known and used for decades in the mechanical industries [1], allowing to predict the structure response subject to dynamic loadings. However, most of those analyses are performed under linear conditions, which can be applied in most of the cases. But in the case of bolted assemblies, the friction joint dynamic behaviour generally can induce some nonlinearities in the structure response from a certain level of vibration. Then, the classic linear approach cannot be used anymore.

A literature review [2] has been achieved in order to give an insight of the dynamic nonlinearities of bolted structures from an experimental, analytical and numerical points of view. First, it is explained the main physical phenomena behind the joint nonlinearities. The main factors that lead to this nonlinear behaviour are the friction phenomena and the clapping (micro-impacts) that can occur in case of looseness in the joint according to R.A. Ibrahim and C.L. Pettit [3]. The former cause comes from the sliding and sticking states in the contact surface area due to a complex shear stress field and a non-uniform contact pressure applied by the bolts as it has been shown by Yaxin Song, D. Michael McFarland, Lawrence A. Bergman, and Alexander F. Vakakis [4]. The localised zones being in sliding state are called microslip zones. They induce coulomb friction energy dissipation, resulting in force-displacement hysteresis loops, as it has been shown by S. Bograd, P. Reuss, A. Schmidt, L. Gaul, M. Mayer [5]. This energy dissipation has an effect on the damping in the structure dynamics. Indeed, two forms of damping can be identified: the structural damping due to the material characteristics, and the dry friction damping due to the energy dissipation in the bolted joint. For simple Single Degrees Of Freedom (SDOF) systems, this friction damping increases with an increasing level of vibration (or excitation force). The stiffness of the structure is also affected and decreases with an increasing level of vibrations. These affect the Frequency Response Function (FRF) of the system.

As previously said, in a design process, it is critical to predict the dynamic response of an assembled structure. However, even nowadays, bolted surfaces are assumed to be glued in most FEM, which is an assumption only valid for low levels of vibrations. Many analytical and numerical models have been developed to predict the nonlinear dynamical behaviour of bolted assembled systems and are referenced in the literature review. Thanks to the development of FEA and computational capabilities, it is today possible to implement the joint characteristics in a numerical model. There are several ways to do

D. Di Maio (✉)
University of Bristol, Bristol, UK
e-mail: dario.dimaio@bristol.ac.uk

G. Kerschen (ed.), *Nonlinear Dynamics, Volume 1*, Conference Proceedings of the Society for Experimental Mechanics Series, DOI 10.1007/978-3-319-15221-9_35

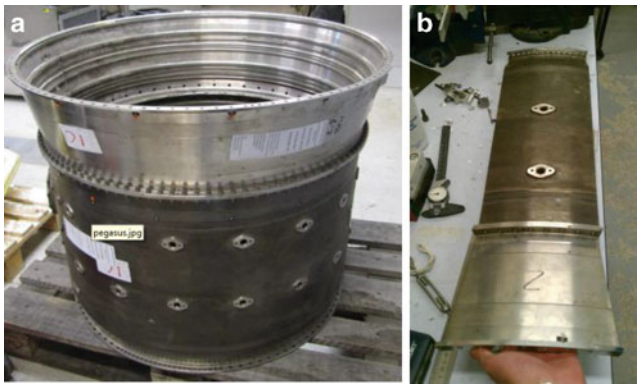

Fig. 35.1 (**a**) Combustion Chamber Outer Casing (CCOC) and High Pressure Chamber (HPC) from a Rolls-Royce engine (*Left*) – (**b**) CCOC-HPC assembly cut section (*Right*)

so, some are more accurate although there are more computational consuming and some are easier to implement and faster to solve, but generally less accurate. A first method consists in implementing contact elements such as Iwan elements [6] or Valanis models [7] usually composed of springs and coulomb friction elements are able to predict an accurate response of a bolted structure, but they are very computational consuming. Another technique developed by H. Ahmadian, M. Ebrahimi, J.E. Mottershead and M.I. Friswell [8] consists in inserting a thin-layer of nonlinear elements between the two surfaces in contact. It has the advantage of solving the numerical model faster, but it requires a complex parameters updating with experimental data.

In modal analysis, a correlation between experimental and numerical data is often required to update the FEM, even in linear conditions (low vibration levels). Indeed, many parameters have a great sensitivity on the frequency response, such as the structural damping and the joint parameters (bolt preload, friction coefficient, etc.). An algorithm is generally used as an optimization function to update the numerical FRF (generally obtained with a Harmonic Balance Method) and the experimental FRF, as it has been shown by Marc Böswald and Michael Link [9].

From an experimental point of view, most papers about bolted joint nonlinearities are about single degrees of freedom systems which require a minimum amount of sensors, having a limited residual effect on the structure response. However, for industrial structures, which can have a large number of degrees of freedom, specific experimental techniques must be used to avoid a change in behaviour too important due to sensors glued to the structure. These techniques, such as laser vibrometer measurements [10] are contactless, avoiding any potential structural perturbation from the measurement material.

In the aerospace industry, many revolution components from the engine are assembled by flange bolted joints which are likely to induce some dynamic nonlinearities as it has been previously explained earlier. For several years, it has become an important research field from the gas turbine industry. Particularly, the nonlinearities caused by contact interactions between engine parts have just begun to be better understood. For example, in this seminar, E. Chatelet proposed a contact area identification process using full-field displacement surface measurements in a simple structure subject to harmonic forcing of different levels [11]. This study focuses on the Combustion Chamber Outer Casing (CCOC) and High Pressure Chamber (HPC) from a Rolls-Royce engine (see Fig. 35.1) which is assembled using a bolted flange. For these complex structures containing a large number of degrees of freedom, the joint nonlinearity is mode dependant, as it has been introduced by C. Schwingshackl, D. Di Maio and I. Sever [12]. That is to say, the nonlinearity can be more or less important regarding the excited mode. The aim of this research is to study this mode dependency of the nonlinearity caused by a bolted flange of a simplified model of an aircraft engine casing section. Then, it is proposed to define some criteria explaining this mode dependency and allowing to define which modes could show the most nonlinearities due to the friction joint dynamics. Both experimental and numerical modal testing methodologies will be proposed. It is further proposed to approach the problem from strain analysis, which is quite a novelty in terms of dynamic nonlinearity study. As few studies have been done using this approach so far, a critical point of view will be made regarding the relevance of this method. It should be possible to assess whether a strain analysis technique is a good indicator of nonlinearity caused by bolted joints.

Some nonlinear studies have already been performed on a section of an CCOC-HPC assembly. However, because of the complex geometry of the actual structure, the modal analysis was not easy to correlate with a numerical model. Thus, it will attempt to reproduce a simplified cut section of the CCOC-HOC assembly so that correlations can be easily made between experimental and numerical data. This will be the structure studied in this project. The research methodology has been proposed during the research proposal stage [13]. The methodology presented in the present document has been improved compared to the first proposal. As previously said, both numerical and experimental investigations are performed in this project. This is why, the research methodology is divided into two main axis:

- The numerical model of the structure
- The experimental investigation of the structure

A correlation between the numerical and experimental models is attempted during the whole process. Figure 35.2 a diagram of the main process of this research project. This aims to give an insight of the global methodology. Each stage will then be further developed in the next chapters.

35.2 Structure Design (CAD) and Manufacturing

The aim of the design process was to simplify the CCOC-HOC cut section Fig. 35.1b with the following assumptions:

- The curvature of the casings are assumed negligible
- Thicknesses of left and right parts are constant
- All ribs or equivalent are removed
- There is only the friction plan for the joint positioning (internal cylinder of the right plate removed)
- The compressor radius is considered constant (which leads to a flatness between left and right plate and a constant width for the left plate)

The CAD of the simplified flange structure can be seen in Fig. 35.3a. The structure needs to be made of stainless steel in order to avoid corrosion that could appear in the vicinity of the joint that could affect its dynamic behaviour. The blank materials have been order to external steel companies. All manufacturing processes have been achieved in the University of Bristol workshops. However, because of the manufacturing capabilities and some process issues that occurred, all the tolerances could not be met.

35.3 Experimental Model Validation- Linear Case

Although the main objective of this project is to study the nonlinear behaviour induced by the bolted joint dynamics, it is essential to start with a linear analysis. It is assumed that the bolted joint does not induce any nonlinear phenomenon if the vibrations levels in the structure are small. From an experimental point of view, that means that the excitation force needs to be relatively small compared to higher levels that could lead to nonlinear responses. From a FEM point of view, the changing parameters from the linear to the nonlinear model are the contact interface characteristics. For the linear model, it is simply assumed that the flanges are “merged”. Thus, there is a linear continuity between the left and the right parts of the structure.

35.3.1 Modal Analysis

The first step of the linear stage is to perform a numerical modal analysis and an experimental modal testing. This has for objective to identify the natural frequencies of the first modes of interest of the structure, with the associated mode shapes. Then, a correlation process will be performed between the experimental and numerical data in order to update the FEM. This updated FEM will be used for further linear and nonlinear analysis. This is one of the reasons why a linear model needs to be performed in a first stage.

35.3.1.1 Numerical Linear Finite Element Model

In the meshing process of the FEM, several types of element types have been investigated. It has been concluded that solid elements need to be used in the case of contact problems. In this case, the structure has been meshed with solid tetrahedral parabolic elements. The mesh size has been optimized so that a good compromise is done between the results accuracy and the calculation time. The meshed structure is shown on Fig. 35.4. It can be noticed that the mesh size is refined in the bolted joint area as this is the area of interest where stress gradients can be important. The nodes belonging to the left and right surfaces in contact are merged.

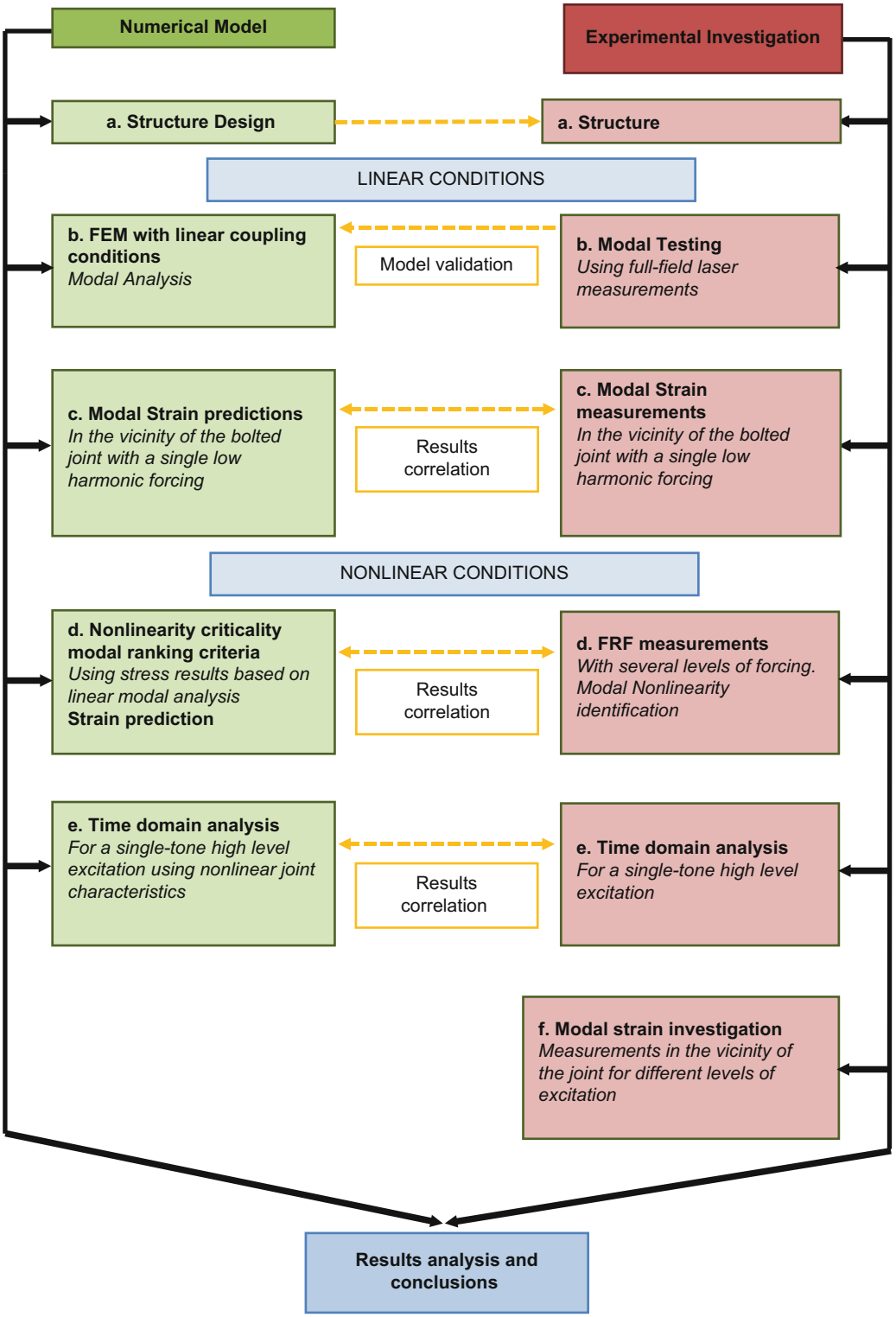

Fig. 35.2 Schematic of the project

A modal analysis is performed with a frequency range of 0–500 Hz. This analysis gives the mass normalized modal eigenvectors Φ_n [1] with the associated natural frequencies of the structure. The resulted mode shapes are essential to find the optimized locations of the drive point and sensors that will be set up for the experimental tests. Indeed, the drive point being the excitation location needs to be chosen so that all the modes of interest can be excited. From this first linear modal

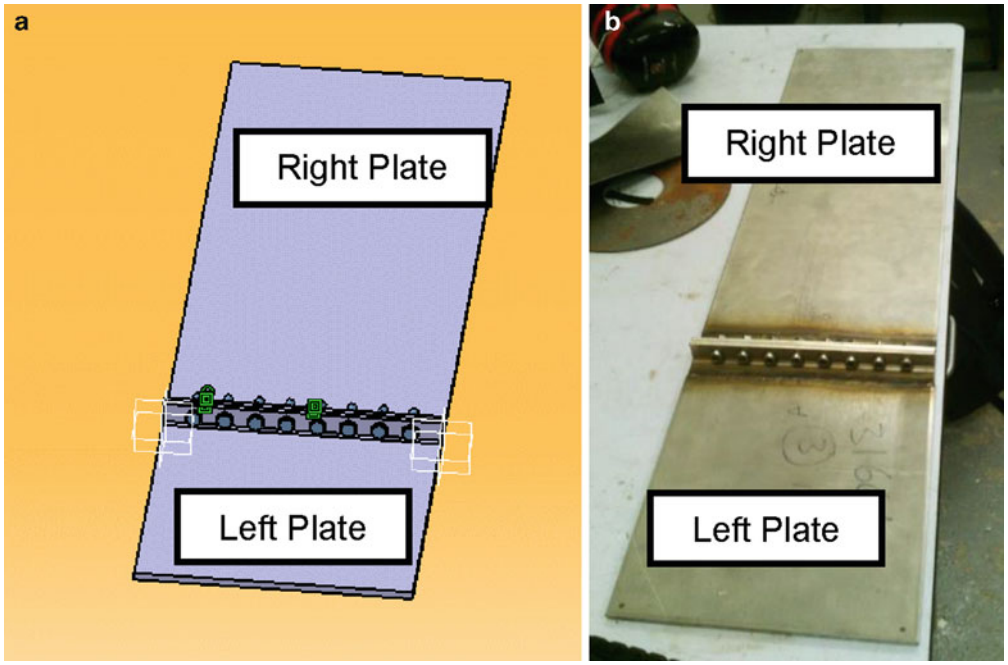

Fig. 35.3 (**a**) *Left* – CAD of the simplified flange structure. (**b**) *Right* – Manufactured simplified flange structure

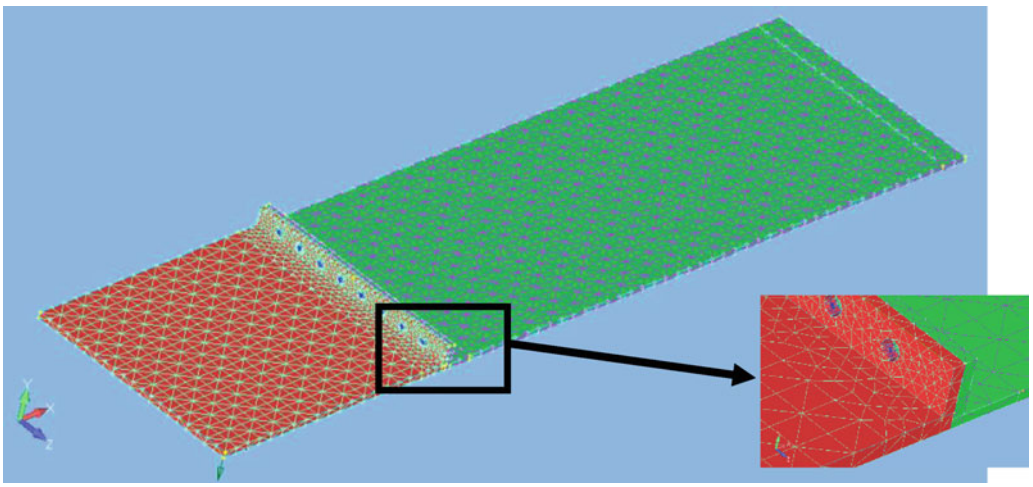

Fig. 35.4 Flange structure mesh (tetrahedral solid parabolic elements)

analysis, it is possible to notice that mode shapes are typical from classic plate structural behaviour, which seems logical regarding the flange structure geometry. This has the advantage simplifying the modal analysis methodology explained in the introduction compared to the complex mode shapes given by the actual CCOC-HPC assembly cut section in Fig. 35.1b.

35.3.1.2 Experimental Linear Modal Testing

Modal testing was performed using a Scanning Laser Doppler Vibrometer (SLDV). The flange structure was bolted using nylock nuts that prevent the bolts to get loose under dynamic loadings. A fixed tightening torque (10 Nm) was chosen and will remain the same for all the experimental tests. The structure was suspended to achieve free-free conditions. Thanks to the mode shapes predicted by the FEM, test planning could be carried out and the best excitation location identified. It was located at the lower left hand corner of the structure. Fig. 35.5a the SLDV system outside a sound booth in which the test set up was made, as shown in Fig. 35.5b.

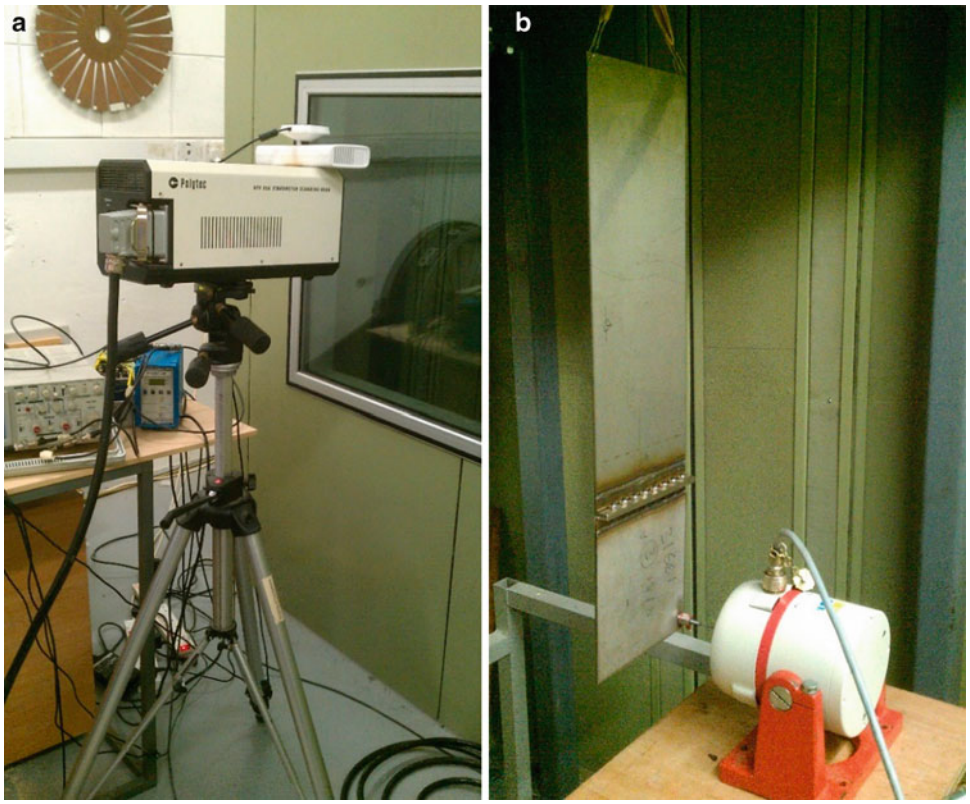

Fig. 35.5 (**a**) *Left* – Polytec Laser Vibrometer (*LV*) – (**b**) *Right* – Suspended structure and shaker

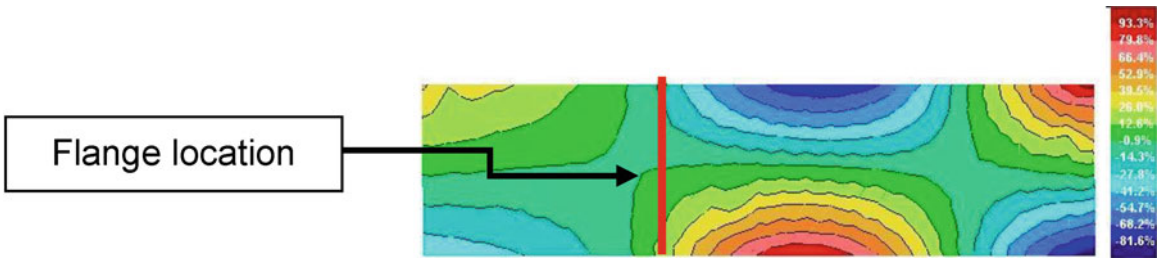

Fig. 35.6 Experimental mode shape of mode 4 (T2) obtained by vibrometry measurements

The FRFs measured by the laser were post-processed by ICATS modal analysis software [14]. An example of experimental mode shape is shown in Fig. 35.6.

35.3.1.3 Updating Process

As both experimental and numerical linear modal analysis were achieved, a correlation can be made between the obtained data in order to update the linear FEM. The mode shapes obtained experimentally using the SLDV measurements are slightly different from those obtained by finite element modal analysis as well as the natural frequencies. Then, a FEM updating process must be performed using the software *FEMtools* [15]. The aim of the updating process is to select some numerical model parameters (in our case the material properties) that will be updated so that the mode shapes and the natural frequencies of the numerical model fit with the experimental results with a limited error. In other words, the mode shapes are scaled once updated. A sketch of the process is presented in Fig. 35.7.

The first step is to import the experimental test data, which is a group of FRFs (as much as scanning points). Then, a normalized sum of those FRFs is performed in order to extract the poles (at the resonance peaks). The FRFs are then reconstructed to remove the noise from measurements. The Scan geometry needs to be superposed with the appropriate FEM surface. There is then a pairing process of each scanning point to the closest nodes. A first superposition process can be made before the updating process to check whether the FE mode shapes are fine, eventually the updating process can start. Several

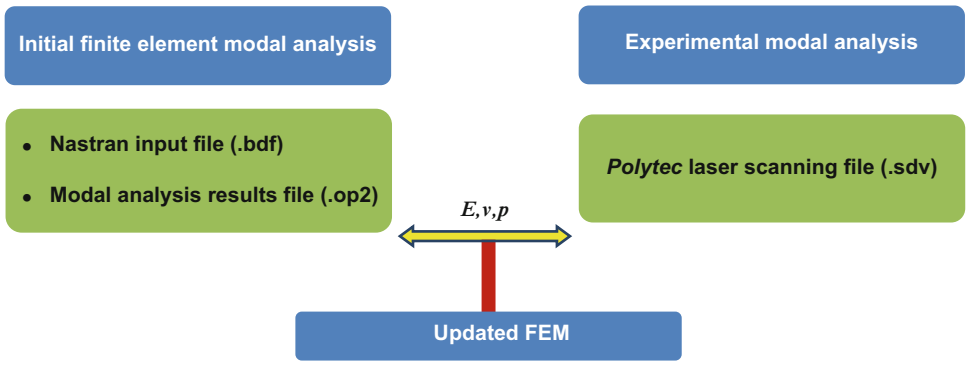

Fig. 35.7 Modal updating process

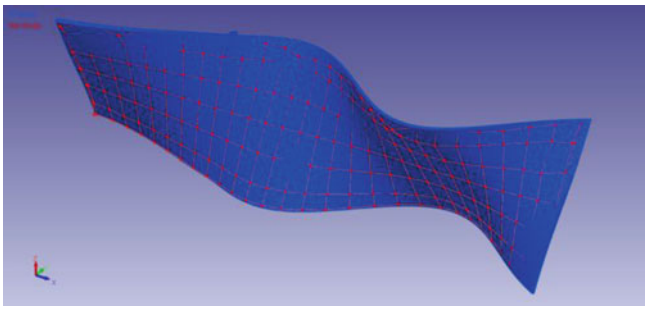

Fig. 35.8 Experimental mode shape (*red*) fitted with the updated finite element mode shape (*blue*)

updating criteria can be chosen. In this presented case, both the natural frequencies and the mode shapes can be correlated by using the Modal Assurance Criterion (MAC) [21]) given as follow:

$$MAC\ (r,q) = \frac{\left|\{\Phi_{FEM}\}_r^T \{\Phi_{Exp}\}_q\right|}{\left(\{\Phi_{FEM}\}_r^T \{\Phi_{FEM}\}_r\right)\left(\{\Phi_{Exp}\}_q^T \{\Phi_{Exp}\}_q\right)}$$

Where $\{\Phi_{FEM}\}_r$ is the numerical modal vector of mode r and $\{\Phi_{Exp}\}_q$ is the experimental modal vector of mode q.

The global young modulus E is selected as the only parameter required to be updated. Finally, the correlation function needs to be defined. In this case, it was chosen the CCABS which basically computes the derivative of the response with respect to each parameter and iterates the process by changing the parameters until a given error percentage is reached. Eventually, the initial young modulus that was set to $E = 210000\ Mpa$ has been updated to $E = 204955\ Mpa$. A maximum of 2 % of error between the numerical and actual natural frequencies and mode shapes was achieved. Figure 35.8 shows an example of fitted mode shape from numerical and experimental data obtained using the updating process by *FEMtools* [15].

35.4 Nonlinearity Criticality Modal Ranking Criteria

As introduced earlier in the paper, the dynamic nonlinearities induced by bolted joints are mode dependent. Then it is important to predict which modes (within a chosen frequency range) will show the most critical behaviour. One of the objectives of this project is to find a way to rank critical nonlinearity based on a linear FE model. An assumption for doing that is to develop some criteria based on a stress analysis using linear modal analysis of the linear FEM. The first stage is to determine the relevant stress components and their location in the vicinity of the joint. R.A. Ibrahim and C.L. Pettit (2003) [3] investigated that the two main physical phenomenon in the bolted joints leading to dynamic nonlinearities are (a) the micro/macroslips occurring in the contact area and (b) localised joint separation that could lead to a “clapping” phenomenon. The friction condition, or the stick/slip limit, can be described in terms of shear stress components within a contact surface area. For example, an infinitesimal cube of a bolted joint contains the two parts in contact and the contact surface area; a simplified stress state can be described as shown in Fig. 35.9. In this case, it is assumed that only the components shown on the figure have an influence on the friction state between the two parts.

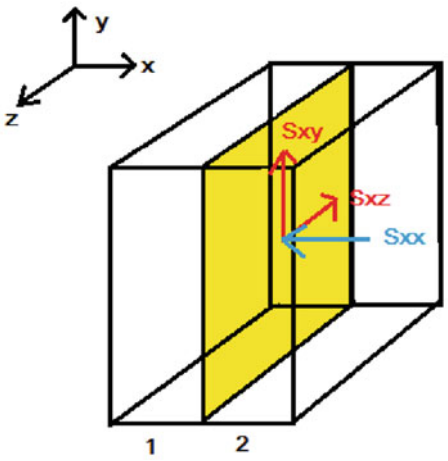

Fig. 35.9 Stress components having an influence on friction between parts 1 and 2, the yellow surface being the contact area

The total shear stress component of a point in the contact plane is calculated in Eq. (35.1)

$$\tau = \sqrt{\sigma_{xy}^2 + \sigma_{xz}^2} \tag{35.1}$$

The slip condition is reached if

$$\tau > \mu * \sigma_{xx} \tag{35.2}$$

with μ the friction coefficient, and σ_{xx} the normal component of stress.

In the case of our flange structure, the normal component of stress is mainly given by the surface pressure induced by the bolt preloads. The shear stress is induced by the external dynamic loadings. Then, it is relevant to take σ_{xy} *and* σ_{xz} in the contact plane as references for the stick/slip condition. The separation phenomenon occurs when the normal component of stress goes down to zero at the contact interface. In other terms, it can be described as the sum the normal stress induced by external forces ($\sigma_{xx,ef}$) other than the bolt pressures and the normal stress induced by the bolt pressure ($\sigma_{xx,bp}$). A local separation occurs when $\left|\sigma_{xx,ef}\right| > \left|\sigma_{xx,bp}\right|$. Then, it is relevant to analyse the normal stresses values obtained in the vicinity of the joint on the lower surface of the plate. Indeed, a separation could only occur close to this surface in the case of this flange structure.

The ranking criteria will be based on cases (a) and (b) separately and a ponderation for each case will be applied. For case (a), the shear stresses σ_{xy} and σ_{xz} fields will be analysed in the contact interface plane using the linear FE modal analysis. Although the linear model does not take the bolt preloads into account (since the contact surfaces are assumed merged), this should give an insight of the modal influence on those shear stresses. It is also important to note that modal analysis gives unscaled mode shapes; the absolute values of stress are not relevant also because the interest is to define a rank. For case (b), the normal stress field is analysed along the interface line of the lower surface of the structure. The modal stress results are not presented in this paper**.** Figure 35.10 shows a table of the shear stresses obtained for mode 6, showing the highest values within the first 10 modes. Figure 35.11 shows a table of the normal stress obtained for mode 7 showing the highest values within the first 10 modes.

It is obvious that the maximum value of stress itself does not have a relevant meaning. The surface area of high stress has also been taken into account. In this analysis, it was noticed that the bending modes show the highest values for the separation criteria (case (b)). The torsional modes show the highest shear stress values which seem logical. Then, they are the most likely to show microslip phenomenon (case (a)). Finally, assuming that the case (a) is twice more critical as case (b), after applying this ponderation (physical assumption), it was obtained the final nonlinear criticality ranking below (1 being the most critical), as presented in Table 35.1.

Note that the modes studied are slightly different from the ones obtained with the updated FEM. Then, mode B5 (normally mode 9) does not appear here. However, it will be attempted to validate this prediction ranking with experimental data for the most critical ones (T3, T4, B4, T2).

Stress component	Max value (MPa)	Shear stress field in the contact interface plane
σ_{xz}	49.3	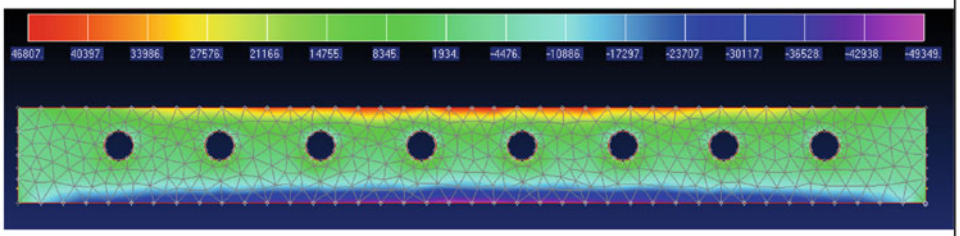
σ_{xy}	20.5	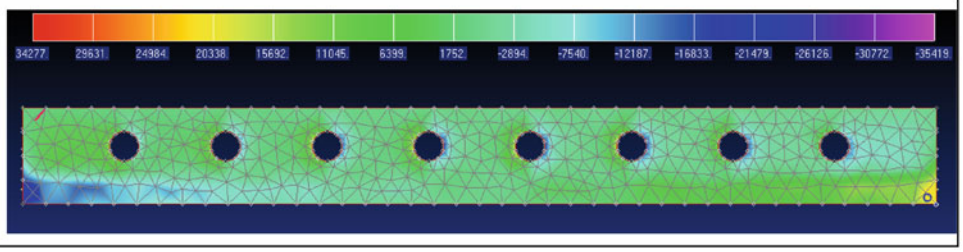

Fig. 35.10 Stress fields for mode 6

Stress component	Max value (MPa)	Normal stress in the vicinity of the interface line (lower surface of the structure)
σ_{xx}	150.1	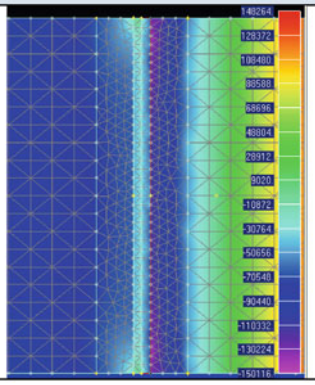

Fig. 35.11 Stress filed for mode 10

Table 35.1 Ranking of modes based on stress criteria

Ranking	Mode	Type
1	6	T3
2	8	T4
3	7	B4
4	4	T2
5	5	B3
6	2	T1
7	3	B2
8	9	
9	1	B1

35.5 Nonlinear Modal Testing of the Flange Structure

This section will present an attempt to validate the nonlinearity criticality ranking modal testing methods [1]. In many vibration nonlinearity researches presented in the literature review [2], the nonlinearity is usually identified using the Frequency Response Function (FRF) of the structure within a relevant frequency range and the appropriate experimental set up. In those studies, a single mode is generally selected and several FRFs are generated around its natural frequency for several level of forcing input. Then, if the friction joint induces nonlinearities, they can be highlighted when the different FRFs are not superposed. For example, Eric Chatelet and his colleagues [13] have shown this effect using a single degrees of freedom (SDOF) friction joint structure. For a fixed normal force applied on the assembled parts, they generated several FRFs for increasing levels of tangential forcing. The receptance (displacement response divided by the input force) first decreases because of increasing damping due to microslip. Then, the joint becomes loose (macroslip) and the receptance increases again. There is also an important frequency shift to the left induced by a decreasing joint stiffness. FRFs for every mode of interest will be measured. Then, identification of the nonlinearities through specific post-processing methods will be carried out. Finally, the most critical modes will be compared to the prediction ranking established using the linear FE modal analysis.

35.5.1 Experimental Set Up

As previously said, the main objective is to generate some FRFs for each mode for several levels of excitation. This modal testing process will be carried out for a single force input point and a single output response point. Those two points have been set using the FE linear modal analysis. The output response location needs to be close to the flange if it is required to capture the nonlinearities (which are mainly localised around the joint). The structure itself is suspended vertically in the same way as for the linear modal testing. The excitation direction is set to be horizontal (perpendicular to the flange structure's main plane), in order to limit the effect of pre-stress cause by the inertia of the structure. The global experimental set up is illustrated in Fig. 35.12.

The structure is excited using a horizontal shaker (*LDS v406*). This shaker is controlled by the *LMS* acquisition module (*LMS SCADAS III*) via an intermediate amplifier (*LDS PA25E*). A force transducer (*PCB 208 C03*) is placed between the shaker tip and the excitation point on the structure's upper surface. The output response is captured by an accelerometer (*PCB 333 M07*) glued over the flange on the upper surface. The *LMS* acquisition is fitted with a signal processing software which is able to perform signal control. The measurements are performed with three types of control:

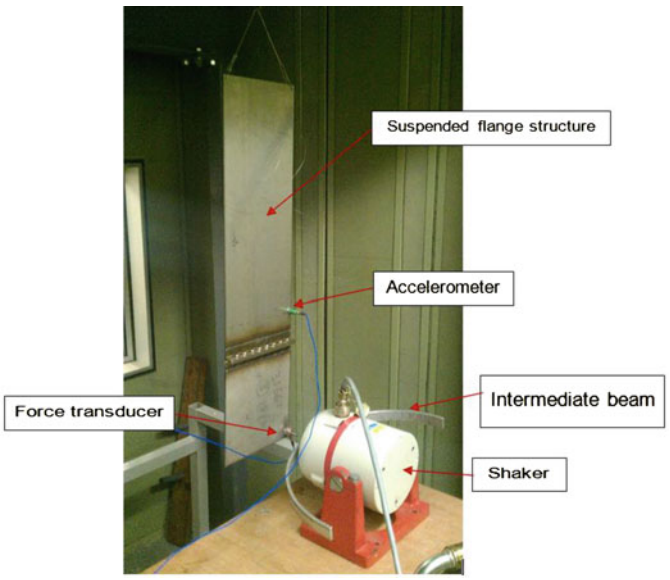

Fig. 35.12 Experimental setup

- ***Without control***: the output signal voltage is fixed. The advantage of this technique is its execution rapidity. It is convenient to quickly scan a large frequency range and generate a FRF. However, it is not relevant when it comes to comparing the FRFs for different levels of vibration, since both force and acceleration can vary all along the scan.
- ***Acceleration control*** (or amplitude control): the response output is controlled. Then, the force varies around the natural frequency. Approaching the natural frequency peak, the force decreases while the acceleration amplitude remains constant.
- ***Force control***: the force input level is controlled. Then, the output response varies while the force amplitude remains constant. The acceleration increases when approaching the frequency peak. This is the most usual type of FRF generation process.

It can be seen in Fig. 35.12 that an intermediate beam is added between the shaker and the structure. It aims to create more impedance at the excitation location. The beam was not tuned for all modes but for some particular resonances, the beam resonated and thus reducing the energy required by the shaker to excite the structure.

35.5.2 Modal Testing

35.5.2.1 Modal Testing Without Control

The first stage of the modal testing consists in scanning the whole frequency range of interest with low excitation amplitude (linear coupling conditions). A frequency range of 0–600 Hz was defined for a low excitation force and the resonances of the test structure were identified. Three levels of output signal were chosen corresponding to Low, Medium and High; this was done in order to identify response peak distortion due to nonlinearities. After reduced frequency ranges were defined for each mode, and then it was possible to test those separately with three levels of excitation. Unfortunately, the results were not satisfying without control, since the chosen levels were not high enough to observe any nonlinearity.

Modal Testing with Force Control

The next step has been to perform the FRF measurements with force control. Then, it is a more relevant control type to compare the different modes to each other with different levels of forcing. However, although it seems to be the best FRF measurement technique, it is also the most difficult to control for the *LMS* controller. Indeed, when approaching a natural frequency, the shaker amplifier struggles to deliver enough power to maintain a given level of forcing. Those measurements have been performed for three levels of force amplitude: 0.5, 1 and 2 N. Again, it has been noticed that for most of the tested modes, those amplitudes were not high enough to induce any significant nonlinearities. Besides, the experimental FRFs were too noisy because of the control difficulty encountered.

Modal Testing with Acceleration Response Control

This last measurement stage has been the most successful to generate FRFs showing the nonlinearities induced by the flange bolted joint. Here, this is the output response which is controlled (in our case as an acceleration). In order to compare the tested modes to each other, it has been attempted to set similar acceleration amplitudes for every modes. However, this has not been possible for some modes which observability was low compared to others. For example, mode 5 shows a low observability and the maximum output response (acceleration) which could be achieved was very low compared to the average maximum of every other mode. There was a limited power capacity because of the amplifier used for the shaker.

Measurement Process

The measurement process was:

- Define a reduced frequency range for each mode of interest.
- Define the sweep frequency step: 0.05 Hz in our case. Indeed, it has to be small enough to capture enough data points around the natural frequency peak, but not too small so that the sweep time of a mode is not too long.

- Define the controlled acceleration level for each FRF generation.
- Repeat the frequency sweep for several levels of acceleration up to the maximum amplifier capacity or control limits.

The overall measurement process has been rather long. Indeed, although this modal testing process seems trivial, there are many external factors that are likely to lead to measurements issues. For instance, the way the structure is suspended, the shaker tip is positioned and attached are two sources of measurement dispersion.

Data Post-processing

Most of the modes of interest in this study show some nonlinearities, the advantage of performing the measurements with acceleration control is that most individual FRFs generated are linearized and can be analysed using linear modal analysis tools. In the case of force control, a complex nonlinear post-processing is often required as the FRFs generated can be highly distorted for high levels of force. This is why, for the convenience of measurements and data post-processing, the nonlinear identification is performed using the amplitude control technique. Figure 35.13 shows the regeneration of the experimental FRF. Figure 35.14 shows the overlap of several regenerated FRFs.

Another nonlinearity indicator is the normalized modal damping coefficient defined as the ratio of the modal damping coefficient of the linearized FRF of a given level of vibration by the one of the lowest level of vibrations. Figure 35.15 shows the results of this type of analysis (Fig. 35.16).

This graph, in Fig. 35.15, does not give relevant nonlinear information. Indeed, the modal damping is supposed to be a parameter affected by a nonlinearity induced by a friction joint. Only mode 8 shows an important increase in modal damping although most other modes also show a slight increase in damping. However, it can be noticed that mode 4 shows a decrease in modal damping, which was not expected but can be explained as seen further. This is partly due to the curve fitting process performed using *ICATS*, where the damping coefficient is sensitive to the fitting quality. Then, it has been decided to study the evolution of peak level instead of modal damping coefficient, although those parameters are similar. The normalized peak evolution seems to be a more relevant nonlinearity indicator in the case of our flange structure. Indeed, the modes showing a nonlinear trend can be observed here. Modes M6, M7 and M8 show a clear decrease in peak level with increasing vibration amplitude. On the other hand, modes M12 and M4 show an increase in peak level which will be further explained. Finally, the last nonlinearity indicator is the normalized Natural Frequency (NF) evolution of each linearized FRF. Indeed, a nonlinearity caused by a bolted joint is often associated with a shift in frequency due to a decrease in joint stiffness with an increasing level of vibrations (as it has been explained in the literature review [2]). However, the actual change is frequency was rather small and data are not reported in this paper. The NF shift can be clearly observed here for mode M4, M6 and M8, although its normalized value is relatively low (less than 1 % in the tested frequency range).

From all those nonlinear indicators analysis, an actual nonlinear criticality ranking can be established and compared with the prediction. However, only the four most critical modes will be retained as the other modes (the least nonlinear) are not easy to compare with the data acquired. It is important to note that all modes could not be tested properly for several reasons previously explained. However, from the measurements done on similar structures [12], those four most critical modes seem relevant (Table 35.2).

Mode 7 (B4) data was probably wrong. Indeed, a "jump" phenomena appears on the high vibration level FRFs that probably comes from a control issue. Then, it has been inserted in the most nonlinear modes with caution. Some further measurements would have been necessary for this mode. Although the ranking was not exactly similar using the FEM

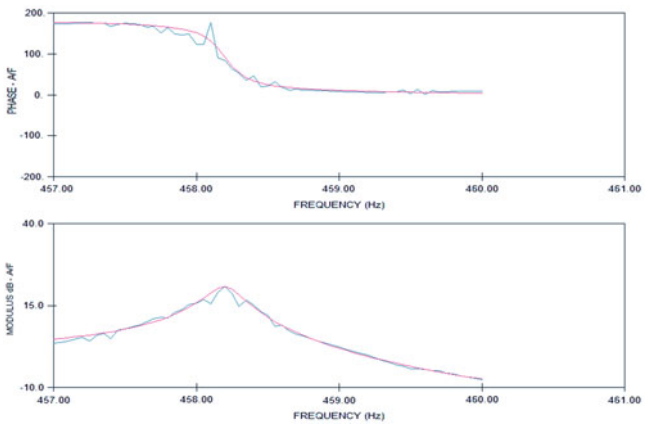

Fig. 35.13 FRF curve fitting process in ICATS for mode 10 (the *green curve* being the experimental data and the *red* one being the regenerated linearized FRF)

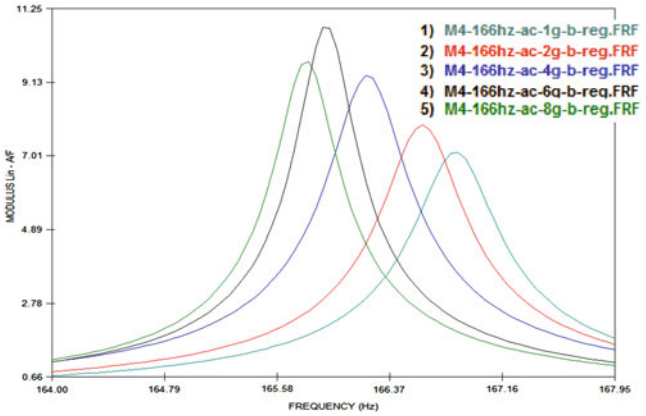

Fig. 35.14 Linearized FRFs for mode 4

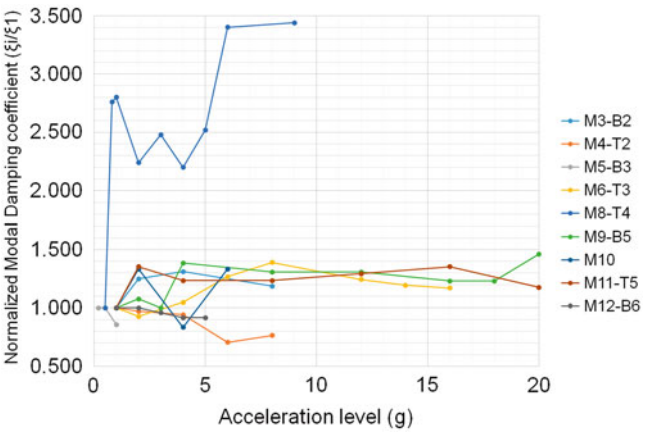

Fig. 35.15 Evolution of the Normalized Modal Damping as a function of the acceleration level (g)

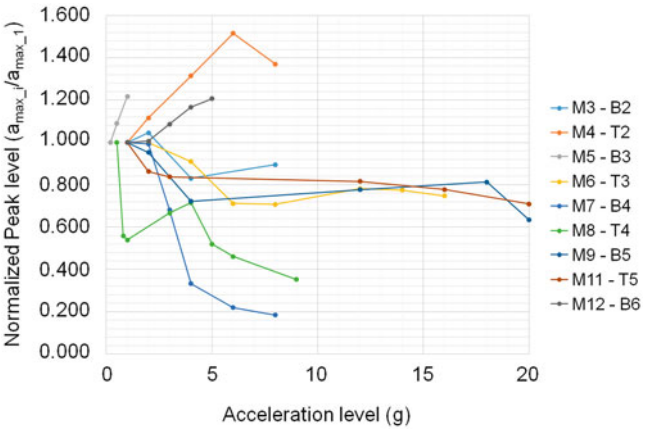

Fig. 35.16 Evolution of the Normalized Modal FRF peak levels as a function of the acceleration level (g)

Table 35.2 Simulated and experimental ranking of nonlinear modes

FEM prediction ranking	Experimental ranking	Mode	Type
2	1	8	T4
3	2	7	B4
4	3	4	T2
1	4	6	T3

prediction criteria, those four most critical modes were captured. This means that the criticality ranking criteria can be partially validated. It is not an accurate technique but allows to identify the modes likely to show the most nonlinear behaviour. Another conclusion to this experimental analysis is the nature of nonlinearity that can be different for every mode. The influence of the bolted joint dynamics on the structure behaviour varies from one mode to another. That confirms

the assumption that the nonlinearities induced by friction joints are mode dependant. For instance, mode 4 (T2) shows an increase in accelerance peak level with an increasing vibration level, whereas mode 8 (T4) shows the opposite. The type of nonlinear behaviour shown by the former mode has been widely observed in bolted structure dynamics [2].

35.6 Nonlinear Dynamic Investigation Using Strain Analysis

So far, the nonlinear analysis has been performed using classic modal testing tools, that is to say, mainly based on FRFs generated using a single output response. Most nonlinear vibration analysis are based on those methods. The vibration nonlinearity induced by friction joints is mode dependant as the stress field in the vicinity of the joint is specific to each mode. From the linear FE modal analysis, an assumption has been made that the torsional modes are the most likely to show microslip behaviour in the contact interface as the shear stress is important as well as its surface area. The bending modes are more likely to show a joint separation behaviour as the normal stress along the joint line is more important than torsional modes. Those assumptions need to be validated by experimental data as well as further numerical analysis based on strain/stress outputs instead of acceleration in a single point.

35.6.1 Experimental Strain Measurements

35.6.1.1 Strain Gages Setup

It has been seen in Sect. 35.4 that the critical stress, likely to lead to nonlinear behaviours, are located both at the contact interface (especially the shear stress components) and on the bottom surface of the structure along the joint line for the normal stress components. However, the contact interface strain/stress components are not measurable with the common strain measurement techniques. Strain gauges were planned at locations on the casing of the test structure and in order to keep the generation data sensible four points were selected. Two measurement points were selected at the edge and two at the middle of the test structure. Each pair were displaced to be one on the short and one on the long flange, as shown in Fig. 35.17. This layout was planned to capture possible changes across the flange for an excitation given at the shorter component.

It was possible to measure σ_{xx}, σ_{zz} and σ_{xz} (plane stress). However, for the case of interest, σ_{xx}, which could induce a partial separation of the bolted joint, and σ_{xz}, which was related to the friction behaviour of the bolted joint (even though it is not located at the joint interface, it could give a good insight), were relevant to the test. Now, in terms of strain components (the measurable quantity), the Hooke strain–stress relationship for plane stress gives:

$$\sigma_{xx} = \frac{E}{1-\nu^2}\left(\epsilon_{xx} + \nu\epsilon_{zz}\right) \tag{35.3}$$

$$\sigma_{xz} = \frac{E}{1-\nu^2}\left(1-\nu\right)\epsilon_{xy} \tag{35.4}$$

Then, ϵ_{xx}, ϵ_{zz} and ϵ_{xz} are required to get the stress components of interest. This is possible to measure those strain components with three components gages or so called rosettes [17]. The 45° rosettes gages were carefully attached on the casing surface,

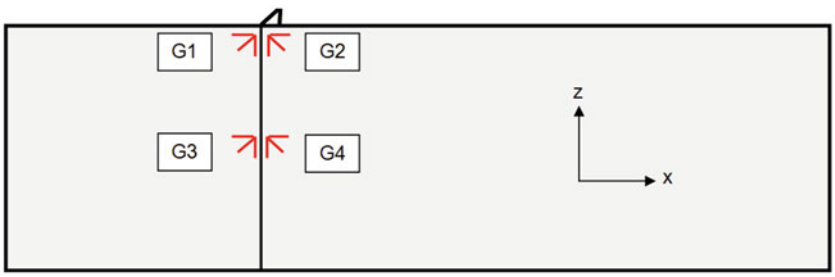

Fig. 35.17 Measurement points for the strain gauges

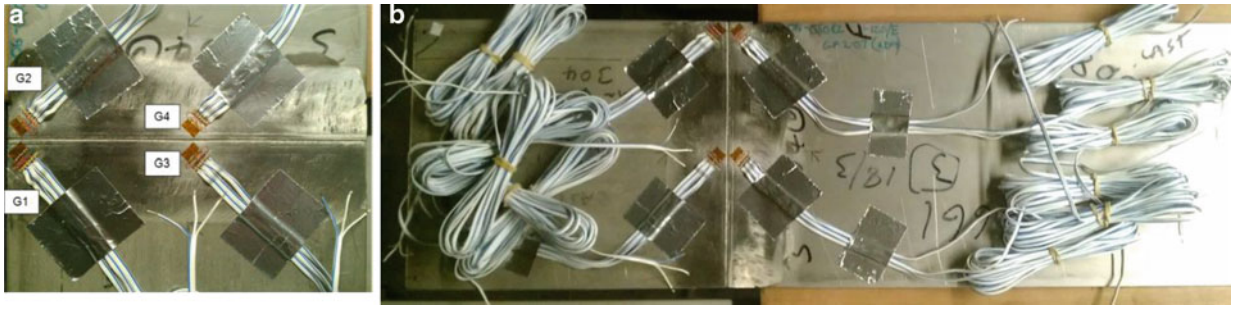

Fig. 35.18 Flange structure equipped with four rosette gages

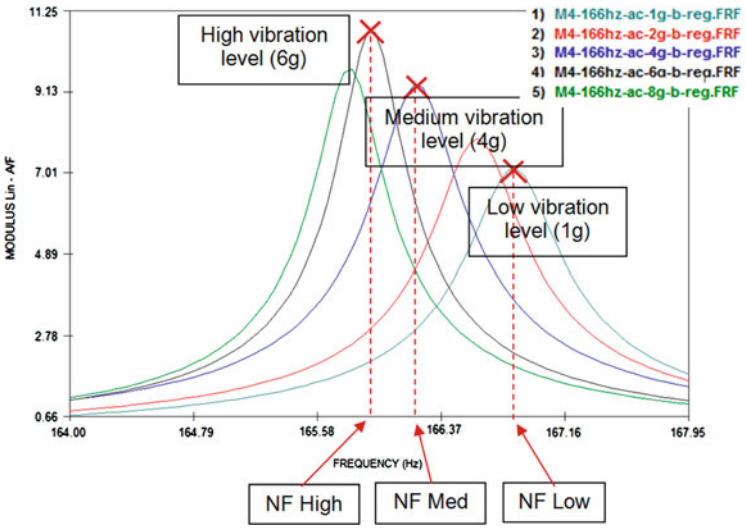

Fig. 35.19 Example of FRF for mode 4 (T2)

as shown in Fig. 35.18. This has been done with a particular attention as those are very sensitive sensors. It is clear from Fig. 35.18 that many cables are not connected to the gauges and these are seen as possible source of damping in the system.

35.6.1.2 Experimental Process

One of the main objectives of this investigation is to capture some information based on strain data that could reveal and identify nonlinear behaviours due to the bolted joint dynamics. The proposed experimental method is to capture the strain components of interest (for every gages) for the first 12 modes with a low, medium and high vibration levels, see for example mode 4 (T2) in Fig. 35.19. In order to remain consistent with the previous nonlinear FRFs measurements, the structure is excited in the same configuration (suspended in its vertical position) as it can be seen in Fig. 35.20. Single tone excitation measurement was executed for every controlled level of vibration. For each modes, three measurements are performed using a low, medium and high acceleration amplitude (at the accelerometer position) determined using the nonlinear FRFs previously acquired. For each level, the nonlinear natural frequency is chosen.

The force, acceleration and strain data are acquired via a *National Instrument* acquisition card. It is then processed with a *LabVIEW* software specifically created for this purpose. Below is a diagram of the whole acquisition chain used for this strain measurement campaign (Fig. 35.21).

The *LabVIEW* acquisition software is designed in such a way to acquire both the acceleration from the accelerometer, the force from the force transducer and the twelve strain components from the strain gages. Once the desired acceleration or force level is reached by manually changing the shaker amplifier gain, and the natural frequency is set, all those input data are recorded during 10 s (steady state response). This acquisition time is chosen so that the Fast Fourier Transformation (FFT) of the signals done during the post-process.

Most values of strain amplitudes obtained during those measurements are very low (between 1 and 100 $\mu\epsilon$). As a result, most strain signals are very noisy. This can be explained by the natural noise delivered by the strain gages relatively high. In some cases, the Signal to Noise ratio was inferior to 5. Then, it was necessary to post-process the signal in order to retain

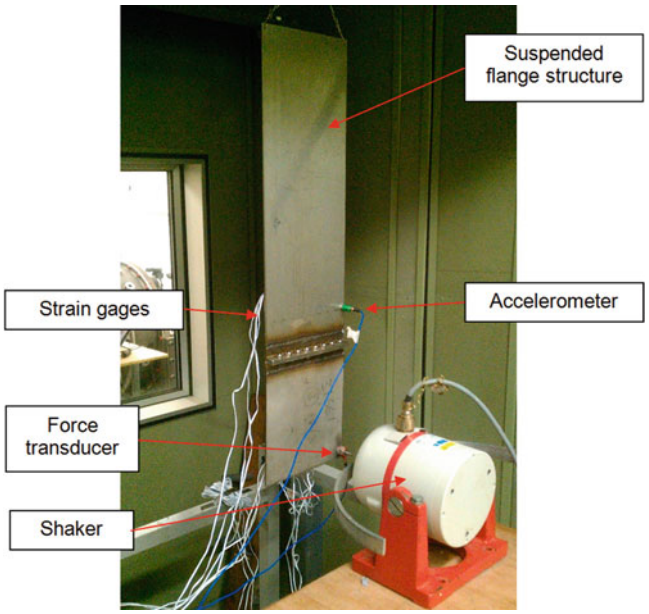

Fig. 35.20 Test setup with strain gauges

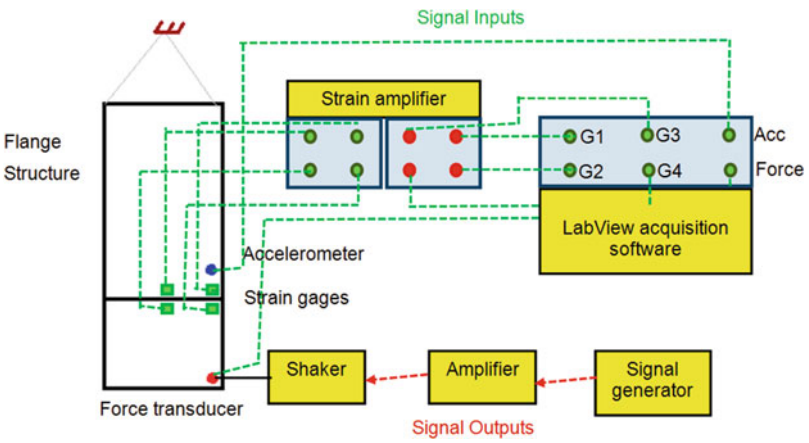

Fig. 35.21 Acquisition setup

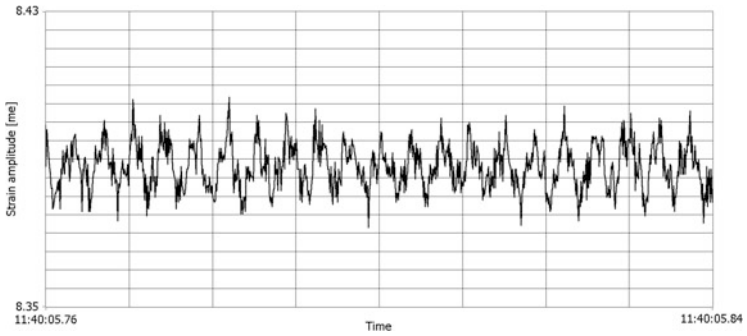

Fig. 35.22 Time domain signal of ϵ_{xx} of G1 for mode 6 (T3) at a level of vibration of 2g

only the useful information from the data acquired. For linear conditions, the strain signals are supposed to be sine waves like the force and acceleration. But this was not the case because of this noise issue. For example, Fig. 35.22 shows a portion of the time domain signal acquired of the normal strain captured by G1 for mode 6 ($f = 270\ Hz$) for a level of excitation of 2 g (linear conditions). Many high frequency components can be seen, most of them are due to the gage noise.

35.6.2 Signal Post-processing

Nonlinearities manifest by a number of additional spectral components multiple of the fundamental one, which is the response to a single tone excitation waveform. These harmonics can be observed in the acceleration, velocity or displacement output but this should also be observed in the strain signals Therefore a spectral analysis of the strain signal is performed.

35.6.2.1 Notations

As many strain components, gages, levels of vibrations and harmonic orders are used in this analysis, a notation has been chosen containing all information:

$$G_k \epsilon^i_{xx\,H_j} \tag{35.5}$$

Where the following subscripts mean:

- i: level of vibration (1, 2 or 3 for Low, Medium or High)
- k: Gage number (1, 2, 3 or 4)
- xx: Strain component (xx, zz *or* xz)
- j: Harmonic order (1, 2 or 3)

For example:

$$G_1 \epsilon^3_{xx\,H_2}$$

is the second harmonic amplitude of the normal strain given by gage 1 for a high level of vibrations.

35.6.2.2 Post-processing Objectives

As it has been previously said, the main objective of this study is to assess the relevance of strain analysis for highlighting the effect of dynamic nonlinearities caused by bolted joints. It was realized that being the values of strains very low their absolute values were not considered important. Indeed, this nonlinear experimental investigation is not suited for establishing a nonlinear criticality ranking based on absolute values of strain amplitudes. Instead, below is a listing of analysis suggestions that have been performed to study the impact of joint nonlinearities on strain:

- Is there a discontinuity in some strain components fundamentals between two facing gages when the level of vibration increases?
- Is there a discontinuity in some strain components harmonics between two facing gages when the level of vibration increases?
- Does the strain data give more information about harmonics caused by dynamic nonlinearities than the acceleration output signal?

In order to answer those problems, a post-processing program using *LabVIEW* is created. It allows to perform the spectral analysis of every measured signals (acceleration, force and strain components) and gives the amplitudes of the fundamental (H1), the second harmonic (H2) and the third harmonic (H3).

The amplitudes of fundamentals and harmonics need to be normalized between the three levels of vibrations. Two different normalization methods are used:

- (a) Normalization of all values with respect to the value obtained for the low level of vibration (for both acceleration, force and strain components):

$$Normalized\ value\ (a) = \frac{G_k \epsilon^i_{xx\,H_j}}{G_k \epsilon^1_{xx\,H_j}} \tag{35.6}$$

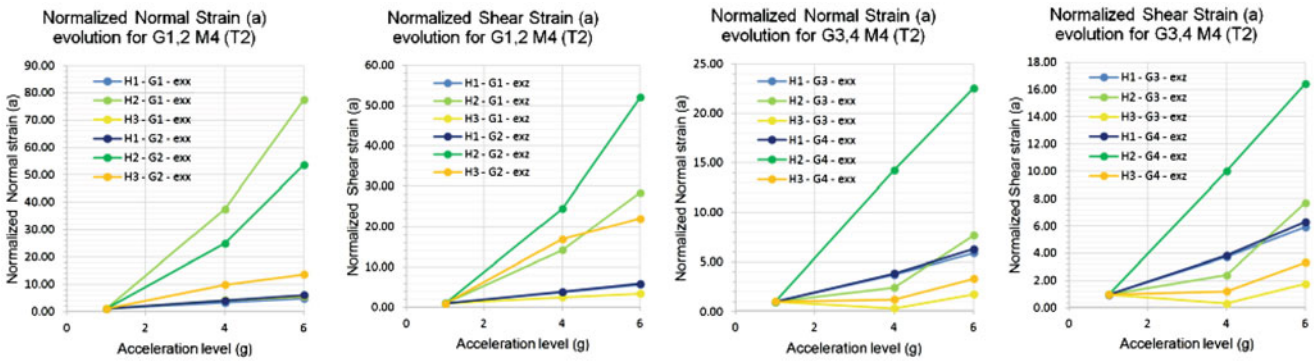

Fig. 35.23 Evolution of the normalized (a) values of normal and shear strain for gages 1,2,3 and 4 as a function of the acceleration level (g) for mode M4 (T2)

- (b) Normalization of the second and third harmonics (H2 and H3) with respect to the fundamental amplitude (for both acceleration, force and strain components):

$$Normalized\ value\ (b) = \frac{G_k \epsilon^i_{xx\,H_j}}{G_k \epsilon^i_{xx\,H_1}} \tag{35.7}$$

Then, the first type of normalization should allow to observe any kind of nonlinearity from a low to high vibration level. For a linear behaviour, every curve (normalized values as a function of the vibration level) should be linear. If a curve shows something different than a line, it could come from nonlinearities caused by the joint. However, it was discovered that the harmonic values can be close to zero in linear conditions. Then, this normalization method is not relevant anymore since it relies on the absolute values obtained for a low level of vibration. This is why, the second type of normalization seems to be more relevant to show any discontinuity. For more convenience, the normalized value is given in percentages. If no nonlinearity appears, there should not be any harmonic, giving a normalized value of 0 %. However, it only shows information about the second and third harmonic values. This is why a combination of two normalization methods is proposed in this nonlinear analysis.

35.6.3 Strain Results Analysis

Strain data is analysed by generating some graphs representing the normalized values of acceleration, force and strain components as a function of the level of acceleration (low, medium and high). For each mode, a separated graph is generated for every gauge association (1 and 2 or 3 and 4) and for every output result type (acceleration, force, normal strain and shear strain). And this is done for the two types of normalization previously explained. Modes 4, and 8 are presented in this paper. The first type of normalization previously explained is identified with an index (a) while the second type is represented by the index (b).

35.6.3.1 Mode 4 (T2): 166 Hz

A perfect linear behaviour would show horizontal lines for the harmonics (as they would theoretically be zero) and two superposed linear curves for the fundamentals. In this case, the same trends are observed for both the normal and shear strain. The fundamental curves (H1) are almost superposed in every case. That means, no discontinuity is observed from the fundamental level. However, the second harmonics get large from the medium level of forcing. In terms of discontinuities, the normalized values for the second and third harmonics are higher for gauges 2 and 4. That could show a discontinuity between the left and right plate, with more strain nonlinearities at the right plate. The graphs presented Figs. 35.23 and 35.24 show the strain data for gauges 3 and 4 (middle of the plate) when normalization type (a) and (b) are used.

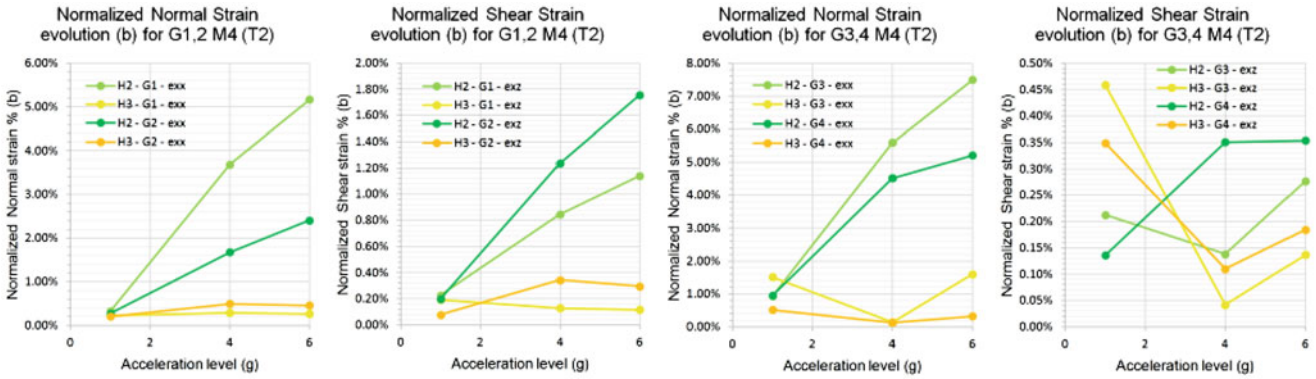

Fig. 35.24 Evolution of the normalized (b) values of normal and shear strain for gages 1,2,3 and 4 as a function of the acceleration level (g) for mode M4 (T2)

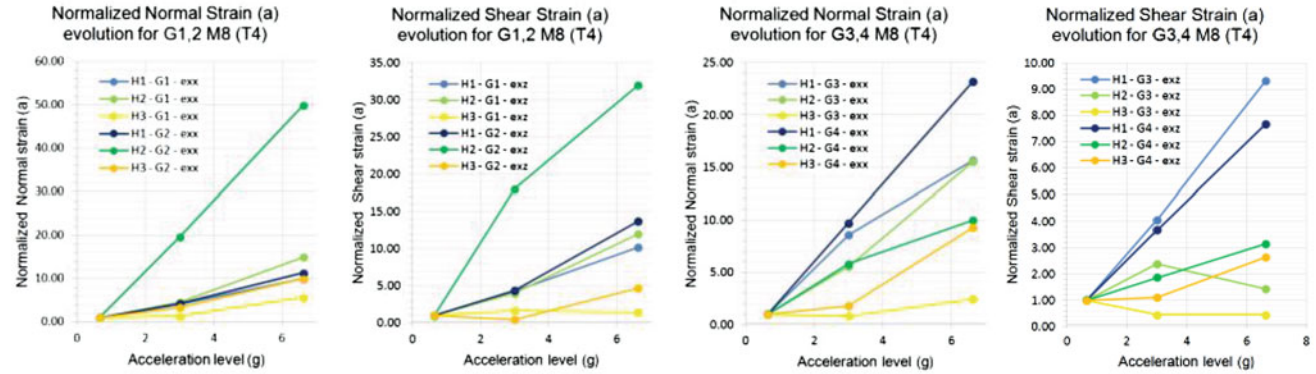

Fig. 35.25 Evolution of the normalized (a) values of normal and shear strain for gages 1,2,3 and 4 as a function of the acceleration level (g) for mode M8 (T4)

The first feature observed is the increase in second harmonics with an increasing level of vibrations, which indicates that this mode shows a nonlinear behaviour. It can be seen here that the normalized values of harmonics are more significant for the normal strains (up to 7 % of the fundamental) from the medium level of vibration. This is only the case for the second harmonic though since the normalized H3 are always below 1 %. Besides, discontinuities are observed between the left and the right plate in the second harmonic of normal and shear strain. In the case of normal strain though, the left plate shows more important H2 values.

35.6.3.2 Mode 8 (T4): 359 Hz

For gage 1 and 2, $G_2\epsilon^3_{xxH_2} > G_1\epsilon^3_{xxH_2}$ and $G_2\epsilon^3_{xzH_2} > G_1\epsilon^3_{xzH_2}$. This could be due to a discontinuity (higher nonlinearity on the right plate). For gauges 3 and 4, discontinuities can be observed for H1, H2 and H3 for the high level of vibrations, especially for the normal strains (Fig. 35.25).

For gage 2, a high relative second harmonic is observed from the medium level of forcing (for both normal and shear strain), showing a high nonlinearity. Moreover, this nonlinearity seems to be localised on the right plate since $G_2\epsilon^{2,3}_{xxH_2} > G_1\epsilon^{2,3}_{xxH_2}$ and $G_2\epsilon^{2,3}_{xzH_2} > G_1\epsilon^{2,3}_{xzH_2}$. However, no conclusion can be made from the strain measurements of gages 3 and 4 (Fig. 35.26).

The force and acceleration graphs are not presented in this present document as they would add too much data. However, a similar trend has been observed for every mode presented above. The acceleration harmonics normalization of type (b) usually follows the same trend as $G_2\epsilon^2_{xxH_2}$. This seems reasonable as both values are measured on the same plate and are rather close (less than 50 mm). However, the normalized values are generally higher for the strain data than the acceleration, which shows the relevance of using the strain data as a nonlinear indicator instead of acceleration. From this nonlinear strain experimental investigation, several conclusions can be made to assess this nonlinearities identification method:

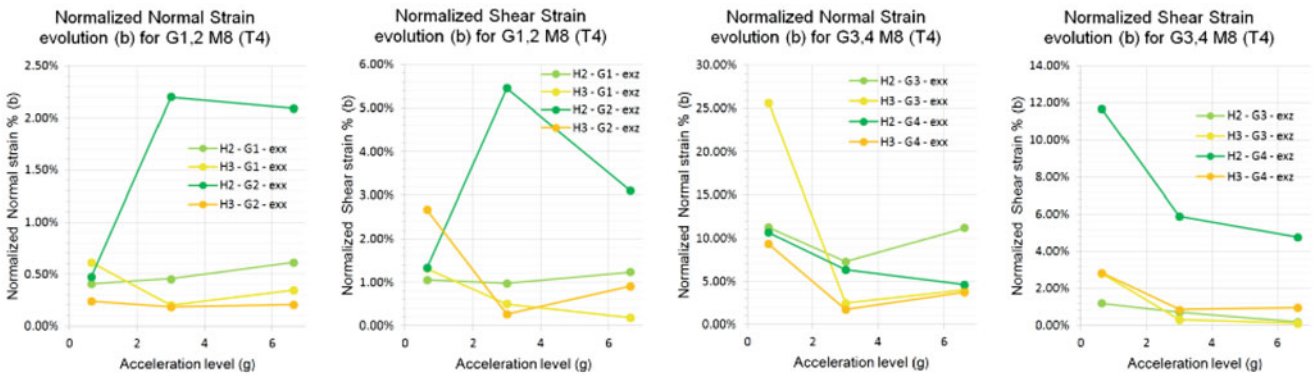

Fig. 35.26 Evolution of the normalized (b) values of normal and shear strain for gages 1,2,3 and 4 as a function of the acceleration level (g) for mode M8 (T4)

- For every modes showing the highest nonlinearities identified using classic modal testing methods, some nonlinear patterns have been confirmed using strain analysis.
- One of the advantage of strain analysis over classic modal testing is the ability to capture some local nonlinearities due to the joint. For instance, some discontinuities have been shown between the left and the right plate, highlighting the influence of the bolted joint on the structure. Besides, different nonlinear features were observed between the (1,2) and (3,4) gage couples, highlighting the localised nature of nonlinearities induced by the bolted joint.
- Another advantage of strain measurements is that the sensors (strain gages) have a lower influence on the structure behaviour as accelerometers could have (in terms of added mass). However, the gage cables could have added a slight damping to the structure.
- However, in opposition to the classic modal testing method, no defined way to quantify the nonlinearities has been clearly found so far. Two normalization methods have been proposed which do not show the same nonlinear features, although the second one (b) seems to be the most relevant.
- Another disadvantage of strain measurements is that the absolute values can be very low and even close to the level of noise generated by the strain gages. This can induce some odd results as it has been observed for modes 7 and 8. Indeed, if the fundamental value of a strain component is low, it becomes uncertain to study the evolution of its relative harmonics as a function of the vibration level.
- Finally, it was noticed a limitation in space where the gages could be glued on the structure. In the case of friction joints, special strain measurement have to be used to know the strain field within the contact interface (still not well known nowadays). However, the FEM could be used to correlate those values of strain if the values of strain are known in another region of the structure.

35.7 Linear Correlation for Model Validation

A linear strain investigation has also been performed in order to compare the normal and shear strains of each mode and to validate the FEM with strain outputs.

35.7.1 Linear FRF Correlation

The strain components of the numerical model are generated using a frequency response function based on the linear modal analysis. In this type of numerical analysis, a structural damping [1] can be added to the solver. This parameter has an important impact on the response level of the structure subjected to a harmonic excitation. After several trials and errors, an optimized value of structural damping is set to 0.5 %. However, the value chosen did not produce perfect correlation between simulated and measured response. This would be reflected on the strain values calculated and therefore it was decided to use trends of strains of components and compare those between the numerical and experimental linear analysis.

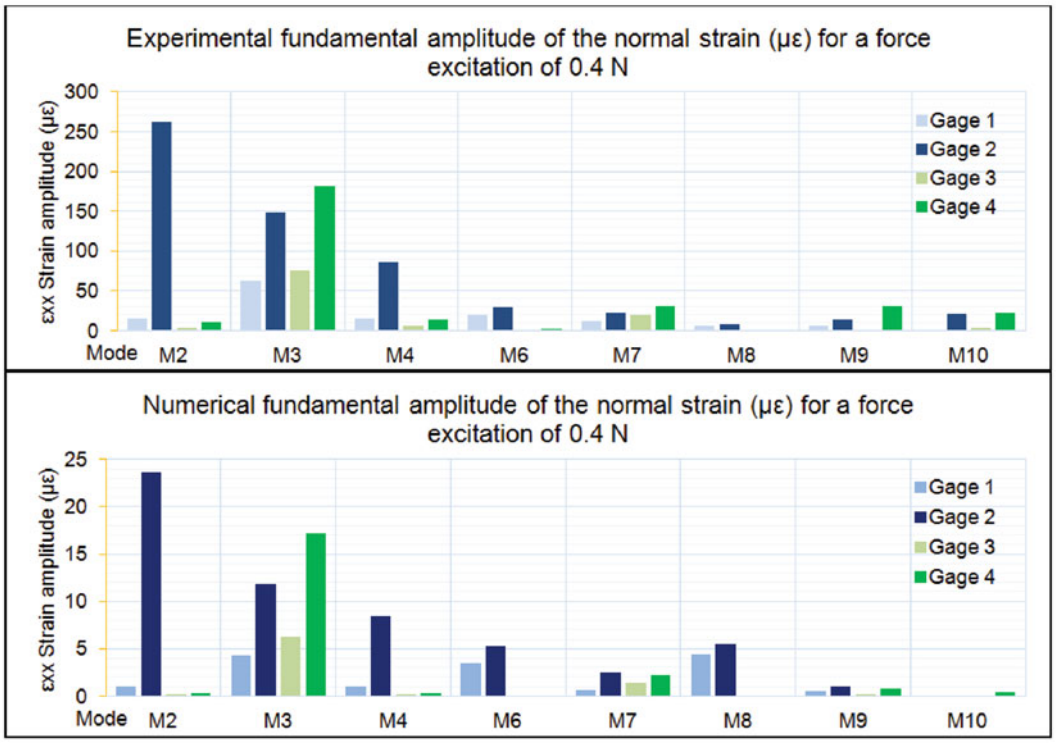

Fig. 35.27 Experimental and numerical fundamental amplitudes of normal strain ($\mu\varepsilon$) for a harmonic force excitation of 0.4 N

35.7.2 Linear Modal Strains Correlation

The numerical FRF analysis requires a fixed periodic input (a force in our case). This suggested that the excitation force level is controlled in both numerical and experimental linear tests. From the previous experimental measurements, a forcing value giving quasi-linear conditions is set to 0.4 N. Then, the normal and shear strain components are measured at each natural frequency of the first ten modes for both experimental and numerical linear analysis. The graphs, in Figs. 35.27 and 35.28, present the linear strain results obtained experimentally and with the linear FEM for the strain gages positions presented in Fig. 35.18. It can be observed that the normal strains are well correlated between the measurements and the model whereas some differences are noticed for the shear strain component. This is can be explained by several reasons. The errors can come from the uncertainties in the measurements in the way the shear strain has been computed from the rosette components and the fact that the values are close to the natural noise level of the strain gages. This could also come from the numerical model as the output points chosen are not exactly at the actual gage position. Besides, the mesh is probably not fine enough to capture accurate values of strain since the gradient can be rather high around the bolted joint. The normal strain amplitudes are always higher for gages located on the right plate. This can be explained by the difference in thickness between the left and right plate. It is thinner on the right plate, giving higher normal strain values. This is not the case for the shear strain though. Moreover, as expected, the shear strain amplitudes are higher for the torsional modes (especially modes 2, 4 and 6). However, there is an unexplained ten factor between the experimental and numerical values.

35.7.3 Numerical Time Domain Nonlinear Analysis

As the linear FEM has been validated, a nonlinear analysis can be performed and compared with the experimental results. These analyses will be performed in the time domain. Indeed, it would also have been interesting to generated nonlinear FRFs to be compared with the experimental results. However, in finite element analysis, this generally induces a complex process combining the Multi-Harmonic Balance Method (MHBM) and an alternating frequency time method as it has been seen during the ASME Turbo Expo [11] in the paper written by A. Herzog, M. Krack, L. Scheidt and J. Wallascheck [18]. This numerical process involves additional software not available in this study. Several time-domain nonlinear analyses are

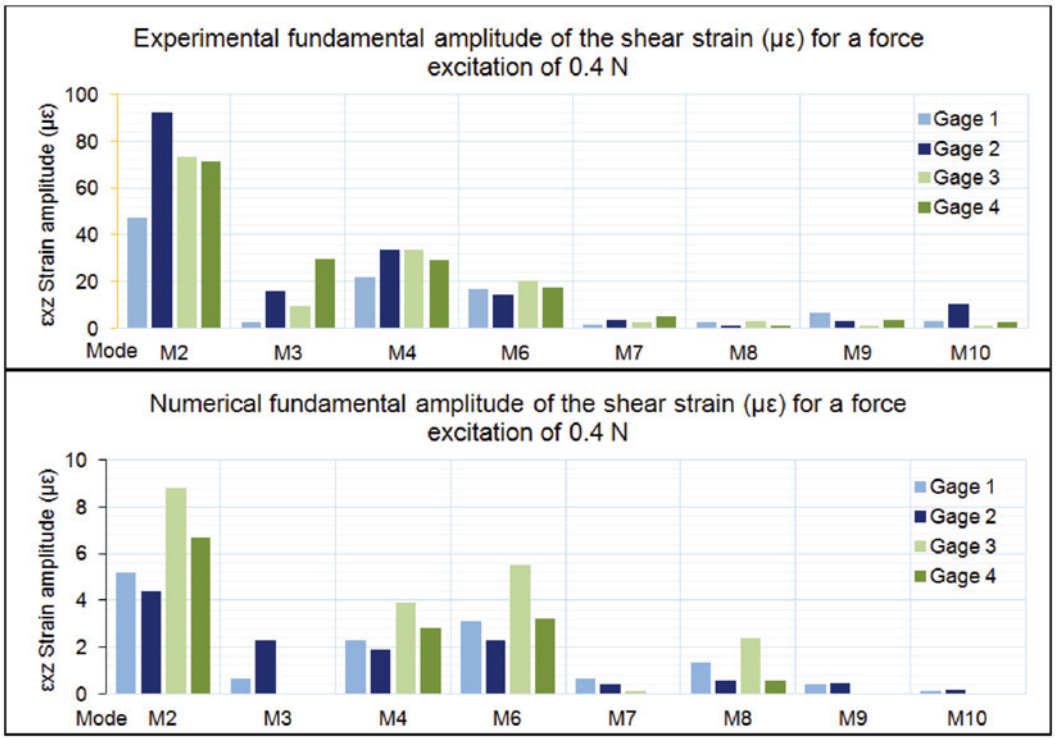

Fig. 35.28 Experimental and numerical fundamental amplitudes of shear strain ($\mu\varepsilon$) for a harmonic force excitation of 0.4 N

performed for the most critical modes (M4 and M8) using low and high excitation forcing levels. The objective is to compute the time response of the flange structure in terms of acceleration and strain for the natural frequencies of modes 4 (T2) and 8 (T4). The structure is subjected to a harmonic force input with low and high amplitude.

35.7.3.1 Nonlinear Model Parameters

Joint Interface Modelling

In Finite Element Analysis, there are several ways to model friction joints. Most of them have been presented in the Literature Review [2]. For bolted joints, the most common process consists in modelling the bolts with rigid elements. These are elements that connect two nodes in a rigid way, one being the "master", the other the "slave" (the displacement of the slave only depends on the master's one). A first model has been created using rigid elements for the bolts and shell elements for the rest of the structure [19]. Part of the bolted joint of the flange structure model can be seen in Fig. 35.29.

This has the advantage of being a linear and simple model (leading to a relatively short computational time). It is able to give a first insight of the linear mode shapes and associated natural frequencies. However, it does not capture any nonlinear behaviour induced by the friction joint. Another possible modelling technique consists in inserting a thin layer of element with nonlinear properties between the flanges. H. Ahmadian, M. Ebrahimi, J.E. Mottershead, M.I. Friswell (2002) [8] have developed several bolted joint finite element model using this technique. The thin layer elements are given material nonlinear properties such as an elastic–plastic behaviour so that it behave in the nonlinear way from a given level of vibrations. This has the ability to fit the nonlinear measured response with a low relative error. However, this usually works for a single mode analysis and the material properties need to be identified using measurement data. The last type of friction joint modelling technique is the use of contact elements at the contact interface of the bolted joint [20]. In a simplified way, the finite element solver projects the vector normal from the surfaces in contact. It then creates contact elements when these normal intersect elements from the facing surface elements. These contact elements are then given friction properties. In our case, it was used a glued contact model for the linear model (flange surfaces considered merged) and a coulomb friction model for the nonlinear model. These contact elements are also called phenomenological models as they represent the friction force as a function of the relative displacement between the surfaces in contact. They are Iwan model [6] composed of Jenkins

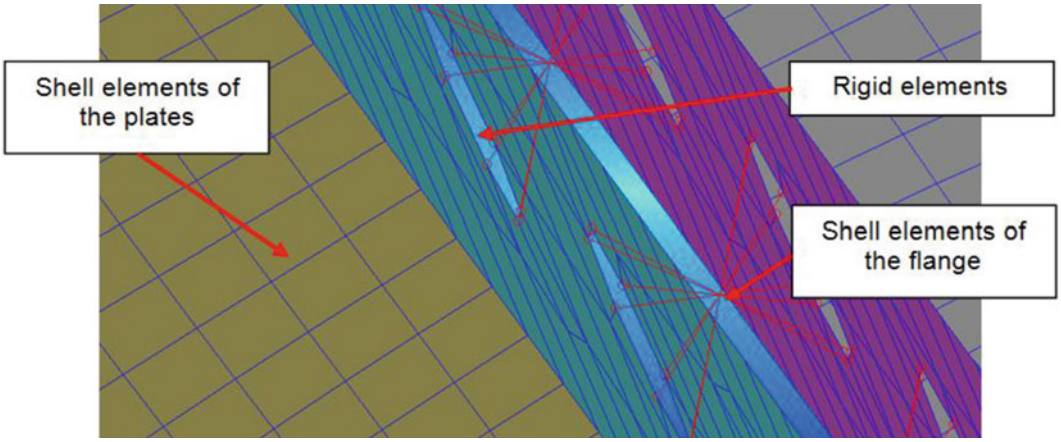

Fig. 35.29 Finite element model of the flange structure using rigid elements for the bolts and shell elements for the plates and flange

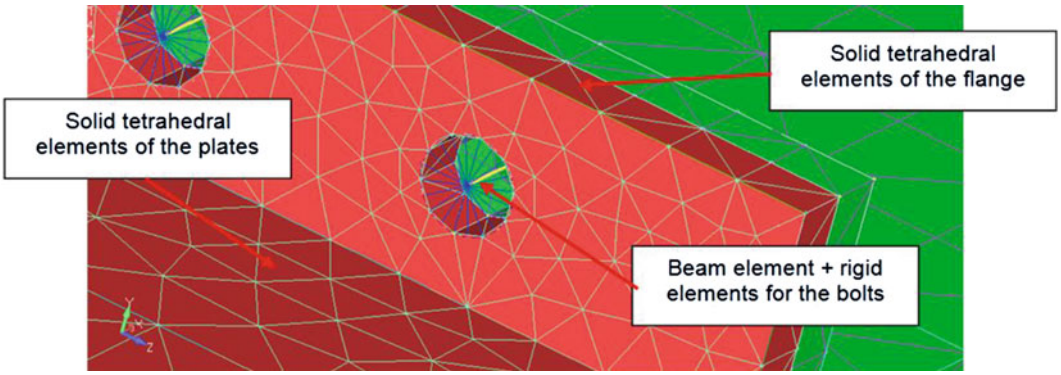

Fig. 35.30 Nonlinear FEM mesh of the flange structure (zoom on the bolted joint)

elements (spring element in series with a coulomb element) in parallel. This is the type of nonlinear elements used in the flange structure nonlinear model. These have the advantage of reproducing an accurate vibration response compared to an actual model. However, as it will be further noticed, this type of FEM has the disadvantage of being very computational time consuming. As previously said, the contact elements have many contact properties. The most important ones are the friction model used and the associated friction coefficient. In our case, the Coulomb friction model is chosen as this is the most commonly used in the industry. It is associated with a friction coefficient which is set to 0.3, being an average value for steel against steel friction.

Bolts Modelling

In the case of contact elements, it is also important to model the effect of bolts on the flange. There are several ways to model the bolts. As it has seen in the previous paragraph, in the case of a linear model, they are usually removed from the model as well as their preload. In the case of a nonlinear model where the joint dynamics are modelled, the pressure applied by the bolt on the flanges is computed by the use of contact elements. The bolts with their associate preload are either modelled with solid elements (nuts and screws) or with the association of beam and rigid elements as it can be seen in Fig. 35.30.

The later possibility is chosen as it simplifies the model. The preload values need to be the same as used during the measurement process. For the actual bolt tightening, a torque wrench was used and set to a torque value of 10 N.m. The normal bolt preload can be estimated from this tightening torque with the relationship below [20]:

$$P = \frac{T}{K \times d}$$

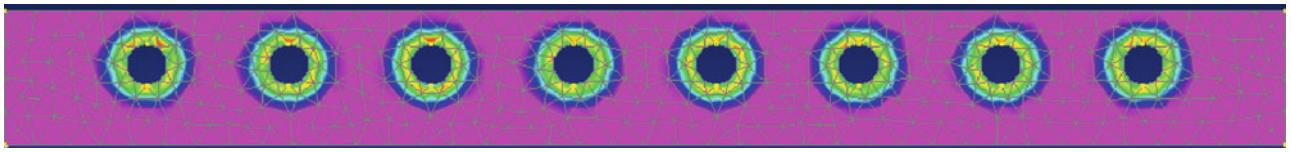

Fig. 35.31 Contact pressure computed by the nonlinear FEM with only the bolt preloads as an input (*purple* being the min and *red* the max pressure)

With:

- T: Tightening torque (10 N.m)
- K: nut factor (estimated to 0.2 according to [20] for steel bolts
- d: Nominal bolt diameter (6 mm)

Then, the calculated preload is $P = 8333\ kN$. This is the value of compression force given to the beam elements modelling the bolts. A static FEA has been performed with only the bolt preloads as an input. The contact pressure on the flange interface is shown in Fig. 35.31.

Plates and Flanges Modelling

In the case of dynamic analysis using contact elements, solid elements need to be used for the surfaces being in contact. This is why, all the rest of structure is modelled using solid tetrahedral parabolic elements although it increases a lot the number of elements compared to a shell element model. The associated material properties are:

- Mass density: $\rho = 7800\ kg.m^{-2}$
- Young Modulus: $E = 204955\ Mpa$
- Poisson's ratio: $\nu = 0.3$

Boundary Conditions and Solution Type

As we want to reproduce the structural behaviour achieved in the measurements, similar boundary conditions are set. That is to say, the structure itself is in free-free conditions, although the actual wire suspension must have had an impact on the response compared with perfect free-free conditions of the numerical model. The force input is a sinusoidal nodal force at the actual input location. The acceleration, normal and shear components of strain are set as output requests at the actual positions of the sensors. The solution type is an advanced nonlinear transient response. Then, the solver parameters also need to be set. The most important parameters are the time step and the number of steps. Those parameters depend on the force input frequency, the maximum frequency component that it is required to capture, the spectral analysis resolution desired, and the transient response time. Several trials and errors have been tested in order to find the best compromise of time step and number of steps for every analysis.

35.7.3.2 Time-Domain Results for the Critical Modes

As previously said, four nonlinear FEA are performed: two per critical mode (with a low and high forcing levels). The forcing levels are set to 5 and 50 N in both cases for respectively the low and high levels. The high value is higher than what had been achieved during the experimental campaign. This is another advantage of performing a numerical analysis, as high level of vibrations can be achieved. The objective is to observe nonlinear features that can be compared between the low and high levels of vibrations. To do so, a similar signal post-process as in the measurement campaign is used with an appropriate *LabVIEW* program. The second type of normalization (b) seen in Sect. 35.6.2.2 is used to study the evolution of acceleration and strain harmonics as a function of the excitation level.

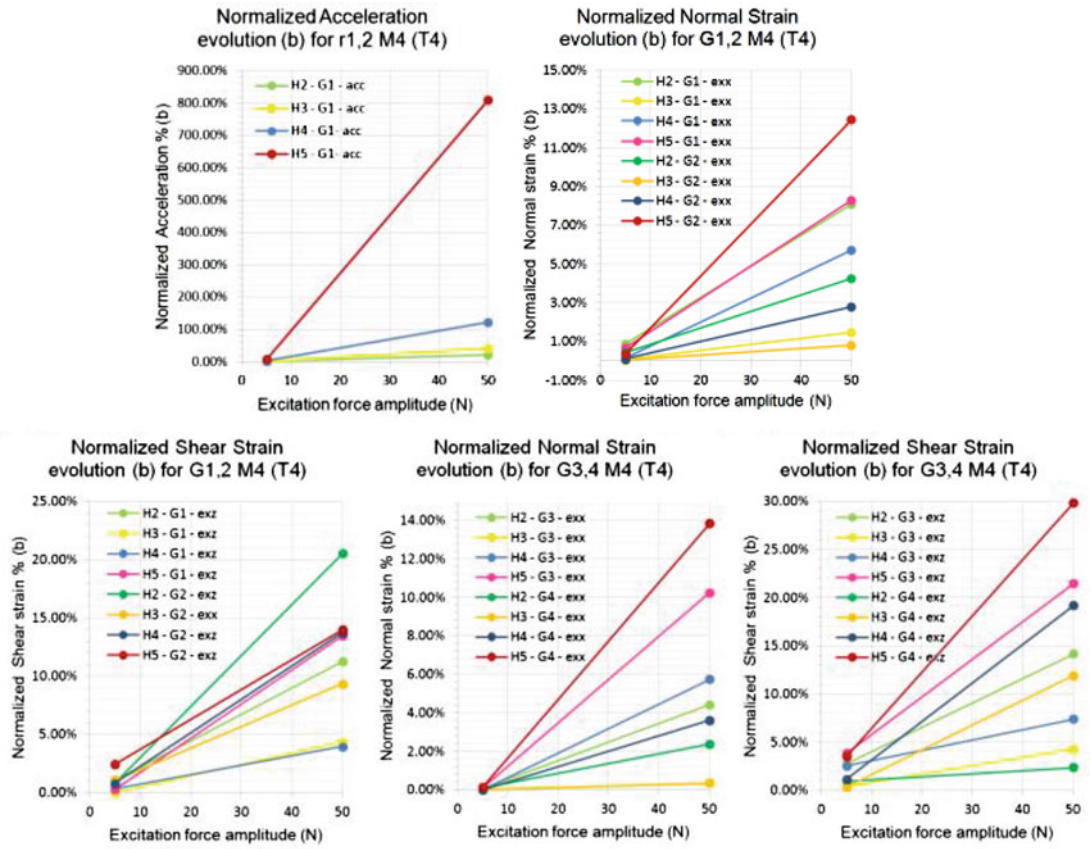

Fig. 35.32 Evolution of the normalized (b) numerical acceleration, normal and shear strains for a low and high levels of excitation forcing of mode 4 (170 Hz)

Mode 4 (T2)

The FE linear natural frequency of mode 4 is 170.2 Hz. Then, this is the chosen value for the excitation force frequency. The band width is set to 1,000 Hz in order to capture up to the fifth harmonic of the fundamental frequency. The time step chosen for sampling this mode is 0.0005 *s*. The number of steps is set to 1,000, giving a total simulated time of 0.5 s. As said before, the main disadvantage of contact elements in a FEM is their impact on the computational time. Indeed, the total simulation time for one analysis was 6 h (to simulate 0.5 s of actual behaviour). The time response seems to be in steady state from 0.3 s for the 5 N excitation case. Below are the results of normalized values of acceleration and strain harmonics as a function of the excitation force amplitude. Some interesting features were observed up to the fifth harmonic (Fig. 35.32).

It can be seen from the normalized acceleration plot that harmonics amplitudes become important for the high forcing level. The fifth harmonic is unexpectedly high (800 % of the fundamental). This is probably due to a too high time step. However, more interesting nonlinear features can be observed on the normalized strain plots. First, almost all relative harmonic amplitudes increase with the level of forcing, showing that the higher the excitation force, the more nonlinearities are caused by the bolted joint. This is especially the case for the fourth and fifth harmonics. There also seems to be some nonlinearity discontinuities between the left and right plate according to the difference in harmonic levels between G1 and G2 or G3 and G4. However, no conclusion can be made about this feature as there is no logical pattern. Sometimes, the harmonic levels on the right plate are higher than the left plate and the other way round. Figure 35.33 shows a part of the time response of $G4\epsilon_{xz}^2$ with the associated spectral analysis. It is obvious that nonlinearities appear as the time response is not a perfect sinusoidal signal. This is highlighted by the harmonic peaks that are relatively high compared to the fundamental amplitude.

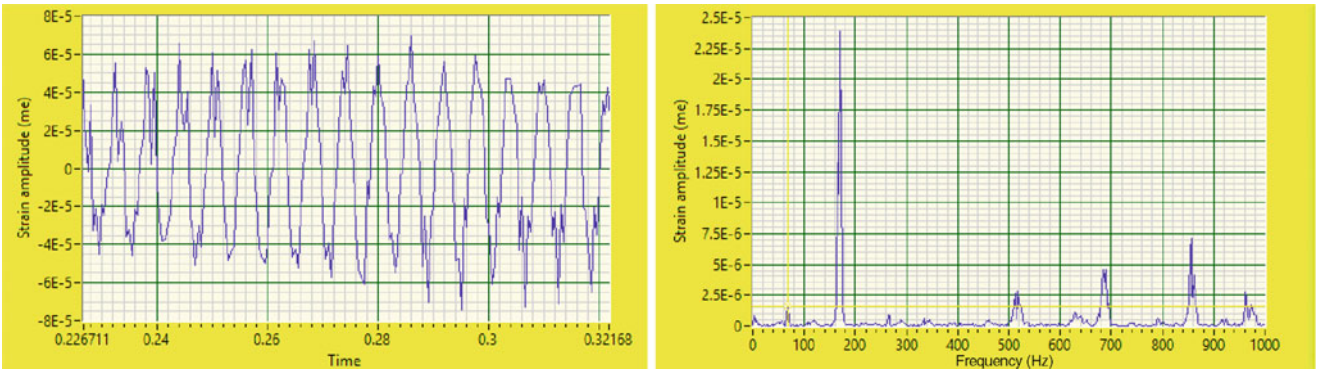

Fig. 35.33 Numerical time response of $G4\epsilon_{xz}^2$ with the associated FFT

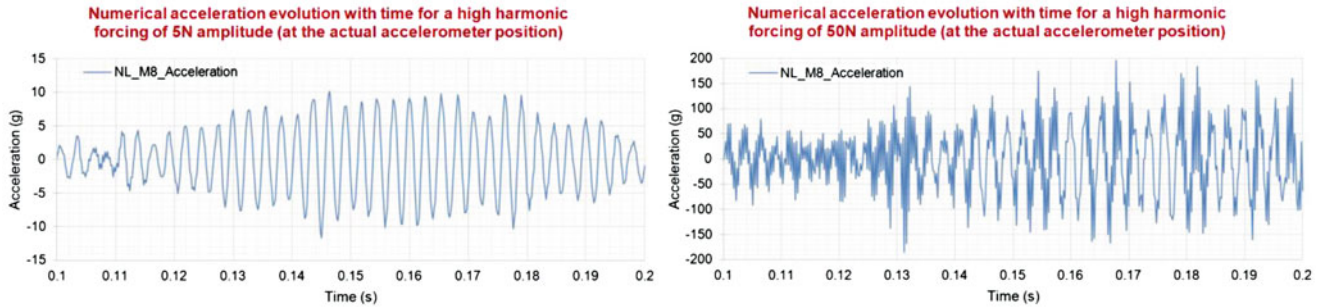

Fig. 35.34 Time domain numerical acceleration evolution of mode 8 (370 Hz) for 5 and 50 N of excitation force amplitudes

Mode 8 (T4)

The FE linear natural frequency of mode 8 is 370.8 Hz. Then, this is the chosen value for the excitation force frequency. This time the bandwidth is set up to 2,500 Hz in order to capture up to the fifth harmonic of the fundamental frequency and using a time step of 0.0002 *s*. The number of steps is set to 1,000, giving a total simulated time of 0.2 s. Figure 35.34 are the acceleration responses for the low and high excitation forces. It can be noticed that there is an important low frequency component in addition to the fundamental that could be explained by the boundary conditions. Indeed, the FE solver has probably struggled to compute the analysis without any constraints (free-free conditions). However, as for mode 4, the interest is in the normalized values of harmonics in this analysis. But the nonlinearities can already be highlighted from those graphs since high frequency components appear on the high excitation force plot (Fig. 35.35).

As for mode 4, the first interesting trend to observe for almost every curve is the increase in normalized harmonic level with an increasing excitation force level. This shows that the nonlinearity caused by the bolted joint is higher for the high forcing level. This is the case for both acceleration and most strain components for all gauges, showing that strain is also an interesting nonlinearity indicator such as acceleration. The shear strain components of G1 and G2 show a discontinuity between the left and the right plates as $G_2\epsilon_{xzH2,3}^2 > G_1\epsilon_{xzH2,3}^2$. There also seems to be a shear strain discontinuity between G3 and G4 as $G_4\epsilon_{xzH3}^2 > G_3\epsilon_{xzH3}^2$. As a partial conclusion, this FE nonlinear analysis has shown that a FEM containing contact elements with friction properties allows to capture the dynamic nonlinearities induced by a bolted joint. Indeed, the acceleration and strain components outputs show similar nonlinear features than it was obtained in the experimental analysis. That is to say, a global increase of normalized harmonics with an increasing level of vibrations in the structure for both acceleration and strains. The advantage of the numerical model is its ability to capture some nonlinear features of level of vibrations that could not be achieved using the experimental set up. However, there are several drawbacks in this type of nonlinear Finite Element Model. First, there are a large number of uncertainty sources such as the errors on the friction coefficient, the errors on bolt preloads and the friction model used by the contact elements which is maybe not accurate enough to capture the actual joint behaviour. The mesh size in the contact area is also critical. The other disadvantage is the computational time which can be very large when contact elements are used. In our case, it took more than 6 h to simulate less than 1 s of structure dynamics.

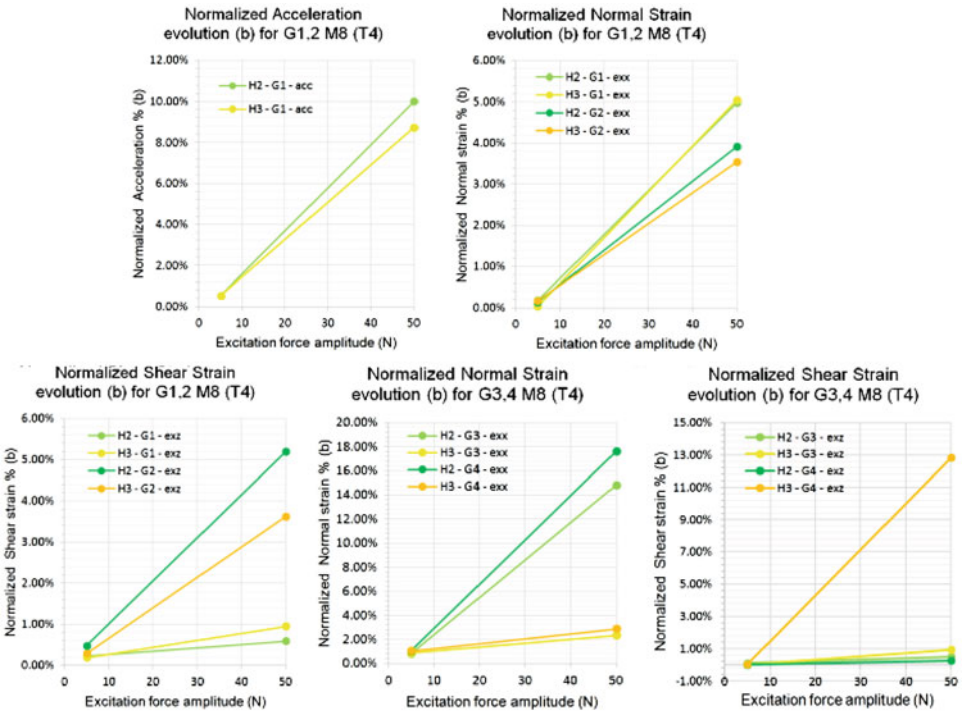

Fig. 35.35 Evolution of the normalized (b) numerical acceleration, normal and shear strains for a low and high levels of excitation force of mode 8 (370 Hz)

35.8 Conclusions

This paper presented a research work focussed on nonlinear dynamics of bolted flanges. A section of a Rolls-Royce aero-engine casing was redesigned in order to remove several geometrical details but preserving its major dynamic properties. The objective was to study the nonlinear dynamics by measuring and analysing the strains across the flange. The work was dived in several stages each of which assured that the level of knowledge about the modal characteristics of the components were as complete as possible. So, linear modal analysis was carried out for performing model updating. A ranking of the mode shapes to be tested up to nonlinear vibration was attempted by using strain analysis. This ranking was experimentally validated by performing modal testing under nonlinear conditions and which were executed using different control methods. An FE model of the flange was built using contact elements at the flange location. This enabled the time response analysis and prediction of strains for given excitation mode. The test structure was equipped with strain gauges at four locations across the flange. Nonlinear testing was carried out and strain data acquired and analyzed. Both theoretical and experimental data were correlated. The research showed that strains can be sensitive to nonlinearity even for smaller levels of vibrations than the actual required for accelerometers. The ranking based on strain analysis showed that torsional modes tend to present more nonlinearity than the bending ones. Additional work must be carried out in this direction. Specifically, in the area of nonlinear response prediction of FE models. This is still base on numerical integration which is very time consuming and therefore limiting the data generation and analysis.

References

1. Ewins DJ, Modal testing theory, practice and applications, 2nd edn. RSP
2. Blandin C (2013) Identification of dynamic nonlinearities of bolted structures. MSc project literature review report from the University of Bristol
3. Ibrahim RA, Pettit CL (2003) Uncertainties and dynamic problems of bolted joints and other fasterners. J Sound Vib 279(2005):857–936
4. Song Y, McFarland D, Bergman A, Vakakis F (2005) Effect of pressure distribution on energy dissipation in mechanical lap joint. AIAA J 43(2):420–425
5. Bograd S, Reuss P, Schmidt A, Gaul L, Mayer M (2010) Modeling the dynamics of mechanical joints. Mech Syst Signal Process 25(2011):2801–2826
6. Oldfield M, Ouyang H, Mottershead E (2004) Simplified models of bolted joints under harmonic loading. Comput Struct 84(2005):25–33
7. Gaul L, Lenz J (1997) Nonlinear dynamics of structures assembled by bolted joints. Acta Mech 125:169–181

8. Ahmadian H, Ebrahimi M, Mottershead JE, Friswell MI (2002) Identification of bolted-joint interface models. Proc ISMA2002 IV: 1741–1748
9. Böswald M, Link M, Identification of nonlinear joint parameters by using frequency response residuals. University of Kassel (Germany)
10. Cazzolato B, Widly S, Codrington J, Kotousov A, Schuessler M (2008) Scanning laser vibrometer for non-contact three-dimensional displacement and strain measurements. From Proceedings of ACOUSTICS 2008
11. Chatelet E, Baranger T, Jacquet-Richardet G, Saulot A (2014) Identification of contact area from full-field displacement surface measurements. Proceedings of ASME Turbo Expo 2014 – GT2014-25504
12. Di Maio D, Schwingshackl C, Sever I, Development of a test planning methodology for performing experimental model validation of bolted flanges
13. Blandin C (2014) Design and finite element linear modal analysis of a simplified aircraft engine casings assembly and research proposal for a methodology for performing the identification of dynamic nonlinearities of a flange bolted structure. From the University of Bristol
14. "ICATS." ICON Suite, 58 Prince's Gate Exhibition Road, London SW7 2PG.
15. "FEMtools". Dynamic Design Solutions N.V. (DDS) Interleuvenlaan 64, B-3001, Leuven, Belgium
16. Vishay Precision Group (2010) Strain gage rosettes: selection, application and data reduction. Tech note TN-515
17. Herzog A, Krack M, Scheidt L, Wallascheck J (2014) Comparison of two widely-used frequency-time domain contact models for the vibration simulation of shrouded turbine blades. Proceedings of ASME Turbo Expo 2014 – GT2014-26226
18. Jensen A (2010) Linear contact analysis: demystified. Finite Element Analysis Predictive Engineering
19. Billings SA (2013) Nonlinear system identification: NARMAX methods in the time, frequency, and spatio-temporal domains. Wiley, Chichester. ISBN 978-1-118-53556-1
20. Brown KH, Morrow C, Durbin S, Baca A (2008) Guideline for bolted joint design and analysis: version 1.0. Sandia National Laboratories
21. Pastor M, Binda M, Harcarik T (2012) Modal assurance criterion. Proc Eng 48:543–548

Chapter 36
The Effects of Boundary Conditions, Measurement Techniques, and Excitation Type on Measurements of the Properties of Mechanical Joints

S. Smith, J.C. Bilbao-Ludena, S. Catalfamo, M.R.W. Brake, P. Reuß, and C.W. Schwingshackl

Abstract This paper investigates how the responses of mechanical joints are influenced by using different experimental setups. The experiments are conducted on both a monolithic beam and a bolted beam, and the beams are excited by hammer tests and a shaker. Multiple boundary conditions are also studied. It is found that the hammer tests performed on the "free" boundary condition monolithic beam (for multiple bungee lengths and positions) had a negligible influence on the system in terms of damping ratio and frequency variation. Multiple sensors attached to the monolithic beam are studied; the effect of multiple accelerometers manifests as a significant shift of frequency and damping due to the additional mass. In the case of the jointed beam, both mirror-like and rough interfaces are used. Several sets of different interface pairs, bolt torques, bolt preloads, excitation frequency sweep rates and bolt tightening orders are considered in this study. The time varying changes in stiffening and damping are measured by testing multiple combinations of the experimental setup at different levels of excitation. The results showed that the mirror-like surface finish for the interface has higher damping values compared to the rough surface across multiple bolt torque scenarios (such as preload and tightening order) and modes of vibration. Guidelines for a more reliable measurement of the properties of a mechanical joint are made based on the results of this research.

Keywords Bolted joints • Nonlinear vibration • Experimental setup • Measurement effects • Testing guidelines

36.1 Introduction

The study and measurement of nonlinear systems is, and will continue to be, a challenging endeavor. Inherent in the measurement of nonlinear systems is the challenge of measuring multiple stable and unstable equilibria, which is paramount for identifying the system level features of a nonlinearity. Much of the difficulty associated with nonlinear systems originates in a poor understanding of the physics governing the nonlinearity. As the system is nonlinear, even small differences in the constitutive models of a nonlinearity can lead to dramatic differences in the system's responses [1, 2].

Often, experimental measurements of a nonlinear system convolute the effects due to the experimental setup and the effects due to the nonlinearity of interest [3, 4]. For instance, a clamped boundary condition is often prohibitively difficult

Sandia National Laboratories is a multi-program laboratory managed and operated by Sandia Corporation, a wholly owned subsidiary of Lockheed Martin Company, for the U. S. Department of Energy's National Nuclear Security Administration under Contract DE-AC04-94AL85000

S. Smith
University of Maryland, Baltimore County, Baltimore, MD, USA

J.C. Bilbao-Ludena
Technical University of Berlin, Berlin, Germany

S. Catalfamo • P. Reuß
University of Stuttgart, Stuttgart, Germany

M.R.W. Brake (✉)
Sandia National Laboratories, Albuquerque, NM, USA
e-mail: mrbrake@sandia.gov

C.W. Schwingshackl
Imperial College London, London, UK
e-mail: c.schwingshackl@imperial.ac.uk

G. Kerschen (ed.), *Nonlinear Dynamics, Volume 1*, Conference Proceedings of the Society for Experimental Mechanics Series, DOI 10.1007/978-3-319-15221-9_36

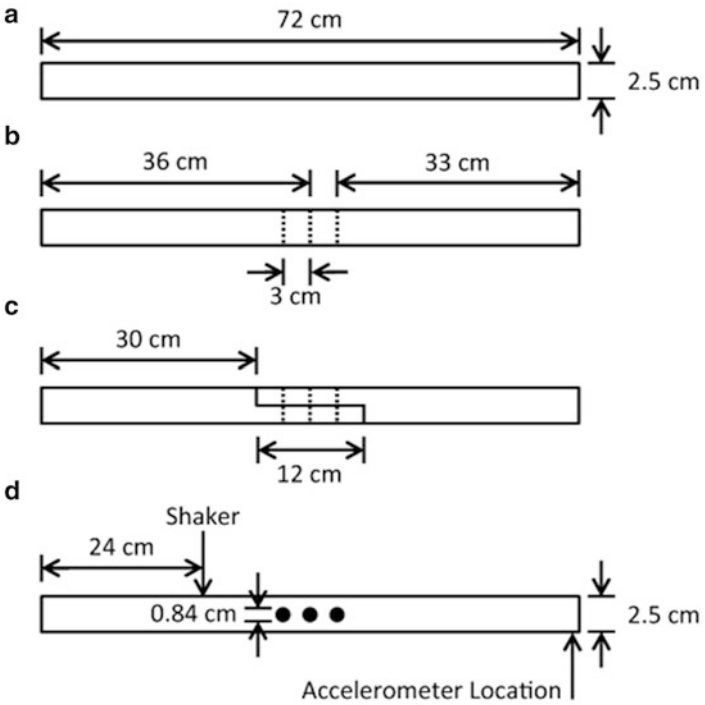

Fig. 36.1 The geometry of the (**a**) monolithic system, (**b**) monolithic system with bolt holes, (**c**) jointed system, and (**d**) top view of the monolithic system with bolt holes. For both the monolithic system with bolt holes and the jointed system, the size and position of the bolt holes and shaker/stinger attachment point are the same

to achieve; in most cases, some amount of torsional stiffness, friction, and even intermittent contact can be introduced by the boundary condition. At the opposite extreme, the free boundary condition is often replicated via bungee cords that act as weak springs. What effect does this added stiffness have on the system though?

In the study of mechanical joints, many questions persist because a complete understanding of the interfacial physics does not, and will not for the foreseeable future, exist [4]. At present, the salient questions of interest in measuring the response of a mechanical joint are:

- How does the mechanical joint affect the system's stiffness?
- How does the mechanical joint affect the system's damping?
- How do these quantities change with excitation parameters (amplitude, frequency, etc.)?

To address these questions, it is paramount that the effects of the mechanical joint are separated from other sources of uncertainty and/or nonlinearity, including the boundary conditions, manner of excitation, and the system itself. In order to approach this problem, the Brake-Reuss beam [5] is proposed as a candidate system for studying lap joints in a dynamic framework. The Brake-Reuss beam (Fig. 36.1) is a set of three separate systems that are designed to determine the effects of a lap joint to a system's dynamic response. The first system (Fig. 36.1a) is a monolithic beam with no mechanical joints, which serves as a reference system that is used to deduce the contribution of the lap joint to the system's damping and stiffness. The second system (Fig. 36.1b) is a monolithic beam with three through-holes, through which bolts are passed and tightened in order to determine the contribution of the bolts (in terms of added mass in addition to stiffness and damping) to the dynamic response. Figure 36.1c shows the third system, in which the lap joint is present. In all three systems, a shaker can be attached via a stinger approximately 24 cm from one end of the beam. The transfer function for the acceleration is then measured at the opposite tip of the beam. Preliminary analysis of this system [5] indicates that there is a strong effect due to the lap joint on the system's frequency response functions. This is an important property as this strong effect is not always discernible in systems with mechanical joints [6].

One significant difference between the present research and the system studied in [5] is that the shaker's attachment to the beams is located along the centerline of the beam. In [5], the shaker's attachment was offset from the centerline, which led to the excitation of the torsional modes in addition to the bending modes of the beam. A result from the preliminary analysis of [5] found that the torsional modes are so sensitive to the interfacial conditions (such as alignment) that the effects of the residual stresses due to the bolt preloads is not distinguishable from other effects. The bending modes, in contrast, are observed in [5] to be sensitive to the residual stresses due to the bolt preloads (and the order in which the bolts are tightened).

In what follows, a more thorough analysis of the system of [5] is presented. This analysis studies the effects of different loading/excitation conditions and boundary conditions. The interfacial properties are also directly measured for different surface finishes, alignments, and bolt torques, and these results are correlated with the properties observed in the frequency response functions. Finally, recommendations for the measurement of nonlinear systems with mechanical joints are made.

36.2 Effects of Boundary Conditions

One method to isolate the effects of a mechanical joint on a system's dynamic response, is to design the test setup to be as linear as possible. To test the different permutations of experimental setups, the monolithic beam (Fig. 36.1a) is used. All test specimen are fabricated from stainless steel 304. The basic experimental setup is shown in Fig. 36.2, which includes the beam, two bungee cords, two PCB 356A03 Triaxial ICP Accelerometers (Accel), two 356A02 Triaxial ICP Accelerometers used in a second experimental setup, a PCB 086C03 ICP Impact Hammer (Hammer), a Bruel & Kjaer PM Vibration Exciter Type 4809 (Shaker), LMS 16 Channel Spectral Analyzer, and a modular support rig. The excitation effects are tested in two groups: first with the impact hammer, and second with the shaker. In the first test, the mode shapes and natural frequencies of the beam are measured using a roving hammer technique with 58 impact lines with two impacts on each line. Table 36.1 contains the modal frequencies and damping, and Fig. 36.3 displays the mode shapes. The numbering in Fig. 36.3 is for the modes calculated using the Finite Element software ABAQUS 6.10. The first longitudinal mode is the seventh mode of the system, which is not excited during the present experiments.

The first group tested the effects the impact hammer tip type (metal or plastic), the impact force amplitude (high or low), the bungee cord length (0.318 m or 0.1651 m), the location of the bungee cords (inside, 10.2 cm separated centered, or outside, 5.72 cm from edges of the beam), the accelerometers' attachment condition (glued or waxed), the position of the accelerometer cables (hanging, supported out the side, or straight down as shown in Fig. 36.4), and the number of sensors

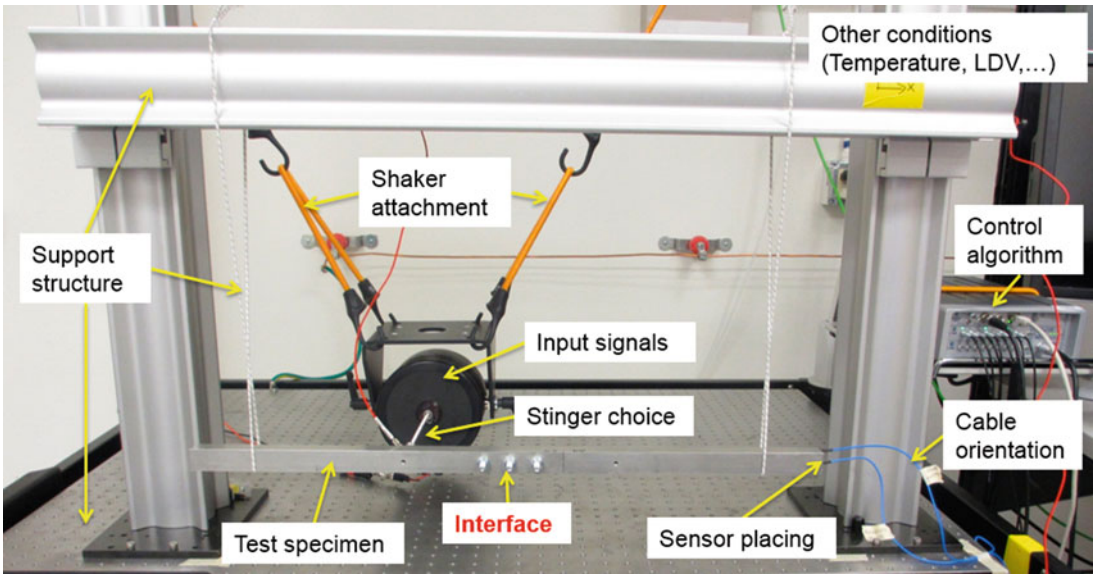

Fig. 36.2 Basic test setup for testing the effects of boundary conditions, excitation techniques, and sensor setup

Table 36.1 Modal testing results on the monolithic beam

Mode	Frequency [Hz]	Modal damping [%]
1st Bending	246.3	0.03
2nd Bending	674.5	0.04
3rd Bending	1, 308.5	0.03
1st Torsional	1, 965.0	0.03
4th Bending	2, 130.7	0.04
5th Bending	3, 126.8	0.04
2nd Torsional	3, 931.8	0.05

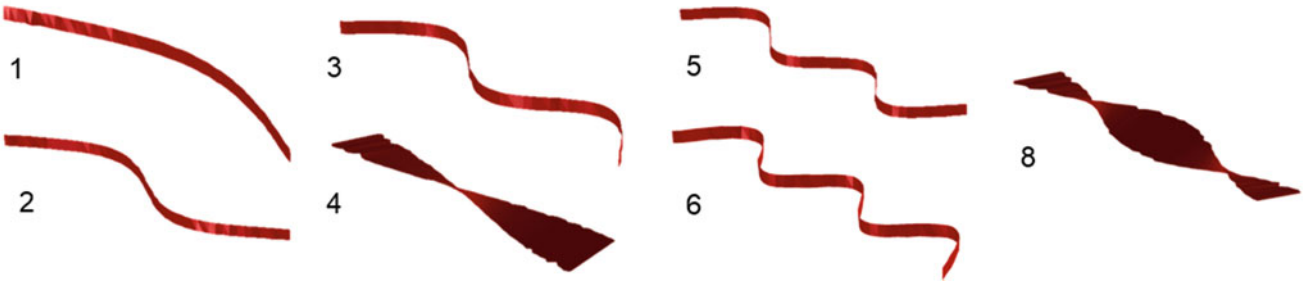

Fig. 36.3 Mode shapes measured in modal analysis

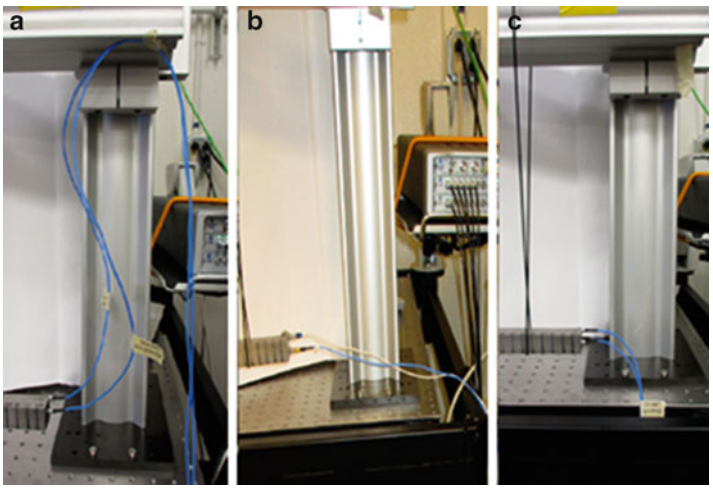

Fig. 36.4 Sensor cable positions: (**a**) supported above, (**b**) supported across, and (**c**) unsupported

Table 36.2 Experimental setups tested for nonlinear influences

Test number	Bungee cord type	Bungee cord location	Bungee cord length (m)	Accelerometer mass (grams)	Accelerometer attachment technique	Hammer mass (grams)	Accelerometer cable orientation
1	White	Inside	0.318	1	Glue	160	Above
2	White	Inside	0.318	1	Glue	235	Above
3	White	Outside	0.318	1	Glue	160	Above
4	White	Outside	0.1651	1	Glue	160	Above
5	Black	Outside	0.318	1	Glue	160	Above
6	Black	Outside	0.318	1	Wax	160	Above
7	Black	Outside	0.318	10.5	Wax	160	Above
8	Black	Outside	0.318	1	Glue	160	Across
9	Black	Outside	0.318	1	Glue	160	Unsupported

on the specimen. The various tests, not including multiple sensors, are listed in Table 36.2. The tests are run with a single impact in order to not average any measured nonlinear response out of the results. The resulting frequency response functions (FRFs) are shown in Fig. 36.5. In order to verify that the test beam is isolated from all sources of external excitation aside from the impact hammer, the support structure is impacted after each change in the bungee cord location or length, at three different locations: at the center of the cross bar, at a location adjacent to the bungee cord, and at the attachment location to the table. The results of these tests show that there is not any significant nonlinearities in any of the test setups, which is desirable. The only significant nonlinearities appear in the torsional modes, which are constrained by the bungee cords; the severities of the nonlinearities are listed in Table 36.3. These nonlinearities could potentially be avoided by an alternative attachment method of the bungee cord to the end of the beam. In the absence of being able to manufacture the beam to attach to the bungee cords in a specific manner, the principle option for an alternative attachment method would be to glue to the bungee cords to the ends of the beam; however, this is dependent on the strength of the glue and whether the bungee is stretched before being glued.

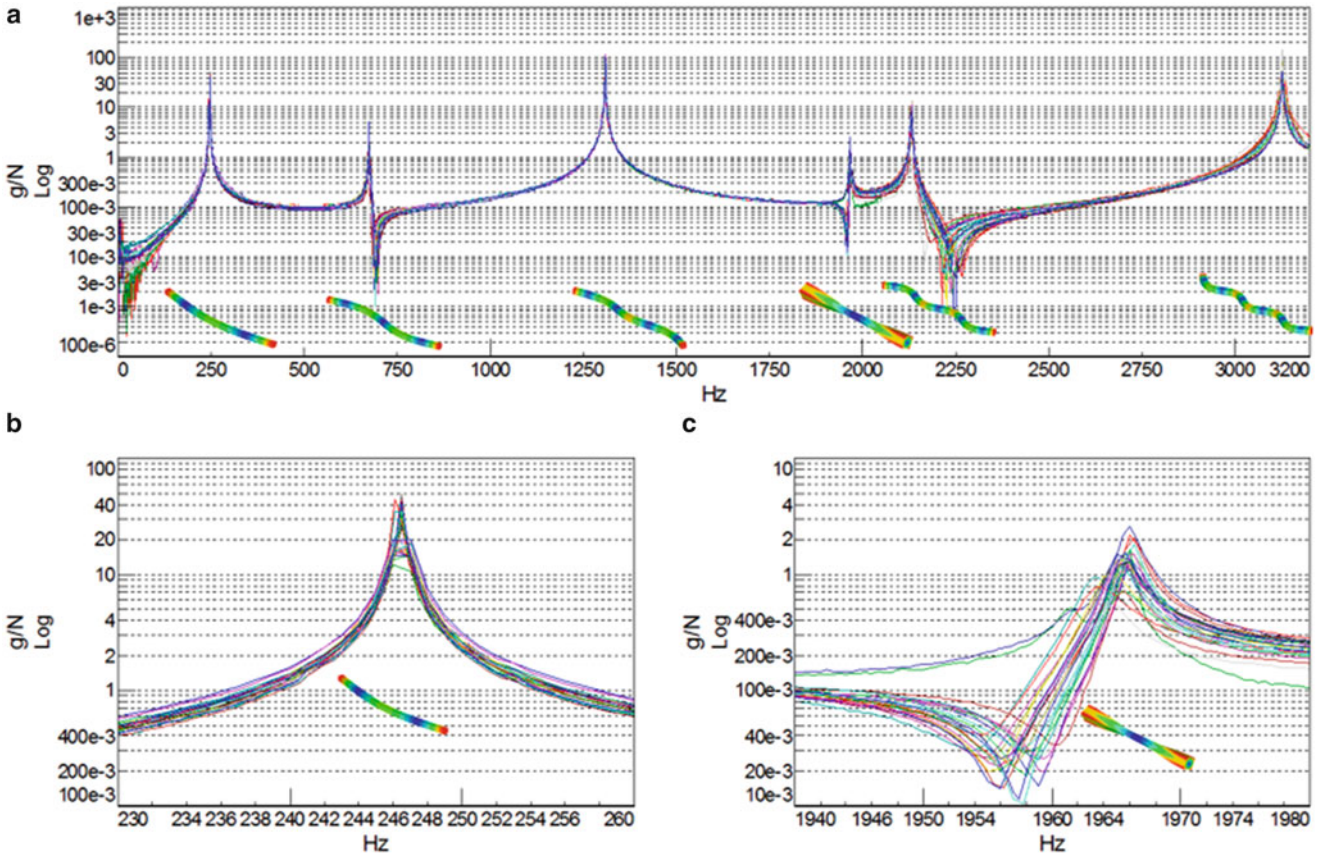

Fig. 36.5 The FRFs for the experimental setups listed in Table 36.2, for (**a**) the entire frequency range studied, (**b**) the first natural frequency, and (**c**) the fourth natural frequency

The final impact hammer test of the monolithic beam is multiple sensors placed on the beam; since the mass of the accelerometers are much smaller than that of the beam (approximately 0.02 % of the beam's mass), it is predicted that effects of more sensors would not be noticeable. Sensors that have a mass of 5 g are placed onto the beam as shown in Fig. 36.6 in four different testing scenarios. The results (Fig. 36.7) show that the torsional modes are most effected by the added masses, resulting in a 17 Hz shift in the first torsional mode and increased damping in the second torsional mode. The severities of the nonlinearities are listed in Table 36.3. As can also be seen in Figs. 36.7b and c, both the reference response and the response of loading scenario three are grouped together in the fourth mode while the reference response and the response of loading scenario one are grouped together in the seventh mode. This is a result of the additional sensors' placement on a node of those modes. The shift in frequency and damping could be associated with the sensors changing the moment of inertia of the beam at the anti-nodes of vibration.

36.3 Effects of Excitation and Measurement Conditions

The second series of experiments utilizes a shaker to excite the beam. The type of stinger, amplitude of excitation, type of signal, sweep direction, and the use of a Polytec OFV-55x Fiber-Optic Interferometer (LDV) compared to an accelerometer are studied. The shaker is attached to the beam with a PCB 208A03 force transducer at the location indicated in Fig. 36.8. The type of stinger is tested first to determine which stinger causes the smallest deviations from the FRFs measured using the impact hammers. The stingers tested are shown in Fig. 36.9 and the results generated by supplying a sweep signal are shown in Fig. 36.10. These results show that the wire and M2 stingers have a significant influence on the response of the system; the two stingers listed also excited the torsional mode which should not have been excited with the position of the stinger on the beam. The torsional modes being excited indicates that the stingers are bending and the restoring force is causing energy to be inputted into the mode.

Table 36.3 Severity of the nonlinear influence from different experimental setups on the natural frequency and modal damping of the beam

Category		Effect on frequency	Effect on damping	Notes
Hammer	Metal	REF	REF	Frequency range with good coherence: 0–8 kHz
	White plastic tip	Low	Low	Frequency range with good coherence: 0–3.2 kHz
	Metal tip with added mass (75 g)	Low	Low	More energy input into structure at low frequencies
Bungees	Full length (13″)	REF	REF	
	Half length	Low	Low	Marginal frequency shifts (1 Hz)
	Inside position	Low	Low	Marginal frequency shifts (1 Hz)
	Outside position	Low	Low	Marginal frequency shifts (1 Hz)
Accelerometers	2 accelerometers glued	REF	REF	Accelorometers glued at one end of the beam, each 4 g
	2 accelerometers attached via wax	Low	Low	Marginal frequency shifts (1 Hz)
	Number of sensors: Scenario 1 (Fig. 36.6)	Mid	Mid	Moderate change in frequency and damping
	Number of sensors: Scenario 2 (Fig. 36.6)	High	High	Frequency shifts from 1 Hz to 30 Hz down (mode dependent); torsional & higher bending modes highly damped
	Number of sensors: Scenario 3 (Fig. 36.6)	High	Low	The frequency shifted up for 2nd torsional but down for higher modes, damping has minor changes
	Cable orientation: up, down, on table	None	Low	Cable down causes slightly higher damping for some modes (+0.01 %)
Test rig		None	None	impacts on different spots of the test rig & table

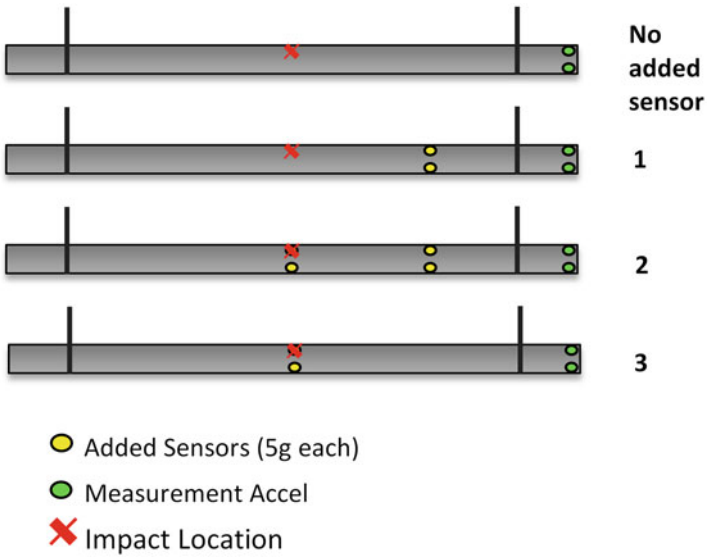

Fig. 36.6 Added sensor testing scenarios

The subsequent shaker excitation experiments use the 10–32 UNF stinger, which has the smallest influence on the response of the beam, and the corresponding FRFs are shown in Fig. 36.11. The severities of the nonlinearities for all shaker tests are listed in Table 36.4. The FRFs show that the use of the LDV only has the largest frequency shift, resulting from the removal of the accelerometers, and the white noise has extra peaks between the third and fourth peak, which could be from stinger modes being excited more than when sweep signals are generated.

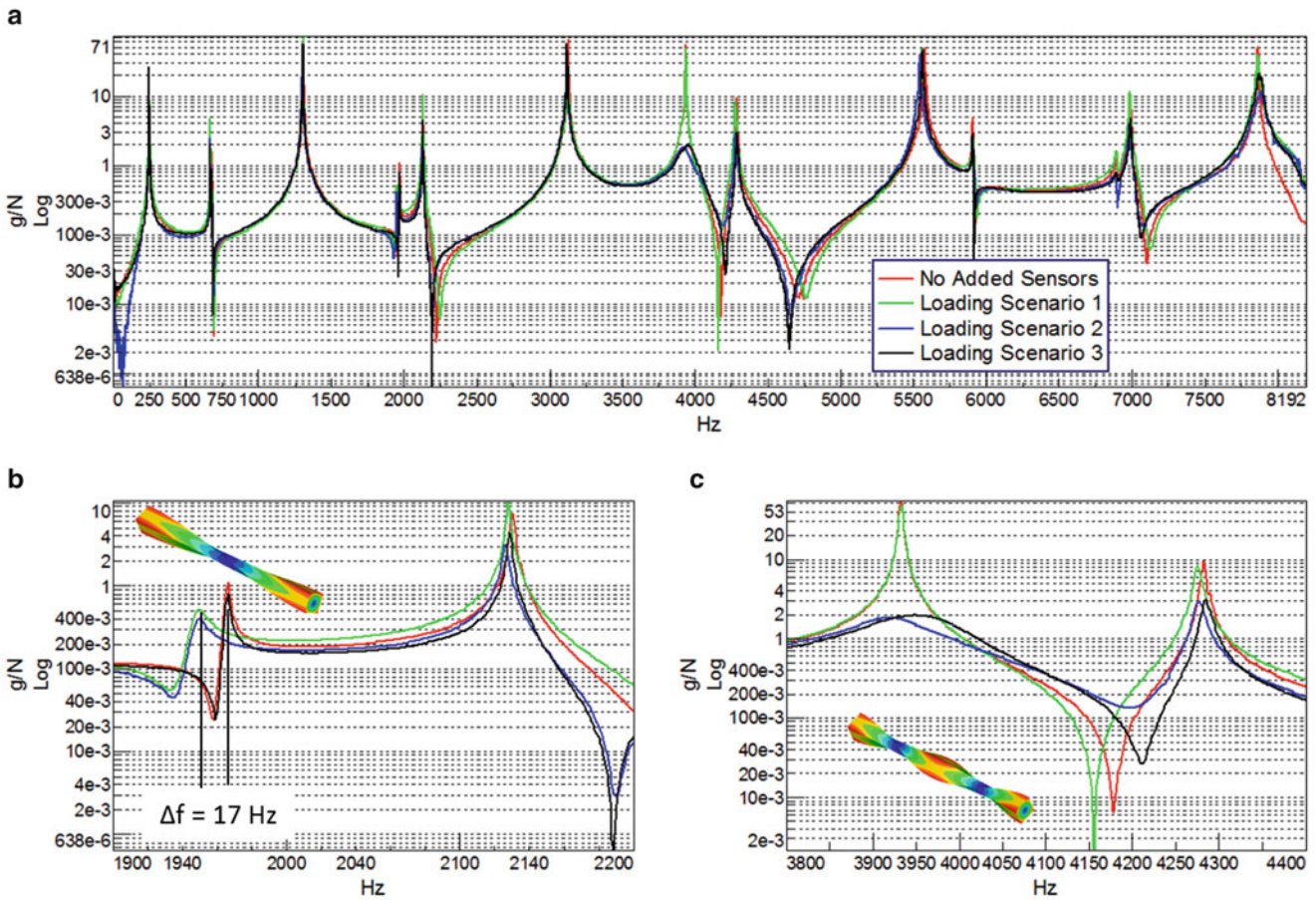

Fig. 36.7 The FRFs of the added mass test scenarios for (**a**) the entire frequency range, (**b**) the fourth and fifth natural frequencies, and (**c**) the seventh and eighth natural frequencies

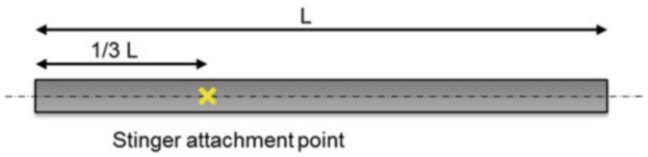

Fig. 36.8 Location of the shaker attached to the beam

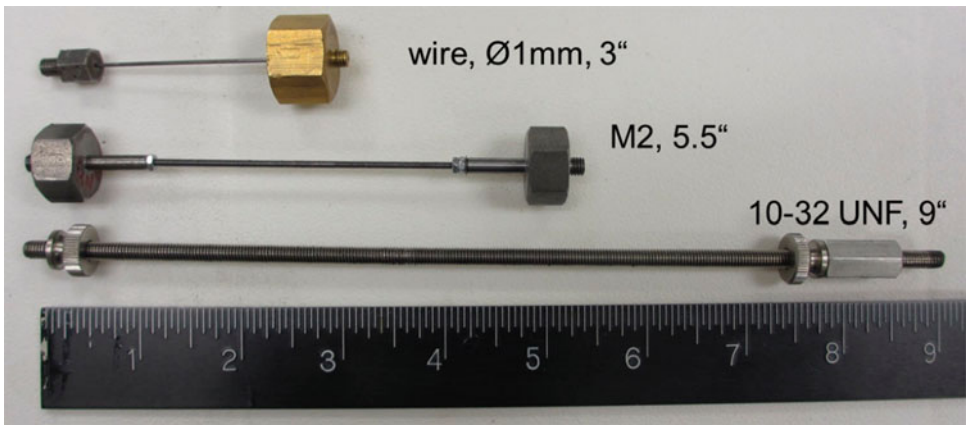

Fig. 36.9 The three stingers tested for nonlinear effects

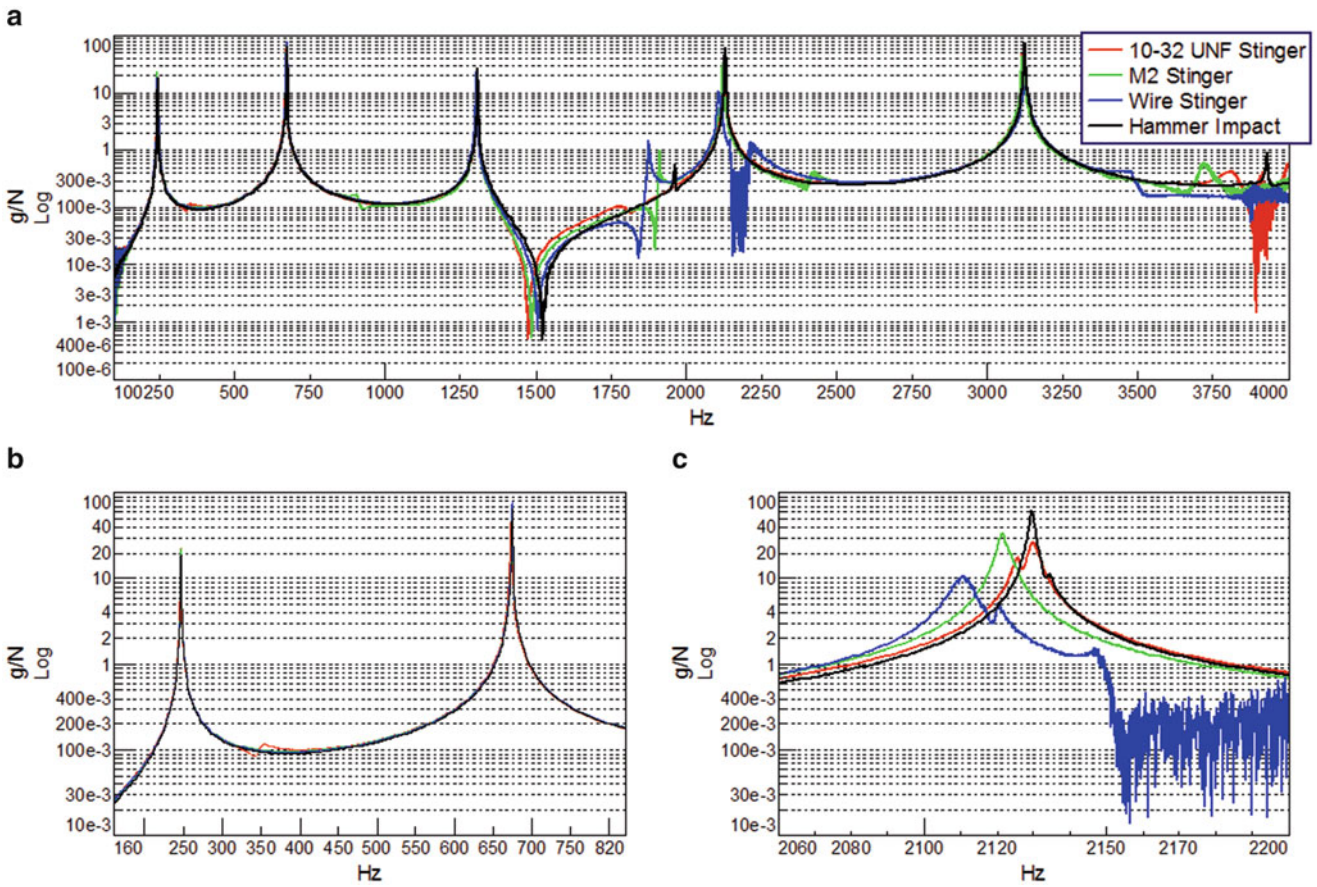

Fig. 36.10 The FRFs of the stinger tests and one impact test for (**a**) the entire frequency range, (**b**) the first and second natural frequencies, and (**c**) the fourth natural frequency (as measured with the impact hammer)

36.4 The Jointed Beam

The nonlinearities in a jointed beam currently are difficult to identify comprehensively due to the variability in the interfacial conditions (surface finish, alignment, asperity distribution, residual stresses, machining variations and curvature, etc.). The profile influences the pressure distribution as well as the friction in the joint. Two different surface finishes are used in this study: a rough finish and a mirror-like finish. The rough finish specimens are manufactured using wire electric discharge machining (EDM) and the mirror finish by laser cutting and polishing. The rough finish specimens developed a warped interface, such as the one shown in Fig. 36.12. The pressure distribution of the interfaces is mapped using FujiFilm Prescale Light Weight and Mid-Sensitivity films, with 5, 10, and 20 Nm torques on the bolts holding the specimens together, shown in Fig. 36.13. The bolts are torqued to half the listed torque then to the full torque value in order to achieve a more uniform pressure distribution. The results of the pressure test shows that the rough interface specimens' pressure distribution is dependent on the bolt tightening order; whereas the mirror-like interface is independent of the order as the pressure distribution approximately is constant.

The jointed beams are then tested using the shaker with a constant sweep up or a stepped sine force control signal. The first test is of the bolt tightening orders, shown in Fig. 36.14, using the constant sweep signal, with results shown in Fig. 36.15 for the rough interface specimens and Fig. 36.16 for the mirror-like interface specimens. The results for the rough interface specimens shows that the response of the beam is more dependent on which outside bolt is tightened first; while the mirror interface response shows that it is independent of the tightening order. The beams are then tested using a sine step force control signal with different levels of bolt torque magnitude (hand tightened, 3, 5, 8, 10, and 20 Nm), shown in Figs. 36.17 and 36.18 for the rough interface specimens and mirror-like interface specimens, respectively. The response for the rough interface specimens appears to converge to a saturation point at approximately 10 Nm; however when the torque is increased further the response changes indicating that a saturation point was not reached. The mirror-like interface specimens' response shows that saturation is reached around 8 Nm.

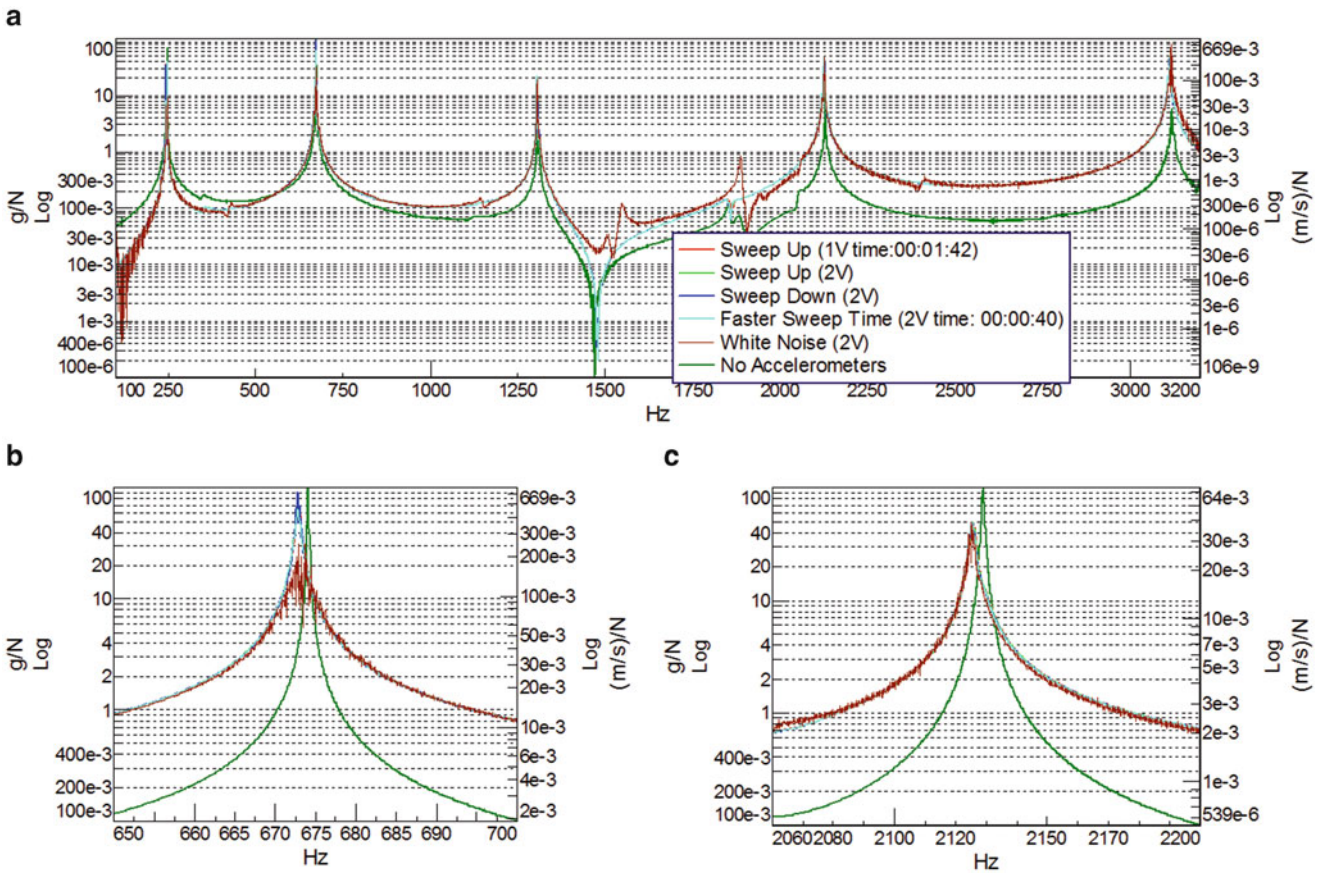

Fig. 36.11 The FRFs of the shaker signal tests over (**a**) the entire frequency range, (**b**) near the second natural frequency, and (**c**) near the fourth natural frequency

Table 36.4 Severity of the nonlinear influence of shaker test setups on frequency and damping of the beam

Category		Effect on frequency	Effect on damping	Notes
Stingers	Impact test	REF	REF	
	10-32 UNF (9″ length)	Low	Low	No torsional modes excited, matches best to hammer tests
	M2 (5.5″ length)	Mid	None	Frequency-shift down
	Wire (3″ length)	Mid	None	Frequency-shift down, torsional modes excited, stinger bending occurs
Excitation Amplitude (V)	High (2 V, sweep up)	REF	REF	
	Low (1 V, sweep up)	None	Low	Marginal frequency shifts (1Hz)
Signals	Sweep up	REF	REF	
	Sweep down	None	Low	Linear structure tested
	Sweep rate low (10 Hz/s)	Low	None	Needs to be investigated in more detail
	Sweep rate high (80 Hz/s)	Low	None	Needs to be investigated in more detail
	White noise	Low	Low	Noisy FRF, no anti-peaks
Accelerometers	Two accelerometers glued	REF	REF	
	No accelerometers (LDV)	Mid	Low	Frequency-shift to slightly higher frequency

Fig. 36.12 The rough interface specimen's warped interface

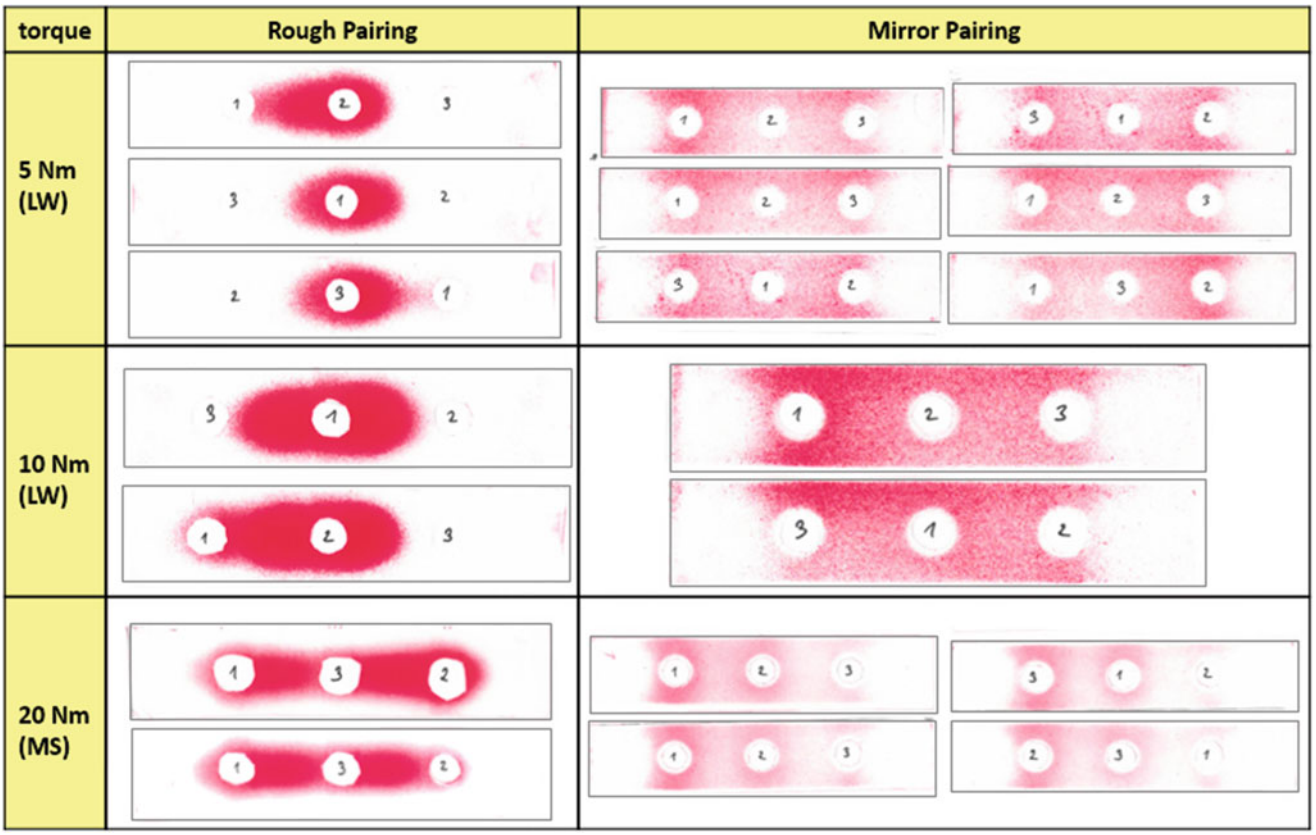

Fig. 36.13 Pressure distributions of the specimens with bolt tightening order indicated on each pressure distribution

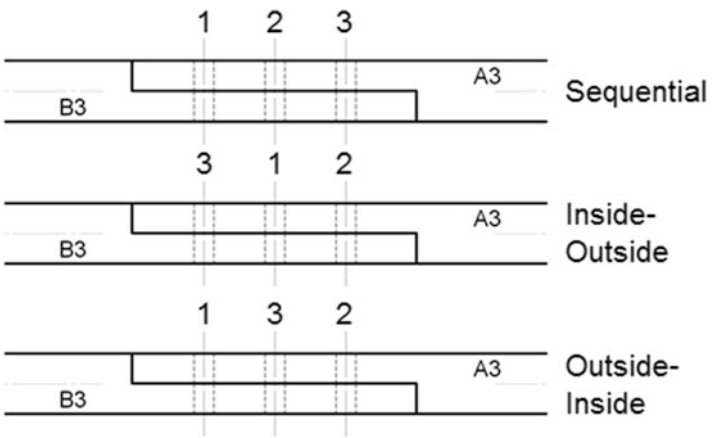

Fig. 36.14 Bolt tightening order shown on a mock joint

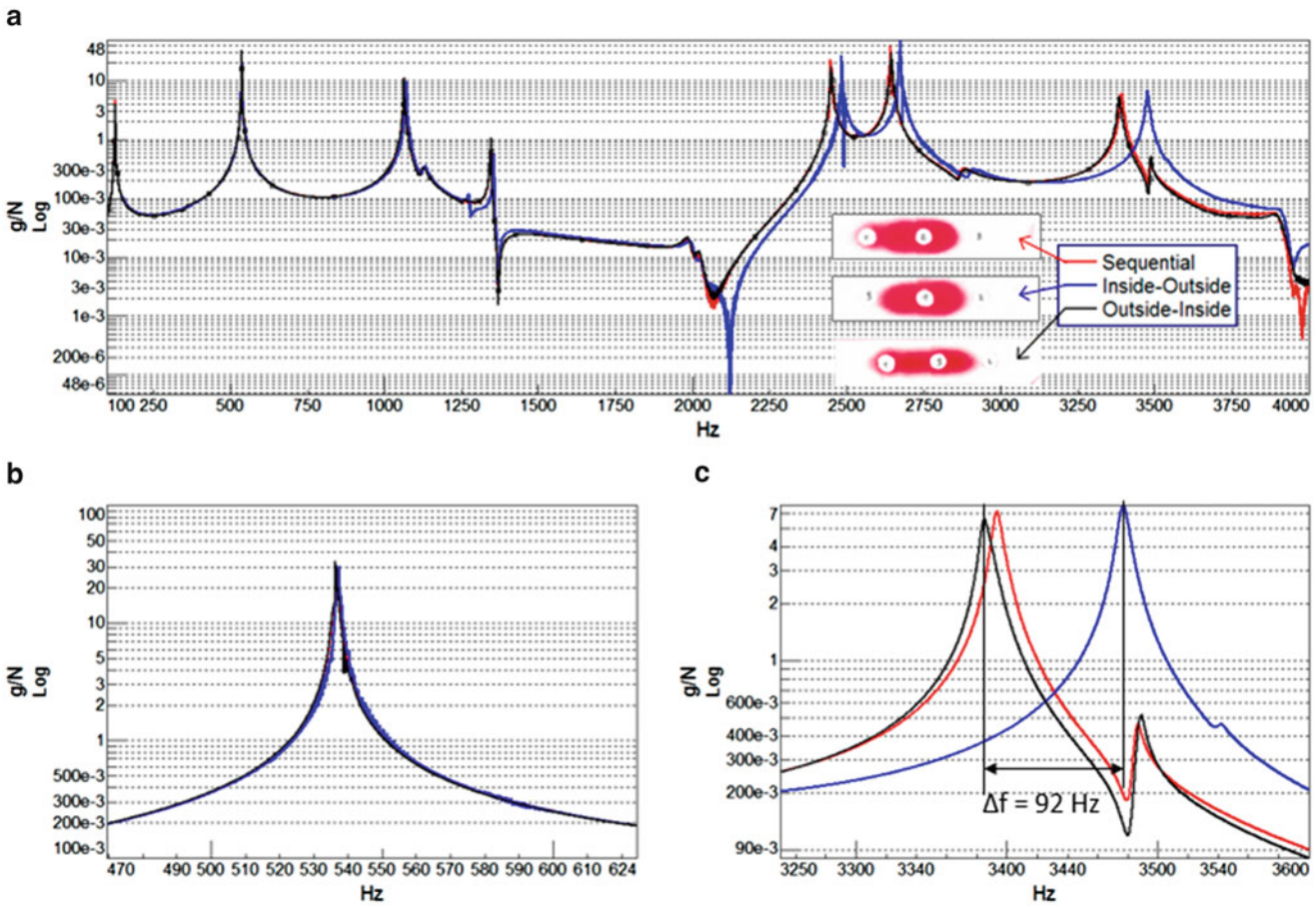

Fig. 36.15 The FRFs of the bolt tightening order of the rough interface for (**a**) the entire frequency range, (**b**) near the second natural frequency, and (**c**) near the seventh natural frequency. The tightening orders are: sequential from one side to the other (*red*), the middle then the outer bolts (*blue*), and the outer then the middle bolt (*black*)

There is little repeatability in the responses of jointed structures, due to the roughness of the interfaces being different on the micro-scale from specimen to specimen and from experiment to experiment [5]. To assess experiment-to experiment variability, the following procedure is used:

- The reference test is conducted after the assembly is first bolted together with a specified bolt torque.
- The beams are disassembled then immediately reassembled with the same specified bolt torque, and immediately tested.
- The beams are disassembled and reassembled with the same specified bolt torque, then allowed to rest for approximately 600 s before being tested.
- Lastly, the bolts are then retorqued back to the specified bolt torque level without disassembling the beams, and then tested.

The responses of the rough interface specimens and mirror-like interface specimens are shown in Figs. 36.19 and 36.20, respectively, for this series of tests. Unlike previous measurements of this system [5], the experiment to experiment variability is found to be low. The discrepancy between this result and [5] is potentially due to the excitation of the torsional modes in [5] but not in the present work, and warrants further investigation. The final experiment is to study the effects of the sine step force control step direction, shown in Fig. 36.21. The results show that the response is direction independent, which is in stark contrast to nonlinear systems like the Duffing oscillator.

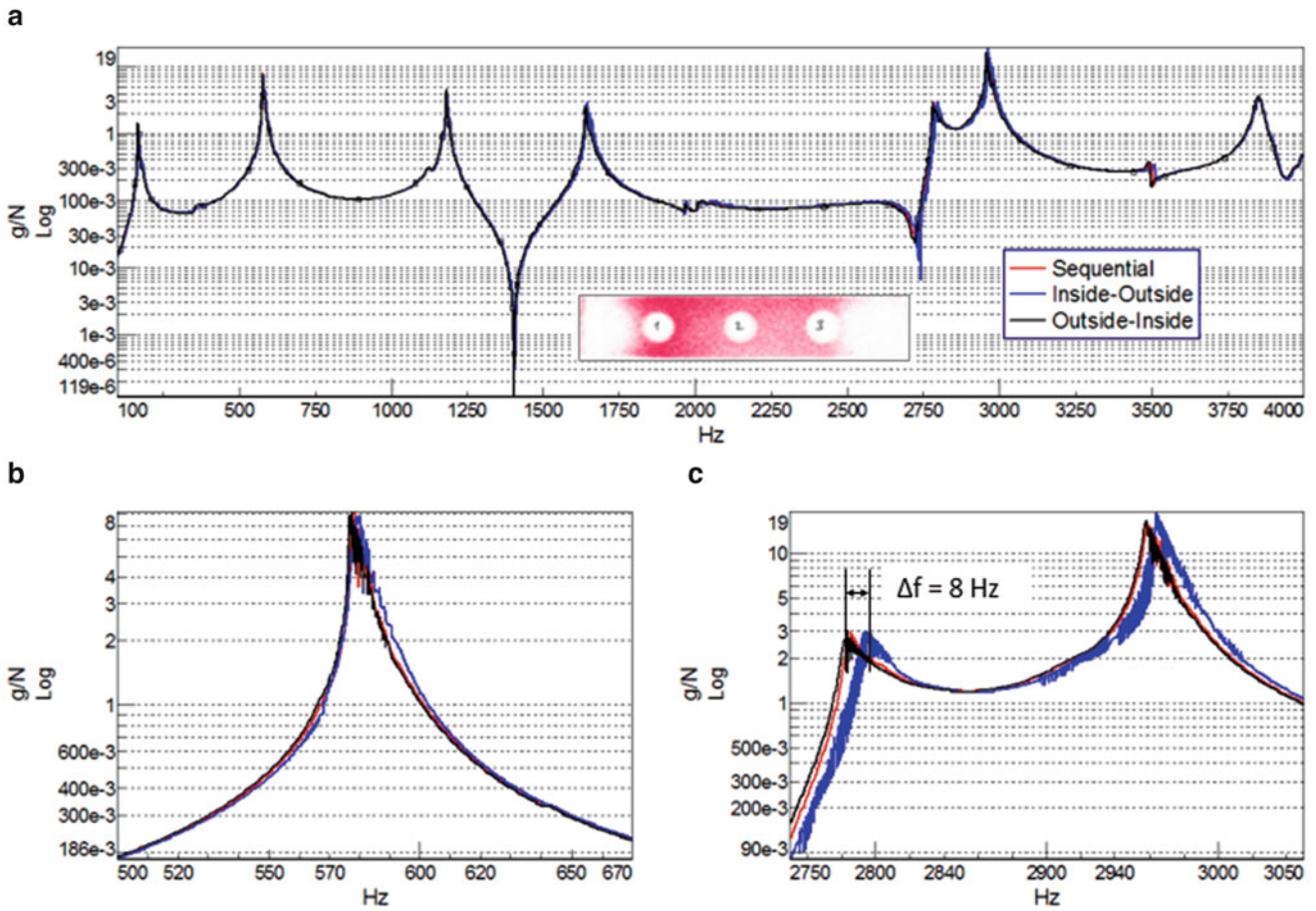

Fig. 36.16 The FRFs of the bolt tightening order of the mirror interface for (**a**) the entire frequency range, (**b**) near the second natural frequency, and (**c**) near the seventh natural frequency. The tightening orders are: sequential from one side to the other (*red*), the middle then the outer bolts (*blue*), and the outer then the middle bolt (*black*)

36.5 Conclusions

This research sought to identify a set of best-practices for conducting experiments of nonlinear systems, specifically those with jointed interfaces. The effects of the boundary conditions, excitation techniques, and measurement techniques on the measurements of the system's stiffness and damping properties are studied. Specific recommendations from this preliminary work are:

- For impact hammer measurements, the tip and hammer mass do not significantly affect the measurements of damping and stiffness. Thus, the impact hammer configuration should be chosen based on the frequency range of interest with harder tips without added mass being more appropriate to study higher frequencies.
- The responses of systems with free boundary conditions created via the use of bungee cords are insensitive to the bungee length, stiffness and position.
- The use of accelerometers, even when they are a small fraction of the mass of the system (0.02 % in the present work), can significantly affect the measurements of damping and stiffness. If used, accelerometers should be located away from node points, and the number should be kept to a minimum.
- For shaker excitation, care should be used in selecting an appropriate stinger. Of those tested, the thinner stingers are found to exhibit bending, which results in the appearance of nonlinearities in the system's frequency responses.
- The excitation sweep rate, magnitude, and direction are not found to have significant effects for the present system.
- The conditions of the interface have significant effects on the responses of the system, and future work should aim to thoroughly quantify the interface conditions.

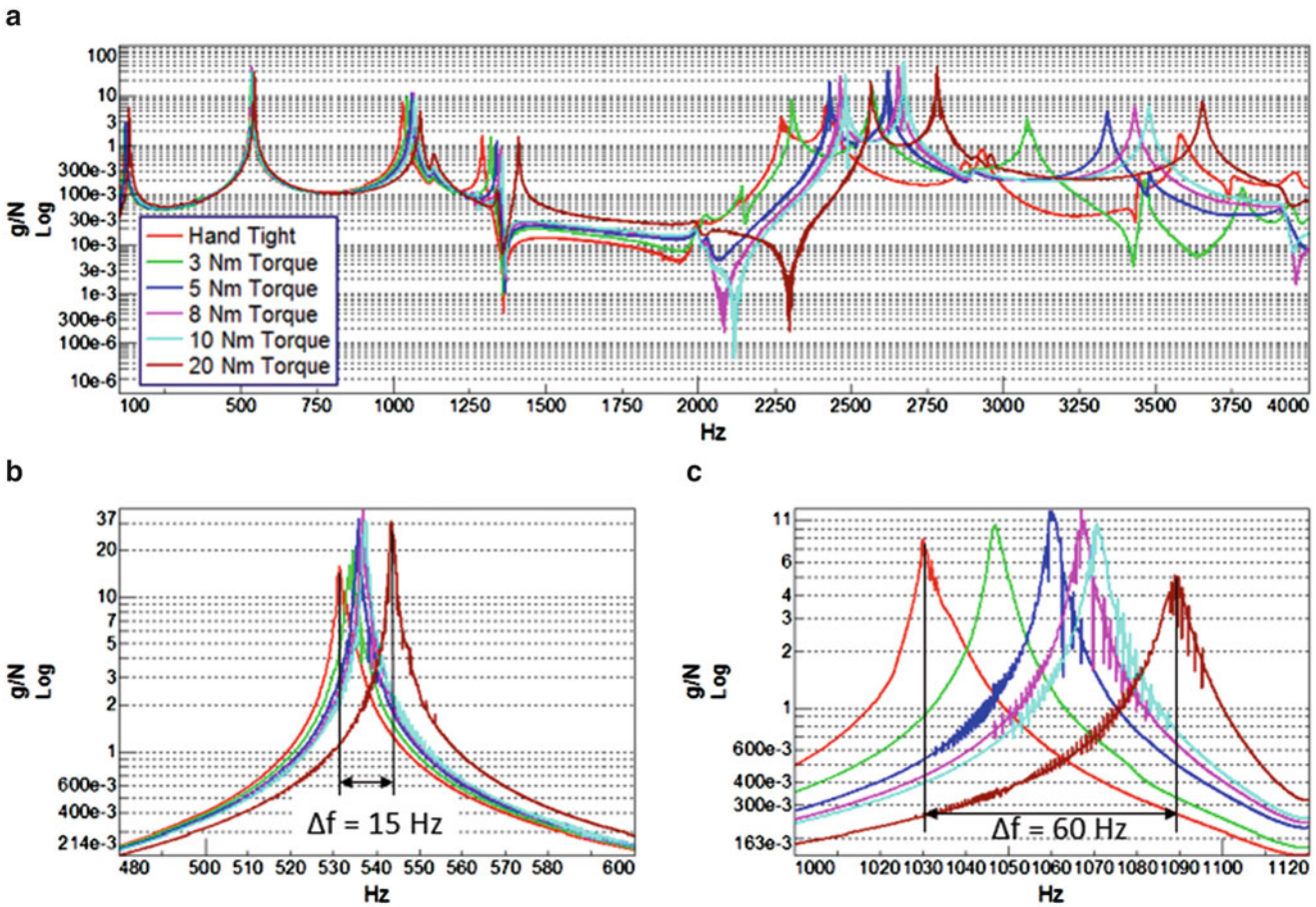

Fig. 36.17 The FRFs of the bolt torque of the rough interface for (**a**) the entire frequency range, (**b**) the second natural frequency, and (**c**) the fourth natural frequency

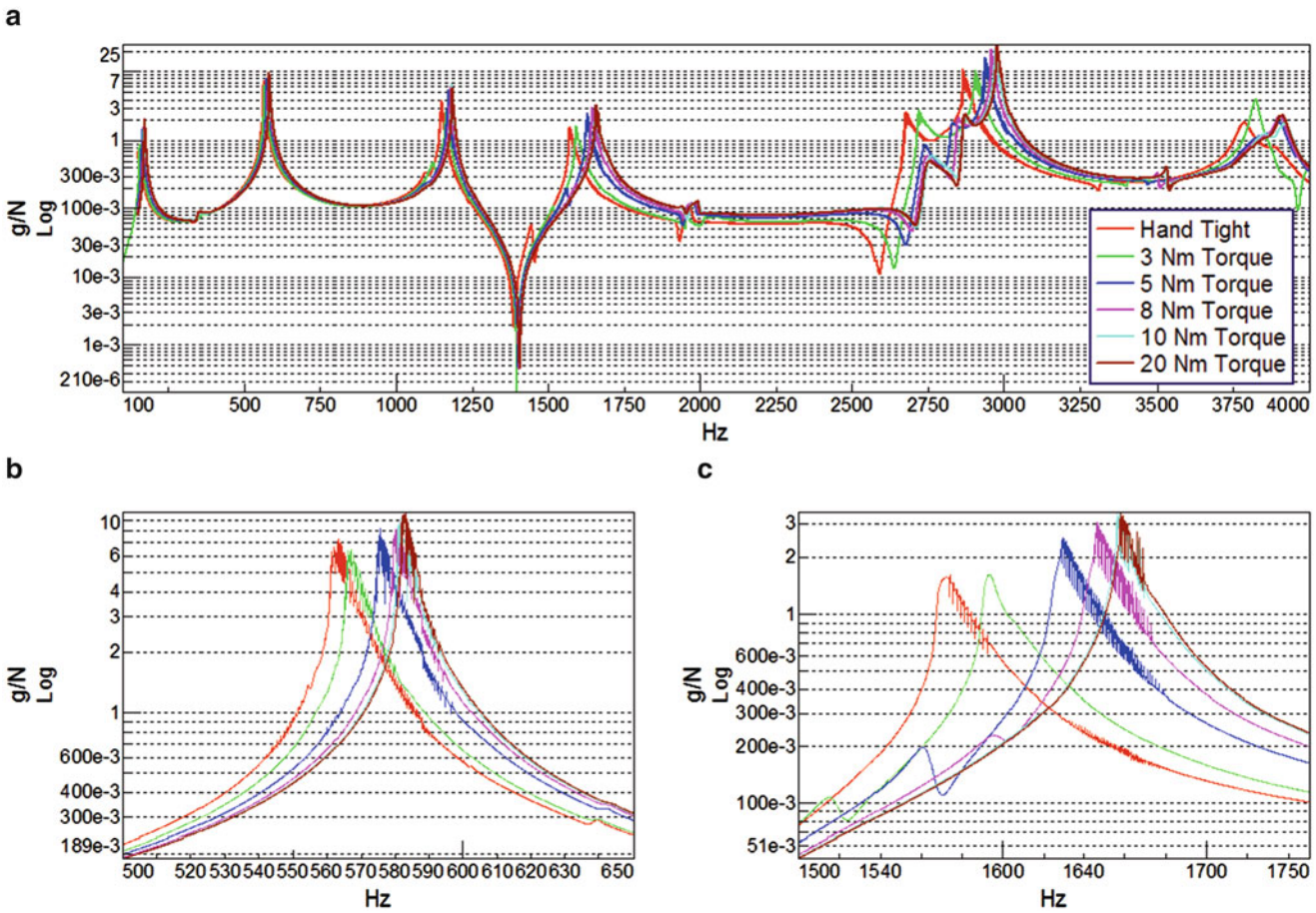

Fig. 36.18 The FRFs of the bolt torque of the mirror interface for (**a**) the entire frequency range, (**b**) the second natural frequency, and (**c**) the fourth natural frequency

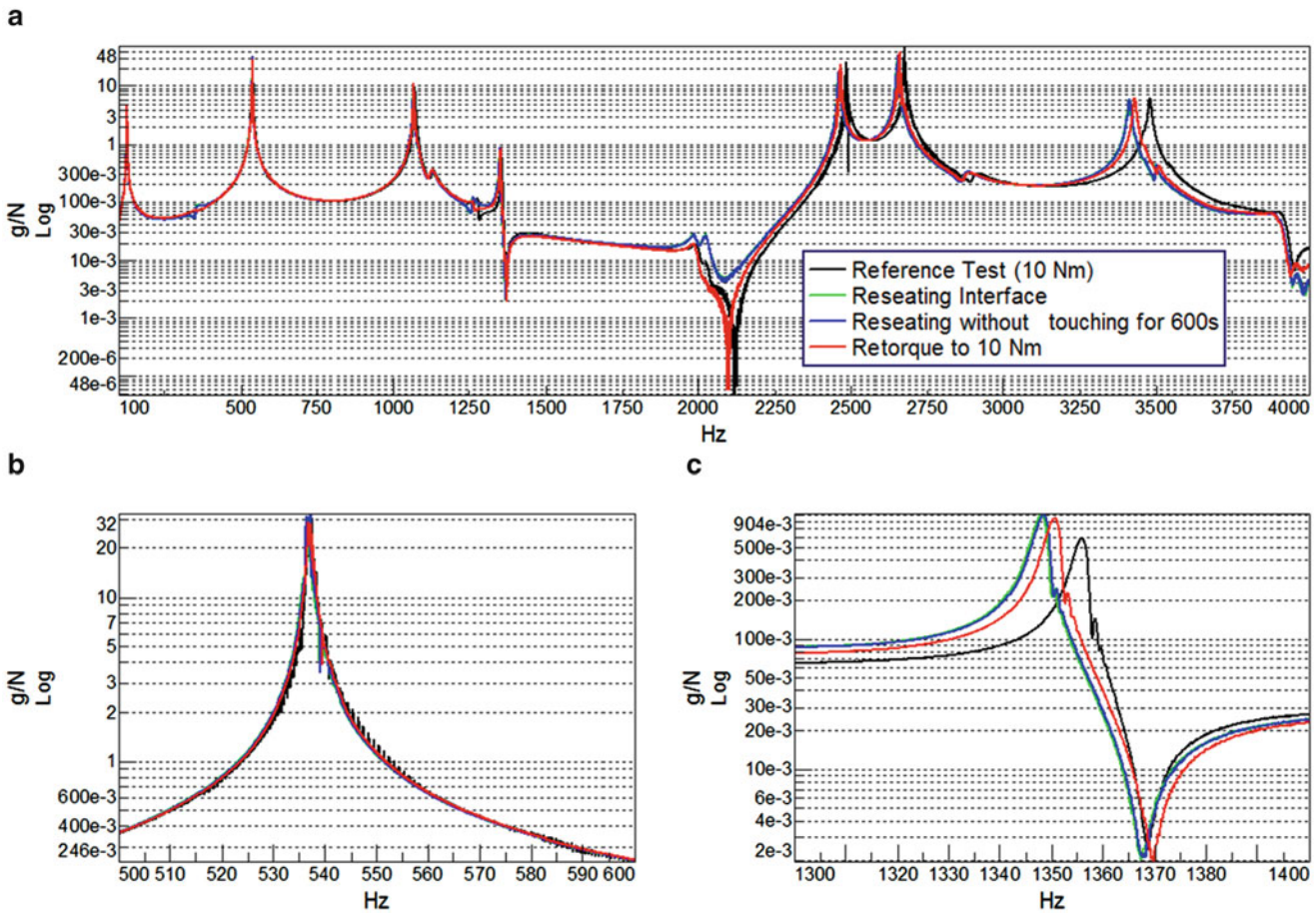

Fig. 36.19 The FRFs of the rough interface repeatability test for (**a**) the entire frequency range, (**b**) near the second natural frequency, and (**c**) near the fourth natural frequency

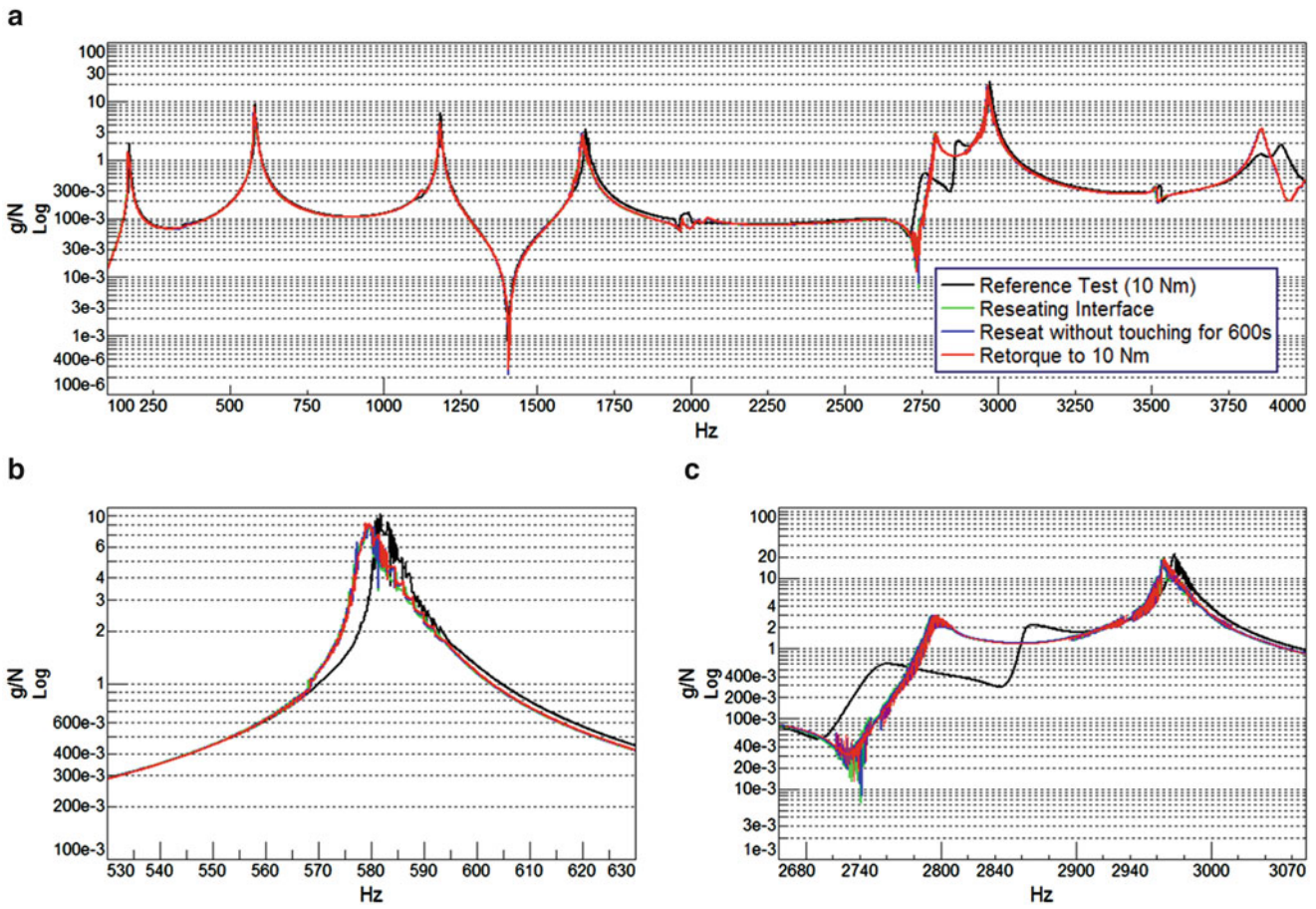

Fig. 36.20 The FRFs of the mirror interface repeatability test for (**a**) the entire frequency range, (**b**) near the second natural frequency, and (**c**) near the fourth natural frequency

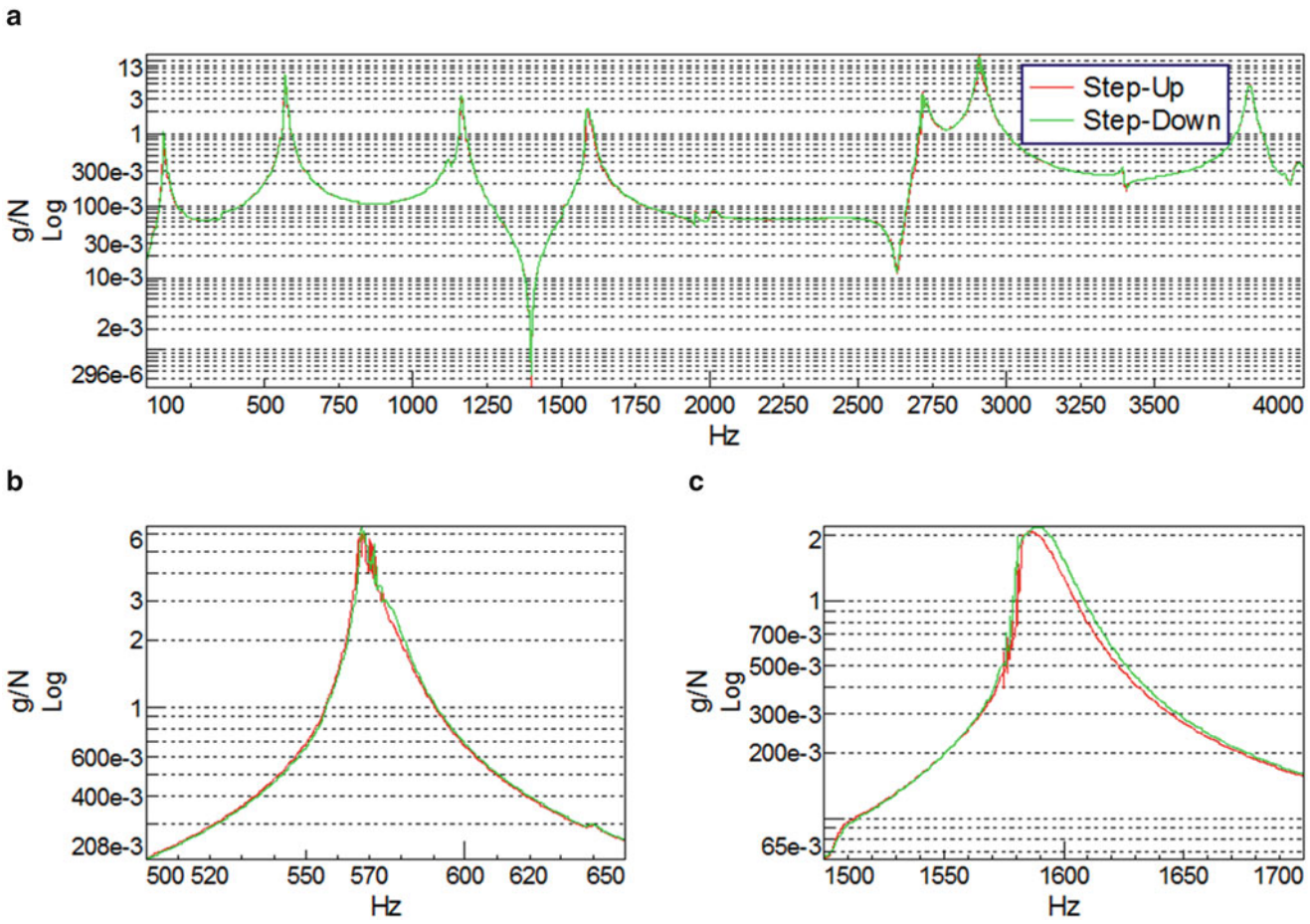

Fig. 36.21 The FRFs of the step direction for (**a**) the entire frequency range, (**b**) near the second natural frequency, and (**c**) near the fourth natural frequency

References

1. Brake MR (2014) The role of epistemic uncertainty of contact models in the design and optimization of mechanical systems with aleatoric uncertainty. Nonlinear Dyn 77:899–922
2. Brake MR (2013) The effect of the contact model on the impact-vibration response of continuous and discrete systems. J Sound Vib 332:3849–3878
3. Schwingshackl CW, Joannin C, Pesaresi L, Green JS, Hoffmann N (2014) Test method development for nonlinear damping extraction of dovetail joints. IMAC XXXII a conference and exposition on structural dynamics, Orlando, Feb 2014
4. Segalman DJ, Gregory DL, Starr MJ, Resor BR, Jew MD, Lauffer JP, Ames NM (2009) Handbook on dynamics of jointed structures. Sandia National Laboratories, Albuquerque, SAND2009-4164
5. Brake MR, Reuss P, Segalman DJ, Gaul L (2014) Variability and repeatability of jointed structures with frictional interfaces. IMAC XXXII a conference and exposition on structural dynamics, Orlando, Feb 2014
6. Sracic MW, Allen MS, Sumali H (2012) Identifying the modal properties of nonlinear structures using measured free response time histories from a scanning laser Doppler vibrometer. IMAC XXX a conference and exposition on structural dynamics, Jacksonville, Feb 2012

Chapter 37
Numerical Model for Elastic Contact Simulation

D. Botto and M. Lavella

Abstract Recently, interest has been growing among the engineering community to develop predictive models for the effect of joints on the tribology of jointed structures. The ability to predict contact forces and force-displacement relations of joints is key in enabling simulations to predict forced response and wear of jointed structures. Only for a limited number of contact geometries has a solution in closed-form been found, and it is available in literature. The finite element method has been used to a great extent to solve problems of elastic bodies in contact, but the iterative solution of large models is very demanding. This work deals with the development of a numerical procedure that utilizes the stiffness matrices of the bodies in contact modeled with the finite element method. The matrices are reduced with a lossless static reduction, and their small dimensions make the iterative solution of the contact problem very fast. Results are compared with contact models found in literature and the sample results agree well with corresponding exact solutions.

Keywords Contact • Friction • Hysteresis loop • Wear • Simulation

37.1 Introduction

The foundations of the static contact problem in elasticity were laid down by Hertz [1], who obtained formulas for contact pressure and approach between bodies in contact under the assumption that the area of contact was elliptical. The general problem of contact of a linearly elastic body in contact with a frictionless rigid foundation was formulated by Signorini [2, 3]. The existence and uniqueness of the solution of the Signorini-like problems were investigated in [4], and in [5] Duvuat and Lions proved that the true contact area and surface displacements are those which minimize the total strain energy, provided that there is no interpenetration between contact bodies.

Variational methods were applied to non-Hertzian contact problem to a great extent and in [6] Kalker proposed an alternative method based on total complementary energy.

These earlier works did not include the effect of friction that was addressed later. In [7] a restricted class of contact problems with Coulomb friction were formulated under the assumption that the contact area is known, while in [8] the dry friction problem was studied in conjunction with rolling contact.

Solutions in closed-form of the contact problem, in terms of normal and tangential forces, have been found only for a limited number of contact geometries, such as sphere [9, 10], nonspherical bodies in Hertz contact [11], and, most recently, rounded flat punch [12].

Numerical methods are needed to handle non Hertzian contact, bodies that cannot be approximated with elastic half-space, or anisotropic materials. Among the numerical approaches it is worth mentioning the earlier work of Conry and Seireg [13], and the finite element (FE) approach proposed by Chan and Tuba in [14]. Within the FE method contact problems are generally approached using either the penalty method or the Lagrange multiplier, implemented in pure formulation or in its standard regularizations, i.e. perturbed and augmented. In the Lagrange multiplier method, violations of the contact condition are handled with Lagrangian multipliers, which are additional degrees of freedom (dof) which cause an increase of the dimensions of the FE model. The penalty method introduces contact stiffness (also called penalty stiffness) which is a predetermined property of the contact element, and its value is crucial both for the accuracy of the results and for convergence of the iterative calculation.

In this work a novel procedure is proposed to solve the contact problem, both in terms of normal and tangential forces and area of contact, split into its adhesion and sliding portions. This method utilizes the stiffness matrices of contact bodies

D. Botto (✉) • M. Lavella
Department of Mechanical and Aerospace Engineering, Politecnico di Torino, Corso Duca degli Abruzzi, 24, Torino 10129, Italy
e-mail: daniele.botto@polito.it

G. Kerschen (ed.), *Nonlinear Dynamics, Volume 1*, Conference Proceedings of the Society for Experimental Mechanics Series, DOI 10.1007/978-3-319-15221-9_37

modeled with finite elements. These matrices are exported from the pre-processor of a commercial FE software, and reduced with a lossless reduction method, so that they can be handled with an in-house software.

The contact problem is solved in terms of displacements, by estimating an initial contact area, or adhesion area in the case of a tangential problem, and then iterating the contact area till convergence. Due to its reduced dimensions the proposed method is very fast, and accurate within the limit of the accuracy of the FE model from which the reduced matrices come. The contact geometries are not limited to special cases, and moreover, the isotropic assumption on the elastic material is relaxed. The friction contact is characterized by its hysteresis loop, namely the tangential-force against the relative displacements between the contact bodies. The aim of this paper is to provide a simple and effective method to estimate the main contact parameters, namely the tangential stiffness (the friction coefficient is a input data) and the energy dissipated by the hysteresis loop, for contact geometries not restricted to special cases.

37.2 Notation and Convention

Throughout this paper vectors and matrices are denoted by boldface letters. If not explicitly stated otherwise vectors are column vectors. A vector **e** of ones is defined, and its dimension is set according to the current equation. Index notation with smallcase x, y, z, is used to describe Cartesian components of forces and displacements, while subscript 1 and 2 refer to contact bodies. Letters c and δ used as index refer to nodes on potential contact area and distant nodes respectively.

37.3 Normal Contact Problem

To solve the normal contact problem means to find the contact area and the normal stress, or pressure, distribution on that area. In the numerical method proposed in this work the pressure distribution is replaced with discrete forces applied to the points of contact, and the contact area is approximated with a set of points. The proposed method has been developed under the following assumptions:

- The material of the contact bodies are linearly elastic, and the deformation are small.
- The roughness is neglected, and the contact surfaces are assumed perfectly smooth.
- An Amonton-Coulomb model of friction is used, and it is assumed that this model holds locally at each contact point. Moreover, the friction coefficient is constant.
- The normal and tangential contact problems are assumed uncoupled, and the tangential forces are determined once the contact area and the contact forces are known. In the method proposed in this work this assumption is not compulsory, but it has been set to compare the numerical results with the analytical solution found in the literature.

37.3.1 Method of Solution

The normal contact problem is formulated imposing the equation of compatibility of displacements, the displacements-forces relations, and the equation of equilibrium.

Compatibility of displacements At any point in the potential contact area the sum of the elastic displacements, of the separation between the bodies, and the rigid bodies approach must be greater than or equal to zero. This condition is written as

$$\mathbf{h}\,(x,\,y) + (\mathbf{u}_{1z} - \mathbf{u}_{2z}) + (\delta_{1z} - \delta_{2z})\,\mathbf{e} \;\geq\; 0 \tag{37.1}$$

where $\mathbf{h}(x,y) = \mathbf{z}_1 - \mathbf{z}_2$ is the separation of the profiles in the undeformed state, $\mathbf{u}_z$ the elastic displacement along the vertical direction, and δ the rigid-body approach.

Displacements-forces relation The displacements-forces relation is given through a stiffness matrix that comes from a FE model. Accordingly

$$\mathbf{K}\,\mathbf{u} = \mathbf{f} \tag{37.2}$$

where **K** is the reduced stiffness matrix of the full FE model; **u** and **f** the vectors of displacements and forces in the master nodes respectively. Reduction can be performed with the method proposed by Guyan [15] where the master nodes, i.e. the nodes keep into the system after the reduction, are the nodes defining the potential area of contact plus a set of distant nodes. Nodes defining the potential contact area must be selected a priori, by the observation of the bodies to bring into contact, and the set must be complete enough to provide for the real contact area, at least within the range chosen for the rigid-body approach. The distant nodes are far from the contact area, theoretically at a infinite distance, and are used to define the rigid-body approach and as reference to determine the contact stiffness. The Guyan reduction of the stiffness matrix is lossless, and none of the information of the full FE model of the elastic body are lost with this reduction.

Equation of equilibrium Within the potential contact area the forces acting on each point must be in equilibrium

$$\mathbf{f}_{c1} + \mathbf{f}_{c2} = 0 \tag{37.3}$$

Moreover, the sum of all the forces acting along the z-axis must balance the applied load F_N normal to the contact surface

$$\mathbf{e}^T \mathbf{f}_{cz} = F_N \tag{37.4}$$

where $\mathbf{f}_{cz}$ is the z-component of the forces within the potential contact area only. For the point belonging to the potential contact area the condition of normal contact can now be stated as follows

$$\mathbf{h}(x, y) + (\mathbf{u}_{1z} - \mathbf{u}_{2z}) + (\delta_{1z} - \delta_{2z})\ \mathbf{e} \begin{cases} = 0, & \text{inside contact area} \\ > 0, & \text{outside contact area} \end{cases} \tag{37.5}$$

while

$$\mathbf{f}_{1z} = -\mathbf{f}_{2z} \begin{cases} = 0, & \text{outside contact area} \\ > 0, & \text{inside contact area} \end{cases} \tag{37.6}$$

Method of solution The stiffness matrix **K** in [2] is the reduced matrix of the full FE model. In this matrix only the degrees of freedom (dof) associated to contact and distant nodes have been kept, namely master dof and nodes, while the others dof has been removed. Since at this stage only the normal contact problem is under investigation a further reduction is needed, in order to eliminate dof u_x and u_y parallel to the contact surface. The displacement-force relation is arranged so that after partition in the form

$$\begin{bmatrix} \mathbf{K}_{zz} & \mathbf{K}_{zx} \\ \mathbf{K}_{xz} & \mathbf{K}_{xx} \end{bmatrix} \begin{Bmatrix} \mathbf{u}_z \\ \mathbf{u}_x \end{Bmatrix} = \begin{Bmatrix} \mathbf{f}_z \\ \mathbf{f}_x \end{Bmatrix}, \tag{37.7}$$

the normal dof u_z are separated from the tangential dof. For convenience in Eq. 37.7 u_x represents the tangential displacements in both direction x and y. The second Eq. in 7 yields

$$\mathbf{u}_x = \mathbf{K}_{xx}^{-1} (\mathbf{f}_x - \mathbf{K}_{xz} \mathbf{u}_z), \tag{37.8}$$

that substituted in the first of Eq. 37.7 gives

$$\mathbf{K}_z \mathbf{u}_z = \mathbf{f}_z - \mathbf{K}_{xx}\ \mathbf{K}_{xz}^{-1} \mathbf{f}_x. \tag{37.9}$$

From Eq. 37.9 the reduced stiffness matrix is seen to be

$$\mathbf{K}_z = \mathbf{K}_{zz} - \mathbf{K}_{zx}\ \mathbf{K}_{xx}^{-1}\ \mathbf{K}_{xz}. \tag{37.10}$$

In general the normal and tangential forces are coupled, but the effect upon the normal force of the tangential force can be neglected. In this case the normal problem can be then solved as if the contact were frictionless. It has been shown [16] that within this assumption only a little loss of information is achieved. In this work the uncoupling assumption has been made and, according to this assumption, Eq. 37.9 becomes

$$\mathbf{K}_z \mathbf{u}_z = \mathbf{f}_z, \tag{37.11}$$

as $\mathbf{f}_x = 0$. Dof of nodes belonging to the potential contact area, but lying outside the true contact area can be eliminated from Eq. 37.11. To this end the stiffness matrix in Eq. 37.11 is parted in its components associated to the nodes i and o, inside and outside the true contact area respectively, and distant nodes δ,

$$\begin{bmatrix} \boldsymbol{K}_{zii} & \boldsymbol{K}_{zio} & \boldsymbol{K}_{zi\delta} \\ \boldsymbol{K}_{zoi} & \boldsymbol{K}_{zoo} & \boldsymbol{K}_{zo\delta} \\ \boldsymbol{K}_{zi\delta} & \boldsymbol{K}_{zo\delta} & \boldsymbol{K}_{z\delta\delta} \end{bmatrix} \begin{Bmatrix} \mathbf{u}_{zi} \\ \mathbf{u}_{zo} \\ \mathbf{u}_{z\delta} \end{Bmatrix} = \begin{Bmatrix} \mathbf{f}_{zi} \\ \mathbf{f}_{zo} \\ \mathbf{f}_{z\delta} \end{Bmatrix}, \tag{37.12}$$

The second equation in 9 gives the displacements of outside nodes

$$\mathbf{u}_{zo} = -\mathbf{K}_{zoo}^{-1} \left(\mathbf{K}_{zoi}\mathbf{u}_{zi} + \mathbf{K}_{zo\delta}\mathbf{u}_{z\delta} \right), \tag{37.13}$$

provided the forces $\mathbf{f}_{zo}$ on nodes outside the contact area are zero. Substituting Eq. 37.13 into the first of Eq. 37.12 yields

$$\mathbf{K}_{zi}\mathbf{u}_{zi} + \mathbf{K}_{z\delta}\mathbf{u}_{z\delta} = \mathbf{f}_{zi}, \tag{37.14}$$

where the reduced stiffness matrices are seen to be

$$\begin{aligned} \mathbf{K}_{zi} &= \mathbf{K}_{zii} - \mathbf{K}_{zio}\, \mathbf{K}_{zoo}^{-1}\, \mathbf{K}_{zoi}, \\ \mathbf{K}_{z\delta} &= \mathbf{K}_{zi\delta} - \mathbf{K}_{zio}\, \mathbf{K}_{zoo}^{-1}\, \mathbf{K}_{zo\delta}. \end{aligned} \tag{37.15}$$

Equation 37.14 holds both for bodies 1 and 2, and the sum of these two equations, combined with equation of equilibrium three yields

$$\mathbf{K}_{1zi}\mathbf{u}_{1zi} + \mathbf{K}_{2zi}\mathbf{u}_{2zi} + \mathbf{K}_{1z\delta}\mathbf{u}_{1z\delta} + \mathbf{K}_{2z\delta}\mathbf{u}_{2z\delta} = 0. \tag{37.16}$$

The compatibility of displacements Eq. 37.1 at nodes inside true contact area gives

$$\mathbf{u}_{2z} = \mathbf{h}(x, y) + \mathbf{u}_{1z} + (\delta_{1z} - \delta_{2z})\,\mathbf{e} \tag{37.17}$$

where, for convenience, the rigid displacements of body 2 have been set to zero. This assumption does not introduce any approximation in the solving equation because, see Eq. 37.17, what really matters is the relative rigid-body displacement. Substituting Eq. 37.16 into 17 gives the solving equation

$$(\boldsymbol{K}_{1zi} + \boldsymbol{K}_{2zi})\ \mathbf{u}_{1zi} = -\mathbf{u}_{1z\delta} + \mathbf{K}_{2zi}\,(\delta_1\mathbf{e} + \boldsymbol{h}_\mathbf{i}). \tag{37.18}$$

that is a linear system in the unknowns $\mathbf{u}_{zi}$, provided the nodes defining the true contact area are known.

The algorithm to solve for the normal contact problem is very simple to implement:

1. At the first iteration, for a given rigid body approach δ_1, the contact area is guess by choosing all the nodes within the interpenetration area.
2. Displacements $\mathbf{u}_{zi}$ for body 1 are determined with Eq. 37.18, while for body 2 are computed using Eq. 37.17.
3. Normal forces $\mathbf{f}_{zi}$ acting on inside nodes i are computed according to Eq. 37.14 for both bodies. Nodes on which the force is equal or less than zero are removed from the set i.
4. Displacements $\mathbf{u}_{zo}$ of nodes o outside the contact area are given by Eq. 37.13.
5. Equation 37.1 is used to check compatibility of displacements for nodes o outside the true contact area. Nodes whose displacements do not pass this check are moved into the set of nodes i.
6. With the new partition between nodes inside and outside contact area the stiffness matrices in Eq. 37.15 are updated, and the iterative process restart from point 2.

37.4 Tangential Contact Problem

Once the contact area has been determined the tangential contact problem is formulated assuming the Coulomb's friction law.

37.4.1 Method of Solution

The displacement-force relation is re-arranged so that after partition in the form

$$\begin{bmatrix} \mathbf{K}_{xx} & \mathbf{K}_{xz} \\ \mathbf{K}_{zx} & \mathbf{K}_{zz} \end{bmatrix} \begin{Bmatrix} \mathbf{u}_x \\ \mathbf{u}_{xz} \end{Bmatrix} = \begin{Bmatrix} \mathbf{f}_x \\ \mathbf{f}_z \end{Bmatrix}, \tag{37.19}$$

the vertical displacements $\mathbf{u}_z$ can be re-written as a function of the in plane displacements

$$\mathbf{u}_z = \mathbf{K}_{zz}^{-1} \left(\mathbf{f}_z - \mathbf{K}_{zx} \mathbf{u}_x \right). \tag{37.20}$$

Eq. 37.20 substituted in the first of Eq. 37.19 gives

$$\mathbf{K}_x \mathbf{u}_x = \mathbf{f}_x - \mathbf{K}_{zz}\, \mathbf{K}_{zx}^{-1} \mathbf{f}_z. \tag{37.21}$$

where the reduced stiffness matrix $\mathbf{K}_x$ is

$$\mathbf{K}_x = \mathbf{K}_{xx} - \mathbf{K}_{xz}\, \mathbf{K}_{zz}^{-1}\, \mathbf{K}_{zx}. \tag{37.22}$$

Under the assumption that the normal and the tangential forces are uncoupled the force $\mathbf{f}_z$ in Eq. 37.21 can be neglected and Eq. 37.22 becomes

$$\mathbf{K}_x\, \mathbf{u}_x = \mathbf{f}_x. \tag{37.23}$$

With a further reduction dofs outside the contact area can be eliminated. The stiffness matrix in Eq. 37.23 can be parted into the inside and outside the contact area, and distant nodes

$$\begin{bmatrix} \boldsymbol{K}_{xii} & \boldsymbol{K}_{xio} & \boldsymbol{K}_{xi\delta} \\ \boldsymbol{K}_{xoi} & \boldsymbol{K}_{xoo} & \boldsymbol{K}_{xo\delta} \\ \boldsymbol{K}_{xi\delta} & \boldsymbol{K}_{xo\delta} & \boldsymbol{K}_{x\delta\delta} \end{bmatrix} \begin{Bmatrix} \mathbf{u}_{xi} \\ \mathbf{u}_{xo} \\ \mathbf{u}_{x\delta} \end{Bmatrix} = \begin{Bmatrix} \mathbf{f}_{xi} \\ \mathbf{f}_{xo} \\ \mathbf{f}_{x\delta} \end{Bmatrix}, \tag{37.24}$$

so that in-plane displacements uxo can be written

$$\mathbf{u}_{xo} = -\mathbf{K}_{xoo}^{-1} \left(\mathbf{K}_{xoi} \mathbf{u}_{xi} + \mathbf{K}_{xo\delta} \mathbf{u}_{x\delta} \right), \tag{37.25}$$

as the forces $\mathbf{f}_{xo}$ acting on nodes outside the true contact area are zero. Substituting Eq. 37.25 into the first of Eq. 37.24 the displacement-tangential force relation in the reduced form becomes

$$\mathbf{K}_{xi} \mathbf{u}_{xi} + \mathbf{K}_{x\delta} \mathbf{u}_{x\delta} = \mathbf{f}_{xi}, \tag{37.26}$$

and where the reduced stiffness equations are seen to be

$$\mathbf{K}_{xi} = \mathbf{K}_{xii} - \mathbf{K}_{xio}\, \mathbf{K}_{xoo}^{-1}\, \mathbf{K}_{xoi}, \tag{37.27a}$$

$$\mathbf{K}_{x\delta} = \mathbf{K}_{xi\delta} - \mathbf{K}_{xio}\, \mathbf{K}_{xoo}^{-1}\, \mathbf{K}_{xo\delta}. \tag{37.27b}$$

In Eq. 37.26 the master nodes are the nodes that define the true contact area, which comes from the solution of the normal contact problem. The true contact area can be split into two portions, namely the portion where the contact forces are less or

equal than the maximum friction force, where nodes adhere to each other, and the portion where the contact forces exceed the maximum transmissible friction force, where sliding occurs between corresponding nodes in contact. It is convenient to split the matrix in Eq. 37.26 into nodes in adhesion and sliding mode

$$\begin{bmatrix} \mathbf{K}_{xiaa} & \mathbf{K}_{xias} \\ \mathbf{K}_{xisa} & \mathbf{K}_{xiss} \end{bmatrix} \begin{Bmatrix} \mathbf{u}_{xia} \\ \mathbf{u}_{xis} \end{Bmatrix} + \begin{bmatrix} \mathbf{K}_{x\delta a} \\ \mathbf{K}_{x\delta a} \end{bmatrix} \{\mathbf{u}_{x\delta}\} = \begin{Bmatrix} \mathbf{f}_{xia} \\ \mathbf{f}_{xis} \end{Bmatrix}, \tag{37.28}$$

and solve the second equation in 37.28 for the displacements in the sliding portion of the contact area

$$\mathbf{u}_{xis} = \mathbf{K}_{xiss}^{-1}\mathbf{f}_{xis} - \mathbf{K}_{xiss}^{-1}\left(\mathbf{K}_{xisa}\mathbf{u}_{xia} + \mathbf{K}_{xi\delta s}\mathbf{u}_{xi\delta}\right). \tag{37.29}$$

Tangential contact forces cannot exceed the maximum allowable friction force, then the tangential forces $\mathbf{f}_{xis}$ in Eq. 37.29, which act on sliding nodes, can be replaced with the normal contact forces multiplied by the coefficient of friction, namely $\mu\mathbf{f}_{zis}$. Substituting for $\mathbf{u}_{xis}$, Eq. 37.29, in the first of Eq. 37.28 gives

$$\mathbf{K}_{xia}\mathbf{u}_{xia} + \mathbf{K}_{x\delta}\mathbf{u}_{x\delta} + \mathbf{f}_{zxis} = \mathbf{f}_{xia}, \tag{37.30}$$

where the stiffnesses and the generalized forces are

$$\mathbf{K}_{xia} = \mathbf{K}_{xiaa} - \mathbf{K}_{xias}\,\mathbf{K}_{xiss}^{-1}\,\mathbf{K}_{xisa}, \tag{37.31a}$$

$$\mathbf{K}_{x\delta} = \mathbf{K}_{x\delta a} - \mathbf{K}_{xias}\,\mathbf{K}_{xiss}^{-1}, \tag{37.31b}$$

$$\mathbf{f}_{zxis} = \mathbf{K}_{xias}\,\mathbf{K}_{xiss}^{-1}\left(\mu\mathbf{f}_{zis}\right). \tag{37.31c}$$

Summation of Eq. 37.30 written for body 1 and 2 yields

$$\left(\boldsymbol{K}_{1xia} + \boldsymbol{K}_{2xia}\right)\,\mathbf{u}_{1xia} + \mathbf{K}_{1x\delta}\mathbf{u}_{1x\delta} + \left(\mathbf{f}_{1zxis} + \mathbf{f}_{2zxis}\right). \tag{37.32}$$

considering that the displacements and the contact forces of the corresponding nodes in adhesion mode are the same. Moreover, the displacements of distant nodes on one of the contact bodies can be assumed to be zero, without loss of generality.

37.5 Results

The problem of a cylinder in contact with a plane was used as a test case of the method. The numerical solution was compared with the Hertzian solution. The material used in the calculation has a 0.3 Poisson ratio and a 200,000 N/mm^2 modulus of elasticity. The diameter of the cylinder was 10 mm. Figure 37.1 shows the maximum contact pressure and the contact length. Figure 37.2 shows the stress distribution for a normal load of 3,790 N. Figure 37.3 shows the distribution of the tangential stress calculated with a normal and tangential load of 1,000 N and 257 N respectively and a friction coefficient 0.6. Results agree with each other very well.

37.6 Conclusion

Previous works have addressed numerical methods to solve the contact problem with Coulomb friction, and these procedures are currently implemented in commercial finite element software. In this study we propose a different approach, also based on a finite element model, to solve the problem of elastic bodies in contact. The proposed method maintains the great flexibility, in terms of contact geometry, allowed by the finite element model, and the solution of the contact problem is not restricted to special geometries or within the half space assumption. Moreover, the proposed method works for contact bodies of anisotropic materials, while analytical solutions assume only isotropic material. Linear elastic material must still

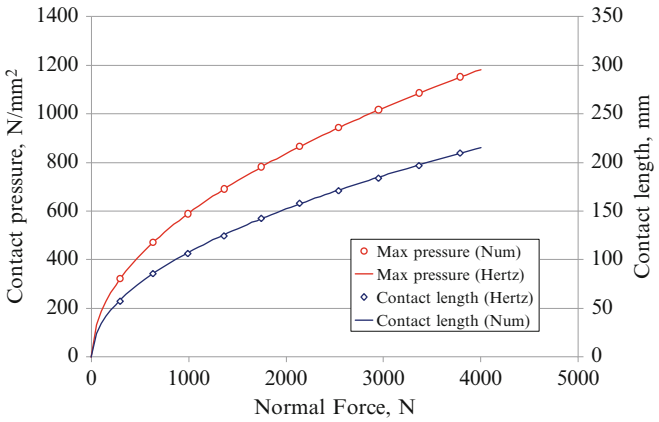

Fig. 37.1 Comparison of the maximum contact pressure and contact length

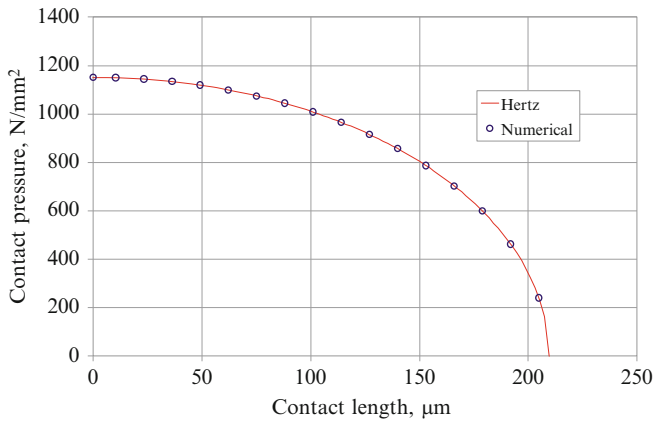

Fig. 37.2 Normal pressure distribution

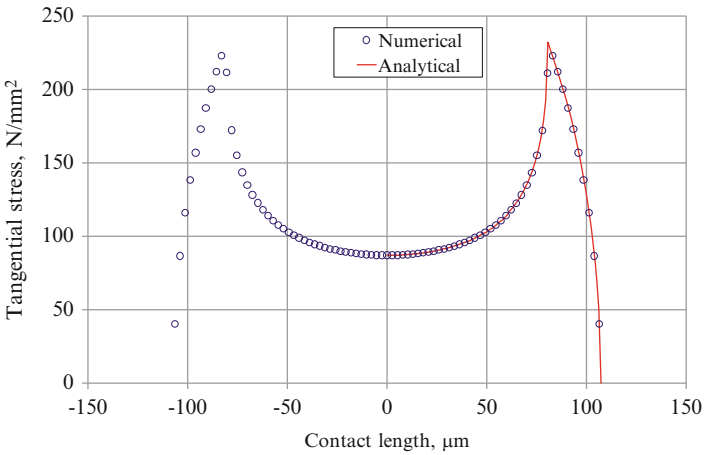

Fig. 37.3 Tangential stress distribution

be assumed. This method has been validated against simple geometries of which the analytical solution of the contact problem is known. With the proposed method it is possible to compute:

- the contact area and pressure distribution,
- the tangential stress distribution, and the adhesion and sliding portion of the contact area,
- the hysteresis loop of the tangential forces against the relative displacements from which the contact stiffness and dissipated energy can be determined.

The proposed method is convenient to be used for wear simulation, where the contact geometries change as a results of the wear process. Moreover the hysteresis loop determined with this method can be implemented in a numerical solver to predict the forced response of structure with contact interfaces.

References

1. Hertz H (1882) Über die Berührung fester elastischer Körper. Journal für die reine und angewandte Mathematik 92:156–171
2. Signorini A (1933) Sopra alcune questioni di elastostatica, Atti della Società Italiana per il Progresso delle Scienze (in Italian)
3. Signorini A (1959) Questioni di elasticità non linearizzata e semilinearizzata. Rendiconti di Matematica e delle sue applicazioni 18:95–139 (in Italian)
4. Fichera G (1964) Problemi elastostatici con vincoli unilaterali: il problema di signorini con ambigue condizioni al contorno, Memorie della Accademia Nazionale dei Lincei, Classe di Scienze Fisiche, Matematiche e Naturali (in Italian) 7(2): 91–140
5. Duvaut G, Lions J (1972) Les inéquations en mécanique et en physique. Dunod, Paris
6. Kalker JJ (1977) Variational principles of contact elastostatics. J Inst Math Appl 20(2):199–219
7. Duvaut G, Lions JL (1971) Elasticité avec frottement. J de Mécanique 10:409–420
8. Kalker JJ (1979) The computation of three-dimensional rolling contact with dry friction. Intern J Numer Meth Eng 14(9):1293–1307
9. Cattaneo C (1938) Sul contatto di due corpi elastici, Accademia dei Lincei, Rendiconti (in Italian), Serie 6(27): 342–348, 434–436, 474–478
10. Mindlin RD, Deresiewicz H (1953) Elastic spheres in contact under varying oblique forces. ASME Trans J Appl Mech 20:327–344
11. Deresiewicz H (1957) Oblique contact of nonspherical elastic bodies. J Appl Mech 24(4):623–624
12. Ciavarella M, Hills D, Monno G (1998) The influence of round edges on the indentation by a flat punch. Proc Inst Mech Eng Part C J Mech Eng Sci 212:319–328
13. Conry TF, Seireg A (1971) A mathematical programming method for design of 190 elastic bodies in contact. J Appl Mech 38:387–392
14. Chan S, Tuba IS (1971) A finite element method for contact problems of solid bodies – Part I. Theory and validation. Int J Mech Sci 13:615–625
15. Guyan RJ (1965) Reduction of stiffness and mass matrices. AIAA J 3(2):380–380
16. Johnson KL (1985) Contact Mechanics. Cambridge: Cambridge University Press

Chapter 38
Efficient and Accurate Consideration of Nonlinear Joint Contact Within Multibody Simulation

Florian Pichler, Wolfgang Witteveen, and Peter Fischer

Abstract For the integration of flexible bodies into the multibody simulation the Component Mode Synthesis (CMS) has been established as a standard reduction tool. In the case of flexible bodies containing joints with a large spatial distribution the CMS is not suitable. In order to capture the local nonlinearities inside the joints the CMS reduction base is extended with problem-oriented trial vectors which are computed based on trial vector derivatives. The focus of this contribution is on the extension of the mentioned reduction method to general multibody dynamic systems. It will be reported how the trial vectors need to be modified in order to remove the rigid body content. Also the consideration of the contact forces in the vector of generalized forces will be discussed. Finally the method will be demonstrated on a car pendulum system with a pendulum designed as a multilayer sheet structure. The time integration is performed with a modified HHT solver. It can be reported, that the suggested approach gives an excellent balance between accuracy and computational effort.

Keywords Multibody simulation • Model order reduction • Jointed structures • Joint contact

Nomenclature

$\hat{\mathbf{M}}$	Generalized mass matrix
$\mathbf{C_q}$	Constraint jacobian
$\mathbf{C}$	Constraint equations
$\mathbf{f}_{(t)}$	External force vector
$\mathbf{f}_{c(\mathbf{x})}$	Nonlinear contact force vector
$\mathbf{K}$	Stiffness matrix
$\mathbf{M}$	Mass matrix
$\mathbf{Q}$	Generalized forces
$\mathbf{q}$	Generalized coordinates
$\mathbf{q}_f$	Vector of the flexible coordinates
$\mathbf{R}$	Translational DOFs
$\mathbf{x}$	Vector of FE DOFs
$\tilde{\mathbf{K}}$	Reduced stiffness matrix
$\tilde{\mathbf{M}}$	Reduced mass matrix
m	Number of constraint equations
n	Number of generalized coordinates
n_{FE}	Number of FE DOF
$q_{f,i}$	Trial vector scaling factor or flexible coordinate
r	Number of considered trial vectors

F. Pichler (✉) • W. Witteveen
University of Applied Sciences Upper Austria - Wels Campus, Stelzhamerstr. 23, 4600 Wels, Austria
e-mail: florian.pichler@fh-wels.at

P. Fischer
Graz University of Technology - FTG Institute of Automotive Engineering Graz, Inffeldgasse 11/II, 8010 Graz, Austria

G. Kerschen (ed.), *Nonlinear Dynamics, Volume 1*, Conference Proceedings of the Society for Experimental Mechanics Series, DOI 10.1007/978-3-319-15221-9_38

s	Number of considered static deformation mode shapes
t	Number of considered JTVs
v	Number of considered vibration mode shapes
α, β, γ	Parameters for HHT solver
$\boldsymbol{\varphi}_i$	Trial vector i
$\boldsymbol{\lambda}$	Vector of Lagrange multipliers
$\boldsymbol{\Phi}$	Matrix containing all trial vectors (reduction base)
$\boldsymbol{\Phi}_{CMS}$	Reduction base for CMS
$\boldsymbol{\Phi}_{free}$	Reduction base containing *free-free modes*
$\boldsymbol{\Phi}_S$	Matrix containing static deformation modes
$\boldsymbol{\Phi}_{TVD}$	Matrix containing all TVDs
$\boldsymbol{\Phi}_T$	Matrix containing JTVs
$\boldsymbol{\Phi}_V$	Matrix containing vibration modes
$\boldsymbol{\theta}$	Rotational DOFs

38.1 Introduction

Complex mechanical structures commonly consist of different substructures which are connected by joints. The overall dynamic behavior of such structures can be strongly influenced by the nonlinear contact forces inside the joints, especially in case of joints with a large spatial distribution.

In engineering practice structures including nonlinear contact forces are commonly analyzed with the direct Finite Element Method (FEM). If the jointed structure needs to be considered in a multibody simulation, where it can be connected to other rigid or flexible bodies and undergo a large spatial rigid body motion, a different strategy needs to be applied. Linear flexible bodies are commonly considered with the Component Mode Synthesis CMS (see [1–3]) in the multibody simulation. For local nonlinearities like in jointed structures the trial vectors used for the CMS are not suitable and therefore in [4] a problem oriented extension of the common reduction base is presented. Therefore special joint trial vectors (JTVs) which are based on trial vector derivatives (TVDs) are used. The theory of these joint trial vectors will be briefly reviewed in Sect. 38.2.1.

In this paper the JTVs will be applied to a multibody system. In Sect. 38.2.2 it will be reported how the nonlinear contact forces inside the joints of the flexible structure need to be considered in the vector of generalized forces of the multibody system. If a floating frame of reference formulation (FFRF) is used to describe the flexible body in the multibody simulation the used trial vectors need to be free of any rigid body content. Furthermore some simplifications in the mass matrix and the quadratic velocity vector can be achieved if the trial vectors are chosen to be *free-free modes*.

Finally a 2D car pendulum model is used in order to demonstrate that JTVs are suitable to consider nonlinear contact inside jointed structures within multibody simulation.

38.2 Theory

The first part of the theory section reviews the principle idea of using trial vector derivatives for the computation of joint trail vectors. In Sect. 38.2.2 it is described how the vector of nonlinear contact has to be considered in the vector of generalized forces for the multibody system.

38.2.1 Brief Review of Joint Trial Vectors Based on Trial Vector Derivatives

In this section an efficient and accurate approach for contact computation in combination with model order reduction will be briefly discussed. This approach was introduced by Witteveen and the author in [4, 5] and is based on the computation of TVDs. For the sake of readability a short review on the theory is given here. A detailed derivation can be found in [4].

For jointed flexible structures which are modeled by FEM a penalty formulation of the contact phenomenon [6, 7] leads to an equation of motion in the form of

$$\mathbf{M}\ddot{\mathbf{x}} + \mathbf{K}\mathbf{x} = \mathbf{f}_{(t)} - \mathbf{f}_{c(\mathbf{x})} \tag{38.1}$$

with the $(n_{FE} \times 1)$ vector $\mathbf{x}$ of nodal degrees of freedom (DOFs) and the $(n_{FE} \times n_{FE})$ mass matrix $\mathbf{M}$ and stiffness matrix $\mathbf{K}$ of the structure. The $(n_{FE} \times 1)$ vector $\mathbf{f}_{(t)}$ contains the external forces and the nonlinear contact forces are collected in the $(n_{FE} \times 1)$ vector $\mathbf{f}_{c(\mathbf{x})}$. In order to reduce the number of DOFs in Eq. (38.1) model order reduction via projection is one possibility. The principle idea is to approximate the vector $\mathbf{x}$ by a linear combination of r time invariant $(n_{FE} \times 1)$ trial vectors $\boldsymbol{\varphi}_i$ with the time varying scaling factors $q_{f,i}$

$$\mathbf{x} \approx \sum_{i=1}^{r} \boldsymbol{\varphi}_i q_{f,i} = \boldsymbol{\Phi}\mathbf{q}_f . \tag{38.2}$$

In terms of matrix and vector notation the r trial vectors are collected as columns in the $(n_{FE} \times r)$ matrix $\boldsymbol{\Phi}$ and the scaling factors in the $(r \times 1)$ vector $\mathbf{q}_f$. In the context of multibody dynamics this scaling factors are also called flexible coordinates. Inserting Eq. (38.2) into Eq. (38.1) and pre-multiplying with $\boldsymbol{\Phi}^T$ leads to a reduced system

$$\tilde{\mathbf{M}}\ddot{\mathbf{q}}_\mathbf{f} + \tilde{\mathbf{K}}\mathbf{q}_f = \boldsymbol{\Phi}^T\mathbf{f}_{(t)} - \boldsymbol{\Phi}^T\mathbf{f}_{c,(\boldsymbol{\Phi}\mathbf{q}_f)} \tag{38.3}$$

with $r < n$ and the $(r \times r)$ reduced mass matrix $\tilde{\mathbf{M}} = \boldsymbol{\Phi}^T\mathbf{M}\boldsymbol{\Phi}$ and the $(r \times r)$ reduced stiffness matrix $\tilde{\mathbf{K}} = \boldsymbol{\Phi}^T\mathbf{K}\boldsymbol{\Phi}$.

If CMS is used the reduction base $\boldsymbol{\Phi}$ is a combination of v vibration mode shapes (= normal modes) collected in the $(n_{FE} \times v)$ matrix $\boldsymbol{\Phi}_V$ and s trial vectors which are basically deformation shapes due to static loads in the $(n_{FE} \times s)$ matrix $\boldsymbol{\Phi}_S$

$$\boldsymbol{\Phi}_{CMS} = [\boldsymbol{\Phi}_V \ \boldsymbol{\Phi}_S] . \tag{38.4}$$

Both types of trial vectors are a function of the mass and stiffness matrix used for the computation. Because of the nonlinearities due to contact the stiffness matrix becomes state dependent. Consequently a certain trial vector is state dependent as well. Due to model order reduction [Eq. (38.2)] the state dependency of a trial vector leads to a dependency on the trial vector weighting factors collected in the vector $\mathbf{q}_f$. The first order $(n_{FE} \times 1)$ TVDs $\left(\frac{\partial \boldsymbol{\varphi}_i}{\partial q_{f,j}}\right)$ can therefore be used to approximate the change of a certain trial vector due to the deformation state. A general derivation for the TVDs can be found in [4, 8–11]. In [4] also a practical computation algorithm for contact problems is given.

According to [4] for both, vibration mode shapes and static deformation shapes the TVDs can be computed along

$$\frac{\partial \boldsymbol{\varphi}_i}{\partial q_{f,j}} = \mathbf{K}^{-1}\frac{\partial \mathbf{K}}{\partial q_{f,j}}\boldsymbol{\varphi}_i \tag{38.5}$$

as long as inertia related terms are neglected.

Using the first order TVDs to approximate the state dependency of a certain trial vector provides $2\,(v+s)^2$ potential new trial vectors. This number is by far too high for an efficient model order reduction. Therefore in [4] a weighted proper orthogonal decomposition (POD) [12, 13] is used to determine the important directions of the space spanned by all the TVDs. The practical computation of the $(n_{FE} \times 1)$ additional joint trial vectors $\boldsymbol{\varphi}_{T,i}$ based on TVDs is performed by solving the eigenvalue problem

$$\begin{aligned} \boldsymbol{\Phi}_{TVD}^T\mathbf{K}\boldsymbol{\Phi}_{TVD}\boldsymbol{\phi}_i &= \lambda_i\boldsymbol{\phi}_i \\ \boldsymbol{\varphi}_{T,i} &= \frac{1}{\sqrt{\lambda_i}}\boldsymbol{\Phi}_{TVD}\boldsymbol{\phi}_i \end{aligned} \tag{38.6}$$

with the $\left(n_{FE} \times 2\,(v+s)^2\right)$ matrix $\boldsymbol{\Phi}_{TVD}$ containing all TVDs.

The number of additional joint trial vectors $\boldsymbol{\varphi}_{T,i}$ used for model order reduction is depending on the considered structure. In [4] an possible estimator for this number is given. The final reduction space is given as

$$\boldsymbol{\Phi} = [\boldsymbol{\Phi}_V \ \boldsymbol{\Phi}_S \ \boldsymbol{\Phi}_T] \tag{38.7}$$

with the $(n_{FE} \times t)$ matrix $\boldsymbol{\Phi}_T$ containing t joint trial vectors based on TVDs.

38.2.2 Consideration of Contact Forces in the Framework of Multibody Simulation

The equations of motion for a multibody system containing flexible jointed structures, described in the floating frame of reference formulation (FFRF), are given in this subsection. In combination with the constraint equations the equations of motion can be written as

$$\hat{\mathbf{M}}(\mathbf{q})\ddot{\mathbf{q}} + \mathbf{C}_{\mathbf{q}}^{T}(\mathbf{q})\boldsymbol{\lambda} = \mathbf{Q}(\dot{\mathbf{q}}, \mathbf{q}, \mathbf{t}) \tag{38.8}$$

$$\mathbf{C}(\mathbf{q}) = \mathbf{0} \tag{38.9}$$

where $\mathbf{q}$ denotes the $(n \times 1)$ vector of generalized coordinates and the $(n \times n)$ matrix $\hat{\mathbf{M}}(\mathbf{q})$ represents the mass matrix of the system. The $(n \times 1)$ vector $\mathbf{Q}(\dot{\mathbf{q}}, \mathbf{q}, \mathbf{t})$ includes the generalized forces. $\mathbf{C}(\mathbf{q})$ and $\mathbf{C}_{\mathbf{q}}$ denote the $(m \times 1)$ constraint equations and the constraint jacobian of the size $(m \times n)$. Finally $\boldsymbol{\lambda}$ is the $(m \times 1)$ vector of Lagrange multipliers. For more details on multibody dynamics the interested reader is referred to [14]. The vector of generalized forces can be further decomposed in

$$\mathbf{Q} = \mathbf{Q}_v + \mathbf{Q}_e + \mathbf{Q}_{c,f} \tag{38.10}$$

with $\mathbf{Q}_v$ being the quadratic velocity vector, $\mathbf{Q}_e$ including the generalized external forces and $\mathbf{Q}_{c,f}$ containing the generalized forces due to contact forces and the generalized flexible forces.

For the body i in the multibody system the equations of motion can be written as

$$\mathbf{M}^i\ddot{\mathbf{q}}^i + \mathbf{C}_{\mathbf{q}^i}^{T}\boldsymbol{\lambda} = \mathbf{Q}_v^i + \mathbf{Q}_e^i + \mathbf{Q}_{c,f}^i. \tag{38.11}$$

In a partitioned matrix form Eq. (38.11) can be written as

$$\begin{bmatrix} \mathbf{m}_{RR}^i & \mathbf{m}_{R\theta}^i & \mathbf{m}_{Rf}^i \\ & \mathbf{m}_{\theta\theta}^i & \mathbf{m}_{\theta f}^i \\ \text{sym.} & & \mathbf{m}_{ff}^i \end{bmatrix} \begin{bmatrix} \ddot{\mathbf{R}}^i \\ \ddot{\boldsymbol{\theta}}^i \\ \ddot{\mathbf{q}}_f^i \end{bmatrix} + \begin{bmatrix} \mathbf{C}_{\mathbf{R}^i}^T \\ \mathbf{C}_{\boldsymbol{\theta}^i}^T \\ \mathbf{C}_{\mathbf{q}_f^i}^T \end{bmatrix} \boldsymbol{\lambda} = \begin{bmatrix} \left(\mathbf{Q}_v^i\right)_R \\ \left(\mathbf{Q}_v^i\right)_\theta \\ \left(\mathbf{Q}_v^i\right)_f \end{bmatrix} + \begin{bmatrix} \left(\mathbf{Q}_e^i\right)_R \\ \left(\mathbf{Q}_e^i\right)_\theta \\ \left(\mathbf{Q}_e^i\right)_f \end{bmatrix} + \begin{bmatrix} \mathbf{0}_R \\ \mathbf{0}_\theta \\ \left(-\tilde{\mathbf{K}}^i\mathbf{q}_f^i + \boldsymbol{\Phi}^{i\,T}\mathbf{f}_c^i\right)_f \end{bmatrix} \tag{38.12}$$

where $\mathbf{f}_c^i$ denotes the $(n_{FE} \times 1)$ contact force vector of the jointed structures. The vector of generalized coordinates is partitioned into the translational DOFs $\mathbf{R}$, the rotational DOFs $\boldsymbol{\theta}$ and the flexible coordinates $\mathbf{q}_f$. A detailed insight into the separate submatrices of $\mathbf{M}^i$ can be found in [14–16].

A simplification of the mass matrix $\mathbf{M}^i$ and the quadratic velocity vector $\mathbf{Q}_v^i$ can be achieved by choosing the trial vectors to be so called *free-free modes* (see [15, 16]) and by setting the body coordinate system to the center of mass in the undeformed state. Thereby the terms $\mathbf{m}_{R\theta}^i = \mathbf{0}, \mathbf{m}_{Rf}^i = \mathbf{0}$ and $\left(\mathbf{Q}_v^i\right)_R = \mathbf{0}$ vanish. In general trial vectors do not fulfill the criteria of *free-free modes*. If a FFRF is used to describe the flexible body, it is furthermore required that the chosen trial vectors do not contain any rigid body content. In the literature two different strategies can be found to transform an arbitrary set of trial vectors into *free-free modes*. Most commonly the Mode Shape Orthogonalization (see [17]) is used. In [17] an additional generalized eigenvalue problem

$$\left(\tilde{\mathbf{K}} - \omega\tilde{\mathbf{M}}\right)\mathbf{y} = \mathbf{0} \tag{38.13}$$

is solved to obtain a new set of trial vectors

$$\boldsymbol{\Phi}_{free} = \boldsymbol{\Phi}\mathbf{Y}. \tag{38.14}$$

The $(n_{FE} \times r)$ matrix $\mathbf{\Phi}_{free}$ contains trial vectors which are *free-free modes* and the $(r \times r)$ matrix $\mathbf{Y}$ contains the r eigenvectors computed from Eq. (38.13). The rigid body content is removed by rejecting the columns of the matrix $\mathbf{\Phi}_{free}$ which are corresponding to zero eigenvalues of Eq. (38.13).

In [16] a different method for separating a set of trial vectors into pseudo-free-surface modes and rigid body modes is proposed. This method also leads to a set of new trial vectors which have the advantageous properties of *free-free modes*.

The system of second order differential equations defined in Eq. (38.12) still has to satisfy the constraint equations $\mathbf{C(q)} = \mathbf{0}$. For time integration of the equations of motion in this work a HHT solver (see [18, 19]) is used. Therefore the systems jacobian has to be computed and the following system of equations has to be solved

$$\begin{bmatrix} \frac{1}{1+\alpha}\hat{\mathbf{M}} + \left(\frac{1}{1+\alpha}\left(\hat{\mathbf{M}}\ddot{\mathbf{q}}\right)_{\mathbf{q}} + \left(\mathbf{C}_{\mathbf{q}}^T\boldsymbol{\lambda}\right)_{\mathbf{q}} - \mathbf{Q}_{\mathbf{q}}\right)\beta h^2 - \mathbf{Q}_{\dot{\mathbf{q}}}h\gamma & \mathbf{C}_{\mathbf{q}}^T \\ \mathbf{C}_{\mathbf{q}} & \mathbf{0} \end{bmatrix} \begin{bmatrix} \Delta\ddot{\mathbf{q}} \\ \Delta\boldsymbol{\lambda} \end{bmatrix} = \begin{bmatrix} -\mathbf{e_1} \\ -\frac{1}{\beta h^2}\mathbf{e_2} \end{bmatrix} \tag{38.15}$$

where h denotes the step size and α, β, γ are parameters for the HHT solver. In Eq. (38.15) the subscripts $(\,)_{\mathbf{q}}$ and $(\,)_{\dot{\mathbf{q}}}$ denote a derivation with respect to the vector of generalized coordinates respectively the vector of generalized velocities.

38.3 Numerical Example

A 2D car pendulum model including an additional point mass as shown in Fig. 38.1 is used to demonstrate the method described in Sect. 38.2. The pendulum is designed as a flexible multilayer sheet structure and rotationally fixed to the car. The central sheet metal (400 mm × 20 mm × 1 mm) is connected with the two outer metal sheets (300 mm × 20 mm × 1 mm) via beams at three locations. The flexible structure has been modeled out of steel in the FE software *Abaqus* [19] and the resulting mass and stiffness matrices have been imported into *Scilab* [20] for all following computations. The entire model of the structure has $n_{FE} = 3009$ DOFs whereof 2709 DOFs are involved in the joint contact. For the computation of the contact forces a simple node-to-node penalty contact as given in [6] is used. The differential algebraic equations describing the multibody system as defined by Eqs. (38.8)–(38.9) have been solved with a modified HHT-solver (see [18, 19]) written in *Scilab*.

38.3.1 Evaluation of the Reduction Base

In order to evaluate the proposed reduction base the car pendulum model is computed with the model parameters defined in Table 38.1. With this values the dynamic response of the system is reduced to the behavior of a simple cantilever. The first 12 used *free-free modes* computed with Mode Shape Orthogonalization out of five normal modes, six static deformation modes and 20 JTVs are visualized in Fig. 38.2.

The external force f_{ext} is applied as a smoothed step function using a half wave cosine. In Fig. 38.3 the convergence of the Euclidean norm of the contact force vector with respect to the number of considered joint trial vectors is plotted.

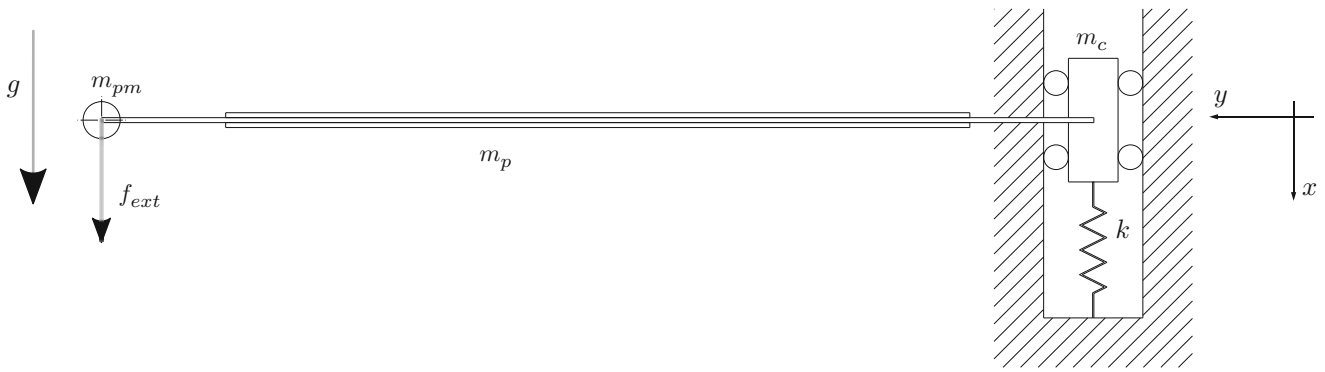

Fig. 38.1 2D car pendulum model

Table 38.1 Model parameters case 1

$m_c = 1e^{-6}\,\mathrm{kg}$	$m_{pm} = 1e^{-6}\,\mathrm{kg}$
$m_p = 0.157\,\mathrm{kg}$	$k = 5e^4\,\frac{\mathrm{N}}{\mathrm{m}}$
$f_{ext,Amp} = 1.5\,\mathrm{N}$	$g = 0\,\frac{\mathrm{kgm}}{\mathrm{s}^2}$

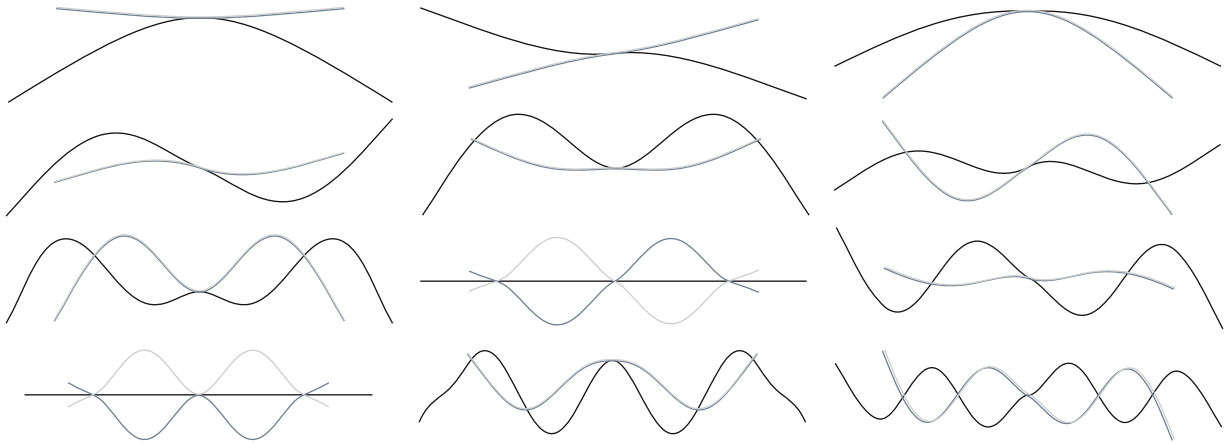

Fig. 38.2 First twelve used trial vectors of the matrix $\mathbf{\Phi}_{free}$

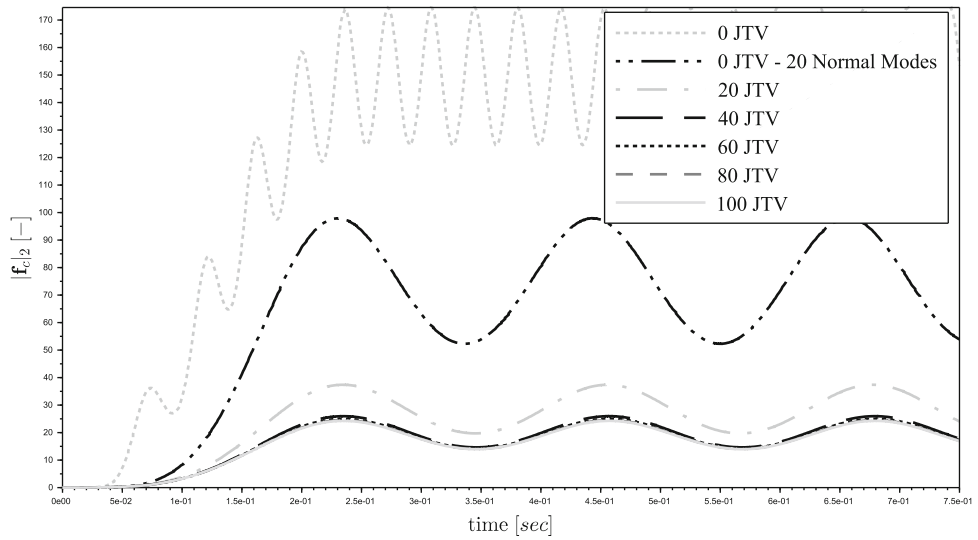

Fig. 38.3 Comparison of Euclidian norm of the contact force vector $|\mathbf{f}_c|_2$ for different numbers of JTVs

The results show that for this structure with 40 additional joint trial vectors a converged solution in terms of contact forces can be achieved. It can also be seen that the use of additional normal modes does not lead to as good results as the use of joint trial vectors. This results are in analogy with the conclusion presented in [4] where additionally a comparison to a full nonlinear computation is given.

38.3.2 Dynamic Simulation

In order to get a dynamic response which also involves a motion of the car the model parameter are changed to the values listed in Table 38.2. In this case no external force is used and only constant gravity is applied. The system is simulated with 60 JTVs, 20 JTVs and 20 additional normal modes. The results for the vertical displacement of the car and the point mass are plotted in Figs. 38.4 and 38.5. The figures show that the accurate consideration of the contact forces inside the joints not only influences the deformation of the flexible structure itself but also affects the motion of the connected rigid bodies. It can also be seen that the results for 20 JTVs are nearly identical with the converged solution computed with 60 JTVs while the results for additional normal modes are not.

Table 38.2 Model parameters case 2

$m_c = 0.25\,\mathrm{kg}$	$m_{pm} = 0.02\,\mathrm{kg}$
$m_p = 0.157\,\mathrm{kg}$	$k = 100\,\frac{\mathrm{N}}{\mathrm{m}}$
$f_{ext,Amp} = 0\,\mathrm{N}$	$g = 9.81\,\frac{\mathrm{kgm}}{\mathrm{s}^2}$

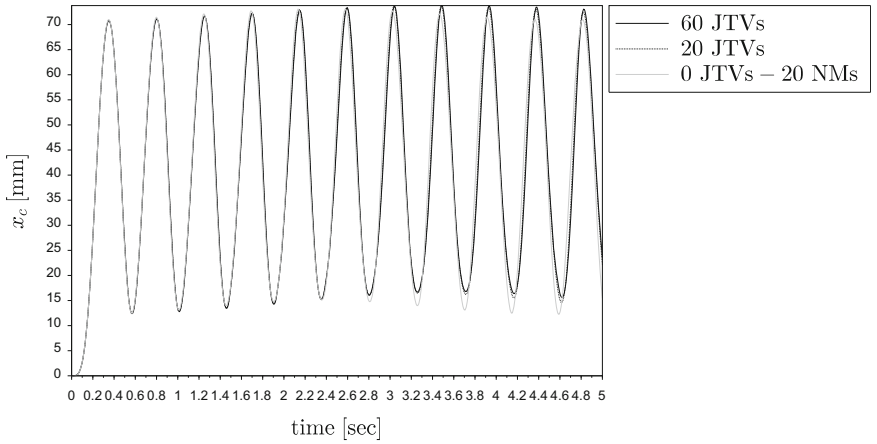

Fig. 38.4 x-displacement of the car for different numbers of JTVs

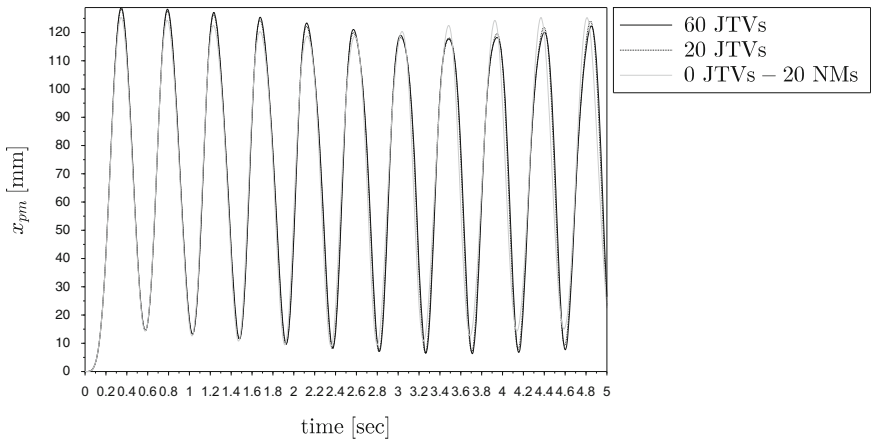

Fig. 38.5 x-displacement of the point mass for different numbers of JTVs

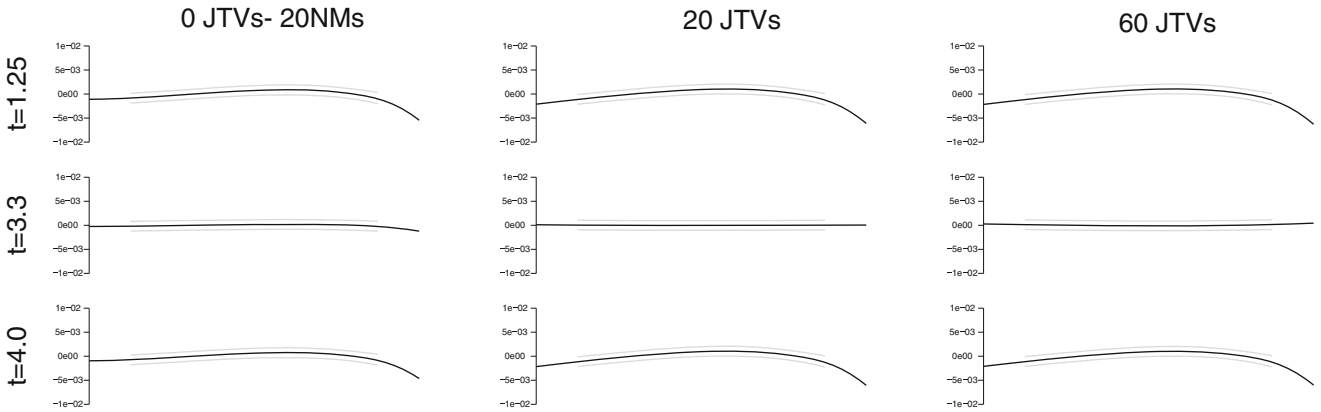

Fig. 38.6 Deformations for different instants of time for 20 additional NMs, 20 JTVs and 60 JTVs

The flexible deformations of the sheet metal structure for three different instances of time are plotted in Fig. 38.6. It can be seen that without the use of JTVs the deformations and therefore also the stresses inside the flexible structure are not computed correctly. This can have major influence on further computations (for example fatigue) carried out based on the results of the multibody simulation.

In terms of numerical efficiency it can be reported that the use of 20 JTVs compared to 20 additional normal modes leads to nearly the same computational effort (less than 10 % higher) but the results are much more accurate by the use of JTVs.

38.4 Conclusion

In this paper the reduction base presented in [4] has been used to get an accurate consideration of the contact inside jointed flexible structures within a multibody simulation. The additionally used joint trial vectors are based on trial vector derivatives and are a problem oriented extension of common reduction bases.

Furthermore it has been reported how the nonlinear contact forces need to be considered in the equations of motion of a multibody system. For the use of trial vectors in combination with a FFRF all rigid body content of the trial vectors needs to be removed. Two different strategies known from the literature have been reviewed. Both strategies additionally guarantee that the finally used trial vectors have the advantageous properties of *free-free modes*.

The example of a 2D car pendulum conformed that the JTVs form an appropriate reduction base for the consideration of joint contact within multibody simulation. Furthermore the accurate computation of the deformation of the flexible structure and the motion of the connected rigid bodies can be performed with very low computational effort.

Acknowledgements This project was supported by the program "Regionale Wettbewerbsfähigkeit OÖ 2010–2013", which is financed by the European Regional Development Fund and the government of Upper Austria.

References

1. Qu ZQ (2004) Model order reduction techniques with applications in finite element analysis. Springer, London
2. Craig RR, Bampton MCC (1968) Coupling of substructures for dynamic analyses. AIAA J 6(7):1313–1319
3. Craig RR (1985) A review of time-domain and frequency-domain component mode synthesis method. In: Combined experimental/analytical modeling of dynamic structural systems. Proceedings of the joint mechanics conference
4. Witteveen W, Pichler F (2014) Efficient model order reduction for the dynamics of nonlinear multilayer sheet structures with trial vector derivatives. Shock Vib 2014:16 pp. Article ID 913136
5. Witteveen W, Pichler F (2014) Efficient model order reduction for the nonlinear dynamics of jointed structures by the use of trial vector derivatives. In: Dynamics of coupled structures. Conference proceedings of the society for experimental mechanics series, vol 1. Springer, London, pp 147–155
6. Wriggers P (2006) Computational contact mechanics, 2nd edn. Springer, Berlin/Heidelberg [Number ISBN-10: 3-540-32608-1]
7. Laursen TA (2002) Computational contact and impact mechanics. Springer, Berlin/Heidelberg [Number ISBN 3-540-42906-09]
8. Idelsohn SR, Cardona A (1985) A load-dependent basis for reduced nonlinear structural dynamics. Comput Struct 20(1–3):203–210. Special issue: Advances and trends in structures and dynamics
9. Idelsohn SR, Cardona A (1985) A reduction method for nonlinear structural dynamic analysis. Comput Methods Appl Mech Eng 49(3):253–279
10. Friswell MI, Mottorshead JE (1995) Finite element model updating in structural dynamics. Kluwer Academic, Dordrecht
11. Slaats P, de Jongh J, Sauren A (1995) Model reduction tools for nonlinear structural dynamics. Comput Struct 54(6):1155–1171
12. Chatterjee A (2000) An introduction to the proper orthogonal decomposition. Curr Sci 78(7):808–817
13. Volkwein S (2014) Model reduction using proper orthogonal decomposition. http://www.uni-graz.at/imawww/volkwein/POD.pdf. Accessed 12 September 2014
14. Shabana AA (2005) Dynamics of multibody systems, 3rd edn. Cambridge University Press, Cambridge
15. Escalona J, Valverde J, Mayo J, Domínguez J (2003) Reference motion in deformable bodies under rigid body motion and vibration. Part I: theory. J Sound Vib 264(5):1045–1056
16. Sherif K, Irschik H, Witteveen W (2012) Transformation of arbitrary elastic mode shapes into pseudo-free-surface and rigid body modes for multibody dynamic systems. J Comput Nonlinear Dyn 7(2):021008
17. Friberg O, Karhu V (1990) Use of mode orthogonalization and modal damping in flexible multibody dynamics. Finite Elem Anal Des 7(1): 51–59
18. Negrut D, Rampalli R, Ottarsson G, Sajdak A (2006) On an implementation of the hilber-hughes-taylor method in the context of index 3 differential-algebraic equations of multibody dynamics (detc2005-85096). J Comput Nonlinear Dyn 2(1):73–85
19. Deassault Systemes (2012) Abaqus theory manual 6.12
20. Scilab (2014) Version 5.5.0, http://www.scilab.org/

Chapter 39
Model Reduction for Nonlinear Multibody Systems Based on Proper Orthogonal- and Smooth Orthogonal Decomposition

Daniel Stadlmayr and Wolfgang Witteveen

Abstract Flexible multibody simulation, subject to holonomic constraints, results in nonlinear differential algebraic systems. As computation time is a major issue, we are interested in applying model order reduction techniques to such multibody systems. One possible method called Proper Orthogonal Decomposition is based on minimizing the displacements euclidian distance while the more recently presented method Smooth Orthogonal Decomposition considers not only displacements but also their time derivatives. After a short introduction to the theory, this contribution presents a comparison of both methods on an index-reduced system. The methods are tested against each other in order to identify advantages and disadvantages.

Keywords Model reduction • POD • SOD • Flexible multibody systems • Karhunen-Loève

Nomenclature

$\dot{\boldsymbol{X}}$	Velocity snapshot matrix
$\boldsymbol{\lambda}$	Lagrangian multiplicators
$\tilde{\boldsymbol{q}}$	Re-transformed full DOFs
$\boldsymbol{C_q}$	Constraint Jacobian
$\boldsymbol{C}$	Constraint vector
$\boldsymbol{M}$	Model mass matrix
$\boldsymbol{M}_{ext}$	Extended mass matrix
$\boldsymbol{q}, \dot{\boldsymbol{q}}, \ddot{\boldsymbol{q}}$	Generalized DOFs and time derivatives
$\boldsymbol{Q}$	Generalized force vector
$\boldsymbol{q}_{red}$	Reduced DOFs
$\boldsymbol{X}$	Position snapshot matrix
α	1st Baumgarte parameter
β	2nd Baumgarte parameter
$\boldsymbol{\gamma}$	Baumgarte stabilization
$\boldsymbol{\Phi}$	Reduction matrix

39.1 Introduction

Multibody system (MBS) simulations are commonly modeled by automated modeling strategies. Due to easier automatisms mainly redundant sets of coordinates are chosen. Unfortunately by using redundant degrees of freedom (DOFs) one ends up with a larger set of coordinates than typically needed. Even though several of these rather unnecessary DOFs are commonly restrained by constraint equations, all DOFs enter the solver algorithm and therefore must be handled. Although computation resources increase rapidly it is wishfull to simplify multibody systems to the essential DOFs—the minimum set of coordinates. When dealing with flexible multibody systems even further DOFs are added, representing a finite element

D. Stadlmayr (✉) • W. Witteveen
University of Applied Sciences Upper Austria - Wels Campus, Stelzhamerstr. 23, 4600 Wels, Austria
e-mail: daniel.stadlmayr@fh-wels.at; wolfgang.witteveen@fh-wels.at

G. Kerschen (ed.), *Nonlinear Dynamics, Volume 1*, Conference Proceedings of the Society for Experimental Mechanics Series, DOI 10.1007/978-3-319-15221-9_39

(FE) body described via well known reduction processes like e.g. Computational Mode Synthesis [1, 2]. As the number of modes characterizing the flex-body must be chosen prior to the multibody simulation, one may end up with a too high number of flex-body coordinates. During the last decades several MBS coordinate reduction methods, based on constraint orthogonalization [3] and coordinate partitioning [4] have been proposed. Heirmann et al. [5] presented a hypothetical combination of coordinate transformation and coordinate partitioning. More recently Proper Orthogonal Decomposition (POD), also known as Karhune-Loève Decomposition [6] has been proposed as a reduction method to implicit differential-algebraic equation (DAE) systems of differential index (d-index) one [7]. Smooth Orthogonal Decomposition (SOD) was proposed in the field of randomly excited vibration systems to extract linear normal modes and natural frequencies by Chelidze [8]. Chelidze [9] recently applied SOD as a model order reduction tool to linear dynamical systems with local nonlinearities. This paper compares POD and SOD model reduction on a planar nonlinear flexible multibody system of differential index one. The first part introduces the d-index one multibody system as well as the reduced order model derived by flat Galerkin projection as proposed by Ebert [7]. The second part gives a short review about the POD and SOD Method and their relation to each other. In the third part a planar flexible slider crank example is investigated. Finally results are discussed and summarized.

39.2 Multibody System Modelling

39.2.1 Full Order Modelling

Assuming a flexible multibody system subject to holonomic constraints, the later modelling strategy produces a d-index three nonlinear DAE system of second order as shown in Eq. (39.1).

$$\begin{aligned} \boldsymbol{M}(\boldsymbol{q}) \cdot \ddot{\boldsymbol{q}} + \boldsymbol{Q}(\boldsymbol{q}, \dot{\boldsymbol{q}}, t) + \boldsymbol{C_q}^T \cdot \boldsymbol{\lambda} = 0 \\ \boldsymbol{C}(\boldsymbol{q}) = \boldsymbol{0} \end{aligned} \tag{39.1}$$

The number of rigid DOFs may be defined for planar examples by $k = 3 \cdot b$ with b as the number of bodies included. Adding a flex-body, l further flexible DOFs appear. The total number of DOFs is given by $n = k + l$. Further let m be the number of constraints $\boldsymbol{C}\,(\boldsymbol{q})$. In order to use ODE solver packages, both d-index and order reduction must be carried out. The derived d-index one system is presented in Eq. (39.2).

$$\underbrace{\begin{bmatrix} \boldsymbol{M}\,(\boldsymbol{q}) & \boldsymbol{C_q}^T\,(\boldsymbol{q}) \\ \boldsymbol{C_q}\,(\boldsymbol{q}) & 0 \end{bmatrix}}_{\boldsymbol{M}_{ext}(\boldsymbol{q})} \cdot \begin{pmatrix} \ddot{\boldsymbol{q}} \\ \boldsymbol{\lambda} \end{pmatrix} = \begin{pmatrix} \boldsymbol{Q}\,(\boldsymbol{q}, \dot{\boldsymbol{q}}, t) \\ \boldsymbol{\gamma}\,(\boldsymbol{q}, \dot{\boldsymbol{q}}) \end{pmatrix} \tag{39.2}$$

Assuming $\boldsymbol{M}_ext$ is nonsingular, Eq. (39.2) can be solved for $\ddot{\boldsymbol{q}}$ and $\boldsymbol{\lambda}$:

$$\begin{pmatrix} \ddot{\boldsymbol{q}} \\ \boldsymbol{\lambda} \end{pmatrix} = \boldsymbol{M}_{ext}^{-1} \cdot \begin{pmatrix} \boldsymbol{Q}\,(\boldsymbol{q}, \dot{\boldsymbol{q}}, t) \\ \boldsymbol{\gamma}\,(\boldsymbol{q}, \dot{\boldsymbol{q}}) \end{pmatrix} = \begin{pmatrix} \boldsymbol{A}\,(\boldsymbol{q}, \dot{\boldsymbol{q}}, t) \\ \boldsymbol{\Lambda}\,(\boldsymbol{q}, \dot{\boldsymbol{q}}) \end{pmatrix} \tag{39.3}$$

In order to avoid the drift problem, the Baumgarte stabilization [10] $\boldsymbol{\gamma} = -\boldsymbol{C}_{\boldsymbol{qq}}\,(\dot{\boldsymbol{q}}, \dot{\boldsymbol{q}}) - \alpha \boldsymbol{C_q} \dot{\boldsymbol{q}} - \beta \boldsymbol{C}\,(\boldsymbol{q})$ is used. Hence, MBS simulation is carried out using the first order d-index one system Eq. (39.4).

$$\begin{aligned} \dot{\boldsymbol{q}} &= \boldsymbol{v} \\ \dot{\boldsymbol{v}} &= \boldsymbol{A}\,(\boldsymbol{q}, \boldsymbol{v}, t) \end{aligned} \tag{39.4}$$

It must be stated that the validity of the above model is strongly depending on the chosen Baumgarte stabilization parameters α and β. Therefore we expect those to be chosen correctly for all upcoming considerations. For further insight into the topic of (flexible) multibody system dynamics the interested reader is referred to Shabana [11].

39.2.2 Reduced Order Modeling

Flat Galerkin projection, defined by Eq. (39.5), projects a high dimensional original system onto some smaller subspace $\mathcal{Y}$ spanned by $\boldsymbol{\Phi}$. The projection matrix $\boldsymbol{\Phi}$ may be derived from various methods, in our case POD and SOD. $\boldsymbol{\Phi}$ is split into a dominant part $\boldsymbol{\Phi}_r$ and a neglectable part $\boldsymbol{\Phi}_{n-r}$. Neglecting the second part of the subspace, the projection changes from a pure transformation into an approximation.

$$\boldsymbol{q} \approx \tilde{\boldsymbol{q}} = \boldsymbol{\Phi}_r \cdot \boldsymbol{q}_{red} \quad \boldsymbol{\Phi}_r \epsilon \mathbb{R}^{nxr},\ \boldsymbol{q} \epsilon \mathbb{R}^r,\ r \ll n \tag{39.5}$$

Applying the flat Galerkin projection to the mechanical system defined in Eq. (39.4), it must be stated that according to the work of Ebert [7] the reduction process may transform the DOFs but must not change any constraint equations as this could lead to unphysical phenomena. Considering this restriction, the reduced model is defined in Eq. (39.6).

$$\begin{aligned} \tilde{\boldsymbol{v}} &= \boldsymbol{U}_{red}^T \cdot \dot{\boldsymbol{q}}_{red} \\ \dot{\tilde{\boldsymbol{v}}} &= \boldsymbol{U}_{red}^T \cdot \boldsymbol{M}_{ext}\left(\tilde{\boldsymbol{q}}\right)^{-1} \cdot \begin{pmatrix} \boldsymbol{Q}\left(\tilde{\boldsymbol{q}}, \tilde{\boldsymbol{v}}, t\right) \\ \gamma\left(\tilde{\boldsymbol{q}}, \tilde{\boldsymbol{v}}\right) \end{pmatrix} \end{aligned} \tag{39.6}$$

With

$$\boldsymbol{U}_{red} := \begin{bmatrix} \boldsymbol{\Phi}_r & \boldsymbol{0} \\ \boldsymbol{0} & \boldsymbol{I}_m \end{bmatrix} \tag{39.7}$$

with $\boldsymbol{I}_{n-r}$ being a unit matrix of dimension m. It must be stated that due to the nonlinear character, the projection must be carried out in each time-step t_i repetitive with re-evaluated system matrices/vectors $\boldsymbol{M}$,$\boldsymbol{Q}$, etc.

39.3 Reduction Methods

39.3.1 Proper Orthogonal Decomposition

During the last couple of years, the linear Galerkin projection method POD established as a commonly used model reduction technique [6]. It is based on the idea of finding a proper orthogonal subspace to the observation space given by observation data. The subspace to be found minimizes the euclidean distance in terms of the captured signal energy. Let $\boldsymbol{X} \epsilon \mathbb{R}^{nxh}$ be the time-series of a multibody simulation with $t = [t_0, \ldots, t_h]$. In the field of POD the observation data matrix $\boldsymbol{X}$ is called $snapshot - matrix$, meaning every column vector $\boldsymbol{q}_i$ represents a snapshot of the system at time t_i. The method of POD investigates this snapshot matrix $\boldsymbol{X}$ in order to define a low-dimensional subspace, spanned by $r-$ basis vectors, so-called Proper Orthogonal Modes (POMs), with $r < n$. Therefore $\boldsymbol{X}$ is processed by the singular value decomposition (SVD) in Eq. (39.8)

$$\boldsymbol{X} = \boldsymbol{\Phi} \cdot \boldsymbol{\Sigma} \cdot \boldsymbol{W}^T \tag{39.8}$$

The $n\ x\ n$ SVD-matrix $\boldsymbol{\Phi} = [\boldsymbol{\phi}_1, \ldots, \boldsymbol{\phi}_n]$ consists of already mentioned POMs $\boldsymbol{\phi}_i$, also called left singular vectors, defining the orthogonal subspace to $\boldsymbol{X}$. The column vectors $\boldsymbol{w}_i$ summarized in $\boldsymbol{W}$ are called right singular vectors. The dimension of the orthogonal subspace may be defined by the singular values, also called Proper Orthogonal Values (POVs), arranged in the diagonal matrix $\boldsymbol{\Sigma} = diag\left(\sigma_1, \ldots, \sigma_n\right)$ with $\sigma_1 \leq \sigma_2 \leq \ldots \leq \sigma_n$. The singular value σ_i indicates the amount of signal energy captured by the associated basis vector $\boldsymbol{\phi}_i$. As the singular values decrease rapidly, a *drop-point*, as indicated in Fig. 39.1 may be found which characterizes the number of basis vectors $\boldsymbol{\phi}_i$ needed to span an orthogonal subspace delivering sufficient result quality. Assuming a drop-point is detectable within $r-$ singular values, the model reduction matrix $\boldsymbol{\Phi}_r \epsilon \mathbb{R}^{n\,x\,r} = [\boldsymbol{\phi}_1, \ldots, \boldsymbol{\phi}_r]$ with $r < n$ can be defined. As a matter of fact, if there is no drop-point detectable, the system may not be reducable. Further, POMs $\boldsymbol{\phi}_i$ may also be derived from the eigenvalue problem given in Eq. (39.9)

$$\boldsymbol{X} \cdot \boldsymbol{X}^T \cdot \boldsymbol{v}_i = \lambda_i \cdot \boldsymbol{v}_i \tag{39.9}$$

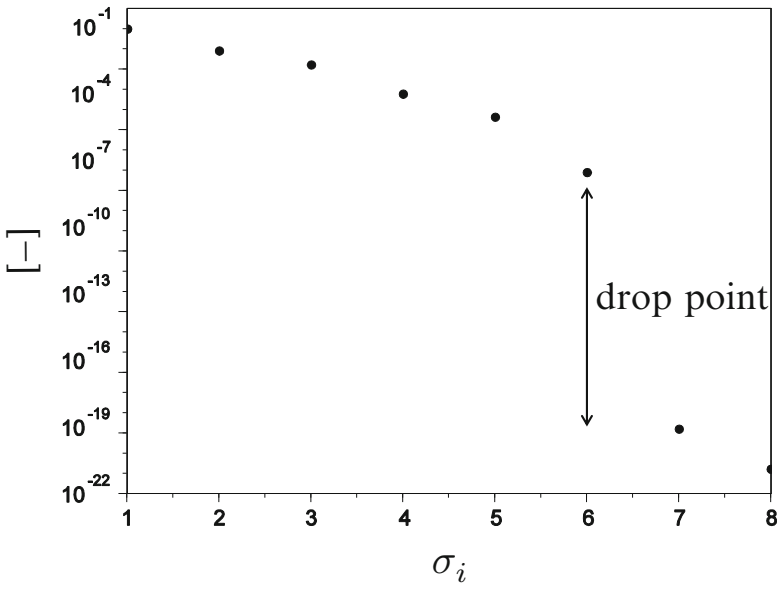

Fig. 39.1 Singular values

with

$$\boldsymbol{\phi}_i = \frac{1}{\sqrt{\lambda_i}} \cdot \boldsymbol{X} \cdot \boldsymbol{v}_i \tag{39.10}$$

and POVs defined as $\sigma_i = \sqrt{\lambda_i}$.

Recalling the linear Galerkin projection, the system transformation is defined as

$$\tilde{\boldsymbol{q}} = \boldsymbol{\Phi}_{red} \cdot \boldsymbol{q}_{red} \tag{39.11}$$

It is worth mentioning, that if all basis vectors $\boldsymbol{\phi}_i$ are used, the projection in Eq. (39.11) is only transforming the system but achieves no reduction at all.

39.3.2 Smooth Orthogonal Decomposition

Chelidze [8] introduced a *SmoothKarhunen-Loève Decomposition* called Smooth Orthogonal Decomposition (SOD). The method has been used as a model order reduction tool for linear systems with local nonlinearities in [9]. Similarities to POD are not only found in the name but also in the basic process of Smooth Orthogonal Modes (SOMs) and -Values (SOVs). Given a snapshot matrix $\boldsymbol{X}_{SOD} \epsilon \mathbb{R}^{hxn}$, which may be simply the transposed POD snapshot matrix, SOD further rests on the velocity snapshot matrix $\dot{\boldsymbol{X}}_{SOD}$. SOMs and SOVs are derived by solving the generalized eigenvalue problem in Eq. (39.12).

$$\boldsymbol{\Sigma}_{\boldsymbol{X}_{SOD}\boldsymbol{X}_{SOD}} \cdot \boldsymbol{v}_i = \lambda_i \cdot \boldsymbol{\Sigma}_{\dot{\boldsymbol{X}}_{SOD}\dot{\boldsymbol{X}}_{SOD}} \cdot \boldsymbol{v}_i \tag{39.12}$$

With the correlation matrices $\boldsymbol{\Sigma}_{\boldsymbol{X}_{SOD}\boldsymbol{X}_{SOD}} = \frac{1}{n} \cdot \boldsymbol{X}_{\boldsymbol{SOD}}{}^T \cdot \boldsymbol{X}_{SOD}$ and $\boldsymbol{\Sigma}_{\dot{\boldsymbol{X}}_{SOD}\dot{\boldsymbol{X}}_{SOD}} = \frac{1}{n} \cdot \dot{\boldsymbol{X}}_{\boldsymbol{SOD}}{}^T \cdot \dot{\boldsymbol{X}}_{\boldsymbol{SOD}}$. The SOVs are hereby given as λ_i and SOMs are defined as $\boldsymbol{\phi}_i = \boldsymbol{v}_i^{-T}$. Depending on the number of snapshots taken into account, the general eigenvalue problem solver may fail and therefore SOMs can be derived from the general singular value decompositions Eq. (39.13).

$$\begin{aligned} \boldsymbol{X}_{SOD} &= \boldsymbol{W}_1 \cdot \boldsymbol{\Sigma}_1 \cdot \boldsymbol{\Phi}^T \\ \dot{\boldsymbol{X}}_{SOD} &= \boldsymbol{W}_2 \cdot \boldsymbol{\Sigma}_2 \cdot \boldsymbol{\Phi}^T \end{aligned} \tag{39.13}$$

with SOMs again defined as $\boldsymbol{\phi}_i$. SOVs are derived by the term-by-term division of $diag\left(\boldsymbol{\Sigma}_1^T \cdot \boldsymbol{\Sigma}_1\right)$ and $diag\left(\boldsymbol{\Sigma}_2^T \cdot \boldsymbol{\Sigma}_2\right)$.

Proceeding as already explained for the POD method, the flat Galerkin reduction consists of $r-$ SOMs indicated by a drop-point found in the SOVs as seen in Fig. 39.1. Due to the velocity snapshot matrix, SOD is not only accounting static but also dynamic characteristica. While POD minimizes the euclidean distance of the captured signal energy, in other words maximizes the energy in the projected signal, SOD further maximizes the variance (the smoothness) in the projection. In this manner SOD finds deterministic trends, which may be of interest for MBS reduction. Taking a look onto Eq. (39.12) and substituting the unity matrix $\boldsymbol{I}$ for $\boldsymbol{\Sigma}_{\dot{\boldsymbol{X}}_{\boldsymbol{SOD}}\dot{\boldsymbol{X}}_{\boldsymbol{SOD}}}$ the POD method is derived from the SOD method by the SVD of $\boldsymbol{X}_{\boldsymbol{SOD}} = \boldsymbol{W}_1 \cdot \boldsymbol{B}_1 \cdot \boldsymbol{\Phi}^T$. Regarding normal mode (NM) identification, Feeny [12] stated that while POD is able to identify NMs for undamped system it fails to identify a linearly damped dynamical system in general. SOD overcomes this drawback and is able to identify a linearly damped dynamical systems NMs as presented by Farooq and Feeny [13].

39.4 Numerical Example

39.4.1 Model Data

The model subject to both reduction methods is presented in Fig. 39.2a. In order to get a maximum set of redundant coordinates, all planar rigid DOFs $\left(x_{cart}, y_{cart}, \phi_{cart}, x_{pendulum}, y_{pendulum}, \phi_{pendulum}\right)$ are used, acting in the respective center of mass. Further, two flex-DOFs, defined by free-free modes, describing the flexible pendulum are added. The MBS therefore consists of $n = 2 \cdot 3 + 2 = 8$ rigid-body and flex-body DOFs. Finally, the following constraints are introduced, representing the carts planar restrictions and a hinge joint between the cart and the pendulum:

$$C_1 : x_c - y_c = 0 \tag{39.14}$$

$$C_2 : phi_c = 0 \tag{39.15}$$

$$C_3 : \begin{bmatrix} x_c - x_p \\ y_c - y_p \end{bmatrix} - \boldsymbol{B}_p \cdot \left(\boldsymbol{u}_p + \boldsymbol{s}_p \cdot \boldsymbol{q}_f\right) = 0 \tag{39.16}$$

With $\boldsymbol{B}_p$ describing the pendulum rotation matrix, $\boldsymbol{u}_p = \left[0, l_p/2\right]^T$ representing the position vector from the pendulums center of mass to the hinge-joint and $\boldsymbol{s}_p \epsilon \mathbb{R}^{lx2}$ representing the first two free-free bending modes. Let the cart further be subject to linear springs and dampers acting in global x and y directions. Given cart mass $m_c = 1\,\text{kg}$, pendulum mass $m_p = 0.004\,\text{kg}$, pendulum length $l_p = 0.8\,\text{m}$, spring stiffness $c_c = 100\,\text{N/m}$ and damping constant $d_c = 0.1$, the model is excited by a sinusoidal force with Amplitude $A = 10\,\text{N}$ and frequency $f = 10\,\text{Hz}$, acting on the rigid cart and forcing it to move diagonal in plane. The simulation is carried out in SciLab v5.5.0—http://www.scilab.org—using the included ODEPACK BDF solver with flexible time stepping for $t_{end} = 1\,\text{s}$. The excitation force and body modes are fitted to excite

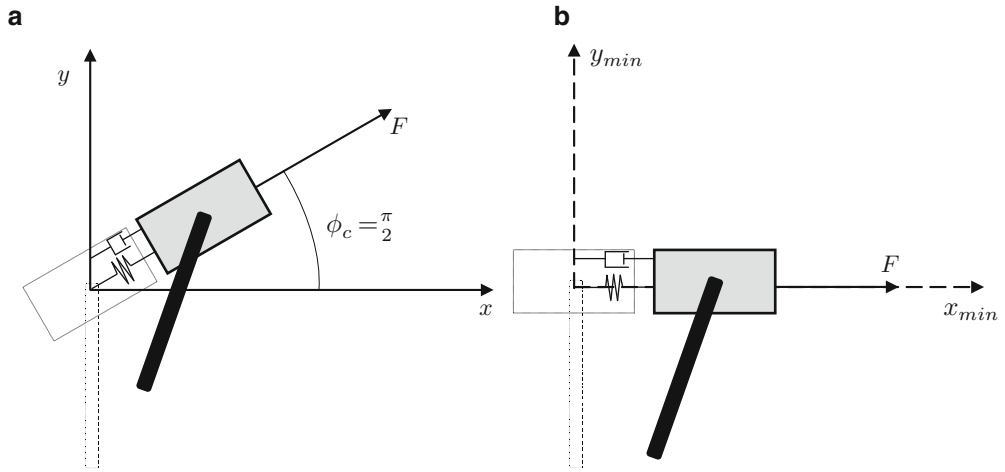

Fig. 39.2 Full and reduced model representation. (**a**) Redundant formulation. (**b**) Minimum set formulation

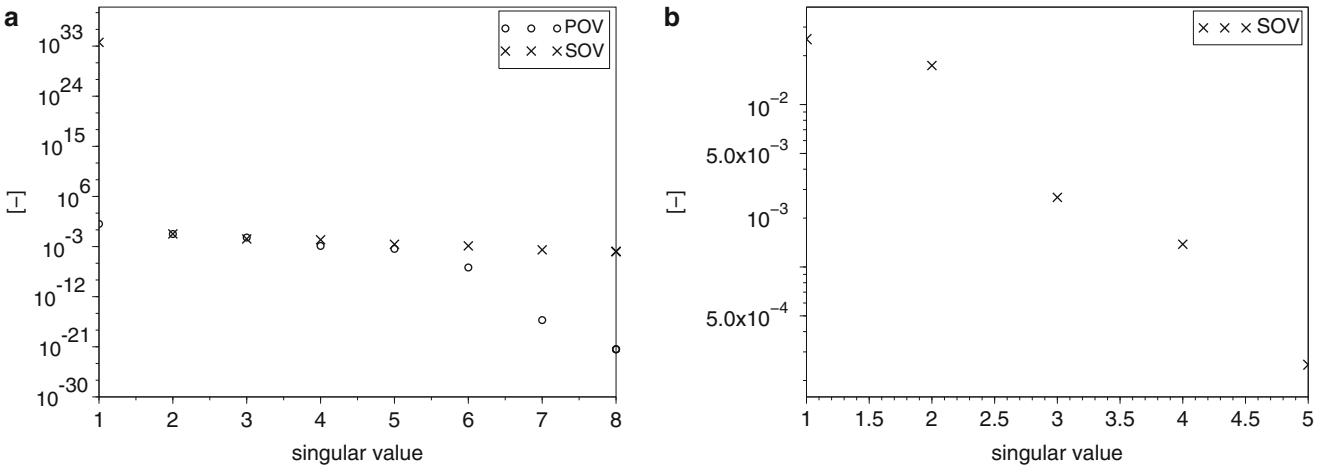

Fig. 39.3 POVs and SOVs plot. (**a**) All POVs and SOVs. (**b**) Independent SOVs

the first flex body mode ($f_1 = 16\,\text{Hz}$) only. The second flex body mode is set to a high eigenfrequency $f_2 > 1\,\text{kHz}$. Considering the given constraint equations which introduce zero rows for restrained DOFs, the snapshot matrices $\boldsymbol{X}$, $\dot{\boldsymbol{X}}$ as well as the correlation matrices $\boldsymbol{\Sigma}_{\boldsymbol{X_{SOD}X_{SOD}}}$ and $\boldsymbol{\Sigma}_{\dot{\boldsymbol{X}}_{\boldsymbol{SOD}}\dot{\boldsymbol{X}}_{\boldsymbol{SOD}}}$ are rank deficient.

39.4.2 Results

A full model simulation collects the snapshot matrices $\boldsymbol{X}$ and $\dot{\boldsymbol{X}}$ at a sample rate of 100 Hz. In a next step, the POD-SVD of $\boldsymbol{X}$ and the generalized SOD-SVD of $\boldsymbol{X}_{SOD}$ and $\dot{\boldsymbol{X}}_{SOD}$ are generated as shown in Fig. 39.3a. As mentioned in the beginning the model reduction techniques should be evaluated on their ability to reduce the redundant set of coordinates to the minimal set of coordinates. The minimal set of coordinates of the given example is defined by $n_{min} = 4$ DOFs, for example $\boldsymbol{q}_{min} = \left[x_{min,c}, x_{min,p}, y_{min,p}, q_{f,1}\right]^T$ as indicated in Fig. 39.2b.

Looking at the POD findings in Fig. 39.3a, a noticeable *drop-point* is detected after $\sigma_{POD,6}$. The POD reduced model-dimension is expected as the snapshot matrix $\boldsymbol{X}$ is of $rank = 6$. The reduction matrix $\boldsymbol{\Phi}_{POD}$ may therefore consist of $r_{POD} = 6$ POMs which project the $n = 8$ original DOFs onto $r_{POD} = 6$ reduced DOFs $\boldsymbol{q}_{red}$. Due to numerical reasons SciLab assigns full rank to the POM matrix instead of the actual rank. Investigating the calculated SOVs in Fig. 39.3a the drop-point between first and second SOV marks an infinite singular value. Regarding Eq. (39.12) and recalling that the velocity correlation matrix $\boldsymbol{\Sigma}_{\dot{\boldsymbol{X}}_{SOD}\dot{\boldsymbol{X}}_{SOD}}$ is singular, the generalized eigenvalue problem yields one infinite eigenvalue for each row/column equal to zero. To get deeper insight into the SOVs, the rank of the SOM matrix is calculated showing rank deficiency. As expected the SOM-rank is calculated to a value of five as it has to be the same as the correlation velocity matrix rank. SOMs $\{\boldsymbol{\Phi}_{SOD,1}, \boldsymbol{\Phi}_{SOD,7}, \boldsymbol{\Phi}_{SOD,8}\}$ are chosen as linear dependent columns which imply that the corresponding SOVs may not be taken into account for SOD model reduction. Dependent SOVs are omitted and the remaining SOVs are plotted in Fig. 39.3b. Although the independent-SOV plot is showing minor drop-points a significant drop-point like POD is missing. As a result all independent SOMs are used to generate the SOD reduced model subspace. Due to the fact that the SOMs are not orthogonal, a Gram-Schmidt Orthogonalization is applied to the SOMs prior to simulation. Examining Fig. 39.4, POD and SOD model results are almost congruent to the full simulation results. Error plots in Fig. 39.5 are derived from the error measure

$$e_i\,[t] = \frac{\Delta q_i\,[t]}{\|max\; q_{red,i}\|} \tag{39.17}$$

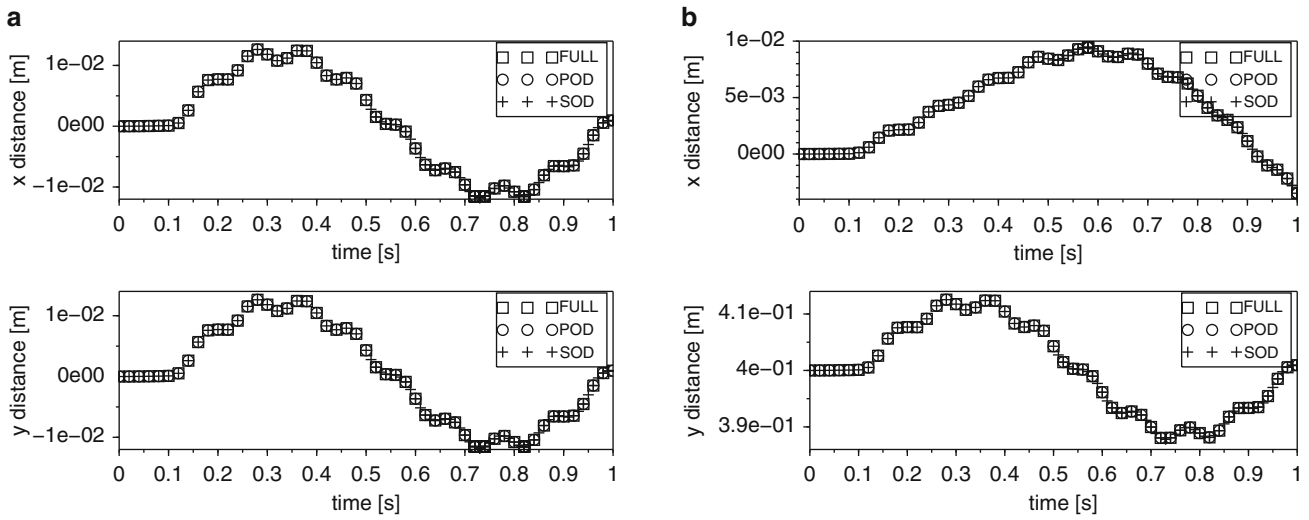

Fig. 39.4 Simulation results—$r_{POD} = 6$ and $r_{SOD} = 5$. (**a**) Cart. (**b**) Pendulum

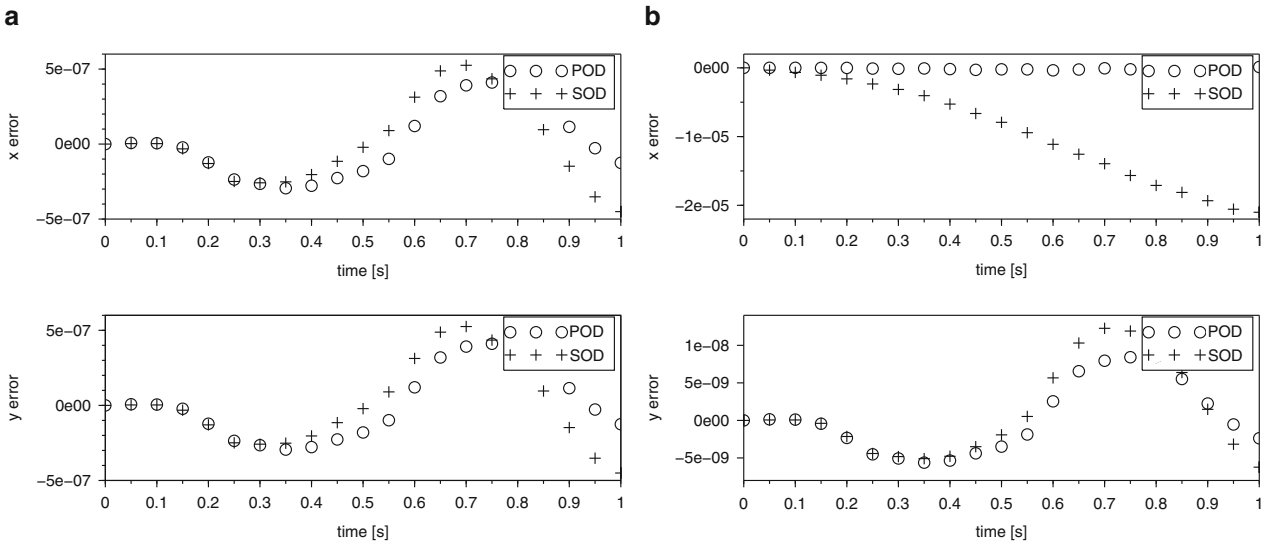

Fig. 39.5 Error plot—$r_{POD} = 6$ and $r_{SOD} = 5$. (**a**) Cart. (**b**) Pendulum

with $\Delta q_i\,[t] = q_{full,i}\,[t] - \tilde{q}_i\,[t]$. Investigating the error plots, the order five SOD model causes a slightly higher error than the order six POD model. Unfortunately, due to the dependent SOMs a further increase of the SOD subspace is not possible. Comparing simulation times, the POD reduced model saves about 12 % compared to the full model while SOD reduces the simulation time by almost 30 %.

Looking at Table 39.1 the POMs may be split into a group of four pendulum bending-modes and into four rigid body modes. The bending POMs thereby also include the second bending mode, which is excited only by numerical diffusion during simulation ($max\left|q_{f,2}\right| \approx 1e^{-23}$) while SOD omits it. Comparing the modes, SOMs similar to POMs can be found, like e.g. $\{\boldsymbol{\Phi}_{POD,2} \leftrightarrow \boldsymbol{\Phi}_{SOD,4}, \boldsymbol{\Phi}_{POD,4} \leftrightarrow \boldsymbol{\Phi}_{SOD,7}\}$.

At the end we would like to report the practically important observation, that the POD approach is more robust in terms of "standard numerical tools" as SOD. To illustrate this statement we increase the sample rate from $100Hz$ to $300Hz$ in order to use more snapshots for SOD, calling the newly generated smooth orthogonal modes refined-SOMs (rSOMs). While the POD rank stays constant for this higher sample rate, the rSOM rank increases. This is related to numerical reasons, as numerical rank determination is in need of high singular value drop-offs which are not present. One rSOM changing from dependent to independent is identified as the first SOM related to the theoretically infinite first rSOV. Given a rSOM-matrix

Table 39.1 Proper-/smooth orthogonal modes

POMs 1:4	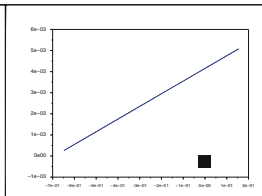	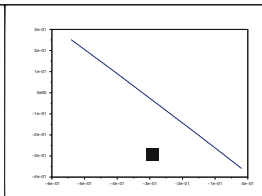	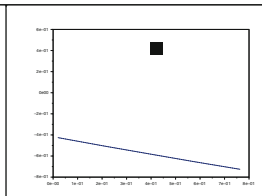	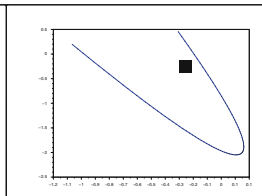
SOMs 1:4	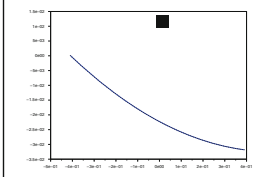	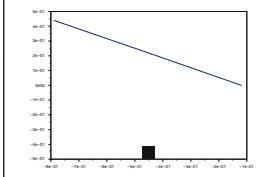	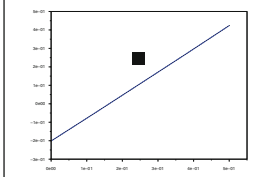	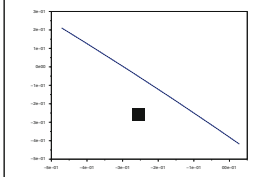
POMs 5:8	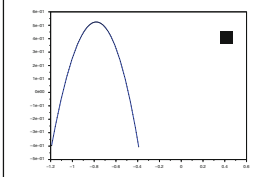	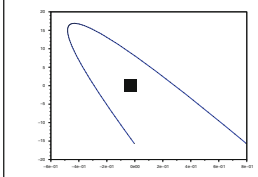	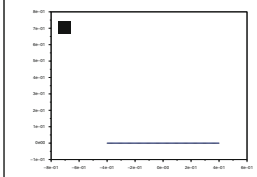	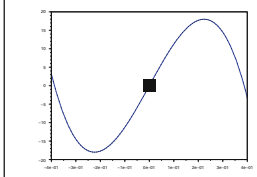
SOMs 5:8	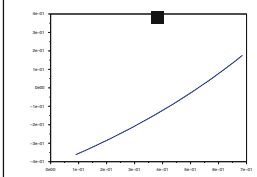	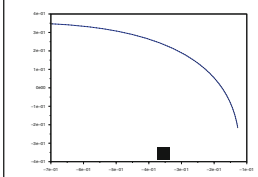	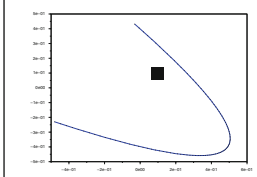	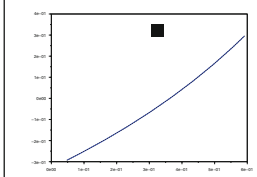

of rank six would indicate six linear independent modes which are not case within this example as the velocity correlation matrix is of rank five. Actually using this $r_{rSOD} = 6$ subspace, the simulation results worsen as indicated in the error plot Fig. 39.6 which implies that SOD is numerically sensitive. It also confirms that the rank computation suffers from the lack of high drop-offs and fails to identify the actual rank.

39.5 Conclusion

This paper tries to compare and evaluate POD and SOD model order reduction applied to a flexible redundant multibody systems. Based on the order reduced d-index one DAE system both reduction methods are summarized and applied to a flexible planar cart pendulum model. The POD reduction identifies two out of four redundant coordinates ending up with a total number of $r_{POD} = 6$ DOFs. Further, the simulation time decreases by about 12 % compared to the full model. SOD reduces the model to $r_{SOD} = 5$ DOFs and reduces the simulation time by about 30 %. POD shows a numerically robust behavior, indifferent to sample-rate variations which is further underlined by a clear singular value drop-point. SOD delivers a smaller reduced model (five SOMs instead of six POMs) and saves about 30 % of simulation time. As SOD is sensitive to sample-rate variations it shows less numerical robustness. Due to the lack of a clear SOV drop-point, numerical rank determination is negatively effected. Finally SOMs need to be orthogonalized prior to reduced simulation in order to achieve a more effective time integration. Both methods presented may suffer from issues when dealing with models starting from locations outside the global origin, meaning initial position values different from zero. As the used type of flat Galerkin projection is approximating the system, omitted DOFs may also lead to loosing their initial conditions. Future work will focus on this initial condition issues as well as on adapted POD and SOD methods in order to end up with models closer to the minimal set of coordinates. Further, in order to minimize not only DOFs but also constraint equations, the constraint restriction posted by Ebert will be softened to allow special types of constraints to be removed.

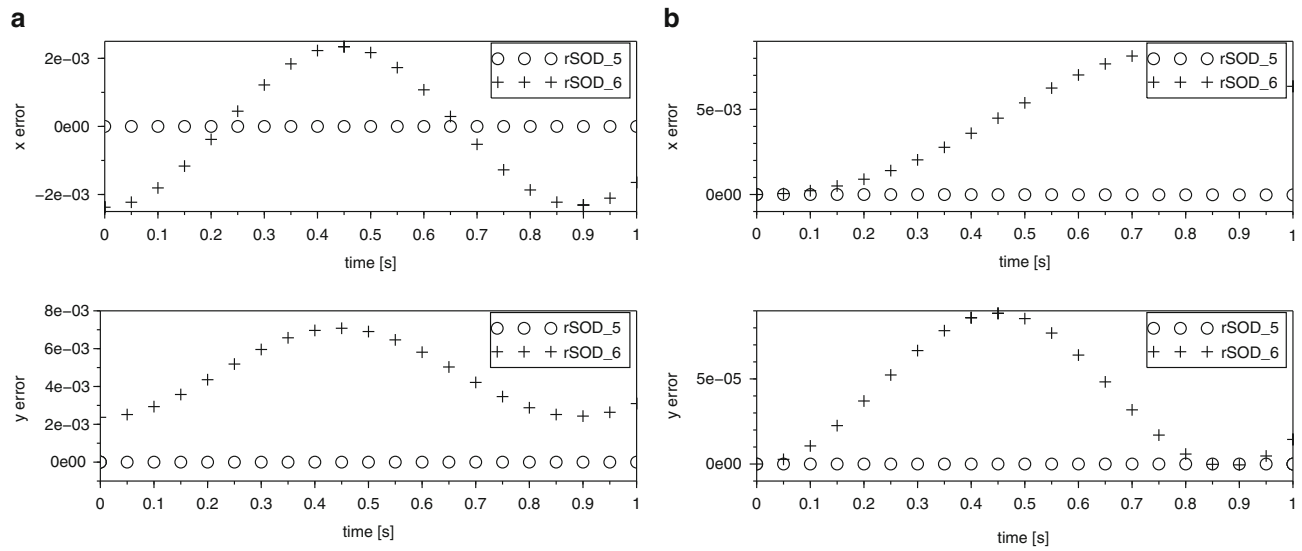

Fig. 39.6 Error plot—$r_{rSOD} = 5$ and $r_{rSOD} = 6$. (**a**) Cart. (**b**) Pendulum

Acknowledgements We gratefully acknowledge the support from the Austrian funding agency FFG in Coin-project ProtoFrame (project number 839074).

References

1. Craig R (1985) A review of time-domain and frequency-domain component mode synthesis method. J Mod Anal 2:59–72
2. Craig R (2000) Coupling of substructures for dynamic analyses: an overview. In: Structural dynamics, and materials conference and exhibit
3. Pennestri E, Valentini P (2007) Coordinate reduction strategies in multibody dynamics: a review. In: Conference on multibody system dynamics
4. Laulusa A, Bauchau O (2007) Review of classical approaches for constraint enforcement in multibody systems. J Comput Nonlinear Dyn 3:1–8
5. Heirman G, Brüls O, Sas P, Desmet W (2008) Coordinate transformation techniques for efficient model reduction in flexible multibody dynamics. In: Proceedings of ISMA
6. Volkwein S (2008) Model reduction using proper orthogonal decomposition. Lecture notes, 2013.09.30-http://www.uni-graz.at/imawww/volkwein/POD.pdf
7. Ebert F (2010) A note on pod model reduction methods for daes. Math Comput Model Dyn Syst 16:115–131
8. Chelidze D, Zhou W (2006) Smooth orthogonal decomposition-based vibration mode identification. J Sound 292:461–473
9. Chelidze D (2014) Identifying robust subspaces for dynamically consistent reduced-order models. In: Nonlinear dynamics. Proceedings of the 32nd IMAC, A conference and exposition on structural dynamics, vol 2
10. Baumgarte J (1972) Stabilization of constraints and integrals of motion in dynamical systems. Comput Math Appl Mech Eng 1:1–16
11. Shabana AA (2005) Dynamics of multibody systems, 3rd edn. Cambridge University Press, Cambridge
12. Feeny B, Kappagantu R (1998) On the physical interpretation of proper orthogonal modes in vibrations. J Sound Vib 211:607–616
13. Farooq U, Feeny B (2008) Smooth orthogonal decomposition for modal analysis of randomly excited systems. J Sound Vib 316:137–146

Chapter 40
Cam Geometry Generation and Optimization for Torsion Bar Systems

Ergin Kurtulmus and M.A. Sahir Arikan

Abstract Moment unbalance is a critical issue in many mechanisms rotating around a certain axis. The common element for eliminating the moment unbalance is a spring attached to the rotary system which can nullify it only at a certain angle or position due to the cosine profile of the unbalance. In order to accomplish this at all angles, torsion bar systems following a cam profile are preferred instead. In this paper, a new method has been developed to generate the exact analytical cam profile on which torsion bar system will roll. Using the moment balance equations and the equations related to the geometry of the cam profile at rotated frames and torsion bar parameters, seven nonlinear differential equations with corresponding initial conditions are obtained. Solution of this set of nonlinear equations determined the cam profile, torsion bar torque profile and the overall system layout. Then, the problem transformed into an optimization problem with an objective of minimizing the maximum amount of torque induced on the torsion bar with certain geometrical and structural constraints, with initial conditions forming the search space. Systematical solution to this optimization problem created a blueprint for the design of a generic system in a constrained volume.

Keywords Moment unbalance • Nonlinear systems • Optimization • Cam geometry • Torsion bar

40.1 Introduction

Moment unbalance is a commonly encountered issue in civil and especially military applications. The problem originates from the fact that the center of mass (CM) of a rotating system does not coincide with the axis of rotation. This excess moment needs to be eliminated for many practical purposes such as to decrease the load on the actuation system or to increase the overall control system performance. Moment unbalance for a typical gun system is depicted in Fig. 40.1 below.

In Fig. 40.1, CM is the center of mass of the total elevating system which includes the gun, the rotor and the mechanisms etc., x_{unb} is the horizontal distance between the rotation axis and CM at zero elevation (assuming the vertical one, y_{unb}, to be zero), α is the elevation angle of the overall system measured from the positive horizontal axis and g is the gravitational acceleration. Then, the moment unbalance is given by the following equation,

$$M_{unb} = m_{unb} g x_{unb} \cos(\alpha) \tag{40.1}$$

where m_{unb} is the total mass of the elevating system. This moment unbalance given by the equation is traditionally eliminated by using equilibrators which mainly include a helical compression spring with a predetermined spring constant. However, they are able to nullify M_{unb} only at a certain angle which is selected to be zero degree, most of the times. This is simply because the moment provided by the spring with certain stiffness cannot match the cosine profile of the unbalance given in equation at all elevation angles. This fact can be observed in the Fig. 40.2. In Fig. 40.2, Moment unbalance profile of a system with an unbalance value of 775 Nm at zero degree elevation is compensated with an equilibrator equipped with a helical spring which has a stiffness of 4,700 N/m. Elevation angle α range is usually between $-10°$ and $+50°$.

E. Kurtulmus (✉)
FNSS Defense Systems Inc., Ankara 06830, Turkey
e-mail: erginkurtulmus@gmail.com

M.A.S. Arikan
Mechanical Engineering Department, Middle East Technical University, Ankara 06800, Turkey

G. Kerschen (ed.), *Nonlinear Dynamics, Volume 1*, Conference Proceedings of the Society for Experimental Mechanics Series, DOI 10.1007/978-3-319-15221-9_40

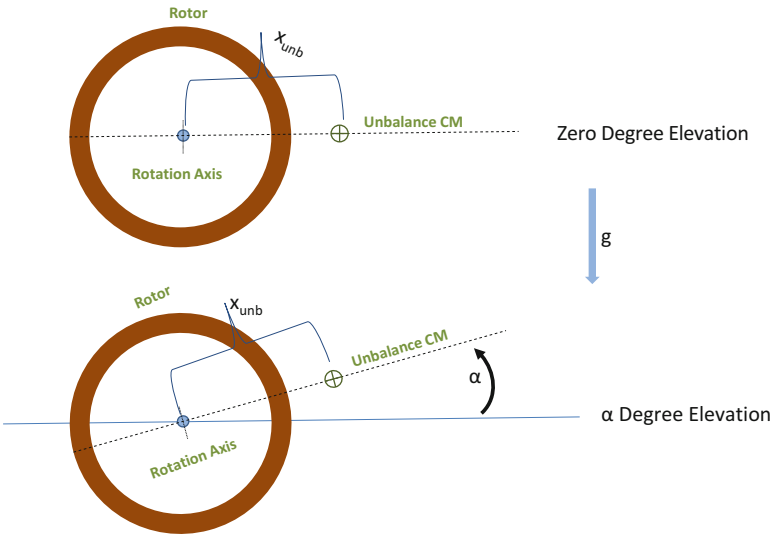

Fig. 40.1 Moment unbalance at a certain elevation angle

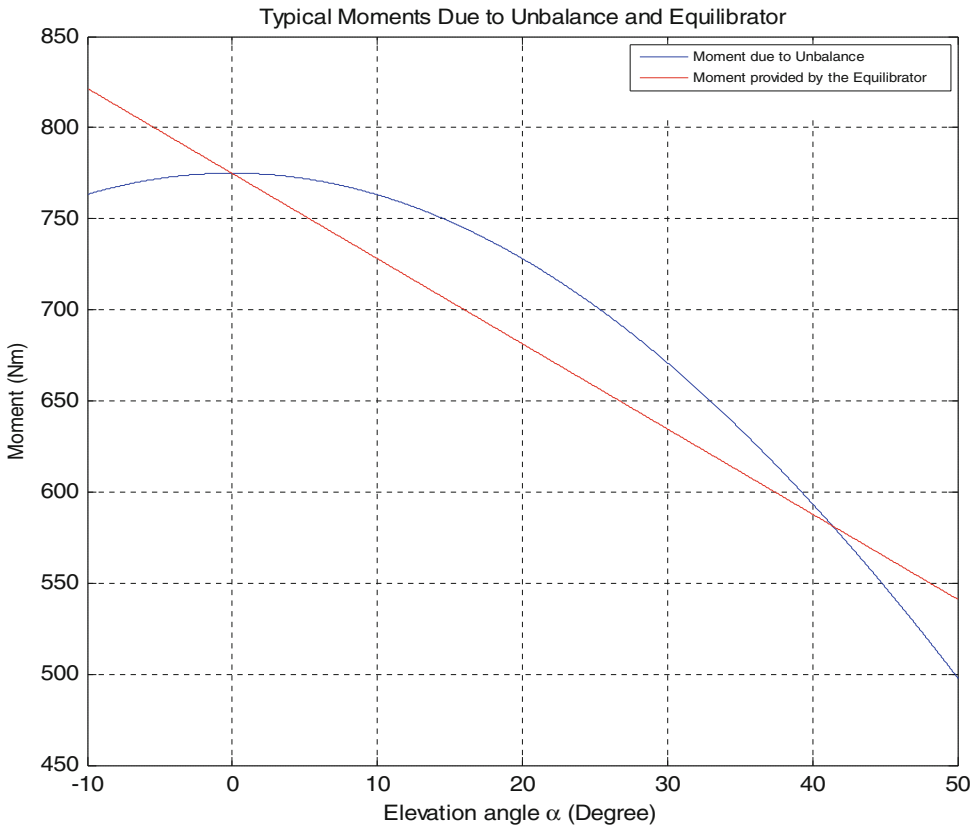

Fig. 40.2 Typical moment profiles for unbalance and the spring loaded equilibrators

In general, the aim is to match moment unbalance profile perfectly or as close as possible at all elevation angles α. In this paper, in order to make that possible, a torsion bar system consisting of a torsion bar, connecting linkages, roller and a special cam profile configuration is discussed. The main focus is on how to generate a cam profile curve and design a torsion bar optimally for a given system with a certain amount of moment unbalance with certain geometrical constraints.

40.2 Modelling of the System

40.2.1 Torsion Bar System Components

The major system components of the torsion bar equilibrator are as follows;

- Torsion Bar
- Connecting Rod
- Roller
- Cam profile (Cam)

These components are illustrated schematically in Fig. 40.3 below.

Torsion bar, with one end fixed while the other end is fixed to the connecting rod via a spline profile and is free to rotate (twist) around the central longitudinal axis, acts as a torsional spring with a certain stiffness. Most of the times, two ends of the torsion bar is machined to form spline profiles in order to transmit torque properly. Connecting rod is a bar which is connected to the torsion bar at one end where all of the torque is transmitted and connected to the roller with a revolute joint at the other end. Roller is a free to rotate element at one end of the connecting rod (connected with a revolute joint) and it is in contact with the cam profile and is rolling along it. In practical applications, it is a roller bearing. Cam is the element with a special curved profile (cam profile) on which the roller moves. In the implementation, the cam is fixed to the rotor, while one end of the torsion bar is fixed to the non elevating turret body. The overall simplified configuration is given schematically in Fig. 40.4.

The coordinate frame is attached to the rotor center with its y-axis pointing towards the opposite direction of the gravity, while x-axis is pointing towards the gun (front of the vehicle) and z-axis coincides with the rotation axis. While the total elevating mass (and thus the rotor) tends to rotate in the clockwise direction under the effect of gravity due to M_{unb} (assuming no torques applied by the actuators and the elevation rate is constant), the cam profile pushes the roller downwards (since the cam and the rotor are fixed together). This, in turn, tends to rotate the connecting rod and to twist the torsion bar in the counter clockwise direction. Any twisting action (angular deflection) on the torsion bar in the counter clockwise direction generates contact forces between the roller and cam profile. These contact forces tend to rotate the rotor in the counter clockwise direction and hence acts to balance the system.

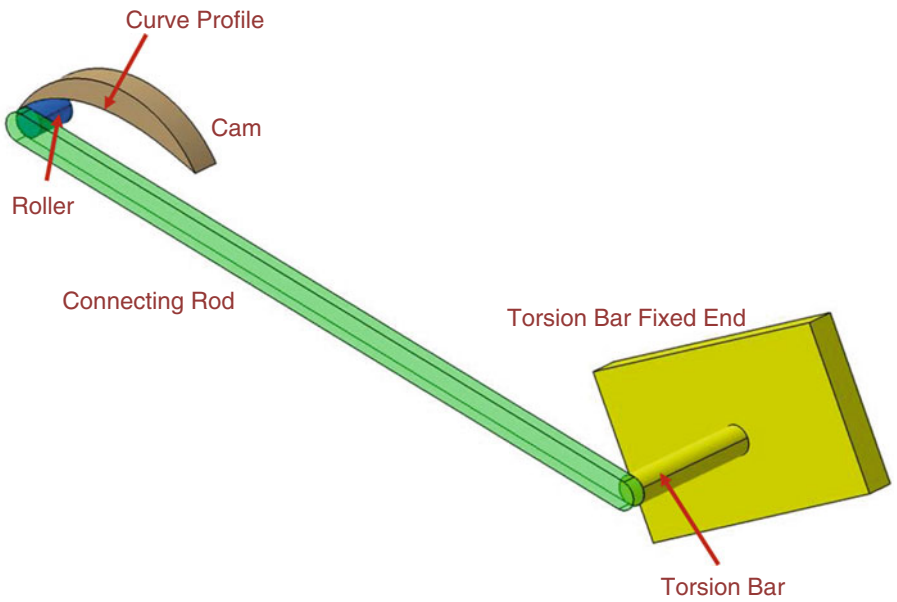

Fig. 40.3 Components of the torsion bar system

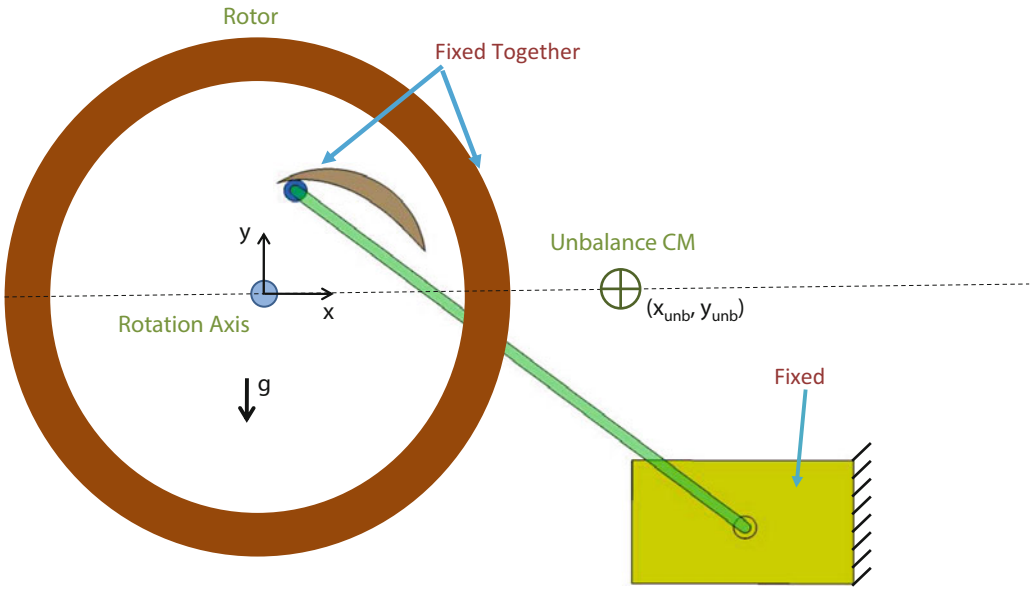

Fig. 40.4 Overall simplified configuration of the system

40.2.2 Mechanical Behavior of the Torsion Bar

A torsion bar can be assumed to have a circular cross section with diameter d and to be under the effect of pure torque. Then, the angle of twist θ_t and maximum torsional shear stress τ_{max} for a solid round bar is given by [1]

$$\theta_t = \frac{TL}{GJ} \tag{40.2}$$

$$\tau_{\max} = \frac{Td}{2J} \tag{40.3}$$

where T is the torque applied to the bar, L is the length of the bar, G is the modulus of rigidity and J is the polar moment of inertia which is

$$J = \frac{\pi d^4}{32} \tag{40.4}$$

for a solid round bar. Then, the torsional spring constant k becomes

$$k = \frac{\pi d^4 G}{32L} \tag{40.5}$$

Although it is true that no spring is linear in reality, the equations above are commonly used for practical modeling purposes and the assumptions which makes them valid can be found in [1].

According to the von Mises's stress theory, under the pure shear stress conditions due to torsion, yielding starts when the following is met [2]

$$\tau_{\max} = \frac{1}{\sqrt{3}} S_y \tag{40.6}$$

where S_y is the yield strength of the bar material. Using Eqs. (40.2), (40.3) and (40.6), and we find and define

$$\theta_{tall} = \frac{2LS_y}{\sqrt{3}dG} \tag{40.7}$$

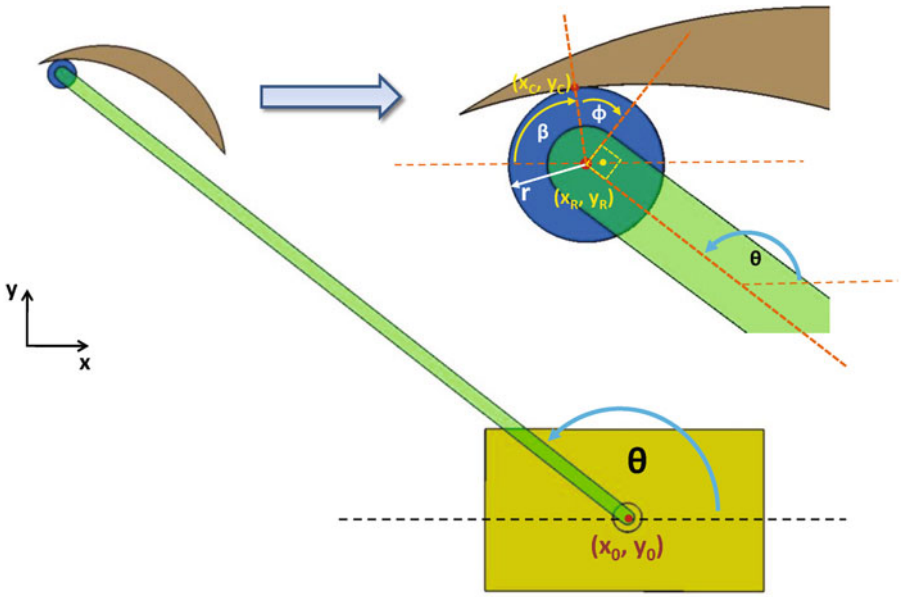

Fig. 40.5 Position and orientation variables for the system

$$f_s = \frac{\theta_{tall}}{\theta_{t_{\max}}} = \frac{2\pi d^3 S_y}{16\sqrt{3} T_{\max}} \tag{40.8}$$

where θ_{tall} is the maximum allowable twist angle for the torsion bar in order not to yield, T_{max} is the maximum amount of torque on the bar, $\theta_{t_{max}}$ is the twist angle of the bar when T_{max} is applied and f_s is the safety factor of the design.

40.2.3 System Variables

Measuring from the coordinate frame explained earlier and referring to Fig. 40.5, the variables defining the position and the orientation of the system are as follows; $\mathbf{x_0}$ and $\mathbf{y_0}$ are the coordinates of the fixed end of the connecting rod where it is connected to the torsion bar i.e., where common axis of rotation of the torsion bar and the connecting rod passes, $\mathbf{x_c}$ and $\mathbf{y_c}$ are the coordinates of the point of contact between the roller and the cam, $\mathbf{x_R}$ and $\mathbf{y_R}$ are the coordinates of the roller center, **r** is the radius of the roller, **θ** is the angle of the connecting rod measured from positive x-axis, **β** is the angle of the common normal to the roller and the cam profile measured from the negative x-axis, φ is the pressure angle which is the angle between the common normal and the direction of the velocity vector of the roller.

The pressure angle φ is actually the tangent of the ratio of the components of the contact force acting on the follower (the roller) resolved along the normal to the roller velocity direction and along the roller velocity direction, respectively [3] and β is the direction of the contact force between the cam and roller. Also, since the connecting rod and the roller are rotating about the point (x_0,y_0), pressure angle is determined to be

$$\phi = 270^\circ - \beta - \theta \tag{40.9}$$

Elevation angle α shown in Fig. 40.1 is the independent variable of the system as all of the other variables are functions of it.

40.2.4 Balance Equations of the System

In order to derive the balance equations of the system, the overall system is analyzed in two free body diagrams. The free body diagram of the rotor-cam subsystem is given in Fig. 40.6 below.

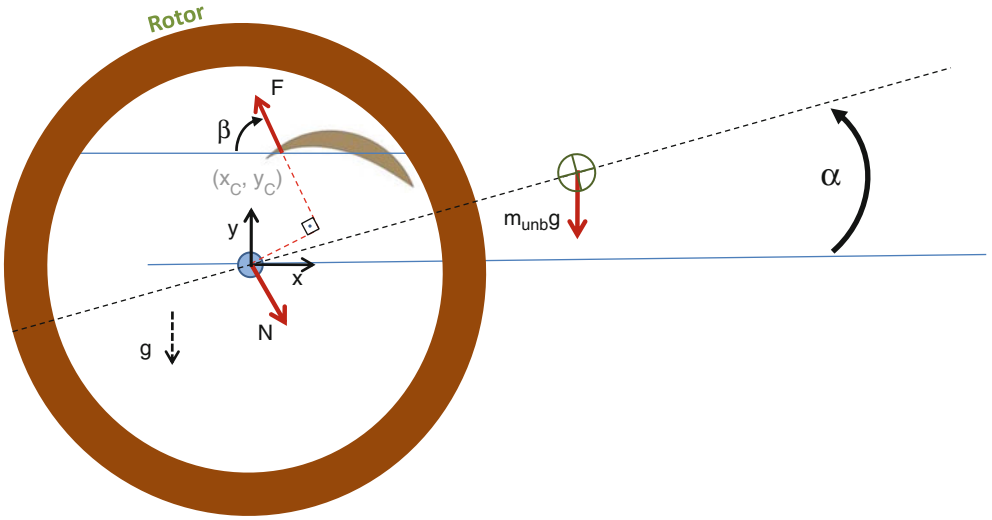

Fig. 40.6 Free body diagram of rotor-cam subsystem

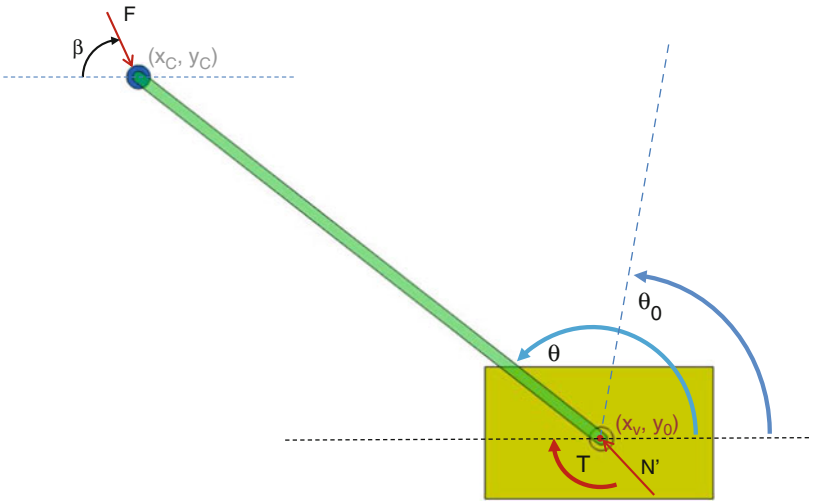

Fig. 40.7 Free body diagram of the roller-connecting rod-torsion bar subsystem

F is the contact force applied by the roller to the cam and N is the reaction force applied by the rotor bearings to the rotor. Hence, in order to have zero net moment along the z-direction

$$\sum M_z = F\left(x_c \sin(\beta) + y_c \cos(\beta)\right) - m_{unb} g x_{unb} \cos(\alpha) = 0 \tag{40.10}$$

must hold for all $\alpha \in [\alpha_{\min}, \alpha_{\max}]$, assuming y_{unb} is zero at $\alpha = 0$. The weight of the cam is assumed to be negligible compared to other forces. Also, the free body diagram of the roller-connecting rod-torsion bar subsystem is given Fig. 40.7 above. Equating the total moment about the point (x_0, y_0) gives

$$\sum M_{(x_0,y_0)} = F\left[(x_0 - x_c)\sin(\beta) + (y_0 - y_c)\cos(\beta)\right] - T = 0 \tag{40.11}$$

$$T = k\left(\theta - \theta_0\right) \tag{40.12}$$

where θ_0 is the initial orientation of the connecting rod where no torque is induced on the torsion bar and N' is the reaction force. Here, the weight of the connecting rod and the roller is assumed to be negligible. Also we have the following geometrical relations for the system

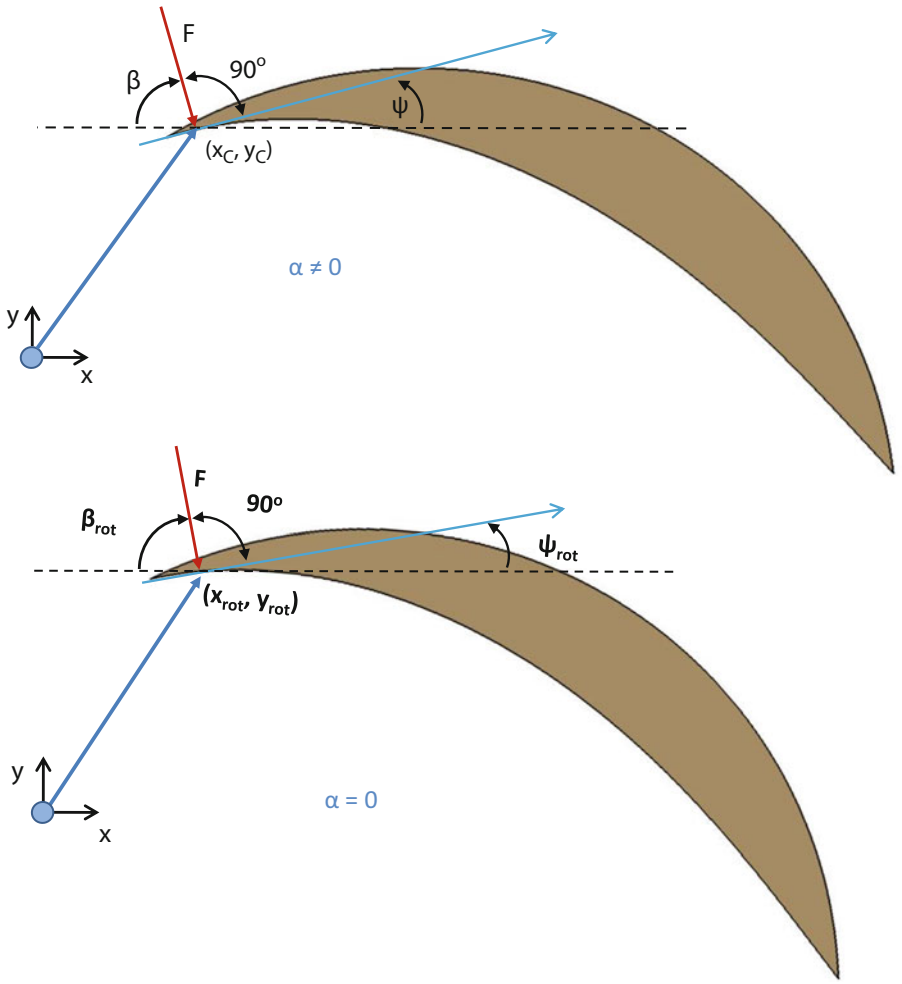

Fig. 40.8 Geometrical cam profile condition at $\alpha \neq 0$ and its mapping to $\alpha = 0$

$$\begin{aligned} x_c &= x_0 + L_{rod}\cos(\theta) - r\cos(\beta) \\ y_c &= y_0 + L_{rod}\sin(\theta) - r\sin(\beta) \\ L_{rod} &= \left[(x_R - x_0)^2 + (y_R - y_0)^2\right]^{1/2} \end{aligned} \tag{40.13}$$

40.2.5 Set of Equations Defining the Cam Profile Curve

The paramount question becomes how to generate the cam profile curve such that equations and hold for all $\alpha \in [\alpha_{\min}, \alpha_{\max}]$ i.e., the moment unbalance is nullified for all α. Recalling that (x_c, y_c) is the contact point when the elevation angle is α, cam profile geometry can be analyzed using the Fig. 40.8. The contact condition dictates that direction of the contact force F should always be perpendicular to the tangent line with orientation **ψ** (measured from the positive x-axis) at the contact point (x_c, y_c) of the candidate curve as shown in Fig. 40.8 for a generic elevation angle $\alpha \neq 0$. Thus we have

$$\beta + \psi = 90^\circ \tag{40.14}$$

Suppose that the top configuration ($\alpha \neq 0$) in Fig. 40.8 is the case where the system is elevated α degrees. If this configuration is rotated in the clockwise direction, intact, to the one where $\alpha = 0$, the bottom configuration in Fig. 40.8 is obtained. Then following relations are obtained

$$\begin{aligned} \psi &= \psi_{rot} + \alpha \\ \beta &= \beta_{rot} - \alpha \end{aligned} \tag{40.15}$$

Thus, the point (x_{rot}, y_{rot}) is the rotation of the contact point (x_c, y_c) about the origin by α degrees in the clockwise direction while ψ_{rot} and β_{rot} are the new values of ψ and β when the rotation is performed. Since the set of points (x_c, y_c) represent the contact points for a certain α, in order to determine the cam profile curve, the set of points (x_{rot}, y_{rot}) (which are their mapping to the initial configuration $\alpha = 0$) need to be determined. They are related to (x_c, y_c) by the following relation

$$\begin{bmatrix} x_{rot} \\ y_{rot} \end{bmatrix} = \begin{bmatrix} \cos(\alpha) & \sin(\alpha) \\ -\sin(\alpha) & \cos(\alpha) \end{bmatrix} \begin{bmatrix} x_c \\ y_c \end{bmatrix} \tag{40.16}$$

Moreover, using Eq. (40.15) and referring to Fig. 40.8 we have

$$\psi = \tan^{-1}\left(\frac{dy_{rot}}{dx_{rot}}\right) + \alpha \tag{40.17}$$

Also, using Eqs. (40.14) and (40.17) and it follows

$$\dot{y}_{rot} - \tan\left(90^\circ - \beta - \alpha\right)\dot{x}_{rot} = 0 \tag{40.18}$$

Moreover, differentiating Eq. (40.16) with respect α yields

$$\begin{bmatrix} \dot{x}_{rot} \\ \dot{y}_{rot} \end{bmatrix} = \begin{bmatrix} -\sin(\alpha) & \cos(\alpha) \\ -\cos(\alpha) & -\sin(\alpha) \end{bmatrix} \begin{bmatrix} x_c \\ y_c \end{bmatrix} + \begin{bmatrix} \cos(\alpha) & \sin(\alpha) \\ -\sin(\alpha) & \cos(\alpha) \end{bmatrix} \begin{bmatrix} \dot{x}_c \\ \dot{y}_c \end{bmatrix} \tag{40.19}$$

where

$$\begin{bmatrix} \dot{x}_{rot} \\ \dot{y}_{rot} \end{bmatrix} = \begin{bmatrix} \frac{dx_{rot}}{d\alpha} \\ \frac{dy_{rot}}{d\alpha} \end{bmatrix} \text{ and } \begin{bmatrix} \dot{x}_c \\ \dot{y}_c \end{bmatrix} = \begin{bmatrix} \frac{dx_c}{d\alpha} \\ \frac{dy_c}{d\alpha} \end{bmatrix} \tag{40.20}$$

Using Eqs. (40.18)–(40.19) and, it follows

$$[-\cos(\alpha)\,x_c - \sin(\alpha)\,y_c - \sin(\alpha)\,\dot{x}_c + \cos(\alpha)\,\dot{y}_c] - \tan\left(90^\circ - \beta - \alpha\right)[-\sin(\alpha)\,x_c + \cos(\alpha)\,y_c + \cos(\alpha)\,\dot{x}_c + \sin(\alpha)\,\dot{y}_c] = 0 \tag{40.21}$$

40.2.6 Overall System Equations

Combining the balance equations and the cam profile curve equations, the following set of nonlinear differential equations are obtained

$$\begin{aligned} &F\,(x_c \sin(\beta) + y_c \cos(\beta)) - m_{unb} g x_{unb} \cos(\alpha) = 0 \\ &F\,[(x_0 - x_c)\sin(\beta) + (y_0 - y_c)\cos(\beta)] - k\,(\theta - \theta_0) = 0 \\ &[-\cos(\alpha)\,x_c - \sin(\alpha)\,y_c - \sin(\alpha)\,\dot{x}_c + \cos(\alpha)\,\dot{y}_c] - \tan(90^\circ - \beta - \alpha)\,[-\sin(\alpha)\,x_c + \cos(\alpha)\,y_c + \cos(\alpha)\,\dot{x}_c + \sin(\alpha)\,\dot{y}_c] = 0 \\ &x_{rot} - [\cos(\alpha)\,x_c + \sin(\alpha)\,y_c] = 0 \\ &y_{rot} - [\sin(\alpha)\,x_c + \cos(\alpha)\,y_c] = 0 \\ &x_c - [x_0 + L_{rod}\cos(\theta) - r\cos(\beta)] = 0 \\ &y_c - [y_0 + L_{rod}\sin(\theta) - r\sin(\beta)] = 0 \\ &\text{with initial conditions} \\ &[F(0) \quad \beta(0) \quad \theta(0) \quad x_c(0) \quad y_c(0) \quad x_{rot}(0) \quad y_{rot}(0)] \end{aligned} \tag{40.22}$$

In the set of Eqs. (40.22), seven nonlinear equations have seven unknowns (system variables) **[F(α), β(α), θ(α), $\mathbf{x_c}$(α), $\mathbf{y_c}$(α), $\mathbf{x_{rot}}$(α), $\mathbf{y_{rot}}$(α)]**, where all of them are functions of the independent variable $\alpha \in [\alpha_{\min}, \alpha_{\max}]$ with $[\alpha_{\min}, \alpha_{\max}] = [-8°, 48°]$ for our study case. Observing the set of equations given by Eq. (40.22), cam profile generation problem largely deviates from classical cam profile problems generally discussed in [4] and [5], due to the conditions imposed by the balance equations. Set of variables [x_0, y_0, k] are selected to be three of the design parameters. In order to solve the Eq. (40.22) set, initial conditions **[F(0), β(0), θ(0), $\mathbf{x_c}$(0), $\mathbf{y_c}$(0), $\mathbf{x_{rot}}$(0), $\mathbf{y_{rot}}$(0)]** needs to be determined. Let us define **[β(0), $\mathbf{x_c}$(0), $\mathbf{y_c}$(0)]** also to be design parameters, since they define the first contact point and the initial slope of the cam profile. Since L_{rod} is a function of β(0), x_c(0), y_c(0), x_0, y_0, then **θ(0)** is determined from the 6th and 7th equations of the Eq. (40.22) set. Then, **$\mathbf{x_{rot}}$(0), $\mathbf{y_{rot}}$(0)** are determined from the 4th and 5th equations of the Eq. (40.22) set, while **F(0)** and θ_0 are determined from the 1st and 2nd equations of the equation set. Thus, it turns out that the set of parameters **[$\mathbf{x_0}$, $\mathbf{y_0}$, $\mathbf{x_c}$(0), $\mathbf{y_c}$(0), k, β(0)]** are defined to be the design parameters of the system. Determination of the design parameters completely defines the set of initial conditions.

40.3 Solution and Optimization of the System Variables

Thus, equation can be solved for a given region of α if the solution exists. However, due to some structural and design concerns, the solutions must satisfy some constraints. Specifically, the initial conditions must lie within certain regions. At the same time, some of the parameters of the system must have small or large values. All of these lead to a multi objective constrained optimization problem with a search space $[x_0 \quad y_0 \quad x_c(0) \quad y_c(0) \quad k \quad \beta(0)] = S \in \mathbb{R}^6$

40.3.1 Constraints and Objective Function of the Optimization Problem

As any other working system, this one also must satisfy some constraints in order to serve the design purpose. Specifically for our application, the set of constraints can be summarized in Eq. (40.23). The 1st, 2nd, and 3rd constraints come from structural installation requirements, the 4th constraint limits the boundaries of the cam profile, the 5th constraint puts a lower limit for the minimum radius of curvature and the 6th constraint puts a lower limit on the static factor of safety. 7th constraint limits the maximum value of the pressure angle since a lower φ means a better transmission of force into action (higher transmission angle). Finally, 8th constraint limits the length of the torsion bar.

Objective function of the optimization problem should be to overcome the moment unbalance M_{unb} in an efficient and effective manner. Quantitatively, this means maximum amount of torque applied on the torsion bar T_{max} should be minimum. Furthermore, the maximum amount of contact force between the roller and cam F_{max} should be minimum structural purposes.

$$
\begin{aligned}
&1)\ L_{rod} \le L_{rod_{\max}} \\
&2)\ x_0 \in [x_{0_{\min}}, x_{0_{\max}}] \ \text{ and } y_0 \in [y_{0_{\min}}, y_{0_{\max}}] \\
&3)\ x_c \in [x_{c_{\min}}, x_{c_{\max}}] \ \text{ and } y_c \in [y_{c_{\min}}, y_{c_{\max}}] \\
&4)\ \sqrt{(x_{rot_{\max}} - x_{rot_{\min}})^2 + (y_{rot_{\max}} - y_{rot_{\min}})^2} \le c \\
&5)\ \min\left(\left| \frac{\left(1+\left(\frac{dy_{rot}}{dx_{rot}}\right)^2\right)^{3/2}}{\frac{d^2 y_{rot}}{dx_{rot}^2}} \right| \right) / r > w \\
&6)\ f_s \ge f_{s_{\min}} \\
&7)\ \phi \le \phi_{\max} \\
&8)\ L \le L_{\max}
\end{aligned}
\tag{40.23}
$$

Combining all of these requirements yields

$$\begin{aligned} \text{minimize } & \langle J(\alpha) = a_1 T_{\max}(\alpha) + a_2 F_{\max}(\alpha) \quad \alpha \in [\alpha_{\min}, \alpha_{\min}] \rangle \\ & \text{subject to} \\ & \langle \text{constraints given by (40.23)} \rangle \end{aligned} \tag{40.24}$$

where a_1, a_2 are weights of the objective function J(α). Selection of the constraints given by and determination of the objective function J(α) with its weights lie in the core of both the problem and its solution and drastically affects the outcomes. Statement of the optimization problem has similarities with the one in [6], except for that, we have two objectives embedded into the problem instead of a single one. The optimization problem is a complex problem due to nonlinearity of equations and the constraints and the considerable breath of the search space S.

40.4 Optimal Solution and Results

Solution of the problem stated by Eqs. (40.22) and (40.24) produces the optimal point $[x_0^*, y_0^*, x_c^*(0), y_c^*(0), k^*, \beta^*(0)]$ which in turn generates the complete solution $[F^*(\alpha), \beta^*(\alpha), \theta^*(\alpha), x_c^*(\alpha), y_c^*(\alpha), x_{rot}^*(\alpha), y_{rot}^*(\alpha)]$, of which the set $[x_{rot}^*(\alpha), y_{rot}^*(\alpha)]$ represents the coordinates of the optimal cam profile curve. Implementation and the solution of the optimization problem is performed by using MATLAB built-in hybrid optimization which applies Simulated Annealing method with a combination of fmincon (minimization of constrained nonlinear multivariable functions).

40.4.1 System Parameters for a Specific Case

In our study case, the system $m_{unb} = 620$ kg, with $x_{unb} = 1.25$ m and $y_{unb} = 0$. Determination of the limits on the search space, $[x_0 \quad y_0 \quad k \quad \beta(0) \quad x_c(0) \quad y_c(0)] = S \in \mathbb{R}^6$ is done by interpretation of some geometric limitations, equations, and the constraints given by, whenever possible. Limits of the search space are given in Table 40.1 below.

Also, the values $a_1 = 1$ and $a_2 = 0.35$ are selected for the objective function. The roller radius is selected to be r = 23 mm. The material properties of the torsion bar are assumed to be G = 79,300 MPa, $S_y = 1{,}350$ MPa. The values used for the set of inequality constraints are given in Table 40.2 below.

40.4.2 Optimal Solution for the Given System

Optimization process produced the optimal design point $[x_0^*, y_0^*, x_c^*(0), y_c^*(0), k^*, \beta^*(0)] = [322.75, -226.5, 100.51, 7.20, 5{,}955.82, 115.80]$. The cam profile and the overall system configuration for this optimal point is schematically given in Fig. 40.9 below. The blue curve represents the cam profile and the line represents the connecting rod for the optimal solution at elevation angle of $\alpha = 0°$. The red disk represents the roller. The blue curve and the line represent the system when $\alpha = 48°$ while the green curve and the line represent the system when $\alpha = -8°$.

The contact force F between the cam and the roller versus the elevation angle α for the optimal solution is shown in Fig. 40.10 below. Torque applied on the torsion bar T versus elevation angle is shown in Fig. 40.11. Angles associated with the cam profile and the connecting rod versus the elevation angle is shown in Fig. 40.12. Some of the important results concerning the torsion bar and the overall configuration are summarized in Table 40.3 below.

Observing Table 40.3, it can be seen that the obtained results are satisfying the constraints. In Table 40.3, selection of f_s yielded the torsion bar length L and diameter d. Selection has been made such that it is above the lower limit specified in the 6th inequality of Eq. (40.23) and L satisfies the 8th inequality of Eq. (40.23). Also ρ_{min} stands for the minimum radius of

Table 40.1 Limits of the search space for optimization

	x_0(mm)	y_0(mm)	$x_c(0)$(mm)	$y_c(0)$(mm)	k(Nm/rad)	β(0)(Deg)
Range	[240, 440]	[−180, −380]	[−20, 280]	[−120, 120]	[2,500, 15,000]	[100, 170]

Table 40.2 Values used for the inequality constraints

	c (mm)	w	f_{smin}	φ_{max} (Deg)	L_{max} (mm)	L_{rodmax} (mm)
Value	200	4	1.5	55	1,200	350

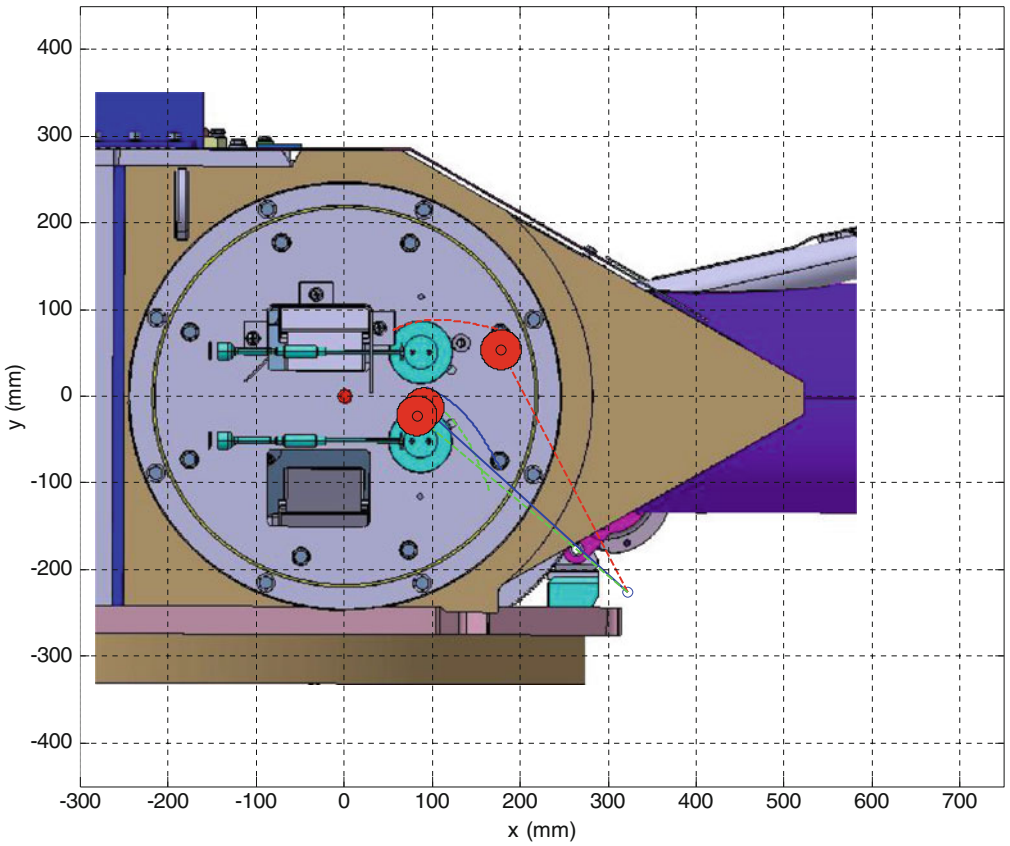

Fig. 40.9 Cam profile and the overall system configuration for the optimal solution at elevation angles of $\alpha = 00$ (*Blue*), $\alpha = -80$ (*Green*) and $\alpha = 480$ (*Red*). *Red disk* represents the roller

curvature of the cam profile curve which is constrained by the 5th inequality of Eq. (40.23). Furthermore, the cam boundary is specified by the 4th inequality of Eq. (40.23).

40.5 Conclusion

In this paper, in order to generate a cam profile for any given moment unbalance such that the residual moment unbalance is nullified at all elevation angles, the set of nonlinear equations, including the balance equations and the cam geometry equations, are derived. In order to solve these set of equations, six meaningful design parameters are selected such that determination of these leads to the determination of the initial conditions of the set of nonlinear equations. Afterwards, a search space related with the selected design variables a are defined. Furthermore, set of inequality constraints related with the overall structural geometry and cam profile geometry is defined. Finally, defining a meaningful objective function for the system led to a multi objective constrained optimization problem which complex by its nature. Using the commonly available optimization methods, optimal solution(s) has been found and the weights of the objective function and the values of the constraints are determined by several trail and errors by running the developed codes several times. This was due to the fact that, no straight forward method exists for determination of these values for a general multi objective constrained optimization problem. The assumption made in the derivation of the equations is the cam, the connecting rod and roller weights are negligible compared with the contact forces and the torsion bar torque. Although, the obtained results confirm these assumptions, inclusion of these weights into the set of equations can be easily made by assuming the weights and centers of masses of the mentioned elements. When these inclusions are made, it has been observed that solution of the resulting equations yielded minor deviations in the cam profile curve, as expected, when the rest of the parameters are kept unchanged. One of the important observations made is that, If the distance between the pivot point (x_0, y_0) and the initial contact point $(x_c(0), y_c(0))$ is decreased the torque applied by torsion bar T becomes more advantageous in terms of its

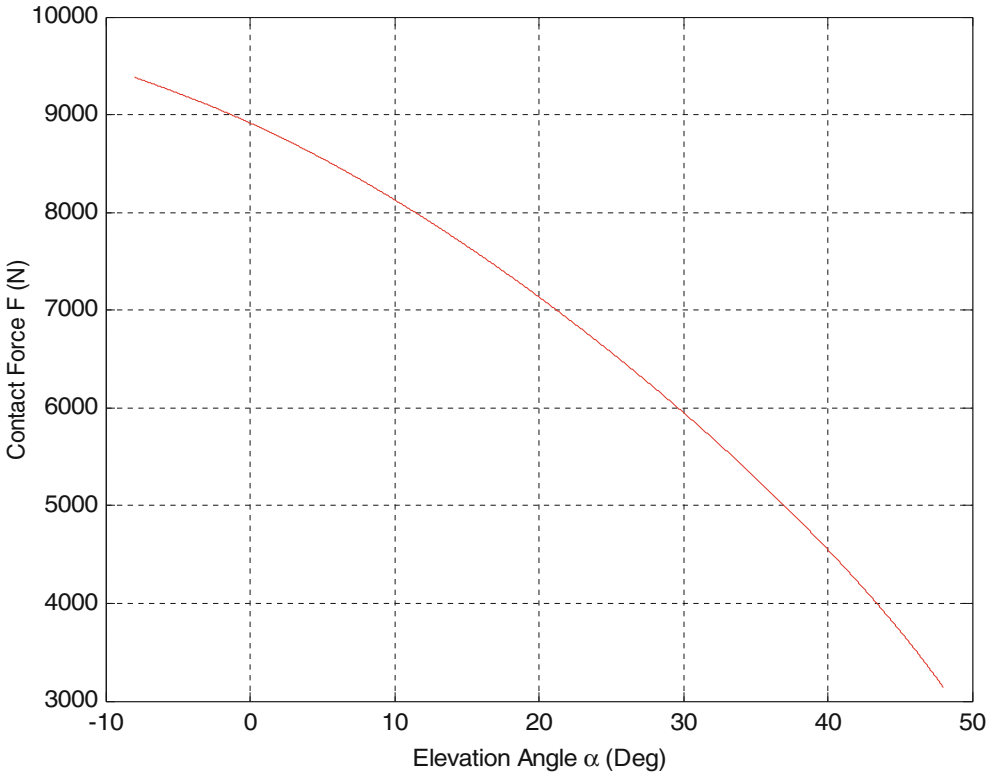

Fig. 40.10 Contact force F between the cam and the roller for the optimal solution versus elevation angle α

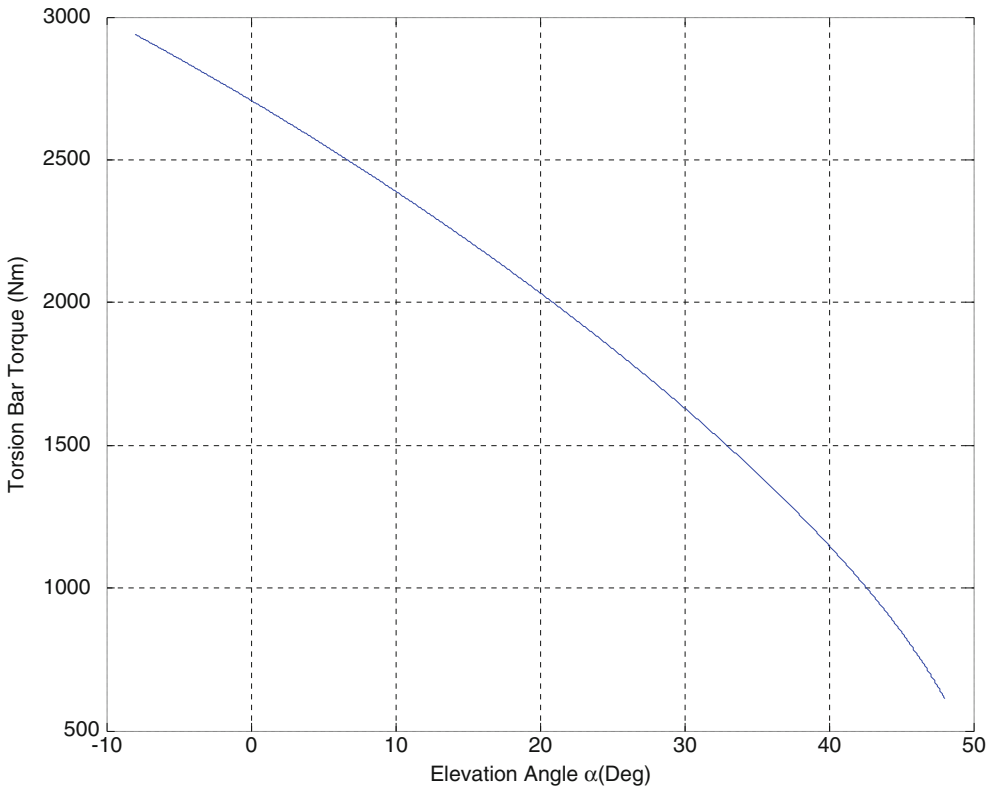

Fig. 40.11 Torque applied on the torsion bar T for the optimal solution versus elevation angle α

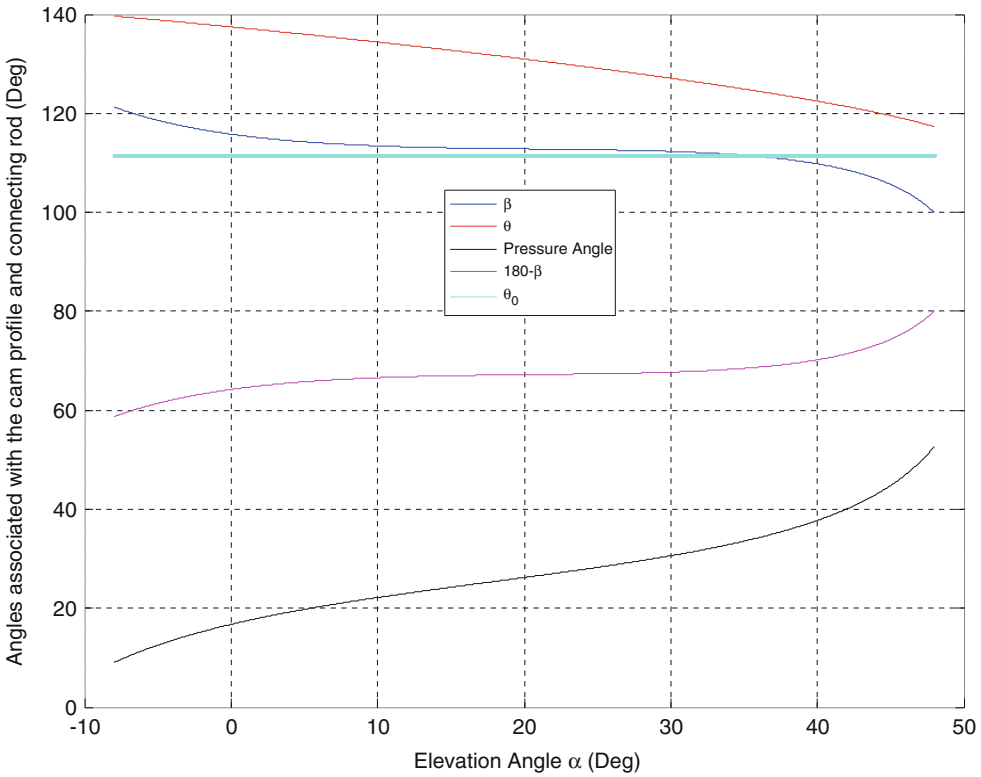

Fig. 40.12 Angles associated with the cam profile and the connecting rod versus elevation angle α

Table 40.3 Obtained results for system and the torsion bar for the optimal solution

Torsion bar		Overall system	
d (mm)	30.85	$\mathbf{F_{max}(N)}$	9, 384.9000
L (mm)	1, 184.00	$\mathbf{\varphi_{max}(N)}$	52.67
k (Nm/rad)	5, 955.82	$\mathbf{x_R(mm)\ @\ \alpha = 0^0}$	90.50
$\mathbf{T_{max}(Nm)}$	2, 939.80	$\mathbf{y_R(mm)\ @\ \alpha = 0^0}$	−13.50
$\mathbf{T_{min}(Nm)}$	613.74	$\mathbf{\rho_{min}(mm)}$	103.55
$\mathbf{\theta_{tmax}(Deg)}$	28.28	$\mathbf{L_{rod}(mm)}$	315.13
$\mathbf{\theta_{tall}(Deg)}$	43.20	$\mathbf{\theta_0(Deg)}$	111.4082
$\mathbf{f_s}$	1.5275	**Cam Boundary (mm)**	197.43

ability to overcome the moment generated by the reaction force F. However, since the pivot point (x_0, y_0) is getting closer to the contact point $(x_c(0), y_c(0))$, θ_{tmax} has to increase in order to span the same amount of elevation angle which leads an increase in T_{max}. Also, an increase in $x_c(0)$, results in lower contact force F which tends to decrease the amount of torque T applied by the torsion bar. However, an increase in $x_c(0)$ results in a longer cam profile curve length since we are getting away from the rotation center and still need to span the same amount of elevation angle. This increased total curve length, in turn, necessitates a larger θ_{tmax} which means a larger T_{max}. These observations show the complex nature of the problem and an obvious need for an optimization. It should also be noted that, the set of values which defines the constraints and the weights in the objective function plays a crucial role in determination of the optimal solution and even in the existence of solutions.

References

1. Budynas R, Nisbett J (2006) Shigley's mechanical engineering design, 8th edn. McGraw-Hill, New York
2. Solecki R, Jay Conant R (2003) Advanced mechanics of materials. Oxford University Press, Oxford
3. Ambekar AG (2010) Mechanism and machine theory. Prentice-Hall, New Delhi
4. Chen FY (1982) Mechanics and design of cam mechanisms. Pergamon Press, New York
5. US Army Materiel Command (1970) Engineering design handbook equilibrators. US Army Materiel Command, Washington, DC
6. Xiao H, Zu JW (2009) Cam profile optimization for a new cam drive. J Mech Sci Technol 23(10):2592–2602

Chapter 41
Dynamics Modeling and Accuracy Evaluation of a 6-DoF Hexaslide Robot

Enrico Fiore, Hermes Giberti, and Davide Ferrari

Abstract Parallel Robots are commonly preferred in place of Serial Robots for tasks in which the working volume is limited, compared to the overall extension of the machine, but where the accuracy requirements are very high. In fact, since the errors do not sum together in series, the positive effect of the closed-loop linkages arrangement is a lower overall sensitivity of the end-effector positioning to the various sources of error. The precision depends on many factors among which the flexibility of the components plays a fundamental role. This paper investigates the contribution of belt-driven and screw-ball-driven linear transmission systems to the overall flexibility of the HexaSlide parallel architecture, using an ADAMS®model. The six Degrees-of-Freedom (DoF) of its mobile platform are provided through the actuation of the same number of Linear Transmission Units (LTUs), fixed to the base, while its links have fixed length. The LTUs are integrated together in the robot. The first eigenfrequencies are mapped in a systematic manner over the whole workspace, using a discretized grid of poses.

Keywords Parallel kinematic machines • Robot • Belt-drive • Linear transmission • Nonlinear system

41.1 Introduction

In order to have a better understanding of which is the behaviour of floating offshore wind turbines and sailing boats in their operating conditions unsteady aerodynamic experiments are performed inside wind tunnels [1]. For this reason it's useful to equip the civil-environmental section of the Politecnico di Milano wind tunnel with a 6-DoF manipulator to perform hardware-in-the-loop simulations. In addition to this kind of simulations there also exist tank testings and full scale simulations. These three types of simulation are complementary and fundamental to validate through experimental datas numerical codes found in CFD softwares. The reason why these experiments are so important is that by recreating as realistically as possible their working conditions it is possible to have a better exploitation of wind energy for what concerns wind turbines, and a better knowledge of the phenomena involved in the maneuver stages of sailing boats. During these simulations it's important to take into account not only the interaction between air and structure but also the hydrodynamic contribution given by the sea water, which will be reproduced by the robot solving in real-time a mathematical model of the waves' motion. To this end a 6-DoF parallel kinematic architecture called Hexaslide has been chosen and optimized by means of a genetic algorithm [2], and the method applied for the optimization has been described in [3]. During the optimization the isotropy of the robot has been taken into account following the theory presented in [4, 5]. The Hexaslide architecture is made up of six links of fixed length connecting a mobile platform to six different rails. In this way six independent PUS type kinematic chains can be identified. While having a smaller working volume with respect to serial robots, in general parallel kinematic manipulators ensure high dynamic performances and precisions in addition to a higher stiffness and a great load capability. Furthermore the actuating system of the Hexaslide is entirely placed on the ground resulting in a lower overall moving mass of the manipulator. Since the robot can't be placed outside of the wind tunnel test section, the TCP position should be as low as possible in the vertical direction in such a way to maximize the test section space exploitable to move the scale model. Indeed the zone near the ceiling is characterized by a turbulent flow and it's important that the scale models, in particular the tip of the turbine blades, stay outside of this zone. The peculiar layout of the Hexaslide's links allows to reduce the vertical size of the manipulator and in addition it prevents the risk of self-collision between the machine's elements. After the optimization the drive system has been sized in a similar way to the one presented in [6] using a mechatronic approach which has been described in [7–9]. The forces and moments exchanged between the scale models and the platform will be measured through a 6-axis balance. So it's important to determine if the vibrations recorded by the balance are the result of

E. Fiore • H. Giberti (✉) • D. Ferrari
Mechanical Engineering Department, Politecnico di Milano, Via La Masa 1, 20156 Milano, Italy
e-mail: hermes.giberti@polimi.it

G. Kerschen (ed.), *Nonlinear Dynamics, Volume 1*, Conference Proceedings of the Society for Experimental Mechanics Series, DOI 10.1007/978-3-319-15221-9_41

the robot approaching a resonance condition or if they are just caused by the scale model. Therefore a flexible multibody model of the robot has been set up with the aim of mapping its first eigenfrequency all over the working space, considering three scenarios: ideal linear transmission unit; flexible belt driven transmission unit; flexible ballscrew transmission unit.

The following sections are organized as follow: Sect. 41.2 describes the inverse kinematics of the Hexaslide; Sect. 41.3 introduces the multibody model describing: (1) links modeling as flexible bodies by means of beam elements (2) belt flexibility, as a function of the position of the slider along its rail, (3) screw flexibility and screw nut coupling modeling. The numeric results are given in Sect. 41.4.

41.2 Hexaslide Kinematics

Given the TCP position and the mobile platform orientation, $\Theta = \{\alpha, \beta, \gamma\}$, it is possible to find each slider position, q_i, by performing the inverse kinematics analysis. With reference to Fig. 41.1, for the ith kinematic chain it is possible to write:

$$\mathbf{l}_i = \mathbf{d}_i + q_i \hat{\mathbf{u}}_i \qquad \text{with} \qquad \mathbf{d}_i = \mathbf{p} + [R]\mathbf{b}'_i - \mathbf{s}_i \tag{41.1}$$

The [R] matrix is the rotational matrix used to switch from the mobile frame to the fixed one, and it is function of the platform orientation Θ. After some simple mathematical passages you get:

$$q_i = \mathbf{d}_i^T \hat{\mathbf{u}}_i \pm \sqrt{\mathbf{d}_i^T (\hat{\mathbf{u}}_i \hat{\mathbf{u}}_i^T - [I])\mathbf{d}_i + l_i^2} \tag{41.2}$$

Once solved the inverse kinematics it is possible to find the relationship between the slider velocity and the velocity of the TCP. It can be shown that for the ith kinematic chain the following expression holds:

$$\hat{\mathbf{n}}_i^T \hat{\mathbf{u}}_i \dot{q}_i - [\hat{\mathbf{n}}_i^T (\mathbf{b}_i \times \hat{\mathbf{n}}_i)^T]\mathbf{W} = 0 \tag{41.3}$$

where $\mathbf{W} = [\dot{x}, \dot{y}, \dot{z}, \omega_x, \omega_y, \omega_z]^T$ is a vector containing both the translational and angular components of TCP velocity. Considering all the six links the previous relationship can be expressed through the Jacobian matrix $[J]$ as:

$$\mathbf{W} = [J]\dot{\mathbf{q}} \tag{41.4}$$

The Jacobian matrix represents the relationship intercurring between the sliders velocity and the TCP velocity. Under the hypothesis of small displacements it is possible to use the Jacobian matrix to relate the small variations of the sliders position to the variation of the robot pose as follows:

$$\Delta\mathbf{X} = [J]\Delta\mathbf{q} \tag{41.5}$$

This relationship allows to compute the TCP positioning error due to the linear units accuracy.

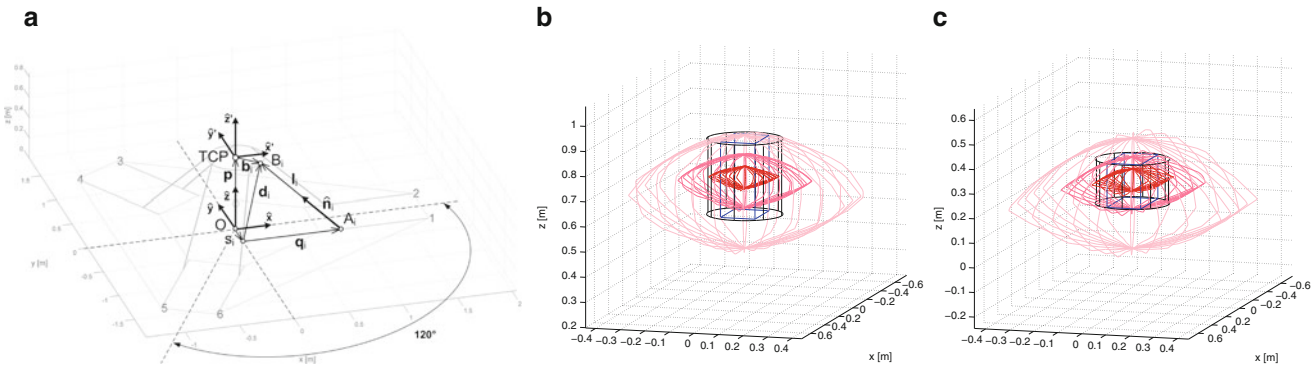

Fig. 41.1 Hexaslide kinematics and working spaces. (**a**) View details of Hexaslide robot. (**b**) Desired working space vs. robot working space, boat. (**c**) Desired working space vs. robot working space, turbine

41.3 Multibody Model

In order to investigate its behaviour all over the working space, a flexible multibody model of the robot has been set up in ADAMS®. Reference markers have been used both for the modeling and the analysis phases. A marker is a reference system characterized by an origin, whose location is expressed with respect to another marker, and by its axes orientation. In particular the most important markers are the *Origin* and the *TCP*, which represent respectively the fixed and the mobile frame. All the other markers used for the creation of bodies, constraints, and forces, have been parametrized in such a way that by changing the TCP coordinates all the elements that constitute the manipulator would rearrange themselves in the new configuration. It is reasonable to assume that the first eigenmodes of the manipulator involve the links' bending stiffness due to their particular shape. During the modeling phase the platform has been considered as a rigid cylinder. As a matter of fact the idea is to have a real platform which consists of a set of aluminum plates with appropriate ribs designed to prevent the plates' bending, in such a way to have a final structure which is at the same time stiff and light. As regards inertia, a mass of 50 kg has been considered for the platform, with an additional contribution of 1,164 kg given by the 6-axes balance. All the analyses have been made imposing null conditions of velocity and acceleration for both the sliders and the platform. For each pose ADAMS®finds an equilibrium condition and linearizes the system around this configuration. At this point the first eigenvalues are computed and stored in a *.txt* file.

41.3.1 Links Modeling

Since the links are long and slender, they have been modeled as discrete beam elements. This kind of elements is made of a set of segments, which essentially are rigid bodies, connected by means of a force field used to simulate the bending, axial and torsional stiffness of a beam. Each segment has been treated as a steel hollow cylinder. In ADAMS®discrete beam elements can be automatically created using the *viewflex* tool. By the way this kind of tool prevents the parametrization of the markers needed to create the segments and the force fields. In order to connect two adjacent segments through a force field, two marker are crated, the first one belonging to the jth segment and the second belonging to the $(j+1)$th one. Indeed the *element_like beam* force field requires two markers between which to be applied. It's important that the two markers called respectively CG_j and CG_{j+1}, have the x-axis lying on the same line, while their y and z axes must be parallel. For what concerns the second moments of area, they have been calculated as follows:

$$I_{yy} = I_{zz} = \frac{\pi(R^4 - r^4)}{4} \qquad I_{xx} = \frac{\pi(R^4 - r^4)}{2} \tag{41.6}$$

assuming the x axis as the beam axis.

41.3.2 Belt Modeling

Belt driven transmission units (BDTU) are made of a polyurethane band wrapped around two pulleys, one of which is the driver. The sliders are attached to this band through their carrier, which has the function of discharging the moments and the force components perpendicular to the rail axis on the ground. Since the band is thin and not so massive, its inertial contribution has been neglected, as well as the inertial contribution of the pulleys because during the analyses the motor is supposed to be blocked. After these considerations the BDTUs were modeled as elastic forces with variable stiffness. For the ith BDTU two markers have been defined (P_i and Q_i) positioned along the rail axis at a distance of ± 0.6 m from the position assumed by the slider when the TCP's coordinates are $\mathbf{p} = (0,\ 0,\ 0.7)^T$ with null orientation. Then two forces were defined, the first between the slider center of mass and the P_i marker, and the latter between the slider and the Q_i marker. These forces were defined as follows:

$$F_i = c_{spec}\frac{l_i - l_0(q_i)}{l_0(q_i)} = k_{eq}(q_i)(l_i - l_0(q_i)) \tag{41.7}$$

where l_0 represents the length of the portion of band between the slider and one of the two marker P_i and Q_i before the beginning of the analysis, while l_i is the real distance between the two markers after small displacements. The c_{spec} constant

is the product between an equivalent Young's modulus, which takes into account the various materials present in the band, and an equivalent section area that changes due to the presence of belt teeth. l_0 has been defined as a design variable which is updated before each analysis. In the *machinery* toolbox of ADAMS®is available a wizard that allows to simulate a flexible belt as a set of rawplugs connected by force fields. The reason why this approach has been discarded is that for each belt about a hundred rawplugs and force fields are needed; each rawplug substantially is a rigid body, and a so huge number of bodies requires an enormous calculation time and memory.

41.3.3 Screw Modeling

For the ball-screw transmission unit (BSTU) modeling a 1.2 m long steel beam has been considered. Unlike for what has been done for the BDTU, in the BSTU's case the inertia of the screw can't be neglected as it consists of a massive solid cylinder rotating at high speed around its axis. Similarly to what have been done for the links modeling, the screw has been treated as a discrete flexible element. One of the ends of the screw has been constrained through a cylindrical joint, leaving the rotation around the screw axis free, while the one connected to the motor has been fixed to the ground since, as told before, during the analyses the motor is supposed to be blocked. In order to define the constraints two markers have been defined: P_i for the fixed end and Q_i for the other one. The reason why such a simplified model has been considered is that the purpose of this work is to have an idea of how the system first eigenfrequencies change allover the working space and not to describe in a detailed way the contact phenomena involved in the screw-nut coupling.

41.3.3.1 Screw-Nut Coupling Modeling

Simulating the screw-nut coupling is difficult since one of the two bodies between which the constraint is applied changes as the robot pose varies. In other words, depending on where the slider is, the screw segment to which the constraint is applied changes. In order to bypass this problem, a fictive body has been introduced with the following characteristics: this body has been modeled as solid cylinder; its center of mass is coincident with that of the slider; its revolution axis coincides with the feed axis of the slider. A screw type constraint has been applied between this body and the slider, in such a way that a displacement Δq of the slider involves a rotation $\Delta\theta$ of the fictive body around its axis according to the following relationship:

$$\Delta\theta = \frac{2\pi}{p_h}\Delta q \tag{41.8}$$

where p_h is the pitch propeller. The next step is to add a constraint between the fictive body and the screw segment so that a rotation of the first involves an identical rotation of the latter. Whereby a *general constraint* has been used. In ADAMS®geometrical constraints are considered as a set of equations of the type:

$$\mathbf{\Phi}_k(\mathbf{q}) = 0 \qquad \text{with} \qquad k = 1, \ldots, n_c \tag{41.9}$$

where n_c represents the number of constraints. For example a spherical joint can be treated as the following set of equations:

$$\begin{cases} x_{marker_1} - x_{marker_2} = 0 \\ y_{marker_1} - y_{marker_2} = 0 \\ z_{marker_1} - z_{marker_2} = 0 \end{cases} \tag{41.10}$$

Similarly a *general constraint* allows to define any geometrical constraint by writing a function that will be imposed equal to zero during all the analysis. The function used to define the *general constraint* is:

$$function = az(M_{fictivebody}, M_{j-segment}) \tag{41.11}$$

where the *az* function computes the angular displacement between two markers along their *z*-axis. The $M_{j-segment}$ marker has been parametrized in such a way that if the slider is in correspondence of the jth segment it is coincident with the fictive body's geometrical center, otherwise it is coincident with the jth segment's geometrical center. This result is achieved by using two *step* functions resulting in an auxiliary function defined as:

$$h(\xi) = \begin{cases} 1 & \text{if} \quad -\frac{L_{seg}}{2} \leq \xi \leq \frac{L_{seg}}{2} \\ 0 & \text{otherwise} \end{cases} \tag{41.12}$$

where ξ represents the relative distance between the $M_{fictivebody}$ marker and the jth segment's geometrical center. Since now only the method to create the constraint between the slider and a generic segment of the screw has been described. It's now necessary to find a way to choose which of the screw segments should appear in the *general constraint*. To this end a design variable has been created, defined as follows:

$$n = floor\left(\frac{q - q_0 + L_{screw}/2}{L_{screw}}\right) n_{segments} + 1 \tag{41.13}$$

where q_0 is the position assumed by the slider when it is in correspondence of the middle of the screw. Indeed the $M_{j-segment}$ marker will be the one corresponding to the nth segment. In the end a displacement of the slider involves a rotation of the fictive body that produces a rotation of the nth segment of the screw. It can be stated that the slider displacements are contrasted by an elastic force that is directly proportional to the torsional stiffness of the screw.

41.4 Numerical Results

The working space has been dissected using vertical planes. On each one of these planes the projection of the working space has been discretized, and the first eigenfrequencies of the manipulator have been mapped. To do so, for each point of the grid, all the values assumed by the first eigenfrequency changing the orientation of the TCP have been considered, and the minimum one has been chosen. The final result is a map of the minimum eigenfrequency of the robot regardless of its orientation.

In Fig. 41.2 the maps of the eigenfrequencies for the ideal transmission unit [(a) and (b)], the BDTU [(c) and (d)] and the BSTU [(e) and (f)] are shown.

As can be seen, by considering the flexibility of the transmission unit the system eigenfrequencies become lower. By the way, while considering the worst case represented by the BDTU the system, the system eigenfrequencies are still plenty higher than both the maximum frequencies at which the robot will be handled and the maximum frequencies of the aerodynamic phenomena, which are lower than 3 Hz. Whereby it's reasonable to assume that the robot vibrations don't affect the positioning errors of the TCP.

41.5 Conclusions

In this paper a vibration analysis of the Hexaslide manipulator has been done. This approach is complementary to the work presented in [10], where large sinusoidal motions have been imposed to the mobile platform. A flexible multibody model has been created in ADAMS®to compute the system eigenfrequencies all over the working space for three different cases, with or without the transmission units. To this end, the system has been linearized around an equilibrium configuration by ADAMS®for different poses. Finally the eigenfrequencies have been mapped on different planes in which the 3D working space has been divided. From the analysis of these maps it is possible to see that the flexible transmission units reduce the minimum eigenfrequencies value. However they are still sufficiently higher than the frequencies at which the robot will be excited.

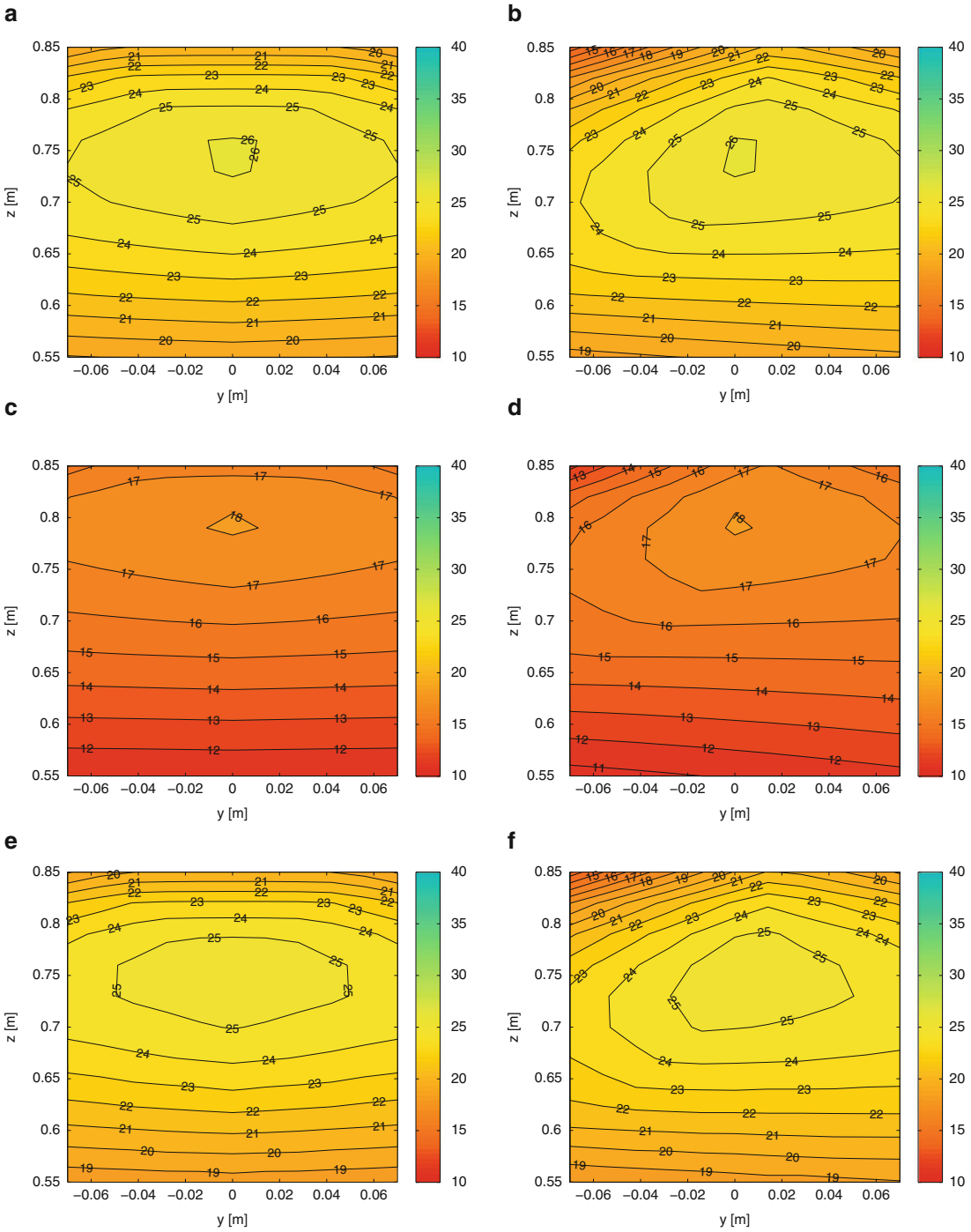

Fig. 41.2 Maps of the eigenfrequencies expressed in [Hz] on 0° and 90° planes with three kinds of transmission units. (**a**) $\phi = 0°$ plane, with ideal transmission units. (**b**) $\phi = 90°$ plane, with ideal transmission units. (**c**) $\phi = 0°$ plane, with BDTU. (**d**) $\phi = 90°$ plane, with BDTU. (**e**) $\phi = 0°$ plane, with BSTU. (**f**) $\phi = 90°$ plane, with BSTU

References

1. Bayati I, Belloli M, Ferrari D, Fossati F, Giberti H (2014) Design of a 6-DoF robotic platform for wind tunnel tests of floating wind turbines. Energy Procedia J 53:313–323
2. Ferrari D, Giberti H (2014) A genetic algorithm approach to the kinematic synthesis of a 6-DoF parallel manipulator. In: IEEE multi-conference on systems and control, Antibes, 8–10 October 2014

3. Cinquemani S, Ferrari D (2014) A genetic algorithm optimization for independent modal space control technique. In: IEEE multi-conference on systems and control, Antibes, 8–10 October 2014
4. Legnani G, Tosi D, Fassi I, Giberti H, Cinquemani S (2010) The point of isotropy and other properties of serial and parallel manipulators. Mech Mach Theory 45(10):1407–1423
5. Legnani G, Fassi I, Giberti H, Cinquemani S, Tosi D (2012) A new isotropic and decoupled 6-DoF parallel manipulator. Mech Mach Theory 58:64–81
6. Giberti H, Ferrari D (2014) Drive system sizing of a 6-DoF parallel robotic platform. In: Proceedings of ASME 12th biennial conference on engineering systems design and analysis, ESDA2014, Copenhagen, 25–27 June 2014
7. Giberti H, Cinquemani S, Legnani G (2011) A practical approach to the selection of the motor-reducer unit in electric drive systems. Mech Based Des Struct Mach 39(3):303–319
8. Giberti H, Cinquemani S, Legnani G (2010) Effects of transmission mechanical characteristics on the choice of a motor-reducer. Mechatron Elsevier J 20:604–610
9. Giberti H, Clerici A, Cinquemani S (2014) Specific accelerating factor: one more tool in motor sizing projects. Mechatron Elsevier J 24(7):898–905
10. Giberti H, Ferrari D, Negahbani N (2015) A belt-driven 6-DoF parallel kinematic machine. In: IMAC XXXIII a conference and exposition on structural dynamics, Orlando, 2–5 February 2015

Chapter 42
A Belt-Driven 6-DoF Parallel Kinematic Machine

Navid Negahbani, Hermes Giberti, and Davide Ferrari

Abstract Parallel Kinematic Machines (PKMs) attract researchers and companies, because they are claimed to offer several advantages over their serial counterparts, like high structural rigidity and high dynamic performance. Indeed, the parallel kinematic arrangement of the links provides higher stiffness and lower moving masses that reduce inertia effects. PKMs have better dynamic performance, however, most of them have a complex geometrical workspace shape and highly non linear input/output relations. To actuate PKMs, rigid high-cost transmission systems are typically used in order to obtain high precision performance: Ball-screw-driven units have good stiffness and good precision for short and medium travel while linear motors have zero backlash, high stiffness, high velocities and accelerations and high costs. This work investigates the possibility to use in their place Belt-Driven Servomechanisms (BDS), which are more suitable for applications that require long actuation travels, high velocities and accelerations, and also low costs. The model of a belt-driven unit is carried out and then the task-space error analysis of a 6-Degrees-of-Freedom (DoF) robot with Hexaglide architecture is performed considering its most critical poses and using a sensitivity approach with respect to belt rigidity, gearbox backlash and friction. The minimum accuracy of the robot over its workspace is finally found with a systematic methodology.

Keywords Parallel kinematic machines • Error evaluation • Timing-belt-drive • Linear transmission • Sensitivity analysis

42.1 Introduction

Over the years, many analytical models for belt-driven transmissions have been presented. Kulkarni et al. [1] proposed the usage of elastic transmission elements for precision position control applications. The characteristics of elastic systems were analyzed and transmission elasticity and friction were identified as the main obstacles to obtain high precision positioning. Hance and his colleagues [2, 3] used linear equation of motions for BDS. Lee and Huang [4] hired a non-linear third order polynomial function as the spring stiffness coefficient for improving the motion equations of Hance.

In the field of fluid-structure interaction problems, in particular to investigate the behaviour of offshore wind turbines and sailing boats, unsteady aerodynamic experiments should be performed inside wind tunnels [5]. The large-amplitude floating motion will be provided to the scale models with a robotic device, emulating the sea water with Hardware-in-the-Loop (HIL) techniques. To this end, a 6-DoF parallel kinematic architecture called Hexaglide was chosen because potentially able to best match the given requirements. The Hexaglide was developed for the first time at the ETH in Zürich as a milling tool machine [6]. It has six independent kinematic chains of PRRS type, in which constant length links connect the mobile platform to six linear actuated rails. According to the preliminary specifications presented in [5], the Hexaglide which is presented in this work, should have long rails, thus BDS was used and its non-linear properties are considered. The dimensions of this PKM were optimized by a generic algorithm [7] and the applied method has been explained in [8]. The cost functions of the optimization process have concerned with the property of isotropy, following the theory presented in [9, 10]. In [11] the drive system was mechanically sized using a mechatronic approach which was presented in [12–14], but all the elements were assumed as rigid bodies. Now, the flexibility of the belt, the backlash in the gearbox and the friction, need to be included in the model of the robot. In the previous works, these factors are not considered at the same time, so that belt-drive servomechanisms must be further investigated. This paper investigates the influence of the mentioned factors using a sensitivity approach. The wind tunnel robot is the application case. The error evaluation is applied for the mobile platform pose, that is the set of Tool Center Point (TCP) coordinates and platform orientation.

N. Negahbani • H. Giberti (✉) • D. Ferrari
Mechanical Engineering Department, Politecnico di Milano, Via La Masa 1, 20156 Milano, Italy
e-mail: hermes.giberti@polimi.it

G. Kerschen (ed.), *Nonlinear Dynamics, Volume 1*, Conference Proceedings of the Society for Experimental Mechanics Series, DOI 10.1007/978-3-319-15221-9_42

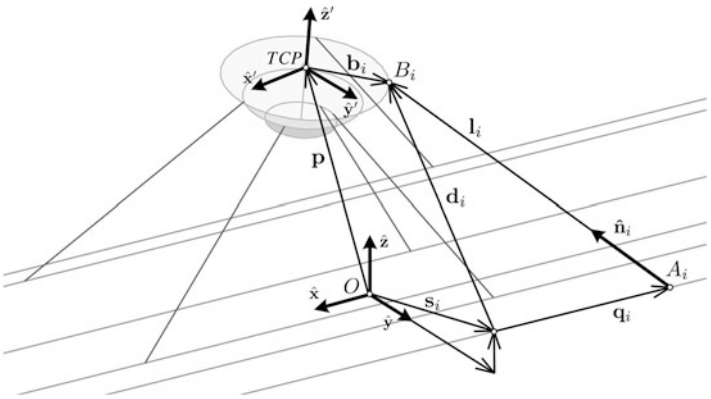

Fig. 42.1 View details of Hexaglide robot [5]

The following sections are organized as follow: Sect. 42.2 describes the inverse kinematics and dynamics of the Hexaglide; Sect. 42.3 derives the equations of motion of the BDS considering: (1) belt flexibility, as a function of the position of the slider along its rail, (2) backlash in the gearbox, and (3) friction. The error evaluation methodology is explained in Sect. 42.4, while the numeric results are given in Sect. 42.5.

42.2 Hexaglide Robot

42.2.1 Inverse Kinematics

Inverse kinematics analysis can be perform for parallel robots, so each slider position, q_i, can be found from TCP position and mobile platform orientation, $\Theta = \{\alpha, \beta, \gamma\}$. With reference to the quantities showed in Fig. 42.1, the inverse kinematics of the Hexaglide robot was solved in Eq. (42.1) and presented in [5].

$$q_i = d_{i,x} \pm \sqrt{l_i^2 - d_{i,y}^2 - d_{i,z}^2} \tag{42.1}$$

42.2.2 Inverse Dynamics

Inverse dynamics is the calculation of forces and torques at the robot actuated joints in order to produce the desired motion of the mobile platform. A multi-body model is implemented in Simulink using the SimMechanics library. Inverse dynamics is solved considering two payloads: a scale model of a sailing boat and a scale model of a offshore wind turbine.

SimMechanics can not solve the inverse dynamics of the parallel robots by applying platform motion directly. For solving this problem, first desired platform motions are given to Eq. (42.1) and desired slider motions are calculated. Then, desired slider motions are applied to the robot SimMechanics model and forces at the robot joints are computed.

42.3 Dynamic Analysis of BDS

BDS consists of a motor, a gearbox and a belt linear unit. The slider is driven by converting the rotational motion to the linear motion. Motor torque and slider inertia, cause the length variation in belt because of its elasticity properties, thus belt-drive is considered as a spring-mass model, as shown in Fig. 42.2.

Previous studies considered the equivalent stiffness coefficient of the belt either constant [2, 3], or a position dependent polynomial [4], while in this work equivalent stiffness coefficient of the belt is variable as a function of slider position, considering elastic properties of belt and dynamics behaviour of the slider. Regarding to strength of material, equivalent stiffness coefficient of body, K, with axial load is defined by $K = EA/L$, where E, A and L are respectively elastic modules, the section area (EA is axial rigidity) and length of the body. The stiffness coefficients of the belt (K_1, K_2 and K_3)

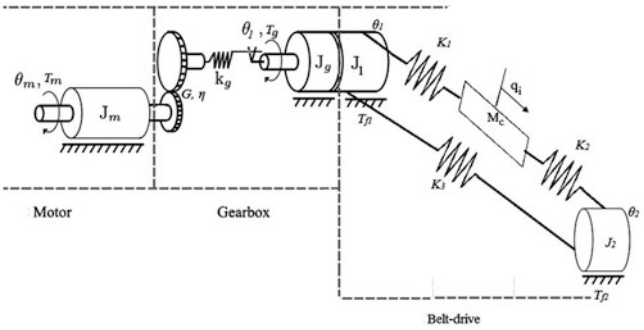

Fig. 42.2 Mass-spring model of the belt drive

are calculated by $K_1 = EA/(L_1 + q_i)$, $K_2 = EA/(L_2 - q_i)$ and $K_3 = EA/L$. K_1 and K_2 are function of slider position q_i. L_1 is the distance between initial position of slider and center of driver pulley, L_2 is defined as distance between initial position of slider and the center of driven pulley $(L - L_1)$ and L is the distance between center of driver pulley and center of driven pulley.

By improving the equations of motion presented in [2], Eq. (42.2) is derived for each BDS by using Lagrange method. The formulated equations in [15, 16] are applied in order to calculate the backlash in gearbox. They are modified to be use in Hexaglide robot and with BDS actuators:

$$\begin{aligned} &M_c\ddot{q}_i + K_1(q_i)(q_i - R\theta_1) + K_2(q_i)(q_i - R\theta_2) + F_f = F_{i,x} \\ &J_m\ddot{\theta}_m = T_m - T_g/(\eta G) \\ &(J_g + J_1)\ddot{\theta}_1 + R\left[K_1(q_i)(R\theta_1 - q_i) + K_3(R\theta_1 - R\theta_2)\right] + T_{f1} - T_g = 0 \\ &J_2\ddot{\theta}_2 + R\left[K_2(q_i)(R\theta_2 - q_i) + K_3(R\theta_2 - R\theta_1)\right] + T_{f2} = 0 \end{aligned} \tag{42.2}$$

where T_m, J_m, J_g and M_c are motor torque, motor inertia, gearbox inertia and slider mass, respectively. Also F_f and F_{i_x} are slider friction force and reaction force between ith slider and ith robot link, respectively. T_{f_1} and T_{f_2} are related to friction torque in pulleys. θ_m, θ_1 and θ_2 are the angular position of driver motor, driver pulley and driven pulley. R is radius of pulleys. J_1 and J_2 are the momentum of inertia of driving and driven pulleys. T_g is backlash torque. η is gearbox mechanical efficiency and G is the gearbox ratio ω_{in}/ω_{out}.

T_g is calculated in Eq. (42.3), where k_g is torsional stiffness of the gearbox and θ_b is the backlash in the gearbox.

$$T_g = k_g \begin{cases} \frac{\theta_m}{G} - \theta_1 - \theta_b & \frac{\theta_m}{G} - \theta_1 \geq \theta_b \\ 0 & -\theta_b \leq \frac{\theta_m}{G} - \theta_1 \leq \theta_b \\ \frac{\theta_m}{G} - \theta_1 + \theta_b & \frac{\theta_m}{G} - \theta_1 \leq -\theta_b \end{cases} \tag{42.3}$$

The friction force is estimated using the exponential form presented in Eq. (42.4):

$$F_f = (M_c g - F_{i,z})\left[\mu_k + (\mu_s - \mu_k)e^{-(\dot{q}_i/V_s)^2}\right]\text{sign}(\dot{q}_i) + C_v\dot{q}_i \tag{42.4}$$

where μ_s is the static coefficient of friction, μ_k is the kinetic coefficient of friction and $F_{i,z}$ is the normal reaction force between ith slider and ith robot link. C_v is the viscous friction parameter and V_s is the characteristic velocity of the Stribeck friction.

BDS equations of motion are solved by Simulink and the results are integrated in the model of the Hexaglide robot.

42.4 Error Evaluation

The error evaluation of the TCP position and platform orientation is important to understand what is the positioning resolution of the robot in the task-space in each of 6-DoF. To identify the critical poses the following steps are applied. First step: critical poses of the Hexaglide robot workspace are found via kinematic mapping of the error from joint- to task-space.

Second step: to probe the dynamic behaviour of the robot in a systematic and significant way, the found critical poses are used as the initial positions and orientations for the robot motion, and about each of them, a sinusoidal large-amplitude movement is independently imposed on every coordinate of the mobile platform. Third step: the error is caused by belt flexibility, backlash in gearbox, and friction coefficient of BDS guideline, this step is devoted to understand sensitivity of error according to mentioned reasons in worst condition.

From kinematic analysis of the Hexaglide robot we know that $\mathbf{W} = [J]\dot{\mathbf{q}}$, where $[J]$ is the Jacobian matrix, $\dot{\mathbf{q}} = [\dot{q}_1, \dot{q}_2, ..., \dot{q}_6]^T$ collects the sliders velocities, while $\mathbf{W} = [\dot{x}, \dot{y}, \dot{z}, \omega_x, \omega_y, \omega_z]^T$ is the velocity vector of the platform. Defining $\mathbf{X} = [x, y, z, \alpha, \beta, \gamma]^T$ as the robot pose vector, Eq. (42.5) is satisfied for small variations.

$$\Delta\mathbf{X} = [J]\Delta\mathbf{q} \tag{42.5}$$

In the presence of identical actuators and transmissions, the robot is assumed rigid with ideal joints, thus BDS is the only source of error. It is reasonable to assume that the errors in the sliders positions are all limited by an equal maximum value $\Delta q_{\max}$. The infinity norm best represents the actual situation of the error kinematic mapping, as explained in [10].

$$\|\Delta q\|_\infty \leq \Delta q_{\max} \tag{42.6}$$

Maximum error of TCP position and platform orientations are found by Eq. (42.7).

$$\Delta\mathbf{X_{max}} = [J] \begin{Bmatrix} 1 \\ 1 \\ \vdots \\ 1 \end{Bmatrix}_{6\times 1} \Delta q_{max} \tag{42.7}$$

Figure 42.3 shows the distribution map of $\Delta y_{\max}$ error over the workspace of the Hexaglide. Critical poses and the maximum error in the task-space are identified for all platform coordinates and reported in Table 42.1.

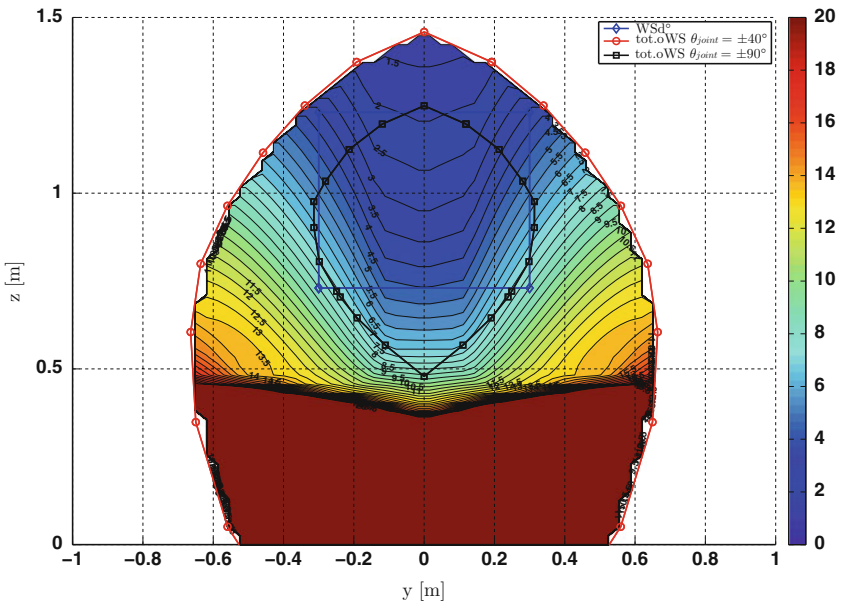

Fig. 42.3 Error of y TCP position

Table 42.1 Critical points of initial position and orientations for each movement

Movement	TCP position (m)			Platform orientation		
	x_0	y_0	z_0	α_0	β_0	γ_0
x − mov.	0	0.3	1.23	±15°	±15°	±15°
y − mov.	0	0	0.98	±15°	±15°	±15°
z − mov.	0	0.3	0.98	±15°	±15°	±15°
α − mov.	0	0.3	0.73	−	±15°	±15°
β − mov.	0	0.3	0.73	±15°	−	±15°
γ − mov.	0	0.3	0.73	±15°	±15°	−

Table 42.2 Maximum amplitudes and frequencies of the desired movements

Movement	Amplitude		Frequency (Hz)	
	Wind turbine	Sailboat	Wind turbine	Sailboat
x − mov.	0.50 m	−	0.7	1.5
y − mov.	0.30 m	−	0.7	1.5
z − mov.	0.25 m	−	0.7	1.5
α − mov.	15°	5°	0.7	1.5
β − mov.	15°	10°	0.7	1.5
γ − mov.	15°	10°	0.7	1.5

In the next step, the pose error $\mathbf{e_X}$ is computed using Eq. (42.8):

$$\mathbf{e_X} = \mathbf{X_d} - \mathbf{X} \tag{42.8}$$

$\mathbf{X_d}$ and $\mathbf{X_d}$, respectively are the desired and the actual poses.

Then, the most critical poses, with the largest $\mathbf{e_X}$ are probed with large amplitude sinusoidal motions given independently on each coordinate of the platform, but these motion laws wouldn't have zero initial position, velocity and acceleration and the sudden change would create impulse actuation forces. Therefore, the sinusoidal motion is initially smoothed by a five order polynomial function, as shown in Eq. (42.9). A_i and f are amplitude and frequency of movement respectively and Table 42.2 shows these parameters for each movement. $\mathbf{X_o}$ is the initial platform pose.

$$X_i = X_{o_i} + \begin{cases} a_5 t^5 + a_4 t^4 + a_3 t^3 & t \le t_c \\ A_i \sin(2\pi f(t - t_d)) & t > t_c \end{cases} \tag{42.9}$$

In a case that BDS consist of a rigid belt and a gearbox without backlash, motor rotation is calculated from slider position by Eq. (42.10) and by applying Eq. (42.1) the sliders positions are obtained.

$$\theta_{m,\text{ref}} = q_{i,\text{ref}}\, G/R \tag{42.10}$$

Then this slider movement applied to the implemented SimMechanics model in order to find the simulated TCP position and platform orientation. Hence, the error between ideal system and the system which includes gearbox backlash, belt flexibility and friction is calculated, apart from the control. In correspondence to the maximum yielded error which is occurred in each DoF and the related motions [Eq. (42.9)], the worst case is calculated. By comparing the results of each DoF and motion the maximum error is found.

Finally, maximum errors and its RMS are computed by considering the worst condition obtained in previous step. By taking in to account the different values of belt drive parameters including belt rigidity, backlash in gearbox and friction coefficient the behavior of errors are analyzed. The BDS parameters are obtained from commercial catalogues. The most effective parameter is found. The sensitivity of the task-space error for Hexaglide robot with BSD actuators is obtained by parameters variation. Next section is devoted to numerical solution for the specific system that will be used in wind tunnel.

Table 42.3 Data of system

Belt-drive	Reducer	Motor
$M_c = 8.67\,\text{kg}$	$k_g = 7.53\text{e}4\,\text{Nm/rad}$	$J_m = 24.2\text{e}{-4}\,\text{kg m}^2$
$R = 0.0414\,\text{m}$	$J_g = 1.1\text{e}{-4}\,\text{kg m}^2$	
$J_1 = J_2 = 1.0004\text{e}{-3}\,\text{kg m}^2$	$G = 25$	
$EA = 3{,}625{,}000\,\text{N}$	$\eta = 0.95$	
$L = 4\,\text{m}$		
$L_1 = L_2 = 2\,\text{m}$		
$\mu_k = 0.1$		

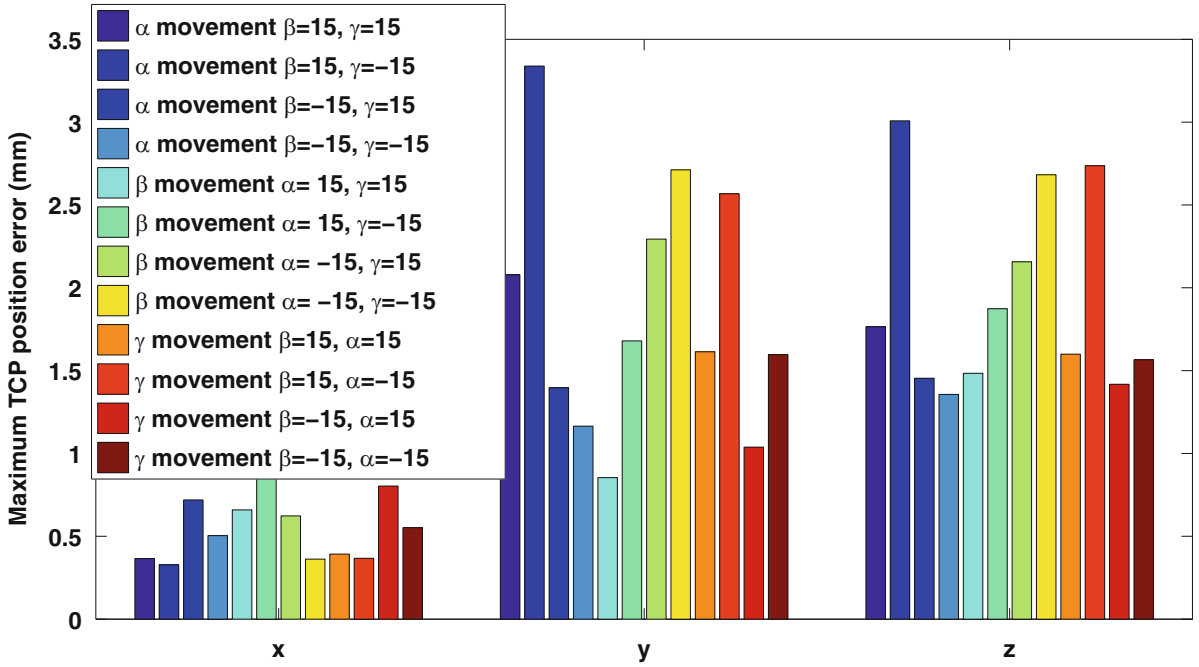

Fig. 42.4 Maximum error of TCP position when sailboat installed on platform

42.5 Numerical Results

Numerical results were achieved by using data from belt drive (Thomson linear motion system WH120), motor (Kollmorgen AKM Servomotor AKM63L) and reducer (Thomson linear motion system VT115-025) catalog, as can be seen in Table 42.3.

Figures 42.4 and 42.5 show maximum error for TCP position and platform orientation in each movement, when sailing boat scale model is installed on the platform. The sailboat and wind turbine have the same behavior when they are installed on the platform, thus the graphical results of the wind turbine is not shown.

According to Figs. 42.4 and 42.5, the critical movement occurs in α movement when $\beta = 15°$ and $\gamma = -15°$. TCP position and platform orientations errors are investigated in this critical movement for different rigidity of belt, gearbox backlash and friction coefficient. Different movements of platform are shown in Figs. 42.4 and 42.5 by different colour. The worst situations in these figures are illustrated in Table 42.4.

Figures 42.6a, b and 42.7a, b show maximum error of TCP positions and platform orientations for different rigidity of belt, backlash of gearbox and friction coefficient, which are all indicated in Table 42.5. Values are presented in Table 42.5 are chosen from minimum value to maximum value which are presented in commercial BDS catalogs. The achieved maximum errors correspondent to values of Table 42.5 are briefly described in Table 42.6. Table 42.6 is including maximum TCP position error and maximum platform orientation error in each BDS. The achieved maximum errors are the worst situations of the robot operation. This worst conditions are occurred in maximum backlash value (13 arcmin) and minimum friction coefficient (0.02).

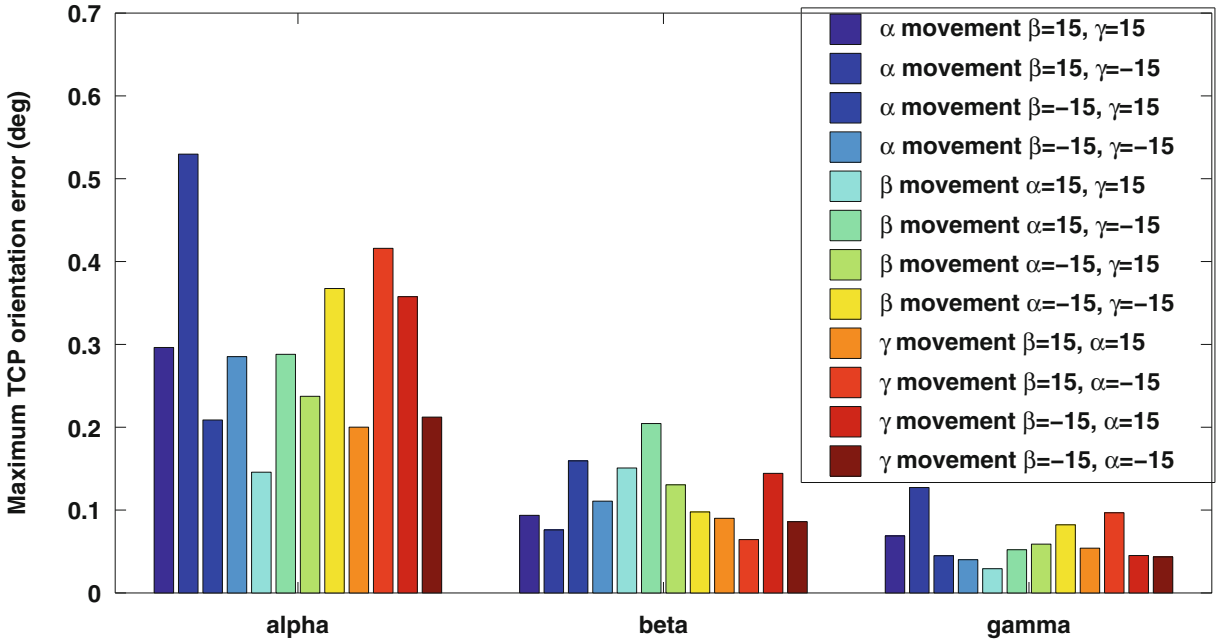

Fig. 42.5 Maximum error of mobile platform orientation when sailboat installed on platform

Table 42.4 Maximum value of the maximum errors and RMS of errors

			Maximum	
			Sailboat	Wind turbine
Maximum error	TCP pos.	x	0.89 mm	0.57 mm
		y	3.34 mm	3.20 mm
		z	3.01 mm	2.88 mm
	Platform orie.	α	0.53°	0.45°
		β	0.22°	0.13°
		γ	0.13°	0.11°
RMS error	TCP pos.	x	0.32 mm	0.3 mm
		y	1.63 mm	1.52 mm
		z	1.63 mm	1.60 mm
	Platform orie.	α	0.23°	0.21°
		β	0.07°	0.06°
		γ	0.06°	0.05°

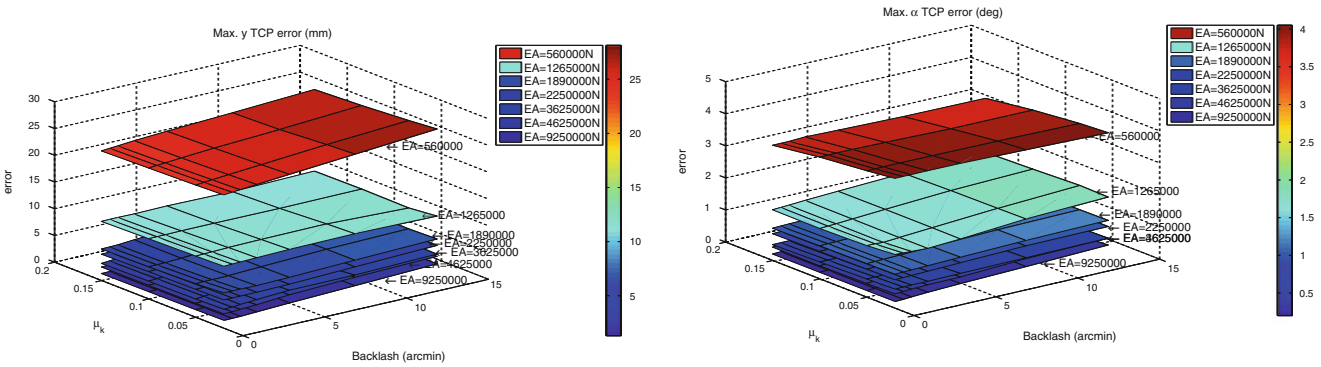

Fig. 42.6 Maximum error of TCP position and mobile platform orientation for different rigidity, backlash and friction coefficient when sailboat installed on platform. (**a**) y direction. (**b**) α orientation

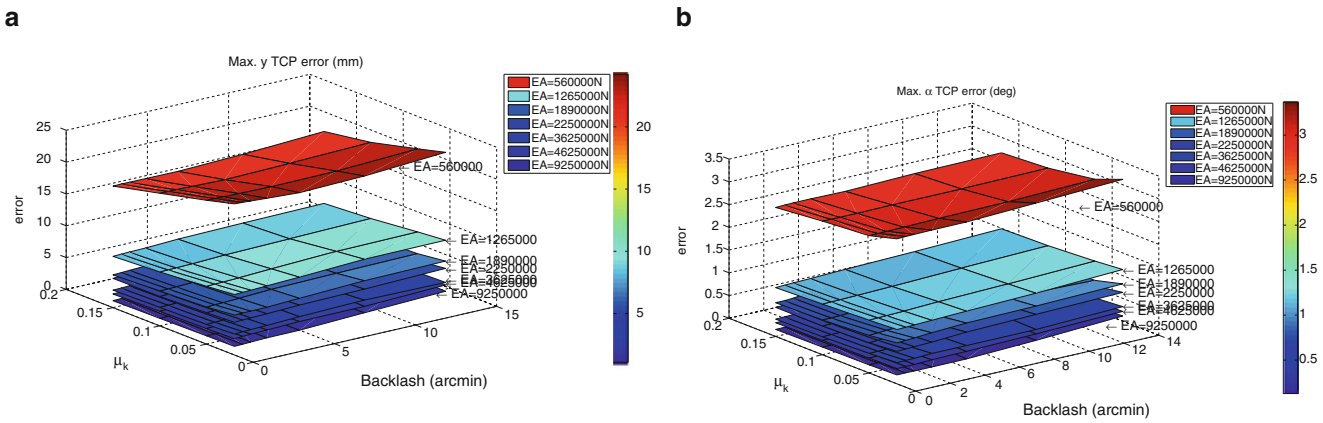

Fig. 42.7 Maximum error of TCP position and mobile platform orientation for different rigidity, backlash and friction coefficient when wind turbine installed on platform. (**a**) y direction. (**b**) α orientation

Table 42.5 Values of belt rigidity, gearbox backlash and friction coefficient are used in numerical analysis

$EA\,(N)$	Backlash (arcmin)	μ_k
560,000	0	0.02
1,265,000	0.5	0.05
1,890,000	1	0.1
2,250,000	2	0.15
3,625,000	4	
4,625,000	8	
9,250,000	13	

Table 42.6 Maximum value of the TCP position error and platform orientation in different belt rigidity

	Max. error in sailboat		Max. error in wind turbine	
$EA\,(N)$	Pos. (mm)	Ori. °	Pos. (mm)	Ori. °
560,000	28.14	4.05	24.3	3.36
1,265,000	12.07	1.96	10.42	1.37
1,890,000	7.56	1.22	7.14	1.06
2,250,000	6.69	1.02	5.99	0.87
3,625,000	4.82	0.66	3.76	0.56
4,625,000	4.32	0.66	3.67	0.46
9,250,000	2.92	0.45	2.52	0.35

Figures 42.6a, b and 42.7a, b are presented for two cases in y position and α orientation. The remain other TCP positions and platform orientations have same behaviour. The results illustrate error decreases by increasing rigidity of belt, rising the friction coefficient and declining the backlash. Looking more closely at the trend of error, it can be seen rigidity of the belt is the most important factor. Hence, the belt rigidity is the most influencing factor.

42.6 Conclusion

Hexaglide robot and linear transmission actuators were explained in Sects. 42.1 and 42.2, respectively. A model of BDS by considering the non-linearity of the system was carried out in Sect. 42.3. Positioning error of the Hexaglide robot with BDS actuator was evaluated in Sect. 42.4. Large sinusoidal motions were used for the mobile platform, this approach is complementary to the work presented in [17], where the vibration analysis is presented to evaluate the first natural frequency of the PKM. The critical poses of workspace was found by the kinematic mapping of the error. The inverse dynamic problem was solved with BDS actuators. TCP position error and platform orientation error were calculated for different belt rigidity, backlash in gearbox and friction coefficient in worst case.

It can be said that BDS is a good actuator for the examined 6-DoF robotic application, with accuracy approximately of 3 mm in TCP position and 0.5° in platform orientation in the case of sailing boat payload, and with accuracy of 2 mm in TCP

position and 0.2° in platform orientation in the case of wind turbine payload. According to the results shown in Figs. 42.6a, b and 42.7a, b, belt rigidity plays crucial role in the error of the system. BDS with belt rigidity more than 3,000 kN is suggested to be used for the wind tunnel device.

References

1. Kulkarni AS, El-Sharkawi MA (2001) Intelligent precision position control of elastic drive systems. IEEE Trans Energy Convers 16(1):26–31
2. Hace A, Jezernik K, Sabanovic A (2007) SMC with disturbance observer for a linear belt drive. IEEE Trans Ind Electron 54:3402–3412
3. Hace A, Jezernik K, Sabanovic A (2005) Improved design of VSS controller for a linear belt-driven servomechanism. IEEE/ASME Trans Mechatron 10:385–390
4. Lee T-F, Huang A-C (2011) Vibration suppression in belt-driven servo systems containing uncertain non-linear dynamics. J Sound Vib 330: 17–26
5. Bayati I, Belloli M, Ferrari D, Fossati F, Giberti H (2014) Design of a 6-DoF robotic platform for wind tunnel tests of floating wind turbines. Energy Proc J 53:313–323
6. Honegger M, Codourey A, Burdet E (1997) Adaptive control of the Hexaglide, a 6-DoF parallel manipulator. In: Proceedings of IEEE international conference on robotics and automation, vol 1, pp 543–548
7. Ferrari D, Giberti H (2014) A genetic algorithm approach to the kinematic synthesis of a 6-DoF parallel manipulator. In: IEEE multi-conference on systems and control, Antibes, 8–10 October 2014
8. Cinquemani S, Ferrari D (2014) A genetic algorithm optimization for independent modal space control technique. In: IEEE multi-conference on systems and control, Antibes, 8–10 October 2014
9. Legnani G, Tosi D, Fassi I, Giberti H, Cinquemani S (2010) The point of isotropy and other properties of serial and parallel manipulators. Mech Mach Theory 45(10):1407–1423
10. Legnani G, Fassi I, Giberti H, Cinquemani S, Tosi D (2012) A new isotropic and decoupled 6-DoF parallel manipulator. Mech Mach Theory 58:64–81
11. Giberti H, Ferrari D (2014) Drive system sizing of a 6-DoF parallel robotic platform. In: Proceedings of ASME 12th biennial conference on engineering systems design and analysis, ESDA2014, Copenhagen, 25–27 June 2014
12. Giberti H, Cinquemani S, Legnani G (2011) A practical approach to the selection of the motor-reducer unit in electric drive systems. Mech Based Des Struct Mach 39(3):303–319
13. Giberti H, Cinquemani S, Legnani G (2010) Effects of transmission mechanical characteristics on the choice of a motor-reducer. Mechatron Elsevier J 20:604–610
14. Giberti H, Clerici A, Cinquemani S (2014) Specific accelerating factor: one more tool in motor sizing projects. Mechatron Elsevier J 24(7): 898–905
15. Dwivedula RV, Pagilla PR (2012) Effect of compliance and backlash on the output speed of a mechanical transmission system. J Dyn Syst Meas Control 134(3):031010(1–9)
16. Pastorino R, Naya MA, Pérez JA, Cuadrado J (2011) Geared PM coreless motor modeling for drivers force feedback in steer-by-wire systems. Mechatronics 21(9):1043–1054
17. Giberti H, Ferrari D, Fiore E (2015) Dynamics modelling and accuracy evaluation of a 6-DoF Hexaslide robot. In: IMAC XXXIII a conference and exposition on structural dynamics, Orlando, 2–5 February 2015

Chapter 43
Bearing Cage Dynamics: Cage Failure and Bearing Life Estimation

Silvio Giuseppe Neglia, Antonio Culla, and Annalisa Fregolent

Abstract Nowadays, given the widespread use of rolling bearings in mechanical applications, an important topic is investigate which parameters influence their wear in order to estimate the real bearing life. The cage is one of the critical element in the bearing, its dynamics is complex and nonlinear due to the intermittent contacts with various elements (e.g. balls and races) with a resulting not regular trajectory of its center that can lead to the cage failure. While the races have a simple rotational motion, the balls usually have a more complex dynamics due to the stick-slip motion and the action of the external contact forces. In this work a lumped model of the cage is presented focusing of its possible kind of motions: cage in free-flight (just inertial and Coriolis forces act on it), race contact, balls contact, race and balls contact. A numerical code is developed taking into account a three DOFs model for the cage, contacts and lubrication.

The goal of this work is to identify the most important parameters influencing the motion and the life of the cage. Furthermore, some chaotic aspects in the dynamics of the bearing are investigated to understand their influence on the cage failure.

Keywords Ball bearings • Contact dynamics • Cage motion • Deterministic chaos • Stick-slip

43.1 Introduction

One of the problems affecting roller bearings is the not regular motion of the cage (i.e. retainer) that separates the balls. Such motion is due to the various contacts between the cage and the bearing elements that can lead to premature bearing failure [1]. The cage dynamics is a complicate phenomenon to describe through a computational model and it is not well understood, in the past years many works have been done on it [2–4].

Between the cage and the balls there is a very small clearance which allows the balls to drive the cage (see Fig. 43.1a), the cage bounces repeatedly on the balls and the contact forces can be very high. Since the cage also must be free to move, its movement can generate vibrations that can adversely affect performance.

Aim of this work is to simulate a different cage geometry (see Fig. 43.1b) in which the ball-cage clearance is smaller than the cage-race one, in order to study the magnitude of the contact interactions and if the limited number of cage-balls impacts can improve the bearing life.

The analysis is done with a planar model of the cage (three degrees of freedom) similar to the one presented in [3], the balls are studied with two degrees of freedom taking into account both dynamical and kinematics aspect in order to simulate pure rolling and stick-slip motion. All the interactions during the cage motion are modeled using the contact Hertz theory [5].

The bearing parameter used for the simulations are shown in Table 43.1.

43.2 Cage Dynamics

During the bearing motion the cage can have four different behaviors:

- *Free flight*
- *Contact with the race*

S.G. Neglia (✉) • A. Culla • A. Fregolent
Dipartimento di Ingegneria Meccanica e Aerospaziale, Università di Roma La Sapienza, Via Eudossiana 18, 00184 Rome, Italy
e-mail: silvio.neglia@uniroma1.it

G. Kerschen (ed.), *Nonlinear Dynamics, Volume 1*, Conference Proceedings of the Society
for Experimental Mechanics Series, DOI 10.1007/978-3-319-15221-9_43

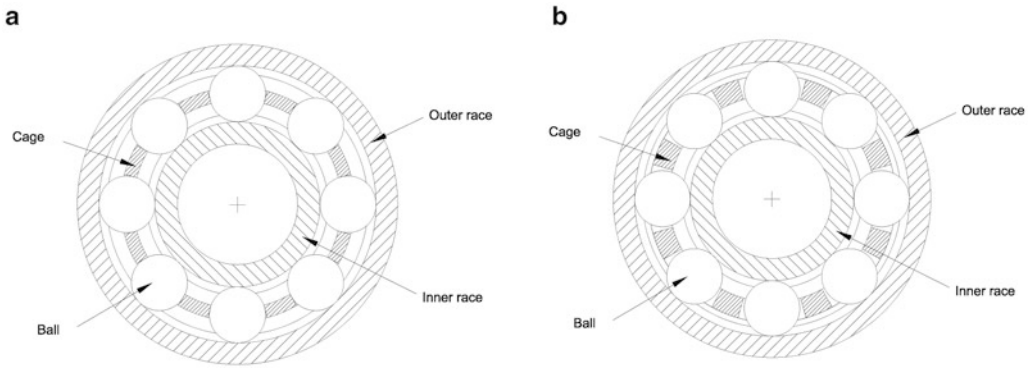

Fig. 43.1 Common bearing (**a**), new type of bearing (**b**)

- *Contact with the balls*
- *Contact with the balls and with the race*

In the free flight motion, the cage is subjected only to the centrifugal and the Coriolis forces. There are no external forces acting on it.

In case of contact with the race, the interaction between cage and race is considered.

In case of contact with the balls, there is a single contact with a ball or a multiple contacts with different balls at the same time.

The contact with the balls and with the race case, describes all the possible phenomena that can occur on a bearing, because there are contacts with the race and with the balls at the same time.

In Fig. 43.2 two reference systems of the studied problem are shown.

OXY is the reference system fixed with the frame (inertial reference system), while oxy is the cage-fixed one (local reference system).

The planar motion of the cage is described with three degrees of freedom (DOFs):

- Translation about the X axis
- Translation about the Y axis
- Rotation about its center

The three Lagrangian coordinates are $\rho(t)$, $\beta(t)$ and $\alpha(t)$. By convention $\beta(t)$ is chosen clockwise while $\alpha(t)$ is counterclockwise.

The dynamic description of the cage is obtained via the Euler's equations (for the angular position of the cage) and with the D'Alambert's equations of motion (for the displacements in the fixed reference frame).

The differential system written in Eq. (43.1), describes the entire cage dynamics.

$$\begin{bmatrix} I_z & 0 & 0 \\ 0 & M_c & 0 \\ 0 & 0 & M_c \end{bmatrix} \begin{bmatrix} 1 & 0 & 0 \\ 0 & \sin\beta(t) & \cos\beta(t) \\ 0 & \cos\beta(t) & -\sin\beta(t) \end{bmatrix} \begin{Bmatrix} \ddot{\alpha}(t) \\ \ddot{\rho}(t) - \rho(t)\dot{\beta}^2(t) \\ 2\dot{\rho}(t)\dot{\beta}(t) + \rho(t)\ddot{\beta}(t) \end{Bmatrix} = \begin{Bmatrix} M_z(t) \\ F_X(t) \\ F_Y(t) \end{Bmatrix} \tag{43.1}$$

The acceleration contribution $\rho(t)\dot{\beta}^2(t)$ is the centrifugal acceleration, while $2\dot{\rho}(t)\dot{\beta}(t)$ is the Coriolis' acceleration.

The contact interactions $F_X(t)$, $F_Y(t)$ and $M_z(t)$ are the results of all the impacts that occur in the bearing.

The system (43.1) can be rewritten in matrix form as:

$$\mathbf{MR}(t)\ddot{\mathbf{x}}(t) = \mathbf{F}(t) \tag{43.2}$$

Table 43.1 Bearing parameters

Name	Value	Description
Outer race		
E_{out}	200 GPa	Young Modulus
ρ_{out}	$7,800\,\mathrm{kg/m^3}$	Density
ν_{out}	0.3	Poisson ratio
R_{out}	0.0186 m	Radius
Ω_{out}	2,000 RPM	Angular velocity
Inner race		
E_{in}	200 GPa	Young Modulus
ρ_{in}	$7,800\,\mathrm{kg/m^3}$	Density
ν_{in}	0.3	Poisson ratio
R_{in}	0.01 m	Radius
Ω_{in}	0 RPM	Angular velocity
Balls		
E_B	200 GPa	Young Modulus
ρ_B	$7,800\,\mathrm{kg/m^3}$	Density
ν_B	0.3	Poisson ratio
R_B	0.003 m	Radius
I_B	$3.2 \cdot 10^{-9}\,\mathrm{m^4}$	Moment of inertia
M_B	$8.9 \cdot 10^{-4}\,\mathrm{kg}$	Mass
n	12	Number of balls
Cage		
E_c	1.73 GPa	Young Modulus
ρ_c	$1,500\,\mathrm{kg/m^3}$	Density
ν_c	0.3	Poisson ratio
R_c	0.0173 m	External radius
r_c	0.0146 m	Internal radius
I_z	$7.6 \cdot 10^{-7}\,\mathrm{m^4}$	Moment of inertia
M_c	0.003 kg	Mass
Other parameters		
f_{SOT}	0.103	Spiral orbit tribometer friction
f_{POD}	0.1	Pin-on-disk friction
ρ_m	$2 \cdot 10^{-4}$ m	Cage-race nominal clarence
C_r	$2 \cdot 10^{-4}$ m	Pocket-ball nominal clarence
K_{out}	$4.01 \cdot 10^5$ N/m	Cage-outer race stiffness
D_{out}	50 Ns/m	Cage-outer race damping
K_{in}	$2.9 \cdot 10^5$ N/m	Cage-inner race stiffness
D_{in}	50 Ns/m	Cage-inner race damping
K_B	$2.3 \cdot 10^5$ N/m	Cage-ball stiffness
D_B	50 Ns/m	Cage-ball damping
R_P	0.0156 m	Pitch radius
γ	3 s/m	Dynamical friction force slope

43.2.1 Free Flight

In case of free flight motion the are no forces acting on the cage:

$$\mathbf{F}(t) = \mathbf{0} \tag{43.3}$$

The dynamical equations of the cage are:

$$\begin{Bmatrix} \ddot{\alpha}(t) \\ \ddot{\rho}(t) - \rho(t)\dot{\beta}^2(t) \\ 2\dot{\rho}(t)\dot{\beta}(t) + \rho(t)\ddot{\beta}(t) \end{Bmatrix} = \begin{Bmatrix} 0 \\ 0 \\ 0 \end{Bmatrix} \tag{43.4}$$

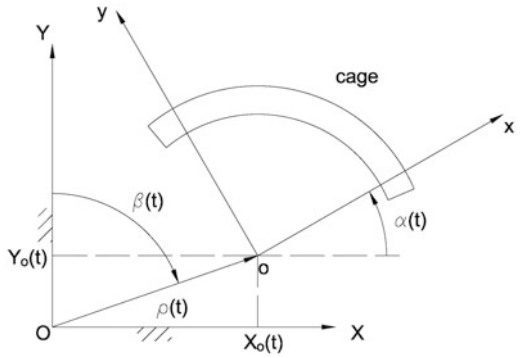

Fig. 43.2 Fixed and local reference system

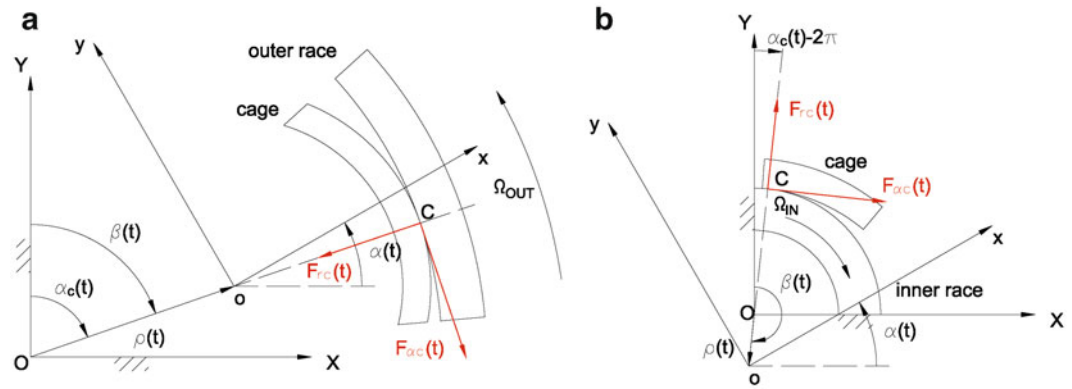

Fig. 43.3 Cage-outer race contact (**a**), cage-inner race contact (**b**)

43.2.2 Race Contact

There will be cage-race contact if:

$$\sqrt{X_o^2(t) + Y_o^2(t)} = \rho(t) \geq \rho_m \tag{43.5}$$

The contact angle $\alpha_c(t)$ calculated in the fixed reference system is equal to:

- $\alpha_c(t) = \beta(t)$ for an outer race contact (Fig. 43.3a)
- $\alpha_c(t) = \beta(t) + \pi$ for an inner race contact (Fig. 43.3b)

The contact forces projected into the proper reference systems are:

$$\begin{Bmatrix} M_z(t) \\ F_X(t) \\ F_Y(t) \end{Bmatrix} = \begin{bmatrix} 1 & 0 & 0 \\ 0 & \sin\beta(t) & \cos\beta(t) \\ 0 & \cos\beta(t) & -\sin\beta(t) \end{bmatrix} \begin{Bmatrix} F_{\alpha c}(t) R_c \\ -F_{rc}(t) \\ \pm F_{\alpha c}(t) \end{Bmatrix} \tag{43.6}$$

the $+$ and the $-$ signs represent the cage-outer race and cage-inner race contact, respectively.

$F_{\alpha c}(t)$ and $F_{rc}(t)$ are the forces acting on the cage in the local reference system oxy.

$$\begin{cases} F_{rc}(t) = C_{sr}\,[\rho(t) - \rho_m] \\ F_{\alpha c}(t) = -f_{POD}\,F_{rc}(t)\mathrm{sgn}[\mathrm{v_{rel}(t)}] \end{cases} \tag{43.7}$$

The friction coefficient f_{POD} is obtained by experimental tests using the *pin-on-disk*, in this test the sliding effect is more influent of the rolling one. The direction of the frictional tangential friction force $F_{\alpha c}(t)$ is obtained through the signum of the relative velocity $v_{rel}(t)$ of the contact point C.

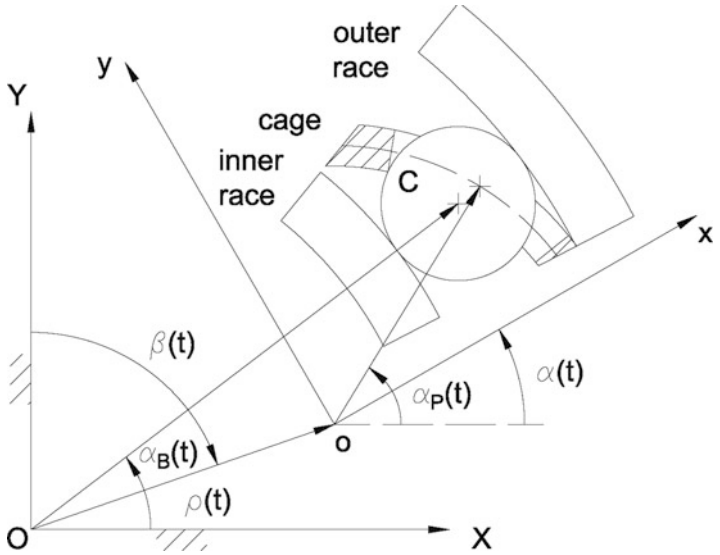

Fig. 43.4 Contact between the cage and the ball

For outer race contact the relative velocity is:

$$v_{rel}(t) = \dot{\rho}(t) - \rho(t)\dot{\beta}(t)\tan\beta(t) - R_c\dot{\beta}(t)\tan\beta(t) - \Omega_{out}R_{out} \tag{43.8}$$

while for inner race contact it is:

$$v_{rel}(t) = \dot{\rho}(t) - \rho(t)\dot{\beta}(t)\tan\beta(t) - R_c\dot{\beta}(t)\tan\beta(t) + \Omega_{in}R_{in} \tag{43.9}$$

43.2.3 Ball Contact

$\alpha_P(t)$ is the angular location of cage pocket in the local reference system oxy (Fig. 43.4).

The generic pocket has the following angular location:

$$\alpha_{Pi}(t) = \alpha(t) + \frac{2\pi}{n}(i-1) \tag{43.10}$$

The initial position of $\alpha_B(t)$ (for $t = 0$) for a generic ball is:

$$\alpha_{Bi}(0) = \frac{2\pi}{n}(i-1) \tag{43.11}$$

Let us assume that if $\rho(t)$ is very small, so there will be coincidence the two reference centers $O \equiv o$, this assumption is not completely false because in a bearing usually $\rho(t) \simeq 0.1$ mm (Fig. 43.5).

There will be cage-ball contact if:

$$|\alpha_B(t) - \alpha_P(t)|\, R_P > C_r \tag{43.12}$$

where $\alpha_B(t)$ is the angular location of the ball in the fixed reference system OXY.

With the used assumption R_P may be confused with R_c.

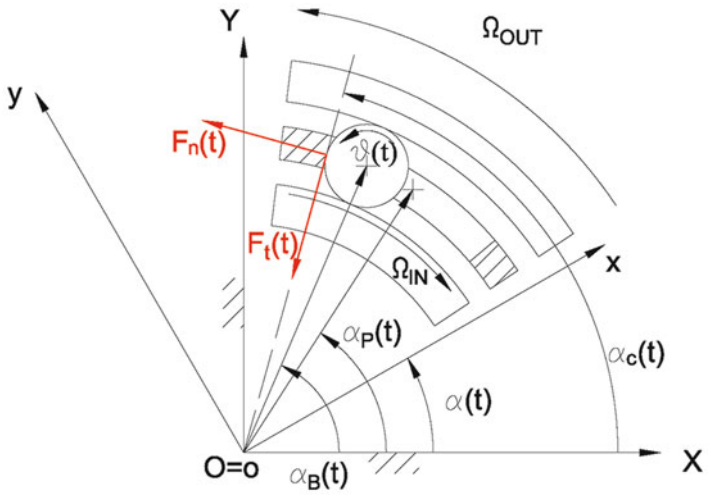

Fig. 43.5 Forces due to the cage-ball contact

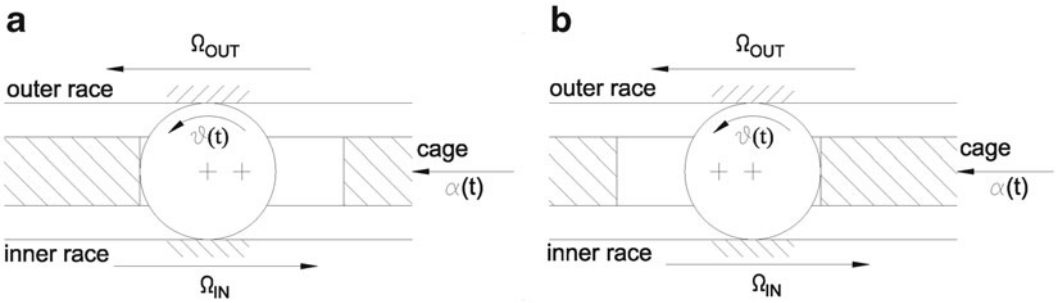

Fig. 43.6 Cage-ball front contact (**a**), cage-ball rear contact (**b**)

Two different ball-cage contact cases can occur:

- Ball front contact if $\alpha_B(t) > \alpha_P(t)$ Fig. 43.6a
- Ball rear contact if $\alpha_B(t) < \alpha_P(t)$ Fig. 43.6b

The contact angular location $\alpha_c(t)$ is:

- $\alpha_c(t) = \alpha_B(t) + \frac{R_B}{R_P}$ for a Ball front contact
- $\alpha_c(t) = \alpha_B(t) - \frac{R_B}{R_P}$ for a Ball rear contact

The forces $F_n(t)$ and $F_t(t)$ acting on the cage are shown Fig. 43.5 and they are calculated as follows:

$$\begin{cases} F_n(t) = C_{sr}\left[\alpha_B(t) - \alpha_P(t)\right] R_P \\ F_t(t) = f_{SOT} F_n(t) \end{cases} \tag{43.13}$$

The friction coefficient f_{SOT} is obtained by experimental tests using the *spiral orbit tribometer*, in this test both sliding and rolling effects are influent.

$F_n(t)$ and $F_t(t)$ must be projected on the fixed reference system OXY in order to obtain $\mathbf{F}(t)$:

$$\begin{Bmatrix} M_z(t) \\ F_X(t) \\ F_Y(t) \end{Bmatrix} = \begin{bmatrix} 1 & 0 & 0 \\ 0 & -\cos\alpha_c(t) & -\sin\alpha_c(t) \\ 0 & -\sin\alpha_c(t) & \cos\alpha_c(t) \end{bmatrix} \begin{Bmatrix} F_n(t) R_c \\ F_t(t) \\ F_n(t) \end{Bmatrix} \tag{43.14}$$

43.3 Ball Dynamics

By considering the system in Fig. 43.7, where the inner race (body 1), the ball (body 2) and the outer race (body 3) are shown.

$\mathbf{F}_n(t)$ and $\mathbf{F}_t(t)$ are the contact forces between cage and ball, they are opposite to those acting on the cage:

$$\begin{cases} F_n(t) = -C_{sr}\left[\alpha_B(t) - \alpha_P(t)\right] R_P \\ F_t(t) = -f_{SOT} F_n(t) \end{cases} \tag{43.15}$$

The forces $F_n(t)$ and $F_t(t)$ act on the ball only when a cage-ball contact occurs.

Assuming $R_{in} \gg R_B$ it is possible to use cartesian coordinates (x and y) instead of the cylindrical ones, as shown in Fig. 43.7, in this coordinate system $x(t) = \alpha_B(t) R_P$ is the displacement of the ball's center.

All the forces acting on the ball are shown in Fig. 43.7, and they represent:

- $\mathbf{F}_c(t)$ (Centrifugal force on the ball)
- $\boldsymbol{\psi}_x(t)$ (Friction force between outer race and ball)
- $\boldsymbol{\psi}_y(t)$ (Normal force between outer race and ball)
- $\mathbf{F}_n(t)$ (Normal force between cage and ball)
- $\mathbf{F}_t(t)$ (Tangential force between cage and ball)
- $\boldsymbol{\phi}_y(t)$ (Normal force between inner race and ball)
- $\boldsymbol{\phi}_x(t)$ (Friction force between inner race and ball)
- $\mathbf{P}$ (Weight of the ball)

43.3.1 Pure Stick Motion

The ball lies in a pure stick motion if the following kinematics and dynamical conditions are verified:

$$\begin{cases} \mathbf{v}_{P,2}(t) = \mathbf{v}_{P,1}(t) \\ \mathbf{v}_{Q,2}(t) = \mathbf{v}_{Q,3}(t) \\ |F_n(t)| < \phi_x(t) - \psi_x(t) \\ |F_t(t)| < -\phi_x(t) - \psi_x(t) \end{cases} \tag{43.16}$$

where the subscript index represents the point (via the letter) and the part (via the number) on which the velocity is considered.

For the second Newton's law along y, we obtain:

$$F_c(t) + F_t(t) - \psi_y(t) + \phi_y(t) - P = 0 \tag{43.17}$$

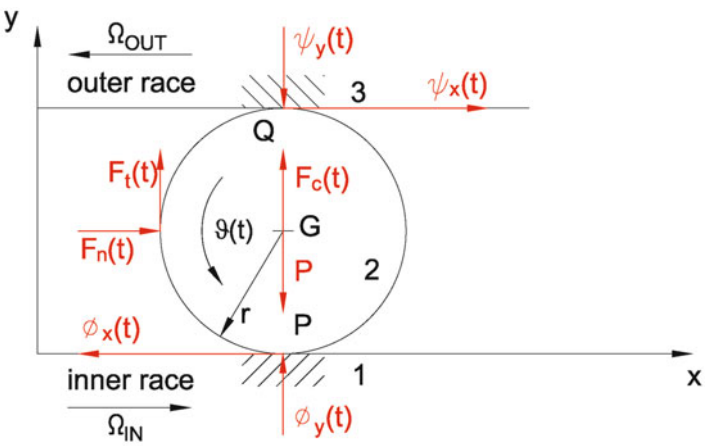

Fig. 43.7 Dynamical system in cartesian coordinates

The weight P can be neglected if the bearing has a vertical revolutional axis, the normal force between the outer race and the ball is actually the bearing's pre-load ψ_y (const. in time) and the centrifugal force $F_c(t)$ is expressed by:

$$F_c(t) = M_B \frac{\dot{x}^2(t)}{R_P} = M_B \dot{\alpha}_B^2(t) R_P \tag{43.18}$$

Equation (43.17) is rewritten as:

$$\phi_y(t) = \psi_y - M_B \dot{\alpha}_B^2(t) R_P - F_t(t) \tag{43.19}$$

According to the Coulomb-Morin law, the static friction forces can be expressed as:

$$\begin{cases} \psi_x = f_{SOT} \psi_y \\ \phi_x(t) = f_{SOT} \phi_y(t) = \psi_x - f_{SOT} M_B \dot{\alpha}_B^2(t) R_P - f_{SOT} F_t(t) \end{cases} \tag{43.20}$$

Equation (43.16) leads to:

$$\begin{cases} \dot{\alpha}_B(t) = \frac{R_{in}(\Omega_{OUT} - \Omega_{IN}) + 2R_B \Omega_{OUT}}{2R_P} \\ \dot{\vartheta}(t) = \frac{R_{in}(\Omega_{OUT} + \Omega_{IN}) + 2R_B \Omega_{OUT}}{2R_B} \\ |F_n(t)| < -f_{SOT} M_B \dot{\alpha}_B^2(t) R_P - f_{SOT} F_t(t) \\ |F_t(t)| < -2\psi_x + f_{SOT} M_B \alpha_B^2(t) R_P + f_{SOT} F_t(t) \end{cases} \tag{43.21}$$

In the pure rolling case, the equations of motion are:

$$\begin{cases} \ddot{\alpha}_B(t) = 0 \\ \ddot{\vartheta}(t) = 0 \end{cases} \tag{43.22}$$

with the following initial conditions:

$$\begin{cases} \alpha_{Bi}(0) = \frac{2\pi}{n}(i-1) \\ \dot{\alpha}_{Bi}(0) = \frac{R_{in}(\Omega_{OUT} - \Omega_{IN}) + 2R_B \Omega_{OUT}}{2R_P} \\ \vartheta_i(0) = 0 \\ \dot{\vartheta}_i(0) = \frac{R_{in}(\Omega_{OUT} + \Omega_{IN}) + 2R_B \Omega_{OUT}}{2R_B} \end{cases} \tag{43.23}$$

43.3.2 Stick-Slip Motion

When the stick conditions (43.21) are not verified, the external forces and torques acting on the ball are bigger than the static friction forces between ball and races, the relative velocity of the contact point is different to zero.

In this case the ball begins to slip on the races and the new equations of motion are:

$$\begin{cases} M_B \ddot{\alpha}_B(t) R_P = F_n(t) + \psi_x(t) - \phi_x(t) \\ I_B \ddot{\vartheta}(t) = F_t(t) R_B + \phi_x(t) R_B + \psi_x(t) R_B \end{cases} \tag{43.24}$$

where this time $\phi_x(t)$ and $\psi_x(t)$ are dynamical friction forces, expressed by:

$$\begin{cases} \psi_x(t) = \mu_d^I \psi_y(t) \\ \phi_x(t) = \mu_d^{II} \phi_y(t) \end{cases}$$

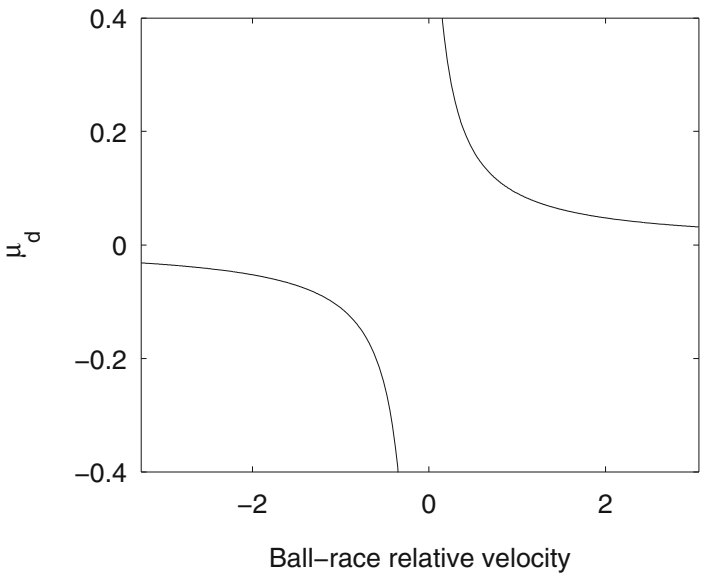

Fig. 43.8 Dynamical friction coefficient

where μ_d^I and μ_d^{II} are the dynamical friction coefficients between ball and outer race and between ball and inner race, respectively:

$$\begin{cases} \mu_d^I = -\frac{f_{SOT}\,\mathrm{sgn}\left[v_{Q,2}(t)-v_{Q,3}\right]}{1+\gamma\left|v_{Q,2}(t)-v_{Q,3}\right|} = -\frac{f_{SOT}\,\mathrm{sgn}\left[-\dot{\vartheta}_B(t)R_P-\dot{\vartheta}(t)R_B+\Omega_{out}R_{out}\right]}{1+\gamma\left|-\dot{\alpha}_B(t)R_P-\dot{\vartheta}(t)R_B+\Omega_{out}R_{out}\right|} \\ \mu_d^{II} = -\frac{f_{SOT}\,\mathrm{sgn}\left[v_{P,2}(t)-v_{P,1}\right]}{1+\gamma\left|v_{P,2}(t)-v_{P,1}\right|} = -\frac{f_{SOT}\,\mathrm{sgn}\left[-\dot{\vartheta}_B(t)R_P+\dot{\vartheta}(t)R_B-\Omega_{in}R_{in}\right]}{1+\gamma\left|-\dot{\alpha}_B(t)R_P+\dot{\vartheta}(t)R_B-\Omega_{in}R_{in}\right|} \end{cases} \tag{43.25}$$

The dynamical friction coefficients expressed in Eq. (43.25) takes into account also the direction of the relative velocity between ball and races.

γ represents the slope of the non linear dynamical friction coefficient shown in Fig. 43.8.

43.4 Results

In this section the kinematic and dynamic results for a single cage revolution are shown, a probabilistic analysis is done in order to demonstrate that the new cage geometry increases the cage life reducing the number of dangerous impacts in the bearing.

Figure 43.9 shows that the radial displacement $\rho(t)$ of the cage appears to have an harmonic solution with a varying mean value. This behaviour is a results of the various forces acting on the cage (e.g. inertial, contact, friction), this kind of solution is purely chaotic because it is possible to predict the solution shape but its location is unpredictable in time.

The various contacts in the bearing give to the cage motion a variable dependent solution, each variation in the bearing parameters (geometrical and dynamical) will affect the cage behavior.

43.4.1 Kinematic Results

In Fig. 43.10, all the displacements and the velocity of the three degrees of freedom of the cage are shown. It is important to underline that the angular position $\alpha(t)$ of the cage has a linear trend (Fig. 43.10a), as expected for the constant velocity of the shaft Ω_{out}, but its velocity $\dot{\alpha}(t)$ (Fig. 43.10b) oscillates in a non predictable way around the pure rolling velocity of the balls group. This aspect is due to the collisions between balls and cage and between race and cage during its motion.

In this particular cage revolution the cage is always in contact with the race because $\rho(t) > \rho_m$, the solutions $\rho(t)$ and $\dot{\rho}(t)$ have an harmonic behaviour with a varying mean value and a varying amplitude, respectively. The harmonic behavior

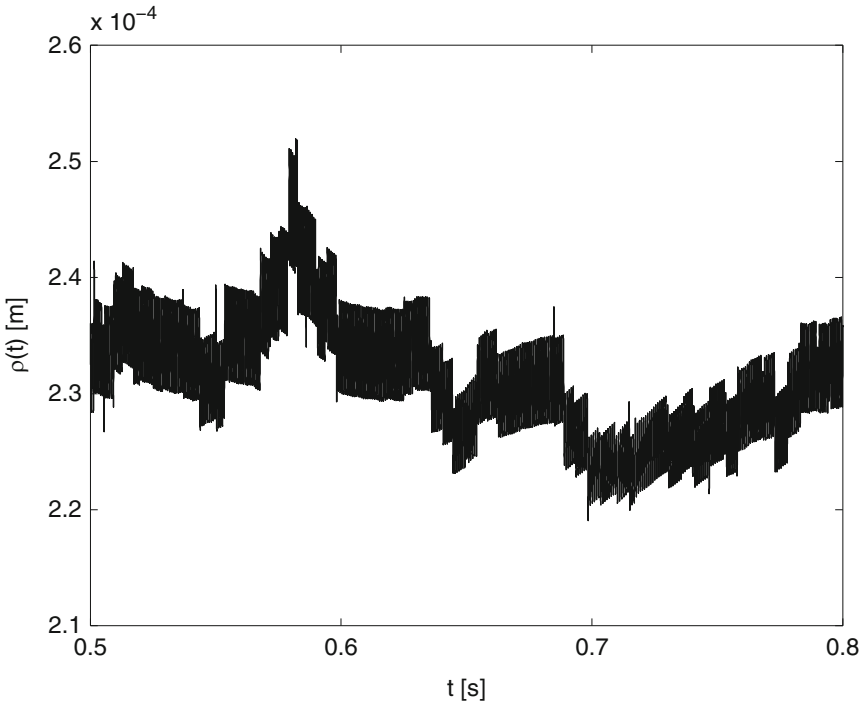

Fig. 43.9 Radial displacement ρ(t)

of the solutions is a due to the contacts between the cage and all the bearing elements, that are modelled with an harmonic oscillator, where the stiffness is obtained via the Hertzian model.

As for the $\alpha(t)$ (Fig. 43.10a) also the angular positions of a generic ball, $\alpha_B(t)$ and $\vartheta_B(t)$, have a linear trend (Fig. 43.11a, c), while the angular velocities $\dot{\alpha}_B(t)$ and $\dot{\vartheta}_B(t)$ oscillate around a constant value.

According to the kinematic and geometric parameters of the bearing (Table 43.1), the pure rolling angular velocities for a generic ball are $\dot{\alpha}_B(t) = 145$ and $\dot{\vartheta}_B(t) = 755$ rad/s, the oscillating solutions presented in the plots suggest that there is always a stick-slip motion of the ball during the simulation. The sliding behaviour is important in the ball dynamics and it has a relevant influence on the cage motion.

43.4.2 Dynamic Results

The cage-balls interactions are plotted in Fig. 43.12. Instead of having a continuous solution for the forces between cage and balls (typical scenario for the common cage geometry Fig. 43.1a), the new cage geometry induces just few collision in a complete cage revolution, this phenomenon suggests a reduction of the cage wear during its motion.

The cage-race interactions, shown in Fig. 43.13, are more continuous than the cage-balls collisions, the plots show that the cage is always in contact with the race and the interactions have the same magnitude of the cage-balls forces for this particular cage revolution.

As the angular velocity of the shaft Ω_{out} is constant, the acceleration of the cage must be zero or very close to this value (the contacts in the bearing have an effect on the cage angular velocity), this aspect is very clear from the torque plots (Figs. 43.12c and 43.13c). The magnitude of M_{zB} il always zero unless there is a ball-cage collision where the torque is in any case very low, and M_{zR} is continuous but still very low in magnitude and with a zero mean value.

Considering a very long simulation ($t = 5$ s) the force results are completely different.

In Fig. 43.14, the absolute value of the interactions are shown, the cage-race forces are almost constant to a $F_R(t) \simeq 12$ N while the cage-ball forces are impulsive and they reach very high values ($F_B \in [50;\ 150]$ N).

While the cage-ball forces are very high in magnitude, it is important to reduce the number of contacts adopting the new cage geometry.

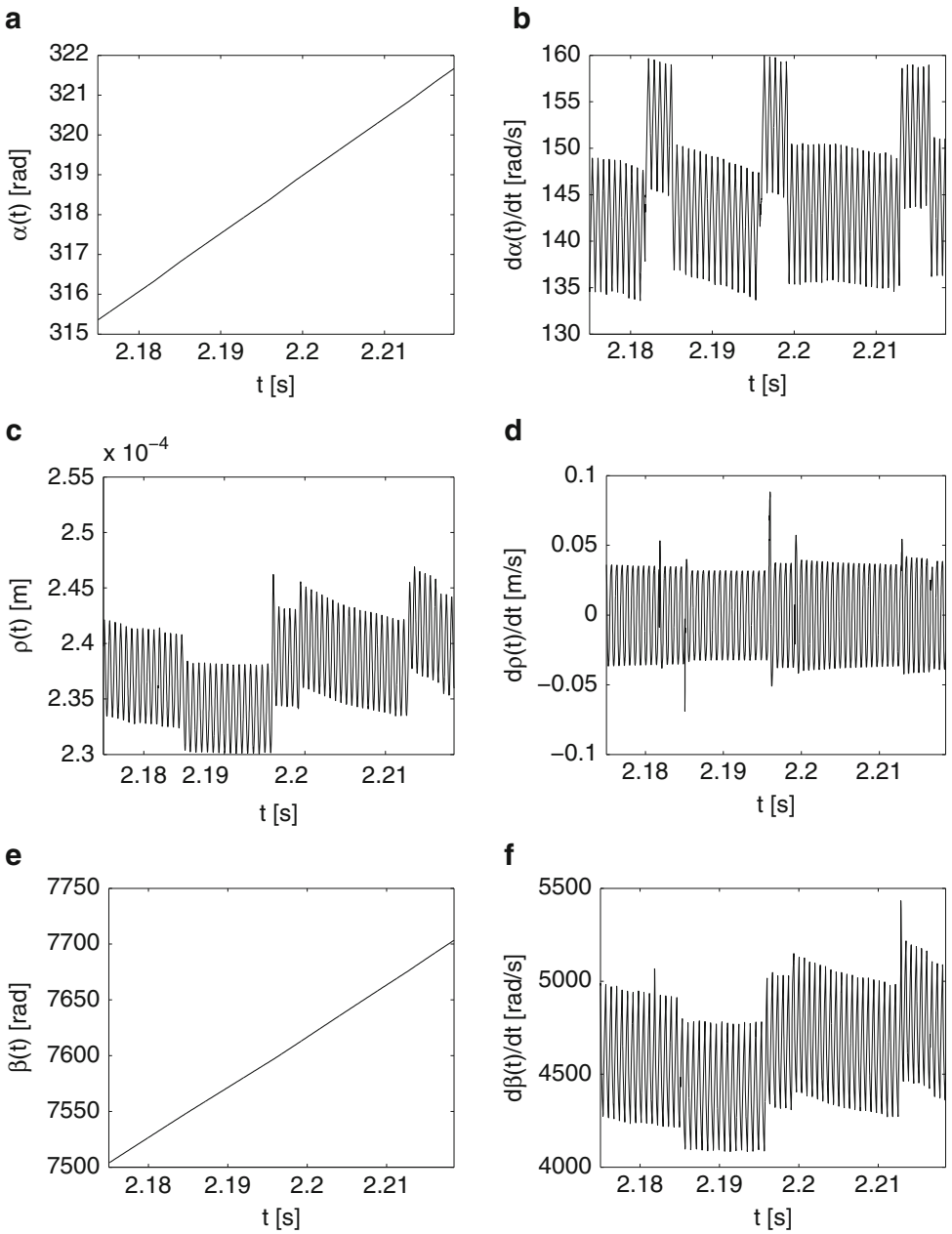

Fig. 43.10 Cage kinematic solutions: angular displacement (**a**), angular velocity (**b**), center radial displacement (**c**), center radial velocity (**d**), center angular displacement (**e**), center angular velocity (**f**)

43.4.3 Probabilistic Analysis

The probabilistic density function (pdf) of the cage-race forces is very similar to the normal distribution (Fig. 43.15a), the normal probability plot in Fig. 43.15b shows that the force distribution is a Gaussian distribution for $F_R \in [11; 17]$ N that are also the values in the most probable range $p \in [-3\sigma; 3\sigma]$.

For the cage-balls forces, the pdf is completely different from the normal distribution (Fig. 43.16a), because of the dispersion of the signal ($F_B < 30$ N and $F_B > 60$ N) but the most probable value of F_B is three times bigger than the cage-race probable value.

This result confirms that the cage-balls forces are dangerous for the bearing, and the new cage geometry, reducing the number of impacts, increases the bearing life.

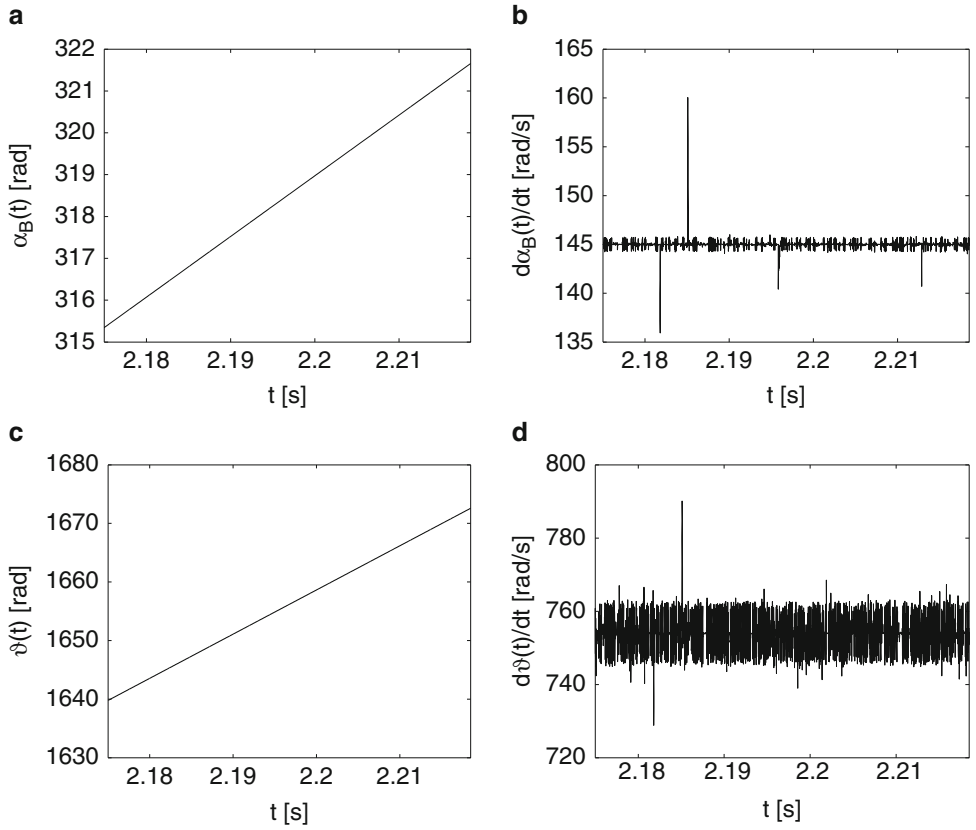

Fig. 43.11 Generic ball kinematic solutions: ball angular displacements (**a**, **c**), ball angular velocities (**b**, **d**)

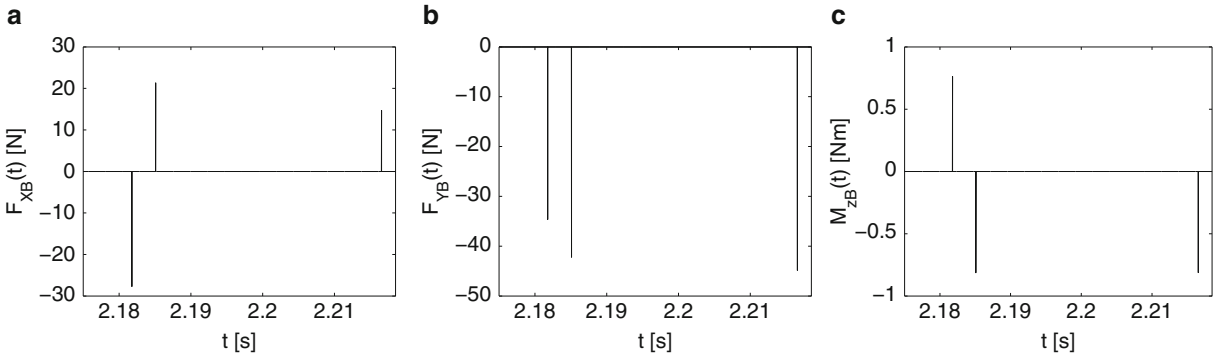

Fig. 43.12 Cage-balls interactions: force along X (**a**), force along Y (**b**), torque (**c**)

43.5 Concluding Remarks

In this paper a different geometrical solution for the cage of the rolling bearing is presented. The idea is to design the retainer with a cage-ball clearance bigger than the cage-race one in order to reduce the number of cage-ball contacts.

A lumped dynamical model is used to simulate both the cage and the balls motions, the cage is studied with three degrees of freedom while the balls are modelled taking into account not only the pure rolling motion but also the slip one.

The kinematic and dynamical results obtained, show that the balls have a switching motion from stick (pure rolling) to slip (sliding) on the races.

The contact forces analysis highlights the big impact of the ball forces on the cage, the different geometry of the cage allows just few cage-ball impact in a single cage revolution, this design solution can increase the bearing life.

Acknowledgements This research is supported by European Space Agency ESA-ESTEC, The Netherlands.

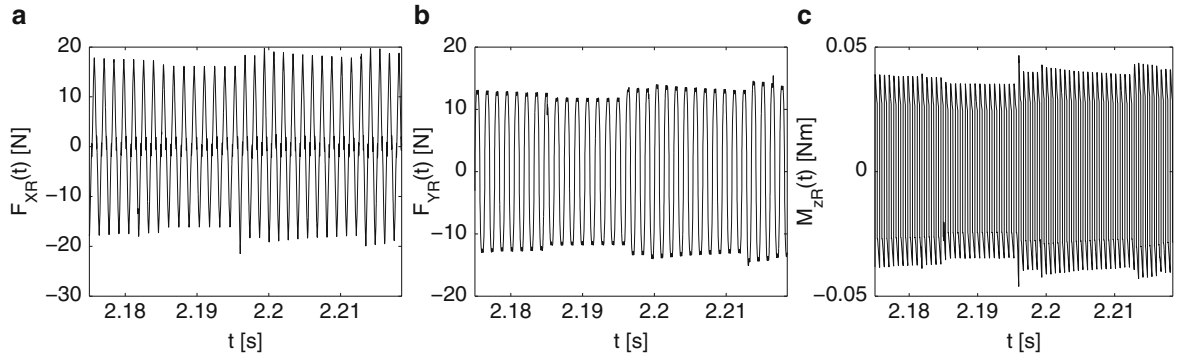

Fig. 43.13 Cage-race interactions: force along X (**a**), force along Y (**b**), torque (**c**)

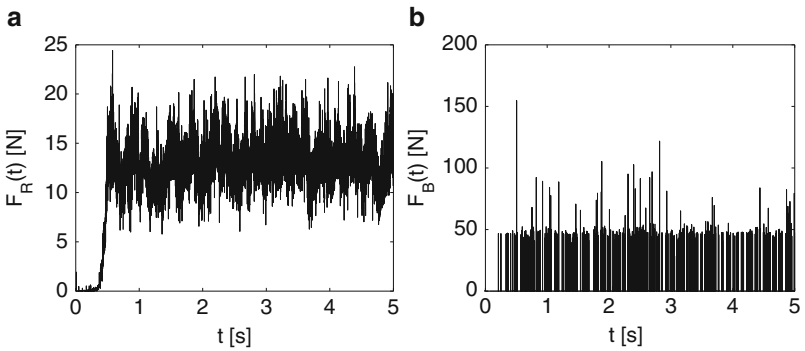

Fig. 43.14 Cage-race contact force (**a**); cage-balls contact force (**b**)

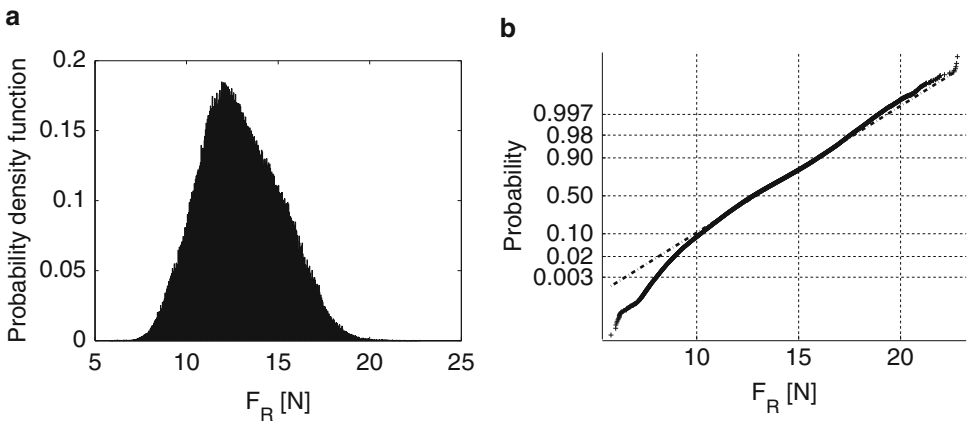

Fig. 43.15 Probability density function (**a**) and normal probability plot (**b**) between cage and race

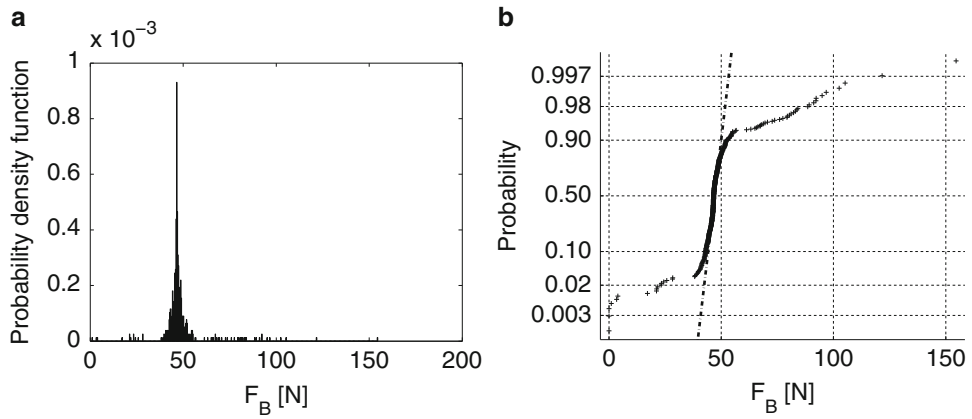

Fig. 43.16 Probability density function (**a**) and normal probability plot (**b**) between cage and balls

References

1. Kingsbury E, Walker R (1994) Motions of an unstable retainer in an instrument ball bearing. ASME Trans J Tribol 202:202–208
2. Boesiger EA, Donley AD, Loewenthal S (1992) An analytical and experimental investigation of ball bearing retainer instabilities. ASME Trans J Tribol 114:530–539
3. Kannel JW (1978) A simplified model of cage motion in angular contact bearings operating in the EHD lubrification regime. ASME Trans J Lubr Technol 100:395–403
4. Walters CT (1971) The dynamics of ball bearings. ASME Trans J Lubr Technol 93:1–10
5. Johnson KL (1985) Contact mechanics. Cambridge University Press, Cambridge

Chapter 44
Bias Errors of Different Simulation Methods for Linear and Nonlinear Systems

Yousheng Chen, Kjell Ahlin, and Andreas Linderholt

Abstract Responses of mechanical systems are often studied using numerical time-domain methods. Discrete excitation forces require a transformation of the dynamic system from continuous time into discrete time. Such a transformation introduces an aliasing error. To reduce the aliasing error, different discretization techniques are used. The bias errors introduced by some discretization techniques are studied in this paper.

Algebraic expressions of the bias error obtained for some discretization methods are presented. The bias error depends on the assumption of the characteristics of the load between two subsequent time steps; here the zero-order, first-order and Lagrange second-order assumptions are studied. Different simulation methods are also studied for numerical evaluation of the derived theoretical bias errors. The discretization techniques are implemented for Runge–Kutta, the Digital Filter method and the Pseudo Force in State Space method.

The study is carried out for both a linear and a nonlinear system; two numerical examples assist in validating the theory. Perfect matches between the numerically estimated bias errors and the theoretical ones are shown. The results also show that, for the nonlinear example, the fourth order Runge–Kutta method produces data that gives less accuracy in the following system identification than the Digital Filter and the used single step Pseudo Force in State Space method do.

Keywords Bias error • Numerical methods • Digital filter • State space • Frequency response function

44.1 Introduction

In simulations, time domain methods are the most general in terms of restrictions of nonlinearities, periodicity etc. Such a computer based simulation is generally based on discrete time steps. Hence, a transformation of the system's description from continuous in time to discrete is necessary. Such a transformation introduces an aliasing error, which can give a considerable error to in the simulated response. To reduce the aliasing error, different discretization methods can be utilized, however, the discretization methods also cause bias errors.

The bias error depends on the assumption made on the input between two successive samples. Commonly used discretization methods are the zero-order-hold (step invariant) and non-casual first-order-hold (ramp invariant) methods, which are described in [1]. These methods require the sampling frequency to be large enough to ensure accuracy. To improve the accuracy further, the Taylor series based second-order-hold discretization algorithm was proposed in paper [2]. The second-order-hold equivalent discretization algorithms, using forward, center, backward and Taylor were studied for stability consideration in [3].

The effect of different discretization methods has traditionally been studied on linear systems. In paper [4], the bias error of the zero-order-hold (ZOH) and first-order-hold (FOH) discretization schemes for a linear system were derived. In this paper, the theoretical bias error of the LSOH discretization scheme is shown, and then the analysis is extended to also consider an example where the system has a significant nonlinearity. The theoretical discretization dependent bias errors for a linear system and a system with a hardening spring are derived for the ZOH, FOH and Lagrange second order hold (LSOH) method.

In addition to different discretization methods, different numerical algorithms are also studied in this paper. The ZOH, FOH, and LSOH are implemented for three numerical methods; the traditional fourth order Runge–Kutta (RK4), the Digital

Y. Chen (✉) • A. Linderholt
Department of Mechanical Engineering, Linnaeus University, Växjö, Sweden
e-mail: yousheng.chen@lnu.se

K. Ahlin
Xielalin Consulting, Akersberga, Sweden

G. Kerschen (ed.), *Nonlinear Dynamics, Volume 1*, Conference Proceedings of the Society for Experimental Mechanics Series, DOI 10.1007/978-3-319-15221-9_44

Filter (DF) method and the single step Pseudo Force in State Space (PFSS) method. The DF method using the FOH for calculation of time response of a nonlinear system is proposed in [4] and it has then been extensively studied in [5, 6]. In this paper, the LSOH is for the first time proposed for the DF simulation method. The PFSS method is a recently developed state space based force feedback method [7, 8], in which the nonlinear feedback force is updated adaptively. In this paper, the single step PFSS method is proposed, which is a modified PFSS method since the nonlinear feedback force is updated for each time step.

The bias error is illustrated using a linear multiple-degree-of-freedom system (MDOF) and a nonlinear system that consists of a single-degree-of-freedom system (SDOF) and a cubic spring, e.g., a Duffing system. Frequency response functions (FRFs) are utilized to demonstrate the bias error introduced by the different methods. The bias errors are illustrated by comparisons between the theoretical FRFs for the system and the FRFs calculated using the simulated time data. The nonlinear example is not as straightforward to analyze since traditional FRFs are not defined for nonlinear systems. In this study, the problem is solved by using the reverse-path (RP) method [9]. With this method, linear FRFs which describe the underlying linear system and the nonlinear coefficients can be obtained. Hence, the reverse path method is used on simulated data and the identification result is compared with theoretical data to show the bias error due to different discretization methods.

44.2 Theoretical Background

It is essential to make a transformation of a model from continuous time to discrete time, when discrete time loads are to be used. No exact solution exists, when a given continuous transfer function, H(s), is converted into a discrete time transfer function H(z). The reason is that H(s) is based on the complete frequency range $f \in [-\infty, +\infty]$, while H(z) is based on $f \in [-\mathrm{fs}/2, +\mathrm{fs}/2]$ where fs is the sampling frequency.

Different discretization assumptions of the input will give different discrete transfer functions of the system. Commonly used discretization assumptions are the impulse invariant, ZOH, FOH, and LSOH.

For a general nonlinear mechanical system, the governing equation of motion can be expressed as

$$\mathbf{M}\ddot{\boldsymbol{q}} + \mathbf{C}\dot{\boldsymbol{q}} + \mathbf{K}\boldsymbol{q} + \boldsymbol{g}\left(\boldsymbol{q}, \dot{\boldsymbol{q}}\right) = \boldsymbol{f}\left(t\right) \tag{44.1}$$

in which $\mathbf{M}$, $\mathbf{C}$, $\mathbf{K}$ are the mass, damping and stiffness matrices respectively, while $\ddot{\boldsymbol{q}}$, $\dot{\boldsymbol{q}}$, $\boldsymbol{q}$, $\boldsymbol{g}$ and $\boldsymbol{f}$ are the acceleration, velocity, displacement, nonlinear function of the displacement and velocity as well as the external force vector respectively.

A state vector composed by the displacement $\boldsymbol{q}$ and velocity $\dot{\boldsymbol{q}}$ such that $\boldsymbol{x}^T = \left[\boldsymbol{q}^T \ \dot{\boldsymbol{q}}^T\right]$ is defined. Further, the non-zero elements of the load vector $\boldsymbol{f}$ and $\boldsymbol{g}$ are put into the excitation vector $\boldsymbol{u}$. Hence, the nonlinear feedback forces are included in the excitation vector $\boldsymbol{u}$. Then, with a proper Boolean distribution matrix $\boldsymbol{P}_u$;

$$\boldsymbol{P}_u\boldsymbol{u} = \boldsymbol{f} - \boldsymbol{g}\left(\boldsymbol{q}, \dot{\boldsymbol{q}}\right) \tag{44.2}$$

and Eq. 44.1 can be recast into a state space form as

$$\begin{aligned} \dot{\boldsymbol{x}} &= \mathbf{A}_\mathrm{c}\boldsymbol{x} + \mathbf{B}_\mathrm{c}\boldsymbol{u} \\ \boldsymbol{y} &= \mathbf{C}_\mathrm{c}\boldsymbol{x} + \mathbf{D}_\mathrm{c}\boldsymbol{u} \end{aligned} \tag{44.3}$$

The matrices $\mathbf{A}_\mathrm{c}$, $\mathbf{B}_\mathrm{c}$, $\mathbf{C}_\mathrm{c}$ and $\mathbf{D}_\mathrm{c}$ are the continuous state-space matrices which are constant for linear and time-invariant (LTI) systems. The $\mathbf{A}_\mathrm{c}$ and $\mathbf{B}_\mathrm{c}$ matrices can be written as:

$$\mathbf{A}_\mathrm{c} = \begin{bmatrix} 0 & \mathbf{I} \\ -\mathbf{M}^{-1}\mathbf{K} & -\mathbf{M}^{-1}\mathbf{C} \end{bmatrix} \mathbf{B}_\mathrm{c} = \begin{bmatrix} 0 \\ \mathbf{M}^{-1} \end{bmatrix} \boldsymbol{P}_u \tag{44.4}$$

To obtain a numerical solution for general excitations, the system has to be converted into a time discrete form;

$$\boldsymbol{x}\left(nT + T\right) = \boldsymbol{e}^{\mathbf{A}_\mathrm{c}\mathrm{T}}\boldsymbol{x}(nT) + \mathbf{B}_\mathrm{c}\int_{n\mathrm{T}}^{n\mathrm{T}+\mathrm{T}} \mathrm{e}^{\mathbf{A}_\mathrm{c}(nT+T-\tau)}\boldsymbol{u}\left(\tau\right)d\tau \tag{44.5}$$

Here, T is chosen as a fixed time-step.

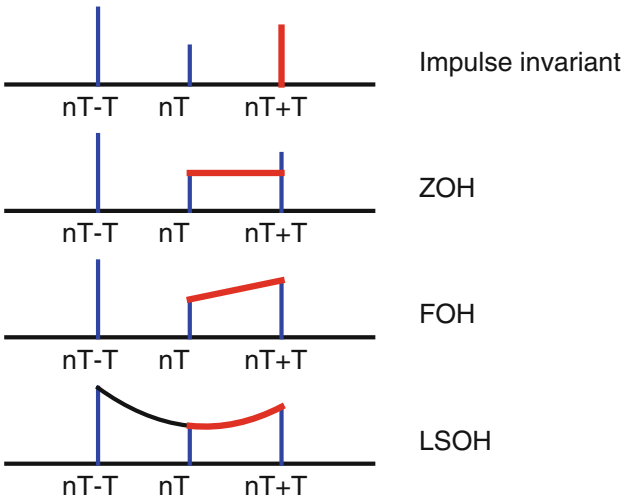

Fig. 44.1 Different assumptions of a discrete load, $\boldsymbol{u_d}(\tau)$, in the interval [nT, n$T + T$]

The integral expression in Eq. 44.5 can only be calculated approximately for a general loading $\boldsymbol{u}$. Hence, a bias which depends on the assumption on the load that is used in the integration is introduced. Different assumptions on a discrete load u_d that are considered in this paper can be seen in Fig. 44.1.

As shown in Fig. 44.1, for the impulse invariant, only the discrete value at (n$T + T$) is used. For step invariant, the value at nT is used for the whole interval. For ramp invariant, a linear function from the value at nT to the value at (n$T + T$) is used. Finally, for LSOH, a second order polynomial fit to the values at (n$T - T$), nT and (n$T + T$) is used.

44.2.1 Aliasing Error

In general, the sampled response y(t) of a system will suffer from aliasing. The spectrum of the sampled response $Y_a(f)$ will have contributions from the original spectrum $Y(f)$ centered around multiples of the sampling frequency f_s [4].

$$Y_a(f) = Y(f) + \sum_{n=1}^{\infty} Y\,(f - nf_s) + Y\,(f + nf_s) \tag{44.6}$$

As an example, the theoretical FRF for an undamped SDOF system with mass m and spring stiffness k is given below.

$$H(f) = \frac{1}{k - m(2\pi f)^2} \tag{44.7}$$

Using the formula shown in Eq. 44.6 the aliased FRF for the undamped SDOF system can be expressed as

$$H_a(f) = \frac{1}{k - m(2\pi f)^2} + \sum_{n=1}^{\infty} \frac{1}{k - m(2\pi\,(f - n \cdot f_s))^2} + \frac{1}{k - m(2\pi\,(f + n \cdot f_s))^2} \tag{44.8}$$

For $f = 0$, the sum can be shown to have a compact expression:

$$\mathrm{H}_a(0) = \frac{\sqrt{k/m}}{2kf_s} \cot\left(\frac{\sqrt{k/m}}{2f_s}\right) \tag{44.9}$$

This result is related to the discretization method known as impulse invariant which will be shown next. For an impulse invariant assumption, the discrete transfer function for an SDOF system can be expressed using the residue and pole as follows [4]

$$H(z) = \frac{\mathrm{T}\left(2\mathrm{Re}\left\{\mathrm{R}\right\} - z^{-1}\exp\left(\mathrm{Re}\left\{\lambda\right\}\mathrm{T}\right)\cdot\left(2\mathrm{Re}\left\{\mathrm{R}\right\}\cdot\cos\left(\mathrm{Im}\left\{\lambda\right\}\mathrm{T}\right) - 2\mathrm{Im}\left\{\mathrm{R}\right\}\cdot\sin\left(\mathrm{Im}\left\{\lambda\right\}\mathrm{T}\right)\right)\right)}{1 - 2z^{-1}\exp\left(\mathrm{Re}\left\{\lambda\right\}\mathrm{T}\right)\cdot\cos\left(\mathrm{Im}\left\{\lambda\right\}\mathrm{T}\right) + z^{-2}\cdot\exp\left(2\mathrm{Re}\left\{\lambda\right\}\mathrm{T}\right)} \tag{44.10}$$

where T, R and λ denote the time increment, residue and pole, $\mathrm{Re}\{\cdot\}$ and $\mathrm{Im}\{\cdot\}$ denote the real part and the imaginary part respectively. For an undamped SDOF system, the residue and pole are given by:

$$\mathrm{R} = \mathrm{j}\frac{\sqrt{k/m}}{2k}\ \lambda = \mathrm{j}\sqrt{k/m} \tag{44.11}$$

Inserting these expressions into Eq. 44.10, and letting $z = 1$ (i.e. $f = 0$) gives

$$H\left(z=1\right) = \frac{\sqrt{k/m}}{2kf_s}\cot\left(\frac{\sqrt{k/m}}{2f_s}\right) \tag{44.12}$$

Equations 44.12 and 44.9 are identical, which means that the discrete transfer function using the impulse invariant transformation has the same value as the theoretical aliased transfer function at zero frequency. It shows that it is aliasing that creates the error when sampled data are used. The aliasing error can be decreased by using different discretization methods for the approximation of two successive samples in the cost of a bias error.

44.2.2 Bias Error

In this section, the theoretical bias errors for the impulse invariant, ZOH, FOH, and LSOH discretization techniques are derived. The bias error is described for both linear and nonlinear systems.

44.2.2.1 Linear Systems

Using different discretization techniques, see Fig. 44.1, for the integration of the input in Eq. 44.5 may be seen as a convolution between the discrete load history u_d and a convolution kernel $\mathrm{w}(\tau)$, see Eq. 44.13.

$$u\left(\tau\right) = \int_{-\infty}^{+\infty} u_d\left(v\right)w\left(\tau - v\right)dv \tag{44.13}$$

The convolution kernels for the impulse invariant, ZOH, and FOH methods are given below [4]. For the impulse invariant:

$$w_1\left(\tau\right) = \frac{1}{T}\delta\left(\tau\right) \tag{44.14}$$

where $\delta(\tau)$ is the Dirac delta function.

For the ZOH:

$$w_2\left(\tau\right) = \tfrac{1}{T},\ 0 \le \tau < T \tag{44.15}$$

For the FOH:

$$w_3\left(\tau\right) = \begin{cases} 0, & \tau < -T \\ \frac{1}{T}\left(\frac{\tau}{T} + 1\right), & -T \le \tau < 0 \\ \frac{1}{T}\left(-\frac{\tau}{T} + 1\right), & 0 \le \tau \le T \\ 0, & \tau > T \end{cases} \tag{44.16}$$

Using the LSOH assumption, the input force between $\left[nT,\, nT + T \right]$ can be expressed as

$$\boldsymbol{u}\left(nT + t\right) = \frac{t^2 - tT}{2T^2}\boldsymbol{u}\left(nT - T\right) + \frac{t^2 - T^2}{-T^2}\boldsymbol{u}(nT) + \frac{t^2 + tT}{2T^2}\boldsymbol{u}\left(nT + T\right) \tag{44.17}$$

And the convolution kernel for the LSOH:

$$w_4\left(\tau\right) = \begin{cases} 0, & \tau < -T \\ \dfrac{\tau^2 + 3\tau T + 2T^2}{2T^3}, & -T \le \tau < 0 \\ \dfrac{T^2 - \tau^2}{T^3}, & 0 \le \tau < T \\ \dfrac{\tau^2 - 3\tau T + 2T^2}{2T^3}, & T \le \tau < 2T \\ 0, & \tau \ge 2T \end{cases} \tag{44.18}$$

A convolution in the time domain corresponds to a multiplication in the frequency domain. The Fourier transform of the convolution kernel associated with impulse invariant becomes

$$\mathcal{F}\left(w_1\left(\tau\right)\right) = 1 \tag{44.19}$$

where $\mathcal{F}\left(\cdot\right)$ denotes the Fourier transform. For the ZOH:

$$\mathcal{F}\left(w_2\left(\tau\right)\right) = \frac{\sin\left(\pi f/f_s\right)}{\pi f/f_s}e^{-j\pi f/f_s} \tag{44.20}$$

For the FOH:

$$\mathcal{F}\left(w_3\left(\tau\right)\right) = \left(\frac{\sin\left(\pi f/f_s\right)}{\pi f/f_s}\right)^2 \tag{44.21}$$

Finally, for the LSOH:

$$\mathcal{F}\left(w_4\left(\tau\right)\right) = \frac{\left(1 + \mathrm{j}\pi f/f_s\right)e^{-\mathrm{j}4\pi f/f_s}\left(1 - e^{\mathrm{j}2\pi f/f_s}\right)^3}{\left(-\mathrm{j}2\pi f/f_s\right)^3} \tag{44.22}$$

Using these different discretization techniques, see Fig. 44.1, results in a reduced aliasing error. However, a bias error is introduced. The normalized bias error can be expressed in the frequency domain as

$$\begin{cases} e_i^{amp} = \left|\mathcal{F}\left(w_i\left(\tau\right)\right)\right| - 1 \\ e_i^{phase} = \varphi\left(\mathcal{F}\left(w_i\left(\tau\right)\right)\right) \end{cases} \quad i = 1, 2, 3,\ 4 \tag{44.23}$$

where e_i^{amp} denotes the amplitude error compared with the theoretical spectrum, while e_i^{phase} denotes the phase error in the estimated spectrum and i represents different discretization methods. The FRFs can be expressed as the ratio between the response spectrum and the input spectrum. As the input is known, the spectrum can be calculated without error. Therefore, the FRFs share the same bias error as the response spectrum. In the following section, the bias error is shown by comparing the biased FRF with the theoretical FRF.

As seen in Eq. 44.23, the impulse invariant method has no bias error. Only the convolution kernel for the ZOH, FOH, and LSOH discretization methods together with their corresponding spectra are shown in Fig. 44.2. The resulting bias errors are shown in Fig. 44.3.

As can be seen in Figs. 44.2 and 44.3, the bias spectrum of the ZOH has zeros for multiples of the sampling frequency which helps to decrease the aliasing problem. The ZOH has a quite nice amplitude error but a large phase error. This may lead to stability problem for a nonlinear system since the nonlinear forces are feedback into the system and in a feedback system, phase errors may lead to instabilities. For the FOH, the spectrum is quite flat around the sampling frequency which makes it very efficient to eliminate aliasing.

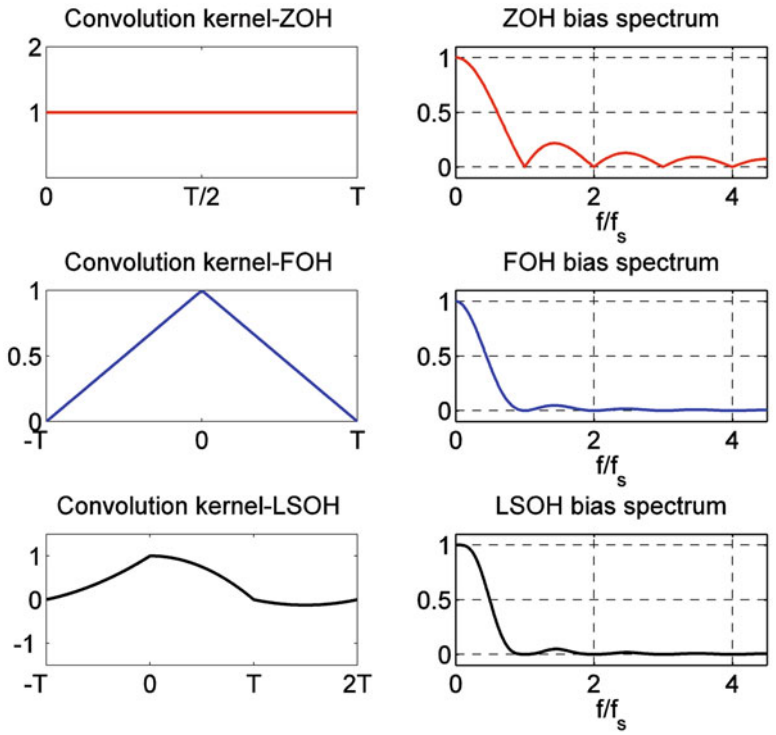

Fig. 44.2 Convolution kernel, to the *left*, and bias spectrum, to the *right*, for the ZOH, FOH, and LSOH

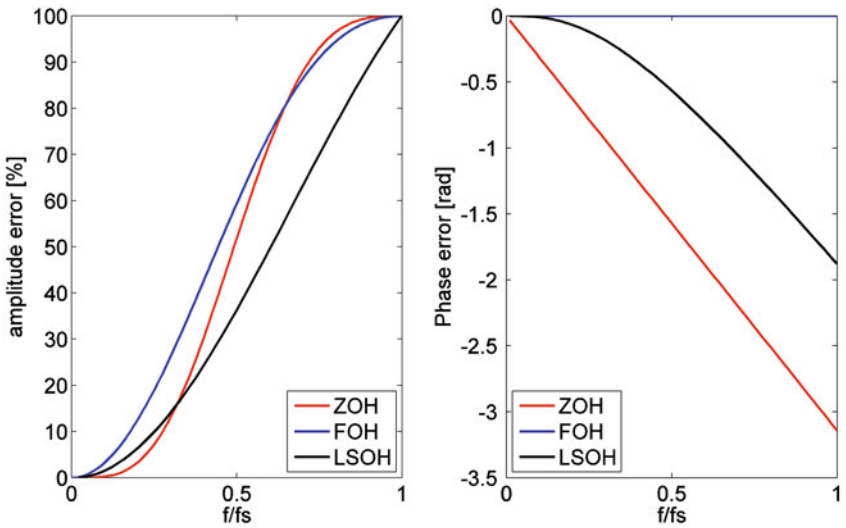

Fig. 44.3 Bias errors for the ZOH, FOH and LSOH; amplitude error to the *left* and phase error to the *right*

Although the FOH has a larger bias error than the ZOH, the zero phase error and its efficient reduction of aliasing lead to its use in many applications. The bias spectrum for the LSOH is approximately equal to one around the low frequencies and very flat around the sampling frequency where it has much smaller amplitude error than the FOH method. However, the LSOH suffers with phase error, but it starts at zero for low frequencies which indicates that the LSOH is a good compromise between aliasing and bias error.

44.2.2.2 Application to Nonlinear Systems

In order to extend the bias error analysis method to a nonlinear system, the nonlinear system is desirably expressed as an underlying linear system and nonlinear coefficients. This is done by using the RP method. Then, the theoretical bias error derived for a linear system can be applied for the underlying linear system. To understand the bias error in the nonlinear coefficients, it is necessary to understand how the nonlinear forces are treated in the different simulation methods.

The forced responses of nonlinear mechanical systems can be calculated using several different time integration methods. In this paper, the RK4, single step PFSS, and DF method are studied.

The RK4 Method

The most commonly used Runge–Kutta method is that of order four known as RK4. The recursion formula for RK4 is

$$x_{n+1} = x_n + \frac{(k_1 + 2k_2 + 2k_3 + k_4)}{6} \tag{44.24}$$

where

$$\begin{cases} k_1 = x\left(t_n, x_n\right)\Delta t \\ k_2 = x\left(t_n + \frac{\Delta t}{2}, x_n + \frac{k_1}{2}\right)\Delta t \\ k_3 = x\left(t_n + \frac{\Delta t}{2}, x_n + \frac{k_2}{2}\right)\Delta t \\ k_4 = x\left(t_n + \Delta t, x_n + k_3\right)\Delta t \end{cases} \tag{44.25}$$

In the RK4, the nonlinear force is calculated using the previous displacement, which then contributes to all the four derivatives calculations.

The DF Method

In the DF method, the underlying linear system is described by its residues and poles and nonlinearities are treated as external forces. Eq. 44.1 can be rewritten as

$$\mathbf{M}\ddot{\boldsymbol{q}} + \mathbf{C}\dot{\boldsymbol{q}} + \mathbf{K}\boldsymbol{q} = \boldsymbol{f}(t) - \boldsymbol{g}\left(\boldsymbol{q}, \dot{\boldsymbol{q}}\right) \tag{44.26}$$

Using the Laplace transformation and the modal superposition theorem for an MDOF system, the FRF for output at DOF i and input at DOF j of the underlying linear system can be expressed as

$$H_{ij}(s) = \sum_{r=1}^{N} \frac{R_r}{s - \lambda_r} + \frac{R_r^*}{s - \lambda_r^*} \tag{44.27}$$

Where R_r are the residues, λ_r are the poles, r is the mode number, N denotes the number of modes and ' * ' denotes complex conjugate. For the discrete time ($nT + T$), the response of the underlying linear system at DOF i, $q_i\ (nT + T)$, due to input at DOF j, f_j, can be calculated using the convolutional integral:

$$\begin{aligned} q_i\ (nT + T) &= \sum_{r=1}^{N} \left\{ \int_0^{nT+T} R_r e^{\lambda_r (nT+T-\tau)} f_j\ (\tau)\, d\tau + \int_0^{nT+T} R_r^* e^{\lambda_r^* (nT+T-\tau)} f_j\ (\tau)\, d\tau \right\} \\ &= \sum_{r=1}^{N} \left\{ e^{\lambda_r T} q_i(nT) + R_r e^{\lambda_r T} \int_0^T e^{-\lambda_r \tilde{\tau}} f_j\ (\tilde{\tau} + nT)\, d\tilde{\tau} + e^{\lambda_r^* T} q_i(nT) \right. \\ &\qquad \left. + R_r^* e^{\lambda_r^* T} \int_0^T e^{-\lambda_r^* \tilde{\tau}} f_j\ (\tilde{\tau} + nT)\, d\tilde{\tau} \right\} \end{aligned} \tag{44.28}$$

The above equation illustrates that $q_i\ (nT + T)$ can be calculated with a recursion formula using only $q_i(nT)$ and the input signal in the interval $[nT, nT + T]$. The discretization methods used to approximate the input between two discrete times define the methods, such as the ZOH, FOH, and LSOH discretization methods. The filter coefficient for ZOH and FOH were derived in [4–6]. Therefore, only the LSOH filter coefficients are derived here. Considering N modes, the Z-domain representation of Eq. 44.28 for the LSOH, can be expressed as

$$
\begin{aligned}
H_{ij}(z) = \Bigg\{ & \frac{\frac{R_r}{2\lambda_r^3 T^2}\left(-2-2\lambda_r^2 T^2-3\lambda_r T+(2+\lambda_r T)e^{\lambda_r T}\right)}{1-z^{-1}e^{\lambda_r T}} \\
& + \frac{z^{-1}\frac{R_r}{2\lambda_r^3 T^2}\left(4\lambda_r T+4-\left(4-2\lambda_r^2 T^2\right)e^{\lambda_r T}\right)}{1-z^{-1}e^{\lambda_r T}} \\
& + \frac{z^{-2}\frac{R_r}{2\lambda_r^3 T^2}\left(-2-\lambda_r T+(2-\lambda_r T)e^{\lambda_r T}\right)}{1-z^{-1}e^{\lambda_r T}} \\
& + \frac{\frac{R_r^*}{2\lambda_r^{*3} T^2}\left(-2-2\lambda_r^{*2} T^2-3\lambda_r^* T+\left(2+\lambda_r^* T\right)e^{\lambda_r^* T}\right)}{1-z^{-1}e^{\lambda_r^* T}} \\
& + \frac{z^{-1}\frac{R_r^*}{2\lambda_r^{*3} T^2}\left(4\lambda_r^* T+4-\left(4-2\lambda_r^{*2} T^2\right)e^{\lambda_r^* T}\right)}{1-z^{-1}e^{\lambda_r^* T}} \\
& + \frac{\frac{R_r^*}{2\lambda_r^{*3} T^2}\left(-2-2\lambda_r^{*2} T^2-3\lambda_r^* T+\left(2+\lambda_r^* T\right)e^{\lambda_r^* T}\right)}{1-z^{-1}e^{\lambda_r^* T}} \Bigg\}
\end{aligned}
\tag{44.29}
$$

Equation 44.29 shows that a set of filter coefficients are needed for each individual mode included in the simulation. By putting the numerator and denominator in vector form

$$
N_{ijr} = \frac{R_r}{2\lambda_r^3 T^2}\begin{bmatrix} -2-2\lambda_r^2 T^2-3\lambda_r T+(2+\lambda_r T)e^{\lambda_r T}, \\ 4\lambda_r T+4-\left(4-2\lambda_r^2 T^2\right)e^{\lambda_r T}, \\ -2-\lambda_r T+(2-\lambda_r T)e^{\lambda_r T} \end{bmatrix} D_{ijr} = \left[1, -e^{\lambda_r T}\right] \tag{44.30}
$$

the filter coefficient a_{ijr} and b_{ijr} can be calculated as follows [4]

$$
\begin{aligned}
a_{ijr} &= \mathrm{Re}\left(D_{ijr} * D_{ijr}^*\right) \\
b_{ijr} &= 2\mathrm{Re}\left(N_{ijr}\right) * \mathrm{Re}\left(D_{ijr}\right) + 2\mathrm{Im}\left(N_{ijr}\right) * \mathrm{Im}\left(D_{ijr}\right)
\end{aligned}
\tag{44.31}
$$

These filter coefficients are valid for the LSOH assumption. With the filter coefficients, Eq. 44.29 can be rewritten as

$$
H_{ij}(Z) = \sum_{r=1}^{M} \frac{b_{ijr}^0 + b_{ijr}^1 z^{-1} + b_{ijr}^2 z^{-2} + b_{ijr}^3 z^{-3}}{1 + a_{ijr}^1 z^{-1} + a_{ijr}^2 z^{-2}} \tag{44.32}
$$

By treating a nonlinear force as an external force, Eq. 44.32 can be used to calculate the nonlinear response. For the example that the nonlinear element is located between dof j and ground, the response of the nonlinear system at time $n\mathrm{T}+\mathrm{T}$ can be rewritten as

$$
\begin{aligned}
\tilde{q}_i(nT+T) = & \sum_{r=1}^{M} b_{ijr}^0\left(f_j(nT+T) - g_j(nT+T)\right) + b_{ijr}^1\left(f_j(nT) - g_j(nT)\right) \\
& + b_{ijr}^2\left(f_j(nT-T) - b_{ijr}^2 g_j(nT-T)\right) \\
& + b_{ijr}^3\left(f_j(nT-2T) - b_{ijr}^3 g_j(nT-2T)\right) - a_{ijr}^1\tilde{q}_i(nT) - a_{ijr}^2\tilde{q}_i(nT-T)
\end{aligned}
\tag{44.33}
$$

A rearrangement of Eq. 44.33 so that all the unknowns are at the left hand side and all the known parameters are at the right side, leads to

$$
\tilde{q}_i(nT+T) + \sum_{r=1}^{M} b_{ijr}^0 g_j(nT+T) = O_r \tag{44.34}
$$

where $O_r = \sum_{r=1}^{M} b_{ijr}^0 f_j(nT+T) + b_{ijr}^1\left(f_j(nT) - g_j(nT)\right) + b_{ijr}^2\left(f_j(nT-T) - b_{ijr}^2 g_j(nT-T)\right) + b_{ijr}^3\left(f_j(nT-2T) - b_{ijr}^3 g_j(nT-2T)\right) - a_{ijr}^1\tilde{q}_i(nT) - a_{ijr}^2\tilde{q}_i(nT-T)$ The equation is recognized as being a nonlinear equation in $\tilde{q}_i$ with g_j being a nonlinear function of $\tilde{q}_i$, which can be solved using the secant method.

The Single Step PFSS Method

The basic idea of the single step PFSS method is to treat nonlinear forces as external forces and formulate the underlying linear system in state-space form.

To begin with, a linear state-space model for the underlying linear system, see Eq. 44.3, is defined. Then, the state-space model is discretized using one of the discretization techniques. The discretized system can be represented as

$$\begin{cases} \boldsymbol{x}\left(nT+T\right)=\boldsymbol{A}_d\boldsymbol{x}(nT)+\boldsymbol{B}_d\boldsymbol{u}(nT) \\ \boldsymbol{y}\left(nT+T\right)=\boldsymbol{C}_d\boldsymbol{x}\left(nT+T\right)+\boldsymbol{D}_d\boldsymbol{u}\left(nT+T\right) \end{cases} \tag{44.35}$$

in which the state vector at time $t=nT+T$ is obtained from information from the previous time step at $t=\mathrm{n}T$. As shown in [1], for the FOH the discrete system matrices calculated from Eq. 44.5 are given as

$$\begin{cases} \boldsymbol{A}_d=\mathrm{e}^{\boldsymbol{A}_c T} \\ \boldsymbol{B}_d=\frac{1}{T}{\boldsymbol{A}_c}^{-1}{\boldsymbol{A}_c}^{-1}\left(e^{\boldsymbol{A}_c T}-\boldsymbol{I}\right)^2\boldsymbol{B}_c \\ \boldsymbol{C}_d=\boldsymbol{C}_c \\ \boldsymbol{D}_d=\boldsymbol{D}_c+\boldsymbol{C}_c\left(-{\boldsymbol{A}_c}^{-1}+\frac{1}{T}{\boldsymbol{A}_c}^{-1}{\boldsymbol{A}_c}^{-1}\left(e^{\boldsymbol{A}_c T}-\boldsymbol{I}\right)\right)\boldsymbol{B}_c \end{cases} \tag{44.36}$$

When the input force and the grounded nonlinear element are at the same DOF j, then the response at DOF i can be calculated as

$$y_i\left(nT+T\right)=\boldsymbol{C}_d\left(\boldsymbol{A}_d x(nT)+\boldsymbol{B}_d\left(f_j(nT)-g_j(nT)\right)\right)+\boldsymbol{D}_d\left(f_j\left(nT+T\right)-g_j\left(nT+T\right)\right) \tag{44.37}$$

A rearrangement of Eq. 44.37 so that all the unknowns are at the left hand side and all the knowns are at the right hand side gives

$$y\left(nT+T\right)+\boldsymbol{D}_d g_j\left(nT+T\right)=\tilde{O} \tag{44.38}$$

where $\tilde{O}=\boldsymbol{C}_d\left(\boldsymbol{A}_d x(nT)+\boldsymbol{B}_d\left(f_j(nT)-g_j(nT)\right)\right)+\boldsymbol{D}_d f_j\left(nT+T\right)$.

As for the DF method, $\tilde{O}$ is completely determined by the past values together with the currently applied force. This function can be solved using the secant method for each time step.

Identification Method

For a nonlinear system, the underlying linear system together with nonlinear coefficients are identified using the RP method in this paper. The bias errors are shown for the underlying linear system and the estimated nonlinear coefficients.

The RP method is a common strategy for nonlinear system identification, and it has been proposed to many nonlinear systems [10, 11]. The fundamental idea of the RP method is to redefine the system as a MISO (Multiple-Input/Single-Output) and treat the nonlinear forces as artificial inputs.

As an example, the RP method for a Duffing system is illustrated below. The governing equation for a Duffing system can be written as

$$m\ddot{q}+c\dot{q}+kq+pq^3=f(t) \tag{44.39}$$

The Fourier transform of both sides of Eq. 44.39 renders in

$$\left(-\omega^2 m+jc\omega+k\right)Q\left(\omega\right)+p\mathcal{F}\left(q^3\right)=F\left(\omega\right) \tag{44.40}$$

Using the RP method, the Duffing system can be represented in the frequency domain as a MISO system as shown in Fig. 44.4 and Eq. 44.41.

$$H^{-1}\left(\omega\right)Q\left(\omega\right)+\mathrm{p}\left(\omega\right)\mathcal{F}\left(q^3\right)=F\left(\omega\right) \tag{44.41}$$

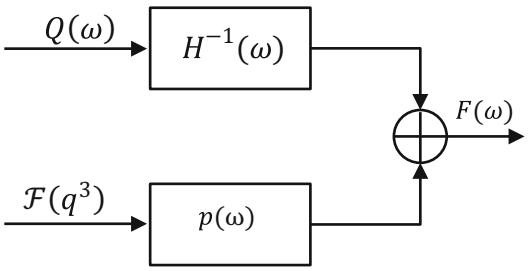

Fig. 44.4 The RP method illustrated for a Duffing system

With the denotation $\mathcal{F}\left(q^3\right) = Q_3\left(\omega\right)$, the equation can be rearranged in a matrix form as

$$\left[\, H^{-1}\left(\omega\right) \mathrm{p}\left(\omega\right) \right] \begin{bmatrix} Q\left(\omega\right) \\ Q_3\left(\omega\right) \end{bmatrix} = F\left(\omega\right) \tag{44.42}$$

Multiplying both sides of Eq. 44.42 with $\left[\, \mathrm{Q}^*\left(\omega\right)\ \mathrm{Q}_3^*\left(\omega\right) \right]$

$$\left[\, H^{-1}\left(\omega\right) \mathrm{p}\left(\omega\right) \right] \begin{bmatrix} Q\left(\omega\right) \\ Q_3\left(\omega\right) \end{bmatrix} \left[\, Q^*\left(\omega\right)\ Q_3^*\left(\omega\right) \right] = F\left(\omega\right) \left[\, Q^*\left(\omega\right)\ Q_3^*\left(\omega\right) \right] \tag{44.43}$$

$$\left[\, H^{-1}\left(\omega\right) \mathrm{p}\left(\omega\right) \right] \begin{bmatrix} Q\left(\omega\right) Q^*\left(\omega\right) & Q\left(\omega\right) Q_3^*\left(\omega\right) \\ Q_3\left(\omega\right) Q^*\left(\omega\right) & Q_3\left(\omega\right) Q_3^*\left(\omega\right) \end{bmatrix} = \left[F\left(\omega\right)\ Q^*\left(\omega\right)\ F\left(\omega\right) Q_3^*\left(\omega\right) \right] \tag{44.44}$$

Taking the expected value of both sides of Eq. 44.45 and using the definition of auto-spectral density and cross-spectral density, the equation can be rewritten as follows

$$\left[\, H^{-1}\left(\omega\right) \mathrm{p}\left(\omega\right) \right] = \left[\, G_{FQ}\ G_{FQ_3} \right] \begin{bmatrix} G_{QQ} & G_{QQ_3} \\ G_{Q_3Q} & G_{Q_3Q_3} \end{bmatrix}^{-1} \tag{44.45}$$

where, as an example, G_{FQ} denotes the cross-spectral density between the input force $F(\omega)$ and the response $Q_3(\omega)$. Similarly, $G_{Q_3Q_3}$ denotes the auto spectral density of the nonlinear force $Q_3(\omega)$. From Eq. 44.45, the underlying linear system $H^{-1}\left(\omega\right)$ and the nonlinear coefficient $\mathrm{p}(\omega)$ can be identified.

Bias Error for Nonlinear Systems

As a nonlinear system can be modelled as an underlying linear system and nonlinear coefficients, the bias error for a nonlinear system are shown for its underlying linear system $H^{-1}\left(\omega\right)$ and the nonlinear coefficients $\mathrm{p}(\omega)$. The derived theoretical bias error expression for a linear system can be used for the underlying linear system $H^{-1}\left(\omega\right)$. The bias error for the nonlinear coefficients $\mathrm{p}(\omega)$ depends on how the nonlinear forces are treated in the simulation methods.

For the RK4 method, the nonlinear forces are calculated using the previous displacement which makes the nonlinear coefficients biased. The bias error for the estimated nonlinear coefficient can be explained by Eq. 44.45. As can be seen in this equation, the inverse of the FRF and the nonlinear coefficient are estimated at the same time using the simulated response and the input force, which indicates that the bias error for the estimated nonlinear coefficient should be the same as the bias error for the estimated inverse of the FRF. For the DF and single step PFSS methods, the nonlinear force are calculated exactly using the simulated response for each time step, which gives no bias error for the nonlinear coefficients. The bias error for a nonlinear system will be illustrated using a Duffing system in the following section.

44.3 Numerical Examples

Two numerical examples; one for a linear system and one for a nonlinear system are studied. The linear example is designed to check different discretization methods' ability to handle aliasing. The nonlinear example is studied to verify the theoretical bias error for the estimated FRF and nonlinear coefficients derived in the previous sections.

44.3.1 A Linear System

An FE model of a rectangular steel plate is studied. A condensed model having a grid of 12 by 12 nodes (144 DOFs), with a resulting mass matrix **M** and a stiffness matrix **K** of size 144 by 144, is used. The plate hangs in springs at the four corners. A modal damping starting at 1 % at the first mode and gradually decreasing to 0.1 % for the highest mode is assumed. This is achieved by creating a suitable, non-physical damping matrix **C**. A measurement of an FRF using a burst random force is simulated, see Fig. 44.5. The force is applied to DOF 1 and the displacement at DOF 49 is calculated. The sampling frequency is 1,200 Hz, and the length of the input signal is 393,216 samples.

The responses of the system are simulated using the RK4, DF, and single step PFSS method. Four different discretization techniques (impulse, ZOH, FOH, and LSOH) are tested for each simulation method. The estimated FRFs obtained from all three simulation methods are compared with the theoretical FRF. It is first verified that, for a linear system, all three simulation methods give identical results when the same discretization technique is used. Therefore, only the results from the DF method are shown in Figs. 44.6 and 44.7.

Using a sampling frequency within the system's frequency range and an alias protected input force, different methods' ability to handle aliasing can be checked. Figs. 44.6 and 44.7 show that the impulse invariant and ZOH give large errors, which indicates that the aliasing of the system response could be disastrous, if not taken care of. It is also shown that the FOH gives a reasonable small error. The LSOH discretization gives the smallest error among the tested discretization methods; this indicates a good compromise between the aliasing error and the bias error. Hence, the FOH and LSOH methods are recommended to be used to reduce the aliasing error.

44.3.2 A Nonlinear System

An SDOF system with a cubic spring (a Duffing system) shown in Fig. 44.8 constitutes the nonlinear example.

The governing equation of motion can be represented by Eq. 44.39 with $m = 1$ kg, $c = 1.25$ Ns/m, $k = 4{,}000$ N/m, $p = 3.5e9$ N/m^3. A random force f polluted with noise, 1 Mega samples long with sampling frequency 500 Hz, is applied.

The response of the nonlinear system is simulated using all three methods. System identifications are made in the frequency domain using the reverse path method for all the simulated data. From an identification, the FRF of the underlying

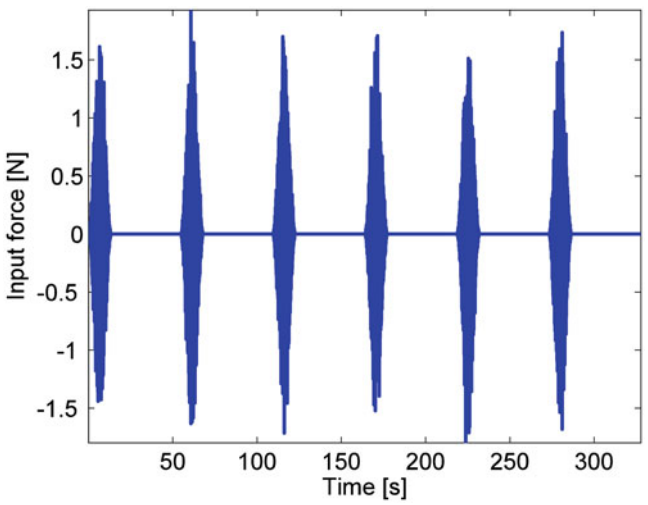

Fig. 44.5 A burst random input force used for the linear example

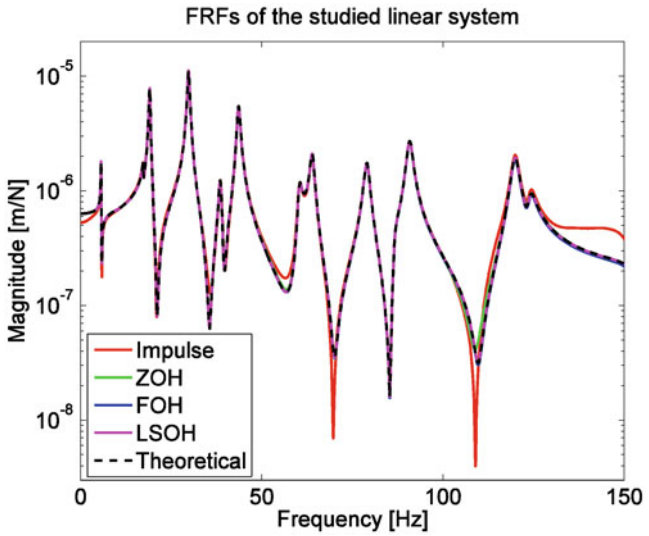

Fig. 44.6 The theoretical FRF (shown in *black*) of the tested linear system is compared with the estimated FRFs stemming from the DF method with different discretization techniques. The estimated FRF from impulse, ZOH, FOH and LSOH is in *red*, *green*, *blue*, and *purple* respectively

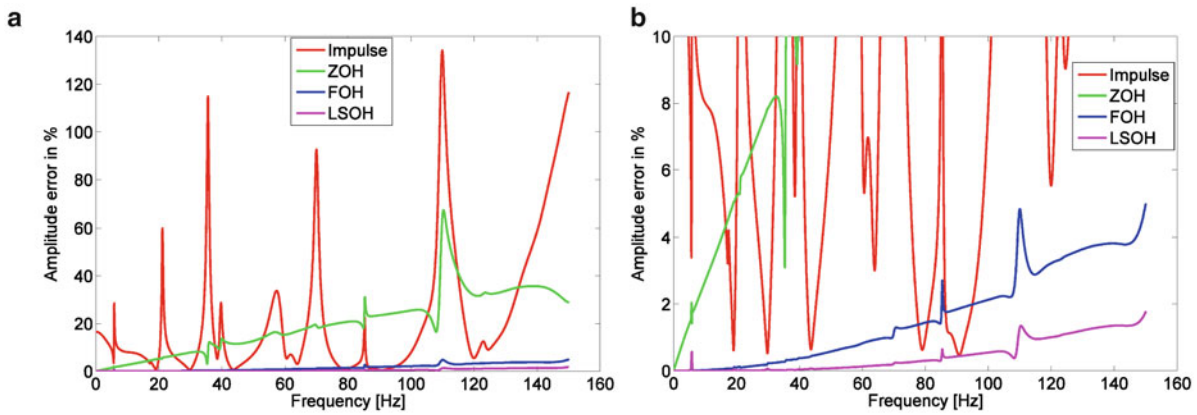

Fig. 44.7 An example of the amplitude error in percent of the estimated FRFs stemming from the DF method using impulse, ZOH, FOH and LSOH discretization techniques (**a**) overview, (**b**) a zoom in

Fig. 44.8 An SDOF system with a cubic spring, used in the nonlinear example

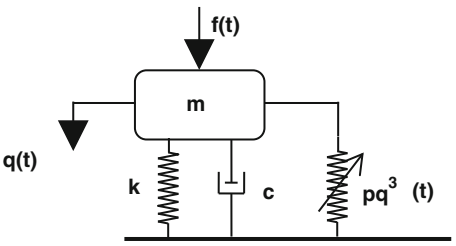

linear system and the nonlinear coefficient are obtained. These are compared with the theoretical ones for each simulation method with three different discretization techniques (the ZOH, FOH, and LSOH). The results for the RK4, DF, and single step PFSS, are shown in Figs. 44.9, 44.10, 44.11, 44.12, 44.13, 44.14, 44.15, 44.16, and 44.17 respectively.

From Figs. 44.7, 44.8, and 44.9, the bias error for the estimated underlying FRF from RK4 simulations, show the same behavior as the theoretical bias error. The bias error for the estimated nonlinear coefficient shows the same trends as the theoretical bias error for the estimated FRF, but upside down. The reason for this bias is that the nonlinear force taken into account in the simulation is not calculated using the estimated responses.

From Figs. 44.10, 44.11, 44.12, 44.13, 44.14, and 44.15, the bias error of the estimated FRF for the linear part of the tested system using the DF and single step PFSS method matches the derived theoretical bias error. No bias error exists for the estimated nonlinear coefficient from the RP method when the DF or single step PFSS simulation method is used. As explained in the DF and PFSS method, the nonlinear force is calculated exactly using the approximated response at each time step. Thus, there is no bias error for the nonlinear coefficient estimated using the simulated response.

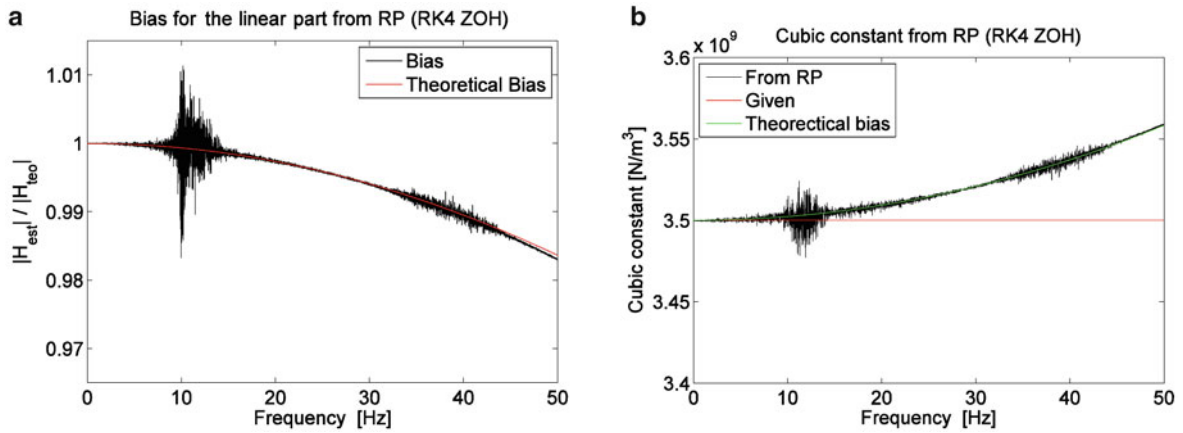

Fig. 44.9 Identification results for the nonlinear example calculated using the RK4 with the ZOH discretization (**a**) Bias error for the estimated linear system compared with the theoretical bias. (**b**) The estimated nonlinear coefficient compared with the used value and theoretical bias

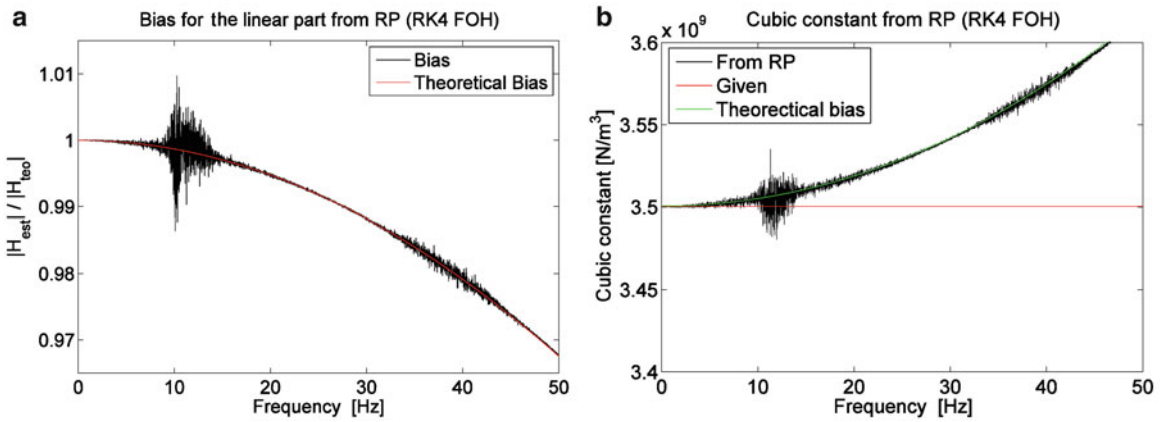

Fig. 44.10 Identification results for the nonlinear example calculated using the RK4 with the FOH discretization (**a**) Bias error for the estimated linear system compared with the theoretical bias. (**b**) The estimated nonlinear coefficient compared with the used value and theoretical bias

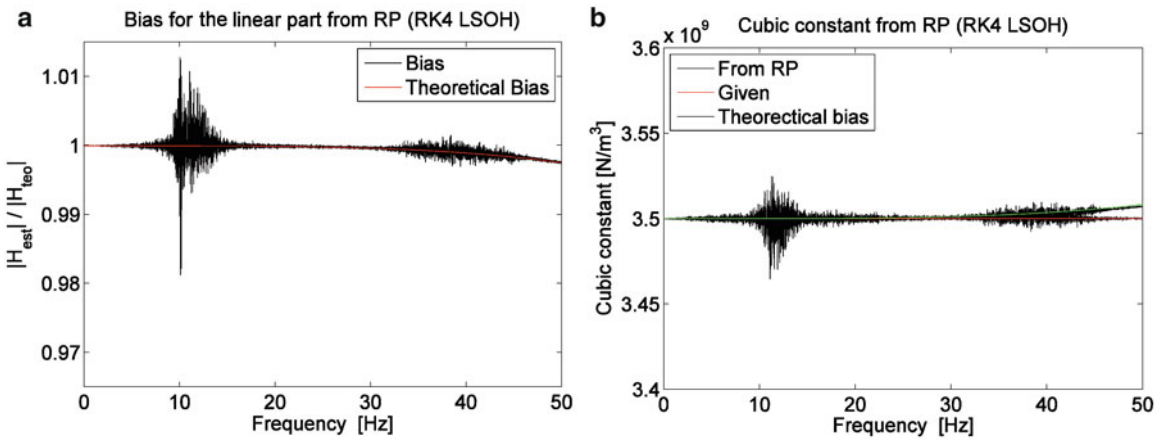

Fig. 44.11 Identification results for the nonlinear example calculated using the RK4 with the LSOH discretization (**a**) Bias error for the estimated linear system compared with the theoretical bias. (**b**) The estimated nonlinear coefficient compared with the used value and theoretical bias

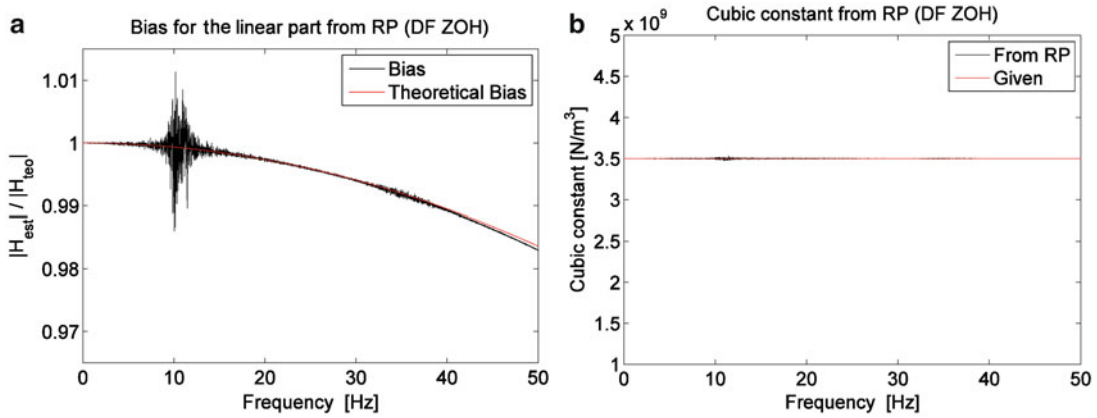

Fig. 44.12 Identification results for the nonlinear example calculated using the DF method with the ZOH discretization (**a**) Bias error for the estimated linear system compared with the theoretical bias. (**b**) The estimated nonlinear coefficient compared with the theoretical value

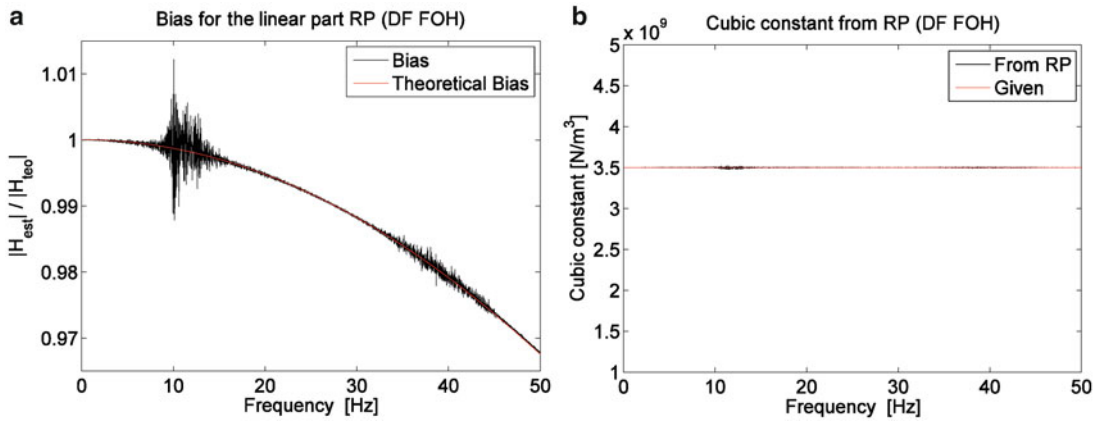

Fig. 44.13 Identification results for the nonlinear example calculated using the DF method with the FOH discretization (**a**) Bias error for the estimated linear system compared with the theoretical bias. (**b**) The estimated nonlinear coefficient compared with the theoretical value

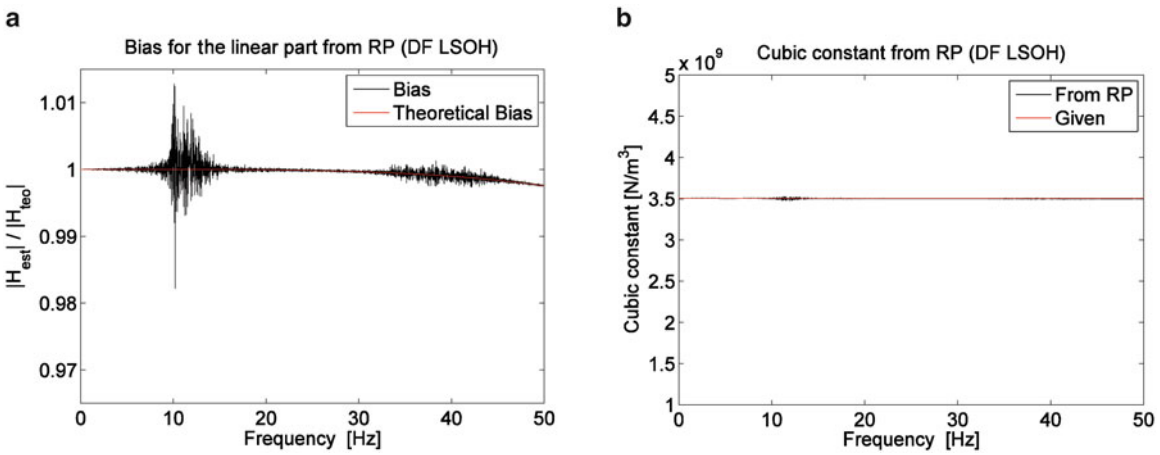

Fig. 44.14 Identification results for the nonlinear example calculated using the DF method with the LSOH discretization (**a**) Bias error for the estimated linear system compared with the theoretical bias. (**b**) The estimated nonlinear coefficient compared with the theoretical value

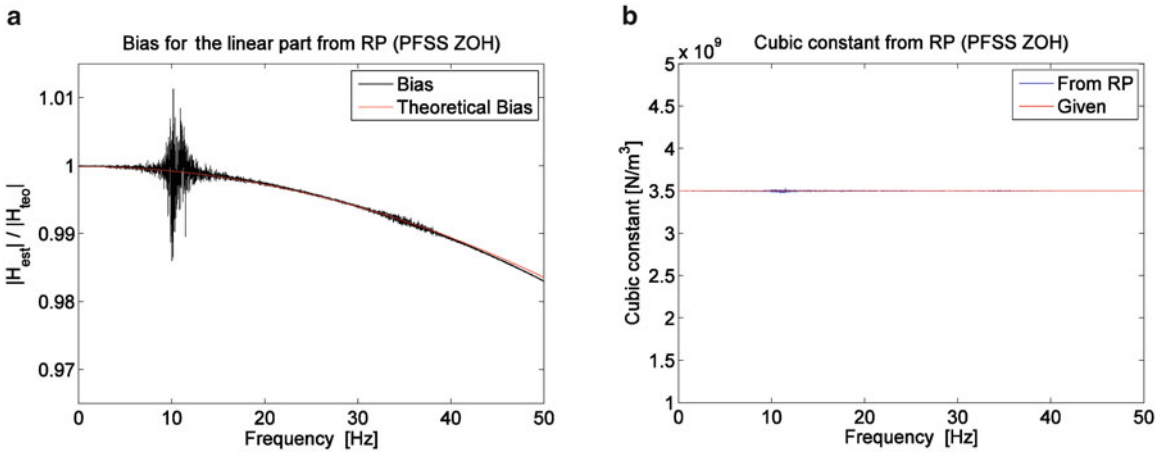

Fig. 44.15 Identification results for the nonlinear example calculated using the single step PFSS method with the ZOH discretization (**a**) Bias error for the estimated linear system compared with the theoretical bias. (**b**) The estimated nonlinear coefficient compared with the theoretical value

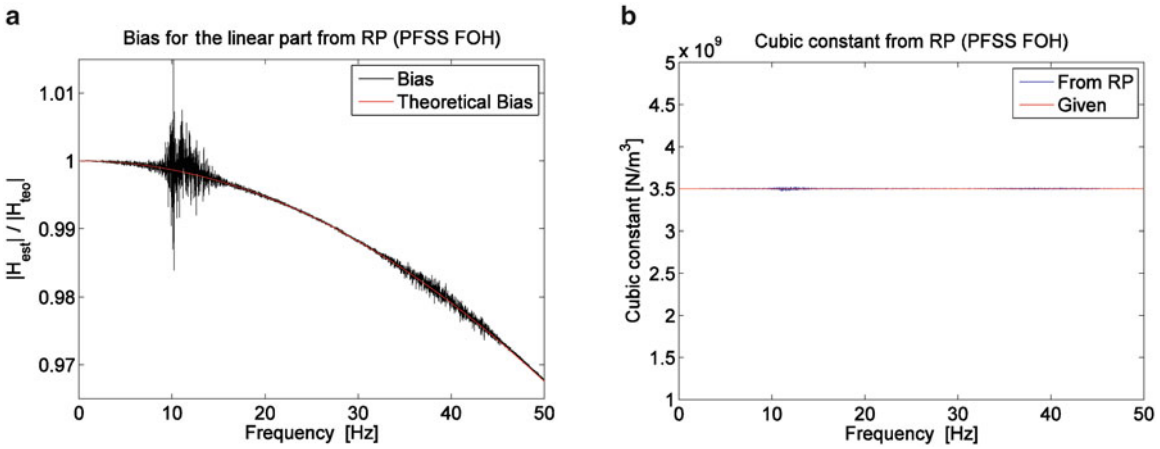

Fig. 44.16 Identification results for the nonlinear example calculated using the single step PFSS method with the FOH discretization (**a**) Bias error for the estimated linear system compared with the theoretical bias. (**b**) The estimated nonlinear coefficient compared with the theoretical value

44.4 Conclusion

When working with sampled data, a transformation of the system description from the time domain to the discrete domain is needed. Such a transformation introduces an aliasing error. In this paper, the impulse invariant is studied to show the aliasing error, which can be clearly seen in the linear example. The aliasing is handled by making different approximations between two successive sample points. However, these approximations create bias errors. As illustrated in the linear example, the impulse invariant and ZOH method give large errors. The FOH and LSOH discretization are recommended for numerical time integration. The LSOH discretization gives smaller bias error than the other discretization techniques, which can be used to improve the accuracy of the simulation methods.

By studying the convolution kernels and the Fourier transforms, the theoretical bias error has been derived for the discretization methods: ZOH, FOH and LSOH. The result has been verified with numerical simulations using both a linear and a nonlinear system.

In the nonlinear example, forced time responses of a Duffing system is studied using the RK4, DF, and a new method named single step PFSS with different discretization techniques (the ZOH, FOH and LSOH). The reverse-path (RP) method is used to identify the FRF of the underlying linear system and the nonlinear coefficient. The bias error for the linear part of the system matches the theoretical bias error for all three simulation methods investigated.

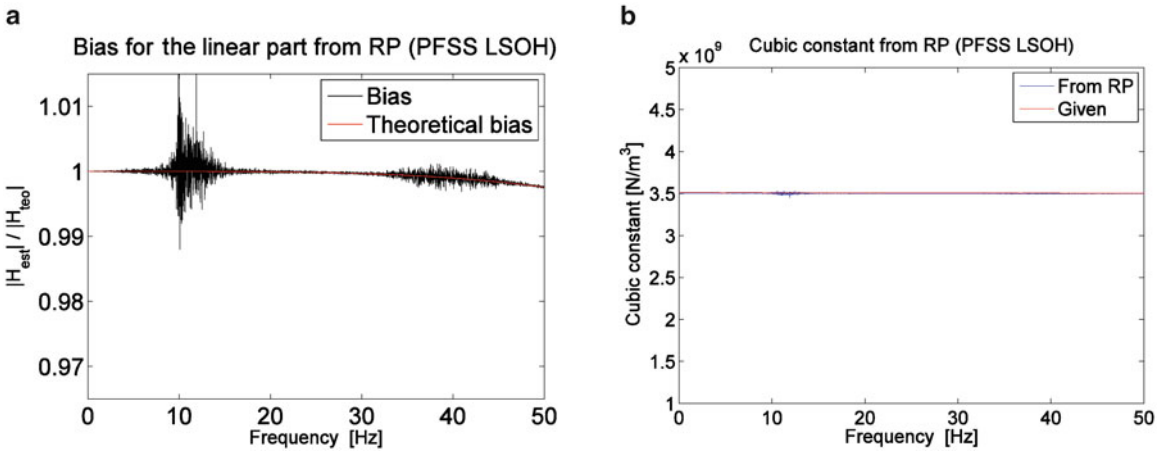

Fig. 44.17 Identification results for the nonlinear system calculated using the single step PFSS method with the LSOH discretization (**a**) Bias error for the estimated linear system compared with the theoretical bias. (**b**) The estimated nonlinear coefficient compared with the theoretical value

There is no bias error for either the DF method or the single step PFSS method since the nonlinear forces are calculated explicitly for each time step. However, as shown in this study, the estimated nonlinear coefficient is biased for the RK4 method and the bias error depends on the discretization method. Therefore, the DF and single step PFSS methods are recommended for system identification of nonlinear systems.

References

1. Franklin GF, Powell JD, Workman M (2006) Digital control of dynamic systems. Elis-kagle Press, Half Moon Bay
2. Zhang Z, Chong KT (2009) Second order hold and taylor series based discretization of SISO input time-delay systems. J Mech Sci Technol 23:136–148
3. Yaghoubi V, Vakilzadeh MK, Abrahamsson T (2014) Efficient simulation method for nonlinear structures. In: Proceedings of the 9th international conference on structural dynamics, EURODYN, Portugal
4. Ahlin K, Magnevall M, Josefsson A (2006) Simulation of forced response in linear and nonlinear mechanical systems using digital filters. In: Proceedings of the international conference on noise and vibration engineering (ISMA), Leuven
5. Josefsson A (2011) Identification and simulation methods for nonlinear mechanical systems subjected to stochastic excitation. PhD thesis, Blekinge Institute of Technology
6. Magnevall M (2011) Simulation and experimental methods for characterization of nonlinear mechanical systems, Karlskrona. PhD thesis, Blekinge Institute of Technology
7. Yaghoubi V, Abrahamsson T (2014) An efficient simulation method for structures with local nonlinearity. In: Proceeding of IMAC XXXII, Orlando
8. Chen Y, Linderholt A, Abrahamsson T (2014) Frequency response function calculations of a nonlinear structure- a comparison of numerical methods. In: Proceeding of the conference on structural dynamics, IMAC XXXII, Orlando
9. Bendat JS (1990) Nonlinear system analysis and identification from random data. Wiley, New York
10. Josefsson A, Magnevall M, Ahlin K, Broman G (2012) Spatial location identification of structural nonlinearities from random data. Mech Syst Signal Process 27:410–418
11. Magnevall M, Josefsson A, Ahlin K, Broman G (2012) Nonlinear structural identification by the “reverse path” spectral method. J Sound Vib 331:938–946

Chapter 45
Internal Resonance and Stall Flutter Interactions in a Pitch-Flap Wing in the Wind-Tunnel

E. Verstraelen, G. Kerschen, and G. Dimitriadis

Abstract Nonlinear aeroelastic phenomena such as store-induced LCOs, transonic buzz and stall flutter are the burden or modern aircraft: they reduce the performance and can even limit the flight envelope in both civil and military cases. Several nonlinear setups were studied experimentally in the last decades by the scientific community but most of them have pitch and plunge degrees of freedom and feature a rigid wing. In this paper, we study a new nonlinear aeroelastic apparatus that features nonlinear pitch and flap degrees of freedom, coupled with a flexible wing. The model is tested experimentally in the wind tunnel to determine its dynamic behaviour. Preliminary observations demonstrate that the system undergoes a supercritical Hopf bifurcation due to the hardening nonlinearity followed by an amplitude jump that is the consequence of either dynamic stall (i.e. stall flutter) or internal resonance (i.e. interaction between the hardening nonlinearity and higher modes).

Keywords Wind-tunnel testing • Nonlinear aeroelasticity • Stall flutter • Internal resonance • Bifurcations

45.1 Introduction

Aeroelasticity is the result of mutual interactions between vibrating modes of a flexible structure and aerodynamic loads. It can lead to linear flutter or, in the nonlinear case, to limit cycle oscillations (LCOs) such as store-induced LCOs, transonic buzz and stall flutter. Such phenomena limit the performance or even the flight envelope of aircraft and have therefore been widely studied by the scientific community during the last 30 years.

A wide range of experimental setups was developed in order to make and validate models or simply to understand the underlying physics of different aeroelastic phenomena. Most of them are characterised by a stiff wing with pitch and plunge degrees of freedom (DOFs) and sometimes a control surface DOF. Setups with a linear structural part and aerodynamic nonlinearity were developed by Amandolese [1], Abdul Razak et al. [2, 3] and Dimitriadis et al. [4] to study stall flutter. Poirel et al. [5] studied laminar separation flutter thanks to another linear setup. The Pitch And Plunge Apparatus (PAPA) was used to test flutter control mechanisms at transonic airspeeds by Mukhopadhvay [6]. Several structurally nonlinear setups were built such as the Nonlinear Aeroelastic Testbed Apparatus (NATA) [7, 8] which uses a cam system to get different continuous nonlinearities on the pitch and plunge DOFs. The NATA was also used by Dowell et al. [9] for teaching purposes. Abdelkefi et al. [10] developed and modelled a different setup using a leaf spring. Conner et al. [11] extensively studied both numerically and experimentally the effects of freeplay in control surfaces. Tang et al. [12] tested an aileron flexible in flap, lag and torsion with freeplay at the root. Most of these structurally nonlinear setups use ball bearings which also introduces nonlinear frictions and hysteresis.

The apparatus we propose in the present study is the Nonlinear Pitch and Flap Wing (NLPFW). It is a flat plate with pitch and flap DOFs inspired by the wing invented by Hancock et al. [13] and used in a book by Wright et al. [14] for teaching purposes. It is structurally hardening and does not feature any bearing thanks to specially designed leaf spring and clamps inspired by the work of Platten et al. [15]. Separation of the airflow occurs at high oscillation amplitudes, which also leads to aerodynamic nonlinearity. This paper presents the NLPFW and provides an experimental investigation of its dynamic behaviour at both wind-off and wind-on conditions. Particular emphasis is given to the appearance of stall flutter and internal resonance phenomena.

E. Verstraelen (✉) • G. Kerschen • G. Dimitriadis
Department of Aerospace and Mechanical Engineering, University of Liège, Liège, Belgium
e-mail: everstraelen@ulg.ac.be; g.kerschen@ulg.ac.be; gdimitriadis@ulg.ac.be

G. Kerschen (ed.), *Nonlinear Dynamics, Volume 1*, Conference Proceedings of the Society for Experimental Mechanics Series, DOI 10.1007/978-3-319-15221-9_45

45.2 Experimental Setup

The experimental apparatus is installed in the Wind-Tunnel of the University of Liège. The model is designed to achieve very low damping (≈0.3 % at wind-off conditions) and flutter at an airspeed of around 12 m/s. To achieve such a low structural damping, the setup does not use any bearings or rotational springs. The pitch and flap restoring torques are provided by a specially designed leaf spring and nonlinear clamps.

The design of the NLPFW (shown in Fig. 45.1) is based on the Hancock wing theoretically developed by J.Hancock during the 1980s [13] and drawn in Fig. 45.2. It is a stiff thin rectangular unswept flat plate with span $s = 750$ mm, chord $c = 200$ mm, thickness $t = 4$ mm and an aspect ratio of 3.75. It is hinged at its root at $0.3c$ from the leading edge. As a result it features two rigid DOFs: a pitch rotation θ and a flap rotation γ. The axis system OXYZ is fixed. The flexural axis, e_s, is parallel to the leading edge and passes by the hinge while the axis e_c is the root of the wing. The pitch angle θ is defined as the angle formed by the axis e_c and X i.e. it measures the rotation around the axis e_s. The flap angle γ is the angle formed by the axis e_s and Z which means that it measures the rotation around the axis e_c.

The stiffness in both pitch and flap is provided by a thin C75S leaf spring. It is 100 mm long, 70 mm large and 0.7 mm thick. It is clamped on the flat plate and on the roof of the test section of the wind-tunnel using two nonlinear clamps. Figure 45.3a draws the geometry of these clamps and Fig. 45.3b plots the nonlinear restoring torque of the pitch DOF and

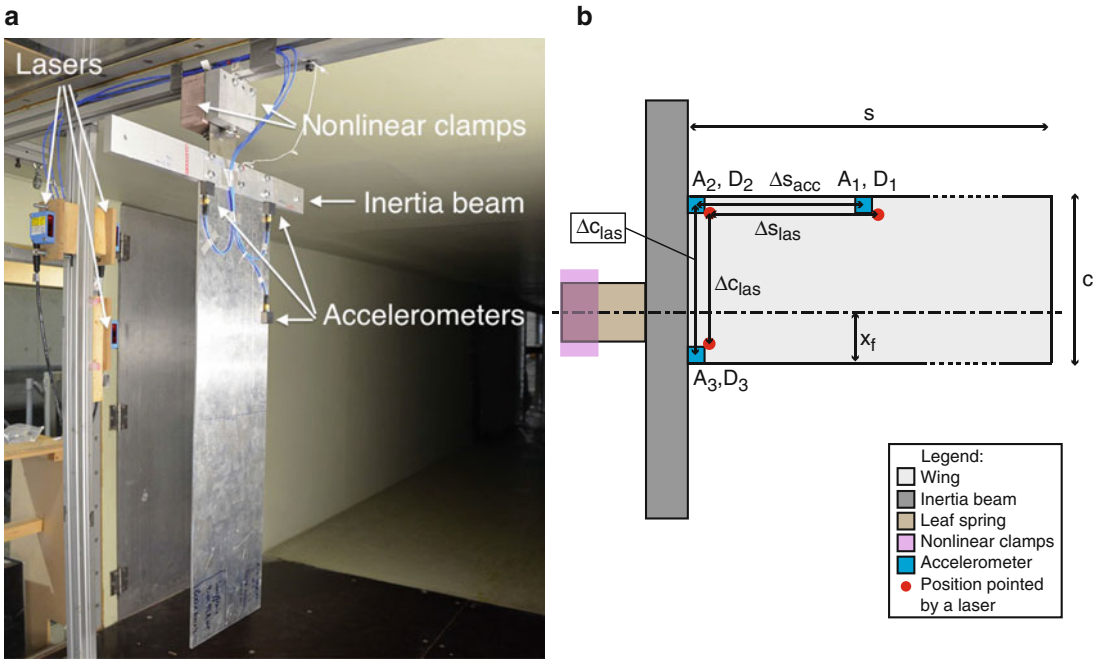

Fig. 45.1 Experimental setup showing wing, support and transducers. (**a**) Photo of the setup in the wind-tunnel. (**b**) Diagram showing transducer locations and major components of the NLPFW

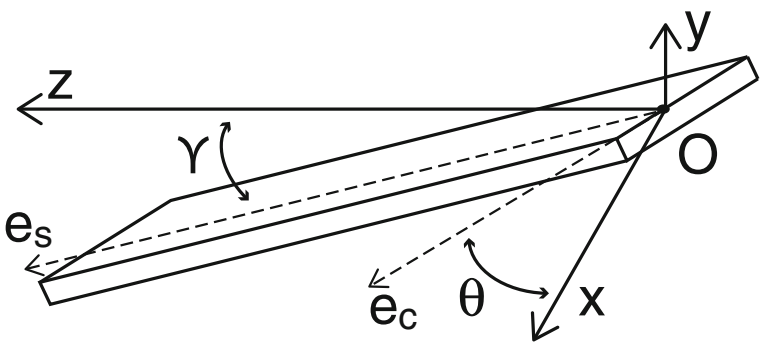

Fig. 45.2 Schematic of the Hancock wing

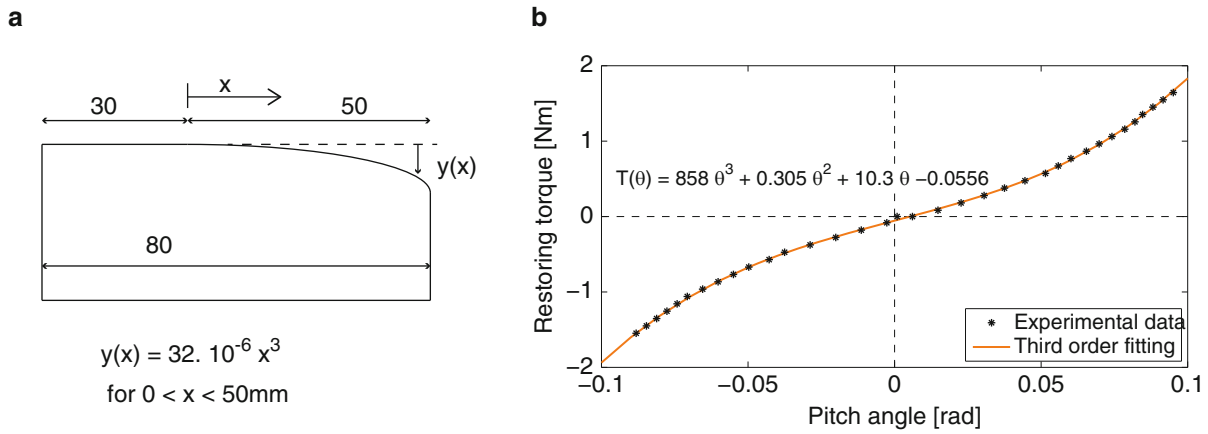

Fig. 45.3 Characteristics of the nonlinear clamps. (**a**) Sketch of the clamps. (**b**) Experimental restoring torque curve of the pitch DOF

Table 45.1 Wind-off characteristics of the NLPF

Characteristic	Symbol	Value	Unit
Dimensions of the wing			
Span	s	750	[mm]
Chord	c	200	[mm]
Thickness	t	4	[mm]
Flap properties			
Linear stiffness	K_γ	≈5	[Nm/rad]
Inertia	I_γ	0.42	[kg m^2]
Damping	ζ_γ	≈1	[%]
Frequency	f_γ	0.85	[Hz]
Pitch properties			
Inertia	I_θ	0.029	[kg m^2]
Linear stiffness coefficient	K_θ	10.3	[Nm/rad]
Quadratic stiffness coefficient	$K_{\theta,2}$	≈0	[Nm/rad^2]
Cubic stiffness coefficient	$K_{\theta,3}$	858	[Nm/rad^3]
Damping	ζ_θ	≈0.3	[%]
Frequency	f_θ	3.1	[Hz]
Position of the sensors			
Distance between A_1 and A_2	Δs_{acc}	200	[mm]
Distance between A_2 and A_3	Δc_{acc}	180	[mm]
Distance between D_1 and D_2	Δs_{las}	205.5	[mm]
Distance between D_2 and D_3	Δc_{acc}	168.5	[mm]

a third order fitting. It was measured statically by applying masses to the pitch DOF and measuring the resulting deflection using a digital inclinometer with a resolution of 0.1°. The flap stiffness is linear in the displacement range considered.

Finally, a 500 mm × 50 mm × 15 mm beam is bolted at the junction between the flat plate and the leaf spring (see Fig. 45.1a, b). It increases the rotational inertia of the system and consequently decreases its flutter speed to make it in the target speed range: [10–15] m/s. Table 45.1 summarises the wind-off characteristics of the NLPF.

The displacements are measured by the means of 3 Sick OD2-P300W200I0 laser sensors with a sensitivity of 9.6 mV/mm and a range of 100–500 mm. The accelerations are measured using three MEMS DC accelerometers with a sensitivity of 100 mV/G and a range of ±30 G. The sampling frequency of these two instruments is set to 1,000 Hz. The position of the sensors is shown in Fig. 45.1b. The accelerometers A_2 and A_3 and the lasers D_2 and D_3 are placed at the root of the wing. As a result there is no torsion of the flat plate and the pitch accelerations and displacements can be computed as in displayed in Eqs. (45.1) and (45.2) assuming a stiff plate.

$$\ddot{\theta} = (A_2 - A_3)(\Delta c_{acc})^{-1} \qquad [\text{rad/s}^2] \tag{45.1}$$

$$\theta = \arctan[(D_2 - D_3)(\Delta c_{las})^{-1}] \qquad [\text{rad}] \tag{45.2}$$

At low energy levels -typically before the flutter speed- this hypothesis is also valid for the flap accelerations, measured using accelerometers A_1 and A_2 (see Eq. (45.3)) and for the flap displacement, measured using lasers D_1 and D_2 (see Eq. (45.4)).

$$\ddot{\gamma} = (A_1 - A_2)(\Delta s_{las})^{-1} \qquad [\text{rad/s}^2] \tag{45.3}$$

$$\gamma = \arctan[(D_1 - D_2)(\Delta s_{las})^{-1}] \qquad [\text{rad}] \tag{45.4}$$

At high energy levels -typically the LCOs cases- the rigid plate hypothesis is not valid. A new variable ϕ (see Eqs. (45.5) and 45.6) is introduced to quantify the deformations of the flat plate: subtracting the signal of accelerometer A_2 (or laser D_2) from the signal of accelerometer A_1 (or laser D_1) cancels the pitch contribution and gives an idea of displacements and accelerations due to the vibrations of the plate.

$$\ddot{\phi} = A_1 - A_2 \qquad [\text{m/s}^2] \tag{45.5}$$

$$\phi = D_1 - D_2 \qquad [\text{m}] \tag{45.6}$$

45.3 Results

Three types of tests were carried out to study this system:

1. Modal analysis at wind-off is performed.
2. The variation of the modal parameters with the airspeed is investigated.
3. The super-critical behaviour of the system is explored through the limit cycles (LCOs) amplitudes frequencies and mode-shapes.

45.3.1 Wind-Off Modal Analysis of the System

Hammer testing was used to carry out mind-off modal analysis. The wing was impacted five times in 24 different locations using a hammer instrumented with a force gauge. The response was measured with a single accelerometer placed on the trailing edge at the tip of the wing. Since it is very difficult to excite the leaf spring with the hammer its deflections are extracted from a model with shell finite elements of the whole structure computed by the means of the Finite Element package SAMCEF. Figure 45.4 shows the first six modes and the positions of the three accelerometers A_1 A_2 and A_3. No clear modes were identified between 10 and 27 Hz, probably due to nonlinear effects. A shaker test at different vibration levels is planned in the near future. The model predicts the existence of an in-plane mode between modes 3 and 4. Nevertheless this mode is aligned with the airflow and should not contribute greatly to the important dynamics of the system. The six mode shapes are the following:

1. First mode: first flexural mode of the leaf spring and no deformation of the flat plate. It is equivalent to γ, the flap DOF of the Hancock wing.
2. Second mode: first torsional mode of the leaf spring and no deformation of the flat plate. It is equivalent to θ, the pitch DOF of the Hancock Wing.
3. Third mode: second flexural mode of the leaf spring and first flexural mode of the flat plate.
4. Fourth mode: second flexural mode of the leaf spring and second flexural mode of the flat plate.
5. Fifth mode: first torsional mode of the flat plate.
6. Sixth mode: second flexural mode of the leaf spring and third flexural mode of the flat plate.

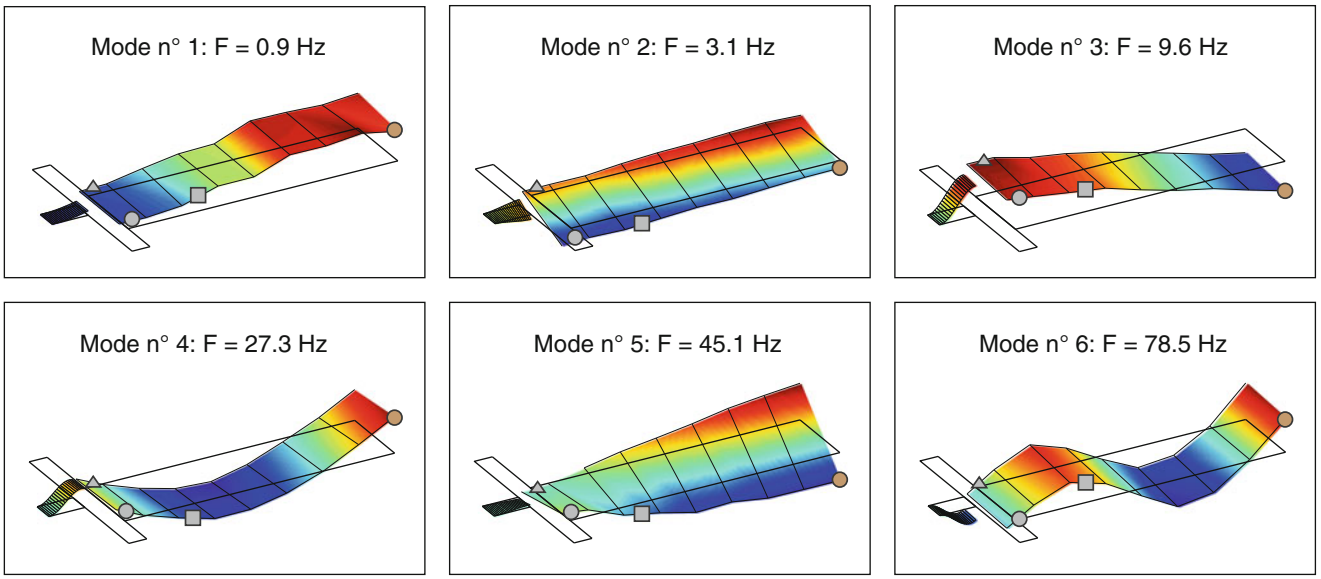

Fig. 45.4 Modes shapes of the NLPF. The *brown dots* indicate the position of the accelerometer used for the modal analysis. The *grey square*, *dots* and *triangles* respectively show the position of the accelerometers A_1 A_2 and A_3 (Color figure online)

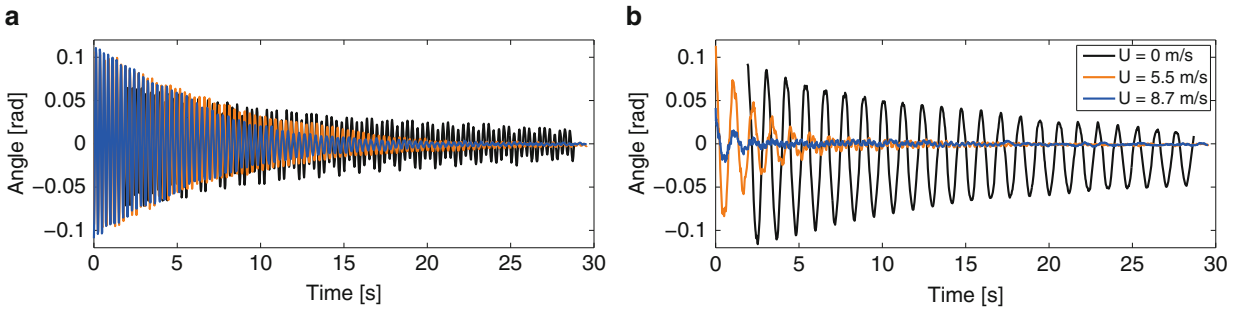

Fig. 45.5 Response of the system at sub-critical airspeeds released from an initial pitch and flap angle of 0.1 rad. (**a**) Pitch response. (**b**) Flap response

45.3.2 Wind-on Study of the System

45.3.2.1 Variation of the Modal Parameters with Airspeed

The variation of the damping and frequency of the system were studied using free decays. For each stabilised airspeed, the system was given an initial pitch and flap angle then was released. Figure 45.5 shows pitch and flap responses at three different airspeeds. The damping of the pitch angle increases slowly while the damping of the flap angle becomes large. The wind-on frequency of the system was computed from these free decays using Fast Fourier Transform (FFT) or Wavelet Analysis. The damping was computed using an exponential curve fit of the Hilbert Transform of the responses. Figure 45.6 shows the variation of frequency and damping of the first two modes with airspeed. It is a classical frequency vs airspeed diagram of a system that flutters: the flap damping increases monotonously while the pitch damping first increases until 9 m/s then decreases until flutter occurs. The modal properties of the flap mode are very scattered because the damping was so high that the system could only undergo a few oscillations before going back to rest. The frequency diagram is also quite common for flutter systems: the pitch and flap frequencies move closer to each other as the airspeed increases until flutter occurs. The variation of the frequency and the damping of modes 3–6 is not displayed here because these modes are not influenced in the velocity range considered, which means that the do not participate in the flutter mechanism.

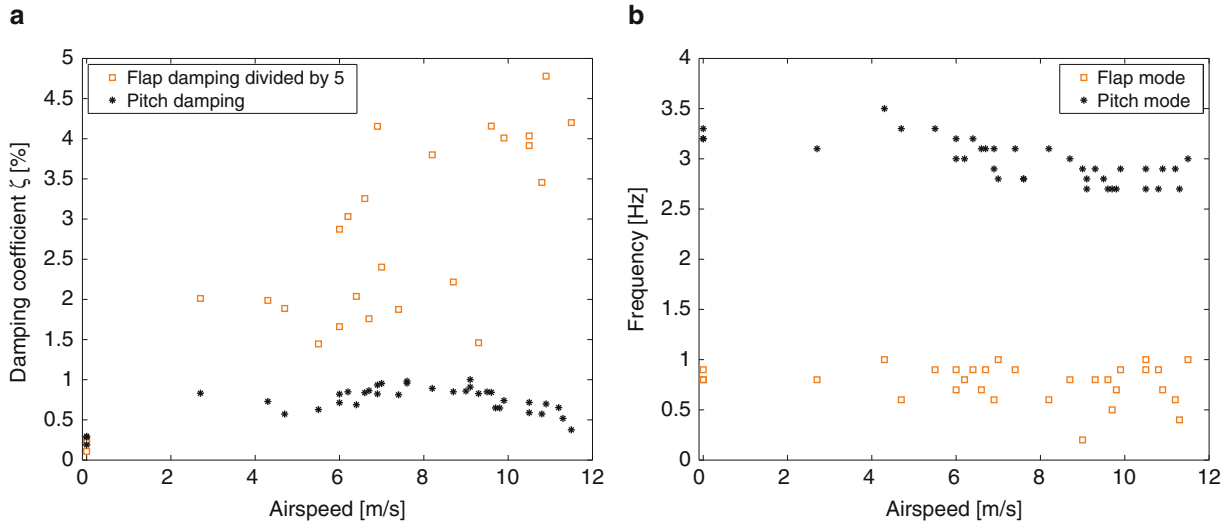

Fig. 45.6 Variation of the modal parameters of the pitch and flap DOFs with the airspeed before the flutter. (**a**) Damping. (**b**) Frequency

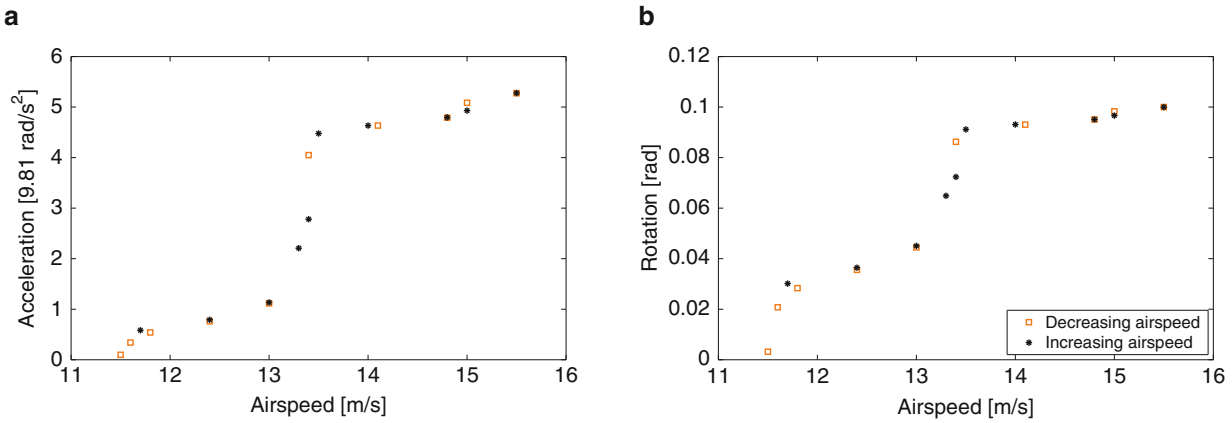

Fig. 45.7 Bifurcation diagram of the pitch DOF. (**a**) RMS acceleration. (**b**) RMS displacement

45.3.2.2 Limit Cycle Oscillation Amplitude and Shape Variation with Airspeed

Figure 45.7a and b respectively show the evolution of the pitch Root Mean Square (RMS) acceleration and displacement (right) with airspeed. The black dots correspond to increasing airspeed tests while the orange squares are related to decreasing airspeed tests. Both sets of points appear to lie on the same curve, which suggests that there is no hysteresis in the system. The bifurcation at 11.5 m/s is a supercritical Hopf: the LCOs were self-excited and manually exciting the system using a rope did not lead to a jump on a branch of higher amplitude. The displacement curve and the acceleration curve both show similar trends: the LCOs start at 11.5 m/s and their amplitude increases smoothly up to 13.5 m/s. At 13.5 m/s a jump occurs: the RMS acceleration is increased by a factor of 5 and the RMS displacement is increased by a factor of 2. After this jump, the amplitude increases slowly with airspeed. A test with wool tufts showed that separation of the airflow occurs after the jump for pitch amplitudes of around 8°. Figure 45.8b–e contains four pictures of the wool tufts placed as displayed in Fig. 45.8a at four time instances of the same half cycle. The top row of tufts, which corresponds to the red one in Fig. 45.8a, lies near the leading edge of the wing while the bottom row, which corresponds to the green one, lies near the trailing edge. The following phenomena occur:

- t_1: the pitch angle is small and increasing, the tufts stick to the wing because the airflow is attached.
- t_2: the pitch angle is large and the front line of tufts (top) is detached from the wing which indicates separation of the airflow near the leading edge. The second line of tufts is much less affected by separation than the first line.
- t_3: the pitch angle is larger than at t_2. The airflow is now separated on both the leading and trailing edges.
- t_4: the pitch angle is small and the airflow is re-attached on the wing.

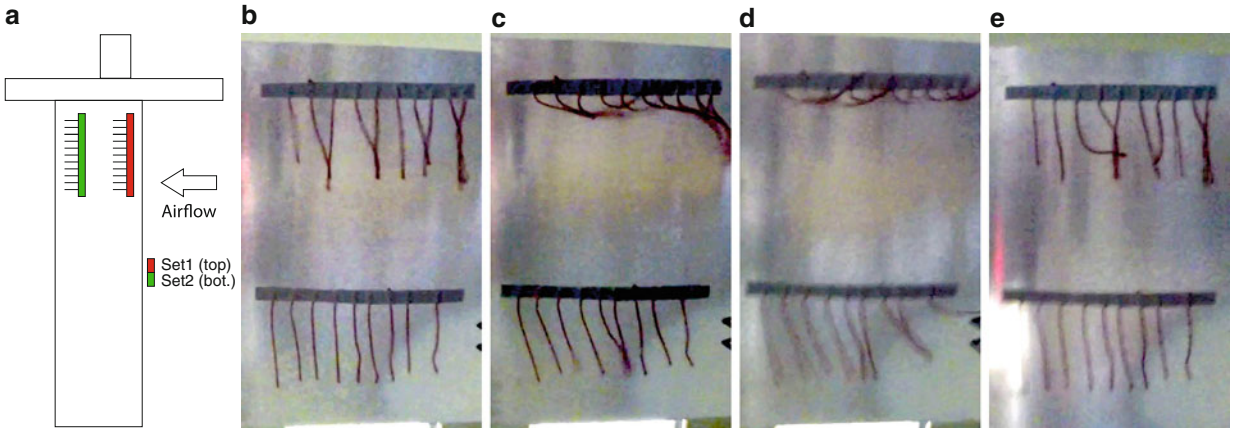

Fig. 45.8 Pictures of wool tufts on the wing during a cycle of half period of stall flutter at 14.9 m/s. The air flows from the top to the bottom on pictures (**b**)–(**e**). (**a**) Position of the tufts on the NLPF. (**b**) t_1: beginning of the half cycle, small increasing pitch angle and attached flow. (**c**) t_2: middle of the half cycle, large pitch angle and separation of the airflow on the leading edge. (**d**) t_3: middle of the half cycle, large pitch angle and separation of the airflow on both the leading and trailing edges. (**e**) t_4: end of the half cycle, small decreasing pitch angle and attached flow

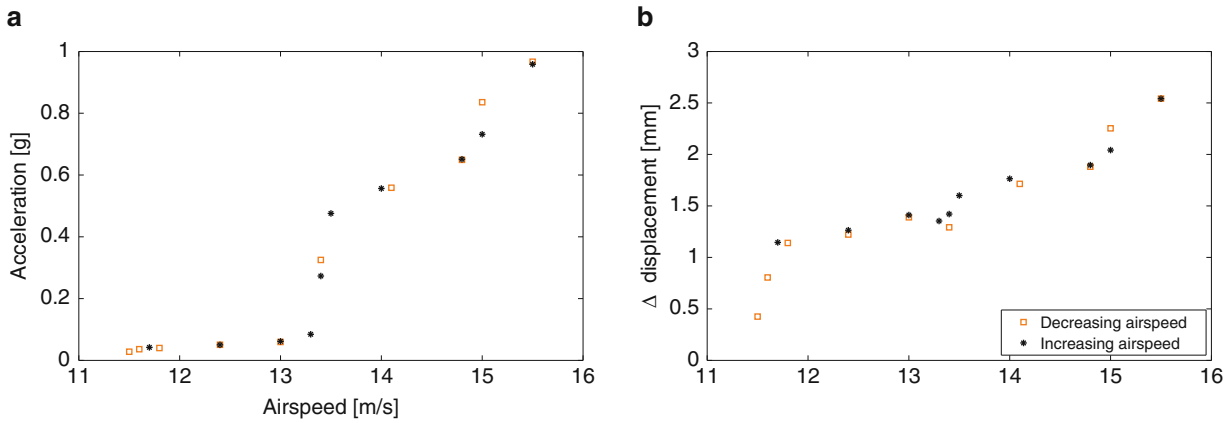

Fig. 45.9 Bifurcation diagram of ϕ the plate deformations DOF. (**a**) RMS acceleration. (**b**) RMS displacement

Figure 45.9 depicts the variation of $\ddot{\Phi}$ RMS acceleration (a) Φ RMS displacement (b) with airspeed. There are significant qualitative differences between Figs. 45.7 and 45.9. The acceleration increases very slowly between 11.5 and 13.5 m/s. Then its amplitude is increased by a factor of 10 after the jump. It increases slowly again after the jump until a second jump occurs at 15 m/s, albeit much smaller than the first one. The displacement diagram shows a smooth increase in RMS displacements with airspeed without any jump. High amplitude acceleration and low amplitude displacement suggests vibrations of the flat plate.

Figures 45.10 and 45.11 plot the comparison of the time series of the pitch accelerations $\ddot{\theta}$ and the measurements of the accelerometers A_1 and A_2 respectively before and after the jump. Below the jump speed, a single important harmonic at the LCO fundamental frequency f_0 around 3 Hz dominates the dynamics and very small components at higher frequency can be noticed. Above the jump speed the pitch acceleration's frequency reaches 4 Hz and the $4f_0$ harmonic becomes large but the motion is still dominated by the fundamental frequency. The accelerations A_1 and A_2 on the other hand see their higher frequency components become as large as the 4 Hz component and they are not in phase anymore. This also suggests vibrations of the flat plate.

45.3.2.3 Limit Cycle Oscillation Frequency Variation with Airspeed

Waterfall plots are depicted in Fig. 45.12. They plot the FFT of the LCO responses at different airspeed and demonstrate the frequency values of all the peaks. It looks smooth but the vertical axis is not continuous. Figure 45.12(left) concerns the pitch frequencies and features the following peaks:

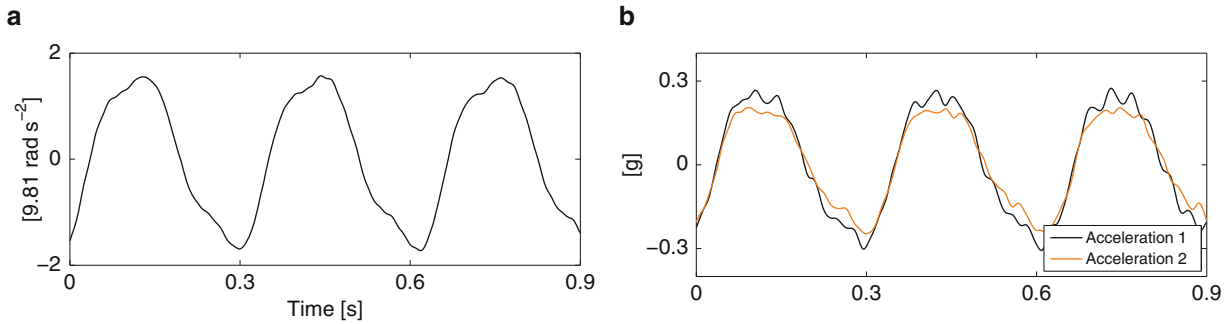

Fig. 45.10 Time series of the LCO response at 13 m/s. (**a**) Pitch acceleration. (**b**) A_1 and A_2 accelerations

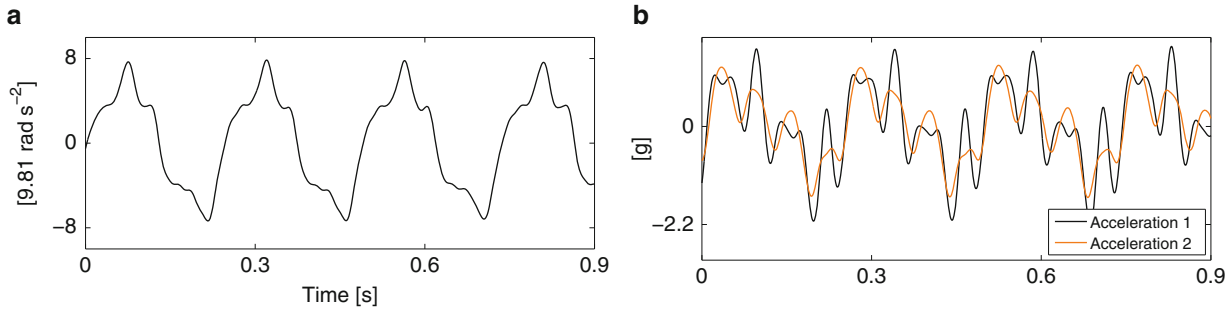

Fig. 45.11 Time series of the LCO response at 13.5 m/s. (**a**) Pitch acceleration. (**b**) A_1 and A_2 accelerations

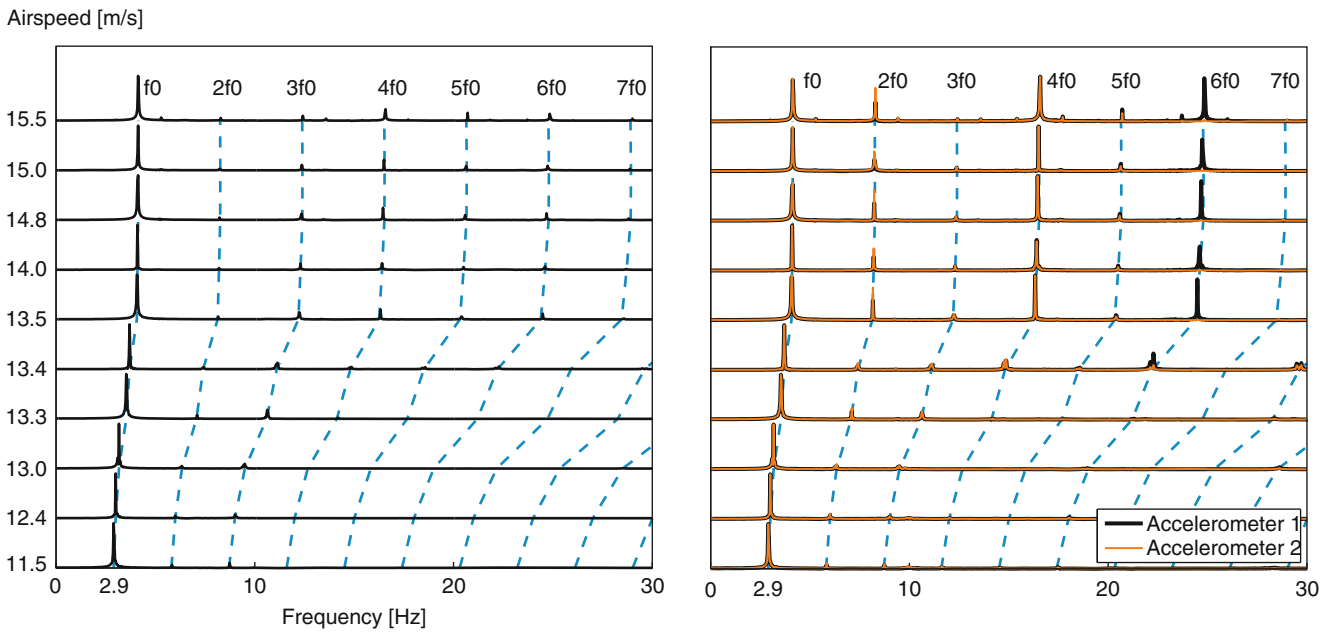

Fig. 45.12 Waterfall plot of the pitch acceleration $\ddot{\theta}$ (*left*) and of the accelerations A_1 and A_2 (*right*)

- The fundamental frequency, f_0, lies at 2.9 Hz at 11.5 m/s and reaches 4.1 Hz at 15.5 m/s.
- A small third harmonic, $3f_0$, lies at 11.5 m/s and its strength does not grow with airspeed compared to the f_0.
- The fourth and sixth harmonics, $4f_0$ and $6f_0$ emerge after the jump (13.5 m/s) and their strength does not grow with airspeed compared to f_0 either.
- The fifth harmonic, $5f_0$ appears after the jump and its amplitude increases slightly with airspeed compared to the amplitude of the fundamental frequency.

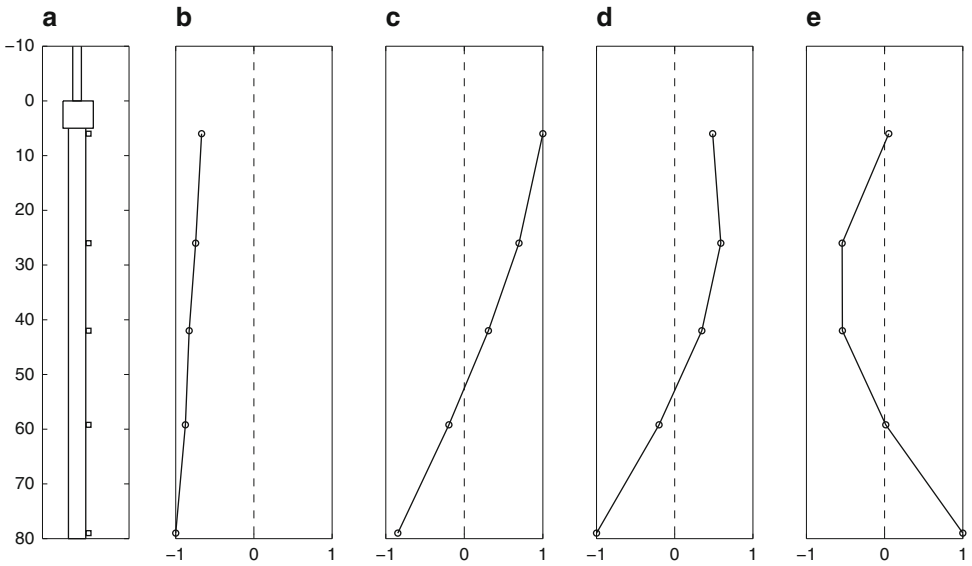

Fig. 45.13 Mode shapes of the strongest harmonics of the NLPFW at 14.9 m/s. (**a**) Position of the accelerometers. (**b**) Fundamental frequency: $f_0 = 4.1$ Hz. (**c**) Second harmonic: $2f_0 = 8.2$ Hz. (**d**) Fourth harmonic: $4f_0 = 16.4$ Hz. (**e**) Sixth harmonic: $6f_0 = 24.6$ Hz

Figure 45.12(right) displays the evolution of the frequency of the accelerometers A_1 and A_2. It features the following peaks:

- The fundamental frequency, f_0 lies at 2.9 Hz at 11.5 m/s and reaches 4.1 Hz at 15.5 m/s.
- The second harmonic, $2f_0$ contributes to the motion from 11.5 m/s but its strength explodes after the jump.
- The fourth and sixth harmonics, $4f_0$ and $6f_0$ start at small amplitude right before the jump (13.4 m/s) and their strength becomes similar to the strength of the fundamental harmonic after the jump (13.5 m/s). It is interesting to notice that the fourth harmonic is strong on both A_1 and A_2 while the sixth one is only affecting A_1 which suggests that they have different mode shapes.
- The third and fifth harmonics and a few other small peaks emerge as airspeed increases but their strength is very small and they to not contribute greatly to the dynamics of the system.

The origin of these spatial differences of accelerations can be investigated by plotting mode-shapes of the wind-on system. These modes-shapes are measured using five accelerometers placed on the trailing edge of the flat plate as displayed in Fig. 45.13a. This accelerometers setup does not allow the quantification of torsional effects but the first torsion mode is at much higher frequency and energy than the modes considered here. Moreover torsion would lead to a linear increase of the acceleration as we move towards the tip of the wing and it would be noticed on the mode shapes. The mode shapes of the strongest modes are the following:

- Figure 45.13b depicts the fundamental LCO mode at 4.1 Hz. All the accelerometers measure a large acceleration in phase, which suggests a motion dominated by the second mode. The measurements also suggest the presence a small modal component similar to the first mode.
- Figure 45.13c displays the mode shape of the second harmonic. It is similar to the third wind-off mode and their frequencies are rather close (8.2–9.6 Hz). This means that there might be modal interactions.
- Figure 45.13d shows the mode shape of the fourth harmonic, which does not look like any other wind-off mode shape. Its frequency is not close to any other wind-off modal frequency either.
- Figure 45.13e plots the mode shape of the sixth harmonic. It is similar to the fourth wind-off mode and their frequencies are close as well: 25–27.3 Hz, which means that there also might be modal interactions. Wind-on shaker tests are planned in the near future to evaluate the variation of frequency of the flexible modes with the airspeed and with the amplitude of the excitation to determine whether there is modal interaction.

45.4 Discussion of the Results

All the results presented above highlight the presence of an initial supercritical Hopf bifurcation at 11.5 m/s and two hypotheses were made to explain the jump at 13.5 m/s:

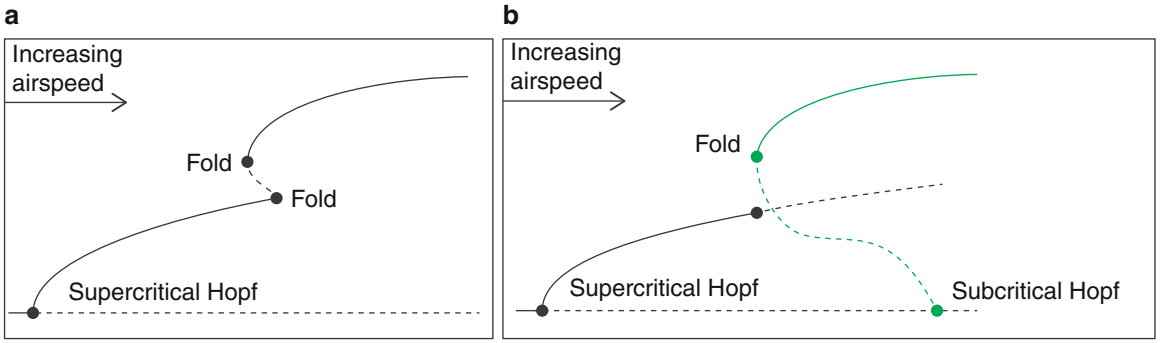

Fig. 45.14 Theoretical bifurcations of the NLPFW. (**a**) Amplitude jump due to modal interactions. (**b**) Amplitude jump due to stall flutter

1. The jump is due to internal resonance. In this case the bifurcation diagram looks like Fig. 45.14a: the initial branch is due to the hardening nonlinearity and the jump is due to internal resonance between the nonlinear stiffness and higher modes. The separation of the airflow highlighted using wool tufts is just a result of the large amplitude of the pitch oscillations.
2. The jump is the consequence of stall flutter. Such a bifurcation diagram is drawn in Fig. 45.14b: the initial branch is still due to the hardening nonlinearity but it intersects with a subcritical stall flutter branch at the jump velocity. The separation of the airflow, shown using wool tufts, is the origin of the jump and the emergence of high frequency plate harmonics is just a consequence of the large amplitude of the motion.

45.5 Conclusion

This study presents a new aeroelastic apparatus characterised by a low structural damping, continuous hardening and no hysteresis thanks to a bearing-free design. Unlike most setups studied in the past the flutter is caused by pitch and flap instead of pitch and plunge. It exhibits classical flutter characteristics for airspeeds between 0 and 11.5 m/s. Then the amplitude is limited by the structural hardening which leads to limit cycle oscillations. At 13.5 m/s a jump occurs that leads to strong pitching oscillations and vibrations of the flat plate. It is still not clear if this jump in amplitude is a result of internal resonance i.e. they are the cause of the jump or if they are just a consequence of the increase in the pitching amplitude. Further testing is planned with shakers or inertial exciters to help understand the non-linear dynamics of the structural system and to study the evolution of the third and fourth wind-off modes with the airspeed.

Acknowledgements The authors would like to acknowledge the financial support of the European Union (ERC Starting Grant NoVib 307265).

References

1. Amandolese X, Michelin S, Choquel M (2013) Low speed flutter and limit cycle oscillations of a two-degree-of-freedom flat plate in a wind tunnel. J Fluids Struct 43:243–255
2. Abdul Razak N, Andrianne T, Dimitriadis G (2011) Flutter and stall flutter of a rectangular wing in a wind tunnel. AIAA J 49(10):2258–2271
3. Abduk Razak N, Rothkegel JI, Dimitriadis G (2012) Experiments on a pitch-plunge wing undergoing limit cycle oscillation. In: Proceedings of the structural dynamics and materials conference, Honolulu
4. Dimitriadis G, Li J (2009) Bifurcation behavior of airfoil undergoing stall flutter oscillations in low-speed wind tunnel. AIAA J 47(11): 2577–2596
5. Poirel D, Mendes F (2014) Experimental investigation of small amplitude self-sustained pitch-heave oscillations of a NACA0012 airfoil at transitional reynolds numbers. AIAA J 52(8):1581–1590
6. Mukhopadhvay V (1999) Transonic flutter suppression control law design using classical and optimal techniques with wind-tunnel results. In: Proceedings of structural dynamics and materials conference, St. Louis
7. O'Neil T, Gilliatt H, Strganac TW (1996) Investigations of aeroelastic response for a system with continuous structural nonlinearities. In: Proceedings of the structural dynamics and materials conference, Salt Lake
8. Silva WA, Strganac TW, HAjj MR (2005) Higher-order spectral analysis of a nonlinear pitch and plunge apparatus. AIAA 2005-2013 Proceedings of the 46th AIAA/ASME/ASCE/ASC Structures, Structural Dynamics, and Materials Conference, Austin, Texas, April 18-21

9. Dowell EH, Clack R, Cox D, Curtiss HC Jr, Edwards JW, Hall KC, Peters DA, Scanlan R, Simiu E, Sisto F, Strganac TW (2004) A Modern course in aeroelasticity. Kluwer Academic Publishers, Dordrecht
10. Abdelkefi A, Vasconcellos R, Nayfeh AH, Hajj MR (2012) An analytical and experimental investigation into limit-cycle oscillations of an aeroelastic system. Nonlinear Dyn 71(1–2):159–173
11. Conner MD, Tang DM, Dowell EH, Virgin LN (1997) Nonlinear behavior of a typical airfoil section with control surface freeplay: a numerical and experimental study. J Fluids Struct 11:89–109
12. Tang DM, Dowell EH (2011) Aeroelastic response induced by free play, Part 2: theoretical/experimental correlation analysis. AIAA J 49(11):2543–2554
13. Hancock GJ, Wright JR, Simpson A (1985) On the teaching of the principles of wing flexure-torsion flutter. Aeronaut J 89:285–305
14. Wright JR, Cooper JE (2007) Introduction to aircraft aeroelasticity and loads. Wiley, Chichester
15. Platten MF, Wright JR, Cooper JE, Dimitriadis G (2009) Identification of a nonlinear wing structure using an extender modal model. J Aircr 46(5):1614–1626